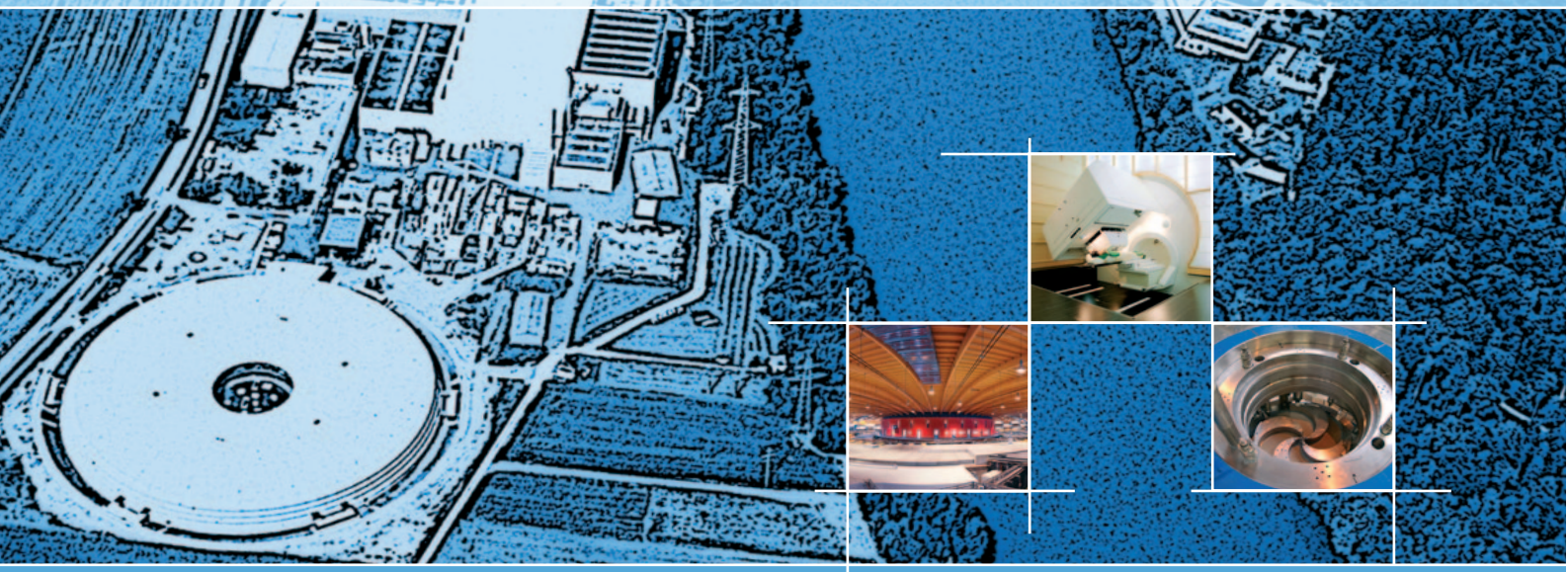
PAUL SCHERRER INSTITUT

PSI

DIPAC 2009

9th European Workshop on Beam Diagnostics and Instrumentation for Particle Accelerators



May 25 – 27, 2009

Basel, Switzerland

Hotel Mercure

Scope

The biannual DIPAC Workshop provides a unique forum for the exchange of information and experience regarding the latest developments in the field of beam diagnostics and instrumentation for particle accelerators worldwide. The program includes invited and contributed talks, poster sessions, discussion groups, an industrial exhibition and a tour of the accelerator facilities at PSI.

Deadlines

Abstract submission:	March 1, 2009
Early registration:	March 31, 2009
Regular registration:	May 8, 2009

Programme Committee

Volker Schlott (chair)
Peter Cameron
Bernd Dehning
Jean-Claude Denard
Mario Ferianis
Peter Forck
Eiji Kikutani
Alex Lumpkin
Andreas Peters
Uli Raich
Günther Rehm
Kees Scheidt
Hermann Schmickler
Mario Serio
Tom Shea
Kay Wittenburg

Local Organizing Committee

Volker Schlott (chair)
Marlen Bugmann
Jan Chrin
Micha Dehler
Goran Marinkovic
Patrick Pollet
Thomas Schilcher
Cécile Vock



http://dipac09.web.psi.ch/


art/Basel
RAMADA
PLAZA

Foreword

The 9th European Workshop on Beam Diagnostics and Instrumentation for Particle Accelerators (DIPAC) was held at Hotel Mercure in Basel, Switzerland, from May 25-27, 2009. It was a great pleasure for the Diagnostics Section of the Paul Scherrer Institute (PSI) to have organized this event and a privilege to have hosted an unprecedented 210 participants.

DIPAC 2009 provided a unique forum for both experts and novices to share their experience and to exchange information and opinions in the field of beam diagnostics. The conference centre at Hotel Mercure together with the comfortable ambience of the roof garden created a workshop atmosphere that fostered lively discussions regarding latest developments and new concepts in instrumentation at particle accelerator facilities worldwide, ranging from low energy gun and injector test facilities to high energy, high intensity hadron accelerators and colliders. Diagnostics and instrumentation issues at synchrotron radiation user facilities, accelerator-based cancer therapy centers and next generation LINAC-based single pass FELs were also been incorporated as an integral part of the DIPAC 2009 program.

The Scientific Program included ten invited talks, fourteen contributed orals and a record number of 115 poster contributions divided into three poster sessions. Oral sessions were followed by half-an-hour of questions and informal discussions, adding to the workshop atmosphere of DIPAC 2009. The Program Committee and the Workshop organizers would like to express their full appreciation for the high quality of oral and poster contributions, which were absolutely crucial for the overall success of this event.

A two-day industrial exhibition was arranged in the midst of the conference centre allowing participants to readily maintain their contacts to instrumentation companies and to remain informed of the latest developments and technological achievements.

The workshop banquet took place at the historic site of Schloss Bottmingen on the outskirts of Basel. Quite apart from the delightful ambience and the high gastronomical standard of Swiss cuisine, workshop participants were also able to appreciate the Swiss public transportation system by undertaking a *Tram* journey to and from the banquet venue.

A visit to Paul Scherrer Institute with guided tours of the synchrotron radiation facility Swiss Light Source (SLS) and the Proton Cancer Treatment Facility (PROCSAN) completed the workshop, providing a comprehensive overview of accelerator and instrumentation activities at PSI.

Finally, this Workshop would not have been possible without the tremendous efforts and support of many around me. I take this opportunity to express my sincere gratitude to members of the Programme Committee, the Local Organizing Committee, the Workshop Staff and the Editors of these Proceedings. Thank you to each and every one of you!



Volker Schlott, DIPAC 2009 Chair

Program Committee

Volker Schlott (Chair)	PSI
Peter Cameron	BNL
Bernd Dehning	CERN
Jean-Claude Denard	SOLEIL
Mario Ferianis	ELETTRA
Peter Forck	GSI
Eiji Kikutani	KEK
Alex Lumpkin	AAI/ANL and FNAL
Andreas Peters	HIT
Uli Raich	CERN
Gunter Rehm	DIAMOND
Kees Scheidt	ESRF
Hermann Schmickler	CERN
Mario Serio	INFN/LNF
Tom Shea	SNS/ORNL
Kay Wittenburg	DESY

Local Organizing Committee

Volker Schlott (Chair)	PSI
Marlen Bugmann	PSI
Jan Chrin	PSI
Micha Dehler	PSI
Goran Marinkovic	PSI
Patrick Pollet	PSI
Thomas Schilcher	PSI
Cecile Vock	PSI

Editorial Board

Jan Chrin	PSI
Michaela Marx	DESY
Volker R.W. Schaa	GSI
Volker Schlott	PSI

Contents

Foreword . . . iii
Committees . . . iv
Contents . . . v
Photo Gallery . . . viii
MOOA01 – Instrumentation Requirements for Different Accelerator Types . . . 1
MOOA02 – Performance of and First Experience with the LHC Beam Diagnostics . . . 6
MOOA03 – Beam Diagnostic System of XFEL/SPring-8 . . . 11
MOOB01 – Highlights from BIW'08 . . . 14
MOOB02 – Commissioning Results of Beam Diagnostics for the PETRA III Light Source . . . 19
MOOB03 – SSRF Beam Diagnostics System Commissioning . . . 24
MOOC01 – Global Fast Orbit Feedback System Down to DC using Fast and Slow Correctors . . . 27
MOOC02 – Digital BPM Systems for Hadron Accelerators . . . 32
MOOC03 – FEM Simulations - a Powerful Tool for BPM Design . . . 35
MOOC04 – Status of Beam Imaging Developments for the SNS Target . . . 38
MOPD01 – Non-Destructive Beam Position Measurement in a Proton Therapy Beam Line . . . 41
MOPD02 – Orthogonal Coupling in Cavity BPM with Slots . . . 44
MOPD04 – Alignment Monitors for an X Band Accelerating Structure . . . 47
MOPD05 – Installation and Commissioning of a Complete Upgrade of the BPM System for the ESRF Storage Ring . . . 50
MOPD06 – Design of Beam Position Monitors for the IFMIF-EVEDA accelerator . . . 53
MOPD07 – Development of the RF Cavity BPM of XFEL/SPring-8 . . . 56
MOPD08 – Bunch by Bunch Feedback System using iGp at KEK-PF . . . 59
MOPD09 – The Measurement of Beam Intensity using the LHC BPM System . . . 62
MOPD10 – Experimental Verification of Particle-in-Cell Simulation Results Concerning Capacitive Pickup Devices . . . 65
MOPD11 – Investigation of Precise Pipeline-Type ADCs in a Burst Regime for a Single-Shot BPM . . . 68
MOPD12 – Design of a Resonant Stripline Beam Position Pickup for the 250 MeV PSI XFEL Test Injector 71
MOPD13 – Implementation of an FPGA-Based Local Fast Orbit Feedback at the DELTA Storage Ring . . 74
MOPD14 – A Resonant First Turn BPM for the Positron Intensity Accumulator (PIA) at DESY . . . 77
MOPD16 – Comparative Studies of RF Beam Position Monitor Technologies for NSLS II . . . 80
MOPD17 – Performance of Exponential Coupler in the SPS with LHC Type Beam for Transverse Broadband Instability Analysis . . . 83
MOPD18 – Design of the Stripline Kickers for ALBA . . . 86
MOPD19 – High Resolution BPMs with Integrated Gain Correction System . . . 89
MOPD20 – BPM System Upgrades in the PETRA III Pre-Accelerator Chain during the 2008 Shutdown . . 92
MOPD21 – SNS Beam Diagnostics: Present Status and Future Plans . . . 95
MOPD23 – Emittance Measurement Devices in the Muon Ionization Cooling Experiment (MICE) . . . 98
MOPD24 – An Overview of the Proposed Beam Diagnostic for ASTRID2 . . . 101
MOPD25 – TheTransverse and Longitudinal Beam Characteristics of the PHIN Photo-Injector at CERN . 104
MOPD26 – Physics and Technical Design for the Second High Energy Dispersive Section at PITZ . . . 107
MOPD27 – SPIRAL2 Injector Diagnostics . . . 110
MOPD29 – First Beam Tests of the CLIC Power Extraction Structure with the Two-Beam Test Stand . . . 113
MOPD30 – Beam Diagnostics for SPIRAL2 RNB Facility . . . 116
MOPD31 – Beam Diagnostics in the CNAO Injection Lines commissioning . . . 119
MOPD32 – Beam Diagnostics at the ALBA Linac . . . 122
MOPD33 – Diagnostics Overview of the Taiwan Photon Source . . . 125
MOPD40 – BunchView - A Fast and Accurate Bunch-by-Bunch Current Monitor . . . 128
MOPD41 – Impact of Environmental Variability on Vibrating Wire Monitor Operation . . . 131
MOPD42 – ProfileView - A Data Acquisition System for Beam Induced Fluorescence Monitors . . . 134
MOPD43 – Implementation of the Electronics Chain for the Bunch by Bunch Intensity Measurement Devices for the LHC . . . 137
MOPD44 – Charge and Laser Beam Energy Monitor for Sparc LINAC . . . 140
MOPD45 – The DCCT for the LHC Beam Intensity Measurement . . . 143
TUOA01 – Sliced Beam Parameter Measurements . . . 146
TUOA02 – Optical Diffraction Radiation Interferometry as Electron Transverse Diagnostics . . . 151

TUOA03 – Electron Scanner for SNS Ring Profile Measurements . . . 155
TUOA04 – Electron Beam Diagnostics for the European XFEL . . . 158
TUPB02 – Beam Induced Fluoresence Monitor and Imaging Spectrography of Different Working Gases . 161
TUPB03 – The LHC Synchrotron-Light Monitors . . . 164
TUPB04 – High Current Ion Beam Investigations on Inorganic Scintillation Screens . . . 167
TUPB05 – Fast Wire Scanner Calibration System . . . 170
TUPB06 – Transverse Profile Monitors based on Fluorescence for IFMIF-EVEDA Accelerator . . . 173
TUPB07 – The Beam Profile Monitor for SPIRAL2 . . . 176
TUPB08 – Design of a Nozzle-Skimmer System for a Low Perturbation Ionization Beam Profile Monitor . 179
TUPB09 – Emittance Measurement using Undulator Radiation at the ESRF Storage Ring . . . 182
TUPB10 – Beam Profile Monitoring at COSY via Light Emitted by Residual Gas . . . 185
TUPB11 – Fast and High Accuracy Wire Scanner . . . 188
TUPB12 – Beam Test of the FAIR IPM Prototype in COSY . . . 191
TUPB13 – IR Photon Array Detector for Bunch by Bunch Transverse Beam Diagnostics . . . 194
TUPB14 – Diagnostics for High Power Ion Beams with Coherent Fiber for IFMIF-EVEDA Injector . . . 197
TUPB15 – Experience with YAG and OTR Screens at ALBA . . . 200
TUPB16 – A Compact Electron Photon Diagnostic Unit for a Seeded FEL . . . 203
TUPB18 – VIMOS, Beam Monitoring for SINQ . . . 206
TUPB20 – First Experience at SARAF with Proton Beams using the Rutherford Scattering Monitor . . . 208
TUPB21 – Detectors for Slowly Extracted Ions in HIRFL-CSR . . . 211
TUPB22 – Design Report of a Non-Destructive Emittance Instrument for RAL's Front End Test Stand FETS 213
TUPB23 – Measurement of Electron Cloud Density With Microwaves in the Fermilab Main Injector . . . 216
TUPB24 – Beam Halo Monitor using Diamond Detector for Interlock Sensor at XFEL/SPring-8 . . . 219
TUPB25 – The Design and Implementation of the Machine Protection System for the FERMILAB Electron Cooling Facility . . . 222
TUPB26 – A Concept to Improve the Availability of PETRA III by Correlation of Alarms, Timestamps and Post-Mortem-Analysis . . . 225
TUPB27 – Feasibility Study of an Optical Fibre Sensor for Beam Loss Detection Based on a SPAD Array 228
TUPB28 – Loss Monitor on Basis of Diffusive Radiation from Rough Surfaces . . . 231
TUPB29 – Beam Based Development of a Fiber Beam Loss Monitor for the SPring-8 X-FEL . . . 234
TUPB30 – Flexible Core Masking Technique for Beam Halo Measurements with High Dynamic Range . . 237
TUPB31 – Configuration and Validation of the LHC Beam Loss Monitoring System . . . 240
TUPB32 – Design Specifications for a Radiation Tolerant Beam Loss Measurement ASIC . . . 243
TUPB33 – Systematic Study of Acquisition Electronics with a High Dynamic Range for a Beam Loss Measurement System . . . 245
TUPB35 – Velocity of Signal Delay Changes in Fibre Optic Cables . . . 248
TUPB37 – Coherent Optical Transition Radiation as a Tool for Ultra-Short Electron Bunch Diagnostics . . 251
TUPB38 – Bunch Length Measurements at the Radiation Source ELBE . . . 254
TUPB40 – Time Resolved Spectrometry on the Test Beam Line at CTF3 . . . 257
TUPB41 – Investigation of Extremely Short Beam Longitudinal Measurement with a Streak Camera . . . 260
TUPB42 – A Compact Single Shot Electro-Optical Bunch Length Monitor for the SwissFEL . . . 263
TUPB43 – Towards an Ultra-Stable Reference Distribution for the New PSI 250 MeV Injector . . . 266
TUPB44 – On the Limitations of Longitudinal Phase Space Measurements using a Transverse Deflecting Structure . . . 269
TUPB46 – Temporal Profiles of the Coherent Transition Radiation Measured at FLASH with Electro-Optical Spectral Decoding . . . 272
TUOC01 – Beam Position Measurement with Sub-Micron Resolution . . . 275
TUOC02 – Cavity BPM Designs, Related Electronics and Measured Performances . . . 280
TUOC03 – LCLS Cavity Beam Position Monitors . . . 285
TUPD02 – Position Pickups for the Cryogenic Storage Ring . . . 288
TUPD03 – Experience with the Commissioning of the Libera Brilliance BPM Electronics at PETRA III . . 291
TUPD04 – Dual Beam X-ray Beam Position Monitor . . . 294
TUPD05 – Improvement of the Fast Orbit Correction on the ESRF Storage Ring . . . 297
TUPD06 – Optimisation Studies of a Resonant Capacitive Pick-Up for Beam Position Monitoring of Low Intensity, Low Velocity Antiproton Beams at FLAIR . . . 300
TUPD08 – An FPGA Based Data Acquisition System for a Fast Orbit Feedback at DELTA . . . 303

TUPD10 – Beam Tests with Libera in Single Pass Mode . . . 306
TUPD11 – The BPM Measurement System in HIRFL-CSR . . . 309
TUPD12 – BPM System and Fast Orbit Feedback Upgrade for the Taiwan Light Source . . . 312
TUPD13 – Photodiode-based X-ray Beam-Position Monitor with High-Spatial Resolution for the NSLS-II Beamlines . . . 315
TUPD14 – Characterization Tests of the Beam Position Monitor Series Production for the TBL line of the CTF3 at CERN . . . 318
TUPD15 – Particle Identification Devices in MICE . . . 321
TUPD16 – Baseband Tune Measurements at GSI SIs^{-1}8 using Direct Digitized BPM Signals . . . 324
TUPD17 – Phase and Amplitude Measurements for the SPIRAL2 Accelerator . . . 327
TUPD18 – Longitudinal Emittance Measurement Using Particle Detectors . . . 330
TUPD19 – Beam Profiling and Measurement at MIBL . . . 333
TUPD20 – Design and Operation of a Current Monitor under Heavy Heat Load . . . 336
TUPD21 – A “Not-Interceptive” Faraday Cup in the CNAO Low Energy Injection Lines . . . 339
TUPD22 – Beam Based Measurements of the RF Amplitude Stability at FLASH using a Synchrotron Radiation Monitor . . . 342
TUPD23 – Detectors for Absolute Luminosity Measurement at DAFNE . . . 345
TUPD24 – High Dynamic Range Spectral Analysis in the kHz Band . . . 348
TUPD25 – Machine Protection System for PETRA III . . . 351
TUPD26 – LHC BLM Single Channel Connectivity Test using the Standard Installation . . . 354
TUPD27 – Upgrade of the Timing System at the Australian Synchrotron . . . 357
TUPD29 – First Measurements of the Longitudinal Phase Space Distribution using the New High Energy Dispersive Section at PITZ . . . 360
TUPD30 – Measurement Devices for the SPARC Synchronization System . . . 363
TUPD31 – Ytterbium Fiber Laser for Electro-Optical Pulse Length Measurements at the SwissFEL . . . 366
TUPD32 – Ultra-Fast mm-Wave Detectors for Observation of Microbunching Instabilities in the Diamond Storage Ring . . . 369
TUPD33 – First Light for Optical Transition Radiation Monitor at the J-PARC . . . 372
TUPD34 – Beam Transverse Profile Monitor based on Residual Gas Ionization for IFMIF-EVEDA Accelerator 375
TUPD36 – Target Materials for a Low Energy Pepper-Pot Emittance Device . . . 378
TUPD37 – Synchrotron Radiation Monitor and Mirror at SSRF . . . 381
TUPD38 – Two-Dimensional Ionization Beam Profile Measurement . . . 384
TUPD39 – Investigation of the Light Yield of Luminescent Screens for High Energetic and High Brilliant Electron Beams . . . 387
TUPD40 – Carbon Fibre Damage in Accelerator Beam . . . 390
TUPD41 – Status of the Laser-Based Beam Profile Instrument for the RAL Front End Test Stand . . . 393
TUPD42 – Design of a New Emittance Meter for LINAC4 . . . 396
TUPD43 – Synchrotron Radiation Monitor for Bunch-Resolved Beam Energy Measurements at FLASH . 399
TUPD44 – High Energy Emittance Measurement at SPARC . . . 402
TUPD45 – Screen Monitor Design for the SwissFEL . . . 405
TUPD46 – Undulator Radiation Measurements at LCLS using K-edge X-Ray Absorption Techniques . . . 408
WEOA01 – Local Beam Loss and Beam Profile Monitoring with Optical Fibers . . . 411
WEOA02 – Intensity and Profile Measurement for Low Intensity Ion Beams in an Electrostatic Cryogenic Storage Ring . . . 418
WEOA03 – Data Acquisition and Error Analysis for Pepperpot Emittance Measurements . . . 421
WEOA04 – Beam Diagnostic Developments for FAIR . . . 424
WEOB01 – Beam Diagnostics and RF Systems Requirements for the SwissFEL Facility . . . 427
WEOB02 – Recent Results from the Optical Replica Synthesizer Experiment in FLASH . . . 430
WEOB03 – Physics Requirements for Linac Stabilizations and Technical Solutions . . . 433

Appendices **439**
List of Authors . . . 439
Institutes List . . . 447
Participants List . . . 455



Photo Gallery, Courtesy of Benedikt Oswald


In-flange.CT
In-flange.NPCT
Passion for Purity




for particle accelerators, synchr
beamlines and radio telescopes
Measurement Principle
Flux Concentrator
(Split Toroid)
GMR-Sensor
Amp
Test Setup

INSTRUMENTATION REQUIREMENTS FOR DIFFERENT ACCELERATOR TYPES

B.J. Holzer, CERN, Geneva, Switzerland

Abstract

At present more than 15000 particle accelerators exist worldwide, being built and optimised to handle a large variety of particle beams for basic research and applications in industry and medicine. Diagnostic tools have been developed and optimised according to the special requirements of these machines and to meet the demands of their users. Storage rings for ultra cooled heavy ion beams, third generation synchrotrons for the production of high brilliant radiation, super conducting protons machines working at the energy frontier and finally linear electron accelerators for FEL applications or high energy physics are just the most prominent representatives of the large variety of accelerators. Each of them needs highly sophisticated tools to measure and optimise the corresponding beam parameters. Accordingly the issue addressed here is not to cover in full detail the different diagnostic devices but rather to concentrate on the aspects and needs as seen by the accelerator physicists and machine designers.

GENERAL CONTEMPLATIONS

The considerations presented here try to give a general overview about the needs in beam diagnostics for quite different machines. Clear enough there are beam parameter "standards" as orbits, beam intensity and lifetime that have to be measured, controlled and displayed in any machine. But given the large variety of accelerators optimised for different purposes there are also quite special needs and beyond the standards we will mostly outline the requirements of these beam parameters that need highly sophisticated measurements devices.

The spectrum of up to date accelerators covers a wide range: Proton or heavy ion storage rings running at the energy frontier as HERA, TEVATRON, RHIC and clear enough the LHC, and on the other side the low energy proton or heavy ion machines that are optimised for medical therapy. Then clear enough there are the special requirements of the electron machines that are optimised for synchrotron light production - be it as 3rd generation light sources or as FEL linacs. And in the end the planned high energy linear colliders that are not yet in their construction phase but already now set requirements for beam stability and control that have not been reached yet. These examples represent the extremes at least concerning the diagnostic tools that had to be established and we hope that talking about these, the large variety of accelerators that exist today like betatrons, cyclotrons, proton linacs are automatically included.

HIGH ENERGY PROTON MACHINES

The most prominent one today is clearly the Large Hadron Collider LHC [1] at CERN whose main parameters are listed in Table 1.



Figure 1: The LHC storage ring at CERN, Geneva.

Beam Parameters: The Standards

As in any (circular) accelerator the standard beam parameters that have to be measured are first of all the orbit and the tune in the two transverse planes. The requirements here differ not too much from other proton of heavy ion machines: beam sizes in the order of a millimetre or a certain fraction of it, and the usual golden rule to measure and control the orbit on the level of a tenth of the transverse beam dimension does not impose strong conditions on the beam position monitor system.

Table 1: LHC Main Parameters

LHC	
proton energy	7 TeV
particles per bunch	$1.2*10^{11}$
number of bunches	2808
beam current	0.582 A
stored beam energy	362 MJ
beam size (arc)	1.2mm ... 0.3 mm
bunch length	8 cm

Figure 2 shows one of the very first LHC beam orbits that were obtained during the beam commissioning in 2008. Before correction, the proton orbit in LHC in both planes was in the order of 5-10 mm, still to high for intense beams and clearly beyond the level that is required for high energy operation. After a few correction cycles however the required level of 1-2 mm rms had already been obtained.

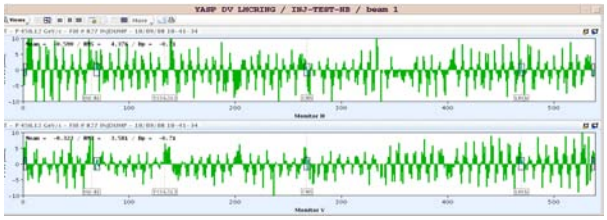


Figure 2: The very first beam steering in LHC.

An example for a tune signal in such a machine is shown in Fig. 3: It has been taken at the HERA collider [2] and shows the horizontal (left) and vertical (right) tune signal during luminosity operation: The tunes are set to their ideal values and - most important for these machines they are perfectly uncoupled.

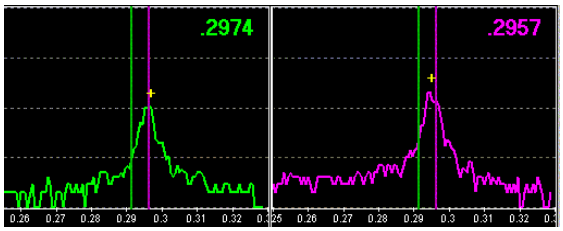


Figure 3: HERA tune measurement during luminosity operation.

More relevant than the bare measurement of the tunes in these high energy proton rings is the stability of the working point: The tunes have to be kept close to the design values during the complete machine cycles. Strong dynamic effects during the acceleration and decaying eddy currents during the injection and luminosity operation lead to intolerable drifts in the tune frequencies that have to be compensated [3]. A precise tune detection is needed that disentangles the two peaks even during operation close to the coupling resonance where these machines usually have to be operated. Unlike to electron machine however a strong beam excitation is excluded as it would destroy the beam quality. Therefore a very sensitive tune measurement is required combined with a sophisticated peak detection algorithm to control the tunes even at the coupling resonance. Figure 4 shows as an example the tune controller of the HERA proton ring: The trim quadrupoles used to control the working point are addressed bitwise allowing tune scans/control on a very precise manner and as demonstrated in the plot the diagnostics and control worked without problems even if the two tunes were interchanged during the operation [4].

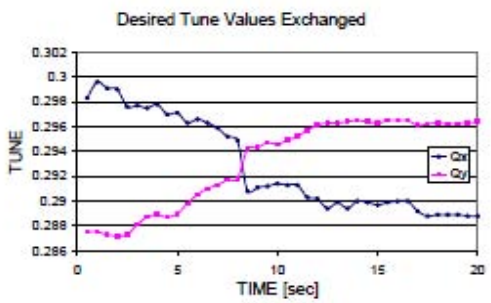


Figure 4: HERA tune controller: clear distinction of the working point even when crossing the tunes.

The Non-Standards

Beam quality in hadron machines is always a critical issue as scattering effects, instabilities and mismatch of orbit or optics during the beam transfer can easily lead to intolerable growth of the beam emittance and unlike to electron machines no damping effect due to synchrotron radiation can cure it. The emittance budget - especially during beam transfer - in these machines therefore is in general very tight: As an example we list in Table 2 the tolerances that are foreseen for the LHC pre-accelerator chain: Only small emittance growth is allowed and especially during the injection into the LHC the beam quality has to be guaranteed.

Table 2: Emittance Budget for the LHC Pre-accelerators

	E_k [GeV]	ε* [π μm]	σ [mm]
LINAC	0.0001 – 0.05	~1.0	
BOOSTER	0.05 – 1.4	2.5	0.3 – 6.5
PS	1.4 - 26	3.0	0.3 – 15
SPS	26 - 450	3.5	0.1 – 6
LHC	450 - 7000	3.7	0.1 - 2

To illustrate the problem, the effect of an offset Δa during beam injection is shown schematically in Fig. 5: Due to filamentation the original offset smears out in phase space and leads to emittance that is - as a rule of thumb - increased quadratically with the error [5].

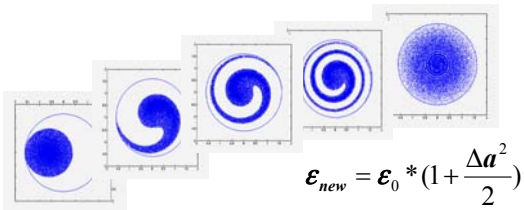


Figure 5: Schematical illustration of beam filamentation in phase space.

Similar effects exist for mismatched beam optics. To avoid these problems the beam position and angle as well as the optics mismatch have to be measured and eventually corrected. The well known keywords for the beam diagnostics in this context are (OTR)-screens, wire scanners and residual gas monitors.

In the case of LHC the beam energy is already high enough that even the synchrotron light emitted by the beam can be used as diagnostic tool [6]. The problem lies in the high energy and intensity of the stored beam. In LHC up to 2808 bunches are filled with 10^{11} protons each and carry an energy of up to 362 MJ. Diagnostics based on material interacting with the beam like wires or screens can not be applied anymore. Tests have been performed in the context of machine safety where a SPS beam of nominal energy (450 GeV) was dumped on a fixed target (Fig. 6).

Even at this relatively low energy severe damage occurs on any material that is hit directly by the beam.

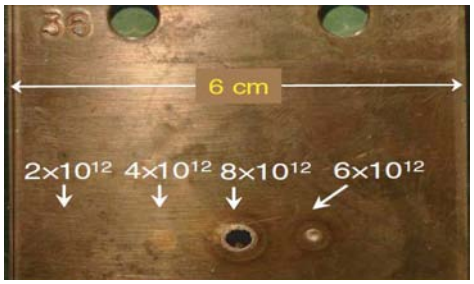


Figure 6: beam dump tests of a 450 GeV proton beam, being extracted from the SPS and dumped on a Cu target.

Wires or screens (Fig. 7) used so far in other machines, therefore are limited to very low beam intensities and the diagnostic tools foreseen in these cases are synchrotron light and residual gas monitors.

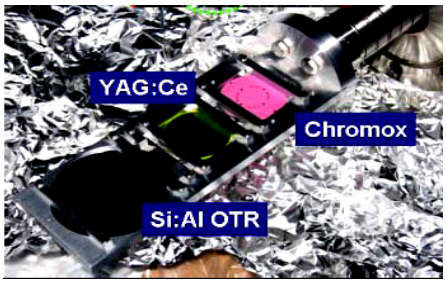


Figure 7: OTR and scintillating screens as diagnostic tools for low energy beams [7].

The strongest requirement for any high energy storage ring is related to the machine protection system: Given the LHC beam parameters any uncontrolled beam loss can easily lead to a quench of the super conducting magnets or even lead to severe damage of the storage ring components. Fig. 8 shows the result of an analysis that has been performed, studying magnet errors in the LHC and the resulting beam losses. In case of a severe magnet failure the damage level for machine components is reached already after 2 ms - corresponding to 25 turns in the machine.

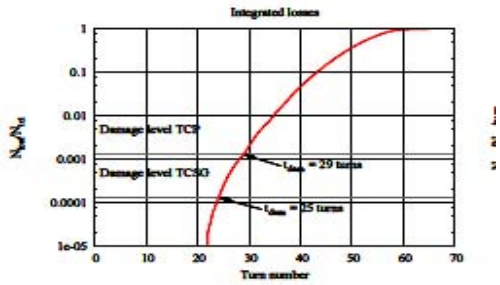


Figure 8: particle losses in LHC after a severe magnet failure: The damage level for machine components is reached already after 25 turns [8].

A very sensitive and at the same time fast beam loss monitoring system has to be established and completed by direct diagnostics of the hardware components [9]. At the same time fast beam current monitors are needed to detect beam losses on the level of $\Delta I/I = 10^{-6}$ on a turn by turn basis [10].

HADRON THERAPY MACHINES

Compared to the big super conducting storage rings discussed before, these machines are in a certain sense representing the other extreme. The typical beam energies of some MeV represent for the control and safety issues of the machine not really a problem. Typical beam parameters like several millimeter beam size and intensities of some 10^{10} particles per cycle neither set strong requirements for the beam diagnostics. The real challenge in this case lies in the control of the beam stability: Both concerning beam orbit and intensity the tolerances are tight and given by the medical application. These devices are driven typically by cyclotrons [11] or nowadays synchrotrons as e.g. in the case of the HIT project (Fig. 9) whose parameters are listed in Table 3:



Figure 9: Layout of the Hadron Therapy Complex HIT

In the case of synchrotron based concepts the beam extraction in general is performed by a typical slow extraction scheme where the beam is put close to the third integer resonance (schematically shown in Fig. 10) and a smooth rf excitation is applied to increase the emittance in a controlled way and to obtain a constant extraction intensity.

Table 3: Typical Parameters of a Hadron Therapy Machine

HIT project	
particles	p, C, He, O
beam energy	50-430 MeV/u
beam size	4-10 mm
extraction time	1-10 s
extraction intensity	10 6 - 4*10 10 ions/spill
beam power	360 W dc

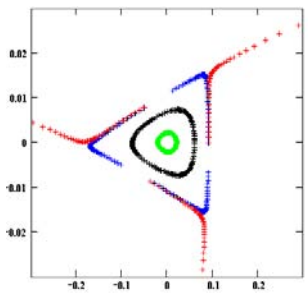


Figure 10: Schematical view in phase space of the slow extraction mechanism.

In the case of the HIT project the stored beam intensity of 10^{10} particles has to be extracted within a time span of typically ten seconds and the obtained intensity during this process should be constant on a level of 1 %. As a consequence the diagnostic elements have to measure beam currents in the order of fractions of nA in a non-destructive manner. The technique applied here in general is based on secondary emission monitors [12] and an example is shown in Fig. 11.

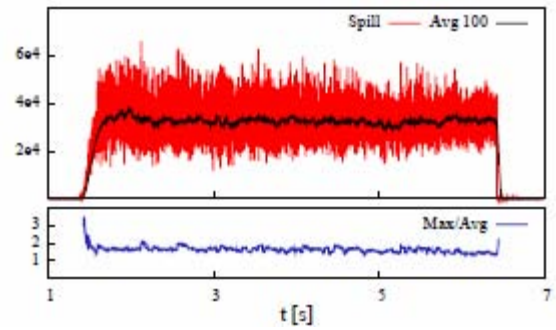


Figure 11: Measured particle flux during the slow extraction in HIT. The spill intensity corresponds to fractions of nA and has to be kept constant on a level of percent.

SYNCHROTRON LIGHT SOURCES

The modern 3rd generation synchrotron light sources represent for the case of electron accelerators again an extreme in beam quality and parameters and correspondingly in the requirements for the diagnostic tools. Here the standards like energy, tunes and beam intensity do not set severe restrictions to the diagnostic designers. The big challenge in this case is the measurement and control of the beam size and orbits. Both are closely related to the emittance and so of major importance for the brillance of the synchrotron light.

The brilliance of a synchrotron light source is given by

$$B = \frac{number\ of\ photons}{4\pi^2 \varepsilon_x \varepsilon_y * s * 0.1\% BW * A}$$

where BW indicates the bandwidth of the emitted light. Beside the beam intensity, the transverse emittances ε_x and ε_y are the main quality factor for these machines and usually these values are much smaller than those obtained in the high energy colliders as LEP or HERA-e. In Table 4 the beam energy and emittances are listed for a number of modern light sources. Values in the range of some nano meters are obtained.

Table 4: Energy and Emittance of Modern Light Sources

	ε_x (nmrad)	E (GeV)		ε_x (nmrad)	E (GeV)
PETRA 3	1	6	SLS	4.4	2.4
SPRING 8	3.4	8	ELETTRA	7	2.4
APS	3	7	BESSY 2	6	1.9
ESRF	3.9	6	SPEAR 3	18	3
DIAMOND	2.5	3	MAX 2	9	1.5
SOLEIL	3	2.5	ANKA	90	2.5

Again the golden rule for orbit stability and control is a required BPM resolution in the order of 10 % of the beam size. Referring now e.g. to the PETRA 3 light source [13] which is in the commissioning phase at present, we have to deal with beam sizes in the order of micro meters. 220 electrostatic beam position monitors (BPMs) are forseen in this storage ring that are supposed to measure the closed orbit with a resolution of 0.3 μm (rms). Beside this high quality BPMs the synchrotron light itself is clearly used as diagnostic tool in these machines. However again the requirements are extreme and the beam parameters demand state of the art techniques.

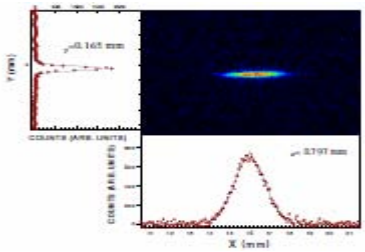


Figure 12: Synchrotron light image of the electron beam in the APS accumulator ring.

Applying Heisenberg's uncertainty principle to the synchrotron light diagnostics [14] we obtain an equation that relates the resolution for position measurements to the opening angle $\Delta\psi=1/\gamma$ of the light cone:

$$\Delta\sigma = \lambda * 2\Delta\psi$$

Assuming e.g. an electron beam of 1 GeV and a wavelength of the emitted light of λ = 500nm we obtain for the uncertainty of the position measurement $\Delta\sigma$ = 500 μm, by far not small enough to meet the requirements. Any position measurement in modern light sources therefore is principally limited by this diffraction effect. To overcome this problem interferometric techniques are applied and pinhole cameras [15].

SASE FELS

Referring to the measurement of "standard parameters" that we already discussed in the previous examples, for the FEL machines we are allowed to state that there are no standards. The beam parameters are pushed to new limits and completely new techniques are needed to diagnose them. As an example the European X-FEL project [16] under construction at present at the DESY institute is sketched in Fig. 13: The 3.4 km long device consists of several linear accelerator parts, 2 bunch compressors and finally a 250m long undulator section where the SASE process takes place.

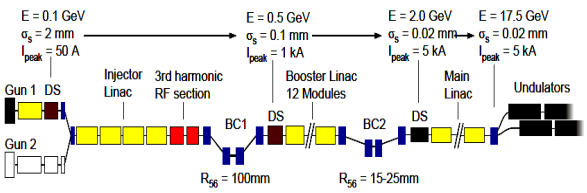


Figure 13: The European X_FEL project at DESY.

The parameters of this machine are listed below (Table 5); the special requirements marked in red. Again, according to the special parameters of the particle beam in these machines and the characteristics of the emitted light, dedicated measurement devices have to be developed: The SASE process is principally of statistical nature and so the properties of the single bunches have to be measured. Therefore any diagnostic tool has to be non destructive, based on single pass -single bunch signals and very fast to provide input for the control system within a bunch train.

Table 5: Parameters of the European X-FEL Project

Euro X-FEL	
light wave length	1Å
beam energy	20 GeV
normalised emittance	1.4 mm mrad
undulator length	250 m
beam pulse length	650 μs
number of bunches	3250
bunch spacing	250 ns
bunch length	70 fs
brilliance (photons/0.1%BWmm^{2}mrad^{2}s)	5*10 ^{33}
absolute emittance	4*10 $^{-11}$ m*rad

Especially the orbit stability within the undulator is of crucial importance as here the electron beam has to overlap with the light fan produced. A stability of the orbit in the order of 3 μm for the rms orbit is required inside the complete undulator length of 250 m. To achieve these constraints a so-called intra bunch feedback system is required that can measure the orbit of a single bunch within a conversion time of 200 ns, analyse the measurement and apply correction settings for the upstream bunches within the bunch train. Those requirements cannot be fulfilled by standard button pick up monitors. To achieve the high precision/ resolution and even more the fast response time required by the Intra Bunch Train Feedback System, new techniques had to be developed and the keywords here are resonant strip line BPMs and re-entrant cavity monitors. Beside the measurements of the beam orbit, the emittance of the bunches are of major importance for the SASE process. Being defined - much like in a proton machine - by the properties of the particle source the beam emittance has to be kept constant over the complete beam transport system and acceleration procedure. Even more it is the so-called slice emittance that determines the SASE process: During its path along the undulator the bunch interacts with the emitted light and micro bunches (slices) are formed that define the coherent emission. The measurement of these slice emittances requires time resolutions of smaller than pico seconds. In general it is based on transverse deflecting RF structures that shear the bunch e.g. into the vertical plane to project the horizontal versus longitudinal bunch profile onto a screen and a streak camera. Using this technique a time resolution of sub-pico seconds is achieved and the emittance of the micro bunches can be obtained. An example of such a measurement, obtained at FLASH is shown in Fig. 14. The length of the slices in this case corresponds to 30 femto seconds.

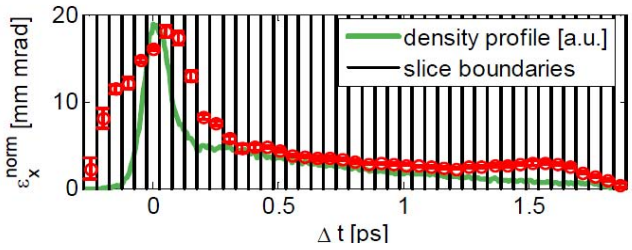


Figure 14: Slice emittance measurement at FLASH.

REFERENCES

[1] O. Brüning et al,"LHC Design Report", June 2004, CERN-2004-003.
[2] S. Herb, "Tune Measurement with Chirped Exci-tation in the Hera Proton Ring", EPAC'96, Sitges, June 1996, MOPCH31, p. 7984 (1996); http://www .JACoW.org.
[3] B. Holzer, "Impact of Persistent Currents on Accelerator Performance", Part. Acc. 1996, Vol 54, 55 and CERN-96-03, 1996.
[4] S. Brinker et al "A Tune feedback System for the HERA Proton Storage Ring", Edinburgh, June 2006.
[5] B. Goddard, "Injection and Extraction", Contr. to CERN Accelerator School, Frascati, Nov. 2008.
[6] R.Jones, "Performance of and First Experiences with the LHC Beam Diagnostics", this workshop.
[7] L. Badano et al, "The Beam Diagnostic System for the FERMI@ELETTRA Photon Injector" ,DIPAC 2007, Venice, Italy.
[8] A. Gomez, "Redundancy of the LHC Machine Protection System", Thesis at the Univ. Barcelona, to be published.
[9] M. Werner, M. Zerlauth, "A Fast Magnet Current Change Monitor for Machine Protection in HERA and the LHC", ICALEPS, Geneva 2005.
[10] M. Werner, K. Wittenburg, "Very fast beam losses at HERA and what has been done about it", ICFA Advanced Beam Dynamics Workshop, Tsukuba 2006.
[11] M. Jermann et al, "The PROSCAN Project" PSI Scientific and Technical Report 2003 / Volume VI.
[12] D. Ondreka, U. Weinrich, "The Heidelberg Ion Therapy (HIT) Accelerator Coming into Operation", EPAC'08, Genoa, June 2008.
[13] PETRA III Technical Design Report, DESY 2004.
[14] G. Kube, "Specific Diagnostic Needs for Different Machines", CERN Accelerator School, Dourdan, June 2008.
[15] G. Kube, "Review of Synchrotron Radiation Based Profile Measurments", DIPAC Venice, 2007.
[16] M. Altarelli et al, "The European X-Ray Free Electron Laser", Technical Design Report, DESY 2006-097.

PERFORMANCE OF AND FIRST EXPERIENCES WITH THE LHC BEAM DIAGNOSTICS

O. R. Jones*, CERN, Geneva, Switzerland

Abstract

During the 2008 LHC injection synchronisation tests and the subsequent days with circulating beam, the majority of the LHC beam instrumentation systems were capable of measuring their first beam parameters [1]. This included the two large, distributed, beam position and beam loss systems, as well as the scintillating and OTR screen systems, the fast and DC beam current transformer systems, the tune measurement system and the wire scanner system. The fast timing system was also extensively used to synchronise most of this instrumentation. This presentation will comment on the results to date, some of the issues observed and what remains to be done for the next LHC run.

THE LHC BTV SYSTEM

There are a total of 37 TV beam observation systems (BTV) of 7 different types installed in the LHC. Each BTV station is equipped with two screens; a 1mm thick alumina plate (scintillator) and a 12μm thick titanium foil to produce Optical Transition Radiation OTR. The alumina plates are very sensitive and can observe single bunches of well below 10^9 particles, but due to their thickness significantly perturb the beam. The number of photons emitted by the OTR is much less than that of the alumina screen, on the other hand the perturbation to the beam is minimal allowing multiple monitors to be used at the same time as well as multi-turn observation.

First Results from the LHC BTV System

During commissioning the beam was initially steered through the transfer lines and different sections of the machine using the alumina screens, producing very clear but completely saturated images (See Fig. 1).

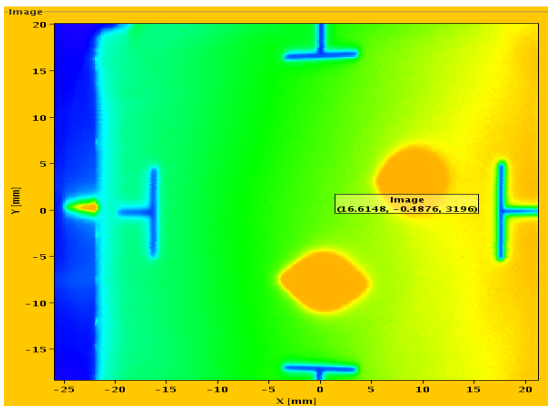


Figure 1 : The first full turn in the LHC as seen by the BTV system (10/9/2008).

*Rhodri.Jones@cern.ch

After this first step the OTR screens replaced the alumina screens as they reduced the blow-up of the beam, reduced the radiation due to beam losses and produced images well suited for analysis with good linearity and no saturation. The possibility of observing OTR emission for even the lowest intensity pilot bunches (2×10^9 protons) was due to the high sensitivity of the standard CCD cameras.

The BTV monitors performed well and were extensively used during all the synchronization tests and for the first circulating beam in the LHC. They provided a quick, reliable tool for the operators in this initial commissioning phase.

Outlook for the LHC BTV System

Due to the expected radiation levels in the injection regions a gradual replacement of the standard CCD cameras with less sensitive radiation hard cameras is foreseen. This will result in losing the possibility to observe single pilot bunches in OTR mode.

THE LHC BLM SYSTEM

The purpose of the LHC BLM system is threefold: to protect the LHC equipment from damage; to avoid beam induced magnet quenches; to observe losses for machine parameter tuning such as the adjustment of collimators. The protection requirements led to the placement of detectors at all likely loss locations, resulting in over 4000 installed monitors mainly around the quadrupole magnets and in the collimator regions. These are either 1.5 litre N_2 filled ionisation chambers or 10cm long Secondary Emission Monitors (SEM). The signals of almost all monitors are compared with pre-defined threshold values which, if exceeded, result in a retraction of the beam permit signal and consequently a beam dump. The BLM monitor acquisition systems for both half sectors served by a given access point are concentrated on the surface, with a redundant link to the beam interlock system transmitting the beam permit signal to the dump system.

Early Performance of the LHC BLM System

Fig. 2 shows the readings of all ionisation chambers around the ring during single turn operation with Beam 1. The bias level of the acquisition is given by the current injected into each channel to continuously test their status. A variation in this test current can be seen for the individual channels as a result of different settings in the front-end electronics. This will have to be better adjusted in all front-end cards before the next running period. The large reading left of IP1 is due to the dump of the beam on the TCT collimator.

The signal to noise level can be better assessed if this bias current level is subtracted, giving a noise level two



Figure 2 : BLM readings along the ring (logarithmic scale). In green the integrated signal from each ionisation chamber over the last 5.2 seconds updated every second. In red the corresponding threshold setting for each monitor.

orders of magnitude smaller than the signal from a pilot bunch of intensity 2×10^9 dumped on a tertiary collimator. This signal to noise level should be sufficient to use the loss patterns from a single pilot bunch of 5×10^9 to allow a subsequent safe, quenchless injection of a total intensity up to 5×10^{11}.

There were two beam induced triggers of the Quench Protection System (QPS) during the injection tests which allowed an attempt at quench reconstruction using the BLM system. The loss patterns observed were located near the centre of a bending magnet, in the dispersion suppressor right of IP2 and left of IP3. The impact angle was 250 µrad in one case and 730 µrad in the other. In both cases the area had sufficient BLM coverage to allow an attempt at reconstruction. Knowing the bunch intensity, impact location and loss distribution widths it was possible to constrain the simulations to give an estimate of the energy deposited in the coil. This was found to be ~15 mJ.cm^{-3} compared to the 30 mJ.cm^{-3} expected.

Outlook for the LHC BLM System

The incident in sector 3-4 implies that almost all BLMs in sector 3-4 will have to be dismantled. The subsequent consolidation required around the LHC means that in the other warmed sectors, at every other quadrupole magnet, some BLMs and cable trays have to be dismounted, while in the sectors remaining cold the new cable tray installation for the upgraded QPS will impact BLM installations. In addition to this unforeseen work, some consolidation was already planned to improve the system after the experience with first beam in the machine:

- Separation of the high voltage supply cables for the SEM and ionisation chambers. This aims to reduce the observed cross talk between the two systems.
- Implementation of a system to allow a full remote reset of the front-end electronics. This will involve the addition of a small mezzanine card to all front-end electronics cards.
- Noise check of the signal cable network. Any poor connections or cables will be repaired.

Some additional work is also foreseen on the BLM software, notably:

- The design of an application to allow the BLM threshold settings to be loaded and checked in the database.
- The test of a software package for handling machine critical settings along with the definition of procedures for manipulation of those settings.

THE LHC BPM SYSTEM

The LHC BPM system is comprised of 1054 beam position monitors, the majority of which (912) are 24mm button electrode BPMs located in all arc quadrupole cryostats (SSS). The remaining BPMs are enlarged (34mm or 40mm) button electrode BPMs mainly for the stand alone quadrupoles, or stripline electrode BPMs used either for their directivity in the common beam pipe regions or for their higher signal level in the large diameter vacuum chambers around the dump lines.

The beam position acquisition electronics is split into two parts, an auto-triggered, analogue, position to time normaliser [2] which sits in the tunnel and an integrator/digitiser/processor VME module located on the surface. Each BPM measures in both the horizontal and vertical plane, resulting in a total of 2156 electronic channels.

First Results from the LHC BPM System

The beam threading mode was used to provide the first turn position data to the operator GUI. This is a totally asynchronous acquisition mode, where any triggers obtained within a specified gate are stored, processed & published. From the very first shot into LHC the BPM system gave excellent results whilst operating in this mode. Combined with the powerful on-line optics software available it allowed quick diagnostics to be made on BPM polarity and machine optics errors.

Test of the Intensity Limit for the BPM System

The LHC BPM system can work in one of two sensitivity ranges – high or low. The threshold for the sensitivity change is conceived such that any reflections at the level of -20dB do not retrigger the system. In the high sensitivity setting the BPM system was foreseen to work correctly with bunch intensities in the range 2×10^9 to 2×10^{10} protons, with the low sensitivity working from 2×10^{10} to 2×10^{11} protons. In order to test the lower limit for auto-trigger detection the bunch intensity was varied from below 1×10^9 to around 3×10^9, while counting the number of correctly triggered BPMs in the arc of Sector 2-3. Fig. 3 shows the results obtained, along with the predicted performance of a typical electronics channel measured in the laboratory. The lower limit for correct BPM functioning can therefore be stated as being 1.5×10^9 protons per bunch.

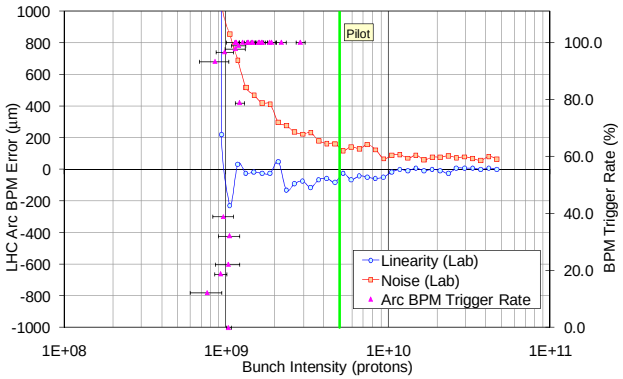


Figure 3 : BPM auto-trigger threshold determination – HIGH sensitivity mode (10/8/2008).

Early Performance of the LHC BPM System

The performance of the LHC BPM system has been characterised for very low intensity, single bunch operation both in trajectory and orbit mode. From the trajectory analysis of 31 injections during the synchronisation tests for Beam 1 the overall rms variation in position over a timescale of some ten minutes was generally seen to be between 150-400µm. This order of magnitude is consistent with the electronic noise estimations shown in Fig. 3 for bunch intensities in the range 2×10^9 to 5×10^9 protons.

Once the beam started to circulate for more than 1 second, the asynchronous orbit acquisition of the BPM system (IIR mode) could be used. This provides an update of the average orbit over the last few thousand bunch positions every second. The data for this mode is routed via the orbit feedback controller, which republishes it to external clients. This allowed much of the acquisition module of the orbit feedback system to be tested and debugged with real data. The operator GUI was capable of retrieving and displaying this data, providing a continuous update of the orbit at 1Hz.

Fig. 4 shows the results of some 15 minutes worth of horizontal orbit data, with similar results obtained in the vertical plane. It can be seen that the rms noise on the measurement for the majority of the machine is between 5µm and 15µm. The alternating high/low noise peaks follow the beta function (with 45° BPM sampling), indicating that a large fraction of this noise results from the beam itself, induced by the known corrector dipole power converter current ripple. The resolution of the BPM system in orbit mode with a single pilot bunch is therefore better than ~5µm.

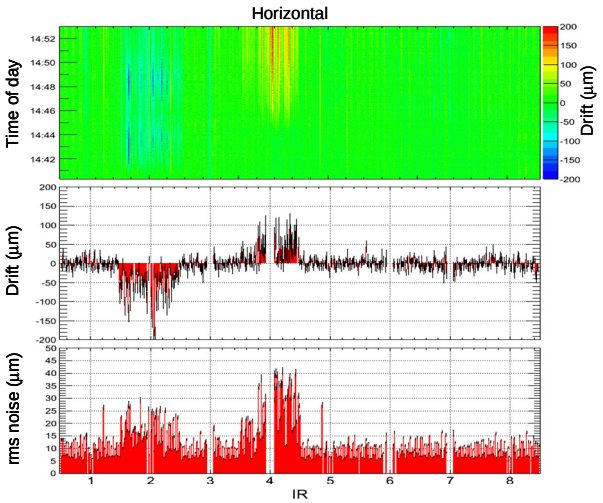


Figure 4 : Orbit stability – HIGH sensitivity mode (12/9/2008).

An oscillation of the position in Point 2 and a drift of the position in Point 4 are also clearly visible. These variations were traced to changes in the air temperature of the surface electronics racks in these locations and may be unacceptable for nominal LHC operation. Investigations are therefore underway to try to eliminate this problem.

Outlook for the LHC BPM System

The main consequences of the Sector 3-4 incident are:

- The dismounting, test and re-installation of the BPMs and electronics in the damaged area.
- The test of all BPM electrodes in-situ for contamination after cleaning.
- The addition of spring clamps on the BPM ports for all sectors remaining cold, which implies the disconnection & re-connection of over 2000 external BPM cables.

Due to these interventions, over half of the machine will have to be re-commissioned. A BPM intensity card [3] will also be installed throughout the machine to allow each BPM to give intensity information.

THE LHC TUNE, CHROMATICITY AND COUPLING MEASUREMENT SYSTEMS

The LHC base-line tune, chromaticity and coupling measurement system consists of three independent acquisition chains per beam and relies on the diode-based, base-band-tune (BBQ) technique developed for the LHC

and now also used in all CERN synchrotrons. The layout of these systems is described in detail in [4].

Of the three systems per beam, the first is dedicated to passive beam spectra observation and ensures a continuous data logging for post-mortem analysis, passive beam quality monitoring and fixed displays in the control room. This passive system observes any residual beam oscillations or externally produced beam excitation.

The second system is intended for 'on-demand' tune measurement, with excitation provided using dedicated tune kickers or fast frequency sweeps ('chirp' signals) via the LHC transverse damper.

The third system is dedicated to Phase Locked Loop (PLL) tune operation, again using the transverse damper as excitation source.

While the PLL hardware has been commissioned, the limited time did not permit a PLL setup with beam. Excitation via the tune kickers was also not attempted.

First Results from the LHC Q, Q' & |C| Systems

An extensive report on all the initial results from these systems can be found in [5]. Fig. 5 shows the tune spectra and corresponding turn-by-turn data before and after correction of the horizontal tune for beam 2, which was initially close to the half-integer resonance. The shift in the horizontal tune and increased number of detected turns (i.e. lifetime) after the tune trim are clearly visible. The availability of this system at a very early stage, capable of tune measurement with a limited number of turns, provided a means to quickly adjust the injection tunes. This allowed the beam to circulate long enough to attempt the first RF beam capture.

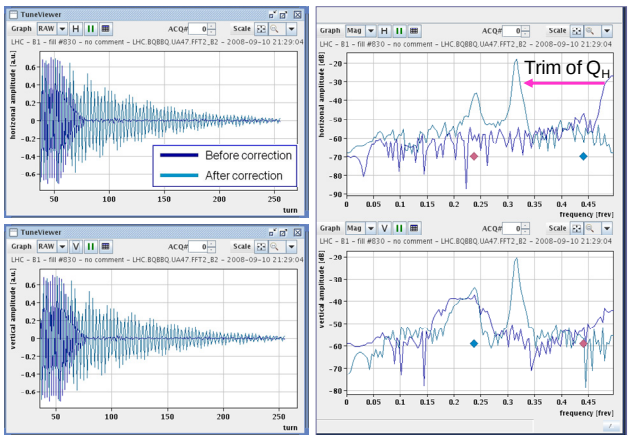


Figure 5 : First measurement and correction of tune using the LHC BBQ system.

This system was also used in conjunction with chirp excitation via the transverse damper giving a first estimate for coupling in the LHC, which was found to be $|C| \approx 0.07$.

Outlook for the LHC Q, Q' & |C| Systems

The next step required to fully commission the LHC tune, chromaticity and coupling systems will be to turn on and optimise the PLL tune systems. This will allow chromaticity measurement via RF modulation and also the first attempts at tune, coupling and chromaticity feedback.

The other special transverse and longitudinal monitors, namely the head-tail/instability monitors, the wall current monitors and the Schottky monitors remain to be fully commissioned.

THE LHC BCT SYSTEM

Beam current transformers of two different kinds provide intensity measurements for the beams circulating in the LHC rings, as well as for the transfer lines from the SPS to LHC and from LHC to the dumps.

The LHC BCTDC Systems

The DC current transformers (BCTDC) measure the mean current of the circulating beam. Because of their operational importance, two independent systems are installed per ring. Four ranges, provided simultaneously, are used to cover the entire beam dynamic range from a few 10^9 to 5×10^{14} protons (~3µA to ~900mA) [6].

First Results from the LHC BCTDC System

The main application used to view the BCTDC acquisition was a fixed display which was refreshed once per second. Fig. 6 shows such an acquisition for Beam 2 on September 12th 2008, with 4 successive injections of a single pilot bunch ranging in intensity from 3.5×10^9 to 6×10^9 protons and circulation times of 100 seconds to 40 minutes. The BCTDC used for this measurement was the operational system (A) while the spare (B) was kept for test and development. The automatic range selection was set to the highest sensitivity with a full scale of 5×10^{11} protons.

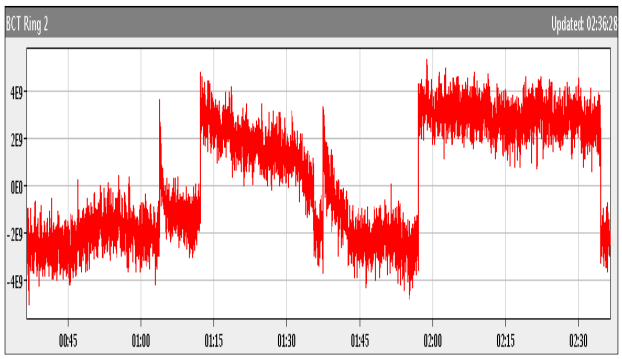


Figure 6 : First circulating beam in ring 2 seen by BCTDC A (12/9/2008).

The noise on the signal corresponds to an rms of 7×10^8 protons for a one second integration time, which is equivalent to 1.3µA. A similar value is found for the slow fluctuations observed over several hours. This result is very good and meets expectations, although it is also a reminder that the BCTDC can only measure single pilot bunches with a limited accuracy of around 20%. A small,

negative offset of ~2.5×10^9 (4.5µA) was also observed and will be automatically corrected for in the future.

The LHC Fast BCT (BCTFR/BCTFD) Systems

The LHC fast BCT systems are capable of measuring bunch to bunch intensity on a turn by turn basis [7]. Four such systems are installed in the LHC ring – one operational system and a hot spare for each beam. Each system has two parallel measurement bandwidths acquiring simultaneously with two different gains. Similarly two systems per beam are installed in the LHC dump lines. The dump line fast BCTs do not measure bunch to bunch, but give only the total intensity.

First Results from the BCTFR System

During the early injection tests where the beam passed through LSS4R, and in the subsequent commissioning with circulating beam the fast BCT was used in capture mode, triggered by the RF pre-injection pulse, to observe the LHC pilot bunch with intensities ranging from 2×10^9 to 6×10^9 protons.

This short time with beam in the LHC was very useful to verify the correct functioning of the complete acquisition chain from detector to the operator GUI. There are still numerous things to be addressed before the full functionality of the system is reached, including commissioning of the lifetime algorithm and items related to the machine-protection system such as safe beam flag transmission and fast beam current decay monitoring. The detectors and acquisition chains of the fast BCTs in the dump line still remain to be commissioned.

THE LHC WIRESCANNER SYSTEMS

A total of 8 linear wire scanners are installed in the LHC for measuring the transverse density profile of the beam. Each beam is equipped with 2 wire scanners in both horizontal and vertical planes, with one available for operation and the other intended as a fully functional back-up. The scanning speed of these systems is 1 ms^{-1}.

First Results from the BWS System

Only beams with very low intensity were available for testing the LHC wirescanners (2×10^9 to 6×10^9 protons circulating at 450 GeV). The first profiles were obtained with the electronics working in turn by turn mode, which does not distinguish between individual bunches. Due to the low intensity the measured profiles are quite noisy, but still well defined. Shown in Fig. 7 is the vertical profile acquired for Beam 2.

Outlook for the LHC Wirescanner System

It is intended to implement the individual bunch acquisition mode ready for use during the next LHC run. This will use the standard BI Digital Acquisition Board (DAB64x) fitted with the 40MHz integrator mezzanine cards of the fast BCT system. In this mode a profile can be produced for one or several arbitrarily selected bunches.

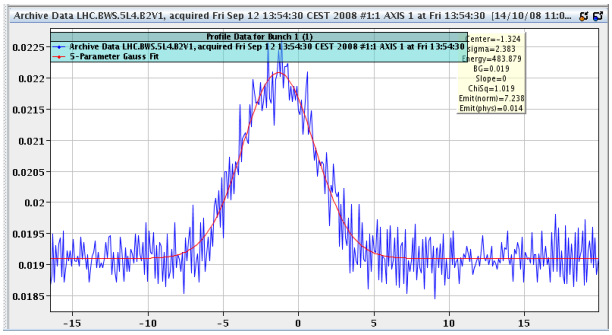


Figure 7 : Vertical wire scan on a single circulating pilot bunch (12/9/2008).

SUMMARY

The first few days of LHC running proved to be a very successful time for all the Beam Instrumentation systems. This was in no small part thanks to the years of planning, installation, testing and hardware commissioning carried out by all members of the BI Group with the help of many other Groups & external collaborators.

There is still a lot of work remaining to be done, however. A near complete re-commissioning of the BPM and BLM systems will be required after major interventions both in sector 3-4, and in the other sectors being consolidated as a result of the sector 3-4 incident. There are significant improvements being made to the synchrotron light monitor optical layout after the initial installation experience and it is also foreseen to install the three remaining US-LARP collision rate monitors (fast ionisation chambers) for the high luminosity interaction regions.

REFERENCES

[1] R. Jones, “First Results from the LHC Beam Instrumentation Systems”, LHC-Performance-Note-006 (2009).

[2] D. Cocq, “The Wide Band Normaliser : a New Circuit to Measure Transverse Bunch Position in Accelerators and Colliders”, Nucl. Instrum. Methods Phys. Res., A 416, 1998.

[3] J. Gonzalez et al., “Measurement of Beam Intensity using the LHC BPM System”, these proceedings, DIPAC09 (2009).

[4] M. Gasior et al., "An Overview of the LHC Transverse Diagnostics Systems", CERN-LHC-PROJECT-Report-1166 (2008).

[5] R. J. Steinhagen et al., “First Results from the LHC BBQ Tune and Chromaticity Systems”, LHC-Performance-Note-007 (2009).

[6] P. Odier et al., “The DCCT for the LHC Beam Intensity Measurement”, these proceedings, DIPAC09 (2009).

[7] D. Belohrad et al., “Implementation of the Electronics Chain for the Bunch by Bunch Intensity Measurement Devices for the LHC”, these proceedings, DIPAC09 (2009).

BEAM DIAGNOSTIC SYSTEM OF XFEL/SPring-8

H. Maesaka#, S. Inoue, T. Ohshima, S. Matsubara, A. Higashiya, M. Yabashi, T. Shintake and Y. Otake,
RIKEN/SPring-8, 1-1-1, Kouto, Sayo, Hyogo, 679-5148, Japan
H. Ego, K. Yanagida and H. Tomizawa, JASRI/SPring-8, 1-1-1, Kouto, Sayo, Hyogo, 679-5198, Japan

Abstract

We present the design and the performance of the beam diagnostic system of XFEL/SPring-8. The XFEL facility requires sub-μm resolution beam position monitors (BPM), screen monitors with less than 10 μm resolution, high-speed beam-charge monitors and a temporal structure measurement system with less than 10 fs resolution. We developed an rf cavity BPM system that uses the TM110 mode at 4760 MHz. The estimated position resolution was 0.2 μm. For the screen monitor, we designed a custom lens system having 2.5 μm resolution and variable magnifications from 1 to 4. For the charge measurement, we developed a high-speed differential current transformer (CT). The rise time of the CT signal was 0.2 ns and common-mode noise was considerably reduced. To measure the temporal beam structure, we developed a C-band (5712 MHz) transverse deflecting cavity that has a disk-loaded backward traveling wave structure. This cavity can resolve a beam into a few fs fragments. Thus, the beam-diagnostic system satisfies the demands of the XFEL accelerator.

INTRODUCTION

An x-ray fre-electron laser facility at SPring-8 (XFEL/SPring-8) [1] is under construction to generate coherent and extremely intense x-rays, where various new applications are expected in life sciences, material sciences, etc. The target wavelength is less than 0.1 nm. The XFEL light is generated by a self-amplified spontaneous emission (SASE) process.

A schematic layout of the XFEL facility is illustrated in Fig. 1. An electron beam with a normalized emittance of 0.6 π mm mrad is generated by a thermionic electron gun. The beam is accelerated to 8 GeV by the following series of rf accelerator cavities: 238 MHz pre-buncher, 476 MHz booster, L-band (1428 MHz), S-band (2856 MHz) and C-band (5712 MHz) accelerators. In the mean time, the bunch length is shortened from 1 ns to 30 fs by using a velocity bunching process of the sub-harmonic acceleration cavities and a bunch compression process of the three magnetic chicanes. Finally, the peak current becomes 3 kA without substantial emittance growth. The electron beam is finally fed into in-vacuum undulators, and an XFEL light is generated. The undulator period is 18 mm and the maximum K-value is 2.2.

In order to maintain the high gain SASE process at an x-ray wavelength, we need to monitor the beam position, the transverse beam profile, the beam charge, the beam arrival timing and the temporal bunch structure at each acceleration stage. The resolution of the beam-position monitor in the undulator section is required to be less than 0.5 μm so as to maintain an overlap between the electron beam and radiated x-rays with 4 μm precision. The transverse beam profile should be measured with a spatial resolution of less than 10 μm. The required resolution of the temporal bunch structure is less than 10 fs.

In this paper, firstly we show an overview of the beam diagnostic system, and then we describe the design and the performance of each diagnostic device.

#maesaka@spring8.or.jp

OVERVIEW OF THE BEAM DIAGNOSTIC SYSTEM

The diagnostic system of XFEL/SPring-8 [2,3] consists of high-resolution rf cavity beam position monitors (RF-BPM), precise screen monitors (SCM), high-speed differential current transformers (CT) and a transverse rf deflector system. The quantities of these monitors are summarized in Table 1, and are shown in Fig. 1. A detailed description of each monitor is given in the next section.

Table 1: Summary of the Number of Beam Monitors

	Number of Monitors
RF cavity BPM	56
Screen Monitor	43
Current Transformer	30
Transverse RF Deflector	1

DESIGN AND PERFORMANCE OF EACH DIAGNOSTIC DEVICE

RF Cavity BPM

Since the details of the RF-BPM are reported in Ref. [4], we summarize the performance of the RF-BPM. The RF-BPM cavity consists of two cylindrical cavity resonators: a TM110 dipole resonator for the position detection and a TM010 monopole resonator for the phase reference and the bunch charge measurement. We designed an RF-BPM cavity with a resonant frequency of 4760 MHz and a detection electronics equipped with an IQ (In-phase and Quadrature) demodulator. We tested the RF-BPM system in the SCSS test accelerator [5] with a 250 MeV electron beam and a 0.3 nC bunch charge. The position resolution was 0.2 μm and the beam arrival timing resolution of the TM010 cavity was 25 fs.

Screen Monitor

The transverse beam profile is monitored by a SCM. We use a fluorescent screen, such as Ce:YAG for a low-

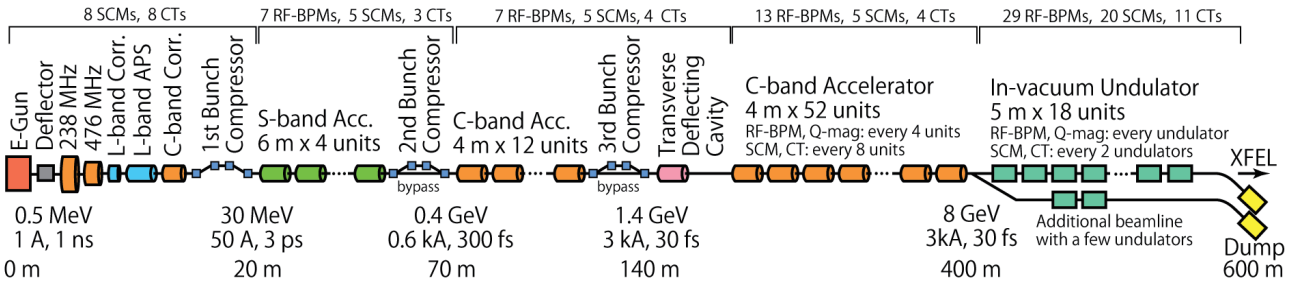


Figure 1: Schematic layout of the XFEL facility. The number of monitors for each section is also shown.

energy beam (less than 100 MeV) and an optical transition radiation (OTR) screen for a high-energy beam.

To achieve the required spatial resolution of less than 10 μm, we newly designed an imaging system [6] comprising a custom lens system and a motorized zoom mechanism from 1x to 4x. Figure 2 shows a photograph of the imaging system. The OTR light from the screen passes through the lens, and forms an image on the CCD camera. The lens and the camera are mounted on motorized stages so that both the magnification and the focus can be adjusted remotely. The optical resolution was 2.5 μm from a measurement of a grid distortion target.

We prepared a thin stainless-steel screen (0.1mm-thick) for an OTR radiator, as shown in Fig. 3, to reduce the radiation damage to other components due to the beam divergence. The central elliptical part is the 0.1mm-thick radiator and it is supported by a 1mm-thick frame. This screen is a stack of ten 0.1mm-thick foils processed by a photo-etching technique, and these foils are unified by a diffusion bonding method. The surface roughness of the screen is several 10 nm and the flatness is 3 μm.

The SCM system was installed into the SCSS test accelerator and tested with an electron beam. Figure 4 (A) shows an OTR image of an electron beam horizontally squeezed by Q-magnets. The horizontal width of this image was evaluated to be 13 μm (standard deviation), which is consistent with the natural divergence due to the beam emittance. Almost the same image as OTR was observed with a Ce:YAG screen, as shown in Fig. 4 (B).

Current Transformer

The main purposes of the CT are beam charge measurements to monitor the appropriate beam transportation and the beam arrival timing measurement to adjust the timing of accelerator components. In the SCSS test accelerator, some commercial CTs are used for these purposes. However, we found that the CT signal was influenced from substantial noise coming from the thyratron of a klystron power source. Therefore, we developed a high-speed differential CT [7] so as to reduce the noise and to improve the temporal response.

A schematic view of the differential CT is shown in Fig. 5. The CT has four outputs: two are positive and the others are negative. By subtracting a negative signal from a positive one, we can remove any common-mode noise. Since the pickup coil is of single turn, the rise time of the output pulse is expected to be small. The beam-position

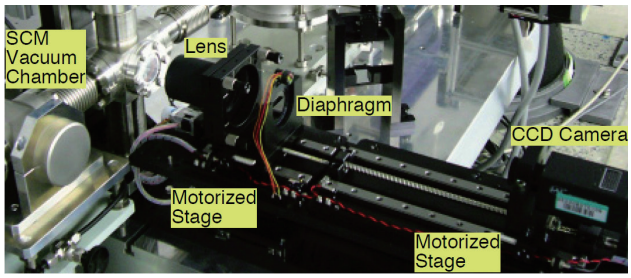


Figure 2: Photograph of the screen monitor.



Figure 3: Thin stainless steel OTR screen.

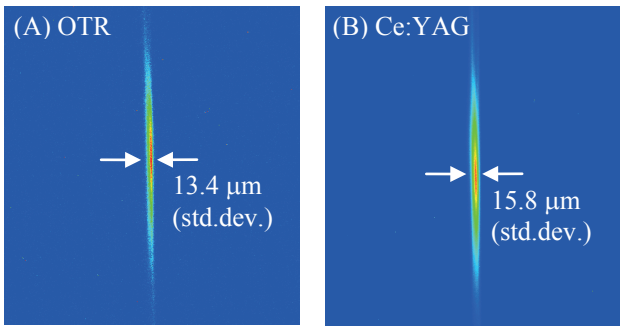


Figure 4: Beam images taken by (A) an OTR screen and (B) a Ce:YAG screen. The magnification of the lens is 4. The horizontal beam size is minimized by Q-magnets.

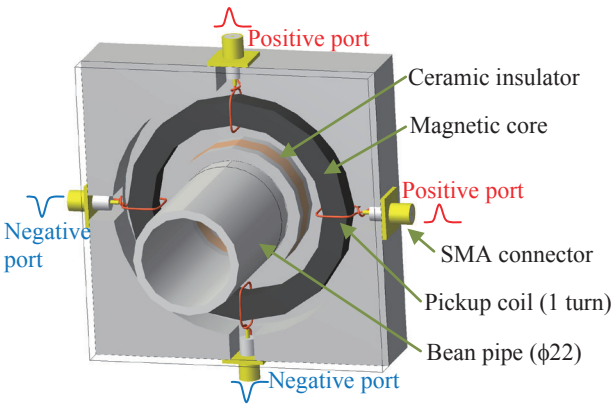


Figure 5: Schematic view of the differential CT.

dependence is eliminated by averaging the signals from all four ports.

We tested the differential CT in the SCSS test accelerator. Some waveforms of the signals are plotted in Fig. 6. A sharp pulse signal was obtained, and the rise time was 0.2 ns. External common-mode noise was reduced to 1/10. Thus, the design performance of the differential CT was confirmed.

Transverse RF Deflecting Cavity

We use a transverse rf deflecting cavity (RFDEF) to measure temporal bunch structures of an electron beam, such as the slice emittance and the energy-vs.-time distribution. An electron beam is swept by transverse deflecting rf fields and the temporal profile is converted to a transverse distribution. When we set the center of the bunch to rf phase of zero-crossing, we can linearly stretch the temporal structure.

An RFDEF cavity, named RAIDEN [8], was newly designed as illustrated in Fig. 7. The structure of RAIDEN is a periodically disk-loaded waveguide that has race-track-shaped irises to separate horizontal and vertical modes. The resonant frequency is selected to be the C-band (5712 MHz) so as to fully utilize the C-band accelerator resource and to obtain a higher deflecting voltage. The resonating mode is the HEM11-5π/6 mode of backward travelling-wave type. The basic performance of the RAIDEN cavity was confirmed by a low-level rf measurement of a 7-cell model.

The RFDEF system will be installed downstream of the third bunch compressor. We use two 1.7m-long RAIDEN tubes powered by a 50 MW klystron and generate a deflecting voltage of 40 MV at the crest phase. The 1.4 GeV electron beam can be resolved with a few fs precision by the RFDEF. The transverse distribution of the stretched beam is recorded by the above-mentioned SCM after a 5 m drift space. Although we have the RFDEF at the third bunch compressor only, we can measure the temporal structure at the first and second bunch compressors by using bypass lines of second and third bunch compressors.

SUMMARY AND PROSPECTS

We developed an rf cavity BPM, a screen monitor, a current transformer and a transverse rf deflector for XFEL/SPring-8. The position resolution of the RF-BPM system was 0.2 μm. The optical resolution of the OTR screen monitor was 2.5 μm. The rise time of the CT output pulse was 0.2 ns and common-mode noise was eliminated. The performance of a C-band RAIDEN cavity for the transverse rf deflector system was confirmed by a low-level rf measurement. Thus, the performance of the developed beam-diagnostic system is sufficient to monitor the electron beam of the XFEL facility.

The design work of the beam diagnostic system is almost complete, and mass-production has just started. Installation of accelerator components will start from July 2009. The first XFEL light will be generated in 2011.

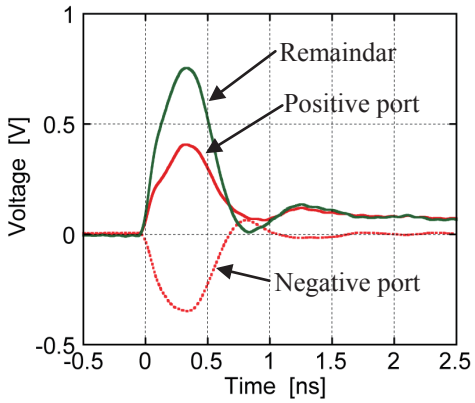


Figure 6: Waveforms of the differential CT.

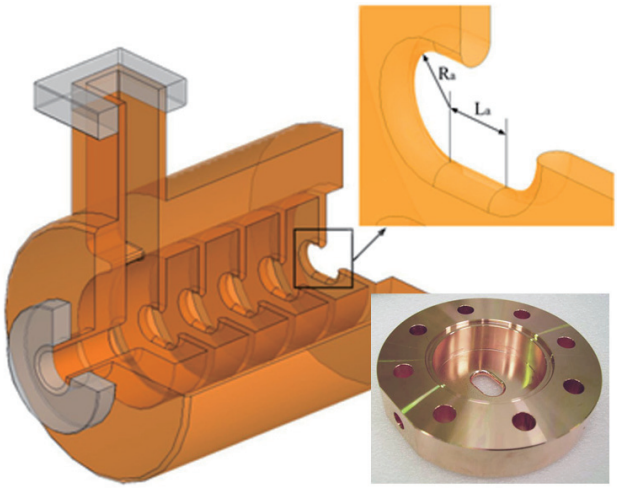


Figure 7: Schematic drawing of the C-band RAIDEN cavity. A photograph of a cell piece is also shown.

REFERENCES

[1] T. Shintake *et al.*, "Status of X-ray FEL / SPring-8 Machine Construction", Proc. of EPAC'08, (2008).

[2] Y. Otake *et al.*, "Development Status of a Beam Diagnostic System with a Spatial Resolution of Ten Micron Meters for XFEL", Proc. of EPAC'08 (2008).

[3] Y. Otake *et al.*, "Development Status of Beam Monitor System at XFEL/SPring-8", Proc. of PAC'09 (2009).

[4] H. Maesaka *et al.*, "Development of the RF Cavity BPM of XFEL/SPring-8", in these proceedings.

[5] H. Tanaka *et al.*, "Operation Status of the SCSS Test Accelerator", Proc. of EPAC'08 (2008).

[6] K. Yanagida *et al.*, "Development of Screen Monitor with a Spatial Resolution of Ten Micro-meters for XFEL/SPring-8", Proc. of LINAC'08 (2008).

[7] A. Higashiya *et al.*, "Development of a Beam Current Transformer for the X-FEL Project in SPring-8", Proc. of FEL'07 (2007).

[8] H. Ego *et al.*, "Design of the Transverse C-band Deflecting Structure for Measurement of Bunch Length in X-FEL", Proc. of EPAC'08 (2008).

HIGHLIGHTS FROM BIW08

F. Sannibale, Lawrence Berkeley National Laboratory, Berkeley, CA 94720, U.S.A.

Abstract

The 13th edition of the Beam Instrumentation Workshop (BIW08) took place at the Granlibakken Conference Center on the beautiful shores of Lake Tahoe in California during the first week of May 2008. About 130 participants registered for the workshop. Included in the program during the three and a half days were three tutorials, eight invited and seven contributed oral presentations, and more than 50 poster contributions. A discussion group session and the vendor exhibition simultaneously held with the single day poster session, afforded many opportunities for informal discussion and idea exchange between attendees. During the workshop, the 2008 Faraday Cup Award that recognizes innovative achievements in beam diagnostics was also presented. In this talk, I will present the highlights from BIW08. The overall quality of the contributions was notably high, which made the selection of the topics for this talk quite difficult. Although I endeavoured to produce a balanced choice of highlights, the final list is surely incomplete due to time limitations of the talk, and also it unavoidably reflects my personal point of view and preferences.

INTRODUCTION

When the DIPAC09 Programme Committee proposed me to present a talk and write this contribution on the highlights of the 2008 edition of the Beam Instrumentation Workshop (BIW08), the first question I asked myself was: why a highlights talk?

Several answers came soon to my mind. First, it could be a good way to inform people in the community that did not attend BIW08 on what happened and on what interesting was presented during the workshop. Second, it could stimulate a tighter link between the two main international workshops on beam diagnostics and instrumentation that alternates every other year between Europe and USA. Last but not least (for me), the preparation of the talk and paper would give me a unique chance and opportunity to read and learn from the large number of contributions presented during the workshop.

So I decided to accept the challenge and soon started to work on it. Of course, as everything in this world, there are always drawbacks in every situation, and this one was not an exception. The quality of most of the contributions was significantly high and for obvious time and space limitations only a limited number of highlights could be picked. This made the selection process very difficult. Additionally, even for the selected contributions, only few slides and paragraphs could be used. The forced choice was to describe only general concepts without many details in the attempt of stimulating the reader interest and to refer to the BIW08 proceedings for deeper information.

The selection criteria used in the highlights choice included novelty, originality, broadness of interest, quality of the work and so on. At the same time, when possible and reasonable, an attempt of spreading the choice over different fields, particle species, and geographical locations was done.

Unavoidably, personal interest and bias played a role in the selection as well, and I apologize in advance to the authors of those contributions that have been undeservedly excluded from this incomplete list of highlights.

OLD & NEW IN BIW08

With BIW08, the Beam Instrumentation workshop was at its 13th edition. The structure of the workshop gradually evolved over the years into the present shape that has been pretty much constant over the last editions. BIW08, during the three and half days included 3 tutorial talks, 8 invited and 7 contributed oral talks, plus two special talks. The single poster session included ~ 50 contributions and was held simultaneously with the vendor exhibition in order to facilitate informal discussion and information exchange. The workshop also included a more formal discussion session and the presentation of the 10th Faraday Cup Award, sponsored by Bergoz Instrumentation and assigned by the BIW Program Committee to the authors of innovative beam instrumentation [1].

BIW registered ~ 130 attendees and 9 vendor exhibitors and for the first time in this edition two new initiatives were introduced. Partial financial support for graduate and under-graduate students was offered, and the proceedings of the workshop were published on the JACoW open World Wide Web database [2]. With these initiatives, the BIW Program Committee tried to boost the interest to beam diagnostics in new generations of engineers and physicists, and to facilitate a free and wider diffusion of the workshop publications.

More information on BIW08 can be found elsewhere [3].

CONTRIBUTIONS HIGHLIGHTS

The selected highlights will be presented by loosely following the contribution category, starting with the Faraday Cup Award, going through tutorial, invited and oral contributions, and finishing with posters.

Faraday Cup Award

The 10th Faraday Cup Award was assigned to Suren Arutunian of the Yerevan Physics Institute of Armenia for the invention, construction and successful test of the diagnostic system "A Vibrating Wire Scanner" [4].

Figure 1 shows a 3D view of the core part of the instrument. A metallic wire is stretched through a region where the magnetic field due to a couple of permanent magnets situated on the wire support itself is present.

An oscillating current is then applied to the wire that due the presence of the magnetic field starts to oscillate. The wire is part of a tuned oscillator circuit that drives the oscillation on the natural mechanical resonance of the wire (typically at few kHz). If the cable is now scanned through the beam under measurement, the interaction of the cable with the beam ultimately generates heating with consequent temperature change and dilation of the wire. Such dilation causes a variation in the wire mechanical resonance with frequency shift proportional to the number of particles in that part of the beam that is interacting with the wire. By scanning the wire and recording the frequency shift at each position it is then possible to measure the beam profile.

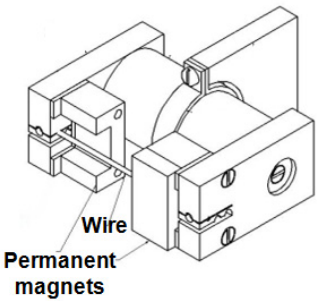


Figure 1: Vibrating wire scanner. Courtesy of S. Arutunian.

The vibrating wire monitor presents a relatively slow response time (tenths of seconds per single position measurement when the system is in air, seconds when in vacuum). On the other hand, it is very sensitive, showing its best performance when measuring low intensity beams and halos. The system has been already successfully tested with ion, proton, electron and photon beams. In a particularly interesting application at the Advanced Photon Source in Argonne, the vibrating wire monitor was used with hard x-ray synchrotron radiation to perform quality beam profile measurements [5]. In such application the monitor was installed in air downstream a thick flange of the storage ring vacuum chamber. The flange absorbed all the synchrotron radiation apart for hard x-ray photons with energy sufficient to go through the thick vacuum flange.

Tutorials

Tutorial talks are a unique characteristic of BIW. The long time allocated for the presentation (75 min plus 15 min of discussion) makes of these contributions something more close to a lecture than to a talk. Speakers are selected among experts on the topic and are requested to explain the matter starting from basics. Tutorials target mainly newcomers and experts from other fields that are interested to learn more about the presented topic, but are actually welcomed and appreciated by most of the attendees.

At BIW08 the three tutorial topics included lasers in beam diagnostics, vacuum technology in accelerators, and digital signal processing using field programmable gate arrays (FPGA). It was quite difficult deciding among the three excellent contributions, but at the end I selected the tutorial on FPGAs by Javier Serrano [6] for the complete and exhaustive presentation and for the importance that the FPGA technology is being assuming in accelerator physics. As a proof of this, a significant number of FPAG applications were presented during the BIW08 poster session [7-10].

In his tutorial Serrano historically introduces the argument, explains the main components and architecture of FPGAs and their functionality. All the design phases and steps that allow transforming abstract ideas into a real digital circuit are clearly described. The focus of the tutorial is concentrated on digital signal processing using FPGAs, which plays a central role in beam diagnostics and instrumentation applications. Special emphasis is also given to the design techniques for a “safe design” that avoids undetermined and/or inconsistent states.

In summary, the tutorial was a comprehensive and clear presentation of the subject, useful to beginners, curious ones but also to the more experts.

Invited Talks

The invited talks were selected by the BIW08 Program Committee at the time when the LCLS, the hard x-ray free electron laser at SLAC, was in the initial part of the commissioning, and the LHC teams at CERN were refining their tools and instruments in preparation for the incoming commissioning. The talks reflected such a situation with an invited by J. Frisch dedicated to the first beam measurements at the LCLS [11], and a couple of talks on two among the “hottest” issues in the design of the CERN collider, “LHC machine protection” by B. Dehning [12], and “radiation damage in detectors and electronics” by R. Lipton [13]. The future of the high energy physics based on accelerators was presented by a motivating talk by M. Zisman with title “future accelerator challenges in support of high-energy physics” [14], while the talk “The CLIC Test Facility 3 instrumentation” by T. Lefevre [15] described the activity of the group at CERN working for demonstrating the technology for future high energy colliders. Two of the talks were reviews of beam diagnostics techniques with are receiving great attention in the community, “electro-optic techniques in electron beam diagnostics”, by J. van Tilborg [16] and “transition, diffraction and Smith-Purcell radiation diagnostics for charged Particle Beams”, by R. Fiorito [17]. The last invited was presented by the author of this paper presenting some new measurement techniques and instrumentation developed at the Advanced Light Source (ALS) in Berkeley [18]. The remaining part of this section includes more details on four of these invited contributions.

In his talk, Frisch, presented a number of impressive measurements at LCLS showing an already high level of beam characterization after a relatively short period of commissioning. Figure 2 shows an example of such measurements where the longitudinal phase space occupied by the beam was measured using in combination

a transverse deflecting cavity and a spectrometer. The results were already showing the beam quality that would allow the LCLS to successfully lase at Angstrom wavelengths in spring 2009.

An unexpected presence of coherent radiation at the OTR screens along the linac made those profile monitors diagnostics unusable, and indicated the presence of longitudinal structures in the bunch with characteristic length comparable (and probably shorter) than visible wavelengths. Beam profiles measurements were performed by using wire scanners.

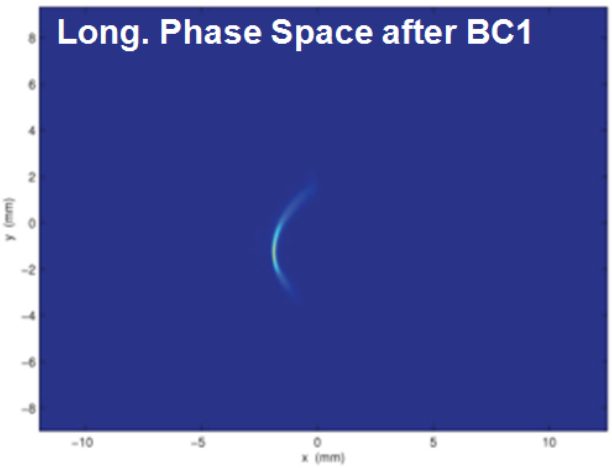


Figure 2: Beam longitudinal phase space measured after the first LCLS bunch compressors. The vertical is the time axis and the horizontal is the energy one. Courtesy of J. Frish.

In his complete and clear review of electro-optic techniques in beam diagnostics, van Tilborg started with a theoretical introduction followed by an extensive description of the different schemes, including time and frequency domain, scanning and single shot applications. Numerous experimental data per each of the schemes were also included.

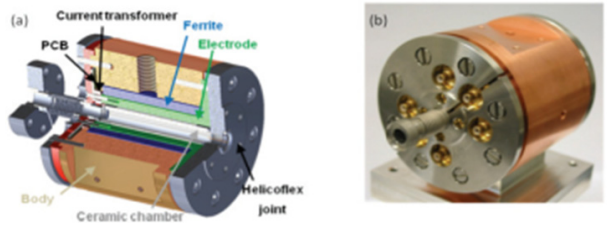


Figure 3: Inductive beam position monitor with 100 nm resolution under development at CTF3. Courtesy of T. Lefevre.

CTF3 facility at CERN has been primarily built to demonstrate by 2010 the key technological challenges for the construction of CLIC a high luminosity 3TeV e+-e- collider based on the “two-beam” accelerator scheme.

Lefevre in his talk pointed out that another major task of CTF3 is to develop and demonstrate the challenging beam diagnostic for the main linac of CLIC. For example, beam position monitors with 100 nm resolution, femtosecond synchronization techniques and high dynamic range beam imaging systems with up to 5 orders of magnitude dynamic range are required. Figure 3 show one of the high resolution beam position monitor under characterization at CTF3.

A novel bunch length monitor developed at the ALS was presented by the author of this paper. In all real accelerator, the longitudinal bunch distribution is never completely smooth and shows a random modulation of the profile. Due to different reasons (longitudinal dispersion, shot to shot variations, etc.) such a modulation changes turn to turn in circular machines, or shot to shot in linear ones. These randomly changing modulations are ultimately responsible for the incoherent radiation emitted by the bunch. If the intensity of the radiation is measured passage to passage it will show random fluctuations as well. It has been shown [19] that the absolute length of the radiating bunch can be measured by measuring the passage-to-passage variance of the radiation intensity in a part of the spectrum where the emission is fully incoherent. The ALS monitor implements this idea in a simple, non-destructive scheme that can be used with any kind of radiation, in both circular and linear accelerators, including those cases where the very short length of the bunches makes difficult the use of other techniques. The monitor was successfully tested at the Advanced Light Source using synchrotron radiation from a dipole [20].

Contributed Orals

Among the contributed oral talks, the one by P. Evtushenko on profile measurements using optical diffraction radiation (ODR) performed at CEBAF [21] is representative of the increasing interest on ODR for performing non-desctructive beam profile measurements. Indeed at BIW08, three contributions concerning ODR based diagnostics were presented. The invited talk by Fiorito [17] offered a complete review of OTR, ODR and Smith-Purcell based diagnostics systems, from both the theoretical and experimental point of view. The mentioned oral contributed by P. Evtushenko, presented instead a number of ODR measurements with a 4.5 GeV and several tens of μA beam at CEBAF. The results showed the potential use of ODR as relative beam size monitor.

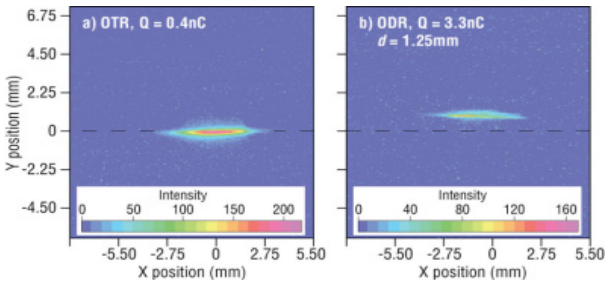


Figure 4: OTR vs. ODR comparison measurement performed at the Advanced Photon Source. Courtesy of A. Lumpkin.

Because of the diffraction radiation characteristics, a significant number of photons in the visible range can be obtained only at high beam energies and high average currents. In their poster contribution [22], A. Lumpkin and collaborators investigated the possibility of using ODR as diagnostic for beams with relativistic gamma factor "down" to the thousand range. Figure 4 shows an example of the ODR measurements performed at the Advanced Photon Source at Argonne.

Posters

Choosing the poster highlights was surely the most difficult task. Among the large number of contributions, I made a first selection that included ten posters [23-32] followed by another one that brought down the number to three.

The contribution by J. Munson and collaborators was selected because of two reasons. First, as the longest paper title I ever saw: "Injection of Direct-Sequence Spread Spectrum Pilot Tones into Beamline Components as a Means of Downconverter Stabilization and Real-Time Receiver Calibration". Secondly and more seriously, because of the particularly interesting content. They describe a successful bench test at TJNAF of a technique that allows combining a reference/calibration tone with a beam signal without deteriorating the beam signal. In order to do that, a special technique was used. Pseudo-random numbers were generated and used to code the tone signal expanding it into a large number of normal components with individual intensities at the noise level. The coded signal was then combined with a simulated beam signal and sent to a receiver. The signal at the receiver can be used as it is for the beam signal analysis, or by reversing the coding process the tone can be extracted from the signal and used for calibration purposes.

The contribution by T. Hoffman and co-authors, "Beam Quality Measurements of the Synchrotron and HEBT of the Heidelberg Ion Therapy Center", is representative of the significant activity devoted worldwide to the study and development of cancer therapy accelerators. Beam diagnostics in cancer therapy facilities plays a very peculiar role. Reliability, calibration and precision are obviously mandatory and of paramount importance in such machines. The poster describes the measurements of the carbon beam slow extraction ("spill") at the Heidelberg facility in Germany. The spill structure is redundantly measured by using ionization chambers, scintillators and beam loss monitors. A "spill pause" is important and used to minimize undesired healthy tissue exposure. If the spill pause does not work properly a fast "RF knock-out" kills the beam within a spill.

The last poster contribution that I want to mention is "Creating a Pseudo Single Bunch at the ALS — First Results" by G. Portmann. In 3rd generation light sources, users performing experiments requiring a long relaxation time are usually satisfied by dedicated special runs where few buckets are filled and several hundreds of ns gaps separate the bunches each other. Portmann and collaborators developed and installed in the ALS ring a fast kicker capable of kicking a bunch every turn (~ 1.5 MHz repetition rate). The kicker pulse duration is less than 80 ns FWHM and allows kicking a single bunch in the middle a ~ 100 ns gap. In this way, such a bunch can be stably set on a displaced orbit. By collimating out the synchrotron radiation from the other bunches on the the regular orbit, a pseudo single bunch operation can be obtained in those beamlines where the displacement is sufficiently large. The paper describes the successful test of the scheme performed at the ALS. Multiple kicker schemes are also presented together with some interesting alternative modes of operation where the beam is kicked every n-th turn.

ACKNOWLEDGEMENTS

The author wants to thank the DIPAC09 organizers for the invitation and the BIW Program Committee for organizing the BIW08 workshop. A very particular acknowledgement goes to all BIW08 contributors that with their high quality work made of BIW08 a very interesting workshop and gave me the possibility of preparing this contribution.

REFERENCES

[1] http://www.faraday-cup.com/
[2] http://accelconf.web.cern.ch/accelconf/
[3] http://www.als.lbl.gov/biw08/
[4] S.G. Arutunian, Proceedings of the 13th Beam Instrumentation Workshop (BIW08), Tahoe City, CA USA, May 2008, p. 1.
[5] G. Decker, *et al.*, Proceedings of the 13th Beam Instrumentation Workshop (BIW08), Tahoe City, CA USA, May 2008, p. 111.
[6] J. Serrano, Proceedings of the 13th Beam Instrumentation Workshop (BIW08), Tahoe City, CA USA, May 2008, p. 29.
[7] H. Bui, *et al.*, Proceedings of the 13th Beam Instrumentation Workshop (BIW08), Tahoe City, CA USA, May 2008, p.155.
[8] J. Weber and M. Chin, Proceedings of the 13th Beam Instrumentation Workshop (BIW08), Tahoe City, CA USA, May 2008, p. 215.
[9] M. J. Chin, *et al.*, Proceedings of the 13th Beam Instrumentation Workshop (BIW08), Tahoe City, CA USA, May 2008, p. 399.
[10] C.-Y. Yao, W. E. Norum and Ju Wang, Proceedings of the 13th Beam Instrumentation Workshop (BIW08), Tahoe City, CA USA, May 2008, p. 419.
[11] J. Frisch, *et al.*, Proceedings of the 13th Beam Instrumentation Workshop (BIW08), Tahoe City, CA USA, May 2008, p. 49.
[12] B. Dehning,, Proceedings of the 13th Beam Instrumentation Workshop (BIW08), Tahoe City, CA USA, May 2008, p. 59.
[13] R. Lipton, Proceedings of the 13th Beam Instrumentation Workshop (BIW08), Tahoe City, CA USA, May 2008, p. 79.

[14] M. Zisman, Proceedings of the 13th Beam Instrumentation Workshop (BIW08), Tahoe City, CA USA, May 2008, p. 39.
[15] T. Lefevre, Proceedings of the 13th Beam Instrumentation Workshop (BIW08), Tahoe City, CA USA, May 2008, p. 93.
[16] J. van Tilborg, *et al*., Proceedings of the 13th Beam Instrumentation Workshop (BIW08), Tahoe City, CA USA, May 2008, p. 69.
[17] R. B. Fiorito, Proceedings of the 13th Beam Instrumentation Workshop (BIW08), Tahoe City, CA USA, May 2008, p. 85.
[18] F. Sannibale, *et al*., Proceedings of the 13th Beam Instrumentation Workshop (BIW08), Tahoe City, CA USA, May 2008, p. 103.
[19] G. Stupakov, M. Zolotorev SLAC-PUB 7132, 1996.
[20] F. Sannibale, *et al*., Phys. Rev. Special Topic –Accel. And Beams **12**, 032801 (2009).
[21] P. Evtushenko, *et al*., Proceedings of the 13th Beam Instrumentation Workshop (BIW08), Tahoe City, CA USA, May 2008, p. 133.
[22] A. H. Lumpkin, *et al*., Proceedings of the 13th Beam Instrumentation Workshop (BIW08), Tahoe City, CA USA, May 2008, p. 359.
[23] J. Musson, T. Allison and C. Hewitt, Proceedings of the 13th Beam Instrumentation Workshop (BIW08), Tahoe City, CA USA, May 2008, p. 169.
[24] T. Kamps, *et al*., Proceedings of the 13th Beam Instrumentation Workshop (BIW08), Tahoe City, CA USA, May 2008, p. 185.
[25] T. J. Maxwell, D. Mihalcea and P. Piot., Proceedings of the 13th Beam Instrumentation Workshop (BIW08), Tahoe City, CA USA, May 2008, p. 225.
[26] J. Pogge, *et al*., Proceedings of the 13th Beam Instrumentation Workshop (BIW08), Tahoe City, CA USA, May 2008, p. 231.
[27] M. Boscolo, *et al*., Proceedings of the 13th Beam Instrumentation Workshop (BIW08), Tahoe City, CA USA, May 2008, p. 265.
[28] T. Ieiri, *et al*., Proceedings of the 13th Beam Instrumentation Workshop (BIW08), Tahoe City, CA USA, May 2008, p. 275.
[29] T. Hoffmann, *et al*., Proceedings of the 13th Beam Instrumentation Workshop (BIW08), Tahoe City, CA USA, May 2008, p. 309.
[30] G. Portmann, *et al*., Proceedings of the 13th Beam Instrumentation Workshop (BIW08), Tahoe City, CA USA, May 2008, p.313.
[31] D.S. Todd, D. Leitner and M. Strohmeier, Proceedings of the 13th Beam Instrumentation Workshop (BIW08), Tahoe City, CA USA, May 2008, p. 329.
[32] F. Becker, *et al*., Proceedings of the 13th Beam Instrumentation Workshop (BIW08), Tahoe City, CA USA, May 2008, p. 339.

COMMISSIONING RESULTS OF BEAM DIAGNOSTICS FOR THE PETRA III LIGHT SOURCE

K. Balewski#, G. Kube, K. Wittenburg, A. Brenger, H.-T. Duhme, V. Gharibyan, J. Klute, K. Knaack, I. Krouptchenkov, T. Lensch, J. Liebing, Re. Neumann, Ru. Neumann, G. Priebe, F. Schmidt-Föhre, H.-Ch. Schröder, R. Susen, S. Vilcins-Czvitkovits, M. Werner, Ch. Wiebers,
Deutsches Elektronen Synchrotron DESY, Hamburg, Germany

Abstract

PETRA III is a new hard x-ray synchrotron radiation source which will be operated at 6 GeV with an extremely low horizontal emittance of 1 nmrad. This new facility is the result of a conversion of the existing storage ring PETRA II into a light source. The conversion comprises the complete rebuilding of one eighth of the 2304 m long storage ring, which will then house 14 undulator beam lines, the optical and experimental hutches, and the modernization and refurbishment of the remaining seven eighths. In addition two 100 m long damping wiggler sections have been installed which are required to achieve the small design emittance. Construction, installation and technical commissioning have been finished middle of March and then the commissioning with beam started. In this paper we present the results that have been achieved during commissioning with special emphasis on the role of diagnostic systems.

INTRODUCTION

At DESY the former storage ring PETRA II with a circumference of 2304 m has been converted into a dedicated light source PETRA III [1], [2]. This new source is a third generation, hard x-ray facility similar to APS, ESRF and SPRING8 and serves as a supplement to the X-FEL which will be build at DESY. The basic parameters are given in table 1.

Table 1: PETRA III parameters

Parameter	**PETRA III**	
Energy / GeV	6	
Circumference /m	2304	
Total current / mA	100	
Number of bunches	960	40
Lifetime / h	24	2
Emittance (horz. / vert.) /nm	1 / 0.01	
Number of insertion devices	14	

The emphasis of the conversion was on achieving a very small horizontal emittance and to solve the stability problems that are usually connected with high brightness beams.

#klaus.balewski@desy.de

The number of insertion devices is rather modest for a machine of this size but this due to the fact that the conversion should be cost effective.

PETRA II consisted of eight almost identical parts which are usually called octants. One of the octants has been completely removed and replaced by a new experimental hall of almost 300 m length and 30 m width (see Fig. 1).

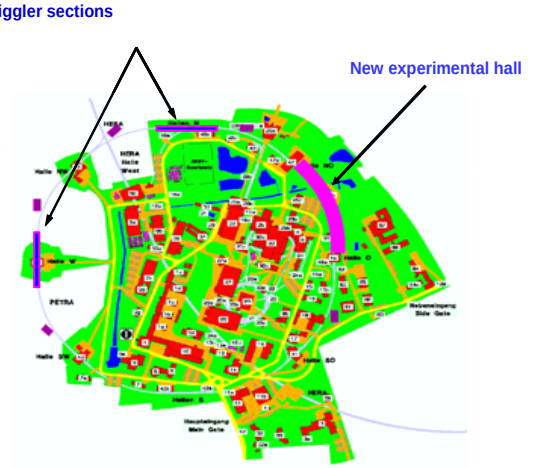


Figure 1: Ground Plan of the DESY site with the PETRA ring. The new experimental hall (purple) is situated between the PETRA halls North-East and East and the damping wiggler sections are in the North and West.

This new hall houses the experimental huts and supplies 9 straight sections in a DBA lattice to install insertion devices. The concept of canted undulators has been applied so that PETRA can be equipped with 14 undulators. Presently 3 two meter long undulators have been installed.

The geometry and the lattice of the remaining seven so called old octants have been kept. The existing hardware was reused if possible but refurbished and modernized to fulfil the high demands on reliability of a light source.

The emittance of the combination of the seven old octants and the new octant is roughly 4 nm rad, well above the design goal. Damping wigglers have been installed to enhance the radiation damping of the machine and thereby reduce the emittance to the required value [3]. These damping wigglers [4], [5] have been accommodated in the long straight sections in the North and West.

The conversion was finished middle of March and then the commissioning of PETRA III started.

Commissioning of an accelerator requires lots of different diagnostics. The instrumentation for PETRA III has been described in detailed elsewhere [6], [7]. In the following the commissioning procedure and the role of diagnostics will be presented.

COMMISSIONING OF THE TRANSFER LINE

The transfer line is a 190 m long transport channel between DESY and PETRA. It consists basically of a very long straight part of about 160 m length, including a drift space of almost 100m and a short arc in front of PETRA that ends at the injection septum.

The essential elements for commissioning were the 10 screen monitors and two current monitors close to the beginning and the end of the transfer line. Screen monitors have been chosen in addition to eight normal BPMs because they have the obvious advantage of measuring both the position and the profile. With the help of the screen monitors it was easy to get the beam through the channel within about 3 hours. Additional time was devoted to improve the transfer efficiency and to roughly check the optics.

A computer model of the transfer line has been set up which allows to calculate different beam parameters and in particular the beam profile at the different screen monitors. By comparing the theoretical profiles with the measured it could be verified that the profiles agree within 10 % which is sufficient for the time being.

The above mentioned straight section contains a long drift space where three screen monitors have been installed which will allow the determination of the DESY beam emittances and the optics at the end of the drift space. These parameters will then serve as input for matching the optics of the transfer line to the required values at the end.

The eight BPMs of the transfer line, three at the beginning and five at the end, have been commissioned as well [8]. The BPMs worked well right from the beginning and the readings agree with the measured positions of the screen monitors. With the help of these BPMs the trajectory in the transfer line will be checked in the future since efficient injection into PETRA requires stable conditions in particular the stability on vertical position and angle is rather critical. A feedback to control these parameters can be installed.

In addition two scrapes have been installed in the transfer line. They can be used to tailor the beam from the synchrotron if necessary.

COMMISSIONING OF THE STORAGE RING

The first commissioning phase of the machine was done without damping wigglers simply to reduce complexity. The primary objectives were to store and accumulate beam and to set up part of the bunch by bunch feedback system to condition the vacuum system with as high current as possible. In addition first tests of different diagnostic elements should be carried out which are for example necessary for the future operation with wigglers and undulators.

First Turn and Stored Beam – BPM System

The first goal was to get the beam around and to store beam.

To set up the septum amplitude and timing two screen monitors have been installed one just behind the septum and the other 90° in horizontal betatron phase behind the septum. Apart from these two screens no more have been installed to avoid possible (vacuum) problems in the long run. The success of the first goal depended completely on the reliable operation of the BPM system in particular on the turn by turn capability.

Because of the importance of the BPM system the specifications have carefully worked out [9]. It has been decided to purchase the latest version of the BPM electronics from I-Tech (Libera brilliance) and it has been checked, if possible, at other storage rings that the electronics fulfils the requirements [10]. The commissioning of the BPM system is described in a companion paper to this conference [11].

The survival of the beam could be easily checked with the sum signals of the BPMs which serve in this case as a huge number of intensity monitors. If one got stuck somewhere the position information easily helped to correct the trajectory so that the beam was transported further. The first turn was completed on Easter Sunday after two quadrupoles with the wrong polarity had been identified and the optics was locally changed in order to circumvent a problem with another quadrupole. The first and even a tiny bit of the second turn could be also seen on an AC current monitor.

In order to store the beam the trajectory in the new octant, where all the small gap chambers are located, had to be corrected empirically so that the beam survived for up to a few hundred turns. The next step was to turn on the rf-system, to set the rf-phase correctly and then about 10% of the initially injected particles were stored.

Preparation for Accumulation

Next it was aimed to get the optics of the machine as close as possible to the theoretical values. The integer part of the tune was determined by analysing difference orbits in the vertical and horizontal plane. To determine the non-integer part of the tune and other important machine parameters such as chromaticities a reliable tune measurement is absolutely necessary. The non-integer part of the tune was first measured with a special monitor being just dedicated to run in the turn by turn mode. But in most cases the tune was measured by exciting the beam with white noise by the kicker magnets of the bunch by bunch feedback and measuring the response with the transverse feedback detector.

In this way the tunes and chromaticities could be set close to the design values and the orbits could be corrected within 2mm horizontally and 1.5 mm vertically.

Orbit correction was limited by the fact that the position of the BPMs was just known within ± 1.5 mm.

After these corrections the on-axis injection efficiency was close to 100%.

In order to improve the aperture of the storage ring the machine was scanned with bumps at those locations where aperture limitations are likely to be expected i.e. close to the small gap undulator chambers in the new octant and the synchrotron light absorbers in the damping wiggler sections.

After having empirically centred the beam at the critical positions accumulation was set up. First up to 1 mA was piled up in a single bunch. The current was deliberately limited to this value because for higher single bunch currents the peak current could be so high that the corresponding peak voltage could damage the front-end of the monitor electronics [12]. In addition to the current limitation attenuators have been installed to protect the front-end of the monitor electronics. This problem will be relaxed in the future because the bunches will be longer when operating with wigglers so that even the attenuators can be removed. Operation with wigglers will allow reaching the design single bunch current of 2.5 mA.

As the next step the kicker timings were set up correctly so that multi-bunch fillings are possible. Presently 40 bunches are evenly filled and at that time the current was limited to about 5 mA due to transverse coupled bunch instabilities.

Increasing the Current – Bunch by Bunch Feedback

For efficient conditioning of the vacuum system currents of at least 40 mA should be stored. It was expected that the current in PETRA III would be limited by coupled bunch instabilities [13]. That's why the old PETRA II transverse bunch by bunch feedback system [14] has been reinstalled and a new transverse and longitudinal system has been installed. The new system has a bandwidth of 62.5 MHz allowing to evenly fill up to 960 bunches (distance between bunches 8ns) whereas the old system has just a bandwidth of 5 MHz so that even fillings of up to 80 bunches are possible.

The old system was put very quickly into operation, since it is known very well, in order to get rid of transverse instabilities. A current of up to 20 mA was achieved and now the current was limited by longitudinal instabilities. During the next commissioning phase the longitudinal system will be activated to overcome this limitation.

In addition to the deliberately set limit for the single bunches a limit on the total current was also applied. Because of HOM heating there exists the danger to damage the BPMs. Limiting the HOM power due to transient heating to 5 W the resulting current limit is [15]

$$I_{tot} \leq 3.6mA \cdot \sqrt{N}$$

where N is the number of bunches. For an even filling of 40 bunches the limit for the total current is approximately 23 mA. In case of operation with wigglers the situation is relaxed because of the longer bunches. For the next commissioning phase temperature measurements at selected monitors have been prepared so that the above mentioned limit can be checked.

Above the importance of tune measurements was already mentioned. Tune measurement via external excitation under feedback operation is obviously difficult because of the strong damping. Already in the past an alternative way was found to measure the tune with feedback and this method was applied at HERA and is applied at DORIS [16], [17]. Looking at the signal just behind the analogue detector of the feedback system (DS) it can be seen that the noise level is reduced close to the tunes (see fig.2 and 3).

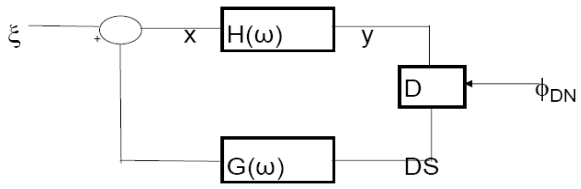


Figure 2: Schematic layout of a feedback system: Beam dynamics is described by H(ω) and the feedback effect by G(ω). The feedback detector is denoted by D and the noise associated with the detector by Φ_{DN}. The signal behind the detector is denoted by DS. External disturbances of the beam are indicated by ξ.

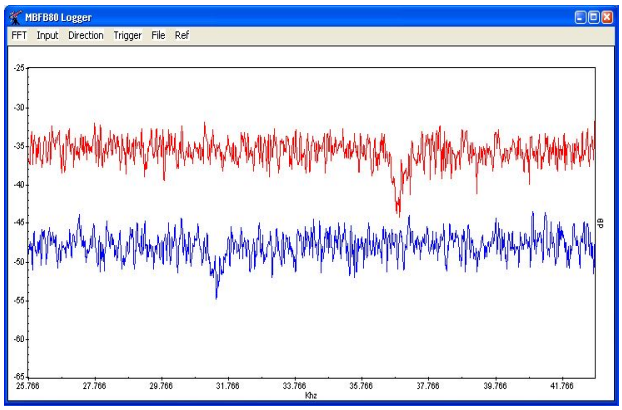


Figure 3: Signal measured behind the detector (DS). The dips in the noise spectrum at the tunes are clearly visible.

This result can be understood if one assumes for simplicity that the beam dynamics is given by a harmonic oscillator and the feedback effect is a differentiator leading to damping. The detector signal is then given by

$$H(\omega) = \frac{1}{\omega_0^2 - \omega^2}; \quad G(\omega) = i\omega\Gamma;$$

$$DS(\omega) = \frac{1}{\omega_0^2 - \omega^2 + i\omega\Gamma}\xi + \frac{\omega_0^2 - \omega^2}{\omega_0^2 - \omega^2 + i\omega\Gamma}\phi_{DN}$$

At the tunes $\omega = \omega_0$ the detector signal is reduced if the damping of the feedback Γ is non zero. Observation of

these signals shows (i) if the feedback is working and (ii) offers the possibility to measure the tunes.

Preliminary Parameter Studies of PETRA III

With the help of the orbit as well as the tune measurement several properties of PETRA III can be determined. During the first commissioning phase several of these measurements have been performed as preparations for the next phase and to test procedures.

The circumference of the machine has been determined. For each of the four sextupole families, the dependence of the tune on variation of the rf-frequency was measured for three different current settings of the sextupoles. The results were three different lines "rf-frequency vs. tune" for each sextupole family. These lines intersect for zero momentum error and the corresponding frequency is the centre frequency. This frequency determines also the circumference of the machine or precisely the orbit that passes on average through the sextupoles. Fig.4 shows an example of such a measurement.

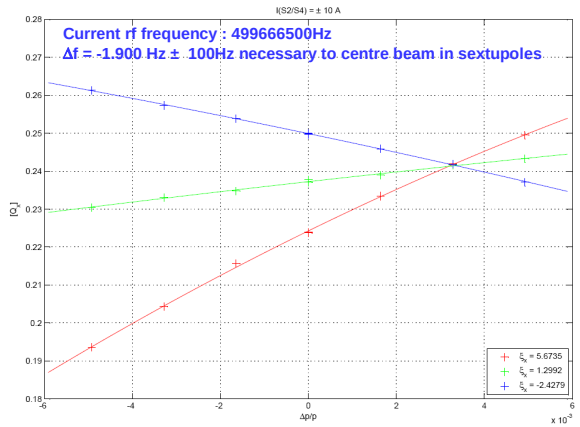


Figure 4: Tune vs. momentum error (rf-frequency) for one sextupole family. The lines intersect for zero momentum error and the corresponding frequency defines the circumference of the machine.

As a by-product of the above measurement the dispersion is determined. For the time being both the horizontal and the vertical dispersion are considerably distorted. Actually this is not really a surprise but simply reflects the fact that the orbit is not well enough corrected. The measured dispersion distortions of up to 10 cm are in accordance with the orbit distortion of 2 mm horizontally and 1.2 mm vertically.

During the first commissioning phase it did not make sense to correct the orbit to a level better then 1 or 2 mm since the position of the monitors was only known within ± 1mm. To make progress beam based alignment (BBA) is mandatory and this is foreseen for the next phase. The BBA procedure has already been tested with a single power quadrupole and found to be working.

Another important procedure is the determination of the orbit response matrix (ORM) and the latter analysis for example with loco. This procedure has been tested with a small number of horizontal and vertical correctors and analyzed. No principle optic error has been identified but there is a small deviation from theory. This will be analyzed in more detail during the next phase.

TESTS OF DIFFERENT INSTRUMENTS

Current Monitors

A fast current monitor which is able to measure the current of individual bunches has been installed and tested. In combination with a marker system it allows to identify bunches and their individual current. This information is important for top-up operation. Basically top-up operation has been prepared and can be applied during this year.

A DC monitor to measure precisely the current and lifetime of the beam has also been successfully tested.

Temperature Sensors

Temperature sensors are installed at several places in particular to survey the temperature of the absorbers in the new octant and in the damping wiggler sections. The temperatures of these elements are available in the control system. If the temperature of some of these sensors exceed a predefined threshold an alarm is sent to the machine protection system to prevent the destruction of the controlled vacuum component. For details on the machine protection system see the contribution to this conference [18].

Movement Detection of the BPMs

The stability of the BPM locations, especially those close to the undulators, are critical because the measured beam position enters into the orbit feedback. Any kind of misreading will result in mis-steering of the beam. The location of the BPMs in the new octant is therefore detected with a special wire system. Basically the position of a wire firmly fixed to the BPM is measured against 4 electrodes which are connected either to the ground or the girder.

Some of the monitors have been successfully tested. The position information of the BPMs will enter the orbit feedback system.

EMITTANCE MEASUREMENT

Two diagnostic beamlines and a laser wire-scanner were built up for longitudinal and transverse emittance measurements. They will be commissioned in the next phase. The following subsections give a short overview, details can be found in Ref. [6].

X-Ray Diagnostic Beamline

A diagnostic beamline for x-ray bending magnet synchrotron radiation was installed at the end of the new octant to image the beam spot onto a high resolution CCD camera system. Imaging will be performed with two

interchangeable x-ray optics: (i) a high resolution compound refractive lens (CRL) system (31 beryllium lenses, ≈ 2 μm resolution), and (ii) a pinhole camera system (0.5 mm thick tungsten blade with circular hole of 20 μm, ≈ 20 μm resolution) for lower resolution in standard operation. A Si monochromator crystal (311 reflection in Laue geometry) will be used to reflect 20 keV photons onto the detector system (Hamamatsu AA50 beam monitor) which is installed outside of the vacuum system.

Optical Beam Line

The optical beamline for bunch length diagnostics uses visible synchrotron radiation from a standard dipole magnet in the old octants. A water cooled Cu mirror extracts the optical part of synchrotron radiation from the dipole, and an optical relay system guides the light about 25 m to a streak camera system (Hamamatsu C5680 Streak Camera) which is housed in an experimental hut outside the tunnel. To be prepared for measurements of the transverse beam size in the optical spectral region as well, all optical elements are designed and proven to be as precise as possible (peak to valley wavefront aberration of λ/20 at 632 nm).

Laser-Wire Scanner

A laser-wire scanner is providing horizontal and vertical profile measurements within tens of seconds with a sub-percent accuracy. For such a resolution the laser-wire diameter has to be below 10μm which is verified by in-situ calibrations (see Fig. 5). The laser light will be transported from the laser hut 6 m above the PETRA tunnel to a vertical and horizontal optical table positioned around the vacuum chamber. Both tables are equipped with scanning, focusing and diagnostics optics [6]. All installations are finished and the commissioning will follow as soon as stable beam conditions will be achieved.

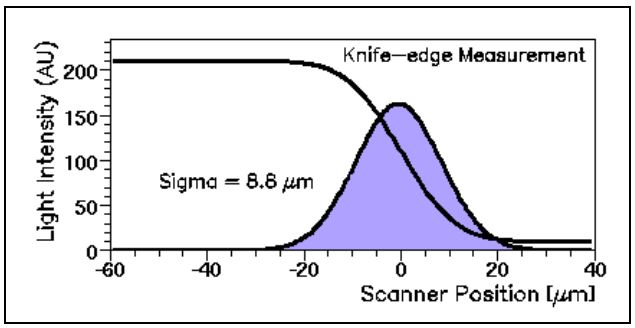


Figure 5: A sample of laser spot size measurement at focus. A knife-edge scan is differentiated to obtain a beam profile.

SUMMARY

The first commissioning phase of PETRA III went smoothly and very fast. No major problem was encountered. Detailed investigation of the machine will be part of the next phase. The success of the first phase is certainly due to sufficient diagnostics that worked well right from the beginning. At this point also the support and commitment of those who took part in the commissioning is greatly acknowledged.

REFERENCES

[1] PETRA III Technical Design Report, DESY 2004-035
[2] K. Balewski et al., "PETRA III: a new high Brilliance Synchrotron Radiation Source at DESY", EPAC '04
[3] K. Balewski, W. Decking, "Optimization of Low Emittance Lattices for PETRA III", EPAC '04
[4] M. Tischer et al., "Status of the PETRA III Damping Wigglers", EPAC 06
[5] M. Tischer et al., "Damping Wigglers at the PETRA III Light Source", EPAC 2008
[6] K. Balewski et al., "The beam diagnostic instrumentation for PETRA III", Proc. Of BIW'08, Lake Tahoe, California, to be published
[7] G. Kube et al., "Overview of the Diagnostics Systems of PETRA III", EPAC 2008
[8] F. Schmidt-Föhre, "BPM system upgrades in the Petra III pre-accelerator chain during the 2008 shutdown ", these proceedings
[9] K. Wittenburg et al., "PETRA III Beam Position Monitor Electronic: Requirements and technical Specifications; Tendering and Contract Management"; Version 1.92
[10] K. Balewski, I. Krouptchenkov, K. Wittenburg, Examination of the Bunch Current and Bunch Pattern Dependence of the LIBERA BPM Electronic, Visit of ESRF". DESY-MDI internal Report Nr. 2006 – 1; September 2006
[11] A. Brenger et al., "Experience with the commissioning of the Libera Brilliance BPM electronics at PETRA III", these proceedings
[12] G. Kube, M. Werner, "Signal Level Calculation for the PETRA III Beam Position Monitor System" DIPAC 2007, Venice, Mestre, Italy and G. Kube, "Sensitivity Estimation for the PETRA-III Beam Position Monitors based on a Boundary Element Method", DESY technical note 2007-1
[13] K Balewski, R. Wanzenberg, "Beam Current Limitations in the Synchrotron Light Source PETRA III",EPAC '04
[14] D. Heins, et al., "Wide Band Multi-Bunch Feedback Systems for PETRA". DESY 89-157; November 1989
[15] R. Wanzenberg, DESY, private communication
[16] R.D. Kohaupt, DESY, private communication
[17] J. Klute, DESY, private communication
[18] T. Lensch and M. Werner., "Machine Protection System for PETRA III", these proceedings

SSRF BEAM DIAGNOSTICS SYSTEM COMMISSIONING*

Y.B. Leng#, K.R. Ye, W.M. Zhou, Y.Z. Chen,
SSRF, SINAP, Jiading, Shanghai 201800, P.R. China

Abstract

SSRF is a 432 m-circumference synchrotron light source with a 150MeV linac, a 3.5GeV full energy booster, and a 3.5GeV storage ring. Principal diagnostics systems have been installed and nearly all have been commissioned during past two years. Data have been obtained on beam position, beam profile, current, and synchrotron radiation diagnostics beamline on the storage ring. Multi bunch transverse feedback system has been applied on the ring. Results for the 150MeV electron beams in the linac, up to 3.5GeV in the booster, and 3.5GeV in the ring will be presented.

INTRODUCTION

SSRF is a 3.5 GeV energy dedicated electron synchrotron radiation source. Recently the commissioning performance goals of the whole facility were met. Multi-bunch beam intensity of the ring has reached 200mA. At 200 mA, the lifetime is larger than 10 hour with all ID gaps closed. The commissioning process went very rapidly. Instrumentation played a critical role [1].

Table 1 shows the primary specification of the various diagnostics systems.

Table 1: SSRF Beam Instrumentation Specifications

Location	Measurement	Specification
Injector	Beam position	Resolution 100μm@1.67MHz
	Beam profile	Resolution 200μm@2Hz
	Bunch charge	Relative accuracy 2%
	Energy	Relative accuracy 0.1%
	Emmitance	Relative accuracy 10%
	DC current	Resolution 50μA@10kHz
	Tune	Resolution 0.001@200Hz
Ring	Beam position	Resolution 10μm@694kHz Resolution 1μm@10Hz
	Beam profile	Resolution 10μm
	Beam length	Resolution 2ps
	DC current	Resolution 10μA@1Hz
	Tune	Resolution 0.0001

To meet above requirements a beam instrumentation system, consisting of 61 stripline BPMs, 152 button BPMs, 2 DCCTs, 11 Wall Current Monitors (WCM), 3 ICTs, 1 faraday cup, 18 screen monitors, 2 tune monitors, 3 transport line slits, 2 ring scrapers, 1 multi bunch feedback system and 1 dedicated diagnostics beam line, has been developed, implemented and commissioned during past 4 years.

The data acquisition system for beam instrumentation is designed on EPICS platform, which follows “standard model” architecture. Five kinds of IOCs were used in this system: VME bus IOC, Libera embedded IOC, PXI bus IOC, scope embedded IOCs, and soft IOC [2].

BEAM POSITION MONITORS

Position Measurement

Beam position monitor system fully equipped with Libera EBPM processors, which provides raw ADC data, turn by turn (694kHz @ ring, 1.67MHz @ booster) data, fast application (10kHz) data and close orbit (10Hz) data at the same time, is the most powerful tools during the commissioning and machine study of SSRF.

Beam position in the LINAC is calculated from raw ADC data of Libera. 40um position resolution and 3pC bunch charge sensitivity have been reached during commissioning. Calibrated by ICT, the sum signal of BPM has been use to give a fast estimation of bunch charge and transport efficiency of LINAC during daily operation.

For the booster raw ADC data and turn by turn (1.67MHz) data are much useful than others. Synchronized by gun-shot trigger the raw ADC data could deliver first turn information. In this way 30 BPMs around the booster ring acted as beam arriving monitor to help operator tuning the machine to store injected beam during the day one commissioning. Decimated turn by turn data from all BPMs is used to present dynamic beam orbit during energy ramping.

For the Ring first turn information derived from raw ADC data help operator to determine beam loss location and tuning machine to store the first beam very quickly (few hours). SA data (10Hz), which position resolution reaches hundred nm level, resents precise closed orbit of the ring. Calibrated by DCCT the sum signal of SA data also could be used to present beam current and calculate beam lifetime. The beam spectrum (FFT of fast application data) is ideal tools to identify orbit noise source. With one million samples the frequency range of beam spectrum could cover from .1 Hz to 5 kHz. Current dependent instability has been observed with this tool. Global turn by turn capability and 3 um position resolution provides a powerful platform for accelerator physicists and operators to perform Response matrix measurement, Optics optimization, global and local phase advance measurement and phase space measurement.

*Work supported by Chinese Academy of Science
#leng@sinap.ac.cn

Figure 1 shows position resolution test result for COD measurement of the Ring.

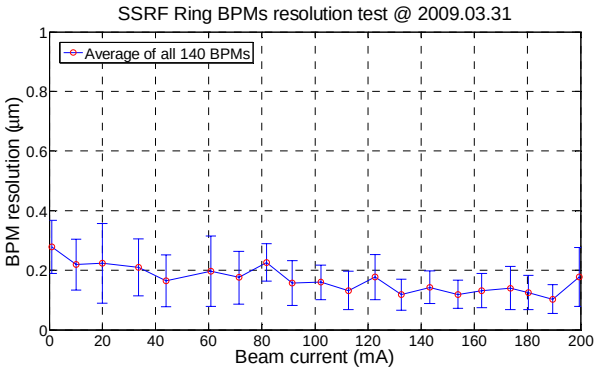


Figure 1: Ring BPM COD resolution test.

Tune Measurement

The Ring and Booster share the same tune monitor design, which is based on continuous harmonic excitation method. The measurement system employs a LAN based function generator, which output, after splitting and amplification, is fed to a strip line kicker. A dedicated BPM pickup equipped with Libera processor is used to observe the beam spectrum and betatron peaks. The betatron tunes and beam sizes have been measured under various configurations of function generator to figure out the best setup. The resolution of tune measurement is better than 0.001. Fig. 2 shows the Booster tune drift during ramping.

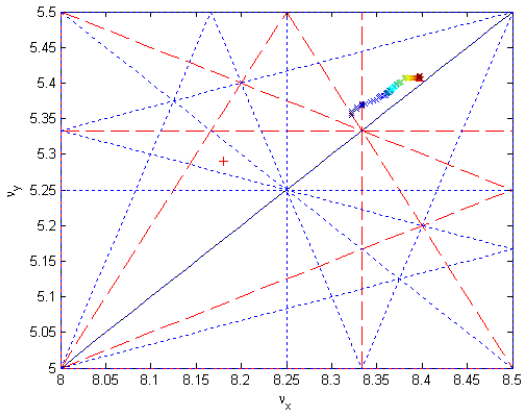


Figure 2: Booster tune drift during ramping.

Filling Pattern Monitor

A filling pattern monitor, which consists of a dedicated BPM pickup, a PXI based IOC and waveform recorder module (Acquiris DC252, BW 2GHz, sampling rate 8GHz), has been developed to perform bunch charge measurement and filling pattern observation in the Ring. By summing the BPM pickup voltage signals of four buttons in RF combiners, the position sensitivity is considerably reduced. Calibrated by DCCT readings the filling pattern monitor reaches 1pC resolution at 1nC range for bunch charge measurement.

DIAGNOSTICS BEAM LINE

The ring synchrotron radiation diagnostics beam line works with visible light, which consists of five branches for different measurements: an imaging system focused on source point to monitor electron beam profile; two SR interferometers (horizontal and vertical) to perform the precise beam size measurement; a 2D streak camera (HAMAMAZU C5680) for bunch length measurement and multi bunch instability study; a fast gated camera (gate width 3ns) for injection optimization [3].

The imaging system was ready on day one and the first stored beam was confirmed with this device. The interferometers have been online since June 2008. Experiments with high current beam (larger than 30mA) shows the beam size measurements deviation is about 1μm. The beam sizes have been measured with this device under various beam current conditions, which is shown in Fig. 3.

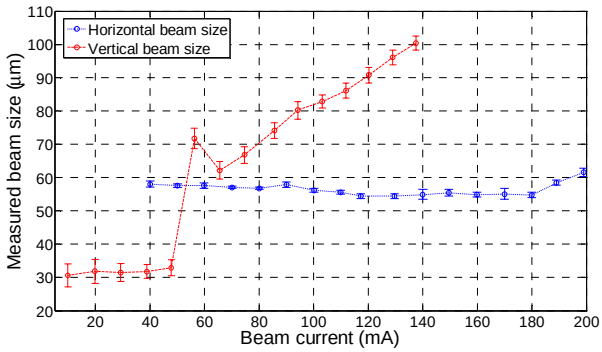


Figure 3: Beam size measured by interferometer.

The primary tests of streak camera and fast gated camera showed the performance of them agreed with the FAT report from producers. Both of them will be put online soon. Another Xray pinhole camera is in manufacture stage and will be installed in the same location to measure beam profile and position for cross checking.

TRANSVERSE FEEDBACK

The SSRF ring transverse feedback is a digital system based on Spring8 board. Two dedicated ID BPMs located in the second straight section are used to detect transverse movement. Separate horizontal and vertical stripline kickers, located in injection straight, are used to apply base band correction kick to the beam. The kicker electrodes are individually driven with opposite polarities by 100 kHz - 250 MHz, solid-state, commercial BONN amplifiers.

Beam size blow-up introduced by multi bunch instability is observed with interferometer in both vertical and horizontal plane. The current thresholds of instability are around 45mA and 190mA respectively (Fig. 3). After applying transverse feedback, the beam size is minimized down to normal level. The attenuation for betatron oscillation is larger than 40dB, which is proved by beam

spectrum calculated from Libera turn-by-turn data. Fig. 4 shows measured beam sizes with feedback on & off.

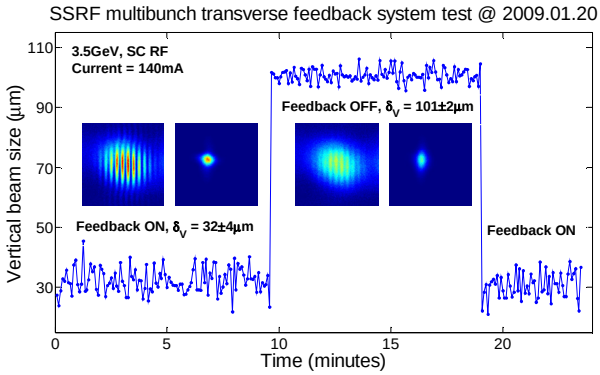


Figure 4: Measured beam size @ feedback on & off.

BEAM INTENSITY MONITORS

3 integration current transformers (ICT) manufactured by Bergoz are placed at the end of Linac, low energy transport line and high energy transport line respectively. Outputs of ICTs are fed to a scope embedded IOC (TEK DPO7054). Bunch charge information is derived from sampled ICT waveform. With this configuration Linac bunch charge and Booster transfer efficiency have been measured. A faraday cup is employed as a reference at the end of LINAC.

11 Wall current monitor (WCM) manufactured by TOYAMA is chosen to present the longitudinal distribution of the beam in the Linac (2), low energy transport line (2), Booster (1) and high energy transport line (3).

Stored beam current in the Ring and Booster is measured using parametric current transformer (DCCT) manufactured by Bergoz. A mounting, cooling and shielding system has been fabricated based on SPEAR3 design for installation of NPCT toroid. Both offline test and online test indicate that the resolution of DCCT system is better than 2μA @ 1Hz for the Ring and 30uA @ 10 kHz for the Booster. Fig. 5 shows resolution evaluation result of the Ring DCCT.

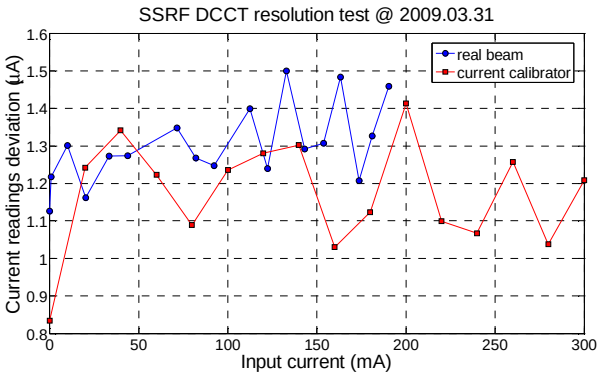


Figure 5: Ring DCCT resolution evaluation result.

PROFILE MONITOR

Fluorescent screen / OTR beam profile monitors are installed in the Linac (5), low energy transport lines (3), Booster (4), high energy transport line (3), and Ring (2) for visual observation of beam profile and position. The luminescent screen is instrumented with a gated CCD camera, which is synchronized with “Gun fire” events via main timing system. Video signals will run through video cables and video multiplexer into PXI IOC.

SCRAPER & SLIT

A horizontal and vertical combined scraper is installed in the injection section to get information about the transverse beam distribution, to eliminate possible beam halos and to establish an alternative method for measuring beam life time in the storage ring. Scraper motion control is implemented in a dedicated PXI-based diagnostics IOC. Ten microns repeatability of blade motion is achieved. The same design was used for transport line slits.

SUMMARY

The diagnostics system has passed commissioning stage and been online for regular operation. Sub-micron level position resolution and turn by turn measurement capability make BPM system the most important toolkits in commissioning and daily operation. All other beam instruments such as DCCT, tune monitor, multi bunch transverse feedback and so on work well and have demonstrated the required performance. Fast orbit feedback system and Xray pinhole camera will be commissioned in the soon future.

ACKNOWLEDGEMENTS

The authors would like to thank everyone who contributed to this work through discussions and suggestions, in particular Guenther Rehm and Micheal Abbot (Diamond), Bob Hettel, James safranek, Jeff corbett and Jim Sebek (SLAC), Toshiyuki MITSUHASHI (KEK), Takeshi Nakamura (SPRING-8), Jean-Claude Denard (Soleil), Hsu Kuo-Tung (Taiwan Light Source), Cao Jian-She and Ma Li (IHEP), and Sun Bao-Geng (NSRL).

REFERENCES

[1] G.M.Liu, H.H.Li, W.Z.Zhang, etc., “Commissioning of the SSRF Storage Ring”, EPAC’08, Genoa, Italy, June 2008, p. 2079 (2008).

[2] Y.B.Leng, W.M.Zhou, Y.Z.Chen, etc., “SSRF Beam Instrumentation System”, ICALECS’07, Knoxville, US, Oct. 2007, p. 205 (2007).

[3] K.R.Ye, Y.B.Leng, J.Chden, etc., “Synchrotron Radiation Monitor and Mirror at SSRF”, this proceedings.

GLOBAL ORBIT FEEDBACK SYSTEMS DOWN TO DC USING FAST AND SLOW CORRECTORS

N. Hubert*, L. Cassinari, J-C. Denard, A. Nadji, L. Nadolski,
Synchrotron SOLEIL, Gif-sur-Yvette, France

Abstract

Beam orbit stability is a crucial parameter for 3rd generation light sources in order to achieve their optimum performance. Sub-micron stability is now a common requirement for vertical beam position. To reach such performance, Global Orbit Feedback Systems are mandatory. This paper describes the different design approaches for Global Orbit Feedback Systems. A few machines can use a single set of strong correctors. Most of them have their strong corrector bandwidth limited by eddy currents in aluminum vacuum chamber, or power-supply speed together with the required digitization granularity. Then, a second set of fast correctors is required for high frequency correction. But Fast and Slow Orbit Feedback Systems cannot work together with a common frequency range, they fight each other. An earlier solution has been to separate fast and slow systems by a frequency dead-band. This approach does not allow correcting efficiently the orbit shifts due to the gap movements of the increasingly sophisticated insertion devices that are installed on new machines. The different solutions that have been recently implemented are reviewed.

INTRODUCTION

Third generation light sources are built for producing high brilliance photon beams. Brilliance improvements have mainly been achieved by emittance reduction in both planes. The vertical emittance and beta functions define the beam size and divergence, which leads to the beam stability requirements. Commissioned in 1987, Super-ACO had a design vertical beam size of 230 µm in its straight sections. This parameter for NSLS II, to be commissioned in 2013, is ~2 µm, which is 100 times smaller. Position and angular stability requirements, usually one tenth the rms beam size σ_z and beam divergence σ'_z respectively, call for position stabilities of 20 µm for Super-ACO and 0.2 µm for NSLS II. Sub-micron stability is a formidable challenge that can only be achieved by implementing global orbit feedback systems. These systems are increasingly sophisticated in order to combine slow and fast corrections at the required speed and stability levels. Machines presently in operation with only a slow orbit feedback system should be able to profit at reasonable cost of the addition of a fast system using a set of cheap fast correctors that works together with the slow ones. The same scheme will also provide a cheaper solution to the new machines with very small beam sizes.

*nicolas.hubert@synchrotron-soleil.fr

BEAM STABILITY REQUIREMENTS

For most beamlines, beam stability implies photon flux stability. They select the photon flux through a slit. The slit defines a beam size aperture for beamlines equipped with a focusing optics and an angular aperture for those equipped with a non-focusing optics. The flux variation is worse with smaller slits. Then the usual requirement $\Delta z/\sigma_z$ or $\Delta z'/\sigma'_z \leq 10\%$ leads to $\Delta I/I \leq 0.5\%$. Let's note that the photon beam size is diffraction limited and the beam divergence is that of the bending magnet or ID photon source; these effects convolved with the electron beam emittance gives the resulting photon beam an emittance larger than that of the electron beam, especially for low energy beamlines. However, for hard X-ray beamlines the electron beam dominates both beam size and divergence.

The effect of the beam position noise on the photon flux depends also on the integration time T_i of the experiment. The position noise components at frequencies higher than $1/T_i$ appear as an emittance growth, not as a photon flux fluctuation. Then the emittance ellipse ε_c describing the electron beam position and angle fluctuations can be added quadratically with the stable photon beam emittance ε_0 for obtaining an effective photon beam emittance ε_{eff}:

$$\varepsilon_{eff}^2 = \varepsilon_c^2 + \varepsilon_0^2 \quad (1)$$

In this case, high frequencies instabilities do not really affect the stability of the photon flux; they only decrease its intensity in a stable way. One can consider as noise source only the part of the position spectrum that is at frequencies $F < 1 / T_i$.

PERTURBATION SOURCES

To fulfil their tight stability requirements, great care is taken in the design and construction of the new machines. Nevertheless, there are still some remaining perturbations to be suppressed by global orbit feedback systems. Perturbation sources can be sorted in decreasing order of their time period [1].

Long Term

With time periods comprised between a few hours and a few minutes, air and cooling water temperatures are important [2]. Changes in air temperature affect the position of Beam Position Monitors (BPMs) and of magnets. In the first case, only the beam position readings are affected. In the latter one, there is an amplification of magnet movements on the beam orbit. Phenomena like sun and moon tides may have an impact of 10 to 30 µm.

Medium Term

Experimental Hall activities often introduce beam orbit perturbations with a time period of a few seconds. Typically, a moving crane can create orbit distortions of 1 to 100 µm peak-to-peak, which is incompatible with user operation. Fast switching magnets for dichroism experiments for example, create perturbations coming from the experimental hall. It can cause position noise of 10 µm and 5 µm respectively in H and V planes [3].

Changes in insertion device settings are also sources of orbit change. Even with feedforward corrections for each ID that strongly reduce orbit changes, perturbations of a few micrometers remain. This is even larger if the feedforward power-supplies involved are not perfectly synchronized [3].

Short Term

Typical Booster cycling frequencies, between 1 and 10 Hz, may affect beam stability. Moreover, vibrations from the ground, cooling water circuits or rotating machinery are transmitted to the vacuum chamber and magnets. It gets amplified at the girder resonance frequencies. The girder vibration modes lie between 10 and 60 Hz, depending on the design. Finally, the 50 or 60 Hz mains and their harmonics usually appear in beam spectra.

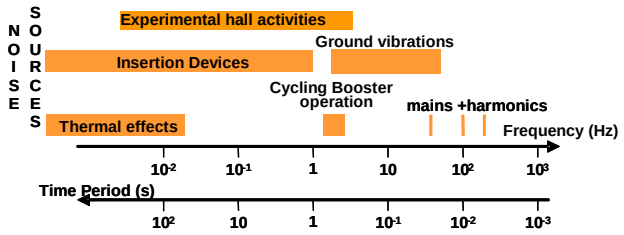


Figure 1: Spectral representation of perturbation sources in a storage ring.

The beam spectrum is machine dependent. A measurement at ELETTRA in shown in Fig. 2. Vibration of quadrupole magnets at 23 Hz as well as the 50 Hz mains frequency and its harmonics are clearly apparent [4]. Fast orbit correction systems are mandatory to suppress those perturbations.

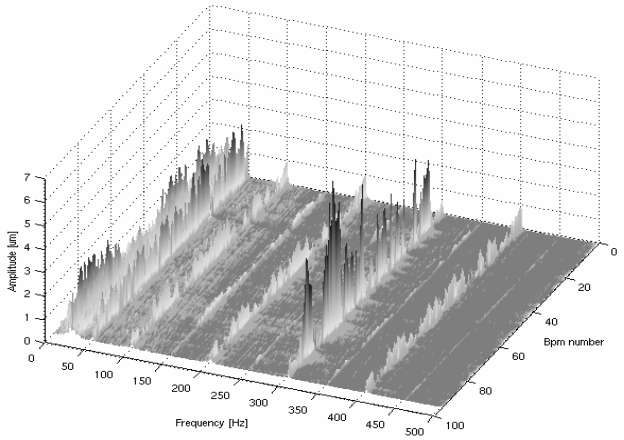


Figure 2: Plot of ELETTRA BPMs amplitude spectra.

GLOBAL ORBIT CORRECTION

The most commonly used algorithm for beam position correction is based on Singular Value Decomposition (SVD) [5]. It provides the inverse response matrix R^{-1} to be used for computing the corrector additional current ΔI:

$$\Delta I = R^{-1} * \Delta U \qquad (2)$$

ΔU is the difference between actual and reference orbits. The correction method is global since it uses all (or a large part of) BPMs and correctors. Local feedback systems are efficient, but a limited number of them can be implemented on a Storage Ring because residual imperfections of a few percent outside the local correction areas add up and spoil the beneficial effects of each local system. Global feedback systems are often preferred with the increasing number of user controlled IDs that perturb the beam orbit.

CORRECTOR SPEED ISSUES

The performance of automatic orbit correction systems, and in particular their bandwidth, will directly depend on the bandwidth of the power-supplies and correctors used for this correction. The important part of the correction spectrum lies between 0 and 150 Hz.

Storage rings are equipped with a set of dipole steering magnets for correcting the closed orbit. Their iron-core makes the magnetic field stronger. Their power supplies must be very stable. In some SR facilities like DIAMOND [6], ESRF-U [7], ELETTRA [8], SLS [9], or SPEAR3 [10], those strong correctors are also used for fast correction. But for one or more of the following reasons, these correctors might not be able to perform fast corrections:

- DAC granularity: On the one hand, the strong correctors must have a large dynamic range for correcting long term alignment drifts; on the other hand, fast corrections need a very fine granularity but over a small amplitude range. As an example, NSLS II stability requirements would imply a granularity of 3 nrad over a full scale of 0.8 mrad if applied to the strong correctors. Choosing two different sets of correctors has been preferred for avoiding power-supplies that at the same time are fast, strong, and have a high granularity [11]. The lower cost is also a motivation.
- Bandwidth limitations: Corrector inductance and power supply rise-time can limit the speed of the correctors. But most often, the limitation comes from the eddy currents in the vacuum chamber that suppress the magnetic field on the beam trajectory. With strong correctors located over aluminum vacuum chambers (or any high conductivity material), those eddy currents will reduce the feedback bandwidth to a few Hertz, incompatible with fast orbit correction. In this case other correctors dedicated to fast correction, can be added. At SOLEIL and NSLS II dedicated power-supplies drive air coil magnets installed

over stainless-steel bellows. In this way, bandwidths over 2 kHz are achievable, as shown in fig. 3.

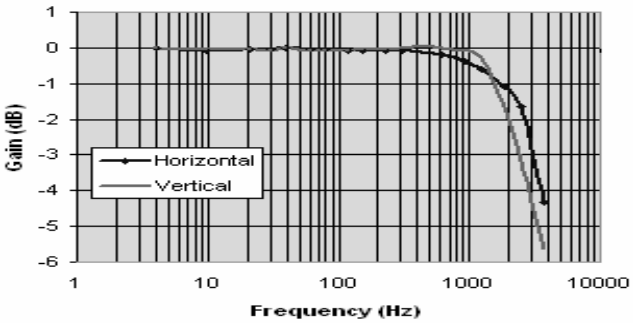


Figure 3: Bandwidth of dedicated power supply + fast air-coil corrector over a stainless steel bellow measured at SOLEIL.

- Historical reasons: older machines with slow corrector power supplies or with correctors installed over aluminium vacuum chambers can implement a fast global orbit feedback at relatively low cost by adding air correctors over stainless steel sections of their vacuum chamber.

FAST AND SLOW ORBIT CORRECTIONS WORKING TOGETHER

We now consider orbit feedback systems with two different sets of magnets for fast and slow corrections. If the two systems are active within a common frequency range they will fight against each other causing quickly a power supply saturation of the weakest system, usually the fast one. A test at SOLEIL showed that the Fast Orbit FeedBack (FOFB) could reach saturation after only ten cycles of the Slow Orbit FeedBack (SOFB). Different approaches have been used over the years, in order to keep up with the increasingly tight stability requirements.

Frequency Dead Band

The first approach was to separate the frequency domains of the 2 systems. This method was used at ESRF, limiting its FOFB bandwidth to 0.1 Hz on the low frequency side [12]. The SOFB had a typical frequency range, from DC to 0.02 Hz. The main advantage is to keep completely independent the two systems. The dead-band needs to be wide enough [13]. The problem with this solution is that all beam spectrum components into the deadband are not corrected and that this frequency range is not always quiet (insertion devices, crane, etc…)
With the increasing number of exotic insertion devices controlled by the users in a wide speed range together with tighter beam stability requirements, this frequency domain cannot be left without correction.

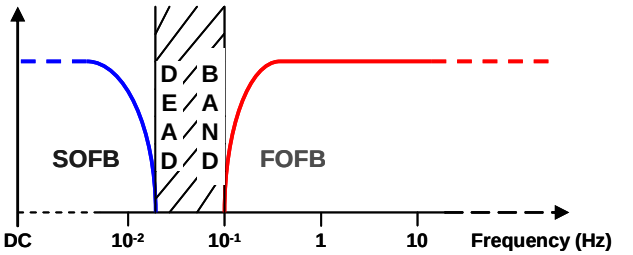


Figure 4: Frequency dead-band between slow and fast orbit feedback systems.

Fast Correction Alone, Down to DC

Then, another approach is to use a Fast Orbit Feedback System alone, with an active frequency range down to DC. It solves the problem of uncorrected perturbations at low frequencies, but presents a limitation due to the relative weakness of fast correctors. They are generally designed to correct small perturbations at high speed (thanks to their low inductance), but have a limited amplitude range of correction (~20 µrad) that brings the correctors into saturation after a few hours or days. The problem can be solved by periodically downloading the DC part of the fast correctors into the slow ones as follows:
Read first the DC-current profile ΔI_{FOFB} of the fast correctors. From this profile and the response matrix R_{FOFB} one computes the difference orbit ΔV:

$$\Delta V = R_{FOFB} * \Delta I_{FOFB} \quad (3)$$

Then this orbit can be corrected with the slow correctors using their inversed response matrix R^{-1}_{SOFB}:

$$\Delta I_{SOFB} = R^{-1}_{SOFB} * \Delta V \quad (4)$$

When applying this new setting ΔI_{SOFB} to the slow corrector, the fast orbit feedback will automatically compensate the transient perturbation and bring the DC-current in its correctors down to 0. This download process can be applied manually or done automatically at a defined rate or after detecting that the fast correctors are close to saturation. This method was used in operation for a few months at SOLEIL with one download a day at the beginning and later a download rate of 10 seconds (fig 5).

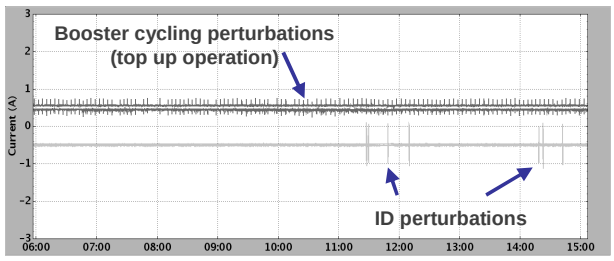


Figure 5: Trend (9 hours operation) on two SOLEIL fast correctors with DC download algorithm.

With this approach, the orbit stabilization efficiency depends on the fast corrector placement. But because of

the lack of space, they are generally less numerous than the strong correctors and are installed at the ends of the straight sections where stability requirements are the tightest. Fewer correctors do not correct as many spatial modes and the long term stability in the arcs is affected.

A similar downloading process can be applied periodically to the RF frequency for correcting the orbit circumference drifts. An external process extracts the dispersive part from the corrector pattern and calculates the new frequency to apply to the RF master oscillator. DIAMOND [14] and SOLEIL [15] correct the dispersion part of the orbit in this way, every ~10s.

Interaction between Fast and Slow Orbit Feedback Systems

This approach makes the slow and fast systems work together in the low frequency range. It combines the advantages of the two systems: very good long term stability for every source point and correction in the whole frequency spectrum.

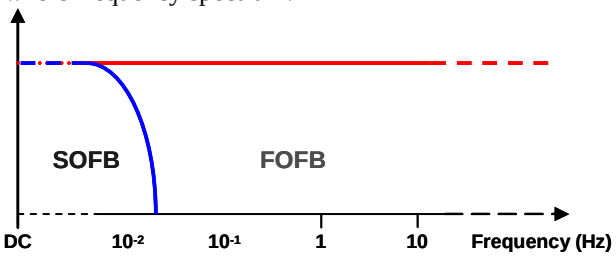


Figure 6: Slow and Fast Orbit Feedback System on a common frequency domain.

As previously mentioned, a common correction frequency range quickly leads to fast correctors saturation. An interaction between the two systems can actually solve the problem.

APS developed a FOFB system that, although not correcting down to DC, has nevertheless a frequency overlap with the SOFB. To make the two systems work together, the slow system predicts the slightly different orbit at its next iteration and transfers it as a new reference to the fast system. As a consequence the Fast System will not see the perturbation created by the slow correction and will not try to compensate it [16]. ALS adopted a similar algorithm, extending the FOFB bandwidth down to DC [13]. But in those two machines, the fast correctors are a subset of the slow ones. At SOLEIL with a set of fast correctors different from the slow ones the combined system was not stable. The different sets of correctors lead to different residual orbits. Even if their contributions are small, those errors accumulate and the current in the fast correctors go to saturation after a few minutes of operation.

The solution presently in operation at SOLEIL consists in combining the orbit prediction algorithm with the DC download algorithm. At each iteration, the SOFB does the following:

- Calculate the new setting $\Delta I1_{SOFB}$ to apply to the slow correctors in order to cancel the difference ΔU between actual and golden orbits:

$$\Delta I1_{SOFB} = R^{-1}_{SOFB} * \Delta U \quad (5)$$

- Predict the orbit change ΔW after correction:

$$\Delta W = R_{SOFB} * \Delta I1_{SOFB} \quad (6)$$

Because of the residual orbit, ΔW is not equal to ΔU.

- Calculate the new setting $\Delta I2_{SOFB}$ to apply to the slow correctors to cancel the DC part of the fast corrector currents. From (3) and (4) we have:

$$\Delta I2_{SOFB} = R^{-1}_{SOFB} * R_{FOFB} * \Delta I_{FOFB} \quad (7)$$

- At the same time subtract the orbit change ΔW from the reference orbit of the FOFB system and apply the new setting ΔI_{SOFB} to the slow correctors given by (5) and (7):

$$\Delta I_{SOFB} = \Delta I1_{SOFB} + \Delta I2_{SOFB} \quad (8)$$

In short, the slow system corrects two defects: i) the difference between actual and golden orbits and ii) the orbit created by the fast correctors DC component. The FOFB system, running simultaneously, is automatically relieved of the DC part in its correctors and does not fight the slow correction thanks to the periodic change of its reference orbit.

Efficiency

The beam stability benefits greatly from the combination of the two systems. At SOLEIL one of the important improvements has been the long term stability at the bending magnets (BM) source points. Indeed, as the fast correctors are located upstream and downstream of each straight section, the stabilization in the arcs was not efficient enough with the FOFB alone. On the BM photon beam slow drifts up to 15 µm could be observed in the vertical plane. With the two feedback systems working together, those drifts have been reduced to about 2 µm (Fig. 7).

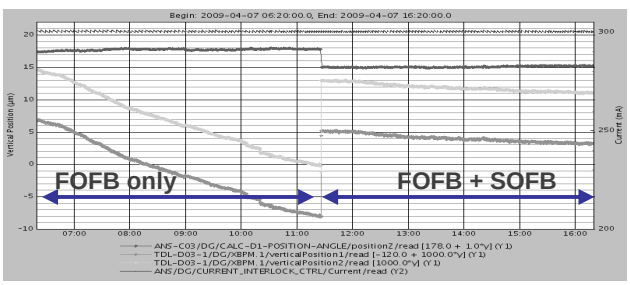


Figure 7: Vertical orbit stability at a BM source point measured by an e-BPM (grey) and a photon-BPM (orange and green).

ORBIT FEEDBACK SYSTEMS STATUS

This section presents a description of the FOFB implementations in several storage rings worldwide (Table 1). Depending on the machine specific criteria (stability requirements, technical possibilities, historical or cost reasons) a solution with one or two sets of correctors has been implemented. It influences the correction bandwidth; it is generally greater with systems with specific fast correctors (150 Hz to 500 Hz) than with systems using strong correctors for fast corrections (60 Hz to 130 Hz). Nevertheless, at lower frequencies both solutions give an equivalent efficiency. One common characteristic for all systems is the continuous frequency range of efficiency from DC to the 0 dB point without any frequency dead band. This has become mandatory with the increasing number of user controlled insertion devices installed on today's light sources.

Table 1: Fast Orbit Feedback implementations in storage rings:

SR Facility	FB type (users operation)	Number of sets of correctors	Bandwidth
ALBA*	Fast	1	DC-130 Hz
ALS	Slow + Fast	1 (fast corr. are a subset of slow ones)	DC-60 Hz
APS	Slow + Fast	1 (fast corr. are a subset of slow ones)	DC-100 Hz
DIAMOND	Fast	1	DC-130 Hz
ELETTRA	Fast	1	DC-150 Hz
ESRF	Slow + Fast	2	DC-150 Hz
ESRF-U*	Fast	1	DC-150 Hz
NSLS II*	Slow + Fast	2	DC-500 Hz
PETRA III*	Slow + Fast or Fast	2	Dead-band or DC-500 Hz
SLS	Fast	1	DC-100 Hz
SOLEIL	Slow + Fast	2	DC-250 Hz
SPEAR3	Fast	1	DC-100 Hz
SSRF*	Slow + Fast	2	DC-100 Hz

* Feedback systems that are not yet commissioned

CONCLUSION

Several machine implemented a scheme with the fast correction performed by strong correctors. Such a scheme applies mainly to new machines in the design phase, but with some conditions on old ones (stainless steel vacuum chambers, power-supplies at high update rate, and laminated corrector yoke). It has been demonstrated that slow and fast orbit feedback systems with different sets of correctors can work together. That solution applies to new machines by solving the power supply granularity problem posed by the increasingly tight stability requirements and also to many old machines to implement fast correctors over stainless steel bellows at the end of the straight sections. Then, it becomes possible for many machines to implement a stability upgrade at a reasonable cost.

ACKNOWLEDGEMENTS

I would like to thank Christoph Steier (ALS), Eric Plouviez (ESRF), Guenther Rehm (DIAMOND), and Marco Lonza (ELETTRA) for fruitful discussions on Fast Orbit Feedback Systems. I also thank all the other colleagues who sent me extensive information on their orbit feedback systems.

REFERENCES

[1] L. Nadolski, "Between Model and Reality II", Beam Diagnostics CAS 08, Dourdan.
[2] M. Böge, "Orbit Stability at the SLS", IWBS 04, Grindelwald.
[3] L. Nadolski et al, "Orbit Stability Status and Improvement at SOLEIL", EPAC 08, Genoa.
[4] M. Lonza et al., "BPM Detectors Upgrade for the ELETTRA Fast Orbit Feedback, DIPAC 07, Venice.
[5] V. Schlott, "Global Position Feedback in SR Sources", EPAC 2002, Paris.
[6] M. T. Heron et al.," Performance and future development of the Diamond Fast Orbit Feedback System", EPAC 08, Genoa.
[7] E. Plouviez et al., "Improvement of the fast orbit correction on the ESRF storage ring", these proceedings.
[8] M. Lonza et al.,"Commissioning of the ELETTRA Fast Orbit Feedback System", PAC 07, Albuquerque.
[9] T. Schilcher et al., "Commissioning and operation of the SLS Fast Orbit Feedback", EPAC 04, Lucerne.
[10] A. Terebilo et al., "Fast Global Feedback System in SPEAR3", EPAC 06, Edinburgh.
[11] L.H. Yu et al., "The Performance of a Fast closed orbit Feedback System with Combined Fast and Slow Correctors", EPAC 08, Genoa.
[12] E. Plouviez et al., "Upgrade of the Global Feedback of the ESRF Storage Ring", DIPAC 05, Lyon.
[13] C. Steier et al.," Operational Experience Integrating Slow and Fast Orbit Feedbacks at the ALS", EPAC 07, Lucerne.
[14] J. Rowland et al., "Status of the DIAMOND Fast Orbit Feedback System", ICALEPCS 07, Knoxville.
[15] L. Nadolski et al., "Beam Position Orbit Stability Improvement at SOLEIL", PAC 09, Vancouver.
[16] C. Schwartz et al., "Compensating the Frequency Deadband of the APS Real-Time and DC Transverse Orbit Correction Systems, PAC 01, Chicago.

DIGITAL BPM SYSTEMS FOR HADRON ACCELERATORS*

J. Belleman†, S. Bart-Pedersen, G. Kasprowicz, U. Raich, CERN, Geneva, Switzerland

Abstract

The CERN Proton Synchrotron has been fitted with a new trajectory measurement system (TMS) [2]. Analogue signals from forty beam position monitors are digitized at 125 MS/s, and then further treated entirely in the digital domain to derive the positions of all individual particle bunches on the fly. Large FPGAs handle all digital processing. The system fits in fourteen plug-in modules distributed over three half-width cPCI crates. Data are stored in circular buffers of large enough size to keep a few seconds-worth of position data. Multiple clients can then request selected portions of the data, possibly representing many thousands of consecutive turns, for display on operator consoles. The system uses digital phase-locked loops to derive its beam-locked timing reference. Programmable state machines, driven by accelerator timing pulses and information from the accelerator control system, direct the order of operations. The cPCI crates are connected to a standard Linux computer by means of a private Gigabit Ethernet segment. Dedicated server software, running under Linux, knits the system into a coherent whole.

INTRODUCTION

The CERN Proton Synchrotron (PS) is a 200 m diameter 26 GeV alternating-gradient synchrotron built in 1959. It is part of the injector complex that prepares protons and ^{208}Pb ions for the LHC.

The PS is equipped with forty electrostatic BPMs, each delivering three analogue signals: A horizontal and vertical displacement signal, Δ_x, Δ_y and an overall sum Σ. The 120 BPM signal channels are digitized using LTC2255, 14 bit, 125 MS/s ADCs, and the digital sample streams are then further processed into per-bunch positions using Xilinx Virtex-4 FPGAs. Results are stored into a memory large enough to store several seconds worth of data (Fig. 1).

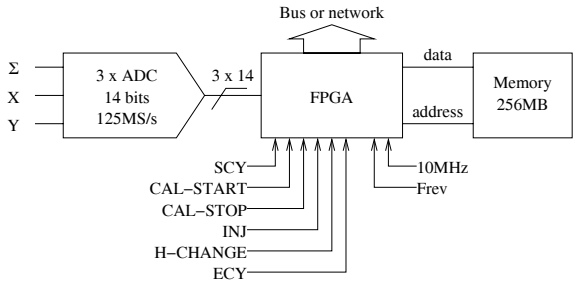


Figure 1: Signal processing block diagram for one BPM.

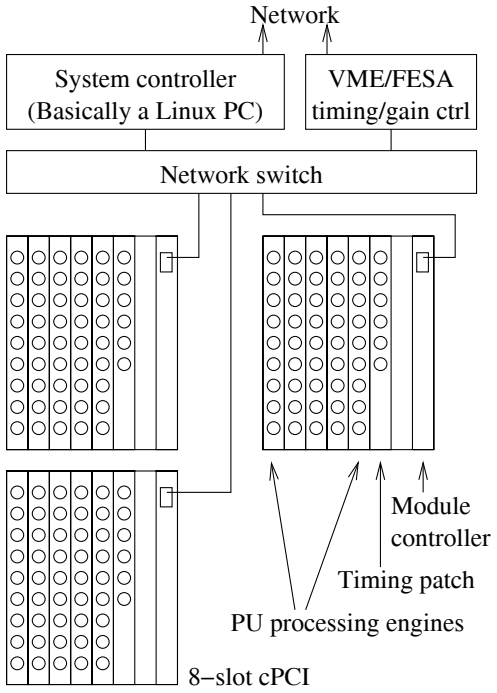


Figure 2: TMS block diagram.

Nine channels, corresponding to three BPMs, are combined on a single cPCI digitizer module. This module is the only board that has been custom designed for this application. Fourteen of these modules are distributed over three half-width cPCI crates (Fig. 2). Each crate also contains a standard, off-the-shelf Concurrent Technologies PP410 module controller. A private Gigabit Ethernet segment connects the module controllers to a Supermicro Core ™ i7, model 5046-XB system controller. The system controller also acts as a BOOTP server and NFS file server for the cPCI processor boards. The three module controllers and the system controller all run Fedora Linux. A server daemon running on the system controller provides an RPC-based interface through which the whole system appears as a coherent single instrument. The server can handle multiple simultaneous independent clients. The system was built to CERN's specification by British industry [1].

For reasons of standardization and uniformity, a server based on CERN's Front-End Software Architecture (FESA) mediates between the TMS and control room ap-

* We acknowledge the support of the European Community-Research Infrastructure Action under the FP6 "Structuring the European Research Area" programme (DIRAC secondary-Beams, contract number 515873)

† Jeroen.Belleman@cern.ch

plications. The FESA server is responsible for informing the TMS of the accelerating cycle to be treated at the appropriate time, and for collecting and publishing data requested by the control room operators. It also controls BPM pre-amplifier settings, maintains and applies calibration data and provides access to diagnostic information. It runs on a processor installed in a separate VME crate, with network connections to both the TMS private segment and to the accelerator control network. The VME crate furthermore contains the hardware to generate the various timing pulses and interrupts, and to control the BPM preamplifiers.

SIGNAL PROCESSING

The system determines the position of the centre of charge of each particle bunch by integrating each of the BPM signals, Σ, Δ_x and Δ_y over the length of the bunch and normalizing against Σ [2][3].

$$X = S_x \frac{\Delta_x}{\Sigma} + E_x \qquad (1)$$

The integration is implemented as a simple addition of the samples belonging to a given bunch. The integrals are then piped into a circular buffer. The actual position calculation (1), which also involves scaling (S_x) and a correction for BPM alignment errors (E_x), is deferred to the time at which data is actually requested for display.

Due to the high-pass frequency response of the BPMs, the base line of the signal droops so that the integral over a full bunch period would tend to zero. To fix this, base line restoration is applied before integration. This is done by passing the ADC data through a numerical filter with a response complementary to the high-pass characteristic of the BPM channel (Fig. 3). The base line is then nominally

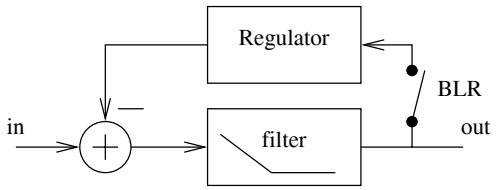


Figure 3: Principle of Base Line Restoration.

flat, but at an indeterminate value, potentially very large. A Base Line Restoration timing signal (*BLR*), is used to collect samples from the baseline to be pumped into a feedback regulator that drives the baseline toward zero.

Beam-synchronous Timing

The bunch-wise processing of the input signals requires beam-synchronous timing signals. The task is complicated by the use of bunch splitting or merging, changing the harmonic number of the machine, possibly several times in a single cycle.

Each of the BPM processing channels implements a numerical Phase Locked Loop (PLL) algorithm, locking a Numerically Controlled Oscillator (NCO) to the revolution frequency F_{rev} prior to beam injection, and to the BPM Σ signal afterward (Fig. 4). All required beam-synchronous

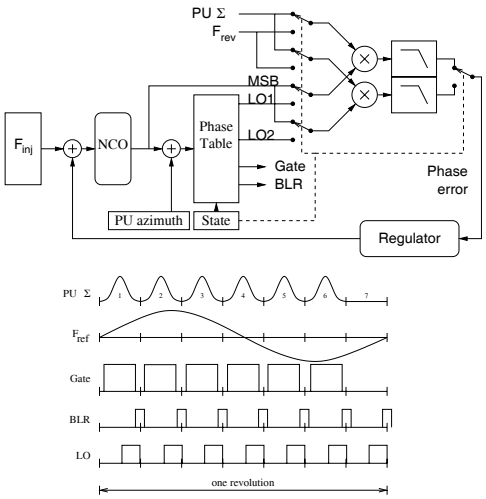


Figure 4: Principle of beam-synchronous signal generation.

signals are then derived from this PLL. The *LO* signal is needed to compare the phase of the Σ signal with the reconstructed reference frequency to close the loop. A *Gate* signal designates the samples belonging to each bunch. A *BLR* signal is generated for Base Line Restitution.

Event Sequencing

From the point of view of the TMS, the acceleration cycle is punctuated by six events produced by the accelerator timing system (Fig. 1). The events mark the start and end of an acceleration cycle, the beginning and end of a calibration period, beam injection, and the instants at which bunch splitting occurs. Some events may happen more than once in a given acceleration cycle. None of these events are under the control of any of the clients of the TMS, thus decoupling the system's behaviour from the clients' whims.

The events drive a state machine that can be freely programmed to traverse any desired sequence (Fig. 5). A few states are reserved as Start, End, or Error states. Each state has an associated internal signal routing –the switches in Fig. 4–, and tables for the generation of *LO*, *Gate* and *BLR* signals. The appropriate state machine program is selected and loaded prior to the start of each acceleration cycle. The state machine programs are kept in a number of small text files, one for each type of acceleration cycle. Loading one takes about 20 ms.

Of the six timing events used, only one, the injection trigger (INJ), needs to be accurate to within one RF period, thus marking the first RF bucket to be filled. All the other timing pulses are synchronized using the site-wide 10 MHz standard clock. The ADC sampling clock and all of the

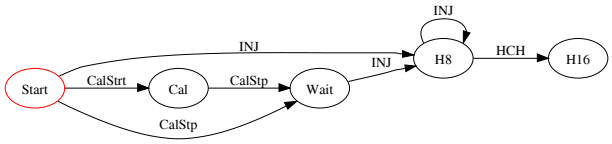


Figure 5: A state machine controls the system's behaviour according to the occurrence of accelerator timing events.

signal processing are also locked to this standard, so the whole system marches to the same beat. The effect of an event is delayed according to the azimuthal position of each BPM with respect to the injection point, thus ensuring the same data structure in every channel.

SOME MEASURED RESULTS

While no in-depth comparison of the new TMS with the old system has yet been completed, it has delivered a number of interesting results. The possibility of the TMS to acquire over many, many turns is very useful for injection and ejection studies. The system will also deliver data to the Automatic Beam Steering (ABS), which calculates field corrections in order to optimize the beam injection trajectory. A few examples of P^+ beam acquisitions are shown in Figs. 6, 7 and 8.

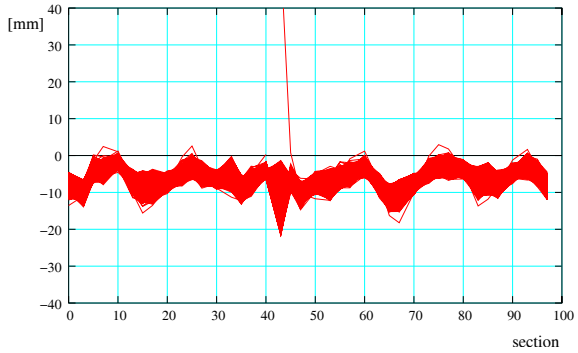


Figure 6: A 1000-turn injection trajectory of a single-bunch P^+ beam. The beam is injected in section 43. During the first few-hundred turns, it makes large excursions around its equilibrium orbit.

CONCLUSION

The new trajectory measurement system delivers both individual bunch trajectories and averaged orbits, over a large number of consecutive turns [4]. It advantageously replaces the old CODD trajectory measurement system, which could only measure a single two-turn trajectory every 5 ms, and which was blind during bunch splitting.

The TMS has been running since September 2008. Software to allow convenient use by the control room crew is nearing completion. Measurements that previously needed painstaking collection of small parcels of data spread over many successive acceleration cycles can now be acquired

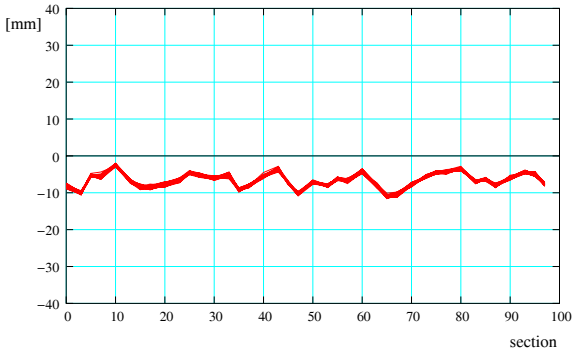


Figure 7: A 25-turn trajectory of a single-bunch P^+ beam a few thousand turns after injection. The beam now follows the same trajectory turn after turn.

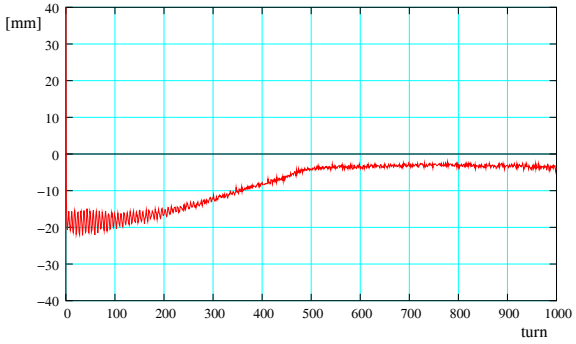


Figure 8: The position of a P^+ bunch in PU43 over 1000 turns starting from injection, showing injection oscillations and the collapse of the injection bump.

in a few seconds and in a single shot. The system has been demonstrated to have no trouble delivering over 700000 points of contiguous trajectory data, or full-cycle turn-by-turn positions from selected BPMs. However, network bandwidth, post-processing power and FESA overhead impose a limit of 200000 points delivered to the end user.

REFERENCES

[1] Alpha-Data/Beam Ltd., "The CERN Trajectory Measurement System: Support and Development Information", `http://portal.beam.ltd.uk/support/cern`

[2] J.M. Belleman, "A New Trajectory Measurement System for the CERN Proton Synchrotron", DIPAC'05, Lyon, June 2005, CTTM01, pp. 137-139, `http://www.JACoW.org`

[3] G. Kasprowicz, J.M. Belleman, U. Raich, "Digital Beam Trajectory and Orbit System for the CERN Proton Synchrotron", DIPAC'07, Mestre, May 2007, TUPB09, pp. 75-77, `http://www.JACoW.org`

[4] E. Bravin, J. Belleman, M. Chanel, M. Ludwig, E. Métral, G. Métral, J.P Potier, U. Raich, R, Scrivens, R. Steerenberg, "Specification of the Beam Position Measurement in the PS Machine", AB-Note-2004-001-ABP, January 2005.

FEM SIMULATIONS – A POWERFUL TOOL FOR BPM DESIGN

P. Kowina, P. Forck, W. Kaufmann, P. Moritz, GSI Darmstadt, Germany
F. Wolfheimer, T. Weiland, TU Darmstadt, Germany

Abstract

This contribution focuses on extensive simulations based on Finite Element Methods (FEM) which were successfully applied for the design of several Beam Position Monitor (BPM) types. These simulations allow not only to reduce the time required for BPM prototyping but open up new possibilities for the determination of characteristic BPM features like signal strength, position sensitivity etc. Since a precise visualization of the signal propagation along the BPM structure is possible, effects like field inhomogeneities or cross-talks between adjacent electrodes can be controlled. Moreover, modern simulation programs enable to define a charge distribution moving at non relativistic velocities, which has an impact on the electromagnetic field propagation. It is shown that for slow ion beams the frequency spectrum of the BPM signal depends on the beam position. Simulation methods are discussed in the context of different BPM realizations applied in hadron accelerators. All simulations described in this paper were performed using CST Suite ® [1].

LINEAR-CUT BPM

Proton and ion synchrotrons are usually operated at the bunching frequency f_{rf} in the order of few MHz. In these accelerators bunches typically have a length of a several meters. For such beam parameters linear-cut BPMs are preferred due to its excellent linearity of the position determination and the independence of the measurements in the orthogonal directions [3]. Moreover, the full transversal coverage by the electrodes allows precise position measurements even for the beams with transversal large and complex charge distribution. An example of such a BPM, sometimes called "shoe-box" due to its cuboid shape, is shown in Fig. 1. Also other geometrical realizations, having e.g. elliptic cross section, show the same electromagnetic properties, see [4] and references therein.

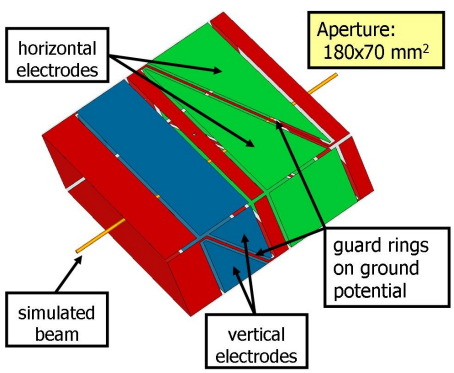


Figure 1: An example of the linear-cut BPM [2].

The most important BPM parameter is its *position sensitivity*, defined as an response of the BPM on the beam displacement [3].

Assuming the bunches much longer than the BPM itself, the electric field propagation in the BPM can be well approximated with TEM wave traveling on a wire. The eventual influence of effects caused by non-relativistic beams is minor and can be neglected. Based on this assumption the BPM position sensitivity can be experimentally determined using so called stretched wire method, see e.g. [5]. In this method the amplitude changes of the signals induced in the electrodes are measured as a response on the changing wire position.

Similarly, position sensitivity can be obtained by means of FEM-based simulations that allow optimization of the BPM design entering in the time consuming prototyping phase. Since simulations enable three dimensional field visualization, the field inhomogeneities or distortions effecting BPM linearity caused by e.g. structure discontinuities can be found and eliminated.

The optimizations performed for linear-cut BPMs with rectangular as well as elliptic cross sections and different electrode arrangements are described in Refs. [2, 4, 6]. It was investigated how the presence of different BPM components like e.g. guard ring influence the position sensitivity and linearity of the position determination. In order to investigate the influence of the whole environment on the position readout, the complete BPM was modeled together with the surrounding vacuum chamber [7]. All components were defined with realistic material permittivity and conductivity. The volume was divided in 3-dimensional hexahedral meshes with typically 10^6 to 10^7 cells – depending on the model complexity. The number of meshes is mainly blown-up by small curved parts or elements oriented diagonally with respect to the main coordinates. The beam was simulated as a traveling wave on a wire using the CST Time Domain Solver and thus reproducing the stretched wire method. An excitation was defined as a Gaussian shaped pulse with length of 5 μs corresponding to the bandwidth of 200 MHz. The position sensitivity was calculated from S-parameters expressed in frequency domain as described in [2]. The goals in optimization of the BPM design were: i) enlarged position sensitivity, ii) linearity of the position determination, ii) reduction of the offset between electrical and geometrical center of the BPM and iv) independence of measurements with respect to the orthogonal directions.

Here we concentrate on the aspect of cross-talk between adjacent BPM electrodes that decreases the difference of

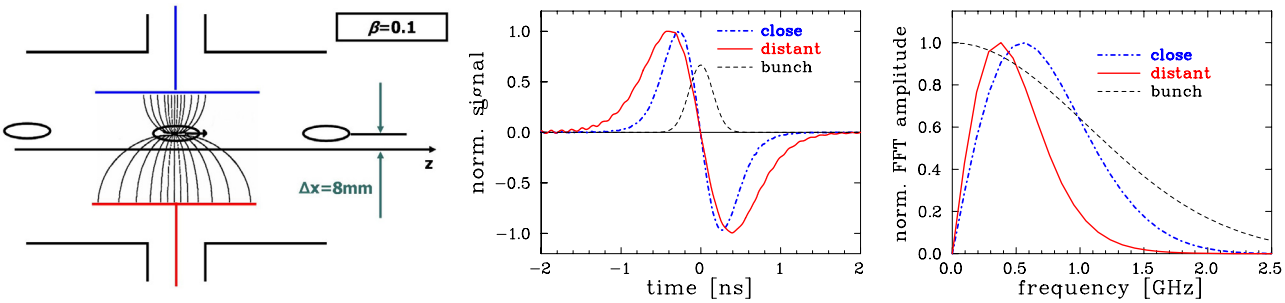


Figure 2: The charge distribution of the bunch moving with $\beta = 0.1$ for 8 mm displaced beam (left). Corresponding signals induced in BPM electrodes (middle) and their frequency spectra (right), for further parameters see text.

signal amplitudes and, in consequence, diminishes BPM position sensitivity. The cross-talk can be measured as response through BPM using network analyzer connected to both electrodes. The result are frequency dependent S21 parameters. Similar cross-talk determination was performed by means of FEM simulations for the geometry shown in Fig. 1 and two different realizations: based on metal coated ceramic or using metal plates. The results are summarized in Table 1.

Table 1: Cross-talk for Geometry from Fig. 1 and Realizations Based on Ceramics and Metal Plates

	ceramics	**metal plates**
no guard ring, 2 mm gap	-8.1 dB	-10.8 dB
with guard ring	-20.8 dB	-22.5 dB

The advantage of the ceramics based solution is its high mechanical stability and relatively easy positioning even of the very complex geometries that consist many elements [4]. The ceramic plates are coated from the inner side with thin metal sheet (typical thickness 50 μm). The shape of electrodes, guard rings etc. is formed by cutting out the fragments of metallization. However, a disadvantage of such solution is the significantly larger (compared to metal plates) coupling capacitance between adjacent electrodes caused by a large relative permittivity of ceramics $\epsilon_r = 9.6$. The better separation could be achieved by increasing the spacing between electrodes. However, for the investigated geometry this distance can not be extended much beyond 2 mm without significant distortion of the electric field in the gap neighborhood. The insertion of the separating ring in the gap between adjacent electrodes, see Fig. 1 improves electrodes separation by more than 10 dB,see Table 1 resulting in an increase of the position sensitivity by factor of two. The maximal reduction of cross-talk would be possible for a geometry based on metal plates equipped with separating ring but is hard due to complicated mechanical alignment of many separate BPM parts. In addition, simulations showed that such a small change in the geometry makes the position sensitivity less frequency dependent [2]. Similar results were obtained for the BPM with elliptic cross section [6].

LOW β EFFECTS FOR BUTTON BPM

In contrast to the assumptions in the previous section for bunch length comparable to the BPM length an influence of the effects due to non relativistic beams on the signal registered in the electrodes becomes more significant. An example for such an accelerator is FAIR proton linac presently under design at GSI [8, 9]. Its accelerating cavities will be driven with a frequency of 325 MHz. In this accelerator BPMs will be installed in several locations over 30 meters of the p-Linac. The beam energy varies along the p-Linac from 3 MeV to 70 MeV corresponding to a beam velocity $0.1 \leq \beta \leq 0.37$. A button type BPM geometry was chosen due to its compact mechanical realization and short insertion length to fit into the short inter-tank sections of the CH-cavities [8]. An additional problem that has to be faced is the rf–power leakage from accelerating cavities, that is especially disturbing in the inter–tank sections, where some BPMs are supposed to be installed. This may require analysis of the beam position on higher rf harmonics.

The position sensitivity of the BPM for non relativistic beams was theoretically investigated by R. Shafer in [10]. The author showed that the BPM sensitivity depends on its geometry, beam energy end frequency on which beam position is analyzed. However, this 2-dimensional formula can not be directly applied to the 3-dimensional BPM geometry, especially for button type BPMs.

The numerical simulations for low β beams were performed by means of CST PARTICLE STUDIO® [1] using the wake-field solver. As a source of excitation a pencil like beam was defined with a Gaussian-shaped longitudinal charge distribution that moves with $0.1 \leq \beta \leq 0.3$. The length of bunches was $\sigma = 150$ ps at a bunch frequency of 325 MHz. The simulated BPM model consists of four planar buttons of Ø 14.4 mm mounted within a beam pipe of Ø 30 mm. The position of the simulated beam was varied in 2 mm steps within the transverse plane in a range of ± 10 mm. The positions in vertical and horizontal direction were calculated from amplitudes of the signals induced in the opposite BPM electrodes using the 'delta over sum'-method (see Ref. [2]).

For non relativistic beams the electromagnetic field propagation is faster than the beam itself. Since the electric field distribution has a significant longitudinal com-

ponent [10] the distribution of the induced charge in the BPM electrodes depends on the relative distance between beam end electrode as shown in Fig. 2 (left): For the closer electrode the longitudinal charge expansion is more narrow than for more distant electrode. It means that signals registered in the closer electrode will have not only higher amplitude but also will be much shorter than that measured on the opposite BPM side, see Fig. 2 (middle). In this figure the signals registered in the electrodes obtained in the simulations for single bunch moving with the velocity of $\beta = 0.1$ are presented. Note that the amplitudes of the both signals Fig. 2 (middle) were normalized to unity for better visualization. The results of Fourier Transformation on these signals are shown in Fig. 2 (right). In the frequency spectrum of the signal registered in the distant electrode high frequency components are strongly suppressed. In consequence, the position calculated form both signals depends strongly on evaluation frequency. The response of the BPM was compared for the first three harmonics of the accelerating frequency, i.e. at 325 MHz, 650 MHz and 975 MHz and for $\beta = 0.1$ and $\beta = 0.3$ are shown in Fig. 3. For $\beta = 0.1$ the position sensitivity, given by the slope of the displayed curves, is significantly higher for the higher frequencies, what is in line with theoretical predictions of Shafer [10] and simulations presented in Ref. [11]. However, it is worth to be emphasize, that the sensitivity at the higher frequencies is larger only close to the BPM center but drops rapidly already for few millimeter beam displacement. For higher beam velocities i.e. for $\beta \geq 0.3$ the electric charge distribution squeezes [10] approaching more TEM wave. Thus the difference between longitudinal expansion of the signals registered in the opposite electrodes become negligible. Therefore, the position sensitivities for $\beta = 0.3$ is almost constant regardless the frequency at which they are analyzed. The effects described above are even stronger in the two dimensional position map. In Fig. 4 each node of grid corresponds to simulated beam position. The reconstructed beam positions show nonlinearities of the position readings. The strength of these distortions grows with the beam displacement typically for button type BPMs [3]. However, for the beam with $\beta = 0.1$, the position maps for first three rf harmon-

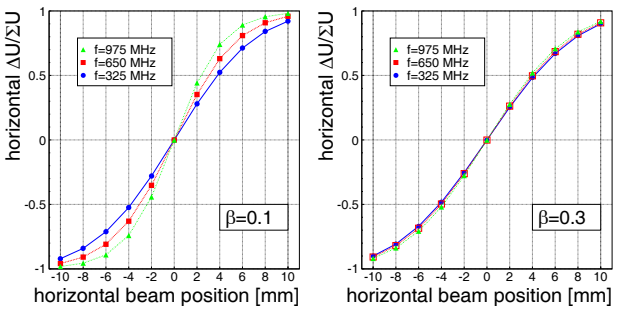


Figure 3: Reconstructed horizontal beam position calculated using 'delta-over-sum' algorithm from signal registered in horizontal buttons for zero vertical beam displacement.

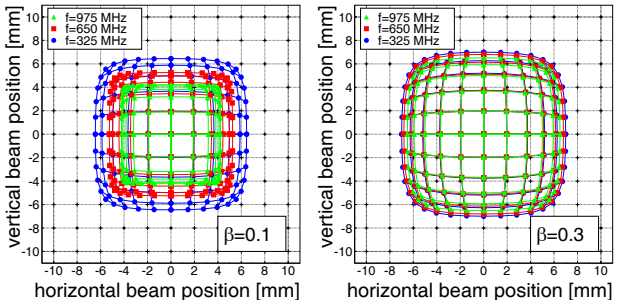


Figure 4: BPM response on variation of transverse beam position for $\beta = 0.1$ (left) and $\beta = 0.3$ (right).

ics significantly diverge from each other. These differences vanish for $\beta \geq 0.3$, Fig. 4 (right). This has to be taken into account when installing BPMs in different locations along the p-Linac: for each location a separate table with correction parameters specific for the given harmonic number and beam velocity have to be prepared. Moreover, BPMs are only usable for limited beam displacement. For this particular case for $\beta = 0,1$ and 3rd harmonics BPM is completely insensitive for the beam displacement larger than ± 5 mm i.e. exceeding $\sim$30 % of BPM aperture. Therefore, it should be kept in mind, that the choice of the rf harmonics is always trade between reduction of the influence of rf–leakage on the BPM signals and reduction of usable BPM aperture.

SUMMARY

The simulations based on finite element methods are very helpful to test different BPM approaches without time consuming prototyping. An 3-dimensional visualization of the field propagation allows to understand complex processes which simplifies optimization of BPM design. Moreover, simulations are successfully used for cases that could not be investigated using a test bench, i.e. for the non relativistic beams.

REFERENCES

[1] `http://www.cst.com`
[2] P. Kowina et al., *Proc. DIPAC'05,*, `POM033`, Lyon, p.114 (2005).
[3] P. Forck et al., *CAS "Beam Diagnostics"*, Dourdan (2008).
[4] P. Kowina et al., *Proc. DIPAC'07*, `TUPB16`, Venice (2007).
[5] D. Nölle et al., *Proc. LINAC 04*, `TUP69`, Lübeck, p.428 (2004) and references therein.
[6] P. Kowina et al., *Proc. EPAC'06*, `TUPCH013`, Edinburgh, p.1022 (2006).
[7] P. Kowina *CARE-ABI Workshop Lüneburg 2006*, see `http://adweb.desy.de/mdi/CARE/Lueneburg/ABI-Lueneburg.htm` (2006).
[8] "FAIR Baseline Technical Report", Vol. 2, GSI Darmstadt, Germany, 2006, p.335.
[9] L. Groening et al., *Proc. LINAC'06*, `MOP061`, Knoxville, p.186 (2006).
[10] R.E. Shafer, *Proc. BIW 1993*, Santa Fe, p.303 (1994).
[11] S.J. Park et al., *Proc. DIPAC'03*, `PT14`, Mainz, p.199 (2003).

STATUS OF BEAM IMAGING DEVELOPMENTS FOR THE SNS TARGET

T. J. Shea, C. Maxey, T. J. McManamy, ORNL, Oak Ridge, Tennessee, USA
D. Feldman, R. Fiorito, A. Shkvarunets , UMD, College Park, Maryland, USA

Abstract

The Spallation Neutron Source (SNS) continues a ramp up in proton beam power toward the design goal of 1.4 MW on target. At Megawatt levels, US and Japanese studies have shown that cavitation in the Mercury target could lead to dramatically shortened target lifetime. Therefore, it will be critical to measure and control the proton beam distribution on the target, in a region of extremely high radiation and limited accessibility. Several sources of photons have been considered for imaging the beam on or near the target. These include a freestanding temporary screen, a scintillating coating, Helium gas scintillation, optical transition radiation, and a beam-heated wire mesh. This paper will outline the selection process that led to the current emphasis on coating development. In this harsh environment, the optics design presented significant challenges. The optical system has been constructed and characterized in preparation for installation. Optical test results will be described along with predictions of overall system performance.

MOTIVATION

The design of targets for megawatt class accelerators is generally limited by material issues such as radiation damage, the ability to adequately cool the structures and the stresses generated by thermal profiles, coolant pressures and short pulse effects. Performance usually improves with more compact targets, while the engineering challenges increase. A key parameter for design is the beam profile and peak current density for a given beam energy since this drives the peak radiation damage rate, the peak volumetric heating in the target and the peak heating in any window system the beam passes through. The containment structure for liquid metal targets are also subject to cavitation damage for short pulse operation and studies for SNS and JSNS mercury targets have shown this may be a sensitive function of peak current density [1]. Generally, targets that are designed for high performance are close to the engineering limits and subject to potential damage if the beam density or power increases. Development of diagnostic systems which give accurate beam profile information during full power operation would allow targets to be safely designed with less engineering margin and with improved lifetime estimates based on radiation damage. Rapid detection of high beam density could be used to trip the beam for target protection.

As shown in Fig. 1, the SNS will operate at beam powers exceeding 1 MW by late 2009. Currently, from a location 9.5 meters upstream of the target, a harp provides the last profile measurement. This multi-wire device and upstream instrumentation provide data that help predict the properties of the beam at the target. Unfortunately, the estimated uncertainty of the current density prediction exceeds 25%. Assuming that the target's damage rate scales with the fourth power of the peak current density, a 30% increase in this parameter would reduce the target lifetime by over 60%. At J-PARC, another high power facility with a liquid metal target, the situation is significantly better. Their multiwire monitor sits much closer to the target and recent studies have demonstrated agreement between this device and image plate activation analysis [2]. During commissioning at the SNS, the situation was also better. A temporarily installed Al2O3:Cr screen provided a full 2 dimensional image of the beam at the target [3]. This uncooled device was removed in 2006 before high power operation began. Due to the valuable data provided by the temporary system, and in anticipation of high power levels, a new beam on target imaging system is being developed.

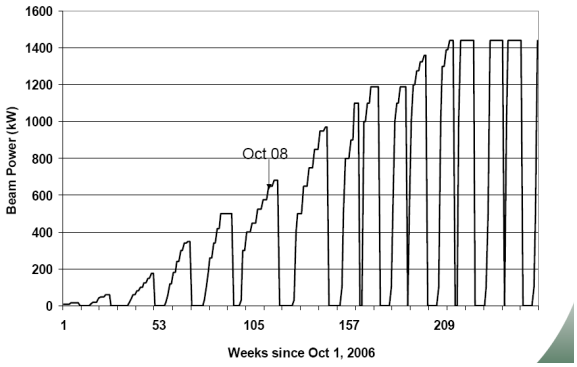


Figure 1: Ramp-up of SNS beam power.

IMAGING OPTIONS

Several sources of photons were considered. Their relative yields were calculated and are summarized in Table 1. In this table, the screen refers to a typical Chromium doped alumina material that was used in the temporary target imaging system. For the future, one option is to install a similar screen for low power tune-up after each target replacement. Before the pulse repetition rate is ramped up to achieve full power, the target would have to be retracted, the screen robotically removed, and the target reinserted. This procedure could take over one week and therefore impact operations.

Since a water-cooled shroud surrounds the target, a second option is to coat this shroud with a thin luminescent material. Heating of the scintillator would be limited, and it could be used during full power operations. As this option was selected for the initial deployment, it receives a detailed treatment in the next section.

Optical transition radiation is produced at the unmodified target surface. For 1 GeV protons, photon

yield is very low, but still may produce a detectable signal. Helium at a pressure of one atmosphere surrounds the target, leading to another source of photons. Excited by energy deposition from the incoming protons, this 99.9% pure gas will scintillate primarily in the shorter wavelengths of the visible spectrum. Helium fills the 2-meter long flight path between the target face and the proton beam window (which separates this region from the upstream accelerator vacuum). Therefore, to measure an accurate beam profile, optics with a shallow depth of field must be employed. Table 1 shows the estimated photon yield from a 10 mm thick slab of gas. When other sources are used to image the beam, Helium scintillation from a much thicker section could contribute a noticeable background.

At LANL in July of 2008, experiments were performed to observe both OTR and He scintillation with an 800 MeV proton beam. For this experimental configuration, a single pulse of $2.7 \cdot 10^{13}$ protons should have produced $3 \cdot 10^{8}$ visible photons within the imaging system's acceptance. Unfortunately, this initial test did not produce a discernable image. This was primarily due to two factors. The experiment was performed parasitically to a target test experiment and this led to severe constraints on the optical performance. In addition, a high gamma dose caused large background in the camera system. Follow-on experiments are anticipated.

Not shown in the table is the option of thermal incandescence. The most relevant example of this technique is employed for the SINQ target at PSI [4]. Although the light intensity is not proportional to beam current density, the system's sensitivity to off-normal conditions makes it an excellent input to a machine protection system.

Table 1: Photon Yields from the 1 GeV SNS Beam

Source	**Photon Yield (photons/proton/steradian)**
Screen (Cr:Al2O3)	$2*10^{+2}$
Coating (Cr:Al2O3)	$2*10^{+1}$
Optical Transition Radiation	$3*10^{-4}$
Helium scintillation (10 mm)	$3*10^{-3}$

Coating Development

Due to some early success and a tight schedule, a flame-sprayed Al2O3:Cr coating has been selected for the first replacement targets. During the LANL experiment mentioned above, several coating samples were tested and the results are shown in Fig. 2. To understand these results and further develop the coating process, collaboration was forged between SNS, ORNL's Material Science and Technology Division, and SUNY Stony Brook's Center for Thermal Spray Research.

Samples were analyzed with X-Ray diffraction and electron microscopy to determine the coating structure. These results were correlated with luminescent intensity measured by laser spectroscopy. UV excitation, and in some cases, proton beam excitation. The samples that were flame sprayed with large particle sizes retain enough alpha phase alumina to efficiently scintillate. Higher temperature and velocity processes (D-gun and plasma spray) fully melt the particles and produce a less porous coating, but would require an undesirable high temperature anneal to restore the alpha phase. With the goal of depositing a functional coating without overheating the expensive target assemblies, the collaboration continues to map the parameter space of material properties and spray conditions.

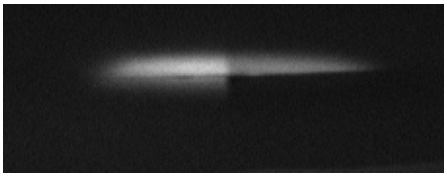


Figure 2: Test at LANL. Lower right quadrant: D-gun coating. Other quadrants: lower temperature flame sprayed coatings. Upper left: 1% Chromia. Upper right: 5% Chromia. Lower left: 0.5% Chromia.

At high beam power, the peak target surface temperature could approach 150 degrees C. Because the luminescent efficiency and decay time constant are both temperature dependant, gated imaging is being explored to simultaneously measure the beam profile and the temperature distribution.

OPTICAL SYSTEM

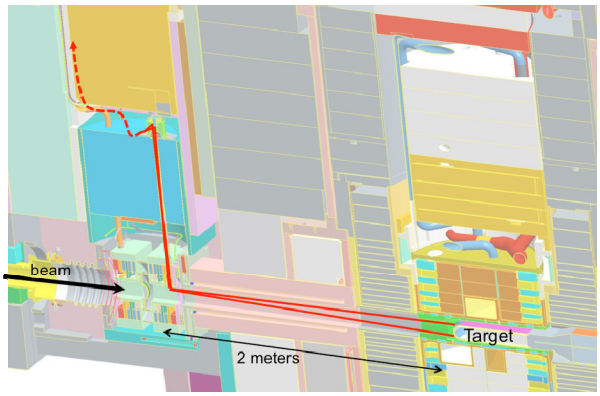


Figure 3: Optical path. Solid lines depict the reflective path and the dotted line depicts the beginning of the 11.5 meter long fiber bundle.

Imaging System Description

The proton beam imaging system was designed around a 25 mm viewport that extends 1.1 m vertically through a shielding plug above the proton beam window (PBW). A convex diamond-turned aluminum mirror mounted to the top surface of the proton beam flight tube (Fig. 4) serves as the input aperture of the imaging system.

The image from the convex mirror is reflected upward through the viewport, to a 45-degree flat diamond-turned aluminum mirror, that directs the light into a custom high-purity fused silica triplet lens. The turning mirror and lens are housed in a robust optics block securely mounted to the top of the PBW shielding plug (Fig. 4). The image

from the triplet lens is formed on the front face of an 11.5 m high-purity fused silica fiber optic imaging bundle (10,000 fibers) that terminates in a custom C-mount lens for attachment to a digital camera.

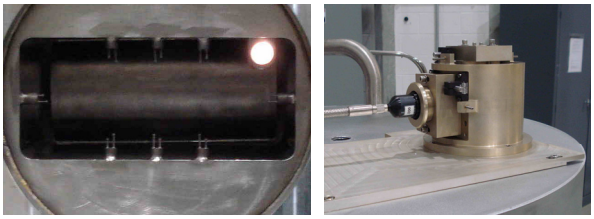


Figure 4: Left: Parabolic imaging mirror in PBW, reflecting viewport (illuminated). Right: Optics block, located 1 meter above parabolic mirror, with imaging lens and imaging fiber attached

Imaging System Design Considerations

The imaging system was designed to ensure that the necessary field of view would be preserved in the presence of several alignment uncertainties. In addition, the imaging fiber bundle was a long-lead-time item being manufactured in parallel with the other design activities and the manufacturer's specification on the input aperture of the fiber was nominally 1.1 mm with a +/- 10% tolerance. The design of the imaging system was based on the minimum fiber aperture of 1.0 mm with the goal of producing an image that was about 35% smaller than the minimum fiber diameter, to account for various alignment uncertainties. If the fiber were delivered at nominal aperture diameter (as expected) this margin would increase to about 42%. The resolution of the imaging system would be dictated by the projected size of the individual fiber elements. At the nominal fiber aperture diameter, the projected diameter of each individual imaging fiber onto the surface of the scintillator target would be 2.5 mm.

The use of an off-axis aspheric mirror as the input optic for the imaging system was motivated by field of view and imaging performance considerations but produced some distortion in the raytrace models (Fig. 5).

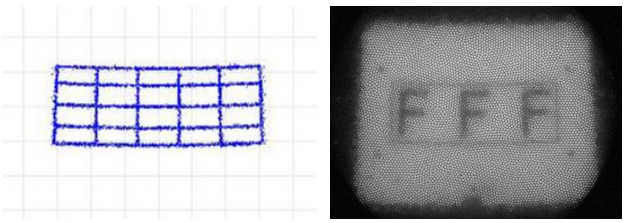


Figure 5: Left: optical modelling result showing anticipated image distortion. Right: Imaging system test target showing region of interest bounded by rectangle.

The optical throughput of the system is a function of the geometric loss from the scintillator to the input aperture, geometric loss within the imaging system itself, reflective losses at each optical element, packing fraction loss at the fiber and attenuation within the fiber itself. When all of these were taken into consideration, the system loss from the scintillator to the camera was calculated as 69 dB.

Imaging System Performance

Measurements of the assembled optical system were conducted using imaging targets with the 70 mm by 200 mm region of interest bounded by a rectangular border. The images produced (example shown in Fig. 5) indicated that the image was about 42% smaller than the fiber aperture, suggesting that the fiber bundle was delivered at near nominal diameter and that the resulting field of view is about 9.5º. The image geometry correlates reasonably well with the predicted distortion from the optical model, as shown in Fig. 5. Optical throughput of the system was measured using an illuminated integrating sphere at the object plane of the system with the output of the C-mount lens coupled into a silicon detector/amplifier. The optical loss was found to be approximately 65 db, which correlates well with the calculated loss of 69 db.

OUTLOOK

Installation of the optics and coating of a new target are both scheduled for Summer of 2009. Although significant risk remains, the goal is to achieve pulse by pulse imaging during the next run. An R&D program will continue to support development of more advanced coatings and optical components. Other applications are also under consideration.

ACKNOWLEDGEMENTS

Many people contributed to this effort over the past years including: G. Bancke, W. Blokland, A. Brunson, K.C. Goetz, E. Kenik, M. Lance, S. McTeer, F. Montgomery, S. Murray, M. Plum, S. Sampath, K. Thomsen, R. White.

REFERENCES

[1] B. Riemer, et. al, "Cavitation Damage Experiments for Mercury Spallation Targets at the LANSCE – WNR in 2005", Proc. Spallation Materials Technology 8, Taos, NM, October 2006.

[2] S. Meigo, et al., "Beam Commissioning of Spallation Neutron and Muon Source at J-PARC", Proc. PAC 2009, Vancouver (2009).

[3] T. J. McManamy, et. al., "SNS Target Viewscreen Design and Operation", AccApp 2007 Conference, Pocatello, UT (2007).

[4] K. Thomsen, "VIMOS, Beam Monitoring for SINQ", these proceedings (2009).

NON-DESTRUCTIVE BEAM POSITION MEASUREMENT IN A PROTON THERAPY BEAM LINE*

D.T. Fourie, L. Anthony, A.H. Botha, J.L. Conradie, J.L.G. Delsink, J.G. de Villiers, P.F. Rohwer, P.A. van Schalkwyk, iThemba LABS, P.O. Box 722, Somerset West 7129, South Africa
J. Dietrich#, Forschungszentrum Jülich, D-52425 Jülich, Germany

Abstract

Non-destructive beam position monitors (BPMs) have been in use at iThemba LABS for several years in the neutron therapy and radioisotope production beam lines, as well as in the transfer lines between the two K8 injector cyclotrons and the K200 separated-sector cyclotron. The sensitivity of these BPMs is limited by noise and pickup from the RF systems to about 300 nA in the high-energy beam lines. For proton therapy, using the scattering method, position measurements at beam currents as low as 20 nA have to be made. A new and more sensitive BPM as well as the electronic measuring equipment, using RF pickup cancellation and improved filtering, have been developed and installed in the proton therapy beam line. The BPM, the electronic equipment and the results of measurements at beam currents down to 10 nA for 200 MeV protons are described.

INTRODUCTION

Variable energy beams of light and heavy ions from ECR ion sources, as well as polarized protons, are used for nuclear physics research at iThemba LABS [1]. A high intensity 66 MeV proton beam can be switched between vaults for neutron therapy and radioisotope production for medical and industrial purposes. Proton therapy has been practised since 1993 with a 200 MeV beam at beam intensities of between 20 nA and 70 nA, using gas-filled multi-wire and segmented ionization chambers for beam position measurements. Non-destructive BPMs [2,3] that can fit in any of the standard beam diagnostic chambers together with other diagnostic elements were developed and installed in the high intensity beam lines. The sensitivity of these BPMs is not sufficient for use in the proton therapy line, owing to the dimensional restrictions on their length, noise in the solid state multiplexers and pickup from the main and the two flat-topping RF systems, that operate at the third and fifth harmonics, as well as from the rebunchers, that operate at the second and fourth harmonics.

The usefulness of the existing BPMs, not only for beam alignment and position monitoring, but also for detecting sources of beam instability, provided the incentive to investigate the possibility of building BPMs with greater sensitivity. Since beam phase measurements [4] in the separated-sector cyclotron could be made at beam currents in the nA range by cancellation of the relatively large pick-up signal, it seemed feasible that the same technique could be used for BPMs in the beam lines, where the level of the pick-up signals is much lower, to improve the sensitivity to such an extent that they can be used in the proton therapy beam line and perhaps also in the nuclear physics beam lines, where low intensity beams with variable energy are used. Tuned BPMs [5] were not considered because of the variable frequency operation of the accelerators. A new BPM, and a test set-up for signal processing electronics, similar to that which is used for beam phase measurements, was designed and built from available amplifiers, filters and measuring equipment. From past experience with the BPMs it is known that the level of the pick-up is the lowest at the third harmonic, i.e. at 78 MHz, for the 200 MeV proton beam. At 66 MeV the pick-up signal that is caused by the flat-topping system of the light-ion injector cyclotron is the lowest at the fifth harmonic, i.e. at 81.8 MHz. The third harmonic flat-topping system of the separated-sector cyclotron causes a much larger disturbance. The signal processing equipment was therefore built to operate in a 10 MHz band centred at 80 MHz.

THE BPM

The influence of the electrode dimensions on the signal level and harmonic content for different beams was calculated according to the method described by Timmer et al. [6]. The BPM electrodes are considered as capacitors that are charged by the beam and discharged through a resistor connected to ground. To verify the order of magnitude of the calculated value, a simpler and less accurate method, which assumes that charge appears only on the inside of the electrodes when the beam enters the BPM, and similarly disappears from the inside when the beam leaves it, was used to calculate the beam pulses with Laplace transforms. With the second method the pulse form differs, as can be expected, significantly from those of the first, but there is good agreement between pulse and harmonic amplitudes. The main BPM dimensions are shown in Fig. 1. To obtain larger harmonic

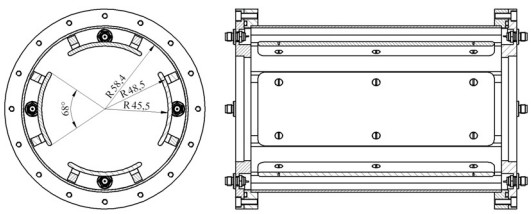


Figure 1: Cross-sectional views of the BPM.

*Work supported by BMBF and NRF, Project-codes: SUA 06/003 and GUN2075288.
#j.dietrich@fz-juelich.de

amplitudes than with the existing BPMs it was found necessary to deviate from the previous design by increasing the length of the electrodes to 170 mm, which is the physical length of the 200 MeV proton beam pulses. The BPM can therefore no longer fit into the standard diagnostic vacuum chambers and has to be installed separately from these chambers. A further increase in the length would result in an increase in the amplitudes of the first few harmonics of the beam pulses but was not implemented to take future space requirements into consideration. Each electrode extends over an angle of 68 degrees and has an inner radius of 45.5 mm to prevent interception of beam. The inner diameter of the beam pipe where the BPM is installed is 73 mm. SMA connectors on both sides of each electrode provide the facility to terminate the electrodes on both sides. Numerical field analyses, using finite element methods with the program TOSCA [7], showed that for a beam diameter of 10 mm the image charge on an electrode is 23.5% of the beam charge. The calculated rms signal levels, with only one termination on each electrode, for 1 nA proton beams are 10.7 nV for the fifth harmonic (81.86 MHz) at 66 MeV and 7.1 nV for the third harmonic (78 MHz) at 200 MeV, assuming homogeneous charge distributions in the beam pulses and pulse lengths of 13 and 9 degrees, based on previously determined beam pulse lengths as measured with capacitive phase probes, respectively. The calculated height of the beam pulses depends strongly on the assumed pulse length but the amplitudes of the harmonics do so to a much smaller degree. For heavy ion beams the signal levels are appreciably higher than that of the 66 MeV proton beam. The amplitudes of the lower harmonics are not sensitive to the inner probe radius and capacitance.

SIGNAL PROCESSING

Figure 2 shows a simplified block diagram of the electronic equipment for processing the beam signals. Because of the occasional high radiation dose in the area where the monitor is installed the multiplexer, comprising of electromechanical RF switches, and the first two amplifiers were installed in a separate electronics area and connected to the BPM through 20 m long cables, with solid outer conductors. The remaining equipment in Fig. 2 was installed in the control room, about 40 m away from the first two amplifiers. The overall attenuation in the cables is 1.57 dB. Included in the gain of the first amplifier, which has a noise figure of 1.2 dB, is the loss of the 1 dB attenuator at its input, which is essential for stability when connecting the input to a long cable. The overall amplification factor, including the cable loss and the 3.3 dB attenuation in the signal combiner, is 71.9 dB, which means that for 1 nA proton beams an amplitude of 42.4 μV for the fifth harmonic at 66 MeV and 28 μV for the third harmonic at 200 MeV can be expected at the input of the lock-in amplifier. Included in the final amplifier stage are an amplifier that limits the output signal level and an attenuator for protection of the final amplifier. To cancel the pick-up signal from the RF systems the beam signal is combined with the appropriate harmonic generated by a synthesizer with a signal of the main RF system as a reference. The phase and amplitude of the harmonic can be adjusted by computer control. This can be done by using previously measured calibration data of the synthesizer, or by measuring the phase and amplitude of the combined signals and those of the synthesizer signal separately. From these values the required phase and amplitude settings of the synthesizer can be calculated, provided that the amplitude and phase of the pick-up signal are stable. Noise in the output signal of the combiner is filtered in the lock-in amplifier, which provides filters with time constants ranging from 0.1 ms to 30 ks with 6, 12, 18 and 24 dB/octave roll-off. The effective time constant is approximately equal to the selected time constant, times the number of dB/octave roll-off as a multiple of 6 dB.

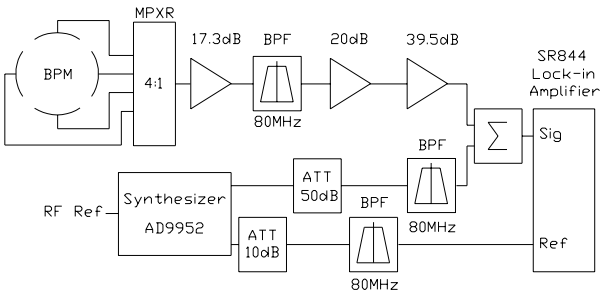


Figure 2: A simplified diagram of the signal processing equipment.

RESULTS OF MEASUREMENTS

Measurements were made mainly on the 66 MeV proton beam since it was the most often available. In terms of pickup it is the worst case since one of the RF systems, the flat-topping system of the injector cyclotron for light ions, operates at the measuring frequency. For 200 MeV only harmonics from the main RF systems contribute to pickup.

For the 66 MeV proton beam the measured amplitude of the fifth harmonic, after amplification, is 37 μV/nA. The calculated value is about 11% higher. For the 200 MeV proton beam the measured amplitude is 26.5 μV/nA. These measurements were made after pickup cancellation and at such high beam intensities and long time constants that the resultant pick-up signal and noise were insignificant.

The beam pulse amplitude of the 66 MeV proton beam has been measured at a beam current of 10 μA, with both ends of the electrodes terminated with 50 Ω resistors, one of these being the input resistance of a 40 dB wideband amplifier. The measured amplitude is 170 mV and the calculated value is 127 mV. The amplitude of the beam pulses is enhanced by the inductance in the leads that connect the electrodes to the feedthroughs. The effect of the inductances can also be seen in the presence of oscillations in the tail of the measured pulses. Since the electrodes are essentially transmission lines and not

capacitors, it is to be expected that the measured amplitudes will be higher than the calculated ones. This, and the effect of the inductances have been verified by modelling the BPM electrodes with a circuit analysis program. The use of a different type of feedthrough, which will allow connections with much less inductance, is planned.

The amplitude of the pick-up signal varies from week to week since the amplifiers of the RF systems are retuned during beam energy changes. The pick-up signal level during operation with the 66 MeV proton beam is typically below 10 µV. For a nominal signal level of 7 µV the amplitude varied, partly due to noise, by plus and minus 1 µV over a 6-hour period. Variations in the amplitude and phase of the signal from the synthesizer are negligible compared to those of the pick-up signal. The combined pick-up and synthesizer signals can be reduced in a single step to below 1 µV by measuring the amplitude and phase of the synthesizer and the combined signals and adjusting the synthesizer signal to newly calculated settings. For the 200 MeV proton beam the amplitude of the pick-up signal, without cancellation with the synthesizer signal, is typically 2.4 µV.

The overall limitation to the lowest beam intensity at which the BPM can be used is determined by the time constants of the filters for noise reduction that are acceptable and measurement accuracy that is required. To keep the measured noise level below 2 µV, a time constant of 3 s and 24 dB/octave roll-off were selected. For a time constant of 1 s and the same roll-off, the noise level increases to above 3 µV.

Figure 3 shows measured BPM signals as well as estimated beam positions, based on measured and calculated beam signals as a function of the actual beam position. The difference between the estimates, based on measurement and calculation, is due to the different beam sizes and the dispersion in the beam directly downstream from the switcher magnet. From figure 3 it is clear that the BPM has to be calibrated, as was done with the BPMs that were built previously.

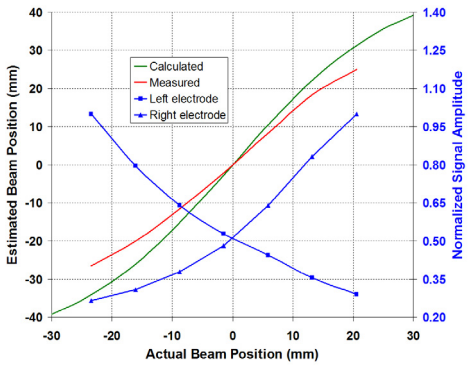


Figure 3: The calculated and measured beam position estimates as a function of the beam displacement. The measured beam position is the difference over the sum of the measured electrode signal s, multiplied with the inner radius of the BPM electrodes. For the calculated beam position, the signal levels on the electrodes were determined with the computer program TOSCA, for different positions of a 10 mm diameter beam. The actual beam positions in the BPM were calculated from the excitation current of the switcher magnet.

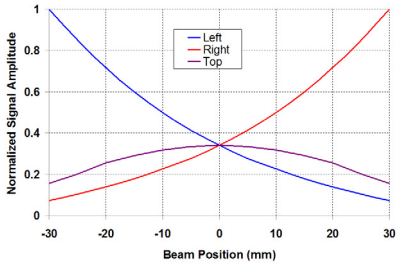


Figure 4: The calculated BPM signals as a function of horizontal displacement of a 10 mm diameter beam.

CONCLUSION

The lower beam current limit at which the BPM and the signal processing equipment described above can be used is a function of the acceptable measurement time and the required positional accuracy. At a beam current of 10 nA, the measurement time is estimated at fifteen seconds per electrode for a positional accuracy of 1 mm, provided there are no beam current variations during the measurement of the signals on the four electrodes. To eliminate the effect of such variations further averaging of the measured values is required.

REFERENCES

[1] J.L. Conradie et al., "Improvements to the iThemba LABS Cyclotron Facilities", Cyclotrons'07, Catania, October 2007, MOPPRA04, p. 140 (2007); http://www. JACoW.org.

[2] J. Dietrich et al., "Beam Position Monitor Development for iThemba LABS Cyclotron Beam Lines", EPAC'04, Lucerne, July 2004, THPLT047, p. 2589 (2004); http://www.JACoW.org.

[3] J. Dietrich et al., "Operational Experience with Beam Alignment and Monitoring using non-destructive Beam Position Monitors in the Cyclotron Beam Lines at iThemba LABS", DIPAC'05, Lyon, June 2005, POM027, p. 96 (2005); http://www.JACoW.org.

[4] J.L. Conradie et al., "Beam Phase Measurement in a 200 MeV Cyclotron", EPAC'06, Edinburgh, June 2006, TUPCH077, p. 1187 (2006); http://www. JACoW. org.

[5] M. Dehler, "Resonant Strip Line BPM for Ultra Low Current Measurements", DIPAC'05, Lyon, June 2005, POW021, p. 286 (2005); http://www.JACoW. org.

[6] J.H. Timmer et al., Nucl. Inst. and Meth. in Phys. Res. A568 (2006) 532.

[7] http://www.vectorfields.co.uk/.

ORTHOGONAL COUPLING IN CAVITY BPM WITH SLOTS

D. Lipka*, D. Nölle, M. Siemens, S. Vilcins, DESY, Hamburg, Germany
F. Caspers, CERN, Geneva, Switzerland
M. Stadler, D. M. Treyer, PSI, Villigen, Switzerland
H. Maesaka, T. Shintake, RIKEN/SPring-8, Hyogo, Japan

Abstract

XFELs require high precision orbit control in their long undulator sections. Due to the pulsed operation of drive linacs the high precision has to be reached by single bunch measurements. So far only cavity BPMs achieve the required performance and will be used at the European XFEL, one between each of the up to 116 undulators [1]. Coupling between the orthogonal planes limits the performance of beam position measurements. A first prototype build at DESY shows a coupling between orthogonal planes of about -20 dB, but the requirement is lower than -40 dB (1%). The next generation cavity BPM was build with tighter tolerances and mechanical changes, the orthogonal coupling is measured to be lower than -43 dB. This report discusses the various observations, measurements and improvements which were done.

INTRODUCTION

A cavity BPM consists of a coaxial dipole resonator with four symmetric arranged slots and a reference resonator, see Fig. 1. A charged particle beam excites electromagnetic fields. Antennas in the slots and the reference resonator observe a voltage. The signal used from the dipole resonator is the TM_{11} mode (the dipole mode is spatial filtered due to the slots), which is proportional to the beam offset times charge. Charge and phase normalization are done with the signal from the reference resonator (TM_{01} mode which is proportional only to the charge), see Fig. 2, such that the beam position is observed. The phase relation between dipole and reference resonator is used to determine the sign of the displacement.

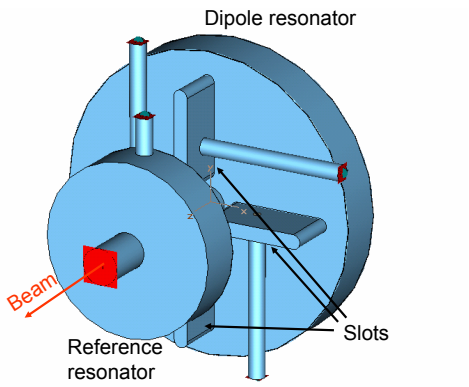


Figure 1: Design view of a cavity BPM, here only the vacuum parts are shown.

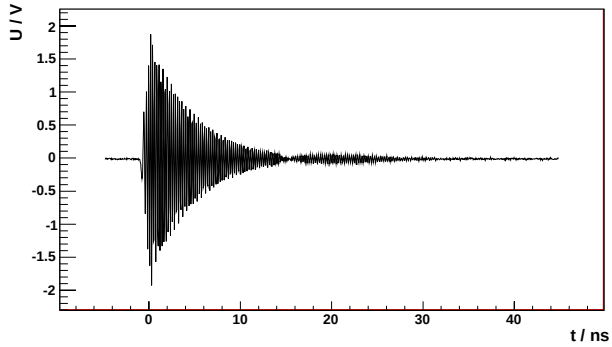


Figure 2: Time domain response signal from reference resonator with visible reflexion after about 14 ns.

Both transverse beam displacements are measured by using two orthogonal feedthroughs (ports) of the dipole resonator, the other two ports are terminated by 50 Ω loads. When the beam is only shifted in one direction with respect to the electromagnetic axis of the BPM only one port should show an offset. With a coupling of both planes the other port will give a signal too, see Fig. 3. If the resulting coupling is larger than requested this limits the BPM performance.

This paper shows the investigation of the coupling for two prototypes (one of the first and one of the second generation) with two methods. The reason of the coupling is evaluated and possible improvements are named.

FIRST CAVITY BPM GENERATION

Three prototypes have been produced at DESY. The design originally developed at SPring-8 [2] was changed according to the boundary conditions of the European XFEL with a resonance frequency of 4.4 GHz. One prototype was installed at FLASH in 2008, see Fig. 4. The BPM can be moved in both transverse directions by stepper motors. The ports are connected with 1.5 m long cables (H&S SUCOFORM SM141) followed with 120 m long cables (RFS LCF 78-50JA 7/8" CELLFLEX) each. The signals are taken with an oscilloscope, 20 GSamples/s. In Fig. 3 the signal from the orthogonal port shows a different decay time compared to the *correct* port. This leads to the assumption that the loaded quality factor is increased. The signals shown in Fig. 2 and Fig. 3 top indicates a reflexion

* dirk.lipka@desy.de

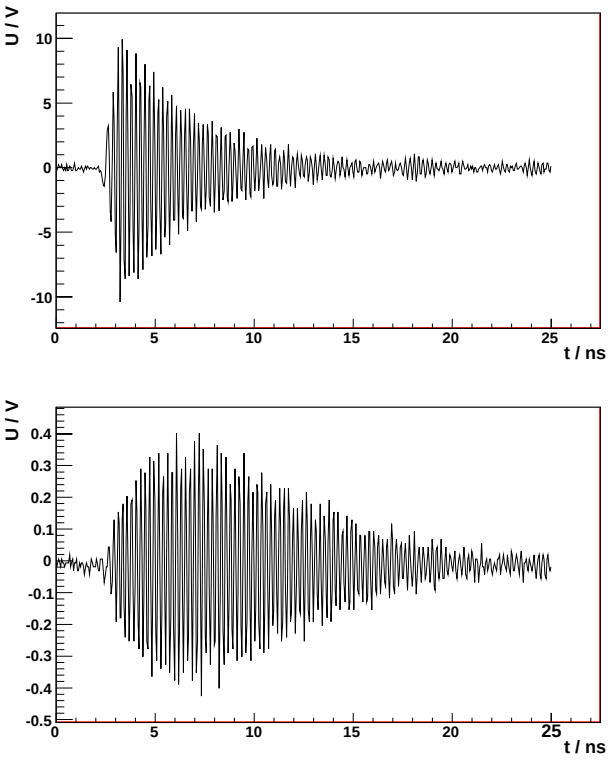


Figure 3: Time domain response signal of dipole resonator. Top: with beam offset of 1.08 mm, bottom: from the orthogonal port. Note the different vertical scales.

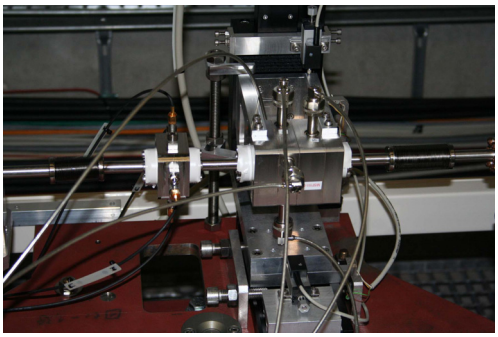


Figure 4: Photo of the installed cavity BPM first generation at FLASH.

after about 14 ns which could influence the quality factor. The reflexion is caused by the interface between the 1.5 m and 120 m long cables. The Fourier transformed signal of Fig. 3 shown in Fig. 5 gives a smaller bandwidth of the coupled signal at the same frequency, an indication of a larger quality factor too.

To estimate the amount of coupling the maximum level at the resonance frequency is taken as a function of beam offset in one transverse direction, see Fig. 6. With increasing offset both ports show an increasing level, the coupling is about -20 dB (10%) which is above the requirement of 1%. Therefore this signal influences the performance of

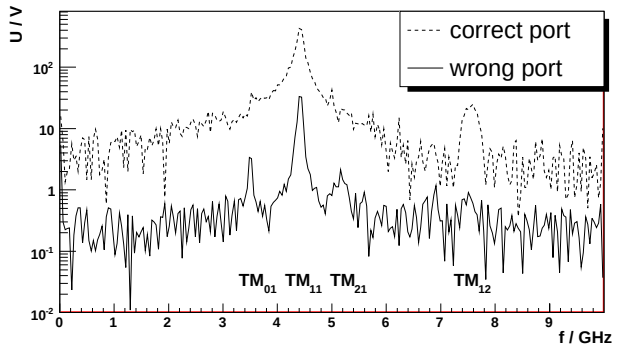


Figure 5: Fourier transformation of signals shown in Fig. 3. Monopole mode leakage at 3.5 GHz is observed too. The first quadrupole mode (TM_{21}) at 5.2 GHz and the second dipole mode (TM_{12}) at 7.6 GHz are visible.

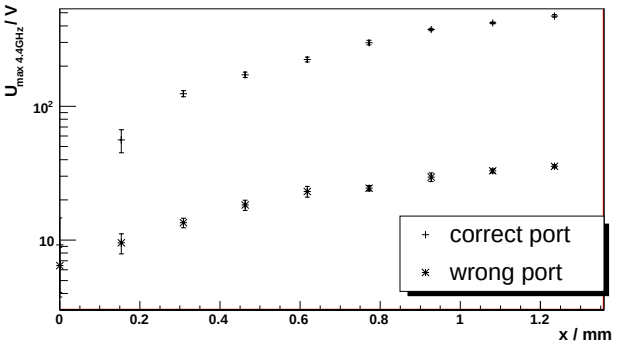


Figure 6: Maximum level at dipole resonance frequency as a function of beam offset for both ports. Error bars are the standard deviation of several measurements.

the BPM.

The transmission of the orthogonal ports of the BPM was measured with a network analyzer without long cables shown in Fig. 7. Here one can see the same level of coupling.

To derive the reason of the coupling CST simulations [3] are performed with shifting non-cylinder-symmetric components of the BPM. An agreement of the transmission measurement was found (see Fig. 7) by shifting one slot by 0.09 mm with respect to his center position (the defined tolerance was ± 0.2 mm). The resonance frequency of the measured BPM was 4.408 GHz, therefore the measured data are shifted, which is within the accepted tolerance of ± 10 MHz. The dipole mode is on the shoulder of the first quadrupole mode therefore the baseline of the transmission is increasing with frequency in Fig.7. But this quadrupole mode has only negligible influence to the measured offset position.

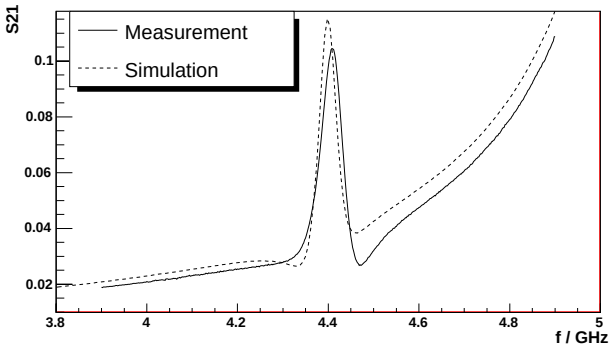


Figure 7: Transmission between orthogonal ports of at FLASH installed BPM without long cables: measurement and simulation (shift of slot position: 0.09 mm).

SECOND CAVITY BPM GENERATION

The next prototypes have been produced with a resonance frequency of 3.3 GHz. The lower resonance frequency was chosen to be able to design cavity BPM with larger beam tube and the same performance like the undulator cavity BPM. This gives the possibility to use the same electronics at different positions of the beam distribution system. The mechanical tolerance of the slot position is tightened to ± 0.05 mm and the vacuum tube connection of the slots are closed (compared to the origin design [2]). Due to the lower resonance frequency the baseline transmission is increased. The closed vacuum tube connection decreases the baseline transmission again, shown in Fig. 8. A small peak is observed at the resonance frequency, but

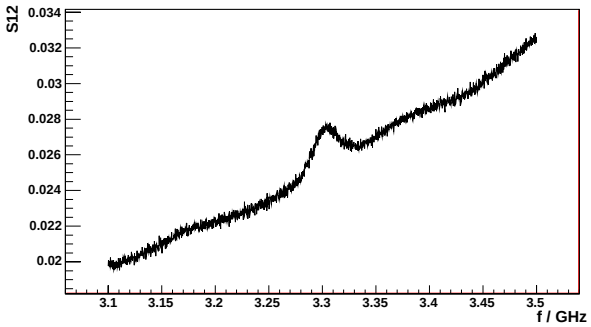


Figure 8: Measured transmission of the second generation cavity BPM between orthogonal ports.

not significant like in Fig. 7, note the different scales. One BPM of the second generation was used to replace the first generation prototype in FLASH, see Fig. 9. The same measurement as a function of beam offset was done, see Fig. 10. The orthogonal port gives a small peak at the resonance frequency but it does not increase with larger beam offset (a larger beam offset range was used compared to Fig. 6). Therefore from this data one can estimate an upper limit of the coupling of -43 dB.

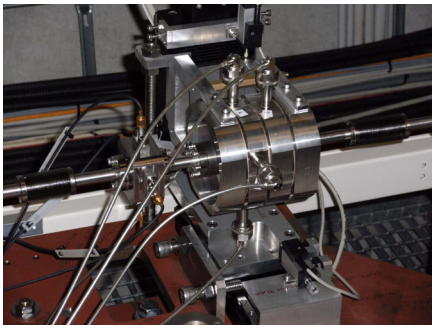


Figure 9: Photo of the installed cavity BPM second generation at FLASH.

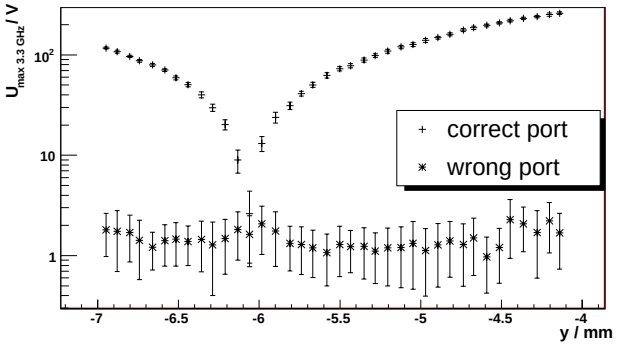


Figure 10: Maximum level at dipole resonance frequency of second prototype as a function of vertical mover position for both ports. Error bars are the standard deviation of several measurements. BPM center is at about -6.08 mm.

SUMMARY

The first cavity BPM generation for the European XFEL showed a coupling of orthogonal port signals measured with beam and verified with transmission measurement of -20 dB. The reason was a too loose tolerance of the position of the slots. By tightening the tolerance the coupling is reduced and measured to be lower than -43 dB. It turns out that coupling is sensitive to geometric errors of a cavity BPM. Thus it can be used as one measure in the quality control process of the series.

ACKNOWLEDGMENT

The author thanks Thomas Traber for his support to the measurement with the Network Analyzer.

REFERENCES

[1] M. Altarelli *et al.*, "The European X-Ray Free-Electron Laser", Technical design report, `http://www.xfel.eu/en/documents/` 2007.

[2] H. Maesaka *et al.*, "Beam position monitor at the SCSS Prototype accelerator," Proceedings of APAC 2007, Indore, India, 2007.

[3] Computer Simulation Technology, `http://www.cst.com`.

ALIGNMENT MONITORS FOR AN X BAND ACCELERATING STRUCTURE

M. Dehler, J.-Y. Raguin, A. Citterio, A. Falone, Paul Scherrer Institut, Switzerland
W. Wuensch, G. Riddone, A. Grudiev, R. Zennaro, A. Samoshkin, D. Gudkov, CERN, Switzerland
G. d'Auria, M. Elashmawy, Sincrotrone Trieste, Italy

Abstract

Currently an X band traveling wave accelerator structure is under development in a collaboration between CERN, PSI and ELETTRA. At PSI and ELETTRA, it will serve for longitudinal phase space compensation at the respective FEL projects, where CERN will use it to test break down limits and rates in the high gradient regime. The design employs a large iris, $5\pi/6$ phase advance geometry, which minimizes transverse wake field effects while still retaining a good efficiency. In addition, we plan to use an active monitoring of the beam to structure alignment and to include two wake field monitors coupling to the transverse higher order modes. These allow steering the beam to the structure axis giving a higher precision than mechanical alignment strategies. Of special interest is the time domain envelope of these monitor signals. Local offsets due to bends or tilts show up as distinct patterns, which should be easily detectable via basic measurements.

INTRODUCTION

Within the context of the GLC and NLC projects, a considerable effort has been going on in developing high power X band RF systems for high energy e^+e^- colliders[1]. After the conclusion of these projects, the recent decision by CLIC to change their principal RF frequency from 30 GHz to an European X band frequency near 12 GHz has given a renewed push to X band development. A big RF structure fabrication and testing program involving major laboratories around the world is under way.

A relatively new application for X band technology is in free electron lasers. LCLS compensates nonlinearities in the longitudinal phase space with an X band structure in order to improve bunch compression. The European FEL projects SPARC, FERMI@ELETTRA and PSI-XFEL also plan to employ it for the same purpose. In that context, a collaboration between CERN, PSI and ELETTRA has been set up to develop suitable structures. While being operated at the PSI-XFEL and the FERMI FEL, an ultra long performance test also important for CLIC, these are also going to be submitted to break down tests at CERN.

Looking at the PSI-XFEL, beam voltages up to 30 MeV are required using only a limited power in the order of 40 MW at the structure, which means a fairly efficient structure. On the other hand, the beam has a relatively modest energy of 250 MeV, so that we are relatively sensitive to transverse wakes. So we need to make a good compromise between a high shunt impedance, generally associated with low apertures, and a low transverse kick, demanding the opposite. The structure will have no HOM damping. But two wake field monitors are foreseen to align the structure to the beam and to minimize transverse kicks.

The monitor use TE type coupling to the dipole modes in the structure to reject the fundamental as well as higher order longitudinal modes. A special feature is, that we also make use of the fact that wave propagation inside the RF structure is relatively slow at a few percent of the speed of light. The spread out pulse response of the wake monitors not only contains information about the offset but also about higher order misalignments as structure tilts. So basic measurement procedures using only the envelope of the output signal are possible.

FUNDAMENTAL MODE PROPERTIES

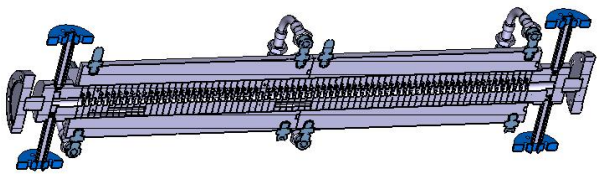


Figure 1: Cut through X band accelerating structure.

For both ELETTRA and PSI specifications, a single structure with 750 millimeter active length is the most appropriate solution. The NLC structure type H75 ($5\pi/6$ phase advance) has been chosen as the most suitable candidate for the testing program. The original H75 design, with all iris aperture, thickness and ellipticity of the iris varying along the structure, provides an accelerating gradient of 65 MV/m for 80 MW input power and was successfully tested up to 100 MV/m with a SLAC mode launcher [2, 3], which we also use here. The relevant parameters are summarized in Table 1.

Table 1: Structure Specifications

Beam Voltage	30 MeV
Max. Power	29 MW
Iris diameter	9.1 mm (avg.)
Wake field monitors	up/downstream
Operating temp.	40 deg. C
Fill time	100 ns
Repetition rate	100 Hz

WAKE FIELD MONITOR

To measure the beam offset inside the structure, we couple to the lowest dipole mode. Minimum perturbation of the fundamental mode and maximum information in the output signal, easily post processed, are the principal design criteria. Where and how to couple, what to expect as a signal is shown in the following.

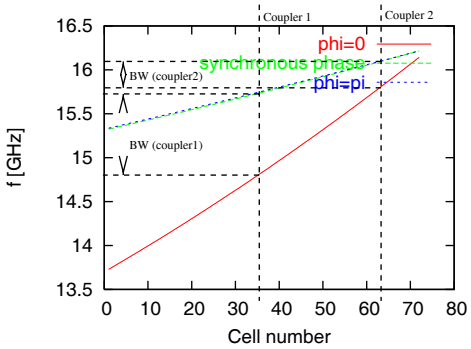


Figure 2: Limits of lowest dipole band and synchronous frequency versus cell number. Also shown the location of the wake field couplers with their respective bandwidths.

The distribution of bandwidths and synchronous frequencies of the lowest dipole band inside the whole structure (Fig. 2) shows three characteristic frequency bands. Dipole modes in the region of 15.3 to 16.1 GHz will be trapped modes, localized in the inside of the structure, where there are cells propagating these frequencies. These trapped modes start in an upstream cell with a field distribution corresponding to a π mode and continue with a decreasing phase advance to the downstream cell, where it goes to zero. The coupling with the beam is most pronounced in the cell, where the resonance corresponds to the synchronous frequency and phase. Resonances below 15.3 GHz (π mode of cell 1) extend from the input coupler to the cell where the phase advance goes to zero. Most of these modes will have weak kick factors, since their frequency does not correspond to one of the synchronous frequencies. The last region contains high kick modes above 16.1 GHz, their fields extend into the output coupler.

With this in mind and assuming, that introducing the monitors will not distort this modal pattern, we are able to choose suitable locations for the wake field monitors. Dipole wakes excited by offsets in the upstream half of the structure correspond to modes which are concentrated in the middle of it. Actually, if we put a monitor in cell 36, it will have a bandwidth of 14.8 to 15.7 GHz (the width of the dipole band in cell 36), the corresponding modes have their synchronous phases in the upstream half and will signal offsets there. For the downstream coupler, we are restricted by the width of the dipole band – a reasonable compromise is cell 63, which sees wakes excited in cells 40-63.

What are the design criteria for the monitor? In order to effectively measure offsets, the wake monitor should reject signals coming from all monopole modes, fundamental as well as higher ones. These are best suppressed by selectively coupling to the transverse electric components of the hybrid dipole modes, something achieved by a suitable orientation of the coupling waveguide.

One option is to use radially oriented waveguides coupling head-on to the cell and a second to have a waveguide in parallel to the beam axis being side coupled, similar to the design of the damped detuned structure, but coupling only to one select cell. Side coupling has the advantage,

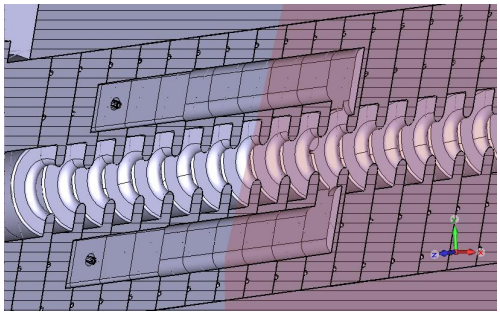


Figure 3: Cut through structure showing the geometry of the downstream wake monitor cell.

that we can have a longer waveguide damping down any residual signal from the fundamental mode, which may enter due to mechanical misalignments. Also, there is enough space to integrate a transition from the waveguide to coaxial and use a standard 50 Ω vacuum feedthrough to connect the front end. We chose this option, the coupler design is similar to the HOM coupled cells of the damped detuned structures, the difference being that we couple only to one cell and have the wave guide electrically shorted on one side (Fig. 3).

The coupling strength corresponds to a loaded Q of around 800 for a zero phase advance of the dipole and gives sufficient signal amplitudes. The effect on the fundamental mode parameters is only minor: A 10 % drop in group velocity and Q, the R/Q stays virtually unchanged.

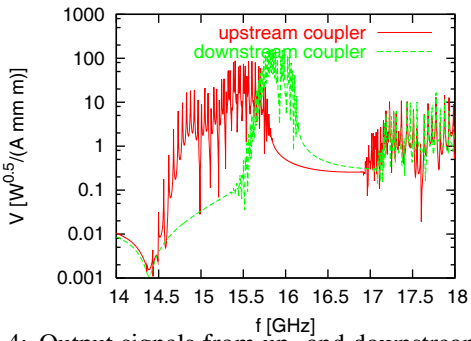


Figure 4: Output signals from up- and downstream monitors vs. frequency.

The wake monitor signals shown in the following were obtained from a dual resonator equivalent circuit, where the elements of the resonators describing the TE and TM components of the hybrid dipole mode and their mutual couplings are fitted from the results of numerical computations. (See [4] for more details, and [5] for special modifications used). Figure 4 shows the signal spectra computed for the up- and downstream couplers. As can be expected from the previous discussion, we see two distinct frequency bands corresponding to the synchronous frequencies in the two parts of the structure.

Of special interest is the time domain evolution of the transverse wakes. A given dipole mode is excited by the beam dominantly in the 'synchronous' cells, where his resonant frequency corresponds to the synchronous one. The mode does not build up instantaneously, but the energy de-

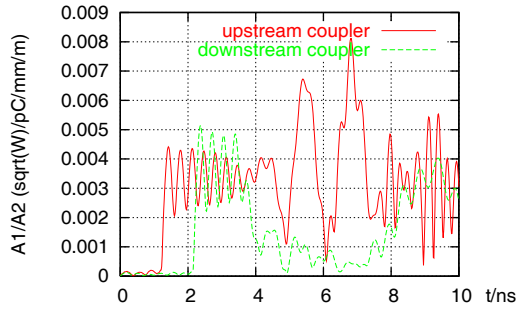


Figure 5: Signal envelope from up- and downstream monitors vs. time.

posited by the beam in this synchronous cell needs time to get distributed in the structure – the distance between the synchronous cell and the wake field monitor leads to a time delay, before the signal shows up in the monitor signal. Signals from different part of the structure have a different delay. In the output signal (Fig. 5), this results in an initial rectangular pulse (with some beating on top) of 2-3 nanoseconds length.

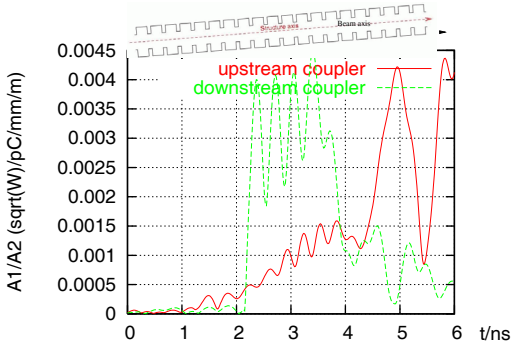


Figure 6: Signal envelope up- and downstream monitors vs. time assuming structure axis tilted to beam axis.

The beam offset in individual parts of the structure is correlated to different synchronous frequencies and this in turn with different delays in the time domain signal. So it is a valid question, whether we can identify also tilts with respect to the beam. A tilted structure is aligned with the beam in the middle, whereas the extremities are offset generating a transverse signal. The resultant wake monitor signals are shown in Fig. 6. The upstream monitor is the more significant one in this case, it sees the total front half of the structure. Where a constant offset gives a more or less rectangular pulse like in fig. 5, we now have a ramp starting at zero (no offset in the middle) and growing linearly to the peak (high offset at beginning). The downstream signal is similar but not as pronounced, since it sees only part of the structure. In the case of bends, dispersion effects smearing out the signal are too strong to see a clear pattern.

What is the effect of mechanical tolerances on the resolution of the monitors? The beam passes through the structure, sees random non correlated offsets of individual cells and will, independent of the global offset, excite wake fields and wake signals showing up as noise in the measure-

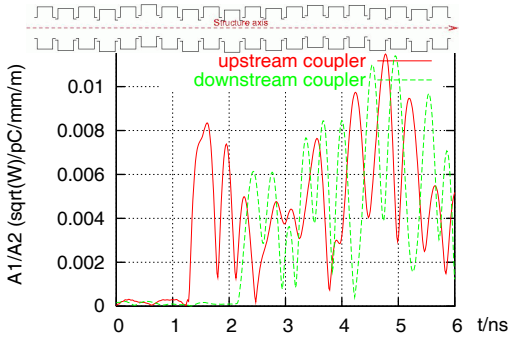


Figure 7: Signal envelope up- and downstream monitors vs. time assuming random, uncorrelated misalignment of individual cells in the structure.

ment. We implemented a model for that into the equivalent circuit model and simulated it [5]. Figure 7 shows an example for the output. The peak random offset signal in the first four nanoseconds is roughly a factor two larger than the equivalent signal for a constant offset (Fig. 5). Said otherwise, a structure with a random cell offset of 1 μm rms creates a signal proportional to a systematic offset of 2 μm – we would have a resolution limit of 2 μm. Resolutions below 10 μm, corresponding to a mechanical cell to cell alignment of better than 5 μm, seem entirely realistic.

CONCLUSION AND OUTLOOK

An X band structure for the new CLIC reference frequency has been designed, used for high gradient testing at CLIC and as a prototype structure for the PSI-XFEL/FERMI projects. It offers an efficient fundamental mode performance with a wide aperture minimizing transverse wake field effects. Two wake monitors in the structure giving information about offsets and tilts of the structure allow a high quality alignment to the beam. The RF design and mechanical construction is nearly finished, we are currently in the transition into fabrication. Structures for high power testing are expected to be ready toward the end of 2009.

REFERENCES

[1] C.E. Adolphsen et al, " International study group progress report on linear collider development", SLAC-R-559, SLAC-R-0559, SLAC-559, SLAC-0559, KEK-REPORT-2000-7, LCC-0042, ISG Progress Report, April 2000.

[2] `http://lcdev.kek.jp/ISG/ISG9.ZL2.pdf`

[3] C. Nantista et al, "Low-field accelerator structure couplers and design techniques", Phys.Rev.ST Accel.Beams, 7:072001 (2004).

[4] R.M. Jones et al, "Wakefield damping in a pair of X-band accelerators for linear colliders", Phys.Rev.ST Accel.Beams 9:102001,2006.

[5] M. Dehler et al, "X-band rf structure with integrated alignment monitors", Phys.Rev.ST Accel.Beams, in print.

INSTALLATION AND COMMISSIONING OF A COMPLETE UPGRADE OF THE BPM SYSTEM FOR THE ESRF STORAGE RING

B.K. Scheidt, F. Epaud, ESRF, Grenoble, France

Abstract

The ESRF Storage Ring has, over the last 3 winter months, been fully equipped with new electronics for its BPM system while causing a minimum disturbance to its large community of X-ray beam-line users. The Libera-Brillance is now doing the treatment of the weak RF signals on all 224 BPM stations, and has replaced the old RF-Multiplexing system that had served reliably for 17 years. This paper describes the precautions that had been taken to make the whole transition as smooth as possible, with regards to the reliability for the SR operation and the positional stability of more than 40 X-ray beams. Information is given on the network & computer control, based on the Tango distributed control system and its device-servers and tools. Results will be presented to demonstrate the strongly improved performance and functionality in every field of application, and that will make this new BPM system the key component in the near future's upgraded orbit stabilization system.

HISTORY, MOTIVATION , CHOICE OF TECHNICAL SOLUTIONS

The agreed upgrade program of the ESRF light source, including that of the accelerator complex [1], has created an opportunity to modernize drastically the old BPM system of the SR. For its orbit control and beam stabilization (incl. feedbacks) the ESRF SR depended on 2 separate and independent systems, both of in-house design & conception : 1) The slow BPM system of 224 stations that had been conceived 20 years ago, and 2) the fast-BPMs with only 32 stations and 16 (vert.) & 32 (hor.) correctors for fast-feedback.

Both BPM types use blocks with 4 buttons for vacuum wall-current pick-up of the RF signal. At the time of conception (i.e. before 1990) of the slow system it was believed that fast & high-resolution beam position measurements would not be possible with the button-type of BPMs (and its RF electronics for signal treatment) and that instead X-BPMs, installed on numerous X-ray beam-lines would satisfy those fast needs. However, such X-BPMs suffered from intrinsic limitations and have never satisfied these requirements.

To overcome this, additional, independent BPM blocks were installed with electronics for fast measurements. Their purpose and usage has evolved progressively over the years, from first pure local fast feedbacks to finally a pure global SR ring feedback system to which very recent improvements were made to cover the full frequency band of the needed orbit stabilization [2].

The slow BPM system had an addition to its basic functionality with a high-resolution 'quasi' Turn-by-Turn measurement mode [3] that, with a stable & reproducible synchronization to an orbit kicker, allows the precise measurement of the SR lattice parameters. But it does not have a genuine single turn capacity, and for injection studies or for coping with severe injection problems, this old system requires certain conditions (4 strong injection currents for a single measurement) that are today no longer compatible with operation needs, nor with restrictions imposed by radiation safety regulations.

The satisfaction of today's requirements on the performance and functionality of a BPM system is no longer realistic through an 'in-house' design because of the technical complexity of different fields inside such system like RF signal treatment, digital signal conditioning through FPGAs, and interfacing with computer networks. This argument applies also to the ability to exercise the rigorous quality-control that is needed for production of a large series of units.

A few years ago the BPM needs of the new synchrotron light sources DLS and Soleil [4,5] had been satisfied successfully, in collaboration with them, by a commercial product called 'Libera-Electron' of the Instrumentation Technologies company [6]. Subsequently this product has provided more light sources for their BPM needs. [7,8,9]

This original product, after being fully employed & analysed by the DLS and Soleil [10,11], was improved in 2007 by a successor called 'Libera-Brilliance'. A total of 8 units of this product were procured at the end of 2007 and tested at the ESRF, during the first half of 2008, for full compatibility with the ESRF needs and the ESRF particularity of (multiple-) single bunch fillings.

VERIFICATIONS ON PROTOTYPES

These single bunch fillings yield an electric signal from the pick-up buttons that reaches a high peak voltage (upto 100V), and is very rich in harmonics (at 355KHz revolution frequency) in the frequency spectral domain. Both aspects can pose a problem to the Libera in terms of degradation of its performance, notably its low noise characteristic and its reproducibility for different SR currents & filling patterns : a) the input electronics may not have fully linear transmission characteristics for such high peak voltage, and b) certain spectral lines of the input signal may mix in an un-expected way with some of the Liberas 'internal' frequencies (the rates of the ADC convertors and the RF 'cross-bar' switches for internal calibration purposes) or some of its harmonics.

The old ESRF system had employed, directly after the pick-up buttons , RF bandpass filters (352 MHz, 40MHz bandwidth) and our long experience of their robustness, reliability and stability is such that we rely on these same components, now employed just in front of the Libera RF inputs, i.e. after ~20m of RG223 RF cable.

This solves the peak-voltages' question, but is of no remedy to excess noise in the output results due to a combination of small intrinsic ADC dislinearities and the internal mixing of the many frequency components that un-avoidably enter the system and that randomly fall in or out the bandwidth of the output signal, and that is generally made worse under the following conditions : 1) rich RF input spectrum (i.e. single bunch filling), 2) non-identical phase of the 4 RF inputs (i.e. due to un-equal RF cable lengths), 3) operating the ADC in the upper half of its dynamic range. 4) operating with the 4 RF inputs of strongly different amplitudes.

These problems had already been experienced with the original Libera-Electron and found a satisfactory solution in applying so-called 'offset-tuning' [4,10], a technique that allows to put the exact ADC' sampling rate at a slightly different value from an exact harmonic (304 for ESRF) of the orbit revolution frequency.

We did extensive verifications on the spectral contents of the so-called FA output (10KHz) that ultimately serves for fast orbit feedback and therefore the most sensitive to such spurious noise. Such noise lines clearly appear in the FA spectrum if the bad conditions are sufficiently fulfilled, but can then be 'moved', by adjusting the offset tune value, out of the bandwidth of interest.

Moreover, attention was paid to getting the new RF cables of reasonable good equal length (the average (over 224 BPMs) is 21mm maximum difference in a set of four), and we run the ADCs (by using the standard Libera AGC) in the lower half of their full dynamic range.

INSTALLATION & COMMISSIONING

The SR is divided in 32 cells of 7 BPMs each, and a first full cell was equipped in sept 2008 with exclusively Liberas, and 2 more full cells in dec. just 2 weeks before the 4 weeks winter shutdown. This allowed to gain confidence with the both the system and with the work & tools for this transition. This was important since the re-cabling and re-organisation of electronics in the receiving cabinets was irreversible. The 4 weeks shut-down therefore could be used to do a maximum of 13 more cells meaning that (a possibly) delicate re-start was now faced with 2 equal halves of the SR under a different BPM system. The remaining half was done at a rhythm of 3 cells per week, on its MDT day with about 4 hours of beam cut and subsequently ~8 hours more of new beam-based BPM offset measurements. The latter was needed to compensate for a change of positional offset between the old and the new electronics, and so the ensure that, after each stage of installation, the beam-lines would endure a minimum of X-ray beam displacement.

COMPUTER CONTROL & READ-OUT

The interfacing software that controls the 224 Liberas and acquires their data is based on the Tango control system [12] that is now widely used at both the ESRF and a few other European light sources. So far we have been using the original Tango device server of the Soleil Liberas that was developped more than 2 years ago.

We have at present one device server per Libera. Embedding this server, in principle possible since the Libera is a Linux based computer, has so far not been achieved mainly due to the modest floating point performances of the ARM processor. This may be reconsidered now with the new release firmware 2.0 but is not of high priority. Instead we have 224 device servers running on 4 dedicated Linux computers that each are equipped with powerful configurations (Dual core Pentium 4 running at 2.5 GHz with 3 GBytes RAM) and connected to a dedicated Ethernet VLAN with 1 GBits links. The 32 cells hosting each 7 Liberas are connected with 100 Mbits links.

On top of these 224 device servers is another Tango device server which collects the X and Z positions data using Tango Group calls : each read command is sent in parallel to all of the 224 lower level devices within 15 milli-seconds. This higher level device server also performs many other tasks like the positions corrections according to the SR current, the periodic storage into the ESRF History Database of the X & Z positions, the RMS values of scalable fast and slow buffers, and a number of maintenance & survey parameters.

The reliability of this dense and complex software structure was a serious challenge, also because it was based on the Soleil Tango server that we had limited familiarity with ourselves and to which we had to make a number of modifications in order to include both particular requirements for the ESRF and new functionalities that became available in new Libera firmware releases. This challenge was meet despite the little time available for testing purposes as the SR continuously depends on this BPM system to satisfy the light source users without interruption.

As to Liberas' firmware : All units were delivered (Nov. 2008) with the 1.82 release, and in Jan. 2009 we started to test the 2.00 release. At the time of editing this paper we have nearly half of the units upgraded to a subsequent 2.02 release that patches a discovered bug (the PM crashing the DSC daemon), includes some improvements and now also has the Communication Controller [15] (for FA data distribution, original design DLS) integrated & supported by the company.

Another major task was the development of the tools to, from a central point, properly install new firmware releases to all units and to subsequently upgrade the associated device-servers with it. Despite the optimization of these tools, the whole procedure of upgrading the full Libera system to a new firmware (in particular for the 1.8 to 2.0 releases) is very time consuming, also since the system is in quasi-continuous use for SR orbit control.

In addition to this, a restructured Tango device server, that is planned to replace the old Soleil Tango server next month, is being prepared and tested. Next to that higher level applications are being developed to allow the operation crew to more fully benefit from the new & high performance features of this new BPM system, and to

allow an adapted control & read-out for beam dynamics studies like injection and lattice measurements.

RESULTS & PROSPECTS

A total of 15 Liberas units (out of 230 procured) needed repair action on the site of the manufacturer. Only a few of these problems arrived while in active use for orbit measurement & control, the majority had been trouble-shooted by simple & quick verifications with RF test signals strait after installation in their cabinets.

Presently only the SA (10Hz) output is used for continuous and routine beam orbit monitoring and control in the SR. The performance of the Libera system has been verified in terms of precision, resolution and reproducibility to satisfaction. On average a few out of the 224 stations are out-of-use, mainly because of recurrent problems with the quality of an SMA connector or an RF-cable, or some un-explained variation of the signal obtained from a button. The Tango device server scrutinizes the quality of a position result by verifying the 'coherency' between the 4 signals of each BPM, and an automatic rejection is carried-out in case a single signal drifts or fluctuates in excess of a small threshold.

The DD output for Turn-by-Turn measurement needs precise adjustments of the timing signals & internal delay values so to ensure that in an acquisition each station is strictly synchronised on the same turn, and with a minimum of leakage or smearing with neighbouring turns. [13] This adjustment was easy to achieve with single shot injections and measuring the Sum signal. However, for even more stringent T-b-T measurements a so-called MAF filter can be installed that is free of such smearing [14]. The use of this special filter, and its preceding timing adjustments was so far done (i.e. tested) to satisfaction on 3 cells only.

The timing signals for the PM buffer, for analysis after a beam-loss or some other triggerable event, have been installed and tested. This revealed a software problem in the 2.00 release that has been corrected since.

The Interlock function is activated on only 8 stations and only in the vertical plane with a +/- 0.7mm threshold. A new software release soon will allow to avoid the systematic triggering on a beam-loss which causes unnecessary confusion to our existing accelerator interlock & protection system.

The Sum signal (of the 4 button signals) shows a very good stability that allows its exploitation at different data-rate outputs. On the SA data a beam lifetime measurement averaged over the large number of Libera units shows a better resolution than that obtained with the PCT current monitors. On the DD data the same Sum signals allow a precise measurement & study of accumulation & injection efficiency.

The rudimentary air-conditiong & temperature control of the technical galleries where the cabinets, housing the 7 Libera units, are situated have made necessary the installation of new doors, plates and ventilators to avoid the ventilators inside the Libera itself reaching the maximum rates. This work has been done sofar on 5 cells with the remainder to be finished before this summer.

A large network of fibre-optics is already installed and ready to be connected-up for the distribution of the 10KHz FA data between all Liberas and a small number of feedback processors. This distribution is handled by a so-called Communication Controller [15] that runs in parallel on the FPGA in each Libera, and facilitates its exploitation in the near future's complete upgrade of the SR orbit stabilization system.

REFERENCES

[1] P. Elleaume et al, "Upgrade of the ESRF Accelerator Complex", WEPC010, EPAC-2008, Genoa

[2] E. Plouviez et al, "Improvements of the Fast Orbit Correction on the ESRF Storage Ring", this DIPAC-09 workshop

[3] K. Scheidt et al, "Breaking New Ground with High-Resolution T-b-T BPMs at the ESRF", IT-08, DIPAC-01, Grenoble

[4] G. Rehm et al, "Performance Verification on the Diamond e-BPM Electronics", POM028, DIPAC-05, Lyon

[5] J-C. Denard et al, "Preliminary Test of a new BPM system for Soleil", POM007, DIPAC-05, Lyon

[6] Instrumentation Technologies, Libera-Brillance, http://www.i-tech.si/index.php

[7] M.Lonza et al, "BPM Detectors Upgrade for the Elettra Fast Orbit Feedback ", TUPB04, DIPAC-07, Venice

[8] Y.B. Leng et al, "Data Acquisition and Analysis in SSRF BPM System", TUPC015, EPAC-08, Genoa

[9] C.H. Kuo et al, "Beam Position Monitoring Upgrade for the TLS", PAC-09, Albuquerque

[10] G. Rehm ,"Digital e-BPMs at Diamond : Operational Experience and Integration into a Fast Global Orbit Feedback", mod1a01, DIPAC-07, Venice

[11] N.Hubert et al, "The Soleil BPM and Orbit Feedback Systems", TUPC020, DIPAC-07, Venice

[12] A. Goetz et all ,"Future of Tango", FOPA01, Icalepsc-07, Knoxville

[13] J-C. Denard et al, "Behaviour of the BPM System during the first weeks of Soleil Commissioning", TUPCH008, EPAC-06, Edinburgh

[14] A. Kosicek et al, "Modified Digital Filtering Makes Possible 'True & Pure' T-b-T Measurements", BIW-08, Lake Tahoe

[15] I.S. Usun et al, "Initial Design of the Fast Orbit Feedback System for the Diamond Light Source", P3_030, Icalepsc-05, Geneva

DESIGN STATUS OF BEAM POSITION MONITORS FOR THE IFMIF-EVEDA ACCELERATOR

I. Podadera*, B. Brañas, A. Ibarra, CIEMAT, Madrid, Spain
J. Marroncle, CEA-Saclay, Gif-sur-Yvette, France

Abstract

The IFMIF-EVEDA accelerator [1] will be a 9 MeV, 125 mA CW deuteron accelerator which aims to validate the technology that will be used in the future IFMIF accelerator. Non-interceptive Beam Position Monitors pickups (BPMs) will be installed to measure the transverse beam position in the vacuum chamber in order to correct the dipolar and tilt errors. Depending on the location, the response of the BPMs must be optimized for a beam with an energy range from 5 up to 9 MeV and an average current between 0.1 and 125 mA. Apart from the broadening of the electromagnetic field due to the low-beta beam, specific issues are affecting some of the BPMs: tiny space in the transport line between the RFQ and cryomodule (MEBT), cryogenic temperature inside the cryomodule, phase and energy measurement in the diagnostics plate (DP), and debunching and big vacuum pipe aperture at the end of the high energy beam transport line (HEBT). For this reason different types of BPMs are being designed for each location (MEBT, cryomodule, DP and HEBT). In this contribution, the present status of the design of each BPM will be presented, focusing on the electromagnetic response for high-current low-beta beams.

INTRODUCTION

The design of the beam position monitors for the high-current low-energy accelerator IFMIF-EVEDA is facing important challenges due to the broadening of the electromagnetic detectors, the radiation environment and the debunching along the line, as described in [2]. The main use of the beam position monitors will be the monitoring of the transverse position of the beam centroid along the accelerator by calculating the differential signal from the vertical and horizontal pair of electrodes of the device. This parameter will be used to correct the dipole errors of the different elements and transport safely the beam along the accelerator. In addition, the bunch phase will be also measured in order to tune the rebuncher and the superconducting cavities. Last but not least the beam position monitors in the diagnostics plate will be in charge of measuring the mean energy of the particles by using the Time of Flight technique. The BPMs are expected to provide sufficient phase accuracy (using the sum signal) for this measurement.

The main beam parameters in which these monitors will work are summarized in Tab. 1. In normal operation, the accelerator will work with CW beams but during commissioning time the beam will be mostly pulsed with low duty factors. Therefore, both CW and pulsed operation has to be foreseen during the design phase. For a proper design of the monitors a first rough estimation can be done by implementing simple analytical models. However, powerful 3D electromagnetic software should be used for a more careful optimization of the geometry, the monitors response and the coupling to the beam. Presently these tools are being used for the design of the monitors all along the accelerator. The status of the design will be presented hereafter.

Table 1: Range (approx.) of the Beam Properties for the BPMs at IFMIF-EVEDA

Beam parameter	**Min. Value**	**Max. Value**
Energy E (MeV)	5	9
$\beta = v/c$	0.0727	0.0975
Peak current I_b (mA)	10	125
Average current $\langle I_0 \rangle$ (mA)	0.1	125
Pulse length T_p (ms)	1	CW
Duty factor (%)	0.1	CW
Bunch length σ_z (ns)	0.1	1.7
Transverse size $\sigma_{x,y}$ (mm)	1	20

LAYOUT AND REQUIREMENTS

Global Layout

Figure 1 sketches the distribution of the different types of beam position monitors inside the accelerator. A total of 18 monitors will be placed on the accelerator, distributed in at least four types of monitors (see Tab. 2) due to the different requirements at each section as detailed hereafter.

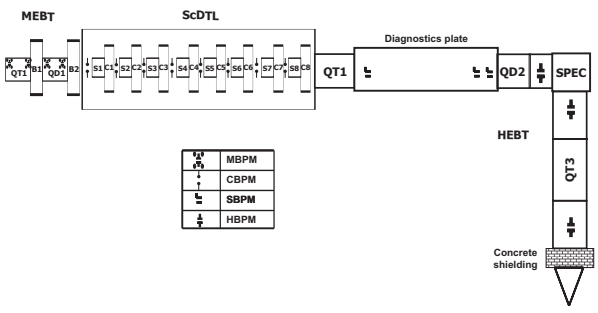


Figure 1: Distribution of the Beam Position Monitors along the accelerator.

* ivan.podadera@ciemat.es

Table 2: Summary of BPMs at IFMIF-EVEDA

Beamline	Aperture	Number
MEBT	48 mm	4
scDTL	50 mm	8
D-Plate	100 mm	3
HEBT	130 – 200 mm	3
TOTAL		18

Matching Section

Due to the beam dynamics requirements and the compactness of the beamline, the Beam Positions in the line between the RFQ and the cryomodule (MBPMs) will be located inside each quadrupole, like done for the SPIRAL2 project [4]. To maximize the charge induced in the electrodes, lobes are used instead of buttons. The mechanical assembly is simplified by using capacitive electrodes instead of striplines (either shorted or matched). The latest will make more complex the design and assembly of the monitor inside the quadrupoles. Small coaxial connectors -i.e. SMA- will be used as electrical vacuum feedthroughs to limit the mechanical interference with the poles of the quads.

Cryomodule

The BPMs inside the cryomodules (CBPMs) are located between each superconducting Half Wave Resonator and superconducting solenoid. The most important criteria to choose the proper monitor in this area is the reliability of the assembly. For this reason, button feedthroughs used for other accelerators will be installed in this area. To maximize this criteria the same button feedthroughs installed at the LHC [5] have been chosen as first option. They provide a 60° subtended angle in the center of the button (button diameter of 24 mm and the same vacuum aperture.

Diagnostics Plate

Apart from helping to the transport of the beam, the BPMs in the DP (SBPMs) are devoted to measure accurately the beam phase in order to tune the rebuncher cavities and the superconducting cavities during the different commissioning phases of the elements in the accelerator. The other main goal of the beam position monitors in this region is the measurement of the Time of Flight between the monitors. Three monitors will be used for that purpose. Two of them will be located as far as possible from each other, and the third one very close to one of the other two. The goal of the last monitor is to limit the a priori knowledge of the mean energy of the beam. In this way the number of bunches between the monitors is known. The distance between the first two monitors can be evaluated by assuming a certain phase accuracy of the BPMs -2°- and length accuracy -100 μm-. A distance of monitors between 2 m and 3 m is chosen. That gives an energy resolution of less than 10 keV for 5 MeV and 20 keV for 9 MeV. In addition, the distance gives a safe margin in case the accuracies are worse than expected.

HEBT

Three are the main issues for the monitors in this region (HBPMs): 1) the debunching of the beam coming from the last superconducting cavity [2], 2) the big beam pipe aperture and 3) the transverse beam size [6]. The first two decrease the output signal level and the resolution of the monitors. Only the fundamental harmonic -175 MHz- will be left at the end of the beamline. The last one modifies the sensitivity of the monitor and an analytical expression has to be used as given in [7].

ELECTROMAGNETIC SIMULATIONS

To evaluate the signal response of the monitors to the IFMIF-EVEDA beam and optimize the design, several codes are being used. For a realistic 3D simulation of the model with a low-beta particle beam as excitation source, the wakefield solver inside the code CST PARTICLE STUDIO™ is used. It provides the time response of the monitor to a certain pencil beam. The main results obtained are summarized in the following.

CBPMs

The sensitivity of the BPMs is simulated with the 3D solver by moving horizontally the excitation (particle beam) and evaluating the response at each of the four buttons. Figures 2 and 3 show the results of those simulations for the Δ_H/Σ, $S_{\Delta_H/\Sigma}$, and log-ratio, S_{dB}, method respectively for the fundamental frequency and the first harmonic (175 and 350 MHz) for horizontal $x = 0$ and diagonal $x = y$ beam movements.

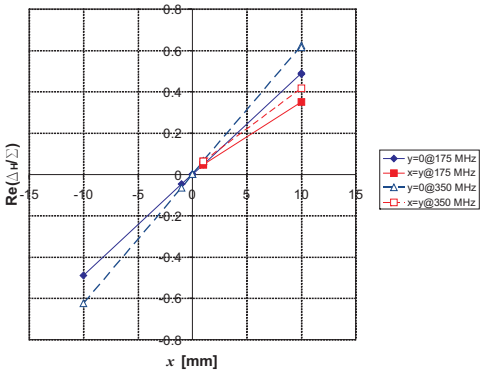


Figure 2: Simulation of the real part of the Δ_H/Σ method for the CBPM at $\beta = 0.0728$ with $\sigma_z = 15$ mm for the fundamental and first harmonic.

To crosscheck the results of the electromagnetic simulations an estimation of the log-ratio sensitivity can be given with the approximative analytical formula as given in [8].

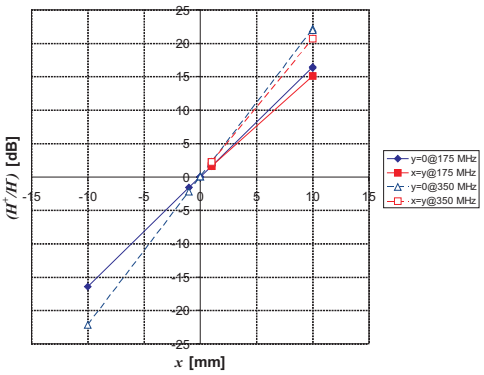


Figure 3: Simulation of the real part of the log-ratio method for the CBPM at $\beta = 0.0728$ with $\sigma_z = 15$ mm for the fundamental and first harmonic.

Table 3 summarizes the calculated horizontal sensitivities of the first CBPM at $\beta = v/c = 0.0728$ for different transfer function methods (Δ/Σ and log-ratio) [7]. The agreement between the simulated and analytical expressions is reasonable. It has to be noticed that the analytical expression is given for a cylindrical electrode and not for a button one. That could explain the slight discrepancy between the simulated and the analytical values.

Table 3: Comparison of Simulated and Analytical Sensitivities of the First CBPM for Different Transfer Fuctions

Energy E	5 MeV
Bunch length σ_b	15 mm
Simulated $S_{\Delta/\Sigma}$@175 MHz	0.0489 mm^{-1}
Simulated S_{dB}@175 MHz	1.6394 dB/mm
Analytical S_{dB}@175 MHz	1.57984 dB/mm
Simulated $S_{\Delta/\Sigma}$@350 MHz	0.0621 mm^{-1}
Simulated S_{dB}@350 MHz	2.2098 dB/mm
Analytical S_{dB}@350 MHz	2.1856 dB/mm

SBPMs

In this section the monitors require the best resolution and accuracy to achieve the best beam characterization. Stripline monitors are the present choose due to the high mechanical stability and good phase response for different beam offsets [3]. The geometry of the four lobes coaxial lines are simulated to match the dipolar and geometrical mode of the line to the external load $Z_0 = Z_{dip} = Z_{geom} = \sqrt{Z_{sum} Z_{quad}} = 50\ \Omega$. In this way the monitors could be used not only with narrowband electronics but also with broadband [9, 10]. Figure 4 shows the optimization of the angular geometry of the striplines to match the dipolar and geometrical impedances with the external load as function of the body radius (external radius of the coaxial line). The angle of the electrodes is fixed to two values: 45° and 60°, and the internal radius of the line to 50 mm. For 60° angle, the optimum is found between 64 and 66 mm.

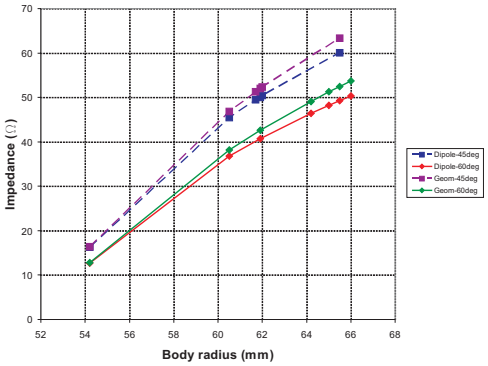


Figure 4: Optimization of the geometry of the four short-end stripline monitor.

CONCLUSIONS

Beam Position Monitors will be essential devices for the tuning and operation of the IFMIF-EVEDA accelerator. Although the low-energy affects the quality of the measurement, the simulations of the BPMs presented here have shown that they perfectly adapted for the measurement of the IFMIF-EVEDA beam. After finishing the design optimization of all the devices, some prototypes will be constructed in the next future and will be characterized in a test bench to verify the results obtained in the simulations.

ACKNOWLEDGEMENTS

We would like to acknowledge the support and the fruitful discussions with L. Soby and C. Boccard from the CERN and P. Forck from GSI. We also want to thank the help from the all the IFMIF-EVEDA ASG team.

REFERENCES

[1] A. Mosnier, A. Ibarra, A. Facco, EPAC'08, p. 3539, Genoa, Italy (2008).

[2] I. Podadera et al., Proceedings of HB2008, Nashville, USA (2008).

[3] S. Kurennoy, LINAC'00, p. 172, Monterey, USA (2000).

[4] R. Ferdinand, Presentation at SPIRAL2 Week 2009, Caen, France (2009).

[5] C. Boccard, Proceedings of CARE Workshop, Lueneburg, Germany (2007).

[6] C. Oliver et al., Proceedings of EPAC'08, p. 3041, Genoa, Italy (2008).

[7] J. D. Gilpatrick, PAC'97, p. 2090, Vancouver, Canada (1998).

[8] R. Shafer, AIP BIW'93,319, p. 303, Santa Fe, USA (1994).

[9] C. Deibele, S. Kurennoy, PAC'05, p. 2607, Knoxville, USA (2005).

[10] S. Kurennoy, PAC'07, p. 4111, Albuquerque, USA (2007).

DEVELOPMENT OF THE RF CAVITY BPM OF XFEL/SPRING-8

H. Maesaka#, S. Inoue, T. Ohshima, S. Matsubara, T. Shintake and Y. Otake,
RIKEN/SPring-8, 1-1-1, Kouto, Sayo, Hyogo, 679-5148, Japan
H. Ego, JASRI/SPring-8, 1-1-1, Kouto, Sayo, Hyogo, 679-5198, Japan

Abstract

We describe the design and performance of the rf cavity beam position monitor (RF-BPM) for the x-ray free-electron laser project at SPring-8 (XFEL/SPring-8). The required position resolution is less than 0.5 μm. To achieve this demand, we designed an RF-BPM that has a TM110 cavity to detect the beam position and a TM010 cavity to obtain the beam charge and phase reference. The resonant frequency is 4760 MHz for both cavities. We designed a detection circuit equipped with IQ (In-phase and Quadrature) demodulators. We installed the BPM system into the SCSS test accelerator and performed a beam test. We observed a position sensitivity of approximately 0.1 μm and a position resolution of less than 0.2 μm at a 0.3 nC bunch charge. We evaluated the resolution of the beam arrival timing measurement with the phase being between the TM010 resonator and a reference rf signal. The temporal resolution was 25 fs. These results are sufficient for the beam tuning of XFEL/SPring-8.

INTRODUCTION

The x-ray free-electron laser project at SPring-8 (XFEL/SPring-8) [1] is underway to open a new era of life sciences, material sciences, etc. The XFEL/SPring-8 facility consists of an electron injector with a thermionic cathode, C-band high-gradient accelerators and short-period in-vacuum undulators. XFEL/SPring-8 is designed to generate a coherent x-ray beam at an angstrom wavelength by a self-amplified spontaneous emission (SASE) process.

One of the most important technical issues is to overlap the electron beam with radiated x-rays throughout the undulator section with high precision. The position difference between the electron beam and the x-rays must be less than 4 μm [2]. Therefore, we require the resolution of the beam position monitor (BPM) to be less than 0.5 μm. Among various types of BPMs, only an rf cavity BPM (RF-BPM) can achieve this demand, because of its high beam-cavity coupling. There exist some past experimental reports with nanometer-level resolutions [3-5].

It is also important to monitor the time difference between a beam and a reference rf signal. The temporal precision of the XFEL accelerator is demanded to be less than 50 fs [6]. An RF-BPM has a capability to detect beam arrival timing from the phase of an excited rf signal.

We designed a BPM system comprising an RF-BPM cavity and a detection circuit in order to achieve the required resolution. This system was installed into the SCSS test accelerator, which was built to demonstrate the feasibility of XFEL/SPring-8, and has been operating as FEL at extreme ultraviolet (EUV) FEL since 2006. Our BPM system was tested with a 250 MeV electron beam. In this paper, we describe the design of this system and the results from beam tests.

DESIGN OF THE RF-BPM SYSTEM

The RF-BPM uses a TM110 dipole resonant mode in a cylindrical cavity to measure the beam position. The longitudinal electric field, E_z, of TM110 is expressed as

$$E_z = E_0 J_1\left(\frac{\chi_{11} r}{a}\right) \cos\varphi \; e^{j\omega t}, \qquad (1)$$

where E_0 is a constant that represents the field amplitude, J_1 is a first-order Bessel function of the first kind, $\chi_{11} \simeq 3.8$ is the first root of $J_1(r) = 0$, a is the cavity radius and ω is the resonant angular frequency. Since $J_1(r)$ can be approximated by a linear function near the axis, the amplitude of the TM110 field excited by an electron beam is proportional to beam displacement.

The voltage amplitude of the output signal from the TM110 cavity can be written as [7]

$$V = V_1 q x + j V_2 q x' + j V_3 q + V_n, \qquad (2)$$

where q, x and x' are the beam charge, the beam position and the slope of the beam trajectory, respectively. $V_1 q x$ is the in-phase component proportional to the beam position, $jV_2 q x'$ is the quadrature-phase component coming from the beam slope, $jV_3 q$ is also the quadrature-phase component due to leakage of the parasitic TM010 monopole mode and V_n are the other components, such as a thermal noise. To obtain beam position information, we have to scale the signal with the beam charge and determine the sign with a phase reference. Therefore, we prepared an additional TM010 mode cavity in the same cavity block to provide charge and phase information.

Based on concepts mentioned above, we designed the RF-BPM illustrated in Fig. 1. For the TM110 cavity, the rf signal is picked up through a coupling slot that is decoupled to the TM010 monopole mode in order to minimize the third term of Eq. 2 ($jV_3 q$). The resonant

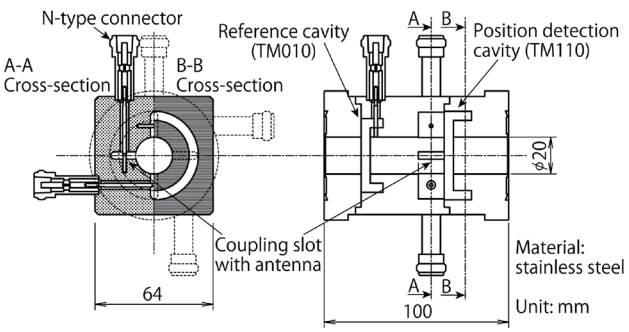


Figure 1: Drawing of the RF-BPM cavity.

#maesaka@spring8.or.jp

frequency is 4760 MHz for both TM110 and TM010 cavities. Although the acceleration rf frequency is 5712 MHz, the BPM frequency is intentionally shifted so as to avoid any background due to the dark current synchronized with the acceleration rf. Some other parameters of the RF-BPM are summarized in Table 1.

The RF-BPM signal is processed by an IQ (In-phase and Quadrature) demodulator (IQ-DEM), as shown in Fig. 2. In order to improve the resolution in the SCSS test accelerator, where a different electronics with a logarithmic amplifier is used [8], we newly developed IQ-DEM type electronics. The rf signal from the RF-BPM is fed into an attenuator switch so as to extend the dynamic range, because the required value is 100 dB (sub-μm – a few mm), while the dynamic range of the IQ-DEM is 60 dB. The baseband signal from the IQ-DEM is recorded by a 12-bit VME A/D converter [9]. The basic performance was verified with a CW rf signal. The amplitude linearity error was less than 1% and the phase error was less than 1 degree when the input rf voltage was more than 10% of the full scale (100 mV). The obtained performance is sufficient for beam-position measurements in XFEL/SPring-8.

RESULTS FROM THE BEAM TEST

We tested the RF-BPM system in the SCSS test accelerator. A photograph of the installed RF-BPM is shown in Fig. 3. The cavity was mounted on a movable stage to align the cavity along the beam axis and to confirm the beam position dependence of the signal. The beam energy was 250 MeV and the beam charge was 0.3 nC. The transverse beam diameter was approximately 0.2 mm (FWHM). We measured the position sensitivity, the position resolution and the beam arrival timing resolution. We describe the results in the following subsections.

Position Sensitivity

We obtained the position sensitivity by moving the BPM position while the electron beam trajectory was fixed. One of the plots of ADC counts versus BPM positions is shown in Fig. 4. The sensitivity was measured to be more than 20 ADC counts per 1 μm. Since the ADC noise is a few counts, the position sensitivity is approximately 0.1 μm.

Position Resolution

The position resolution can be measured by using three adjacent RF-BPMs. The first and third BPMs predict the position at the second BPM, assuming a straight beam trajectory. The position resolution is determined from the residual, which is the difference between the detected position of the second BPM and the expectation.

A resolution measurement was performed with the three BPMs illustrated in Fig. 5. All of the electromagnets between the BPMs were turned off so that the beam trajectory would be straight. The distribution of the residual in the horizontal direction is shown in Fig. 6. The width of this histogram is the convolution of the position

Table 1: Parameters of the RF-BPM Cavity

	TM110 cavity	TM010 cavity
Resonant Frequency	4760 MHz	4760 MHz
Loaded Q factor	50	50
Number of ports	4 (X: 2, Y: 2)	1
Signal amplitude at the 50 ohm port	14 mV/μm/nC (peak)	200 V/nC (peak)

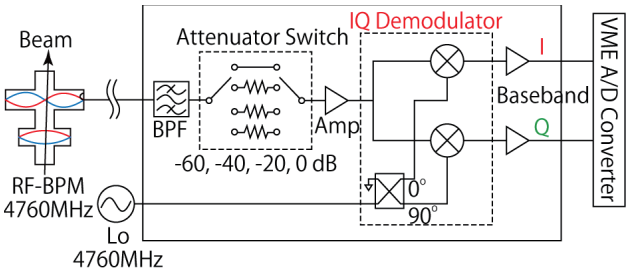


Figure 2: Block diagram of the RF-BPM electronics.

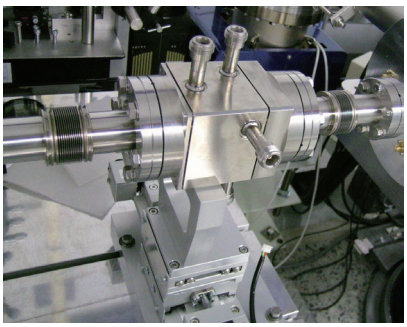


Figure 3: Photograph of the RF-BPM cavity.

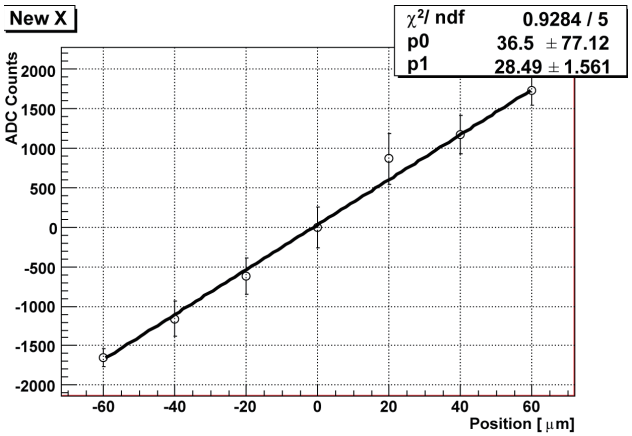


Figure 4: ADC count of the RF-BPM at each position. The error bars show the standard deviation of the histogram of the ADC data. A linear function fitted to the data is also plotted.

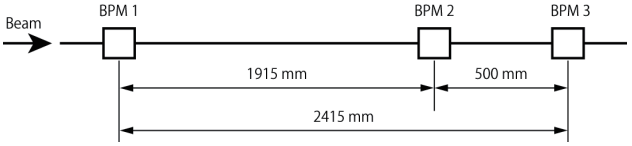


Figure 5: Arrangement of the three BPMs for the resolution measurement.

uncertainties of the three BPMs. Assuming that the resolutions of the three BPMs were same, the position resolution, σ_{BPM} , was calculated by the following equation by means of an appropriate error propagation:

$$\sigma_{\mathrm{BPM}} = \frac{L_1+L_2}{\sqrt{2({L_1}^2+L_1L_2+{L_2}^2)}}\,\sigma_{\mathrm{res}} \simeq 0.773\,\sigma_{\mathrm{res}}\ , \qquad (3)$$

where L_1 and L_2 are the distance between the BPM 1 and 2 and that of the BPM 2 and 3, respectively, and σ_{res} is the standard deviation of the residual distribution. Since we found that the conversion coefficient of the ADC counts to the beam position had a systematic error of 10%, we increased σ_{BPM} by 10%. Finally, the position resolution of the RF-BPM was measured to be less than 0.2 μm, as tabulated in Table 2.

Beam Arrival Timing Resolution

The beam arrival timing can be measured by the phase of the TM010 resonator. In the SCSS test accelerator, the beam arrival timing jitter was measured to be approximately 50 fs [6] with this method. However, the temporal resolution of the RF-BPM, itself, was not evaluated at that time. Therefore, we measured the temporal resolution by using the two neighboring BPMs (the BPM 2 and 3 in Fig. 5).

Figure 7 shows the distribution of the phase difference between the two TM010 cavities. The standard deviation is 0.0459 degree of 4760 MHz, corresponding to 27 fs. The temporal resolution is $1/\sqrt{2}$ of this value if the resolutions of the two BPMs are same. We found that the beam arrival timing jitter of the BPM 2 was 30% different from that of the BPM 3. Therefore, we increased the resolution by 30% as a systematic error. Consequently, the temporal resolution of the RF-BPM was obtained to be 25 fs ($= 27\ \mathrm{fs}\ /\ \sqrt{2}\ \times 1.3$).

CONCLUSIONS

We designed an RF-BPM system to achieve a sub-μm resolution required for the XFEL facility. The performance of the RF-BPM system was confirmed by an electron beam of the SCSS test accelerator. The position sensitivity was 0.1 μm and the position resolution was less than 0.2 μm. The temporal resolution on the beam arrival timing was evaluated to be 25 fs. These results are sufficient for the XFEL facility.

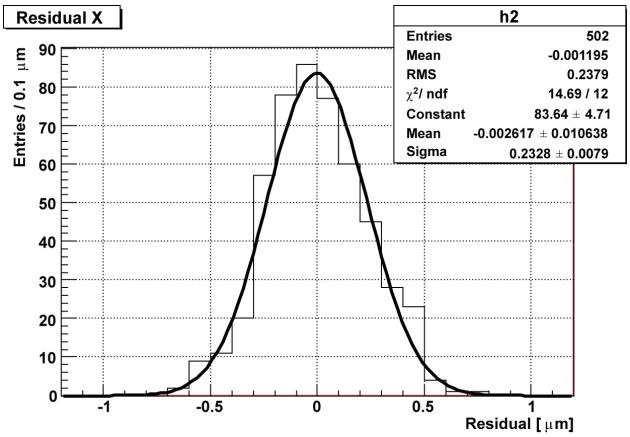


Figure 6: Residual distribution of the position resolution measurement. The histogram was fitted by a Gaussian.

Table 2: Position Resolution of the RF-BPM

	Horizontal	Vertical
Position resolution	0.198 μm	0.171 μm

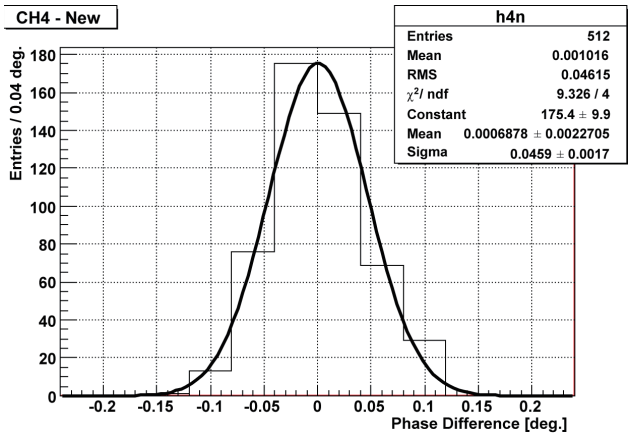


Figure 7: Phase difference between the TM010 cavities of the BPM 2 and 3. The histogram was fitted by a Gaussian.

REFERENCES

[1] T. Shintake *et al.*, "Status of X-ray FEL / SPring-8 Machine Construction", Proc. of EPAC'08, (2008).
[2] T. Tanaka, H. Kitamura and T. Shintake, Nucl. Instrum. Meth. A 528, 172 (2004).
[3] T. Slaton *et al.*, "Development of Nanometer Resolution C-band Radio Frequency Beam Position Monitor in The Final Focus Test Beam", SLAC-PUB-7921 (1998).
[4] V. Vogel *et al.*, "Performance of a Nanometer Resolution Beam Position Monitor System", UCRL-CONF-216283 (2005).
[5] T. Nakamura, "Development of Beam-position Monitors with High Position Resolution", Master thesis, Univ. of Tokyo (2008).
[6] Y. Otake *et al.*, "Timing and LLRF System of Japanese XFEL to Realize Femto-second Stability", Proc. of ICALEPCS'07 (2007).
[7] T. Shintake, "Development of Nanometer Resolution RF-BPMs", Proc. of HEAC'99 (1999).
[8] H. Maesaka *et al.*, "Beam Position Monitor at the SCSS Prototype Accelerator", Proc. of APAC'07 (2007).
[9] T. Fukui *et al.*, "A Development of High-speed A/D and D/A VME Boards for a Low Level RF System of SCSS", Proc. of ICALEPCS'05 (2005).

BUNCH BY BUNCH FEEDBACK SYSTEM USING iGp AT KEK-PF

R. Takai#, M. Tobiyama, T. Obina, J. W. Flanagan, M. Tadano, T. Mitsuhashi,
KEK, 1-1 Oho, Tsukuba, Ibaraki 305-0801, Japan

Abstract

A transverse bunch-by-bunch feedback system using iGp feedback signal processors has been tested at the KEK-PF. The system consists of a bunch position detection system using 1.5 GHz components of the beam (3 x f_{RF}), iGp feedback signal processors, and a transverse feedback kicker with a high power amplifier. It shows sufficient performance to suppress instabilities completely up to a beam current of 450 mA. Results of the mode analysis of the instabilities using the grow-damp function of the iGp are also shown.

INTRODUCTION

Photon Factory electron storage ring (PF-ring) has been operated in a single- or multi-bunch mode of 2.5 GeV. In the multi-bunch operation, several coupled-bunch mode instabilities are observed in both transverse and longitudinal planes as a stored beam current increases. As for the transverse instabilities, we have suppressed them by using a bunch-by-bunch feedback system developed based on that of SPring-8 [1]. Although this feedback system had worked without major problems since the installation of 2005, we are now planning to replace it to that using "integrated General purpose signal processors (iGp)", which have been developed by the collaboration of KEK, SLAC, and INFN-LNF [2]. The iGp is equipped with not only a greater flexibility for the change of tunes, but also many GUI panels that enable us to remotely change various parameters on digital processing such as coefficients of an FIR filter. It has already been used in the longitudinal bunch-by-bunch feedback system of PF-ring, and succeed in suppressing longitudinal dipole oscillations sufficiently [3]. In order to confirm its effectiveness for transverse instabilities, we have constructed the transverse feedback system using the iGp, and tested its basic performance. The details and some experimental results of the tentative feedback system are presented herein.

The main parameters of PF-ring are listed in Table 1.

Table 1: Main Parameters of PF-ring

Beam energy	2.5	GeV
Circumference	187	m
RF frequency f_{RF}	500.1	MHz
Harmonic number	312	
Revolution frequency f_{rev}	1.603	MHz
Betatron tune ν_x / ν_y	9.6 / 5.28	
Damping time τ_x / τ_y	7.8 / 7.8	ms
Stored current (single/multi)	50 / 450	mA

FEEDBACK SYSTEM

The transverse bunch-by-bunch feedback system is mainly composed of three sections, an analogue front-end detection, a digital signal processing, and a beam correction. The block diagram of the whole system is shown in Fig. 1.

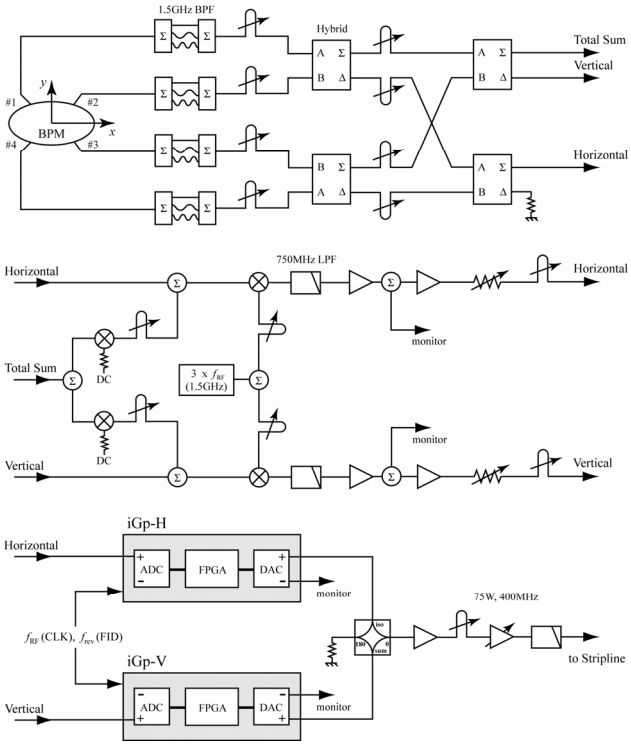


Figure 1: Block diagram of the transverse feedback system using the iGp.

Front-end Detection Section

The beam signals picked up by a 4-button BPM are processed individually via a 1.5 GHz bund-pass filter (BPF) which consists of a power combiner/splitter and three delay cables. The output signals are summed by hybrid circuits (M/A-COM, H-183-4) and converted into three signals, Horizontal, Vertical, and Total Sum. After offset components in Horizontal and Vertical are cancelled by using Total sum, the transverse position of each bunch is detected by a synchronous detection at the 3rd harmonic of the RF frequency (3 x f_{RF}). The timing of the signal processing is precisely adjusted with line stretchers while a single bunch is stored.

#ryota.takai@kek.jp

Signal Processing Section

A key component of the iGp is a FPGA board including 8-bit 1GSPS ADCs, one FPGA chip (Xilinx, Vertex-II), and 12-bit 1GSPS DACs. The FPGA functions as a 16-tap FIR filter designed so as to have a maximum gain at a betatron frequency and achieve a phase shift of 90 ◦ between the pickup and the feedback kicker. Figure 2(a) and 2(b) show frequency responses of the horizontal and vertical FIR filters used in the experiment, respectively. These responses can be easily changed through the GUI.

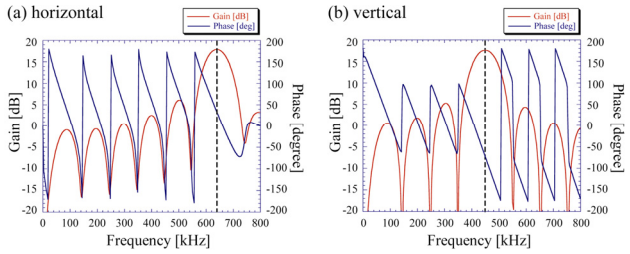


Figure 2: Frequency responses of the horizontal and vertical FIR filters.

The detected signal from the front-end section is digitised by ADCs operated at the RF frequency of 500 MHz, and then applied the FIR filter and a 1-turn delay function inside the FPGA. The processed signal is converted to analogue by DACs operated at 500 MHz, and summed to that of another transverse degree by an external hybrid.

Figures 3(a) and 3(b) are the input and output signals of the iGp measured at the single-bunch operation, respectively. The extraction of the betatron-frequency component and the DC-offset cancelling are implemented simultaneously with the 500 MHz clock signal.

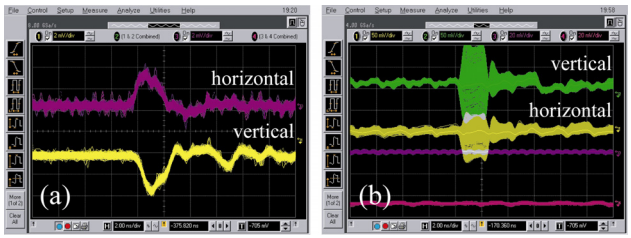


Figure 3: Input and output signals of the iGp for a single bunch.

Corrector Section

The correction signal from the iGp is amplified with a 75 W broadband amplifier (Amplifier Research, 75A400), and fed to a stripline kicker whose length is 45 cm. One of the ends of the stripline electrode is connected to a high-power attenuator. The attenuated signal from the stripline is used to monitor the correction signal associated with the beam-excited signal.

EXPERIMENTAL RESULTS

Overview

In order to prevent the onset of the transverse ion-trapping instabilities, test experiments of the iGp feedback system are performed with 280 out of 312 buckets filled. The bunch spacing is 2 ns. We apply the longitudinal bunch-by-bunch feedback and the RF phase modulation so as to suppress the longitudinal dipole and quadrupole oscillations. According to past experience, the transverse instabilities are excited more strongly as the magnet gap of in-vacuum undulators (ID gap) becomes narrow [4]. Therefore, in the first stage, we fix the ID gap to the maximum value of 45 mm.

Under such conditions, we injected the beam with the iGp feedback system working. As a result, the feedback system showed sufficient performance to suppress the transverse instabilities, and we succeeded in storing a 450 mA current which is the typical value for user operation. Without the transverse feedback, the stored beam was not lost, but the severe horizontal oscillations were observed. We could also confirm that the transverse instabilities were damped immediately if we closed the feedback loop again.

Figures 4(a) and 4(b) show the transverse beam profile measured by a CCD camera for the open- and closed-loop conditions, respectively. We can see that the horizontal beam size is reduced by closing the feedback loop. To quantify the effect, we performed Gaussian fits to horizontal projections of the profiles, and compared them as shown in Fig. 4(c). In this case, the horizontal beam size decreases by approximately 20 %.

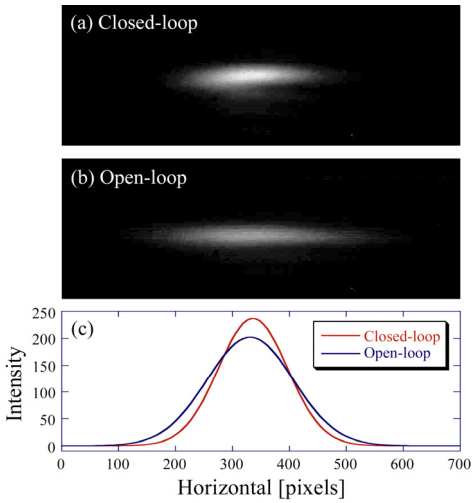


Figure 4: Transverse beam profiles measured by a CCD camera.

Mode Analysis of Instabilities

The iGp can hold two FIR filter coefficient sets in an internal memory of the FPGA, and switch them with arbitrary timing. This function enables us to perform the transient-domain analysis of instabilities for the

horizontal and vertical plane, individually [5]. In Figs. 5(a) and 5(b), results of the transient-domain analysis for the horizontal plane are illustrated. The time interval from the start of data acquisition to the resumption of the horizontal feedback was set to be 12.5 ms. The stored beam current at this time was 370 mA.

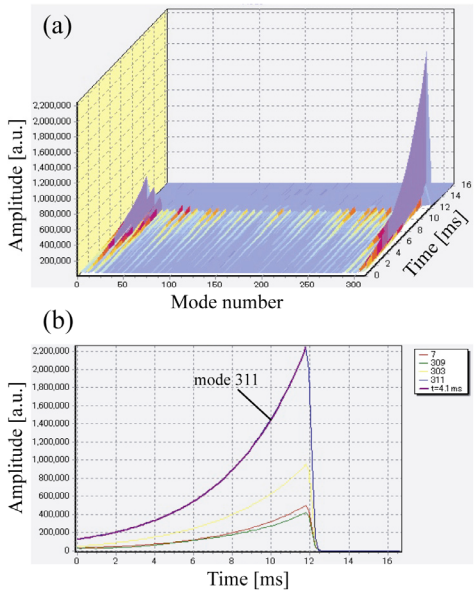


Figure 5: Time evolution of the modes of the horizontal instabilities.

Mode 311 (-1), which is the highest order mode, is most strongly excited among all modes in the horizontal plane. It is also shown that this mode is recaptured easily when we resume the horizontal feedback after the 12.5 ms interval, and suppressed immediately. Fitting exponential functions to the growing part of mode 311, we can estimate the growth time of 4.1 ms. This value changes depending on various parameters such as the stored beam current and the vacuum pressure. In the case of a 450 mA current, although the most strongly excited mode is 311, its growth time shortens to 3.7 ms. On the other hand, the damping time of mode 311 is sufficiently short in both currents, approximately 0.1 ms (160 turns).

We performed the same measurement for the vertical plane. Noticeable instabilities were, however, not observed in this plane even if the vertical feedback was turned off completely.

ID-gap Dependence

When we narrowed the ID gap with a 370 mA current, the growth time of instabilities decreased obviously, while the excited modes did not change. The growth time of horizontal mode 311 was measured for several values of the ID gap and the result is shown in Fig. 6. It shows us that the instability grows rapidly in smaller gap less than 10 mm. According to the intuition, the observed instabilities seem to have been excited by the resistive-wall instability. The resistive-wall instability should, however, occur in the vertical plane as observed at SPring-8 and ESRF [6,7]. In this case, we could not observe any instabilities in the vertical plane even with the minimum gap of 4 mm. In addition, we cannot also explain that the highest order mode is most strongly excited, because the transverse impedance of the resistive-wall instability should be inversely proportional to the square root of the frequency [8]. Further investigations are required to identify the cause of these phenomena.

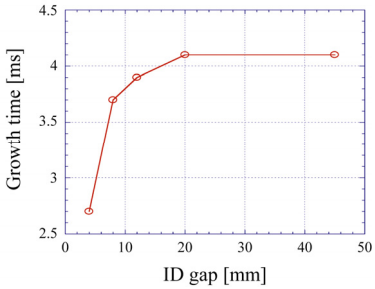


Figure 6: Dependence of the growth time of horizontal mode 311 on the ID gap.

SUMMARY AND FUTURE PLAN

We have constructed and tested a transverse bunch-by-bunch feedback system using the iGp at PF-ring. The feedback system has shown sufficient performance to suppress the transverse instabilities up to a beam current of 450 mA. We have also performed the transient-domain analysis of instabilities, and determined that the highest order mode 311 of the horizontal plane grows most rapidly among all instability modes. The growth time of this mode has changed depending on a stored beam current and a magnet gap of in-vacuum undulators. It has shown a drastic decrease especially in smaller magnet gap less than 10 mm.

We are now constructing the transverse feedback system using the iGp for ordinary use, which has two feedback loops, aiming at the installation within this year. After the installation, we continue the study to identify the cause of the transverse instabilities at PF-ring.

ACKNOWLEDGEMENT

The authors are grateful to Drs. J. Fox and D. Teytelman for useful discussions. We would also like to thank members of the PF light source division for their support of the machine studies.

REFERENCES

[1] W. X. Cheng, *et al.*, Proc. EPAC06 (2006) 3009.
[2] D. Teytelman, *et al.*, Proc. EPAC06 (2006) 3038.
[3] T. Obina, *et al.*, Proc. BIW08 (2008) TUPTPF015.
[4] T. Obina, *et al.*, PF-Ring Report 895 (2006).
[5] M. Tobiyama, *et al.*, PRST-AB **9** (2006) 012801.
[6] T. Nakamura, *et al.*, Proc. PAC01 (2001) 1969.
[7] R. Nagaoka, *et al.*, Proc. EPAC00 (2000) 1158.
[8] K. Bane, *et al.*, Proc. PAC93 (1993) 3375.

THE MEASUREMENT OF BUNCH INTENSITY USING THE LHC BPM SYSTEM

J.L. Gonzalez*, E. Calvo, D. Cocq, R. Jones, CERN, Geneva, Switzerland

Abstract

A convenient way of having beam bunch intensity information available all around the LHC ring is to use the beam position monitor (BPM) system. The principle is to add the BPM signals, process them and make the result compatible with the time-modulation method used for transmitting the position over a fibre-optic link. In this way the same acquisition system can make both position and intensity data available. This paper describes the technique developed and presents the first intensity measurements performed on the CERN-SPS and LHC.

INTRODUCTION

The LHC beam position system is comprised of more than 1070 beam position monitors, the majority of which are electrostatic button electrode pick-ups. Each BPM provides both position and intensity information. The acquisition electronics is split into two parts, an analogue front-end, which sits in the tunnel, and an integrator/digitiser/processor VME module located on the surface [1]. Transmission from tunnel to surface is carried out using a time-encoded signal over a single mode fibre-optic link. A digital multiplexer, located in the position to time normaliser board [2], allows for either position or intensity selection, eliminating the need for a separate optical transmission system and digital acquisition boards for the intensity measurement. A WorldFIP fieldbus is used to control the tunnel stations.

THE LHC BPM SYSTEM

The LHC BPM system is foreseen to work with bunch intensities ranging from 1.5×10^{9} to 2×10^{11} protons, using two sensitivity settings (low or high). Figure 1 shows the basic layout of the system. Each normaliser module gets the high frequency beam signals of the horizontal or the vertical electrodes and filters them using a pair of matched, 70 MHz, low-pass filters in order to significantly reduce any bunch length dependence due to the shortening of the bunch during acceleration. The filter is followed by a passive combiner, which makes the analogue sum of these signals available for further processing in the beam intensity board. Intensity information can actually be transmitted either directly using the optical output of the intensity module or via the normalisers, since the signal produced is compatible with the time-modulation method used for encoding the beam position.

Intensity Measurement Principle

Figure 2 depicts the intensity measurement principle. An analogue input multiplexer selects for which of the two counter-rotating beams the intensity will be measured. The input signal is the combination of the horizontal and vertical sum signals from the two associated normalisers. Detecting the zero crossing of the BPM signal triggers both the laser "*Start*" pulse and the constant current discharge source after a predefined delay.

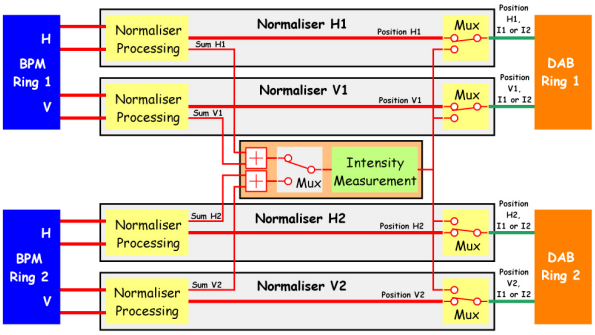


Figure 1: LHC position and intensity measurement system layout.

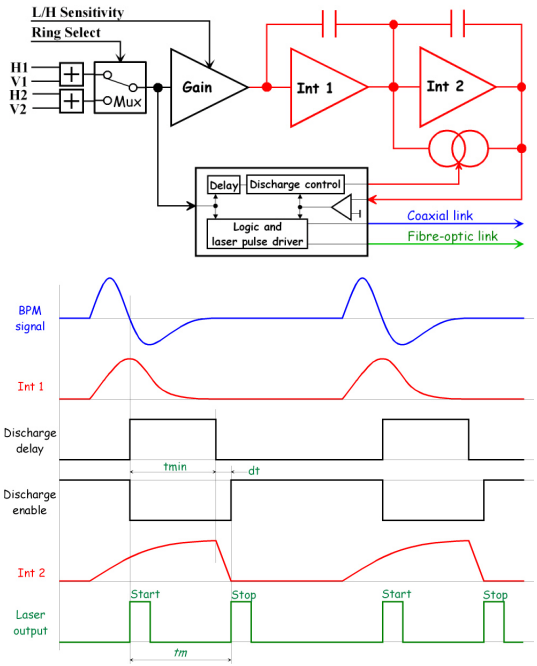


Figure 2: Intensity measurement principle and related waveforms.

The sensitivity control input adapts the gain to the beam dynamic range. The resulting signal is then integrated twice and a fast comparator produces the laser "*Stop*" pulse when the output voltage of the second integrator reaches zero, due to the constant current discharge. The *Start* and *Stop* pulses have a duration of 1ns and the

* jose.luis.gonzalez@cern.ch

intensity information is encoded in the time t_m between the two pulses, which can vary from 8.5ns to 11.5ns.

Laboratory Measurements and Simulations

700 Intensity modules have been installed throughout the LHC ring. Each of them has been tested and calibrated on a dedicated test bench, using a PC-driven "intensity beam simulator" to emulate the sum-outputs of a pair of normalisers. The measured linearity is better than ±4%. In order to verify that the accuracy is within the 10% specified for the system, further measurements in both frequency and time-domain were carried out on the whole analogue front-end, including the LHC button pick-up, the flange, actual cabling and the normaliser.

A unit Gaussian pulse excitation signal (909ps full width at half maximum) was used for time-domain network analyzer measurements. Such pulse response analysis had already previously been used to correct PSpice® simulation models to fit acquired data [3].

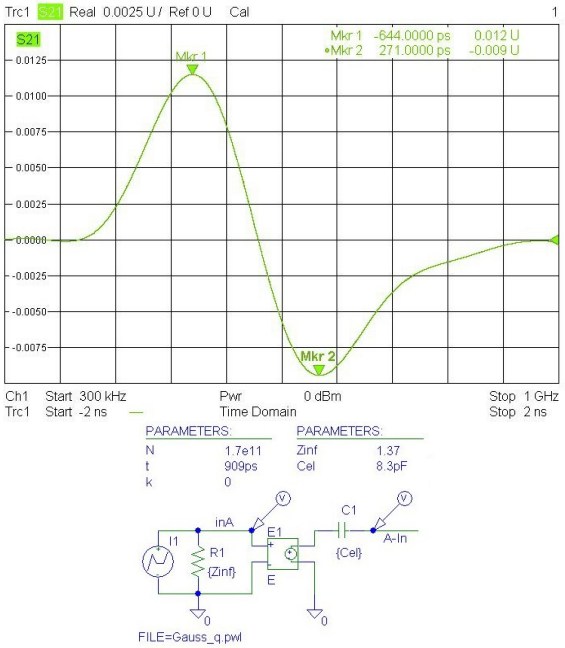


Figure 3: Measured pulse response of the LHC button pick-up and the electronic PSpice® simulation model.

The differentiated pick-up response and the simulation model are presented in Figure 3. A set of parameters are used to identify both the button electrical characteristics and the input-pulse charge content and duration.

Since the pick-up introduces around 40dB attenuation, any subsequent measurements were noisy. The normaliser and the associated wiring were therefore measured separately from the pick-up. Figure 4 shows the sum response to the same unit Gaussian pulse and the hardware equivalent PSpice model that fits the acquisitions.

The normaliser sum signal is produced by a passive combiner that adds the signals of two identical branches composed of input couplers, constant-resistance low-pass filters and matching attenuators. External wiring is simulated using another filter and the resulting losses are included in the input attenuator. Model parameters have been adjusted to obtain the same pulse response as the reference measurement.

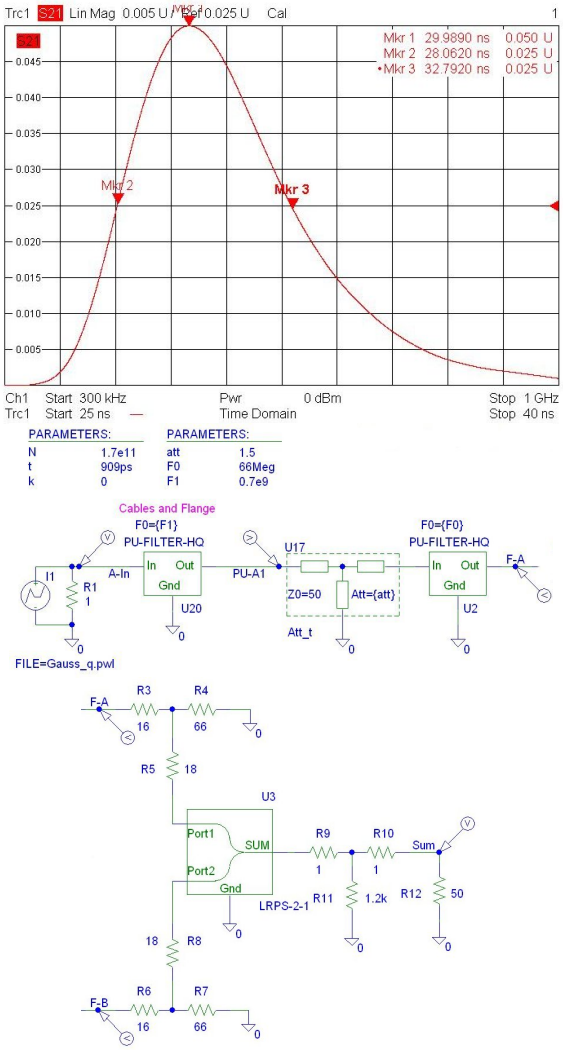


Figure 4: Network analyzer time-domain measurement of the normaliser sum-output and partial schematic of the equivalent simulation model.

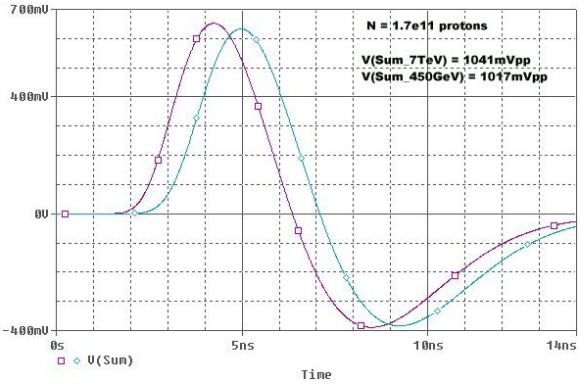


Figure 5: Simulated normaliser sum signal responses to the LHC bunch at 450 GeV and 7 TeV.

The results of full system simulation, from button to normaliser sum-output are presented in Figure 5. Notice that the sum signal variation, due to bunch length effects

in going from beam injection to collision, is only 24mV$_{pp}$ (about 2%), while the bunch length σ changes from 375ps to 252ps. The sum signal can therefore be considered as linearly proportional to the bunch intensity and its transfer function versus the number *N* of bunch protons is:

$$Sum_{\mathrm{mV_{pp}}} = 6.06 \times 10^{-9} N$$

This is used to scale the internal calibrator of the normaliser and that of the test bench beam simulator to give bunch intensities.

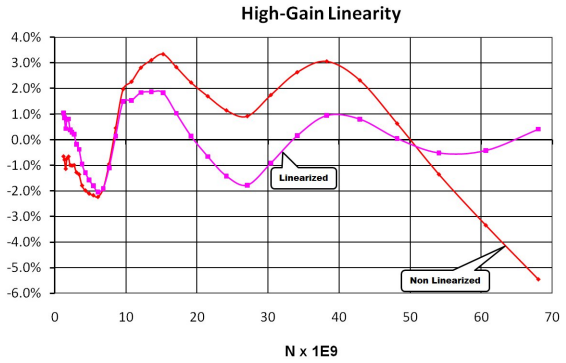


Figure 6: Linearization graph from the test bench.

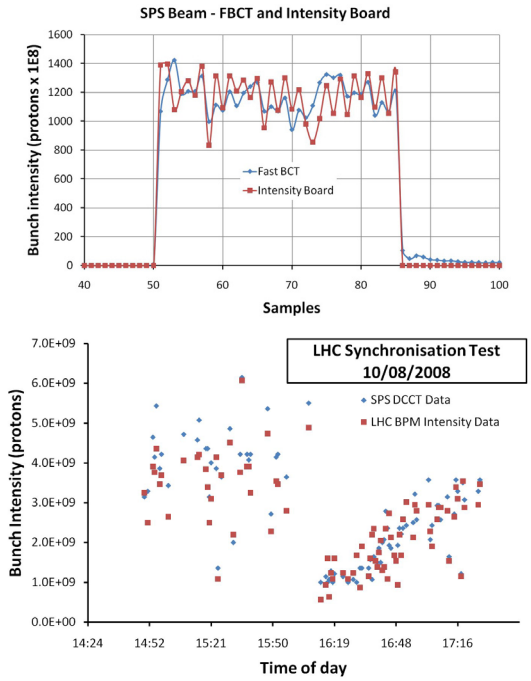


Figure 7: SPS (top) and LHC (bottom) measurements.

The 48dB range of the "intensity beam-simulator" extends from 1.2×10^{9} to 3×10^{11} protons per bunch. The intensity module covers it using two sensitivity ranges of 35dB each, with an overlapping region. The high sensitivity mode guarantees a linearity around ±2%, as illustrated with the example in Figure 6, while that of the low sensitivity is close to ±4%.

FIRST BEAM MEASUREMENTS

The first beam acquisitions showed a systematic offset of the intensity reading [4]. This was found to come mainly from the final cabling layout and small neglected electronics effects and led to the time-domain analysis previously discussed. Figure 7 presents actual proton beam measurements on both the CERN-SPS and from first beam in the LHC. The SPS trace shows the bunch by bunch intensity profile of a 72 bunch LHC type batch, taken on a single turn. It can be seen that the intensity module and the fast beam transformer are in reasonable agreement to within the accuracy possible due to the bandwidth limitations of the transformer. The LHC plot shows a comparison of the SPS DCCT data and a BPM intensity module at the end of the first LHC sector for single, very low intensity, pilot bunch injection over a few hours. Even working close to its detection threshold the intensity module can be seen to give a reliable measurement of the bunch intensity injected in the LHC.

CONCLUSION

An intensity module has been designed and built to provide bunch intensity measurements from each beam position monitor located in the LHC. As this was added at an advanced stage in the beam position project, the intensity module had to encode the intensity information using the same pulse modulation technique as the beam position system. Despite this tight constraint the BPM intensity card has shown to perform remarkably well, with a linearity of around 2% and an accuracy better than the 10% requested for the system.

ACKNOWLEDGEMENTS

We wish to thank L. Jensen for implementing the acquisition software, as well as J. Albertone and T. Bogey for their precious help during the installation in the LHC tunnel. We are particularly indebted to S. Ben Amor for testing and calibrating the whole hardware production.

REFERENCES

[1] E. Calvo et al., "The LHC orbit and trajectory system", presented at DIPAC 2003, Mainz, Germany. CERN-AB-2003-057 BDI.

[2] D. Cocq, "The wide band normaliser – a new circuit to measure transverse bunch position in accelerators and colliders", Nuclear Instruments and Methods in Physics Research A 416 (1998) p.1-8.

[3] J.L. Gonzalez, "Using Mathcad, MATLAB and PSpice for electronics simulations", Proceedings of the 4th CARE-HHH-ABI Workshop on "Simulation of BPM Front-End Electronics and Special Mechanical Designs", Lüneburg (Germany), 2006, p.82-85.

[4] R. Jones, "First Results from the LHC Beam Instrumentation Systems", LHC Performance Note 006, 2009.

EXPERIMENTAL VERIFICATION OF PARTICLE-IN-CELL SIMULATION RESULTS CONCERNING CAPACITIVE PICKUP DEVICES*

M. Ruf†, L.-P. Schmidt, University of Erlangen-Nuremberg, Germany
S. Setzer, Siemens AG, Healthcare Sector, Erlangen, Germany

Abstract

For beam position monitoring purposes, three different approaches have been applied to investigate and compare pickup button and electron beam spectrum characteristics. Results on this simulative approach are presented. Induced pickup currents have been calculated both with an analytical and a numerical method. An experimental validation of these simulation results has been conducted with the 6-MeV electron beam from a linear accelerator for medical purposes. The measurements were conducted under non-vacuum conditions. Good agreement between particle-in-cell simulation and experimental data was achieved concerning pickup power spectral distribution and dependence from beam current and beam displacements although non-negligible electron spread during air passage of the electron beam cannot be avoided.

INTRODUCTION

Multi-energy particle accelerators are widely used in cancer treatment facilities [1]. High efforts are being made to ensure precise generation of the beam as well as high precision irradiation and thus to minimize the risk of harming the patient. However, in a clinical environment, unavoidable effects can influence beam position. For multiple-angle treatment, medical accelerators usually comprise rotatable gantries, where the effects of mass and earth's magnetic field can cause beam displacements. Moreover the vicinity of magnetic resonance systems, even if positioned in a different treatment room, was found to be responsible for minor misalignments to the intended beam path. Besides other measures to monitor and stabilize the beam profile, position measurement and correction of the beam is advantegeous for radiation stability.
In this paper, investigations on capacitive pickup devices are presented. A comparison between analytically calculated pickup characteristics and simulation results obtained with the software package CST PARTICLE STUDIO (CST PS) is given. Moreover, particle-in-cell (PIC) simulation results are compared to measurements conducted with test probes and the 6-MeV electron beam from a Siemens medical linear accelerator. In contrast to usual beam position monitoring, these measurements have been conducted under non-vacuum conditions, as in therapy applications particles propagate through a certain distance in air before reaching the patiet.

* Work supported by Bayerische Forschungsstiftung in the project "MEDieMAS - Effiziente Bestrahlungsgeräte für Krebstherapie (Efficient radiation systems for cancer therapy)", file number AZ-735-07
† marcel@lhft.eei.uni-erlangen.de

SIMULATIVE APPROACHES

To calculate the induced current on pickup probes and their spectral distribution, two alternative approaches based on different calculation methods have been applied:

Analytic Calculation in Matlab

An analytic approach for calculating the beam induced currents on capacitive pickups has been implemented in *Matlab* software. The developed tool is based on a numerical analysis given in [2]. The induced current on a pickup probe is calculated from the displacement current across the area of the pickup device. The influence of different bunch shapes is accounted for by the useage of weighted point charges. Therefore, the point charge is spread over a normalized distribution describing the bunch shape. The induced current on the button is then obtained by integration of the individual weighted point charge contributions at every sample of a given time interval. The total current can be calculated by considering the total number of particles and thus, the total charge in the bunch.
For spectral analysis of the pickup signals, the developed tool applies a Fast-Fourier-Transformation (FFT) to the signal in time domain which comprises the currents induced from a selectable number of bunches in a bunch train. The power levels contained in the beam spectrum fundamental and a number of bunch harmonics are then derived.

Particle-in-Cell Analysis in CST PS

To introduce pickup geometry parameters not covered by the Matlab analytic approach, like metal thickness and RF feed, PIC simulations [3] have been conducted in the full 3D electromagnetic solver software package *CST PARTICLE STUDIO*. Open boundaries have been chosen to avoid reflections of beam generated fields in the simulation volume. The induced currents are observed by mode selective time domain monitors in the vicinity of the waveguide ports. Further data processing is done in CST's postprocessing toolbox.

Comparison of Calculation Methods

To validate the later experiment, Matlab analysis and PIC simulations were applied to a setup also used in the conducted measurements. The test setup consists of disk-shaped pickup plates connected to a 50 Ω semi-rigid coaxial line (see below). Plate geometry as well as beam characteristics were chosen as the input parameters of the Matlab tool. The complete test pickup geometry was fully modeled in CST PS as indicated in Fig. 1.

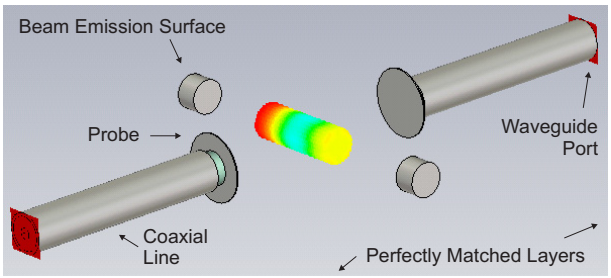


Figure 1: 3D model of CST PS simulation setup showing two opposite circular pickups as well as emission surfaces for the beam.

Figure 2 shows the induced currents on a 3 mm diameter pickup plate calculated both analytically and numerically and the basic agreement between the two. The Matlab generated curve shows the expected derivation of the Gaussian bunch shape, which is not as obvious in the PIC generated plot due to the high β of the beam. The reason for the oscillation following the main peak in the PIC plot can be found by mode separation of the CST signal monitor in time domain: The ringing is due to higher order modes excited in the coaxial line [4].

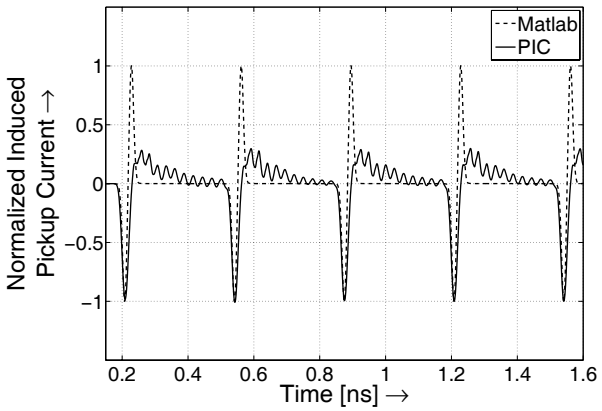


Figure 2: Comparison of pickup current signals in time domain gathered with Matlab analysis (dashed) and PIC code (solid) for a circular pickup with diameter d=3 mm and a 6 MeV electron beam. The curves have been normalized to the maximum induced current obtained by the Matlab calculation.

EXPERIMENTAL VERIFICATION

The application of a charged particle beam to the patient in the case of cancer therapy requires the beam to propagate through a certain distance of air. To validate the calculated pickup behavior, measurements have been conducted with the multi-energy, high-β electron beam generated by a Siemens medical linear accelerator. The measurements have been conducted in an area where in treatment applications the beam already propagates through air towards the patient.
As space is limited in a medical accelerator environment, pickup buttons have been preferred over stripline pickups due to the smaller dimensions of the buttons. The test probes have been manufactured as flat, disk-like extensions of the inner conductor of a 50 Ω semi-rigid coaxial line which was DC-decoupled by means of a Bias-T. The accelerator employs a 3 GHz RF source, thus the pickup current was investigated with a spectrum analyzer covering the frequency range up to 40 GHz.

Spectral Distribution of Pickup Power

In Fig. 3, a comparison between the simulated and measured harmonic content of the pickup signal is given for the first three beam harmonics. For spectral analysis of the simulated time signals, a bunch train of 40 electron bunches has been taken into consideration. The side lobes of the main spectral peaks in Fig. 3 are artefacts of the FFT which was applied to the bunch train in time domain.

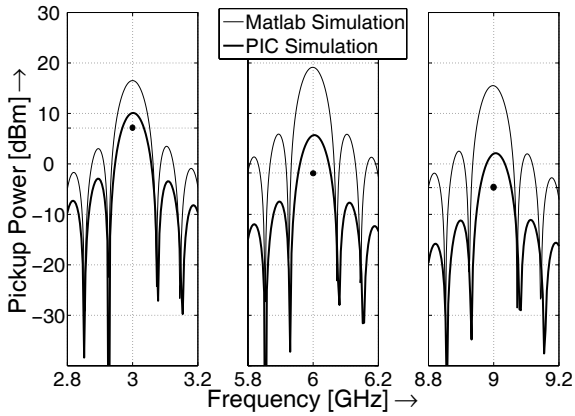


Figure 3: Comparison of spectral power distribution between Matlab simulation (fine), PIC simulation (bold) and measurement (dots). Despite beam spreading, the measured values are in close vicinity to the simulation results.

The figure reveals a mismatch between the power spectra obtained with Matlab and PIC code simulation. The deviation between the two curves can be attributed to different time signals. For generation of Fig. 3, the distance of the probe to the beam center has been increased compared to Fig. 2, which results in time domain signal deviations. The measured pickup power values at the fundamental and the

2nd and 3rd harmonic are indicated as bold circles in the figure. The degradation compared to the PIC-generated values is most probably due to beam spreading which occurs when the electron beam propagates through air. However, the measured power levels are still in acceptable vicinity to the simulated values.
It was validated that smaller disk probes lead to a higher sensitivity as stated in [5]. The measured sensitivity of a 3 mm diameter probe was 1.7 dB/mm, whereas the sensitivity of a 12.5 mm probe was measured to be 0.8 dB/mm. As promised by PIC simulations, the beam harmonic with the highest contained power was 6 GHz for the smaller disk and 3 GHz for the larger disk.

Pickup Current vs Beam Current

Figure 4 shows the rising pickup current when the beam current is increased. In the measurement, the beam current was increased by a factor of ten, causing the pickup current to increase by the same amount as expected. The inset of Fig. 4 compares the measurement results to PIC simulations, where the beam current increase was introduced by a rise in total bunch charge. Simulation and measurement are in good agreement. The 6 GHz harmonic of the beam spectrum is the highest component in the pickup spectrum due to button geometry (3 mm diameter in this case).

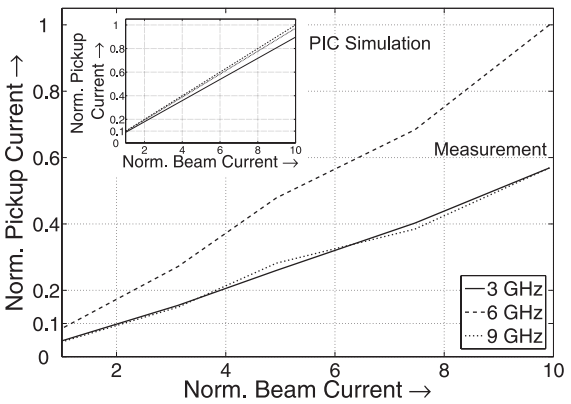


Figure 4: Comparison of PIC simulation and measurement concerning pickup current versus beam current. Both simulation and measurement data are normalized to the maximum ocurring pickup current showing nearly the same linear dependence in the plot.

Pickup Current vs Beam Displacement

Investigations have been conducted concerning the dependence of the pickup current from beam displacements. The distance between the probe and the beam center can easily be varied in simulation. In the test measurements, beam displacement was emulated by displacing the probe instead of displacing the beam.
Figure 5 shows the outcome of both simulations and measurement of the 6 GHz component of the displaced beam. Although non-negligible beam spreading during air passage can be assumed, good agreement between measurement and simulation is achieved.

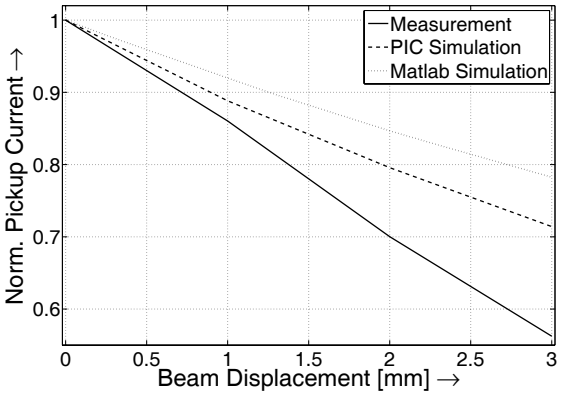


Figure 5: Simulation and measurement results on 6 GHz beam harmonic as a function of beam displacement. “0 mm” refers to the initial distance of the probe to the beam center (15 mm). The plots have been normalized to the respective currents at the initial position.

CONCLUSION

Analytical, numerical and experimental approaches have been applied to investigate the properties of capacitive pickup buttons, to be used for particle beam position monitoring. A Matlab tool has been developed based on the integration of induced currents of weighted point charges. The simulation results have been compared against particle-in-cell simulations conducted in full 3D electromagnetic simulation software. To validate simulation results, measurements with test pickups have been carried out employing the electron beam of a 6- to 25-MeV medical linac. Good agreement was achieved between the two simulation approaches and the measurements, although the beam passed a certain distance in air environment. Consequently, the applied codes represent promising tools for further investigations in this field.

REFERENCES

[1] C.J. Karzmark, C.S. Nunan, E. Tanabe, “Medical Electron Accelerators”, New York: McGraw-Hill, Inc., 1st ed., 1993.

[2] P. Strehl, “Beam Instrumentation and Diagnostics”, Berlin: Springer Verlag Berlin-Heidelberg, 1st ed., 2006.

[3] S.J. Park, J.H. Park, Y.S. Bae, W.H. Hwang, J.Y. Huang, S.H. Nam, Y.S. Cho, J.M. Han, S.H. Han, B.H. Choi, “Design of BPM PU for Low-Beta Proton Beam using MAGIC Code”, DIPAC’03, Mainz, May 2003, PT14, pp. 199-201, 2003.

[4] J. Hinkson, “ALS Beam Instrumentation - Beam Position Monitoring”, unpublished, 2000.

[5] R.E. Shafer, “Beam Position Monitoring”, AIP Conference Proceedings, vol. 212, pp. 26-58, 1989.

INVESTIGATION OF PRECISE PIPELINE-TYPE ADCS IN A BURST REGIME FOR A SINGLE-SHOT BPM*

A. Kalinin, ASTeC Daresbury Laboratory STFC, Warrington, UK
S. Artinian, Bergoz Instrumentation Ltd, Saint Genis Pouilly, France

Abstract

In the EMMA Accelerator turn-by-turn BPM, the ADC should execute several successive fast rate measurements with a clock burst triggered by the bunch on each turn. We investigated a work of some fast pipeline-type ADC ICs in a burst regime where a minimal burst length is decided by the ADC latency. The results show that pipeline-type ADCs a main merit of whose is a high precision are usable in a beam-triggered single-shot BPM as well as in other event-triggered systems. The set-up used for the investigation illustrates the measurement arrangement in the EMMA BPM. The employed technique described can be used for detailed investigation of a single shot BPM noise.

INTRODUCTION

On the EMMA Accelerator [1], the bunch trajectory is to be measured on each turn in 84 circumference points. The turn is $T = 55.2$ns. The bunch executes up to ten turns, and its trajectory is spirally enlarging in the horizontal plane, sweeping about a half of the pickup aperture. For machine tuning, the bunch can be made circulating larger number of turns on a stationary orbit.

Aiming at a compact and inexpensive EMMA BPM system, we, first of all, use in it a multiplexing of two pickup signals in each plane into a single channel where the second signal is delayed by $T/4 = 13.8$ns. The BPM synchronous detector output is a pair of spaced as above single polarity pulses about 5ns length each. On each turn, the ADC measures these two beam pulses and then makes two measurements of the DC pedestal.

Next, in the system, as a time reference signal for synchronous detection and clocking the ADC, the beam signal itself is used. [2] This approach allows first, to avoid a cumbersome network of external reference distribution from BPM to BPM, and second, to use a single synchronous detector (and a single ADC) instead of the I/Q scheme where a double set of each is required.

Trying to find optimal solutions for the EMMA BPMs in particular, and for the single shot BPMs that are now in demand, in general, we had tended towards ADC of the pipeline type. Being sufficiently fast, consuming low power, being comparatively inexpensive, a pipeline ADC has a solid advantage of high accuracy in comparison to a flash ADC.

We saw also that with ability to work in the burst regime, the pipeline ADCs could make possible precise measurements in any event-triggered system, for instance, in accelerator-based high energy particle detectors.

* The work was done within a BASROC/ CONFORM/ /EMMA Project, and was supported by the UK Science and Technology Facilities Council, and by Bergoz Instrumentation Ltd.

In this paper we report results of some initial burst regime investigation. Our investigation has not covered a broad range of modern ADC ICs available on market. We have not made chip-to-chip statistic measurements for that ADC that fits the purpose. Our immediate result is that an ADC has been identified for which the regime is feasible albeit with use of some additional facility.

TEST SET-UP

We used commercial ADC Evaluation Boards. A differential burst was directly fed into the ADC clock inputs. The burst was taken from a generator 81150A (Agilent Tecnologies). The clock period was 14ns.

At the ADC analog inputs, three circuits were used: (1) the ADC inputs were short to the ADC internal reference; (2) the inputs were connected to the differential outputs of an operational amplifier (differential gain $G_{2d} = 1$) whose inputs were short to GND; and (3) the ADC inputs were connected to the same amplifier one input of which was fed from a non-inverting preamplifier ($G_1 = 4$, 50Ohm input impedance). Amplifiers AD8000 and ADA4939 (both from Analog Devices) were used.

A preamplifier input pulse signal of about 13bit resolution was taken from another output of the 81150A generator. A DC pedestal that in the case of single polarity input pulse makes a full ADC range usable was introduced in the preamplifier.

The ADC output was observed using a logic oscilloscope DL9505L (from Yokogawa Electric Corp.). For each kind of measurements, a 64-shot array was recorded, using manual trigger. For the ADC latency of m clock periods, the readings of the samples of number $m + j$, $j = 1,2,...,4$ were recorded by setting the oscilloscope logic cursor at these samples.

ADC TEST

We tested two ADCs: MAX1427 (15bit, 80MHz, $m = 3$ cycles, from MAXIM) and AD6645ASQ (14bit, 105MHz, $m = 3$ cycles, from Analog Devices).

A response of the first ADC (with the inputs short to the ADC reference) to a clock burst is shown in Figure 1 where a full horizontal size is about 7μs. The burst is shown on the upper trace DRY (it is the ADC's Data Ready signal). After the start, one can see that the ADC readings have a long transient: from big (negative) values through some ringing to a noise floor at four least bits (on the right from the cursor line which is distanced from the start by 4.4μs). Obviously, this ADC is not suitable for a single shot BPM.

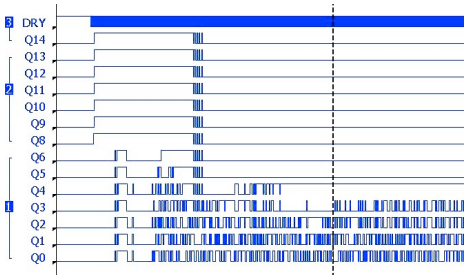


Figure 1: A screenshot of MAX1427 readings.

The AD6645 transient lasts one clock period. It was measured with the inputs short to the ADC reference. Table 1 gives mean values and standard deviation values in the decimal units (a full ADC range is 16384) for the samples $j = 1,2,...,4$. Histograms of the readings (mean is subtracted) for the last three samples are shown in Figure 2 left (the colours used are given in Table 1).

Table 1: AD6645 transient

j	1	2	3	4
mean	92	4.0	4.6	4.5
std	25	0.90	0.99	0.87
colour	–	blue	yellow	green

Note both the mean and the std of the first sample are unstable and change significantly from day to day, with a change of PS voltages, etc.

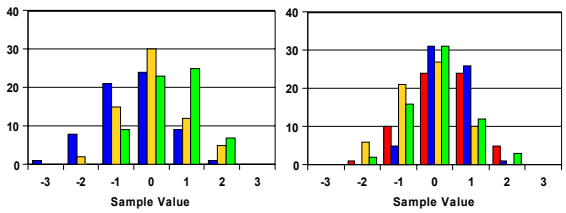


Figure 2: Histograms of AD6645 readings. Left/right, without/with awakening pulse.

One can see that from the sample $j = 2$ forth, the ADC has a resolution that appears to be its ultimate resolution. Accuracy of the first sample can be improved using an obvious idea to 'awake' the ADC with an additional clock pulse in advance to the burst. The effect of the pulse can be seen in Table 2 and Figure 2 right (sample $j = 1$ is red). With an awakening pulse, the AD6645 really gets ready for a burst measurement.

Table 2: Effect of awakening pulse

j	1	2	3	4
mean	5.3	5.4	5.6	5.0
std	0.89	0.79	0.86	0.87

For the case above, the pulse was 50ns length, and the advance was (-1)μs. We investigated the awakening effect by changing the pulse length in the range 10ns to 100ns and the advance in range (-0.1)μs to (-4)μs. No indication of resolution deterioration was observed. It's worth to note that with increase of the advance over about (-4.5)μs the resolution steeply got deteriorated.

A pulse in some advance to the beam is usually easily available at accelerators. Pulse distribution to a set of BPM cards can be made using some common wire in the backplane bus.

ADC INPUT CIRCUIT TEST

The noise, pedestal, and signal measurements discussed below were all done with a 50ns awakening pulse in advance (-1)μs to the burst.

Noise

An ADC readings noise of a circuit with a differential amplifier (DA) (whose inputs are short to GND) is given in Table 3 and in Figure 3 left.

Table 3: Noise with differential amplifier

j	1	2	3	4
mean	6.6	6.3	6.4	3.4
std	1.57	1.57	1.58	1.72

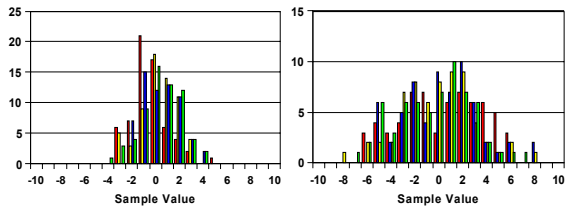


Figure 3: ADC readings noise with differential amplifier (left) and of full circuit (right).

Averaging standard deviations in Table 2 and 3 as $\overline{std_{2,3}} = \sqrt{\sum std_{2,3j}{}^2 / 4}$, one gets $\overline{std_{\mathrm{DA}}} = \sqrt{\overline{std_3}^2 - }$ $= -\overline{std_2}^2 = 1.37 = 183\mu\mathrm{V}$. That is 1.25 times larger than output noise estimation 148μV calculated using the datasheet amplifier output noise density $9\mathrm{nV}/\sqrt{\mathrm{Hz}}$ and the datasheet ADC bandwidth 270MHz.

An ADC readings noise of a full circuit with a preamplifier is given in Table 4 and in Figure 3 right. Calculating $\overline{std_4} = 3.19$, and using $\overline{std_3} = 1.61$, one can estimate the preamplifier output noise as 370μV which is

Table 4: Noise of full circuit

j	1	2	3	4
mean	8.3	8.4	7.9	5.6
std	3.42	3.13	3.06	3.15

about 2 times larger than a datasheet estimation 190μV. What causes this excess it is necessary to investigate. Here we take the noise $\overline{std_4} = 3.19$ merely as a reference in the pedestal and signal measurements below.

Pedestal

The pedestal differential magnitude was $P = -1\text{V}$. The ADC input AIN was shifted down to $-P/2$, the input $\overline{\text{AIN}}$ was shifted up to $+P/2$, close to the range ends $\mp 0.55\text{V}$. With a positive pulse at the preamplifier input, each ADC input goes to its opposite range end. This arrangement makes a full ADC range 2.2V usable.

The pedestal magnitude was measured as $(-0.986)\text{V}$ (mean value), well within the ADC gain error (<10%). The histogram was similar to the histogram of a full circuit in Figure 3.

The average standard deviation was $\overline{std_{\text{P}}} = 3.20$. Comparing it to $\overline{std_4} = 3.19$, one can conclude that a DC pedestal had not brought an additional noise.

Signal

The circuit total gain $G_{\text{t}} = 4$ was chosen to match the synchronous detector output range (about 0.5V max) and the ADC range. In the measurements below, we kept the preamplifier input pulse magnitude well within the range, how it will be with a beam, namely, about half of it. We used a 13bit generator pulse 5V attenuated with a resistive attenuator 26dB.

First, we measured a 22ns length pulse that covered both $j = 1,2$ samples. The pulse had a flat top, so, if some sampling time jitter was there, no additional magnitude noise should be generated. The mean pulse magnitudes and their standard deviations are given in Table 5. The histograms are similar to the pedestal histograms.

Table 5: A 22ns pulse

j	1	2	3	4
mean, V	+0.0041	+0.0165	–0.978	–0.987
std	3.48	3.59	$\overline{std_{\text{P5}}} = 3.12$	

Next, we measured a pair of identical 7ns pulses (shown in Figure 4 left) that were similar to BPM output pulses. As pulse tops were not ideally flat, we adjusted the clock signal delay to have maximal readings, i.e., to sample a pulse apex. The measurement produced results given in Table 6 and Figure 4 right, and in Figure 5 where shot-to-shot samples are shown.

One can see that the pulse magnitude distribution has got some tails. Besides, some drift-like noise component has appeared that is common for both $j = 1,2$ samples. Indeed, calculating a correlation coefficient $\rho_{12} = \overline{(s_{1k} - mean_1)(s_{2k} - mean_2)}/(std_1 \cdot std_2)$ where k is the sample number, one gets $\rho_{12} = +0.26$ whereas for the 22ns pulse the coefficient is about –0.05. For the pedestal it lies typically within ±0.1.

Most probably, a common noise component is caused by a clock delay drift. Distribution broadening may occur due to a clock jitter. For the 81150A generator a datasheet jitter amounts to 25ps. We observed its contribution directly, by moving the sample moment from the apex by 1ns. On the slope, the standard deviation of each pulse had got doubled. This experiment shows importance of providing flatness of the BPM output pulse top, discussed in [2].

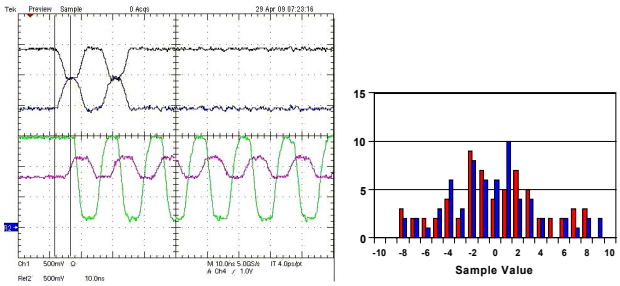


Figure 4: Left, the signals at the ADC inputs (top), the CLK signal (pink), and the DRY signal (green). Right, the pulse magnitudes (means are subtracted).

Table 6: Two identical 7ns pulses

j	1	2	3	4
mean, V	+0.0031	+0.0056	–0.983	–0.987
std	4.07	3.82	$\overline{std_{\text{P6}}} = 3.17$	

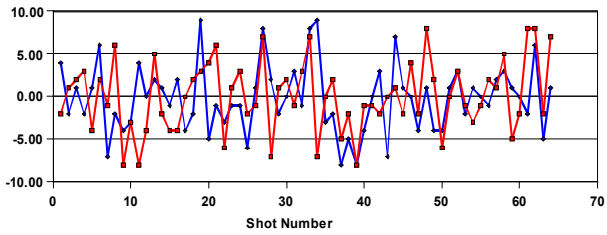


Figure 5: Shot-by-shot samples (means are subtracted).

SUMMARY

We advertise an ADC AD6645 (from Analog Devices) that can be used in a burst regime for precise measurements in a single shot BPM as well as in other event-triggered systems, provided with an awakening pulse.

We've described a simple set-up for pipeline-type ADC tests. An employed technique can be used for detailed investigation of a single shot BPM noise.

ACKNOWLEDMENTS

We are grateful to R. J. Smith for his effective support of this work.

REFERENCES

[1] S. L. Smith, "EMMA, the World's First Non-Scaling FFAG Accelerator", PAC'09.

[2] A. Kalinin, "Towards Sub-Micrometer Resolution of Single-Shot Strip Line BPM", EUROTeV-Report-2008-56.

DESIGN OF A RESONANT STRIPLINE BEAM POSITION PICKUP FOR THE 250 MEV PSI-XFEL TEST INJECTOR

A. Citterio, M. Dehler, D.M. Treyer, B. Keil, V. Schlott, L. Schultz, PSI, Villigen PSI, Switzerland

Abstract

The 250 MeV PSI X-FEL Test Injector will use resonant stripline beam position monitor (BPM) pickup as standard BPMs to reach the desired single bunch resolution in the order of 10 µm in a charge range of 10 to 200 pC. This paper presents the electromagnetic design of the pickup that was performed with Microwave Studio. The pickup was optimized in terms of the main radiofrequency (RF) characteristics - frequency, shunt impedance, unloaded and loaded Qs - of the resonant modes of interest, in order to obtain the signal characteristics required by the electronics, that samples the pickup signals directly at 5 GSamples/s [1]. Mechanical aspects of the design are also presented, with particular attention to the tuning pin solution for stripline alignment. Based on the simulated geometry, one pickup prototype was built and tested and the correct characteristics of the resonant modes were verified.

OVERVIEW

To provide the desired position resolution in the ten micrometer range along the 250 MeV PSI-XFEL injector, about 25 standard beam position monitors are foreseen to measure and stabilize the beam position within ~10% of the final beam size. The choice of a 500 MHz resonant stripline pickup and a 5 GSample/s direct sampling electronics [1] based on existing PSI designs [2] allowed a cost-efficient solution and fast prototyping of pickups and electronics as well as of the digital signal processing firmware and software. At the desired bunch charge range from 200 pC down to 10 pC, resonant striplines are superior e.g. to button pickups since they concentrate the output signal spectrally at a high signal-to-noise ratio, thus enabling higher position resolution with narrowband processing, even for single shot operation and low bunch charges [3]. The main advantage over cavity pickups is the significantly reduced cost and development time especially for the electronics, since the low Q and comparatively low frequency allow direct sampling by the 5 GSample/s Domino Ring Sampler (DRS) chip of the BPM electronics, without the need for an analog mixer scheme or a low-jitter clock distribution [1]. A schematic sketch of four resonant stripline electrodes (two per plane) is depicted in Fig. 1.

This BPM topology supports four independent TEM eigenmodes of operation $\underline{V_0} = (V_1, V_2, V_3, V_4)$:

- sum mode, or monopole mode: $V_{0,M} = \frac{1}{2}(1,1,1,1)$
- two delta modes, or dipole modes: $V_{0,D_x} = \frac{1}{\sqrt{2}}(1,0,-1,0)$ and $V_{0,D_y} = \frac{1}{\sqrt{2}}(0,1,0,-1)$
- quadrupole mode: $V_{0,Q} = \frac{1}{2}(1,-1,1,-1)$

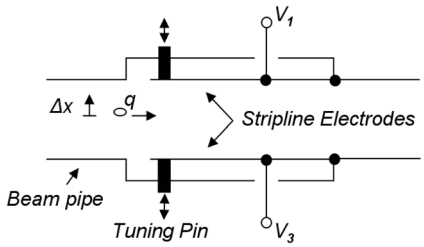


Figure 1: Resonant stripline pickup, one plane only.

The ratio of the signal voltages from opposing electrodes depends on the transversal beam position:

$$x \sim \frac{\Delta}{\Sigma} \text{ with } \Delta = (V_3 - V_1) \text{ and } \Sigma = (V_3 + V_1)$$

Each mode has a characteristic impedance and frequency spectrum that influences the BPM performance, representing the criteria for the pickup selection [4]. The pickup sensitivity, defined as the ratio of opposite voltages per beam offset in [dB/mm], is determined by the normalized shunt impedances and the loaded Qs:

$$S_x\,[dB/mm] \sim 20\,log(1 + 2s_x \cdot 1mm), \qquad (1)$$

$$s_x\,[1/mm] \sim \sqrt{2\frac{(R/Q)_{D_x}}{(R/Q)_M}\frac{Q_{l,D_x}}{Q_{l,M}}}\Bigg|_{x=1mm} \qquad (2)$$

The detection method employed is signal stretching by ringing filter, followed by direct sampling and digital envelope detection. To maintain high sensitivity of signal envelope voltage to beam position for the complete duration of the signal, the following conditions must be satisfied: at the appearance of the output signal $Q_{l,D}/Q_{l,M} \geq 1$, and the dipole and monopole frequencies must coincide, i.e. $f_D = f_M \pm 1$ MHz. The frequency of the resonant stripline pickup was chosen equal to 500 MHz, which is well in the bandwidth range of the DRS4 sampler chip. The frequency choice also enabled easy adaptation of the design already used at the SLS linac and transfer lines [2], allowing electronics development and tests with existing SLS linac pickups while the new spectrally and mechanically improved pickup was being developed.

CONCEPTUAL DESIGN AND RESULTS

Prototype Design

Figure 2 shows geometry and mechanical solutions adopted for the prototype pickup.

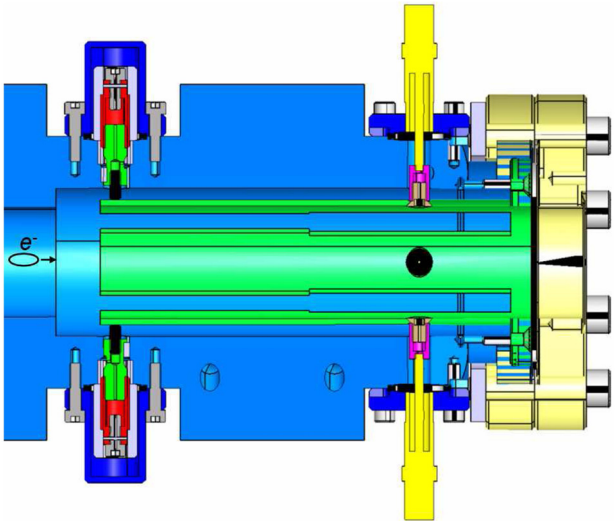


Figure 2: Pickup prototype for the PSI-XFEL Injector.

The beam pipe dimension of 38 mm was maintained as inner diameter of the stripline. To have a maximum response magnitude at the resonance, the stripline length must be equal to a quarter resonant wavelength, i.e. $l = 150$ mm. Once the overall adopted geometry was tuned, this length was reduced to 138.4 mm. A first tuning of the pickup was performed on the width of the stripline slots. Because the loaded Qs must be lower than that of the ringing filter (max. 30), but not too low to keep the spectral energy density high at 500 MHz, an initial width of 11 mm was chosen for the slots, resulting in eigenmodes with $Q_l \sim 8$. Moreover, because longer slots correspond to a closer proximity of the resonant modes, the length of the slots was made equal to the length of the stripline itself. This ensures a few MHz difference between monopole and dipole frequencies. Afterwards, according to the design described in [5], each slots was modified and the initial width of 11 mm was reduced to 9.3 mm for the first half of the stripline, which now presents two different widths. In fact, this configuration corresponds to add a capacitive load, which will only affects the electrodes at different potentials, as e.g. for the dipole mode case. Consequently the dipole and quadrupole modes will move down in frequency towards the sum mode. The final tuning of the frequency spectra was obtained by adjusting the position of the ports. The feedthroughs (50 Ω line impedance) are put in the region where the magnetic field of the modes is mostly concentrated. Simulations show a sensitivity of the port position with the frequency modes of about +1 MHz/mm in the beam direction, depending also on the geometry of the rest of the structure. The contact with the electrodes is guaranteed by means of Cu-Be screws fixed on the feedthrough antennas. Concerning the pickup alignment with respect to the beam pipe, a tolerance of 10 µm was considered for the concentricity, giving a tolerance of 5 µm for the electrical center.

Four ceramic screws of 4 mm diameter put at 5 mm from the open end of the stripline allow the alignment of the stripline (with a satisfying precision). A detailed view of the feedthroughs and tuning pins complex are shown in Fig. 3.

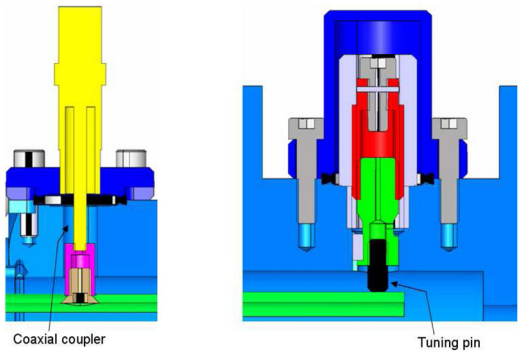


Figure 3: Details of the feedthroughs (left) and tuning pins (right).

Simulation Results, Measurements and Redesign

The BPM prototype was tested for both S-parameters and beam measurements and the results were compared to the simulations. Table 1 shows the eigenmode frequencies and their obtained Q factors. Microwave Studio was used to compute the eigenmodes both directly (second column in Table 1) and the mode group delay analysis (third column). With this method the S-parameters are obtained at first by a frequency sweep of the pickup. Then they are suitably combined to obtain the four mode reflection coefficients S_{mode}, i.e. the eigenvalues of the scattering matrix **S**. Finally, the group delay of mode reflection coefficients corrected for the single pass delay of feed lines $(dS_{mode}/d\omega) - 2\tau$ is computed. The frequency where the mode group delay is maximal is the mode resonance frequency. The agreement of the two simulation methods is better than 1 MHz for the frequencies, and also quite good for the Q factors. The condition $Q_{l,Dipole} \geq Q_{l,Monopole}$ previously described is satisfied. Since in the simulations a magnetic symmetry plane has been defined longitudinally, the two dipole modes are identical. From the shunt impedance values computed, $(R/Q)_M = 10.6\,\Omega$ and $(R/Q)_D = 44\,\text{m}\Omega$ at 1 mm, the expected sensitivity is $S = 1.57$ dB/mm. Using a model of pickup, electronics, and detection algorithm, this results in an estimated position resolution of 5.5 µm for 200 pC beam charge.

While the loaded Qs measured match very well with the estimated values, the measured frequencies are larger than expected: ~+9 MHz for the monopole and ~+6 MHz for the dipole modes. To explain this difference, further MWS simulations were performed: imperfections of the simulated geometry explain in fact part of the frequency error. These imperfections concern an approximated geometry of the flanges at the feedthroughs and of the tank near the tuning pins, and a wrong dielectric constant value used for the ceramic alignment screws. A sum of these effects can justify ~+6 MHz for the monopole mode and ~+5 MHz for the dipole and quadrupole modes. The cause of remain-

Table 1: Simulated and Tested Mode Frequencies and Quality Factors

	MWS Eigenmodes			MWS S-params.			Measurements	
Mode	f_0 [MHz]	Q_u	Q_l	f_0 [MHz]	Q_u	Q_l	f_0 [MHz]	Q_l
Monopole	499.82	1067	6.3	500.31	∞	5.7	509	6.4
Dipole X	500.23	1159	7.5	501.03	∞	7.3	507	7.7
Dipole Y	500.23	1159	7.5	501.03	∞	7.3	506	7.4
Quadrupole	500.35	1145	8.2	501.39	∞	8.4	506	8.2

ing error could be identified in an imperfect stripline alignment. In the mechanical alignment procedure, a rod with the same diameter as the beam pipe away from the electrode was inserted through the pickup. The tuning screws were adjusted inwards until the torque increased and then the rod was removed. Because of the force from the tuning screws, the electrodes could be bent away from the beam pipe inner surface even further when the road was removed, reducing the capacitive load between tank and stripline. This fact is confirmed by the simulations: 0.1 mm misalignment of the all four electrodes away from the beam pipe inner surface increases the eigenmode frequencies by a few megahertz. Finally, the crosstalk measured among orthogonal dipole modes is in the order of 0.1%.

The prototype was installed at the Linac of SLS and then tested with an electron beam. Figure 4 shows the amplitude for one of the four filtered pickup electrode voltage for unknown offset beam position and 0.85 nC bunch charge.

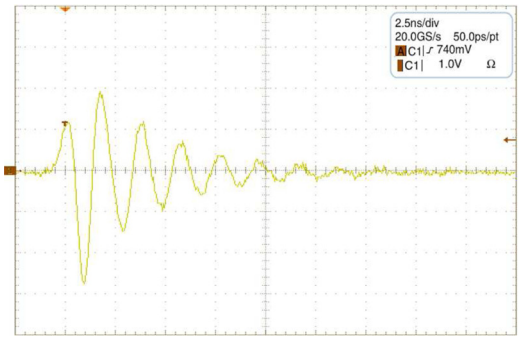


Figure 4: Lowpass filtered pickup electrode voltage at the end of cables. Filters used: Mini-Circuits SLP-1000.

Average initial amplitude is 5.25 V peak to peak. Accounting for cable attenuation and rescaling for the bunch charge of interest, the electrode voltage from fundamental resonance of monopole mode is ~2.11 V_{pp} at 0.2 nC. This is 0.7 dB more than the predicted value of 1.94 V_{pp}.

Because of the the error found in the frequency modes, the stripline was redesigned, changing in length of the electrodes by few millimeter and in widths of the slots by a few tenths of millimeter. To make the alignment of the feedthroughs easier, the gap width between bushing and inner surface of the coaxial coupler was increased from 0.5 to 1.25 mm. The mechanics of the tuning pins itself was simplified, allowing a faster mounting and minimizing in the same time the effect of the depth of the recess around the tuning pin on the fields.

The new specifications after the upgrade of the pickup are shown in Table 2. Frequencies and loaded Qs refer to MWS simulated S-parameters analyzed according to the mode group delay, and match well with the simulated values obtained by looking directly for the eigenmodes.

Table 2: Simulated Mode Frequencies and Quality Factors for the New Design Of the Resonant Stripline Pickup

Mode	f_0 [MHz]	Q_u	Q_l
Monopole	500.31	1358	6.15
Dipole X,Y	499.95	1461	7.59
Quadrupole	499.95	1493	8.71

The sensitivity decreases from 1.57 dB/mm to 1.53 dB/mm; however, the ratio $Q_{l,Dipole}/Q_{l,Monopole}$ is 5% larger. The theoretical resolution limit for the chosen BPM electronics remains unchanged at 5.5 µm. The signal levels are 0.6 dB larger.

CONCLUSIONS

The obtained results indicate that the designed resonant stripline pickup allows to reach the desired position resolution in the order of 10 µm in the PSI FEL test injector. The fabrication and the test of a prototype allowed to identify and solve, also by means of mechanics improvements, critical aspects, thus optimizing the eigenmode spectrum and resulting BPM performance.

REFERENCES

[1] B. Keil, S. Lehner., S. Ritt, "Application of a 5 GSPS Analogue Ring Sampling Chip For Low-cost Single-shot BPM Systems", Proc. EPAC 2008, Genoa, Italy, 1167 (2008).

[2] M. Dehler, et al., "BPM System for the Swiss Light Source", Proc. PAC 1999, New York, USA.

[3] D. M. Treyer, "Low latency high resolution single-shot Beam Position Monitors", Proc. DIPAC 2007, Venice, Italy.

[4] M. Dehler, "Resonant Stripline BPM for Ultra Low Current Measurement", Proc. DIPAC 2005, Geneva, Switzerland.

[5] M. Dehler, G. Behrmann, S. Vilcins, M. Siemens, "Stripline devices for FLASH and European XFEL", proc. of 2008 Beam Instrumentation Workshop, Lake Tahoe, CA, USA.

IMPLEMENTATION OF AN FPGA-BASED LOCAL FAST ORBIT FEEDBACK AT THE DELTA STORAGE RING

P. Towalski*, P. Hartmann, G. Schuenemann, D. Schirmer, T. Weis, G. Schmidt, S. Khan
Zentrum fuer Synchrotronstrahlung DELTA, TU Dortmund, D-44221 Dortmund, Germany

Abstract

The beam orbit of the 1.5 GeV electron storage ring DELTA showed a variety of beam distortions with a pronounced frequency spectrum mostly caused by girder movements and ripples of the magnet power supplies. In order to enhance the orbit stability to at least 300 Hz bandwidth a global fast orbit feedback (FOFB) is under consideration. As a prototype an FPGA based local fast orbit feedback at a 10 kHz data acquisition rate has been developed. The digitized orbit data are distributed from I-Tech Libera and Bergoz MX-BPMs [1] to an FPGA board via a fibre interconnected network based on the Diamond Communication Controller [2]. The correction algorithm is written in VHDL and the corrections are applied with digital power supplies connected to the FPGA board through RS485 links. The first operational tests of the system achieved an effective damping of orbit distortions up to 350 Hz. The paper will give an overview on the layout of the FPGA-based local orbit feedback system, will report on the results of the measured uncorrected orbit distortions at DELTA and the stability enhancements that could be achieved by the local feedback system.

INTRODUCTION

The beam stability at the storage ring Delta is affected by low frequency distortions during the ramp of our booster BoDo and beam oscillations caused by mains power supplies generating distortions with the frequency of 50 Hz and its harmonics up to approx. 350 Hz. Furthermore girder movements at their resonance frequencies, excited by ground vibrations, lead to displacements of magnetic elements of the accelerator, particularly the quadrupoles and therefore detoriate the photon beam stability at the beam lines. In order to supply higher brilliance synchrotron radiation a global fast orbit feedback is under consideration in connection with the existing slow orbit feedback working at frequencies at about 0.1 Hz. For this reason a local fast orbit feedback in the vertical plane (see Fig. 1) has been developed to prove the feasibility of the planned feedback and to test designated methods and components.

LOCAL ORBIT BUMPS

The dependency between the corrector strength θ_j at the corrector j and the orbit z_i at position i can be described using the orbit response matrix $\boldsymbol{R}$:

$$R_{ij} = \frac{\partial z_i}{\partial \theta_j} \tag{1}$$

The calculation of the expected orbit $\vec{z}$ can be achieved by superposing the effects of all corrector θ_j:

$$\vec{z} = \boldsymbol{R}\vec{\theta}. \tag{2}$$

Using the technique of singular value decomposition (SVD) the calculation of a pseudoinverse is possible even if $\boldsymbol{R}$ is a singular matrix. The corrector strength θ_j for given orbit $\vec{z}$ is then directly derived from the pseudoinverse $\boldsymbol{R}^+$ of the response matrix $\boldsymbol{R}$ via:

$$\vec{\theta} = \boldsymbol{R}^+ \vec{z}. \tag{3}$$

The vector $\vec{z}$ represents the required orbit, the vector $\vec{\theta}$ represents the best approximation of the appropriate corrector strength to apply. Appropriate in the sense of being the best solution is achieved by the method of a least square fit. The superposition of two orbit bumps using four correctors allows for the adjustment of the orbit at bpm14 and 15. The bumps are created with the correctors vcor1 to vcor4 (see Fig. 1) mounted at appropriate positions [3].

A response matrix $\boldsymbol{R}$ for all of the 54 BPMs and four correctors was measured with beam. In a next step the pseudoinverse of $\boldsymbol{R}$ was used to calculate the corrector coefficients for the two orbit bumps using four correctors. Orbit bump induced crosstalk between bpm14 and bpm15, as well as the influence on the orbit outside the feedback section was less then 10 %, verified at 7 control BPMs.

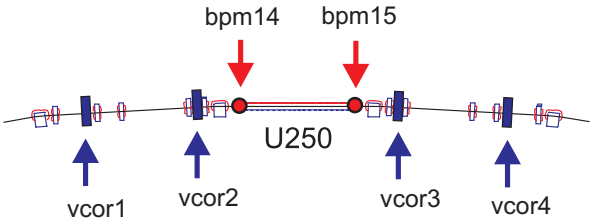


Figure 1: Setup of the vertical fast local orbit feedback at DELTA consisting of an undulator (U250), two beam position monitors (BPMs) and four vertical correctors (vcor).

ORBIT DISTORTIONS

To identify the typical orbit distortions, a frequency spectrum was created from decimated turn-by-turn data

* patryk.towalski@udo.edu

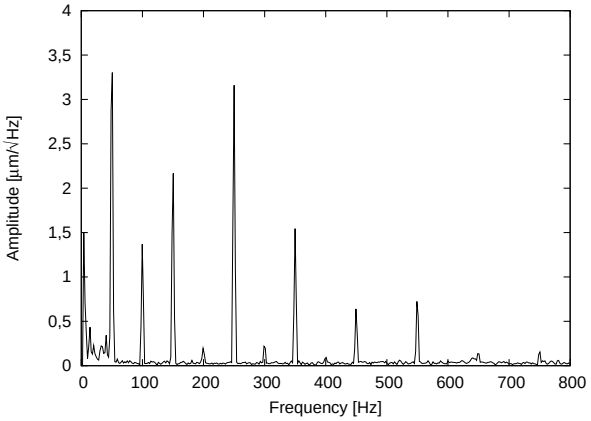


Figure 2: Spectral rms orbit deviation versus frequency.

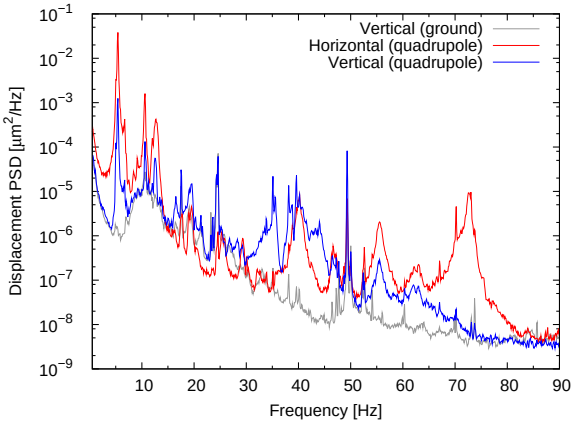


Figure 3: Displacement PSD horizontal and vertical on a quadrupol and vertical on the ground.

taken by an I-Tech Libera electronic [4] installed at bpm14. The experimental results are shown in Fig. 2. Apart from distinctive distortions at 50 Hz and its harmonics, caused by the mains power supplies, low frequency perturbations in the range of 5 Hz have been observed.

Girder oscillation has been measured using geophones [5] during regular beam operation to identify the source of these low frequencies. One geophone capable to measure in three dimensions was attached to a quadrupole, a second one (measuring in one dimension) was mountend vertically on the floor. The geophones create a voltage proportional to the speed of their movement. This voltage was amplified and then recorded using a "LeCroy WaveSurfe 454" oscilloscope at a sampling frequency of 500 Hz.

MATLAB [6] was used to calculate the spectral power density (PSD), to apply a Hamming window function and to convert the velocity data to real displacement. Figure 3 shows the experimental results. Excitation frequencies of 5.3 Hz, 10.6 Hz and 12.5 Hz are caused by girder resonances. These oscillations lead to a time dependent transverse misalignment of the quadrupoles [7], influencing the orbit.

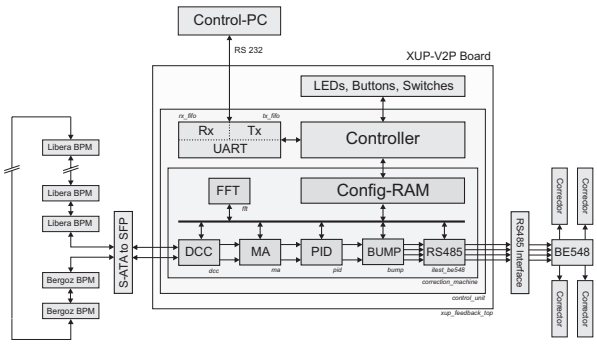


Figure 4: Block diagramm of the correction system of the local fast orbit feedback implemented in VHDL.

IMPLEMENTATION OF THE LOCAL FAST ORBIT FEEDBACK SYSTEM

The fast local orbit correction has been implemented as a classic control loop. Each element of the loop can influence the control dynamics by delay or bandwidth.

The orbit position has been measured at bpm14 and 15 with I-Tech Libera Electron [4] BPMs, equipped with the Diamond Communication Controller allowing to distribute the fast orbit position data over a glas-fibre network at a rate of 10 kHz.[1] The BPMs digital filters have a latency time of about 300 µs at a bandwidth of 2 kHz.

The data processing takes place on the Xilinx XUP-Virtex-II Pro Development Board [8], available through the Xilinx University Program. It is, similar to the I-Tech Liberas, equipped with a Virtex-II Pro FPGA. The correction system was implemented using the hardware description language VHDL. It is controllable using a connected standard-PC. The data processing is done in modules, which can be seen in Fig. 4.

The position data sent to the network from bpm14 and bpm15 (see Fig. 1) is received from the Diamond Communication Controller [DCC in Figure 4] in a first step. During a settable time window (60 µs in our case) received position data is passed to a moving average filter/low pass filter [MA]. In this way the dc-part and therefore the interference with the existing slow orbit correction is eliminated. Calculation of the correction values is done by a standard proportional, integral and derivative controller [PID]. The D-fraction is set to zero to minimize the influence of data noise. In a next step the desired orbit is converted into corrector currents using equation (3) to create a superpostion of the two four corrector bumps [BUMP]. The new desired current values are converted into a serial data stream [RS485] and are distributed via the RS485 interface to the corrector magnet power supplies. The time for correction calculation on the board is approximately 0.2 µs and therefore negligible.

The power supplies BE548 from the company iTest are

[1] Future plans include the connection of existing analog Bergoz BPMs into the fast orbit positition data network. For reference please see G. Schuenemann [1].

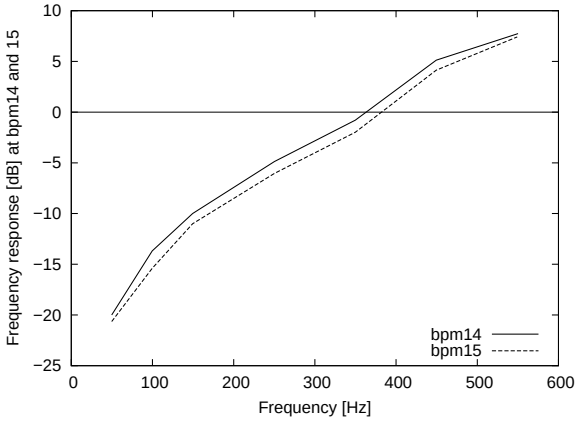


Figure 5: Frequency response at bpm14 and 15.

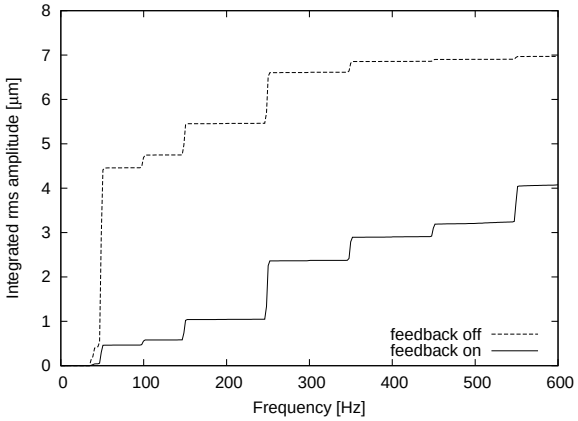


Figure 6: Integrated rms ampl. with feedback on and off.

used as four-quadrant power supplies (± 24 V, ± 10 A). They are connected to the four corrector magnets vcor1 to vcor4 (see Fig. 1 and 4). The minimum time delay after reception of new desired values is 40 µs. The additional delay to reach steady state depends on the desired current variation and the coils inductance. In our case 5 A can be applied in approx. 220 µs. This corresponds to a slew rate of 20833 kA/s.

The magnetic field of the corrector magnets varying in time induces eddy currents in the vacuum chamber. The frequency response was measured using an inductance coil inside the chamber. The vacuum chamber cut-off frequency (-3 dB) was estimated to 1.7 kHz.

The minimum latency for the control loop is about 400 µs resulting in a controller resonance frequency of about 1.25 kHz. Assuming oscillations with a current change of 5 A the total delay increases to 620 µs causing a shift of the resonance frequency of the control loop to 800 Hz.

Increasing this resonance frequency and thereby increasing the attainable cut-off frequency is in principle possible by further reducing the delay.

RESULTS

The frequency response being the ratio of distortion amplitudes with and without orbit feedback was measured with beam at bpm14 and 15. The experimental results are shown in Fig. 5. The amplitude ratios have been determined at strong distortion frequencies only, intermediate values have been interpolated linearly. The cut-off frequency at bpm14 turned out to be 355 Hz, bpm15 has a cut-off frequency of 370 Hz. A total damping of -20 dB at a frequency of 50 Hz has been obtained with the controller.

Figure 6 shows the integrated rms amplitude with and without orbit feedback obtained at bpm14 (averaging over multiple spectra). Due to strong intensity fluctuation of the girder movements in the lower frequency range the integrated rms amplitude would be spoiled by this random effect. To avoid this, frequencies below 40 Hz were removed from the spectrum.

In summary a substantial overall reduction of the orbit distortions below 350 Hz has been achieved in a first approach. Based on this results a future global orbit feedback will be designed and installed at the DELTA storage ring in the near future.

ACKNOWLEDGMENTS

We thank the Diamond Light Source, Didcot, U.K. for providing the Diamond Communication Controller and here especially G. Rehm, I.S. Uzun, M.G. Abbott and N. Hubert from the SOLEIL Light Source for special assistance. We also thank the Electronics Lab of the physics faculty for special electronic developments and J. Altmann for supplying the geophones.

REFERENCES

[1] G. Schuenemann et al., “FPGA Based Data Acquisition System for Fast Orbit Feedback at the electron storage ring Delta”, this conference.

[2] I. S. Uzun et al., “Initial Design of the Fast Orbit Feedback System for Diamond Light Source”, Proc. 10th ICALEPCS.

[3] Nicolas Zebralla, “Feedbacksysteme, lokales, digitales, Orbitfeedback”, internal report

[4] Instrumentation Technologies, “Libera Electron User Manual 1.46”, 2007.

[5] SENSOR Nederland bv, “SM-6 Geophones”, 2003, http://www.iongeo.com/content/includes/pdfs/SM6_121026.pdf.

[6] The MathWorks Inc., 3 Apple Hill Drive, Natick, MA 01760-2098, United States.

[7] J.A.Balmer et al., “Measurement of Ground Vibrations and Calculation of their Effect on the Diamond Light Source”, Proc. EPAC 2000.

[8] Xilinx, Inc., “Xilinx University Program Virtex-II Pro Development System Hardware Reference Manual”, 2008, http://www.xilinx.com/univ/XUPV2P/Documentation/ug069.pdf.

A RESONANT FIRST TURN BPM FOR THE POSITRON INTENSITY ACCUMULATOR (PIA) AT DESY

M. Hüning[#], R. Jonas, J. Lund-Nielsen, F. Schmidt-Föhre, DESY, Hamburg, Germany

Abstract

The Positron Intensity Accumulator PIA at DESY is used to accumulate the intensity and damp down the emittance of the positrons produced in the Linac II before they are injected into DESY II. Up to 13 shots are collected and damped. During the damping process the (base band) peak current is increased by about a factor 4. Therefore the signal from the circulating beam can be up to 50 times bigger than the injected beam and hence overload any first turn detectors. The injected beam however is bunched by the 3 GHz RF of the linac. By filtering the 3 GHz component of the antenna signal and subsequent demodulation it is possible to set up a BPM system detecting exclusively the injected beam.

INTRODUCTION

The Linac II at DESY is an electron-positron linac delivering beams of 450 MeV. In order to reduce the transversal and longitudinal emittances of the beam it is injected into the accumulator and damping ring PIA [1]. PIA is a small ring with approximately 28 m of circumference. The revolution frequency therefore is 10.4 MHz. It is an octagon with 2 stretched and 2 shortened straights. Injection takes place in one of the short straights. The eight dipoles are combined function magnets and in addition there are 4 horizontally focusing and 4 horizontally defocusing quadrupoles. Each of the dipole chambers contains a button BPM. These BPMs and their readout however are optimized for measuring the closed orbit with 10.4 MHz bunches. Sufficient accumulations and damping are required in order to obtain a usable signal.

For monitoring the energy at the end of the Linac it is desirable to measure the beam position of the injected beam at a position with large dispersion. A suitable position for this is the first long straight, approximately 7 m from the injection septum. Here the dispersion is the largest and there is sufficient space to install a new BPM. It was decided to use a BPM of the PETRA III type [2]. This is a button type BPM with a large bandwidth.

SETUP

In order to separate the signal of interest from noise and the low frequency signal of the circulating beam, the pickup signal is first band-pass filtered (Figure 1). With a cavity-type BPM this could have been achieved directly at the source. But this would have required a completely new design while the PETRA III type BPM could be used with only minor modifications. The BPM has a diameter of approximately 98 mm.

The buttons are arranged with an angle of 45° to the usual coordinates of x and y. In this way the electrodes are less likely to be hit by stray particles from the low energy tail of the injected beam. The beam position then has to be calculated from a linear combination of the rotated coordinates.

By mixing with a 3.375 GHz reference the signal is converted to 375 MHz. The exact frequency and phase of the reference is not important as long as it is the same for all buttons. The signal is further improved by low-pass filtering and subsequent amplification. Finally it is fed into the actual BPM electronics.

The beam position is processed by readout electronics of the AM/PM type [3]. It was originally designed for the FLASH linac. In the AM/PM electronics a difference in voltage is translated into a phase difference of two normalized signals. In this way the BPM signal becomes independent of the beam current over a large dynamic range.

Given the high operating frequency of 3 GHz a phase shift between the individual buttons is likely. With a simplified model of the BPM it was calculated that a phase shift between corresponding buttons causes a reduction of the linear range of the BPM. The tolerable phase shift however was found to be up to 60° which can be achieved with a careful setup. With this phase shift the deviation of the measured from the real beam position increases from 1 mm to 2 mm at a beam position of 10 mm.

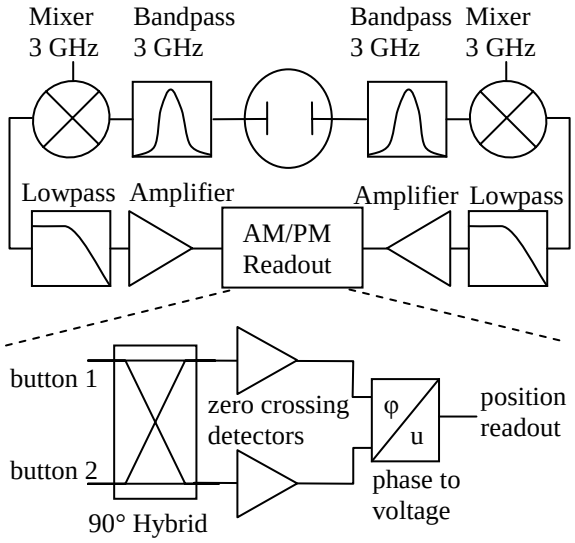


Figure 1: Block diagram of the BPM readout.

[#]markus.huening@desy.de

CHARACTERIZATION

Before beam operation the BPM was tested with a network analyzer connected to various pairs of buttons. It was found that the buttons have a high-pass characteristic with a cut-off at approximately 300 MHz. Because of the large diameter of the beam pipe the RF can propagate into the pipe above a frequency of 1.87 GHz, the lowest waveguide mode. While this will not influence the direct interaction of the beam with the electrode, it allows parasitic modes and wakes from nearby parts of the machine to couple to the electrodes. A great deal of ringing has to be expected.

In order to preserve the large acceptance of the ring it is not possible to change for a smaller beam pipe radius. This prevents the most obvious way to suppress interaction with signals from other parts of the machine.

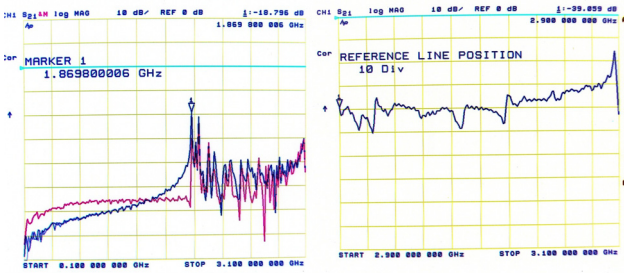


Figure 2: Frequency Response of the BPM.

The raw signals of the buttons have been investigated with a spectrum analyzer in zero span mode (Figure 3). The spectrum analyzer was triggered with a PIA trigger and the sweep was set to 320 ms, a full cycle of the PIA accumulation. The center frequency was first set to 2.998 GHz, the linac frequency. This way the 13 injections are clearly visible with a spacing of 20 ms. The power at the peak of one such pulse was measured with -57 dBm. Switching to 125 MHz one sees the accumulation of intensity in the ring. After 13 injections -47 dBm are measured. At the end of the accumulation cycle the 12th harmonic system is switched on for better bunch compression. At this point the intensity increases by approximately 8 dB.

The second measurement was taken at 125 MHz because the high-pass characteristics of the buttons suppress the lower frequency signals. The difference between 2.998 GHz and 125 MHz amounts to 10 dB at the last injection. Considering that there is a factor of 13 between the injected and the accumulated beam one would expect a difference of approximately 20 dB. Indeed this is the case after compression when the power spectrum shifts towards higher frequencies.

It was also checked that the signal at injection really correlates with beam. When the trigger of the linac gun is removed, the signal is gone. Noise sources like the kicker magnet nearby the BPM continue pulsing in this case. The signal-to-noise ratio therefore can be assumed to be at least 10 dB.

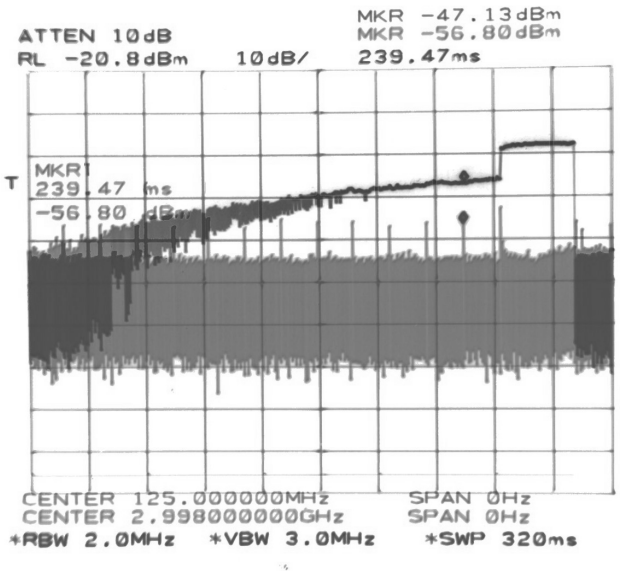


Figure 3: Frequency selected response of a single button, photographed from a spectrum analyzer in zero span mode. Two frequencies are shown, 125 MHz and 3 GHz.

MEASUREMENTS

The Beam Position Signal was measured with a positron beam. In the electron case the situation is more favourable. Therefore it was assumed that it would surely work if the positron case did.

Figure 4 shows the response of the BPM to an injected pulse of $8 \cdot 10^8$ positrons. As expected there is considerable ringing visible. The beam pulse has a maximum duration of 50 ns. The following single values were taken circa 30 ns from the onset of the pulse.

During the measurement there was a timing jitter of a few nanoseconds. Therefore the measurements were post processed by shifting them to an equal rising edge. With the timing jitter removed the signal had a RMS variation of 13 mV.

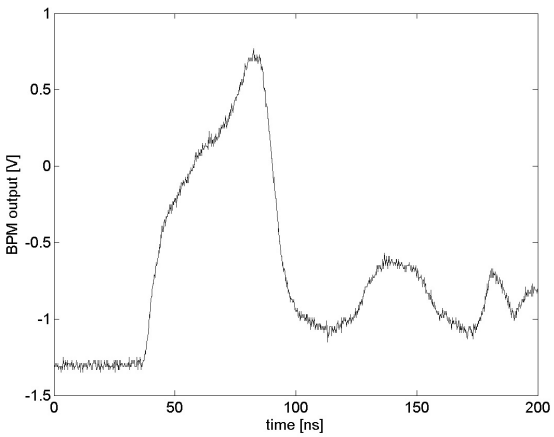


Figure 4: Beam Position Signal.

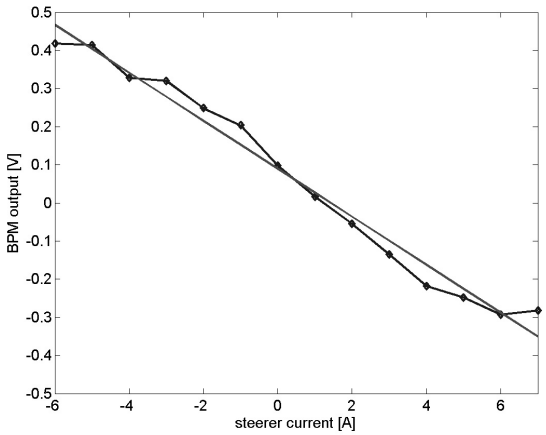


Figure 5: Vertical movement by a steerer magnet 5 m upstream the BPM. Outsize this range beam loss occured.

Since the coordinates of the BPM are rotated by 45° from the machine coordinates each pair of buttons is equally sensitive to horizontal and vertical movement. First the BPM was calibrated with a vertical steerer approximately 5 m upstream. Figure 5 shows the result. The steerer moves the beam 1.5 mm/A at the position of the BPM. So the total displayed range is 19 mm. Beyond this range the beam intensity is reduced by beam loss. The corresponding measurements were ignored.

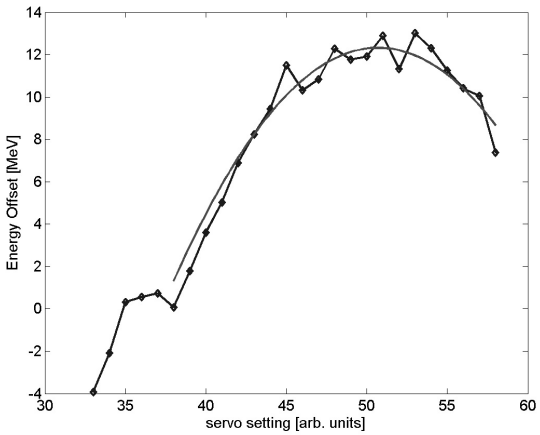


Figure 6: Energy variation by adjusting two acceleration sections of the linac. The nominal setting is 45.

The slope is 63 mV/A, hence 42 mV/mm. This is the calibration regarding the actual vertical displacement of the beam. Along the axis of the BPM the displacement is actually larger. The RMS jitter of 13 mV mentioned above then translates into 300 µm. This is not the resolution of the BPM but includes actual beam jitter.

The same calibration constant can be used for the horizontal axis. With this and together with the known dispersion at the location of the BPM it is possible to measure the energy variation of the injected beam. The beam energy is adjusted with the so called “servo”. This is a phase shifter moving the phases of the two last acceleration sections of the linac against each other. The abscissa in figure 6 is the setting of the servo, by coincidence it is close to the actual phase-shift. At the time of the measurement the optimal setting of the servo was 45. As can be seen the linac is operated close to the maximum of the servo. All measurements were cross-checked with a nearby viewscreen.

In figure 4 a slope can be observed on the BPM signal in the range of interest between 50 ns and 80 ns. This was attributed to an energy chirp of the beam pulse. Indeed the pulse is cropped when the energy is moved towards the acceptance limits of PIA.

CONCLUSION

A first turn BPM has been installed in PIA. By RF-filtering it cleanly separates the injected from the stored beam. Due to the necessary large aperture of the BPM the cut-off frequency of the beam pipe is lower than the bunch frequency and hence the operating frequency. It does – however – deliver reasonable results that are good enough to be used for setting up the machine and possibly for automating the energy control of the linac.

REFERENCES

[1] A. Febel, G. Hemmie, “PIA, the Positron Intensity Accumulator for the PETRA Injection”, PAC 1979, IEEE Trans on Nucl Sci Vol. NS-26, No 3, 3244

[2] G. Kube et al., “Overview of the Diagnostics Systems of PETRA III”, Proc. of EPAC 08, Genoa, 2008

[3] G. Vismara, “The Comparison of Signal Processing Systems for Beam Position Monitors”, Proc. of DIPAC 99, Chester, UK, 1999

COMPARATIVE STUDIES OF RF BEAM POSITION MONITOR TECHNOLOGIES FOR NSLS II*

O. Singh#, I. Pinayev, NSLS-II Project, BNL, Upton, NY 11973, U.S.A.
G. Decker, B.X. Yang, APS, ANL, Argonne, IL 60439, U.S.A.

Abstract

Sub-micron beam stability is a necessary performance requirement for the NSLS II light source, a substantial challenge testing the limits for currently available RF beam position monitoring methods. Direct performance comparisons between commercially available BPMs and Advanced Photon Source in-house developed BPM were made at the APS storage ring. Noise floor, fill pattern dependence, and intensity dependence were investigated and correlated with photon diagnostics at the beam diagnostic beamline at APS sector 35. Key results are presented.

INTRODUCTION

The comparative tests of different BPM receivers were performed at APS. The key features of the experimental arrangement are shown in Figure 1. The Libera Brilliance receiver [1] was connected to the S36A:P0 BPM station in the diagnostics straight. An in-house built APS FPGA-based BPM receiver [2] was connected to the S35B:P0 BPM station. Both stations use 4-mm diameter pick-up electrodes mounted on an 8-mm high vacuum chamber of a diagnostics undulator. Horizontal separation of the buttons is 9.6 mm center-to-center. Separation between 35B:P0 and 36A:P0 is about 4 meters. Bergoz electronics [3] was used for S35B:P1 and S36A:P1 equipped with 10-mm buttons mounted on the approximately 4x8 cm elliptical vacuum chamber.

At a distance of 30.045 meters from the center of the ID straight is a vertically moveable horizontal slit, and at 29.5 meters is a horizontally moveable vertical slit. Both the slit size and center are adjustable with high accuracy using stepper motors. The beamline uses an hourglass-shaped beryllium window to separate the ring vacuum from the beamline vacuum. By using this shape, heat is more efficiently removed, albeit at the expense of transmogrifying the transverse profile of any transmitted photon beam.

The slit assemblies are accessible and their motion can easily be calibrated against a reference dial indicator to quantify mechanical motion. Preliminary measurements indicate backlash at the level of 20 microns, although there are indications that repeatability is significantly better than this, below 5 microns.

Both horizontal and vertical calibrations were performed at 35-ID. The main idea was to independently determine the absolute calibration of S35B:P1 and S36A:P1 from the slit/flux monitor combination, and compare the results with the lattice model.

Because S35B:P0 and S36A:P0 used experimental electronics, they have not been calibrated against the ring model. Instead, the local bump scans provide absolute calibration data for these electronics, in addition to supplying absolute calibration data for the front-end photon BPMs.

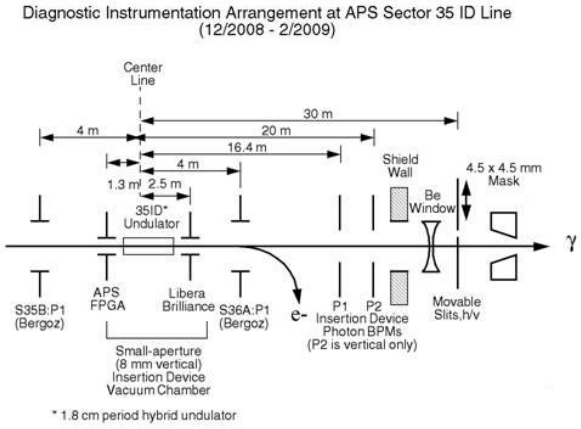


Figure 1: Diagnostics arrangement for 35-ID source point. Distances are approximate.

OBSERVING NOISE SPECTRUM OF CIRCULATING BEAM

During studies the Libera Brilliance signal level was manually set and direct measurement (no switching) was selected. The APS FPGA-based BPM receivers were in routine configuration. 262144 data points at a revolution frequency of 271.6 kHz were collected for both devices and the observed horizontal beam motion spectra are shown in Fig. 2.

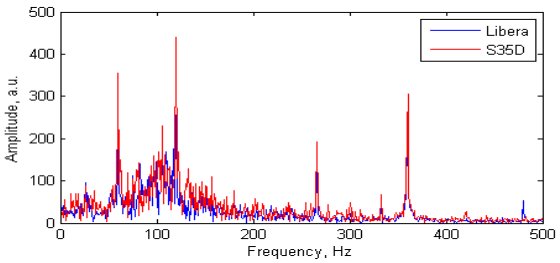


Figure 2: Overlaid spectra of beam motion in the horizontal plane. The data are from both Libera Brilliance and FPGA based receiver.

Excellent agreement of the two sets of data was found. The finest details are a perfect fit (see Fig. 2-4).

* Work supported by U.S. Department of Energy, Office of Science, Office of Basic Energy Sciences, under Contracts DE-AC02-98CH10886 and DE-AC02-06CH11357.
#singh@bnl.gov

As can be seen from Figures 3 and 4, Libera Brilliance has less noise than the APS FPGA-based receiver.

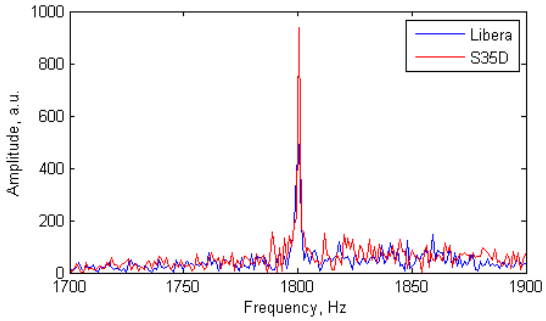


Figure 3: Synchrotron motion line observed by Libera Brilliance and FPGA-based receivers.

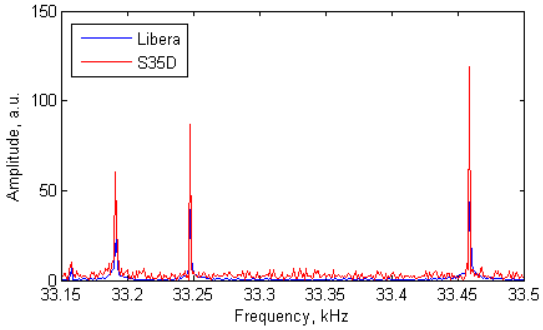


Figure 4: Details of horizontal beam motion in 30 kHz region observed by Libera Brilliance and FPGA-based BPM receivers.

INJECTION TRANSIENT STUDIES

The injection trigger signal was split and used to start simultaneous data acquisition for both the APS FPGA-based BPM receiver and Libera Brilliance. Final fine alignment on the time axis was done during post processing. The relative delay was the same for both planes. The transients are shown in Fig. 5 and Fig. 6.

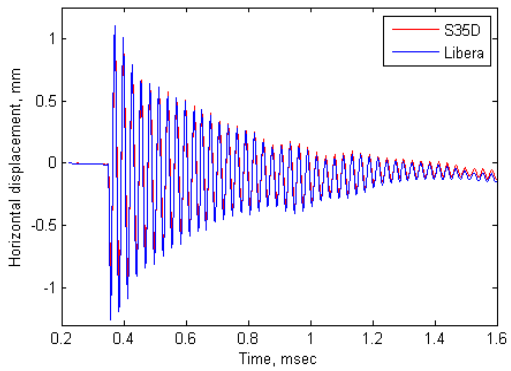


Fig. 5: Horizontal transient caused by the injection kickers. There is remarkable agreement in the two curves except for a small offset observed towards the end of the transient.

The vertical transient has good agreement but not as good as for the horizontal plane.

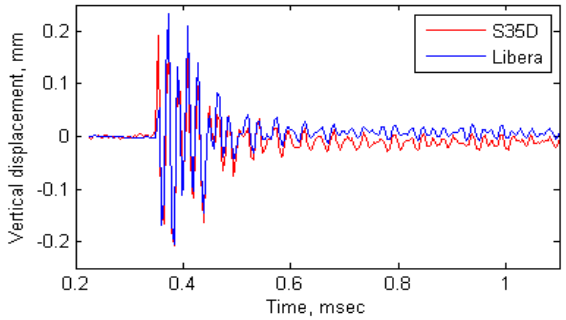


Figure 6: Vertical transient caused by injection kickers.

FILL PATTERN DEPENDENCE

Fill pattern dependence was considered as a perceptible intensity dependence seen when a gap in the 324 bunch fill pattern is present while maintaining constant total circulating charge. A single button was attached to a four-way splitter at the input to the Libera Brilliance module. Intensity dependence was simulated by large horizontal steering. For the uniform fill of 90 mA beam in 324 bunches was used.

The beam was refilled to 102 mA and then with a mismatched kicker (IK2 had 9 kV instead of normal 6 kV), part of the beam was blown away. 270 bunches had full charge and 10-15 bunches on each side had reduced charge. Again dependences of beam position and measurement noise on signal intensity were found. The process of refill and cleaning followed by measurements was repeated to obtain a fill pattern with 75 mA and a larger hole.

For the more direct study of the dependence of position and noise on signal intensity, all readbacks associated with a certain level were averaged and the standard deviation was found. The peak-to-peak position variations did not exceed 80 nm for both planes (see Fig. 8). The noise levels are shown in Fig. 7.

With a high level signal for all three patterns the noise was around 5 nm in the horizontal plane and 10 nm in the vertical plane (due to the difference in the programmed sensitivities). Reduction of the signal level increased noise in both planes by a factor of 3. In the medium range, change of the beam position readback with fill pattern was about 80 nm for both planes.

For the Bergoz BPM receivers in similar conditions, drift was 50 nm in the horizontal plane and 170 nm in the vertical plane. For the APS FPGA-based receivers, drift was 240 nm in the horizontal plane and 680 nm in the vertical plane. So, the Bergoz and Libera Brilliance had comparable performance, while the APS FPGA-based module was a factor of 3 worse.

Table 1 shows results from data logged for 24 hours while top-up was running with the 24-bunch (154 ns spacing) fill pattern. A single button was connected to a 4-way splitter and then into the Bergoz inputs, and a second button was sent into a second splitter and routed to the Libera Brilliance. For both receivers the simulated electron beam was on center (i.e., after splitter signals

were directly connected to inputs). The Libera data rate is 9.82 Hz with 2 Hz low-pass filtering. The Bergoz is one sample per minute, with a 20-second time constant filtering. In general, the variation in the vertical plane is larger due to the calibration factor difference for the unrotated button geometry (for Libera K_x/K_y=0.407).

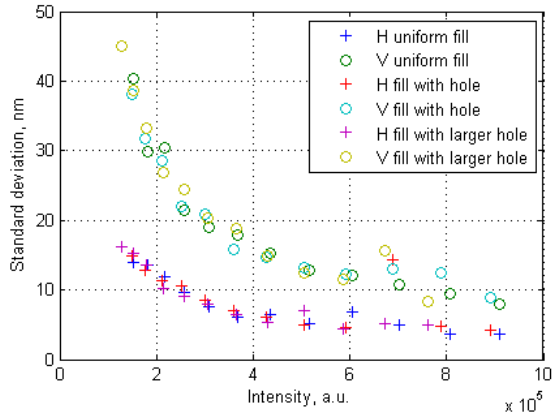


Figure 7: Libera Brilliance beam position measurement noise dependence on intensity for different fills.

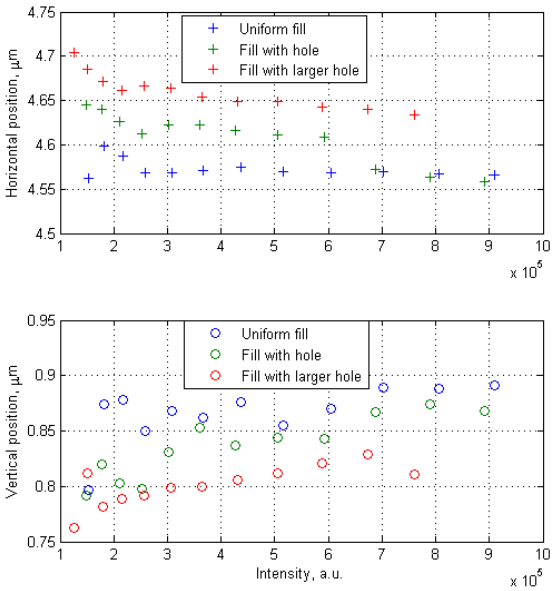


Figure 8: Beam position measured by Libera Brilliance vs. intensity for different fills.

The performance was also verified for beam with a simulated "offset" by the installation of a 4 dB attenuator into one of the four inputs for both receivers.

The drift performance of the Bergoz unit is somewhat better than the first data set; perhaps the rack temperature was more stable. The Libera Brilliance rms values seem to have increased by about 70% for the horizontal plane, and 33% for the vertical plane and now their ratio is more in line with the ratio of calibration factors. The summarized data are shown in Table 1. As mentioned before, the signal bandwidth was different for the two units. To make comparison more direct, the position signals from the Libera Brilliance were averaged using a 20 sec Hanning window: the corresponding noise is shown in parentheses.

Table 1. Summarized data for BPM receivers drifts during 24 hours of top-up operation.

	Bergoz		Libera Brilliance	
	X, nm	Y, nm	X, nm	Y, nm
Rms motion for centered beam	54.0	90.6	7.6 (4.1)	27.1 (22.1)
Rms motion for beam with offset	44.0	49.5	12.8 (6.1)	36.6 (25.2)

BPM CALIBRATION USING SLIT

The flux monitor installation was completed in December, 2008 and first measurements with beam were conducted on December 22. Local steering of the undulator beam across a slit provides a very clean profile measurement. By displacing the slit by a known calibrated amount and repeating the local bump scan of the particle beam, the measured profile is displaced. Determination of the amount of displacement by extrapolation from the source RF BPMs provides a cross-calibration relating measured electron beam position to slit position. For each of the data sets, a straight line fit was made. For the FPGA BPM receivers, the residuals to the fits of the data are ±1 micron out of a full-scale range of about half a mm, or ±0.2% nonlinearity. It was found that calibration factors for FPGA electronics were 16.6% off in the vertical plane and 22.9% in the horizontal plane.

For the Libera Brilliance, the loaded internal calibration factors were K_x = 2778000 nm and K_y = 6831000 nm. It was found that vertical calibration factors should be decreased by 3.9% for the vertical plane and by 2.1% for the horizontal plane.

CONCLUSION

There is excellent agreement between observations of beam motion with a Libera Brilliance and APS FPGA-based receiver, with the Libera Brilliance unit having less noise in the high-frequency part of spectrum. For fill pattern dependence, Libera Brilliance outperformed both the APS FPGA-based unit and the Bergoz BPM receiver.

Calibration factors for Libera Brilliance found from the numerical calculations are in good agreement with photon slit scans, while FPGA receivers are off by as much as 20%.

REFERENCES

[1] http://www.i-tech.si
[2] G. Decker et al., "Performance of FPGA-Based Data Acquisition for the APS Broad Band Beam Position Monitor System," Proc. of BIW'08, pp.155-160.
[3] http://www.bergoz.com

PERFORMANCE OF EXPONENTIAL COUPLER IN THE SPS WITH LHC TYPE BEAM FOR TRANSVERSE BROADBAND INSTABILITY ANALYSIS*

R. de Maria, BNL, Upton, New York, J.D. Fox, SLAC, Menlo Park, California, USA
W. Höfle, G. Kotzian, G. Rumolo, B. Salvant, U. Wehrle, CERN, Geneva, Switzerland

Abstract

We present the performance and limitations of the SPS exponential coupler [1] for transverse instability measurements with LHC type beam. Data were acquired in 2008 in the SPS in the time domain with a bandwidth of up to 2.5 GHz. The data were filtered to extract the time evolution of transverse oscillations within the less than 5 ns long LHC type bunches. We describe the data filtering techniques and show the limitations of the pick-up due to propagating modes.

INTRODUCTION

Two types of transverse instabilities limit the single bunch intensity of proton beams in the SPS. On the one hand with multi-bunch beams such as the LHC nominal beam with 25 ns bunch spacing the electron-cloud instability limits the maximum intensity per bunch [2]. On the other hand for very high bunch intensities the single bunch transverse mode coupling instability (TMCI) is a limitation as well [3]. Common to both instabilities is the appearance of high frequency signals caused by oscillations within the bunch. Diagnostics to probe the nature of the instabilities, their spectral components and time evolution must be able to resolve oscillations within the bunch.

Due to the relevance of the electron cloud driven instability and its adverse effect on the transverse emittance (blow-up) and because some of the LHC upgrade scenarios beyond ultimate luminosity call for bunch intensities higher than the LHC ultimate bunch intensity of 1.7×10^{11} protons per bunch where the TMCI may limit performance, an R&D program was launched to optimally diagnose and possibly cure these transverse single bunch instabilities by a wide band transverse feedback system [4].

The quest to adequately diagnose the instabilities motivated the analysis of existing pickup/kicker structures in the SPS and to evaluate their performance.

Exponential couplers were built and installed in the SPS [1] and are readily available. A fast digital oscilloscope was used to acquire the data from the pick-up with offline post processing to correct for imperfections, in order to evaluate the pick-up performance and provide the means to accurate diagnose the instabilities.

In the following we present the results of these activities, explain the elements of the acquisition chain, show some sample measurements and discuss the post processing methods. Conclusions are drawn and future plans outlined.

* Work supported by DOE and CERN

EXPONENTIAL PICKUP AND ACQUISITION CHAIN

The main component of the acquisition chain is a stripline pickup where the stripline has s-dependent (s being the coordinate in beam direction) width that translates in an s-dependent coupling constant. The distance of the stripline from the vacuum chamber diminishes as the width decreases such as to preserve a constant line impedance of 50 Ω. If the coupling, i.e. the electrode shape, is exponential the resulting transfer function is almost flat in amplitude instead of having the typical notches of a constant width stripline pick-up. The absolute value of the transfer function in frequency domain is [1]

$$|F(\omega)| = \frac{K\omega l/c}{\sqrt{a^2 + \frac{4\omega^2 l^2}{c^2}}} \sqrt{1 + e^{-2a} - 2e^{-a}\cos(2l\omega/c)} \tag{1}$$

and the phase is

$$\mathrm{Arg}\{F(\omega)\} = \arctan\left[\frac{2\frac{\omega l}{c}\sin\frac{2\omega l}{c} + a\left(e^a - \cos\frac{2\omega l}{c}\right)}{2\frac{\omega l}{c}\left(e^a - \cos\frac{2\omega l}{c}\right) - a\sin\frac{2\omega l}{c}}\right] \tag{2}$$

where l is the kicker length, K a coupling constant and a is describe the exponential tapering ([1]). We assumed ultra-relativistic beams, $v = c$. Normally the pick-up is installed with the beam passing the wide end of the strip first, we will call this *forward* installed. A backward installed coupler has the beam interacting the narrow end of the strip first. Note that the coupler is directional and signals are always extracted at the upstream ports.

A drawback of the exponential coupler is its nonlinear phase response, but it can either be corrected by numerically filtering the data or in the case of a pickup-kicker combination one can take advantage of the mirrored phase response for a backwards installed coupler. With one coupler (kicker or pick-up) installed backward and the other forward we expect to compensate for an overall linear phase response.

The pickup has four electrodes at ± 45 degrees to the horizontal plane which allow to measure both bunch intensity, as well as horizontal and vertical displacement. In the SPS there are a total of four such pickups installed, two usually cabled for horizontal operation and two for vertical operation. The tests concentrated on the vertical observations, plane in which the electron cloud effect causes a high frequency instability.

The pickup could not be tested on a bench, but we measured with a network analyzer the properties of the electrodes, cables and hybrids. The installation orientation of

the pickup cannot be tested without beam, the stripline being a matched 50 Ω system. A dedicated experiment with short bunches showed that one of the four pickups under test was installed backwards, opposite of what would be the expected default orientation, a relict from past operation with anti-protons, see Fig. 1. Another critical part

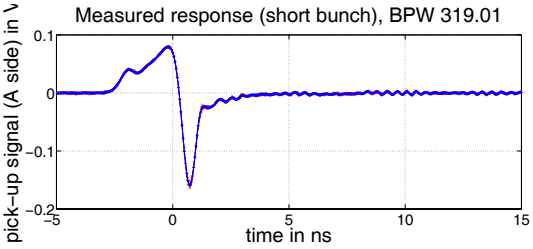


Figure 1: Measured pick-up response to single short bunch (backward installation).

are the long cables that bring the signals to the surface. While the attenuation was as expected and not a major concern, we found, rather unexpected, the nonlinear dependence of phase with frequency in these corrugated cables [5] to further spoil the performance of the pick-up when signals were observed in the time domain: with short bunches and long cables a "ringing" can be observed. This is illustrated in Fig. 2 where we compare the calculated time domain response of the pick-up to a gaussian bunch of length $4\sigma = 1$ ns, in forward (solid blue line) and backward (dashed) installation direction with and without the required cable, as actually installed. The bunch is shown for comparison (red curve) and the responses have been normalised to have a peak value of 1.

Resistive combiners were used to sum signals from the two pairs of electrodes and an Anzac H-9 hybrid was used to produce sum and delta signals. Care must be taken not to saturate the hybrid. In the final set-up used the hybrid was installed on the surface, with cables from the tunnel precisely matched in length. The attenuation from the cables (5 dB to 20 dB in the frequency region of interest) gives additional protection to avoid saturation of the hybrid—the attenuation is in any case in the signal chain. 6 db and 3 dB attenuators were further installed at the cable ends and 20 dB for the sum signal to equalize the voltage level to the delta signal in the scope. With this setup the signal levels were oscillating between 10 mV to 1 V depending on the bunch intensity.

For data acquisition we used a Tektronix DPO7254 digital oscilloscope capable of a maximum sampling rate of 40 GS/s. For most of the measurements two channels (sum and delta) were recorded reducing the maximum sampling rate to 20 GS/s. Bunch synchronous triggering was available (each turn) allowing efficient use of the memory of the oscilloscope. With the installed memory of 20 M samples per channel, one batch of LHC beam ($\simeq 8\mu$s) could be recorded for hundreds of turns or a single bunch for $\simeq 20'000$ turns.

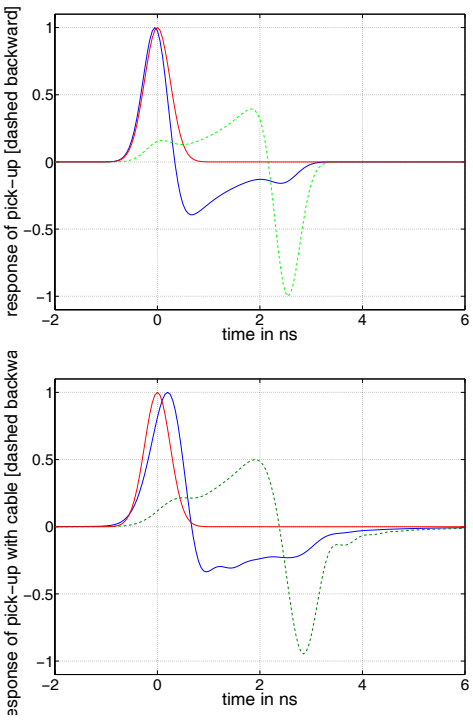


Figure 2: Pick-up response to gaussian bunch without and with cable. Red line represents the bunch intensity, blue and dashed line the signal distorsion of a forward and backward pickup installation respectively.

MEASUREMENTS

We acquired data during machine development study sessions in the SPS in 2008 at injection with LHC beam and up to nominal LHC beam intensity ($> 1 \times 10^{11}$ protons per bunch) subject to the electron cloud instability (Fig. 5) and single bunch beam with and without RF (Fig. 3-4) for TMCI diagnostics and to search for machine impedance [6].

Figure 4 shows the frequency content of one single bunch demonstrating the flatness of the response compared to a traditional stripline. A multi bunch measurement shows that the stripline picks up in the delta signal experiences high Q resonances above $\simeq$1.6 GHz. The frequency of 1.6 GHz can be associated with the TE_{11} mode cut-off frequency of 1.64 GHz (calculated for a vacuum pipe diameter of 107 mm). For the sum signal the signals of the related resonance in the pick-up cancel due to the symmetry of the mode. Careful inspection of the sum signals reveals the presence of spectral components close to the TM_{01} mode (2.1 GHz calculated, 2.2 GHz observed) and the TE_{21} mode (2.7 GHz calculated, 2.4 GHz observed). Analysis of delta signals from a single captured bunch show the absence of a line at the TM_{01}, as expected (monopole mode), but the 2.4 GHz signal is again observed. Note that the TE_{21} is of quadrupolar symmetry and both, delta and sum signals can be excited with the beam not centered in the pick-up.

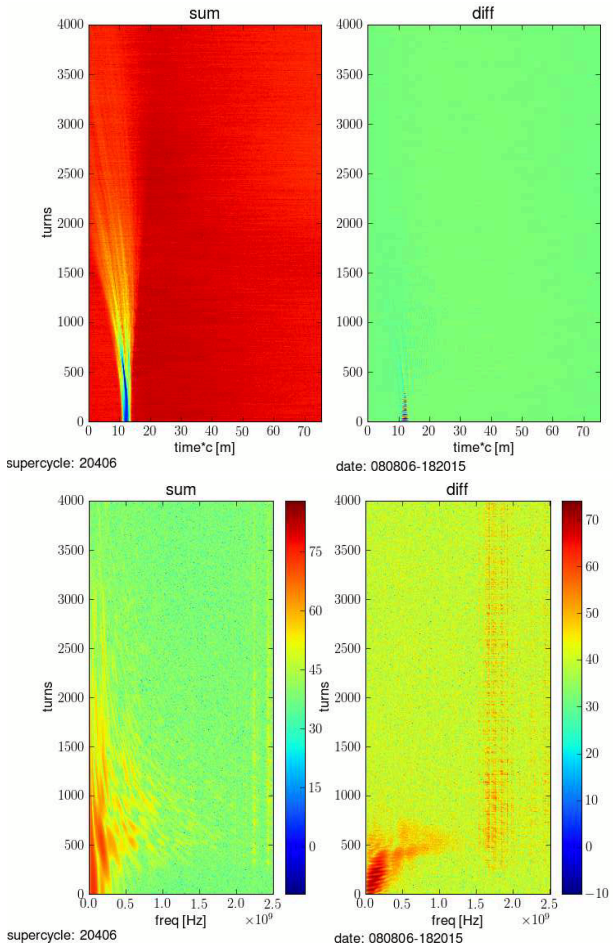


Figure 3: Debunching in the SPS, time domain data reconstructed and spectrum of sum and difference signal from a vertical pick-up. Bunch is unstable and lost.

Delta signals show some distortions, which are supposedly due to strip line imperfections. In order to extract the interesting oscillatory part these distortions can be removed by a comb filter (1-tap notch).

CONCLUSIONS

We demonstrated the performance of the available wide band exponential couplers in the SPS and outlined the signal processing necessary to extract the relevant bunch oscillations. The pick-up worked as expected, but a number of shortcomings such as a systematic distortion of the delta signal due to non-equal electrodes remains to be understood and efficiently removed from the data through calibration. During the 2009 SPS run we plan to continue the measurements for instability analysis. One of the couplers will also be equipped with high power hybrids and loads (200W range) allowing it to be used for excitation purposes and to measure beam transfer functions.

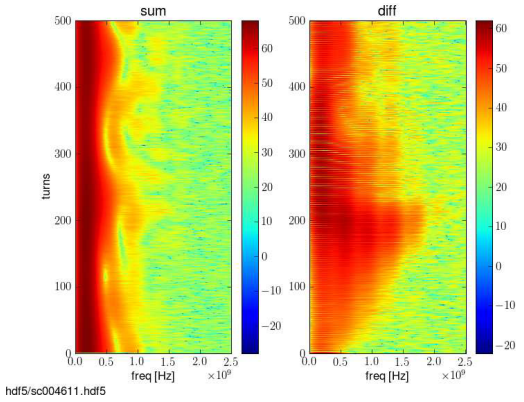


Figure 4: Evolution of spectra (sum and difference) for captured single bunch, transversely unstable.

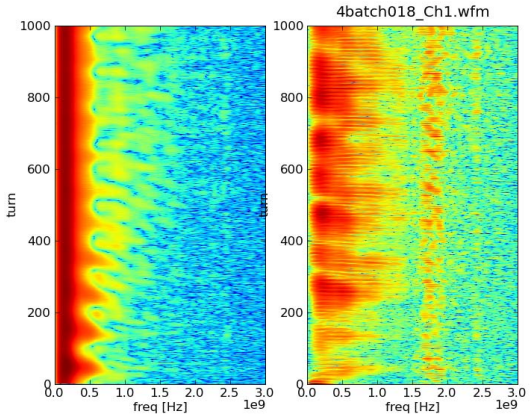


Figure 5: Evolution of spectra (sum and difference) for one LHC bunch in a bunch train subject to e-cloud transverse instability.

ACKNOWLEDGMENTS

The authors are thankful to T. Bohl, T. Linnecar, G. Papotti, G. Arduini, E. Métral, E. N. Shaposhnikova, F. Caspers for the discussion and help in the MD studies.

REFERENCES

[1] T. Linnecar, CERN-SPS-ARF-SPS/78/17, CERN, Geneva (1978)

[2] G. Arduini et al., 31st Advanced Beam Dynamics Workshop, Napa, CA, USA, CERN-2005-001, p. 31–47, CERN, Geneva (2005)

[3] B. Salvant et al., Proceedings Beam07, p. 113–118, CERN-2008-005, and B. Salvant et al., EPAC 08, Genoa, p. 1694–1697 (2008)

[4] J. D. Fox et al., PAC'09, Vancouver, BC, May2 009, paper TH6REP078 (2009)

[5] G. Kotzian et al., PAC'09, Vancouver, BC, May 2009, paper TH5RFP033 (2009)

[6] B. Salvant et al., PAC'09, Vancouver, BC, May 2009, paper FR5RFP047 (2009)

DESIGN OF THE STRIPLINE AND KICKERS FOR ALBA

U. Iriso*, T.F. Günzel and F. Pérez
CELLS, Ctra. BP-1413 Km 3.3, 08290 Cerdanyola, Spain

Abstract

The design of stripline kickers shall be adapted to match the line impedance, maximize the effective beam kick, reduce the heat load and minimize the transverse coupling impedance. These kickers are used for either tune measurements or transverse feedback. We describe the ALBA design of these kickers for the Storage Ring.

INTRODUCTION

The term "striplines" refers to a configuration of longitudinal electrodes that may be used either as beam pickup (to extract information about the beam motion), or beam kickers (to change its motion). Their design should be taken with due care. The electrodes must be adapted to match the line impedance, reduce heat load, and minimize the transverse coupling impedance. Moreover, when used as active devices, we shall maximize the beam kick efficiency.

ALBA has designed different stripline kickers. In the following we use the word "striplines" to the combination that allows the dual purpose of beam pickup and beam excitation, and "kicker" to the one used only to excite the beam. The two designs are:

- Storage Ring Stripline: only one unit is installed in the machine. Its purpose is to provide the beam excitation for tune measurements. In early phases of the commissioning, this unit will be also used for tune measurements. Thus, its length is $\lambda/4$, being λ the bucket length (λ =2 ns in our case). See Fig. 1, left.

- Feedback Kickers: in order to cure the fast transverse instabilities, we will install two of these kickers (horizontal and vertical). See Fig. 1, right. Since their purpose is only beam excitation, their length is $\lambda/2$.

In this report we describe the steps followed for the design of these devices.

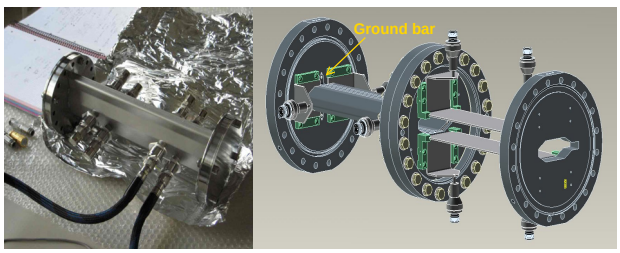


Figure 1: Stripline (left) and hor and ver kicker (right).

* ubaldo.iriso@cells.es

STORAGE RING STRIPLINE

In this case, we design a four-electrodes striplines for either beam measurement or beam excitation. We describe the line impedance matching, the effective kick produced by the stripline, and its coupling impedance.

Line Impedance Matching

First, the electrodes shall be matched to the line impedance. A four-electrode stripline supports 4 independent TEM eigenmodes: sum, dipole horizontal, dipole vertical, and quadrupole modes (see Fig. 2. left). Typically, when the purpose of a stripline is the beam position measurement, these devices are designed using the traditional sum-mode matching with wide electrodes to maximize the beam signals [1]. For the dual purpose case, we have adopted the compromise relation [1]:

$$Z_L = Z_{\mathrm{dipole}} = \sqrt{Z_{\mathrm{sum}} Z_{\mathrm{quad}}}\,. \qquad (1)$$

where $Z_L = 50\Omega$, and we have assumed that the hor and ver dipole modes are identical (which, as seen "a posteriori", is a good approximation).

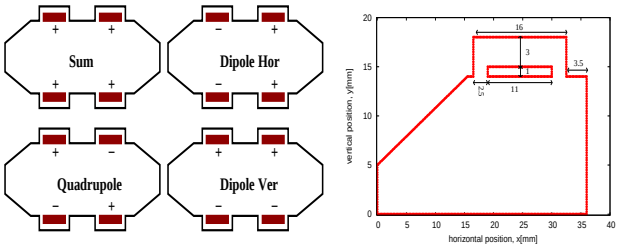


Figure 2: Independent modes in a four-electrode stripline (left), and geometry of one forth of it (right).

For symmetry reasons and because of the low coupling between the strips, the differences between the 4 aforementioned modes can be neglected and it is common to focus the study on one forth of the vacuum chamber [2]. As the results will show (see Table 1), this is not a bad approximation. Each of these eigenmodes has a characteristic impedance that can be easily computed with simple transverse 2-d electrostatic codes (in this case, we use SUPERFISH). The final geometry for one forth of the vacuum chamber is shown in Fig. 2, right.

The results for the 4 modes are shown in Table 1. Note that $\sqrt{Z_{\mathrm{sum}} Z_{\mathrm{quad}}} = 51.16\Omega$, and so the last condition in Eq. 1 is fulfilled with $\sim 2\%$ of discrepancy.

Table 1: Impedance of the SR Stripline for Each Eigenmode

	Sum	Dipole Hor	Dipole Ver	Quad
Z(Ω)	52.78	50.89	50.05	49.59

Effective Kick

The shunt impedance Z_{sh} of a kicker made out of two electrodes of length l and spaced with a distance d is [4]

$$Z_{sh} = 2Z_0\left(\frac{2g\beta c}{d\omega}\right)^2 \sin^2\left(\frac{\omega l}{c}\right), \qquad (2)$$

where Z_0 is the vacuum impedance, ω refers to the kick angular frequency, c is the speed of light, and g is the geometrical factor [4]. Figure 3 shows the shunt impedance for the stripline and the vertical feedback kicker (which will be seen in the next Section). Note the difference between the nodes position (corresponding to $\lambda/4$ and $\lambda/2$, respectively) and the significant difference between shunt impedances at $\omega = 0$ GHz (1.3 kΩ vs 45 kΩ). Since the purpose of the stripline is just the beam excitation for tune measurements, this shunt impedance is sufficient.

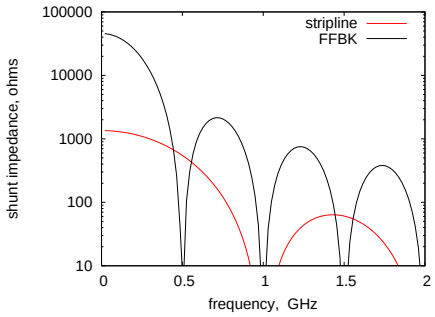


Figure 3: Shunt impedance of the stripline and vertical feedback kicker.

Coupling Impedance

Since the loss of a stripline is inversely proportional to the bunch length of only 4.6mm, the losses are quite high, namely 23W. Under the assumption that above the cutoff-frequency most wake fields propagate away from the stripline, the remaining losses at the device are slightly above 15W. But it can be even a bit more if the modes trapped at the feedthroughs do not couple well to propagating modes. Figure 4 shows the stripline impedance spectrum, where on distinguishes two separate parts: the characteristics of a stripline (below ∼ 6 GHz) and of a BPM button (around 10 GHz).

On the other hand the vertical and horizontal transverse impedance of 180Ω/m and 263mΩ/m are small compared to the storage ring transverse impedance budget.

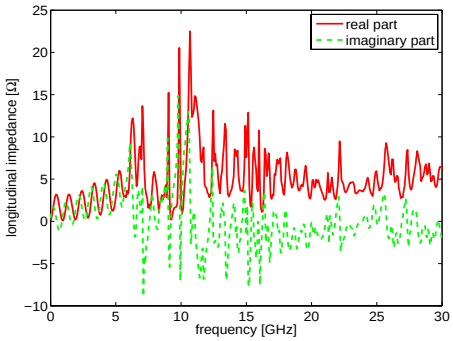


Figure 4: Spectra of the longitudinal impedance.

STORAGE RING FEEDBACK KICKERS

As in the ALBA storage ring resistive wall coupled instabilities are expected already at moderate currents a dedicated feedback kicker is needed for each transverse plane. Our design is based on the one of SLS/Elettra[3]. Since its purpose is to damp the coupled bunch instabilities, the electrodes length is $\lambda/2$. The drawback of this solution is the significant geometrical impedance these devices produce.

Line Impedance Matching

In this case we will only use the dipole configuration (+ -), and the line impedance matching is straightforward. Figure 5 shows both vertical and horizontal kickers dimensions. The ver kicker consists of two parallel plates placed inside a cylindrical chamber, where the distance between them is equal to the vertical dimension of the SR beam pipe. The hor kicker follows the general SR chamber geometry, where we have introduced a ground plate between the two electrodes to reduce the transverse beam impedance (see below).

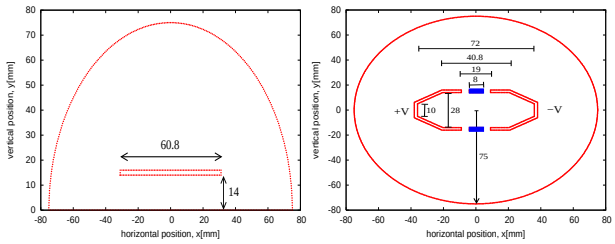


Figure 5: Transverse geometry of the vertical (right, half-geometry) and horizontal kickers (right).

Effective Kick

In this case, the goal is that the effective kick can cure the CBI, i.e. feedback damping time τ_F should be faster than CBI growth time.

The maximum kick $\Delta\theta_k$ produced by the feedback system shall correspond to the maximum beam transient x_{max}. With the proper phase advance between the kicker and the pickup, the feedback damping time τ_F is [4]:

$$1/\tau_F = \frac{\Delta\theta_k}{2x_{max}} f_0 \sqrt{\beta_p \beta_k} \qquad (3)$$

where f_0 is the revolution frequency, β_p and β_k are the beta function at the pick-up and kicker.

The kick produced to a elementary particle crossing between two electrodes is:

$$\Delta\theta_k = e\sqrt{2PZ_{\rm sh}}/E \ , \qquad (4)$$

where Z_{sh} for the hor and ver kickers are shown in Fig. 3 and Table 2, P=100 W is the amplifier power and E=3 GeV is the beam energy.

On the other hand, the (fastest) resistive wall (RW) instability growth time τ as a function of the beam intensity I is:

$$1/\tau = \frac{I}{2E/e}\frac{f_0(\langle\beta\rangle R_\perp)}{\sqrt{(1-Q_0)f_0}} \ , \qquad (5)$$

where $\langle\beta\rangle$ is the beta function, Q_0 is the fractional betatron tune, and $R_\perp$ is the transverse rw impedance for f=1 GHz.

Figure 6 shows the instability growth time as a function of the beam intensity using the parameters in Table 2, compared to the feedback damping time assuming a maximum transient of $x_{\rm max} = 1$ mm.

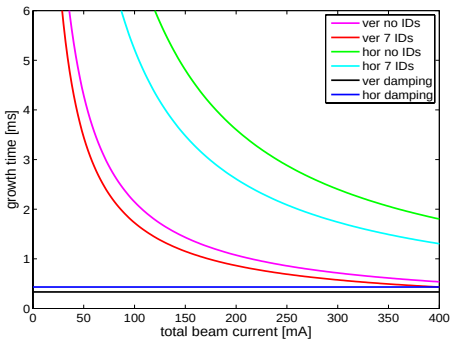


Figure 6: Damping rate needed for both planes for different machine configurations at zero chromaticity.

Table 2: Parameters Determining Feedback Damping and rw Instability Growth Times

Parameter	unit	Hor	Ver
β_p, β_k	m	8.9, 8.6	5.6, 5.1
Z_{sh}	kΩ	45.7	10.1
$\langle\beta\rangle R_\perp$ (w.o. IDs)	k$\Omega\sqrt{\rm GHz}$	210	600
$\langle\beta\rangle R_\perp$ (with IDs)	k$\Omega\sqrt{\rm GHz}$	290	750

Coupling Impedance

The geometrical coupling impedance of the hor and ver feedback kickers are calculated with GdfidL and shown in Table 3. The ceramical supports in the electrodes provide mechanical stability, and a slight improvement in the impedance in both cases. The power loss of the hor kicker could be reduced by almost a factor 4 with the introduction of the ground plate and now is only 56 W.

As for the vertical kicker, a countermeasure to reduce this power loss is currently being investigated. First analysis show that the power loss in the ver kicker can be reduced by about a factor of 2-3 by reducing the gap between the edge flanges and the electrodes (from 5mm to 1mm).

Table 3: Geometrical Coupling Impedance of the Kickers

	$Z_V[\frac{k\Omega}{m}]$	$Z_H[\frac{k\Omega}{m}]$	$\kappa_\parallel[\frac{V}{pC}]$	P[W]
ver kicker	1.67	0.78	0.57	179
hor kicker	0.43	0.55	0.18	56

The longitudinal impedance spectra contain many resonances. The analysis of the eigenmode vertical kicker spectrum shows that the shunt impedances of the resonances remain below the threshold of LCBIs. Around 4 GHz, the shunts reach values of already half of the threshold.

Whereas the values of transverse impedance are acceptable within the storage ring impedance budget, the power loss is of larger concern. By summing up the individual loss factors of the resonances below the cutoff frequency of the beam chamber ($\lesssim$ 6 GHz), a better appreciation of the power dissipation was achieved. A power loss of around 100 W for the vertical kicker is calculated, the horizontal one is only 33 W. The endplates, the feedthroughs and occasionally the ground plate were identified as parts of highest heat load. We plan to perform a finite element analysis to evaluate the temperature rise along the vertical kicker.

SUMMARY

Striplines and kickers at ALBA are presented. The analysis of their designs show that they are properly adapted to the line impedance, and their design fulfills the goals of tune excitation (for the stripline) and feedback damping (for the kickers). A potential concern can be the power loss in the vertical kicker, for which a first countermeasure is being investigated.

ACKNOWLEDGMENTS

We are very grateful for the engineering support from M. Cornelis, suggestions from our Cinel colleagues, and useful comments from M. Dehler and V. Schlott (SLS).

REFERENCES

[1] C. Deibele, S. Kurennoy, "Matching BPM stripline electrodes to cables and electronics", Proc. of PAC'2005. Knoxville (USA), 2005.

[2] C. Mariette, et al., "Excitation stripline for Soleil Fast transverse feedback", Proc. of DIPAC'2007, Venice, 2007.

[3] M. Dehler et al, "Current status of the ELETTRA/SLS transverse multibunch feedback", Proc. of EPAC'00, Vienna (Austria), 2000.

[4] A.W. Chao and M. Tigner (Ed.), "Handbook of Accelerator Physics and Engineering", 2nd printing, 1998. Ch.7.

HIGH RESOLUTION BPMS WITH INTEGRATED GAIN CORRECTION SYSTEM*

M. Wendt#, C. Briegel, N. Eddy, B. Fellenz, E. Gianfelice, P. Prieto, R Rechenmacher, D. Voy,
Fermilab, Batavia, IL 60510, U.S.A.
N. Terunuma, J. Urakawa, KEK, Tsukuba, Japan

Abstract

High resolution *beam position monitors* (BPM) are an essential tool to achieve and reproduce a low vertical beam emittance at the KEK *Accelerator Test Facility* (ATF) damping ring. The ATF *damping ring* (DR) BPMs are currently upgraded with new high resolution read-out electronics. Based on analog and digital down-conversion techniques, the upgrade includes an automatic gain calibration system to correct for slow drift effects and ensure high reproducible beam position readings. The concept and its technical realization, as well as preliminary results of beam studies are presented.

INTRODUCTION

The generation and preservation of low emittance beams is mandatory to achieve a high luminosity in the next generation linear acceleration-based lepton collider for *high energy physics* (HEP). Therefore, the damping and extraction of electron beams with ultra-low vertical emittance of < 2 pm is a mission critical goal [1], and has to be demonstrated at the damping ring of the KEK Accelerator Test Facility (ATF) [2]. This requires various optimization methods to steer the beam along an optimum ("golden") orbit with minimum disturbance of non-linear field effects. A high resolution BPM system is one of the important tools; it needs to meet as initial specifications

- A resolution of ~100-200 nm in a "narrowband" mode.
- A high resolution (some μm) turn-by-turn measurement option.
- An automatic gain correction system, to compensate slow drift effects in the analog part of the read-out electronics – e.g. due to temperature variations, aging effects of components, etc.

The BPM concept was initiated as KEK/SLAC/Fermilab collaboration [3] in frame of the Global Design Initiative (GDE) of the International Linear Collider (ILC) activities. Today this ATF DR BPM upgrade collaboration is backed by Japan-US funds, with Fermilab as core partner.

As proof of principle prototypes and beam studies are performed on 20-of-96 BPM stations with new read-out hardware:

- 714MHz-to-15MHz downmix / calibration module (located in the ATF accelerator tunnel)
- VME-based digital signal processing and timing electronics, currently based on the commercial *Echotek* digital receiver (will be replaced by in-house digitizers).
- Various FPGA-firmware, control and diagnostics drivers and software (C++, VxWorks, Linux) and an EPICS interface to the ATF controls (V-system).

THE ATF DAMPING RING

The 1.2 GeV ATF damping ring is equipped with 96 button-style BPM pickups, and part of the Accelerator Test Facility (ATF) complex, which includes an S-Band electron linac, and an extraction beam-line (ATF2).

Table 1: ATD DR Machine and Beam Parameters

beam energy E	=	1.28 GeV
beam intensity, single bunch	≈	~1.6 nC ≡ 10^{10} e^- (≡ I_{bunch} ≈ 3.46 mA)
beam intensity, multibunch (20)	≈	~22.4 nC ≡ 20 x 0.7 10^{10} e^- (≡ I_{beam} ≈ 48.5 mA)
f_{RF}	=	714 MHz (≡ t_{RF} ≈ 1.4 ns)
f_{rev}	=	f_{RF}/330 ≈ 2.16 MHz (≡ t_{rev} ≈ 462 ns)
bunch spacing t_{bunch}	=	2/ f_{RF} ≈ 2.8 ns
batch spacing	=	t_{rev}/3 = 154 ns
repetition freq. f_{rep}	=	1.56 Hz (≡ t_{rep} = 640 ms)
beam time t_{beam}	=	460.41 ms (≡ 996170 turns)
vert. damping time τ	≈	30 ms
hor. betaron tune (typ.)	≈	15.204 (≡ f_h ≈ 441 kHz)
vert. betaron tune (typ.)	≈	8.462 (≡ f_v ≈ 1 MHz)
synchrotron tune	≈	0.0045 (≡ f_s = 9.7 kHz)

Table 1 lists some relevant machine and beam parameters of the ATF damping ring. In standard operation a single bunch is injected on axes from the S-Band linac. After ~200 ms all injection oscillations are fully damped, and the beam stays for another ~400 ms in the ring, before being extracted. Optional multi-batch / multi-bunch operation can be set up on a cycle-by-cycle basis (no extraction), with up to three equally spaced batches, each containing 1…20 bunches, spaced by 2.8 ns.

* This work supported by a high energy physics research program of Japan-USA cooperation, and by the Fermi National Accelerator laboratory, operated by Fermi Research Alliance LLC, under contract No. DE-AC02-07CH11359 with the US Department of Energy.
#manfred@fnal.gov

THE ATF DR BPM UPGRADE

The currently installed read-out system for the 96 button style BPMs does not meet the requirements in terms of resolution, reproducibility, intensity independence and turn-by-turn measurement capabilities to tune the ATF damping ring to the ultimate low vertical emittance goal of < 2 pm. In the past (2006–2008) several upgrade efforts have been made, testing new read-out electronics on 20 button-style BPMs. Recently (2009) an improved analog downmix unit with integrated calibration system has been investigated at six BPM locations.

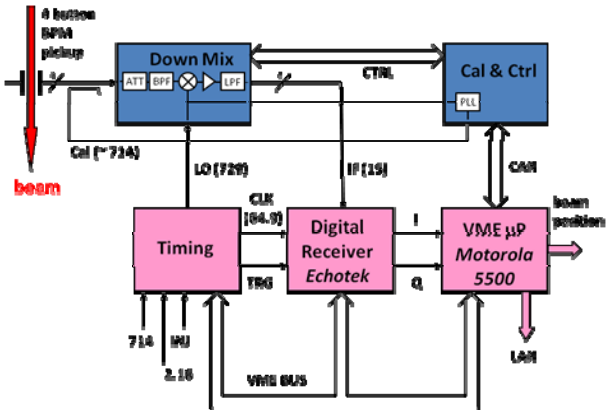


Figure 1: ATF Damping Ring BPM upgrade system.

Figure 1 shows an overview of the upgraded read-out system for a single BPM location. The downmix and calibration units are located inside the accelerator tunnel, converting 714 MHz beam signals from the four button-style BPM electrodes to an IF of 15.145 MHz. The digital receiver (commercial *Echotek* VME-board) and most of the auxiliary hardware (timing, VME processor, CAN-bus controller, power supplies, etc.) are located outside the tunnel.

Button-style BPM Signal Processing

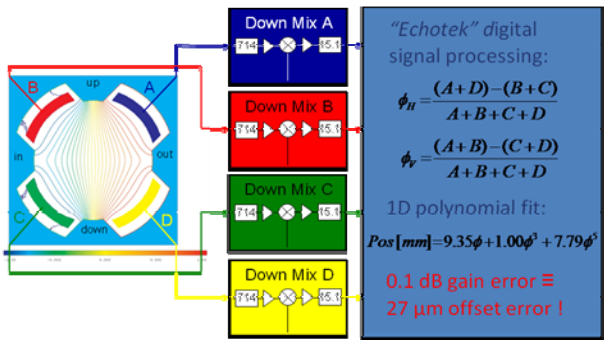


Figure 2: BPM signal processing schema.

The button-style BPM pickup, which is the only unchanged component of the upgrade project, utilizes four "button" electrodes, arranged symmetrically under 45^0 into the vacuum chamber of 24.4 mm diameter. Figure 2 shows the signal processing schema, which is based on a two-step down converting process:

1. Analog: 714 MHz to 15.1 MHz
2. Digital: 15.1 MHz to DC (baseband, I/Q)

The filtered (CIC & FIR) I/Q signals of each electrode are summed in quadrature, and the magnitude results of the A, B, C and D pickup signals are arranged as normalized horizontal or vertical displacement information (Fig. 2). Some of the pickup non-linearities are taken into account by applying a 5^{th} order polynomial to fit the calculated equipotentials.

Analog Downmix and Calibration Unit

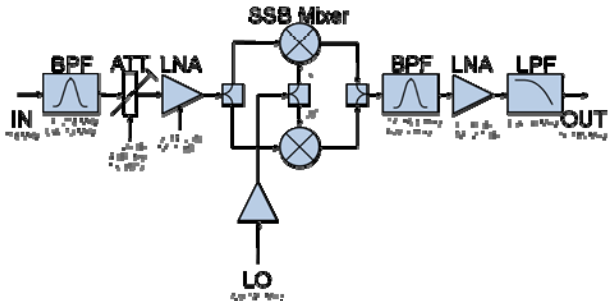


Figure 3: Analog downmixer (1-of-4 channels).

An analog downconverter is required to match the high-pass transfer impedance of the button electrode (0.74 Ω @ 714 MHz) to the pass-band (~40 MHz) of the *Echotek* digital receiver (105 MSPS). Figure 3 shows the simplified block schema of one downmix channel; bandpass filters, gain-stages and attenuators are used for signals conditioning. The 15.1±1.5 MHz IF band-pass defines the signal waveform at the output, which decays within ~400 ns to allow time resolved turn-by-turn measurements (Fig. 4, left). The circuit offers a >90 dB dynamic range, plus 40 dB by gain switching element (Fig. 4, right).

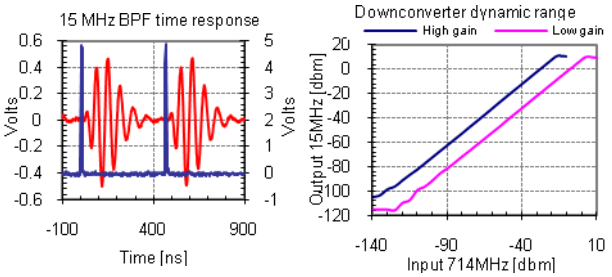


Figure 4: Measured performance of the downmix unit.

A 10 dB directional coupler at the input is used to apply an internally generated calibration signal (Fig. 1), which is used to compensate slow drift effects in the analog signal path, e.g. due to temperature changes or component aging effects. The calibration signal is generated by a fractional PLL from the 729 MHz LO-signal, the frequency is ~400 kHz above/below the 714 MHz beam signal, within the pass-band of the analog processing chain. The simultaneous detection of reflected and transmitted (through the button BPM) calibration signals is performed only in narrowband mode, by utilizing separate down-converters in the digital receiver. For each channel (X: A, B, C or D) a correction term:

$$X_{corr} = \frac{A_{Cal} + B_{Cal} + C_{Cal} + D_{Cal}}{4\,X_{Cal}}$$

is derived from the detected calibration signals, and multiplied to each of the beam signals.

Digital Signal Processing

A commercial 8 channel digital receiver (*Echotek* ECDR-GC814) VME-board, based on 14-bit 105 MSPS *Analog Devices* AD6645 A/D converters, is currently used for the digital signal processing. Each channel is equipped with a 4-channel direct downconverter (DDC) ASIC (GC-4016 *Graychip*), which holds the I/Q mixer, NCO, digital filters (CIC & FIR), and other signals processing elements. Two fundamental operating modes are programmed for the ATF DR BPM signal processing:

- **Wideband (turn-by-turn, TBT) mode**
  5-stage CIC: decimate by 4
  CFIR: 7-tap boxcar, decimate by 2
  PFIR: 1-tap, no decimation
- **Narrowband mode**
  5-stage CIC: decimate by 2746
  CFIR: 21-tap raised cosine, decimate by 2
  PFIR: 64-tap raised cosine, decimate by 2

In case of the narrowband mode, two additional *Graychip* channels, for the detection of reflected and transmitted calibration signals, have to be activated. Their NCO frequencies are tuned to the corresponding calibration frequencies (15.14545 MHz ± 400 kHz). In the final ATF BPM system configuration the *Echotek* digital receiver will be replaced by an equivalent, in-house designed VME digitizer board.

All required reference signals (LO, clock, trigger, etc.) are locked to the 714 MHz damping ring RF, generated by an in-house developed VME timing board (Fig. 1). The 69.24 MSPS clock frequency defines 32 data samples per turn, which are decimated by 8 in wideband, turn-by-turn mode. The given 5-stage CIC filter limits the bandwidth to ~1 MHz. In narrowband mode the decimation is set to 10984, which results in samples spaced by 158 µsec, and a bandwidth of ~500 Hz. All data post-processing and control activities are handled in a VME *Motorola* 5500 processor board, which also controls the local CAN-bus.

PRELIMINARY RESULTS

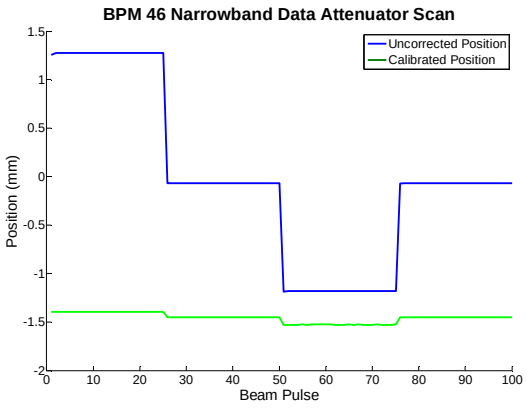


Figure 5: Calibration system test at BPM # 46.

Figure 5 shows a proof-of-principle beam test of the automatic gain correction system. Gain errors in the analog signal processing stages may occur due to temperature drifts or component aging effects, a typical 0.1 dB gain error in one channel corresponds to a 27 µm displacement error (position offset). Introducing an extreme gain error of 4 dB in a single channel, results in a ~1.3 mm offset error in the uncorrected case, which is corrected to <50 µm using the reflected calibration signal.

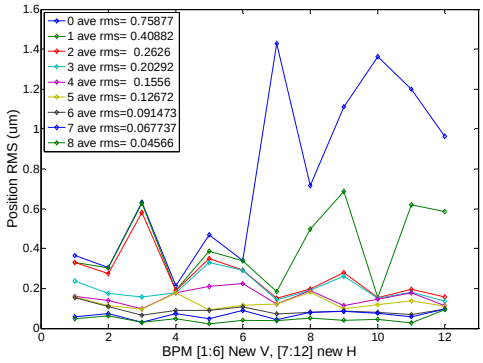


Figure 6: BPM resolution in narrowband mode.

The narrowband mode resolution of the upgraded BPM read-out electronics has been analyzed by taking 1280 consecutive data samples (~200 msec), starting at turn # 400,000, i.e. the beam is fully damped. A 126 tap box-car filter is applied on the data to reject the 50 Hz power ripple, followed by an SVD analysis to decompose the beam motion from the systematic noise of the BPM hardware. As Figure 6 indicates, the resolution seems to be <200 nm, after applying a reasonable cut of the first three modes..

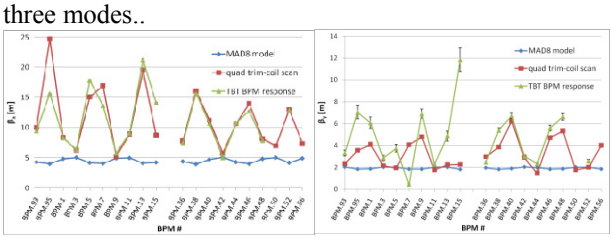


Figure 7: Comparison of measured and theoretical β-functions.

The TBT mode was tested by Fourier analyzing the BPM response (2048 turns) to coherent beam oscillations [4], excited by a kicker. The single pass resolution is found to be <10 µm RMS. Figure 7 compares theoretical and measured (TBT kicked beam and quad scan methods) β-functions at the 20 BPM locations.

REFERENCES

[1] Y. Honda, et.al., Phys. Rev. Lett. 92, 054802 (2004).
[2] J. Urakawa, PAC'97, Vancouver, B.C., Canada, May 1997, pp. 444-448.
[3] P. Prieto, et.al., BIW'08, Lake Tahoe, CA, U.S.A.
[4] J. Borer, C. Bovet, A. Burns, G. Morpurgo, EPAC'92, Berlin, Germany, March 1992, pp.1082-1084.

BPM SYSTEM UPGRADES IN THE PETRA III PRE-ACCELERATOR CHAIN DURING THE 2008 SHUTDOWN

F. Schmidt-Föhre, A. Brenger, G. Kube, R. Neumann, K. Wittenburg
Deutsches Elektronen-Synchrotron DESY, Hamburg, Germany.

Abstract

The new synchrotron light source PETRA III is powered by a chain of pre-accelerators including Linac II, PIA, transfer lines, and DESY II. The whole chain is equipped with upgraded versions of diagnostic systems that were installed during the 2008 shutdown. This paper presents the upgrade of the beam position monitor (BPM) systems at PIA together with the transfer lines and DESY II. All systems rely on the 'Delay Multiplex Single Path Technology' (DMSPT). It is demonstrated that the self-triggered design of the BPM electronics is specifically suited to the different needs of such a heterogeneous pre-accelerator chain. Structures and dependencies of the BPM systems will be described in detail.

INTRODUCTION

With the decision at DESY in 2004, to upgrade the injector storage ring PETRA II to a new high-brilliance 3rd generation synchrotron light source PETRA III, it was also decided to refurbish and upgrade the whole existing pre-accelerator chain during the 2008 shutdown [1]. This upgrade process also included the diagnostics systems in the pre-accelerators. Using different bunch patterns at a design beam current of 100mA, PETRA III will deliver brilliant synchrotron light for up to 14 user undulator beamlines. Minimum bunch spacings of 8ns (optional 4ns) are foreseen with 40ps long bunches in the multi bunch mode consisting of 960 equally spaced bunches (f_{RF} = 499.6645 MHz, $f_{revolution}$ = 130.1 kHz).

To ensure stable top-up operation for PETRA III, the chain of pre-accelerators has to maintain stable conditions for bunch injection including controlled high timing accuracy and reasonably low emittance in the transfer line (E-Weg). This was accomplished by the refurbished and partly renewed pre-accelerator diagnostic systems, in particular using upgraded versions of DMSPT-type button-type BPM systems in most of the sections. This article gives an overview over these upgrades in the individual pre-accelerator sections, which were upgraded specifically taking into account their specific demands.

PREACCELERATOR BPM SYSTEMS

The PETRA injector chain is illustrated in Fig. 1. It consists of five different sections: (i) the injector Linac II (450MeV, 2,998GHz) which is used for positron and electron acceleration, (ii) the Positron Intensity Accumulator ring PIA (10,4 MHz/125 MHz, 450 MeV) which serves for intensity accumulation and re-formation of the linac time structure to match the subsequent synchrotron DESY II, (iii) the intermediate transfer line (L-Weg), (iv) the booster synchrotron Desy II which is used to accelerate single bunches up to a particle energy of 6 GeV, and (v) the transfer line (E-Weg) towards Petra III.

BPM UPGRADE DESIGN GOALS

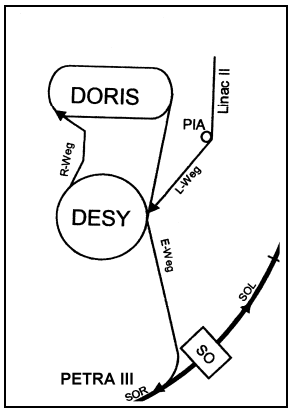


Figure 1: Petra III preaccelerator chain at DESY (Linac II, PIA, L-Weg, DESY II, E-Weg).

Prior to the upgrade in 2008, the DESY II booster synchrotron already used 24 BPM systems, while all other preaccelerator sections were not equipped with BPMs for regular operation before. Therefore an implementation of electrostatic button BPMs at certain accelerator and transport in positions defined by the accelerator optics was desired. The schedule for the upgrade of DESY II contained the refurbishment of the 24 existing button-type BPM chambers, buttons, cabling, and discrete signal conditioning front-end electronics.

In addition, the accumulation in PIA and the energy ramping in DESY II put high demands on the dynamic measuring range of the associated BPM systems. Before the upgrade, the existing BPM system of DESY II was designed to measure the maximum BPM signal level in the upper ADC count range with fixed input signal attenuation. Therefore low level input signals could not be measured. The upgraded BPM electronic system is intended to be able to cope with the high dynamic BPM signal ranges, enabling measurements in the full dynamic range of the BPM input signal.

For control of the injection process, the accumulation and energy ramping procedures in the circular accelerators, other types of measurements called '1st-turn' and 'turn-by-turn' were desired. Those kind of measurements store the BPM button signal information at each of the BPMs for a certain number of individual turns, delivering a turn-by-turn beam position history when reading the turn buffers of the BPM electronics. This operation mode can also be used for tune measurements.

IMPLEMENTATION

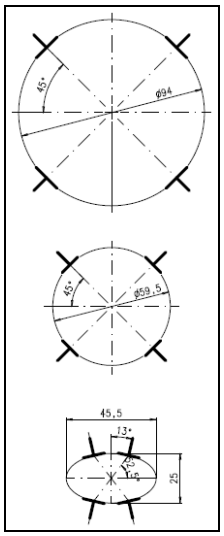


Figure 2: Vacuum chamber cross sections for the new BPMs.

Tree types of new BPM vacuum chambers were installed at PIA (1 monitor chamber), L-Weg (5 + 8), and E-Weg (8). They have different cross sections depending on the vacuum chamber cross section at the corresponding BPM position (Fig. 2).

5 new BPMs were installed in the transfer line between LINAC II and PIA,. The corresponding electronics use resonant signal detection schemes due to the special beam properties (2,998 GHz prebunched, quasi-continuous beam) of the LINAC II and are covered by another article [2].

The remaining BPM systems in PIA and the following pre-accelerator sections use BPM detector electronics of the DMSPT type for data acquisition as shown in Fig. 3.

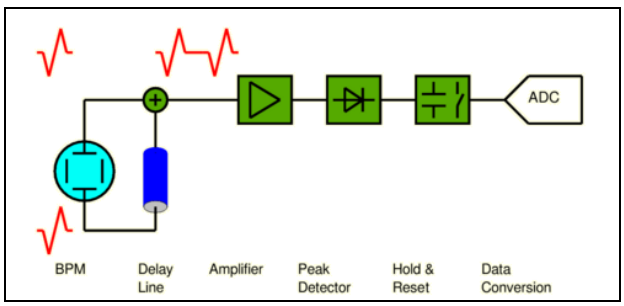


Figure 3: delay-multiplex single path technology (DMSPT) BPM signal acquisition principle [3].

This technology, originally developed in 1986 for the HERA accelerator (R. Neumann, DESY), chains all four button pickup signals on one analog processing channel by use of a delayline-combiner network, delivering individual electrode signal data. The use of only one single processing channel equalizes most dominant channel parameters (attenuation, frequency and phase response, inherent and induced noise). This reduces signal processing differences only to the well-adjusted passive delayline-combiner-cabling network (located in the vicinity of the pickups) and to the system-inherent stochastic ADC phase- and amplitude jitter. Thus, the pulse-chaining principle results in high accuracy, low drifts, and a high common-mode-rejection (CMRR). The BPM pickup signal acquisition stage uses a simple self-triggered diode clipping peak-hold detector to sample the low pass filtered peak-held signal by an 8-bit Flash-ADC. An auto-reset of the charge-memory after the ADC sampling completes the self-trigger process, eliminating typical external jitter problems. Together with the ADC the analog front-end module holds the acquisition logic for compilation of all of the 4 sampled peak BPM input signal values into a stream of two clocked output data words.

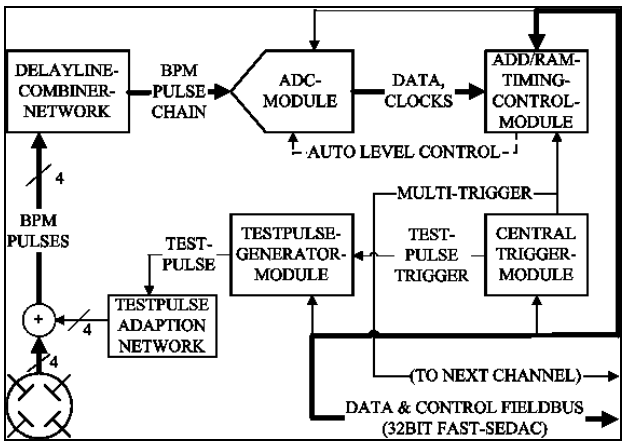


Figure 4: modular BPM single channel system setup.

In the following step, the sampled button signal data are processed in an ADD/RAM timing-control module as shown in Fig. 4 (main signal acquisition path is marked by bold lines). This module incorporates an FPGA logic with enhanced averaging-adder functionality (up to 128 stages) and state processing circuitry for timing and memory storage (e.g. RAM mode for PIA and DESY). In addition, the design variants for PIA and DESY storage rings contain the digital ALC loop controller for increased dynamic input signal acquisition capability.

The ADD/RAM timing-control module receives a serial revolution-clock-synchronized, so called multi trigger signal that carries encoded injection- and ejection-time-frame information. This information is delivered by a centralized trigger module that utilizes the central timing information of the accelerator section for arming of the BPMs.

As a special feature, for increased reliability and reduced repair time (MTTR) for the whole accelerator chain, front-end test pulse generation was added for all BPM channels in all pre-accelerator sections except Linac II, enabling online testability throughout the whole measuring chain. All BPM modules mentioned above use an upgraded version (Fast, 32bit) of the DESY in-house SEDAC fieldbus for data, status and control communication.

The upgraded BPM electronics at PIA and DESY offer '1st-turn' and 'turn-by-turn' measurement features by the so called ‘RAM mode’, as well as facilitating single-pass measurements in the so-called ‘live mode’. They also contain a fast, hardware-controlled automatic-input level control logic (ALC, implemented by a digital input attenuator control loop), to enable correct ADC dynamic range levelling over nearly the whole BPM input signal level range (typ. factor 50 at PIA - where the lowest two accumulation steps cannot be measured due to sub-

threshold suppression) and to prevent overload of the detectors [2]. For configuration purposes, the acquisition starting point (DESY II segment, PIA accumulation cycle and turn number) for live and RAM mode and the number of acquisition windows and window length can (RAM mode only) can be selected. Channel configuration is completed by the number of turns used for averaging and the input level damping mode (automatic or manual, enabling selectable damping values).

The upgraded BPM systems in the transport lines measure the position of single bunches passing by in live mode only, armed by the ejection triggers of the preceding accelerator stages (PIA, DESY II). First tests in this mode show, that the required resolution of < 300µm (RMS) for a single bunch of 10^{10} particles at certain BPM positions in the E-Weg is fulfilled (e. g. E-Weg BPM at 178m provides a theoretical resolution of < 300µm driven by an input signal intensity of 7% of full scale – detailed measurements are currently under investigation) .

In addition to the BPM hardware upgrade, the whole control system software was renewed and upgraded to provide a PETRA III compatible control system environment (TINE/CDI, Java). All upgraded BPM control system software is designed using modular server/client architecture. It ensures hardware timing-related readout of BPM button signal and status data from the ADD/RAM modules via the SEDAC fieldbus with the required 6,25 Hz update rate, an example of which is shown in the BPM client application snap-shot example in Fig. 6. After attenuation-correction of the delayline-combiner-netzwork, position calculation from the individual button signals is accomplished by software



Figure 5: typical modular BPM system crate example (4 BPM channels).

using the well-known Δ/Σ equation [4]. Generation and import of reference files can be used for orbit difference evaluation, whereas periodic logging of BPM position and status data into common control system archives serves as a commonly used data backup that can be viewed and analyzed offline using available control system archive analysis tools.

CONCLUSION AND OUTLOOK

The comprehensive and specific upgrades of all preaccelerator sections were discussed. The usage of a small number of different BPM chamber types for all sections in combination with a commonly established and upgraded BPM electronics system design is successfully adapted to the specific needs of the related pre-accelerator sections. It was demonstrated that the BPM electronics system upgrade enhancements (ALC, RAM mode) fulfil the section-specific requirements of the pre-accelerators, and facilitate a stable and reliable operation for PETRA III. Integration of the RAM mode of the BPM electronics into the control system software is planned for second half-year of 2009.

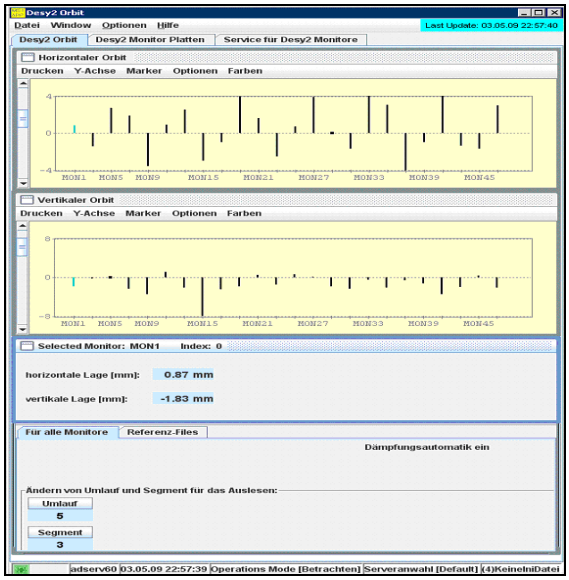


Figure 6: BPM application program example (client).

ACKNOWLEDGEMENTS

We acknowledge M. Hüning and J. Maidment for their comprehensive support [5]. We also thank T. Traber for fruitful discussions and J. Neugebauer for his substantial support during systems installation and testing.

REFERENCES

[1] Technical Design Report “PETRA III: A low Emittance Synchrotron Radiation Source”, Editors K. Balewski et al., DESY 2004-035.

[2] M. Hüning et. al., “A resonant first turn BPM for the position intensity accumulator (PIA) at DESY”, MOPD14, these proceedings.

[3] T. Traber and R. Neumann, “Simulation of BPM Electronics at DESY”, CARE-Meeting, Lüneburg, March 2007, p. 14 (2007).

[4] K. Wittenburg et al., ”PETRA III Beam Position Monitor Electronic: Requirements and technical Specifications; Tendering and Contract Management”; Version 1.92 (2007).

[5] M. Hüning and J. Maidment, private communication.

SNS BEAM DIAGNOSTICS: PRESENT STATUS AND FUTURE PLANS

A. Aleksandrov, Oak Ridge National Laboratory, Oak Ridge, TN 37830, USA

Abstract

The Spallation Neutron Source accelerator systems will deliver a 1.0 GeV, 1.4 MW proton beam to a liquid mercury target for neutron scattering research. The accelerator complex consists of an H- injector, capable of producing one-ms-long pulses at 60 Hz repetition rate with 38 mA peak current, a 1 GeV linear accelerator, an accumulator ring and associated transport lines. The accelerator systems are equipped with variety of beam diagnostics. The beam diagnostics played important role during beam commissioning, they are used for accelerator tuning and monitoring beam status during production runs. The requirements to the various diagnostics systems are changing in the process of beam power ramp up. This talk will give an overview of the evolution of the major SNS beam diagnostics systems: commissioning, operation, power ramp up, and power upgrade.

INTRODUCTION

The SNS accelerator complex consist of an H^- injector, capable of producing one-ms-long pulses with 38 mA peak current, chopped with a 68% beam-on duty factor and a repetition rate of 60 Hz to produce 1.6 mA average current, an 87 MeV Drift Tube Linac (DTL), a 186 MeV Coupled Cavity Linac (CCL), a 1 GeV Super Conducting Linac (SCL), a 1 GeV Accumulator Ring (AR), and associated transport lines. After completion of the initial beam commissioning at a power level lower than the nominal, the SNS accelerator complex is gradually increasing the operating power with the goal of achieving the design parameters in 2009. Results of the initial commissioning and operation experience can be found in [1]. The SNS Power Upgrade Project (PUP) [2] aims at doubling the beam power by increasing SCL and AR beam energy to 1.3 GeV and peak current in the linac to 59 mA. The SNS baseline design included diverse suite of beam diagnostics [3], which, in main part, were brought on line simultaneously with other accelerator systems and played crucial role in fast and successful SNS commissioning and power ramp up. As the SNS operation is shifting more and more toward neutron production for users the roles and requirements for the beam diagnostics are changing as well. This paper describes the status and development plans for the major beam instrumentation systems.

BEAM INSTRUMENTATION ROLES

The beam time in the SNS operational schedule is divided in free parts: neutron production, machine tune up for production, and machine study periods.

Neutron Production Period

The neutron production period currently takes 80% of the scheduled beam time and this fraction is increasing steadily. The most important performance metric during this period is beam availability. Therefore only systems directly involved in beam delivery are of high importance. Beam instrumentation systems triggering the Machine Protection System (MPS) fall in this category. These include the Beam Loss Monitors (BLMs), distributed along the accelerator, the beam-in-gap detector (CHUMPS) in the Medium Energy Beam Transport (MEBT) line responsible for detection of the MEBT chopper failure, the Differential Beam Current Monitor (DBCM) protecting the MEBT chopper target, the beam dump current detectors (NCDs) protecting beam dumps from excessive power, and the beam current on target monitor (BCM25) monitoring beam power delivered to the neutron target. These systems have to operate at the beam rate up to 60 Hz and if any one fails the beam in the machine is inhibited.

Machine Tune Up Period

The machine tune up period is required after each maintenances period and currently takes about 10% of the scheduled beam time. If any one or even several systems fail operation is still possible. The most important performance metric during this period is accuracy of data, easy of use (user friendliness), and speed. Operators should be able to perform tune up as quickly as possible with as little support from diagnostics experts as possible. The main systems for machine tune up are the Beam Position and Phase Monitors (BPMs) and the Wire Scanners (WSs). These systems have to operate at a reduced pulse rate of 1-2 Hz. The BLMs are also used for the fine tuning of the losses.

Machine Study Period

About 10% of the scheduled beam time is dedicated for the machine study. All available diagnostics could be used during this period. If any one or even several systems fail operation is still possible. The most important performance metric during this period is accuracy of data. Physicists usually do measurements often with help from diagnostics experts. Some of the diagnostics systems for machine study can be of experimental nature or in prototype stage of development. Beam halo and transverse profile measurements in the ring are examples of such systems. These systems are required to operate at a reduced pulse rate of 1-2 Hz.

SNS BEAM DIAGNOSTICS

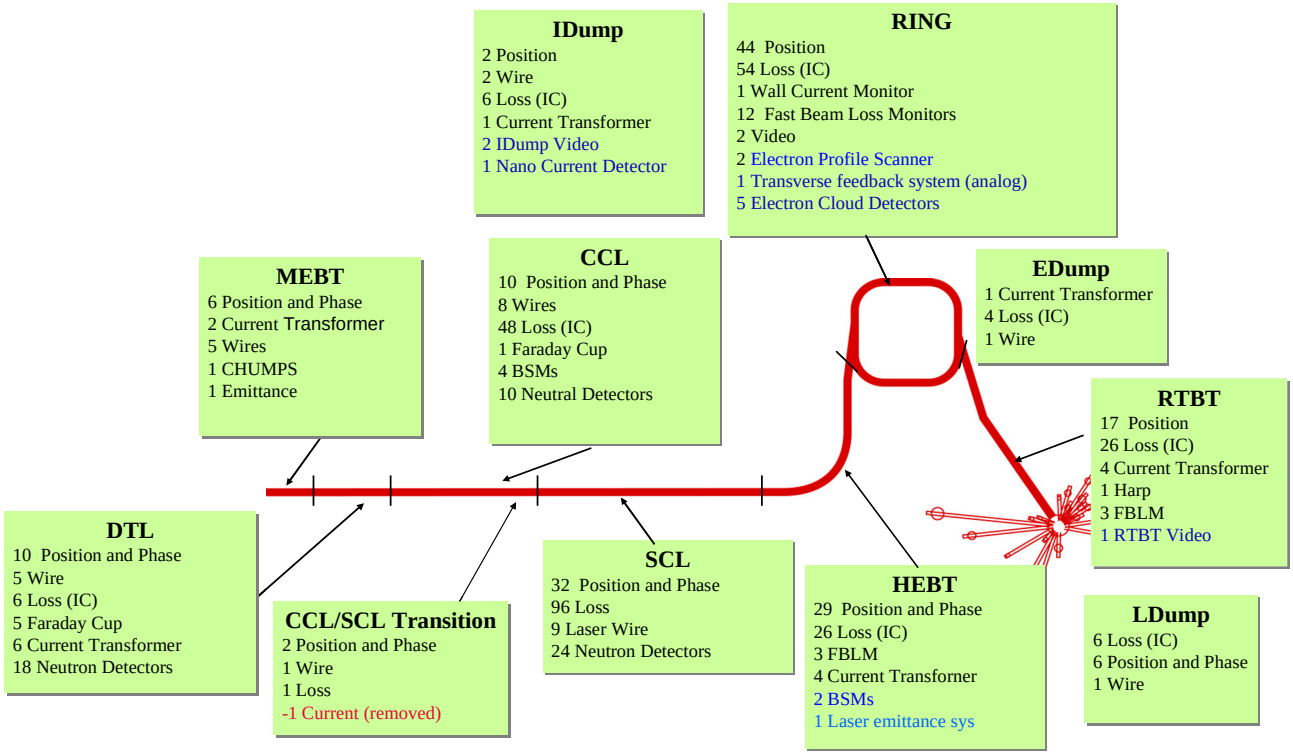


Figure 1: SNS Beam Diagnostics.

Beam Loss Monitors

The SNS BLM system consists of 362 radiation detectors measuring secondary radiation due to beam loss. BLMs are used as MPS device to shutdown the beam if the integral loss is above threshold. SNS uses ionization chambers (IC) as its main BLM device. This is due to their simple design and immunity to radiation damage. In addition to ICs we use several type of PMT based detectors. The data acquisition system is VME based. The BLM system has been quite reliable and caused less than 10 hours of beam down time during last year. To further improve reliability we are developing new front-end electronics with independent hot swappable modules with individual high voltage power supplies in each module.

Beam Position and Phase Monitors

Beam phase measurements are the main tool for linac tune up. Position measurements are used for trajectory correction in the linac, ring injection set up and centering beam on dumps and target. BPM system utilizes strip line pick up electrodes in all parts of the accelerating complex. Narrow band RF front-end electronics is used in the linac and the HEBT, base band front-end electronics is used in the ring and the RTBT. All BPM systems use PCI digital interface. In the near term we plan to add more BPMs in the transfer lines and upgrade timing system. In longer term we plan to redesign the data acquisition electronics to mitigate part obsolescence and PC compatibility problems.

Transverse Beam Profile Measurements

Conventional stepping wire scanners are used for measuring transverse beam profile in the normal conducting linac and beam transport lines. The wire scanners deliver reliable profiles with dynamic range of about 100, which is sufficient for the beam core matching bunt not sufficient for beam halo and loss study. We are investigating possibilities to increase the dynamic range to 10^3 - 10^4 by upgrading the front-end electronics and/or by modifying the wire scanner design.

A laser based transverse profile measuring system, or Laser Wire (LW) is used in the SCL. The LW delivers reliable data on a quite day but often suffers from laser beam position jitter due to environmental noise. A typical variation of the laser beam position during a day is shown in Fig. 2. We have identified the main sources of the vibrations and will implement mitigation measures during the next shutdown. The LW has a capability of measuring profiles with high time resolution allowing observing beam size variation within a single mini-pulse as shown in Fig. 3.

There was no base line diagnostics for measuring beam profile in the SNS ring. We installed and successfully tested a prototype of non-perturbing Electron Beam Profile Monitor EBPM [4]. The EBPM has a capability of

measuring profiles with high time resolution allowing observing beam size variation within a single turn in the ring mini-pulse as shown in Fig. 3. An ionization profile monitor is under development as an alternative device of measuring transverse beam size in the ring.

A conventional slit/grid device is used for measuring transverse phase space footprint of the beam in the Medium Energy Beam Transport (MEBT) line. Its performance has been improving steadily.

A non-perturbing laser wire based transverse emittance measuring station will be installed in the High Energy Beam Transport line by the end of 2009 [5].

Measuring the beam halo is considered to be important for increasing beam power and reducing beam loss. There is no a dedicated beam halo measuring device at the moment. We developed a current measuring system for HEBT scrapers capable of measuring an intercepted beam charge down to 10^{-5} level. This system can be used for transverse halo evaluation or can become a basis for a dedicated halo monitor.

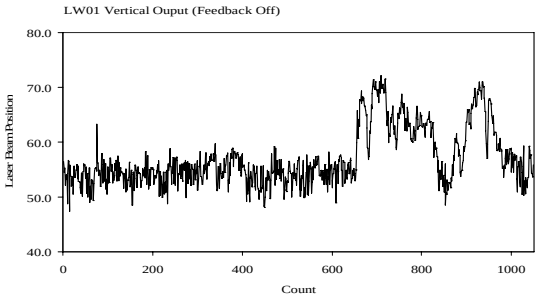


Figure 2: Laser beam position (arbitrary units) vs. time (1 sec/count) in the SNS Laser Wire system.

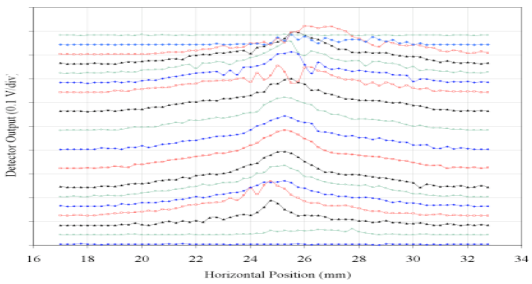


Figure 3: Transverse beam profile in the SCL measured with 20 nsec steps within a single mini-pulse.

Longitudinal Beam Profile Measurements

There are two types of diagnostics in use for longitudinal bunch profile measurements. A Laser Bunch Shape Monitor (LBSM) is installed in the MEBT, four Bunch Shape Monitors (BSMs) are installed in the CCL, and two BSMs are installed in the HEBT [6]. These measurements proved to be useful for linac set up, troubleshooting and machine study. The BSMs have very large dynamics range up to 10^4-10^5 as illustrated by a typical bunch profile measurement shown in Fig. 4 and Fig. 5

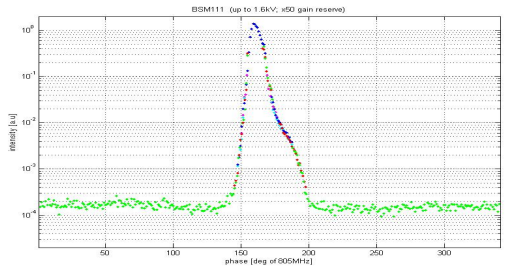


Figure 4: Longitudinal bunch profile measured in CCL.

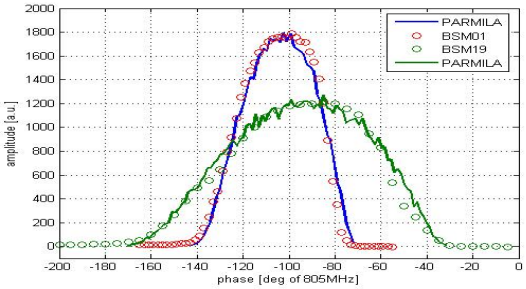


Figure 5: Longitudinal beam profiles measured in the HEBT compared to simulation.

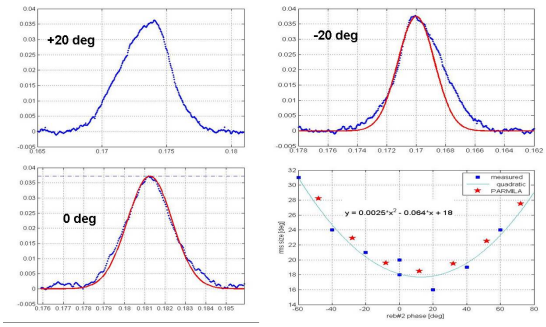


Figure 6: Bunch profile measurements in the SNS MEBT. Plots on top are for the buncher phase shifted from the nominal set point. Bottom left is for the nominal buncher setting. Bottom right is comparison of RMS bunch width vs. buncher phase dependence with the PARMILA simulation.

ACKNOWLEDGEMENT

ORNL/SNS is managed by UT-Battelle, LLC, for the U.S. Department of Energy under contract DE-AC05-00OR22725.

REFERENCES

[1] S. Henderson, Proc. EPAC 2008, p.2892.
[2] S. Henderson et al., Proc. EPAC 2006, p. 345.
[3] T. Shea, Proc. DIPAC 2005, p. 6.
[4] A. Aleksandrov et al., these proceedings .
[5] J. Dong-o et al., Proc. PAC 2009.
[6] A. Aleksandrov et al., Proc. PAC 2007, p. 2608.

EMITTANCE MEASUREMENT DEVICES IN THE MUON IONIZATION COOLING EXPERIMENT

P. Kyberd, School of Engineering and Design,Brunel University,UK (for the MICE Collaboration)

Abstract

The Muon Ionisation Cooling Experiment (MICE) at the ISIS[1] accelerator located at the Rutherford Appleton Laboratory will be the first experiment to study muon cooling with high precision. The proposed operation of the experiment is described, and performance measurements on the crucial detector components are presented.

THE MICE EXPERIMENT

Introduction

The MICE experiment is designed to measure the performance of a cooling channel based on the design from Study II for a Neutrino Factory[2].

In this design the muon beam is passed through a series of absorbers of low atomic number to reduce the muon energy, each absorber followed by a set of RF cavities working at 201.25 MHz which accelerate the beam to the original energy. In MICE a small part of this cooling channel will be tested by measuring precisely the momentum and position of each muon as it enters and leaves the channel. From these measurements an input beam of given emittance can be synthesised[3] and the emittance of the resulting output beam measured. The results will allow a reliable prediction of the performance of the full channel. A set of plates of variing thickness (diffuser) placed just before the first emittance measurement is used to vary the incoming beam characteristics and allow a wider range of input beams to be synthesised.

The experiment runs parasitically in ISIS, by dipping a titanium target into the beam. The structure of the ISIS beam imposes constraints on the operation of the MICE target and beamline. ISIS runs at 50Hz and during each cycle a few$\times 10^{13}$ protons are injected into the ring and accelerated over the following 10ms to 800 Mev. If the titanium target enters the beam too early very few pions are produced and the beam is severely disrupted by energy loss and multiple scattering; thus the target can only intersect the beam during the last one to two milliseconds. The target is only dipped once per second, to minimise the disruption to other ISIS users. The required event rate of 600 muons per second then requires a readout and detector system capable of operating at MHz. We must be able to determine the phase of the RF in the cavities as the muons pass through the cavities, which requires sub nanosecond timing.

Overview

A schematic of the MICE beam and cooling channel is shown in Figure 1. The interactions of the protons with the target produce a spray of pions. The pions at 25° are focussed by a triplet and then bent to enter a superconducting solenoid which projects through the wall of the machine hall. Muons produced by pion decay in the solenoid are captured by the field and enter the MICE hall, where they are bent, focussed by two additional triplets and then enter the MICE cooling channel. Two Cerenkov counters, used for particle identification, are placed before the channel; a scintillator based timing system is placed before and after the channel and used as part of the particle identification system and for the timing with respect to the RF phase. Finally a ranger is used to confirm the identity of particles which traverse the full channel.

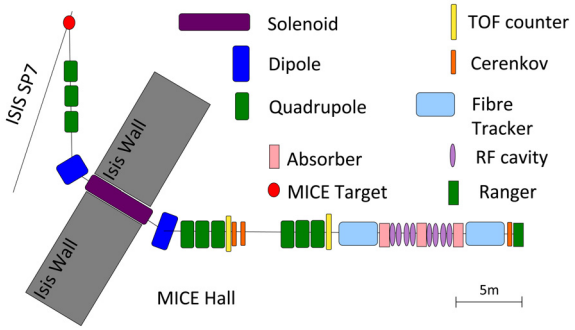


Figure 1: Schematic of MICE beam and cooling channel.

Muon Production

Once per second the MICE target is dipped into the beam. It was a titanium blade of length 35 mm which presents a target 1 mm wide and 10 mm deep. Simulations[4] show that 1.4×10^{12} protons must intercept the target in order to generate a flux of 600 *good* muons per target dip. (*Good* muons refer to those which are captured by the MICE beam line and traverse the whole cooling channel). Studies in 2006 allowed us to measure the external diameter of the beam and show that the target was capable of intercepting the beam during the last two milliseconds of the cycle and still clear the beam envelope before the next pulse. The number of muons produced can be varied by adjusting either the timing of the start signal or the depth of travel.[5]

Pions produced and captured by the upstream magnets are bent through a hole in the ISIS vault where they enter an eight metre superconducting solenoid with a field of five Tesla. The pions decay into muons which are captured by the field and emerge to be bent and foccused into the MICE experiment.

Superconducting Spectrometer

The measurement of beam cooling, relies on the accurate determination of particle position and momentum both before and after the cooling channel. To make this measurement MICE have built a pair of identical spectrometers. To make an accurate measurement of both position and momentum without disturbing the trajectory of the muons, MICE needs a system with low mass, high efficiency and good resolution. This is provided by scintillating fibre detectors sitting, radius 30 cm, in a four Tesla superconducting magnet whose field is uniform to the level of 3 parts per mil. The tracker is read out by visible light photon counters (VLPCs)[6, 7] held at 9K, using the D0 central fibre tracker read-out and electronics system[8]. The tracker consists of five stations, each one consists of three doublet layers at 120° to each other to provide a space point (Figure 2a). They are held in a carbon fibre space frame with an overall length of 110cm. In order to measure position without disturbing the muon trajectory thin fibres must be used (350 microns in diameter). Such fibres produce very little light and so visible light photon counters are used. The VLPC combination of very high efficiency with low background allow good track measurement even with these slender fibres. The fibres are laid up in doublet layers Figure 2b to ensure complete coverage. The position resolution achievable in such a setup is actually better than that required for the measurements and since the most expensive part of the the system is the readout system, the individual fibres are bundled together in groups of seven (as shown in the Figure 2b and each bundle feeds one channel. Increasing the size of the fibres would ease the construction of the detectors, but the resulting fibre thickness leads to unacceptable multiple scattering.

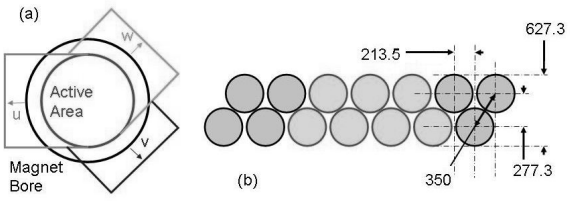


Figure 2: a) Three views per station. (b) Doublet layer shaded fibres bundled to form one channel (all distances in microns).

Five modules were then mounted onto a carbon fibre frame and their positions accurately measured using a coordinate measuring machine to produce a tracker. The tracker was then placed inside a black carbon fibre cylinder and supported on an aluminium space frame with the beam axis pointing vertically upward. A cosmic ray telescope was created using a trigger scintillator just above the tracker and a four inch layer of lead blocks followed by a second trigger scintillator. The lead ensured that the system only triggered on muons of momentum 130 MeV/c or greater. Data was taken using this arrangement between July 2008 and November 2008. The second tracker has since been completed and testing has just restarted on both trackers.

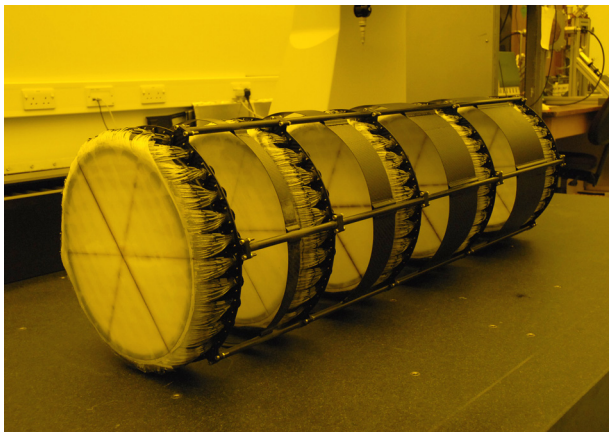


Figure 3: Completed tracker.

Results from the first tracker were analysed by: creating clusters from one or two neighbouring channels in each view and clusters with greater than two photo-electrons are kept. Space points are defined as a cluster in each view from a given station, where the distance between two pairwise intersections is small enough. Any remaining clusters are used to create space points. Sets of three space points from distinct stations are tested for collinearity; the tracks of those that pass are extrapolated to the other two stations and the closest space point to the extrapolated track is taken as part of that track as long as it lies inside a small road around the extrapolation. Finally each set of 3, 4 or 5 points is passed to the Kalman filter track fit [10] and the combination with the smallest χ^2 per degree of freedom is kept. The points thus used are removed from consideration and the process repeated until all the space points have been removed or no more tracks are found. From these tracks the light yield and the resolution of the tracker can be determined. Figure 4 shows the mean light yield is eleven photo-electrons. The yield of individual layers varies from 8.6 to 11.2 p.e. Figure 5 shows the diffference between the extrapolated track and the hit position in x, y is similar. The values of 583 microns in X and 597 microns in Y and consistent with the design goal of 470 microns, once the extrapolation errors are taken into account.

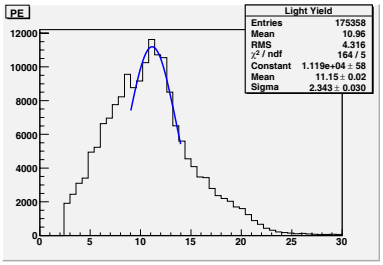


Figure 4: Light yield Histogram : all channels tracker 1.

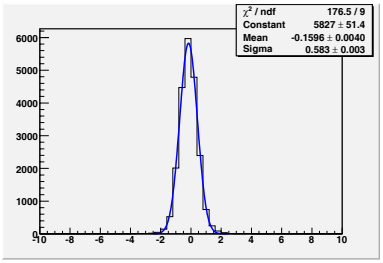


Figure 5: Residuals.

TOF Counters

A TOF detector is made of two layers of scintillator slabs. The first layer has vertical slabs and the second has horizontal slabs. Each slab is equipped with two PMTs, one at each end and each feeding a TDC to measure the absolute time of the hits. The system has a very fast and precise response time but corrections still need to be applied to obtain our design resolutions. First light propagation down the scintillator: this can be estimated both by the time difference between the two PMTs which define a single hit; and by the position measured in the orthogonal view in events with only a single hit in each view. Next because a leading edge discriminator is used the time at which the discriminator registers a hit is dependent on the size of the pulse *(time walk)*. Finally the propagation time down the readout cables has a dispersion which must be removed by measurement. During running in December 2009[11] a small amount of data was taken, concentrated in the area in the centre of the counters and which allowed the calibration of 9 *pixels* in TOF0 and 2 *pixels* in TOF1. The corrected time of flight distributions (Figure 6) shows a clean separation between pions and muons and approaches the design resolution.

Future Work

The second tracker is currently being measured using cosmic rays. Runs later in 2009, with the decay solenoid powered will allow a complete calibration of the TOF system and the measurements on the emittance of the input beam will commence towards the end of the year.

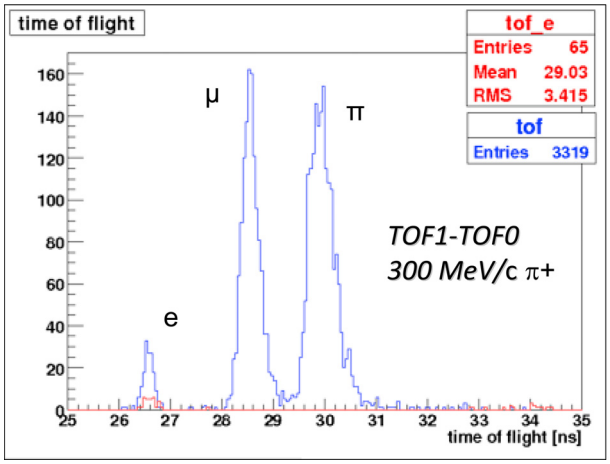


Figure 6: Time of Flight between the TOF counters for a *positron* (red) and *pion* (blue) beam.

REFERENCES

[1] Findlay, DJS, ISIS: Pulsed neutron and muon source, Prepared for Particle Accelerator Conference (PAC 07), Albuquerque, New Mexico, 25-29 Jun 2007 http://www.isis.rl.ac.uk

[2] Feasibility Study-II of a Muon-Based Neutrino Source, eds. S. Ozaki, R. Palmer, M. Zisman, and J. Gallardo, BNL-52623 (2001) www.cap.bnl.gov/mumu/studyii/FS2-report.html

[3] Statistical weighting of the MICE Beam. C.T. Rogers EPAC'08, 11th European Particle Accelerator Conference, 23-27 June 2008, Genoa, Italy

[4] T. Roberts. MICE beamline analysis TRD Sept 2004. Presented to MICE Collaboration Meeting, 10th Feb 2005. www.mice.iit.edu/cm/cm11/cm11_roberts_g4beamline.ppt

[5] Paul Smith. The Development of the Target Mechanism for the Muon Ionisation Cooling Experiment (MICE) Thesis Sheffield University 2008

[6] M. Petroff and M. Stapelbroek, Photon-Counting Solid-State Photomultiplier, IEEE TRANSACTIONS ON NUCLEAR SCIENCE 36 (FEB, 1989) 158162.

[7] M. Petroff and M. Atac, High-Energy Particle Tracking using Scintillation Fibers and Solid-State Photomultipliers, IEEE TRANSACTIONS ON NUCLEAR SCIENCE 36 (FEB, 1989) 163164.

[8] D0 Collaboration, V. M. Abazov et al., The Upgraded D0 Detector, Nucl. Instrum. Meth. A565 (2006) 463537, physics/0507191.

[9] MICE technical reference document, 2004. http://www.isis.rl.ac.uk/accelerator/MICE/TR/MICE_Tech_ref.html

[10] A. Cervera-Villanueva, J. J. Gomez-Cadenas, and J. A. Hernando, RecPack a reconstruction toolkit, Nucl. Instrum. Meth. A534 (2004) 180183.

[11] Karadzhov Y., Bonesini M., Graulich J.S., Tsenov, R. TOF Detectors Time Calibration http://mice.iit.edu/mnp/MICE0251.pdf

AN OVERVIEW OF THE PROPOSED BEAM DIAGNOSTIC FOR ASTRID2

J.S. Nielsen#, N. Hertel, S.P. Møller
ISA, Aarhus University, Ny Munkegade 120, 8000 Aarhus C, Denmark.

Abstract

This paper presents an overview of the proposed beam diagnostics for ASTRID2, the new 580 MeV 3rd generation low-emittance synchrotron light source to be built in Aarhus, Denmark. ASTRID2 will use the present ASTRID1 as booster, permitting full energy injection and thereby top-up-operation. The diagnostics will include viewing screens, beam current monitors, electronic beam position monitors, striplines, etc. The description includes both the storage ring and the transfer beam line.

INTRODUCTION

There has been a tremendous development of synchrotron radiation sources over the last two decades since ASTRID1 [1-3] was built. The biggest quantum leap possible came with the introduction of undulators, whereby the photon rate on a target increased by many orders of magnitude. ASTRID1 was not original equipped with insertion devices, although one undulator has been retrofitted. Therefore we have wanted to build a modern machine in Aarhus for several years. This has now become possible through a grant from the Danish government.

Table 1: Main parameters of the ASTRID2 storage ring compared to ASTRID1

	ASTRID2	ASTRID1
Energy [MeV]	580	580
Circumference [m]	45.704	40.00
Current [mA]	200	200
Revolution time [ns]	152.45	133.40
Length of straight sections [m]	2.7	
Number of straight sections	4	1
Horizontal tune	5.23	2.22
Vertical tune	2.23	2.63
Natural emittance [nm]	13	140

The main parameters of the ASTRID2 storage ring are shown in Table 1, together with the corresponding parameters for ASTRID1 as comparison. The major differences are the emittance, which is about ten times smaller for ASTRID2, and the number and length of straight sections. ASTRID2 will allow for 4 insertion devices, as opposed to ASTRID1's single.

The other marked difference is that ASTRID2 will have full-energy injection, and hence top-up operation will be employed. This will in many ways make the machine much more stable. The current will be stable, which means that the Synchrotron Radiation (SR) intensity will be constant. And since the heat load will also be constant, it will be much easier to keep the beam parameters stable, such as the beam positions.

TRANSFER BEAM LINE

The primary purpose of the beam diagnostic in the transfer beam line is to facilitate easy steering of the beam through the beam line, with good transfer efficiency. Since ASTRID1 has not been designed as a rapid cycling booster, the injection rate will be slow (≤0.1 Hz). It is therefore even more essential to have the proper diagnostic and tools to help steering the beam from ASTRID1 to ASTRID2.

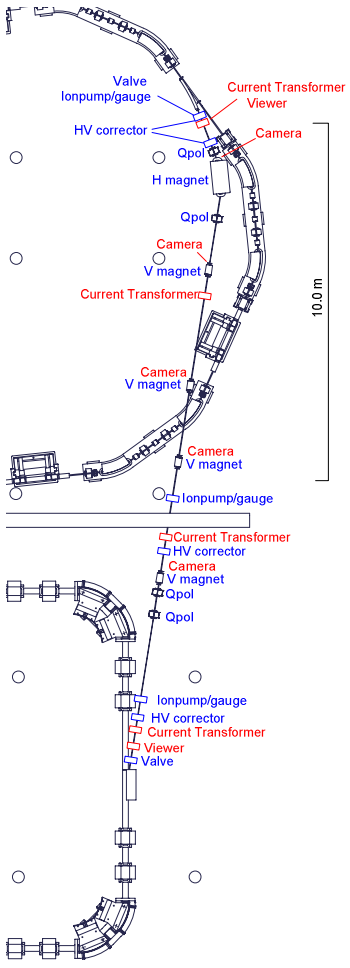


Figure 1: Layout of the transfer beam line from ASTRID1 to ASTRID2.

#jsn@phys.au.dk

To verify proper extraction from ASTRID1 we will soon after the Astrid extraction septum install a **viewing screen**. This will either be of the optical transition radiation type, or a fluorescent screen. The fluorescent screens have a higher sensitivity, but can have problems with saturation (and thereby problems with proper representation of the beam) at higher intensities. At the end of the beam line another viewing screen will be used to centre the beam at the ASTRID2 injection septum channel, and to verify that be beam has not been cut. Using quadrupole scans this viewing screen can also be used to measure the emittance of the extracted beam, and to verify the optical properties of the beam and the transfer beam line.

Since the transfer beam line has to cross the ASTRID2 storage ring, there will be 4 vertical magnets to bring the beam above the ASTRID2 ring. After each of these magnets and after the 30° horizontal magnet we will install cameras to monitor the emitted **Synchrotron Radiation**. This SR light can be used to monitor the beam properties (primarily the position).

To quantity the transfer efficiency a number of **current transformers** will be installed along the beam line. To keep cost down, these will probably be homemade, consisting of a ferrite ring with a small coil mounted in a flange.

Automatic Beam Steering

With the low injection rate, the initial commissioning of the transfer beam line will be somewhat time consuming if done manually. We therefore plan to implement an Automatic Beam Steering (ABS) system to assist commissioning and the daily operation of the transfer beam line. The ABS will take beam positions from the two viewers (beam destructive) and the 5 SR cameras located after the 5 bending magnets (4 vertical and 1 horizontal), and use these positions to calculate new corrector settings.

In the initial phase the system will just sequentially centre the beam on each camera/viewer using the nearest upstream corrector. In phase 2, when the beam has been threaded to the end, the system should measure the response matrix. This will allow position correction to be performed in all of the transfer line in one go. In the third phase the beam will be centred in the quadrupoles, using the quadrupole variation method.

STORAGE RING

The beam diagnostic in the storage ring should not only facilitate the initial storage of the beam, but should more importantly allow for sufficient characterisation of the stored beam (current, positions, emittance, stability, etc.).

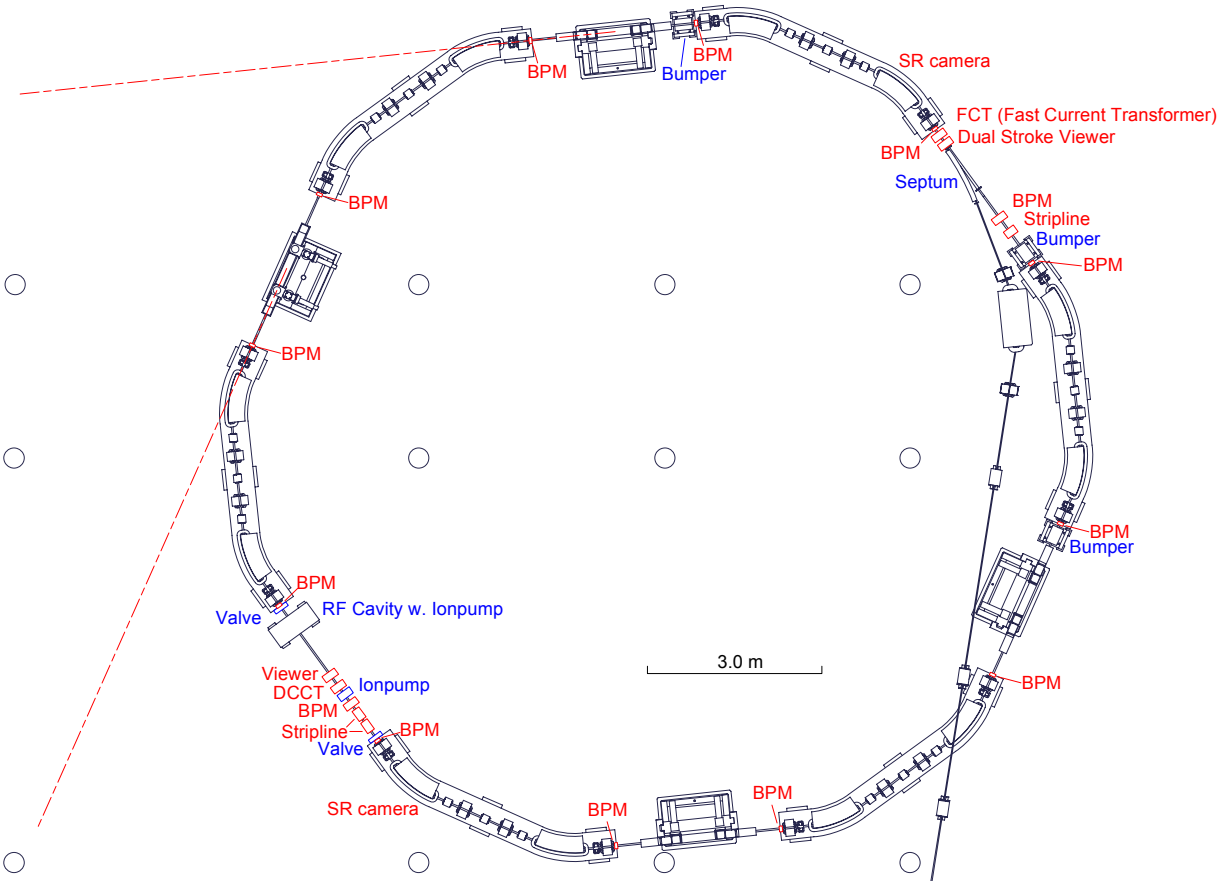


Figure 2: An overview of the ASTRID2 storage ring showing the locations of diagnostic elements. The small circles are pillars in the building.

Initial Storage

To facilitate the initial storage, two **viewing screens** will be installed. One dual-stroke viewing screen will be installed just after the injection septum. Fully inserted this will allow monitoring the beam coming out of the septum. Partly inserted it will permit monitoring the beam after one turn. Opposite the injection straight in the RF and diagnostic straight, another viewing screen will allow monitoring the beam after half a turn.

To quantify the injection efficiency a **Fast Current Transformer** (FCT) will be installed just after the injection septum. This will allow determining the injected current, and the turn-by-turn loss. Since we here have much higher requirements for bandwidth, accuracy, and vacuum compatibility, this will most likely be a high quality commercial product.

Current

One of the most important parameter of the stored beam is the current. We plan to install a commercial **DC Current Transformer** (**DCCT**) in the diagnostic straight.

Beam Positions

Absolute control of the beam position is of course essential to the Synchrotron Radiation user. In order to facilitate this, we will install Beam Position Monitors (BPMs) of the button type at the end of each arc. With 6 arcs, we will have a total of 12 BPMs.

The read-out electronics will be of the multiplexed analog type. We are presently testing a card developed at MAX-lab [4]. The MAX-lab card is designed for 300 MHz, which is their 3rd harmonic. At 315 MHz, which is our 3rd harmonic there is 3 dB attenuation in the input filters. It is possible to change the input filters and make the card operate at other frequencies (say 105 MHz or 210 MHz).

Quadrupole Shunts

In order to perform offset calibration of the BPMs and for beta function measurement, all of the quadrupoles will be equipped with quadrupole shunts. Copying the MaxLab solution, we plan the shunts to be power resistors in series with solid state relays. For each magnet we will have a few circuits, say at 1% and 2%. By having individual control of each shunt, we will with two shunts have the possibility of 3 shunt currents (say for instance 1%, 2%, and 3%).

Tunes

We will install two sets of **striplines** at 45° for tune measurement. One set will be installed in the injection straight and another set will be installed in the RF and diagnostic straight. Tunes will be measured using a swept spectrum analyser. The output from the tracking generator will be connected to one stripline through an amplifier, and input of the spectrum analyser will be connected to another stripline.

Initially we will not install any transverse feedback systems, but we will install a set of striplines at 90°, for future use. For use as a longitudinal pickup we will install a short circular tube in the diagnostic straight. Two extra BPMs will be installed, one in the injection straight, and one in the RF and diagnostic straight, for various diagnostic purposes.

Emittance

At two places (at the first bending magnet after injection, and at a bending magnet opposite injection) we plan to install **Synchrotron Radiation (SR) cameras** to monitor the beam properties. Besides giving an easy visual inspection, the pictures can also be analysed in real time (up to some tens of Hz), and a number of electron beam properties can be extracted. By measuring the beam size we will have a measure of the emittance of the stored electron beam, and the position of the SR-light on the camera will directly be a measure of the position of the electron beam. The visual representation of the beam, can often be very useful, for example in diagnosing instabilities.

TIMELINE

The project has been approved, and we are presently preparing for contract negotiation. The timeline of the project is given in Table 2.

Table 2: Timeline of the project

Year	
2009	Design and order
2010	Delivery and installation
2011	Commissioning of the ring and installation (transfer) of the first beam lines
2012	Transfer of the remaining beam lines
2013	Full operation

REFERENCES

[1] R. Stensgaard. *ASTRID, The Aarhus Storage Ring*, Physica Scripta, Vol. T22, p 315, 1988.

[2] S.P. Møller. *ASTRID, A Storage Ring for Ion and Electrons*, Proc. of EPAC'88, p. 112.

[3] J.S. Nielsen and S.P. Møller. *New Developments at the ASTRID Storage Ring*, Proc. of EPAC'98, p 406.

[4] Private communication. Robert Nilsson, MAX-lab.

THE TRANSVERSE AND LONGITUDINAL BEAM CHARACTERISTICS OF THE PHIN PHOTO-INJECTOR AT CERN

O. Mete, CERN, Geneva and EPFL, Lausanne, Switzerland
E. Chevallay, A. Dabrowski, S. Doebert, K. Elsener, V. Fedosseev, T. Lefèvre, M. Petrarca, CERN, Geneva, Switzerland
D. Egger, EPFL, Lausanne, Switzerland; R. Roux, LAL, Orsay, France

Abstract

The laser driven RF photo-injectors are recent candidates for high-brightness, low-emittance electron sources. One of the main beam dynamics issues for a high brightness electron source is the optimization of beam envelope behavior in the presence of the space charge force in order to get low emittance. Within the framework of the second Joint Research Activity PHIN of the European CARE program, a new photo-injector for CTF3 has been designed and installed by collaboration between LAL, CCLRC and CERN. Beam based measurements have been made during the commissioning runs of the PHIN 2008 and 2009 including measurements of the emittance, using multi-slit technique. The demonstration of the high charge and the stability along the long pulse train are between the goals of this photo-injector study as also being important issues for CTF3 and the CLIC drive beam. In this work the photo-injector will be described and the first beam measurement results will be presented and compared with the PARMELA simulations.

INTRODUCTION

A photo-injector was proposed as a new electron source for CTF3 (CLIC Test Facility 3) and later for the CLIC (Compact Linear Collider) drive beam [1, 2]. After the installation of the PHIN photo-injector at CERN, the longitudinal and the transverse properties of the commissioning beam have been measured in a range of parameters. In laser-driven RF photo-injectors the transverse phase space dynamics are influenced by several issues like time dependency of the RF field, space charge effects and transverse focusing. The adjustment of the laser properties such as spot size, radial and temporal distribution can effectively be used to control the properties of the beam in both directions. During the high charge operation at low energies, the space charge force is the dominating effect for emittance growth. The space charge effect can be compensated with the field created by a focusing magnet. The laser spot size dependence of the transverse size and emittance of the beam has been investigated for the laser spot sizes of 2 mm, 3 mm and 4 mm. The transverse emittance was measured with the multi-slit method in a range of focusing magnet current to study the emittance compensation. This method is applicable to the low energy, space charge dominated beams [3, 4].

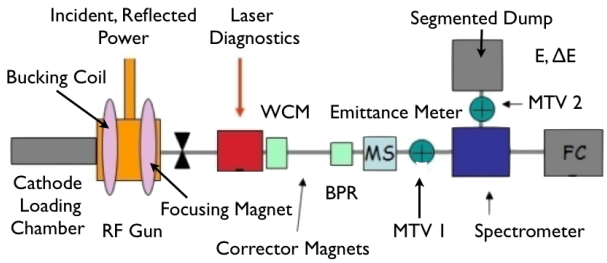


Figure 1: The PHIN photo-injector layout.

SET-UP

The beamline consists of three sections, cathode transfer chamber, RF gun and the beam measurements section (see Fig. 1). A semiconductor Cs_2Te cathode was introduced on one end of a 2+1/2 cell RF gun in order to extract the electrons. The cathode has been studied at the CERN photo-emission laboratory and demonstrated a lifetime to allow >100h run at a 3% quantum efficiency for a 262 nm laser wavelength. The so called "bucking coil" was installed in parallel to the cathode surface to maintain zero magnetic field in this location. This is to prevent the back-bombardment of the electrons onto the cathode surface that decreases the cathode lifetime and the achievable amount of extracted charge. Another magnet follows in the exit of the gun as a transverse focusing element and ensures the emittance compensation. A Nd:YFL oscillator produces the laser pulses at a repetition rate of 1.5 GHz with an average power of ~300 mW. The oscillator has the fundamental wavelength of λ ~1047 nm and a pulse width of τ ~8 ps [5]. The laser diagnostics was placed close to the gun as shown in Fig. 1 providing the alignment of the laser and the cathode after the laser table. The third section of the beamline consists of several diagnostics tools: a wall current monitor (WCM) and a beam position RF monitor (BPR) have been included. A set of corrector magnets have been also installed for horizontal and vertical corrections in addition to the focusing magnet. For the emittance measurement a 2 mm thick tungsten multi-slit mask was utilized. The mask has 25 slits each having a width of 100 μm. FLUKA [6] simulations showed that the mask is able to totally stop a 5.5 MeV electron beam allowing the electron transmission only through the windows while 20% of the incoming electrons are backscattered. An OTR (Optical Transition Radiation) screen was used in the system to image the

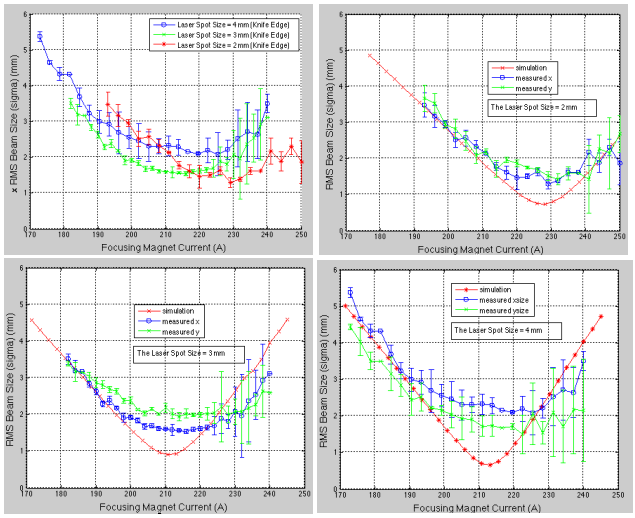


Figure 2: Focusing magnet scans for the transverse beam size measurement for different laser spot sizes.

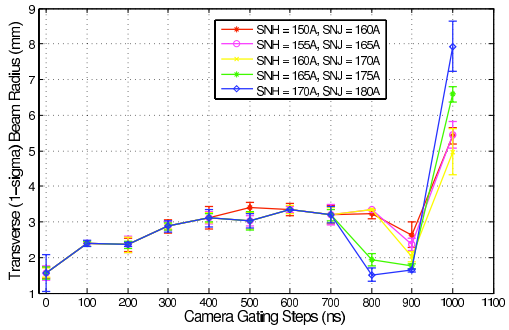


Figure 3: The transverse beam size measurement along the 1.2 µs long train.

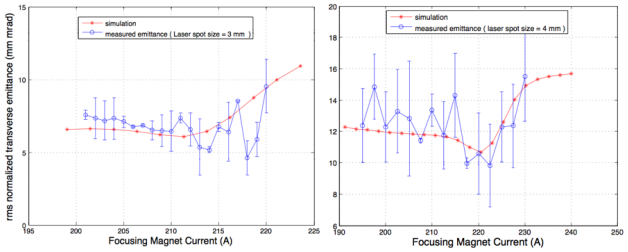


Figure 4: The transverse normalized rms emittance vs focusing magnet current for laser size of 3 mm (left) and 4 mm (right).

beamlets after the slits. A Faraday cup was placed after the emittance-meter for charge measurements. The energy spread measurement has been done with a spectrometer, installed in the end of the beamline. The spectrometer consists of a dipole magnet placed before the Faraday cup, a ceramic screen and a CCD camera. When the dipole is active the beam is transmitted to the spectrometer line instead of dumping in the Faraday cup. In the second PHIN run (March 2009), the CCD camera in the emittance-meter has been replaced by a intensified CCD camera allowing to use a aluminum OTR screen. It has been chosen as a better solution than using a more sensitive ceramic screen that often saturates in the usual operation electron intensity. A segmented dump has been also installed and tested in the second PHIN run allowing the measurement of the time resolved longitudinal beam properties .

MEASUREMENTS

For the beam size measurements, simulations depend on the assumption of a round electron beam with a gaussian distribution since the initial properties of the beam resembles the laser properties. As the result of the first run we have observed an asymmetric behavior between the vertical and horizontal components of the beam size. Investigations on the laser alignment and positioning on the cathode, and the background field by the magnetic components in the set-up have been considered as possible sources for this asymmetry. During 2009 run beam size scans have been performed with respect to different laser spot sizes of 2, 3, and 4 mm at 5.5, 5.2 and 5.7 MeV, respectively. The asymmetry was no longer present. The results for that scans are shown in Fig. 2 in comparison with the PARMELA[7] simulations. The simulations and the measurements agree rather well with the exception of the focus region. Although the discrepancy is still under investigation, it could be related to the limited resolution of the optical system or a saturation effect. The transverse emittance and the minimum spot size are scaling with the laser spot size as expected. Since the stability of the beam parameters along a long pulse train is very important for CTF3, the beam size has been measured as a function of time along the train by using a gated camera. The measurement was done with the steps of 100 ns. The gentle increase of the spot size could be explained with an imperfect beam loading compensation during the measurement. The result can be seen on Fig. 3 for different magnet settings. Emittance measurements have been performed over wide a range of focusing magnet current and laser spot size. The emittance scan at energy of 5.7 MeV and 5.2 MeV for the laser spot sizes of 3 mm and 4 mm can be seen in Fig. 4 and compared with the PARMELA simulation. It has been shown that the transverse emittance scales with the laser spot size with the values of around 7 mm mrad at 3 mm and 12 mm mrad for 4 mm laser spot sizes at the focusing region.

The reconstructed phase space can be compared to the PARMELA simulations in Fig. 5. This phase space has been measured as the laser spot size was 3 mm and with the 1.28 nC charge per bunch at 5.2 MeV. The RMS normalized transverse emittance has been measured as 7.3 mm mrad for this given single shot measurement. Time resolved energy of the beam was measured by using a segmented dump. The energy spread was not reliably measurable since a fixed screen in front of the dump caused electron scattering which lead to a factor of 9 widening in the

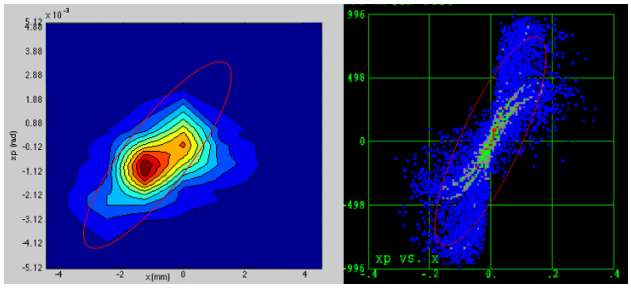


Figure 5: The reconstructed phase space from the measurement (left) and the PARMELA simulation (right).

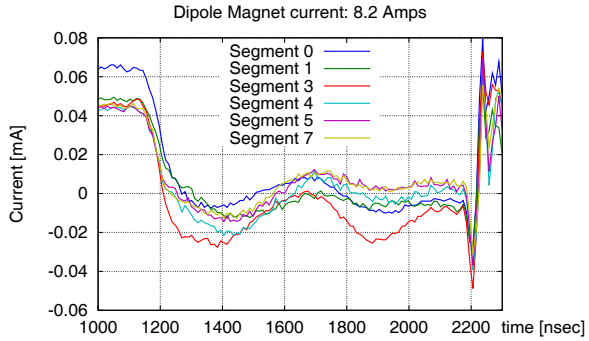


Figure 6: The intensity distribution in the centre of the segmented dump.

transverse size. The screen will be changed to a thin aluminum foil for the next run to avoid this effect. Simulations with GEANT4 [8] showed that the value of energy spread is up to a few percent. Regarding the time resolved aspect of the measurement, the goal was to measure the time variation of the energy along the pulse train. Figure 6 shows the current in the dump for each segment as a function of time. The measurement shows that the energy along the train is stable confirming the stability of the RF system. The beam loading compensation was also studied and optimized by adjusting the timing of the beam versus the RF pulse. Figure 7 shows the successful beam loading compensation. In the presence of the beam, a flat top RF pulse has been obtained resulting in a mono energetic beam. The reflected power is well matched at this point confirming that the input coupler has been adjusted to the correct over-coupling. The beam was consisted of 300 bunches with a charge of 1.28 nC during the measurements with a laser spot sizes of 3 and 4 mm. The measurements, at 2 mm laser spot size, have been done with a charge of 1.09 nC per bunch. The highest achievable charge was 2.53 nC per bunch during the operation.

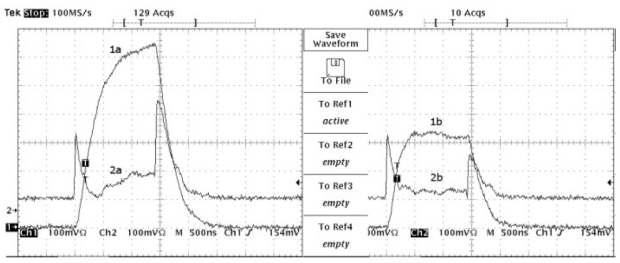


Figure 7: Beam loading. Left: RF power in the gun (1a) and reflected power (2a) when no beam is present. Right: RF power in the gun (1b) and reflected power (2b) when beam is present.

CONCLUSION

The beam measurements revealed the expected behavior agreeing with the simulations within some error ranges. The envelope behavior at the small beam sizes has to be investigated considering the possible limitations from the instrumentation and the laser spot size. The emittance measurements have been improved with respect to the previous run by replacing the CCD camera with an intensified one enabling the usage of an aluminum OTR screen. The simulations for the beam size measurements are consistent with the measurements within a 10% error band of the laser spot size. For the segmented dump, simulations showed that elements in the beamline such as the alumina screen significantly increases the transverse size of the beam, due to multiple scattering and energy loss, to the point this contribution is much larger than the dispersion due to energy spread. Although a reliable energy spread measurement was impossible under this condition, the issue will be solved easily in the next commissioning run by replacing the alumina screen with a thin aluminium OTR screen.

REFERENCES

[1] S. Döbert, "Integration of the PHIN RF Gun into the CLIC Test Facility", MOPLS129, European Particle Accelerator Conference 2006, EPAC'06, Edinburgh, Scotland.

[2] R. Losito, et. al., "The PHIN Photoinjector for the CTF3 Drive Beam", WEPLS059, European Particle Accelerator Conference 2006, EPAC'06, Edinburgh, Scotland.

[3] Min Zhang, "Emittance Formula for Slits and Pepper Pot Measurement", FERMILAB-TM-1988.

[4] S.G. Anderson, "Space-charge Effects in High Brightness Electron Beam Emittance Measurements", Phys. Rev. ST Accel. Beams, APS May, 2002, doi:10.1103/PhysRevSTAB.5.014201.

[5] M. Petrarca, et al., "First Results From the Commissioning of the PHIN Photo-Injector for CTF3", MO6RFP063, Particle Accelerators Conference 2009, PAC'09, Vancouver, Canada.

[6] A. Ferrari, P.R. Sala, A. Fasso, J. Ranft, "FLUKA: A multi-particle transport code" (Program version 2005), CERN-2005-010.

[7] L.M. Young, J. Billen, "The Particle Tracking Code PARMELA", Particle Accelerator Conference 2003, PAC'03, Portland, Oregon, USA.

[8] S. Agostinelli, et.al., "GEANT4: A simulation toolkit", Nucl. Instrum. Meth., A506, 2003, p. 250–303, doi:10.1016/S0168-9002(03)01368-8.

PHYSICS AND TECHNICAL DESIGN FOR THE SECOND HIGH ENERGY DISPERSIVE SECTION AT PITZ*

S. Rimjaem†, J.Bähr, Y. Ivanisenko, M. Krasilnikov, J. Rönsch, F. Stephan,
DESY, 15738 Zeuthen, Germany
M. Joré, A. Variola, LAL, 91898 Orsay, France

Abstract

Research activities at the Photo Injector Test facility at DESY, Zeuthen site, (PITZ) aim to develop and optimize high brightness electron sources for Free Electron Lasers (FELs) like FLASH and the European XFEL. To demonstrate the XFEL operation, an electron bunch train containing 3250 pulses of 1 nC charge at 10 Hz repetition rate is required. The spectrometers and related equipments for studying the longitudinal phase space for such long pulse trains do not yet exist at PITZ. Design and construction of a new high energy dispersive arm (HEDA2) is currently in progress. Besides the requirement to handle long electron bunch trains, the HEDA2 setup is designed to allow high resolution measurements of momentum distribution up to 40 MeV/c, a longitudinal phase space measurement with slice momentum spread down to 1 keV/c and transverse slice emittance measurements at off-crest booster phases. The status of the physics design and technical considerations of this dispersive section will be presented.

INTRODUCTION

The test facility PITZ was built and is developing as a pilot photo injector source for the FELs like FLASH and the European XFEL. The research goal is to produce, optimize and characterize the small transverse emittance electron beam of $\leq$ 1 mm-mrad with a bunch charge of 1 nC and an energy spread of smaller than 1%. In order to fulfill the characterization of high brightness electron beam, the PITZ beam line is continuously upgraded towards the final design (PITZ2) in parallel to the beam operation. The future PITZ2 set up (see Fig.1) will consist of a photocathode RF-gun, a booster cavity, and several diagnostics systems including 3 emittance measurement systems, 3 dispersive arms, an RF deflector, a phase space tomography module, and bunch length diagnostics. One of the key components which will be installed in the PITZ2 beamline is a new cut disk structure (CDS) booster cavity for emittance conservation corresponding to the peak field at the cathode of 60 MV/m [1]. The CDS booster can accelerate electron beams to reach higher energy than the current PITZ setup. This leads to the upgrade of the diagnostics components downstream the booster cavity for supporting the measurements with higher energy electron beams.

* This work has partly been supported by the European Community, contract RII3-CT-2004-506008 and 011935.

† sakhorn.rimjaem@desy.de

To fulfill the beam characterization, besides the intensive measurement program for the transverse phase space optimization the longitudinal phase space is studied using the low energy dispersive arm (LEDA) to measure beam momentum downstream the RF-gun, the first high energy dispersive arm (HEDA1) and the second high energy dispersive arm (HEDA2) to measure the beam momentum behind the booster. The upgraded LEDA and the new HEDA1 have been installed in the current PITZ setup [1]. The old high energy dispersive arm from the previous set up, which is able to measure the beam momentum up to about 16 MeV/c [2], was moved to the end of the beam line. Design and construction of the new HEDA2 is ongoing under the collaboration between DESY and LAL and it is planned to be installed at PITZ in the middle of year 2010.

SETUP

The HEDA2 setup is designed for high resolution measurements of momentum distribution up to 40 MeV/c, a longitudinal phase space measurement with slice momentum spread down to 1 keV/c, and a transverse slice emittance measurements. The contradictory between the measurements of the longitudinal phase space and the transverse slice emittance is the operation at different booster phases. The on-crest or nearly on-crest booster operation is required in the longitudinal phase space measurement for a small momentum spread, while in the transverse slice emittance measurement, the off-crest booster phases conduct the large momentum spread. Since the resolution of the transverse slice emittance measurement at the existing HEDA1 setup is expected to be very good [3], the good resolution of the longitudinal phase space measurement has higher priority in HEDA2 design.

To demonstrate an operation of electron bunches of 1 nC charge for the long bunch train up to 7200 pulses for the FEL at FLASH (720 μs pulse, 10 Hz) and 3250 pulses for the European XFEL (650 μs pulse, 5 Hz), the large beam dump with the size of about $2\times2\times2$ m^3 is required and the existing beam dump in the PITZ straight section is planned to be upgraded to fulfill this requirement. The same size of the beam dump is also needed at the end of the HEDA2 section, but the space in the PITZ tunnel is limited. Thus, the transportation of the beam back to the beam dump in the straight section is foreseen. Three dipole magnets are used for this purpose. The HEDA2 setup (see Fig.2) will consist of 3 dipole magnets, 2 screen stations, a quadrupole magnet, 3 beam position monitors (BPMs) and 2 integrated

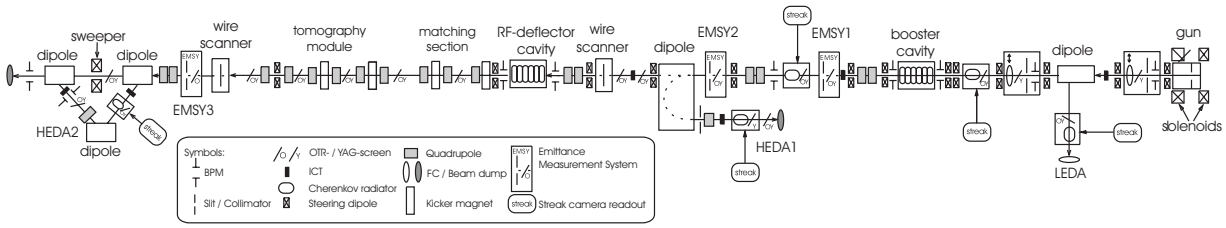


Figure 1: Layout of the future Photo Injector Test facility at DESY, Zeuthen site, (PITZ).

current transformers (ICTs). For characterization of a single bunch out of the long pulse trains, a kicker magnet will be placed in the straight section before the first dipole magnet. The longitudinal phase space will be measured at HEDA2 by using the combination of a spectrometer and a Cherenkov radiator equipped with a streak camera readout or an RF-deflector together with a screen in the dispersive section.

Since the RF-deflector deflects the beam in vertical plane, the first dipole (DISP3.D1) bends the beam in the horizontal direction and functions as the spectrometer for longitudinal phase space measurements using the first screen station (DISP3.Scr1). The second dipole (DISP3.D2) serves in transverse slice emittance measurements using a quadrupole (DISP3.Q1) and the second screen station (DISP3.Scr2) and transports the beam back to the straight section. The third dipole (DISP3.D3) transports the beam to the beam dump. The deflecting angle (α), the input and the output pole face rotation (β_{in}, β_{out}) and the bending radius (ρ) of these dipoles are listed in Table 1.

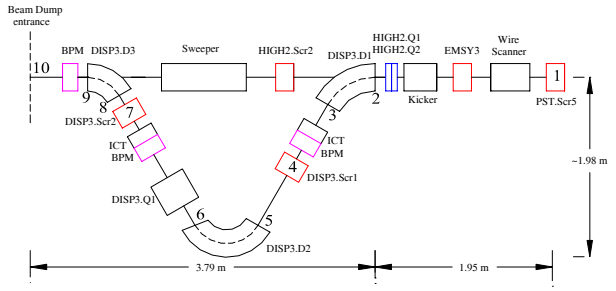


Figure 2: Layout of the foreseen HEDA2 setup.

Table 1: Specifications of Dipole Magnets in HEDA2 Setup

dipole	α (^{o})	β_{in} (^{o})	β_{out} (^{o})	ρ (mm)
DISP3.D1	60	0	0	600
DISP3.D2	-120	0	9	400
DISP3.D3	60	0	0	400

SIMULATIONS AND DESIGN

Reconstructed Longitudinal Phase Space

In momentum and momentum spread measurements, electrons with different momenta are deflected by a dipole magnet with different deflecting angles and resulting in different positions at the dispersive screen as $x = R_{11}x_0 + R_{12}x'_0 + R_{16}\frac{\Delta p_0}{p_0}$, where the matrix elements R_{11}, R_{12} and R_{16} are defined by the matrix transportation from the initial position through the dipole magnet until reaching the dispersive screen. In order to have good resolution for momentum spread ($\frac{\Delta p_0}{p_0}$), the influence of the particle position (x_0) and divergence (x'_0) should be small compared to the momentum contribution.

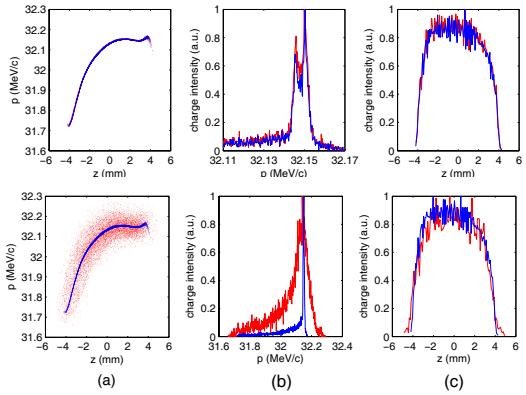


Figure 3: (a). Longitudinal phase space, (b). momentum spectrum and (c). charge profile of simulated particle distributions at the reference screen (blue) compared to its reconstructed distribution at the dispersive screen (red). Top-row pictures show the results from the simulated measurement using the quadrupole focusing at the reference screen and bottom-row pictures show the results in case of without the quadrupole focusing.

For the design of the first dipole as a high resolution spectrometer using the RF-deflector, a reference screen was defined to be the focus position in order to reduce the influence of the beam size. The last screen in the tomography module (PST.Scr5) was chosen to be the reference screen for the longitudinal phase space measurement at the dispersive screen (DISP3.Scr1). The drift lengths from the reference screen to the dipole entrance and from the dipole exit to the dispersive screen were optimized from simulations and they are chosen to be 1950 and 650 mm. The focusing optimization using the first three quadrupole magnets in the tomography module as the triplet quadrupole has been studied and the results are shown in Fig.3. It can be clearly seen that the measurement with the quadrupole focusing should have better resolution. The resolution of the measurement is affected mainly by the initial beam size and the vertical focusing of the beam on the dispersive screen before turning on the RF-deflector is required to gain a good resolution.

The reconstructed slice momentum spread ($p_{rms,slice}$) for different quadrupole focusings have been simulated for the initial particle mean momentum, momentum spread, minimum slice momentum spread and mean slice momentum spread of 32.07 MeV/c, 106.15 keV/c, 0.77 keV/c and 2.88 keV/c, respectively. The results in Fig.4 show that the focusing corresponding to the minimum horizontal beam size (0.06 mm, blue curve) at the reference screen gives better resolution than other cases. The reconstructed distribution fits very well in the center part of the bunch which contains the major part of charge. There is some discrepancy at the head and the tail of the bunch due to the focusing of a certain energy range at the required position. The minimum slice momentum spread of the simulated measurement using the RF-deflector down to 0.96 keV/c can be expected for this focusing condition.

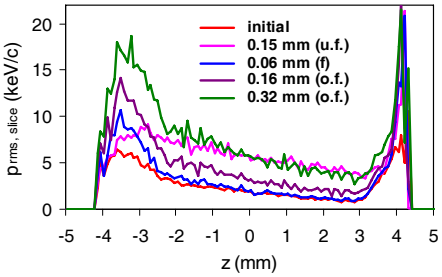


Figure 4: Simulated slice momentum spread compared to its reconstructed at the dispersive screen for different quadrupole focusing corresponding to the rms horizontal beam sizes at the reference screen. The abbreviations u.f., f, and o.f. present the under-focused, focused and over-focused conditions at the reference screen.

Beam Size Calculation

The beam size in the dispersive section will be large due to the large dispersion from the dipole magnet, especially in cases of far off-crest RF phases. Beam sizes along the dispersive section have been studied with the gun and the booster on-crest for the measurement with and without using the RF-deflector. The calculation results in Fig.5 conclude that the aperture of all the components in HEDA2 should be about or larger than 80 mm depending on the locations and the reasonable design for each component. The transverse beam size before and after the exit of the DISP3.D3 dipole can be controlled by using the DISP3.Q1 quadrupole magnet.

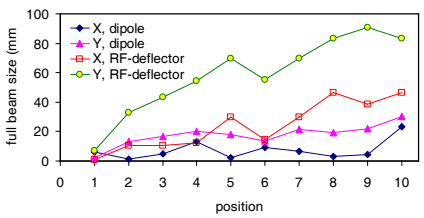


Figure 5: Calculated beam sizes along the HEDA2 section. The position numbers correspond to the numbers indicated in HEDA2 setup in Fig.2.

Dispersive Screen Stations

The DISP3.Scr1 is a multi-purpose screen station for momentum distribution measurements using a YAG and an OTR screen, bunch length measurements using an OTR screen and an aerogel radiator as Cherenkov radiators and a vertical slit for the transverse slice emittance measurements. The design configurations of this screen station are shown in Fig.6. Since the beam spot size in the dispersive section will be large due to the large dispersion, the large screen sizes are needed. The effective screen size of about 80 mm×60 mm for the YAG and OTR screens was chosen and this leads to the large screen actuator. The idea to include the screen actuator inside the actuator bellow has been studied. In order to keep the effort vacuum force that the linear translator needs to take (3000 N), the bellow size of 160 mm diameter will be used. According to this constrain, the OTR screens will have the off-set of about 50 mm from the desired position. Simulation results confirm that this off-set is acceptable for the high resolution in the longitudinal phase space measurements.

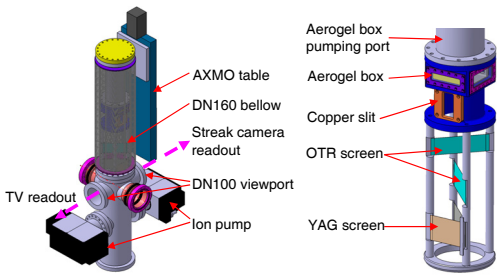


Figure 6: The first screen station in HEDA2 (DISP3.Scr1) including details of screens and slit configurations.

SUMMARY

The HEDA2 spectrometers and related diagnostics, which are foreseen to be installed at PITZ at about the middle of year 2010, will allow the analysis of long bunch trains including measurements of the longitudinal phase space and the transverse slice emittance. The slice momentum spread resolution down to 0.96 keV/c is expected to be resolved using this dispersive section diagnostics. The physics design for the dipole magnets and the simulated measurement conditions are ongoing in parallel to the technical design. An optical system for the longitudinal phase space measurements is under development.

REFERENCES

[1] C. Boulware., "Latest Results at the Upgraded PITZ Facility", FEL'08, Gyeongju, Korea, THAAU05.

[2] J. Rönsch et al., "Recent Measurements of the Longitudinal Phase Space at the Photo Injector Test Facility at DESY in Zeuthen (PITZ)", FEL'07, Novosibirsk, Russia, WEPPH009, p. 342, http://www.JACoW.org.

[3] S. Khodyachykh et. al, "Design of Multipurpose Dispersive Section at PITZ", FEL'06, Berlin, Germany, THPPH020, p. 601, http://www.JACoW.org.

SPIRAL 2 INJECTOR DIAGNOSTICS

P. Ausset, IPN, Orsay, France
T.A. Andre, C. Doutressoulles, B. Ducoudret, C. Jamet, W. Le Coz, F. Lepoittevin, E. Swartvagher, J.L. Vignet, GANIL, Caen, France
C. Maazouzi, C. Olivetto, C. Ruescas, IPHC, Strasbourg, France

Abstract

The future SPIRAL2 facility will be composed of a multi-beam driver accelerator (5 mA/40 MeV deuterons, 5 mA /14.5 MeV/u heavy ions) and a dedicated building for the production of radioactive ion beams (RIBs). RIBs will be accelerated by the existing cyclotron CIME for the post acceleration and sent to GANIL's experimental areas. The injector constituted by an ion source a deuteron/proton source a L.E.B.T. and a M.E.B.T. lines and a room temperature R.F.Q. will produces, transports and accelerates beams up to an energy of 0.75 MeV/u. An Intermediate Test Bench (B.T.I.) is being built to commission the SPIRAL2 injector through the first re-buncher of the M.E.B.T. line in a first step and the last re-buncher in a second step. The B.T.I. is designed to perform a wide variety of measurements and functions and to go more deeply in the understanding of the behaviour of diagnostics under high average intensity beam operations. A superconducting LINAC equipped with two types of cavity will allow reaching 20 MeV/u for deuterons beam. This paper describes injector diagnostic developments and gives information about the current status.

INTRODUCTION AND GENERAL DESCRIPTION OF THE FACILITY

The SPIRAL2 project aims at producing Radioactive Ion Beam (R.I.B.) by ISOL as well as low-energy in-flight methods. A collaboration of several French laboratories is now constructing the SPIRAL2 facility [1] composed of an injector including two E.C.R. sources, a R.F.Q. operating at 88.05 MHz, a LINAC based on 88.05 MHz superconducting independently phase quarter wave superconducting cavities able to accelerate high intensity (5 mA) deuteron beam up to 20 MeV/u and light heavy ion (Q/A= 1/3) beam (1 mA) up to 14.5 MeV. Finally the H.E.B.T. lines will distribute those beams to a beam dump or to the experimental stable ion beam experimental areas or transported to the 200 kW target ion source system. The expected rate of fission is 10^{14}/s

THE SPIRAL2 INJECTOR DIAGNOSTICS

The general layout of the L.EBTs and M.E.B.T. is shown in Fig. 2. The first E.C.R. source produces 20 keV/u light heavy ions (Q/A/=1/3). The second E.C.R. source produces deuterons beam (40 keV) and now according to a new experiment needs proton beam (20 keV) with characteristics very similar to those of the deuteron beam. The two lines merge in the shared L.E.B.T. which goal is to correctly match the beam to the entrance of the R.F.Q. [2].

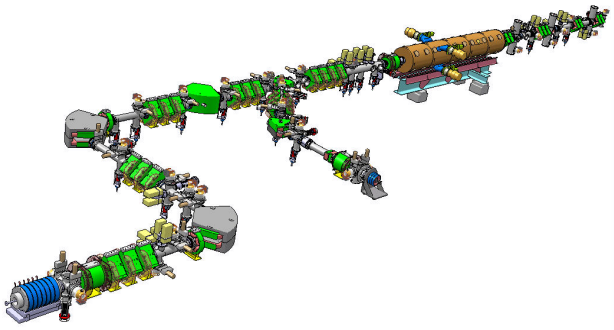


Figure 1: General layout of the SPIRAL2 injector.

Beam Characteristics

The maximum power of the beam under the nominal C.W. mode operation reaches 7.5 kW at the exit of the M.E.B.T. In order to lower the beam average power, Low Duty Factor Pulsed mode operation is also planned for commissioning periods. For this purpose, the operation of the source may be pulsed. A slow chopper located in the shared LEBT may pulse the beam in order to obtain duty cycle as low as 0.1 %. This mode of operation allows also the interceptive diagnostics to withstand the beam during the tuning of the injector. At last, a fast chopper located in the MEBT line removes selected bunches from the beam according to special experiment needs.

Destructive Beam Intensity Measurements

They are carried out by copper made water cooled Faraday Cup in the L.E.B.T and in the M.E.B.T. (end of the line). The first one following the E.C.R. ion source is specially devoted to the tuning of the source. The Faraday cups are designed for a 100 mm aperture in the LEBT and 60 mm in the M.E.B.T. The maximum beam power



Figure 2: Photograph of the Faraday Cup of the L.E.B.T.

sustained by the Faraday Cup is then 1.2 kW (LEBT) and 1.5 kW (MEBT) corresponding to a maximum temperature of 350° K (MEBT). The design has been optimized by thermal simulation under ANSYS software.

Non Destructive Beam Intensity Measurement

A D.C.C.T. (New P.C.T. from Bergoz Company) is located just at the entrance of the R.F.Q. in the L.E.B.T. A home made three layers shielding (Armco, mu metal and copper) protects the sensor from the external leakage magnetic field solenoid.

Extensive tests have been carried at Ganil to check the sensitivity of the D.C.C.T. in the vicinity (7 cm) of the leakage field of a solenoid. It has been measured that the shielding lowers the offset drift from 1 µA/Gauss down to 0.1 µA/Gauss. Results concerning the other main parameters such as bandwidth, drifts with temperature, linearity are in good agreement with the nominal manufacturer specifications.

An A.C.C.T. will be coupled with a D.C.C.T in the M.E.B.T. line in order to fulfil all the foreseen mode of operation of the accelerators. An identical couple of transformers will be installed at the exit of the LINAC to measure as accurately as possible (≤ 1%) the LINAC efficiency transmission. These measurements are required for safety reasons during the daily operation.

Transverse Beam Profiles Measurements

Even during low duty Factor pulse beam operation, SPIRAL2 beams deposit a large amount of energy in any sensor and may reach several hundred W/cm^2 in the LEBT. The evolution of the temperature has been estimated by a crude resolution of the heat equation. An example is given in Fig. 3 in the case of a 150 µm diameter tungsten wire impinged by a 2 cm diameter, 5 mA, 1.5 MeV proton beam, pulse duration: 500 µs, repetition rate: 1 s. The average temperature reaches nearly 900° K after 1 s.

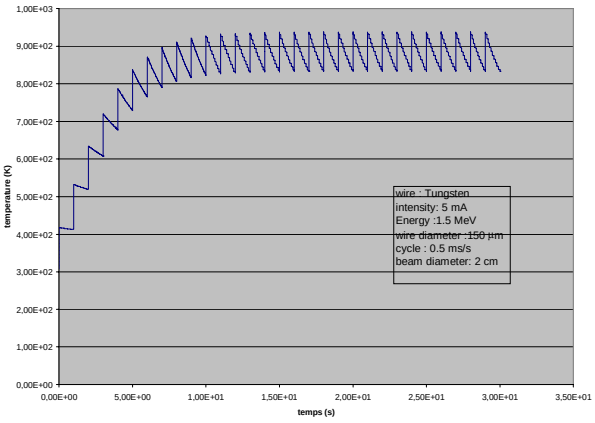


Figure 3: Evolution of the temperature of a 150 µm diameter tungsten wire (see text).

The grid of the sensors is divided in to two categories according to the beam size to be measured: 47 wires of 150 µm diameter tungsten with a spacing of 1 mm for the first one and 47 same diameter tungsten wires (spacing is variable from 1 mm up to 3 mm) for the second category [2]. These wires are welded on an alumina board to obtain a maximum out-gassing rate of 1.10^{-8} Pa.m^3.s^{-1}.

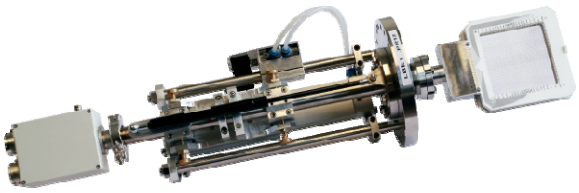


Figure 4: View of the secondary emission beam profiler.

The complete tuning of the beam transport in the L.E.B.T. needs 16 secondary emission beam profiler (variable spacing) and 4 (spacing 1mm) for the M.E.B.T.

Transverse Beam Emittance Measurements

The full transverse characterisation of the beam needs to measure the transverse beam emittance. Water cooled scanner emittancemer also named Allison Scanner has been selected. It is schematically depicted in this Fig. 5.

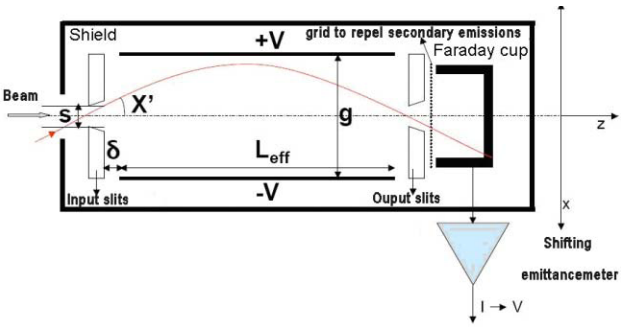


Figure 5: Schematic of the Alison emittancemeter of the L.E.B.T. and M.E.B.T.

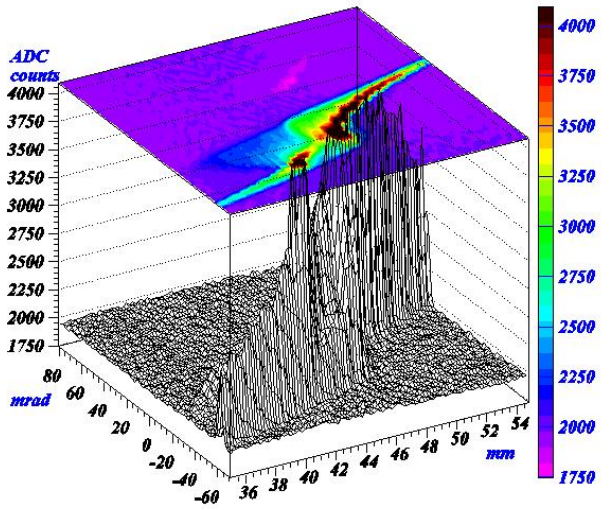


Figure 6: Ion beam emittance measured at the exit of the SPIRAL2 Phoenix source. Beam: Ar 4+, 60 KeV, 15 µA.

The beam current impinges on the narrow slit (width: 0. 2 mm) of the scanner pod. The emerging beamlet passes between a pair of electric deflection plates driven by a linear ramp generator: ± 1.4 kV max (LBET) and ± 4 kV max (M.E.B.T.). For ions passing through the rear slit there is a simple relationship between the initial angle and the instantaneous ramp voltage. The maximum measurable angles are ±100 mrad (L.E.B.T.) and ± 30 mrad (M.E.B.T.). The scanner pod is stepped across the beam to complete the measurement as a function of x and x' (full stroke: 120 mm in the L.E.B.T.). The intensity of the beamlet is measured at each step of the pod.

The prototype of the emittance-scanner has been already tested on the ion source to be installed on SPIRAL2. The result is shown on Fig. 6 in the case of Ar 4+ beam.

Longitudinal Measurements

A fast coaxial Faraday cup, previously used on the Intermediate Test Bench (B.T.I.) will be installed in the M.E.B.T. following the commissioning to measure the bunch lengths. A Fast Faraday cup is under design in collaboration with a manufacturer. This new design may allow the Faraday Cup to withstand a 400 W beam power and the bandwidth is expected to reach 2 GHz in order to measure accurately the bunch length (rise time < 200 ps). This Fast Faraday Cup will be tested at Ganil during the last quarter of this year.

A Fast Current Transformer (upper cut-off frequency: 1.6 GHz) will be installed in the M.E.B.T. upstream of the Linac for beam phase measurements.

COMMISSIONNING OF THE SPIRAL2 INJECTOR

The first step of the commissioning of the SPIRAL2 injector consists to install in the French C.N.R.S. laboratory "L.P.S.C." located at Grenoble, the E.C.R. ion source followed by the first part of the ion L.E.B.T. in order to check the operation of the source at the nominal beam power and to test the behaviour of the diagnostics: Faraday cup, beam profiler, emittancemeter.

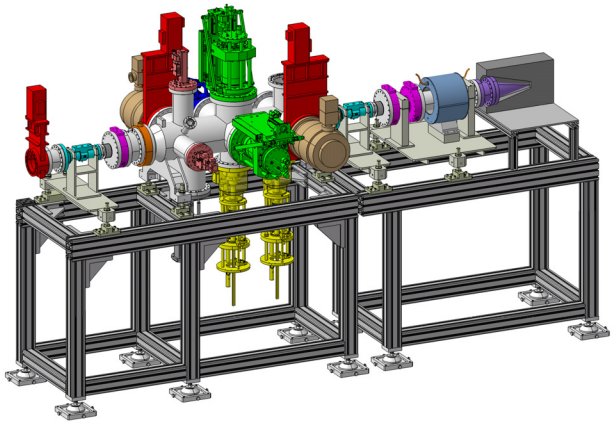


Figure 7: 3D view of the Intermediate Tests Bench (B.T.I.).

In a second step, following the installation of the injector at GANIL, an "Intermediate Tests Bench" named B.T.I. will be assembled as part of the injector commissioning plan. The B.T.I. will be positioned directly after the first re-buncher of the M.E.B.T in order to fully characterize the following beam properties:

- Beam current: D.C.C.T. and A.C.C.T.
- Beam transverse profiles: Secondary emission monitor and residual ionization gas monitor in order to compare the obtained profiles.
- Transverse emittance.
- Longitudinal emittance: Measurement of the bunch length variation with a fast Faraday cup against the variation of the voltage of the re-buncher.
- Phase and energy: A classical arrangement of three P.U. electrodes determines the number of bunches and the energy by time of flight.
- Beam Position: Two Beam Position Monitors will be a copy of the Linac P.U. (length: 39 mm, inner diameter: 48 mm, subtented lobe angle: 60°). Their primary function is to steer the beam to the beam stop. The latter will be used to measure the phase and the beam energy using the time of flight method (cross-check with the previous measurement).

All the diagnostics used on the B.T.I. will be identical to the accelerator ones. The non-intercepting measurements can be made at nearly full duty factor as the beam stop is planned to withstand the beam full power of the M.E.B.T. A second set of measurements with the B.T.I. positioned just downstream of the third re-buncher of the M.E.B.T. is planned.

CONTROL SYSTEM OF THE INJECTOR

EPICS has been selected for the SPIRAL2 control system and therefore for the SPIRAL2 injector. Consequently the architecture is based on industrial adapted solutions VME cards to control the different devices. The EPICS drivers have already been written.

REFERENCES

[1] T. Junquera & al, the high intensity superconducting Linac for the SPIRAL2 project at Ganil, Proceedings of LINAC06, Knoxville, Tennessee USA

[2] P. Bertrand, JL Biarrotte and D. Uriot, Beam dynamics studies for the Spiral2 project, Proceedings of EPAC06, Edinburgh (UK) 2006.

[3] W. Le Coz & al, phase and amplitude measurement for the spiral2 accelerator, this workshop DIPAC 2009, Basel, Switzerland

[4] J.L. Vignet & al, the beam profile monitors for Spiral2 accelerator, this workshop DIPAC 2009, Basel, Switzerland

FIRST BEAM TESTS OF THE CLIC POWER EXTRACTION STRUCTURE IN THE TWO-BEAM TEST STAND*

E. Adli†, University of Oslo, Norway and CERN, Geneva, Switzerland
R.J.M.Y. Ruber, V. Ziemann, Uppsala University, Sweden
R. Corsini, S. Doebert, A. Dubrovskiy, G. Riddone, D. Schulte,
I. Syratchev, CERN, Geneva, Switzerland
S. Vilalte, IN2P3-LAPP, Annecy-le-Vieux, France

Abstract

The two-beam acceleration scheme foreseen for CLIC and the associated radio-frequency (RF) components will be tested in the Two-beam Test Stand (TBTS) at CTF3, CERN. Of special interest is the performance of the power extraction structures (PETS) and the acceleration structures as well as the stability of the beams in the respective structures. After the recent completion of the TBTS, the first 12 GHz PETS has been tested with beam, using so-called recirculation of the RF power inside the PETS. The TBTS allows precise measurement of beam parameters before and after the PETS as well as RF power and phase. Measurements of transverse kick, energy loss and RF power with recirculation are discussed and compared with estimations, including first measurements of pulse shortening probably due to RF breakdown.

INTRODUCTION

The Two-beam Test Stand (TBTS) is a unique and versatile facility devised to test key components of the two-beam acceleration concept that is the basis of the CLIC project [1]. Worldwide it is the only facility where CLIC type power production (PETS) and accelerating structures can be tested with beam. The TBTS is part of the CTF3 complex at CERN [2] that creates a high power drive beam which is then decelerated in order to generate the RF power needed to accelerate a second, probe, beam which is provided by a another linac. The drive beam has a time structure suitable for power generation at all harmonics of 1.5 GHz but is optimised for the nominal CLIC frequency of 12 GHz. It can reach beam intensities up to 30 A, pulse lengths up to 1500 ns and beam energies up to 150 MeV. The probe beam can reach beam intensities up to 0.9 A, pulse lengths up to 150 ns and beam energies up to 170 MeV.

Commissioning of the TBTS drive beam line started last year. As the available drive beam current will be some four times lower than in the CLIC design, the installed PETS has a modified design. It has increased length to 1 m from 0.215 m and is equipped with external RF recirculation [3]: the PETS operates as an amplifier feedback ring driven by the drive beam power. Up to 30 MW of 12 GHz RF power has been produced from a 5 A beam.

THE TWO-BEAM TEST STAND

The TBTS consists of two parallel beam lines for the drive and probe beam and a two meter long test area in each. The layout of the two beam lines is almost identical [4]. The experiments described in this report are performed on the drive beam line. The layout of the line with PETS installation is shown in Figure 1.

Two quadrupole triplets are used to vary and optimise the beam size inside the PETS and on an OTR screen following a spectrometer dipole in order to maximise the energy resolution. Moreover, four steering magnets are available to adjust the orbit inside the PETS with a closed bump. Five inductive BPMs [5] are installed for intensity and position measurements. Their bandwidth allows to observe the position within a bunch train and this is used to determine kicks and energy loss of the beam during normal operation and when a RF breakdown occurs inside the PETS. The achievable resolution to determine the kicks is in the order of a few micro radians and 4×10^{-4} for the energy [6].

The PETS RF recirculation loop contains a variable splitter to control the amount of power in the loop and a phase shifter to tune the loop's length. The RF power and phase are measured through directional couplers connected to 12 GHz diodes and I&Q demodulators.

RECIRCULATION

In the recirculator a fraction of the field g (product of the splitter ratio κ and the round-trip ohmic losses) is coupled

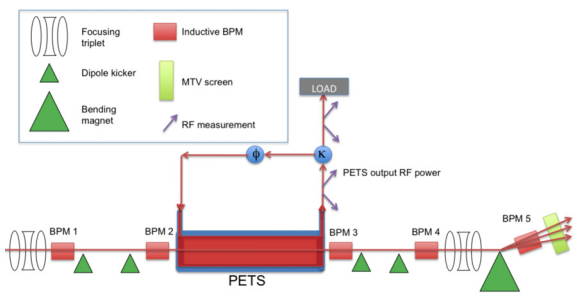


Figure 1: Sketch of the Two-beam Test Stand's drive beam line (not to scale).

* Work supported by the Swedish Research Council, the Knut and Alice Wallenberg Foundation, the Research Council of Norway and the Commission of the European Communities under the 6th Framework Programme Structuring the European Research Area, contract number RIDS-011899.

† Erik.Adli@cern.ch

back into the PETS with an eventual phase-shift ϕ with respect to the beam generated field [7–9]. For a rectangular pulse, neglecting system bandwidth limitations, and keeping all parameters constant one can calculate the peak electric field at the PETS output after M full recirculation cycles, E_M, as [9]

$$E_M = E_{beam} \sum_{m=0}^{M} g e^{j\phi} \quad (1)$$

where E_{beam} is the peak electric output field generated by the beam before the recirculation starts to act. Using the same assumptions the beam energy loss, $\langle U_M \rangle$, can be calculated as [10]

$$\langle U_M \rangle = \Re(E_M) LF(\lambda) - \frac{1}{2} E_{beam} LF(\lambda) \quad (2)$$

where L is the structure length and $F(\lambda)$ the form factor.

RECONSTRUCTION

Extending Eq. (1) to arbitrary beam pulse intensities, while keeping other parameters constant, we use BPM intensity measurements to reconstruct the PETS output peak field, E, the phase of the total field with respect to the beam generated field, θ, and the output power, P. The relative field phase was measured using I and Q demodulator channels on the signal from the PETS output RF window, indicated in Figure 1.

For the 2008 run the recirculator parameters g and ϕ were unknown, and as part of the reconstruction process these parameter had to be identified. A continuous series of 200 logged pulses were used to fit the unknown parameters by comparing the power and phase reconstruction with the RF measurements yielding $g = 0.75$, ϕ = -18 deg [9]. No precise bunch length measurements were available for the run, and an overall scaling factor had therefore to be fitted as well.

The rms difference of the measured and reconstructed power pulses lies within 10% for 75% of the pulses in the series used for the fit. Figures 2 and 3 show examples of reconstructed and measured power and phase.

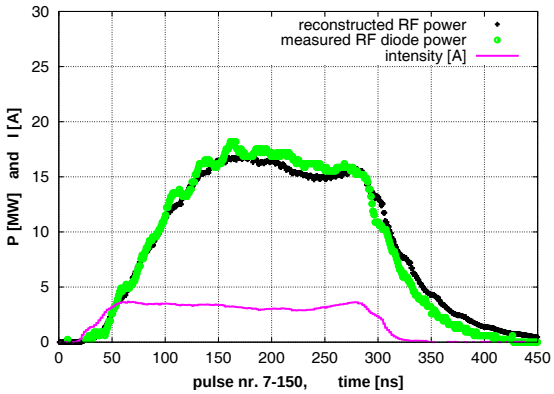


Figure 2: Reconstructed RF power from intensity measurements in black (+), measured RF power in green (o), BPM intensity in magenta (-), for a nominal pulse.

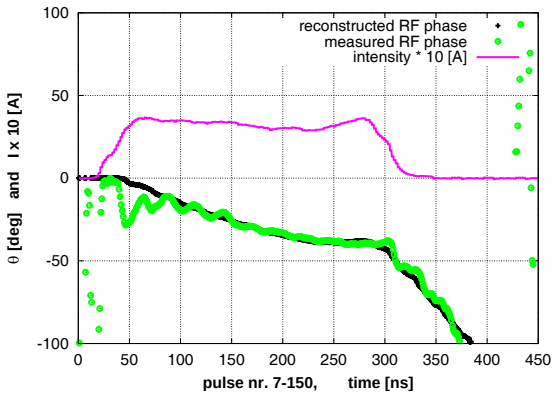


Figure 3: Reconstructed relative field phase from intensity measurements in black (+), measured relative field phase in green (o), BPM intensity in magenta (-), for a nominal pulse.

The beam intensity was gradually increased during the 2008 run, and in specific time intervals the measured RF power pulse was significantly shorter than the power reconstructed from the intensity measurements for a given pulse, as shown in Figure 4. The dynamics of such pulses can be modelled by varying the recirculation gain and phase [8] during the pulse, or, alternatively, by varying the bunch arrival phase [11]. This work is ongoing and the instrumentation of the TBTS proves to be very useful for the understanding of the dynamics of the PETS. The analysis software will be incorporated in the on-line analysis software and will serve as an indicator for breakdown, such that interesting pulses can be automatically stored for further post-processing at a later time.

ENERGY LOSS MEASUREMENTS

The PETS transfers part of the drive beam energy into RF power. In [10] three different approaches for estimating of corresponding beam energy loss are presented. First, we can determine the energy loss from the BPM in the spectrometer [6]. Second, the loss can be deduced from the power measurements in addition to the intensity measure-

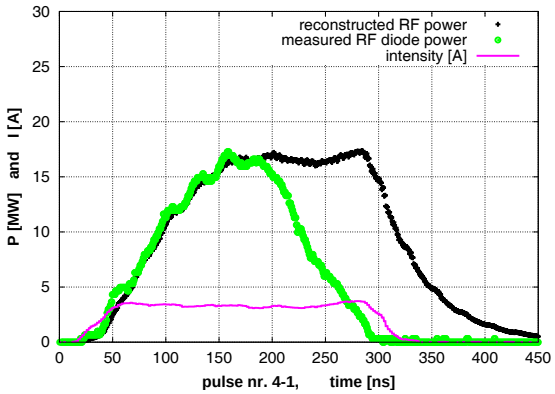


Figure 4: Reconstructed RF power from intensity measurements in black (+), measured RF power in green (o), BPM intensity in magneta (-), for a shortened pulse.

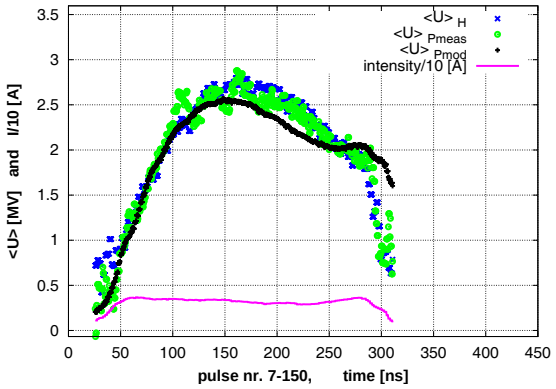


Figure 5: Energy loss estimates based on spectrometer measurements, $\langle U \rangle_H$, in blue (x), PETS power combined with BPM intensity measurements $\langle U \rangle_{P\mathrm{meas}}$, in green (o) and BPM intensity measurements alone, $\langle U \rangle_{P\mathrm{mod}}$, in black (+).

ments. Third, we can can use the intensity measurements alone, combined with Eq. (2). The rms difference between the three estimates lies within 20% for 75% of the pulses in the series used for the fit. Figure 5 shows an example of the mean voltage seen by the beam, along the pulse, estimated using these three approaches.

KICK MEASUREMENTS

For the design of a future two-beam accelerator and its stability it is also important to know if the beam receives any kick on its way through the PETS. Any such kick can be determined using the horizontal and vertical BPM measurements. For simplicity in the commissioning phase we assume here that such a kick would originate in the longitudinal centre of the PETS. From simulations we expect that the kick due to transverse dipole wakes in the PETS should be less than 100 μrad if the incoming beam offset is 1 mm parallel along the PETS centre line. Due to mechanical and electrical BPM offsets, not yet precisely identified, it was not possible to resolve the absolute angle and kick measurements accurately at this stage of operation. We therefore consider only relative changes along the pulse.

Figure 6 shows the estimated vertical offset (y), angle (yp) and kick in the middle of the PETS, for the pulse presented in Figure 4. During the time period that corresponds with the build up of the RF field in the PETS and the external RF power, the kick angle changes with approximately 0.5 mrad. From 250 ns on the kick angle changes with more than 1 mrad in the opposite direction. This could possibly indicate a relation between the beam kick and the field inside the PETS when pulse shortening is observed, and will be studied further during the next run. The horizontal measurements of the same pulse do not show a significant change in kick angle.

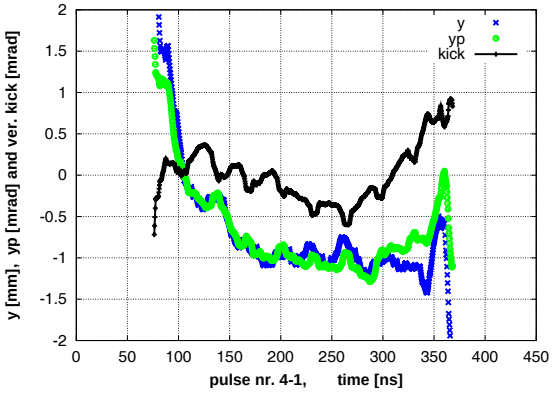


Figure 6: Estimated beam centroid offset, y, in blue (y), beam angle in the PETS, yp, in green (o) and kick angle, in black (+). All quantities are estimated in the middle of the PETS.

CONCLUSIONS

The first beam tests of a PETS in the TBTS have proven the extensive possibilities to correlate beam and RF measurements. Using a simple constant parameter model, a good agreement has been reached between estimations and measurements of the RF power production and beam energy loss. Being in the commissioning phase, work is ongoing to improve the quality of the modelling and measurements and extend their scope. The first results presented here demonstrate already that the TBTS is an excellent tool for studying the PETS dynamics.

REFERENCES

[1] G. Guignard (ed.), "A 3TeV e^+e^- Linear Collider based on CLIC Technology", CERN, Geneva (2000) CERN 2000-008.

[2] G. Geschonke and A. Ghigo (eds.), "CTF3 Design Report", *CERN CTF3 Note 047* (2002)

[3] I. Syratchev et al., "CLIC RF High Power Production Testing Program", EPAC'08 (2008) WEOBG01

[4] R.J.M.Y. Ruber et al., "The CTF3 Two-beam Test-stand Installation and Experimental Program", EPAC'08 (2008) WEPP139

[5] M. Gasior, "An Inductive Pick-up for Beam Position and Current Measurements", DIPAC'03, May 2003, Mainz, p.53, http://bel.gsi.de/dipac2003

[6] M. Johnson, "Beam-based Diagnostics of RF-breakdown in the Two-beam Test-stand in CTF3", *CERN CLIC Note 710* (2007)

[7] R. Ruber and V. Ziemann, "An Analytical Model for PETS Recirculation", *CERN CTF3 Note 092* (2009)

[8] V. Ziemann, "Data Analysis for PETS Recirculation", *CERN CTF3 Note 094* (2009)

[9] E. Adli, "Analysis of the first 12 GHz PETS tests with beam using a constant parameter recirculation model", *CERN CTF3 Note 096* (2009)

[10] E. Adli, "Techniques for the estimations of beam energy loss in the TBTS PETS, applied to the first 12 GHz PETS tests with beam", *CERN CTF3 Note 097* (2009)

[11] Igor Syratchev and Erk Jensen, private communication

BEAM DIAGNOSTICS FOR SPIRAL2 RNB FACILITY

P. Anger, T. Andre, A. Delannoy, E. Gueroult, B. Jacquot, C. Jamet, G. Ledu, A. Savalle,
F. Varenne, J.-L. Vignet, GANIL, Caen, France, J-M. Fontbonne, N. Orr, LPC, Caen, France

Abstract

The SPIRAL2 project is based on a multi-beam driver facility in order to allow both ISOL and low-energy in-flight techniques to produce intense radioactive ion beams (RIB) in a new Facility. A superconducting linac capable of accelerating 5-mA deuterons up to 40 MeV is used to bombard both thick and thin targets. These primary beams will be used for the RIB production by several reaction mechanisms (fusion, fission, etc.) The production of high intensity RIB will be based on fission of uranium target induced by neutrons.

These exotic particles will be produced, ionized, selected in a dedicated production building and transported to the existing CIME cyclotron for post acceleration. After this, they will be used in the present experimental area of GANIL. The construction phase of SPIRAL2 was officially started in 2005.

The beam diagnostics for the production facility allow a pre-tuning with a stable beam followed by an extrapolation to the radioactive beam. Some diagnostic devices may also provide for equipment protections and for the safety systems.

An overview is presented of the diagnostics which will allow tuning and control of the RIB in this new production facility.

SPIRAL2 RNB FACILITY

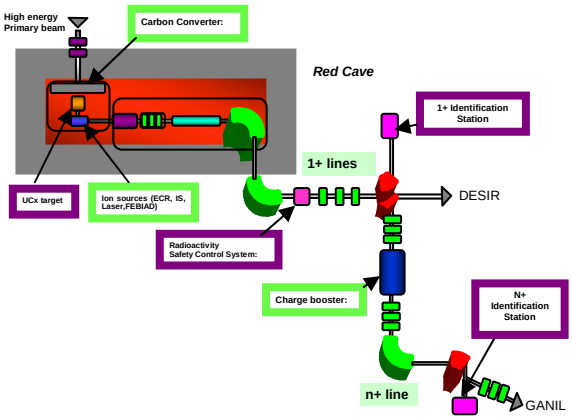


Figure 1: RNB general scheme.

The RNB facility will produce, from a high intensity primary beam, radioactive ion beam in a red radiological cave. The production of high intensity RIB will be based on fission of uranium target induced by neutrons. The mono-charged secondary beams will be selected in the 1+ beam line, used for low energy experiment or multi ionized to be post accelerated in the existing Ganil.

TUNING AND CONTROL METHODS

The tuning principle of the SPIRAL2 beams consists of pre-tuning with a stable beam followed by an extrapolation to the radioactive beam.

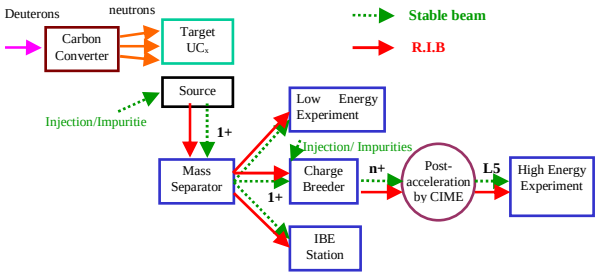


Figure 2: Stable beam tuning and R.I.B. tuning.

PRELIMINARY TUNING IN STABLE BEAM

Beam Intensity Measurement

Measurement of the beam intensity in the lines is based on the use of Faraday cups (Fig. 3) and a linear current to voltage converter. Their measurement dynamics extends from 10^9 pps up to I_{max} (P<50W) with an absolute accuracy of a few percent.

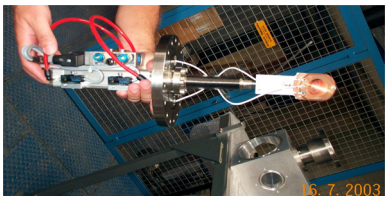


Figure 3: Faraday cup.

Beam Profile and Position Measurement

The measurement of the beam transverse profile in the lines is carried out by secondary emission multiwire profilers (Fig. 4). The principle is based on electron emission under the impact of the beam on wires. The range measurement is 10^9 pps – 10^{13} pps for energy from some keV to 25 MeV/A and the absolute positional accuracy is better than 1 mm.

It gives transverse profile dimensions and the gravity centre of the beam along a horizontal and vertical axis. This information will be distributed via electronic processing according to Ethernet or MODBUS protocol with the Spiral2 Command-Control.

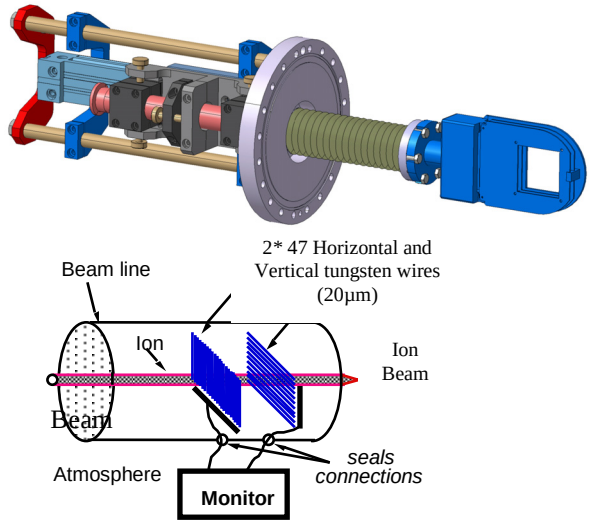


Figure 4: Secondary emission multiwire monitor, principle and picture.

For Spiral2 facilities, electronics components will be far away from the sensor to be protected from the radiation. Studies will therefore have to be conducted on a new electronic device with a length of approximately 20 m of cables (Fig. 5).

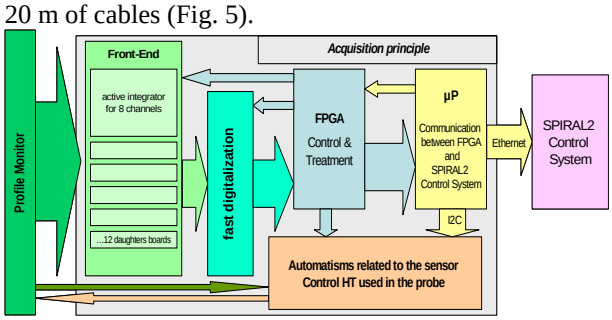


Figure 5: Spiral2 profiler acquisition principle.

RADIOACTIVE ION BEAM TUNING

Low Beam Intensity Measurement

Electrical Measurement. The intensity measurement will have to be carried out using a Faraday cup with logarithmic current/voltage converter, like that used on the SPIRAL1 facility. Their measurement dynamics extend from some 10^7 to 10^{14} pps. This Faraday cup has electric shielding to measure weak beam intensity over a large dynamic range.

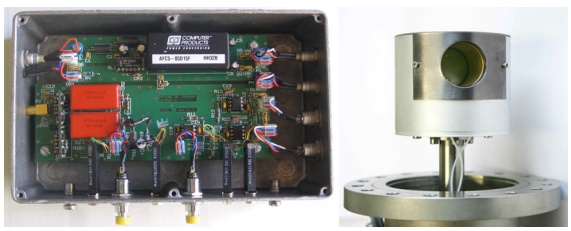


Figure 6: Faraday Cup views and logarithmic converter for low beam intensity.

Beam Radiation Measurement. In the case of "routine intensity measurement" in beam lines, it will be possible to use devices containing implantation foil and semiconductors to measure the beam radioactivity (gamma radiation) and control the transmission in the beam line.

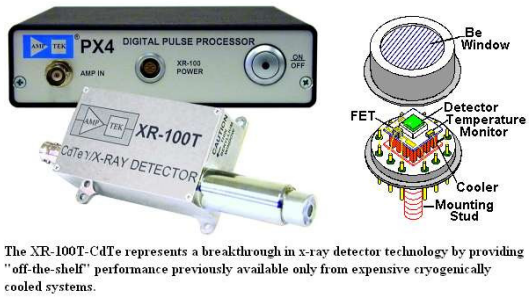


Figure 7: CdTe detector.

These interesting devices are under development at Ganil (resolution: 0.8 % FWHM at 662 keV).

Beam Profile Measurement

Secondary Emission Foil Profiler. Profilers with emissive foil and micro-channel plates will also allow measurement of the transverse profile after CIME, with no lower energy limit. This is a **low intensity** beam profile monitor. The principle is a collection of the secondary electrons in a drift space which are amplified with an MCP stage and collected on an x-y grid for a required resolution of 1 mm. They are currently under development at GANIL (Fig. 8).

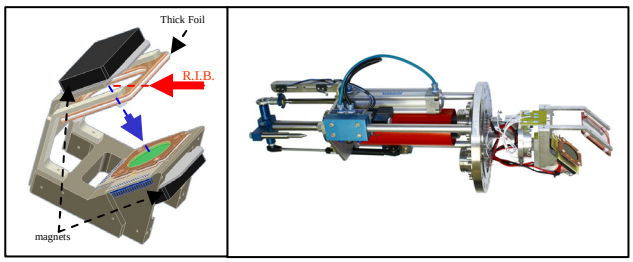


Figure 8: Secondary emission foil profiler: principle and view.

The last Ganil tests results show good performance with high energy beam (5 Mev/A) with a wide range of intensities (10 to 10^{11} pps). The tests will also have to show that this device can measure with a low energy beam in the 1+ and n+ lines of Spiral2 (E < 10 keV/A). Consequently, the configuration of the electric and magnetic fields will have to be extensively optimised to ensure correct guidance of the detected electrons.

Very Low Intensity and Low Energy Profiler. To control the radioactive beam in the low energy line of Spiral2, beam localisation and beam quantification should be carried out. When there is no stable beam pollution, beam detection with electric charge measurement is possible. One solution with weak beam energy would consist in direct interaction of the beam with a micro-

channel plate without emissive foil. This development will start in 2010.

Secondary Emission Multiwire Profiler with Gas Circulation for Post Accelerated Beam. Transverse beam profile measurement in the lines after existing CIME cycloton will be carried out, in most cases, by profilers with gas circulation. The principle is like a gas ionisation chamber. The low limit for this profiler is due to the thickness of the input window. This sensor is under development and the results are very good: Résolution better than 1mm for 10^2 to 10^6pps with a gas pressure of 10mbar of C4H10 or C3F8 and with an input window thickness of 6um of Mylar.

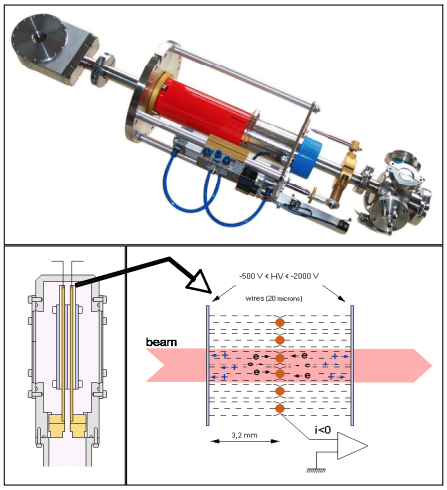


Figure 9: Gas Profiler: view and principle.

DIAGNOSTIC FOR RADIOLOGICAL DOSE CONTROL BY BEAM INTENSITY MEASUREMENT

Beam intensity measurement by electric charge measurement is a possibility which has been studied. If the pollution by a stable beam is not too high, it would be interesting to use electric charge measurement to take a flow measurement on line, thereby limiting the activity downstream. For this, three solutions are studied.

Beam Current Transformer

It is designed for non-destructive measurement.

The coil transformer only measures magnetic field variations so beam modulation is necessary. Since the best measurement resolutions at GANIL for these sensors are of the order of nAe (≈10^{10} pps), an absolute threshold under all conditions lower than ≈10^{11} pps cannot be guaranteed.

Pick-Up

For this measurement, beam modulation is necessary too. The best measurement resolutions for these sensors at low energy (20 keV) are of the order of 10nAe (≈10^{11} pps), an absolute threshold under all conditions lower than ≈10^{12} pps cannot be guaranteed.

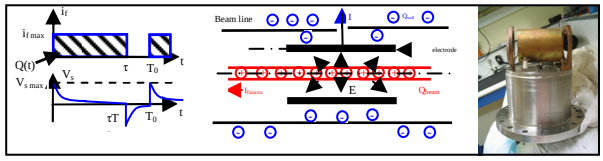


Figure 10: Views of the GANIL pick-up.

Faraday Cup Associated With a Fast Electrostatic Deflector

In order to provide users with a beam which is as continuous as possible, a device equipped with an electrostatic deflector in front of a low intensity Faraday cup which integrates the average intensity could be installed. This electrostatic deflector could deflect, for example, at a frequency of 1 kHz, with a useful ratio for measurement of 5 %, leaving 95 % of the continuous beam for the users (Fig. 11).

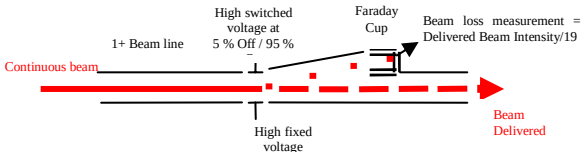


Figure 11: Faraday cup associated with a fast electrostatic deflector.

In this case, a Faraday cup resolution of 2 pAe, by guaranteeing the "deflector" function, provides an indirect resolution of 36 pAe on the beam users. This device could control and guaranty in all circumstances a user beam threshold of about 360 pAe (2*10^9 pps). It is sufficient.

CONCLUSION

The feedback of the Ganil and Spiral1 operation is a major factor contributing to optimum design of the Spiral2 facility and definition of the beam tuning methods. The beam diagnostic definition benefits from this feedback. Some Spiral1 diagnostics will be reused; others are in development.

However all diagnostics will have to answer:

- new and strong nuclear environment requirements (remote handling, simplicity, robustness, reliability),
- requirement for behaviour at high vacuum (low degassing rate at a pressure of 10^{-8} mbar in order to limit the beam losses in the n+ line).

REFERENCES

[1] M. H. Moscatello et al., Technical report of the radioactive beam section of SPIRAL2. Ganil report (2007, DECEMBER).

BEAM DIAGNOSTICS IN THE CNAO INJECTION LINES COMMISSIONING

G. Balbinot, C. Biscari, J. Bosser, E. Bressi, M. Caldara, L. Lanzavecchia, M. Pullia, A. Parravicini, M. Spairani, CNAO, Milan, Italy

Abstract

The CNAO, the first Italian synchrotron for deep hadrontherapy [1-2], is presently in its final step of installation. It will deliver beam of both, Protons and Carbon ions, in three treatment rooms in order to treat solid tumours with active scanning technique.
CNAO beams are generated by two ECR sources [3], able to produce both particle species, and transferred to a RFQ and a LINAC through a Low Energy Beam Transfer line (LEBT) at 8 keV/u and then accelerated up to 7 MeV/u before being injected in the synchrotron ring [4].

A compact and versatile tank containing a complete set of beam diagnostic tools has been intensively used for the LEBT line commissioning successfully concluded in January 2009. In a length of 390mm, the tank houses two wire scanners, aimed to measure vertical and horizontal beam position and transverse profile, a Faraday Cup, for beam current measurement, and two vertical and horizontal metallic plates for beam halo suppression, emittance measurements, beam collimation and particles selection.

Using one tank only, phase space distribution reconstruction can be quickly performed as well as synchronous profiles and intensity measurements.
Five identical tanks are installed in the LEBT line [5], as consequence of a standardization strategy to improve diagnostic monitor knowledge and make maintenance easier.

LEBT LINES GENERAL DESCRIPTION

LEBT lines Beam Diagnostic (BD) elements are schematized in figure 1: the two sectors, called O1 and O2, are dedicated to the respective source and are both equipped with two diagnostic tanks and one 90° dipole spectrometer in order to make the tuning of each source independent from the use of the second one. When one of the Faraday cups upstream the first quadrupole triplet is inserted, the source can be monitored without interfering with the operation of the other one. Beam parameters can be measured also before the spectrometer dipole. The two sectors called L1 and L2, common for both the lines, include the beam injection chopper and a special Faraday cup (CFC) for beam current intensity monitoring.

BD INSTRUMENTATION

Slits

Four Copper plates compose the slits: working two by two the plates create vertical and horizontal slits dedicated to beam scanning, phase space distribution measurements and particle specie selection (downstream the spectrometer).

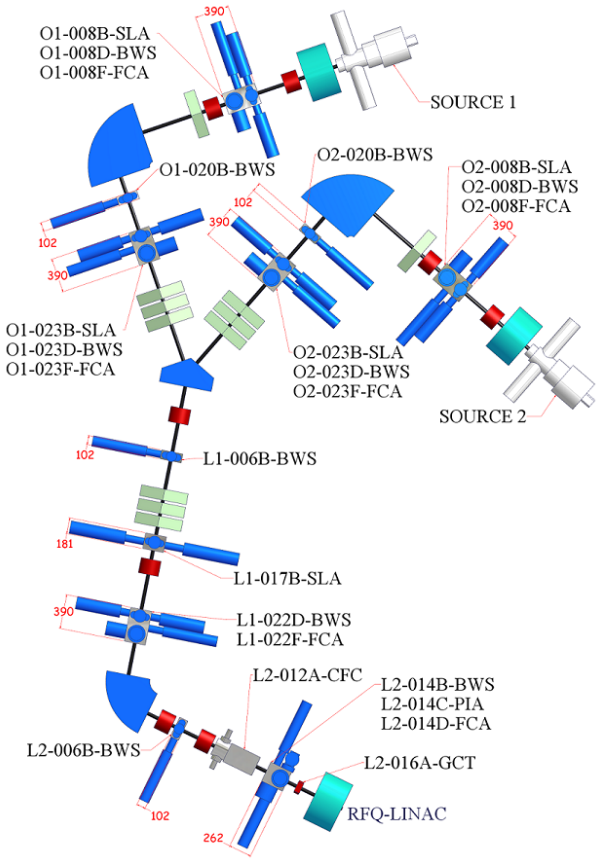


Figure 1: LEBT BD Instrumentation Layout with elements names. SLA are Slits, BWS are Wire Scanner in both planes, FCA is Faraday Cup, CFC is the Chopper Faraday Cup, PIA is Profile Grid and GCT is a current transformer.

Moreover, the plates positioning around the beam allows the beam halo suppression. Slits plates are 1mm shifted longitudinally in order to allow their overlapping; they are also water cooled to dissipate the large beam power (360W). Each plate is driven by a brushless motor at the maximum velocity of 250 mm/s with a position accuracy of about 20 µm: absolute position is read through a linear potentiometer. Secondary electrons emitted as a result of interaction between the beam and the plates can be suppressed by polarizing the plates up to 1kV.

Wire Scanner (WS)

Each 390 mm LEBT tank houses two WSs, one horizontal and one vertical, which can be used to get the beam profile, and in consequence its barycentre, in scanning mode or to measure the beam position stability in watch-dog mode once positioned at the beam border. Beam profiles are computed after having synchronously acquired wire position versus wire current: the motion mechanics is identical to the slits one so the same kind of potentiometer is acquired with the same results in terms of accuracy and resolution. The wire is made of 0.1 mm diameter tungsten wire: one of the two ends is connected to a custom multi-gain amplifier which measures current signals from 1 nA to 1 mA at the maximum frequency of 400 Hz.

Faraday Cup (FC)

The last installed element in the LEBT 390mm tank is a FC made with a Copper round 135 mm diameter cup moved by a pneumatic actuator: it can be used as beam stopper to close, for example, line O2 when the particle specie coming from O1 is required or to measure the beam current and ripple. If coupled with the upper stream slits the FC can performs profiles as well. A repeller ring electrode in front of the cup pushes back secondary emitted electrons while an extra grounded metallic ring between the repeller and the cup avoids that leakage currents deteriorate the beam intensity measurement. LEBT beam is continuous and its intensity is up to 15mA, before species selection; by consequence, the cup is water cooled in order to dissipate the beam power which can be up to 360W. The cup is directly connected to a custom multi-gain amplifier which has a bandwidth up to 15 kHz and a dynamic range from 100 nA to 100 mA.

EXPERIMENTAL RESULTS

Faraday Cup (FC)

The primary use of the FC is the beam current measurement, which is reliable once the effect due to the electrons back scattering is suppressed applying a voltage to the repeller ring. Figure 2 reports the beam current read on the FC versus the voltage applied to the ring: the correct intensity measurement is made by setting the voltage at -350V (or above).

A 390mm tank is also mounted downstream the chopper (tank called L2-014 in Figure 1) where the beam is normally pulsed by the electrostatic chopper. The electronic chain connected to all the FCs has been designed in order to follow the nominal chopped signal as well: one pulse of 100 µs duration every 2 seconds (Figure 3).

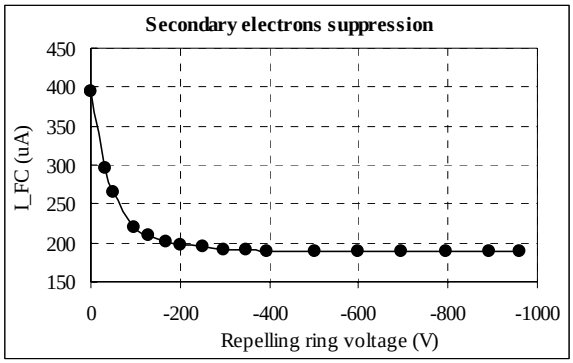


Figure 2: Secondary electrons suppression.

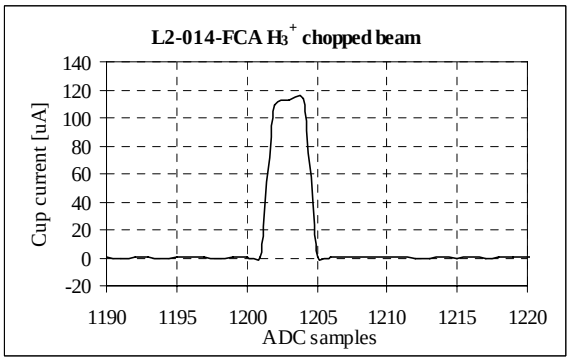


Figure 3: Chopped beam on FC acquired at 25 kHz.

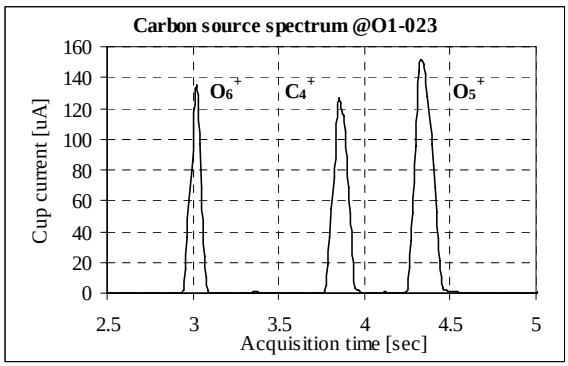


Figure 4: Carbon source spectrum obtained ramping the spectrometer during FC acquisition.

The FC called O1-023F-FCA just downstream the 90° dipole can be used to measure the source spectrum in two different ways: one is moving the upstream horizontal slit acquiring the current on the FC at all the positions; the other method is the acquisition during the dipole ramping current. Figure 4 reports the spectrum using this second procedure.

Wire Scanner (WS)

The two horizontal and vertical WSs, mounted on the 390mm tank, are used for beam profile, beam position and emittance measurements (once accomplished with the

upstream slits): in order to increase the statistic, profile measurement consists of two scans, one entering and one coming out the tank. Figure 5 reports the two overlapped scans of the same measurement.

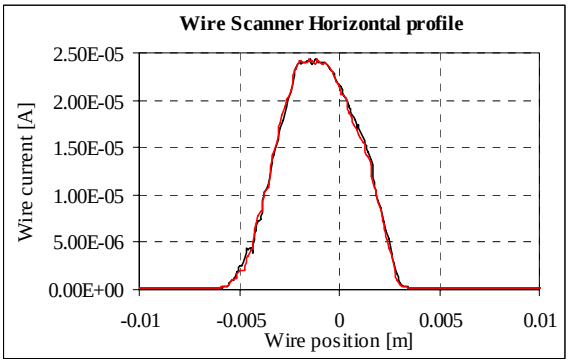


Figure 5: H_3^+ beam horizontal profile in the tank O2-023 with the horizontal plates positioned in ± 5mm respect to the vacuum pipe centre.

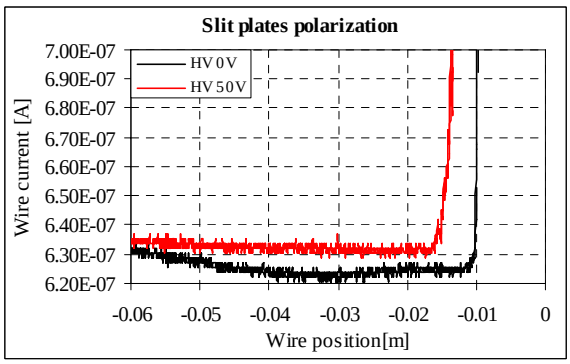


Figure 6: Zoom of two horizontal WS left end profiles for different Slit plates polarisation voltage with Carbon ions beam.

Another use of the WS mounted in the 390mm tank is the watch-dog mode where the wire stays in a fixed position, normally at beam border. In case the wire stays always at the beam centre at the maximum current, the measured wire temperature never exceeds 300 °C which is far from the Tungsten wire melting threshold.

Slit

The four plates of the 390mm tank are used as beam halo suppressor, as collimator for particle selections or as slits for emittance measurements. In order to minimize the effect of the secondary electrons emitted once hit by the beam, the copper plates are all connected to a high voltage power supply (0÷1000V, 30mA). Figure 6 reports the comparison of two horizontal profiles taken with the same WS having slit plates of the same tank polarized at 0V and at 50V. Exceeding 100V polarisation introduces distortions in beam trajectory and profiles.

CONCLUSION

In a single 390mm tank fully equipped with two WSs, four plates and a FC measurements of beam intensity, profile and source ripple can be performed. Moreover, combining different detectors of the same tank like WS and plates, horizontal and vertical emittance can be quickly measured. During LEBT line commissioning, the emittance was computed from a sequence of WS profiles for different positions of the upstream 1mm slit. With a slit step of 1 mm the measure, on one single axis, takes 15 minutes time. Figure 7 shows the vertical phase space distribution at the level of O1-023 tank. By using statistical emittance definition, RMS Twiss parameters and emittance value at 1 sigma are retrieved. The corresponding ellipse is draft on the plot with solid line. The dashed line ellipse is a reference ellipse the user can fix.

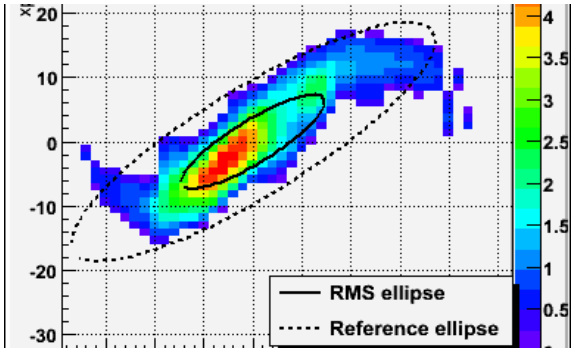


Figure 7: Vertical emittance (x, x') measurement obtained moving vertical slit from -30mm to +30mm and keeping horizontal plates at -5mm and +25 mm in order to select H_3^+ peak and stop all the other species.

REFERENCES

[1] S. Rossi, "Developments in proton and light-ion therapy", EPAC 2006.

[2] M.Pullia, "Status Report on the Centro Nazionale di Adroterapia Oncologica (CNAO)", EPAC 2008.

[3] S. Gammino, L. Celona, G. Ciavola, F. Maimone (INFN/LNS, Catania), R. Monferrato, M. Pullia, E. Vacchieri (CNAO Foundation, Milan), C. Bieth, W. Bougy, O. Tasset (PANTECHNIK, BAYEUX), "Commissioning of the ECR Ion Sources at CNAO Facility", EPAC 2008.

[4] H. Vormann, B. Schlitt (GSI, Darmstadt), G. Clemente, U. Ratzinger (IAP, Frankfurt am Main), S. Minaev (ITEP, Moscow), "RF Tuning of the IH-DTL for the CNAO Linac", EPAC 2008.

[5] J. Bosser, G. Balbinot, S. Bini, M. Caldara, V. Chimenti, L. Lanzavecchia, A. Parravicini (CNAO Foundation, Milan), A.Clozza, V. Lollo, INFN/LNF, Frascati (Rome), Italy, "A compact and versatile diagnostic tool for CNAO injection line", EPAC 2008.

BEAM DIAGNOSTICS AT THE ALBA LINAC

U. Iriso*, A. Olmos, and F. Pérez
CELLS, Ctra. BP-1413 Km 3.3, 08290 Cerdanyola, Spain

Abstract

The commissioning of the ALBA Linac (Autumn 2008) required a careful measurement of the beam parameters. This paper describes the diagnostics devices installed at the ALBA Linac and our experience with them.

INTRODUCTION

The ALBA Linac was supplied by Thales Communications and installed in Spring 2008 at the CELLS site. The installation of the first part of the transfer line Linac to Booster (LTB) and the Diagnostics Line (Lidia) was done simultaneously under the CELLS responsability. The Linac beam commissioning was performed in Autumn 2008. More details about the Linac installation and commissioning are found at Refs. [1, 2].

The Linac is designed to work in two operational modes: Single and Multi Bunch Mode (SBM and MBM, respectively). In SBM, the Linac delivers up to 8 pulses with a bunch spacing that can range between 6 and 50 ns, and a maximum charge of 2 nC total. In MBM, it provides a train between 112 and 1024 ns length with a maximum charge of 4 nC and a fixed bunch spacing of 2 ns. The Linac specifications are listed in Table 1.

Table 1: Linac Parameters. The acronym "ptp" refers to "pulse-to-pulse" variation (rms).

Parameter	SBM	MBM
# of bchs	1 ... 8	56 ... 512
pulse length, ns	≤ 1	112 - 1024
bch spacing, ns	6 - 50	2
charge, nC	≥ 1.5	≥ 3
Bunch purity	$\leq$1%	...
pos. stability* ptp	$\leq$0.2 mm	$\leq$0.2 mm
energy, MeV	$\geq$100	$\geq$100
energy spread	$\leq$0.5%	$\leq$0.5%
energy var. ptp	$\leq$0.25%	$\leq$0.25%
norm. emit, μrad	$\leq 30\pi$	$\leq 30\pi$

Figure 1 shows a sketch of the Linac, LTB and Lidia with the diagnostics systems. Thales responsibility ends after the diagnostics elements installed downstream the second accelerating structure. All components installed after that are CELLS responsability and their goal is to check whether the Linac fulfills the required specifications.

This paper shows the diagnostics components installed at the LTB and Lidia to check the main beam parameters, that is: beam charge, position, and size. Description of the emittance, energy and energy spread measurements is shown in Refs. [2, 3]. Figure 2 shows a picture with the diagnostics devices in the Linac and LTB, which will be seen throughout the text.

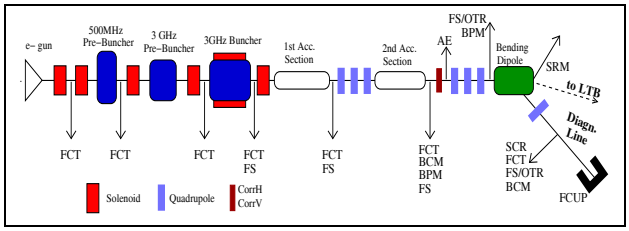


Figure 1: Sketch of Linac and LTB, with the diagnostics location.

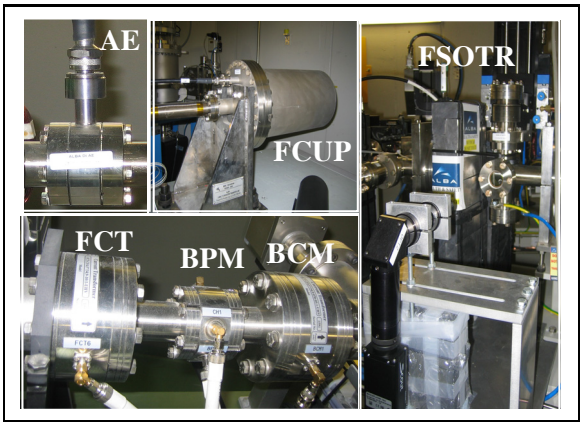


Figure 2: Diagnostics components at the Linac and LTB.

BEAM CHARGE MEASUREMENTS

Beam charge measurements are done using the commercially available Fast Current Transformer (FCT) and Beam Charge Monitors (BCM) [4], and with in-house designs manufactured by Cinel: Annular Electrode (AE) and Faraday Cup (FCUP).

Fast Current Transformers

Fast Current Transformers (FCT) are installed after each active element in the Linac and LTB (see Fig. 1). In total, we have 8 FCTs to monitor the transfer efficiency along the line, and they all have been very useful throughout the Linac commissioning.

Our model is the FCT-CF4"1/2-34.9-40-10:1, with a frequency range 5 kHz - 1.4 GHz. This limited frequency range implies that: 1) precise beam charge measurements

* ubaldo.iriso@cells.es

should not be performed with this device, but use the BCM instead; and 2) the influence of the 3 GHz bunching system cannot be precisely distinguished. For this, we will better use the AE – see next.

Beam Charge Monitors

The Beam Charge Monitors (BCM) measure the charge of very fast pulses with high accuracy (resolution at the pC level) by means of a capacitively shorted transformer coupled to a fast readout transformer in a common magnetic circuit [4].

The BCM is composed by an Integrating Current Transformer (ICT) installed at the vacuum chamber and the integrating electronics card. The ICT model is ICT-CF4"1/2-34.9-40-05:1, the electronics card model is BCM-IHR-E. Both components are "off-the shelf" units calibrated together to allow charge measurements with pC precision.

Their commissioning required due care with the timing signal, and filter out the klystron noise. The latter was a cumbersome task. Figure 3 shows the noise in the ICT with no beam in the Linac but with the klystron "on". This signal is produced by ground loops from/to klystrons, and as a result, the charge inferred by the BCM has an rms noise 150 pC. These ground loops were finnally suppressed wrapping the signal cable around a ferrite coil. Only then the rms noise could be decreased then to 4 pC – see Fig. 4.

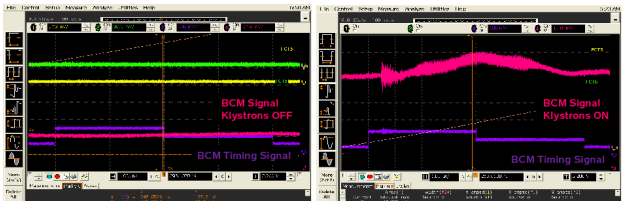


Figure 3: BCM signal with klystrons off (left) and on (right). The pink trace shows the raw ICT signal (before integration by the BCM-IHR-E). Integration by the BCM card the klystron noise produces the 150 pC rms noise shown in Fig. 4.

Annular Electrode

The advantage of the AE with respect to the Current Transformers is its sensitivity and larger bandwidth, which allows to distinguish low beam charges. However, they must be calibrated using the BCM. The AE signal is connected to a 4 GHz scope to see the 3 GHz Linac component in case of phase mismatch. In any case, the scope uses a 10 dB attenuator because the AE signals can be larger than 10 V.

The large AE signals are used to perform bunch purity measurements. Unfortunately, they are limited by ripples and cable reflections to a 2.5%.

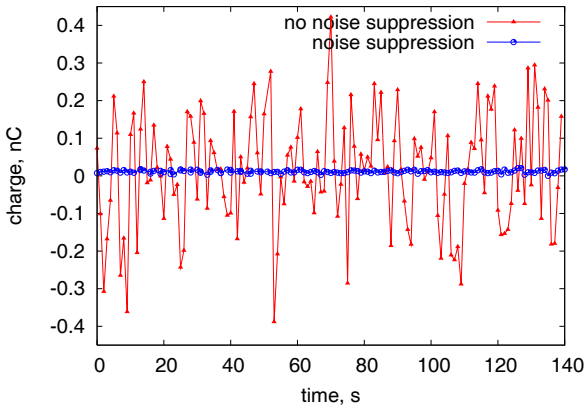


Figure 4: BCM measurements with no beam in the Linac and with klystrons "on", with and without noise suppresion. The rms variation without noise suppression is ±150 pC, with noise suppression is only ±4 pC.

Faraday Cup

The FCUP is the last component at the Diagnostics Line and it is mainly designed as beam stopper. Therefore, it is optimized for charge collection efficiency rather than bandwidth.

The charge measured from this device is calibrated according to the measures of the BCM. The peak-to-peak voltages measured with both AE and FCUP are about a factor 5 larger than the ones measured by the FCTs (see Fig. 5). As the AE, the FCUP signal was attenuated by 10 dB to protect the scope.

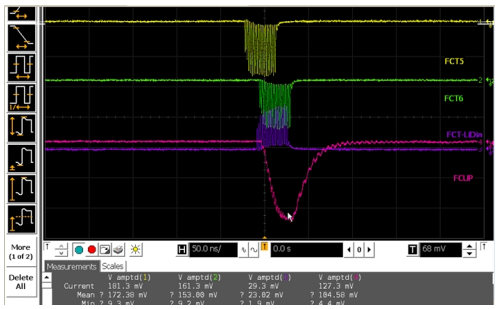


Figure 5: FCUP measurements compared with FCT signals. The FCT-Lidia signal is inverted because the coil is installed backwards.

BEAM TRANSVERSE PROFILES AND POSITION

The Linac specifications required a beam position stability "within a 10% of beam size". Transverse size and position are measured with the Fluorescent Screen and Optical Transition Radiation monitors (FSOTR). Beam position is measured as well with the Beam Position Monitors (BPM).

Fluorescent Screen and OTR

The transverse beam spatial distribution is measured using the "FSOTR". This setup allows to introduce into the beam's path two kind of screens, which emit light upon collision with the electron beam. The first screen is a YAG:Ce screen that emits light by scintillation, the second is an Al-foil that emits transition radiation. The light is finally brought to the CCD camera using an optical system. More details about this monitor can be found at Ref. [5].

The optical calibration was set individually for each FSOTR monitor using reference marks at the screens. Typically, this was 1 pixel = 20μm. However, the absolute position inside the vacuum chamber could not be precisely calibrated. An example image of the beam out of the Linac with the downstream quadrupoles "off" is shown in Fig. 6.

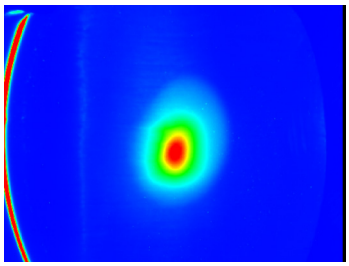


Figure 6: Image of the beam out of the Linac. The picture size is ∼20x16 mm.

Figure 7 shows two histograms of the vertical beam centroid's position (left) and the corresponing vertical beam size (right) inferred using the FSOTR. The absolute vertical position is not properly calibrated and an arbitrarly offset has been substracted.

We can see that the rms displacements in the vertical direction are ±0.04 mm (rms). For an average beam size of $\sigma_y = 1.94 \pm 0.02$ mm (see Fig. 7, right), we conclude that the vertical stability is 2%, much lower than the specified 10%. A similar analysis in the horizontal plane results in a position stability below 1%.

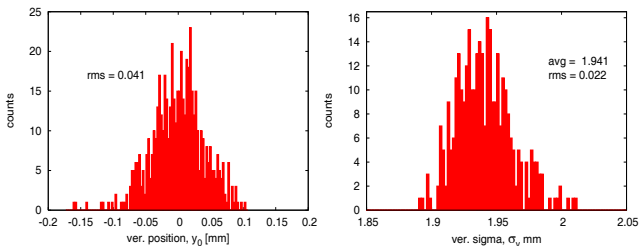


Figure 7: Variation of beam centroid (left) and size (right) inferred using the FSOTR after 700 samples.

Beam Position Monitors

Beam transverse position using the FSOTR are found with good precision, but its drawback is that it is a destructive method. It is therefore convenient to measure the beam position using the 4-buttons BPM.

Most difficulties regarding the BPMs commissioning were related to the proper electronics timing. Once this was achieved, horizontal and transverse position were obtained with an rms noise of $\pm$ 70μm – see Fig. 8. However, this noise can increase by about a factor 3 in case of for low charge beams (around 0.25 nC).

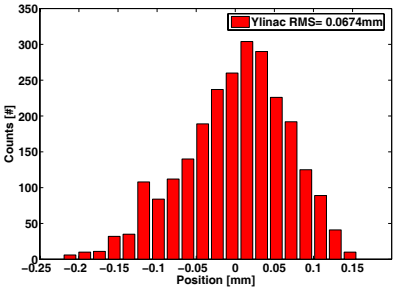


Figure 8: Beam position variation measured with the BPM after 2500 samples with a MBM of 4 nC.

SUMMARY

The experience with the diagnostics components at the ALBA Linac and LTB are presented. All in all, our experience with these devices and their commissioning is good and they allow a proper beam Linac commissioning. Only the bunch purity could not be measured with the proper precision. We would like to highlight that:
1) The charge measurements using the BCM is set to $\pm$ 4 pC after noise suppression.
2) Relative position pulse-to-pulse are better obtained with the FSOTR ($\pm$ 40 μm) than with the BPM ($\pm$ 70 μm).
3) Due care shall be taken with the FCUP and AE because their large signals compared with the FCT signals can damage the scope.

ACKNOWLEDGMENTS

We are very grateful for the engineering support of M. Cornelis, the work of the Controls Group, and help from the Linac Commissioning team.

REFERENCES

[1] A. Falone et al. *Status of the 100 MeV preinjector for the ALBA Synchrotron*, Proc. of EPAC08, Genoa (Italy), 2008.

[2] A. Setty et al. *Commissioning of the 100 MeV preinjector for the ALBA Synchrotron*, Proc. of PAC09, Vancouver (Canada) 2009.

[3] G. Benedetti, U. Iriso and A. Olmos. *Beam measurements at the ALBA Linac*, Proc. of PAC'09, Vancouver (Canada) 2009.

[4] http://www.bergoz.com/

[5] U. Iriso, G. Benedetti, and F. Pérez. *Experience with the YAG and OTR screens at ALBA*, in these Proceedings.

DIAGNOSTICS OVERVIEW FOR THE TAIWAN PHOTON SOURCE

K.T. Hsu, C. H. Kuo, K. H. Hu, C.Y. Wang, NSRRC, Hsinchu 30076, Taiwan

Abstract

A new high brilliant 3 GeV storage-ring-based light source - Taiwan Photon Source (TPS), is planned to be built at National Synchrotron Radiation Research Center. Various diagnostics will be deployed to satisfy stringent requirements for commissioning, operation, and top-off injection of the TPS. Specifications and overview of the planned beam instrumentation system for the TPS are summarized in this report. The efforts including diagnostic devices and subsystems will be addressed also.

INTRODUCTION

The TPS project will be a state-of-the-art synchrotron radiation facility featuring ultra-high photon brightness with extremely low emittance. It consists of a 150 MeV S-band linac, linac to booster transfer line (LTB), 0.15–3 GeV booster synchrotron, booster to storage ring transfer line (BTS), and 3 GeV storage ring. Latest generation diagnostic systems will equip TPS to fulfill its design goals. The storage ring has of 24 DBA lattices cells. It is a 6-fold symmetry configuration. The main beam diagnostics related parameters for the storage ring are shown below in Table 1.

Table 1: Major Parameters of the TPS Booster Synchrotron and the Storage Ring

	Booster Synchrotron	Storage Ring
Circumference (m)	496.8	518.4
Energy (GeV)	150 MeV – 3 GeV	3.0
Natural emittance (nm-rad)	10.32 @ 3 GeV	1.6
Revolution period (ns)	1656	1729.2
Revolution frequency (kHz)	603.865	578.30
Radiofrequency (MHz)	499.654	499.654
Harmonic number	828	864
SR loss/turn, dipole (MeV)	0.586 @ 3 GeV	0.85269
Betatron tune ν_x/ν_y	14.369/9.405	26.18 /13.28
Momentum compaction (α_1, α_2)	-	2.4×10^{-4}, 2.1×10^{-3}
Natural energy spread	9.553×10^{-4}	8.86×10^{-4}
Damping partition $J_x/J_y/J_s$	1.82/1.00/1.18	0.9977/1.0/ 2.0023
Damping time $\tau_x/\tau_y/\tau_s$ (ms)	9.34/ 16.96 / 14.32	12.20/ 12.17 / 6.08
Natural chromaticity ξ_x/ξ_y	-16.86/-13.29	-75 / -26
Dipole bending radius ρ(m)	-	8.40338
Repetition rate (Hz)	3	-

To realize the benefits of the high brightness and small sizes of TPS sources, photon beams must be exceedingly stable both in position and angle to the level of better than 10% of beam sizes and divergence. Table 2 provides the electron beam sizes and angular divergences for selected TPS sources. The most stringent beam measurement and stability requirement will be for the vertical position at the 7 m straight for ID source (σ_y = 5.11 μm); this will require special consideration for measuring both electron and photon beams.

Table 2: The Electron Beam Sizes and Divergence

Source point	σ_x (μm)	$\sigma_{x'}$ (μrad)	σ_y (μm)	$\sigma_{y'}$ (μrad)
12 m straight center	165.10	12.49	9.85	1.63
7 m straight center	120.81	17.26	5.11	3.14
Dipole (1^o source point)	39.73	76.11	15.81	1.11

LINAC DIAGNOSTICS

The TPS 150 MeV linac system was contracted to the RI Research Instruments GmbH (former ACCEL Instruments GmbH) in December 2008 [1]. The delivery schedule is around the border of 2010/2011. Beam instrumentation comprises five YAG:Ce screen monitors for beam position and profile observation, two fast current transformers (FCT) to monitor the distribution of charge and one integrating current transformer (ICT) for monitoring total bunch train charge. Wall current monitors (WCM) formed by equally spaced broadband ceramic resistors mounted on a flexible circuit board, wrapped around a short ceramic break, will also give information on beam charge as well as longitudinal profiles of electron bunches. Linac diagnostics are summarized in Fig.1 and Table 3. All of these mentioned diagnostics will be provided by the vendor. Acceptance test of the linac system will be performed at a temporary site near the TPS main building before its completion and move to the TPS building later. It is also planned that beam position monitors (BPM) might be added between accelerator sections are also planned. These BPMs will be useful for RF phasing monitoring, feedback control and on-line beam position jitter observation.

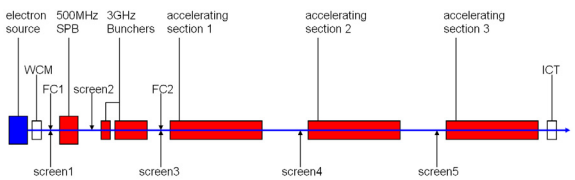


Figure 1: Functional block diagram of the linac diagnostic devices.

Table 3: Linac Diagnostics

Monitor	Quantity	Beam parameters
YAG:Ce screen	5	Position, profile
WCM	1	Intensity distribution
FCT	2	Intensity distribution
ICT	1	Charge at exit of the linac

TRANSFER LINE DIAGNOSTICS

Planned diagnostics for the LTB and the BTS [2] are summarized in Table 4 and 5 respectively. The YAG:Ce fluorescence screens will provide information on beam position and profile. The OTR screens are also considered to be used for high precision of beam emittance and energy spread measurement at the diagnostic branch of the LTB and at selected position of the BTS to avoid saturation of YAG:Ce screens. Integrating current transformer will provide information of beam charge pass LTB and BTS and hence on the beam losses during the injection cycle. The beam trajectory will be monitored with beam position monitors equipped with Libera Brilliance Single-Pass [3], its functionality is similar as the BPM electronics for the booster and the storage ring but is equipped with high gain analogue board to improve its performance for single pass measurement.

Table 4: LTB Diagnostics

Monitor	Quantity	Beam parameters
YAG:Ce/OTR screen	6	Position, profile (1 at diagnostic branch). OTR screen will be adopted for the site of high precision profile measurement to avoid saturation of YAG:Ce screen.
FCT	2	Beam intensity
ICT	1	Beam charge
BPM and single pass electronics	7	Beam position
Energy define slits	1	1 pair of horizontal blade

Table 5: BTS Diagnostics

Monitor	Quantity	Beam parameters
YAG:Ce/OTR screen	3	Position, profile, booster extraction beam emittance.
FCT	1	Beam intensity
ICT	1	Beam charge
BPM and single pass electronics	6	Beam position, relative intensity.

BOOSTER DIAGNOSTICS

Booster [4] diagnostics will provide beam parameters including orbit, working tunes, circulating current and filling pattern, emittances for both planes, bunch length. Planned diagnostics are summarized in Table 6. Fluorescent screens will be installed at injection and extraction section and at the other lattice cells to facilitate booster commissioning, troubleshooting and psychology needing – to see is to believe. The screen material will be YAG:Ce, which has excellent resolution of the beam image and exhibits high sensitivity and high radiation hardness. Booster orbit will be monitored with 60 BPMs with turn-by-turn capability. The BPM electronics will be the same as in the storage ring to simplify maintenance. The sum signal from the receivers can be used to monitor fast history of the beam current.

Circulating current will be measured with Bergoz's NPCT, while bunch pattern will be monitored with a fast current transformer. For tune measurement, the electron beam will be excited with white noise using striplines. The beam response will be observed with a real-time spectrum analyzer connected to the dedicated BPM buttons with the front end. There will be an extra set of striplines for a bunch cleaning system, for users who need a specific filling pattern in the storage ring. Synchrotron radiation from a dipole will be used to observe the beam profile during energy ramping and emittance measurements. The capability to monitor bunch length with a streak-camera will be also provided.

Table 6: Booster Synchrotron Diagnostics

Monitor	Quantity	Beam parameters
NPCT	1	Averaged beam current
FCT	1	Filling pattern
BPM (4 button pick-ups)	60	Beam position
Set of striplines and amplifiers	2	Betatron tune, bunch cleaning system.
YAG:Ce screen (Fluorescent screen)	6	Beam profile and position at injection, extraction, and every lattice cells.
Synchrotron light monitor, profile and streak camera (visible light)	1	Beam size (emittance), bunch length.
Bunch cleaning system	1	-

STORAGE RING DIAGNOSTICS

The beam diagnostics system is designed to provide a complete characterization of the beam and the TPS storage ring [5], including beam closed orbit, size, tune, circulating current, filling pattern, lifetime, chromaticity, beam loss pattern, beam density distribution, emittance, and bunch length. A large number of beam monitors and devices will be installed in the storage ring. The types and quantities of these devices are given in Table 7.

A high precision DC current measurement will be provided by Bergoz's NPCT. The NPCT device provides a resolution of better than 1 $mA/Hz^{1/2}$ and has large dynamic range/ bandwidth, making it a versatile device for measuring lifetime and injection efficiency. Filling pattern of the storage ring observed from the sum signal of BPM buttons by wide bandwidth fast digitizer sampling at RF or a multiple of RF frequency, will enable measurement of the fill charge distribution of each bunch to better than 0.5% accuracy. This information is sufficient for filling pattern control in top-up operation and various studies. Each cell will have five standard RF BPMs mounted on elliptical chambers, up to two primary RF BPMs located in the ID straight section mounted on racetrack chambers; and up to two X-ray photon BPMs (XBPM) per beamline. To achieve the highest level of orbit measurement resolution, the optimization of the

button geometry to obtain a high level of BPM resolution for both standard and primary BPMs is in progress. Prototype BPM equipped with 6.5 mm button diameter and 17.7 mm separations on the 60x30 mm elliptical chamber has been implemented. The BPM constant is around 13 mm in both planes were achieved with adequate linearity. The primary BPM is planned to install in 20 mm height racetrack chamber with monitor constants around 9 mm. BPM mounted on 11 mm small gap ID chamber is also considered. Striplines and a bunch-by-bunch feedback system is also in design phase.

Table 7: Storage Ring Diagnostics

Monitor	Quantity	Beam parameters
NPCT	1	Averaged beam current Beam lifetime
Sum signal of BPM buttons	1	Filling pattern Bunch current
BPM (4 button pick-ups)	168	7 BPM/cell
Set of striplines and amplifiers	2	Betatron tune, bunch cleaning system 2 sets, 1 set = 4 electrodes.
YAG:Ce screen (Fluorescent screen)	1	Beam profile and position just after injection septum
PIN diode type beam loss monitors	2 per cell	Beam loss pattern
Scintillation loss monitor	10	High counting rate or integrated type beam loss monitor
Scrapers	2 sets per plane	1 set = 2 blades

TPS will utilize a distributed beam loss monitoring system based on p-i-n diodes, which are commercially available. For the temporal distribution of the loss particles (on the scale of one turn) scintillation detectors will be used. These can also be used for monitoring the losses of injected electrons near the injection and RF straights.

Two pairs of two-plane adjustable-position scrapers will be installed on the ring to be used both as protective devices as well as diagnostics instruments for accelerator studies. One set of scrapers (H/V) will be installed in the dispersive section to measure the energy distribution of the electron beam. Another set will be installed in a straight section with zero dispersion in order to have information on the transverse size of the electron beam, and to eliminate possible beam halos capable of affecting the insertion devices.

The photon diagnostics for the TPS storage ring will utilize visible and X-ray synchrotron radiation generated in a bending magnet. Planned photon diagnostics devices are summary in Table 8. Visible light beamline will be built to measure various beam parameters by streak camera, CCD camera and interferometer. One or two X-ray pinhole cameras imaging the electron beam from bending magnets is the baseline design for the TPS emittance measurement. As they offer the required resolution and the dynamic range to accurately measure the electron beam size, typically 40x15 μm^2 for 1% coupling, at all currents from below 1 mA to 400 mA. Optimization of the X-ray pinhole system will give the possibility to measure very small beam sizes in a few microns typically. Its main function will be measurement of the electron beam energy spread and monitoring vertical beam size. Measuring the filling pattern by using time correlated single photon counting (TCSPC) method is also considered.

Table 8: Storage Ring Synchrotron Diagnostics

Monitor	Quantity	Beam parameters
X-ray pinhole camera	1	Emittance vertical and horizontal planes. Equilibrium profile Single turn profile Bunch-by-bunch profile.
Time correlated single photon counting system (Visible light or X-ray)	1	Filling pattern Isolated bunch purity
XBPM	1 or 2 per beamline	Position and angle of ID radiations
Visible light synchrotron light diagnostic station, Imaging and streak camera	1	Alternative beam size measurement (emittance), either imaging the vertical polarized synchrotron light or interfereometer.
Streak camera	1	Bunch length

SUMMARY

Beam diagnostics plans for the TPS project are summarized in this report. Detailed design is underway. The critical diagnostic systems, addressing beam stability and low emittance monitoring, are being investigated in the design phase. Delivering a best diagnostics system to satisfy stringent requirements of TPS is the goals.

REFERENCES

[1] Document 2008–BP-8067, “TPS Linac Technical Design Report”, ACCEL Instruments GmbH.
[2] P.J. Chou, et al, “ Design Status of Transfer Lines in TPS”, Proceedings of the PAC09.
[3] I-Tech: http://www.i-tech.si.
[4] H.C. Chao, et al., “Current Design Status of TPS 3 GeV Booster Synchrotron”, Proceedings of the PAC09.
[5] C.C. Kuo, et al., “Progress Report of TPS Lattice Design”, Proceedings of the PAC09.

"BUNCHVIEW"
A FAST AND ACCURATE BUNCH-BY-BUNCH CURRENT MONITOR

F. Falkenstern, F. Hoffmann, P. Kuske, J. Kuszynski,
Helmholtz Zentrum Berlin, Germany

Abstract

BunchView is a system for the direct measurement of the current from each bunch circulating in a storage ring based on the analysis of the RF-signals delivered by a set of striplines. This paper describes the development, achievements, operation, and results of this fast and accurate bunch current monitor built for the BESSY and MLS storage rings.

Using a combination of a 14/16Bit analog to digital converter (ADC), a high-speed FIFO, ECL technique, and FPGAs, a real-time measurement of the fill-pattern with high accuracy and bunch-by-bunch resolution was achieved. The results are identical to the fill-pattern determined by time correlated single photon counting based on synchrotron radiation detected with an avalanche photo diode.

BunchView is fully integrated into the EPICS control system. The data provided by the BunchView monitor give accurate bucket position in the ring and bunch current over a wide dynamic range. The smallest measured single bunch current is less than 100nA. In the future the system will be used in the top-up mode of operation in order to inject beam into the emptiest buckets and thus keep the fill-pattern stable over longer periods of time.

INTRODUCTION

The BESSY machine is a third-generation light source operating at energy of 1.7 GeV with a stored current up to 300 mA. In the storage ring, electrons might be stored in any pattern consisting of up to 400 bunches. Knowledge of the fill-pattern of the buckets in a ring is very important, especially as more sophisticated time-resolved experiments are considered. At the time, BESSY has three modes of operation with special fill pattern: 1st the multi bunch (MB) mode with 350 consecutive filled buckets and a gap of 100 ns for ion-clearing, 2nd the single bunch mode (SB) with up to 20 mA, and 3rd the hybrid mode where a single bunch of 10 mA is injected in the middle of the gap. The operation in top-up mode [1] requires a real-time, high resolution determination of the current stored in each individual bucket.

DIAGNOSTIC TASK

We looked for a detection system, which monitors the current in each bucket with more than 12 bit accuracy and updates the whole fill-pattern of 400 bunches in less than 100 ms. Moreover, the system must be synchronized to the timing control at BESSY and thus gets the bunch number and its corresponding current value as shown in Figure 1.

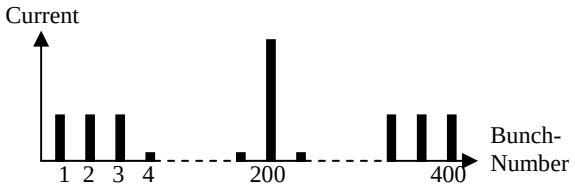


Figure 1: Fill-pattern in the storage ring.

Unfortunately, all commercial oscilloscopes have less than 8 bit amplitude resolution at the 500 MHz analog bandwidth.The best ADC-cards reach at best 10 bit resolution. The main reason is the track-and-hold (T/H) amplifier in the front-end of the ADC where the analog value is stored during the digitalisation process [2]. The hold time is essential for the amplitude resolution of the ADC. At present, many ADCs with a 14/16 bit amplitude resolution and an analog bandwidth of more than 500 MHz are on the market. But they all have a sampling rate below 130 MHz. Operating many ADCs in parallel would overcome this limit, however, would also lead to a more complicated design and a larger size. An alternative method for the data acquisition based on only one ADC and undersampling is used in our monitor and will be described in detail below.

PRINCIPLE OF MEASUREMENTS

In the storage ring the bunches circulate with a well defined revolution time which is 800 ns in case of the BESSY storage ring. Thus every revolution time the same bunch passes by the monitor. It is not necessary to detect all the bunch currents during just one revolution because the distribution of electrons distributed over the buckets does not change that fast. In addition we wanted to average the bunch current values over longer times in order to get a better resolution. Therefore, we decided to use signal undersampling [3].

For a better understanding, first consider a model of the storage ring with only 16 bunches as shown in Figure 2. If only every fifth bunch is sampled we catch all bunches in 5 revolution times and we get the following array of digitized bunch intensities:
"1,6,11,16, 5,10,15, 4,9,14, 3,8,13, 2,7,12".

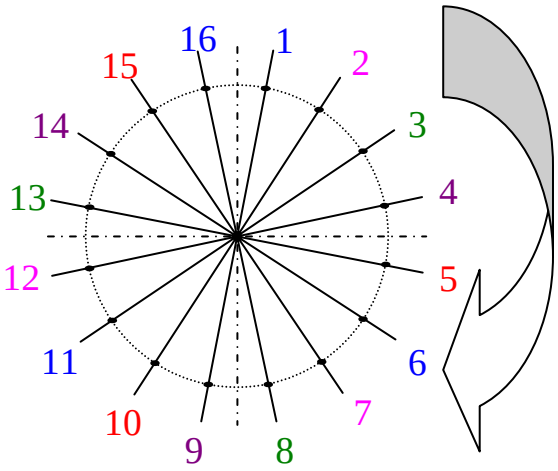


Figure 2: Simplified model with 16 bunches.

With 400 bunches we can not sample every 5th bunch, because we will not catch all bunches in this case.

For 400 and 80 we decided to take a divisional number 7, and so we sample each seventh bucket in the storage rings. In this way we have in 800*7 ns (BESSY) the complete fill-pattern (the whole current information from each bunch) as shown in Fig. 3 and thus the sample rate is reduced to 71.4 MHz (500 MHz/7) well within the specifications for our ADC .

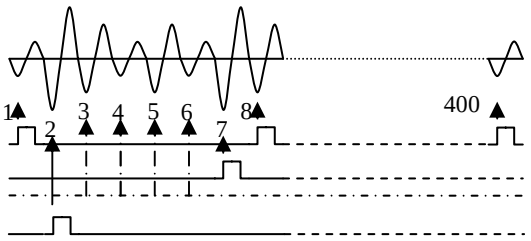


Figure 3: If every 7th bunch is sampled it takes 7 revolution times to acquire the information from each bunch once.

HARDWARE AND SOFTWARE

The original charge of each bunch can be converted in an electric pulse with different special current sensors in the vacuum pipe of the storage ring. We have knob-type BPM pick-up electrodes, a ring electrode and a set of 4 striplines at BESSY. The pick-up electrodes are not used, because they deliver a rather low signal. The ring electrode provides a 1.5 V peak to peak signal for a charge of 0.8 nC corresponding to 1 mA current in the bunch. This sensor is immune to orbit fluctuations in the ring and requires only one vacuum feed through in the vacuum pipe. We have achieved the best results with a set of 15 cm long striplines. They provide a 4.5 Volt signal for 1 mA bunch current. As shown in Fig. 4 the signal has a very good time response with 50 ohm input impedance.

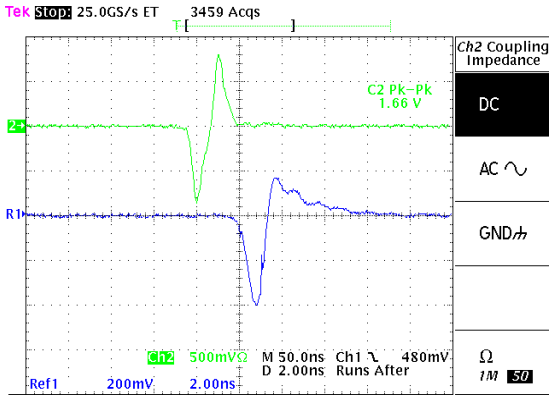


Figure 4: Voltage signals from stripline (in green) and ring electrode (in blue) for a single bunch (0.4 mA) circulating in the storage ring BESSY acquired by a real-time oscilloscope with bandwidth of 500 MHz.

A fast current sensor with high sensitivity and low loss cables are very important for accurate measurements. Bad cables and poor connections to the ADC-board lead to impedance mismatch and cause reflections. A major problem of the current sensor is the time response. The signal from bunches in a train should not overlap. Even with the stripline electrodes the signal of a single bunch extends over 2.3 ns. Note, the bunch spacing could be 2 ns. In order to compensate that, we reshaped the pulse response with a 500MHz low pass filter (LPF) so that influences from neighbouring bunches on the signal are minimized (Fig. 5).

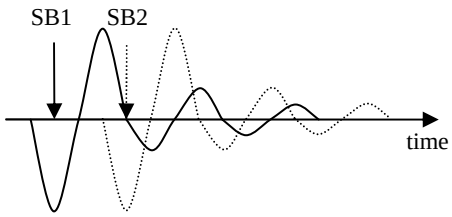


Figure 5: Sampling of the signal from equally populated neighbouring bunches. Signal interference has been reduced with a LPF.

The assembly of the electronics system consists of three main parts. The evaluation board ADC from the Analog Divices, Inc., our control development system and one PXI PC with a FPGA card from the National Instruments, Inc. (Fig. 6).

The power combiner makes the signal less sensitive to the beam position. The filtered bipolar and attenuated sum signal is digitized with the ADC. The sample clock signal for the ADC is derived from the RF master

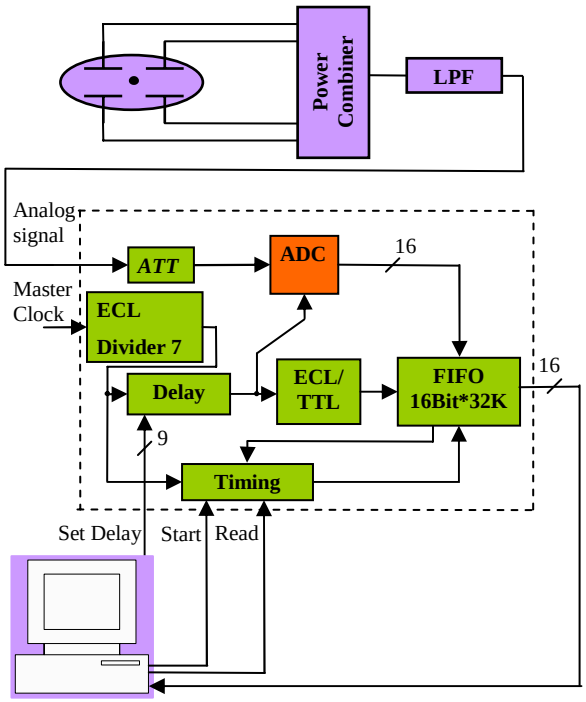


Figure 6: Hardware of the measurement system BunchView.

clock (500 MHz). A low jitter ECL divider and an ECL delay [4] are used in order to create the appropriate sampling times for the acquisition of the top of the signal amplitudes (Fig 3 and 5). The digital data delivered by the ADC are stored in the FIFO. In the 32K*16 bit FIFO up to 80*400 values can be stored. In the next step the data is transferred into the FPGA card (Fig. 7).

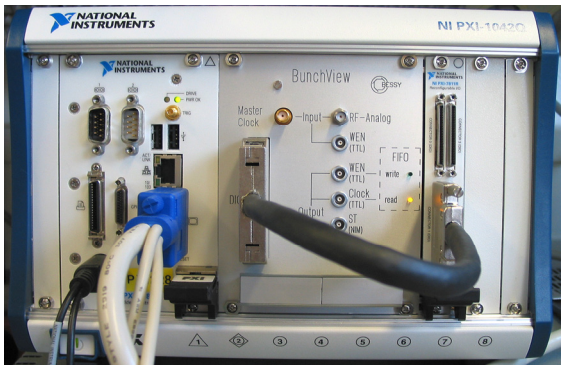


Figure 7: PXI Chassis containing an Embedded System Controller, the BunchView module and the FPGA card.

The fast digital processing in the FPGA card under LabVIEW averages the bunch current for each of the 400 buckets and stores them in the system controller. The LabVIEW host program sorts the data in the right order of bunch number, converts the ADC bits to current (Fig.8), calculates the injection rate, life time, etc. and updates the corresponding EPICS variables.

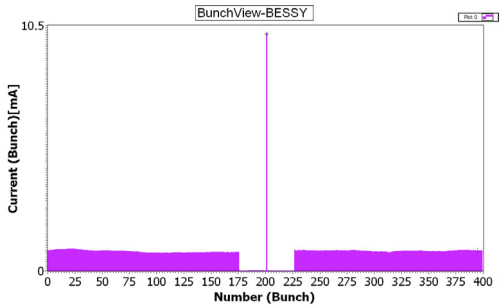
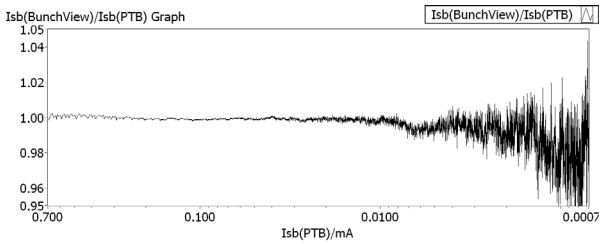


Figure 8: Typical Hybrid fill-pattern at BESSY measured with the BunchView system.

SENSITIVITY AND LINEARITY

For the test of the sensitivity and the linearity of the BunchView system, a current of 1 mA was injected into the storage ring and a scraper was used to reduce the current gradually over a period of two hours. During this time, the SB current was measured simultaneously with our two DCCTs, a photodiode of the PTB [5], and the BunchView system. The results are shown in Figure 9.



Figures 9: Confirmation of the very good linearity and high sensitivity of the BunchView system between 0.7 mA and 700 nA.

SUMMARY

BunchView, a bunch-by-bunch current diagnostics system, based on digital sampling of beam induced stripline signals with a 14/16Bit ADC, has been developed at BESSY and was installed successfully in the BESSY and MLS storage rings. The visualization of details of the fill-pattern already during the injection process gives the operator important information: like false SB position and poor SB purity, poor gap clearing efficiency, etc, which can be immediately corrected. The system is also an indispensable tool for low intensity studies during machine development runs.

REFERENCES

[1] P. Kuske, et al., “Preparations of BESSY for top-up operation” , EPAC'08, Genoa (2008).
[2] National Semiconductor “Specifications and Architectures of Sample-and-Hold Amplifiers”,
[3] D. Buchanan „Performance of an IF sampling ADC in receiver applications”, Analog Devices, Inc.
[4] Micrel Semiconductor “High-Speed PECL”.
[5] R.Thornagel, et al., “The electron storage ring BESSY II as a primary source standard from the visible to the X-ray range” Metrologia, 2001.

IMPACT OF ENVIRONMENTAL VARIABILITY ON VIBRATING WIRE MONITOR OPERATION

S.G. Arutunian, M.A. Davtyan, I.E. Vasiniuk, Yerevan Physics Institute, Yerevan, Armenia
J. Bergoz, Bergoz Instrumentation, Saint Genis Pouilly, France
G. Decker, Argonne National Laboratory, Argonne, IL, USA
G.S. Harutyunyan, Yerevan State University, Yerevan, Armenia

Abstract

The Vibrating Wire Monitor (VWM) was developed for precise transversal profiling/monitoring of charged particle/photon beams. The extremely high sensitivity of VWM is achieved by sensitivity of wire natural oscillation frequency to wire temperature. Due to the rigidity of the wire support structure, the VWM is also sensitive to the environmental parameters. In this paper, it is shown that the main parameter of influence is the ambient temperature. The magnitude and character of this influence is investigated along with the effect of electromagnetic interference on the VWM electronics in an accelerator environment.

INTRODUCTION

VWMs for accelerator beam instrumentation are based on the change in the natural oscillations frequency of a vibrating wire depending on the temperature of the wire and environment in which oscillations take place [1]. During operation these conditions (VWM sensor and electronics temperatures, electromagnetic interference from high power accelerator elements, hyper-radiation, presence of high electric and magnetic fields etc) can change, leading to shifts in measurements.

In vacuum the dominant effect is the sensor temperature since the resonant frequency in first approximation depends exceptionally on the mechanical properties of resonator and weakly depends on electronics.

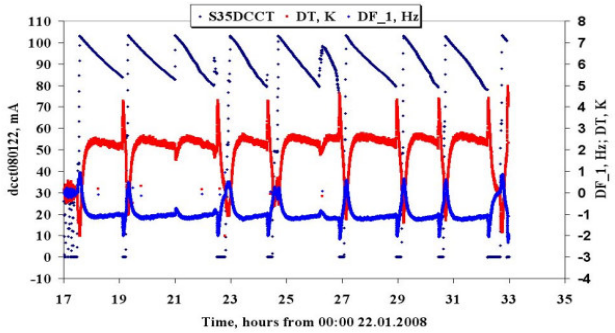


Figure 1: VWM005 reacts to the current change in APS.

Experiments at the APS ANL [2], [3] showed that a five-wire VWM005 reacts to electron beam current even in the case when beam synchrotron radiation does not touch the vibrating wire. In this experiment, a VWM was mounted at terminating flange of APS storage ring. We explained this behaviour by shifts of copper flange temperature. In Fig. 1 we present the time dependence of the VWM005 first wire frequency shift (right axis) that correlates with beam current (left axis). At right axis we also present the calculated wire temperature with shifts of about 2 K and 30 min relaxation time.

EXPERIMENTS

VWM Dependence on Ambient Temperature

To decrease VWM dependence on ambient temperature normally we choose wire material and housing material with the same thermal expansion coefficients. But to accent the question we analyze a sensor with wires and housing made by different materials (housing – bronze, first wire – Kanthal, second wire – stainless steel). As a reference thermometer we used Platinum resistive temperature detector Pt100 (RTD) with 0.03 °C accuracy. Measurements were done by Eurotherm model 2416 PID controller. Calibration of VWM is presented in Fig. 2.

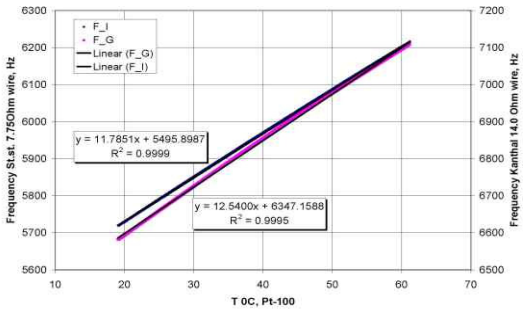


Figure 2: Calibration of two-wire VWM: magenta – Kanthal, blue –stainless steel.

The mean dependences on ambient T are 12.540 Hz/K (in range 6600-7100 Hz) for Kanthal wire and 11.785 Hz/K for stainless steel wire. The frequency measurement accuracy was about 0.01 Hz corresponding to 0.8 mK temperature drift. This value is extremely small so the long-term temperature measurements require detailed investigations to determine the stability of the VWM measuring system. Measurements with VWM and with Pt100 have some essential differences:

- The sensitive element of VWM has a mass of about 2 mg that is less massive than Pt100 (about 50 mg) although VWM contains housing of about 100 g surrounding the wire.

- The autogenerator current for VWM does not exceed 1 mA so the self dissipative power for VWM is about 10 mW which is at least one order smaller than for Pt100.
- The VWM frequency measurement scheme in fact is numerical in contrast to analogue scheme of measurements via Pt100.
- In case of air usage VWM wire is affected by air pressure and humidity and it seems that this problem is less essential for Pt100.

Mercury Thermometer Regulated Thermostat

For long-term drift measurements we prepared a thermostat on the basis of a mercury contact thermometer that regulates the absolute level of temperature. By tuning of the power supply driving the heater on/off control, we achieved reasonable oscillation of the temperature about 0.6 0C by Pt100 thermometer. The oscillation amplitude measured by VWM was 0.1 0C because of greater thermal inertia. The typical temperature paths collected by Pt100 and VWM are presented in Fig. 3.

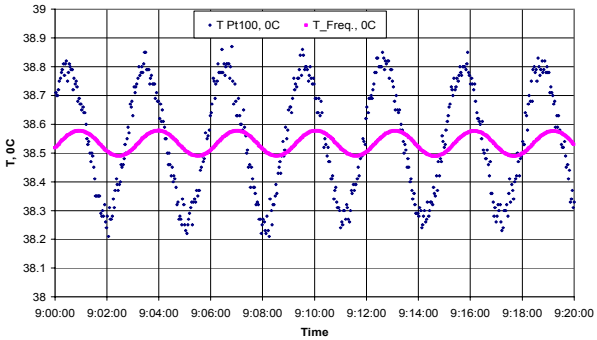


Figure 3: Thermostat on mercury thermometer base: signals from Pt100 and VWM are presented.

Temperature oscillation period was about 3 min and because of different thermal inertia the phase shifts between Pt100 and VWM readings are seen.

Dependence on the Electronics Temperature

To compare measurements of temperature via VWM and Pt100 we placed the sensors in mercury thermometer controlled thermostat and put both electronic units in a box that slowly thermocycled in range 10 ^{0}C...65 ^{0}C. The time resolved signals are presented in Fig. 4. Notable is the difference in temperature scales. The Pt100 readings show mean temperature shifts about 1 ^{0}C when mean temperature of the VWM readings remain stable. We also calculated the differences in subsequent readings of Pt100 and VWM. Because of very slow drift of mean temperature these values represent the measurements errors. Ninety three % of all readings for the VWM lies in range ±0.0015 K while the same fraction for Pt100 lies in range ±0.06 K. The dependences of Pt100 and VWM temperature measurements on the temperature of sensor electronics are presented in Fig. 5. The drift of VWM measurements is essentially absent and for Pt100 we have about -0.02 K_of_readings/K_of_electronics.

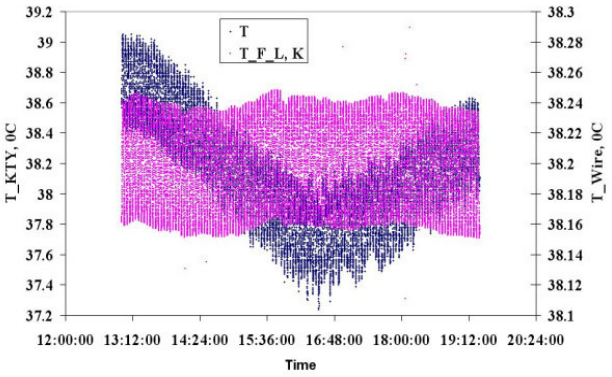


Figure 4: Thermometers are in mercury thermostat and the electronics are thermocycled.

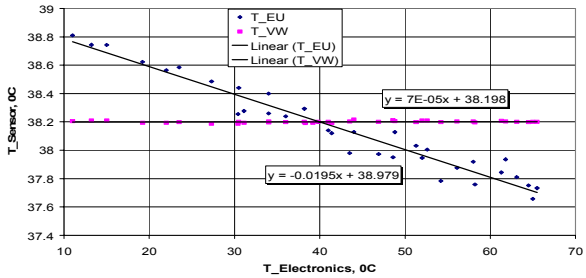


Figure 5: Comparison of the Pt100 and VWM readings dependences on electronics temperature.

Same VWM Sensor and Few Electronic Units

To investigate how large is VWM temperature dependence on the electronic unit components we prepared the following experiment. We placed the VWM005 in mercury thermostat and used one of the wires as reference. The measurements of frequency we provided by 3 electronic units with different essential components (the operational amplifier in autogeneration circuit was chosen from OP37 and NE5534 with different slew rate, the field-effect transistors used in amplitude stabilisation scheme were chosen from 2N3819, 2N5459 and КП305Е). The electronic units were thermocycled in the range 20 ^{0}C...60 ^{0}C. Each electronic unit contains a separate quartz generator IQXO-22C 4.0000M type. Measurements were provided subsequently by specially developed PC controlled multiplexer. For each unit switch on new generation of oscillations by autogeneration scheme about 1 s was needed so for every polling 8 s was chosen. This time was enough to prepare 4-6 correct 1 s measurements. Readings were written to a file every second with a special program that extracted unwanted points. The results of the experiment are presented in Fig. 6. In red the box temperature that contained electronic units is marked. As one can see, very small shifts between units are observed. The readings from the fourth (magenta) unit were shifted at 0.1 Hz in room temperature but this shift remained constant at units heating compared to the fifth unit (green). The shift 0.1 Hz can be explained by the different quartz generators. And vice versa the readings of the fifth unit at

temperatures near 60 ^{0}C decreased compare to the third one (blue).

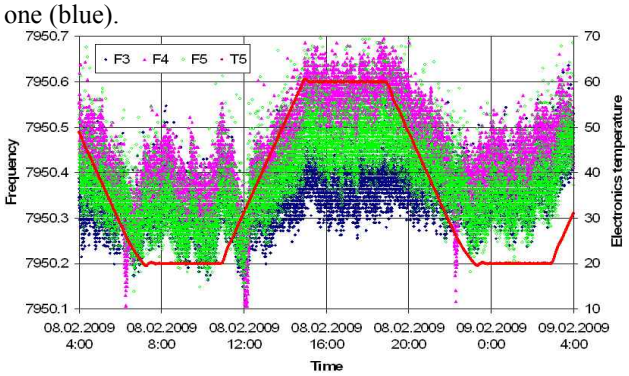


Figure 6: Comparison of the different electronic units with the same VWM sensor.

VWM Regulated Thermostat

To improve the mercury thermometer thermostat we prepared a thermostat on the VWM basis. The 2-wire VWM was used and PID (proportional, differential, differential) control was applied according to one of the VWM wires signals. Simultaneously the second wire frequency was measured and for reference the temperature by Pt100. Sensor Pt100 was mounted on the top side of VWM housing.

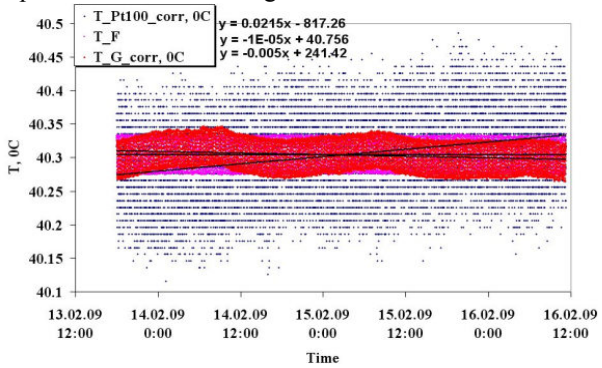


Figure 7: Results of thermostat regulated by VWM thermometer.

The results of 2.5 days of data collection are presented in Fig. 7. Since the readings from first VWM wire (magenta) was used in control by PID-algorithm as reference the time drift of this signal is absent. The second wire measurements show small drift about -0.005 K/day as compared to 0.02 K/day for Pt100 measurements.

Electromagnetic Interferences

For an experiment at the APS in Jan 2008, the electronics of the VWM was placed in the accelerator tunnel in immediate vicinity of magnets. The algorithm for frequency calculation in the VWM is based on the counting of periods of oscillation inside of a one second interval. Count of periods by PIC family microcontroller was provided by external interrupts of measuring signal edge rising. Electromagnetic interferences can create signal edges counted as additional period of oscillations. Each error produces a constant shift of about 1 Hz in frequency measurement. This produced divisible to 1 Hz jumps in data. Effect also depends on specific microcontroller parameters. Typical situation for VWM005 is presented in Fig. 8. The problem can be solved mathematically by special software that past together split data (see Fig. 9). It is preferable to solve this problem by dividing the electronic units of the VWM into two parts: an autogenerator unit and a measurement unit. The first one must be placed in tunnel in which the sinusoidal amplified signal is produced and transfer to the control panel. At the input of measurement unit with microcontroller a special block of low frequency filters must be installed to remove high frequency disturbances.

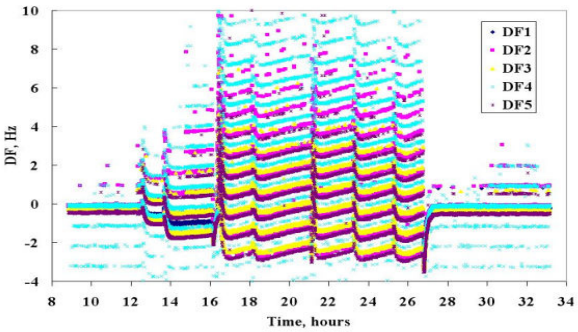


Figure 8: Electromagnetic disturbances 1.04 Hz steps.

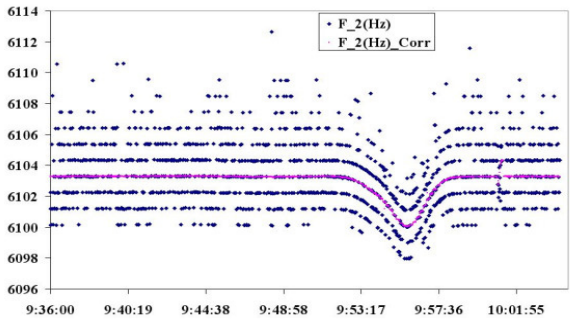


Figure 9: Mathematical treatment of split signal.

CONCLUSIONS

Experiments show that the parameters of absolute stability of VWM temperature measurements are superior to RTD so the VWM can be used not only for beam diagnostics but also for precise and stable thermometry, e.g. for precise measurement of the magnet cooling water temperature with a resolution of 0.01°C [4].

REFERENCES

[1] S. Arutunian, Vibrating wire sensors for beam instrumentation, BIW08.

[2] G. Decker, S. Arutunian, M. Mailian, G. Rosenbaum, First vibrating wire monitor measurements of a hard x-ray undulator beam at the Advanced Photon Source, DIPAC07.

[3] G. Decker, S. Arutunian, M. Mailian, I. Vasiniuk, Hard x-ray synchrotron measurements at the APS with vibrating wire monitor, BIW08.

[4] T. Fukui et al., High precision temperature measurement system, ICALEPCS99.

PROFILEVIEW - A DATA ACQUISITION SYSTEM FOR BEAM INDUCED FLUORESCENCE MONITORS*

R. Haseitl, C. Andre, F. Becker, P. Forck, GSI, Darmstadt, Germany

Abstract

Along the GSI linear accelerator, several Beam Induced Fluorescence (BIF) monitors are installed. Due to the non beam-intercepting measurement principle, multiple BIF monitors can be active simultaneously to observe the beam at different locations. For this novel possibility, the software called ProfileView has been developed, allowing users to view beam profiles coming from several BIF monitors. This contribution describes the different hardware devices of the GSI BIF monitor installation and the according software to control these devices.

MOTIVATION

Beam Induced Fluorescence monitors determine the transversal beam profiles without beam disturbance [1]. Therefore, they are well suited to observe the beam at several positions in the accelerator at the same time. Presently, two BIF monitors are installed in the GSI linear accelerator. In the next two years, a final number of seven BIF monitors will be installed to observe the beam throughout the linear accelerator and in the transfer line to the synchrotron. The readout of the two image intensified cameras of a BIF monitor has formerly been realised with outdated LabView programs. Just one camera could be monitored at a time, so horizontal and vertical profiles had to be measured successively. The new software called ProfileView overcomes these limitations and allows machine operators to view multiple BIF monitors at the same time through an easy-to-use graphical user interface (GUI) which can be seen in Fig. 1. Up to three different BIF monitors can be observed and compared at once. By default, the pressure is the only parameter to tweak the signal strength. For advanced users, every parameter of the system can be fine-tuned in a password protected 'Expert mode'.

HARDWARE

The hardware of the BIF system is in wide parts similar to the hardware of the BeamView system for scintillator screens [2]. Each BIF monitor consists out of the following hardware components depicted in Fig. 2:

- two FireWire cameras (for the horizontal and the vertical profile) with multi-channel plates (MCPs) for image intensification and remote-controllable irises
- a National Instruments Compact Vision System (CVS) [3] or standard PC for camera readout and digital image processing

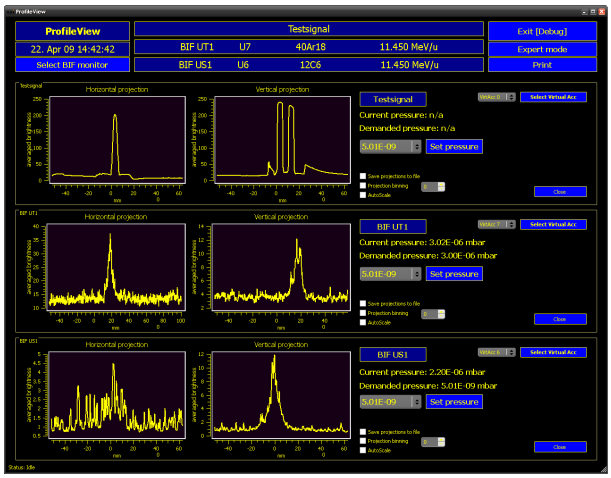


Figure 1: ProfileView graphical user interface.

- Ethernet connected DAC electronics for iris and MCP amplification control
- pressure control unit to inject defined gas pressures into the beam pipe
- timing decoder to trigger the cameras and the image intensifiers
- remote controllable power plugs to reset system components
- a computer running ProfileView to display images and projections and control all hardware devices

Image Acquisition System

To acquire images, standard FireWire cameras (Basler A311f) have been equipped with custom made image intensifiers (Proxitronic) for single photon detection. The cameras are connected to dedicated image processing hardware, acting as middle layer between the camera and the computer running the GUI. For this purpose, an embedded system (National Instruments Compact Vision System 1456 [3]) can be used. This embedded computer is equipped with FireWire interfaces, an FPGA with digital I/Os, network connectivity, a 733 MHz CPU, 128MB RAM and 256MB non-volatile storage. The CVS is capable to control up to 16 cameras connected via FireWire hubs, with four of them running simultaneously. It is programmed via LabView Realtime, FPGA and Vision packages. It is also possible to use a standard Windows PC with FireWire ports and an FPGA card instead of the CVS to achieve higher system performance. Besides some minor adaptations, the software for the CVS and the PC is the same.

* Work supported by EU, project FP6-CARE-HIPPI

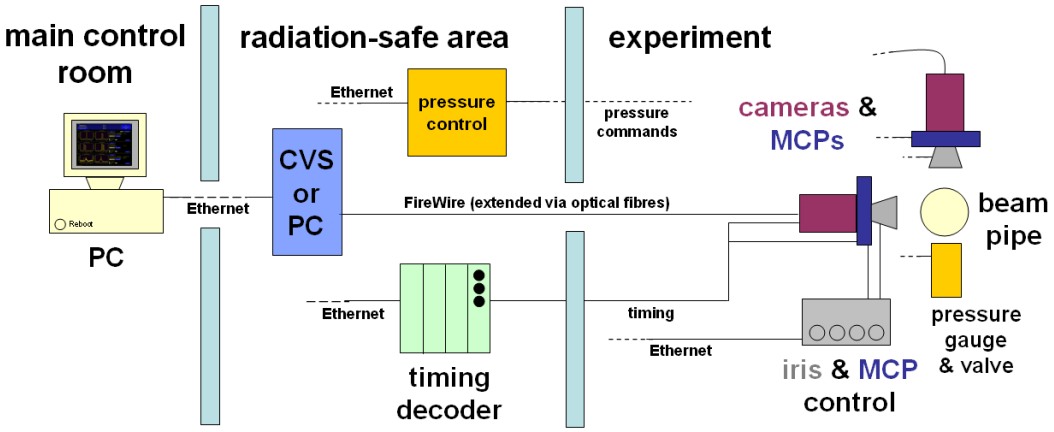


Figure 2: Schematic of the BIF monitor hardware.

Supplemental Hardware

Every device in the BIF system is controlled via Ethernet. To trigger the cameras and the MCPs with respect to the beam pulse, a programmable timing interface is used. The camera iris and the MCP amplification are controlled by a simple DAC electronics. A commercial pressure control unit (Pfeiffer RVC300) creates the pressure bump inside the beam pipe for gas excitation. The typical pressure range for BIF operation is between 10^{-7} and 10^{-5}mbar, using nitrogen as working gas. For remote reset capabilities, all devices are connected to remote controllable power plugs. In case of malfunction, each device can be reset separately. To minimize radiation damage, most of the active electronics is placed outside the accelerator tunnel.

SOFTWARE

The software of the whole BIF system is split into two parts: The image acquisition software is written in LabView and running on the CVS (or PC). The other part called ProfileView is written in C++, displays images and controls all system devices. The CVS and ProfileView communicate with each other via standard Ethernet.

Software on the CVS

The part of the software running on the CVS is responsible for acquiring images and performing calculations on the image data like the computation of projections or histograms. This data is sent across the network to the PC running ProfileView. A specification of the requirements for the CVS software has been created and given to an external company which developed the LabView application and a C++ application programming interface (API) for ProfileView [4]. It has been implemented to serve both use cases, scintillator screens and BIF monitors. The CVS software offers the following features:

- control up to four cameras simultaneously
- calculate histograms and projections of the incoming images
- buffer data in case of heavy network traffic or unavailability of the client
- disable triggers in the FPGA in case the camera is busy processing the last frame
- send the results via Ethernet
- XML interface for CVS and camera control

The functionality is realized with independent image acquisition threads, each controlling one active camera. The default behaviour is sending of projections only (without the original images) to save network bandwidth. If the user wants to observe and save the original images too, it can be enabled in the Expert Mode. The typical bandwidth of uncompressed images with 5 Hz is around 24 MBit/s per BIF monitor. The system is controlled by human readable XML commands, sent over the same socket connection as all other data. To deliver images, processed data and command responses, an application layer protocol is used to distinguish between XML and binary data. The API allows easy access to the arriving data and command submission. Communication takes place over standard Ethernet sockets using the TCP/IP protocol. Since Ethernet is a non-deterministic technology, buffers are implemented on the CVS. When there is heavy network traffic or the client is not ready to receive data, the CVS stores all data in a configurable ring buffer. The submission is continued as soon as the network is not overloaded any more or the client acknowledges the reception of the last data package.

ProfileView

The software part called ProfileView is responsible to receive data from one or more CVS systems and to control all supplemental hardware devices. To understand the interaction of the different classes, a typical startup of a BIF monitor and the following data flow is described:

As soon as a detector is selected in ProfileView, the startup sequence initializes the horizontal and vertical camera of the BIF monitor. The startup procedure sets camera specific attributes, e.g. integration time, gain or video mode. When the cameras are initialized and waiting for

triggers, the CVS is informed to calculate projections of the images arriving in the future and to forward them to the computer running ProfileView.

After camera initialisation, the value for the demanded pressure is sent to the pressure hardware. The pressure control class is implemented as a separate thread, which requests the current pressure in the beam pipe every three seconds. When the user wants to set a pressure, the new value is sent to the hardware and the valve opens to adjust the new pressure accordingly. To avoid flooding the accelerator with atmospheric pressure, only predefined values can be set. An arbitrary value can be entered in the password protected 'Expert Mode'.

A network connection is established to the DAC electronics controlling the camera iris and the MCP. For reasons of hardware protection, the connection has to remain open and the demanded values have to be sent every few seconds. In case of an unexpected disconnection, the hardware closes the iris and shuts down the amplification voltage. This way the MCPs will be left in a safe state in case of a network or software error. For reliability and safety reasons, the GSI-built DAC electronics will be replaced by a commercial programmable logic controller in the future.

Finally the timing hardware is initialized. As soon as the desired event occurs on the GSI timing bus, the timing hardware sends a trigger to the camera to start acquisition of an image and a gate to activate the MCPs.

Once an image arrives at the CVS over the FireWire bus, the projections are calculated and stored in a buffer. A 'network sender' thread takes the oldest buffer element and sends it to the computer running ProfileView. Projections, histograms and images are transferred as binary data, error messages and commands as XML strings.

The complete programming of ProfileView is done in C++ using the Qt framework [5] for platform independent GUI, thread, network and XML functionality. For data processing, extensive use of the Qt signal/slot mechanism is made. When data has been read from the network, a Qt signal, comparable to an interrupt, is raised, with a pointer to the new data as an argument. The GUI layer receives this signal and updates itself with the new data. To avoid read/write concurrency issues, memory locking and acknowledge mechanisms have been implemented. Each hardware device is represented as separate Qt class. A class called gsiBifMonitor combines all device classes into a virtual representation of the physical hardware setup.

USER EXPERIENCE

Typical frame rates in operation are between 5 and 10 Hz. The maximal achievable frame rate of the system depends on the hardware and the data rate (see Table 1). If just the projections are sent to the client, the frame rate is between 50 and 66 frames per second (fps). If the original images of one or both cameras are requested additionally, the maximal frame rate drops considerably and a PC should be used. The data rate of a BIF monitor triggered with 20 Hz grows from 0.8 MBit/s (projections only) over 50 MBit/s (projections and one image stream) to ∼110 MBit/s when both original images are requested. The CVS systems are used for historical reasons, easy system setup and their reliability in operation due to the real-time operating system and the robust hardware. A Windows PC is faster and cheaper, but the non-deterministic operating system can cause an error in very rare occasions.

Table 1: CVS vs. PC Performance Comparison

Requested data	**CVS**	**3 GHz PC**
projections only	∼50fps	∼66fps
proj. with one image stream	∼14fps	∼52fps
proj. with two image streams	∼8,33fps	∼37fps

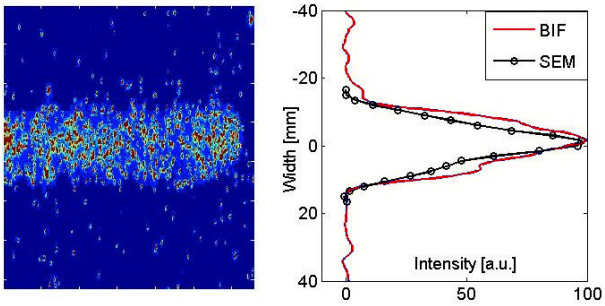


Figure 3: Comparison between a false-color image of BIF and a secondary electron emission grid (SEM).

The results of BIF measurements show the functionality of the measurement principle for different ions in the energy range from 1.4 to 750 MeV/u [1]. For lower energies, secondary electron emission grids (SEM) are the standard diagnostic device at GSI. To validate the measurements of the BIF monitors, data of both systems has been compared. The profiles (average of 5 beam pulses) of a high current (4.5 mA) Ar^{1+} beam with 1.4 MeV/u show good agreement in width and shape between BIF monitors and SEM grids (see Fig. 3 [6]).

REFERENCES

[1] F. Becker, P. Forck et al., "Beam Induced Fluorescence Monitor for Transverse Profile Determination", DIPAC'07, Venice, (2007).

[2] R.Haseitl et al., "BeamView - A Data Acquisition System for Optical Beam Instrumentation", PCaPAC08, Ljubljana, (2008).

[3] Company National Instruments, www.ni.com

[4] Company Ingenieurbüro Hagel, www.ib-hagel.de

[5] Company Qt Software, www.trolltech.com

[6] C. Andre et al., "Commissioning of Beam Induced Fluorescence Monitor at Unilac", GSI Scientific Report 2008, Darmstadt, (2008).

IMPLEMENTATION OF THE ELECTRONICS CHAIN FOR THE BUNCH BY BUNCH INTENSITY MEASUREMENT DEVICES FOR THE LHC

D. Belohrad*, O. R. Jones, M. Ludwig, J. J. Savioz, S. Thoulet, CERN, Geneva, Switzerland

Abstract

The fast beam intensity measurements for the LHC are provided by eight Fast Beam Current Transformers (FBCT). Four FBCTs installed in the LHC rings are capable of providing both bunch-by-bunch and total turn-by-turn beam intensity information. A further four FBCTs, two in each of the LHC dump lines, are used to measure the total extracted beam intensity. In addition to providing intensity information the ring FBCTs also send signals to the machine protection system. This increases the complexity of both the RF front-end and the digital acquisition parts of the signal processing chain. The aim of this paper is to discuss the implemented hardware solution for the FBCT system, in particular with respect to the signal distribution, FPGA signal processing, calibration, and interaction of the FBCTs with the machine protection chain.

INTRODUCTION

The fast BCT measurement system consists of a Bergoz type transformer with a bandwidth from 400Hz to 1.2GHz. This is followed by an RF front-end consisting of an RF distributor, analogue integrator and beam circulating flag (BCF) detector, before entry into a 14bit digital acquisition system.

A simplified block schematic of the fast intensity measurement system is depicted in Fig. 2. In order to maintain the compatibility of the CERN-SPS and the LHC FBCT systems it was decided to use a digital processing chain based on the CERN-SPS system. This uses a DAB64x acquisition card developed by TRIUMF (Canada) on which are mounted two Individual Bunch Measurement System (IBMS) mezzanine cards [1]. The mezzanine cards are used to integrate the incoming signal using a 40MHz integrator ASICs developed for the LHCb experiment. The integrated signal is then digitized and processed on the DAB64x card to produce bunch-by-bunch intensity values.

Four channels (2 DAB64x boards) are used to provide measurements in two dynamic ranges: high gain with full scale=2×10^{10} and low gain with full scale=2×10^{11} particles. For each dynamic range the measurements can be acquired with a high bandwidth (HIBW, 200MHz) for bunch to bunch measurements and a low bandwidth (LOBW, 2.5MHz for low gain and 1.5MHz for high gain) for a timing insensitive total intensity measurement.

* david.belohrad@cern.ch

SIGNAL DISTRIBUTION

The purpose of the RF distributor is to split the beam signal appearing at the output of the transformer [2] into a total of six outputs. Four of these outputs are used for the measurement, and are connected via appropriate protection circuitry to the IBMS mezzanines. The remaining outputs are used for the BCF detector and an oscilloscope.

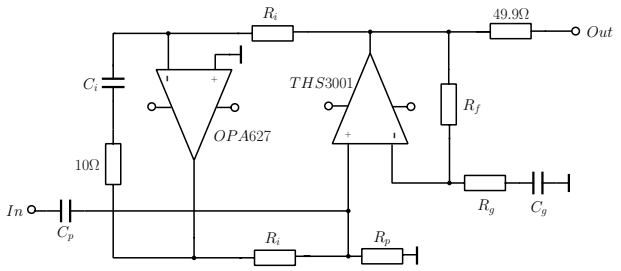


Figure 1: High gain amplifier with offset suppressor.

The signal coming from the transformer is divided by a resistive splitter, is separately amplified and then filtered. The signal amplification for the measurement outputs is dependent on the dynamic range and the bandwidth. Regardless of the bandwidth, the low gain range does not require any amplification as even the LOBW signal creates almost a full scale response at the output of the integrator. An amplification of 30dB and 40dB is required for the HIBW and the LOBW channels respectively for the high gain range.

Maintaining the required bandwidth with high gains is difficult to achieve using voltage feedback operational amplifiers (VFOA). Current feedback operational amplifiers (CFOA) were therefore used. These exhibit higher offset voltages, hence an active feedback to suppress the input offsets was developed (Fig. 1). The implemented method is based on the fact that the measured signal has no DC value. An AC coupled amplifier was designed, and its output actively low-pass filtered, inverted, and injected back to the input of the amplifier. The time constant of the filter is much longer than the one corresponding to the low-frequency cut-off of the measurement transformer.

All filters implemented in the RF distributor are of Gaussian type to ensure that no overshoot occurs in the response to the input signal. The HIBW filters are passive 2^{nd} order LC circuits, and their goal is to reduce the peak amplitude of the incoming beam signal. Fourth order filters consisting of two Sallen-Key blocks were used to implement the LOBW channels.

The entire RF distributor was designed as a VME card. In order to control the impedance of the tracks

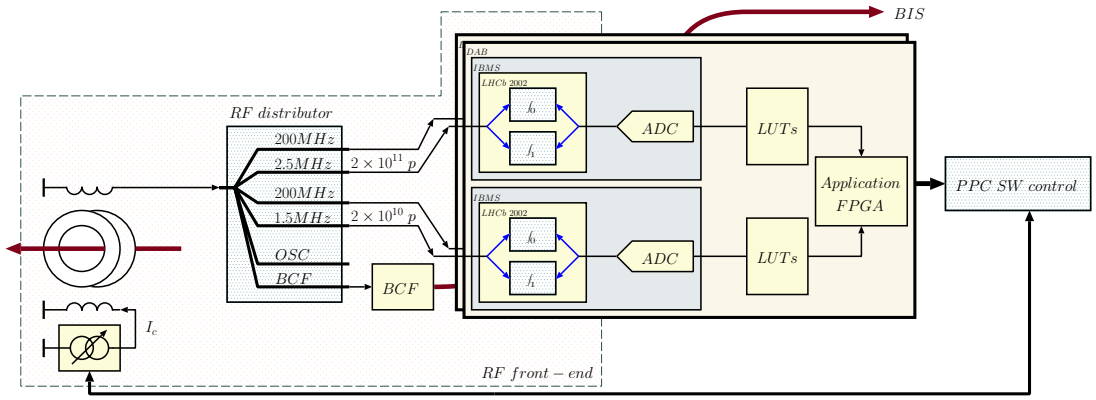


Figure 2: Schematic of the signal processing during the calibration and the intensity measurement.

it was manufactured using four layer composite material. The RF tracks were implemented on a Neltec NY9220 0.256mm thick substrate, which forms the top and the first interior layer of the PCB. The bottom and the second interior layer use standard FR4 material (0.8mm), which is melted by 0.4mm thick prepreg onto the RF substrate. The entire design is protected by a brass shielding. The measured S_{11} using such a configuration was found to be s_{11}=-25dB at 800MHz and s_{11}=-20dB at 1.2GHz.

THE BCF DETECTOR

The LHC Beam Interlock System (BIS) needs the FBCTs to provide information about whether or not there is beam circulating in the LHC. In order to provide this a detection method was implemented using a constant fraction discriminator (CFD) with offset shifting as seen in Fig. 3. By setting the V_{ofs} the threshold at which the CFD triggers can be modified. In order to catch very short pulses appearing at the output of the CFD an ECL flip-flop was connected between the CFD and the processing FPGA. This permits the FPGA, which is clocked at 50MHz, to capture even short signals. The FPGA algorithm for

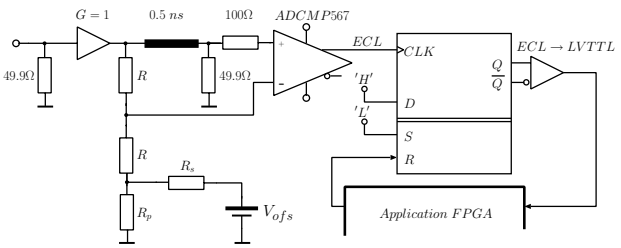


Figure 3: Principal description of the BCF detector for the LHC.

the detection is based on counting the number of events reported by the CFD. A counter value is increased every time the CFD triggers and it is decreased every 100μs. As the LHC turn period is $\approx$ 89μs, the presence of even a single bunch will slowly increase the value of the counter. By exceeding a given count threshold the presence of circulating beam is presumed and this information is passed to the BIS. Once the counter is saturated, it stays in the saturation as long as the CFD triggers at least once per 100μs. When the CFD triggers disappear the counter automatically decrements until the threshold value is reached. At this moment the counter value is reset to zero and the BCF detector reports no circulating beam. The value attributed to the beam presence counter threshold will affect the hysteresis of the detector.

For the LHC start-up a four bit counter depth was chosen and the count threshold set to 75% of the maximum value. The V_{ofs} voltage was trimmed to trigger when 2.5×10^9 particles having $\sigma = 680ps$ appear at the input of the CFD. The noise of the electronics limits the CFD threshold to some 2×10^9 particles for this bunch width.

CALIBRATOR

The calibrator for the LHC FBCTs must generate currents to calibrate all four measurement channels. Two point calibration (offset and gain) is used, implying the use of three currents - 750mA, 40mA and 7.5mA. Both HIBW and LOBW channels for the low gain use the 750mA and 40mA, while the HIBW high gain channel uses the 40mA and 7.5mA. The LOBW high gain channel can only use the 7.5mA, with the offset assumed to be zero.

The operation of the calibrator is depicted in Fig. 4. The calibrator consists of a source of high voltage (HV), a variable current sink (I_c) and switches (Q_1, Q_2). The operation of the calibrator is monitored by an ADC, which measures the voltage over the reference resistance R_m and the DC value of the HV. The calibrator functions in the following way. In the idle mode the HV switch is turned on with transistors Q_1 and Q_2 in the off state. This permits the capacitors C_c to charge via the current passing through the path R_c-C_c-R_d as shown in the picture by the orange arrow. Both capacitors are charged at the same moment. When the calibration is triggered a set of timings is generated. Firstly, the HV switch is turned off and Q_1 opens (current flows). The disconnection of the HV is time consuming, and it takes 8μs to switch off the 200V source. Once this is done, switch Q_1 is opened and with the HV disconnected from the R_c, the current starts to

flow from the lefthand C_c into the current sink I_c (blue arrow). This stabilizes the feedback of the I_c and charges all internal capacitances. Once I_c is stabilized, switch Q_1 is quickly closed while opening Q_2. The current now no longer flows through Q_1 and the dummy resistance R_d, but via the righthand C_c, R_l and the calibration winding L_x (green arrow). As the current sink is already stabilized, concurrent switching of Q_1 and Q_2 provides a very sharp negative current pulse. Under laboratory conditions, using a short cable to connect to a resistive load, a fall time of $4ns$ was measured for a current of $800mA$ (SR=1000V/μs). The calibration cycle is completed by closing switch Q_2 and reconnecting the HV. This permits both capacitors C_c to charge again. The precision with which the current can

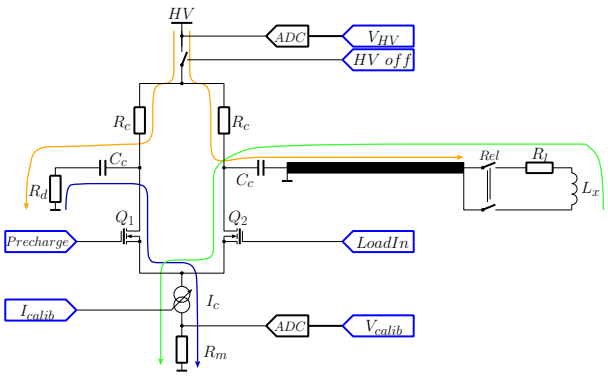


Figure 4: Principle of operation of the LHC BCTF calibrator.

be set is limited by the input offsets of the operational amplifiers (OA) used. As the current sink I_c must quickly react to changes of the load, it is implemented using fast OAs. These limit the uncertainty of the setting of the I_c to ≈1.9mA. This value was not acceptable and therefore a measurement of the voltage over a reference resistance R_m was implemeted. By using low offset OAs and a precision component network for this measurement the uncertainty on the knowledge of the actual current generated is limited to 650μA (9% at 7.5mA).

Figure 5 displays the results of the measured linearity error of the complete calibration and acquisition chain. The values are calculated for a single calibration shot per given calibration current. The calibration pulse is measured by LOBW channels on both gain ranges, digitized and passed via look-up tables correcting the offset and gain of the integrator. The error is calculated with respect to the best linear fit. The value of the error increases towards lower calibration currents. This is caused by worsening of the signal to noise ratio and can therefore be partially reduced using statistics, i.e. calculation of an average for each desired current. This is especially true for the high gain LOBW channel which exhibits increased noise due to the heavy amplification. A single VME card houses both the calibrator and the BCF. All settings, including the BCF threshold value, are stored in a local memory and protected

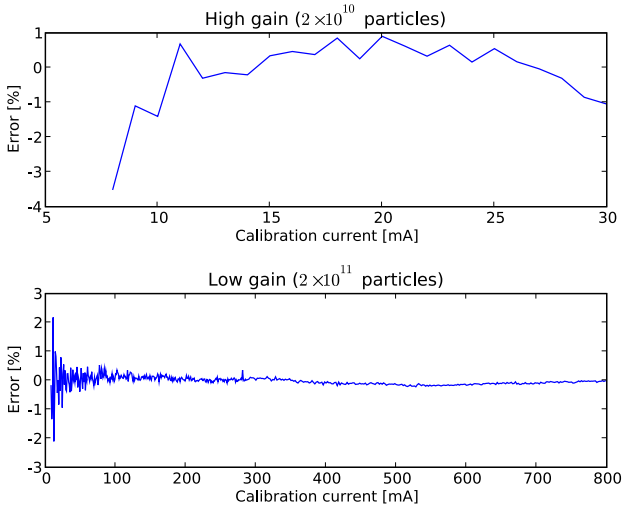


Figure 5: The error of the linearity of the calibration chain for LOBW channels.

against accidental overwrite. The BCF detector connection to the BIS is doubled to ensure redundancy. The calibrator is connected to the calibration turn on the transformer via ≈30 metres of 7/8" air-dielectric Heliflex cable. This type of cable is also used to transfer the beam signal to the RF distributor.

LHC START-UP

The FBCT system as described here was installed in the LHC tunnel in time for the start-up in September 2008. Special attention was paid to install the cables and electronics far from any sources of pulsed currents. The first measurements of the FBCTs with circulating beam did not show any perturbation due to neighbouring equipment. The FBCTs for the dumps, however, do acquire noise induced by the extraction kicker magnets. The performance of these monitors will depend on the relative position in time of this signal with respect to the beam signal.

The complete system was tested during the first few days with LHC beam. The acquisition chain, software and implementation of the control system worked flawlessly. Minor problems were detected in the algorithm used for calibration. These issues are now being solved on a test facility using the SPS fast transformer equipped with the same LHC electronics. The functionality of the BCF detector was not tested due to the very small intensity of the beam which was circulating in the LHC.

REFERENCES

[1] H. Jakob, L. Jensen, R. Jones, J. J. Savioz, "A 40MHz Bunch by Bunch Intensity Measurement for the CERN SPS and LHC", DIPAC'03, Mainz, Germany, 2003

[2] D. Belohrad, P. Odier, S. Thoulet, S. Longo, "Mechanical Design of the Intensity Measurement Devices for the LHC", DIPAC'07, Venice, Italy, 2007

CHARGE AND LASER BEAM ENERGY MONITOR FOR SPARC LINAC*

L. Cultrera#, F. Anelli, M. Bellaveglia, G. Di Pirro, D. Filippetto, E. Pace, C. Vicario, INFN National Laboratories of Frascati, Via E. Fermi 40, Frascati, Italy

Abstract

The experimental setup implemented in the SPARC linac control system used to monitor the laser beam energy and to measure the beam charge by means of a Faraday Cup will be illustrated and discussed. The experimental setup makes use of National Instruments 2 GS/s 8-Bit digitizer board. This tool has been shown to be useful in order to monitor the laser beam energy stability and to evaluate the quantum efficiency of the cathode.

INTRODUCTION

Within the goals of the SPARC high brightness photoinjector [1] the stability of the electron beam plays a crucial role. For this reason a new instrument of measure has been included in SPARC control system: the SPARC beam diagnostic system allows now monitoring continuously the laser energy delivered to the cathode and thus the quantum efficiency of the cathode itself. This new tool allowed us to keep under control the cathode performances in terms of its emission properties (QE mean value and uniformity of emission). The tool, now completely integrated inside the SPARC control system allows also to reconstruct the quantum efficiency map of the cathode surface.

EXPERIMENTAL SETUP

In the following paragraph the experimental setup for monitoring the laser energy and the beam charge and its implementation inside the SPARC control system [2] will be illustrated.

Laser Energy Monitor

The SPARC laser beam energy is measured by means of a fast photodiode (Thorlabs mod. DET210). The signal generated by the photodiode consists in a sharp current pulse with duration of approximately ten ns. The area of the photodiode signal results to be linearly dependent from the energy of the laser pulse. In order to deduce the energy carried out by laser beam, an accurate calibration is carried out by relating the area of the photodiode signal with respect to the laser energy measured by a commercial joulemeter (Molectron mod. J3-05).

A typical calibration curve is reported in Fig. 1. In this figure is evident that the photodiode response can be considered linear, and its slope represents the conversion factor that should be used to convert the area of the measured photodiode signal to the energy of the laser beam pulse.

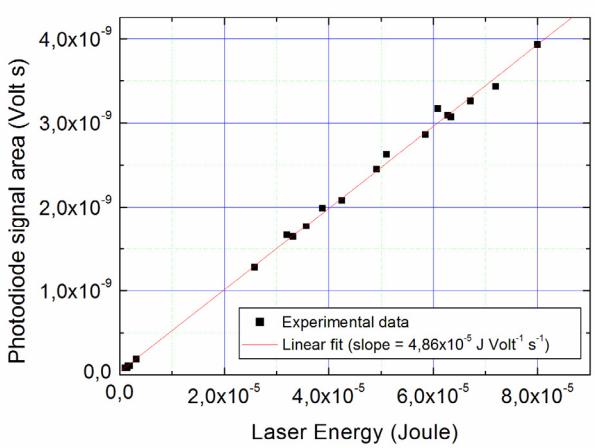


Figure 1: Typical calibration curve for the laser photodiode.

Due to the sensitivity of the photodiode with respect to the relative laser beam position with respect to the detector area the calibration factor is usually verified each time that the operators prepare the laser beam for the SPARC run. Moreover, a pointing procedure of the laser beam to the centre of the cathode is performed by means of a motorized mirror at the end of the optical transfer line. Thus the final path of the laser beam is frequently changed and this affects also the calibration constant. In order to avoid this problem we choose to sample the laser energy before the motorized mirror by means of a beam splitter as shown in Fig. 2 [3].

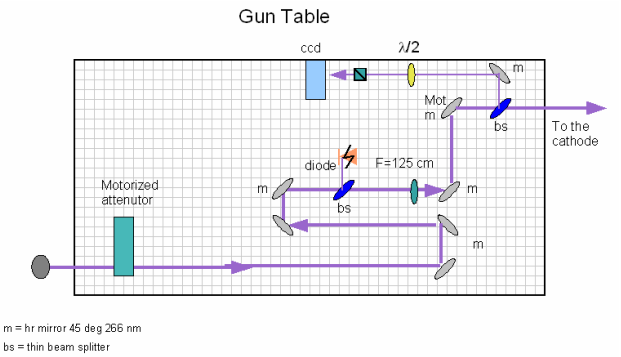


Figure 2: Layout of the final part of the laser beam transfer line. The position of the beam splitter and photodiode is also shown.

With this beam splitter and photodiode configuration, when the motors of the last mirror are used to move the laser spot over the cathode surface, the influence on the measurement of the laser energy pulse became negligible.

*Work supported by Italian National Institute of Nuclear Physics (INFN) and by Ministero Istruzione Università e Ricerca, Progetti Strategici, DD 1834, Dec. 4, 2002, within the SPARC project.
#luca.cultrera@lnf.infn.it

Beam Charge Monitor

In order to measure the beam charge two different techniques are currently used in the SPARC photo-injector. The first one make use of a Faraday cup placed at 1.2 m downstream the cathode surface. The second one is based on Integrating Current Transformer (ICT) that take place at the beginning and at the end of the three accelerating structures that boost the energy of the electron beam up to 150 MeV. We will focus our description to the Faraday cup and on its use in measuring the emission uniformity of the cathode surface. We will describe the use of the ICT as monitor of the bunch charge during routine operation of the SPARC linac.

In Fig. 3 a picture of the SPARC Faraday cup is shown.

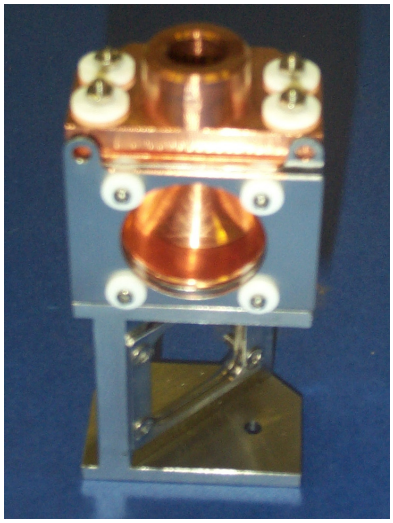


Figure 3: Faraday cup picture.

Signals Acquisition

The analogue signals obtained from the photodiode and from the Faraday cup are sent, one for each channel, through coaxial cables to a an high speed digitizer board (National Instruments NI PCI 5152 2 Gs/s Digitizer Oscilloscope).

The waveforms acquired from the digitizer can be directly manipulated by the local software that runs on the front-end CPU located in the SPARC bunker or can be transferred and analysed at the console level CPUs located in the control room by running dedicated software. The trigger of the digitizer board is achieved through a 10 Hz TTL signal of the SPARC timing system being so independent on the amplitude of the signals on the photodiode or Faraday cup dedicated channels.

ICT are connected using an electronic conditioning from Bergoz (BCM-IHR) that is read using the National Instrument board NI PCI 4070 DIMM.

At this moment the software for two control panels has been written with the aim to characterize the SPARC photocathode. The first one is used to keep constantly under control the laser energy sent to the cathode, the electron beam charge (by using ICT) and thus the quantum efficiency at the photo-injector working point. The second one is used to study the emission uniformity of the cathode by collecting the quantum efficiency map (by using the Faraday cup).

RESULTS

In the following paragraph some preliminary results obtained by integrating the laser energy monitor and the Faraday cup reading inside the SPARC control system will be illustrated.

QE Stability Results

Fig. 4 and 5 reports the result obtained over 24 hours of continuous QE measurement during a typical running shift of the SPARC photo-injector, including some shutdown periods.

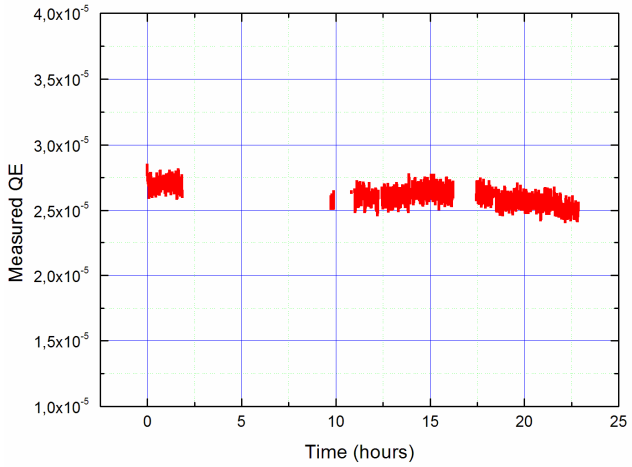


Figure 4: QE monitor results over approximately 24 hours.

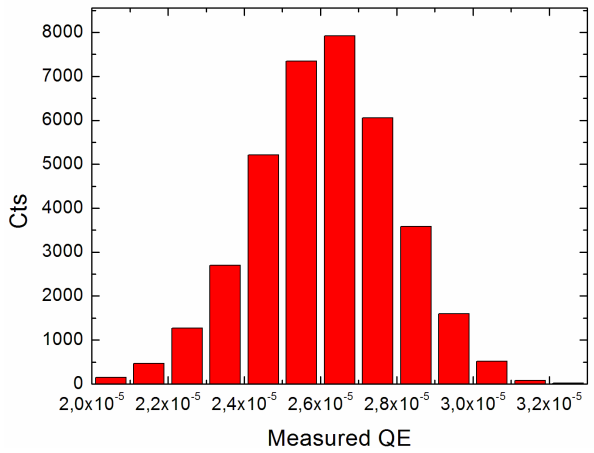


Figure 5: Histogram of the measured QE values during a typical shift.

Experimental data reported in Fig. 4 shows that some fluctuations can be detected in the efficiency of the cathode. We expect that the use of this new tool can be very useful to keep under control any variation of the quantum efficiency.

While in Fig. 4 a small decrease in the QE of the cathode has been revealed, the distribution of the same QE values reported in Fig. 5 shows that the standard mean value and standard deviation were respectively 2.5×10^{-5} and 1.8×10^{-6}.

We plan to use this QE monitor with the aim to build a slow feedback system dedicated to adjust the laser beam energy in order to prevent long term drifts of the electron bunch charge.

QE Uniformity

One of the key parameters of the SPARC photo-injector is the photocathode emission uniformity [1]. By using the Faraday cup and the photodiode, to measure respectively the electron bunch charge and the laser energy, the quantum efficiency can be deduced in a very small area (typically having 150 micron diameter). In order to deduce the QE map the laser beam spot size is tightly focused by means of a suitable fused silica lens and the quantum yield is determined from the slope of the emission curves (collected charge vs. laser energy) far from the space charge saturation regime. By moving the laser spot over the cathode surface the QE map of the cathode can be evaluated [4].

Figure 6 reports a picture of the front end software panel used to elaborate the waveforms acquired from NI 5152 board and related to the photodiode and Faraday cup readings

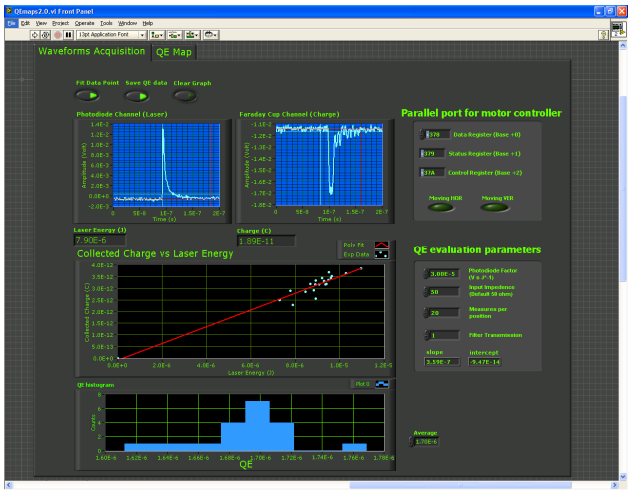


Figure 6: Picture of the front end software at console level used to acquire the emission curves of the photocathode.

Figure 7 reports the quantum efficiency map recorded after the laser cleaning process that was performed in order to restore the uniformity of emission together with a high value of quantum efficiency. Laser cleaning was performed by rastering the laser beam over an area of 3x3 mm^2 [4]. The acquired map shown in figure 6 clearly identify the squared area where the laser cleaning has been carried out giving also a measure of the emission uniformity achieved inside the irradiated area.

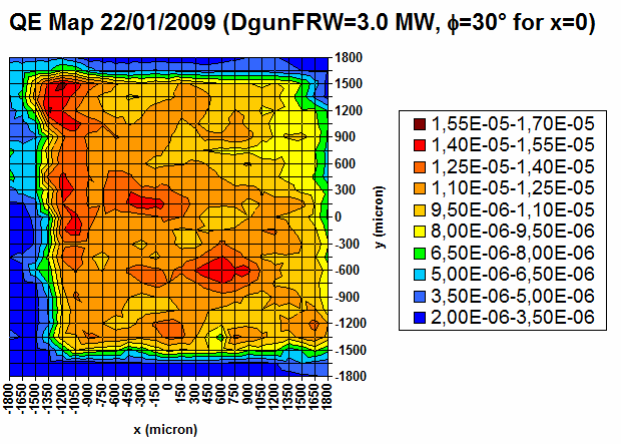


Figure 7: Quantum efficiency map of the SPARC photocathode obtained by data automatically collected through photo-injector control system.

CONCLUSIONS

In this work we have reported the implementation of the laser energy monitor and of the Faraday cup readings within the SPARC control system. The opportunity given by the insertion of this new devices are strongly related to the investigation of electron emission uniformity and to a future realization of a feedback system that will correct an eventual drift of the emission due to the degradation of the quantum efficiency properties of the photocathode.

REFERENCES

[1] SPARC Group, Conceptual Design Report, January 2004; http://www.lnf.infn.it/acceleratori/sparc/.

[2] G. Di Pirro et al, “SPARC contol system”, Proceedings of ICALEPCS07, Knoxville, Tennessee, USA, TPPB25, p.215 (2007); http://www.jacow.org

[3] C. Vicario et al., “Drive laser system for SPARC photoinjector”, Proceedings of PAC 2007 Albuquerque, New Mexico, USA, TUPMN040, p.1004 (2007); http://www.jacow.org

[4] L. Cultrera et al., J. Phys. D: Appl. Phys. 40 (2007) 5965

THE DCCT FOR THE LHC BEAM INTENSITY MEASUREMENT

P. Odier*, M. Ludwig, S. Thoulet, CERN, Geneva, Switzerland

Abstract

The LHC circulating beam current measurement is provided by eight current transformers, i.e. two DC current transformers (DCCT) and two fast beam current transformers (FBCT) per ring. This paper presents the DCCT, designed and built at CERN, including the sensor, the electronics and the front-end instrumentation software. The more challenging requirements are the needed resolution of 1μA rms for a 1s average, and the wide dynamic range of the circulating beam intensity from a single pilot bunch (8μA) to the total ultimate beam current of 860mA. Another demanding condition is the high level of reliability and availability requested for the operation and for the machine protection of this highly complex accelerator. The measurement of the first RF captured beam in ring 2 will be shown to demonstrate that the system is close to meeting these specifications both in terms of resolution and stability.

INTRODUCTION

The DCCTs, based on the fluxgate magnetometer principle [1], measure the mean current of the circulating beam. The DCCTs for LHC were designed according to tight engineering specifications [2] and built at CERN.

HARDWARE

General Layout

The DCCTs are installed in the long straight section in Point 4 of the LHC on a long girder which also supports the FBCT [3].

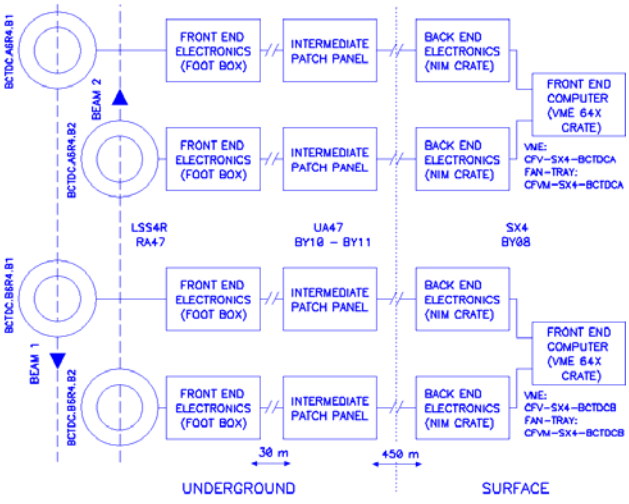


Figure 1: General Layout.

At this location the vacuum chamber is at room temperature and can be baked out to improve the quality of the vacuum. The front end electronics (FEE) is located in a shielded shelter under the girder and thus protected to some degree from beam induced radiation. An intermediate patch panel located in a parallel gallery housing the FBCT electronics provides an underground monitoring facility. The back end electronics (BEE), as well as the Front End Computer (FEC), are located in a surface building in Point 4 (Fig.1). The two systems named A, normally in operation, and B, normally kept as a spare, each contain one 1 DCCT per ring and 1 FEC.

Sensor

Different elements are installed between the external diameter of the vacuum chamber (64mm) and the internal diameter of the DCCT (114mm) [3]. This includes an electrical heater for baking out the vacuum pipe at 200ºC, combined with a thermal insulator and a water cooling circuit to ensure a temperature below 60ºC at the level of the magnetic cores.

The magnetic shielding is made of three layers of Mu-metal plus one external layer of pure iron. The external diameter (265mm) is limited by the second ring vacuum chamber (at this location the 2 beam pipe axes are separated by 192mm).



Figure 2: The DCCT with the connexions for the beam image current.

The "heart" of the DCCT consists of three ring cores of nanocrystalline alloy (inner diameter 146mm, cross-section 190mm^2, μ_i >100000) installed in a copper shielding. To avoid mechanical stresses and vibrations inducing noise, the cores are fixed loosely by flexible clips. Two cores, carefully matched to have an identical magnetization curve, are wound to form the fluxgate sensor. The third core is wound to form the AC part providing the bandwidth extension [4]. A magnetic shielding is placed between AC and DC cores to reduce the modulation ripple crosstalk. Two windings of 4 turns

*patrick.odier@cern.ch

embracing the three cores are used for the feedback and calibration. Two temperature probes (PT100) are fixed on the cores to monitor the DCCT output signal temperature dependence and to provide an alarm in case of overheating during the bake-out phase. The external layer of the shielding, electrically connected to the vacuum chamber via four copper braids on each side, offers a path for the LF components of the beam image current (Fig.2). The HF components pass through the DCCT via a series of capacitors placed around the ceramic gap cancelling the magnetic field induced by the beam current at these frequencies.

Back End Electronics

The BEE consists of separate modules placed in one NIM crate per DCCT (Fig.3). This modular approach allows for future improvement on particular elements and for retrofitting on existing DCCTs.

The SYNCHRO CLOCK generates both the modulation and demodulation clock (at twice the modulation frequency) with an accurate phase shift setting between them. A modulation frequency of 212Hz was chosen to avoid a very low frequency beat between the second harmonic of the modulation and any harmonics of the mains frequency.

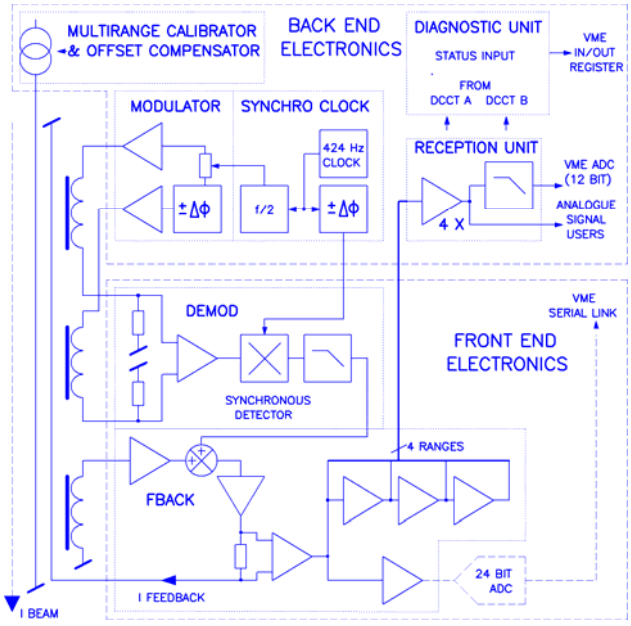


Figure 3: DCCT simplified schematics.

The MODULATOR generates the sinus wave used to modulate the two DC cores far into saturation. Small differences in the two cores are compensated by the amplitude balance and phase shift settings. A demagnetization process is automatically launched at power on.

The MULTIRANGE CALIBRATOR & OFFSET COMPENSATOR (CalPG) can generate a quick calibration sequence which consists of four successive calibrated current pulses sent into the sensor. This is performed on request and synchronously with the acquisition. The module also serves to remotely cancel the static offset.

The RECEPTION UNIT receives the analogue signal of four ranges, provided simultaneously, that cover the entire beam dynamic range from a few 10^9 to $5x10^{14}$ circulating charges (~3µA to ~900mA). After common mode rejection the 4 ranges are low-pass filtered before distribution to the various users. The cut off frequency ranges between 20Hz for the 12 bit ADC and 1.5 kHz for the analogue signal users.

The Acquisition and Control System consists of 4 VME boards served by a Central Processor Unit (CPU): the Timing Generator, the ADC, the Input/Output Registers and the Interface with the Safe Machine Parameter (SMP) System. The 12 bit ADC scans 16 channels (4 ranges and 4 auxiliary signals per DCCT) every 20ms.

The DIAGNOSTIC UNIT, which can be connected to the Input/Output Registers, will perform a crosscheck between systems A and B based on the comparison of the signals and statuses delivered by the DCCTs. The result of this check will help the instrument specialist to select the appropriate operational system.

Front End Electronics

The FEE consists of separate boards placed in one dedicated box per DCCT.

The modulation current of the two DC cores contains a second harmonic proportional to the DC beam current. The DEMOD board performs a synchronous detection of the second harmonic by multiplying the difference of the two modulation currents by the demodulation clock. The resulting signal has its frequency response limited to 10 Hz by a low pass filter.

The FBACK board adds the signals from the DEMOD board and from the AC winding and then generates the feedback current which, when passing through the sensor, cancels the magnetic field induced by the beam current. Measurement of the feedback current over a shunt resistor, taking into account the ratio of the number of turns, is a direct measurement of the beam current. The voltage drop across the shunt resistor is amplified by four different amplifiers providing in parallel the signals to the four ranges (spaced in sensitivity by a factor of 10) and to a fifth range dedicated to a 24 bit ADC. This ADC, soon to be added to the system, will have the highest resolution over the whole dynamic range and will transmit the data to the BEE via a serial link.

FRONT END SOFTWARE

The instrument front-end software runs on the CPU and reads out the ADC, selects an acquisition channel among the four ranges with optimum gain, averages data and controls the calibration. A common front-end software architecture is used to implement a set of real-time actions synchronized by events (acquire, publish). A structured shared memory (device) holds the data and provides the

decoupling between the synchronized real-time activity and the nearly asynchronous user communication. A communication process provides standard but nevertheless client specific communication interface. The real-time Unified Modeling Language (UML) diagram (Fig.4) shows the synchronized communication between the ADC and calibrator (hardware objects boxed), acquisition and machine protection link, device buffers and result publication and user control (software objects circled). During normal acquisition the ADC is triggered at 50Hz, read out and linked to machine protection at 10Hz with the results published at 1Hz. In order to check the instrument precision before first injection into the LHC a quick calibration sequence (grey area) can be triggered. This acquires the noise and calibration signal of all four ranges and lasts some 4 seconds, during which time the machine protection link is disabled.

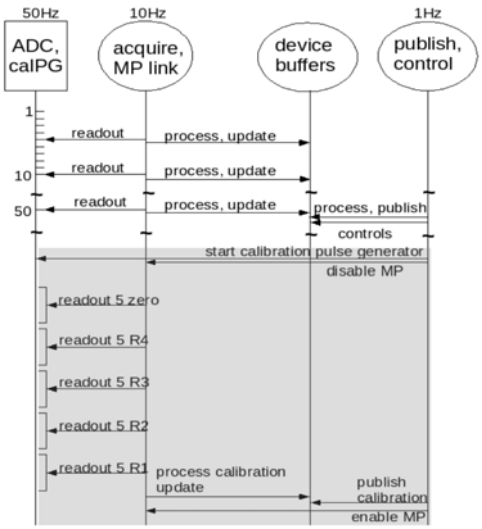


Figure 4: Real-time UML diagram showing hardware and software object invocation with time.

Interfaces and Usage

A standard software interface for general purpose provides the total beam intensity of each ring with a time resolution of 50Hz for the last 30s at an update rate of 1Hz. Further specialist interfaces provide the functionality for calibration and access to special functions such as simulation and client programs within the technical network of the control system. A dedicated optical link provides intensity acquisitions and status information to the LHC machine protection system at a rate of 10Hz.

FIRST RESULTS

During the first days of LHC running a fixed display, refreshed once per second was used to view the DCCT acquisition. It allowed the observation of total beam current as soon as the beam was circulating for more than 1 second (~11000 turns). This was the case for beam 2 on September 12th 2008. The two DCCTs on ring 1 were not commissioned with beam since beam 1 did not circulate for a sufficient duration before the LHC incident on September 19th 2009.

In Figure 5, one can see four successive injections of a single pilot bunch containing from 3.5×10^9 to 6×10^9 protons and circulating for between 100 seconds and 40 minutes. The DCCT used for this measurement was the operational system (A).

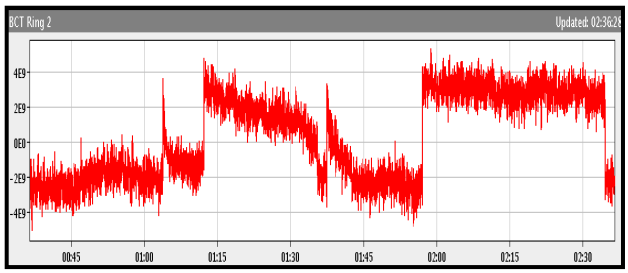


Figure 5: First circulating beam in ring 2 seen by BCTDC A (12/9/2008).

The noise and the slow fluctuation in the signal corresponds to 7×10^8 protons (rms value for a 1s integration time) which is equivalent to 1.3μA. There is a small negative offset of 2.5×10^9 (4.5μA) which should be automatically corrected for in the future.

CONCLUSION AND OUTLOOK

Although the beam time was not sufficient to commission the whole system, the short time with beam did allow confirmation that the DCCTs work as expected and meet the specifications in terms of noise and stability.

There are still numerous things to be commissioned with beam (DCCTs on beam 1, automatic range selection, transmission to the machine protection system and automatic offset correction). Also still to be implemented is the DIAGNOSTIC UNIT and the 24 bit ADC covering the entire dynamic range.

ACKNOWLEDGEMENTS

The authors would like to express their thanks to J.Longo for his invaluable involvement in the project. Thanks are also due to many colleagues in the CERN mechanical workshops for their very high quality work.

REFERENCES

[1] P.Odier, “DCCT TECHNOLOGY REVIEW”, CARE-Conf-2004-023-HHH, Lyon, December 2004.
[2] C.Fischer, R.Schmidt, “On the Measurements of the Beam Current, Lifetime and Decay Rate in the LHC Rings”, LHC-BCT-ES-0001, EDMS 359172.
[3] D.Belohrad, S.Longo; P.Odier; S.Thoulet, “Mechanical Design of the Intensity Measurement Devices for the LHC”, DIPAC’07, Venice, May 2007, WEPB09, p. 253 (2007).
[4] G.Gelato, “Beam current and charge measurement”, Beam instrumentation, ed.J.Bosser, CERN-PE-ED 001-92.

SLICED BEAM PARAMETER MEASUREMENTS

D. Alesini, E. Chiadroni, M. Castellano, L. Cultrera, G. Di Pirro, M. Ferrario, D. Filippetto, G. Gatti, L. Ficcadenti, E. Pace, C. Vaccarezza, C. Vicario, INFN/LNF, Frascati, Italy
B. Marchetti, A. Cianchi, University of Rome Tor Vergata and INFN-Roma Tor Vergata, Italy
A. Mostacci ,University La Sapienza, Roma, Italy
C. Ronsivalle, ENEA C.R. Frascati, Italy

Abstract

One of the key diagnostics techniques for the full characterization of beam parameters for LINAC-based FELs is the use of RF deflectors. With these devices it is possible to completely characterize both the longitudinal and the transverse phase space. In the paper we illustrate the main design considerations for time resolved (sliced) beam parameter measurements using RF deflectors (RFDs). Measurement setups for longitudinal pulse shape as well as phase space and transverse beam slice emittance characterizations are described. The main sources of error are discussed and the design criteria of these devices are presented. In particular the SPARC RF deflector and the related diagnostic lines as well as recent measurement results are shown. Measurement results obtained at LCLS and FLASH are then shortly illustrated.

INTRODUCTION

The characterization of the longitudinal and transverse phase space of the beam at the end of an injector is a crucial point in order to verify and tune all photo-injector parameters. With the use of an RFD it is possible to measure the bunch longitudinal profile and, adding a dispersive system, the longitudinal beam phase space [1,2]. Similarly, since the longitudinal beam distribution can be projected along a transverse coordinate, the transverse emittance of each longitudinal bunch slice can be measured using the quadrupole scan technique [3]. In the first section of the paper we shortly review the basics principles of the longitudinal and transverse beam phase space characterization using an RFD. The main properties of both SW and TW deflecting structures in term of electromagnetic field configuration and performances are discussed in the second section. In the third section we illustrate the typical measurement setups and, in particular, those installed in the SPARC photo-injector [4]. The main measurement results obtained at SPARC are discussed in the fourth section. The last section shows some relevant results obtained at LCLS [5] and FLASH [6] and new proposed techniques.

BEAM DIAGNOSTICS USING RFD

The different types of measurements that can be done with RFDs are based on the property of the transverse voltage (V_{DEFL}) to introduce a correlation between the longitudinal coordinate of the bunch (t_B) and the transverse one (vertical, in general) at the screen position (y_S). The phase of the deflecting voltage is chosen in order to have a zero crossing of the transverse voltage in the center of the bunch, giving a linear transverse deflection from the head and the tail of the bunch itself. After the deflector the transverse kick results into a transverse displacement of each longitudinal bunch slice, proportional to its position with respect to the bunch center. The mechanism is illustrated in Fig. 1.

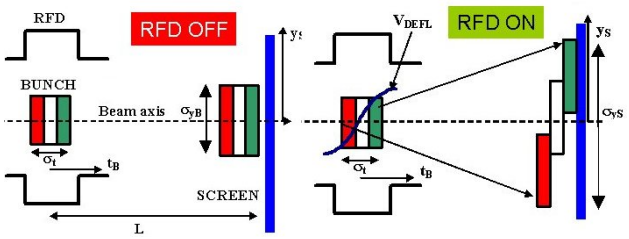


Figure 1: Longitudinal to transverse correlation induced by the RFD transverse voltage.

Since the beam has a finite transverse emittance, the distribution of the deflected bunch at the screen position is the superposition between the deflected beam profile and the transverse size of each bunch slice. In the plot we assumed that all longitudinal slices have the same transverse dimension on the screen (σ_{yB}) and that there is a simple drift (L) between the RFD and the screen. The total vertical rms distribution (σ_{y_S}) at the screen is simply given by [2]:

$$\sigma_{y_S}^2 \cong K_{cal}^2 \sigma_{t_B}^2 + \sigma_{y_B}^2 \tag{1}$$

where $K_{cal} = (V_{DEFL}/E)\omega_{RF} L$, ω_{RF} is the angular frequency of the deflecting voltage and E is the beam energy in eV units. From this formula one can define the resolution length (σ_{tB_RES}) as the bunch length that gives, on the screen, a distribution with rms vertical size equal to $\sqrt{2}\sigma_{yB}$. It is simply equal to:

$$\sigma_{t_B_RES} = E\frac{\sigma_{y_B}}{V_{DEFL}\omega_{RF}L} = \sqrt{E/E_0}\sqrt{\varepsilon\beta_S}\frac{1}{V_{DEFL}\omega_{RF}L} \tag{2}$$

where ε is the transverse normalized emittance of the beam, β_S is the vertical β-function at the screen position and E_0 is the electron rest energy.

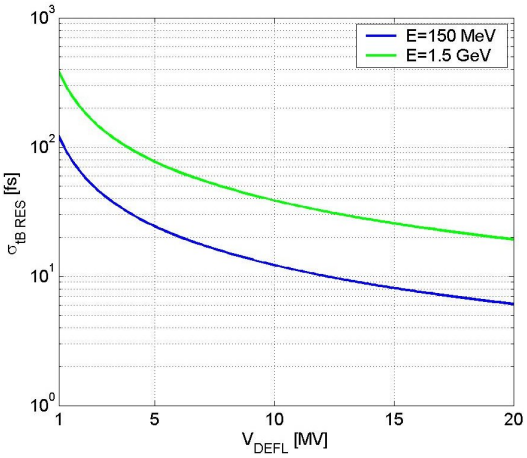


Figure 2: resolution as a function of the transverse deflecting voltage V_{DEFL}. Parameters: ε=1 [mm·mrad], f_{RF}=2.856 [GHz], β_S=1 m, σ_{yB}≅18 μm (@1.5 GeV), σ_{yB}≅58 μm (@150 MeV), L =4 m.

The plot of the resolution as a function of the transverse voltage is reported in Fig. 2 for the set of parameters reported in the figure caption and for two different energies. In the SPARC case, as example, we have that V_{DELF}≅1.5 MV, f_{RF}=2.856 [GHz], σ_{yB}≅100 μm, E≅150 MeV and L≅4m, the typical resolution is then *~130 fs*. From Fig. 2 it is possible to observe that resolution of the order of few ten of *fs* are reachable with standard deflecting structures in the case of a 1.5 GeV beam and below ten *fs* in the case of a 150 MeV beam.

The other important characteristics of such system is that it is possible to self calibrate the measurements. The coefficient K_{cal} that relates the vertical coordinate at the screen with the time coordinate of the bunch can be, in fact, directly calculated measuring the bunch centroid position $\langle y_S \rangle|_{meas}$ on the screen for different values of the RFD phase by the formulae:

$$K_{cal} = \omega_{RF} \frac{\langle y_S \rangle|_{meas_1} - \langle y_S \rangle|_{meas_2}}{\Delta\phi|_{meas_1} - \Delta\phi|_{meas_2}} \tag{3}$$

Typical measurements of the calibration coefficient in the SPARC photo-injector are reported in Fig. 3 for different energies.

A careful discussion of other source of errors in the measurements with RFD is reported in [1,2].

RF DEFLECTING STRUCTURES

Different types of deflecting structures can be used for beam diagnostics. As in the case of accelerating sections, the main differentiation is between the travelling wave (TW) and standing wave (SW) cavities. In general RFDs are multi-cell devices working on the TM_{11}-like mode [7,8]. In all type of structures both the electric (*E*) and the magnetic (*B*) field contribute to the total deflection. Figure 4 shows the two field components on axis (z is the propagation direction). In the plot we also reported the longitudinal electric field on the deflecting plane. From the plot it is possible to observe that the deflecting modes have non-zero derivative of the longitudinal electric field on axis. We will discuss later the effect of such component in the measurements.

Since there are two possible polarities of the deflecting field, polarizing rod or holes are, in general, foreseen to introduce an azimuthal asymmetry in the structure fixing the working polarity itself [7,8].

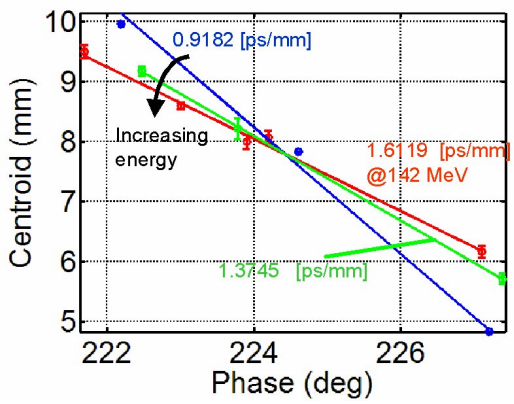


Figure 3: Typical measurements of the calibration coefficient in the SPARC photo-injector for different energies.

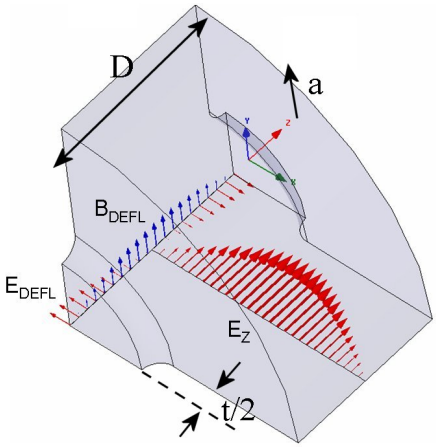


Figure 4: Single cell deflecting structure *E* and *B* field vectors.

Another important characteristic of the deflecting modes is that the transverse force is uniform over a wide region inside the iris aperture and is practically constant over a region with radius of a/2.

In TW devices the iris aperture (a) is the most important parameter to fix the deflection efficiency, group velocity and the attenuation per unit length. Analytical expressions valid in the case of small pitch approximation (t<<D) [7,8] and can be very useful for a first evaluation of the deflecting structures parameters. Typical working mode is the 2π/3. A detailed analysis of such structures is, for example, reported in [2].

SW structures are-multi cell devices working, for example, on the π-mode. Theses structures have, in general a higher efficiency per unit length with respect to the TW ones but the maximum number of cells is limited

to few tens because of mode overlapping. Due to the resonant nature of their electromagnetic field, they requires, in general, circulators to protect the RF source from reflections and they have higher filling times compared to the TW case.

Figure 5 shows, for example, the deflecting voltage and the maximum surface electric field for four types of structures working in S Band at 2.856 GHz. From the plot it is possible to observe that, because of the higher surface electric field, SW multi-cell devices can be used with input power below 10 MW giving V_{DEFL}<7 MV.

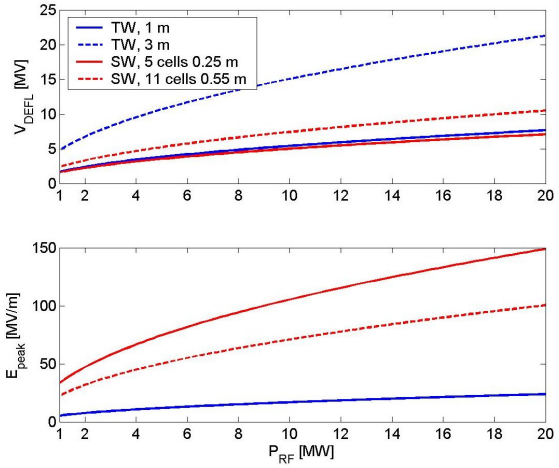


Figure 5: the deflecting voltage and the maximum surface electric field for four types of structures working in S Band at 2.856 GHz.

An example of SW structure is the SPARC RFD [9]. It is a 5 cells SW structure working on the π-mode at 2.856 GHz and fed by a central coupler with coupling coefficient equal to 1. Its transverse shunt impedance is ≈ 2.5 MΩ and gives a deflection of 3 MV with an input power of 2 MW. It is now installed in the SPARC injector (as shown in Fig. 6) for beam diagnostics. More detail can be found in [9].

Induced Energy Spread by RFD

The TM_{11}-like deflecting modes has a non-zero derivative of the longitudinal electric field on axis. This is a general property of the deflecting modes because the deflecting voltage is directly related to the longitudinal electric field gradient through the Panofsky-Wenzel theorem by the formula:

$$\tilde{V}_y = j\frac{c}{\omega}\int \nabla_y \tilde{E}_z e^{j\frac{\omega}{c}z} dz \tag{4}$$

Since this gradient is 90 deg out-of phase with respect to the deflecting voltage, it introduces an energy spread inside the bunch when the deflectors are used for beam diagnostics (in this case, in fact, the phase of the deflecting voltage is set to have zero crossing of the transverse voltage in the center of the bunch).

The contribution of the RFD to the slice energy spread is not negligible and, to the first order depends linearly on the vertical slice size inside the RFD (σ_{yB_RFD}) and can be evaluated by the formula:

$$\sigma_{E_RFD} \cong \frac{\omega_{RF}}{c}\hat{V}_{DEFL}\sigma_{yB_RFD} \tag{5}$$

Typical values, in the case of SPARC, are of the order of 10-20 keV since $\sigma_{yB_RFD}\cong$300 μm.

The contribution of the deflector to the slice energy spread can be taken into account performing two measurements at two different deflecting voltages and using the following formulae to evaluate the sigma σ_{yB_RFD} of each slice.

$$\sigma^2_{y_RFD} = \left(\frac{c}{\omega_{RF}}\right)^2 \frac{\sigma^2_{E_MIS_1} - \sigma^2_{E_MIS_2}}{\hat{V}^2_{DEFL_1} - \hat{V}^2_{DEFL_2}} \tag{6}$$

where $\sigma_{E_MIS_1,2}$ are the two measured slice energy spreads.

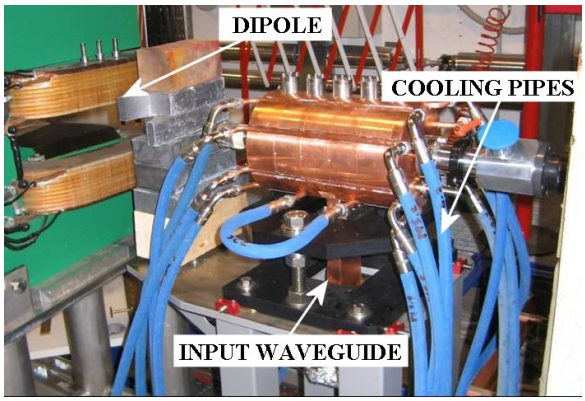


Figure 6: SPARC RFD installed in the LINAC.

MEASUREMENT SETUP

Slice Emittance and Beam Profile

The slice emittance is one of the fundamental parameter that defines the FEL process. It also contains important beam dynamics signature, revelling for instance if the emittance compensation process was performed at its best or not. The technique is similar to the usual quadrupole scan [3]. Because the RFD deflects the beam vertically a set of values for the quadrupoles must be find in advance to change only the horizontal dimension of the beam, keeping constant the vertical size in order to have the same longitudinal resolution.

The typical measurement setup is reported in Fig. 7. The picture and dimensions are referred to the SPARC diagnostics at the end of the 150 MeV LINAC. In case of beam profile and transverse slice emittance measurements the beam image is taken on the screen 1 and the slice beam emittance is measured by the quadrupole scan done by the triplet before the RFD. To correctly choose the quadrupole currents one has to previously measure the projected emittance and the twiss functions before the triplet (through an usual quad scan technique) and find the correct set of quadrupoles knowing the model of the beam line from the triplet to the screen 1.

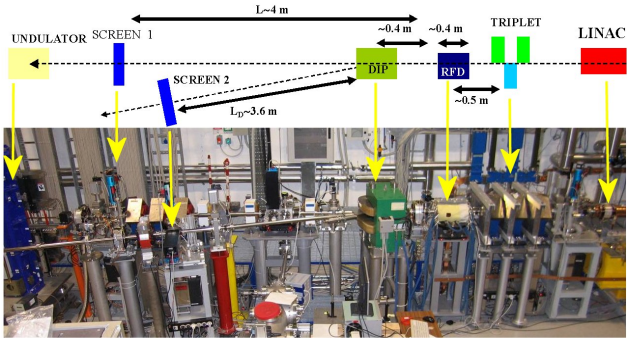


Figure 7: Typical measurement setup. The picture and dimensions are referred to the SPARC diagnostics.

Longitudinal Phase Space

The longitudinal phase space can be characterized using the combination of RFD and dipole as illustrated in Fig. 7. In this case the beam is projected into the screen 2 and, also in this case, in order to have enough longitudinal resolution the vertical dimension at the screen position has to be taken under control. From the phase space picture the slice energy spread can be extrapolated by slicing the beam vertically and measuring the beam thickness in energy as function of time. Also the horizontal β-function at the screen 2 has to be reduced as much as possible in order to reduce the emittance contribution to the energy spread measurement. In any case the dominant systematic error is the energy spread induced by the RFD.

MEASUREMENT RESULTS AT SPARC

The SPARC project is an R&D photo-injector facility for the production of high brightness electron beams to drive SASE and SEEDED FEL experiments in the visible and UV light [10]. The high beam quality produced by SPARC will also allow investigations into the physics of ultra-short beams, plasma wave-based acceleration, and production of advanced X-ray beams via Compton back-scattering. The study of the beam slice properties, such as slice emittance or slice energy spread, allow to deeply investigate the details of emittance compensation method and to tune the machine for best performance. Moreover the knowledge of the beam current, beam energy, slice emittance and slice energy spread gives a complete description of the FEL process.

Beam Profile

Several beam profile measurements have been done at SPARC in different operating condition. Here we report the results obtained during the velocity bunching experiment. The detail of the experiment is illustrated in [10]. The beam is injected in a long accelerating structure at the crossing field phase and it is slightly slower than the phase velocity of the RF wave. In this condition it slips back to phases where the field is accelerating, but at the same time it is chirped and compressed.

The longitudinal beam profile measurements are crucial for this experiment because, while the bunch is compressed, it also change its longitudinal distribution. Figure 8 shows the measured compression ratios versus injection phase in the first travelling wave structure. The red curve has been obtained with PARMELA simulation. The error bars in figure have been computed over the 10 images collected for each measurement, a more detailed study including jitters effects and systematic error will be the subject of future investigations.

We have been operating with a quasi-Gaussian longitudinal laser profile ~7.5 ps FWHM long with 300 μm transverse spot size. The bunch charge was 300 pC. The beam acceleration on crest corresponds to the phases around -75 deg. In this condition the measured longitudinal profiles compared with the PARMELA simulation are reported in Fig. 9 (a), the rms bunch length is length measured at the linac exit was ~3.25 ps with energy of 150 MeV. The beam profile compared with simulation in the case of a compression factor equal to 3 (inj. Phase=-87 deg) is reported in Fig. 9 (b).

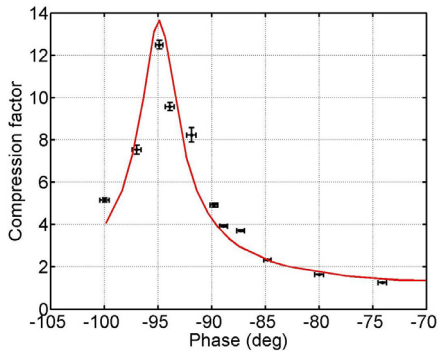


Figure 8: Compression factor versus injection phase, experimental points and PARMELA simulations (red curve).

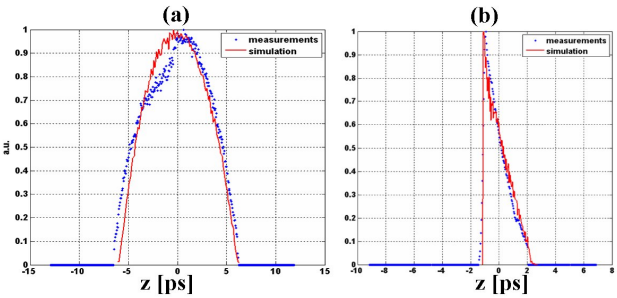


Figure 9: Beam profiles in the velocity bunch experiment @ SPARC; (a) not compressed beam, (b)compression ratio 3.

Slice Emittance

In the plot of Fig. 10 we compare the slice emittance measurement with a beam with 125 pC of charge and a laser spot on the cathode of 320X300 μm with a PARMELA simulation. In this plot we used a technique that we called RUS (Running Slice). It is very hard, especially on the beam tails, to determine the first and the last slice. This assumption however has impact on the position of all the other slices. To overcome this problem and resolve the ambiguity we fix a slice length (in our

case 200 μm) and move it along the bunch in step of about 500 fs.

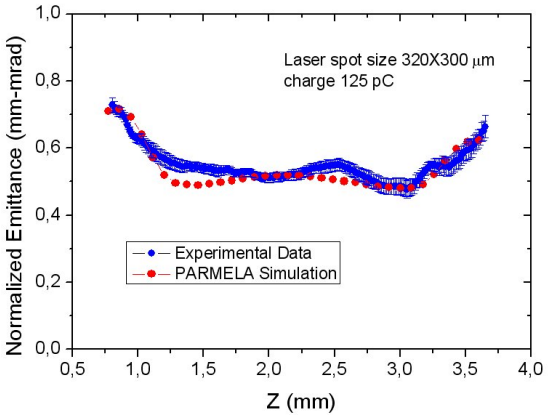


Figure 10: Comparison between slice emittance measurements and PARMELA simulation.

Longitudinal Phase Space

A typical longitudinal phase space measurements is reported in Fig. 11. From the plot the slice energy spread has been extrapolated and is given in Fig. 12, compared with simulations. The main discrepancy between the simulations and the experimental data is given by the RFD contribution that has been estimated by the formula (5) to be ~15 keV. The emittance contribution has not been subtracted from the measurements, but it has been estimated to be less than 10%.

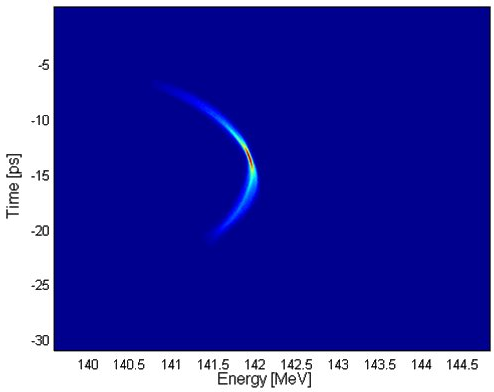


Fig. 11: Longitudinal trace space at 140 MeV.

EXPERIMANTAL RESULTS IN OTHER ACCELERATOR FACILITIES

New important results have been also reached in other accelerator facilities like LCLS or FLASH. In the first case two TW deflecting structures (LOLA type) are installed in the LINAC and allow measurements at low (135 MeV) and high energies (13.5 GeV). By RFD structures several important measurement have been done like the measurement of the increment in the energy spread by laser heating, slice emittance, or verification of the effect of the X-Band cavity in the correction of the chirp in the energy distribution of the beam [5]. Several measurements have been also done at FLASH by a TW 3.6 m long cavity at the end of the injector [6]. Beam profiles and slice emittances in different operating conditions have been done with resolution of the order of 20 fs. Very promising results have been also reached few years ago with circular polarized RF deflectors. [11]. In this case with the same device it is possible to simultaneously measure the longitudinal phase space (without introducing energy spread errors) and the beam profiles. Recent interesting new techniques in the deflecting cavities fabrication adopting aluminium have been also explored [12].

CONCLUSIONS

RFDs are crucial devices for both longitudinal and transverse phase space characterization allowing reaching resolution below 10 fs. The measurement setups and the experimental results, in the case of SPARC, have been shown and discussed. In particular the use of the RFD technique has been fundamental in the velocity bunching experiment at SPARC. A possible solution to take into account the contribution of the RFD in the energy spread slice has been also illustrated. Important new results have been also reached in other accelerator facilities like LCLS or FLASH and the use of the RFD technique allowed measuring laser heating effects or longitudinal phase space correction using X-Band cavities.

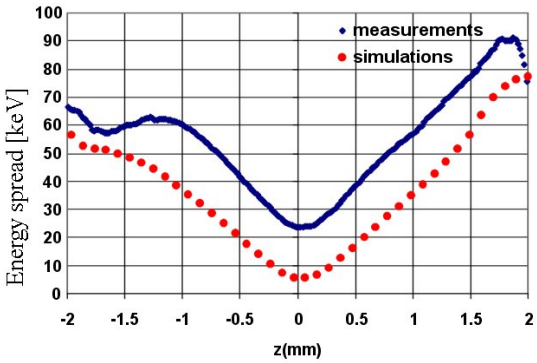


Figure 12: Measurements of the slice energy spread.

ACKNOWLEDGEMENTS

The authors would like to acknowledge P. Emma, C. Gerth and M. Rohrs for the information's and material on LCLS and FLASH measurement results.

REFERENCES

[1] P. Emma, et al., LCLS-TN-00-12, 2000.
[2] D. Alesini, IJMPA, Vol. 22 No: 22 Year: 2007.
[3] M. Minty and F. Zimmermann, Springer, 2003.
[4] B. Marchetti, et al., to be published in Proc. of PAC 09.
[5] P. Emma, et al., to be published in Proc. of PAC 09.
[6] M. Rohrs, et al., Proc. of EPAC 06 and FEL 05.
[7] P. Bernard and H. Lengeler, CERN 68-30, 1968.
[8] G. A. Loew, et al., SLAC Report 17, 1963
[9] D. Alesini, et al., NIM A, 2006.
[10] M. Ferrario et al., to be published in Proc of PAC 09.
[11] J. Haimson, et al., AIP Conf. Proc. 647, 2002.
[12] D. Alesini, to be published in Proc. of PAC 09.

OPTICAL DIFFRACTION RADIATION INTERFEROMETRY AS ELECTRON TRANSVERSE DIAGNOSTICS*

E. Chiadroni†, M. Castellano, INFN/LNF, Frascati, Italy
A. Cianchi, University of Rome Tor Vergata and INFN Tor Vergata, Rome, Italy
K. Honkavaara, G. Kube, DESY, 22607 Hamburg, Germany

Abstract

The characterization of the transverse phase space for high charge density and high energy electron beams is demanding for the successful development of the next generation light sources and linear colliders.

Due to its non-invasive and non-intercepting features, Optical Diffraction Radiation (ODR) is considered as one of the most promising candidates to measure the transverse beam size and angular divergence.

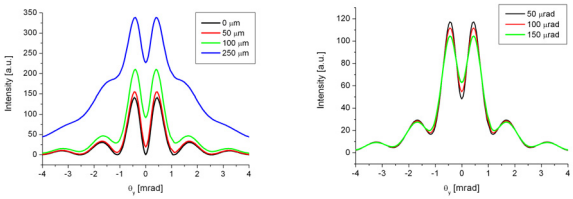
A thin stainless steel mask has been installed at 45^o with respect to the DR target and normally to the beam propagation to reduce the contribution of synchrotron radiation (SR) background. In addition, interference between the ODR emitted on the shielding mask in the forward direction and the radiation from the DR target in the backward direction is observed. This is what we call Optical Diffraction Interferometry (ODRI) which, better than ODR, allows to separate the intrinsic ambiguity between the radiation produced by a single particle passing through a slit with an offset with respect to its center and a gaussian distributed particle beam with standard deviation of magnitude equal to such offset.
Results of an experiment, based on the detection of the ODRI angular distribution to measure the electron beam transverse parameters and set up at FLASH (DESY, Hamburg) are discussed in this paper.

INTRODUCTION

The development of high energy Linear Colliders (LC) [1] and short wavelength Free-Electron Lasers (FEL) [2, 3, 4] requires high quality electron beams, which means small transverse emittance (< 1 mm mrad) and high peak current (≈ kA). Due to the large power density of this kind of beams, a non-intercepting diagnostics needs to be developed and applied. In 1997 one of the authors suggested a new method for the non-intercepting measurement of transverse beam size [5]. The idea is based on the observation of diffraction radiation (DR) emitted by a charged particle beam going through a slit in a metallic foil due to the interaction of the charge electromagnetic (EM) field with the screen surface. The intensity of the radiation increases linearly with the number of charges and is proportional to $e^{-\frac{2\pi a}{\gamma\lambda}}$, where a is the vertical slit aperture, γ the Lorentz factor and λ the emitted wavelength. The factor $\gamma\lambda/2\pi$, called as DR impact parameter, is the natural size of the radial extension of the EM field, thus when $a \cong \gamma\lambda/2\pi$ DR is emitted.

Since the beam goes through the slit, DR is a non-intercepting diagnostics and, therefore, excellent to be used parasitically without disturbing the electron beam.

The aim of our experiment is measuring the transverse beam size and divergence, in order to calculate the transverse emittance, by studying the angular distribution of Optical Diffraction Radiation (ODR). The DR angular distribution is produced by the interference of radiation from both edges of the slit. The visibility of the interference fringes is correlated to the beam size (see Fig. 1, left).



(a) (b)

Figure 1: Theoretical calculation for the angular distribution of the vertical component of ODR for different transverse beam sizes and vertical angular divergences. The simulation has been performed assuming an electron beam energy of 680 MeV, with interference filter (800 nm) and 0.5 mm slit width.

The effect is also affected, in a slightly different way, by the angular divergence of the beam (Fig. 1, right): the ODR angular distribution becomes wider and the intensity of the minimum higher, when the beam divergence increases.

A dedicated analysis of the radiation angular distribution allows then to separate the two effects. If the beam waist is located in the plane of the DR screen, the transverse emittance can be derived with a single non-intercepting measurement.

EXPERIMENTAL APPARATUS

Our experiment is carried out at FLASH (DESY, Hamburg)[7]. FLASH is an excellent facility for this experiment, since it can drive long bunch trains, up to 800 bunches per macropulse allowing a high charge operation, and it has a good long term stability, a small transverse

* Work supported by the European Community Infra-structure Activity under the FP6 "Structuring the European Research Area" program (CARE, contract number RII3-CT-2003-506395)
† enrica.chiadroni@lnf.infn.it

emittance (~ 2 mm mrad), and a high electron beam energy, approaching 1 GeV.

Our experimental set-up is placed in the by-pass beam line (Fig. 2) very far (about 40 m) from the dipole magnets in order to minimize the contribution of synchrotron light coming from them.

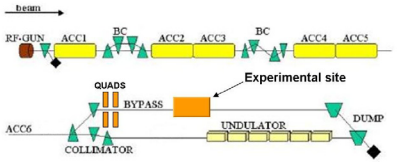


Figure 2: FLASH layout and experimental site.

The experimental set-up consists of two aluminated silicon screens (DR screen), one with the mask the other one without it (cfr. Fig. 5). A motorized actuator allows to insert the desired screen in the vacuum pipe under an angle of 45^o with respect to the beam direction. The target is of fundamental importance for the success of the experiment, since damaged edges and/or an uneven surface may change the interference effects, resulting in a blurred angular distribution.

The DR screen is constructed by lithographic technique starting from a silicon nitride wafer and opening two slits, one of 0.5 mm and the other of 1 mm aperture, by means of chemical etching. The slits on the DR screen are separated by 2 cm, and this space between the slits on the second DR screen without a mask, is used as a standard OTR (Optical Transition Radiation) screen. The main advantage of the silicon nitride with respect to SiO_2 [8] is a much less etching rate which preserves the silicon substrate from damages and makes the surface much more uniform. An aluminum layer is deposited by sputtering on the target to enhance the reflectivity.

ODR MEASUREMENTS

In the first phase of the experiment we had to cope with a very strong background of synchrotron radiation produced not only by the last dipole but also by some strong quadrupoles of the by-pass transport line. Although the distance of these optical elements was more than 40 meters far from our ODR screen, the vacuum pipe acted as an optical guide, producing the pattern shown in Fig. 3. The OTR angular distribution was almost covered and could be distinguished with difficulty.

A big effort, both in beam handling and software development, was required in order to reach a good background subtraction and the elimination of the “salt-and-pepper” noise produced by X-rays. At the end we were able to prove a good qualitative agreement between the experimental data and the simulations, as shown in Fig. 4.

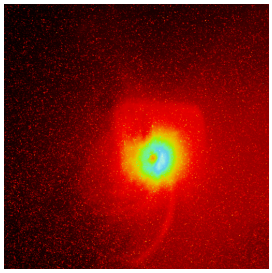


Figure 3: OTR angular distribution covered by the synchrotron radiation background.

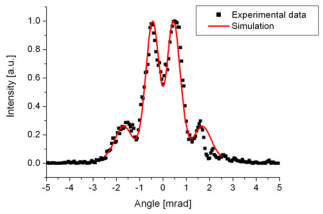


Figure 4: Experimental ODR profile, after background subtraction, and comparison with theory. Beam parameters: 680 MeV, 0.7 nC, 25 pulses, 2 s, 800 nm. Fit parameters: 610 MeV, 0.5 mm, σ_y=80 μm, $\sigma_y^{'}$=125 μrad.

OPTICAL DIFFRACTION RADIATION INTERFEROMETRY

To reduce the synchrotron radiation background and to distinguish the effects of rms beam size and beam offset within the slit on the angular distribution, a stainless steel shield with larger cuts (2 mm and 1 mm, respectively) is mounted at 45^o respect to DR target. The electron beam direction is normal to the shield. The sketch of the screen and the shield is in Fig. 5.

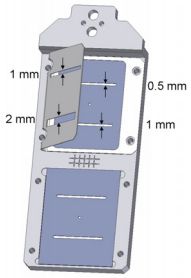
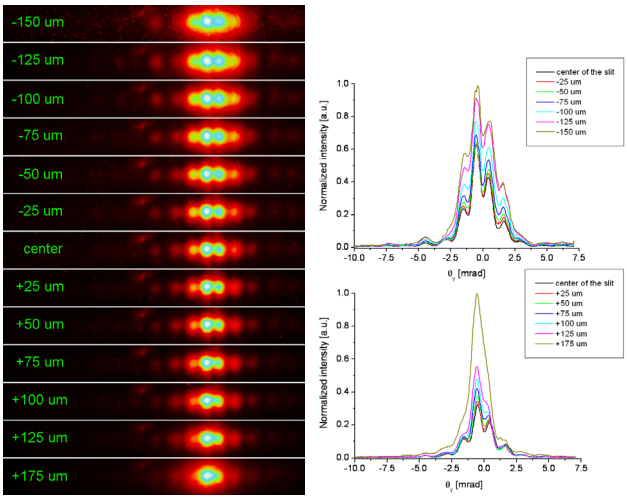


Figure 5: Sketch of the new screen together with its shielding mask.

In our experimental conditions, with an ODR emitted wavelength of 800 nm and 1 GeV electron beam energy, the size of the 1 mm cut on the shield is not large enough to prevent the production of ODR in forward direction. The forward ODR from the shield is then reflected by the DR screen and it interferes with backward ODR produced by the DR screen itself. The amplitudes of the two sources,

i.e. forward emitted DR from the 1 mm slit and backward emitted DR from the 0.5 mm slit, are different both in intensity and in angular distribution, thus the interference results in the suppression of the central peaks and the enhancement of the side maxima.

A complete transverse scan of the beam position in the slit aperture has been carried out by moving the slit with respect to the beam position from one edge of the slit to the other edge. The results are shown in Fig. 6: the ODRI angular distribution image for different impact parameters is displayed on the left, the corresponding ODRI angular distribution profile is plotted on the right. We moved in steps of 25 μm around the slit center. Due to the fact that it is very hard to align the two slits with a precision of fractions of the emitted wavelength, a different behavior of the experimental distributions was supposed while going from the center of the slit to one edge or towards the other. For these ODRI measurements, FLASH was operated with 13 bunches per macropulse, 0.8 nC per bunch, 2 s CCD exposure time. Polarizer and interference filter to select the 800 nm wavelength were inserted.



(a) (b)

Figure 6: ODRI angular distribution image (left) and profile (right) for different impact parameters.

Fig. 6 shows strong asymmetrical ODRI angular distributions. This asymmetry can only be explained by assuming that the two half planes of the 0.5 mm slit are parallel but not perfectly coplanar. In this case, the field of a particle incident with angle α (in our case, $\alpha = \pi/4$) will be reflected by one half plane earlier than by the other. The phase difference between the two fields, in the approximation of $d << \gamma\lambda$ and $\beta \approx 1$, is $\phi_0 = 4\pi d/\lambda \cos\alpha$ (d is the longitudinal misalignment). A detailed discussion can be found [9].

The scan has been repeated with a smaller transverse beam size, σ_y=78 μm, in order to observe any slight change of the ODRI angular distribution. Let us now focus the attention on the ODRI angular distribution measured with the beam in the center of the 0.5 mm slit. The ODRI angular distributions for both transverse electron beam sizes (89 μm and 78 μm) are compared in Fig. 7 demonstrating the sensitivity of the experiment even on smallest variations of the transverse beam size in the order of a few micrometer.

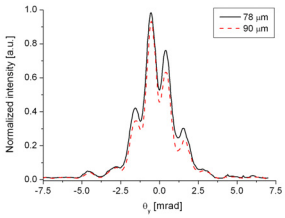
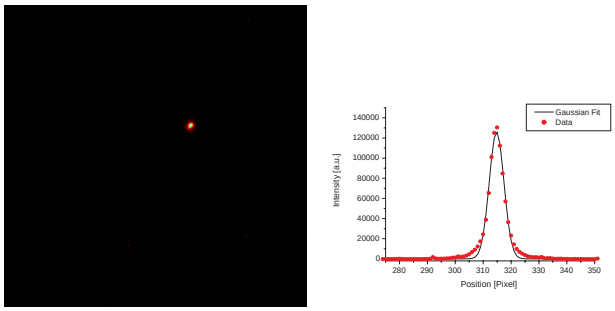


Figure 7: ODRI experimental angular distribution for two different rms vertical beam sizes, σ_y=78 μm and σ_y=89 μm.

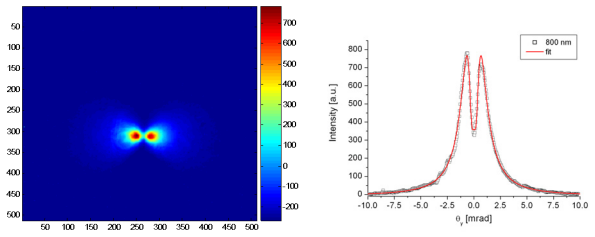
The analysis of the Optical Transition Radiation (OTR) in both image and focal plane allowed the estimation of rms electron beam size (Fig. 8), energy and vertical angular divergence. Fig. 9 (left) shows the OTR angular distribution obtained with an integrated charge of 16 nC (4 bunches of 0.8 nC per macropulse with 5 Hz pulse repetition rate and 1 s camera exposure time). The synchrotron radiation background is subtracted. The interference filter to select the 800 nm wavelength and the polarizer to select the vertical component are inserted. From the fit of the OTR angular distribution profile we estimate a beam energy of 870 MeV and a vertical angular divergence of 150 μrad.



(a) (b)

Figure 8: OTR beam image (left) and its vertical projection (right). The estimated rms beam size is 89 μm.

In order to validate our experimental results, the fitting function has been modified with respect to the [6] formulas by the introduction of an additional phase term, which takes into account the unavoidable non planarity of the two halves of the slit at the level of fractions of wavelength. Furthermore, since the distance between the two screens is of the order of few centimeters, i.e. much less than the formation zone at this energy and wavelength, interference between the forward DR produced by the first slit and the backward DR coming from the second is observed. Thus, both misalignment and phase difference between the two slits are considered as additional fitting parameters. A



(a) (b)

Figure 9: OTR angular distribution (left) and its vertical profile, fit to retrieve beam energy and beam angular divergence (right). The fit takes into account the contribution of the angular divergence.

Gaussian distributed beam both in transverse beam size and angular divergence is assumed.

The results obtained by the fit are presented in Fig. 10 and Fig. 11 for the two beam sizes considered, showing a very good agreement with experimental data.

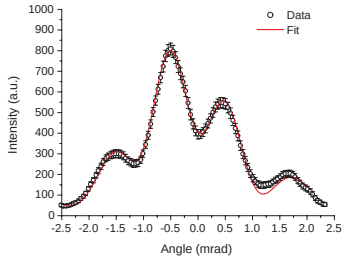


Figure 10: ODRI experimental angular distribution and fit which allows to retrieve beam and geometrical parameters. Fit parameters: 860 MeV, σ_y=83 μm, σ'_y=200 μrad, Δy=12 μm.

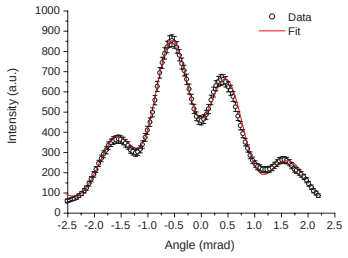


Figure 11: ODRI experimental angular distribution and fit which allows to retrieve beam and geometrical parameters. Fit parameters: 865 MeV, σ_y=70 μm, σ'_y=263 μrad, Δy=13μm.

CONCLUSIONS

A detailed and quantitative study of the ODRI angular distribution, together with the analysis of the OTR in the image and focal plane, has allowed us to demonstrate the feasibility of a single shot emittance measurement in a phase space waist.

The advantage of using ODRI instead of ODR angular distribution is the chance to distinguish the effect due to the transverse beam size to the one due to the beam offset from center of the slit, which, otherwise, are equivalent. Furthermore, since the visibility of fringes is increased, the sensitivity to the beam dimension is higher.

REFERENCES

[1] http://www.linearcollider.org.

[2] M. Altarelli et al. (Eds.), "XFEL: The European X-Ray Free-Electron Laser: Technical Design Report", DESY 2006-097.

[3] http://www-ssrl.slac.stanford.edu/lcls/cdr.

[4] http://www.lnf.infn.it/acceleratori/sparc/.

[5] M. Castellano, Nucl. Instr. and Meth. Phys. Res. A **394**, 275 (1997).

[6] M.L. Ter-Mikaelian, "High-Energy Electromagnetic Processes in Condensed Media" (Wiley-Interscience, New York, 1972).

[7] W. Ackermann et al, *Nature Photonics* **1** 336 (2007).

[8] E. Cianci et al., "Micromachined Silicon Slit for Beam Diagnostic in Particle Accelerator", *Proc. SPIE* **4557**, 242-249 (2001).

[9] M. Castellano et al., "Diffraction Radiation as a Diagnostic Tool at FLASH", Proceedings of Channeling 2008, Erice, Sicily.

ELECTRON SCANNER FOR SNS RING PROFILE MEASUREMENTS*

W. Blokland, S, Aleksandrov, S. Cousineau, ORNL, Oak Ridge, TN 37831, U.S.A.
D. Malyutin, S. Starostenko, Budker Institute of Nuclear Physics, Novosibirsk, Russia

Abstract

An electron scanner has been commissioned to non-destructively measure the transverse profiles in the Spallation Neutron Source (SNS) Ring. The SNS Ring is designed to accumulate on the order of 1.6e14 protons with a typical peak current of over 50 Amps. The electron scanner works by measuring the deflection of 50-75 kV electrons by the electric field of the proton beam. Two electron guns, one for each plane, with dipole correctors, quadrupole magnets and deflectors to shape the electron beam have been installed. This paper describes the system and the initial results.

INTRODUCTION

The electron scanner is the first instrument to measure the transverse beam profiles in the SNS accumulator ring. Alternative profile monitors such as wire-scanners were planned but not installed due to budget restrictions. The electron scanner projects electrons accelerated up to 75 keV through the proton beam as depicted in Fig.1.

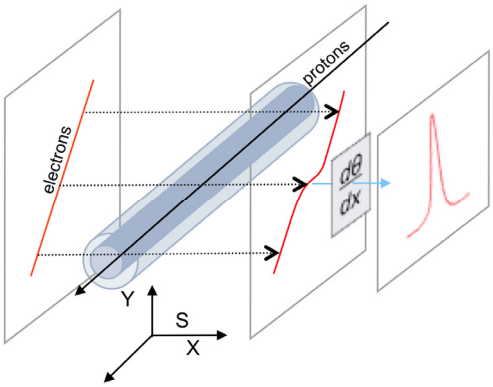


Figure 1: The deflection of the electrons.

The transverse profile is derived from the angle of deflection of the electron beam according to the following formula, see also [1,2,3]:

$$\frac{d\theta}{dx} = \int_L \frac{e}{mv^2} \cdot \frac{\delta(x,y)}{\varepsilon_0} dy$$

where e, m are the electron charge and mass, respectively, v is the velocity, $\delta(x,y)$ is the proton beam density distribution, and θ is the electron beam deflection angle.

This assumes that the path of the electrons is approximately straight, the net energy change to the electrons by the proton beam is close to zero, and the effect of the proton magnetic field can be neglected.

* ORNL/SNS is managed by UT-Battelle, LLC, for the U.S. Department of Energy under contract DE-AC05-00OR22725

ELECTRON SCANNER HARDWARE

The electron scanner layout is depicted in Fig. 2 The different parts are: (1) electron gun, (2) deflection scan system, (3) dipole correctors, (4) quadrupole magnets, (5) vacuum chamber for proton beam, and (6) the phosphor screen.

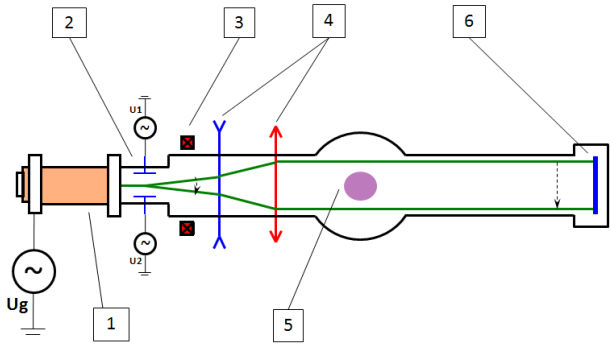


Figure 2: Diagram of electron scanner.

The electron gun produces a pulse of about 1usec of up to 75 keV electrons with a maximum current of 5 mA. The scan system applies a 20 nsec long ramp to the defectors to project the electrons on a diagonal line. The diagonal projection makes the deflection of the electrons by the proton beam visible as a deviation from a straight line. The first quadrupole extends the range of the deflection while the second quadrupole focuses the electron beam such that the electron beam is parallel. The electron gun is pulsed once a second but faster rep rates of up to 5 Hz are possible. The time line is shown in Fig. 3. To minimize the electron beam size, the cathode heating is turned off for a few milliseconds before the acceleration pulse.

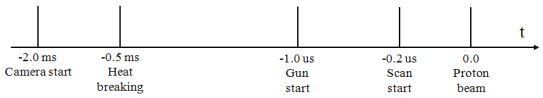


Figure 3: Time diagram.

One vertical and one horizontal scanner are installed in the tunnel, see Fig. 4. GigE Vision CMOS cameras acquire the images from the fluorescent screens. Because the scanners are located in a straight section of the ring, the radiation levels are low enough to not damage the cameras. A single PXI-based computer running LabVIEW controls the cameras, timing, pulse generators and power supplies of the electron scanner.

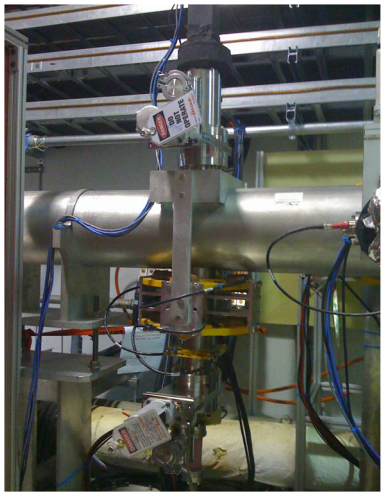


Figure 4: Electron scanner installation.

ELECTRON SCANNER SOFTWARE

The software for the electron scanner consists of four parts:

- Control software that controls the electron scanner hardware, including the timing.
- Simulation software that simulates the projection of the electrons and creates test images for the Analysis software.
- Imaging software that acquires the image of the projected electrons and analyzes the curve to determine the transverse profile.
- Scan software that manages the Control software and the Imaging software to perform multiple acquisitions and produces 3-dimensional images of the beam bunch, e.g. a longitudinally integrated profile.

Both the Imaging and the Scan software interface to EPICS so that the physics applications on the consoles can readout the results.

Image Analysis

The analysis has to take the derivative, dy/dx, of the curve to determine the profile. Because taking the derivative of data, especially pixel data from the camera, can provide noisy results, different analysis methods were tested ahead of commissioning using the Simulation software. These methods were: (1) find the peak in each column of pixels to find an (x,y) pair and take the derivative of all (x,y) pairs, (2) find the peak of a Gaussian fitted to each column of pixels to get an (x,y,z) pair (with z the intensity of the peak), then fit these pairs with a spline and take the derivative of the fit, or (3) fit a spline to all pixels weighted by intensity, and take the derivative of the fitted spline, see Fig. 5. The smoothing provided by the spline and Gaussian fit in method (2) most effectively mitigated the image noise problem and thus yielded the most reliable results. The spline fitting can find a profile even if there are gaps in the electron curve due to low electron density.

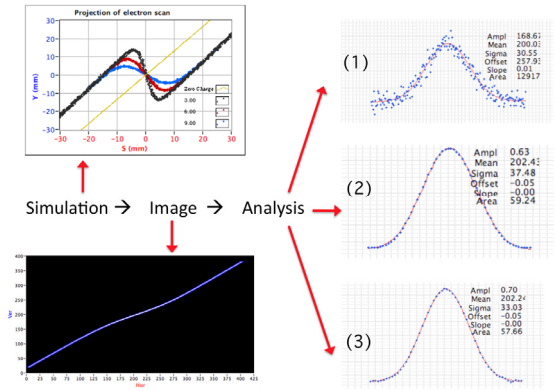


Figure 5: Simulated Electron projections, the generated image and the different profile analysis fittings.

RESULTS

An example of the horizontal projected electron curve is shown in Fig. 6. This data is taken at about 5uC. The bright spot on the right consists of electrons that are outside the 20 nsec deflection scan waveform but still are accelerated by the 1usec long accelerating pulse.

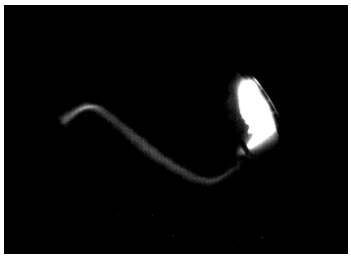


Figure 6: Image of the electron curve.

Because the length of the scan is short, 20 nsec, compared to the bunch length of 600 nsec, we can perform scans at different locations within the bunch. By performing scans at regular intervals throughout entire bunch length, we can create 3-dimensional plots of the bunch, as shown in Fig. 7. The double peak is in the longitudinal direction and is confirmed by the Ring Current Monitor waveform.

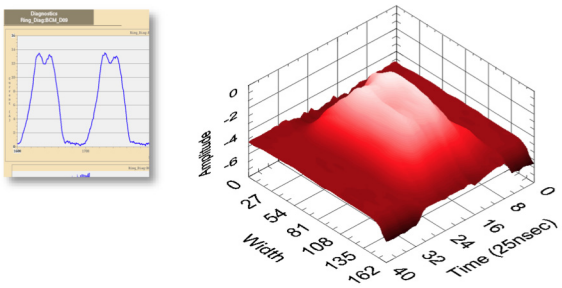


Figure 7: Shown on right is the 3-D profile for a 4 uC bunch in the accumulator ring. The width axis represents the transverse axis of the beam and is given in pixels with 0.3 mm per pixel. The time axis represents the longitudinal axis of the beam and is given in 25 nsec per count. Shown on left is the longitudinal profile as given by a ring beam current monitor.

In addition to viewing different profiles within a single turn, we can also view profiles for any turn during the accumulation cycle. Profiles from multiple accumulation turns, 50/100/200/300/400/500, are shown in Fig. 8. This figure also shows the projection in the longitudinal direction to show the equivalent beam current profile. For this proton beam configuration, the vertical range of the electron scanner is too small for the current proton beam accumulation and thus the profile is truncated.

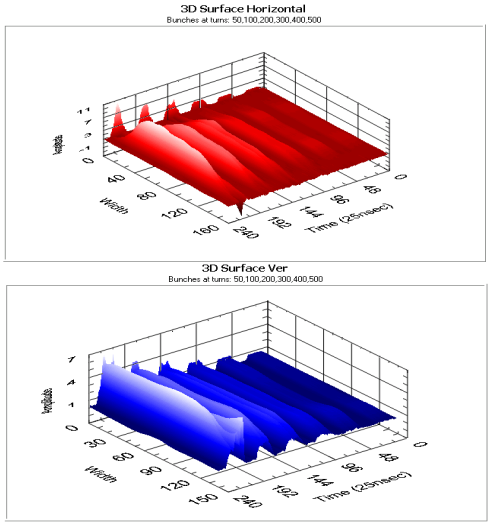


Figure 8: Multiple bunches from both the horizontal (red) and vertical plane (blue) are shown. Width is in pixels at 0.3 mm per pixel. The time scale is in 25 nsec per count.

Evaluation

To verify the results of the electron scanner, we have performed an initial comparison of profiles with the profiles from a Harp located in a downstream transport line for a number of beam configurations, see Fig. 9.

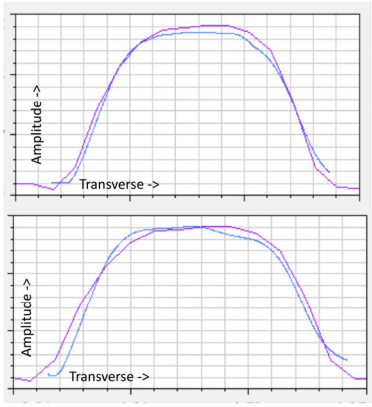


Figure 9: Integrated ELS profiles (purple) of 2.8μC (top) and 6.8μC (bottom) of beam at the 620th turn compared to Harp profiles (blue). Profiles are normalized in RMS and area in order to compare only the shape.

For accurate comparison with Harp results, the ELS profiles were integrated over the full pulse length (600 nsec) in the manner described in the previous section. This comparison was performed for production-style ring beams of various intensities.

To account for optics differences between the ELS and the downstream wire scanners and Harp, the profiles were normalized to the same width and area. The shape of the profiles obtained from the ELS was generally in good agreement with downstream Harp data, especially at high intensity. At the lower intensity settings, the ELS profiles were somewhat broader, though the Harp data was rather noisy and possibly unreliable at these beam intensities.

Individual profiles from 20 nsec slices were qualitatively assessed for a number of beam configurations, including hollow beams and painted beams of various intensities. The profile shapes consistently reflected what was expected for the configuration at hand. A few issues of concern, which are currently under investigation, are the absolute scale of the ELS profiles (in mm), and an artificial tilt of the profile floors.

DISCUSSION

Despite the aforementioned minor problems, the electron scanner has been successful in providing a means of parasitically measuring the ring beam transverse profiles. The ability to obtain profiles for individual 20 nsec slices of beam anywhere along the 1 msec accumulation cycle is a useful feature unavailable in the downstream Harp and wire scanners.

Already some improvements have been made to the electron scanner. The timing jitter has been reduced to improve the accuracy of the longitudinal dimension of the 3-D profile. We replaced the cameras with more light sensitive cameras to improve the visibility of the projected electrons. We found that stray magnetic fields from the ring magnet's bus bar and a nearby corrector dipole affected the path of the electrons. This likely is the cause of the tilt in the measured profile. We plan to magnetically shield the electron scanner. Also, the aperture for the vertical profile is too small and the next version of the electron scanner will remedy this.

SUMMARY

This paper described the successful commissioning of the prototype electron scanners with good qualitative results. Work is in progress to verify the absolute scaling of the profiles and install magnetic shielding.

REFERENCES

[1] P.D. Goldan "Collisionless Sheath---An Experimental Investigation", Phys. Fluids 13, 1055 (1970), DOI:10.1063/1.1693008.

[2] E. Tsyganov et al, "Electron beam emittance monitor for the SSC", PAC1993, pp.2489-2491.

[3] A. Aleksandrov et al, "Feasibility Study of Using an Electron Beam for Profile Measurements in the SNS Accumulator Ring", PAC 2005, pp. 2586-2588.

ELECTRON BEAM DIAGNOSTICS FOR THE EUROPEAN XFEL

D. Nölle, DESY, D-22607 Hamburg, Germany, on behalf of the XFEL Team

Abstract

The European XFEL is an X-ray free-electron-laser that is currently being built in Hamburg. It is organized as an international project and will be a large scale user facility [1,2]. Based on superconducting TESLA technology electron beams of high average power will be sent to several undulator lines simultaneously to produce hard X-rays with high average intensity and a peak brilliance by far superior to any 3rd generation light source. This paper will present the current status of the planning, the development and the prototyping process for the standard electron beam diagnostics of this facility. It will cover the main diagnostic systems, like the BPM system, beam size measurements, charge and beam loss measurements as well as the machine protection system.

INTRODUCTION

The European XFEL (E-XFEL) is a project to construct an international X-ray Free-Electron-Laser user facility close to DESY in Hamburg. The facility will be operated by a limited liability company with shareholders from the participating counties.

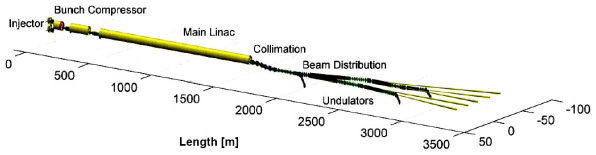


Figure 1: Sketch of the layout of the E-XFEL.

DESY will act as a host lab and leads the accelerator consortium, that is in charge for the construction of the accelerator. Like the FLASH facility [3] E-XFEL will also be based on superconducting TESLA RF technology. Therefore, this machine will provide much higher duty cycle as machines like SCCS and LCLS. An electron beam with a pulse length of 650 µs and a bunch rep rate up to 5 MHz will be accelerated up to 17.5 GeV at a repetition rate of 10 Hz. The shortest XFEL wavelength will be 0.1 nm or about 10 keV. To make optimum use of the high duty cycle, the long bunch trains can be distributed into 2 SASE undulator lines, which will be ramified into additional lines for "secondary undulators" that make use of the spent beam producing either FEL or spontaneous radiation. The time structure of the beam can be adjusted independently for both main SASE undulators (SASE I and SASE II) by means of a kicker septum scheme in the beam distribution system.

While the contracts between the founder states of the XFEL Company are still in the phase of final negotiation, and the signature of the conventions can be expected for summer, the construction phase of the facility has already started. The contracts for civil construction are placed and groundbreaking took place in winter 2008/2009. Also the procurement of main components will start this summer. The construction is scheduled to take about 5.5 years. According to this planning commissioning should start 2014. SASE is expected to follow about 1 year later.

STANDARD BEAM DIAGNOSTICS

This paper focuses on standard beam diagnostics like beam position, charge, beam size and beam loss. These systems are currently in the design phase. First prototypes are under construction or will be available soon. A description of the more specialized diagnostic systems can be found in Ref.[4].

BEAM POSITION MONITOR SYSTEM

Beam position monitors are the backbone of the diagnostic system. E-XFEL will distinguish between standard BPMs with moderate resolution and precision BPMs, where higher performance is required. For the standard BPMs mainly the button type will be used. About one third of the BPMs in the accelerator modules will be re-entrant cavity BPMs. About every third RF-Section of the LINAC, consisting of 4 accelerator modules, will be equipped with monitors of this type to provide a better resolution if required.

Cavity BPMs will be used mainly in and close to the undulator sections. One cavity BPM will be located in each undulator intersection. In addition before and behind the undulator sections there will be some of these cavity BPMs to allow for precise beam based alignment. Further high precision (cavity) monitors with a 40.5 mm beam pipe diameter will be used before the LINAC sections and in the collimation and distribution section. This type will also be used for the Intra Bunchtrain Feedback System (IBFB) developed by PSI [5].

Table 1: Numbers and types of the E-XFEL BPMs

BPM Type	Number	Diameter	Single Bunch Resolution
Standard Button BPM	228	40.5 mm	50 µm
"cold" BPM (Button, Re-entrant Cavity)	101	78 mm	50 µm
Precision BPM (Cavity)	117	10 mm	1 µm
Precision BPM (Cavity)	12	40 mm	1 µm

The BPM system for the E-XFEL will be provided by a collaboration of PSI, CEA and DESY. DESY will take

over the mechanics for all BPMs, except the re-entrant cavity BPMs. These monitors will be supplied by CEA, including monitor and RF-front-end. The BPM electronics, the firmware and embedded software for all BPMs will be provided by PSI, except for the cold re-entrant cavity BPM, where the front-end is supplied by CEA.

Button BPM

Button BPMs will be used as standard BPM for all warm beamlines, except for the undulator sections. Furthermore, they will also be used in the XFEL cryo modules, rigidly connected to the quadrupoles at the end of an accelerator module string [6]. The button BPM electronics will be based on an analogue input stage that transforms the high-frequency broadband signals of the pickups into a low-frequency bandwidth-limited signal pulse of some 10ns length that is sampled directly by a fast ADC and post-processed by an FPGA. First prototypes are already under test at FLASH and PSI.

For the cold variant of this BPM type the development of the BPM body is almost finished. The custom made feedthroughs have passed the cryogenic tests successfully. Only minor changes of the overall design are expected with respect to the current prototype due to system integration issues in the cryo-module.

Re-entrant Cavity BPM

The re-entrant cavity BPM has the potential of better resolution compared to the standard button type [7]. About 30% of the cold BPMs will be of this type. From the mechanical point of view, the interfaces to the outside world of the cryo-module are identical. Also for this BPM the development is quite advanced. The feedthroughs are qualified for the operation in the cold. A prototype is currently mounted in the first E-XFEL cryo-module prototype. The RF front-end based on a down conversion scheme with IQ detection is under development at CEA. The electronics will be integrated into the modular BPM framework developed and supplied by PSI.

Cavity BPM

The requirements on BPM resolution is at most places of the machine rather loose, tight requirements are mainly valid in and around the undulator sections, as well as for few places to steer the beam after the LINAC sections and in beam distribution system. In the collimation section they are also required for the IBFB that is using special low latency electronics. Two types of cavity BPMs will be used. Both types consist of a reference and dipole resonator. Special care is taken for the dipole cavity to optimize the coupling of the dipole mode to the coupling slots [8]. The version for the undulator sections has a 10 mm beam pipe, while the other will be for the standard 40.5 mm beam pipe diameter. From RF point of view both types have the same frequency (3.3 GHz) and Q (70). Therefore, the can be read out with the same type of electronics. The cavity BPM RF front-end, currently developed at PSI, will be based on down conversion and IQ detection. It will ensure high resolution and low drift.

BPM Electronics

The overall BPM electronics system concept developed by PSI follows a modular design approach that maximizes the amount of common hard- and software for the different BPM types in the machine. The BPM electronics will consist of analogue RF front-end (RFFE) modules that are specific for each pickup type, and a generic FPGA-based digital back-end carrier board with two ADC mezzanine modules that is used for all BPMs in the machine. The RFFEs and the digital back-end board with its ADC mezzanine modules are plugged into a common customized crate that contains one generic digital back-end as well as either four button BPM RFFEs or two cavity or re-entrant BPM RFFEs. This generic modular hardware approach that is also employed for the IBFB-specific low-latency BPM and signal processing hardware [9] allows minimizing the overall development and maintenance effort and provides a unified control and timing system interface for all BPMs in the machine.

BEAM SIZE MEASUREMENTS

Like for all other SASE machines emittance control is an important task for the diagnostics, since the optimisation of the emittance transport is essential for the FEL performance. Therefore, E-XFEL will have special sections after the injector, the two bunch compressors and in the collimation section to measure the projected and if possible also the slice emittance. These stations will combine 4 beam size measurements to determine the local twiss parameters as well as the emittance. This allows also controlling the optics and correcting its match to the following sections.

Below 2 GeV (up to the second bunch compressor) the beam size measurements will be done by means of OTR screens. These screens will include on axis and off axis OTR targets. The off axis targets will be used in combination with kicker magnets that deflect a single bunch out of the 650 μs long bunch train onto the screen. In addition this bunch can also be streaked by a transverse mode structure to get access to slice parameters [4]. Resolution of the OTR stations has to be between 30 and 10 μm depending on their location. Since LCLS has reported problems with coherent effects with their OTR systems due to the strongly compressed beam, the E-XFEL OTR chambers provide ports for installation of additional wire scanners in case of such problems in a later stage.

In the high energy sections the beam size is getting to small for OTR diagnostics, and wire scanners will be used for measurements. They have to provide fast scans, i.e. the wire is driven through the beam during one RF-pulse. Nevertheless, OTR systems will also be installed for commissioning purpose and single bunch operation.

On-axis and off-axis operation of the screens requires two different focal spots. In addition imaging of a streaked beam requires large field of view. For both aspects it would be appropriate to focus onto the entire plane. The Scheimpflug's principle, known from large format cameras, allows extending the depth of field by choosing appropriate angles between the object, the image and the lens plane. If these planes have a common intersection line, the entire screen plane is imaged well focused onto the image plane. Therefore an angle of 67.5° between beam axis and screen surface was chosen. A magnification close to 1:1 has to be used to achieve the required resolution. With large view fields large CCD chip cameras will be required.

CHARGE MEASUREMENT

To ensure proper beam transport the transmission has to be close to 100%. Therefore the charge of the bunches has to be measured at various places along the LINAC. Furthermore, charge has to be well controlled for stable SASE operation. The charge monitors will be on the same toroid (current transformer) type that is already in use at FLASH. Significant change will be done for the electronics. Fast sampling ADCs using either numerical integration or data fitting schemes will be used for improved read-out. The electronics of a single toroid will be linked to their neighbours, so that the transmission between two monitors can be checked, and fast alarms can be released in case of problems. The system will be based on digital electronics implemented on µTCA technology. The processing of the alarms will be done by an on-board FPGA of the ADC board.

BEAM LOSS AND MACHINE PROTECTION

Superconducting LINACs are able to transport a large amount of charge and energy due to the high duty cycle. The maximum beam power of E-XFEL is about 600 kW cw at 17.5 GeV. This number indicates that a machine protection system is required to prevent the machine from damage. In this context damage does not only mean mechanical damage of components but also their activation and degradation. Electronics will suffer from high radiation levels in the machine and the undulators will degrade in performance.

Therefore a machine protection system will be installed. The system will process signals from all over the machine. Slow signals from magnets, RF, vacuum and screens will be used to check for the correct machine state and will block beam operation or allow for only single or few bunches depending on the status of the machine. Fast signals from e.g. beam loss monitors or transmission measurements will cause an interrupt of charge production or beam abortion by means of the dump kicker in case of imperfect transmission of the long bunch trains.

The system will be an upgraded version of the FLASH system [10], using similar principles with updated technologies. The logic units collecting and evaluating the input channels and creating the alarms will be based on modern digital processing units. The beam loss monitors will still be based on photomultipliers, but with a readout using fast ADCs and digital signal processing. Both units will be implemented as AMC boards for the µTCA standard.

SUMMARY

The developments for the standard beam diagnostics for E-XFEL are in an advanced state. The design of the main systems is clear, and partners within E-XFEL collaboration are fixed. First prototypes are already under test at FLASH.

REFERENCES

[1] "XFEL Technical Design Report", DESY 2006-097, http://xfel.desy.de.
[2] R. Brinkmann, "The European XFEL Project", FEL´06, Berlin, MOBAU03, p. 24, (2006), http://www.JACoW.org.
[3] V. Ayvazyan, et al., Eur. Phys. J. D, 37, 297, (2006)
[4] C. Gerth, "Electron Beam Diagnostics for the European X-Ray Free-Electron-Laser" DIPAC´07, Venice, MOO2A02, p. 17, (2007) http://www.JACoW.org.
[5] B. Keil et al., "Design of an Intra-Bunch-Train Feedback System for the European X-Ray FEL", Proc. DIPAC'07, Venice, p.232 (2007), http://www.JACoW.org.
[6] D. Nölle et al., „BPMs for the XFEL Cryo-Module", DOPAC´07, Venice, TUPB12, p.84 (2007), http://www.JACoW.org.
[7] C. Simon. et al., "Beam Position Monitors using a Reentrant Cavity", DIPAC´07, Venice, TUPB15, p.93, (2007), http://www.JACoW.org.
[8] D. Lipka, "Cavity BPM Designs related Electronics and measured Performances", TUOC02, this conference,
D. Lipka, "Orthogonal coupling in Cavity BPM with Slots", MOPD02, this conference
[9] B. Keil et al., "The PSI DSP Carrier (PDC) Board – a Digital Back-end For Bunch-to-bunch and Global Feedbacks In Linear Accelerators and Storage Rings", Proc. EPAC 2008, Genoa,, p.3272 (2008)
[10] L. Fröhlich et al., "First operation of the FLASH machine protection system with long bunch trains", LINAC'06, Knoxville, USA, pp. 262–264, 2006

BEAM INDUCED FLUORESCENCE MONITOR & IMAGING SPECTROGRAPHY OF DIFFERENT WORKING GASES*

F. Becker†, C. Andre, P. Forck, R. Haseitl, A. Hug, B. Walasek-Hoehne, GSI, Darmstadt, Germany,
F. Bieniosek, P.A. Ni, LBNL, Berkeley, California, D.H.H. Hoffmann, TUD, Darmstadt, Germany

Abstract

Beam induced fluorescence spectra in the range of 300-800 nm were investigated with an imaging spectrograph. Wavelength-selective beam profiles were obtained for a 5.16 MeV/u sulphur beam in nitrogen, xenon, krypton, argon and helium at 10^{-3} mbar gas pressure. In this paper calibrated BIF spectra of specific gas transitions were identified and corresponding beam profiles presented. The measurement results are discussed for typical applications at the present setup and the future FAIR facility.

MOTIVATION

As conventional intercepting diagnostics will not withstand high intensity ion beams, **B**eam **I**nduced **F**luorescence (**BIF**) profile monitors constitute a preeminent alternative for online profile measurements [1]. At present, two BIF monitors are installed at the GSI UNILAC and several locations are planned for the FAIR high energy beam transport lines [2]. For further optimizations accuracy issues like gas dynamics have to be investigated systematically. Especially the determination of focused beams in front of targets with high line charge densities rely on a careful selection of proper working gas transitions to keep profile distortions as low as possible [3].

EXPERIMENTAL SETUP

Key issue of this experimental layout using an imaging spectrograph with an area scan intensified CCD (ICCD) camera (Fig. 1) was to have both, the spectral information of specific beam induced gas transitions along the diffraction axis and the spatial information about the beam profile width, transition wise along the imaging axis, see Fig. 2. For 150 mm object distance, a chromatically corrected UV-lens of f=50mm and f/2.8 was chosen. A CCD height of 4.9 mm and a total reproduction scale β_{tot}=0.42 yield a 19.5 mm field of view.

Imaging Spectrograph & Gas Composition

The ∅ 70 mm spherical mirror with 140 mm focal length is holographically etched and astigmatism corrected. 140 sinusoidal grooves per mm produce a spectral dispersion of 50 nm/mm and an image field of 8x12 mm on the vertical imaging axis and the horizontal dispersive axis, respectively. With an optical resolution of 33 lp/mm the ICCD limits the spectral resolution to 1.5 nm for an entrance slit $\leq$ 30 μm. The total spectral system efficiency includes all single component efficiencies as a convolution, see Fig. 3 (upper plot). Most limiting factors in the wavelength range $\geq$ 600 nm are the tri-alkali (Na_2KSb)Cs photocathode and the decreasing grating efficiency. Investigation of optical gas spectra relays on a sufficient purity of the actual gas species. In order to measure and control impurities, a resid-

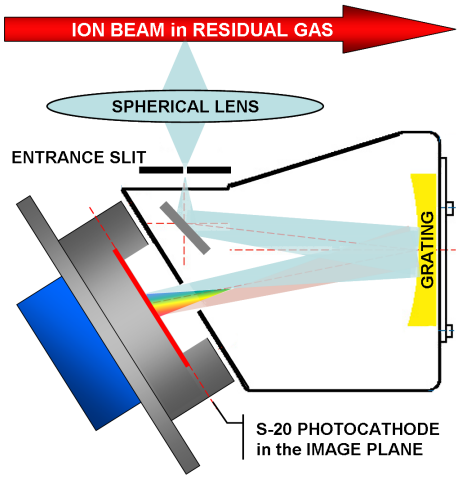


Figure 1: Top-view of the optical path in the diffractive plane. Length of spectrum in the image plane is 10 mm. 1:1 imaging from slit to image plane. All refractive optics adapted to UV-VIS [5]. ICCD performs single photon detection and has a ∅ 25 mm UV-enhanced photocathode with a V-stack MCP [6] and digital VGA camera [7] (bluish).

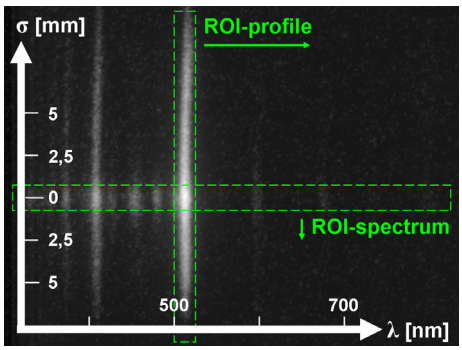


Figure 2: Spectrographic average image n=2000 of $3{\cdot}10^{11}$ S^{6+} ions @ MeV/u in 10^{-3} mbar helium gas, σ_w=1.8mm. Logarithmic gray-scale for better presentation.

* Work supported by EU, project FP6-CARE-HIPPI
† Frank.Becker@gsi.de

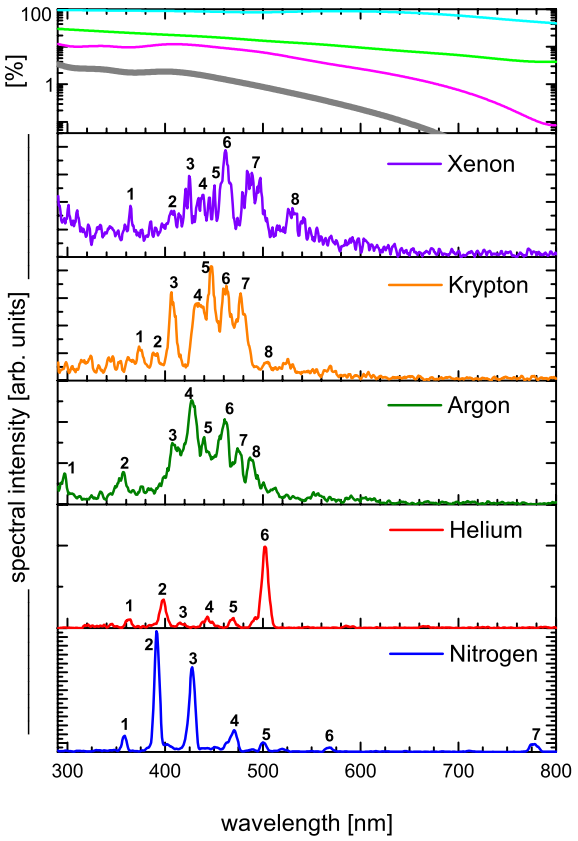


Figure 3: Optical Beam Induced Fluorescence spectra of $3{\cdot}10^{11}$ S^{6+} ions @ 5.16 MeV/u in 10^{-3} mbar residual gases (Xe, Kr, Ar, He, N_2). Most prominent transitions are indicated and described in Table 1. Spectral efficiencies (upper plot) in descending order: lens (blue), grating (green), photocathode (magenta) and total (gray).

ual gas analyzer (RGA) 'quadrupole mass spectrometer'-type was used [8]. Base pressure of the unbaked vacuum system was 10^{-7} mbar, with the typical fingerprint of hydrogen, water, nitrogen and traces of the previously introduced rare gas species like krypton in an argon atmosphere. Although the gas leak system was flushed carefully after each gas exchange, a significant source of residuals was the pressure reducing regulator. In order to keep relative impurities below 5 %, the working pressure for all experiments had to be set to 10^{-3} mbar N_2-equivalent. For set pressures, a gas leak system controls a motorized needle valve so that gas flow rate versus the pump rate allows a dynamic equilibrium. To overcome gas specific variations, the ion gauge (5 % reproducibility) was cross-calibrated to a linear temperature corrected capacitance gauge (0.2 % accuracy), so that the relative error in gas pressure p_{eff} was ≤ 6 %.

DATA ANALYSIS - RESULTS

All optical spectra were recorded during 2000 beam pulses for unchanged accelerator settings. Each single image was recorded as 8-bit bitmap, with the ICCD in photon counting mode. To maintain the dynamic range, the average images were 32-bit float tiffs, see Fig. 2. Further resolution improvement by a factor of ~ 4 was achieved with a cognitive algorithm that determined barycenters of single photon spots and added them as single counts to the VGA-sized matrix [9]. To discriminate spectral peaks against spiky shot noise, Savitzky-Golay fits were applied. Regions of interest (ROI) were chosen like 10 pixel or 40 μm at the beam center for the BIF-spectra in Fig. 3 and like 20 pixel or 16 nm for the transitions specific profile plots in Fig. 4 (mid & bottom).

Table 1: Residual gases (block-wise), observed charge states, observed integral intensity I, I_{gas} normalized to p_{eff} and $I_{gas\&Z}$ normalized to p_{eff} and the e^--density (upper block line). Corresponding transitions as indicated in Fig. 3, central wavelength and relative intensity with respect to the integral intensity (lower block line). Peaks indicated with No.)* are superpositions of several transition lines.

gas species	charge state	$\sum$ I; I_{gas}; $I_{gas\&Z}$ [%]
No.) central-wavelength [nm], *relative intensity [%]*		
Xenon	Xe^+/Xe	41; 86; 22
1) 363, *4*; **2)*** 407, *4*; **3)*** 424, *6*; **4)*** 438, *5*		
5) 450, *2*; **6)*** 462, *12*; **7)*** 484, *16*; **8)*** 530, *5*		
Krypton	Kr^+/Kr	45; 63; 25
1) 373, *4*; **2)*** 388, *3*; **3)** 407, *10*; **4)*** 434, *14*		
5) 447, *12*; **6)*** 463, *12*; **7)*** 477, *13*; **8)*** 505, *2*		
Argon	Ar^+	50; 38; 30
1) 297, *3*; **2)*** 357, *5*; **3)*** 407, *11*; **4)** 427, *19*		
5)* 440, *8*; **6)*** 461, *15*; **7)*** 474, *8*; **8)*** 487, *7*		
Helium	He	21; 4; 26
1) 364, *4*; **2)** 398, *16*; **3)*** 415, *3*; **4)*** 443, *7*		
5)* 470, *5*; **6)** 502, *48*		
Nitrogen	N_2^+/N^+	100; 100; 100
1) 358, *4*; **2)*** 391, *45*; **3)*** 428, *29*; **4)*** 470, *9*		
5) 501, *3*; **6)** 560, *1*; **7)*** 776, *3*		

BIF-Spectra

All spectra were first calibrated to a Hg-Ar-standard and then refined step by step with known transitions of the recorded BIF-spectra. The accuracy for central wavelength is ≤ 1 nm. The investigation was performed with 5 ms long beam pulses of $3{\cdot}10^{11}$ S^{6+} ions at 5.16 MeV/u, focused to a σ_w of 1.8 mm. Obtained BIF spectra are depicted in Fig. 3. They were not normalized to the spectral efficiency of the optical components, which is therefore given in Fig. 3 as well. In Table 1, the observed charge states, relative integral intensities and most prominent transitions are listed. Different signal-to-noise ratios for the gas species are determined by the observed integral intensity I. Beside nitrogen and helium, where spectral lines of optical transitions are separated, lines appear less intense and clustered in groups. Although nitrogen shows the brightest transi-

tions, gases like xenon and krypton show similar integral intensities I_{gas}, normalized with respect to p_{eff}. To account for the electronic stopping power, integral intensities $I_{gas\&Z}$ have been furthermore normalized to the electron-density$\propto$Z. This way, all rare gases show similar relative integral intensities, except for nitrogen having a four times higher integral intensity value. When the ROI was moved from the center to the beam fringes, spectral intensity decreased homogeneously for all gases unlike helium which showed an unequal decrease for different transitions. For proton beams as well as for much heavier Ta beams, similar results were obtained. A more detailed description can be found in [10].

Transition Dependent Profile Data

The spectrally resolved profile plots are presented in Fig. 4. In the upper plot, all gas-species show corresponding profile width, besides helium that shows a factor 2.5 larger σ_w. Transition-wise profile data is shown in Fig. 4 for N_2 (middle and He (bottom). In the case of nitrogen, the transitions 1), 5) and 6) show a slightly increased profile width that can be explained by an upscaling of noise in the profile fringes due to the normalization to a common maximum. He-profile contributions by 1) and 6) show significant shoulders but 2) and 3) do not. Since both He-cases contain weak and strong contributions, noise scaling effects do not explain these results. Assuming excited states of He 1), 2) might have large cross-sections for electron excitation, an 8 mm halo is reasonable, as the mean free path of secondary electrons is in the order of 10 mm, for p_{eff}=4·10^{-3} mbar.

CONCLUSION

As first experimental outcome, optical spectra of nitrogen, xenon, krypton, argon and helium have been successfully recorded. They excellently agree with measurements at lower energies $\leq$ 10 MeV/u in the case of nitrogen [11, 12] and higher energies in the range of 50 MeV/u to 25 GeV/u for nitrogen and xenon [13]. Nitrogen seems to be the most appropriate residual gas, because of its spectral concentration between 390 and 430 nm. In addition, nitrogen shows the highest integral intensities. Especially the four times higher $I_{gas\&Z}$ makes it the right choice, if the stopping power is an issue. For electric fields in the order of 10 kV/mm the trajectories of excited, charged molecules like N_2^+, will be influenced by the beam's space charge and might falsify the profile reading [14]. Therefore one might focus on different selection criteria as larger molecule masses and shorter transition-lifetimes, provided by rare gases like Xe and Kr. Helium is no alternative due to its wrong profile image in the considered pressure range. However, for most beam parameters N_2 is the optimal choice because of its high light yield. Moreover it was shown that all nitrogen profiles show the same profile width. Once a residual gas is selected, optical components can be further optimized.

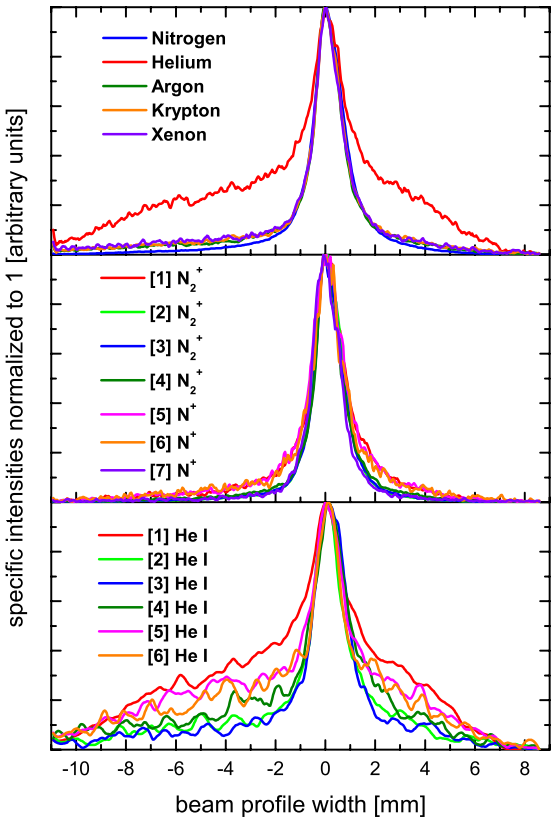


Figure 4: Gas specific beam profiles (upper plot) and transition specific beam profiles for nitrogen (middle) and helium (bottom) as indicated in Fig. 3.

REFERENCES

[1] P. Forck et al., DIPAC'05, ITTA01, p. 223-227 , 2005.
[2] M. Schwickert et al., DIPAC'09 WEOA04, 2009 & FAIR Baseline Technical Report, **Vol. 2**, p. 148-162 , 2006.
[3] F. Becker et al., DIPAC'07, MOO3A02, p. 33-36 , 2007.
[4] company: `www.horiba.com`, CP140-202 140mm Imaging Spectrograph.
[5] company: `www.linos.com`, inspec.x 2.8/50 UV-VIS apochromatically corrected lens system.
[6] company: `www.proxitronic.de`, BV 2581 QY-V 100N.
[7] company: `www.baslerweb.com`, Type 311-f VGA Sony ICX414AL Sensor.
[8] company: `www.pfeiffer-vacuum.de`, Gauge PKR-261, Valve EVR-116, Controller RVC-300, Calibration-Gauge CMR-264, RGA PrismaPlus.
[9] software: `http://rsbweb.nih.gov/ij/`, Img. proc.
[10] F. Becker, "Non-destructive Beam Profile Measurement of high intense HI-Beams", PhD-thesis, Darmstadt, 2009.
[11] R.H. Hughes et al., Phys. Rev., **123**, 2084 (1961)
[12] C. S. Lee et al., "Study of N_2^+ first negative system" Nucl. Instrum. Meth. **B 140**, p. 273-280, 1998.
[13] M. A. Plum et al., "N2 and Xe gas scintilliation @ Cern PS and Booster", Nucl. Instrum. Meth. **A 492**, p. 74-91, 2002.
[14] F.Becker et al., BIW'08, California, TUPTPF054, 2008.

THE LHC SYNCHROTRON-LIGHT MONITORS

A.S. Fisher*, SLAC National Accelerator Laboratory, Menlo Park, CA 94025, USA
A. Goldblatt and T. Lefevre, CERN, Geneva, Switzerland

Abstract

Synchrotron-light telescopes will measure the profiles of the two LHC beams of protons or lead ions, and verify that the abort gap is clear. At collision energy (7 TeV), each telescope will image visible light from a superconducting dipole used to widen beam separation at the RF cavities. At injection (0.45 TeV), this source must be supplemented by a 2-period superconducting undulator 1 m from the dipole. An optical "trombone" delay line will provide the large shift in focus. We discuss the optical design, diffraction, depth of field, and the expected signals over the energy ramp, for emission from the centre and edge of the dipole and from the undulator.

INTRODUCTION

The two LHC synchrotron-light telescopes (BRST [1]) will measure the transverse beam profiles. The abort-gap monitor (AGM or BRSA [2]) will verify that the 3-μs gap contains an acceptably small number of particles, since a partial kick during the rise of the abort kicker may drive them into a magnet and cause a quench.

Protons will be injected at 450 GeV and ramped to collisions at 7-TeV, where they emit enough synchrotron light in superconducting dipoles for imaging. However, arc dipoles are interconnected in a long series of cryostats, with no access to this light. In the IR-4 straight, a chicane of four 9.45-m dipoles widens the beam separation from 194 to 420 mm for RF cavities. As the beam exits the cavities, dipole D3 bends it by 1.57 mrad. In the 62-m drift to the fourth dipole, light from the first 3 m of D3 diverges from the protons, reflects from an extraction mirror at 26 m, and passes through a fused-silica vacuum viewport to optics below the beamline. The dipoles ramp to 3.88 T at 7 TeV, bringing the critical wavelength λ_c from 0.23 mm to 61 nm in an orbit with radius ρ=6 km.

At injection, since the dipole's visible emission is negligible, a short superconducting undulator [3] with N_u=2 periods of λ_u=28 cm was added to the cryostat 937 mm before D3. With B_u=5 T (not ramped), its spectrum for 450-GeV protons peaks in the visible, at 610 nm.

The ALICE detector will study lead-ion rather than proton collisions. With fewer particles and a red-shifted spectrum, this experiment requires separate evaluation.

Since ρ must be the same for proton and ion orbits, at a given dipole field the energy must scale with charge. Lead ions will collide at Z=82 times the 7-TeV proton energy (92 μJ/ion!). The relativistic factor γ scales by Z/A.

EMITTED ENERGY PER PARTICLE

For central dipole radiation, the energy per particle emitted (in both polarizations) into solid angle and frequency $d\xi d\psi d\omega$ (where the horizontal and vertical angles ξ/γ and ψ/γ are conveniently expressed in normalized form) is expressed using modified Bessel functions K [4]:

$$W_d = Z^2 \frac{3}{4\pi^2} W_0 \left(\frac{\omega}{\omega_c}\right)^2 \left(1+\psi^2\right)^2 \left[K_{2/3}^2(\zeta) + \frac{\psi^2}{1+\psi^2} K_{1/3}^2(\zeta) \right] \tag{1}$$

$$W_0 = \frac{e^2}{4\pi\varepsilon_0 c} = 7.6956 \cdot 10^{-37}\ \mathrm{J \cdot s} \tag{2}$$

$$\zeta = \frac{\omega}{2\omega_c}\left(1+\psi^2\right)^{3/2} \tag{3}$$

$$\omega_c = \frac{2\pi c}{\lambda_c} = \frac{3}{2}\gamma^3 \frac{c}{\rho} \tag{4}$$

We model the dipole's edge field as:

$$B(z) = \frac{B_d}{2}\left(1 + \frac{2}{\pi}\arctan\frac{z}{L_e}\right) \tag{5}$$

The edge radiation is then given by [5]:

$$W_e = Z^2 \frac{8}{9\pi^2} W_0 \left(\frac{\omega_c}{\omega}\right)^2 \frac{\left(1-\xi^2+\psi^2\right)^2 + \left(2\xi\psi\right)^2}{\left(1+\xi^2+\psi^2\right)^6} \cdot \exp\left[-\frac{\omega L_e}{\gamma^2 c}\left(1+\xi^2+\psi^2\right) \right] \tag{6}$$

Note that this expression diverges for $\omega << \omega_c$; these low frequencies are emitted as the particle moves from the edge to the uniform field, and so edge and central radiation are not really distinct in this range.

The energy from undulator radiation is given by [4]:

$$W_u = \frac{Z^4}{A^2} N_u^2 K_u^2 W_0 \frac{\left(1-\xi^2+\psi^2\right)^2 + \left(2\xi\psi\right)^2}{\left(1+\xi^2+\psi^2\right)^4} \cdot \left(\frac{2\omega}{\omega+\omega_1}\right)^2 \mathrm{sinc}^2\left(\pi N_u \frac{\omega-\omega_1}{\omega_1}\right) \tag{7}$$

with undulator parameter K_u and first-harmonic ω_1:

$$K_u = \frac{eB_u\lambda_u}{2\pi m_p c} \tag{8}$$

$$\omega_1 = \frac{4\pi\gamma^2 c}{\lambda_u\left(1+\xi^2+\psi^2\right)} \tag{9}$$

OPTICAL CONSIDERATIONS

Depth of Field in the Dipole

Due to the small bend angle, dipole light will be collected over a long path. In the horizontal plane, rays are emitted tangent to the orbit (Fig. 1). They focus in the optical system as if originating at their intersection R with the focal plane. We see which ray angles from a point M

*afisher@slac.stanford.edu

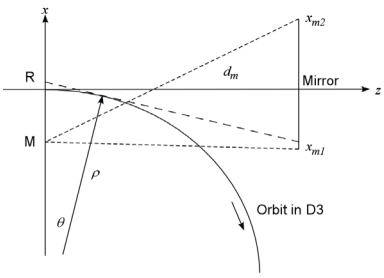


Figure 1: Radiation from a point inside the dipole.

on the focal plane intersect the extraction mirror. Fig. 2(a) plots these positions and angles in phase space. We see that the mirror reflects light from the first 3.2 m of the orbit in D3. The plot also shows the acceptance of a slit placed one focal length after the first focusing optic, in order to select a range of angles from the source plane. The focus is set in the middle of the path determined by the slit.

The beam ellipses from different points along the orbit project onto the *x* axis with small shifts, but the shifts are minimized by focusing in the middle. A sum of the projections along the entire selected path confirms that the broadening is <2% for the full 3 m accepted here.

In vertical phase space (Fig. 2(b)), the large radiation opening angle makes wide radiation phase ellipses that remain centered (since the orbit is straight) but rotate with distance in the dipole, widening the sum of projections. Blurring is again reduced by focusing in the middle of the path, but it becomes a problem for paths over 2 m.

Diffraction

A wide angular spread is needed for a small optical waist and hence for good size resolution. For a given angular width, the TEM_{00} mode has the smallest waist and so offers a lower bound on resolution. A TEM_{00} beam at 400 nm with an RMS size of 330 μm, typical of a beam in D3, has an RMS angular spread of 100 μrad. The vertical angle of dipole radiation from 7-TeV protons is wider, 182 μrad, and a 2-m path gives a (uniform) horizontal spread of 324 μrad. A ZEMAX [6] calculation at 400 nm finds an overall broadening of 5%. Ions, with a smaller γ and so larger angles, give less concern.

Optical System

To match the wide spectrum over the ramp, we focus with two metal-coated mirrors. A crowded rail under the beamline is being replaced by an optical table, allowing space for calibration and focusing (Fig. 3). The first mirror, F1, is 32 m from the source; to form its image on the table, it must demagnify. The second mirror, F2, raises the overall magnification to 0.3, so that the image covers multiple camera pixels. With incidence at 1° to the normal on both spherical mirrors, ZEMAX finds an RMS point spread on the image of 16 μm from aberration.

A design improving on spherical optics was developed. Since any portion of the surface of an ellipse has perfect geometric point-to-point imaging, elliptical mirrors can be devised for any angle of incidence. Indeed, the spot size remains below 1 μm RMS even with source points 1 mm off axis and with the window's slight chromaticity. However, such mirrors are costly, and the geometric blurring from spherical optics is less of a concern than diffraction. Elliptical optics may be useful as an upgrade.

Since the light source shifts by up to 2.8 m during the ramp, from the undulator's centre to 1.6 m inside D3, the optical focus must change. Moving focusing mirrors while maintaining focus and alignment is difficult. Instead, the entering optical path is held constant by an optical "trombone" (Fig. 3). A 2-pass trombone using a 600-mm motorized translation stage can delay by 1200 mm. For up to 3 m, needed to focus in the dipole, a second stage inserts two mirrors into the path on the moving platform, making a 4-pass trombone.

SIGNALS ON THE DETECTORS

Camera

An image-intensified camera (Proxicam HL4 S NIR with a red-enhanced S25 photocathode) replaces a CCD. Combining (1), (6), and (7) with the spectral responses of the camera (300 to 900 nm), the metal-coated mirrors (>380 nm for protected silver) and the viewport (<4 μm, with an opaque notch around 2.8 μm), gives the number of electrons emitted from the photocathode.

Fig. 4 shows the signals in the peak pixel for the expected beam size and the fills of Table 1. The intensifier can brighten these signals, but cannot improve the signal-to-noise ratio from the square root of this photoelectron count. The drop in in-band undulator radiation before the dipole radiation rises causes a crossover region with a deep dip in available light plus blurring from multiple sources. Manipulating the focal-plane slit helps to speed this transition from undulator to dipole.

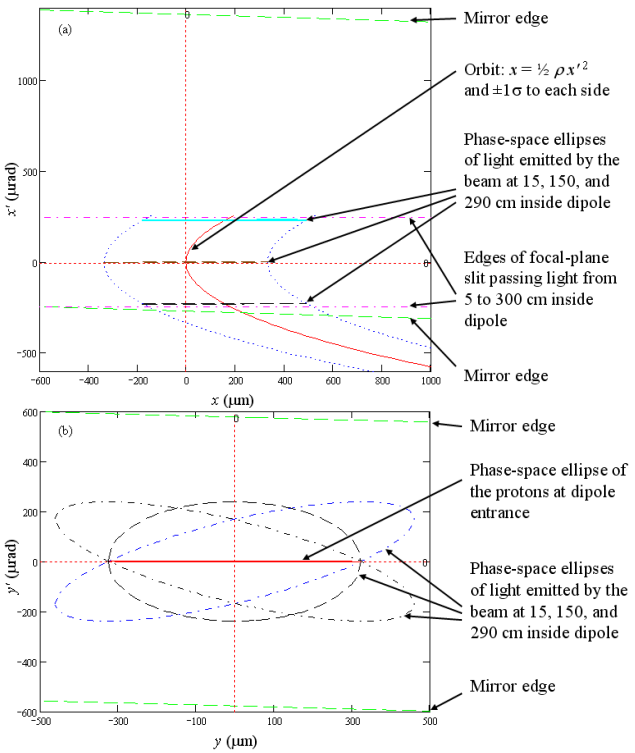


Figure 2: (a) Horizontal and (b) vertical phase space for emission in D3, with the coordinates and the optical focus in middle of the path selected by the slit.

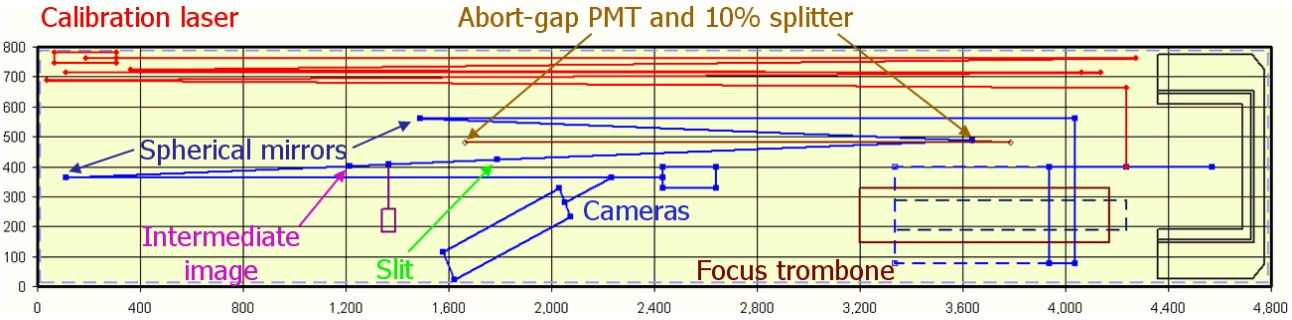


Figure 3: A new 4.8×0.8 m^2 optical table below the beam adds a calibration path and focus trombone. Light enters at right.

At injection, a proton pilot bunch needs an integration time of at least 1 s. For lead ions, there is simply too little light in the visible to see an injected pilot bunch, but with sufficient integration, a full bunch might be imaged. This limitation is lifted once the ramp begins, shifting undulator light out of the infrared.

Abort-Gap Monitor

A beamsplitter between F1 and F2 (Fig. 3) reflects 90% of the light (before cutting by the slit) for imaging and transmits 10% to the AGM. A photomultiplier (PMT) is placed on the split path at the intermediate image from F1, where the light fits easily into the 10-mm photocathode. The gated PMT (Hamamatsu R5916-50) uses a microchannel plate rather than dynodes. The gate allows it to sensitively detect the small gap signal without saturation from the large population elsewhere.

The 3-μs gap is monitored in 30 100-ns bins. The beam-loss monitor group has calculated the proton population per bin at quench threshold [7]. Jowett explains [8] that ions fragment hitting the beam screen and deposit the same energy in a magnet coil as Z protons at the corresponding stage of the ramp. We thus set the threshold at $1/Z$ times the quench limit for protons.

The calculated PMT signals meet the requirement to measure a threshold population to 5% accuracy in 100 ms throughout the ramp—except for lead ions at injection. Since this case is difficult for imaging too, all the light should then be sent to the PMT. This factor of 10 provides sufficient improvement to meet the criterion.

Table 1: Proton and lead-ion fills

	Protons	Ions
Number per pilot bunch	5×10^9	7×10^7
Number per full bunch	1.7×10^{11}	8.2×10^9
Number of bunches, full ring	2808	592

REFERENCES

[1] L. Ponce, R. Jung and F. Méot, "LHC Proton Beam Diagnostics Using Synchrotron Radiation", CERN-2004-007.

[2] C. Fischer, "High Sensitivity Measurement of the Longitudinal Distribution of the LHC Beams", LHC-B-ES-0005.00 rev. 2.0.

[3] R. Maccaferri, M. Facchini, R. Jung, D. Tommasini and W. Venturini Delsolaro, "The 5-T Superconducting Undulator for the LHC Synchrotron Radiation Profile Monitor", LHC Project Report 731, EPAC, 5-9 July 2004, Lucerne, Switzerland.

[4] Albert Hofmann, *The Physics of Synchrotron Radiation*, Cambridge University Press, (2004).

[5] R. Coïsson, "Angular-Spectral Distribution and Polarization of Synchrotron Radiation from a 'Short' Magnet", Phys. Rev. A **20** (1979), pp. 524-528.

[6] ZEMAX Development Corp., http://www.zemax.com

[7] B. Dehning and M. Sapinski, private communication.

[8] J.M. Jowett, "Ions in the LHC", CERN, Chamonix Workshop, 2009.

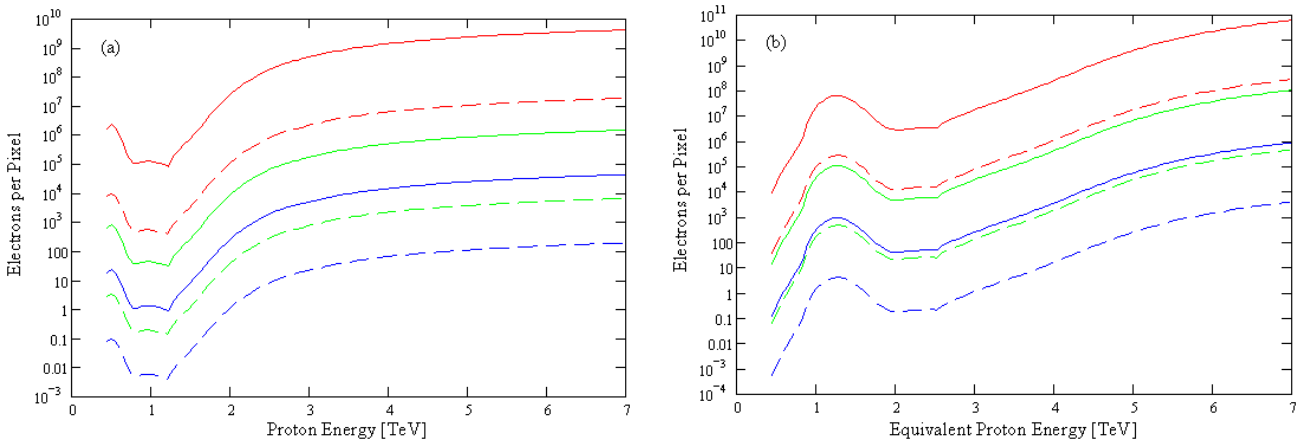


Figure 4: Electrons in the peak pixel of the camera in one turn (dashed curves) and in a 20- ms video interval (solid curves); for a pilot bunch (blue), a single full bunch (green), and a full ring (red). (a) Protons and (b) lead ions.

HIGH CURRENT ION BEAM INVESTIGATIONS ON INORGANIC SCINTILLATION SCREENS

E. Gütlich*, P. Forck, B. Walasek-Höhne, GSI, Darmstadt, Germany
W. Ensinger, Technical University of Darmstadt, Germany

Abstract

At the GSI heavy ion LINAC, the properties of scintillating screens irradiated by the ion beam were studied. Different ion beams from H^+ to U^{28+} in the energy range from 4.8 to 11.4 MeV/u were used with currents up to some mA. The investigations were focused on ceramic materials. Their properties (light yield, beam width and higher statistical moments) were compared with different quartz glasses. The image of each ion beam pulse was recorded by a digital CCD camera and individually evaluated. The recorded beam width shows dependence on the used scintillator material. Additionally, the light yield and beam width depend significantly on the screen temperature. For ZrO_2 the influence of the screen temperature on the statistical moments was investigated. Furthermore, the spectra of the scintillation screens were studied in the UV-VIS region with different ion species.

INTRODUCTION

Since decades, scintillation screens are widely used for beam profile measurement in nearly all accelerator facilities. Moreover, these screens are an essential part of a pepper-pot ermittance system. The realization at GSI, as used for the high current operation of the LINAC, is described in [1]. However, there had been doubts concerning the accuracy of the pepper-pot method [2], which might be related to a possible image deformation by the scintillating screen as reported in [3, 4, 5]. The properties of the luminescent materials (see Table 1) were investigated with ion beams of H^+, C^{2+}, Ar^{10+}, Ni^{9+}, Ta^{24+} and U^{28+} at energies between 4.8 and 11.4 MeV/u and different beam currents as delivered by the LINAC. The typical size of the ion beam was σ = 2 mm. Sensitive scintillation screens, like the single crystal $YAG{:}Ce$ or $ZnS{:}Ag$, were irradiated with lower currents [4]. The ceramic materials with less light yield, like BN, ZrO_2, $ZrO_2{:}Mg$, pure Al_2O_3 and $Al_2O_3{:}Cr$ (Chromox), were investigated and compared to Quartz-glass (Herasil 102) and Quartz-glass doped with Ce (M382). The realised experimental setup and the data aquisition system are described in [4, 6]. The original image of the beam spot was projected to the horizontal and vertical plane of the beam. In this work the results for the horizontal projection are presented, but comparable results were also obtained for the vertical one. For the characterization of the distribution $p_i(x_i)$ not only the centre μ (1st moment) and standard deviation σ (2nd moment) were used, but also the skewness γ (3rd moment, parameter of the asymmetry) and the kurtosis κ (4th moment, the peakedness) [7].

Table 1: Compilation of Investigated Materials

Type	Material	Supplier
Ceramic	ZrO_2 (Z700-20A), $ZrO_2{:}Mg$ (Z507), BN, Al_2O_3, $Al_2O_3{:}Cr$,	BCE Special Ceramics
Quartz glass	Quartz ($Herasil$ 102), Quartz:Ce ($M382$)	Heraeus Quarzglas

SCREEN INVESTIGATION

The interest of pepper-pot emittance measurements arises from the UNILAC high current operation with several mA. As reported in [3, 4, 5], the imaged beam width depends significantly on the temperature of the scintillating screen. An example for high current measurement is shown in Fig.1 where the screens were irradiated by Ar^{10+} with a current of 310 μA within 100 μs delivery time corresponding to $2 \cdot 10^{10}$ ppp. The peak power was 14 kW while the average power was 3.8 W. As expected the light yield of the various materials differs by several orders of magnitude. For the four materials $Quartz{:}Ce$, $ZrO_2{:}Mg$, BN and $Herasil$ the yields dropp significantly during the irradiation. The determined beam width varies within a factor of two. The light yield decreases coincidently with the imaged beam width, but with a slightly different time constant. Since it is known that the light yield reduction is correlated with the screen temperature [3, 4, 5], a break in the beam delivery of 3 minutes was scheduled to let the screens cool down. For $Herasil$, Al_2O_3, $Al_2O_3{:}Cr$ and $ZrO_2{:}Mg$ the light yield and the beam width show reproducible time behaviour and reach a constant value. For Al_2O_3 the light yield is constant whereas for $Al_2O_3{:}Cr$ the yield even increase. In both cases, a broadening of the image width occurr in a reproducible manner. Using a PT100 temperature sensor at the backside of $ZrO_2{:}Mg$ screen the average temperature of 240°C was determined for comparable beam parameters with an average power of 2.3 W (respectively to 3.8 W for the measurements shown in Fig.1). The interpretation of the temperature behaviour is challenging. As reviewed in [8] and [9] the light yield of crystal scintillators like $NaI{:}Tl$, BGO and $CdWO_4$

* E-Mail: e.guetlich@gsi.de

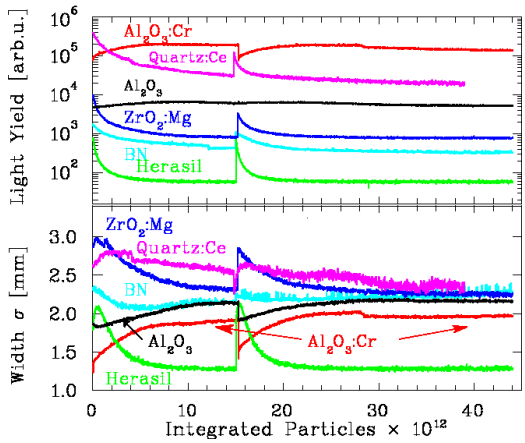


Figure 1: Light yield and beam width for different materials irradiated by 2200 macro-pulses of Ar^{10+} ions with $2 \cdot 10^{10}$ ppp, in 100 μs pulse lenght with 2.6 Hz repetition rate at 11.4 MeV/u ($\sim$300 μA). After 5 min. of irradiation, a 3 min. break was introduced to let the screen cool down, followed by 10 min. irradiation.

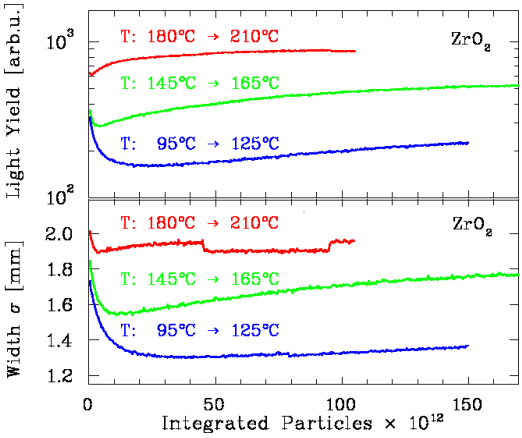


Figure 2: Light yield and beam width for ZrO_2 irradiated by 300-500 macro-pulses of 2 Hz repetition rate with $3.9 \cdot 10^{11}$ ppp H^+ in 4 ms pulse lenght at 4.8 MeV/u.

depends significantly on the temperature. After a certain (material dependent) irradiation time, a steady-state temperature distribution is reached leading in a constant yield and width reading. The equilibrium width reading differs.

For the investigation of the temperature dependence, a Ni layer (heating loop) was sputtered on the backside of ZrO_2 screen to heat the sample up to 300°C. The light yield and the beam width for ZrO_2 with three different heating levels are shown in Fig.2. The sample was irradiated by a proton beam with $3.9 \cdot 10^{11}$ ppp within 4 ms beam delivery and a repetition rate of 2 Hz, corresponding to a peak power of 75 W and an average power of 600 mW. The heating power was kept constant for each curve but the sample was additionally heated by the ion beam. Thus, the temperature on the backside of the sample increases during the irradiation. Beside an initial phase, which is difficult to interpret, one can clearly see that the equilibrium light yied and the imaged beam width increase with the temperature. By heating up the ZrO_2 screen from room temperature to 274°C, the light yield increases by one order of magnitude. In Fig.2 the light yield is increases by a factor of 4 and the imaged beam width increases by a factor of 1.5 in the temperature range from 125°C to 210°C. These reasults clearly point out that the temperature of the ceramic scintillaton screens could be a critical issue, especially for high current ion beams. Further experimental results are reported in [3, 4, 5].

SPECTROSCOPIC STUDIES

The spectroscopic studies on the scintillation screens were performed with the Jobin Yvon Horiba CP140-202 spectrograph [10] and an Image Intensifier CCD Camera (ICCD). The spectra of six different scintillation screens irradiated with a Ta^{24+} and a H^+ ion beam are presented in Fig.3. The spectra are not corrected by the photocathode and the spectrometer efficiency. By comparing the luminescence spectra for the two ion species Ta^{24+} and H^+, some significant differences were observed for Al_2O_3, Al_2O_3:Cr, BN, $Herasil$ and ZrO_2. There is no change in the spectrum of ZrO_2:Mg. By comparing the spetra of pure Al_2O_3 and Al_2O_3:Cr, one can clearly see the influence of the host lattice on the band around 490 nm. The absence of the known line at about 695 nm for Al_2O_3:Cr is not explained till now. The screen temperatures are different for Ta^{24+} and H^+ during the irradiation process, which could cause a slight shift in the spectra. To investigate the influence of the screen temperature on the spectrum, temperature studies were performed, like the one for Fig.2. In Fig.4 three different heating levels were applied on the ZrO_2 scintillation screen. Starting from room temperature with no additional heating to a temperature of $\sim$250°C. For the broad bands, a slight shift into higher wavelength during the heating process was observed. Further more, the bands around 400 nm and 725 nm are strongly effected by the increased temperature. An additional interesting observation is that there is no change in the position for the sharp line around 515 nm in the ZrO_2 spectra with H^+ ions. It turns out that the influence of the screen temperature is bigger for irradiation with H^+ than for Ta^{24+}.

MEASUREMENT RESULTS

Several scintillation materials were investigated under various beam conditions. Different readings of the imaged beam width for various materials were determined even for purpose built crystalline scintillators. These results were obtained with H^+ ions, as well as heavier elements up to U^{28+}. The observed behaviours were reproducible under different beam conditions. The influence of a chromatic abberation of the lens, as well as the light intensity on the CCD-Chip could be excluded to explain the results. Due

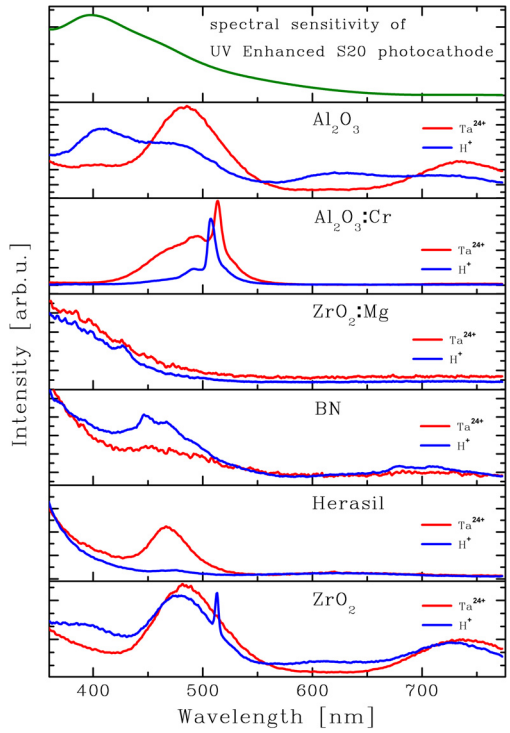


Figure 3: Spectra of the scintillators for Ta^{24+} (in red) and H^+ ions (in blue). Beam parameters for H^+: $4.1 \cdot 10^{11}$ ppp at 4.8 MeV/u, 2 ms pulse lenght, 2 Hz repetition rate. Beam parameters for Ta^{24+}: $8.8 \cdot 10^9$ ppp at 11.4 MeV/u, 100 μs pulse lenght, 1 Hz repetition rate. The spectra are averaged over about 1000 images and they are not corrected by photocathode (top) and spectrometer efficiency.

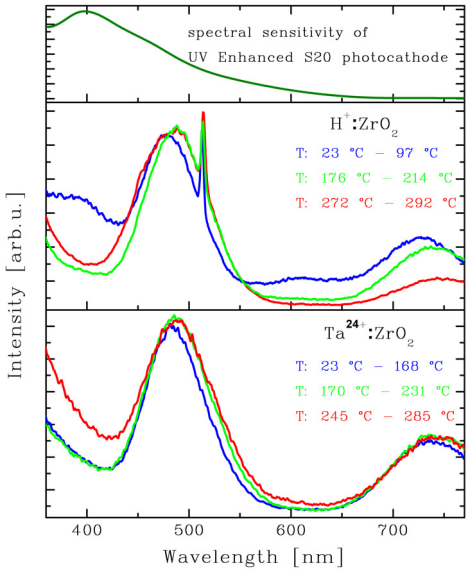


Figure 4: Spectra of ZrO_2 for irradiation with Ta^{24+} and H^+ ions for different heating levels. The beam parameters and the evaluation are the same as in Fig.3.

to the possibly high surface temperature, it is intended to introduce a filter in front of the lens, to avoid image deformation due to IR-radiation. The influence of the surface roughness and grain size has to be investigated for the ceramics. Additionally, the linearity of the investigated scintillating materials has to be determined. Further data analysis are in progress to discriminate between saturation, diffuse refraction and self-absorbtion of scintillation light using the higher statistcal moments. Additional beam-based experiments are required to distinguish between these effects.

For high current applications, the properties are influenced by the temperature of the screens, which is significantly increased during irradiation. This knowledge is essential for choosing a well-suited material for the pepperpot emittance device. Following the high current investigations at least BN and $Quartz$:Ce can not be used due to the permanent degradation [5]. It seems that ZrO_2:Mg and $Herasil$ are good candidates for a high current application. ZrO_2:Mg has a high light yield, it does not show a significant surface modification and its spectrum shows almost no dependence on the ion species. $Herasil$ showed a narrow imaged beam width and being a transparent material the diffuse reflections at the grain boundaries are avoided, but its spectrum shows a significant change for Ta^{24+} compared to H^+. The influence of different ion energies and species on the scintillation process has to be investigated for $Herasil$, because of its transparency. In addition ion beam analysis will be carried out to clarify the open questions.

REFERENCES

[1] T. Hoffmann et al., Proc. Beam Instrum. Workshop, Stanford, USA: p.432, (2000).

[2] J. Pfister et al., Proc. EPAC 2008, Genoa, Italy: p.3449, (2008) and W. Barth, L. Groening, D. Liakin, Proc. DIPAC03 Mainz, p.56 (2003).

[3] E. Gütlich and P. Forck et al., GSI-Scientific Report 2007/2008, p.105(2007)/to be published(2008), (2007 and 2008).

[4] E. Gütlich and P. Forck et al., Proc. Beam Instrum. Workshop BIW, Lake Tahoe, USA: to be published, (2008).

[5] E. Gütlich and P. Forck et al., Proc. SCINT 2009, Jeju, Korea: to be published (2009).

[6] R. Haseitl et al., Proc. PC@PAC, Ljubljana, Slovenia: p.180, (2008).

[7] W. H. Press et al., Numerical Recipes 3rd.Edition, Cambridge University Press, New York, p.724 (2007)

[8] G.F. Knoll, Radiation Detection and Measurement, John Wiley & Son, New York (1999).

[9] G. Blasse, B.C. Grabmaier, Luminescent Materials, Springer Verlag (1994).

[10] Homepage of Horiba Scientific, http://www.horiba.com.

FAST WIRE SCANNER CALIBRATION

J. Koopman, A.G Ollacarizqueta, CERN, Geneva, Switzerland
A. Lokhovitskiy[1], JINR, Dubna, Russia, CERN

Abstract

The fast rotating wire scanners installed in the PS and the PS booster are used for the precise transversal profile measurements in horizontal and vertical planes. The scanners may show large position measurement errors if no special treatment is applied to the acquired data. The aim of the calibration is to obtain a correction algorithm for the systematic position measurement error due to mechanical and electronic offsets.

A new calibration system has been developed and introduced in CERN for the scanners implementing position feedback control. The calibration method is based on a substitution of a particle beam by a laser one where the laser beam position is well known. According to the previous experience the following crucial requirements to the system have been taking into consideration: heavy and mechanically stable design of the calibration bench to reduce mechanical oscillations of scanner parts; automation of the calibration procedure to exclude human errors in data taking, storing and analysis; high precision of the laser positioning; minimization of the total amount of scans and calibration time for each scanner.

SYSTEM OVERVIEW

The setup consists of a massive vacuum tank that can receive either a horizontal or a vertical scanner with 2 viewports at the position where normally the vacuum chamber is situated. A laser beam, split into two parallel beams of nearly equal intensity distant by 2.7 mm by means of special optics, through which the wire travels at high speed, is mounted in front of one viewport. Behind the second viewport a large fixed mirror is positioned.

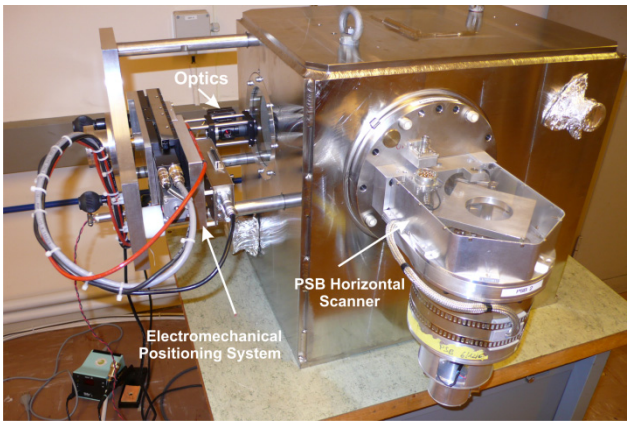


Figure 1: Calibration bench with a horizontal PS booster scanner.

The carbon wire scanning through the beams creates thus twice a shadow detected by one single photo-detector, resulting in 2 negative peaks and otherwise constant signal. Correlating the measured peak positions with the real laser beam position allows the creation of a correction algorithm. For the automation purposes the laser and photo-detector are mounted together on a translation table and moved by a stepping motor (Parker MX80S, stepping motor driven linear stage.).

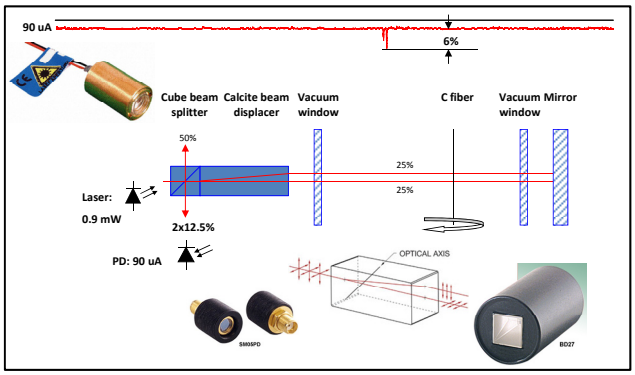


Figure 2: Measurement principal.

An expected and observed signal from the 30 µm C-fiber travelling with a speed of 10 to 20 m/s through a 200 µm (σ) laser beam (1mm diameter) only has a modulation depth ~6%. A precise adjustment of the optical subsystem is required to provide conditions at which a peak detection algorithm works stable. One should note it impacts on the total number of scans which is needed to be done during the calibration of a scanner. A minimal number of bad scans, when peaks cannot be detected precisely, is allowed to make less repeated scans and to extend the life-time of bellows and wires.

Motion Control and Acquisition Electronics

The electronics for the acquisition and control of the wire-scanner movement and laser positioning are hosted in a standard VME64x crate. The motion control card [5] is in charge of the scanner positioning and the laser beam acquisition. The laser movement and position acquisition are controlled through a TVME200/IP-OCTAL-422 card connected to a MIDI crate [6]. Two FESA [3] classes running on a RIO3-8064 CPU card control the system. When a scan is launched, the position of the scanner is measured by means of a precision rotary potentiometer. A 16-bit ADC performs the read-out of each position measurement which is then stored in a 256k memory block. The standard wire-scanner installation acquires the signal coming from a photomultiplier using a logarithmic amplifier. The calibration installation has to use the laser detector signal instead. The signal is read with a 12-bit ADC configured to acquire an external input signal. The measurement in both cases is stored in another 256k memory block of the motion control card. The rate of acquisition is

[1] Arkady.Lokhovitskiy@cern.ch

configurable. For calibration purposes a rate of 200 kHz was used. The laser position is read from the MIDI crate and corresponds to the number of steps the motor displaced from a limit switch with respect to the centre of the chamber.

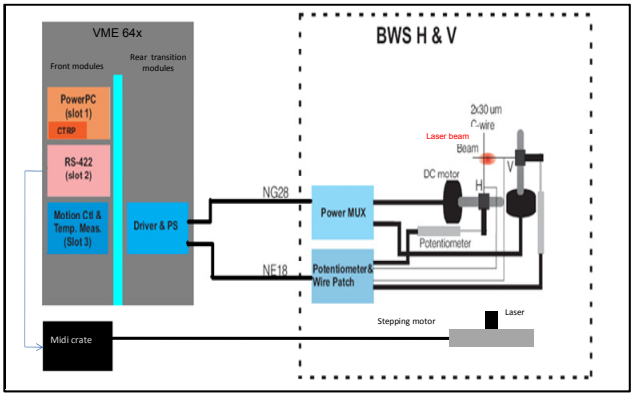


Figure 3: Electronics schematics of the calibration bench.

LOOKUP TABLES

The measured position of the scanner is represented by a signal coming from the potentiometer only contains the information about a motor crankshaft angle (see Figure 3). Because of very high non-linearity of the transmission of the motor rotation to the wire travelling the crankshaft angle cannot be used directly to identify a projected position.

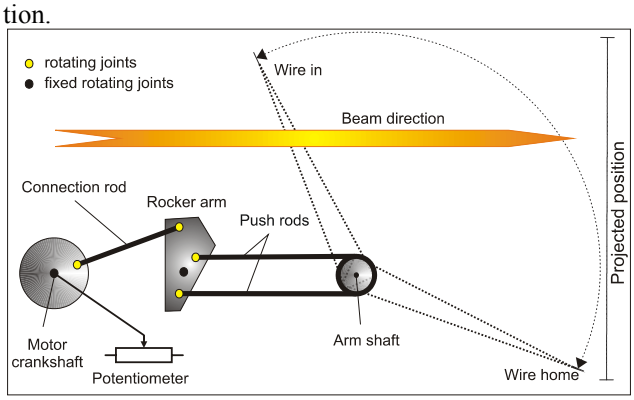


Figure 4: Schematic of a wire movement.

To convert bits into projected positions in the calibration system a method of lookup tables is implemented. Each lookup table contains number pairs $n^{p}(bits) \Leftrightarrow x^{p.p.}(mm)$ covering a significant range of the projected positions. The calibration system uses the theoretical and correction lookup tables. The correction tables are the final output of a calibration procedure and they have to be uploaded to the FESA servers controlling the operational electronics. The theoretical lookup tables (Figure 5) have been calculated once according to geometrical parameters of an ideal scanner (Table 1) by a method described in [1]. They are used to display the calibration results in a form of human readability and may help to unmask some problems with a scanner during its calibration.

Table 1: Geometrical parameters of the kinematic model

Parameter	PS	PS Booster
Crankshaft radius	11 mm	11 mm
Length of connection rod	84.5 mm	84.5 mm
Horizontal distance of motor shaft to rocker shaft	80 mm	80 mm
Vertical distance of motor shaft to rocker shaft	36 mm	36 mm
Radius of rocker arm, motor side	26 mm	26 mm
Radius of rocker arm, wire side	17 mm	16 mm
Angle between rocker and lever	34 deg.	34 deg.
Horizontal distance from rocker centre to fork shaft	164 mm	167.69 mm
Vertical distance from rocker centre to fork shaft	17.25 mm	17.62 mm
Radius of fork shaft	5.75 mm	6.0 mm
qDistance from fork shaft to wire	164 mm	164 mm
Fork angle at home position	-20 deg.	-24 deg
Distance from fork shaft to beam centre	89.75 mm	92.38 mm
Radius of push rod	6.2 mm	6.2 mm

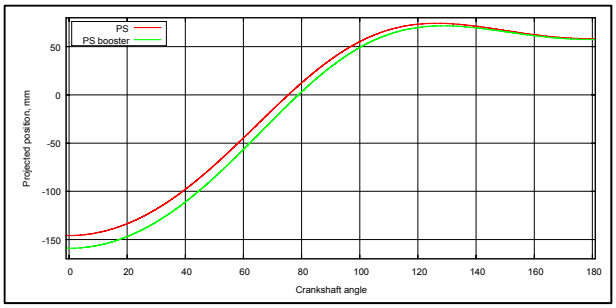


Figure 5: Lookup tables of theoretical projected positions.

CALIBRATION PROCEDURE

A scanner calibration is carried out in 4 steps:

1. A scanner is mounted in the tank and linked-up to the control electronics. To prevent scanner damage the installation integrity and readiness of all the elements in the system have to be verified before the calibration is being started.
2. Verification of the photodiode signal quality and peak visibility by making single scans. Optics adjustment may be required.
3. Automated calibration. At each laser position few scans for each predefined speed (10, 15 and 20 m/s) have to be performed and the detector read out. The acquired data is analyzed and the peaks in the signal accurately located in time scale. An incremental positioning of the laser and a number of repeated scans are set up to perform the minimal needed number of scans for tolerable results. The automated calibration produces 6 correction lookup tables: for each of 3 predefined speeds and for 2 wire movement directions. Figure 6 shows the mismatching between measured and calculated lookup tables of 2 wire scanners for the speed 15 m/s where a laser positioning increment equals to 5 mm.

4. A check of newly created correction lookup tables. The same scans as in the step 3 have to be performed again but already applying the created tables to identify a wire position. An error of a position measurement is defined as $\Delta x = x_{wire}^{p.p}(v_p) - x_{laser}$, where v_p is a potentiometer value of a detected dip(s), $x_{wire}^{p.p}(v_p)$ is a projected position of the wire taken from a correction lookup table, x_{laser} - laser beam position. If the majority of the results are within the range ±0.5 mm the scanner is classified as calibrated and ready to be used for operation. Check results of the scanners from Figure 6 are shown in Figure 7.

Steps 2-4 are executed using a dedicated expert application written in java to handle remotely the calibration task and to process acquired data. The application communicates directly with 2 FESA servers controlling the electronics.

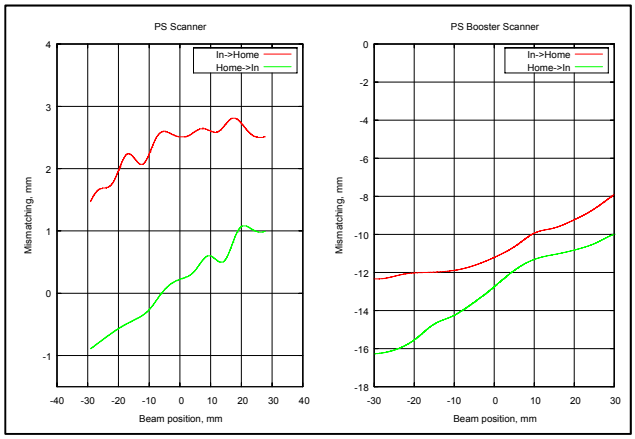


Figure 6: Mismatching between measured and theoretical projected positions of a scanner in PS domain and a scanner in PS booster domain. The wire speed is 15 m/s.

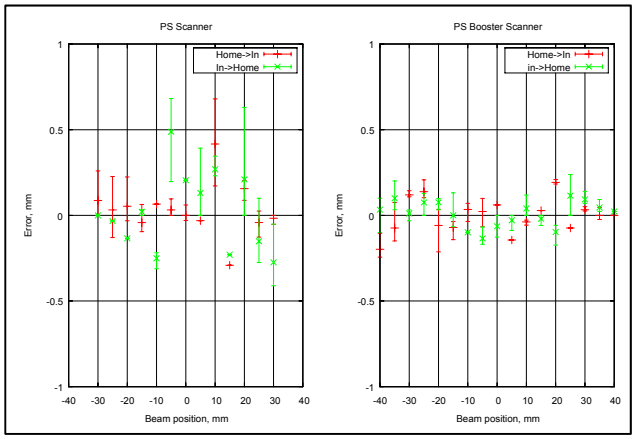


Figure 7: Check results of a scanner in PS domain and a scanner in PS booster domain. The wire speed is 15 m/s.

CONCLUSION

With the new calibration system we achieved the following results: human errors are completely excluded from the calibration task; one scanner full calibration takes only 1 hour if there are no hardware problems (it took half-day formerly); percentage of bad scans is very low when optics are well tuned. During the 2008-2009 shutdown at CERN 13 fast wire scanners including a spare one were calibrated and installed in the PS and the PSB booster at hard time constraints. When the PS and the PS booster started up few comparative profile measurements were done to verify a match of a profile centre-mass with a position measured by a nearest pickup. A Figure 8 shows one comparative measurement.

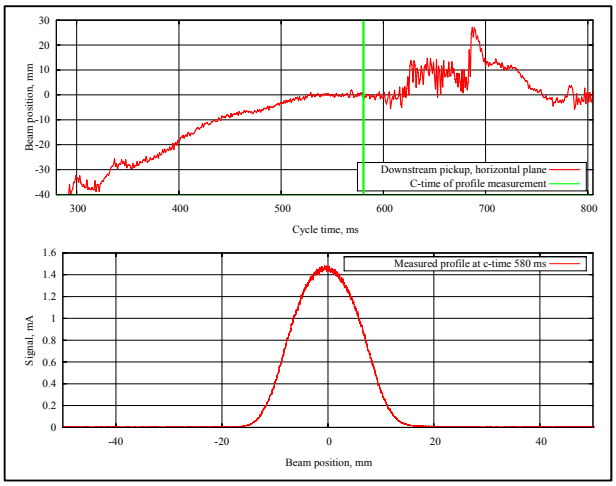


Figure 8: Horizontal profile measurement of a c entred beam in the PS booster: a) beam position from a downstream pickup, b) profile, measured by a wire scanner.

REFERENCES

[1] M. Ludwig, S. Burger, U. Raich, J. Olsfors, “Fast Wire Beam Scanner Movement Control for the PSB”, PS/BD NOTE 2002-210, CERN.

[2] S. Burger, C. Carli, M. Ludwig, K. Priestnall, U.Raich, “The PS Booster Fast Wire Scanner”, Proceedings of DIPAC 2003, Mainz, Germany.

[3] Michel Arruat, Leandro Fernandez, Stephen Jackson, Frank Locci, Jean-Luc Nougaret, Maciej Peryt, Anastasiya Radeva, Maciej Sobczak, Marc Vanden Eynden, “Front End Software Architecture”, Proceedings of ICALEPCS07, Knoxville, Tennessee, USA.

[4] Jan Koopman, “Wire Scanner Calibration Bench - Measurement Principal”, internal document of a section BE-BI-BL, CERN.

[5] Stian E. S. Førde, “Wire Scanner Motion Card”, thesis, Bergen University College, stiford@gmail.com, December 13, 2006.

[6] http://cdsweb.cern.ch/record/294827/files/sl-95-123.pdf

TRANSVERSE PROFILE MONITORS BASED ON FLUORESCENCE FOR IFMIF-EVEDA ACCELERATOR

J.M. Carmona*, B. Brañas, A. Ibarra, I. Podadera, CIEMAT, Madrid, Spain

Abstract

IFMIF-EVEDA prototype accelerator will be a 9 MeV, 125 mA continuous wave (CW) deuteron accelerator, focused on validating the technology that will be used in the future IFMIF facility [1]. In such a high current low energy deuteron accelerator, any interceptive diagnostic could be destroyed. In the quest of non interceptive beam transverse profilers required for IFMIF-EVEDA, two different options are considered: A monitor based on the fluorescence of residual gas developed by CIEMAT and another based on ionization developed by CEA [2]. In this contribution, a description of the beam transverse profile monitor prototype based on fluorescence, together with a brief analysis of the reliability of the profiles captured with this monitor will be presented.

INTRODUCTION

The International Fusion Materials Irradiation Facility (IFMIF) aim is to provide a materials irradiation database for the design, construction, licensing and safe operation of the future Fusion Demonstration Reactor (DEMO) [2]. In such a reactor, high neutron fluxes may generate up to 30 dpa/fpy (displacements per atom/full power year). IFMIF facility will be a dual 40 MeV deuteron accelerator (2 x 125 mA operating in continuous wave), colliding with a liquid lithium target with the aim to produce high neutron fluxes to test new materials.

In the framework of the "Broader Approach", the IFMIF-EVEDA (Engineering Validation and Engineering Design Activities) project includes the construction of an 9 MeV and 125 mA (CW) deuteron accelerator prototype. Most of the components of the accelerator are being developed by France, Italy and Spain [3].

In such high current accelerator, non-interceptive diagnostics are required. Hence, in the following sections, a brief description of the first prototype for the EVEDA fluorescence profile monitor will be provided. Such monitor is actually in design and prototyping phases.

PROTOTYPE PROFILE MONITORS

As part of the diagnostics package, non interceptive profile monitors will be installed along the line of the EVEDA accelerator with the aim to measure and characterize the beam. A fluorescence profile monitor is based on the interaction between the beam particles and the residual (or injected) gas inside the vacuum chamber of the accelerator. Photons are produced due to the excitation and de-excitation of the gas molecules or atoms (in the case of injected atomic gas). This technique has been tested already at different accelerator e.g. CERN-PSB [4] and GSI-UNILAC [5].

The light emitted, can be collected and used for the determination of the beam profiles. The low cross sections between the beam and the gas at those energies (9 MeV), can be counteract by increasing the integration time (taking advantage of CW operation) and optics optimization.

A set of collection optics will be installed to obtain horizontal and vertical projections of the beam at the same position. Briefly it consists of a special optical window and a set of optics plus a detector. Depending on the results of the first prototype, the detector could be finally located in front of the viewport or installed in a safety place inside of a shielded box, using a coherent fibre bundle to transport the image from the viewport to the camera. A movable calibration system and a gas valve will be installed in order to provide spatial calibration and to increase the pressure locally, respectively. Finally, a filter wheel could be installed to select different line transitions.

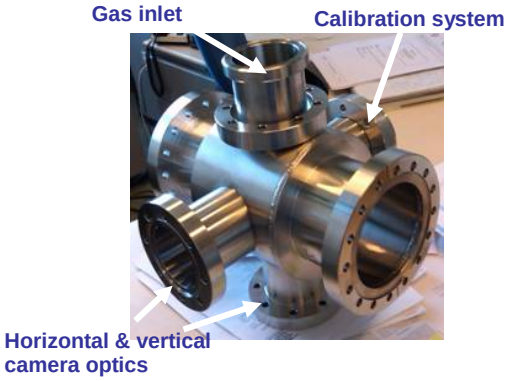


Figure 1: Illustration of the prototype vacuum chamber for the fluorescence profile monitor, showing the vertical and horizontal viewports, as well as those for gas injection and calibration.

Challenges for IFMIF-EVEDA Profile Monitors

The high neutron and gamma fluxes can lead into a permanent damage for electronic devices like detectors or standard fibres. Detectors usually loose dynamic range and contrast with radiation and can become inoperative even at low dose rates [6]. The detector which suits better our requirements must be chosen carefully, taking into account quantum efficiencies, readout times, spatial resolution, dynamic range and rad-hard operation. CCD's and CID cameras from several companies have been considered. To date, the most promising candidate for EVEDA are CID rad-hard cameras because of its dynamic range and rad-hard resistance operation of some models (up to 3 Mrad). Other detectors like PMT's or

*jm.carmona@ciemat.es

APD's have been discarded due to lack in spatial resolution.

A widely known problem is that transmission of optical windows falls with radiation, resulting in decreasing photon counts with time. In order to avoid this setback, the construction of optical windows based on with KU1 and KS-4V quartz glasses are proposed. Transmission for these quartz glasses is ~100% and remains constant for wavelengths above 380 nm at high gamma and neutron flux rates [7, 8].

SHIELD CONCEPT AND IMAGE BUNDLE OPTIONS

High neutron and gamma fluxes are expected during operation of the accelerator inside the vault. In such hostile environment, is essential to design a local shield in case of using sensitive elements. Looking for a optimization of the shield estimations of the neutron and gamma spectra are being made (see Fig. 2). For the monitors that will be located along the HEBT, a dual head and single output coherent fibre bundle are being considered. For the EVEDA prototype monitor, a radiation tolerant CID camera has been selected (see below). Since every pixel in CID cameras is addressable individually, it could be possible to obtain both profile projections with a single camera using the proposed bundle. If this capability is tested successfully, it will cause a cost reduction of the rents.

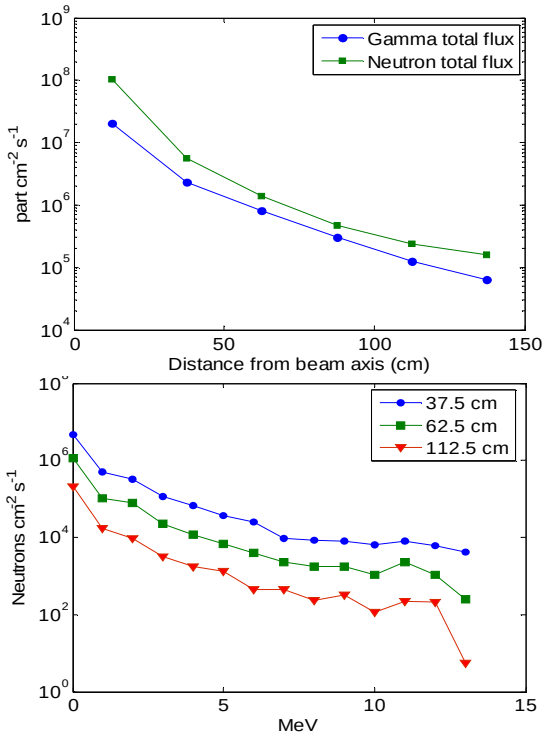


Figure 2: Preliminary estimation of total gamma and neutron fluxes versus the distance from the beam axis (top) and neutron spectra at 3 different distances from the beam axis (bottom) near the beam dump [9].

Coherent Image Bundles Options

A coherent image fibre bundles opens the possibility to move the diagnostic set to a safety shielded location. The image bundle should withstand high gamma and neutron fluxes without darkening (loss transmission).

Nowadays, Fujikura LTD [10] and SCHOTT [11] are suppliers with images bundles in their catalogues. SCHOTT provides good quality large image bundles but no radiation resistant (unless they are shielded). Fujikura LTD has radiation resistant image bundles (FIGR series), but they have a maximum diameter of 3 mm leading into a decrease in spatial resolution.

In order to overcome this drawback, an array of FIGR image bundles can be grouped into a larger one, although spatial resolution of SCHOTT bundles will be still larger.

With the purpose of evaluate the viability of this approach, a Fujikura image fibre bundle will be tested together with the fluorescence profile monitor with a deuteron beam in the next months.

RAD-HARD CID CAMERA

A Thermo Scientific radiation hard CID8726DX6 monochrome camera has been selected for the BTPM prototype. This charge injection device based camera can withstand more radiation levels than standards CCD cameras with relatively low noise in such hostile environments. See table 1 for specifications.

Table 1: CID camera main characteristics

Pixels	786 x 603
Pixel size	17.3 μm x 17.3 μm
Full well capacity	> 100000 electrons
Remote head controller	Up to 50 m
Rad – Hard (at least)	3 Mrad
Outputs	USB 2.0, J2, J1002,…
Gain	x2, x4
Geometric distortion	0 %

The CID8726 camera is cooled down to keep a good S/N ratio even at high gamma fluxes. This camera has lower performances than the best scientific CCD's available, but suitable for profile measurements in hostile environments.

PROFILE RELIABILITY AND GASES

Typically, molecular nitrogen and hydrogen are the main components of the residual gas present inside a beam pipe. The most intense lines come mainly from N_2 and N_2^+ with wavelengths between 385-430 nm and lifetimes about 60 ns [3].

Electric Field Interaction

In high current accelerators (and especially in low *beta* beams) the interaction between the electric field and the excited charged particles of the residual gas could lead into a profile falsification.

For instance, in case of large transition lifetimes, the distance between the points where the excitation and de-

excitation of a particle occurs can be non negligible. In order to avoid the contribution of electric field to beam profiles, transitions coming from non ionized atoms or molecules can be selected like e.g.. Ne I, Ar I, Kr I or Xe I lines, depending on their lifetimes and intensities.

Table 2: Velocities due to thermal motion for different candidate gases

$v_{th}(N_2)$	4.15 x10^{-4} mm/ns
$v_{th}(Ne)$	4.92 x10^{-4} mm/ns
$v_{th}(Ar)$	3.48 x10^{-4} mm/ns
$v_{th}(Kr)$	2.39 x10^{-4} mm/ns
$v_{th}(Xe)$	1.92 x10^{-4} mm/ns

Unlike other accelerators, hydrogen is expected to be the dominant residual gas in EVEDA due to superconducting cavities (at least near them). There are several processes which could turn into emission of photons (with different cross sections) like e.g.

$$D^+ + H_2 \rightarrow D^+ + H_2(n^*) + e^-$$
$$H_2(n^*) \rightarrow H_2(n_0) + h\nu$$
$$D^+ + H_2 \rightarrow D^+ + H_2^+(n^*) + e^-$$
$$H_2^+(n^*) \rightarrow H_2^+(n_0) + h\nu$$
$$D^+ + H_2 \rightarrow D^+ + H(n^*) + H(n^*)$$
$$H(n^*) \rightarrow H(n) + h\nu$$
$$D^+ + H_2 \rightarrow D(n^*) + H_2^+(n) \rightarrow D(n) + H_2^+(n) + h\nu$$

+ Electron impact excitation processes

Thus, injection of another gas could be desirable because of hydrogen low mass and weak transitions in the region of interest among other effects. In the quest of the best gas, high mass, high cross section, a short lifetime and transitions in the visible region are desirable. Neon, Argon, Krypton and Xenon are gases with similar cross sections, with several transitions in the visible region and in the case of Xe, a large mass (131 amu) and some Xe II line transitions with short lifetimes (~6 ns) [5, 12]. Hence, a filter wheel in the design could assure the reliability of the profiles.

Thermal Motion

Thermal motion could be also a source of profile widening also, but even for long lifetimes (~60 ns), the distance between excitation and de-excitation (photon emission) due to this effect is negligible (e.g. 2.5E-3 mm for N_2^+). See table 2.

Estimation of Photons and Resolution

A numerical code has been developed to optimize the design of the monitors along the line. With this tool, beam-gas interaction emissivity, number of photons reaching the detector and the final resolution achievable can be estimated e.g. using the present CID camera, cross section σ~1e-18 cm^2, tube radius ~ 30 mm, distance beam-lens ~200 mm, pressure ~ 3e-6 mbar, lens F/ number ~1.4, efficiency ~ 1%, integration time ~ 100 ms, 125 mA, σ^{rms}~2.5 mm, the expected photons are ~1.57e+7, beam size in front of detector ~0.36 mm being ~21 in detector pixels. As the beam size will change along the HEBT (i.e. from ~2 mm to ~20 mm), an optimization of the monitors should be made. The optics can be selected to obtain a required resolution, e.g. to obtain the same spatial resolution for σ^{rms}~20 mm beam, a 12 mm lens and a distance beam-lens of ~650 mm should be chosen.

ACKNOWLEDGEMENTS

We would like to acknowledge P. Forck and F. Becker from GSI and E. Bravin from CERN for his comments and fruitful discussions.

CONCLUSIONS

IFMIF-EVEDA prototype profile monitor based on fluorescence of residual gas have been presented. At the present design status, this technique looks very promising to characterize the beam transverse profile at such low energies and high deuteron current. Therefore, they could be a key device to carry out non-interceptive transverse emittance measurements by doing quadrupoles scans.

REFERENCES

[1] P. Garin et al., EPAC08 conference proceedings, TUZG01, (2008).
[2] J. Marroncle et al., see this proceedings.
[3] IFMIF Comprehensive Design Report, January 2004.
[4] M.A. Plum et al., Nucl. Instr. And Meth. A 492 (2002) 74-90
[5] F. Becker et al,. "Beam induced Fluorescence (BIF) Monitor for Heavy Ion Beams", BIW 2008, Lake Tahoe, May 2008
[6] S. Hutchins et al., "Radiation tests on solid state cameras for instrumentation", Proceedings of DIPAC 2005, CTWA02.
[7] A. Moroño et al,. Journal of Nuclear Materials 329-333 (2004) 1438
[8] D.V. Orlinski et al., Problems of Atomic Science and Technology, N 3. Plasma Physics (5), (2000) p. 60-63
[9] F. Ogando et al., UNED, private comunication
[10] www.fujikura.co.uk
[11] www.schott.com
[12] NIST Atomic Spectra Database Lines Form. http://physics.nist.gov/PhysRefData/ASD

THE BEAM PROFILE MONITORS FOR SPIRAL 2

J.L. Vignet, A. Delannoy, E. Guéroult, P. Gangant, J.C. Foy, S. Cuzon, C. Houarner, M. Blaizot,
GANIL, BP 55027, 14076 Caen Cedex 5, France

Abstract

In order to visualize the SPIRAL 2 beam dynamics, several beam profile monitors are under development. Multiwires beam profile monitors (SEM) will be used on the driver and RIB lines. Non interceptive beam profile monitor (RGM) should be mounted on the LINAC diagnostics box before experiments room, and low intensity beam profile monitor (EFM) on the RIB lines For the signals acquisition of all this kind of monitor, a new associated electronics will be used. These electronics digitize 94 channels in a parallel system. Each channel integrates the current of the associated wire or strip and performs a current-voltage conversion. The dedicated GANIL data display software has been adapted for these different new monitors.

SPIRAL2 DESCRIPTION

The SPIRAL2 facility is based on a high-power superconducting driver LINAC which delivers a high-intensity, 40-MeV deuteron beam, as well as a variety of heavy-ion beams with mass-to-charge ratio equal to 3 and energy up to 14.5 MeV/u (Table 1). The driver accelerator will send stable beams to a new experimental area and to a cave for the production of Radioactive Ion Beams (RIB). The Accelerator building construction (phase1) will started in 2010 and the RIB production building (phase 2) in 2012 (Fig. 1). The commissioning of the driver should start in 2011 at GANIL.

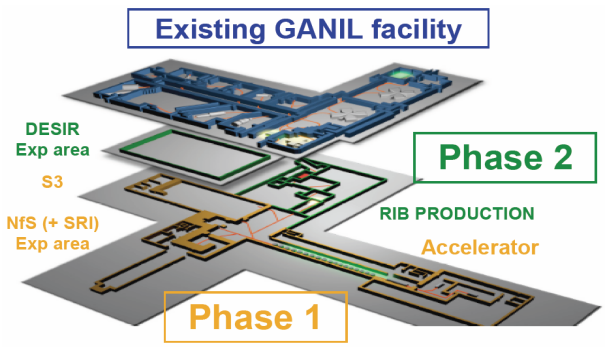


Figure 1 : SPIRAL 2 and GANIL facilities.

DRIVER ACCELERATOR

The Injector, dedicated to protons, deuterons and ions of Q/A=1/3, is mainly composed of two ECR ion sources with their associated LEBT (Low Energy), a warm RFQ and the MEBT (Medium Energy) line connected to the LINAC. The LINAC accelerator is based on superconducting independently-phased resonators. It is composed of 2 families of quarter-wave resonators (QWR) at 88 MHz, 12 resonators with β=0.07 (1 cavity/cryomodule), and 14 resonators at β=0.12 (2 cavities/cryomodule).

STABLE BEAM CHARACTERISTICS

Table 1: SPIRAL 2 Stable Beam Characteristics

	Q/A	Intensity range (mA)	Energy range (Mev/u)	CW beam Power (kWatt)
Protons	1	0-5	2-33	165
Deuterons	1/2	0-5	2-20	200
Ions	≥1/3	0-1	2-14.5	43.5
Ions	≥1/6	0-1	2-8.5	51

RIB PRODUCTION

The 40 MeV, 5 mA deuteron beam impinging on the converter produces an intense neutron flux with a energy centered at 14 MeV. Neutrons induce fission in the UC target located downstream of the target converter. The converter has to withstand up to 200kW beam power. The converter is a high speed rotating target which limits the peak surface temperature of converter materials far below 2000°C. The thermal power deposit in the converter material is dissipated only by thermal radiation.

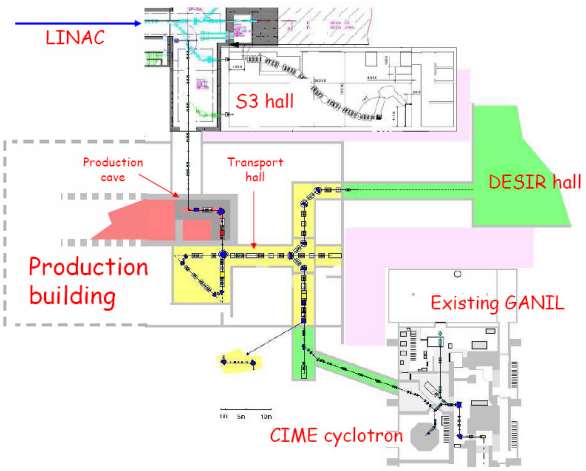


Figure 2 : Radioactive beam facilities.

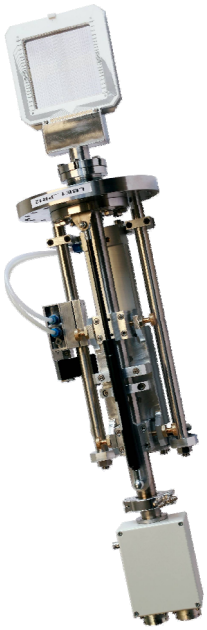
Table 2: Radioactive Beam Characteristics

	Line 1+	Line n+	Existing ganil
Ion mass range	6 to 240	6 to 160	6 to 160
Intensity range (pps)	10^3 to 10^{11}	10^3 to 10^{10}	10^3 to 10^9
Beam energy	10 to 60 keV	10 to 45 keV	1.2 to 20 MeV/u
Example of RIB	132 Sn^{1+} 20 keV	132 Sn^{20+} 400 keV	132 Sn^{20+} 792 MeV

BEAM DIAGNOSTICS

In order to drive the SPIRAL2 beam along the beam transport three kinds of beam profile monitor have been developed at GANIL.

Secondary Emission Monitor (SEM)



These monitors are composed of an horizontal and a vertical grid of golden tungsten wires of 150 µm.

Three kinds of grid can be installed, depending on the maximum size needed to be measured:
- 47 wires with 1 mm spacing for maximum beam size of 30 mm
- 47 wires with three different spacing (1, 2, or 3 mm) for maximum beam size of 80 mm.
- 100 wires with 1 mm spacing for maximum beam size of 100 mm

These wires are welded on an alumina board to obtain a maximum out-gassing rate of 10^{-8} $Pa.m^3.s^{-1}$. The total mechanical precision of this diagnostic is 0.2 mm.

Figure 3 : SEM profiler.

In order to resist the beam power, different duty cycle should be applied and depending on the location on the line. Simulations have been done in order to estimate the temperature of the wires About 70 secondary emission monitors will be installed on the different lines of the SPIRAL 2 facilities.

Table 3 : 5 mA Deuterons on 150 microns tungsten wire.

	LEBT	MEBT	LINAC
Energy	40 keV	1.5 MeV	40 MeV
Wires temperature	650 °C	900 °C	900 °C
Duty cycle	4 ms/s	0.5 ms/s	2 ms/s

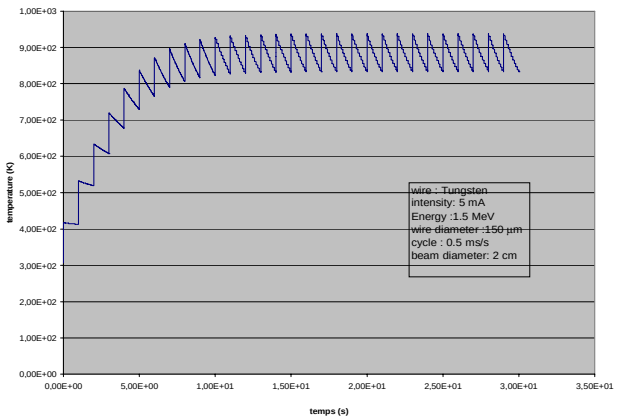
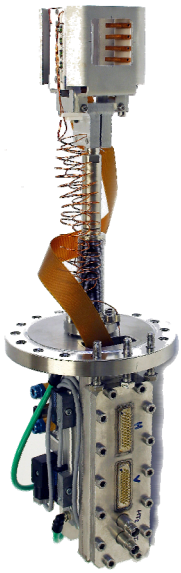


Figure 4: Temperature variation vs beam time on wire.

Non-Interceptive Beam Profile Monitor (RGM)



The principle of this profiler is based on the ionization of the residual gas of the lines by the beam. This diagnostic gives a one-dimensional profile and is composed by a drift space and a signal amplification stage (one micro-channel plate) with an anode of 35 strips spaced by 0.3, 0.5 or 1 mm. The working pressure is 10^{-8} mbar and the desired resolution is 1mm. In order to obtain a low out-gassing, the profiler should be baking at 150 °C.

Figure 5 : RGM profiler.

It will be set up when a high intensity beam monitoring will be needed and will be mounted between the six first Linac cryogenic cavity and just before the high intensity target of experimental rooms.

Low Intensity Beam Profile Monitor (EFM)

A secondary emission foil profiler is under development and will be used on the SPIRAL 2 radioactive beam lines and the experimental rooms. It will monitor low intensity in the range of 10^{1} to 10^{9} pps and low energy beams from 200 keV in order to replace the standard low intensity beam profile witch used gas at 1 atmosphere and has a threshold energy of about 3 MeV by nucleon.

The impact between the beam and the foil will create secondary electrons. These electrons are guided by electric and magnetic field through a drift space.

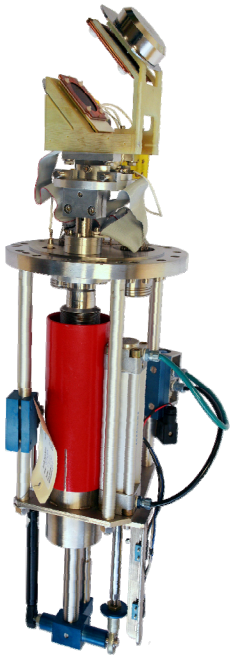


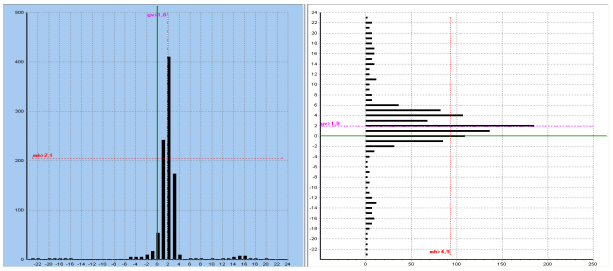
Figure 6 : EFM profiler.

Micro-channel plates will amplify the number of electrons in order to be collected on an X-Y grid. The desired resolution is 1mm in each dimension.

During a test with a $^{12}C^{2+}$ Beam at 5 Mev/u with 10^5 particles per second, the EFM Beam Profile has been compared with a standard gas monitor profile. Acquisition results are shown below.

Standard gas beam profile

Horizontal plane Vertical plane



EFM beam profile

Horizontal plane Vertical plane

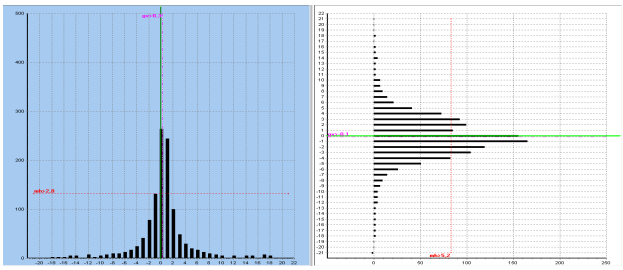


Figure 7 : Beam profile acquisition.

This detector is under redesigning in order to have an homogeneous magnetic field.

ASSOCIATED ELECTRONICS FOR ALL BEAM PROFILE MONITORS

These electronics digitize 94 channels in a parallel system. Each channel integrates the current of the associated wire or strip and performs a current-voltage conversion with two possibilities: passive system for high intensity beams and active system for low intensity beams and electronic deportation (about 20 m for the LINAC).
The front end (active or passive signal integration) is implanted on 12 daughter boards of 8 channels to streamline the maintenance and to keep the electronic modularity. For the digitalization, we have chosen a heavily parallel organization for a good A/D conversion speed (about 4 µs) and a best signal shape conservation. Acquisition of this digital data and their treatments is done by a FPGA (ALTERA Cyclone 3). All the automatisms related to the sensor (high voltages, insertion, Micro-channels plates protection, front end protection) are managed by a microcontroller (FREESCALE 68HCS12). Communication with the command/control (Modbus protocol over TCP/IP) and global equipment setup (integrated WEB server) are managed by a microprocessor (FREESCALE coldfire 5282) executing RTOS. A first prototype of this electronic system (without control of automatisms) was successfully tested in 2008. A pilot series with all facilities will be developed in 2009. The series of 20 electronics for LBE and LME will have to be ready for the end of 2010.

ACQUSITION AND DATA DISPLAY SOFTWARE

Current acquisition and data display software have been modified for the preliminary test with the SPIRAL2 ions source (LPSC, Grenoble) and the new profile monitors. Software provides data display and calculations (Gravity, FWMH) for both normal and variable wires grid monitors. Communication with hardware (TCP/IP Modbus) have been improved to add special controls provided by new profile monitor electronic design (beam over range securities, high supplies, acquisition etc.). All current data storage features and tools (ProfilerDisplay) remain available.

CONCLUSION

The development of these three different kinds of beam profile will permit to cover all the dynamic of the SPIRAL 2 energy and intensity beam. Last test are now in progress to perform RGM and EFM profile solution before fabrication. The first series of the SEM are now installed on the ion source LBE line and will soon be tested under high intensity beam.

REFERENCES

[1] R. Anne et al., A non interceptive heavy ion beam profile monitor on residual gas ionisation, NIM, A329 (1993) 21-28.

[2] R. Anne et al., Beam profile and beam time structure monitors for the extracted beams from the Ganil cyclotrons, 15th International Conference and their application. Caen France 14 – 19 June 1998.

DESIGN OF A NOZZLE-SKIMMER SYSTEM FOR A LOW PERTURBATION IONIZATION BEAM PROFILE MONITOR*

M. Putignano†, C. P. Welsch, Cockcroft Institute and University of Liverpool, UK
K.-U. Kuehnel, Max Planck Institute for Nuclear Physics, Heidelberg, Germany

Abstract

Growing interest in the development of low energy projectiles, in particular heavy ions and antiprotons, calls for new beam instrumentation to be developed to match the strict requirements on ultra-high vacuum and low beam perturbation. When it comes to transverse profile monitoring, a convenient solution for simultaneous determination of both transverse profiles is found in a neutral supersonic gas-jet target shaped into a thin curtain and the two-dimensional imaging of the gas ions created by impacting projectiles. The resolution and vacuum efficiency of this monitor is directly linked to the characteristics of the gas-jet curtain.

In this contribution we describe the design of a nozzle-skimmer system to be used for the creation of the jet curtain in the first prototype of such monitor, together with the geometry and extraction field shape of the experimental chamber which will house the experiment. Using numerical fluid dynamics simulations, we present the effects resulting directly from changes in the geometry of the nozzle-skimmer system on the characteristics of the jet curtain.

INTRODUCTION

Low-energy physics and storage rings are recently attracting growing interest in the scientific community, as remarkable characteristics of quantum systems are most conveniently studied at low projectiles energies in the keV range [1,2].

Development of low-energy storage rings causes widespread beam diagnostic technologies to become obsolete. In particular preservation of the beam lifetime causes perturbing profile monitoring, like e.g. interceptive foils, to be ruled out [3]. Furthermore, existing non-perturbing techniques such as residual gas monitors can take up to about 100 ms [4] to make meaningful measurements, due to the low residual gas pressure, at the expected operating pressure of around 10^{-11} mbar.

A possible solution around these limitations is constituted by a neutral supersonic gas jet target shaped into a thin curtain and bi-dimensional imaging of the gas ions created by impact with the projectiles. Such monitor, as compared to those based on residual gas, allows injection of additional gas, in order to increase the ionization rate, together with efficient evacuation to keep the required vacuum level elsewhere in the storage ring, due to the high directionality of the supersonic jet [5]; furthermore, it allows simultaneous determination of both transversal profiles and even beam imaging.

Crucial to such monitor is the control of the gas-jet in terms of achieved density and directionality. In the following section we present the results of numerical simulations which show that the geometry of the nozzle-skimmer system has a dramatic impact on the final result, and hence plays a central role in the optimization process. We then describe the nozzle skimmer system, the chamber which has been designed to house the experimental validation, the extraction field for the curtain probing experiment, and finally draw our conclusions.

NUMERICAL SIMULATIONS

The most common technique for the creation of a supersonic curtain-shaped gas jet involves the creation of an axis-symmetric jet of great intensity and the subsequent reshaping via collimators, after supersonic speed is attained [6]. Nevertheless, this approach results in several difficulties, amongst which the need of a large setup, which is needed for the gas jet to expand to the desired dimension; the use of large focusing magnetic fields to be coupled to the magnetic moment of the gas molecules, generally O_2; and the use of large quantities of gas, since most gas is collimated out, which results in large stagnation pressure needed at the source. We performed preliminary simulations, showing that it is possible to achieve a curtain-shaped jet by means of a suitable nozzle-skimmer system already at the gas source, if a rectangular slit nozzle and a skimmer shaped as a hollow trapezoidal prism is used in a suitable geometry, instead of the circular nozzle used in common applications.

To show the importance of the geometry of the nozzle-skimmer system for the curtain characteristics, we run several set of simulations, varying 5 geometric parameters, which we will refer from now on as variables, while monitoring 3 relevant observables, as described below.

The variables are: the skimmer aperture angles in the direction parallel (α), and perpendicular (β) to the curtain expansion, the width of the skimmer slit (SW), the depth of the skimmer structure (SD) and the nozzle-skimmer distance (Dist). We observed the Mach Number downstream the skimmer (M), which gives an indication of the efficiency of the expansion and hence of the directionality of the jet, as well as the geometrical dimensions of the gas curtain: width and depth (W and D respectively), which directly affect the resolution of the monitor [5].

* Work supported by the EU under contract PITN-GA-2008-215080, by the Helmholtz Association of National Research Centers (HGF) under contract number VH-NG-328 and GSI Helmholtzzentrum für Schwerionenforschung GmbH.
†corresponding author: massimiliano.putignano@quasar-group.org

When analysing this system we are confronted with 5 variables, resulting in an exceedingly complex set of results, whose mathematical description needs a detailed treatment. In this paper, we will rather express our results in the form of qualitative behavioural trends of each observable as a function of each variable, obtained by varying that variable alone while leaving the others constant.

A trend is intended to be found when the form of the functional relationship between the observable and the variable under investigation is preserved in the simulations regardless of the actual values of the other variables. This way, we are able to draw a table, shown in Fig.1, which summarises the simulated behaviour of each observable (column entry) when the respective variable is increased (row entry).

We identify linear relationships (straight arrows), parabolic relationships (curved arrows), and more complex relationships (circles), where even the form of the functional relationship depends on the value of some secondary variables (indicated inside the circle), and hence, according to our previous definition, a trend is not found.

This last is a qualitatively different behaviour as compared to the first two cases, where the shape of the trend does not depend on the remaining variables, while still the details of the trend, such as the gradient for the linear relationships, will depend on the values of the remaining variables.

In the table the bold orange lines represent the very clear trends, defined as those trends where the average over all points of the best fit Pearson value lies above 90%, while the slim, black lines represents less evident trends, where the average best fit Pearson value lies between 75% and 90%.

	Mach N.	D	W
α	↘	↘	↗
β	↘	⌒↗	→
SW	↘	↘	↗
SD	α	⌒↗	⌒↘
Dist	⌒↘	α, β	α, β

Figure 1: Table of simulated trends.

This table gives an indication of how sensitive the gas jet is to the geometry of the nozzle-skimmer system, hence providing strong evidence in favour of the need of a detailed study for the goal of proper optimization. Furthermore, it also gives an insight as to which variables have a stronger impact on the performance of the jet in termes of directionality (namely α, β and Dist) and curtain width to depth ratio (α and SW).

CHAMBER DESIGN

In order to test the optimization of the jet curtain, it is necessary for the apparatus to fulfil two crucial requirements. First, it should include a nozzle-skimmer system whose geometry can be readily modified and secondly it should include a monitoring system able to deliver the density map of the jet curtain. The density of the curtain is indeed the crucial parameter for the operation of the profile monitor, as the reaction rate and hence the sensitivity will scale with it. In this section we present these two sub-systems.

Nozzle-Skimmer System

The skimmers' holding system, shown in Fig.2, has been designed to grant maximum flexibility. It can accommodate up to two skimmers, which can be fine aligned both angularly (with a 5 degrees range) and longitudinally (within 20 mm). The longitudinal adjustability is obtained by welding the smallest plate (violet) on the end flange of an inner chamber ending with an adjustable bellow, which sits inside the main chamber, welded in turn to the larger plate (green). Such 'nested' chamber design also allows to keep the two skimmers very close to each other and still perform differential pumping between them.

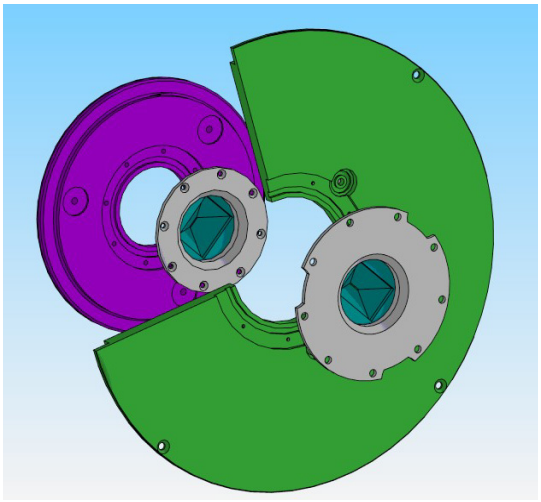


Figure 2: Skimmers holding system, exploded view.

The skimmer system is furthermore designed to allow removing both skimmer holders, detaching the skimmers, and glueing differently shaped skimmers back in place without demounting the whole chamber, hence also preserving its alignment.

An additional structural problem arises with the skimmers, as in order to preserve quasi-laminar flow downstream the expansion fan and hence allow the establishment of a stable supersonic jet, they need to be manufactured with walls thinner than 100 μm. Therefore, due to the large pressure difference across their walls caused by differential pumping, care must be taken to prevent them collapsing towards the low pressure region. Therefore, we chose not to design a variable geometry mechanism, rather manufacturing several skimmers of different geometries, spanning over 18 models 3 different values for α and β, and 2 different values for SW.

Curtain Monitoring

In order to probe the curtain and map its density, our apparatus will rely on electron impact ionization of the gas atoms. The gas ions produced will then be extracted by a 1 keV/m electric field and guided to an MCP stack for amplification, finally hitting a phosphor screen, whose emitted photons will be detected by a CCD camera. The current signal on the second MCP will then give a measure of the number of collected ions, while the CCD camera will show the spatial extension of the collected ions, i.e. the depth of the curtain in the point of interaction with the electron beam. Therefore, coupling this information with the measured spot size of the electron beam and the known electron impact ionization cross sections, the density of the curtain can be calculated.

Due to the relatively large area of gas-jet under investigation (4x4 cm), a ± 12.5mm XY manipulator is attached to the electron gun, so as to increase the spatial range provided by electrical deflection of the electron beam. The experimental chamber designed to this purpose is shown in Fig.3.

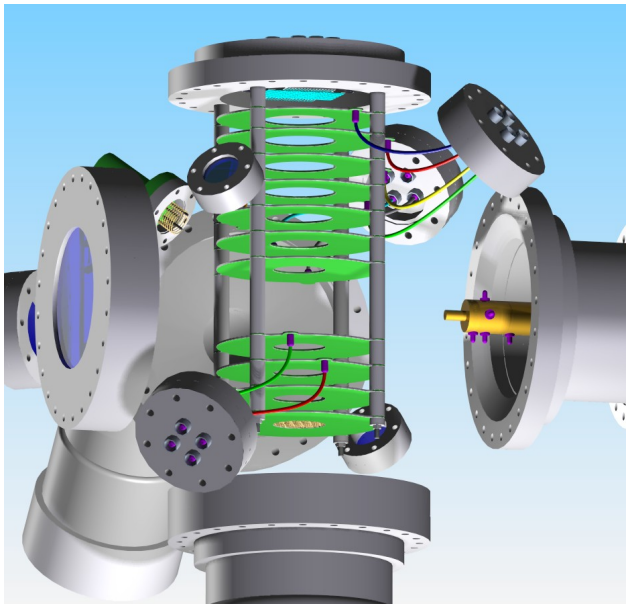


Figure 3: Experimental chamber and extraction system for the density mapping of the supersonic-jet curtain.

The spatial resolution of this mapping scheme depends mainly on the spot size of the scanning electron beam, which can be kept below 2 mm diameter.

On the other hand, the accuracy depends on the quality of the extraction field and on the current stability of the electron beam. The electron gun is tested to yield a beam stable within less than 1% of the nominal current when guided with a current feedback loop. The extraction field has been designed after having carried out extensive simulations with the SIMION 8.0 code. The simulations were intended to optimize the field in the central region of interest in the experiments, around the extraction electrodes axis; it is indeed in this region of interest that interaction between accelerated projectiles and the gas jet will take place in the final application for beam profile monitoring. Following the simulations, the voltages and geometry of the extracting field electrodes have been adjusted to yield the field shown in Fig. 4. This field is homogeneous within a 2.5% in the central region of interest of diameter 40 mm, where the curtain density measurements will lie.

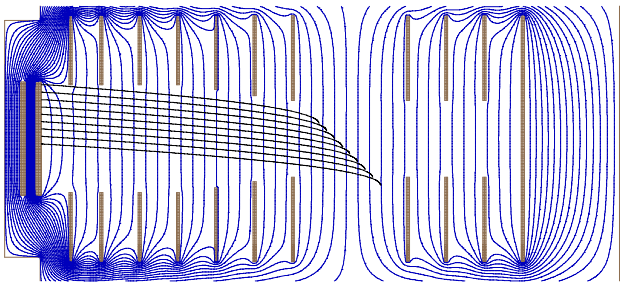


Figure 4: SIMION 8.0 simulated extraction field and tracking of the ions created on the curtain.

CONCLUSIONS

By means of numerical fluid dynamics simulations, it has been possible to highlight the importance of a nozzle-skimmer system geometry for the quality of a curtain-shaped gas-jet for use in a fast, nearly non-perturbing ionization beam profile monitor, suitable for operation at very low energy machines. It was also possible to pinpoint the most relevant observables and predict their behavioural trends when the geometric variables are changed. Finally, an experimental setup was designed to validate the numerical studies and characterize the supersonic gas-jet curtain.

REFERENCES

[1] C.P.Welsch *et al.*, "FLAIR – A facility for low-energy antiproton and ion research", Hyperf. Inter., 172, 71 (2006).

[2] L.H. Andersen *et al.*, "Physics with electrostatic rings and traps", J. Phys. B: At. Mol. Opt. Phys., 37, p. R57-R88 (2004).

[3] J. Harasimowicz, C.P. Welsch, "Beam instrument-ation for the future ultra-low energy electrostatic storage ring at FLAIR", LEAP08, Vienna, September 2008.

[4] T. Honma *et al.*, "Design and performance of a non-destructive beam-profile monitor utilizing charge-division method at HIMAC", Nucl. Instr. and Meth. A, 490 (3), p. 435-443 (2002).

[5] M. Putignano *et al.*, "A Fast, Low Perturbation Ionization Beam Profile Monitor Based on a Gas-jet Curtain for the Ultra Low Energy Storage Ring.", LEAP08, Vienna, September 2008.

[6] Y. Hashimoto *et al.*, "Oxygen gas-sheet beam profile monitor for the synchrotron and storage ring", Nucl. Instr. Meth. Phys. Res. A, 527 (3), 289-300 (2004).

EMITTANCE MEASUREMENT USING UNDULATOR RADIATION

F. Ewald, ESRF, Grenoble, France

Abstract

An additional electron beam emittance measurement that uses X-ray radiation from an undulator at the ESRF storage ring is now installed. The method consists in detecting the monochromatic spatial profile of the fifth harmonic of the undulator spectrum at 29.3 keV. The X-rays are converted to visible light using a scintillating screen which is then imaged to a CCD camera. The emittance value is deduced from the image size, the photon beam divergence, the source distance, and the lattice functions at the source point. The direct use of undulator radiation is advantageous in terms of the precise knowledge of the source position and lattice parameters in the straight section. For this reason this device will find its main application as a horizontal emittance monitor with improved absolute precision compared to that of the pinhole cameras which are making use of bending magnet radiation.

MOTIVATION

The electron beam emittance at the ESRF is currently monitored through two different families of devices: Two pinhole cameras [1] and eight so-called In-Air-X-Ray (IAX) detectors [4]. Both kinds of devices use X-rays emitted from dipoles. While the pinhole cameras deliver both, horizontal and vertical emittance values, the IAX detectors allow for precise measurement of the vertical emittance only. Due to the strong gradient of the beta-function along a dipole and difficulties in the precise determination of the X-ray source point position, the beta-value involved in the emittance calculation from the pinhole cameras is prone to errors. In order to cross-check the results with a different method, an emittance measurement using undulator radiation has recently been set up. The advantage of this method, which will be described in detail in the next section, is the very precise knowledge of the lattice parameters in the center of the straight sections in a storage ring.

BACKGROUND

Assuming that the β-function is well known, we can determine the emittance ε from the electron beam size σ and β at a given point in the storage ring. In our case, the point in which we measure ε, is the center of a straight section, where we can ideally suppose β' and η' to be zero. In reality, however, this may not be true, even if, after all, the values will be small, and β' can be neglected without worries. The electron beam size σ and its divergence σ' are then given by

$$\sigma^2 = \varepsilon \cdot \beta + (\eta\delta)^2 \quad , \quad \sigma'^2 = \varepsilon/\beta + (\eta'\delta)^2 \qquad (1)$$

In an ideal storage ring, the dispersion in the vertical plane would be zero, especially in the straight sections. Since, in reality, this may not be the case, we keep the above relations for both, the horizontal and the vertical plane.

Since the parameters β, η, η' and the energy spread δ are a priori known, measuring the emittance is now reduced to the measurement of the electron beam size. This will be done non-intrusively using the X-ray radiation emitted by the electrons traveling through the magnetic field of an undulator. The X-rays emitted by the electrons are freely propagating towards the detector conserving the divergence σ' of the electron beam at the source point. The X-ray beam size on a screen positioned at a distance D downstream the undulator is then given by the convolution of the electron beam size and the angular distribution of electron trajectories, the finite natural divergence of undulator radiation (σ'_{u}), and an image broadening (σ_{opt}) of the optical system. We assume that we have to deal only with Gauß-distributions, such that the rms X-ray spot size measured on the screen can be expressed by:

$$\Sigma^2 = \sigma^2 + (\sigma' D)^2 + (\sigma'_{\mathrm{u}} D)^2 + \sigma^2_{\mathrm{opt}} \quad . \qquad (2)$$

Substituting σ and σ', as given above, allows to calculate ε from the measured beam size Σ:

$$\varepsilon = \frac{\Sigma^2 - (\eta\delta)^2 - (\eta'\delta)^2 \cdot D^2 - \sigma'^2_{\mathrm{u}} \cdot D^2 - \sigma^2_{\mathrm{opt}}}{\beta + \frac{D^2}{\beta}} \quad . \qquad (3)$$

Under the condition that the working point is located at the peak of an odd undulator harmonic, the natural photon beam divergence and the natural source size can be approximated by [3]:

$$\sigma'_{\mathrm{u}} = \sqrt{\frac{\lambda_X}{2L}} \quad , \quad \sigma_{\mathrm{u}} = \frac{\sqrt{2\lambda_X L}}{4\pi} \quad , \qquad (4)$$

with λ_X being the X-ray wavelength of the respective harmonic, and L the undulator length. The natural source size is of the order of 1 μm at about 30 keV, and therefore negligible in our measurements. The above approximation indicates that, in order to keep the photon divergence small, a high X-ray energy is favourable. In general it is desirable not to work at the peak of the harmonics, but at slightly higher energies, in order to minimise the photon divergence. Therefore, σ'_{u} was calculated using the exact expression for the spatial distribution of undulator radiation rather than using the above equation.

EXPERIMENT

On the basis of a previous experiment [2] the setup is implemented in the beamline ID30, the latter being shared

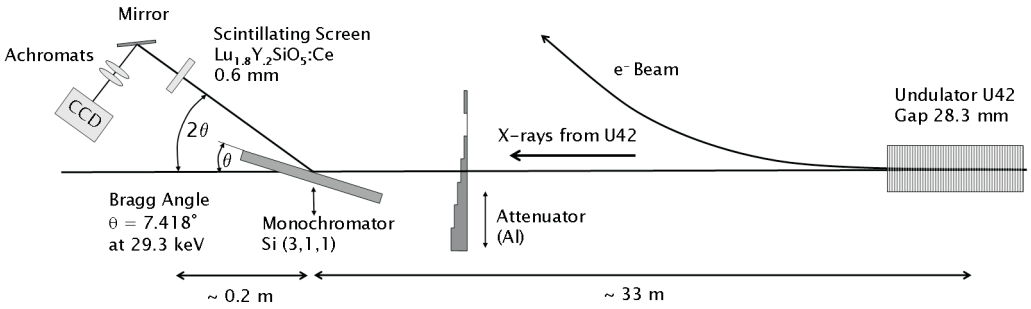


Figure 1: Sketch of the experimental setup seen from the top.

between different groups of the Accelerator and Source Division for testing and development of new equipment for the storage ring. The very compact emittance measurement setup (∼50×50 cm) will be permanently installed in this beamline. A sketch of the setup is shown in Fig. 1. In Tab. 1 the storage ring lattice parameters at the source point, the undulator parameters and the geometry of the setup are summarised. For the present measurements at ID30 we use an undulator with 42 mm period (U42). The undulator gap is set to 28.3 mm. At this value the energy of the 5th harmonic is sufficiently high to minimise the contribution of the natural divergence of undulator radiation. Furthermore, the harmonics are widely spaced such that the lower orders can easily be attenuated without affecting the 5th harmonic.

The radiation emitted from the U42 undulator is sent to a monochromator crystal which selects the desired energy. The monochromator is a 0.5 mm thick and 20 mm × 50 mm large single Si(3,1,1) crystal, mounted onto a motorised rotation stage allowing to scan the Bragg angle. The (3,1,1) crystal cut has been chosen in order to produce a reasonable horizontal footprint of the X-ray beam on the crystal surface of about 20 mm (rms) at a Bragg angle of 7.4°. This reduces the X-ray intensity on the surface, and thereby limits effects of lattice deformation due to local heating. A water cooled aluminium attenuator with variable thickness is placed in front of the monochromator in order to reduce the heatload on the crystal. The high energy radiation which is used in the measurement is mainly transmitted while the low energy radiation is absorbed. Without attenuation the radiation power incident on the monochromator crystal is about 30 W in 16-bunch mode at 90 mA electron beam current (measured with a calorimeter). 4 mm of Al have been introduced in order to reduce the power to roughly 2 W. In order to remove any residual heat, the monochromator crystal is mounted on a water cooled copper block, the thermal connection between the crystal and the copper being a highly heat conducting liquid InGa alloy. The energy calibration of the monochromator is done with the K-absorption edge of Sn, which is located at 29.2 keV. For the emittance measurement the energy is fixed at 29.3 keV which corresponds to the narrowest cone of the natural undulator radiation at the gap value of 28.3 keV. At this energy the natural photon divergence of the undulator radiation is $\sigma'_{\rm u} \approx 3\ \mu$rad. The X-ray energy can be selected with a precision of $\sim 0.01\%$.

Finally, the monochromatic X-ray beam is converted into visible light by a 0.5 mm thick and 15 mm large Cerium doped scintillator crystal $Lu_{1.8}Y_{0.2}SiO_5$:Ce ('Prelude' St. Gobain). A set of achromats is used to image the scintillator onto a digital CCD camera. To avoid radiation damage on both, the lenses and the camera, they are protected with lead and observe the scintillating screen via a mirror. The total blurring induced by the imaging optics is $\sigma_{\rm opt} \approx 20\ \mu$m.

Table 1: Lattice and Undulator Parameters : $\lambda_{\rm u}$...undulator period, L...undulator length, K...undulator K-value at 28.3 mm gap, D...distance to source, E...X-ray energy

Lattice:		**Undulator:**	
$\beta_{\rm x}$	37.6988 m	$\lambda_{\rm u}$	42 mm
$\beta_{\rm z}$	2.9496 m	L	1.62 m
η	0.1343 m	K	0.895
η'	0	D	33 m
δ	0.106 %	E	29.3 keV

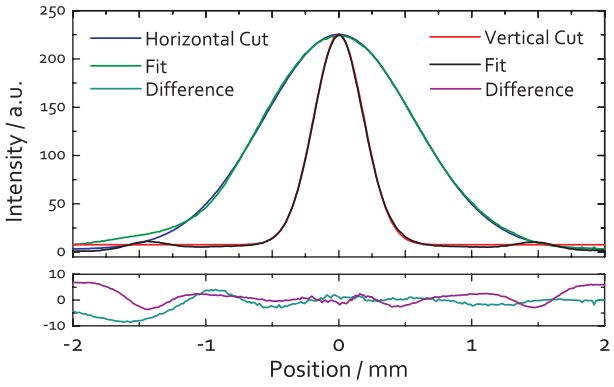


Figure 2: Horizontal and vertical cut through the measured beam profile, the lineouts of the fitted 2-dimensional Gaußian, and their differences.

The images are fitted with a Gaussian intensity profile, from which the rms beam size Σ is extracted. The fit is done on only a small region of the profile of about $1.5 \times \Sigma$. This reduces influences of the background and contributions to the wings of the beam profile which are not coming from the 5th, but higher harmonics. Additionally, the time needed for the fit is strongly reduced if the area is kept small. Therefore the acquisition rate of the system is a few seconds. Fig. 2 illustrates the good agreement between the measured beam profile and the fit.

RESULTS

The emittance value from ID30 is calculated from the measured rms beam sizes on the scintillating screen using Eq. 3. The horizontal and vertical emittances measured in 16-bunch filling at about 70 mA are $\varepsilon_x = 3.9$ nm and $\varepsilon_z = 60$ nm. Tab. 2 compares these values with the other emittance monitoring devices: the pinhole cameras ID25 and D9, and one of the IAX detectors C14. The differences of up to 10% of the vertical emittance values can be explained with the variation of the vertical β-function with respect to the model β due to the coupling around the storage ring. The horizontal emittances measured with ID30 and D9 compare well, while the ID25 value differs considerably.

Table 2: Measured Emittance Values from Undulator Radiation (ID30), the Pinhole Cameras ID25 and D9, and the IAX Detector C14

	ID30	SRW	ID25	D9	C14
horizontal ε_x [nm]	3.9	4.1	6.3	4.1	–
vertical ε_z [pm]	60	55	47	43	53

In order to evaluate the absolute emittance value, the beam size at the position of the scintillating screen was calculated with SRW ('Synchrotron Radiation Workshop' [5]) for different horizontal emittance values and plotted in Fig. 3. To the measured beam size of 540 μm on the screen (corrected for optical blurring), corresponds a calculated emittance value of 4.1 nm. The same calculation is done for different vertical emittance values, keeping the horizontal emittance at 4 nm. The measured beam size of 176 μm corresponds to a vertical emittance of 55 pm. The comparison of the measured emittance values with the calculation clearly shows that the measurements of ID30 and D9 yield the right order of magnitude. The significantly higher horizontal emittance value measured by the pinhole camera ID25 can therefore be doubted, and is most likely due to the uncertainty in the determination of the source distance and horizontal beta value.

As shown in detail in Tab. 3, the uncertainty of the emittance measurement in ID30 is about 2% only in the horizontal plane, but ∼13% in the vertical plane. The latter being mainly due to the high uncertainty of the photon divergence. Therefore, the undulator radiation is at the moment not adapted to exploit the very small emittances of less than 20 pm reached in multi-bunch filling modes. The horizontal emittance measurement, however, is very precise and benefits from the well known lattice parameters in the straight section. The undulator radiation can therefore be used to complement the pinhole camera measurements.

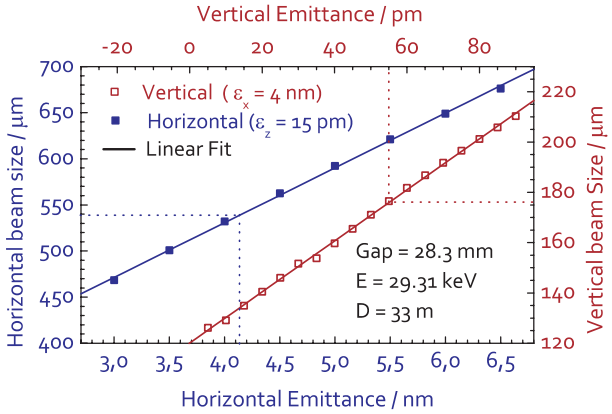


Figure 3: Horizontal and vertical rms beam sizes calculated with SRW for different emittance values.

Table 3: Uncertainties of the Parameters Used to Calculate the Emittance at ID30, and their Influence on the Final Result

	horizontal	**vertical**
3% precision of β_x and β_z	0.5 %	3 %
3% for η_x	0.4 %	–
2% for δ	0.2 %	–
10% uncertainty for σ'_u	0.8 %	9 %
0.2% uncertainty of D	0.15 %	0.5 %
10% image blurring σ_{opt}	< 0.1 %	0.3 %
Total	~ 2 %	~ 13 %

REFERENCES

[1] P. Elleaume, C. Fortgang, C. Penel and E. Tarazona, "Measuring Beam Sizes and Ultra-Small Electron Emittances Using an X-ray Pinhole Camera", Journal of Synchrotron Radiation 2, p. 209 (1995).

[2] E. Tarazona and P. Elleaume, "Emittance measurements at the ESRF", Review of Scientific Instruments 66, p. 1974 (1995).

[3] Kim, "Characterstics of Synchrotron Radiation", Technical Note, Lawrence Berkeley Laboratory (1989).

[4] B. K. Scheidt, "Measurement of vertical emittance with a system of six In-Air-X-Ray projection monitors at the ESRF", DIPAC'07, p. 72.

[5] O. Chubar and P. Elleaume, "Accurate And Efficient Computation Of Synchrotron Radiation In The Near Field Region", EPAC'98, June 1998, p. 1177.

BEAM PROFILE MONITORING AT COSY VIA LIGHT EMITTED BY RESIDUAL GAS*

C. Böhme†, T. Weis, Technical University of Dortmund, Germany
J. Dietrich, V. Kamerdzhiev, Forschungszentrum Jülich, Germany
J.L. Conradie, iThemba LABS, South Africa

Abstract

Scintillation is one of the outcomes of beam interaction with residual gas. This process is utilized for non-destructive beam profile monitoring. Test bench measurements at various gas compositions and pressures have been performed, as well as measurements at the 3.14 MeV cyclotron beam line at iThemba LABS as well as ones with the circulating proton beam at COSY-Juelich. The test bench measurements have been mainly done using a single large photocathode photomultiplier to estimate the photon yield. A multichannel photomultiplier was used along with a lens system to monitor the ion beam profile at iThemba LABS. Experimental results are presented and the challenges of the approach are discussed.

INTRODUCTION

The knowledge of the beam position and profile is essential for the successful operation of an accelerator facility. At hadron accelerators the high beam current limits the use of traditional intersecting methods like wire scanners or secondary electron emission (SEM) grids, because the used materials are heated or melted trough the beam energy. At synchrotrons non destructive methods are preferred to monitor the circulating beam. Several kinds of diagnostic devices, using the products of the interaction between the ion beam and the residual gas, are under development or in use. Usually the devices register the ions and/or electrons produced in collisions of the beam particles with the residual gas. Some attempts have already been made which use the emitted light of the excited residual gas atoms in order to monitor the beam [1]. This method of registering photons has the advantage of being insensitive to electric or magnetic fields. Also the spatial and time resolution is considerably higher, allowing a single pulse measurement. The limitation of this method is the cross section of light emission, which is about three orders of magnitude lower compared to ionization. Nevertheless, a wide range of applications can still be covered with this method.

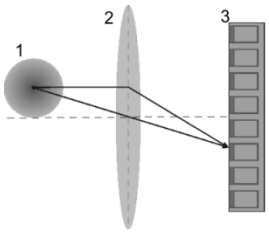


Figure 1: Measurement principle (not to scale): The light from the beam (1) is focused with a glass lens (2) onto the multichannel photomultiplier (3).

MEASUREMENT TECHNIQUE

The light emitted by the residual gas is focused by a glass lens onto a position sensitive multichannel photo-multiplier (PMT) array, as shown in Figure 1. A Hamamatsu PMT (7260-type, 32 channels, 0.7·10 mm photocathode size, 1mm pitch size) was used for the position sensitive measurements. Along with that, a Philips XP2020 single channel PMT (44mm round photocathode) was used for basic research, mainly without an optical lens system in order to have a large aperture angle for the registration of photons. Depending on the amount of photons registered the readout of the PMT was adapted. For low intensities a discriminator was used together with a counter, in order to count the number of events. For high intensities a direct current measurement was performed using a 48 multichannel current digitizer, developed at iThemba LABS.

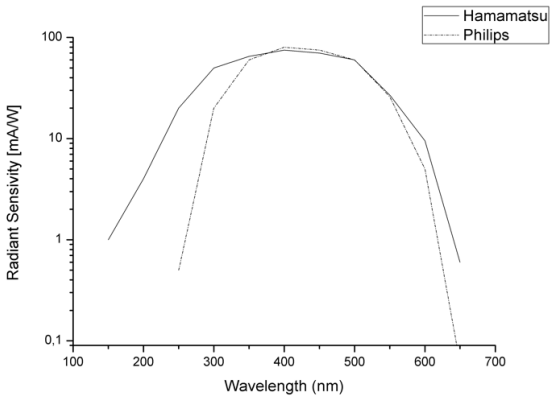


Figure 2: Luminous characteristics of the Photomultipliers used.

PHOTON YIELD

While measuring the beam profile using photons emitted by the residual gas the only controllable parameters of

* Work supported by BMBF and NRF, Project code SUA 06/003
† c.boehme@fz-juelich.de

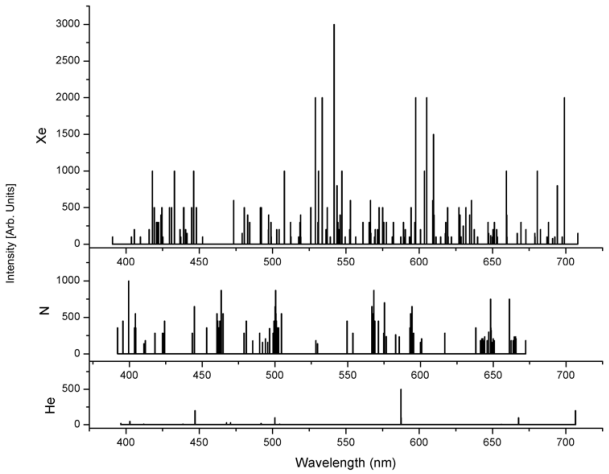


Figure 3: Expected wavelength distribution within the visible range of the investigated gases [3].

the photon yield are the composition and pressure of the residual gas at a given ion beam parameters. Along with the residual gas, one possibility is to intentionally increase the gas pressure in order to increase the photon yield. Although the increase of residual gas pressure is normally not applicable in accelerators and especially within synchrotrons, as the beam passes the region of high pressure many times possibly resulting in emittance increase, it has been successfully tested [2]. While the residual gas mixture is given, the gas to be added can be chosen within certain limits. Two gases are candidates for addition, N_2 and Xe. These gases are used, because both show strong light emission within the visible range (see figure 3) and are also easily pumped out of the vacuum system by the pumps.

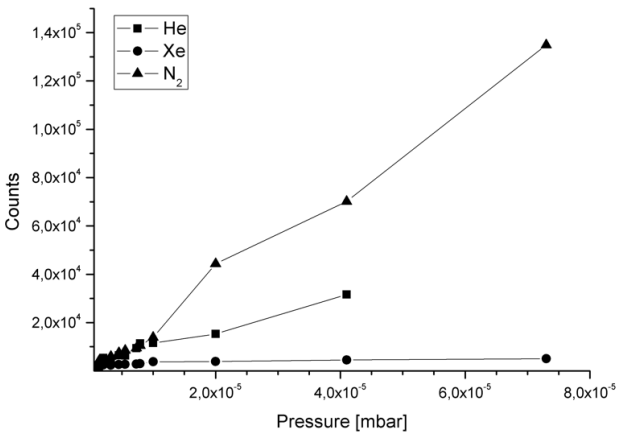


Figure 4: Photon yield for different gas pressures for He (•), N_2 (▲) and Xe (■) at 12keV He ion beam.

Test Bench Measurements

In order to test and enhance the measurement setup before installing it in the synchrotron, a test bench was used. Here the pressure can be varied between about $5 \cdot 10^{-7}$ and $1 \cdot 10^{-4}$ mbar. The test bench is equipped with an ion source which can generate Helium ions up to 20 keV. The experiments have been performed in a special chamber which has been darkened inside to minimize reflections. Upstream the PMT setup a emittance measuring device is installed. This can be used to determine the beam characteristics.

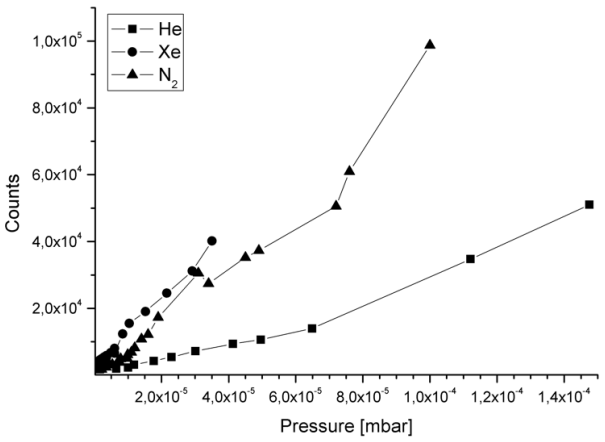


Figure 5: Photon yield for different gas pressures for He (•), N_2 (▲) and Xe (■) at 6keV He ion beam.

With this setup the light production rate with the described gases has been tested at several pressures and for different ion energies. The light emission of helium was also measured, for reference purposes, as helium, which is used in the ion source of the facility, causes a background. The results are shown at Figure 4 and Figure 5. The photon yield shows a linear dependence on gas pressure. Since the cross sections for excitation of the measured gases with protons and Helium ions show different behavior [4], these measurements cannot be transferred directly to experiments within COSY.

Profile Measurements in the Cyclotron Beamline at Low Energies

Measurements were performed at the iThemba LABS cyclotron beamline with a 3.14 MeV proton beam at a residual gas pressure of 10^{-5} mbar and about 300 μA beam current [6]. The Hamamatsu multichannel PMT was connected to the multichannel current digitizer, allowing to take data from all channels simultaniously. The beam position is measured for reference by two BPMs, placed upstream and downstream of the PMT. The beam was deflected with a steering magnet to verify if the position change reported by the BPMs agrees with the PMT measurement. In Figure 6 the measured data is shown together with a Gaussian fit for each measurement. The results of the PMT measurement are in good agreement with the BPM measurement.

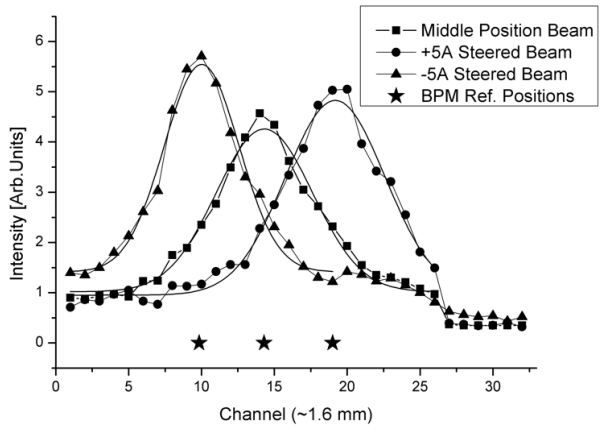


Figure 6: Profile measurements for a 3.14 MeV proton beam shifted with a steerer. The BPMs middle position is adjusted to fit the PMTs one. The channels on the right side are darkened for background measurement.

Measurements in a Synchrotron

To evaluate whether the method is practical for usage in a synchrotron, the multichannel PMT has been installed at COSY Juelich. First measurements have already been reported in [5]. Further measurements had been planned to take place in the proximity to an internal experiment using a gas target. Unfortunately, these measurements could not be completed, because of a strong light background of which the source could not be localized.

CONCLUSIONS

The presented method of monitoring beam profiles with residual gas scintillation seems to be promising. The method has been successfully used at different setups, e.g. the iTemba LABS cyclotron beamline, the JESSICA experiment at COSY Juelich in preparation of the ESS, and also first measurements at the COSY synchrotron have been made, although the original goal of single turn measurements in a synchrotron has not been achieved yet. During the tests the instrumentation was improved, with the current digitizer developed at iThemba labs the readout of the 32 channels is easily possible, even at low light conditions where usually photon counting methods, discriminators combined with counters, would be used. For testing and improving the instrumentation the dedicated test bench has proven to be very useful. One of the next steps is the use of cylindrical lenses to make use of a larger solid angle of the beam. Another possibility would be to generate a fast local pressure bump, which will be tested at COSY Juelich in near future.

ACKNOWLEDGEMENTS

We would like to thank Prof. Dr. A. Schempp and Dr. O. Meusel of the University of Frankfurt am Main, Germany, for providing the ion source used at the test bench described. We also like to thank the operators at the iThemba LABS and H. Pütz at COSY-Juelich for supporting our experiments.

REFERENCES

[1] M.A. Plum et al., Nucl. Instr. Meth. A492 (2002), p.74.

[2] P. Forck et al., Profile Monitors based on residual gas interaction, Proceedings of DIPAC 2005, 223

[3] Spectra of neutral and singly ionized elements from the Astronomical Data Center (ADC) catalog A6016, by Reader J., Corliss Ch.H.: 1981, 'Line Spectra of the Elements', CRC Handbook of Chemistry and Physics; NSRDS-NBS 68

[4] Jaecks, D. et al., Excitation of Ne, Ar, Kr and Xe by He^+ Impact, Physica 36 (1967), 606

[5] J. Dietrich et al, Beam Profile Measurements Based on Light Radiation of Atoms Excited by the Particle Beam. Proceedings of PAC07, 3955

[6] J. Dietrich et al. Non-destructive Beam Position and Profile Measurements Using Light Emitted by Residual Gas in a Cyclotron Beam Line, Proceedings of EPAC08, 1095

FAST AND HIGH ACCURACY WIRE SCANNER

M. Koujili, CERN, Geneva, Switzerland and SeT-UTBM, Belfort, France
B. Dehning, J. Koopman, D. Ramos, M. Sapinski, J. De Freitas, CERN, Geneva, Switzerland
Y. Ait Amira, FemtoST-UFC, Besançon, France
A. Djerdir, SeT-UTBM, Belfort, France

Abstract

Scanning of a high intensity particle beam imposes challenging requirements on a Wire Scanner system. It is expected to reach a scanning speed of 20 m.s^{-1} with a position accuracy of the order of 1 μm. In addition a timing accuracy better than 1 ms is needed. The adopted solution consists of a fork holding a wire rotating by a maximum of 200 $^\circ$. Fork, rotor and angular position sensor are mounted on the same axis and located in a chamber connected to the beam vacuum. The requirements imply the design of a system with extremely low vibration, vacuum compatibility, radiation and temperature tolerance. The adopted solution consists of a rotary brushless synchronous motor with the permanent magnet rotor installed inside of the vacuum chamber and the stator installed outside. The accurate position sensor will be mounted on the rotary shaft inside of the vacuum chamber, has to resist a bake-out temperature of 200 $^\circ$C and ionizing radiation up to a dozen of kGy/year. A digital feedback controller allows maximum flexibility for the loop parameters and feeds the 3 phases input for the linear power driver. The paper presents a detailed discussion of the selected concept and selected components.

INTRODUCTION

Wire scanners are installed and operated on a daily basis on all circular accelerators of CERN. However, they present some drawbacks:

- For high intensity beams the energy deposited by the incident particles on the wire may be sufficient to break the wire [1].
- The wire can also be destroyed due to the energy transferred by the beam to the wire through its accompanying electromagnetic field [2].
- Inaccuracy of position measurement primarily due to vibrations of the mechanics and the wire.
- Vacuum leakage in the bellows due to wear.

To improve the optimization of the luminosity in the Large Hadron Collider (LHC), much higher measurement accuracies than those currently achievable are required. The new performance demands include a wire travelling speed of up to 20 m.s^{-1} and a position measurement accuracy of the order of 1 μm, in addition to a timing accuracy better than 1 ms. This implies the design of a system with extremely little vibration and electro-magnetic interference. Other requirements related to interface and environment issues such as radiation, temperature, vacuum and interactions with the beam must also be accounted for.

The baseline solution (Fig. 1) consists of a small diameter rotary brushless synchronous motor with the rotor's magnetic field provided by permanent magnets, installed inside the vacuum chamber. This rotor is supported on a shaft by roller bearings with materials and solid lubricants to be selected for low outgassing and friction characteristics in vacuum environment. Attached to the same shaft is a fork on which the wire is stretched. In order to minimise the outgassing from the motor, the stator windings which excite the rotor are placed outside the vacuum chamber. The air-vacuum interface is made in the magnetic gap through a low magnetic permeability stainless steel wall. A position transducer to be mounted on the rotating shaft shall provide its absolute angular position for the feedback control loop of the motor and also a highly repeatable relative position during the scan.

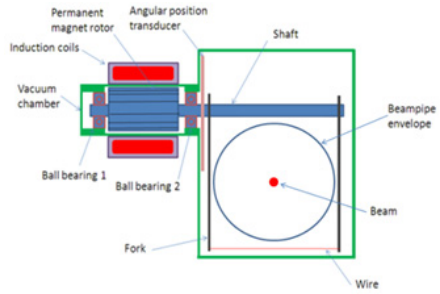


Figure 1: Simplified drawing of the future wire scanner. The green lines enclose the vacuum area.

In this paper, the motor requirements are defined first starting from the wire scanner specifications. Thus, the motor and its power supply are chosen with regard to the constraints obtained in terms of the needed torque, speed, and acceleration. After a brief description of the motor model some simulations achieved on the base of the physical parameters given by the manufacturer are included and commented based on the specifications.

WIRE SCANNER SPECIFICATIONS AND MOTOR CHOICE

In this section, the different requirements to be met by the wire scanner device are listed and used to choose the

motor ensuring the drive function. For the first prototype, a frameless brushless synchronous motor has been chosen taking into account the requirements in terms of dynamics and environmental constraints.

Dynamic Requirements

The driver shaft will have a reciprocating movement of a stroke of $\theta_{max} = 180^\circ$, which will comprise an optimised curve of acceleration and deceleration which will allow reducing the vibration. In order to estimate the required acceleration, the following assumptions are made. The acceleration will be done over 90 $^\circ$ up to a peak velocity of $\Omega_{max} = 200$ rad.s^{-1}(linear speed of $V = 20$ m.s^{-1} with a fork length of 10 cm) and the deceleration to a stop over the remaining 90 $^\circ$ stroke (Fig. 2).

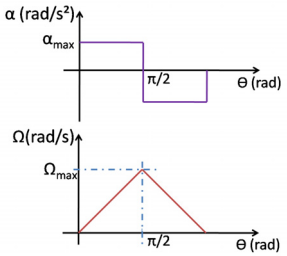


Figure 2: Theoretical angular acceleration (top) and angular speed (bottom) profile of the system.

To reach the peak velocity (200 rad.s^{-1}) in 90 $^\circ$ the motor must provide an angular acceleration α of:

$$\alpha = \frac{1}{2}\frac{\Omega^2}{\theta} = 12755 \text{ rad.s}^{-1}$$

Environmental Constraint Requirements

The rotor materials must have, after bake-out, a total outgassing not exceeding 10^{-9} Pa.m^3.s^{-1}. The permanent magnets on the rotor must have a thermal demagnetizing largely superior to bake-out temperature (200 $^\circ$C). The whole motor must be resistive to a cumulated ionizing radiation dose of 20 kGy (roughly 1kGy/year).

Geometrical Requirements

The motor air gap must be sufficiently thick to allow introducing a low magnetic permeability stainless steel wall.

Motor Choice

The chosen motor for the prototype is a Parker K500-150-5Y frameless synchronous machine proposed in two independent parts: a three phase stator and a permanent magnet rotor with six pairs of poles.

The maximum torque provided at 200 rad.s^{-1} ($T_{max@200rad/s}$) is determined from the datasheet of the manufacturer. The relationship between the maximum torque at 200 $rad.s^{-1}$ ($T_{max@200rad/s}$) and the acceleration provided by the motor (α_{max}) is

$$\alpha_{max} = \frac{T_{max@200rad/s}}{J_r + J_s + J_f}$$

where J_r, J_s, J_f are the inertia constants of the rotor, the sensor moving part and the fork, respectively. This motor can provide more than 2.5 times the acceleration needed for the wire scanner [3]. The rotor lamination is made of standard steel which will be made vacuum compatible. Samarium cobalt alloy has been chosen as adequate magnetic material for the rotor instead of neodymium which is less resistive to temperature. The foreseen glue based fixation of the magnets on the rotor will be replaced by a mechanical solution. The air gap between the rotor and the stator is comprised between 0.7 and 0.85 mm which is large enough to introduce the vacuum chamber barrier [4]. The chamber tightness and its eddy current effect will be tested with the first prototype.

Linear Power Supply

As the wire scanners will be mounted in EMI sensitive environment, the power supplies working on the principle of high frequency switching (PWM) must be avoided. A three-phase linear power supply is currently under design. From simulation (Fig. 4), the maximum current needed by the motor (I_{max}) is 80 A.

The maximum needed voltage is the sum of the maximum back-EMF and the maximum voltage drop across the phase resistor and the synchronous inductor. From simulations, the maximum peak to peak voltage is 120 V.

Starting from the specifications above, the MOSFET power amplifier “PA52 by Apex” has been chosen. It can provide an output voltage of 200 V and a peak current of 80 A with a gain bandwidth product of 3 MHz.

Angular Sensor

The transducer must provide information on the angular position of the shaft for two independent functions with different requirements: an absolute position readout for the motor control with an accuracy of 30 arc minutes (8.7 mrad) r.m.s and a relative position measurement for determination of the wire trajectory with an accuracy of about 5 arc seconds (25 μrad) r.m.s. The signal processing may be performed offline.

The use of an analog position sensor with capacitive coupling between its fixed and moving elements to measure the angular position with high accuracy, resolution and repeatability is under consideration.

As this sensor consists of two printed flat plates (free of electronic components), almost any material can be used for the supporting plate and the conductive traces. This advantage allows making the sensor vacuum compatible and resistive to radiation and temperature.

SIMULATION STUDY

In order to test the validity of the chosen motor with regard to the wire scanner specifications, a simulation study has been achieved starting from the manufacturer characteristics. After the dynamic modelling of the motor, a servo control has been carried out under Matlab/Simulink software. The linear amplifier and angular sensor have been modelled through simple gains.

Dynamic Model of the Motor

The three-phase windings are balanced. As a result, the voltage equations of the three-phase stator windings can be expressed as:

$$v_{an} = i_a r_s + L_s \frac{di_a}{dt} + \lambda'_m.p.\Omega_r.cos(p.\theta_r)$$

$$v_{bn} = i_b r_s + L_s \frac{di_b}{dt} + \lambda'_m.p.\Omega_r.cos(p.\theta_r - \frac{2\pi}{3})$$

$$v_{cn} = i_c r_s + L_s \frac{di_c}{dt} + \lambda'_m.p.\Omega_r.cos(p.\theta_r + \frac{2\pi}{3})$$

where v_{an}, v_{bn}, v_{cn} and i_a, i_b, i_c are respectively the three-phase voltages and currents of the stator windings, r_s and L_s are their resistance and inductance, λ'_m is the maximum flux produced by each permanent magnet, p is the number of pairs of poles and Ω_r and θ_r are the rotor speed and position, respectively.

$$T_e(\theta_r, t) = -K_T \Big[sin(p.\theta_r).i_1(t) + sin(p.\theta_r - \frac{2\pi}{3}).i_2(t) + sin(p.\theta_r + \frac{2\pi}{3}).i3(t) \Big]$$

where K_T is the torque constant.
The motor speed can be expressed as

$$\frac{d\Omega_r}{dt} = \frac{1}{J_T}[T_e - B_m.\Omega_r]$$

where Ω_r is the rotor speed, J_T the total inertia on the shaft and B_m the viscous coefficient.

Simulation Results and Discussion

The following simulation parameters were used: $R_s = 0.245\,\Omega$, $L_s = 1,365$ mH, $K_E = 0.2598$ V.rad.s^{-1}, $p = 6$, $J = 5.8 \cdot 10^{-4}$ kg.m^2. Assuming sinusoidal voltage waveforms in function of the electric angle and by using two specific functions for the initial phase and magnitude of the sine, the following waveforms of angular speed and position have been obtained (Fig. 3). In Fig. 4, the corresponding three-phase voltages and currents are shown. It can clearly be seen that the speed reaches a peak of $\Omega_r = 200$ rad.s^{-1} in less than 90 °, oscillates around this value and decelerates to a stop. This behaviour fulfils the specifications of the wire scanner in terms of maximum values of speed and acceleration. However, there are oscillations which must be minimised in the final test bench by an adequate control strategy. This control must adapt the magnitudes and phases of the three voltage sources in order to optimise the angular speed waveform.

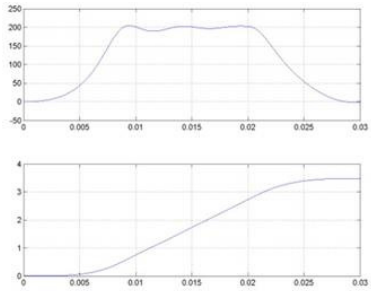


Figure 3: Simulated angular speed (top) and position (bottom) waveforms versus time in seconds.

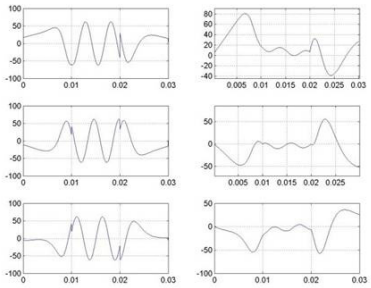


Figure 4: Simulated three phase voltage (left in volts) and current (right in amps) waveforms versus time in seconds.

CONCLUSION

On the basis of simulations one concludes that the prototype of the fast wire scanner actuator is now ready to be built in order to optimize the control and to test the functionalities of the device. A dSPACE® Controller Board will be used as the real-time interface in the bench prototyping. Thereby, the control strategy will be optimized regarding the vibration phenomena and disparities of the physical parameters such as the circuit resistors.

REFERENCES

[1] M. Sapinski, “Carbon Fibre Damage in Accelerator Beam”, these proceedings.

[2] M. Sapinski, T. Kroyer “Operational limits of the wire scanners on the LHC beams”, proceeding of Beam Instrumentation Workshop, May 2008.

[3] M. Koujili, “Study of synchronous frameless Parker motor (K500150-5Y)”, http://project-wire-scanner.web.cern.ch.

[4] D. Ramos, “Cylindrical shell with external pressure according to EN 13445-3:2002”, http://project-wire-scanner.web.cern.ch.

[5] J-P. Louis, E. Hoang, G. Feld, “Actionneurs courant continu et synchrone autopilot”.

BEAM TEST OF THE FAIR IPM PROTOTYPE IN COSY

C. Böhme, Technical University Dortmund, Germany
J. Dietrich, V. Kamerdzhiev#, FZJ, Jülich, Germany
P. Forck, T. Giacomini, GSI, Darmstadt, Germany
D. Liakin, ITEP, Moscow, Russia

Abstract

The advanced ionization beam profile monitor is being developed at GSI for the future FAIR facility in collaboration with ITEP and FZ-Jülich. In January 2009 the IPM prototype was installed in COSY-Jülich. After successful hardware test the beam tests followed. The prototype was operated without magnetic field, thus only residual gas ions were detected. An arrangement consisting of an MCP stack, a phosphor screen, and a CCD camera was used to detect ions. We report the first profile measurements of the proton beam up to 2.8 GeV at COSY.

INTRODUCTION

The Ionization Profile Monitor (IPM), currently under development at GSI, is intended to provide fast and reliable non destructive beam profile measurements at the future FAIR machines as well as the existing accelerators at GSI [1]. The ionisation products are guided to a position sensitive detector by transverse electric field. Two modes of operation are foreseen. Ion detection is used to obtain the profiles with high spatial resolution by means of a phosphor screen (PS) and a CCD camera [2]. Detection of electrons is required to allow for turn-by-turn profile measurements. This will be done by using a multichannel photomultiplier [3]. Collection of electrons makes the presence of a guiding magnetic field necessary in order to prevent the electrons from spreading out. The magnetic system is being designed in collaboration with iThemba LABS, South Africa.

THE IPM SETUP AT COSY

The IPM prototype was installed in COSY to study its performance and gain operational experience. It is not equipped with a magnet; hence only ion detection technique can be applied. An arrangement consisting of an MCP stack (100x48 mm^2), a P47 phosphor screen, and a 656×494 pixel CCD camera is used to detect ions. High voltage electrodes provide the electric field for ion extraction. The IPM prototype actually contains two identical units to provide simultaneous measurements in both, horizontal and vertical, planes. Figure 1 shows the design of the IPM prototype installed in the arc downstream of the cooler telescope.

The cameras are read out by a LabView server application running on a PXI based front end. The user interacts with the front end from the accelerator control room by means of a client program running on a PC. Both the server and client applications were developed by a private company according to the GSI specifications.

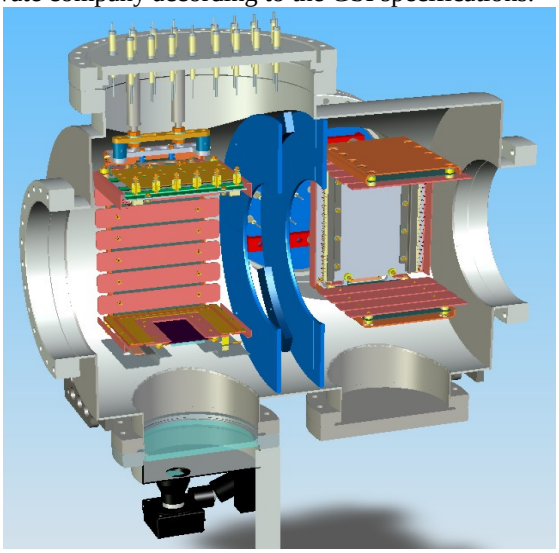


Figure 1: Mechanical design of the FAIR IPM prototype.

In order to be able to monitor and control the aging of the MCPs the monitor is equipped with UV lamps that are capable of homogeneously irradiating the whole MCP surface. This feature is used to correct the detector sensitivity inhomogeneity. Profiles of the polarized and unpolarized proton beams circulating in COSY were measured covering the full energy range of the machine.

BEAM PROFILE MEASUREMENTS

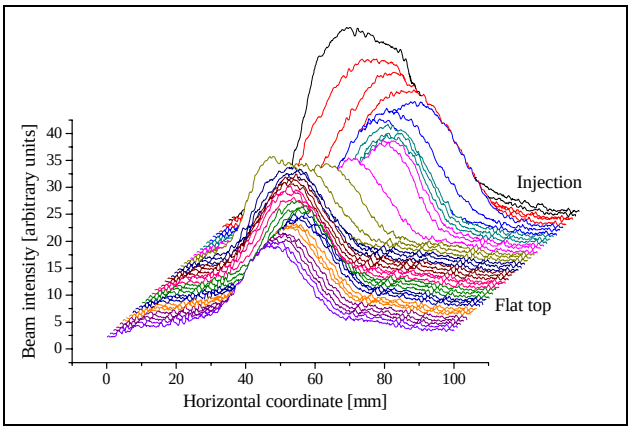


Figure 2: Evolution of the horizontal proton beam profile during injection and acceleration to 1.343 GeV/c. About $3 \cdot 10^9$ polarized protons reached flat top. Time span is 2 s. Corrected for spatial detector sensitivity distribution via UV calibration. 5 pts moving average smoothing was applied.

#v.kamerdzhiev@fz-juelich.de

The beam profile measurements were carried out at various proton beam energies. The ion extraction voltage was set to 4400 V, the MCP voltage to 1950 V and the MCP to PS voltage to 3800 V. The accelerator timing system was set up to trigger the IPM data acquisition before the proton injection occurred and stop it at the end of flat top. Figure 2 shows the fast evolution of the horizontal profile of the polarized proton beam during injection and acceleration to 1.343 GeV/c. The behaviour of the vertical profile is shown in Figure 3. One can clearly see particle losses in both planes. However, only horizontal beam motion is observed. The data was recorded at a rate of 20 profiles per second in each plane. ANKE internal target was on [4].

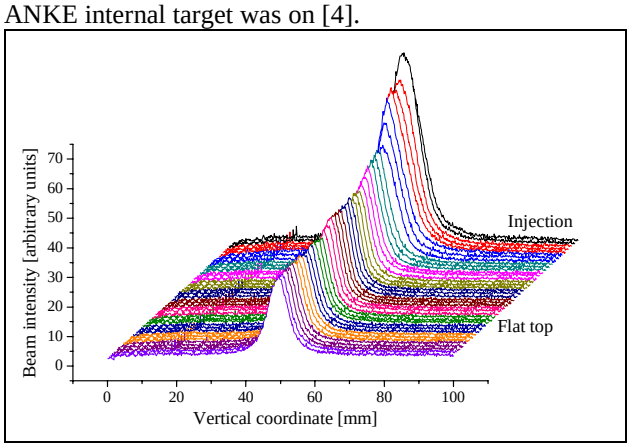


Figure 3: Evolution of the vertical proton beam profile during injection and acceleration to 1.343 GeV/c. About $3 \cdot 10^9$ polarized protons reached flat top. Time span is 2 s.

Figure 4 and Figure 5 show the slow evolution of the horizontal and vertical polarized proton beam profile at 1.343 GeV/c flat top. The beam quality degradation is due to the ANKE internal target which was estimated to be about $3 \cdot 10^{14}$ atoms/cm^2 thick at the time of measurement.

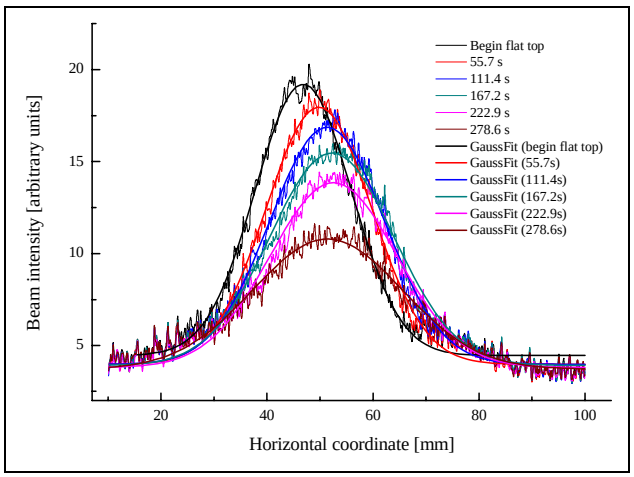


Figure 4: Horizontal profiles of the polarized proton beam at 1.343 GeV/c. The profile measurement started once the flat top was reached. COSY was operating in a 300 s cycle for ANKE experiment. Internal target on.

The acquired profiles agree well with the expected ones and are nicely fitted with a Gaussian, except for some tails in horizontal plane and peaks in the vertical plane (not shown in Figure 5 for readability reasons).

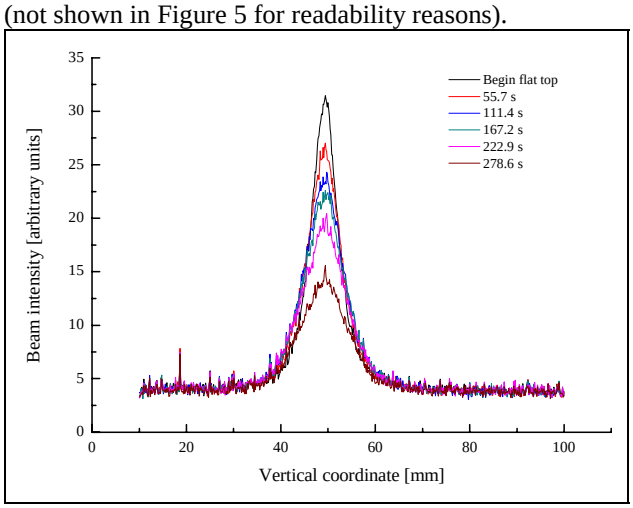


Figure 5: Vertical proton (polarized) beam profiles at 1.343 GeV/c flat top. Recorded during a 300 s COSY cycle with ANKE internal target on.

The profile integrals calculated by the client application agree very well with the beam current measured by the beam current transformer (BCT) (see Figure 6).

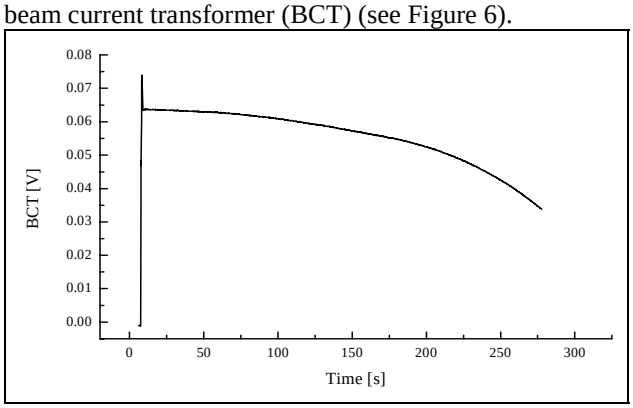


Figure 6: Beam current transformer signal.

EXPERIENCE AND CHALLENGES

Figure 7 shows the horizontal beam (unpolarized protons) image as seen by the CCD camera on the PS. The image width corresponds to the full width (100 mm) of the P47 screen. The beam is intentionally offset to optimize extraction. The unexpected light spot in the centre (horizontally) on the lower edge of the PS may be explained by light reflection. However, it is not yet clear whether it takes place in the glass substrate of the screen or is a result of multiple reflections in the vacuum chamber.

Figure 8 shows the vertical beam image. There are indications that the vacuum window may be contributing to the light reflection. The edges of the PS seem to appear twice in the camera image. This could be due to the light reflection from the screen holder as well. These issues require further investigation and dedicated studies. For example, it would be very useful to study the phenomena mentioned above by varying the beam position at the IPM location. This would allow for better understanding of

geometrical dependencies and eventually, identifying the origin of the problem.

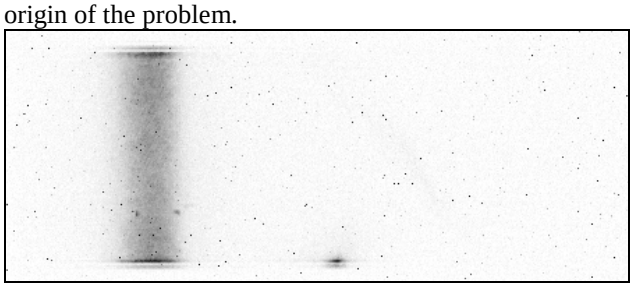


Figure 7: Horizontal beam image as seen by the camera on the PS. The greyscale image is inverted for better readability.

The camera images were cropped using the client application, prior to profile calculation to prevent the phenomena, taking place on the PS edges, from distorting the profiles.

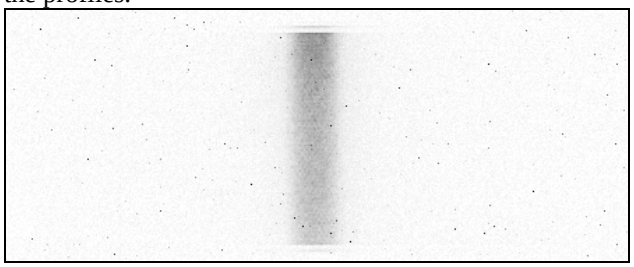


Figure 8: Vertical beam image as seen by the camera on the PS. The greyscale image is inverted for better readability.

The accumulated radiation damage of the CCD chips needs to be characterized quantitatively in order to be able to develop modes of operation assuring the longest possible lifetime. Summing the brightness values for all pixels while there is no beam in the machine and the IPM HV is off could provide a simple and robust way of monitoring the camera condition. A sophisticated algorithm for bad pixel correction is already built into the front end software.

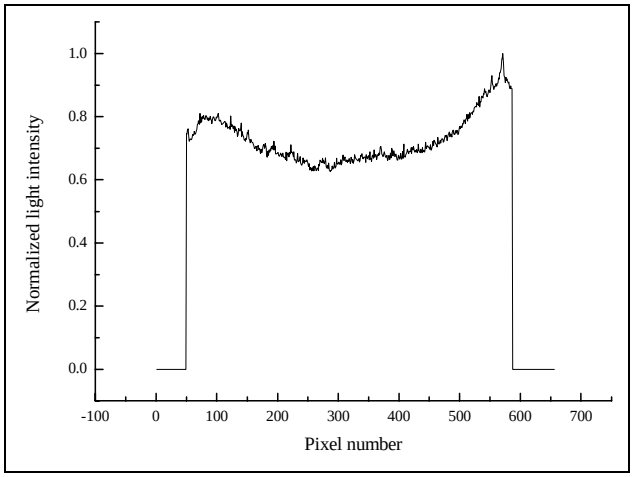


Figure 9: An example of the detector sensitivity distribution measured by illuminating the MCP surface with UV light and observing the PS light with the camera.

The UV lamps (120 nm wavelength) installed in the IPM have proven themselves very useful for monitoring and correction for the detector sensitivity distribution.

Vacuum problems due to operator errors at the early stages of testing showed the necessity to have built-in safety features in the HV power supply control software. Such software was developed and commissioned at FZ-Jülich. The program checks the user input against a series of plausibility criteria. In addition the user is not required to provide the absolute voltages on the electrodes. Instead, physical values, like MCP voltage or MCP to PS voltage are used. These measures made the IPM operation more user friendly and safe.

SUMMARY

The IPM prototype developed by GSI for the future FAIR accelerators was installed in COSY for testing. The monitor was used to measure horizontal and vertical profiles of polarized and unpolarized proton beams in the intensity range of 10^9 to $3{\cdot}10^{10}$ particles in the ring. The data was recorded at a rate of 20 profiles/s in each plane at all beam energies available at COSY. Though all the results reported in this paper are preliminary, they demonstrate that the IPM delivers accurate online beam profile data and can be operated safely and reliably. The values of the profile integrals calculated by the IPM software agree very well with the BCT measurements. The observed evolution of horizontal and vertical proton beam profile throughout the accelerator cycle appears to be consistent with internal target operation and the location of the IPM in the ring.

Undoubtedly, the advanced IPM will be very useful for future beam studies at COSY e.g. beam cooling and injection optimization.

Even though the available software is still under development it allowed for reliable data acquisition and simple analysis.

We plan to replace the PXI based front end with an industrial PC equipped with a fast network card capable of supporting two Gigabit Ethernet cameras generating 200 frames/s each.

REFERENCES

[1] M. Schwickert et al., “Beam Diagnostic developments for FAIR” DIPAC09.

[2] T. Giacomini et al., “Development of a residual gas profile monitor with high resolution and fast readout”, BIW04.

[3] D. Liakin et al., “A Counting Module for an Advanced Ionization Profile Monitor”, EPAC08.

[4] S. Barsov et al., “ANKE, a new facility for medium energy hadron physics at COSY-Jülich”, NIMA, 462, 3, 21 April 2001.

IR PHOTON ARRAY DETECTOR FOR BUNCH BY BUNCH TRANSVERSE BEAM DIAGNOSTICS

A. Bocci, M. Cestelli Guidi, A. Clozza, A. Drago, A. Grilli, A. Marcelli, A. Raco, R. Sorchetti,
INFN – Laboratori Nazionali di Frascati, Via Enrico Fermi 40, I-00044 Frascati RM, Italy
L. Gambicorti,
Istituto Nazionale di Ottica Applicata – CNR, Largo Fermi 6, 50125 Firenze, Italy
A. De Sio, E. Pace,
Università degli Studi di Firenze, Largo Fermi 2 , 50125 Firenze, Italy
J. Piotrowski,
VIGO System SA, 3 Swietlikow Str. 01-389 Warsaw, Poland

Abstract

Beam diagnostics based on synchrotron radiation (SR) may use real time imaging methods that monitor the beam transverse dimensions. In particular the bunch-by-bunch transverse beam diagnostics is a powerful method that allows investigations of transient phenomena in which bunch motion and instabilities are correlated to the position in the bunch train. Such diagnostic methods need photon array detectors with response time from ns to ps range and dedicated fast electronics. At DAΦNE, the e^+/e^- collider of the Frascati National Laboratory (LNF) of the National Institute of Nuclear Physics (INFN), tests with an IR array prototype made of 32x2 pixels and its electronics are in progress. The size of the pixels is ~50x50 μm^2 and their response time ~1 ns. In this contribution we describe an experimental set-up to obtain IR imaging of the SR source and a turn-by-turn and a bunch-by-bunch transverse diagnostics of the stored bunches with a sub-ns time resolution. Preliminary measurements obtained using the IR emission of the SINBAD beamline will be presented. Tests of the array detector with its 64 channels electronics are in progress at the ***T**ime **R**esolved **e+ L**ight* (*3+L*) experiment, a dedicated diagnostics of the DAΦNE positron ring which monitors the longitudinal and transverse dimensions of the positron beam.

INTRODUCTION

Beam diagnostics tools based on synchrotron radiation (SR) are fundamental features of any collider dedicated to high-energy physics experiments and to storage rings optimized as synchrotron radiation sources. Moreover the SR, used for beam diagnostics, gives, as main advantage, a direct and non-destructive system of probing. Typical diagnostics by SR are usually based on expensive imaging techniques that allow measurements of the beam transverse dimensions as well as the longitudinal structure and the bunch length of stored particles (e.g., using a streak camera device). In particular, the real time measurements of the transverse beam dimensions and emittances are growing in interest for next generation of lepton colliders, synchrotron radiation sources and FELs.

In order to measure the beam emittance, the real time analysis of the beam transverse profile is a fundamental requirement of any particle accelerator.

Besides, bunch-by-bunch beam diagnostics is a powerful method for experiments of accelerator physics, such as studies of transient phenomena in which motion and instabilities of bunches depend on the position in the bunch train [1].

Turn by turn and bunch by bunch diagnostics can be implemented using very fast IR, visible, UV or X array detectors (from the sub-ns to the ps range) with dedicated electronics in order to collect and store a large amount of data. Recently at DAΦNE, the Frascati e+/e- collider, measurements of the time structure of synchrotron radiation emitted by the bunches have been performed using uncooled IR photon detectors, achieving a time resolution of a few hundred picoseconds [2]. Future foreseen applications of this technology are based on faster photo-voltaic devices with <100 ps response time and IR uncooled array detectors, to achieve bunch by bunch imaging of the photon source and to investigate transverse instabilities on the DAΦNE rings. In particular, the ***T**ime **R**esolved **e+ L**ight* (*3+L*) experiment, dedicated to beam diagnostics, has been installed in the DAΦNE hall to collect the SR extracted by a bending magnet of the positron ring [3]. The SR is focalized by a set of mirrors in air in front of a fast IR photo-detectors in order to measure longitudinal lengths and transverse sizes of the bunches and to investigate bunch instabilities [4].

This novel device and its electronics have been assembled to test the first transverse diagnostics of the e^+ beam at DAΦNE at IR wavelengths. The device consisting of a fast array detector with 2x32 pixels exhibits a response time of ~1 ns. Preliminary data from single elements of the array and of the electronics have been acquired in order to characterize the assembled device. After completion of the device and its dedicated electronics we could monitor the beam both in the bunch-by-bunch and turn-by-turn transverse modes, two fundamental tools to improve accelerator performances, e.g., at DAΦNE to increase the positron current and the luminosity, and to monitor transverse beam instabilities.

In the following we describe the experimental set-up and present preliminary tests performed with several pixels of the array illuminated by the IR SR emission at the SINBAD beamline of DAΦNE.

EXPERIMENTAL SET-UP

DAΦNE is an e^+/e^- collider, with center of mass energy at 1.02 GeV, designed to operate at high current levels (>2 A) and up to 120 bunches [5]. DAΦNE can work with different bunch patterns: the present typical operation mode is with 105 consecutive electron buckets out of the available 120, with a gap of 15 bunches to avoid ion trapping in the electron beam. In this bunch configuration, the minimum bunch distance is 2.7 ns and bunches are characterized by a Gaussian shape with a bunch length of σ~56 ps.

At DAΦNE an IR photon beam extracted from a bending magnet located in the external arc section of the electron ring is already available for experiments [6]: the infrared SR beamline SINBAD (Synchrotron Infrared Beamline At DAΦNE) is operational since 2001. This beamline is dedicated to Infrared spectroscopy and microscopy and collects radiation at wavelengths from about 10 to 10000 cm^{-1} (1-100 μm). The prototype of the imaging device with its electronics board has been assembled for preliminary tests using the IR light of the SINBAD beamline. A picture of few pixels of the device and of the assembled array is shown in Fig.1.

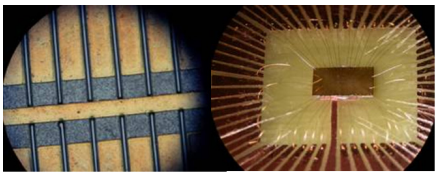


Figure 1: Magnified view of the IR array showing a few pixels of the photoconductive IR detector (left). Interface board and detector showing the connection between pixels and interface board made of gold bonding wires (right).

In this preliminary measurement an interface board has been built and the pixels of the array have been connected by gold bonding wires to the board and finally to the input of an analog electronics board. The dedicated electronics is composed of 64 channels with a bandwidth ≥1 GHz for channel built to amplify signals from the array with a gain of ~40-50 dB (depending on the power supply voltage). In order to characterize each pixel of the array, a four channels oscilloscope has been used to collect and analyze the signals. In the next future we plan to use a fast digital electronics in order to acquire and store the signals and the data of all 64 channels. In these preliminary measurements only four pixels of the array have been connected to the electronics board. These pixels belong to two different lines of the array. A layout of the array detector indicating the tested elements is shown in Fig 2.

The array has been placed at the focus spot of the optical system after the last toroidal mirror of the SINBAD beamline. The SINBAD optical system de-magnifies the source image by a factor 2.3 and its size is estimated about 2.0x1.5 mm at mid-IR wavelengths. The array has been placed in the vertical position in front to the IR spot. Because of the pixel size of the array (i.e. 50x50 $μm^2$) and because only 4 pixels were connected to the electronics, only a small part of the spot can now be monitored by the IR array for now. The signals of the four pixels have been collected at the same time by a scope with four input channels, a bandwidth of 600 MHz and 2.5 Gsample/s.

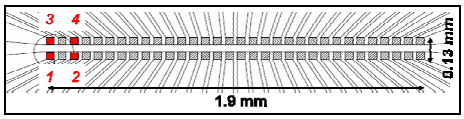


Figure 2: A layout of the IR array detector with its dimensions. Red pixels are those used for the tests.

EXPERIMENTAL DATA

Measurements obtained from a single pixel of the array are shown in Fig. 3. The individual IR emission of the 105 bunches of the beam and the gap can be resolved.

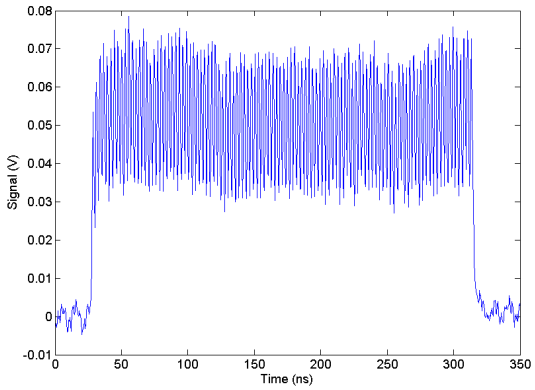


Figure 3: IR signals of the 105 electron bunches collected by one pixel of the IR array detector.

In order to reduce the noise level and to obtain a good S/N ratio the acquisition has been performed by averaging 200 sweeps of waveforms. In this measurement a maximum S/N~36 has been achieved with a beam current of ~1550 mA.

Fig. 3 shows also that the bandwidth of the system is large enough to separate the signals at a distance of ~2.7 ns between bunches even if the response to each bunch is not fast enough to reach the offset level at the beginning of the first bunch. Nevertheless, performing an exponential fit of the signal of the last bunch, a preliminary estimate of the response time of each pixel has been obtained.

The IR signal from the last bunch and its fit are compared in Fig. 4 (blue and red lines, respectively) yielding a response time of the pixel of ~1 ns. Comparing these data with those of other pixels, the response time varies between ~1 and ~1.3 ns. However, we need to underline that, in this configuration, the measurements are limited also by the bandwidth of the scope (600 MHz) limiting the resolution of the measurements.

As an example, two data sets obtained acquiring at the same time the signal of four pixels of the detector are

compared in Fig. 5 and in Fig. 6, with an electron beam current of ~2000 mA and 1700 mA, respectively. The upper panel of Fig. 5 and Fig. 6 shows the signals of pixels 1 and 2 (black and red lines, respectively), the lower the signals of the pixels 3 and 4.

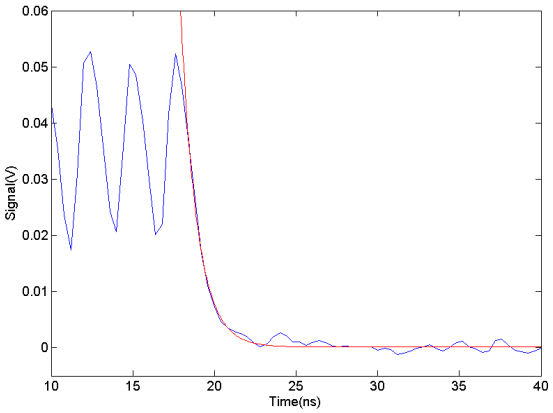


Figure 4: Signal from the last bunch of the train (blue line) and the fit (red line) used to calculate the pixel response time.

Plots in Fig.5 and in Fig. 6 refer to the first and to the last 22 bunches of the train, respectively. Actually, the four pixels measured two different portions of the IR spot and pixels 1 and 2 showed amplitude differences for different bunches, with the signal of pixel 1 always higher than that of pixel 2. The same results have been obtained with pixels 3 and 4, with the signal of pixel 3, at the same level of pixel 1, always higher than pixel 4. We explain this behaviour with a different illumination of the upper pixels (i.e., 1 and 3) collecting the brighter part of the spot. Differences between the relative amplitudes among bunches as measured by different pixels are also observed in both Fig. 5 and in Fig.6 but dedicated measurements are necessary in order to confirm this data.

Work is still in progress to measure the bunch-by-bunch transverse size of the source collecting data from all pixels of the array.

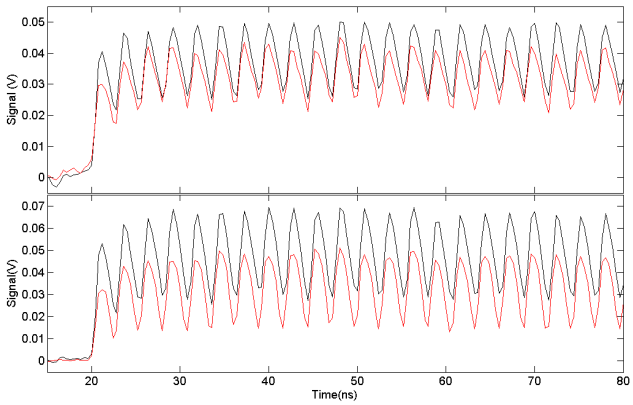


Figure 5: Data from four pixels of the array detector showing the first 22 bunches of the e^- beam (I~2000 mA).

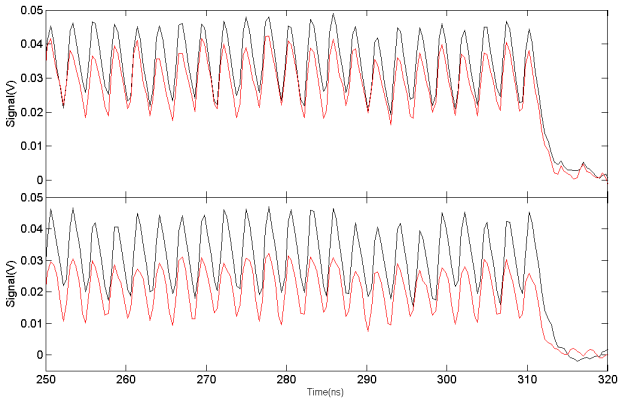


Figure 6: Data from four pixels of the array detector showing the last 22 bunches of the e^- beam (I~1700 mA).

CONCLUSIONS

A first preliminary measurement of few pixels of a fast IR array detector have been performed. Four pixels of an IR array of 64 pixels were connected to four channels of an analog electronic board to test the device placed at the focus of the SINBAD IR beamline at DAΦNE. The measured response time of the pixels is about ~1 ns, sufficient to separate the emission of two consecutive bunches at DAΦNE (~2.7 ns). The signals from the pixels exhibit amplitude differences with respect to each other which can be correlated to the intensity of the source. Work is still in progress to connect all pixels of the array to store a fast transverse IR image of the circulating bunches. We plan also to characterize the linearity of the array elements, to acquire signals with a faster scope to improve the evaluation of the time resolution with a faster digital electronics. The array with the electronics board will be finally installed at the *3+L* experiment, with the goal to monitor the bunch-by-bunch longitudinal and transverse size of the positron beam at DAΦNE. This experiment will represent an important step to improve accelerator performances, e.g., positron beam dynamics and hopefully maximum collider luminosity.

REFERENCES

[1] G. Kube, *Proc. of DIPAC 2007*, 6 (2007).
[2] A. Bocci *et al.*, *Proc. of EPAC 2008*, 1056 (2008).
[3] A. Bocci *et al.*, *Proc. of BIW 2008*, http://www.als.lbl.gov/biw08/talks/Bocci_WednesdayAfternoon.pdf (2008).
[4] A. Bocci *et al.*, *Proc. of PAC 2009*, TH5RFP058 (2009).
[5] C. Milardi *et al.*, *Proc. of PAC 2009*, MO4RAI01 (2009).
[6] M. Cestelli Guidi *et al.*, J. Opt. Soc. Am. A 22 (2005) 2810.

DIAGNOSTICS FOR HIGH POWER ION BEAMS WITH COHERENT OPTIC FIBER FOR IFMIF-EVEDA INJECTOR

F. Senée*, G. Adroit, R. Gobin, B. Pottin, O. Tuske, CEA Saclay, IRFU, F-91191 Gif-sur-Yvette, France.

Abstract

Optical diagnostics based on the excitation of residual gas molecules are routinely used for high intensity beam characterization. Beam intensity, beam position and profile are measured by means of a digital camera. In addition species fraction and profile of each beam are measured using a Doppler shift method. As part of IFMIF-EVEDA project, CEA is in charge of the design and realization of the 140 mA-100 keV cw deuteron source and low energy beam transport line. In the beam line, (D,d) reaction will occur and high neutron flux will be emitted when deuteron beam interacts with surfaces. Moreover gamma ray and activation will also occur. In order to protect diagnostics, coherent optic fibers could be used to transport the beam image outside the irradiated zone. A comparative study of two coherent fibers will be presented (FUJIKURA & SCHOTT), along with the characterization in magnification and transmission of a 610 mm long fiber and its associated optics. To estimate the capability of such fibers to transport beam image, a dedicated experiment has been performed with proton beam produced by the SILHI source. The beam profile has been compared with and without the optic fiber.

INTRODUCTION

The International Fusion Materials Irradiation facility (IFMIF) aims at producing an intense flux of 14 MeV neutrons, in order to characterize materials envisaged for future fusion reactors. Such a machine facility is based on two high power continuous wave accelerator drivers, each delivering a 125 mA D^+ beam at 40 MeV to a liquid lithium target. In the first phase of the "Broader Approach", the IFMIF-EVEDA (Engineering Validation and Engineering Design Activities) project includes the construction of an accelerator prototype with the same characteristics as IFMIF, except a lower energy of 10 MeV instead of 40 MeV for the incident deuteron energy. CEA-Saclay is in charge of the design and realization of both deuteron source and the associated low energy beam transport (LEBT) line. This part, named the IFMIF injector, will be built and tested at Saclay and then moved to Japan. The deuteron beam will be extracted from a 2.45 GHz ECR source based on the SILHI design [1], the Saclay source. It has been developed to produce cw 100 mA proton beams with 95 keV energy. In the framework of preliminary IFMIF studies, SILHI has been tuned to analyze deuteron beam characteristics [2]. That enabled to demonstrate that the emission spectrum in the visible region of deuterium differs slightly from that of proton due to the influence of hyperfine interactions among others. Therefore, all optical diagnostics realized on SILHI and presented in section 2 will be transposable on IFMIF injector. But high neutron flux and gamma rays, emitted when deuteron beam interacts with surfaces, push to use coherent optic fiber to transport the beam image outside the irradiated zone or radiations hardened camera (CID camera). Recent tests of such devices performed on SILHI beam are presented in section 3 and 4.

*franck.senee@cea.fr

OPTICAL BEAM DIAGNOSTICS

The interaction between the proton beam and the residual gas produces excited and ionized gas atoms and molecules. An analysis of the emitted light with different devices allows getting ion beam characteristics.

With Digital Cameras (CCD Camera or CID Cameras)

Direct fluorescence beam profile measurement with digital camera perpendicular to the beam direction allows the following parameter measurement:

- Beam current proportional to fluorescence intensity
- Beam size
- Beam center position
- Beam profile

With Monochromator and CCD Camera

With a digital camera installed in the focal plane of a monochromator with 20° angle. Doppler shift observation of the H_α hydrogen Balmer series allows isolating the fluorescence only resulting from proton beam interaction with the residual gas. As a result, other parameters are achievable:

- Species fraction
- Species fraction beam profile
- Source impurities

With Coherent Optic Fiber, Monochromator and CCD Camera

Adding a coherent optic fiber to transport the beam image outside the irradiated zone and until the device (digital camera or monochromator) seems to be a good solution to prevent these devices from the high neutron flux and gamma ray produced on IFMIF-EVEDA (Fig. 1). All optical diagnostics above should be able to run with this fiber type. That is what we tried to prove with a comparative study made with of two coherent fibers of two manufacturers (FUJIKURA & SCHOTT). Radioprotection simulations show that the radiation level produced by 165 mA deuterons beam at 100 keV should be in the range of 100 mSv/hr around the diagnostic box.

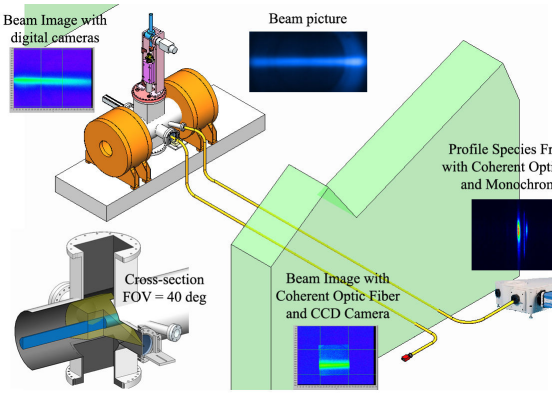


Figure 1: Methods of characterization of the deuteron beam of IFMIF Injector.

FUJIKURA AND SCHOTT COHERENT FIBER SPECIFICATIONS

It seems that only two manufacturers of coherent optic fiber are available: FUJIKURA Japanese Company and SCHOTT USA Company. The main specifications of their coherent optics fiber image transport are presented below (Table 1).

Table 1: Main specifications of two manufacturing coherent optic fiber

Specifications	FUJIKURA	SCHOTT
Model	FISR-30	IG-163
On catalog	No	Yes
Resolution	11200 mm^{-2}	54000 mm^{-2}
Max length	On request	4.575 m
Hardened radiations (650 nm)	Yes (Att=14 dB/km for 1.10^6 rads/hr)	No
Attenuation (650 nm)	0.6 dB/m	1.3 dB/m
Image area	2.7 mm^2	80 mm^2
Image format	Circular	Polygonal
Required magnification	Yes	No
Objective end	Objective lens sleeve (FOV fixed)	C-Mount
Camera end	C-Mount	C-Mount

It appears that the two fibers have got some strengths and weaknesses. Transmission, length and the radiations hardening are the assets of FUJIKURA fibers whereas for the SCHOTT fibers the resolution and the field of view are mutable by changing the objective lens. It would have been interesting to test the two but FUJIKURA fibers are custom-made. Lending it for tests is not possible. So, only one SCHOTT coherent optic fiber of 610 mm long has been characterized with beam profile measurement.

SCHOTT COHERENT OPTIC FIBER CHARACTERIZATION

At first, characterization of the SCHOTT coherent optic fiber was to check its own transmission using a mercury vapor lamp such as light source. The software APILUX will be used to get the transmission of the optical components. After completed the transmission check of the whole optical system with this lamp, the optic fiber transmission with the proton beam has been measured. The optical components used are an objective lens (16 mm), a coherent optic fiber (IG-154, 610 mm, 16 mm^2), a relay lens assembly (IG-1643) and a CCD Camera (Stingray). Finally, the optical system magnification has been determined in order to compare the beam profile obtained with and without the SCHOTT fiber.

Own Fiber Transmission

The obtained ratio between the quantities of light with and without the coherent optic fiber gives the fiber and relay lens assembly transmission. This obtained transmission is 30 %. The relay lens assembly transmission calculated by APILUX is 82 %. One must simply deduce this value to the measured transmission in order to obtain the 610 mm long coherent optic fiber transmission. Therefore, the fiber transmission is 37 %. To compare this result with the spectral transmission given by SCHOTT (Fig. 2), the use of monochromatic light source would have been more suitable. The spectrum of the used mercury vapor lamp has been obtained with monochromator IR550 (Fig. 2). One could note the mercury vapor lamp spectrum is close to the proton beam spectrum (Balmer series).

Transmission of the Whole Optical System for the Proton Beam

To estimate the effective whole transmission system, simulation have been done with APILUX and compared to the experiment results obtained above. The error between the simulation and the experiment is 3 %.

Then the estimated transmission (with APILUX) for whole optical system installed on the proton beam line is 26 ± 3 %. By replacing 610 m long optic fiber by 4.575 m long one, this estimation goes done to 12 ± 3 %. This simulation result doesn't depend on the beam intensity as the light intensity for each Balmer line is directly proportional to the beam intensity [3] (Fig. 2).

Consequently, attenuation will be a decisive parameter in the choice of the coherent optic fiber.

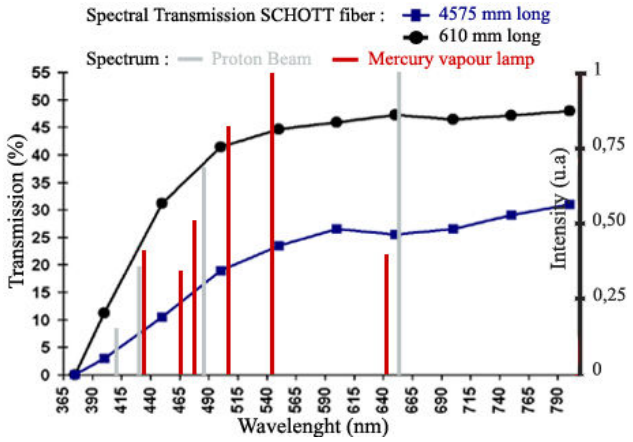


Figure 2: Spectral transmission for a SCHOTT coherent optic fiber of 610 mm and 4575 mm long, mercury vapor lamp and proton beam spectrums.

Optical System Magnification

The magnification is determined by comparing a circular target 20 mm diameter viewed through the optical system with coherent optic fiber and without. The ratio between the two target sizes is 0.64. The field of view with fiber will be thus bigger that without. The Full Width at Half Maximum (FWHM) determined on the beam profile has to be corrected of this value in order to compare the fiber impact on the beam profile.

Beam Profile With and Without SCHOTT Coherent Optic Fiber

The beam profile is deduced from the transverse beam image obtained with the CCD camera (Fig. 3).

This average FWHM difference with and without coherent optic fiber is 10 %. This value is obtained by doing different software corrections on the image such as subtracting the background noise, modifying the Look-Up Table with the pixel maximum luminous intensity. This result could be explained partly by the difference of the field of view: 243 pixels correspond to 69 mm with the optic fiber and 44 mm without. An improved study will be necessary in order to better understand the others involved process but results are promising.

RADIATIONS HARDENED CAMERA IN COMPARISON WITH CCD CAMERA

Radiations hardened cameras operate by Charge Injection Device [4]. One CID8726DX6 designed and manufactured by Thermo CIDTEC (Liverpool, NY) has been tested on the SILHI source with a 25 mm objective lens. Obtained beam profile has been compared with CCD camera results (Fig. 3) for different gains. This CCD camera is the same one used in the above test.

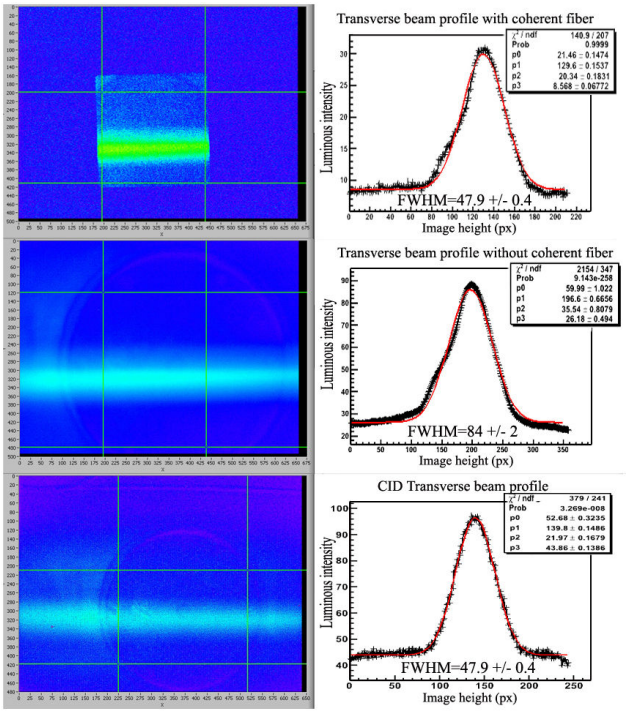


Figure 3: Obtained beam profile from image beam with coherent fiber and without and CID camera.

Taking into account a 0.71 magnification, the obtained difference between CCD FWHM and CID FWHM is 7 %. This result can be explained by the difference between the pixels size (CID pixels are close to 2 times larger than CCD pixels with binning use of 2x2 pixels) but also by the image aliasing. The discrepancy coming from the image aliasing is due to the image format used for the digital acquisition. Further studies are in progress to overcome this trouble. At present time the CID cameras could be used to get the mains characteristics of the beam.

CONCLUSIONS AND PERSPECTIVES

Therefore, it won't be necessary to used coherent optic fiber to get all characteristics of the beam. CID cameras will be used. The cost saving is about factor 3 for coherent optic fiber 5 m long. Nevertheless an optic fiber will be necessary in front of the monochromator to do the Doppler shift analysis. The use of a FUJIKURA fiber is foreseen.

REFERENCES

[1] R. Gobin et al., Rev. Sci. Instrum., 79 (2008) 02B303.

[2] R. Ferdinand et al., "Deuteron Beam Test for IFMIF", EPAC'02, Paris, France, (p. 894-896).

[3] B. Pottin et al., "Optical Beam Profiler for High Current Beams", EPAC'00, Vienna, Austria.

[4] S. Bhaskaran et al., "Performance Based CID Imaging – Past, Present and Future", http://www.thermo.com.

EXPERIENCE WITH YAG AND OTR SCREENS AT ALBA

U. Iriso*, G. Benedetti, and F. Pérez
CELLS, Ctra. BP-1413 Km 3.3, 08290 Cerdanyola, Spain

Abstract

One of the key diagnostics instruments during the ALBA Linac commissioning was the screen monitors that allowed the control of beam size and position. These screen monitors are equipped with a YAG and an OTR screen. This paper describes our screen monitor setup and the experience with both types of screens.

INTRODUCTION

During the ALBA Linac commissioning [1], beam transverse position and profiles are obtained using the setup named "FSOTR" (Fluorescent Screen and Optical Transition Radiation monitor). It includes a Fluorescent Screen (Cerium activated Yttrium Aluminum Garnet, named hereafter "YAG", with chemical formula $Y_3Al_2O_{12}$), and a second screen that produces Optical Transition Radiation (named hereafter "OTR").

After collision with the electron beam, both screens emits light, but their nature differs: YAG screen emits light by scintillation, the OTR screen emits light by Transition Radiation. In both cases, a lens system brings the light to the CCD screen, where the image is collected.

We adopted the solution of YAG and OTR screens in the same setup to obtain a proper beam image for the cases of low and high beam charges. As shown in next Sections, the YAG usage is appropriate for low beam charges because these screens produce lots of light. Its drawback is the saturation at high charges. In these circumstances, the usage of the OTR is convenient, albeit its low photon flux production and so, dynamic range.

In the following, we describe our mechanical setup and experience during the Linac Commissioning, and compare beam images produced with both OTR and YAG screens. We would like to stress that our experience is based with low energy electron beams (up to 100 MeV), which is a relevant factor for both YAG and OTR imaging.

EXPERIMENTAL SETUP

Figure 1 (left) shows a picture of the experimental setup. Using a pneumatic system, the FSOTR monitor allows to introduce either screen into the beam's path. Once the beam collides with either screen, an optical system directs the light to the CCD camera, where the beam image is analyzed.

The optical system is bought off-the-shelf from *EHD-Imaging* with a manually controlled zoom. The working distance of this system is about 300 mm. The CCD camera is *Basler Scout* model, Ethernet controlled, 12-bit resolution, 1034x779 pixels and a square pixel size of 4.65 μm. To minimize the luminic noise, we set the CCD shutter to the minimum time aperture: 100 μs. Since the slowest light emission is the one produced by the YAG screen, and this is only 70 ns [2], this shutter is enough to collect the light produced by either screen.

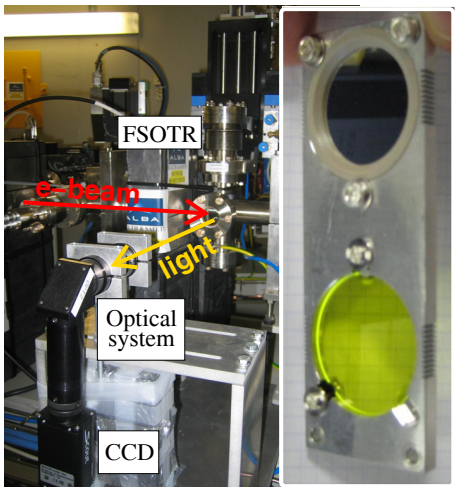


Figure 1: Picture of the FSOTR (right) installed at the Diagnostics line and screen holder with the YAG (bottom yellowish) and OTR screens (top).

Figure 1 (right) shows a picture of the screen holder with the YAG (yellowish and translucent screen) and the OTR ("mirror-like" screen). The YAG screen manufactured by Crytur [2] has a 0.5 mm thickness and 30 mm diameter. The second is a Silicon substrate of 0.3 mm with a thin layer (100 nm) of Aluminum to enhance the transition radiation. The reference marks on the holder edges are used for calibration purposes and image focusing. The calibration in the FSOTR monitors varies from one to another, but it is generally 1 pixel = 20 μm.

BEAM IMAGING WITH YAG SCREENS

The number of photons arriving at the CCD camera produced after a single electron hits the YAG screen is

$$N_{\mathrm{ph}} = Y \times \Omega \,, \qquad (1)$$

where $Y = 35 \times 10^3$ ph/e-/MeV is the YAG photon yield [2], and $\Omega = 4 \times 10^{-4}$ sr is the solid angle covered by the optical system. This means that a single electron at 100 MeV

* ubaldo.iriso@cells.es

produces 1400 photons that arrive to the CCD sensor, assuming 100% efficiency along the optical system. Large photon fluxes are very positive, but in some cases it can has some disadvantages, which are next listed.

CCD Saturation

Pixel or CCD saturation occurs when the image sensors reach their finite charge capacity or their maximum charge transfer capacity. This occurs when the number of photons arriving to the CCD chips is larger than this maximum, which occurs for high areal beam charge densities. In our case, we find this limit at about $2\,\mathrm{nC/mm^2}$.

CCD saturation is easily recognised whenever we reach the maximum pixel intensity in an area around the beam centroid. In this case, 4095 (12-bit digital CCD camera). When CCD saturation is reached, the beam profile image is distorted and so is the image analysis.

YAG Emission Saturation

Fluorescence or scintillating light by the YAG screen is emitted by the de-excitation of atomic states that were previously excited by the passage of an ionizing particle, in this case the electron beam. Above a certain areal beam charge density of the electron beam, the atomic excitation is no longer proportional to the number of electrons crossing the YAG crystal, and a saturation of the light emission is reached. When YAG saturation is reached, the image analysis is not reliable.

YAG saturation is not easily recognized when looking at one single image. This is better distinguished during the quadrupole scan performed to do emittance measurements. Figure 2 shows the horizontal sigma as a function of the quadrupole intensity. As the beam approaches the waist along both branches, the beam size decreases linearly until we enter a pseudo-plateu (between approximately -1.9 A and -1.7 A). This corresponds to a 2 nC beam, for which the charge areal density (1-sigma) at saturation is $1.5\,\mathrm{nC/mm^2}$.

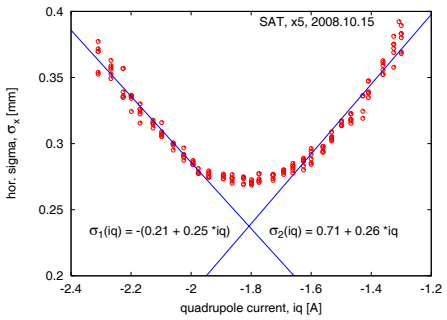


Figure 2: Beam size decreases linearly as we approach the beam waist (approximately at -1.8 A). Below 0.28 mm, the beam size enters a saturation regime. The blue line shows two linear fits to the data at each branch, and stresses the lack of linearity between -1.7 A and -1.9 A, which points the YAG saturation.

Light Reflections and Multiple Scattering

Because the YAG screen is translucent, light produced by the beam itself can be reflected in the beam chamber and distorts the beam image. In our case, since the chamber behind the YAG screen is round, it acts as a concave mirror and this effect enlarges the apparent beam size.

Moreover, due to the YAG screen thickness, multiple scattering inside the screen increases the apparent beam size [3]. Because the screen is tilted 45° in the horizontal direction (and not in the vertical), this effect is more pronounced horizontally than vertically – see Figs. 5 and 6. Figure 3 depicts the effect of the multiple scattering inside the YAG screen.

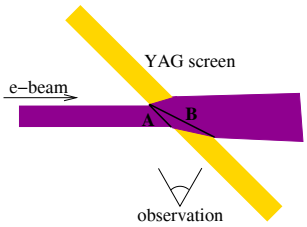


Figure 3: Beam size enlargement due to multiple scattering inside a YAG screen. The distance A appears as B.

BEAM IMAGING WITH OTR SCREENS

An OTR screen produces visible light when a relativistic charged particle crosses the interface of two media with different permittivity ϵ_r. The radiation is emitted in a cone of $\pm 1/\gamma$ towards the optical system, and so reflections inside the vacuum chamber are not an issue. The most critical point is the low photon flux produced with the ALBA Linac beams.

The number of photons N_{ph} generated when a single electron crosses a metal foil is [4]:

$$N_{\mathrm{ph}} = \frac{\alpha}{\pi}(2\ln\gamma - 1)\ln\frac{\nu_2}{\nu_1}\,, \qquad (2)$$

where α is the fine structure constant, γ is the beam relativistic factor, and ν_1, ν_2 is the photon frequency region. Since the OTR light is emitted between $\pm 1/\gamma$, we consider that the same optical system captures all the OTR photons. In this case, one electron at 100 MeV produces about 0.016 photons that arrive to the CCD in the visible range. This is about 5 orders of magnitude lower than the image produced using the YAG screen.

In the first phase of the Linac commissioning, the maximum energy was 70 MeV, for which the OTR signal was too low. We could only use the OTR during the last part of the Linac commissioning, when the Linac was properly optimized and energies > 100 MeV and small emittance beams could be reached.

BEAM SIZE USING YAG AND OTR

Figure 4 compares two cases that illustrate the pros and cons of the beam imaging with YAG (top) and OTR (bottom) screens, and their profile analysis in the vertical direction. In both cases the Linac settings are the same. The effect of reflections and multiple scattering in the YAG screen produces the tails' enlargement. On the other hand, the OTR image has a larger Signal to Noise Ratio (SNR) because of the areal charge density is not very large (in this case, about 0.2 nC/mm^2).

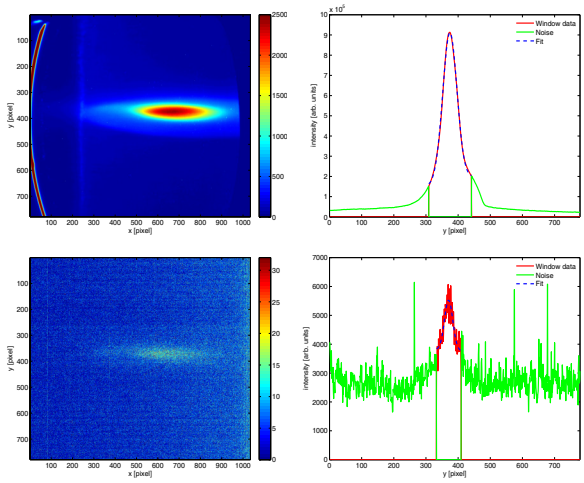


Figure 4: Two beam images and their profile analysis for the same Linac settings using the YAG (top) and OTR (bottom).

Due care shall be then taken during a beam size scan, for example, in the emittance measurements using the quadrupole scan technique. In these cases, the areal beam charge density varies by about one order of magnitude between the beam waist and the scan edges [1].

Figure 5 shows the difference between the horizontal beam size inferred using the YAG and OTR screens. The YAG screen gives a horizontal size which is a factor ~ 2 larger than the beam size inferred using the OTR screen. Note that around the beam waist, the scan is probably affected by saturation.

On the other hand, the vertical beam size (see Fig. 6) does not show such a significant difference because of the screen orientation previously mentioned decreases the effect of the reflections and multiple scattering. In both horizontal and vertical profiles, this difference is more pronounced in the beam waist.

SUMMARY AND OUTLOOK

The ALBA FSOTR monitor and the advantages and disadvantages of using YAG or OTR found during the ALBA Linac comissioning are shown. The images produced using the YAG screen have a photon flux of about 5 orders of magnitude larger than images produced using the OTR screen. However, beam imaging using YAG screens produce CCD or YAG saturation. In this case, we measure CCD saturation for charge densities above 2 nC/mm^2 and YAG saturation above 1.5 nC/mm^2. Light reflections and multiple scatterings produce a beam size overestimation using the YAG screen of about a factor of 2 (horizontally) and about 50% (vertically).

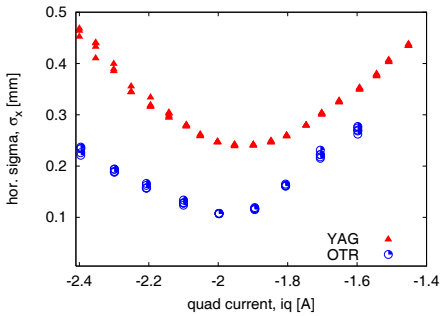


Figure 5: Hor beam sizes during a quad scan, inferred after analysis of the YAG and OTR images (MBM, 4 nC).

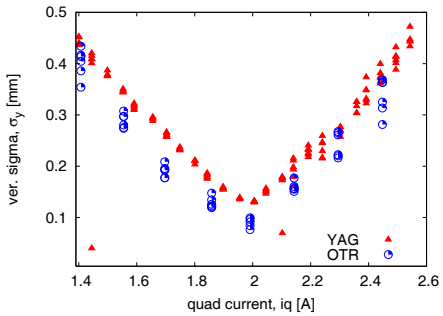


Figure 6: Ver beam size during a quad scan, inferred after analysis of the YAG and OTR images (MBM, 4 nC).

In order to avoid these reflections, it is convenient to use YAG screens optically non-transparent (i.e., with a few µm Si coating). Since ALBA already has all its YAG screens, we have designed a sandblasted stainless steel plate to avoid these reflections. Moreover, this plate has also some marks to provide in-situ calibration.

ACKNOWLEDGMENTS

We are very grateful for the engineering support of M. Cornelis and useful comments from V. Schlott (SLS) and K. Scheidt (ESRF).

REFERENCES

[1] G. Benedetti, U. Iriso and A. Olmos. *Beam measurements at the ALBA Linac*, Proc. of PAC'09, Vancouver (Canada) 2009.

[2] `http://www.crytur.cz/`

[3] E. Bravin, *Transverse Profiles*, CAS on Beam Diagnostics, May 2008, Dourdan (France).

[4] B. Gitter, Optical Transition Radiation, CAA-Tech-Note Internal #24, UCLA Department of Physics, 1992.

A COMPACT ELECTRON PHOTON DIAGNOSTIC UNIT FOR A SEEDED FEL*

J. Bödewadt†, J. Roßbach, University of Hamburg, Germany
B. Polzin, H. Schlarb, A. de Zubiaurre Wagner, DESY, Hamburg, Germany
R. Ischebeck, PSI, Villigen, Switzerland

Abstract

A seeded free-electron laser (FEL) operating in the soft X-ray (XUV) spectral range will be added to the SASE FEL facility FLASH. The seed beam will be generated by higher harmonics of a near infrared laser system. A dedicated transport system will guide the radiation into the electron accelerator environment. Within the seed undulator section compact diagnostic units have to be designed to control the transverse overlap of the photon and the electron beam. These units contain a BPM a wire scanner and an OTR screen for the electron diagnostic. A Ce:YAG screen and a MCP readout for the wire scanner are foreseen to measure the photon beam position.

INTRODUCTION

The free-electron laser in Hamburg (FLASH) offers high brightness photon beam with sub-10 fs pulse length in the vacuum ultra-violet (VUV) and soft x-ray (XUV) regime to various experiments [1] . It operates using the principle of self-amplified spontaneous emission (SASE) where radiation is emitted by a 1 GeV high peak current (∼kA) electron beam in a planar undulator. Due to the start up from shot noise this results in a statistical behavior of the emitted spectrum [2]. Beside that the arrival-time jitter of the FEL pulses is in the order of a few 100 fs which limits the temporal resolution for pump-probe experiments [3] where an external laser system has to be synchronized with the accelerator. One way to reduce this time jitter is to seed the FEL process with an external laser and combine the amplified radiation pulse with near infra-red pulses from the same laser system. Since the two radiation pulses originate from the same source they are intrinsically synchronized. A directly seeded FEL configuration is going to be installed at FLASH in winter 2009 [4]. A 40 m long section upstream the existing SASE undulator will be rebuild for that purpose. Figure 1 shows a general layout of that section. The XUV seed radiation is created by higher-harmonic generation (HHG) from NIR femtosecond laser pulses focused in a rare gas jet and guided through a 15 m long differentially pumped transfer line from a laser laboratory into the adjacent accelerator tunnel and into the electron beam pipe. This transfer line includes two motorized mirror chambers to steer the beam and thus to control the spatial overlap between the electron and the photon beam. In order to obtain the overlap, diagnostic units will be installed at either end of each undulator module. Each unit accommodate an electron beam position monitor (BPM), vertically and horizontally installed wire scanners (WS), an aluminum coated silicon screen for optical transition radiation (OTR) measurements and a Ce:YAG crystal.

SPATIAL OVERLAP

One of the key challenges of the seeding experiment is to achieve the spectral, temporal and spatial overlap. The latter will be obtained by either steering the electron beam onto the photon beam or vice versa. Therefor two pairs of dipole corrector magnets (horizontal and vertical) preceding the sFLASH undulator and two motorized mirrors inside the XUV-seed transfer line will be installed. Each of the mirrors can be steered in two dimensions thus the

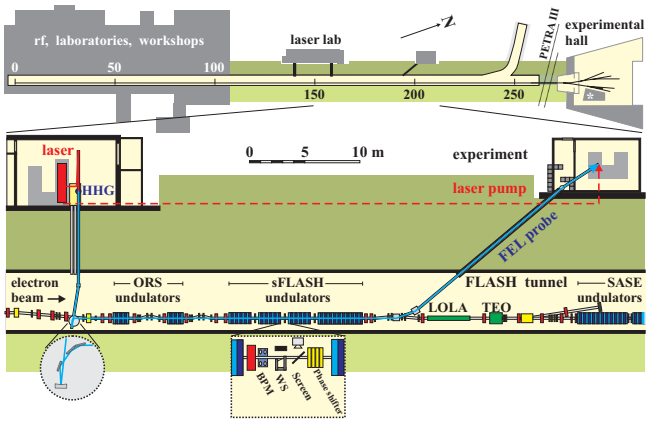


Figure 1: The FLASH facility (top) comprises a 260 m long tunnel housing the linac and undulators of a SASE FEL, followed by an experimental hall. A 40 m long section (bottom) will be rebuilt to accommodate four additional undulators for sFLASH. Seed pulses from an HHG-source in a building adjacent to the FLASH tunnel will be aligned to the electron beam. At the undulator exit, the FEL radiation is sent by mirrors to an experimental hutch. Delayed laser pulses will be sent directly to the hutch for pump-probe applications (dashed line).

* Funded by the Federal Ministry of Education and Research of Germany under contract 05 ES7GU1
† contact: joern.boedewadt@desy.de

position and angle adjustment of the photon beam within the undulator is possible. During the commissioning of the experiment the spatial overlap will be the second of the three step to assure a six-dimensional overlap. After setting the variable-gap undulators to fulfill the resonant condition with respect to the electron beam energy and the seed wavelength, the transverse positions of the seed and the electron beam have to be matched. This will be done by measuring and aligning the two beams at the entrance and the exit of the first undulator module using the OTR and the Ce:YAG screen. The last step to establish seeding is to set the right timing between the two femtosecond pulses to achieve temporal (longitudinal) overlap which will be another challenge [5].

Tolerances

Numerical simulations were performed to estimate the tolerances for the electron beam transverse offset and angle with respect to photon beam [6]. Assuming a tolerance for the radiation power of the seeded FEL of 5% the simulation shows a maximum accaptable offset of 35 μm and a maximum angle of 20 μrad for the two beam with respect to each other. Based on that numbers the position and angle adjustment tolerances for the photon beam were set to 10 μm and 5 μrad respectively.

DIAGNOSTIC UNIT

The sFLASH undulator has three 0.7 m long intersections were a quadrupole, a phase shifter, a dipole corrector coil and a beam diagnostic unit has to be installed. Figure 2 shows a technical drawing of one of these sections. A fourth diagnostic unit will be installed at the entrance of the undulator. The maximum space available for the design is 20 cm. All units will be equipped with a carrier on a linear translation stage to mount a silicon screen, a Ce:YAG crystal and a calibration screen. Together with an appropriate optical system and a CCD camera ,this gives the possibility to measure beam size and position for electron and photon beams on a single shot bases. Furthermore button type beam position monitors (BPM) on the undulator intersection units and a strip line BPM at the undulator entrance will be installed [7]. In addition the first two units accommodates a horizontally and a vertically installed wire scanner with two multichannel plates to detect scattered photons and electrons respectively. Scintillator panels mounted beside the undulator will give the possibility to detect electron showers produced by the wire scanners.

Wire Scanner

The wire scanners were designed and built for a self-seeding option at FLASH [8] and are of the same type as used in the SASE undulator section at FLASH [9]. For sFLASH they will be equipped with a tungsten wire of 15 μm diameter and two carbon wires with 10 μm and 5 μm diameter.

Imaging System

For precise emittance measurement using the four screen method the electron beam size has to be measured with an error better than 10% of the rms beam size. Therefore the imaging system of the diagnostic units has to garantee a resolution of 10 μm/pixel with a design electron beam size of 100 μm. The standard camera system [10] installed at FLASH uses cameras with a pixel size of 9,9 μm [11]. The third and fourth diagnostic unit will operate with these camera types too. A simple 1:1 imaging setup can be used at that positions. For the first and second unit the signal-to-noise ratio of the standard system won't be sufficient to diagnose the XUV photon beam on the Ce:YAG crystal even with a large aperture lens. Therefor a more sensitive EMCCD camera system will be used with a telescope like lens system (see Fig. 3). To avoid image destortions an aspherical lens with a focal length of 80 mm and an diameter of 45 mm is installed right after the vacuum window resulting in an acceptance angle of 30°. Another lens system with a focal length of 75 mm will image the screen on the CCD resulting in a magnification of 0,94. With a camera pixel size of 8 μm the resolution is good enough for precise emittance mesurements and to diagnose the XUV seed beam. Differ-

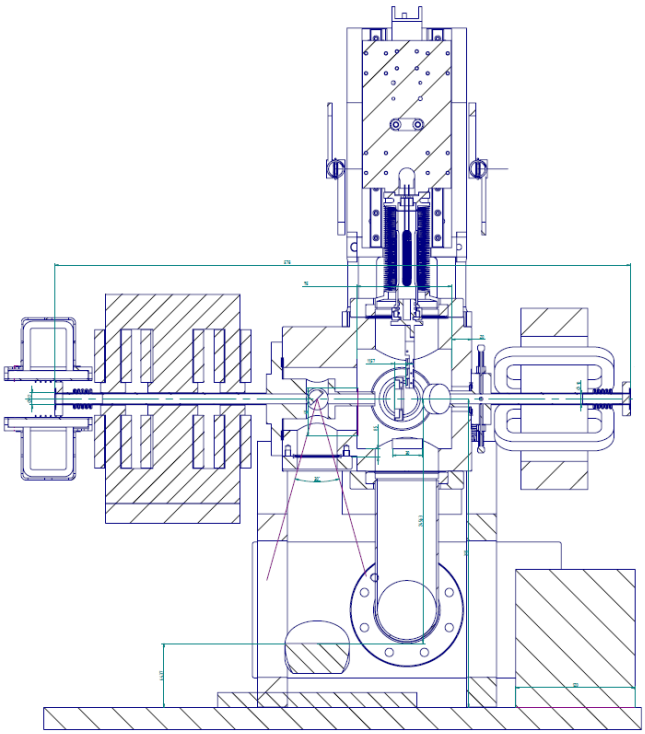


Figure 2: A sectional drawing of the sFLASH undulator intersection. Components from left to right: dipole corrector coil, phase shifter, diagnostic unit, quadrupole. The diagnostic unit accommodate a button BPM (right), wire scanners (vertical type on top), MCP for photon/electron detection and a carrier (left) with a silicon screen and a Ce:YAG crystal. The diameter of the vacuum chamber is 10 mm.

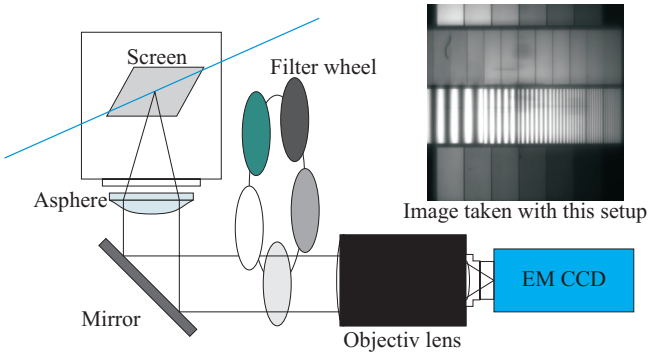


Figure 3: Layout of the imaging system for the OTR/Ce:YAG diagnostics. From the screen emitted radiation is collimated with an aspherical lens ($f = 80\,\mathrm{mm}$) and focused by a commercial lens ($f = 75\,\mathrm{mm}$). A motorized filter wheel allows five different attenuation factors. The small image shows a sine test pattern imaged with this setup.

ent color and grey filters will be installed on a motorized filter wheel to avoid saturation of the CCD and to protect it against high intensity laser beams.

SUMMARY

In order to commission and control the spatial overlap between an XUV photon beam and the electron beam for a direct seeding experiment at FLASH compact diagnostic units were designed. Combining standard beam position monitoring instruments for both electron and photon beams it will work as an essential tool during the first phase of the seeding experiment.

ACKNOWLEDGMENTS

Special thanks to people from different groups at DESY (among them FEB, FH1, MCS, MVS, ZM and Zeuthen). Their support is gratefully acknowledged. The project is supported by the Federal Ministry of Education and Research of Germany under contract 05 ES7GU1.

REFERENCES

[1] W. Ackermann et al., *Operation of a free-electron laser from the extreme ultraviolet to the water window*, Nature Photonics 1 (2007), p. 336.

[2] E. L. Saldin et al., *The Physics of Free Electron Lasers*, Springer Berlin (1999).

[3] A. Azima et al., *Jitter Reduced Pump-Probe Experiments*, Proceedings of DIPAC'07, Venice, (WEPC13).

[4] S. Khan et al., *sFLASH: An Experiment For Seeding VUV Radiation at FLASH*, Proceedings of FEL'08, Gyeongju, (TUPPH072).

[5] R. Tarkeshian et al., *Conceptional Ideas For The Temporal Overlap Of The Electron Beam And The Seed Laser For sFLASH*, Proceedings of FEL'08, Gyeongju, (TUPPH051).

[6] V. Miltchev et al., *Tolerance Studies On The High Harmonic Laser Seeding At FLASH*, Proceedings of FEL'08, Gyeongju, (TUPPH003).

[7] N. Baboi et al., *Beam Position Monitor Calibration at the FLASH Linac at DESY*, Proceedings of PAC'07, Albuquerque, (FRPMN017).

[8] J. Feldhaus et al., *Possible application of X-ray optical elements for reducing the spectral bandwidth of an X-ray SASE FEL*, Opt. Commun., 140 (1997), p. 341.

[9] U. Hahn et al., *Wire scanner system for FLASH at DESY*, Nuc. Inst. Methods **A 592** (2008), p. 189.

[10] G. Grygiel et al., *DOOCS Camera System*, Proceedings of ICALEPCS'07, Knoxville, (WPPA21).

[11] Basler AG, A300-Serie, `http://www.baslerweb.com`

VIMOS, BEAM MONITORING FOR SINQ

K. Thomsen, PSI, Villigen, Switzerland

Abstract

For the neutron spallation source SINQ at PSI a novel visual monitor (VIMOS) has been devised to guarantee correct beam conditions, triggered at the occasion of irradiating the delicate liquid metal target during the MEGAPIE project. VIMOS is looking directly for the most relevant parameter: it checks whether any point on the target is hotter than allowed. For this purpose the incandescence of a glowing mesh right in front of the beam entrance window is observed by means of dedicated radiation hard optics and suitable cameras. Starting from the initial goal of reliably detecting beam anomalies in a timely manner the scope of the system has been extended to serve as a standard device for beam monitoring and fine tuning of the settings of the proton beam transport lines. Over the course of the five years of continuous reliable operation of this unique system valuable experience has accumulated, which is employed for steady improvements of the device with respect to endurance in the radiation environment, calibration, maintenance, and price.

INTRODUCTION

Five years of operation of VIMOS clearly produced a wealth of operational experience and also resulted in some data, which were not expected form the beginning. In the following, a few selected highlights are presented as well as their impact on the course of the further development of the system.

VIMOS in its original configuration derived its sensitivity in part from the spectral response of the imaging tube in the used radiation resistant camera [1]. With a steep cut-off towards the infra-red, the detected signal rises steeply in case mesh-temperatures get higher and more emitted intensity is shifted to shorter wavelengths correspondingly.

INITIAL SENSITIVITY EVOLUTION

One observation at the start of the system five years ago was a significant decrease of the observed signal for identical beam conditions during the first year of operation. This had been attributed to blackening, i.e. an increase of effective emissivity, of the tungsten mesh under proton irradiation [2]. Starting with an effective emissivity of 0.3 and increasing it to 1, results in a reduction of signal in the sensitive wave band of the first VIMOS camera of 100.

Employing the same special tool as during the initial set-up, further evidence for this change in emissivity has been obtained in the meantime. A light emitting diode close to the mesh can be used for fine alignment of the camera. Whereas the image taken in 2005 (Fig. 1, top) clearly shows some reflections these are absent in the corresponding image of 2009 (Fig. 1, bottom).

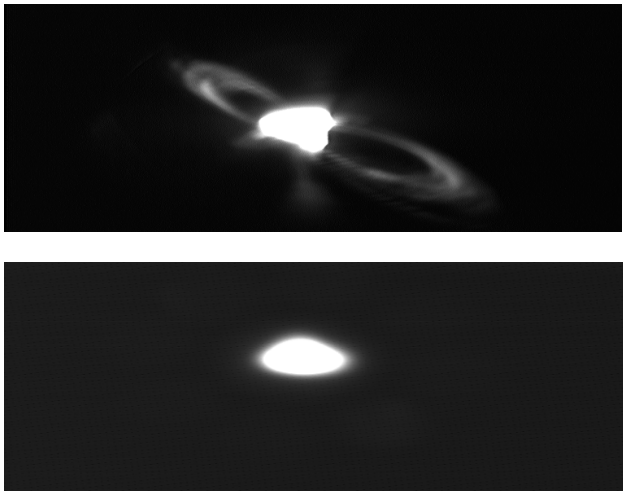


Figure 1: Set-up of the VIMOS camera by means of a special tool with a light emitting diode five years apart. Whereas the top image from the very start of operation features some reflections, nothing of this kind is visible after "seasoning" of the mesh. The absence of reflected light is consistent with the observed decrease in overall signal during the first year of irradiation.

CAMERA LIFE TIME

Initially, the tube based cameras showed very reliable and constant performance over the course of the operation periods at SINQ. During the irradiation of MEGAPIE severe degradation occurred within weeks [3]. The current amplification of some transistors inside the camera was reduced by a factor of five, which, most importantly, lead to a reduction of the usable sensitive area on the entrance window of the camera and to a shift of the image. Whereas there was no immediate loss of sensitivity with respect to the required safety function, because of easy software compensation, the expensive cameras had to be replaced at short intervals to guarantee their full functionality. An increase in the amount of fast neutrons scattered downwards from the target by a factor of two was found responsible for the damage to the cameras, most probably due to these neutrons after thermalisation [4].

A new design of the standard target in SINQ will result in similar neutron fluxes also for a solid target [5]. In order to cut down on camera wear (and maintenance cost) a radiation resistant light guide has been introduced with the aim of placing the camera four meters away at a location with much reduced radiation exposure.

During the irradiation period of 2008 no dramatic deterioration in the transmission of the light guide has been observed. The tube based camera employed during this time exhibited unchanged performance.

For the last 6 weeks of 2008 a standard CCD camera without any shielding was installed to verify the feasibility of using inexpensive semiconductor based devices in principle. This camera exhibited clearly observable degradation in the form of hot pixels, transient as well as more permanent ones, and increased noise already after short exposure. Nevertheless, it worked well over the whole remaining operation period and it delivered all the time signals which demonstrate that it could have been used for a much longer time without endangering the responsiveness of VIMOS.

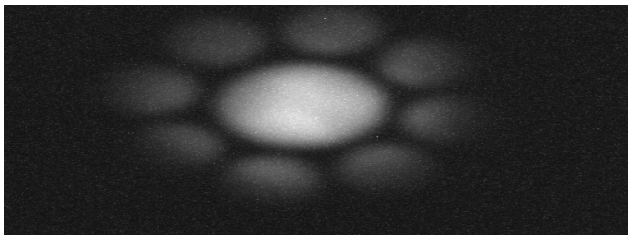


Figure 2: Image obtained through the light guide and with a CCD camera without shielding at the start of operation spring 2009 at nominal beam conditions at 1270 µA.

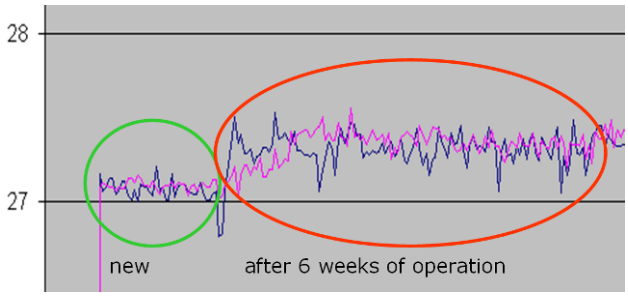


Figure 3: Representative "empty" signal from the first CCD camera, i.e. average over non-illuminated sector of frame, at the start (green circle) and at the end (red oval) of the VIMOS service period. Due to hot pixels the background level shifted just noticeable after irradiation, and fluctuations from frame to frame increased.

EXPANDED FUNCTIONALITY

Assuming that a given light guide can be used for several irradiation periods, i.e. for a minimum of two years, several improvements of the VIMOS system can be implemented:

- Use of inexpensive semiconductor based (CCD) cameras.
- Easy and quick replacement of cameras at the far end of the image guide.
- Splitting of the detected light into diverse optical paths.
- Selecting different wavelengths for better diagnostics.
- Absolute calibration of the image in terms of beam current density.

The first two bullets above were the predominant aim for short-term upgrades of VIMOS. If possible, the running cost of the system had to be reduced while improving the maintainability of the installation. If the lifetime of the optical fibers outlasts the useful operational time of the tube based cameras by at least a factor of two, a significant cost reduction can be achieved in the future.

As reported above, a standard CCD camera showed satisfactory performance during a first test run at the end of 2008, even with out shielding. Adding some graded shielding will definitively minimize camera degradation.

Once it has been proven that semiconductor based cameras can be employed long enough at the new remote position, additional and informative data can be obtained. Splitting the collected light into separate channels allows for keeping the "spectrometer-mode" sensitivity in one "alarm-signal" path while recording a less non-linear response in a second channel.

Measuring the relative signal strengths for two different wavelength-windows enables one to derive the absolute temperature of the glowing mesh rather independent of the losses in the optical transmission. Calibration in a in-active test set-up is then possible. Knowing the exact temperature of the mesh one can determine the heat deposited by the beam when passing through the mesh, and in the end obtain the current density distribution of the proton beam on the target in µA/cm^2.

ACKNOWLEDGMENTS

A large number of colleagues contributed considerably to the development and the successful implementation of VIMOS at SINQ: P. Baron, B. Blarer, V.N. Dang, M. Djiango, R. Dölling, M. Dubs, P.A. Duperrex, T. Dury, G. Dzieglewski, S. Ebers, Y. Foucher, G. Frei, N. Frei, U. Frei, R. Fütterer, K. Geissmann, P. Häberli, G. Heidenreich, P. Hengel, M. Muser, A. Irniger, A. Kalt, R. Kaufmann, E. Langenbach, E. Lehmann, A. McKinnon, A. Mezger, P. Ming, M. Moser, R. Mock, U. Müller, L. Ni†, Ch. Perret, E. Pitcher, L. Podofillini, M. Reder, U. Rohrer, P.A. Schmelzbach, P. Schüttel, T. Shea, B. Sigg, B. Smith, A. Strinning, M. Vatré†, E. Wagner, S. Wagner, W. Wagner, H. Walther, …PSI Accelerator Operator Crews.

REFERENCES

[1] K. Thomsen, VIMOS, near-target beam diagnostics for MEGAPIE, NIMA 575, 347-352, 2007.
[2] K. Thomsen, Advanced on-target beam monitoring for spallation sources, NIMA 600, 38-40, 2009.
[3] C. Fazio and the MEGAPIE collaboration, The MEGAPIE-TEST project: Supporting research and lessons learned in first-of-a-kind spallation target technology, Nuclear Engineering and Design 238, 1471-1495, 2008.
[4] L. Zanini, private communication, 2006.
[5] W. Wagner, M. Seidel, E. Morenzoni, F. Groeschel, M. Wohlmuther, M. Daum, PSI status 2008—Developments at the 590 MeV proton accelerator facility, NIMA 600, 5-7, 2009.

FIRST EXPERIENCE AT SARAF WITH PROTON BEAMS USING THE RUTHERFORD SCATTERING MONITOR

L. Weissman , D. Berkovits, Y. Eisen, S. Halfon, I. Mardor, A. Perry, J. Rodnizki,
Soreq NRC, Yavne 81800, Israel
K. Dunkel, C. Piel, D. Trompetter, P. vom Stein,
Research Instruments GmbH, 51429 Bergisch Gladbach, Germany

Abstract

The first phase of the SARAF high current proton/deuteron accelerator is currently under commissioning. The first experience with 3 mA, pulsed proton beam included the measurement of the energy spectra of the protons of energies up to 2.2 MeV scattered at 45^o from a 0.3 mg/cm^2 thick gold foil. The beam was accelerated by the RFQ and by several superconducting resonators. The energy spectra of the scattered particles were taken for different accelerator settings. The results were compared with time-of-flight and with Monte-Carlo calculations. Monitoring the energy of the scattered particles proved to be a useful tool for beam tune and calibration of the accelerator components such as the RFQ and the superconducting resonators.

INTRODUCTION

SARAF accelerator, a medium energy high current RF superconducting linac of protons and deuterons (2 mA, 40 MeV), is currently under construction at Soreq center [1]. Phase I of the accelerator includes the Electron Cyclotron Resonance (ECR) ion source, Low Energy Beam Transport (LEBT), Radiofrequency Quadruple (RFQ) accelerator-buncher, Medium Energy Beam Transport (MEBT), Prototype Superconducting Module (PSM), Diagnostic plate (D-plate) and beam dumps (Fig. 1). A detailed description of the accelerator is out of scope of this paper and can be found in [1,2] and references therein. At the moment Phase I is fully installed and being commissioned by ACCEL-Research Instruments GmbH, in collaboration with Soreq personnel.

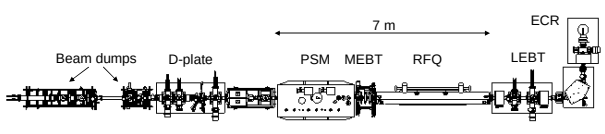


Figure 1: Overview of Phase I of SARAF accelerator.

Most of the beam diagnostics of the SARAF linac are situated on the D-plate. The main diagnostic components are: a slow Faraday cup (FC), set of vertical and horizontal slits and wires for profile and emittance measurements, two phase probes for time-of-flight measurements (TOF), two beam position monitors, a parametric current transformer (from Bergoz) and two fast FCs. Earlier report on the use of the D-plate for proton beam commissioning through the RFQ is given in [3].

Along with traditional beam diagnostics instruments, a Beam Halo Monitor (BHM) station is implemented into the SARAF D-plate [4]. The beam halo is planned to be characterized using a mini FC, on-line and off-line measurements of radiation from LiF target crystals and by monitoring energy spectra of Rutherford Scattered (RS) particles from a thin target gold foil.

The extensive use of the BHM is planned only after full commissioning of Phase I. However, a specific part of the BHM, the RS monitor, was used in the recent commissioning efforts for transport and acceleration of the pulsed proton beam through the RFQ and PSM. In this paper we present results of these measurements.

USE OF THE RS MONITOR FOR TUNING OF THE ACCELERATOR

The Conditions of the Commissioning Tests

Main commissioning tests were done in a mode where both the ECR ion source and the RFQ were pulsed. The timing overlap between these pulses defines the length of the proton pulse. Typically short pulses of 100 μsec duration at a frequency of a few Hz were used. Such low duty cycle (10^{-4}) is necessary for use of interceptive beam diagnostics. The 20 keV pulsed beam from the ECR was transported via the LEBT, bunched and accelerated to 1.5 MeV by the RFQ and further transported and accelerated for the first time by the PSM module. The module contains six Half Wave Resonators (HWR) made of bulk Nb and three 6 T superconducting solenoids inserted among them [5]. The optical elements of the LEBT, MEBT, PSM solenoids and a quadruple doublet after the PSM were set to optimize the beam transmission. However, the beam current measured at the D-plate was 3 mA, corresponding to a 60% transmission from the LEBT, where 5 mA was measured. Most of the beam loss occurred at the low-energy part of the RFQ. This issue will be the subject for further investigations.

Description of the RS Monitor

The energy of the beam as a function of various parameters of the accelerator components was measured at the D-plate by comparing timing signals from the two phase probes (TOF) and the RS monitor measurements (Fig. 2).

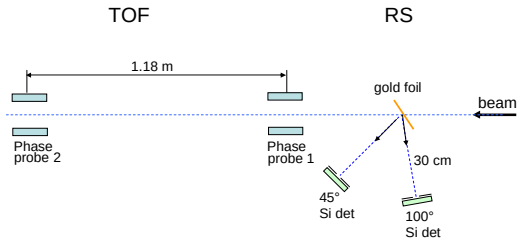


Figure 2.: Schematic presentation of beam energy measurement incorporated into the D-plate.

In the latter case the 0.3 mg/cm^2 thick gold foil was introduced into the beam periphery and the scattered protons were detected by two 500 microns thick Silicon particle detectors (Canberra Inc.), placed at a distance of approximately 30 cm from the target, at the angles of 45 and 100 degrees with respect to the incident beam direction. The gold foil was glued to a graphite frame, which was placed on a target ladder. The foil was introduced slowly in the beam periphery until the counting rate in the Si detectors was satisfactory. The detector signals were amplified and shaped by preamplifiers and spectroscopy amplifiers and were digitized and histogrammed by a data acquisition system. During the first attempts strong pile-up in the detector signals was observed even at very low overall detection rate. This was due to high number of particles in a pulse. This problem was solved by introducing of 2 mm diameter collimators on the detector front, thus reducing its detection solid angle by a factor of 30. In general, use of two detectors provides some experimental flexibility as the detection rate has strong dependence on the scattering angle. In these tests the detector at 45 degrees was mostly used.

Further tests showed various advantages of the RS monitor compared to the TOF technique. The determination of the centroid of the beam energy distribution takes a few seconds, although longer time is needed to obtain good quality spectra. The energy spread of the beam and information on some weak low-energy beam satellites can be obtained from the spectra. At the moment, the disadvantage of RS method is the lack of possibility of independent energy calibration and, hence, the RS energy spectra have to be calibrated using the TOF measurements.

Example of Use of the RS Monitor

Energy spectra were measured for beam traversing through detuned cryogenic resonators, allowing one to study separately the RFQ performance. Evolution of beam energy spectrum as a function of RFQ forward power is presented in Fig. 3. The strong peak at the expected energy (1.5 MeV) appears in the spectrum only at the RF power value higher than 50 kW. The FWHM of the peak is about 20 keV. Contribution to this width comes from the energy spread of the beam, intrinsic energy resolution of the detector, electronic noise and broadening due to finite thickness of the foil. With current energy resolution we have not observed any change in the energy distribution with change of the radial position of the foil. The low energy tail observed in the peak is probably due to propagation of protons during rising of the RF voltage at the beginning of the RFQ pulse. The energy calibration of the RS was done by comparison with TOF results. The spectra are also compared with TRACK Monte Carlo simulations [6]. The various broad peaks observed in the low-energy part of the spectrum of the non-optimal RFQ power are probably due to beams which are not fully synchronised with the RF field. At the moment these peaks are not fully explained by the simulations. These measurements along with the ones done with the standard D-plate instrumentations showed that the optimum RF power for transporting and acceleration of protons through RFQ is above 55 kW.

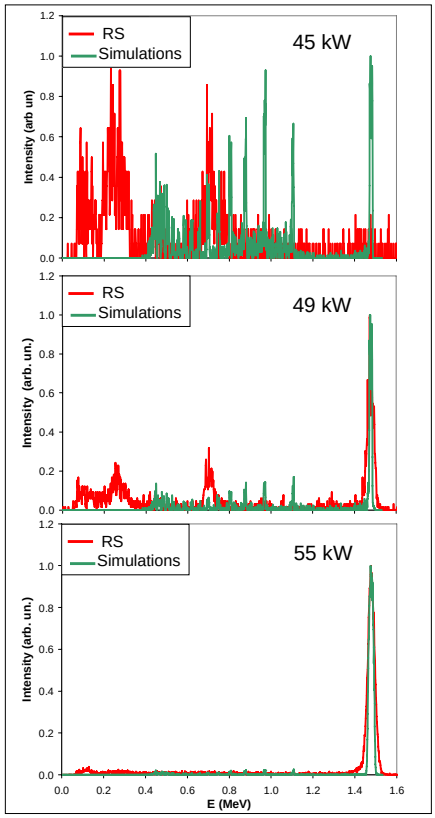


Figure 3: Evolution of proton energy spectrum for the turned off and detuned PSM resonators with increase of the RFQ RF power.

The RS monitor is useful for phasing of individual cavities. For example, energy as a function of the voltage of the first cavity (HWR1) is shown in Fig. 4a. The other five cavities were turned off and detuned. The effect of the cavity accelerating voltage and phase is clearly seen. The energy values determined by the two methods are consistent. As a result of the phasing procedure the synchronous phase of the resonator can be determined. The results are compared with simulation allowing one to

calibrate the resonator voltage. Typically the resonator voltages obtained in the phasing measurements differ by 20-40 % from the initial estimations. Due to the sensitivity of the RS spectra to the bunch energy width the bunching effects of the resonators can be studied (Fig. 4b). The intrinsic energy resolution and effects of scattering on the gold foil were not taken into account in the simulation of the beam energy spread.

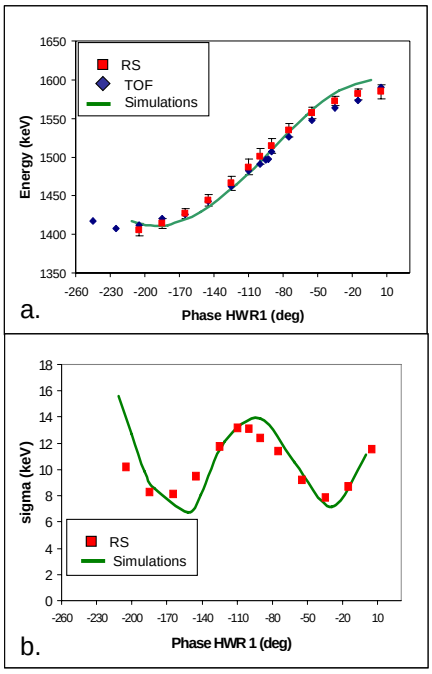


Figure 4: a: Proton energy as a function of HWR1 phase, as determined by TOF and RS b: Gaussian fit width (sigma) of the RS peak as a function of the HWR1 phase. Results are compared to the TRACK simulations.

After performing phasing of individual cavities the parameters of the whole accelerating module can be determined. In the example presented in Fig. 5 the four of the six HWR were operational. The first two resonators were used for bunching of the beam and the other ones for further acceleration. The RFQ power was set to 56 kW. The voltages and phases of the three first resonators were

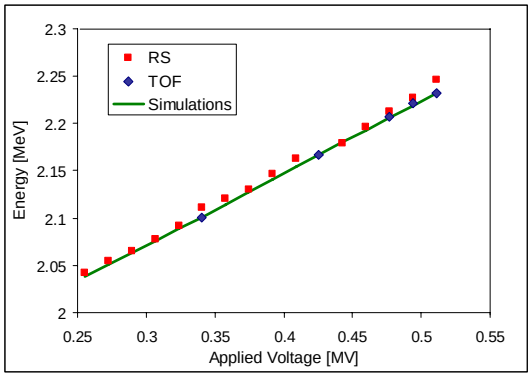


Figure 5: Proton energy as a function of HWR4 voltage, while the three previous resonators also operated.

set to 150 kV and -95°, set to 85 kV and 0°, set to 446 kV and 20° respectively. The phase of the forth HWR was set to -30° and its voltage was increased gradually.

Stable beam operation with all six cavities has not yet been achieved. It became evident that it is necessary to further perform conditioning of the cavities and introduce improvements of their control system. This work is currently in progress.

SUMMARY AND OUTLOOK

The commissioning of Phase I of the SARAF accelerator is on-going. A low duty cycle 3 mA Proton beam has been bunched and accelerated by the RFQ, and consequently re-bunched and accelerated by the PSM up to 2.2 MeV. Monitoring of energy spectra of the scattered protons proved to be a useful tool for tuning of the RFQ and the six superconductive resonators. Prompt determination of the beam energy allows one to perform a fast tune. Details on the energy spread of the beam also can be obtained. The technique is limited to the particle energies corresponding to the stopping range in Silicon smaller than a detector thickness.

Further improvements in the future will include: introduction of an alpha source for in-situ detector calibration, reduction of electronic noise, obtaining information on bunch time distribution using a small diamond detector and fast electronics.

Finalizing the proton and deuteron beam commissioning through the entire Phase I is foreseen for the summer of 2009.

REFERENCES

[1] A. Nagler et al., “Status of the SARAF Project”, LINAC'06, Knoxville, August 2006, MOP054, p. 168 (2006).

[2] I. Mardor et al., “Status of the SARAF CW 40 MeV Proton/Deuteron Accelerator", PAC May 4-9, 2009, Vancouver, Canada, FR5REP087

[3] C. Piel et al., "Phase 1 Commissioning Status of the 40 MeV Proton/Deuteron Accelerator SARAF", EPAC'08, Genoa, June 2008, THPP038, p. 3452 (2008).

[4] I. Mardor et al., "The Beam Halo Monitor of SARAF", LINAC'06, Knoxville, August 2006, TUP010, p. 265 (2006).

[5] M. Pekeler et al., “Development of a Superconducting RF Module for Acceleration of Protons and Deuterons at Very Low Energy”, LINAC'06, Knoxville, August 2006, TUP034, p. 321 (2006).

[6] J. Rodnizki et el., "Lattice Beam Dynamics Study at Low β For SARAF/EURISOL Driver 40/60 MeV 4 mA d&p Superconducting Linac", HB2008, Knoxville, August 2008, WGB15 (2008).

DETECTORS FOR SLOWLY EXTRACTED IONS IN HIRFL-CSR*

R.S. Mao#, J.W. Xia, T.C. Zhao, Z.G. Xu, B. Tang, Z.G. Hu, J.X. Wu, H.S. Xu, G.Q. Xiao, Y.J. Yuan, J.H. Zheng, IMP, Lanzhou, China

Abstract

This paper gives the detectors used for slowly extracted heavy ions from CSR. The beam profiles are measured with viewing screens and anode-striped ion-chambers. The currents are determined with scintillators and ion-chambers. The signal processing system and the measurement results are also presented.

INTRODUCTION

HIRFL-CSR [1] is a double cooling-storage-ring system with a main ring (CSRm) and an experimental ring (CSRe). The beam is accumulated, cooled and accelerated in CSRm, and will be extracted in slow extraction [2] mode for many external-target experiments. The ions can be accelerated to 200~1100MeV/u and the number of stored ions ranges between 10^6 and 10^9. The spill length will be several seconds (actually during the CSR commissioning it was always set to three seconds), so the beam current is about 106 ~ 109pps. In this range, the typical detectors such as the ionization chamber (IC), the scintillator, the diamond monitor or secondary electron monitor (SEM) can be used for beam intensity measurements [3], the gas filled grids and viewing screens for beam profile measurements. These devices are commonly used for many years in GSI, CERN, etc [4][5]. In HIRFL-CSR, the anode-striped ion-chamber is installed to measure the beam profile, and the scintillation screen with CCD to measure beam profile directly for high intensity beam. For beam intensity measurement (lower than 10^9pps), the use of the IC together with scitillator filled the measurement requirements. For the convenience of the commissioning, we installed the scintillator detectors as beam loss monitors on the upside, downside, left side and right side of the beam tube to monitor the beam transmission status and help to judge the beam direction. In Jan. 2008, the beam extracted by RF-knock out method was measured for the first time. The detectors and some results are given below.

IONIZATION CHAMBER AND SCINTILATOR

In the beam line, the IC and scintillator are installed together(similar to the detector of GSI [4]) into the pockets [6] with 60mm×60mm entrance window (50μm stainless-steel), shown in Fig.1. To prevent the detector from radiation damage, it will be pulled in only if it is necessary. The anode-stripped ion-chamber is chosen so that the beam intensity and profile could be measured simultaneously. The plate of the anode and the cathode are made of ultra-thin printed circuit board with the thickness of 0.1mm. The schematic of detector is shown in Fig. 2.

*Work supported by the center government of China and NSFC

#maorsh@impcas.ac.cn

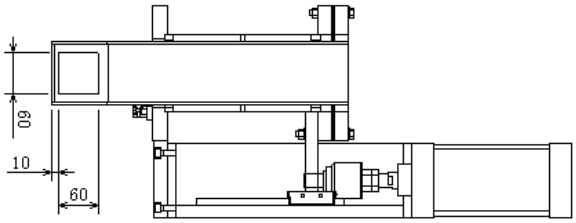


Figure 1: Detector pockets driven by pneumatics (CF150).

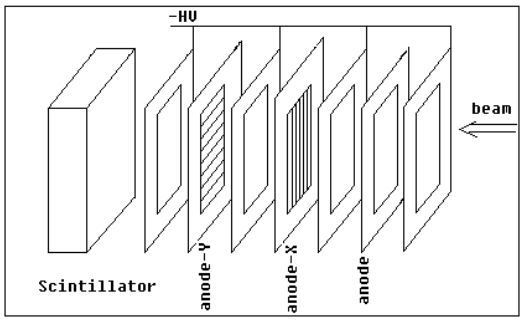


Figure 2: Structure of detector in pocket.

Taking one detector in the beam line as an example, the width of the anode strip is 2.7mm and the interval is 0.3mm, the space between the two plates is 3mm. The sensitive area is 45mm*45mm. At present, the detector gas is air (except one detector filled with nitrogen), but in the future it will be nitrogen for all. The voltage is about -10V~-400V and can be adjusted during measurement process. The current produced by the strip or whole anode of IC is converted to voltage signal using I/V converter and then sampled directly with NI-PXI-6133 A/D card [7]. The real time beam profiles or intensity can be given using the LabVIEW. One of the results is shown in Fig.3 (one strip signal is lost because of the broken cable).

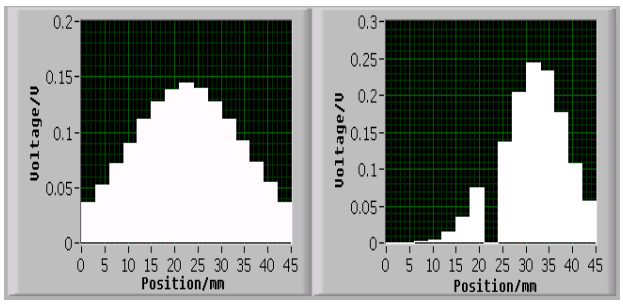


Figure 3: Beam profile left: profile x, right: profile y.

The detector at the experiment terminal is installed in air without pocket, the structure is similar to which installed in beam line, except the sensitive area, the width and the number of the anode strip.

For convenience and low cost, the scintillator is manufactured with the CSI (T1) by IMP. The data acquisition system is based on the NI-PXI-6602 and the LabVIEW software. One of the measurement results of the spill is shown in Fig.4. From that we can see clearly that the frequency of substructure is 50Hz.

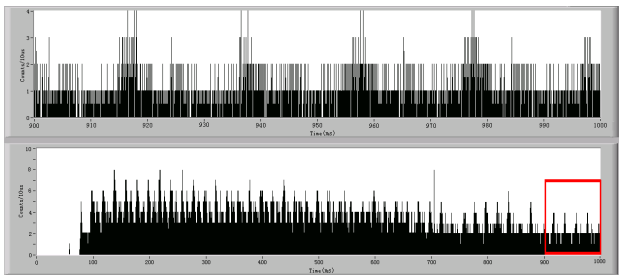


Figure 4: Spill structure (zoomed and total) measured by scintilator (sampling rate is 100 kHz, C6+, 200 MeV/u).

BEAM LOSS MONITOR

At the first commissioning of slow extraction, we installed four scintilators to measure the beam losses. The detectors were located at up, down, left and right position of beam tube, at the point where the pipe is narrow. Normally the counts from four channels will be very low and nearly equal if the beam is at the center of beam tube. Figure 5 shows the counts from the detectors.

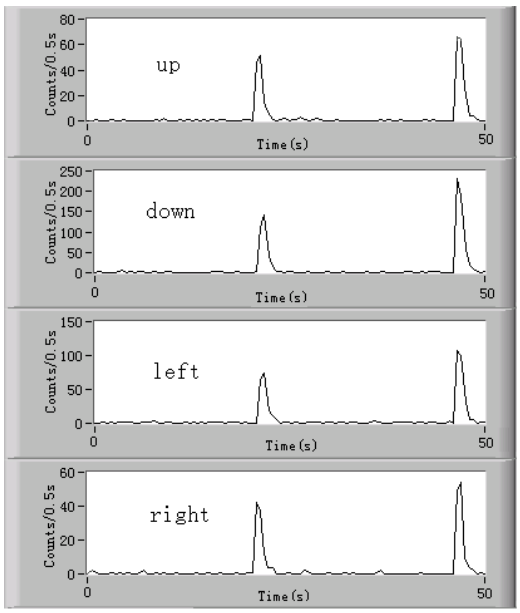


Figure 5: Counts from four scintilators.

VIEWING SCREEN

The chromolux screen with a CCD camera for observation of the light spots is a very simple, reliable profile monitor. Figure 6 is one of the measurement results with slow extraction.

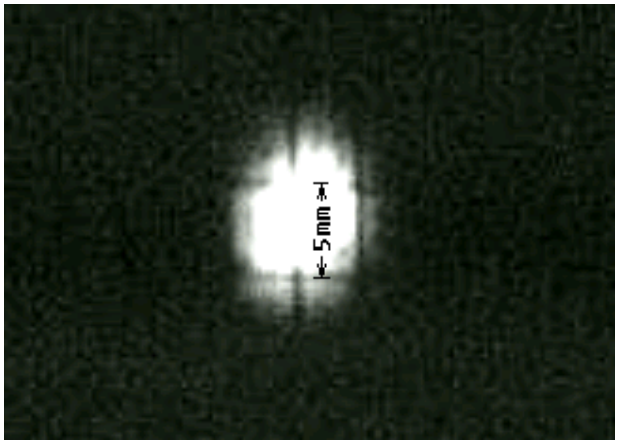


Figure 6: Beam profile (C6+, 200MeV/u).

NEXT STEPS OF DEVELOPMENT

Calibration has to be done for high precision measurement. MWPC for profile measurement of weak beam, such as secondary ions, is still under development. The current-to-frequency converter now is available, and will be used in IC signal processing system soon.

ACKNOWLEGMENT

The authors want to thank all the colleagues at GSI who gave us valuable information and contributed to our work.

REFERENCES

[1] J.W. Xia, et al, “Construction and commissioning of the HIRFL-CSR”, APAC’04, Indore, India, p.534;
[2] Y.J. Yuan, et al, “Design of slow extraction for HIRFL-CSR”, APAC’01, Beijing, China, p.484;
[3] Peter Strehl, “Beam instrumentation and diagnostics”, Springer, 2006;
[4] P. Fork, T. Hoffmann, A. Peters, “Detectors for slowly extracted heavy ions at the GSI facility”, DIPAC’97, Frascati, Italy, p.165.
[5] Peter Fork, “Lecture notes on beam instrumentation and diagnostics”, Joint University Accelerator School, January – March 2008.
[6] O. Klepper, et al, “First steps towards radioactive beams in the experimental storage ring at GSI”, NIMB, Vol70, Issue 1-4, p.427.
[7] http://www.ni.com.

DESIGN REPORT OF A NON–DESTRUCTIVE EMITTANCE INSTRUMENT FOR RUTHERFORD APPLETON LABORATORY'S FRONT END TEST STAND FETS

C. Gabor*, STFC, ASTeC, Rutherford Appleton Laboratory (RAL), OX11 0QX, UK
A.P. Letchford, STFC, ISIS, RAL, OX11 0QX, UK
J.K. Pozimski, STFC, ISIS, RAL, OX11 0QX, UK and
Imperial College London, High Energy Physics Department, SW7 2AZ, UK

Abstract

The RAL front end FETS is currently under construction to demonstrate a fast chopped, high power H^- ion beam at 3 MeV of up to 18 kW. Therefore emittance instruments should use photo detachment because mechanical parts could be affected by heat loading. This emittance instrument uses a dipole to separate negative ions from produced neutrals and a scintillator to measure particle distribution and deflection. This means a careful design of the diagnostic instrument according to other beam parameters and existing focusing elements because reasonable results require high enough phase space advance. A conceptual design layout will be presented considering the current status of the MEBT simulations along with a discussion

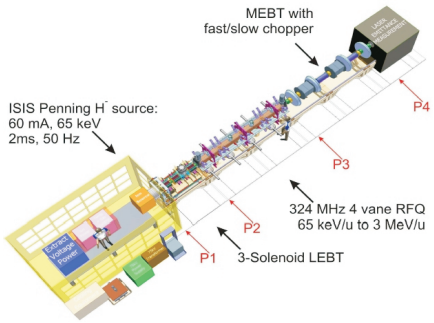


Figure 1: Overview of the FETS set up. The main elements are a Penning type ion source, 3 solenoid LEBT, RFQ and the MEBT consisting of quadrupoles, four buncher cavities and the chopper. The emittance diagnostic and beamdump are located at the end of the beamline.

INTRODUCTION

In order to contribute to the development of high power proton accelerators in the MW range, to prepare the way for an ISIS upgrade and to contribute to the UK design effort on neutrino factories [1, 2] a Front End Test Stand FETS (see Fig. 1) is being constructed at the Rutherford Appleton Laboratory RAL in the UK [3]. The aim of FETS is to demonstrate the production of a 50 to 60 mA, 2 ms, 50 pps chopped beam at 3 MeV with sufficient beam quality. This means in particular very high demands for the chopper unit which provides a fast unit for short rise time and a slow chopper for the long pulse duration. The chopper itself is integrated in a MEBT which firstly has to match the RFQ output to the chopper and secondly to a DTL further downstream both in longitudinal and transverse phase space. The MEBT design is still under discussion [4] and all design schemes are confined by constraints given by a future LINAC but the actual end of the FETS beamline will consist of an emittance instrument and two beam dumps ("diagnostic beam line").

Thus, first studies to investigate changes to adapt the beam parameters to the demands of the test facility FETS are presented. A brief introduction of the applied diagnostics and main parameters of the bending dipole are also provided.

* christoph.gabor@stfc.ac.uk

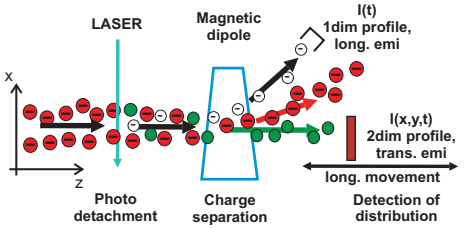


Figure 2: Basic principle of photo detachment ion beam diagnostics The H^- ions get neutralized by laser light. The diagnostics is in general a three stage process: detachment, charge separation and detector.

LASER BASED ION BEAM DIAGNOSTICS

The basic principle of the implemented Photo Detachment Emittance Instrument (PD–EMI) is illustrated in Fig. 2. Compared to more common devices like a slit–grid (harp) and pepperpot scanner the laser acts like a slit whereas the particle detector takes the place of a pepperpot device, therefore the transfer function of PD–EMI is a so called slit–point mapping. In Fig. 2 the laser is parallel to the x–axis therefore the yy' emittance can be measured in a direct way by gathering angle profiles for each y–position of the laser [5, 6].

According to this idea the laser has to rotate to access information of the xx' plane. Previous studies have shown that this would be possible but means a very complicated magnetic design: since the gap of the dipole has to provide enough clearance for a second set of mirror the fringe field can be significant and, even without considering the poor field homogeneity, could cause avoidable beam perturbations. Therefore, in [7] another possibility is presented where a longitudinally movable detector in combination with an image reconstruction method (Maximum Entropy,

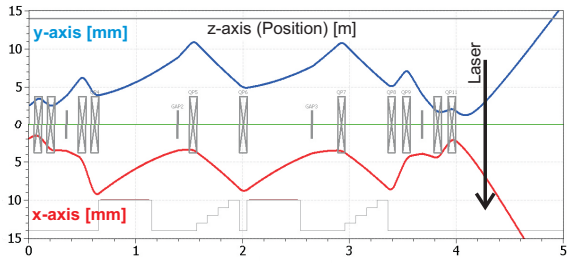


Figure 3: Envelope in x and y direction. The MEBT matches the beam to a future DTL. The possible laser position is marked, at ≈ 4.8 m would be end of diagnostic section followed by beamdump(s).

also called MaxEnt [8]) are able to produce good results of the missing plane, as long as the phase advance, i.e. the differences of the spatial distributions are big enough. The emittance computation is based on several intensity profiles with their transformation matrix $\mathbf{R}$ back to the measurement point. First applications in accelerator science are published in [9, 10] and more recently in [11].

MEBT WITH DIAGNOSTIC DIPOLE

The MEBT is described in [4], the envelope is shown in Fig. 3 matching a DTL (all simulations have been performed with Tracewin [12]). Typically, one plane is convergent and vice versa. Due to a horizontal bending magnet and vertical scanning of the laser the horizontal plane should have a waist to provide a large enough phase advance [7]. The change of the field strength of the last four quadrupoles typically is enough to prepare the ion beam for diagnosis as long as aperture and field strength offer sufficient flexibility.

Important design criteria for the dipole are the reference length which is restricted due to a lack of strong focusing, growing beam size[1] and a long focus. The latter would reduce the phase advance affecting the MaxEnt. The deflection angle and radius are limited by a sufficient returning yoke interfering with the overall length. But the main purpose is to separate three different kind of species: straight forward a beam dump either terminates the undeflected ion beam or neutrals produced by gas stripping (H^0_{RGI}) further upstream. Since the laser scans the beam somewhere in the first half of the magnet the neutrals produced by photo detachment (H^0_{PD}) get a kick and are separated via the following drift from H^- and H^0_{RGI}. All beamlets have to be fully separated to go to either the beamdump or the detector head. For the parameters given in Tab. 1 a max. beam(pipe) of $R_{max.} = \pm 30$ mm is assumed. That gives some safety margin providing more flexibility for other beam conditions (the relatively large gap height should be seen in the same context). This is equivalent with the z_0 position mentioned in Tab. 1 and means the nearest possibility to mount the detector head. But the detector itself might move closer to the photo detachment. Regarding the separation it turns out that the best location for the laser scan is in general close to 30% of total deflection, here at ≈18°. By varying the last four quads of the beamline a mild waist in one plane and a slight divergent beam in the other plane could be achieved (Fig. 4). Compared to Fig. 3 the two transverse planes are swapped to give the waist in the horizontal plane. This is not ideal but technical possible; an alternative is to add more quadrupole. But the latter, as well changing the aperture, is avoided in order to reduce changes to the present MEBT scheme. The field strengths are reduced (not more than 25 T/m) but it could be an issue that the combined PM and EM quadrupoles do not offer enough variability in their field strength [13].

[1] Typical dipole focusing should be avoided since the element's purpose is diagnosis and not beam transportation and it might complicate a point–to–point transformation.

Table 1: The main parameters of the sector dipole. At the moment no gradient or edge focusing is assumed.

Parameter	
Gap height g	60 mm
Pole width	200 mm
Magnetic field, $H^-_{3\,\mathrm{MeV}}$	500.5 mT
Deflection angle α_{H^-}	60°
Bending radius R	0.5 m
Reference path length $l_{arc,\,H^-}$	523 mm
Deflection angle α_{PD}	≈18°
Reference path length $l_{arc,\,\mathrm{laser}}$	164 mm
Drift, straight $d_{H_{PD}}$, z_0 position	360 mm
Total drift, straight $d_{H^0_{\mathrm{RGI}}}$	549 mm

DISCUSSION

Here, in this example the xx' emittance is reconstructed using MemSys5 [14]. The assumed measurement point is exactly at the laser position. The backward transformation can then be described as a pure drift. But this is not mandatory, the phase advance could be also provided by a quadrupole scan or a combination of both. Only the measurement point should be adapted. The assumed example

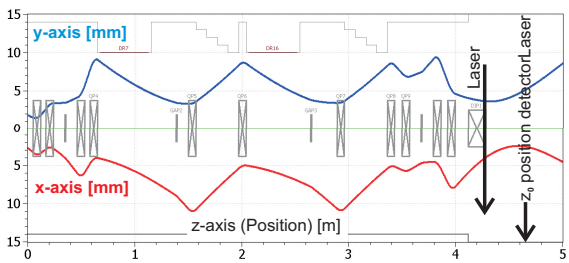


Figure 4: Envelope with adjusted quadrupoles to transport beam through sector magnet and creating a waist in horizontal plane, end of the diagnostic magnet at ≈ 4.8 m.

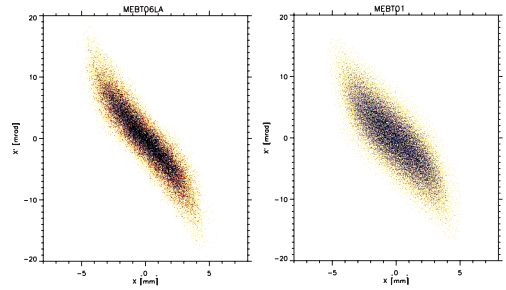


Figure 5: Comparison between original distribution (left) and reconstructed phase space pattern (right) based on MaxEnt.

illustratives some interesting aspects: if the beam path for backward transfromation consists only of the drift of H^{o}_{PD}, the transfer matrix cannot be affected by any other non–linear effects. The angular resolution is given by the drift length of H^{o}_{PD} and spatial resolution of the detector and since the variation of the distance it also changes the resolution. Assuming to transport the beam further upstream back through the dipole the distribution would only see hone fringe field. The result of the investigated example is shown in Fig. 5 and Fig. 6. Five profiles are extracted, at $z_n = 100, 200\,275\,375\,500$ mm, all given in respect to the laser position. This means that the detector has to move from its origin position $z_0 = +360$ mm -160 mm inwards and 240 mm outwards. The total range of 400 mm should be feasible but the nearest position to the laser is close to limit because the H^- beam can either affect the measurement or destroy the detector. Both the emittance pattern as well the fractional emittance show very good agreement between original beam and reconstruction, i.e. the general beam optics and parameters are suitable for MaxEnt. The constant bias in rms–emittance in Fig. 6 is caused by different numbers of particles phase space "pixels".

SUMMARY & OUTLOOK

The paper investigates how good the existing MEBT scheme can match a beam in a diagnostic magnet. It is possible to obtain a beam with a waist in one transverse plane as necessary. Enough phase advance can provided just by a waist, more general a combination of quad–scan and less movable detector are more likely. Some thoughts and parameters important for the design of the sector magnet are discussed. Further studies are important to include fringe field effects and the general influence of the sector magnet compared to an undisturbed beam. Transport simulations regarding the variable field strength of the quadrupoles are also planned, at least for the last four of the MEBT.

ACKNOWLEDGEMENT

The author wants to thank D.S. Sivia for continuous help with problems around MaxEnt and implementing the "emittance application" to MemSys5. C. Plostinar kindly helped with all issues related to the MEBT and particle tracking with Tracewin.

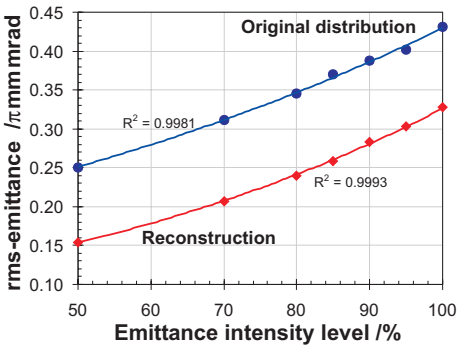


Figure 6: Comparison of the fractional emittance for several intensity levels. The difference is very likely ascribed different numerical integrations (different number of particles).

REFERENCES

[1] T.R. Edgecock, 6th Int. Workshop Neutrino Factories & Superbeams (NuFact04), July/August 2004, Osaka, Japan

[2] Neutron News, vol. 15 (2004), ISSN 1044-8632. See also http://www.isis.rl.ac.uk/

[3] A.P. Letchford et al., "Status of the RAL Front End Test Stand", LINAC 2008, MOP009

[4] C. Plostinar et al., "Front End MEBT Studies for a high power Proton Accelerator", PAC 2009, FR5REP085

[5] C. Gabor, "Untersuchungen zur zerstörungsfreien Emittanzmessung an einem Testaufbau für negative Ionen", Goethe–Universität Frankfurt, IAP, PhD–thesis, 2007

[6] C. Gabor, D.A. Lee, J.K. Pozimski, A.P. Letchford, "Laser–Based Beam Diagnostics for the RAL Front End Test Stand FETS", 11th Int. Conf. on PNNIB, AIP Conf. Proc. 925, p.183, 2006

[7] C. Gabor et al., "Emittance Measurement Instrument for a high Brilliance H^- ion beam", LINAC 2008, TUP084

[8] D.S. Sivia, J. Skilling, "Data Analysis — A Bayesian Tutorial", 2nd edition, Oxford University Press, 2006

[9] G.N. Minerbo, "MENT: A Maximum Entropy Algorithm for Reconstructing a source from Projection Data", Computer Graphics and Image Processing, 10 (1979), pp. 48. . . 68

[10] U. Rohrer, "Introduction of 2–Dimensional Beam Tomography for Monitoring Transverse Beam Emittance at SIN", PSI Ann. Rep 1982, NL 5–6

[11] F. Loehl, "Measurements of the Transverse Emittance at the VUV–FEL", DESY-THESIS 2005-014 (TESLA-FEL 2005-03),Hamburg, 1979

[12] Didier Uriot, CEA, France, didier.uriot@cea.fr, http://irfu.cea.fr/Sacm/logiciels/index3.php

[13] C. Plostinar et al. "A Hybrid Quadrupole Design for the RAL Front End Test Stand FETS", WEPC157, EPAC 2008,

[14] Maximum Entropy Data Consultants Ltd., J. Skilling, S. Gull, "MemSys 5"

MEASUREMENT OF ELECTRON CLOUD DENSITY WITH MICROWAVES IN THE FERMILAB MAIN INJECTOR*

J. Crisp#, N. Eddy, I. Kourbanis, K. Seiya, B. Zwaska, FNAL, Batavia, IL 60510, U.S.A.
S. De Santis, LBNL, Berkeley, CA 94720, U.S.A.

Abstract

Electron cloud density in the Fermilab Main Injector was measured by observing microwave transmission along the vacuum tube. Presence of the electron cloud reduces the velocity of the microwave signal. Both frequency and time domain methods reveal relative cloud density and time evolution. The effect of beam time structure is clearly evident. The accelerator magnetic field effects the distribution of electrons making it difficult to estimate density.

INTRODUCTION

The Main Injector is a synchrotron which accelerates 53 MHz proton bunches from 8 GeV to either 120 GeV or 150 GeV. It has a revolution frequency of 90 kHz. While the Main Injector currently provides over 300 kW of beam power, Project X [1] requires up to 2.1 MW . There is concern about electron cloud instabilities at these beam currents. It is necessary to rely on simulations or models to predict this effect. In this regard, it is prudent to compare measurements of electron cloud development with simulations before extrapolating to higher beam currents.

An electron cloud can be created and trapped in the electromagnetic fields originating from the positively charged proton beam. Depending on the emissivity of the surface and the energy of the electrons striking it, the charge density can increase until the beam fields are neutralized. With the increased beam intensities anticipated, the electron density could adversely affect operation.

Presence of the electron cloud can be measured by observing the propagation of microwaves along the beam pipe [2]. For a uniform distribution of electrons, the phase shift through length L can be estimated as shown below [3].

$$\phi \approx \frac{L}{c}\frac{\omega_p^2}{2\sqrt{\omega^2-\omega_c^2}}, \quad \omega_p \approx 2\pi\, 9\sqrt{\frac{N_e}{m^3}}\ \ plasma\ \ frequency \quad (1)$$

$$\omega_c = beam\ \ pipe\ \ cut-off\ \ frequency$$

The time response of the electron cloud is observed to be faster than the batch structure (~100 nsec). Thus, the phase shift will be modulated with the electron cloud density which in turn follows changes in beam current each turn. The variation in beam current is provided by the gaps required to accommodate injection and extraction kicker rise times. The rotation frequency of 90 kHz results in the largest component in the beam current spectrum. For a phase modulation of ±β radians the sideband amplitude relative to the carrier will be β/2. The amplitude of these sidebands reveals the electron cloud density.

EXPERIMENTAL SETUP

The measurement makes use of existing Main Injector Beam Position Monitors (BPMs) which are 25 cm long shorted stripline pickups. The BPMs and the beam pipe have a 50x120 mm elliptical aperture. BPMs are located inside the downstream end of each quadrupole magnet. The BPMs are connected as shown in Fig. 1 to drive the TE_{11} mode which has the lowest cut-off frequency (1.484 GHz). It is necessary to remove the BPMs from operation which limits acceptable locations.

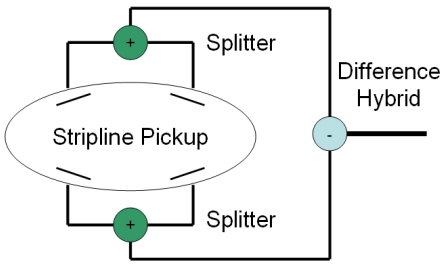


Figure 1: Connections at BPM pickups are configured to couple to the TE_{11} mode and cancel the common beam signal. The coupling was measured at -30 dB through both pickups and 17 m of pipe.

The experimental setup is shown in Fig. 2. An Agilent E4428C signal generator provides the source which is amplified by a mini-circuits ZHL-10W-2G power amplifier. To first order, the mixer detects phase modulation and rejects amplitude modulation. Measurements have been performed at two locations in the Fermilab Main Injector.

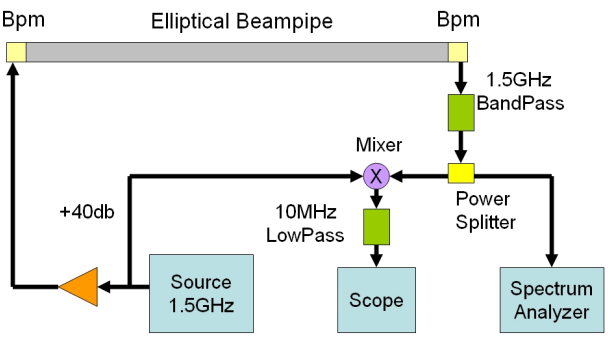


Figure 2: Basic experimental setup.

* Operated by Fermi Research Alliance, LLC under Contract No. DE-AC02-07CH11359 with the United States Department of Energy
#crisp@fnal.gov

MI60 Bend Region

The first two BPMs selected (Q532, 601) were located in a bend region near MI60 service building. They were 12.6 m apart and separated by two dipole magnets and their associated quadrupole. The bend field is 1.4 Tesla at 120 GeV. MI60 has the advantage of high quality ½" heliax cables available to transport the signals to/from the service building with good transmission.

The total transmission including the amplifier, cables, stripline pickups, and the beam pipe is shown in Fig. 3 (red). The peak at 1.538 GHz was chosen for good transmission and good sensitivity. The electron cloud induced phase shift increases near cut-off.

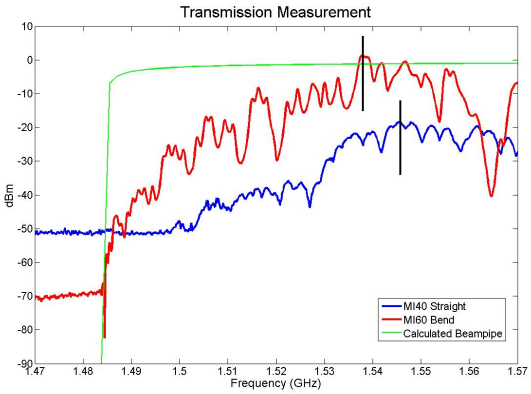


Figure 3: Transmission from MI60 Bend (red), MI40 Straight (blue), and Calculated transmission for our beam pipe. The lines denote the carrier frequency chosen at each location. Measurement includes amp, cables, pickups, and beam pipe.

MI40 Straight Section

For comparison, two BPMs in a dipole free straight section (Q403, 404) were selected near service building MI40. They were separated by 17.6m and a quadrupole magnet. Unfortunately, only RG8 foam cables were available at this location resulting in lower transmission. To drive a larger signal into the beam pipe and mitigate coupling between the cables as well as loss, the power amplifier was moved into the tunnel. The total transmission for this location is shown in Fig. 3 (blue). The carrier frequency of 1.545 GHz provided the best transmission at this location.

MEASUREMENTS

Traditionally, the sensitivity of the electron cloud measurements have been limited by reduced coupling with the beam pipe provided by button style BPMs. The Fermilab Main Injector stripline BPMs provide strong coupling resulting in improved sensitivity. This allows a direct time domain measurement of the phase modulation revealing growth and decay rate of the electron density. Measurements in both the frequency and time domain were taken and compared.

Frequency Domain

One difficulty is the presence of direct beam induced signals in the detector. Harmonics of the 90 kHz revolution frequency are observed above the 1.484 GHz cut-off frequency of the beam pipe. This was not expected for the 1.1nsec sigma gaussian bunches. The carrier frequency is chosen to place the 90 kHz electron cloud induced sidebands between the direct beam harmonics, Fig. 4. The -38 dbc amplitude at MI60 suggests 90 kHz phase modulation of about 50 mrad and at MI40 -65 dbc corresponds to 2.2 mrad peak to peak.

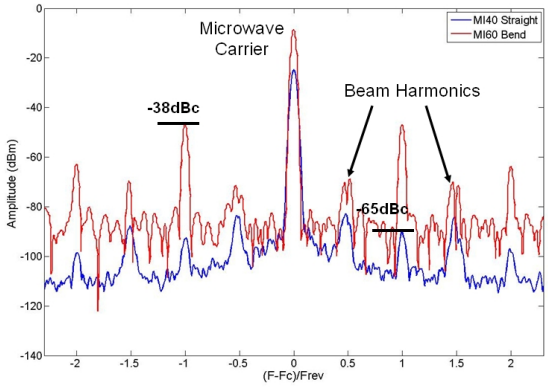


Figure 4: Spectrum of transmitted microwave signal for MI60-red and MI40-blue.

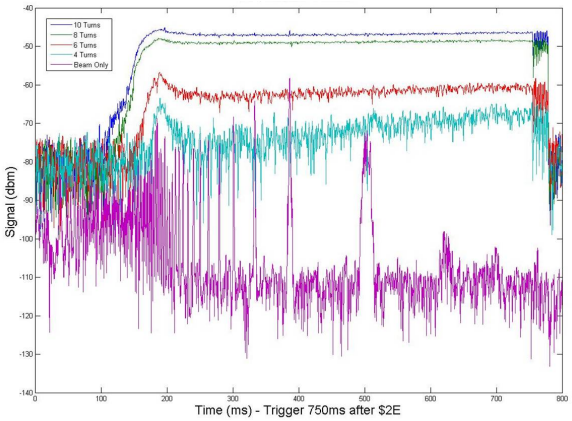


Figure 5: Zero Span Data for MI60. Bunch intensity is about 1e10 for each Booster turn.

The frequencies of the electron cloud induced sidebands are determined by the fixed carrier and are essentially constant throughout the acceleration cycle. However, the direct beam induced rotation harmonics at 17000 times the rotation frequency sweep through the microwave carrier as the beam is accelerated. Figure 5 shows the amplitude at one of the electron cloud induced sidebands from the start of ramp until extraction. The measurement was done by placing the spectrum analyzer in zero-span mode. The lowest trace was taken with no microwave signal and simply shows the direct beam induced harmonics sweeping through the detected frequency. The other traces show how the amplitude of the electron cloud induced sidebands change through the

acceleration cycle at 4 different beam intensities. The peak observed just before 200 msec corresponds to transition, when the bunches are short and have the highest peak current. The last 50 msec of beam is affected by a 'bunch rotation' process that modulates the peak bunch current.

Time Domain

For the time domain measurement, the mixer output is collected with a deep memory scope. At MI60, the scope sampled at 500 MS/s and the data was averaged for 100 turns. At MI40, the sampling rate was reduced to 100 MS/s allowing the data to be averaged over 1700 turns. The direct beam harmonics are larger than the electron cloud induced sidebands. However, they are not correlated with the microwave carrier and thus average away in the time domain, Fig. 6.

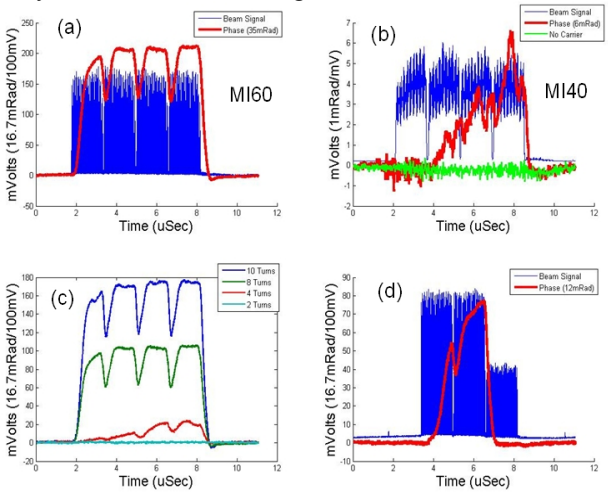


Figure 6: Direct Phase Shift measured at MI60 (a,c,d) for different batch structures and intensities and MI40 (b). Bunch intensity (blue) is 1e10 for each Booster turn.

The first set of measurements where done at MI60 and are complicated by passing through two main bending magnets and one quadrupole, Fig. 6(a,c,d). In Fig. 6(a), the 35mrad phase shift is approximately a square wave with 50% duty cycle and would produce a 45 mrad peak to peak phase shift at 90 kHz. This compares to 50 mrad measured in the frequency domain.

The test was repeated at MI40 through 17.6m of beam pipe, one quadrupole, and no bending magnets, Fig. 6(b). The 3 batch wide, 5 mrad peak 'clipped sawtooth' phase shift of Figure 6(b) would produce a 3.5 mrad peak to peak phase shift at 90 kHz. This compares to 2.2 mrad measured in the frequency domain.

It is believed the strong vertical bend field at MI60 traps the electron cloud in a narrow column centred on the beam [4]. This results in larger electron densities and associated phase shifts. The phase shift measured at MI40 without the bend field is 10 times smaller for the same beam current even with the longer beam pipe.

The development of the electron cloud can clearly be seen with a non-linear dependence on beam intensity Figure 6(c). Apparently, electrons left from previous batches seed the growth of subsequent batches allowing the electron density to reach equilibrium faster. It is interesting that the half intensity batch of Figure 6(d) is unable to sustain the electron cloud. Electron density rise times are 100-200 nsec at typical Main Injector intensities. At lower intensities it can take several μsec.

SUMMARY

From the basic theory, the microwave delay or phase shift is proportional to the electron cloud density. The observed phase shifts are not linearly proportional to beam intensity. For larger intensities, an equilibrium state is seen in the direct phase measurements in the dipole region. Due to a number of factors, the direct phase shift is significantly smaller in the field free straight section but no equilibrium is observed. The results of the direct phase shift in the time domain are in good agreement with the phase modulated sideband amplitude in the frequency domain.

An ideal mixer detects phase modulation and rejects amplitude modulation. A few percent asymmetry was observed between the upper and lower sidebands. This could be caused by a small amount of amplitude modulation suggesting the electrons absorb some of the energy attenuating the microwave carrier.

At this time, only the observed phase shift is reported. To infer the electron cloud density, requires understanding the effects of the magnetic fields and the non-uniform distribution of the electrons which develop. The direct phase data measured within a machine turn reveals how the electron cloud grows and decays. The relative changes observed can be directly compared with simulation results of this process [4, 5]. Evaluating simulations at the present intensities will allow extrapolating to the anticipated intensities to determine what electron cloud mitigation is necessary.

REFERENCES

[1] I. Kourbanis et al. "Current and Future High Power Operation of the Fermilab Main Injector", PAC09 proceedings.

[2] F. Caspers et al. "The CERN SPS Experiment on Microwave Transmission Through the Beam Pipe" PAC05 proceedings.

[3] J. Byrd, S. De Santis, K Sonnad, M. Pivi, "Measurements of the Propagation of EM Waves Through the Vacuum Chamber of the PEP-II Low Energy Ring For Beam Diagnostics", PAC07 Albuquerque, New Mexico, (2007).

[4] M. Furman et al., "Status of Electron-Cloud Build-Up Simulations for the Main Injector", PAC09 proceedings.

[5] P. Lebrun, "Microwave Transmission through the Electron Cloud at the Fermilab Main Injector: Simulation and Comparison with Experiment," PAC09 proceedings.

BEAM HALO MONITOR USING DIAMOND DETECTOR FOR INTERLOCK SENSOR AT XFEL/SPring-8

H. Aoyagi#, T. Bizen, K. Fukami, N. Nariyama, JASRI/SPring-8, Hyogo, Japan
Y. Asano, T. Itoga, H. Kitamura, T. Tanaka, RIKEN/SPring-8, Hyogo, Japan

Abstract

An electron beam halo monitor has been developed in order to protect undulator permanent magnets against radiation damage for the X-ray free electron laser facility at SPring-8 (XFEL/SPring-8). The halo monitor will be installed at the upstream of the undulator and detect the electron beam that might hit the undulator magnets. Diamond detector, which operates in photoconductive mode, is good candidate for electron beam sensor, because diamond has excellent physical properties, such as, high radiation hardness, high insulation resistance and sufficient heat resistance. Pulse-by-pulse measurement suppresses the background noise efficiently, especially in the facilities having extremely high intense beam with low repetition rate, such as XFELs. The feasibility study of this monitor was performed at the SPring-8 compact SASE source (SCSS) test accelerator for XFEL/SPring-8. We observed the unipolar pulse signal with the pulse length of 0.4 nsec FWHM. The beam profiles of the halo can be also measured by scanning the sensor of this monitor.

INTRODUCTION

The XFEL machine is composed of a low emittance electron beam injector, a high gradient C-band accelerator, and in-vacuum undulators. The charge of electron beam is designed to be 1 nC/pulse (60 Hz). Even if the undulator permanent magnets are irradiated continuously with the small part of the electron beam halo, whose energy is 8 GeV or less, the magnetic field is to be degraded [1]. The intensity of the halo part of the electron beam must be monitored during machine operation, and an electron injector must be halted immediately, when the electron intensity exceeds a threshold. The position of core part of the electron beam is controlled accurately, so usually the magnets are not to be irradiated with the core part directly. The halo part of the beam, however, may be broadened by the slight changes of the beam conditions, and may hit the magnets. Therefore, we are considering the machine protection interlock system, which detects overdose of electrons and send an alarm signal to stop the beam operation.

We have been developing a beam halo monitor for the interlock sensor, which is equipped with diamond detectors to measure directly electron intensity of the halo part of the electron beam. Diamond detector, which operates in photoconductive mode, is good candidate for electron beam sensor, because diamond has excellent physical properties, such as high radiation hardness, high insulation resistance and sufficient heat resistance. This diamond detector is based on the technique of X-ray beam position monitors for the SPring-8 X-ray beamlines [2, 3]. We adopted a pulse-by-pulse measurement for the halo monitor, because it suppresses the background noise efficiently, especially in the facilities having extremely high intense beam with low repetition rate, such as XFEL machines.

The detector head of the beam halo monitor is made of CVD diamond [4]. The structure of the diamond detector, which was fabricated by Kobe Steel, Ltd., is shown in Fig. 1. One electrode is for signal reading and the other is for applying bias voltage. The active area is the bottom part of the plate between electrodes. The electron-hole pairs that are created in the active area can be extracted toward the electrodes. The cross section of this active area is designed to have the size of 5 mm by 1 mm. The depletion layer thickness is estimated to 0.3 mm. This detector has a self-sustaining structure, which is not mounted on a package. Therefore the active area of the diamond detector can be put closer to the beam center. The typical dark current is the order of 100 pA at the bias voltage of 100 V. In the case of pulse mode measurements, the dark current does not have effects on the output signal, because the charge from dark current in one pulse is negligibly small.

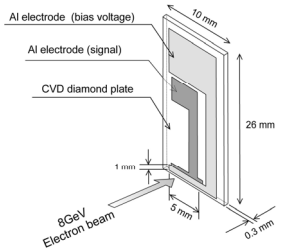


Figure 1: Structure of the diamond detector.

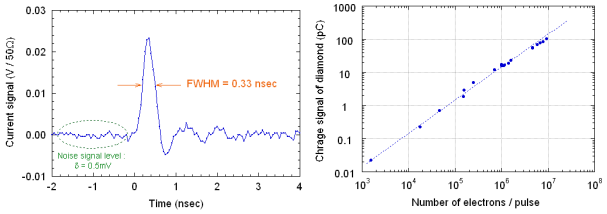
In order to evaluate the basic characteristics of the diamond detectors, such as detection sensitivity against electron beam and linearity, the beam tests have been undertaken at the beam dump of the 8 GeV SPring-8 booster synchrotron [4]. The oscilloscope having the sampling rate of 20 GS/sec and the analogue band width of 4 GHz was used. We prepared low attenuation cables, because the oscilloscope must be set out side of the machine tunnel and the cable length must be long, such as about 20 m. The coaxial cables of 50 Ω are used for impedance matching.

The typical pulse shape of the output signal is shown in Fig. 2 (a). This is one-shot measurement. The bias voltage is +100 V. The number of electron in one pulse is about 10^4. The pulse length of 0.33 nsec FWHM was obtained.

#aoyagi@spring8.or.jp

We took great care in cabling between electrodes on the diamond detector and the coaxial cables. We think that the pulse length of the output signal can be shortened farther using the detector having lower electrical capacitances. The RMS noise signal level is suppressed to about 0.5 mV for one-shot measurements.

The linearity of output signal on injected beam was also demonstrated as shown in Fig. 2 (b). The numbers of incident electron in one pulse were estimated by the output charge from the silicon detector. The output charge from the diamond detector is proportional to the number of incidence electrons in one pulse in the range of around 10^3 to 10^7 electrons/pulse. Minimum number of injected electron beam was nearly 1.5×10^3 /pulse, and we observed typical charge signal of 25 fC, when the bias voltage is +100 V.



(a) pulse shape (b) linearity

Figure 2: Measured data of the diamond detector.

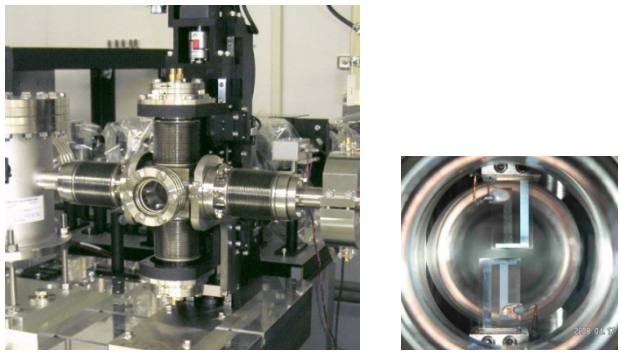
BEAM HALO MONITOR

Figure 3 shows the diamond detectors which are mounted on the beam halo monitor. Each diamond detector is fixed on ICF70 vacuum flange. The RF feedthrough connectors are used on flanges, and the RF coaxial cables for UHV are connected to the electrodes of the detectors with very short wires. Therefore, the pulse length can be shortened, and the detection efficiency can be enhanced. Coaxial cables are used for impedance matching.

Figure 4 shows the beam halo monitor installed at the 250 MeV SCSS test accelerator for XFEL/SPring-8. A pair of detectors is mounted on the upper and lower side of the beam center. The distance between both the active areas of the detectors can be change by one actuator, and the center position of both detectors can be also change by the other actuator. The beam halo monitor is designed to install in front of the permanent magnets array of the undulators. The core of the electron beam passes through between both detectors.



Figure 3: Photographs of the diamond detectors.



(a) (b)

Figure 4: (a) Photographs of the beam halo monitor (b) Seen from on the beam axis.

Feasibility Test

We have carried out feasibility tests of the beam halo monitor at the SCSS test accelerator. The tests have been demonstrated as follows:

- Observation of the signal shape (check of pulse length, existence of ringing) at very low electron beam intensity.
- Evaluation of effect of noise source caused by such a thyratron.
- Evaluation of induction current (effect of wake field) and their suppression.
- Evaluation of signal cause of bremsstrahlung and secondary electrons produced at vacuum pipes, etc.
- Evaluation of effect on laser oscillation when the sensors get close to the electron beam.

Figure 5 shows the pulse shape of the beam halo monitor. The number of electron in one pulse is estimated to be about 4×10^4. The active area of the diamond detector was irradiated with the core part of the electron beam in this measurement. The output pulse length of 0.4 nsec FWHM was obtained. The pulse length is slightly longer than that measured at the 8 GeV SPring-8 booster synchrotron, as shown in Fig. 2 (a), because the cable length used in this measurements was longer by 5 m. The significant ringing was not observed. Figure 5 also indicates that the effect of noise source caused by such a thyratron can be evaluated to be negligible.

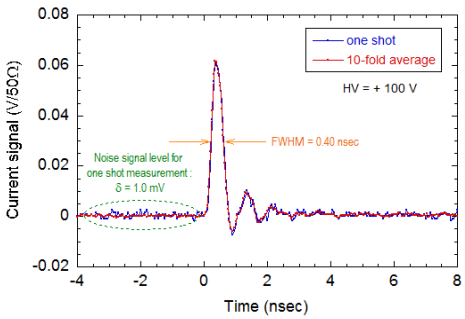


Figure 5: Pulse shape of the beam halo monitor (blue line: 10-fold average, red line: one shot measurement).

We evaluated the effect of induction current, when the electron beam core with high intensity (1.2×10^8 e/pulse) passes through near the detectors. We adopted the low pass filters (LPFs) in order to suppress the effect. Figure 6 shows the effect of induction current and the suppression. The upper part and the lower part show the signal shape without the LPFs and without LPFs, respectively. The effect of induction current can be suppressed by using proper LPFs, and the net signal from e-h pairs, which comes from the halo part of the electron beam, can be measured.

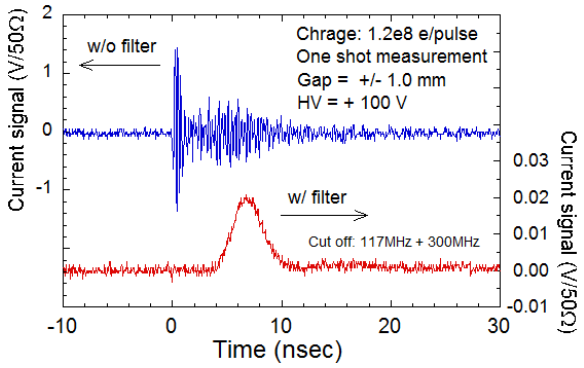


Figure 6: Effect of induction current and the suppression (upper: without LPFs, lower: with LPFs).

We also made an evaluation of signal from the bremsstrahlung and secondary electrons produced at vacuum pipes, etc. Therefore the vertical scanning measurements have been carried out. Figure 7 shows the signal charge as a function of vertical position of the active area of the diamond detector. The aperture of a spatial slit, which is placed just after the end of injector, was varied systematically. The profiles of electron spread by bremsstrahlung and electron scattering is theoretically assumed to be broad. On the contrary, the amount of signal charge at the vertical position over +/-2 mm is lower the detection limit even at the full aperture of the slit. So we think that the signal from the bremsstrahlung and secondary electrons is negligibly small.

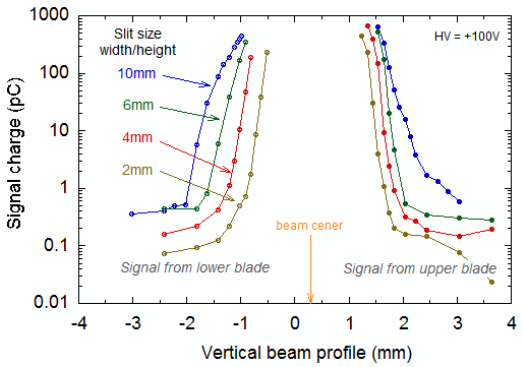


Figure 7: Scanning measurements.

Finally we checked the effect for the laser oscillation when the sensors approach the electron beam as shown in Fig. 8. The intensity of laser oscillation is not to be effected if the distance from the beam center and the diamond detector is more than 1 mm.

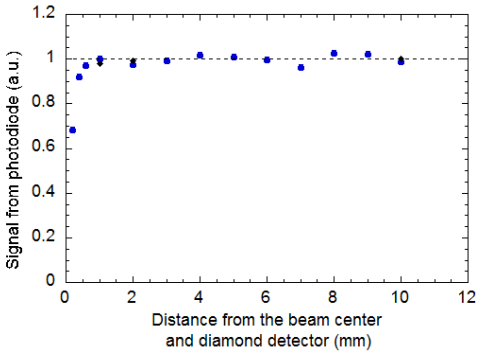


Figure 8: Effect on laser oscillation.

CONCLUSION

We have designed and fabricated the beam halo monitor using the diamond detectors as the sensor of machine protection interlock system at XFEL/SPring-8. The beam test of the monitor has been carried out at the 250 MeV SCSS test accelerator for XFEL/SPring-8. The pulse length of the current signal is 0.4 nsec FWHM. The RMS noise signal level is about 1 mV rms for one-shot measurements. We demonstrated the feasibility of the beam halo monitor. All these results suggest that the electron beam halo monitor is feasible for the interlock sensor to protect the radiation damage of the undulator permanent magnets for XFEL/SPring-8.

ACKNOWLEDGEMENTS

We would like to thank SCSS Test Accelerator Operation Group for their comments on beam tests, and S. Takahashi and A. Watanabe of JASRI/SPring-8 for their supports.

REFERENCES

[1] T. Bizen et al., “High-energy electron irradiation of NbFeB permanent magnets: Dependence of radiation damage on the electron energy", Nucl. Instr. Meth. A 574 (2007) 401.

[2] H. Sakae et al., “Diamond Beam-Position Monitor for Undulator Radiation and Tests at the Tristan Super Light Facility", Journal of Synchrotron Radiation, 4 (1997) 204.

[3] H. Aoyagi et al., “New Configuration of Photoconductive Type Diamond Detector Head for X-ray Beam Position Monitors”, AIP Conf. proc. (SRI2003) Vol. 705 (2004) 933.

[4] H. Aoyagi et al., "Beam Halo Monitor using Diamond Detectors for XFEL/SPring-8", THPC146, EPAC 2008, Genoa, Italy.

THE DESIGN AND IMPLEMENTATION OF THE MACHINE PROTECTION SYSTEM FOR THE FERMILAB ELECTRON COOLING FACILITY *

A. Warner#, L. Carmichael, K. Carlson, J. Crisp, R. Goodwin, L. Prost, G. Saewert, A. Shemyakin,
FNAL, Batavia, IL 60543 U.S.A.*

Abstract

The Fermilab Recycler ring employs an electron cooler to store and cool 8.9-GeV antiprotons. The cooler is based on a 4.3-MV, 0.1-A, DC electrostatic accelerator for which current losses have to remain low (~10^{-5}) in order to operate reliably. The Machine Protection System (MPS) has been designed to interrupt the beam in a matter of 1-2 μs when losses higher than a safe limit are detected, either in the accelerator itself or in the beam lines. This paper highlights the various diagnostics, electronics and logic that the MPS relies upon to successfully ensure that no damage be sustained to the cooler or the Recycler ring.

INTRODUCTION

Stable operations of a 4.3 MeV Pelletron (an electrostatic accelerator) with a 100 mA DC electron beam has lead to the successful demonstration of electron cooling of 8 GeV anti-protons in the Recycler ring [1][2]. The electron beam is transported to interact with the anti-proton beam in a common 20-meter long straight section (i.e. cooling section) after which electrons are separated from the antiprotons and recaptured at the high voltage terminal of the machine; there the beam is dumped in the collector at the energy of 3 kV. Losses during this energy recovery process are kept below, ~ 10 μA. Increased beam loss during this process can lead to a reduction of the terminal voltage and, in turn, an interruption in re-circulation. In severe cases the terminal voltage of the machine can be discharged to near zero in a microsecond, releasing ~3 kJ of stored energy. This so-called full discharge results in an increased vacuum pressure of the accelerating tubes, it can damaged electronics in the terminal and may degrade the electric strength of the tubes [3]. In addition a sustained current loss in a single location could melt and drill a hole in the vacuum chamber. At the R&D stage of the project encountering these types of scenarios indicated a need for an elaborate protection scheme. Twice the electron beam drilled a hole in the vacuum chamber. As a result we limited the current available to DC losses to ~20 μA so that the timescale for melting the beam pipe is of the order of several seconds, in which case the loss monitor system mentioned below insures that the electron beam can be turned off in less than 1 second.

To mitigate these effects fast protection circuitry has been developed at the terminal level as part of a Machine Protection System (MPS) which closes the gun in 1 μs if the terminal voltage decreases because of higher losses. The MPS consists of two interconnected parts: a permit system and a crash recovery system. The permit system monitors several critical machine- and subsystem-related alarms as well as the loss monitors for the entire beam-line. The crash recovery system is a slower, higher-level application which regulates the beam given the status of a range of machine parameters. Figure 1 shows a simplified flow diagram of the whole system.

PROTECTION SYSTEM OVERVIEW

The main hardware components of the protection system comprise: (1) the electron gun's modulator and fast circuitry in the terminal along with its fiber optically connected interface module located at ground level, (2) the beam permit box and (3) an Internet Rack Monitor (IRM) processor which is capable of interfacing up to 64 analog channels with digitization of all 64 channels done by the hardware at 1 kHz.

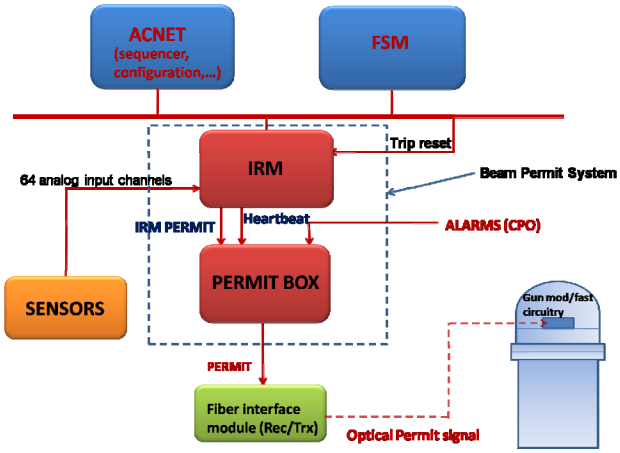


Figure 1: Protection system diagram.

Gun Modulator and Fast Circuitry

The Gun Modulator is located inside the deck enclosure which is inside of the Pelletron terminal. Its output drives the "control electrode" of the electron gun located in the terminal at the top of the accelerating column. The modulator is used to control the beam generated by the electron gun for either cooling antiprotons in the Recycler (DC beam) or for machine diagnostic purposes (Pulsed beam). In the same way the voltage on the grid of a triode tube defines the tube current, the voltage on the control electrode defines the gun current (i.e. electron beam current). Depending on the desired operating mode when producing the electron beam, the modulator either adds an AC voltage to the DC voltage of the control

* FNAL is operated by Fermi Research Alliance, LLC under Contract No. DE-AC02-07CH11359 with the United States Department of Energy.
#warner@fnal.gov

electrode (provided by a separate power supply), or it delivers high voltage pulses to the control electrode. The modulator also serves the function of shutting the gun off rapidly (~1 μs) when the permit signal is removed. In particular, this fast protection circuitry was developed for the case of fast terminal voltage drops due to beam current losses, thus reducing the risk of full discharges [3]. In addition the modulator guarantees that the gun remains clamped off until after the gun's anode supply is totally powered off in the case of a sudden power loss at the terminal while the beam is still on. It was also painstakingly designed to remain protected during high voltage breakdowns of the machine; since the control electrode is known to sustain damaging energy when the machine breaks down the modulator must reliably survive these events. The modulator is actually composed of two separate modules that communicate with each other; the modulator chassis in the Pelletron deck enclosure as mentioned above, and the interface module at ground level. The single purpose of the interface module on the ground is to relay information back and forth between the chassis in the terminal and the control system frontend at ground. The two modules are connected to each other via a number of fiber optic cables.

Beam Permit Box

A variety of operating parameters are monitored at ground level by the beam permit box which issues a permit signal that is transmitted over a dedicated fiber to the modulator in the terminal. This beam permit box forms the hardware interface between the IRM and the interface module at ground level. Additional inputs are provided to the box that allows the sequencer or a manual switch located in the control room to disable beam.

The beam permit box has a fast comparator for monitoring the so-called CPO (capacitive pick off) monitor. The CPO is a device that measures voltage changes at the terminal and depending on the magnitude of the voltage drop and its time derivative, the permit may be removed, inducing a trip. The CPO has a 16nsec rise time and 19 msec fall time and a positive output for a discharge spark. The typical trip level is a 10 kV change on the terminal as measured by the CPO monitor at about 50 kV/V. A CPO signal exceeding the trip level will latch a trip condition and take away the Permit in about 9nsec. A DAC in the IRM provides an analogue trip level. The smallest usable trip level is about 1 kV. A setting larger than 150 kV may never trip. The trip level is accurate to about +/-0.5 kV. The change in voltage must be fast compared to the 50usec AC coupling time constant used in the circuitry. In addition to the Beam Permit, outputs from the beam permit box include a buffered copy of the CPO signal for monitoring in the control room as well as a slightly filtered copy for an ADC channel in the IRM.

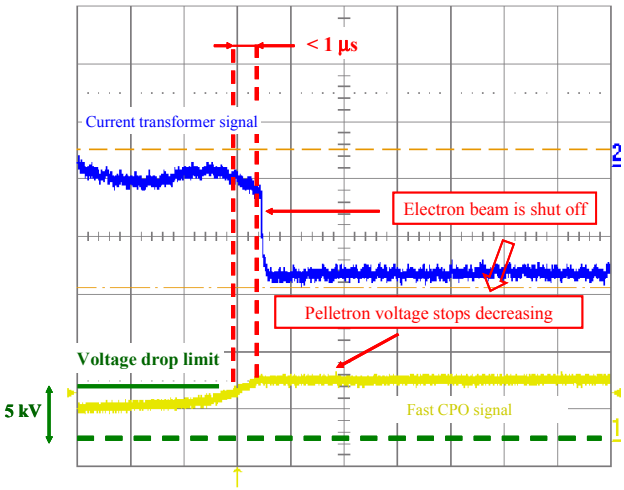


Figure 2: Oscillograms of a recirculation interruption. The yellow trace is the terminal voltage, and the blue trace is the cathode current.

IRM Permit System

The IRM digitizes and monitors 22 loss monitor channels distributed along the entire beam-line along with the CPO signal. Upper and lower threshold limits for each channel that is monitored by this system is downloaded via the control system. A local subroutine then scans each input channel against its limits. Based on the status of the inputs the system provides the permit box with an 'IRM permit' input. It is worth noting that the hardware automatically stores its results into a 64K circular buffer that has room for 512 sets of data which translates into 512 ms of data saved per channel. The local application which operates at 15 Hz runs on the system and supplies an interrupt routine that the underlying system code invokes from the digitizer interrupt; this occurs at the end of the digitization process over an 800 μs period. The interrupt code is invoked when the latest set of 1 kHz data has been stored into the buffer. The system then passes to the interrupt code an indication of where this latest data set is stored within the circular buffer. Since continued execution of the interrupt routine is so important, a heartbeat output line is provided that is driven by the kilohertz interrupt routine logic. It is driven high at the start of the interrupt routine execution and driven low at the end, about 100 μs later, if the maximum of 64 channels is being scanned. Its minimum time can be about 6–10 μs if the first channel reading is out of limits. If the permit box fails to see this heartbeat activity, it assumes there is no active interrupt monitoring going on, a heartbeat trip condition will be latched and the permit will not be issued.

CRASH RECOVERY REGULATION

The gun current is regulated by a Java-based Finite State Machine (FSM) which reduces or switches off the gun current whenever a distinct set of fault conditions are detected and increases the current back to its nominal set point when normal conditions return. This regulation

process is an essential part of the Pelletron operation as it serves to anticipate critical faults, thus improving the overall efficiency of the operational aspects of electron cooling. The FSM provides the following functionalities:

1. Maintains (or recovers) the nominal electron beam current whenever drifts or unexpected changes occur.
2. Reduces the gun current as needed to compensate for soft fault conditions such as vacuum deterioration and slow (i.e. ~ seconds) HV drops.
3. Execute a consistent set of steps and checks whenever the machine needs to recover from a trip. It is particularly important when the trip is due to a large HV discharge.

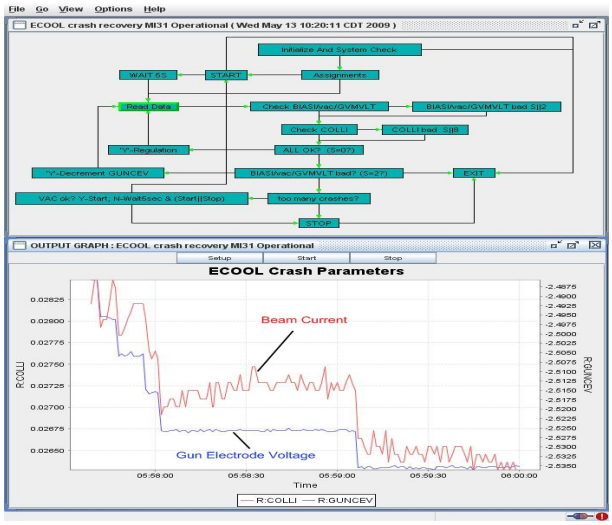


Figure 3: FSM Display. The plot shows the FSM regulating the gun control electrode voltage in order to reduce the beam current back to its nominal value.

The FSM class is imbedded in the Java-based Data Acquisition Engine (DAE) infrastructure that sits on top of the Fermilab accelerator control system (ACNET). The ACNET control system is a 3-tiered system that uses a connectionless User Datagram Protocol (UDP) to connect different machines. The DAE infrastructure refers to a client server model where Java clients use Remote Method Invocation (RMI) to communicate with the DAE servers that are tied directly to the ACNET control system. Each FSM operates in a thin client-server model where the FSM client starts jobs remotely on the server which is bundled with the DAE engines. The FSM server handles all communication with ACNET and all computations. Information such as state transitions and requested data is sent back to the client through RMI

CONTROL SYSTEM INTEGRATION

An integral part of the MPS is the display and analysis of any detected faults. Faults that are detected by the permit systems are time-stamped by the IRM. A persistent FSM logs the data associated with a trip generated by the permit or regulation systems and stores the monitored data in a database. A Java application provides an integrated, graphical display of faults detected by the permit and regulation systems. Figure 4 shows the application's main window where the beam line is schematically represented with all the monitored channels for which the stored data can be accessed (inserts in Fig. 4). Additionally, a display of the fault history along with the first fault in a fault sequence is illustrated.

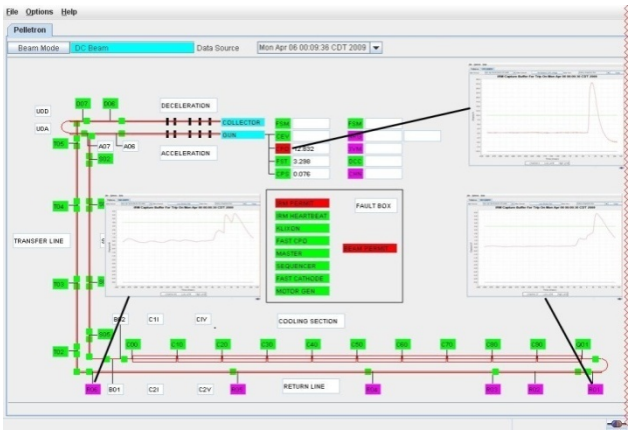


Figure 4: Fault System Display.

SUMMARY

The machine protection system works well and is fully operational. The fast gun circuitry in conjunction with the beam permit box has successfully aided in reducing the frequency of full discharges to about one per year, thus increasing the cooler reliability. The Crash recovery FSM has proven to be very useful operationally as it significantly reduces manual interventions while running beam. It in turn increased the electron beam uptime, which is now close to 92% (except for occasional hardware failures). The FSM infrastructure has become an integral part of the Pelletron's machine protection scheme at various levels and helped in streamlining fault analyses. It not only captures operational knowledge in the regulation script, but also allows for the easy testing and implementation of additional scripts to improve operational efficiency.

REFERENCES

[1] S. Nagaitsev et al., Phys. Rev. Lett. **96**, 044801 (2006).
[2] Pelletrons are manufactured by The National Electrostatics Corporation; www.pelletron.com.
[3] L.Prost and A. Shemyakin, FERMILAB-CONF-05-384-AD (2005).
[4] Guide to Data Acquisition Engine, K. Cahill, Beams Document 666-v1.

A CONCEPT TO IMPROVE THE AVAILABILITY OF PETRA III BY CORRELATION OF ALARMS, TIMESTAMPS AND POST-MORTEM-ANALYSIS

M. Werner, DESY, Hamburg, Germany

Abstract

For current and future accelerators, in particular light sources, high availability is an important topic. Therefore the causes of beam losses must be diagnosed and eliminated as fast as possible. This paper presents a concept using the following signals and data from diagnostic instruments and other sources: i) software alarms transmitted by the control system, ii) hardware alarms received and timestamped by the machine protection system, and iii) Post-Mortem-Analysis. By analysing alarm dependencies and the chronological order of alarms, the cause of the problem can be tracked down. The help of diagnostic instruments is highlighted.

INTRODUCTION

A manual alarm analysis in the case of a beam loss can be a time consuming task. In some cases alarms cause an alarm avalanche, by this hiding the initial alarm. In other cases alarms are mutually dependent and the question arises which alarm occurred first. The following ideas could help to solve some of these problems, and it is intended to use some of them in the context of the Machine Protection System for the new PETRA III light source [1].

SOFTWARE ALARMS

Software alarms are transmitted from the hardware to the server for this hardware via a field bus or via Ethernet or the server generates the alarm by itself. The server sends the alarms to a dedicated alarm server and shows the alarms through the control system interface. The time of an alarm can be determined with a precision in the order of 1 second, and the reaction time is also in the order of 1 second. The alarm description can be very specific, e.g. the name of a magnet circuit (out of hundreds of circuits) can be displayed without big effort. Adding new alarms is just a matter of software.

Non-dangerous events which always cause a beam loss

Alarms from these events can be transmitted by software, and there is no need for a precise timestamp to localize the error, because these events do not depend on other events in a difficult way, so they must be the initial cause of a beam loss. Examples:

- Main dipole or quadrupole power supply breakdown
- RF system breakdown (not triggered by beam loss)
- Mains breakdown

HARDWARE ALARMS

Hardware alarms need dedicated cables, therefore they are limited to critical alarms which need a fast reaction time (order of 1ms) and/or a precise timestamp (order of 1us can be achieved).

Dangerous events which must trigger a fast beam dump

Alarms for these events must dump the beam by the use of the machine protection system (MPS) and they should be timestamped. Together with the timestamps of the other alarms, a statement about the initial alarm can be made in many cases. Examples:

- Cavity sparking
- Vacuum shutter closed
- Temperature too high
- Personal interlock broken (e.g. door opened, emergency button pressed)
- Beam Orbit out of limits or critical BPM not working correctly

Non-dangerous events which need a precise timestamp

These events sometimes cause a beam loss. They should not initiate a beam dump. For alarms from these events the cause of the beam loss cannot be clearly assigned, but if the event occurs shortly before a beam loss, there is a high probability that it is the cause of the beam loss. Examples:

- Main dipole or quadrupole power supply spike
- RF spike
- Mains brownout or spike
- Corrector power supply breakdown

There is an overlap to the software alarms (see above), because, for example, the alarm line for a main dipole power spike will also trigger in the case of a main dipole power failure.

COMBINATION OF SOFTWARE AND HARDWARE ALARMS

A combination of software and hardware alarms can be useful for a group of devices such as corrector magnet supplies: the individual names of the faulty channels can be transmitted by software, while an “OR”-combination of all channels add up to a single hardware alarm to provide a precise timestamp of the first alarm in this group.

ALARM DEPENDENCIES

Studying the way how alarms depend on each other can lead to the initial alarm in some cases even if no timestamps are available. If an interlock door has been opened, the main magnets are switched off and an orbit deviation was observed, it is clear that the opening of the door initially caused the beam loss and all other alarms. See Fig. 1 for typical alarm dependencies.

Independent Alarms

If one of these alarms happens, it is easy to assign the cause of the beam loss. Examples:

- Cavity sparking
- Temperature too high
- Personal interlock broken (e.g. door opened, emergency button pressed)

Dependent Alarms

They can happen as a consequence of another event. Examples:

- Bad Orbit (dependent on magnet currents)
- RF breakdown (sometimes dependent on beam current)

Linear Dependencies

In this case the cause of a problem can be traced back and no timing analysis is necessary. If, for instance, during a beam loss a bad orbit was detected and the main dipole power supply is on error, the problem is the power supply in most cases because the power supply can directly influence the orbit but not vice versa.

Circular or Mutual Dependencies

In this case tracing back the cause of an event can lead to the event itself. An example is a beam loss concurrent with an RF breakdown: an RF breakdown always causes a beam loss, but a beam loss can also lead to RF failure. In this case an analysis of the chronological order of the alarms helps.

CHRONOLOGICAL ORDER OF EVENTS

If the analysis of the dependencies does not show the reason of a beam loss because alarms are circular or mutually dependent, the alarm timestamps can provide more information. The first alarm in an alarm sequence can often point to the initial problem. This first alarm can be a dangerous or a not dangerous alarm. Let us consider the example of a corrector magnet failure (not dangerous) leading to an orbit distortion (detected by a BPM) which is dangerous because then a closed undulator can produce intense light at the wrong place and melt components. Although the BPM triggered the beam dump, the corrector magnet can be identified as source of the beam loss because it happened directly before the beam loss. On the other hand, a corrector magnet fault does not always lead to beam loss if the kick offset of the corrector is small enough.

POST MORTEM ANALYSIS

Post mortem data recording can be triggered by a full or partial beam loss or other events. The recording should cover the interesting time range around the loss, this can be from milliseconds (e.g. for BPM data) until seconds (e.g. for temperature data) with adequate time resolution. All recorders for the different devices (RF, power supplies, BPMs and others) should use the same Post Mortem trigger to allow easy time correlation between the different device groups.

Manual or Automatic Analysis

In many cases automatic analysis of Post Mortem data can help to find the cause of a beam loss or at least support an expert in his manual analysis. For example, a scan of the Post Mortem data of all magnet currents or voltages could reveal anomalies shortly before a beam loss.

Combining Several Data Channels

Useful information can be taken from the BPM Post Mortem data. The evolution of the RMS orbit deviation compared to a reference orbit (taken from the first samples of the Post Mortem data) in both directions can be calculated as well as the evolution of the position sum (trace length) in the horizontal direction. If the sum is constant but the RMS value increases directly before the beam loss, this points to beam instability. If, on the other hand, the sum changes, an RF problem is more likely, because the sum is correlated to the beam energy.

Consistency Checks

Another interesting possibility is the combination of Post Mortem data of BPMs with fast and/or slow orbit corrector magnet currents, using the Orbit Response Matrix (ORM). An inconsistency can directly point to a bad BPM or corrector magnet and help in troubleshooting the orbit feedback system.

AUTOMATICAL ALARM ANALYSIS

Regarding the event dependencies in an accelerator, an automatic analysis of software alarms and the chronological order of hardware alarms can point to the initial cause of a beam loss. For more difficult cases, also Post Mortem data can be automatically analyzed to give concentrated information to the operator. If the source of a beam loss is still unclear, a manual analysis by an expert is necessary, whereas the timestamps and the Post Mortem data are still very helpful.

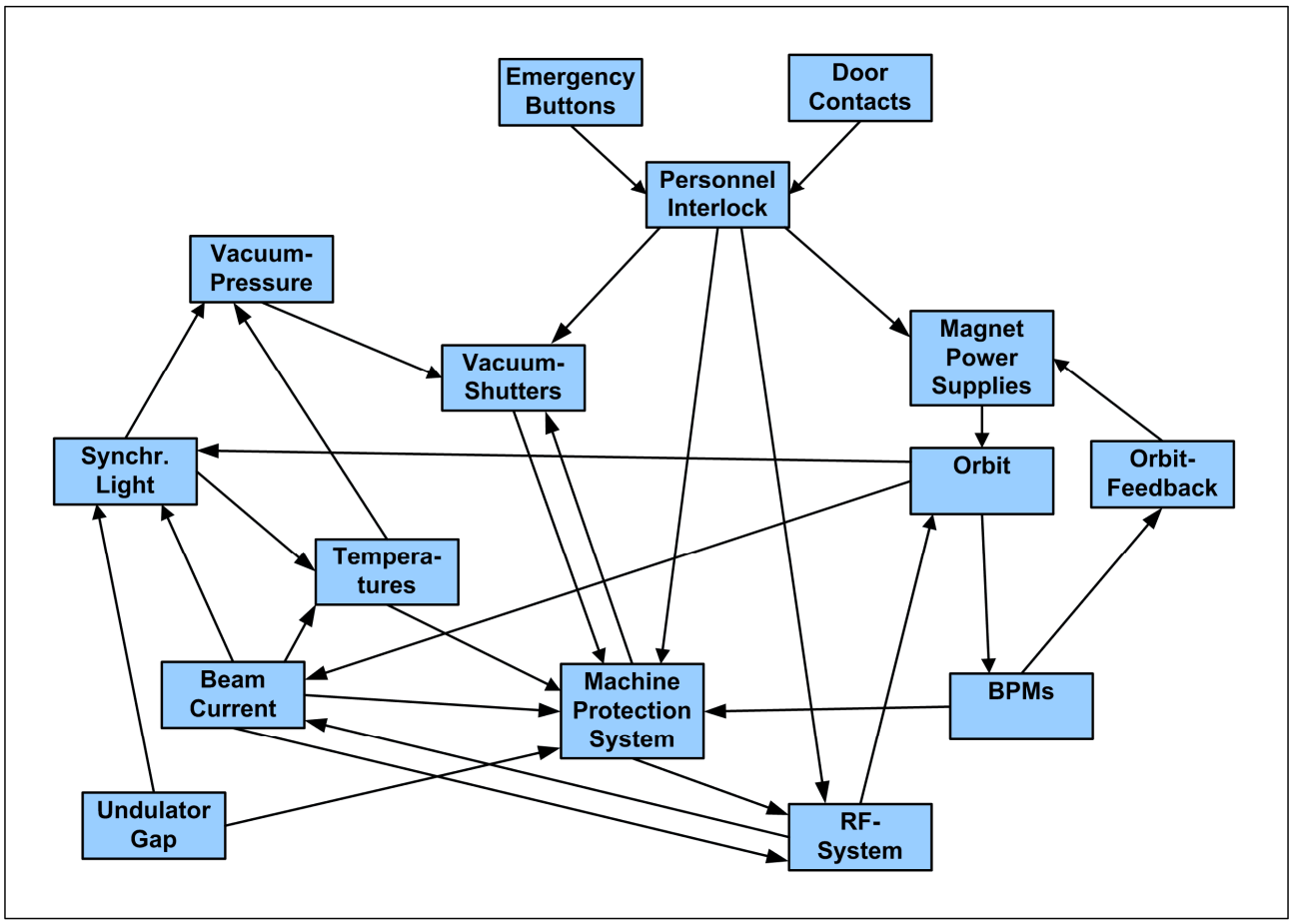


Figure 1: Alarm dependencies. The arrows show in which direction alarms or states influence other alarms and states in the PETRA III light source.

THE BENEFIT OF WARNINGS

Some beam losses can be avoided by observing critical parameters and reacting in time. A software warning system can do this observation automatically and give an acoustical or optical signal to the operator. Examples:

- Beam near position limits (BPM interlock)
- Quadrupole sum of BPM buttons close to limits
- Sum of BPM buttons close to limits (consistency with beam current monitors)
- Vacuum pressure close to limits
- Magnet current close to limit (slow or fast corrector magnets)
- Temperature near limit

CONCLUSION

Ideas and methods were presented to increase the availability of a typical light source by fast automatic or computer-aided manual analysis of beam losses, thereby shortening the downtime. The important role of BPMs in this analysis was shown.

REFERENCES

[1] T. Lensch and M. Werner, “Machine Protection System for PETRA III”, these proceedings.

FEASIBILITY STUDY OF AN OPTICAL FIBRE SENSOR FOR BEAM LOSS DETECTION BASED ON A SPAD ARRAY*

A. Intermite†, Max Planck Institute for Nuclear Physics, Heidelberg, Germany
M. Putignano, C. P. Welsch, Cockcroft Institute and University of Liverpool, UK

Abstract

This contribution describes an optical fibre sensor based on the use of a silicon photomultiplier (SiPM) composed of an array of Single Photon Avalanche Detectors (SPADs). This sensor will be used for the detection and localization of particle losses in accelerators by exploiting the Cerenkov Effect in optical fibres. As compared to conventional vacuum photomultipliers, the SPAD array allows for maximizing the geometrical efficiency of Cerenkov photon detection. The array can be directly integrated into the fibre end while retaining the same quantum efficiency (20%) in the wavelength range of interest. The SiPM is intrinsically very fast due to its small depletion region and extremely short Geiger-type discharge, which is in the order of a few hundreds of picoseconds. Therefore, the combined use of optical fibres and SiPMs seems a promising option for a modern Cherenkov detector featuring subnanosecond timing, insensitive to magnetic fields, capable of single photon detection and allowing for the possibility of realization in the form of a smart structure. We present the layout and operating principle of the detector, its characteristics, and outline possible fields of application.

INTRODUCTION

Beam loss monitor systems are designed for measuring beam losses around an accelerator or a storage ring [1]. Particles showers penetrate the optical fibre and generate Cerenkov radiation. Using two parallel sensors along the most critical parts of the accelerator such as collimators, scrapers and aperture limitations the losses can be detected and localized. To couple the highest number of photons into the fibres, the geometrical features of the sensor have to be optimized. For this purpose a simulation code was developed, to achieve the best collection efficiency with the optical fibres available commercially in the range between 450-550 nm. The Numerical Aperture (NA) of these fibres is chosen considering the meridional and skew rays contribute to the coupling efficiency and the attenuation curves in the specific range of wavelengths where the SiPMs have their highest photosensitivity.

*Work supported by the Helmholtz Association of National Research Centers (HGF) under contract number VH-NG-328 and GSI Helmholtzzentrum für Schwerionenforschung GmbH

† Corresponding author: angela.intermite@quasar-group.org

CERENKOV RADIATION IN OPTICAL FIBRES

A charged particle passing through an optical fibre of large enough radius (a>>λ) produces Cerenkov radiation inside the fibre if its velocity exceeds the phase velocity of light in the medium. Cerenkov photons are immediately generated and the number of photons N_{ph} per wavelength interval λ and distance L is given by [2]:

$$\frac{d^2N_{ph}}{d\lambda\, dL} = 2\pi\alpha z^2 \frac{\sin^2\theta}{\lambda^2} \qquad (1)$$

where α = 1/137 is the fine structure constant, θ is the Cerenkov cone semi-angle, λ the wavelength and L the path length of the particle with charge z in the fibre.

Cerenkov light is emitted on the surface of a cone with an angular opening semi-angle given by:

$$\cos\theta = \frac{1}{n\beta} \qquad (2)$$

where $\beta = v/c$ and n the refractive index of the fiber.

From Eq. (1), the intensity of Cerenkov light increases inversely to the cube of the wavelength as it is plotted in Fig. 1, consequently the blue color dominates in the visible spectrum.

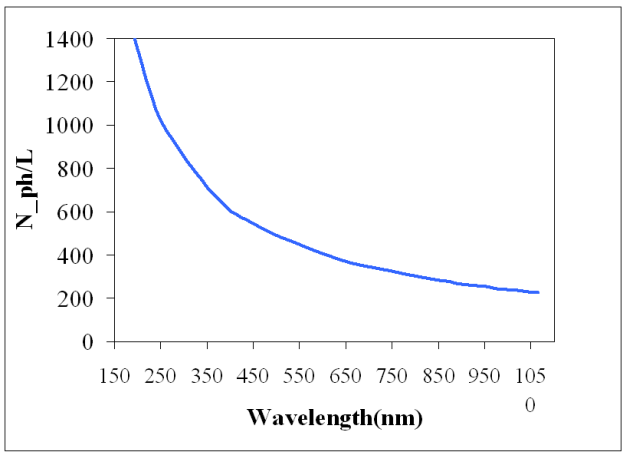


Figure 1: Number of photons produced per incident electron and per unit length L between 193 – 1064 nm.

When we consider the Cerenkov propagation inside a fibre we have to consider the probability of survival of the created photons (Collection Efficiency, CE) in the waveguide: this is determined by NA of the fibre and by the direction of the Cerenkov photons. In Fig. 2 we can see CE as a function of the incidence angle of the charged particle with respect to the fiber axis and the impact parameter, i.e. the shortest distance between the charged

particle trajectory and fiber axis. To calculate CE we considered the contribution of both meridional and skew rays and of the fibre cleaving angle in a C++ code written for the purpose.

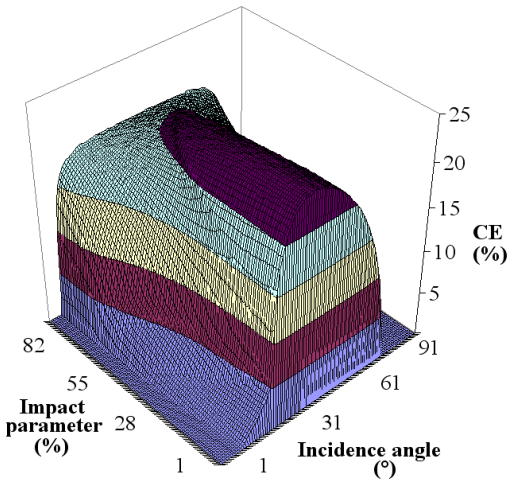


Figure 2: Collection efficiency of Cerenkov photons inside a pure silica optical fibre with NA=0.63.

The collection efficiency increases with the numerical aperture of the fiber as we can see in Fig. 3.

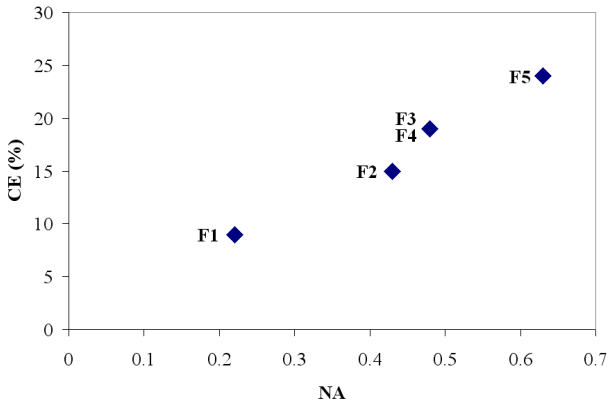


Figure 3: Collection efficiency of Cerenkov photons as a function of the Numerical Aperture (NA) of the optical fibres listed in Table 1. The collection efficiency is independent of the value of the fibre core diameter as it can be seen from the points F3 and F4.

The propagation of Cerenkov light in the fibre depends on the particle shower geometry as well as on the particle and fibre properties. For electrons the threshold energy to emit Cerenkov light in quartz fibre (n=1.46) is about 175 keV and the semi angle of the Cerenkov light is about 46°.

BEAM LOSS DETECTION SYSTEM

The proposed sensor is based on two parallel fibres with high numerical apertures as shown in Fig. 4. Both fibres are connected to two SiPMs with the same features.

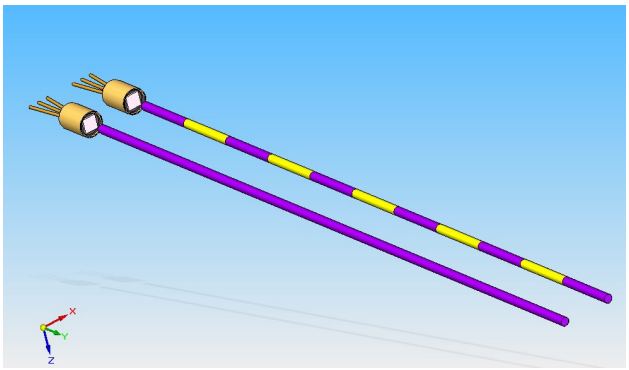


Figure 4: Sketch of the complete arrangement of the optical fibre sensor.

The first fibre, F1 (shown in violet), is used as reference arm. Its geometrical features are chosen to maximize the Cerenkov photons produced in the range between 450-550 nm, in which range the detector has a high Photon Detection Efficiency (PDE) of 15-20%.

The second arm of the sensor will be realized by splicing two fibres with different properties, F1 and F2, respectively indicated in violet and yellow, so that the fibre F2 will have much higher attenuation of F1. In this way the number of Cerenkov photons detected on the composite arm will be smaller than the number of the reference arm F1, with the difference depending on the number of large attenuation sections encountered by the travelling photons. By counting the number of fibres in the second arm it will then be possible to localize losses.

The advantages of this optical fibre sensor with respect to the traditional delay line configuration are:

- The resolution of the sensor depending mainly on the length of the spliced fibres of the second arm. It is therefore possible to achieve resolution of down to a few centimetres, much finer than the resolutions achieved by usual delay line sensors, which are limited by the detector time resolution to about 1 meter. Such finer resolution is particularly relevant when there is the need to monitor losses in narrow spaces as in CLIC Experimental area (CLEX) where the distance between the main beam and the drive beam is about 75 cm. Here this optical sensor, placed perpendicular to the accelerator pipes in a region where losses have been spotted, would allow detecting which pipe the losses came from.
- Each signal is read independently and absolute position calculated from the intensity ratio in the two branches, therefore, there is no overlap of signals and it becomes possible to detect multiple signals without using clock triggers.
- The active surface of the SiPM has the same dimensions of the fibre listed in Table 1 and this reduces the coupling losses between fibres and SiPM.

Optical Properties of Fibres

In this paper we considered multimode step index fibres with a total diameter of 1 mm for simple coupling with a

SiPM of the same dimension. The properties of these fibres are listed in the table below.

Table 1: Properties of optical fibres used in this paper for calculating the collection efficiency.

Fibres	NA	Core Diam. (µm)	Core material
F1	0.22	200	Pure Quartz
F2	0.43	200	Pure Silica
F3	0.48	200	Pure Silica
F4	0.48	400	Pure Silica
F5	0.63	486	PMMA

SILICON PHOTOMULTIPLIER

The Cerenkov light is detected with Silicon Photomultipliers at the end of the fibres. In the last few years, a new kind of planar semiconductor device has come out, namely the SiPM with promising features that could even replace traditional photomultiplier tubes. It is based on a Geiger mode SPAD elementary cell and it consists of an array of *n* independent identical microcells whose outputs are connected together as we can see in Fig. 5. The final output is thus the analog superposition of *n* ideally binary signals. This scheme along with the sensitivity of each individual cell to single photons appears to result in a perfect photosensor capable of detecting and counting single photons in a light pulse.

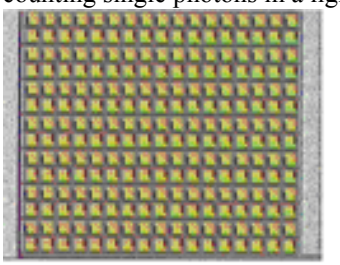


Figure 5: Magnification of a SiPM (courtesy of ST-Microelectronics, Catania).

Every SPAD cell is a p-n junction operating in Geiger mode at a low voltage (≈30 V) and fabricated in silicon planar technology. The junction is biased slightly above the breakdown by an overvoltage around 10% of the breakdown voltage itself, and it remains quiescent until a photon is absorbed in the depletion volume. This gives rise to the development of an avalanche current pulse, which needs a dedicated circuit to quench it, whose total charge is independent of the number of initial photocarriers. The quenching circuit is a passive one (a large-value resistor), which allows to keep the overall circuitry very simple. Such a resistor, in the form of a transparent polysilicon square frame, was integrated on top of the cell's cathode. The cell is square-shaped, with a 50/30 μm side-over-active-area ratio and a resulting 36% fill factor (the active area also includes the polysilicon frame) [3, 4].

It is deposited an antireflective coating layer and reduced the quasi-neutral region thickness above the thin junction depletion layer, in order to enhance the spectral response in the blue and near-ultraviolet wavelength ranges. The expected consequences are low leakage currents, low noise, and good PDE as it can be seen in Fig. 6.

The dimensions of these detectors make their coupling with optical fibres easier without influencing the final coupling efficiency.

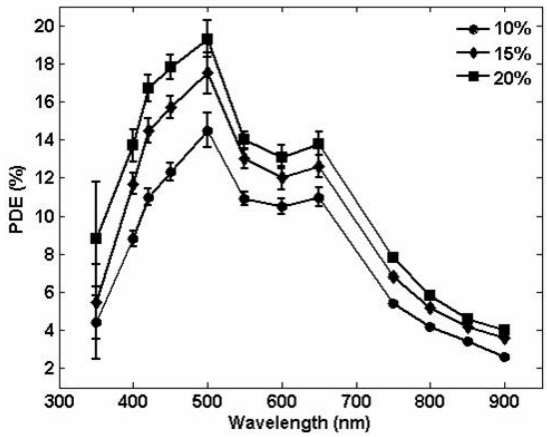


Figure 6: Photon detection efficiency of a SiPM as a function of wavelength (courtesy of ST-Microelectronics, Catania).

CONCLUSIONS

The properties of Cerenkov light emitted inside fibres combined with the lightguide conditions and the performances of SiPMs can be used for detecting and localizing losses in harsh environments such as accelerators. The optical fibre radiation hardness to very high radiation levels, the fast response of the SiPM associated to the sensor and the compact detector dimensions make it a good candidate for beam loss monitoring. To improve the collection efficiency in the range of 450-550 nm high aperture numerical fibres with core diameters between 200 µm and 500 µm are explored.

ACKNOWLEDGMENT

The authors are grateful to Dr Massimo Mazzillo from ST-Microelectronics, Catania and to Prof. Salvo Tudisco, from University of Catania for their continuous collaboration.

REFERENCES

[1] J. V. Jelley, "Cerenkov Effect and Its Applications", British J. of Appl. Phys. 6, 1955, p. 227-232.

[2] P. Gorodetsky et al, "Quartz Fiber calorimetry", Phys. Rev. Lett. 25 (1997) 56.

[3] P. Finocchiaro et al, "Characterization of a Novel 100-Channel Silicon Photomultiplier-Part 1: Noise", IEEE Trans. On Electron Devices 55 (10), October. 2008, p. 2757 - 2762.

[4] P. Finocchiaro et al, "Characterization of a Novel 100-Channel Silicon Photomultiplier-Part 2: Charge and Time", IEEE Trans. On Electron Devices 55 (10), October. 2008, p. 2765 – 2772.

LOSS MONITOR ON THE BASIS OF DIFFUSIVE RADIATION FROM ROUGH SURFACES

S.G. Arutunian*, Zh.S. Gevorkian, K.B. Oganesyan,
Yerevan Physics Institute, Alikhanian Brothers St. 2, Yerevan 375036, Armenia

Abstract

Diffusive Radiation is generated when a charged particle passes through a randomly inhomogeneous medium. Such a situation can be realized when a charged particle slides over a rough metallic surface. One of the important properties of DR is that the emission maximum lies at large angles from particle velocity direction. Therefore it can be used for detection of beam touch to the accelerators vacuum chamber wall in case when generated photons will be observed on the opposite side of the vacuum chamber. Such a diagnostics can be especially useful for monitoring of beam particle losses.

There is substantial interest in the development of different tools for beam diagnostics. Particularly, optical transition radiation is widely used for this goal [1, 2, 3]. With modern powerful optical detectors OTR based devices are very convenient. However there is also a problem with use of OTR. For relativistic particles, TR photons are emitted at very small angles $\theta \sim \gamma^{-1} \ll 1$. DR that we are going to discuss is free from such a shortage. In the present paper we consider the possibility of using of DR from rough surfaces for beam diagnostics.

A charged particle passing through a stack of plates placed in a homogeneous medium is known to be radiating electromagnetic waves. Radiation originates because of the scattering of electromagnetic field on the plates. Considering this problem theoretically it was shown [6, 7] that the spectral angular radiation intensity can be represented as a sum of single scattering I_0 and multiple scattering I_D contributions of pseudophotons

$$I = I_0 + I_D \tag{1}$$

where

$$I_0(\theta,\omega) = \frac{e^2}{2c}\frac{B(|k_0 - kcos\theta|)\sin^2\theta}{[\gamma^{-2} + \sin^2\theta k^2/k_0^2]^2}\frac{\omega^2}{k_0^4 c^2} \tag{2}$$

and diffusive contribution is determined as

$$I_D(\theta,\omega) = \frac{5e^2\gamma^2}{2\varepsilon c}\frac{L_z l_{in}(\omega)}{l^2(\omega)}\frac{\sin^2\theta}{|\cos\theta|} \tag{3}$$

Here L_z is the path of the particle in the medium, θ is the observation angle, $k_0 = \omega/v$, v is the particle velocity, $k = \omega\sqrt{\varepsilon}/c$, B is the correlation function of random dielectric constant field created by randomly located plates. Assuming that parallel plates with equal probability can occupy any point of z axis one finds correlation function as follows

$$B(q_z) = \frac{4(b-\varepsilon)^2 n \sin^2 q_z a/2}{q_z^2}\frac{\omega^4}{c^4}. \tag{4}$$

where $n = N/L_z$ is concentration of plates in the system, a is their thickness, b is their dielectric constant and ε is the average dielectric constant of the system. In Eq. (3), l and l_{in} are average elastic and inelastic mean free paths of photon in the medium. Inelastic mean free path is mainly associated with the absorption of electromagnetic field in the medium. Elastic mean free path is associated with the photon refraction on plates. It depends on the falling angle on plates. In the case when photon falls normally elastic mean free path is determined as follows

$$l = \frac{4k^2}{B(0) + B(2k)} \tag{5}$$

Note that just this quantity enters into spectral angular intensity Eq. (3). Eqs. (3, 5) are correct in the weak scattering limit $\lambda/l \ll 1$ and for observation angles $\theta = \pi/2 - \delta, \delta \gg (1/kl)^{1/3}$. Last restriction over angles appears because when $\theta = \pi/2$ pseudophotons are moving parallel to plates and no any refraction happens and the condition of weak scattering is failed. When the conditions of multiple scattering of electromagnetic field are fulfilled the diffusive contribution to the radiation intensity Eq. (3) is the main one because $I_D/I_0 \sim l_{in}/l \gg 1$. As it is seen from Eq. (3) the radiation intensity is determined by elastic and inelastic mean free paths of photon in the medium. It follows from Eq. (4) that when $ka \gg 1$, $B(2k)/B(0) \sim 1/(ka)^2 \ll 1$. Therefore in both cases $ka \gg 1$ and $ka \ll 1$ the photon mean free path has the form

$$l \sim \frac{k^2}{B(0)} \tag{6}$$

where $B(0) = k^4(b-\varepsilon)^2 na^2/\varepsilon^2$. Substituting this expression into Eq. (6) and taking into account that $k = \omega\sqrt{\varepsilon}/c$, we have

$$l \sim \frac{\varepsilon}{\frac{\omega^2}{c^2}(b-\varepsilon)^2 na^2} \tag{7}$$

Remind that ε is the average dielectric constant of the system which for a layered stack has the form:

$$\varepsilon(\omega) = nab(\omega) + (1-na)\varepsilon_0(\omega) \tag{8}$$

Here ε_0 is the dielectric constant of a homogeneous medium into which plates with dielectric constant $b(\omega)$ and

* femto@yerphi.am

thickness a are randomly embedded. If a homogeneous medium is vacuum then $\varepsilon_0 \equiv 1$. The parameter na is the fraction of the plates in the system.

A rough interface is a region with random fluctuations of dielectric constant that separates two homogeneous semi-infinite media. Suppose that $z = 0$ is the plane distorted by the roughness. The equation of rough surface is determined as follows

$$z = h(\vec{\rho}) \tag{9}$$

where h is a random function and $\vec{\rho}$ is a two-dimensional radius vector in the x, y plane. We suppose that the space $z > h(\vec{\rho})$ is occupied by the vacuum or air and the space $z < h(\vec{\rho})$ by a metal. Usually, for convenience, h is assumed as a gaussian stochastic process characterized by two parameters

$$\begin{aligned} < h(\vec{\rho}) >= 0 \\ < h(\vec{\rho}_1)h(\vec{\rho}_2) >= \delta^2 W(|\vec{\rho}_1 - \vec{\rho}_2|) \end{aligned} \tag{10}$$

where $< \ ... \ >$ mean averaging over the randomness, $\delta^2 =< h^2(\vec{\rho}) >$ is the average deviation of surface from the plane $z = 0$. Because of the translational invariance and isotropy the correlation function W depends on the quantity $|\vec{\rho}_1 - \vec{\rho}_2|$. It follows from Eq. (11) that $W(0) = 1$. Roughnesses at two points located far away from each other are uncorrelated therefore when $|\vec{\rho}_1 - \vec{\rho}_2| \to \infty$, W goes to 0. One can determine correlation length σ as a distance at which correlation function is essentially decreased. Frequently gaussian form for correlation function $W(\rho) = \exp(-\rho^2/\sigma^2)$ is used. The parameters δ and σ experimentally can be found using light scattering from rough surfaces [4]. Depending on the degree of treatment of the surface of a metal δ is of order of several ten angstroms and σ is of order of few hundred angstroms. Another parameter characterizing roughness that plays important role in radiation is the average of modulus of deviation from the reference plane $z = 0$, $R =< |h(\vec{\rho})| >$ [5]. Depending on the degree of treatment of the surface this parameter varies from $0.01\mu m$ to $5\mu m$.

When a charged particle slides over a rough surface it crosses randomly distributed hills and valleys. One can model these hills and valleys as randomly located plates and vacuum spacings between them. Correlation length of the roughness σ plays role of the thickness of the plates. An electromagnetic wave can travel through these hills provided that σ is smaller than the depth of skin layer in the metal. In the optical region this condition will be fulfilled for not very rough surfaces. Moreover if the hills are high enough $2\pi R \gg \lambda$ then one can assume that photon with wavelength λ is propagating through a random stack of parallel plates having one-dimensional randomness of dielectric constant.

For realization of diffusive mechanism of radiation absorption should be weak. This means that the plates should be very thin. Moreover, in metal case their thickness should be less than the depth of skin layer of metals, in order to the photons diffusively propagate over the system. In the optical region a metal skin layer is of order of several hundred angstroms. As was mentioned above for rough surfaces σ which plays a role of thickness is of order of a few hundred angstrom therefore an optical photon can diffuse through hills and valleys of a rough metallic surface. An experiment on radiation from $80\,keV$ energy electrons sliding over rough metallic surfaces was carried out many years ago[5]. An enhancement of radiation intensity compared to normal falling case was observed. Estimations of hill and valley sizes show that conditions for generation of diffusive radiation exist in the experiment [5]. Unpolarized character and spectral angular dependence of observed radiation intensity are well described by diffusive radiation intensity formulae [6]. Hence we think that in the experiments [5] the diffusive radiation was observed. The energy of a charged particle should be enough for penetration of the system with inessential variation of its velocity. In the experiments [5], keV energy electrons were used. For observation of diffusive radiation from protons their energy should be at least several *MeV* in order to penetrate through many hills when sliding over a rough surface. As it follows from Eq. (3) maximum of radiation lies in the region of large angles from particle velocity direction. Using Eq. (3) one can estimate the integrated over all angles number of emitted photons in the interval $\Delta\omega$ as

$$N_{ph} \sim \alpha \frac{L_z l_{in}}{l^2} \frac{\Delta\omega}{\omega} \tag{11}$$

where α is the fine structure constant. The angular part and γ^2 give contribution of order unity except the case of ultrarelativistic particles. It follows from Eq. (11)that the gain of photon yield compared to transition radiation from one interface case is of order $L_z l_{in}/l^2$. Let us estimate this ratio. The inelastic mean free path of the photon in a random stack can be estimated as follows:

$$l_{in} \sim \frac{\lambda}{\pi f Imb(\omega)} \tag{12}$$

where $f \sim na$ is the fraction of plates in the system. Taking into account that $|b| \gg \varepsilon \sim 1$, for the elastic mean free path one gets from Eq. (7)

$$l \sim \frac{\lambda^2}{4\pi^2 b^2 f a} \tag{13}$$

Diffusive photons are absorbed in the system. Only those escape the system that are created on the particle path of order l_{in}. Therefore when estimating the number of emitted from surface photons one should substitute L_z by l_{in} in Eq. (11). Therefore using Eqs.(11-13), for the number of emitted diffusive photons from a rough surface at the frequency interval $\Delta\omega \sim \omega$, we obtain the following estimate

$$N_{ph} \sim \alpha \left(\frac{4\pi b^2 \sigma}{Imb\lambda} \right)^2 \tag{14}$$

Note that in all equations above b is the real part of dielectric constant of metal. It follows from Eq. (14) that the

photon yield does not depend on the averaged distance between hills [5]. It depends on the ratio σ/λ. Radiation intensity increases on the roughness σ increasing. Maximum intensity is achieved for short length waves. These characteristic features were observed in the experiment [5]. Taking the following reasonable values for a metal $b^2 \sim 10$, $Imb \sim 0.1$, $\sigma \sim 100A^o$, $\lambda \sim 4000A^o$ one has $N_{ph} \sim 10$. Thus the photon yield significantly exceeds the transition radiation yield $N_{tr} \sim 1/137$[8]. Note that even for very smooth surfaces $\sigma \sim 100A^o$ the effect is significant. Such a large photon yield allows to use the diffusive radiation for touch beam diagnostics at electron and proton accelerators.

To create a reliable instrument of beam diagnostics based on diffusive radiation corresponding signal from rough surface should be subtracted from background electromagnetic radiation. This background can be created by other mechanisms of radiations in the same spectral range (diffractive radiation, bremsstrahlung and etc). Also very important is to be sure that the detected signal is generated by the beam touch of the selected place in vacuum chamber. As a DR radiator, a special movable area with surface roughness greater than that in vacuum chamber can be prepared. Motion of this area can be realized in longitudinal or tangential directions with shifts comparable with area sizes. Signal of radiation detector modulated with the frequency of motion subtracted from permanent background supplies the specific DR contribution. The frequencies of kHz range can be applied. Another possibility is the more slow motion of area in radial direction. In this case one must watch on the signal intensity in fixed positions of area. Very promising can be idea to create the DR generator area with variable roughness. For this purpose the piezoelectric effect can be used. One can imagine a stack from piezo and non piezo but metal foils of different thickness. The face of such a stack serve as generator of DR. In case of electrical potential loading at stack the geometrical parameters of stack will change and corresponding modulations in detected signal should be registered. Optimal for DR detection system can be imagined section of vacuum chamber with double tap directed in opposite direction. In one tap a few tens square mm DR radiator can be placed and in opposite the DD detectors must be placed. The important advantage of DR usage is that the DR is emitted at large angles relative to the beam propagation direction. This allows to realize a very simple scheme of DR detection in orthogonal direction on the opposite side of the vacuum chamber. For this purpose existing taps in vacuum chamber can be used to minimize distance between the source of radiation and detector. Situation completely differ in traditional wire scanner technique where the detector of secondary particles/radiation are placed at few meter beam downstream. To extract the DR signal from background in vacuum chamber the motion of DR radiator can be used. Very promising is modulation of DR radiator parameter by piezoelectricity. Proof-of-concept experiment in this case do not need great expenditures and can be realized by usage of standard optical detectors.

REFERENCES

[1] L. Wartski, F. Roland, J. Lasalle and G. Filippi, J. Appl. Phys. 46, (1975), 3644.

[2] D.W. Rule, NIM B, 24/25, (1987), 901.

[3] D.W. Rule and R.B. Fiorito, in *Accelerator Instrumentation*, edited by Elliot S. McGrory, AIP Conf. Proc. No 229 (AIP, New York, 1991), p.315.

[4] *Surface Polaritons: Electromagnetic Waves on the Surfaces and Interfaces*, edited by V.M. Agranovich and A.A. Maradudin, Nauka, Moscow, (1985).

[5] F.R. Harutunian, A.Kh. Mkhitarian, R.A. Hovhanissian, B.O. Rostomian and M.G. Sarinyan, Sov. Phys. JETP, 50, (1979), 895 and references therein.

[6] Zh.S. Gevorkian, Phys. Rev. E 57, (1998), 2338; Sov. Phys. JETP, 114, (1998), 91.

[7] Zh.S. Gevorkian, Phys. Rev. Lett., 145, (2006), 185.

[8] V.L. Ginzburg and V.N. Tsytovich, *Transition Radiation and Transition Scattering*, Adam Hilger, Bristol 1990.

BEAM BASED DEVELOPMENT OF A FIBER BEAM LOSS MONITOR FOR THE SPring-8/XFEL

X.-M. Maréchal#, JASRI SPring-8 and XFEL Project RIKEN, Sayo-gun, Hyogo, 679-5198 Japan
Y. Asano, T. Itoga, XFEL Project, RIKEN, Sayo-gun, Hyogo, 679-5148 Japan.

Abstract

To select the best candidate for a fiber based beam loss monitor, glass fibers of different diameter (100~600 µm), index profile (graded/stepped) and from different makers were characterized (signal strength, attenuation, dispersion) at the SPring-8 Compact SASE Source (SCSS). Beam tests showed that at 250 MeV the detection limit corresponding to a 10 mV signal is below 1 pC/bunch over 60 m and 3 pC/bunch over 120 m, with a position accuracy better than 30 cm. The fiber lifetime has been estimated to be over 13000 hours from dose measurements at the SCCS.

INTRODUCTION

Optical fibers have been used as radiation detectors for more than 20 years in a wide range of experiments. Recently several facilities have worked on the development of fiber-based local beam loss detection systems [1]. Fiber-based beam loss monitors offer the possibility to detect beam losses over long distances in real time, with good position accuracy and sensitivity at a reasonable cost. For the undulator section of the 8 GeV SPring-8/XFEL [2], radiation safety considerations set the desirable detection limit at 1 pC (corresponding to a 0.1% beam loss) over more than a hundred meter. While the intensity of the Cerenkov radiation generated in and transmitted down a multimode fiber has been predicted theoretically [3,4], the selection of the optimum fiber is not straightforward. A beam-based approach was therefore chosen to characterize different glass fibers (signal strength, attenuation, dispersion).

EXPERIMENTAL SET-UP

The experiments were carried out at the SCSS, a 1/16th model of the future SPring-8/XFEL The SCSS has a maximum electron energy and repetition rate of 250 MeV and 60 Hz respectively. The optical fiber was set along (for beam loss measurements) or across (for attenuation/dispersion measurement) the accelerator vacuum chamber (Fig. 1). The signals from the photomultiplier tubes (PMTs) set at both end of the fiber are read out with an oscilloscope. A trigger signal from the accelerator master oscillator is used as time reference. The beam current was measured with current transformer (CT) monitors placed along the beam accelerator. Inserting the screen of an optical transition radiation (OTR) monitor into the beam path generates an electromagnetic shower: This artifice is used to simulate a beam loss (stray electrons hitting the vacuum chamber). To measure the attenuation/dispersion of the light signal, the fiber is set across behind an OTR screen. The signal is then measured for different distances (A, B in ig 1b.).

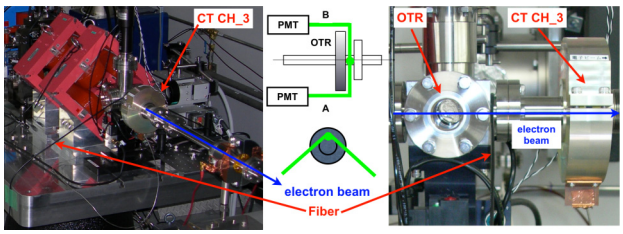


Figure 1: Experimental set-up used for the measurement of the attenuation of the beam loss monitor.

Several kinds of fibers (different diameters, numerical aperture and index profile) were tested (Table 1). All fibers were coated to limit the noise from ambient light. The choice of the photomultiplier (Hamamatsu H6780-02) resulted from a compromise between the fiber attenuation and the characteristics of Cerenkov spectrum. An additional criterion was the possibility to add a connector: The fibers were equipped with FC connectors at both ends to insure easy ("plug and play") and clean connections (low insertion loss) as well as a good reproducibility. With this experimental set-up, it is possible to test the response (signal strength, attenuation, dispersion) of these fibers in realistic (The continuous spectrum of a Cerenkov signal from stray charged particles) and standardized conditions.

Table 1: Main characteristics of the fibers. The numerical aperture of the Fujikura and Corning fibers are respectively 0.2 and 0.39.

Maker	Reference	Index	Length [m]
Mitsubishi	ST100	Step	10.1
Fujikura	GC200/250	Graded	10.2
	GC400/500	Graded	61.4
	GC600/750	Graded	10.1
	SC200/220	Step	10.1
	SC400/440	Step	32.4 & 121.4
Corning	COR200VIS39	Step	25.4

SIGNAL STRENGH AND ATTENUATION

Figure 2 shows the strength of the Cerenkov signal as a function of the fiber length. The signal from the PMT has been normalized by the average beam charge impacting the screen of the OTR monitor. The error bars reflect the standard deviation from the PMT signal (typically taken over a few hundreds samples) as well as the standard deviation of the CT signal (typically less than one

#marechal@spring8.or.jp

percent) and its accuracy (10%). The lines are fits from the measured value according to:

$$S[\mathrm{V/nC}] = S_0[\mathrm{V/nC}]\,10^{-\alpha[\mathrm{dB/km}]x[\mathrm{km}]} \quad (1)$$

where α is the attenuation of the Cerenkov signal expressed in dB/km. α is a convolution of the attenuation of the fiber and the PMT sensitivity. The values obtained from the fit are given in Fig. 3, the uncertainty being larger for the shorter (~ 10 m) fibers.

For Wang et al. [3] the Cerenkov output power is proportional to the square of the fiber diameter D. The results obtained here show that the detector output is proportional to $D^{1.5}$. A bundle of fibers will give a signal weaker than that of a single fiber of equivalent diameter. For the SPring-8/XFEL, the detection limit and length to be surveyed give a minimum diameter of 400 µm.

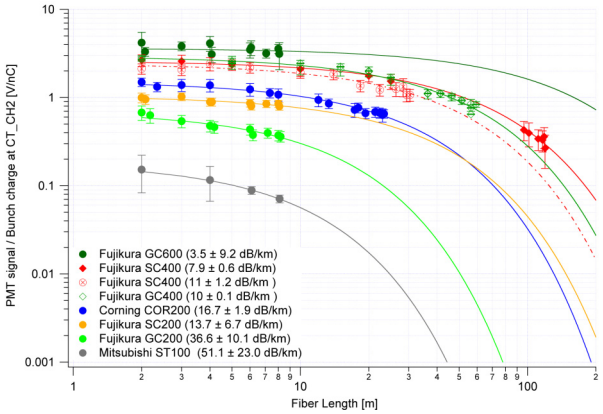


Figure 2: Signal from the PMT normalized by the average beam charge impacting the OTR screen as a function of the fiber length. The legend gives the values of the attenuation obtained from the fits.

DISPERSION

Multimode and chromatic dispersions distort the optical signal as it travels down the fiber, resulting in pulse broadening: Dispersion will affect the time and therefore the spatial resolution of the beam loss detector. Fig. 3 shows the full width at half maximum of the Cerenkov signal measured with the PMTs as a function of the fiber length for the Fujikura GC and SC 400. As can be seen from Fig. 3, the GC and SC 400 have the similar dispersion (≈ 0.14 ns/m within experimental errors): The dispersion of the Cerenkov signal in the fiber is mainly due to chromatic dispersion.

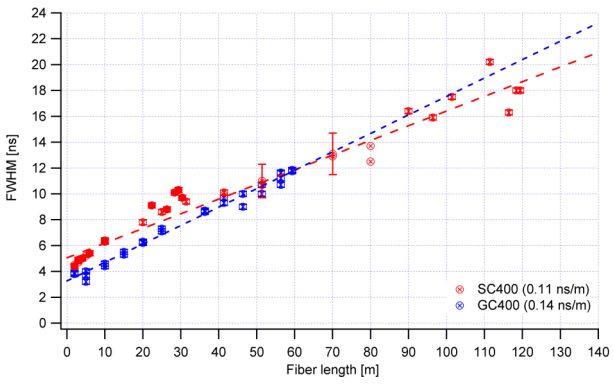


Figure 3: FWHM of the PMT signal as a function of the fiber length.

DETECTION LIMIT

Two methods have been used to evaluate the detection limit of the system: With the fiber set along the accelerator, one has measured either the signal generated by inserting an OTR screen, or the signal from a natural beam loss. In each case, both the signal detected upstream and downstream (with respect to the direction of propagation of the electron beam) were measured. The results, calculated for a detection level set at 10 mV, are summarized in Table 2 for the Fujikura SC400 fiber.

Table 2: Detection limit (Fujikura SC400) at 10 mV

Fiber Length	OTR induced loss		Natural Beam loss	
	Direction with respect to the e- of propagation			
	Upstr.	Downstr.	Upstr.	Downstr.
60 m	0.6 pC	0.9 pC	< 1pC	< 0.1pC
120 m	1.8 pC	2.6 pC	< 3pC	< 0.3 pC

Figure 4 shows a typical signal measured during user operation (lasing at 60 nm) in the SCSS chicane located just before the undulators. No beam loss is detected from the difference between the upstream and CT monitors. The downstream signal is four times larger than the upstream signal: The detection of both signals is therefore important for an optimum operation of the beam loss monitor. The fine structure of the main peaks is also clearly visible: With a temporal discrimination of a few ns, it becomes possible to detect different beam losses occurring within a short distance from each other.

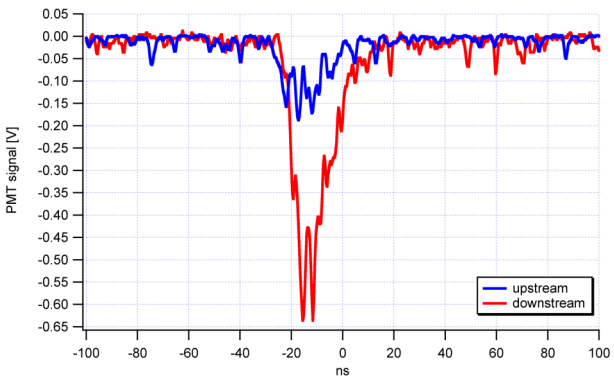


Figure 4: Beam loss signal (Fujikura SC400, single shot, 2.5 GS/s). The fiber is set so that the PMT is located 120 m upstream/downstream from the loss point.

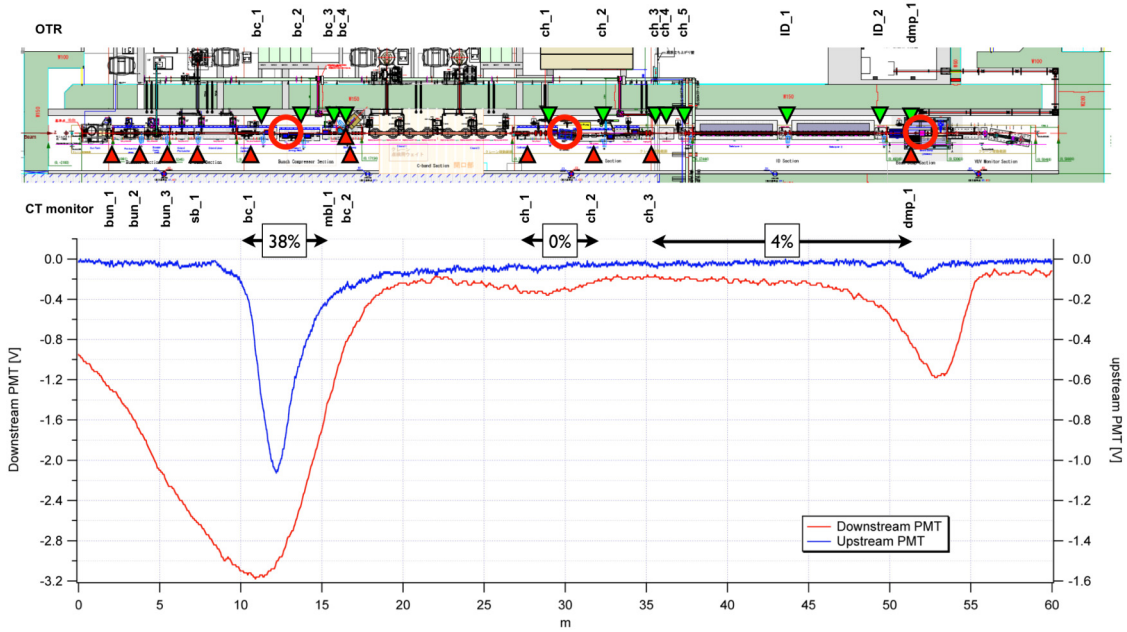


Figure 5: A typical beam loss measured on the SCSS prototype accelerator (single shot). Top: View of the SCSS accelerator with the location of the OTR and CT monitors (green and red triangles respectively). Bottom (b): The signals from the upstream and downstream PMTs. The percentages give the beam losses as measured by the CT monitors. The red circles indicate the position of the loss points.

Figure 5 presents a typical beam loss measured at the SCSS (single shot). The fiber was set along the vacuum chamber, from the first chicane up to the beam dump. The energy of the electron varies from 50 MeV (before the C-band section) up to 250 MeV (after). The signals from both chicanes are clearly visible (although no beam loss is detected by the CT in the second chicane). A few percents of the beam are lost before the beam-dump.

LIFETIME

Optical fibers are known to be susceptible to radiation damage. The production of color centers translates into radiation-induced attenuation, the deterioration of the fiber optical performance being higher at shorter wavelengths. So far no radiation damage has been observed in the 600 to 850 nm range. The fiber lifetime at the Spring-8 8 GeV/XFEL has been estimated using data available for multimode fibers (average 3 dB/km/Gy [5]) and dose measurements at the SCSS (a maximum of 0.008 Gy/h in the ID section in routine operation [6]): Assuming a 1 m length irradiated at the maximum dose, the fiber lifetime is over 13000h for a 1 dB loss.

SUMMARY

The ultimate detection limit of a fiber based beam loss monitor is strongly dependent on the fiber characteristics. While small core fibers are limited to short lengths, for larger core diameters, the practical length will not exceed a few hundred meters, depending on the desired detection level. Beam tests showed that at 250 MeV the detection limit corresponding to a 10 mV signal is below 1 pC/bunch over 60 m and 3 pC/bunch over 120 m. The position accuracy was found to be better than 30 cm.

A practical, online, version of the beam loss monitor is now under development: The signal from fibers set along the vacuum chamber will be read out by a Flash-ADC. The waveforms will be used to determine the position of the beam loss along and perpendicularly to the beam direction. Studies (Numerical and experimental) are planned to estimate the amount of the loss as a function of the amplitude of the signal. First tested on the SCSS this beam loss monitor should be installed on the SPring-8/XFEL when it comes into operation.

ACKNOWLEDGMENTS

We are very grateful to the Corning and Mitsubishi companies who graciously provided samples.

REFERENCES

[1] F. Wulf, this conference.
[2] http://www.riken.jp/XFEL/eng/index.html
[3] Y.-C.Wang, Y.-W. Shi and H.-T.Jiang, Proc. SPIE Vol. 1572, Intl Conf on Optical Fibre Sensors in China, 1991, 32.
[4] S. H. Law, S. C. Fleming, N. Suchowerska, and D. R. McKenzie, Applied Optics, Vol. 45, Issue 36 (2006) 9151
[5] M. N. Ott, "*Radiation Effects Data on Commercially Available Optical Fiber: Database Summary*", NASA Goddard Space Flight Center
[6] X.-M. Maréchal, T. Itoga and Y. Asano, SPring-8 XFEL internal report XFEL SD-08/01, August 2008

FLEXIBLE CORE MASKING TECHNIQUE FOR BEAM HALO MEASUREMENTS WITH HIGH DYNAMIC RANGE

J. Egberts, S. Artikova, MPI-K, Heidelberg, Germany
C.P. Welsch, Cockcroft Institute, Warrington, Cheshire, UK, University of Liverpool, Liverpool, UK

Abstract

The majority of particles in a beam are located close to the beam axis, called the beam core. However, particles in the tail distribution of the transverse beam profile can never be completely avoided and are commonly referred to as beam halo.

The light originating from or generated by the particle beam is often used for non- or least destructive beam profile measurements. Synchrotron radiation, optical transition, or diffraction radiation are examples of such measurements. The huge difference in particle density between the beam core and its halo, and therefore the huge intensity ratio of the emitted light is a major challenge in beam halo monitoring.

In this contribution, results from test measurements using a flexible core masking technique are presented indicating way to overcome present limitations. This technique is well-known in e.g. astronomy, but since particle beams are not of constant shape in contrast to astronomical objects, a quickly adjustable mask generation process is required. The flexible core masking technique presented in this paper uses a micro mirror array to generate a mask based on an automated algorithm.

INTRODUCTION

The detection and possible control of the beam halo is of utmost importance for high energy accelerators, where unwanted particle losses lead to an activation or even damage of the surrounding vacuum chamber. But also in low-energy machines like the USR [1] one is interested in minimizing the number of particles in the tail region of the beam distribution. Since most part of the beam is normally concentrated in the central region, observation techniques with a high dynamic range are required to ensure that halo particles can be monitored with sufficient accuracy. One option to monitor the beam halo is to use light generated by the beam, either through synchrotron radiation (SR), optical transition radiation (OTR), or luminescent screens. In thus case, a special detection technique is required to allow for high dynamic range measurements.

The flexible core masking technique is based on the core masking technique which is well established in astronomy to observe the corona of the sun [2]. For an accurate image acquisition of the corona, an exposure time is required at which a normal camera overexposes due to the bright central region of the sun. The resulting blooming effects will superimpose the corona light and make an accurate image acquisition impossible. Therefore, the central bright region of the sun is masked out to allow for a corona measurement without any negative blooming effects. The same principle can be applied for beam halo measurements, as already shown in [3, 4]. Test measurements of this kind have been performed at CERN by T. Lefèvre et al [5].

Unlike astronomical objects, an accelerator beam's profile is typically variable in shape. A technique using a fixed mask does not suffice any more and a flexible core masking technique is required. Taking advantage of the unique features of *Micro Mirror Arrays (MMA)*, flexible masks required for this technique become feasible.

MICRO MIRROR ARRAY

The *Micro Mirror Array* used for the measurements consists of an array of 1024×768 micro mirrors of $13.68\mu\text{m}\times13.68\mu\text{m}$ size. Each of them can individually be set to $\pm12^\circ$ [6]. Light will then be reflected in different directions depending on the micro mirror state. It is thereby possible to use the MMA as a reflective display which can be utilised as an adjustable mask.

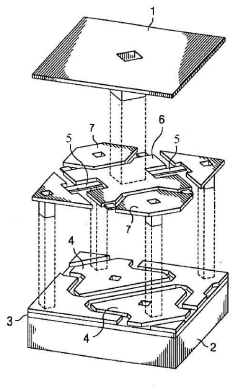


Figure 1: *MMA* Pixel Scheme [7].

Each single pixel of the *MMA* can be separated in a substructure and superstructure. The mirror itself is attached to the superstructure. The substructure of the pixels consists of a silicon substrate (fig.1-2) with an insulating layer (fig.1-3) on top, which isolates the superstructure from the substructure. Upon the insulating layer, there is a thin metallic layer, which forms the lower address electrodes (fig.1-4) and also supports the hinge. The hinge consists of the flexible torsion beam (fig.1-5), the large hinge yokes (fig.1-6), and upper address electrodes (fig.1-7).

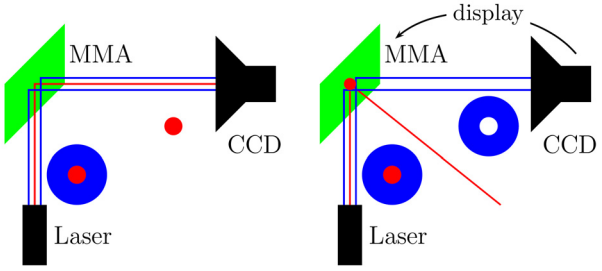
If there is an appropriate potential applied to the upper and the lower electrodes (fig.1-4; 1-7), the electrostatic

force between them induces a torque and causes the hinge to tilt. The torsion beam (fig.1-5) acts as a torsion spring and creates a resisting torque. The hinge is tilted until the resisting torque of the torsion spring and the electrostatic torque are of the same magnitude or until it is stopped mechanically by touching the substructure. Since the pixel is used only in a digital ON-OFF mode, the voltage between the two electrodes is set high enough to cause the maximum deflection.

EXPERIMENTAL SETUP

We simulate a typical (Gaussian) distribution as it can be found in most particle beams, by using a conventional HeNe laser in our lab. The opening angle of the laser of 0.1° corresponds to SR/OTR emitted at some 100 MeV and can be regarded as a realistic approximation of a real particle beam.

The laser beam is reflected by an MMA into an 8Bit CCD-camera that measures the two dimensional beam profile, as illustrated in Fig. 2. If the mask is displayed on the MMA, the central beam core (red) will be deflected while the halo (blue) is still reflected into the CCD-camera. The challenge of measuring a high dynamic range is reduced to the issue a measuring a low intensity which can be done by increasing the exposure time of the camera or by removing neutral density filters that were included before.



(a) Laser profile measurement (b) display beam core on MMA

Figure 2: After the profile is measured (a), its image (red) is displayed on the MMA to mask out the core to only reflect the halo into the camera (b).

MASK GENERATION

The mask is generated by displaying an image of the laser beam core on the *MMA*. Since the *MMA* is a digital device, the grey-scale image acquired by the CCD has to be transformed into a binary image. All pixels above a certain threshold are set to white, and all pixels below are set to black. The mask can then be stretched to the size that is required for the measurement.

The mask generation process consists therefore of three parts, the beam profile measurement, the conversion in a binary image, and the re-scaling of the mask to the desired size. To have a minimal negative effect of any light intensity fluctuations on the mask size during the image conversion, the threshold should be applied at the point of the maximum slope of the intensity distribution. On the other hand, as the mask is resized, the error of the mask shape also increases by the scaling factor. It can therefore be assumed that the total error of the mask is given by

$$\Delta M \propto \left(\frac{\partial I(x)}{\partial x}\right)^{-1} * R, \qquad (1)$$

with ΔM being the error of the mask shape, $I(x)$ being the light intensity distribution at threshold position x, and R being the scaling factor. Assuming a Gaussian shaped intensity distribution, ΔM is minimised by setting the first derivative to zero.

$$\frac{\partial}{\partial x}\left(x\frac{\partial}{\partial x}e^{-\frac{x^2}{2\sigma^2}}\right) = 0 \qquad (2)$$

This yields $x^2 = 2\sigma^2 \Rightarrow x = \sqrt{2}\sigma$. The threshold for setting the 8-Bit grey values to black or white is therefore chosen to be at $1/e$ of the maximum brightness. The highest brightness in an 8-Bit image is $2^8 - 1 = 255$ which gives a threshold of $255/e$.

To avoid an additional rescaling of the mask due to the diverging beam, the beam profile from which the mask is generated is acquired where the *MMA* is located.

MEASUREMENT

A control software was written that is able to control the CCD-camera and the *MMA*. It realises the mask generation and allows for a precise positioning of the mask on the *MMA*. The acquired two dimensional images are projected over 10 pixel rows to achieve a better statistics. Projections of various mask sizes are shown in Fig. 3.

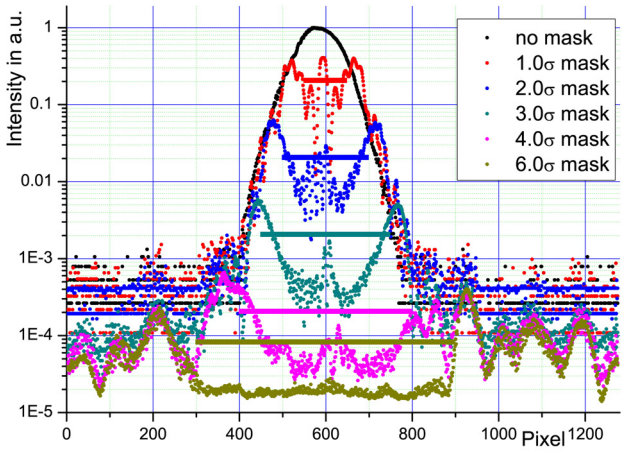


Figure 3: Projected profiles for various mask sizes.

To take full advantage of the 8Bit dynamic range of the CCD-camera, the exposure time is varied for each measurement to achieve an optimum result. In the analysis, the camera output therefore needs to be scaled by the exposure time to grant a quantity proportional to the light intensity.

The camera output was found to be highly linear with respect to the inverse exposure time.

In the central region a strong interference pattern is visible created by the mask. But for the beam halo observation this is of no further interest. In the outer halo region, some pattern is visible that is found to be part of the intrinsic laser beam profile.

Since the pattern outside the beam core is the major limitation to the achievable dynamic range, an iris is used to "cut off" this pattern. As the *MMA* and the mask can both generate interference patterns, the iris is carefully inserted in front of the *MMA* not to cut of any interference patterns caused by the *MMA*. Thereby, the dynamic range was calculated to be 1:300,000 which corresponds to 5.5 orders of magnitude.

Laser Correction

In the method described above, the mask always has to be smaller than the iris to observe a sensible signal. To overcome this limitation, a spatial mode filter can be used to generate a perfect Gaussian beam profile instead of cutting off the fringes.

The basic principle of a spatial mode filter is illustrated in Fig. 4. In the Fourier plane of the first lens, a pinhole is located to filter out higher orders and thereby generate the theoretically predicted Gaussian distribution of a laser beam.

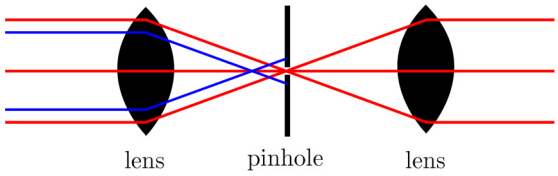


Figure 4: Principle of a spatial mode filter.

The major challenge of setting up the spatial mode filter is the high precision adjustment of the lenses and the pinhole. If the pinhole is misplaced in transverse direction, the beam profile is strongly distorted in one direction. By the use of micrometer screws, this positioning is done very precisely and its negative effects can almost be neglected. In case of a longitudinal misplacement of the pinhole, it is not exactly located in the Fourier plane of the focussing lens. The Fourier transform will still have a spatial component that creates an interference pattern when passing through the pinhole. The correct longitudinal adjustment of the pinhole mainly determines the dynamic range of the resulting Gaussian distribution of the laser beam.

The most reliable method of adjusting the spatial mode filter was achieved by first positioning the pinhole with respect to the first focussing lens. If the focal point of the lens matches the pinhole, the backscattered light between lens and pinhole will be at its minimum. The longitudinal and transversal position of the pinhole can thereby be adjusted very precisely. For the positioning of the second lens, a total focussing effect of the spatial mode filter must be avoided. It proved to be most accurate to focus the laser to a distant point.

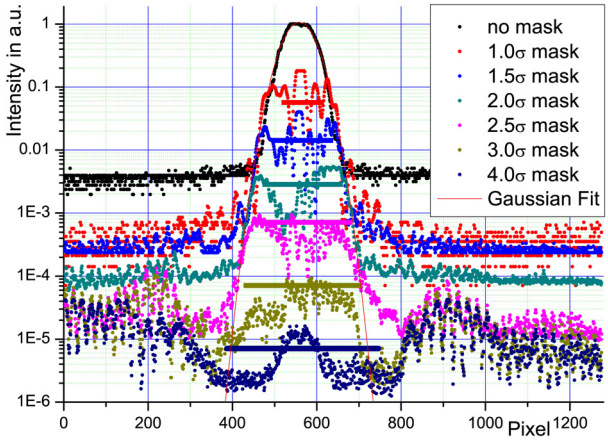


Figure 5: Projected profiles for various mask sizes for a laser beam corrected by a spatial mode filter.

It was possible to achieve a Gaussian shaped laser beam profile over more than four orders of magnitude, as indicated in Fig. 5. Based on this measurement, a dynamic range of six orders of magnitude is calculated.

CONCLUSION

The flexible core masking technique proved to be a reliable method for high dynamic range measurements of up to six orders of magnitude. The disadvantage of the flexible core masking technique is the complex setup and the lower dynamic range in comparison to other measurement techniques like the use of CID-cameras. On the other hand, this technique is a low budget alternative granting high dynamic ranges in short acquisition times.

REFERENCES

[1] C.P. Welsch, J. Ullrich et al., "An ultra-low-energy storage ring at FLAIR", Nucl. Instr. and Meth. A 546 (2005) 405417.

[2] B.R. Oppenheimer et al, "The Lyot Project: Status and Deployment Plans", AMOS Technical Conference, 2003

[3] C.P. Welsch, E. Bravin, B. Burel, T. Chapman, T. Lefèvre, M.J. Pilon, "Alternative Techniques for Beam Halo Measurements", Meas. Sci. Technol. 17 (2006) 2035c

[4] J. Egberts, S.Artikova, C.P. Welsch, E. Bravin, T. Lefèvre, T. Chapman, M.J. Pilon, "Design of a Beam Halo Monitor with Dynamic Range", TUP076, LINAC08, 2008, Victoria, Canada

[5] T. Lefèvre et al., "Beam Halo Monitoring at CTF3", THPLT147, Proc. EPAC 2004, 2004, Lucerne, Switzerland

[6] Texas Instruments, "DMD Discovery 1100 Conroller Board & Starter Kit", 2005

[7] T.J. Meyer AND B.A. Mangrun AND M.F. Reed, "Split Beam Micromirror", Texas Instruments Inc., 2006

CONFIGURATION AND VALIDATION OF THE LHC BEAM LOSS MONITORING SYSTEM

C. Zamantzas, B. Dehning, J. Emery, J. Fitzek, F. Follin, S. Jackson, V. Kain, G. Kruk, M. Misiowiec, C. Roderick, M. Sapinski ,CERN, Geneva, Switzerland

Abstract

The LHC Beam Loss Monitoring (BLM) system is one of the most complex instrumentation systems deployed in the LHC. As well as protecting the machine, the system is also used as a means of diagnosing machine faults, and providing feedback of losses to the control room and several systems such as the Collimation, the Beam Dump and the Post-Mortem. The system has to transmit and process signals from over 4'000 monitors, and has approaching 3 million configurable parameters.

This paper describes the types of configuration data needed, the means used to store and deploy all the parameters in such a distributed system and how operators are able to alter the operating parameters of the system, particularly with regard to the loss threshold values. The various security mechanisms put in place, both at the hardware and software level, to avoid accidental or malicious modification of these BLM parameters are also shown for each case.

INTRODUCTION

The Large Hadron Collider (LHC) is the next circular accelerator being constructed at the European Organisation for Nuclear Research (CERN). It will provide head-on collisions of protons at a centre of mass energy of 14 TeV for high energy particle physics research. In order to reach the required magnetic field strengths, superconducting magnets cooled with superfluid helium will be used. The energy stored in the LHC can potentially damage many elements of the accelerator or could make its operation very inefficient.

The strategy for machine protection and quench prevention of the LHC is mainly based on the Beam Loss Monitoring (BLM) system. At each turn, there will be several thousands of data to record and process in order to decide if the beams should be permitted to continue circulating or their safe extraction is necessary to be triggered. The decision involves a proper analysis of the loss pattern in time and a comparison with predefined threshold levels that need to be chosen dynamically depending on the energy of the circulating beam. This complexity needs to be minimized by all means to maximize the reliability of the BLM system and allow a feasible implementation. The processing of the acquired data and the comparison with predefined threshold levels is needed to be performed in real-time and thus requires dedicated hardware to meet the demanding time and performance requirements.

To overcome such limitations, a great effort has been committed to provide a highly efficient, reliable and feasible implementation of the BLM system by employing various state of the art techniques in analogue and digital electronics, databases and computing, which include redundancies and optimizations across all of its levels of abstraction.

SYSTEM CONFIGURATION

The BLM system is making use of modern field programmable gate arrays (FPGAs), which include the resources needed to design complex processing and can be reprogrammed making them ideal for future upgrades or system specification changes. There is a common FPGA firmware that is deployed to all crates at the Front-End Computer's (FEC) boot procedure or if required could be read from the flash memory on power on.

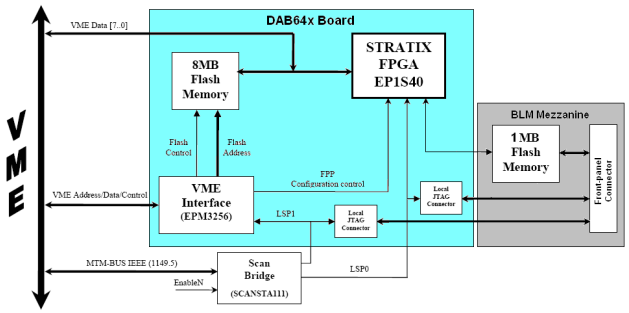


Figure 1: Block diagram of the FPGA firmware deployment and initialisation options.

More specifically, the FPGA configuration can be forced to be loaded either remotely via the FEC and the VME bus, locally via the JTAG connection that is provided in the front panel, or set to auto-configurable by utilising the on-board memory. Figure 1 shows a block diagram of the interconnections in the Threshold Comparator (BLETC) module.

The dataset of thresholds and settings for the complete BLM system during the deployment procedure is split to the relevant parameters for each module. In that way, they include only information which is unique for each monitor, crate or sector that the module will need to protect. Among those it includes the monitor names, their threshold values, the serial numbers for the BLETC and the two acquisition modules [1] which are connected to it, as well as the Connection and Masking matrices. Table 1 shows the complete list of the parameters stored on each processing module.

These channel and board specific parameters are stored in the normally unused space of the configuration memory

Table 1: Parameters Deployed on Each BLETC Module

Name	Data (x32bit)	Description
Thresholds	8192	Threshold values table (16 channels x 12 Running Sums x 32 Energy Levels)
Channel Connected	1	Channel definition: CONNECTED / DISCONNECTED from the BIS
ChannelMask	1	Channel definition: "MASKABLE"/"UNMASKABLE"
BLECF Serial A	1	Acquisition Card's Serial Number (for Channels 1-8)
BLECF Serial B	1	Acquisition Card's Serial Number (for Channels 9-16)
BLETC Serial	2	Threshold Comparator's Card Serial number
BLETC Firmware Version	1	Threshold Comparator's Firmware Version
Expert Monitor Names	128	Expert Monitor Names for the 16 channels.
Official Monitor Names	128	Official Monitor Names for the 16 channels.
DCUM	16	DCUM Numbers of each channel
Family Names	128	Threshold Family Name of each channel
Monitor Coefficients	16	Monitor Threshold Coefficient for each channel
Last LSA Modification	2	Timestamp: Last Modification of the MASTER table in LSA database
Last Flash Modification	2	Timestamp: Last Modification of the non volatile on-board memory
Flash Checksum	1	CRC value for/from the FEC to check the table integrity.
Total	8620	

taking advantage of the high reliability and the non volatile properties of the particular flash memory.

After the initialisation of the module an FPGA process fetches the data from the flash space and makes a local copy in its embedded memory. By design, the processing electronics provide the functionality to update remotely the stored parameters and if safety reasons require it, only local updates can be enforced by an on-board switch. The new settings are loaded from the memory on the FPGA either on request or at the next boot.

STORAGE OF SETTINGS

In order to collect and verify the vast amount of data necessary as well as to automatise the procedure and minimise the errors in future changes several databases have been employed. Those include the Manufacturing and Test Folders (MTF), the LHC Layout and the LHC Software Architecture (LSA) databases.

Initially the data are imported in MTF and are copied and linked together after scrutinous verification to the Layout. The latter provides hierarchical views of the system as well as information on the position in the tunnel and with respect to all other elements of the LHC (see [3]). The complete dataset can be one-way synchronised to LSA where it is split into tables to hold information for each monitor, crate or sector. All the final configuration parameters have been chosen to be stored in LSA, which is the settings management system at CERN. It has been built with high availability in mind and provides significant features like strong security, detailed history of changes, and roll-back to a previous state.

STAGE and FINAL Tables

The LSA database structure uses data staging – the BLM parameters exist in STAGE and FINAL tables. The STAGE tables allow BLM experts to load parameters available from the Layout database, to add the threshold values, and perform consistency checks before persisting the data to the FINAL tables. A dedicated database procedure is used to commit changes made in the STAGE tables to the FINAL tables. Many constraints (rules governing the data) have been implemented within the database to ensure data integrity.

MASTER and APPLIED Tables

The MASTER table content is produced by a database procedure, which combines the data of the various FINAL tables. The threshold values appearing in this table correspond to the absolute limits known from simulations and measurements to protect the different elements from damage.

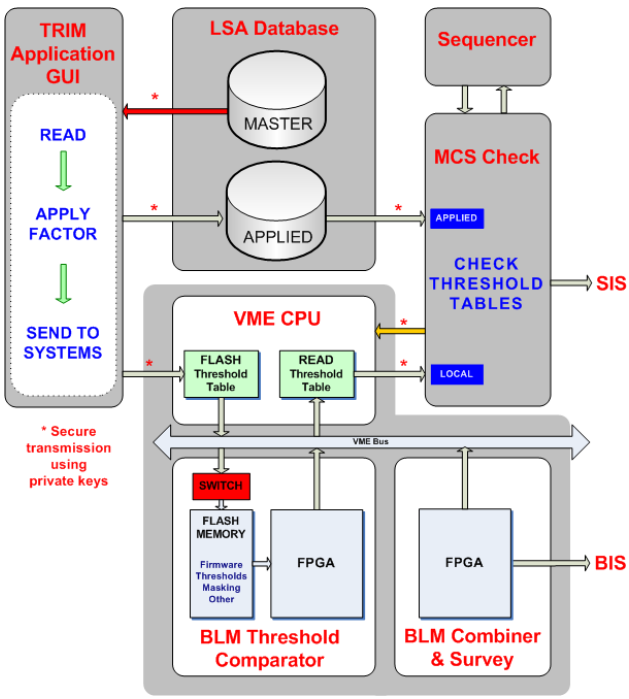


Figure 2: Block diagram of the data flow for the parameters configuration and verification.

A further process triggered by the operators reads the MASTER table, applies unique per monitor threshold coefficients (always < 1) and saves the new table as the APPLIED table. The latter is the table that the FEC sends to the FPGA, if allowed by a role based access system and the on-board switch in the processing electronics. In that way, operators and domain experts can readjust by scaling down the individual threshold values of each monitor, if this is found necessary, without impairing the protection characteristics of the system.

SYSTEM VALIDATION

The overall reliability of a system is augmented by checking as often as possible whether its functionality and performance has remained unchanged. For this reason, several checks have been integrated in the BLM system that either loop continuously or, for those tests that need to alter inputs or outputs of the system, are performed on request when the operation of the accelerator permits. The 'on-request' checks are initiated by the LHC Sequencer before each fill and are dictated to run at regular intervals by the Combiner and Survey (BLECS) module which can disallow a new beam to be injected in the machine.

Continuous Checks

The acquisition chain is tested using a 10pA test signal that is measured directly in the tunnel card. A status flag is raised if there is no response because of the injected signal within 100 seconds. This status flag is caught by the BLETC.

A continuous check of the connectivity and the error-free transmission between the acquisition and the processing modules is based on the double optical line, the embedded information in the packets and two error detection techniques [2], i.e. CRC32 and 8b/10b encoding.

Similarly, the Beam Energy reception is continuously checked and in the case of errors or disconnections the system defaults to the strictest threshold values, i.e. those for the highest energy.

The correct card assignment is performed by checking the embedded serial numbers arriving with every packet against those stored in the database. This function indirectly also checks continuously the correct channel assignment.

A continuous integrity check of the on-board memory that holds the threshold and settings tables is performed by the FEC, currently once per minute, that is able to discover corruption of the parameters.

On Request Checks

The Management of Critical Settings (MCS) Online Check is performed additionally after every update of the crates. The initiated test allows the FEC to read all the currently used parameters by incrementing the energy levels and recording the used threshold values. It subsequently transmits them to the MCS Online Check for comparison. Both the FEC and the Software Interlock System (SIS) receive the PASS/FAIL result.

With the purpose of discovering disconnected or failed channels a modulation of the high voltage supply of the detectors is initiated. (see [4])

The correct operation of the acquisition electronics is tested by enabling a signal of 100 pA to be injected on each input. The BLECS is able to detect the change by using the 1.3 second integrated values recorded.

The ability of the BLETC to generate a beam dump request signal for each of the 'maskable' and 'un-maskable' outputs, and its correct reception by the BLECS is tested by utilising dedicated backplane lines on each crate to issue commands.

Similarly, the correct beam dump requests transmission between the BLECS and the Beam Interlock system (BIS) is tested. In this case the request is transmitted over the ethernet connection available in the FEC.

CONCLUSIONS

In consequence, by performing its requested tasks the BLM system is able to have a constant and very detailed view on the state of the whole machine. This is supported by the back-end infrastructure of the databases, processes and applications to set up and verify its operation as well as to provide failsafe modifications in the future.

ACKNOWLEDGEMENTS

The authors would like to thank the Machine Protection working group, the operators and the Controls and Operations group for their contribution, and especially Daryl Bishop and Graham Waters at TRIUMF for building and supporting the DAB64x board.

REFERENCES

[1] E. Effinger, B. Dehning, J. Emery, G. Ferioli, G. Gauglio, C. Zamantzas, *"The LHC Beam Loss Monitoring System's Data Acquisition Card"*, 12th Workshop on Electronics for LHC and future Experiments (LECC 06), Valencia, Spain.

[2] C. Zamantzas, B. Dehning, E. Effinger, J. Emery, G. Ferioli, *"An FPGA Based Implementation for Real-Time Processing of the LHC Beam Loss Monitoring System's Data"*, Nuclear Science Symposium Conference Record, 2006. IEEE, vol.2, no., pp.950-954, Oct. 29 2006-Nov. 1 2006.

[3] P. Le Roux, R. Billen, J. Mariethoz, *"The LHC Functional Layout Database as Foundation of the Controls System"*, ICALEPCS07, Knoxville, Tennessee, USA.

[4] J. Emery, B. Dehning, E. Effinger, G. Ferioli, H. Ikeda, E. Verhagen, C. Zamantzas, *"LHC BLM Single Channel Connectivity Test using the Standard Installation"*, these proceedings.

DESIGN SPECIFICATIONS FOR A RADIATION TOLERANT BEAM LOSS MEASUREMENT ASIC

G.G. Venturini, B. Dehning, E. Effinger, C. Zamantzas, CERN, Geneva, Switzerland

Abstract

A novel radiation-hardened current digitizer ASIC is in planning stage, aimed at the acquisition of the current signals from the ionization chambers employed in the Beam Loss Monitoring system at CERN. The purpose is to match and exceed the performance of the existing discrete component design, currently in operation in the Large Hadron Collider (LHC). The specifications include: a dynamic range of nine decades, defaulting to the 1 pA-1 mA range but adjustable by the user, ability to withstand a total integrated dose of 10 kGy at least in 20 years of operation and user selectable integrating windows, as low as 500 ns. Moreover, the integrated circuit should be able to digitize currents of both polarity with a minimum number of external components and without needing any configuration. The target technology is the IBM 130 nm CMOS process. The specifications, the architecture choices and the reasons on which they are based upon are discussed in this paper.

INTRODUCTION

It is expected that with the increase in LHC beam intensity an increase in beam losses will be observed as well. Accordingly, the BLM electronics installed in the facility will be exposed to a higher radiation level. The current discrete component front-end electronics will be replaced by an Application Specific Integrated Circuit (ASIC) chip, designed to operate in the radioactive environment and, at the same time, to deliver higher performance. The employment of the new integrated circuit will allow the placement of the acquisition boards closer to the detectors in the most radioactive locations.

DESIGN SPECIFICATIONS

The charge digitizer provides a digital output proportional to the integral of the input current over a time window. Figure 1 shows a functional diagram of the device.

The main objectives of the design are summarized as follows (Table 1):

- *Dynamic range*: nine decades (or 180 dB).
- *Minimum input current*: the ASIC design will be compatible with the different detectors and setups employed in the BLM system, in line with the specifications. Considering a current digitizer based on a current-to-frequency converter, the input-output relationship is given by $f_{OUT} = I_{in}/Q_{REF}$, where Q_{REF} is here referred to as the reference charge. Enabling the user to select different values of the reference charge provides an effective method to scale the maximum and minimum signals, while internally the range of frequencies of operation and the value of the DR are kept constant. As other design-dependent constraints affect the value of the maximum and minimum input currents, care should be taken in the implementation of different input ranges. Additionally, independently of the chosen design, the inverse saturation current of the protection diodes and its variation due to temperature, radiation effects and aging set a limit on the minimum detectable current that can be measured. To overcome this drawback, the protection circuit on the analog input pins will be opportunely designed, to decrease the lower limit under 1 pA. The trade-off between the overload tolerance of the custom-protected inputs and the input leakage will be analyzed to provide a satisfactory solution, to provide a leakage below 100 fA.
- *Bipolar input currents*: the converter should work with currents of either polarity, without requiring any pre-configuration. It is currently under consideration whether or not the converter will provide the same range for each of them or a full and a reduced one. The measurement of dual polarity currents with a single supply device requires the input to be biased at approximately $V_{DD}/2$. The availability of this voltage on an output pin is useful when a circuit is connected to the input and it is thus provided to the user (REFOUT pin in Fig. 1).
- *Radiation tolerance*: the design aims for a Total Ionizing Dose (TID) equal or greater than 10 kGy over a 20 years period. The requirements regarding Transient Dose Effects, maximum Single Event Effects (SEE) rates are being investigated and will be split into maximum Single Event Upsets (SEU) and Single Event Latch-up (SEL) rates.

In addition to the main features listed above, *the acquisition time window* should be selected by the user from a set, by means of dedicated setup pins, the shortest interval being 500 ns. Additionally, care should be taken in the design to ensure a *minimum number of external components*. The components required to assemble an acquisition board are one or more ASICs, a crystal, power management ICs and a controller for data transmission – depending on the selected transmission medium – and a few minor elements, such as decoupling capacitors . A diagram of an acquisition board is shown in Fig. 2, displaying the substantially reduced component count with respect to previous designs.

Table 1: Specifications of the LHC CFC Electronics [1] and ASIC

	Parameter	Value	Units	Comments
Current design	Dynamic range (DR)	nine decades		(1 pA-1 mA)
	Minimum detected current	1	pA	
	Linearity error	less than ±25	%	over the 1 nA-1 mA range
		less than ±100	%	over the 1 pA-1 nA range
	Integration window	40	μs	
	Total integrated dose	500	Gy	in 20 years
ASIC	Dynamic range	nine decades		positive and negative currents
	Minimum detected current	0.1	pA	User selectable, minimum value.
	Linearity error	less than ±25	%	over the upper six decades
		less than ±100	%	over the lower three decades
	Integration window	100, 40 or 0.5	μs	
	Total integrated dose	1×10^4	Gy	in 20 years

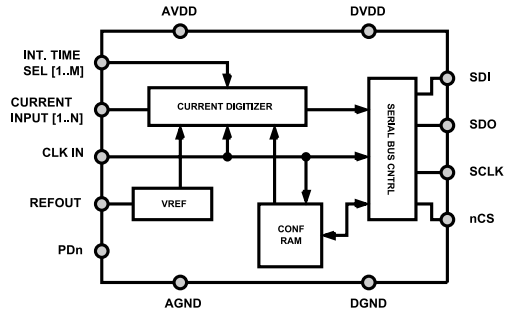


Figure 1: Functional diagram of the current digitizer.

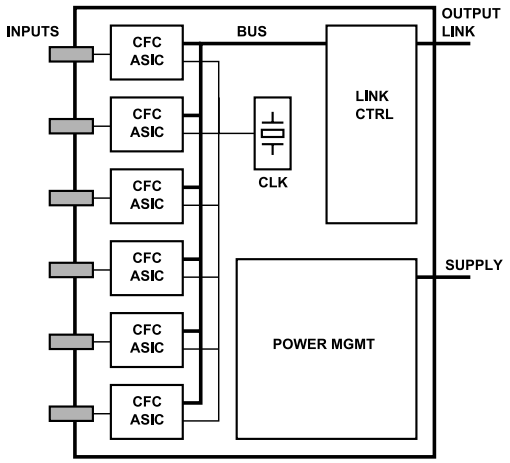


Figure 2: Diagram of an acquisition board showing the reduced number of components required (not to scale).

Several different *architectures* are being considered in the current preliminary study, including the use of a recycling integrator, multiple running integrators, a current steering multivibrator or a delta-sigma modulator. For each design, compatible schemes to provide a conversion within a user specified time window are being considered. A *digital output* shall be provided – therefore the ASIC is a current-input analog-to-digital converter (ADC). Depending on what type of device is to be used to read the output data and transmit it, a different type of bus or interface should be used, allowing a direct interface, which will provide a compatible data rate. As a dynamic range of nine decades requires 30bits, a serial bus allows a significant reduction in the number of output pins. In addition, a daisy chain wiring scheme would allow the connection of several devices on the same board while minimizing the number of wires, required in compact designs.

Although the operational *clock frequency* will be confirmed by system simulations, the design will be carried out for a relatively high clock rate, 10 MHz for the external clock and 100 MHz for the core one. The oscillator input will allow the direct connection of an external crystal.

Additional devices are considered to be included on the same chip: a *total dose sensor*, based on RADFETs. The knowledge of the radiation level to which each chip has been exposed to will give an estimate of the remaining life of the chip, and hence of when the board has to be serviced, and additionally it will provide useful information about the design and the technology itself for further developments. Moreover, since the analog-to-digital characteristic of the converter is affected by temperature changes, a *temperature sensor* will provide useful information to the surface electronics.

CONCLUSIONS

A radiation-tolerant ASIC will be developed at CERN to be employed in the foreseen LHC upgrade. The design will be carried out taking into account system-level specifications, the new devices that are concurrently developed, and will provide an increase in performance over the current design and additional functionality.

REFERENCES

[1] E Effinger, B Dehning, J Emery, G Ferioli, and C Zamantzas. Single gain radiation tolerant LHC beam loss acquisition card. (CERN-AB-2007-028), 2007.

SYSTEMATIC STUDY OF ACQUISITION ELECTRONICS WITH A HIGH DYNAMIC RANGE FOR A BEAM LOSS MEASUREMENT SYSTEM

G.G. Venturini, B. Dehning, E. Effinger, J. Emery, C. Zamantzas, CERN, Geneva, Switzerland

Abstract

A discrete components design for a current digitizer based on the current-to-frequency converter (CFC) principle is currently under development at CERN. The design targets at higher current inputs than similar designs, with a maximum equal to 100 mA and a minimum of 1 nA, as required by the ionization chamber that will be employed in the Proton Synchrotron and Booster accelerators as well as in the LINAC 4. It allows the acquisition of currents of both polarities without requiring any configuration and provides fractional counts through an ADC to increase resolution. Several architectural choices are considered for the front-end circuit, including charge balance integrators, dual-integrator input stages, integrators with switchable-capacitor. Design approach and measurements are discussed in this article.

INTRODUCTION

The Beam Loss Monitoring system employed in the CERN accelerator chain determines the energy density deposed in the individual accelerator elements as well as the residual radiation. For this reason, a wide dynamic range is required, equal to approximately seven decades. The ionization chambers employed are suitable sensors for this purpose, as they are able to provide a current signal with a dynamic range that exceeds the aforementioned requirements. The acquisition electronics must be designed accordingly, in order not to decrease the dynamic range below the system specifications. The dynamic range of the whole chain is limited by the very first stage: the acquisition of the signal has to be carried out with a circuit architecture other than a Miller integrator, since its dynamic range is limited to approximately 60dB.

GENERAL SCHEME OF RECYCLING INTEGRATORS

The general scheme of a recycling integrator is shown in Fig. 1. It contains a loop composed of an integrating system and a comparator block closed by the reset circuitry of the integrator.

The current signal at the input (I_{in}) is integrated and every time the result (V_o) exceeds a threshold (V_{TH}), the integrator is reset, lowering its output again under the threshold value. At the same time, the value stored by a counter is incremented by one unit, to keep track of the acquired charge. At the end of the measurement time window (T_M), the output of the integrator is sampled and its value is combined with the number of resets, according to the formula:

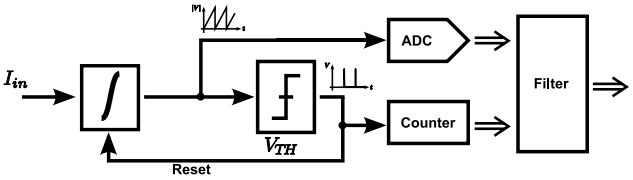


Figure 1: General scheme of a recycling integrator.

$$Q = C\ (V_O(T_M) - V_O(0)) + n\,Q_{REF} \tag{1}$$

Q is the charge acquired in the interval $(0, T_M)$,

n is the number of resets performed during the said time interval,

Q_{REF} is the charge that is lost by the integrator at every reset event,

C is the proportionality factor between the output voltage and the stored charge in the integrator.

Two successive commutations of the comparators are separated by a time interval given by the time required to accumulate a charge equal to the amount subtracted in the last reset. If the input is a constant current, the switching frequency of the comparator is ideally linked to the value of I_{IN} by the following relationship,

$$f_{SW} = \frac{I_{IN}}{Q_{REF}} \tag{2}$$

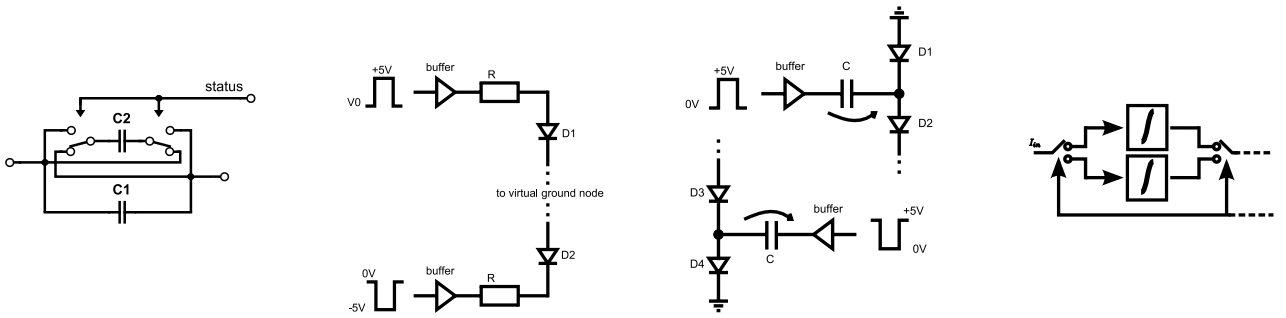
which can be generalized for an arbitrary input waveform as:

$$f_{SW} = \frac{1}{T_{SW}} = \frac{\overline{I_{IN}(t)}\big|_0^{T_{SW}}}{Q_{REF}} \tag{3}$$

$\overline{I_{IN}(t)}\big|_0^{T_{SW}}$ is the average value of the input current in the time interval $(0, T_{SW})$ between two consecutive commutations.

DESCRIPTION OF THE CIRCUITS

The charge-to-voltage conversion of the recycling integrator is determined by the reset circuit, as seen in Eq. 2 (Q_{REF} dependence). According to the specifications of the circuit, several implementations of the described scheme have been performed in this work.



(a) Switchable capacitor system.

(b) Charge injection through a resistor.

(c) Charge injection through a charged capacitor.

(d) Dual integrator input stage.

Figure 2: Reset schemes.

Charge Subtraction Schemes

In the design of recycling integrators, two resets strategies are often employed, the first being short-circuiting the feedback capacitor in the Miller integrator and the second being the injection of an opportune charge Q_{REF} through a current source (I_{REF}) connected to the virtual ground at the inverting node of the amplifier for a fixed amount of time (T_{REF}) [2]. The disadvantages of the former are the introduction of a blind time and a corresponding non-linearity in the digitizer conversion, while the main disadvantage of the latter is its high power dissipation for the considered input currents.

The feedback capacitor has been modified as depicted in Fig. 2a. It is composed by two capacitors C_1 and C_2, connected through a system of switches. When the controlling signal changes status, the connection of C_2 to C_1 is reversed and the charge is shared between the two capacitors. If the capacitance value of both is the same and equal to C, a charge equal to $2\,C\,V_{TH}$ is removed from the integrator.

Another possibility is the use of two integrators as depicted in Fig. 2d. At any time, only one integrator is connected to the input and output of the system through single-pole double-throw switches. While the connected charge amplifier integrates the input signal, the other is being reset. As soon as the output of the active integrator crosses a threshold voltage, the connected and resetted integrator are swapped.

The possibility of injecting a fixed charge into a Miller integrator has also been foreseen. Referring to Fig. 2c, top (bottom) diagram, in absence of triggering, the voltage drop across the capacitor C is 0 V (5 V). When the buffer switches to 5 V (0 V), D_1 (D_4) is reverse biased and D_2 (D_3) is forward biased, transferring the charge to the input node. As the output of the buffer switches back to the initial condition, the diode D_1 (D_4) recharges the capacitor back to the initial condition.

A similar design based on resistors instead of capacitors is shown in Fig. 2b, top (bottom). The diode D_1 (D_2) is forward biased when the output of the buffer is equal to 5 V (−5 V) and prevents a DC current from flowing to the input node when the output of the buffer is 0 V.[3]

Bipolar Currents

The extension to bipolar currents has been implemented adding an additional comparator and threshold and duplicating the injection schemes for both charge polarities. Whenever a comparator flips, the appropriate reset circuit is triggered, bringing the integrator output in the region of operation.

Calibration and Accuracy

To calibrate the converter, the leakage current is compensated through a potentiometer and the conversion factor is adjusted through the timer responsible for the activation of the injection circuit (Fig. 2c, 2b) or regulating the threshold voltage (based on a precision voltage reference, Fig. 2a,2d).

The accuracy of the converter is limited by the accuracy of the instrument used to perform the calibration.

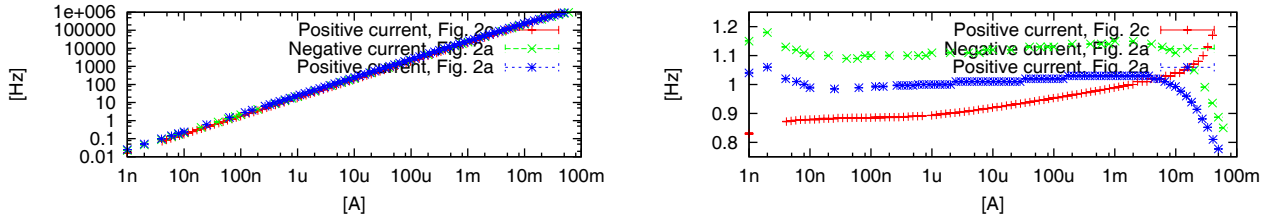
DESIGN CONSIDERATIONS

Dynamic Range

The dynamic range is the ratio of the largest to the smallest detectable signal. The largest signal is limited by the correct operation of the loop. The maximum frequency at which the integrator can be reset, together with the conversion factor, determine I_{MAX}.

The lower limit is set by the standard deviation of the output noise of the system and the residual input leakage after compensation (ΔI_{LEAK}). Although the input leakage is deterministic and may be compensated, its variation with the temperature and aging results in an imperfect matching. The dynamic range assumes the expression:

$$DR = \frac{I_{MAX} T_M}{\Delta I_{LEAK} T_M + \sqrt{S_I T_M + \sigma_{RO}^2}} \qquad (4)$$



(a) Reset frequency

(b) Normalized current-frequency conversion factor

Figure 3: Measurements regarding the considered circuits.

σ^2_{RO} Variance of the error introduced by the readout electronics (e.g. ADC),

S_I Double-sideband current noise at the input, assumed white, stationary and Gaussian.

Linearity

The linearity of the conversion of the charge digitizer depends on the Miller integrator, the uncompensated leakage, the source resistance and the reset circuit.

Taking into account the finite gain-bandwidth product ($GBW = A_0\omega_a$), the finite differential input resistance (R_d) and source resistance (R_s), the Miller integrator has a transfer function equal to:

$$\frac{V_o(s)}{Q_{in}(s)} = -\frac{1}{C}\frac{1}{1+(1/A_0)\left(1+\frac{s}{\omega_a}\right)\left(1+\frac{1}{sCR}\right)} \tag{5}$$

R is given by ($R_d \,/\!/\, R_s$).

From Eq. 5, the behavior of the circuit may be analyzed for high and low frequency operation as follows:

$$V_o(s) = -\tfrac{1}{C}\cdot\tfrac{sCRA_0}{1+sCRA_0}\,Q_{in}(s) \quad \text{for } s \ll GBW \tag{6}$$

$$V_o(s) = -\tfrac{1}{C}\tfrac{1}{1+s/GBW}\,Q_{in}(s) \quad \text{for } s \gg \frac{1}{CRA_0} \tag{7}$$

The inverse Laplace transform of the time response to a charge ramp $Q_{in}(s) = -\frac{\alpha_Q}{s^2}$ is reported in Eq. 8, 9, for Eq. 6, 7 respectively.

$$V_O(t) \approx \frac{\alpha_Q t}{C}\left(1-\frac{t}{2CRA_0}+\ldots\right) \tag{8}$$

$$V_o(t) = \frac{\alpha_Q}{C}\left\{t+\frac{1}{GBW}\left[\exp\left(-GBW\,t\right)-1\right]\right\} \tag{9}$$

At low frequency there is an error approximately equal to $T_{SW}/(2CRA_0)$ (relative) and to $1/GBW$ (absolute) at high frequency. [1]

At all operating points, the following output drift is also present:

$$\frac{dV_O(t)}{dt} = \frac{\Delta I_{LEAK}}{C} + \frac{V_{OS}}{C\,R_s} + \frac{V_O(t)}{C\,R_f} \tag{10}$$

Non-idealities in the reset circuit result in a different charge subtraction depending on the output frequency. Considering the circuits in Fig. 2a, 2c, 2d, the incomplete discharge of the feedback capacitors introduces an error. The change in the output voltage during reset is governed by the combined effect of the time constant of the charge transfer and the slew rate of the amplifier.

The conversion characteristic is also affected by a current offset error, due to the aforementioned ΔI_{LEAK}.

Signal to Noise Ratio

The signal to noise ratio of the converter is given by:

$$SNR = \frac{I_{IN}T_M}{\Delta I_{LEAK}T_M + \sqrt{S_I T_M + \sigma^2_{RO} + n\,\sigma^2_{RST}}}$$

σ^2_{RST} Variance of the charge removed at each reset.

MEASUREMENTS

The measurements on selected circuits are shown in Fig. 3.

CONCLUSIONS

Several possible designs have been proposed that provide an increase in the dynamic range compared to the Miller integrator, up to 160dB, for signals from particle detectors in the range 1 nA-100 mA. The circuits provide a user-adjustable conversion factor, offset compensation and ability to acquire currents of both polarities. SNR and linearity limits have been underlined.

REFERENCES

[1] Analog Devices. Application note: Operational integrators. *Operational Amplifiers*, AN-357:13–15.

[2] E Effinger, B Dehning, J Emery, G Ferioli, and C Zamantzas. Single gain radiation tolerant LHC beam loss acquisition card. (CERN-AB-2007-028), 2007.

[3] Giuseppe Guido Venturini. A study on high dynamic range acquisition electronics for a beam loss monitoring system. Master's thesis, CERN/Politecnico di Milano, 2009.

VELOCITY OF SIGNAL DELAY CHANGES IN FIBRE OPTIC CABLES

M. Bousonville*, GSI, Darmstadt, Germany
J. Rausch, Technische Universität Darmstadt, Germany

Abstract

Most timing systems used for particle accelerators send their time or reference signals via optical single mode fibres embedded in cables. An important question for the design of such systems is how fast the delay changes in the fibre optic cable take place, subject to the variation of the ambient air temperature. If this information is known, an appropriate method for delay compensation can be chosen, to enable a phase stabilised transmission of the timing signals. This is of interest particularly with regard to RF synchronisation applications.

To characterise the velocity of the delay change, the delay behaviour after a sudden temperature change will be described.

When trying to determine the step response, two problems occur. On the one hand, the material parameter of the coating, necessary for the calculation, is typically unknown. On the other hand, the measurement of the step response under realistic conditions is very laborious.

Thus in this presentation it will be shown how the step response and, accordingly, the velocity of the delay change in a fibre optic cable can be calculated by means of theoretical considerations, utilizing the typical geometry of fibre optic cables.

INTRODUCTION

The following analysis was performed as part of the development of the timing system for the cavity synchronisation of the Facility for Antiproton and Ion Research (FAIR) [1-3]. Loose tube cables frequently used in telecommunications are considered. The coating of this cable type can be described as a tube in which the standard single mode fibres (SMF) are loosely inserted (Fig. 1). The fibres and the coating are thus mechanically decoupled. This and the fact that the fibres are about 2% longer than the cable coating means that the tension on the cable to a certain extent does not act on the fibres and thus does not cause any delay change (see Eq. (3)). Accordingly, only temperature fluctuations are responsible for a delay change.

In the following, a way of calculating analytically not only the absolute delay change but also the speed at which such change takes place is presented for the first time.

ABSOLUTE DELAY CHANGE

Signals need the group delay τ to pass through a fibre of length L and group index N_g [4]

$$\tau = \frac{N_g \cdot L}{c}, \tag{1}$$

wherein c stands for the speed of light in a vacuum. With a transmission length of L = 1 km and a group index of $N_g \approx 1.5$, delays of approximately 5 µs, for example, occur. According to [4], a change in the group delay can have two causes. First of all, fluctuations in the temperature T

$$\frac{d\tau}{L \cdot dT} = \frac{1}{c}\left(N_g \frac{dL}{L \cdot dT} + \frac{dN_g}{dT} \right) \tag{2}$$

and secondly, mechanical tension σ acting on the length of the fibre

$$\frac{d\tau}{L \cdot d\sigma} = \frac{1}{c}\left(N_g \frac{dL}{L \cdot d\sigma} + \frac{dN_g}{d\sigma} \right). \tag{3}$$

Both bring about both a change in the length of the fibre and a change in the group index. For a non-jacketed fibre this results, according to Eq. (2) with N_g = 1.4682 at a wavelength of 1550 nm [5], the length expansion coefficient $dL/(L \cdot dT) = 5.6 \cdot 10^{-7}\ \mathrm{K}^{-1}$ and the temperature coefficient of the group index of $dN_g/dT = 1.2 \cdot 10^{-5}\ \mathrm{K}^{-1}$ [6], in a value of

$$\left(\frac{d\tau}{L \cdot dT} \right)_{fibre} = 40 \frac{ps}{km \cdot K}. \tag{4}$$

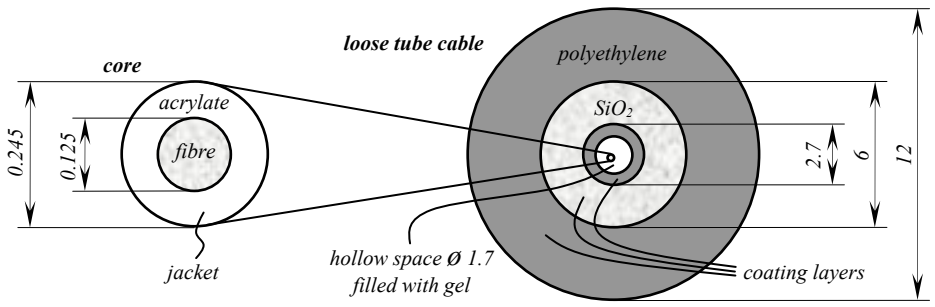


Figure 1: Cross-section of a loose tube fibre optic cable.

*M.Bousonvill@gsi.de

In loose tube cables, however, the fibres are frequently provided with thin jackets (Fig. 1, left), i.e. hollow space of the cable contains tight buffeted cables. According to [4], in tight buffeted cables tensions occur between the fibre and the jacket because of their different temperature expansion coefficients. The tension acting on the fibre in turn, according to Eq. (3) brings about a change in the delay. For the resulting impact on a jacketed fibre,

$$\left(\frac{d\tau}{L\cdot dT}\right)_{jacketed} = \frac{A_j}{A_f} E_j k_j \left(\frac{d\tau}{L\cdot d\sigma}\right)_{fibre} + \left(\frac{d\tau}{L\cdot dT}\right)_{fibre} \quad (5)$$

is obtained, with the cross-sectional areas A_j and A_f of the jacket as well as the fibre, the modulus of elasticity E_j and the linear expansion coefficient k_j of the jacket*. Here, the product $E_j k_j$ represents the change in tension per Kelvin acting on the fibre in a proportion of A_j/A_f. The extent to which delay depends on the temperature is thus greatly influenced by the properties of the fibre jacket. With so-called phase-stable optical fibres [7], the jacket exhibits a negative expansion co-efficient. As a result, the first addend in Eq. (5) becomes negative and partly compensates the second addend. As a result, the function of temperature falls below the value in Eq. (4) exhibited by the non-jacketed fibres.

By way of specific example, delay as a function of temperature will be calculated with Eq. (5) for the conventional loose tube cable shown in Fig. 1. Assuming the following material parameters of the jacket of E_j = $3.3\cdot10^{-5}$ N/mm^2 and $k_j = 7.7\cdot10^{-5}$ K^{-1} (Tab. 1), a value of

$$\left(\frac{d\tau}{L\cdot dT}\right)_{core} = \left(\frac{d\tau}{L\cdot dT}\right)_{cable} = 76\frac{ps}{km\cdot K} \quad (6)$$

results.

If it is now possible to succeed in determining the temperature curve in the fibre after a sudden change in ambient air temperature, the delay change in the cable over time and thus the step response can be determined in conjunction with Eq. (5).

SPEED OF DELAY CHANGE

An exact calculation is not possible since, firstly, the cable manufacturers did not deliver any data on the relevant material parameters and, secondly, the values found in the literature in some cases differ widely (Tab. 1). The only approach that can be taken here, therefore, is to estimate the speed range of the change. In the course of establishing this, it will however be revealed that this estimation is conservative, making it possible to say which value with certainty will not be exceeded.

Two key variables throttle the speed at which the delay changes after a rise in the temperature of the ambient air: the thermal resistance and the thermal capacity of the cable. Heat transfer resistance from the ambient air to the cable can be calculated by [8, p. 315]

$$R_{a\to c} = \frac{1}{\alpha 2\pi r_c L} \quad (7)$$

Here, α is the heat transfer coefficient, r_c stands for the radius and L for the length of the cable. The thermal resistance of the various layers from which the cable is made is calculated according to [8, p. 318]

$$R_{l,n} = \frac{1}{\kappa_n 2\pi L}\ln\left(\frac{r_{e,n}}{r_{i,n}}\right), \quad (8)$$

with thermal conductivity κ, the external radius r_e and the inner radius r_i of the respective layer n. It is assumed that the ambient air moves slightly† at a speed of 2 m/s and thus amounts to α = 13.6 W/(m^{2}K) [8, p. 637]. Moreover, r_c = 6 mm and $\kappa \geq$ 0.33 W/(m·K) for all coating layers. Under these conditions,

$$R_{a\to c} >> R_{l,n} \quad (9)$$

and also significantly greater than the transfer resistances between the layers. By way of approximation, therefore, all thermal resistances except $R_{a\to c}$ are treated as negligible, as a result of which the speed at which the complete cable is heated is underestimated. The heating period now depends only on $R_{a\to c}$ and the thermal capacity of the entire cable, the latter representing the sum of the thermal capacities of all individual layers

$$C_c = \sum_{n=1}^{N} c_{sh,n}\rho_n V_n\,, \quad (10)$$

wherein c_{sh} is specific thermal capacity, ρ density and V the volume of the respective layer n. The product $c_{sh}\cdot\rho$ differs only slightly for the materials typically used and is the lowest in silica glass (see Tab. 1)

$$(c_{sh}\rho)_{SiO_2} = 1.66\cdot10^6\,\frac{Ws}{m^3K}. \quad (11)$$

For Eq. (10), the following can thus be written

$$C_c \geq (c_{sh}\rho)_{SiO_2} V \quad (12)$$

by which the variable C_c was attributed to two known variables. The heating process for the cable now behaves similar to the charging process of a capacitor connected in series to an ohmic resistance. For the time curve of the temperature change in the cable ΔT_c after a sudden rise in the ambient temperature by ΔT_a ,

$$\Delta T_c(t \geq 0) = \Delta T_a\left(1 - e^{-\frac{t}{R_{a\to c}C_c}}\right), \quad (13)$$

* In this approximation, [4] assumes that the modulus of elasticity of the fibre is substantially greater than that of the jacket and the expansion coefficient of the fibre substantially smaller than that of the jacket. This is the case, e.g., with acrylate and polyethylene. Note that the parameters of the fibre are similar to those of fused silica (Tab. 1).

† Strong movements of the air in cable ducts and buildings in which the fibre optic cables are laid in the FAIR are unlikely.

Table 1: Parameter of materials used for fibre optic cables

	k [K^{-1}]	E [N/mm^2]	κ [$W/(m \cdot K)$]	c_{sh} [$J/(kg \cdot K)$]	ρ [kg/m^3]	$c_{sh}\rho$ [$kg/(m^3 \cdot K)$]
SMF [6]	$5.6 \cdot 10^{-7}$					
Fused Silica SiO_2 [9]	$5.5 \cdot 10^{-7}$	71700	1.38	754	2200	$1.66 \cdot 10^6$
Acrylate [10]	$7 \cdot 10^{-5}$ to $7.7 \cdot 10^{-5}$	2400 to 3300	0.17 to 0.19	1400 to 1500	1190	$1.67 \cdot 10^6$ to $1.79 \cdot 10^6$
Polyethylene [10]	$1 \cdot 10^{-4}$ to $3.0 \cdot 10^{-4}$	100 to 300	0.33	1900 to 2300	920	$1.75 \cdot 10^6$ to $2.12 \cdot 10^6$
Aramid fibre [10]	$-2.0 \cdot 10^{-6}$	59000 to 124000	0.04	1400	1440	$2.02 \cdot 10^6$
Steel [8]	$1.6 \cdot 10^{-5}$	190000	15.00	500	7800	$3.90 \cdot 10^6$

results with the time constant of the cable $R_{a\to c}C_c$, for which the following can be written using Eq. (7) and (12)

$$R_{a\to c}C_c \geq \frac{\pi r_c^2 L}{\alpha 2\pi r_c L}\left(c_{sh}\rho\right)_{SiO_2} = \frac{r_c}{\alpha 2}\left(c_{sh}\rho\right)_{SiO_2}. \quad (14)$$

The step response of the delay change is now obtained by multiplying Eq. (13) by the absolute delay change $d\tau/(L \cdot dT)$ of the core[‡]

$$\left(\frac{d\tau}{L}\right)_{cable} = \Delta T_a\left(1 - e^{-\frac{t}{R_{a\to c}C_c}}\right)\left(\frac{d\tau}{L \cdot dT}\right)_{core}. \quad (15)$$

To determine the speed of the delay change, Eq. (15) is differentiate with respect to the time t

$$\left(\frac{d\tau}{L \cdot dt}\right)_{cable} = \frac{\Delta T_a}{R_{a\to c}C_c} e^{-\frac{t}{R_{a\to c}C_c}}\left(\frac{d\tau}{L \cdot dT}\right)_{core}. \quad (16)$$

In this expression we use Eq. (14) as well as $t = 0$ and obtain the maximum delay change speed

$$\left(\frac{d\tau}{L \cdot dt}\right)_{\substack{\max \\ cable}} \leq \frac{2\alpha}{\left(c_{sh}\rho\right)_{SiO_2}} \frac{\Delta T_a}{r_c}\left(\frac{d\tau}{L \cdot dT}\right)_{core}. \quad (17)$$

According to this conservative estimate it can be said that, as the diameter of the cable becomes larger, the speed of the change in the temperature and thus also the delay change in the fibre decreases linearly. In the specific transmission cable in Fig. 1, the following results for a sudden rise in ambient temperature from $\Delta T_a = 1$ K and the value in Eq. (6)

$$\left(\frac{d\tau}{L \cdot dt}\right)_{\substack{\max \\ cable}} \leq 0.208 \frac{ps}{km \cdot K}. \quad (18)$$

If the fibre were to have only the directly contacting acrylate jacket, the delay, assuming the same sudden rise in temperature, would change at ≤ 10.2 ps/(km·s) or 49 times faster. By choosing a thick-coated loose tube cable, the speed of the delay change after a sudden rise in temperature can be significantly throttled.

[‡] $\Delta T_c = dT$

SUMMARY

A formula was established by means of which it is possible to calculate the speed of the delay change in a fibre optic cable. The thermal conductivity, specific thermal capacity and density of the cable coating material do not have to be known for this. Using the analytical formula, it is possible to calculate on the basis of the known cable geometry a value which, based on the approximations, with a high degree of probability will not be exceeded. Of key importance is that the change speed, assume an identical core, is approximately inversely proportional to the cable diameter.

REFERENCES

[1] M. Bousonville and J. Rausch „Universal Picosecond Timing System for the Facility for Antiproton and Ion Research", Physical Review Special Topics - Accelerators and Beams, Volume 12, Issue 4, 2009.

[2] M. Bousonville and P. Meissner „RF Reference Signal Distribution System for FAIR", Proceedings of the European Particle Accelerator Conference, Genua, 2008.

[3] M. Bousonville, Doctoral thesis, Technische Universität Darmstadt, Germany, 2009. http://tuprints.ulb.tu-darmstadt.de/1382

[4] A.H. Hartog, A.J. Conduit and D.N. Payne „Variation of pulse delay with stress and temperature in jacketed and unjacketed optical fibres", Optical and Quantum Electronics, 11, S. 265-273, 1979.

[5] Corning „SMF-28e-Glasfaser Produktinformation", data sheet 2003.

[6] Corning, letter to the author regarding fibre SMF-28e, 2005.

[7] T. Naito et al. „RF Reference Distribution Using Fibre-Optic Links for KEKB Accelerator", Proc. of the Particle Accelerator Conference, Chicago, 2001.

[8] H. Kuchling „Taschenbuch der Physik", Fachbuchverlag Leipzig, edition 16, 1999.

[9] D.R. Lide „Handbook of Chemistry and Physics", CRC Press, edition 65, 1984-85.

[10] Goodfellow, data sheets, 2008. http://www.goodfellow.com

COHERENT OPTICAL TRANSITION RADIATION AS A TOOL FOR ULTRASHORT ELECTRON BUNCH DIAGNOSTICS

Gianluca Geloni, Petr Ilinski, Evgeni Saldin, Evgeni Schneidmiller and Mikhail Yurkov,
DESY, Hamburg, Germany

Abstract

In this contribution we describe how Coherent Optical Transition Radiation can be used as a diagnostic tool for characterizing electron bunches in X-ray Free-electron lasers. The proposed method opens up new possibilities in the determination of ultrashort, ultrarelativistic electron bunch distributions. Our technique is described more extensively in [1], where the interested reader will also find relevant references.

INTRODUCTION

Operational success of XFELs will be related to the ability of monitoring the spatio-temporal structure of sub-100 fs electron bunches as they travel along the XFEL structure. However, the femtosecond time-scale is beyond the scale of standard electronic display instrumentation. Therefore, the development of methods for characterizing such short electron bunches both in the longitudinal and in the transverse directions is a high-priority task, which is very challenging.

A method for peak-current shape measurements of ultrashort electron bunches using the undulator-based Optical Replica Synthesizer (ORS), together with the ultrashort laser pulse shape measurement technique called Frequency-Resolved Optical Gating (FROG) was recently proposed (see references in [1]). It was demonstrated that the peak-current profile for a single, ultrashort electron bunch could be determined with a resolution of a few femtoseconds. The ORS method is currently being tested at the Free-electron laser in Hamburg (FLASH). Novel results will be reported at this conference.

In this paper we present a feasibility study for integrating the ORS setup with a high-resolution electron bunch imager based on coherent Optical Transition Radiation (OTR). Our ideas are discussed in detail in [1], where the interested reader will also find relevant references that are omitted here for reasons of space.

Electron bunch imagers based on incoherent OTR constitute the main device presently available for the characterization of an ultrashort electron bunch in the transverse direction. They work by measuring the transverse intensity distribution. Since no fast enough detector is presently available, the image is actually integrated over the duration of the electron bunch. Therefore, incoherent OTR imagers fail to measure the temporal dependence of the charge density distribution within the bunch. For these reasons, the use of standard incoherent OTR imagers is limited to transverse electron-beam diagnostics, to measure e.g. the projected transverse emittance of electrons. However, it is primarily the emittance of electrons in short axial slices, which determines the performance of an XFEL. Therefore, there is a need for electron diagnostics capable of measuring three-dimensional (3D) ultrashort electron bunch structures with micron-level resolution.

The main advantages of coherent OTR imaging with respect to the usual incoherent OTR imaging is in the coherence of the radiation pulse, and in the high photon flux. Exploitation of these advantages leads to applications of coherent OTR imaging that are not confined to diagnostics of the transverse distribution of electrons. The novel diagnostics techniques described here can be used to determine the 3D distribution of electrons in a ultrashort single bunch. In combination with multi-shot measurements and quadrupole scans, they can also be used to determine the electron bunch slice emittance.

The possibility of single-shot, 3D imaging of electron bunches with microscale resolution makes coherent OTR imaging an ideal on-line tool for aligning the bunch formation system at XFELs. In order to ensure SASE lasing at X-ray wavelengths, a very high orbit accuracy of a few microns has to be ensured in the 200 m long undulator. The resolution of incoherent OTR imagers is not adequate to characterize the position of the center of gravity of an electron bunch with such accuracy. Our studies show that coherent OTR imaging can be utilized as an effective tool for measuring the absolute position of the electron bunch with the required micron accuracy. Finally, the improvement of bunch-imaging techniques up to the microscale level does not only yield a powerful diagnostics tool, but opens up new possibilities in XFEL technology as well.

OPTICAL REPLICA SETUP

We propose to create a coherent pulse of optical radiation by modulating the electron bunch at a given optical wavelength and by letting it pass through a metal foil target, thus producing coherent OTR at the modulation wavelength. The radiation pulse should be produced in such a way to constitute an exact replica of the electron bunch. Reference [1] includes a discussion about how to avoid the influence of self-interaction effects. The optical replica can be used for the determination of the 3D structure of electron bunches. Although other projects may benefit from our study too, throughout this paper we will mainly refer to parameters and design of the European XFEL.

In order to produce the optical replica we need to modulate the electron bunch at a fixed optical wavelength. One may take advantage of an Optical Replica Synthesizer

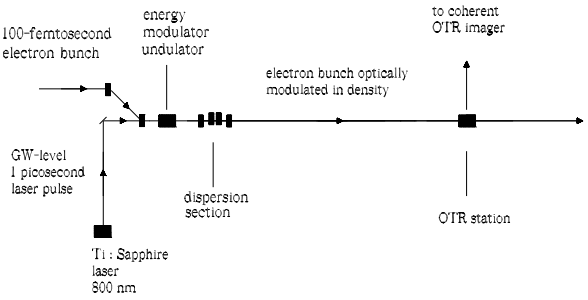


Figure 1: Schematic diagram of the coherent imager. The working principle is based on the optical modulation of the electron bunch and on emission of coherent OTR radiation from the metallic mirror.

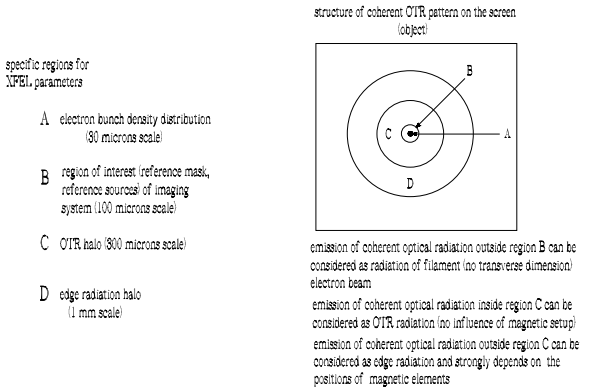


Figure 2: Scheme of the coherent OTR radiation pattern as observed in the object plane for the low electron beam energy case of 2 GeV.

(ORS) modulator, which we suppose to be installed after the BC2 bunch compressor chicane. A basic scheme to generate coherent OTR is shown in Fig. 1.

A relatively long laser pulse serves as a seed for the modulator, consisting of a short undulator and a dispersion section. The central area of the laser pulse should overlap with the electron pulse. In order to ensure simple synchronization, the duration of the laser pulse should be much longer than the electron pulse time jitter, which is estimated to be of order 100 fs. Foreseen parameters of the seed laser are: wavelength $\lambda_m = 800$ nm, energy in the laser pulse 1 mJ and pulse duration (FWHM) 1 ps. The laser beam is focused onto the electron bunch in a short (the number of periods is $N_w = 5$) modulator undulator resonant at the optical wavelength of 800 nm. Optimal conditions of focusing are met by positioning the laser beam waist into the center of the modulator undulator, with a Rayleigh length of the laser beam equal to the undulator length. Since the electron betatron function β, the undulator length L_w and the Rayleigh length of the laser beam are of the same magnitude, the size of the laser beam waist turns out to be about 20 times larger than the electron beam size. As a consequence, we can approximate the laser beam with a plane wave when discussing about the modulation of the electron bunch. The seed laser pulse interacts with the electron beam in the modulator undulator and produces an amplitude of the energy modulation in the electron bunch of about 500 keV. Subsequently, the electron bunch passes through the dispersion section (with momentum compaction factor $R_{56} \simeq 50\mu$m), where the energy modulation is converted into density modulation at the laser wavelength. The electron bunch density modulation reaches an amplitude of about 10%. Finally, the modulated electron bunch travels through the OTR screen. It should be mentioned that OTR screens can be positioned at various locations down the electron beam line where electrons have substantially different energies. In the case of the European XFEL, the electron energy varies from 2 GeV (second bunch compression chicane) up to 17.5 GeV at the undulator entrance. For other machines, these parameters differ. In the case of LCLS, energies will range from about 4.5 GeV to 13.6 GeV.

THE OTR SOURCE

A powerful burst of OTR is emitted, which contains coherent and incoherent parts. The coherent OTR has much greater number of photons, up to 10^{13} i.e. 1μJ per pulse. A detailed study shows that, in our case of interest, we can exploit the Ginzburg-Frank formula for the characterization of the OTR field from a single electron at the OTR screen. Then, the field distribution for the electron bunch at the OTR screen in the space-frequency domain is essentially a convolution in the space domain of the temporal Fourier transform of the charge density distribution and the temporal Fourier transform of the single-electron field. Qualitatively, we can distinguish between four zones of interest, Fig. 2. Information about the electron bunch will be shown to be included in a small region of size $\sigma_r \sim 30\mu$m, region A. The region of interest of the imaging system is characterized by $r < 100$ μm, region B. The field distribution for 100 $\mu\text{m} < r < 300$ μm does not depend on the transverse size of the electron beam, region C. Finally, the position of magnetic structures become relevant at larger distances $r \sim 300$ $\mu\text{m} \sim \gamma\lambda/(2\pi)$, region D.

COHERENT OTR IMAGING

The so called $4f$ filtering architecture is ideal for a coherent OTR imaging setup, Figure 3. We demonstrate that such setup can be used to characterize electron density profiles on the microscale level. Such resolution level can be reached by spatially filtering in the Fourier plane and using a radial-to-linear polarization conversion. In this way, the particle spread function is improved up to the point spread function for a point-like source.

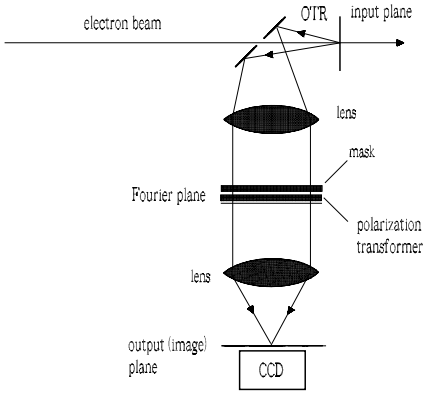


Figure 3: A practical arrangement of the coherent OTR image-processing system. (The hole in the OTR screen is for simplicity of drawing only. A tilted configuration should be used at these wavelengths instead.)

DIFFRACTIVE IMAGING METHODS

Diffractive imaging is one of the most promising techniques for microscale imaging of electron bunches, when a detector records the Fraunhofer diffraction pattern radiated by the electron bunch, and an image can be reconstructed with the help of a phase retrieval algorithm. This reduces the requirements on the optical hardware by increasing the sophistication in the post-processing of the data collected by the system. Besides, a diffractive imaging setup has the same ultimate resolution of the $4f$ coherent imaging setup.

The applications of coherent OTR imaging are not confined to diagnostics of the transverse distribution of electrons projected along the longitudinal axis. Simple extensions allow for the characterization of the 3D structure of electron bunches with a multi-shot measurement. Such an approach involves a combination of real and reciprocal space imaging spectrometers. Both imaging setups use frequency filters to obtain the spectral data of the image. When the filter bandpass is changed, successive images are recorded at different wavelengths. This process is repeated, wavelength by wavelength. The result is the simultaneous knowledge of two "3D cubes" of spectral data, one in the real space $(\Delta\lambda, \Delta x, \Delta y)$ and the other in the reciprocal space $(\Delta\lambda, \Delta\omega_x, \Delta\omega_y)$, having indicated with $\omega_{x,y}$ the spatial frequencies relative to the x and y axis. Application of the Gerchberg-Saxton algorithm allows one to retrieve the spatio-temporal electron-bunch structure. Also, the determination of the projections of the cube of data in reciprocal space onto specific planes of interest is sufficient to reconstruct the electron-bunch structure, even without knowledge about the cube of spectral data in real space. In other words, the optical replica pulse can be measured in the 3D Fourier domain. We name this novel method Frequency-Resolved Optical Diffractive Imaging (FRODI). FRODI can be further developed from a multi-shot to a single-shot technique to measure the 3D structure of a single electron bunch. This is accomplished by splitting the beam and simultaneously measuring orthogonal (x, t), (y, t) and (x, y) projections. The entire traces can be recorded by three detectors, and used to reconstruct the desired 3D electron-bunch structure. Our 3D imaging technique FRODI turns out to be a relatively simple solution to a very complicated problem, as in our case different spatial frequencies are related to different temporal spectra (i.e. spatial frequency and temporal frequency are coupled).

HOLOGRAPHIC METHODS

Fourier-Transform Holography (FTH) is another promising imaging method. FTH is a non-iterative imaging technique, so the image can be reconstructed in a single step deterministic computation. This is achieved by placing a coherent point source at an appropriate distance from the object and having the object field interfering with the reference wave produced by this point source, detecting the interference pattern in the Fourier plane. For optical applications, the resolution of holographic techniques is not limited by size and quality of the point-like source. It is not difficult to produce a pinhole, unresolved at optical wavelengths, and let sufficiently bright radiation through it. The fast, unambiguous and direct reconstruction achieved in FTH is attractive for coherent OTR imaging of electron bunches. Moreover, FTH may also be used to generate a low-resolution image of the bunch to support diffractive imaging techniques. In this case, multiple references can be added to the FTH setup in order to increase the a-priori information available. Multi-shot and single-shot techniques for the characterization of the electron bunch can also be based on FTH setups, and spatio-temporal FTH techniques can also be used [1]. An extension of the method opens up the possibility for single-shot 3D imaging of ultrashort electron bunches.

Finally, time-gated FTH is another class of possible techniques. A hologram records information about the object only when it is illuminated simultaneously by a coherent reference wave. Then, when a short reference is used, the hologram is equivalent to a time-gated viewing system. We propose a method based on time-gated FTH with multiple reference sources capable of characterizing the spatio-temporal structure of individual electron bunches. Multiple, ultrashort (about 10 fs) reference pulses are generated with a varying time-delay, so that several two-dimensional images (frames) of the electron bunch at different position inside the bunch can be reconstructed from a single holographic pattern. We call this technique Holography Optical Time Resolved Imaging (HOTRI).

REFERENCES

[1] G. Geloni, P. Ilinski, E. Saldin, E. Schneidmiller and M. Yurkov, "Method for the determination of the three-dimensional structure of ultrashort relativistic electron bunches", DESY 09-069, online version at http://arxiv.org/abs/0905.1619

SPECTRAL RESPONSE OF A MARTIN-PUPLETT INTERFEROMETER FOR ELECTRON BUNCH LENGTH MEASUREMENTS

C. Kaya*, U. Lehnert, Forschungszentrum Rossendorf, Dresden, Germany

Abstract

At the ELBE Free Electron Laser (FEL) at Forschungszentrum Dresden Rossendorf (FZD) electron bunches having lengths between 1 to 4 ps are generated. It is required to compress these electron bunches to lengths below 1 ps which necessitates diagnosis of the electron bunch parameters. We use a Martin-Puplett interferometer (MPI) which is a modification of the Michelson interferometer, where the beams are linearly polarized at specific orientations. It measures the autocorrelation function of the coherent transition radiation (CTR) from a view screen which is an optical replication of the electron bunch.

The interferometer setup consists of various optical components like polarizers, beam splitter, mirrors and Golay cell detectors. In our measurement a wire grid was used as a polarizer and also as a beam splitter. A thorough understanding of the response of the optical components, as a function of the CTR wavelength range of our interest, is required for correct analysis of the measured signal. We have therefore simulated the response of the entire interferometer setup including the diffraction losses and the window transmission and compared the results to experimental measurements.

INTRODUCTION

ELBE is based on a superconducting electron linac. The ELBE linac is designed to operate with an accelerating field gradient of 10 MV/m so that the maximum design electron beam energy at the exit of the second module is 40 MeV. ELBE delivers an electron beam with an average current of up to 1 mA. The electron source is a DC thermionic triode delivering beam with energy of 250 keV. The gun beam quality predefines the accelerated beam quality. In the ELBE the electron bunch is compressed to 10 ps after the electron beam injector. In the accelerator the electron bunch length is in the range of 1 to 10 ps. We use a Martin-Puplett interferometer (MPI) which is a modification of the Michelson interferometer, where the beams are linearly polarized at specific orientations. It measures the autocorrelation function of the coherent transition radiation (CTR) from a view screen which is an optical replication of the electron bunch.

In our work we want to determine the workable wavelength range for our Martin-Puplett interferometer setup. We have therefore simulated the response of the entire experimental setup. We also describe in this study our measurements of the electron bunch length, which is in the picosecond range. The bunch length is estimated from a frequency domain fit of a specially constructed analytical function to the measured power spectrum of the bunch. The power spectrum is obtained as a Fourier transform of the measured autocorrelation function of the CTR. The CTR autocorrelation function is measured with the help of a Martin-Puplett interferometer.

EXPERIMENTAL SETUP

A polarizing Martin-Puplett interferometer (shown in Fig. 1) is used to analyze the spectrum of the far-infrared radiation. CTR passes through a quartz window and is reflected by a parabolic mirror. Then the CTR is polarized vertically by a wire-grid linear polarizer and made incident on a beam splitter. For our measurements the wire grids are wound from 20 μm gold plated tungsten wire with 100 μm spacing (from center to center), which are used as polarizers and beamsplitters. The reflected beam from the beamsplitter then goes to a roof mirror which is fixed, while the transmitted beam goes to a movable roof mirror. These two reflected beams then interfere and then split by a second beam splitter (analyser) the polarization directions are detected using two Golay cell infrared (IR) detectors.

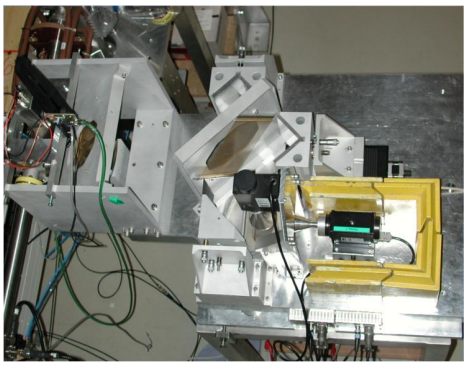


Figure 1: Martin-Puplett Interferometer.

GENERAL DESCRIPTION OF TRANSITION RADIATION

In our experiment the transition radiation is generated when the electron beam is impinged on an aluminum target rotated by 45^0 with respect to the incoming beam (shown in Fig. 2). The spectral energy flux of backward transition radiation is given for electrons by the Ginzburg-Frank formula [1]:

*E-Mail : c.kaya@fzd.de

$$\frac{d^2I}{d\nu d\Omega} = \frac{e^2}{2\pi \in_0 c} \frac{\beta^2 \sin^2(\theta)}{(1-\beta^2 \cos^2(\theta))^2} \quad (1)$$

where I is the spectral energy flux in a solid angle $d\Omega$, β is the ratio of electron velocity to velocity of light (v/c) and θ is the polar angle with respect to the backward transition radiation.

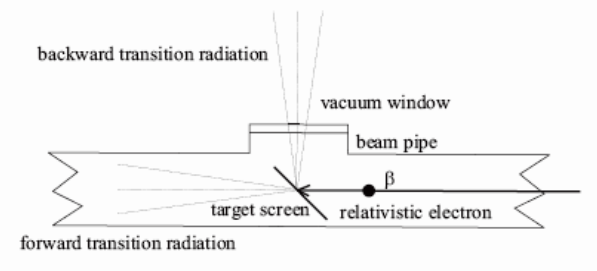


Figure 2: Emission of transition radiation.

The polar angles (opening angle) of the transition radiation for different beam energies are calculated using the above formula (1). The plots (shown in Fig. 3) show that the opening angle of the beam decreases with the radiation energy. Polar angle will be large for low electron energy. This information is useful in determining the optimum distance of the parabolic mirror from the beamline window. The maxima in emission occurs at $\theta = \pm 1/\gamma$, where γ is the Lorentz factor of the electron.

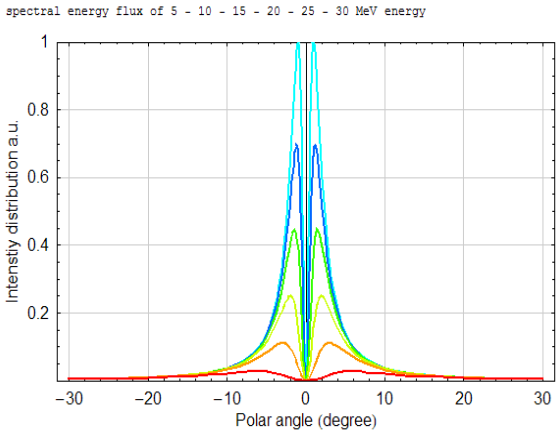


Figure 3: Transverse emission characteristics of transition radiation according to equation (1) for different electron energies of 5-10-15-20-25-30 MeV as behind the ELBE LINAC. Red curve is for 5 MeV electrons, light blue curve is for 30 MeV electrons.

SIMULATION OF OPTICAL COMPONENTS OF INTERFEROMETER

For Martin-Puplett type interferometers the response of the wire grids are found to be strongly bandwidth-limited. In order to determine the workable wavelength range for the interferometer, we compute the interference depth dependence on wavelength. After the first polarizer, the electric field direction of coherent transition radiation is polarized almost vertical. For our simulations we have used vertical electric field direction of CTR before the beamsplitter. In the experiment the beamsplitter wire grid is oriented at 45^0 with respect to the vertical electric field component. Therefore, the electric field divides into two components: (i) parallel to the wire grids and (ii) perpendicular to the wire grids (shown in Fig. 4). If the thickness **d** (20 μm) of the wires and the spacing **s** (100 μm) are small compared to the wavelength of the incident light, the module of the reflection coefficients for the vertical electric field components parallel and perpendicular to the wires can be calculated as follows [2]:

$$|R_{II}| = \left[1 + \left(\frac{2s}{\lambda}\right)^2 \ln\left(\frac{s}{\pi d}\right)^2\right]^{-\frac{1}{2}} \quad (2)$$

$$|R_{\perp}| = \left[1 + \frac{(2\lambda s)^2}{\pi^4 d^4}\right]^{-\frac{1}{2}} \quad (3)$$

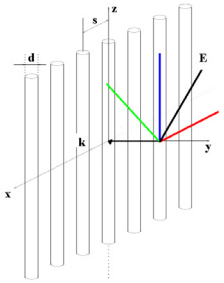


Figure 4: On the beamsplitter vertical electric field (black line) component.

A part of the radiation will also get transmitted through the beamsplitter. When the wire grids is ideal (no absorption or scattering), sum of the reflection and transmission coefficients should be one. We have simulated the vertical and horizontal electric field components after each optical component and obtained the intensities of the radiations reaching the two detectors. We have calculated the relative intensities at both the detectors as a function of frequency (0-3 THz). We have restricted the frequency range to 3 THz because it is the workable limit for the polarizers and beamsplitters. Figure 5 shows the interference depth given by the difference between the signals of the vertical and horizontal detectors.

The lower cut-off frequency at the detector input windows is about 0.5 THz. Using the Martin-Puplett interferometer we can thus measure CTR in the frequency range of 0.5-2.7 THz. This indicates that we can measure bunch lengths between 0.5 and 2 ps with our setup.

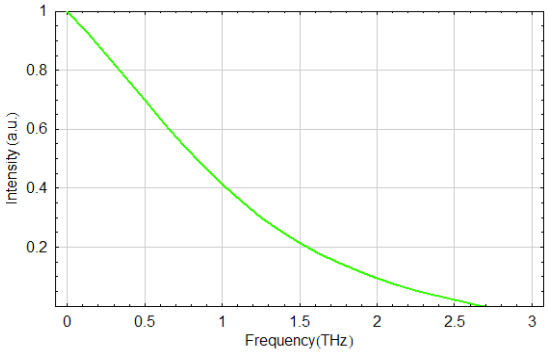


Figure 5: Spectral response of detectors signal. Response of the detectors is difference in between the vertical and horizontal detector signal.

COMPARISON BETWEEN SIMULATION AND EXPERIMENT

In this section, we will describe our analysis of the measured spectra (shown in Fig. 6) of the far-infrared CTR. The shape of the CTR pulse is a "copy" of the electron bunch shape. Measurement of the radiation spectrum give information about the bunch length.

The signal intensities measured at the vertical and horizontal detectors show that the vertical detector signal is much higher than horizontal detector signal for each scan. We have therefore normalized signals on the basis of the fact that since the detectors were identical the mean value of the data measured by the detectors should be equal and the modulation depth, i.e., the difference in the maximum and minimum will be equal as well, as the sum of the two signals must be constant. We define the difference interferogram as the difference of these amplitudes which is autocorrelation function of the radiation pulse. According to the Wiener-Khintchine theorem the fast Fourier transform of the autocorrelation function is the experimental power spectrum.

For simulation, a hypothetical Gaussian shape of the bunch is assumed. We used the general Huygens Fresnel integral in our simulation to account for the diffraction losses on the detector input windows.

The simulated power spectrum thus consists of a product of the Fourier transform of the hypothetical Gaussian shape of the bunch and the factor accounting for the diffraction losses. This function is fitted to the power spectrum to obtain unknown parameters like RMS bunch length and the cut off frequency on the detector input window. As an example we show one of our experimental results where by fitting the spectrum we have obtained the RSM bunch length of 1.3 ps.

CONCLUSIONS

We have calculated the response of the experimental setup as a function of the CTR wavelength which is essential for correct analysis of the measured signal. We have simulated the autocorrelation function where diffraction losses at the detector windows are taken into account. From there we derive an operation range of 0.5-2 ps for the bunch length determination with our MPI. Using MPI measurements and by comparison of the experimental results with our simulations we have estimated the electron bunch lengths. If the electron bunch length is compressed below 0.5 ps we will not be able to measure it with our MPI setup.

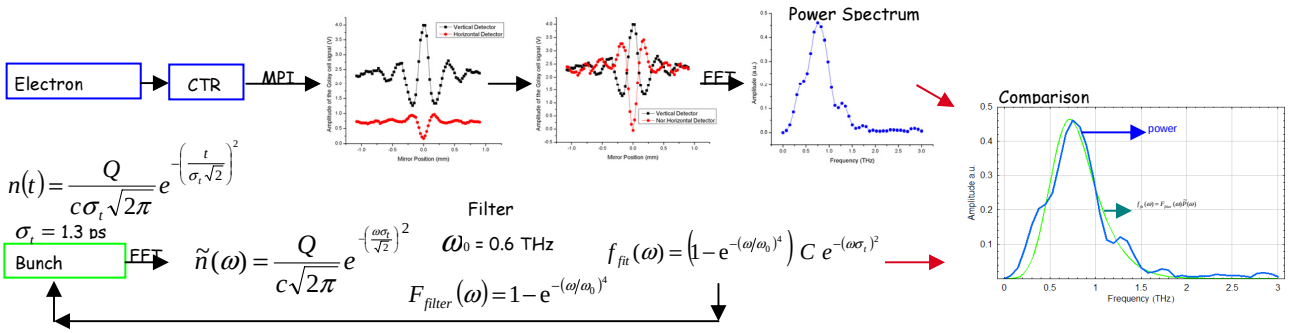


Figure 6: Analysis of measurement, comparison between simulation and experiment.

ACKNOWLEDGEMENTS

I would like to thank Dr. P. Michel and the operators at the ELBE Germany, for supporting my experiments. Also I want to thank Dr. P. Evtushenko at the JLabFEL, USA who had built the setup and for the information we obtained from his thesis.

REFERENCES

[1] V.L. Ginzburg, et al., "Radiation of a uniformly moving electron due to its transition from one medium into another", Journ. Phys. USSR, 9, 1945.

[2] H. Lamb, "On the diffraction in transmission of electric waves by a metallic grating", Proc. London Math. Soc. , Vol. 29, pp. 523-544; 1898.

[3] P. Evtushenko, "Electron Beam Diagnostic at the ELBE Free Electron Laser", PhD thesis, presented at the Technical University Dresden, 2004.

TIME RESOLVED SPECTROMETRY ON THE TEST BEAM LINE AT CTF3

M. Olvegård, A. Dabrowski, T. Lefèvre and S. Doebert, CERN, Geneva, Switzerland
E. Adli, University of Oslo, Norway

Abstract

The CTF3 provides a high current (28 A) high frequency (12 GHz) electron beam, which is used to generate high power radiofrequency pulses at 12 GHz by decelerating the electrons in resonant structures. A Test Beam Line (TBL) is currently being built in order to prove the efficiency and the reliability of the RF power production with the lowest level of particle losses. As the beam propagates along the line, its energy spread grows up to 60%. For instrumentation, this unusual characteristic implies the development of new and innovative techniques. One of the most important tasks is to measure the beam energy spread with a fast time resolution. The detector must be able to detect the energy transient due to beam loading in the decelerating structures (nanosecond) but should also be capable to measure bunch-to-bunch fluctuations (12 GHz). This paper presents the design of the spectrometer line detectors.

CTF3 TEST BEAM LINE

CLIC Test Facility 3 (CTF3) [1] is an electron accelerator test facility at CERN, built by an international collaboration, in order to test CLIC technology [2]. The first part of the machine generates a high current beam (almost 30 A for 140 ns pulse length and bunched at 12GHz), which is transported to the CLic EXperimental area (CLEX). One of the CLIC crucial issues is the reliability and efficiency of the RF power production. This is addressed in CLEX in the Test Beam Line (TBL) [3]. Built in stages, with a first Power Extraction and Transfer Structure (PETS) module installed in 2009, the TBL will experimentally characterize the stability of the drive beam during the deceleration.

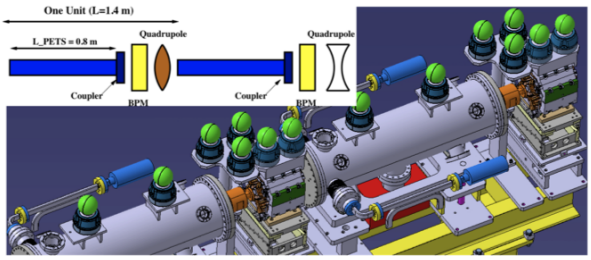


Figure 1: Schematic view of a typical TBL girder containing two PETS modules, 2 BPMs and 2 quadrupole magnets.

In its final form, the TBL will be composed of sixteen identical modules. Each module will consist of a 0.8 m PETS with a coupler, a beam position monitor (BPM) and a quadrupole on a precision movable support, see Fig. 1. The 28 A beam from CTF3 is decelerated by about 5 MeV in each PETS, producing about 150 MW of 12 GHz power. Due to transient effects during the filling time of the PETS, the first 3 ns of the bunch train will have a huge energy spread from the initial energy down to the final energy of the decelerated beam, see Fig. 2. Time-resolved spectrometry is therefore an essential beam diagnostics tool in order to measure the beam energy spectrum after deceleration.

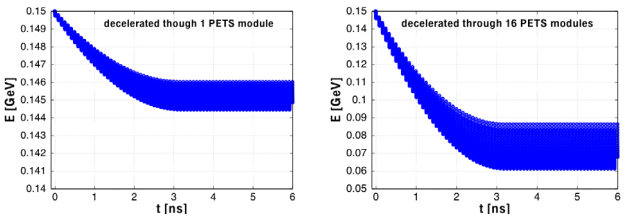


Figure 2: Time resolved energy distribution of decelerated beam after 1 PETS module (left) and 16 PETS modules (right), for the first 6 ns of the 140 ns pulse train.

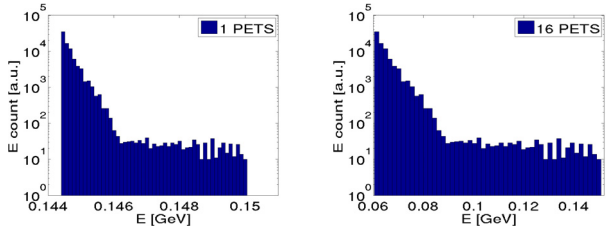


Figure 3: Histogram of the final energy distribution of a 140 ns pulse train after deceleration through 1 PETS module (left) and 16 PETS modules (right).

This paper presents the time resolved spectrometer design for the TBL.

TIME RESOLVED SPECTROMETRY

The spectrometer under design (see Fig. 4), will consist of a bending magnet, which provides an energy dependent horizontal deflection to the electrons, followed by an optical transition radiation (OTR) screen [4] observed by a CCD camera to provide a high spatial resolution profile measurement and then lastly a novel segmented beam dump for the time resolved energy measurement.

The segmented dump is a device composed of parallel metallic plates designed to stop the incident particles. By measuring the deposited charge in each segment, the beam profile can be reconstructed. The material and the dimension of the segments must be optimized depending on the beam parameters, in particular the energy and the expected energy spread. The segments need to be long enough to stop the primary particles. On the other hand the segment thickness must be chosen to optimize the

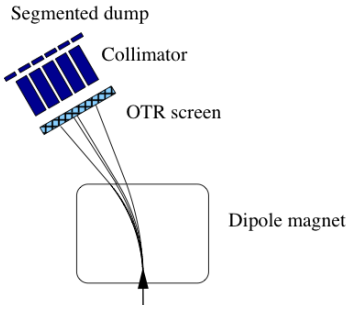


Figure 4: Schematic of the layout of the spectrometer.

spatial resolution, which will suffer from a smearing due to multiple scattering. Moreover, because of the high power carried by the beam, thermal changes must be considered as a crucial issue, as well as radiation effects that will influence the long-term response of the detector.

DESIGN OF SEGMENTED DUMP FOR THE TEST BEAM LINE

The detector design presented here is based on a design of an installed and operational segmented dump at CTF3 [5], but adapted to the unique beam conditions at the TBL. Simulations using the monte-carlo code FLUKA [6] was used in order to optimise the design parameters, based on beam energy with a range of 50 MeV to 150 MeV and on the thermal constraints linked to the high charge beam. Given the thermal constraints the design of the detector will consist of two parts, the first being the design of the active segments, and the second being the design of the upstream collimator, designed to absorb 90% of the full beam power. Since the effects of multiple scattering and the thermal effects of energy deposition are most significant for the higher beam energy, an initial FLUKA study was performed using a 150 MeV electron beam, incident on tungsten. Simulations were performed here assuming an infinitely small beam size.

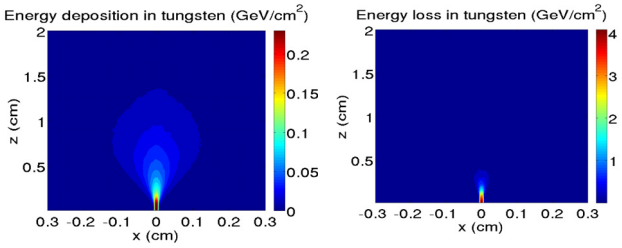


Figure 5: Total energy deposition (left) and energy loss by primary electrons (right) in a tungsten block.

As shown in Fig. 5, the total energy deposited in the material, by both the primary electrons and the secondary particles and photons, was calculated as a function of the longitudinal coordinate z and the transverse coordinate x. In addition, the energy loss by the primary electrons was also scored, as shown on the neighbouring plot. Tungsten was chosen because of its relatively high melting point, and high Z number, thus able to stop the electron beam within a relatively short distance, in order to make the detector as compact as possible. The distributions in Fig. 5 are projected in the longitudinal direction in order to estimate respectively the longitudinal distance needed to stop the primary electrons and also the corresponding EM shower. As shown in Fig. 6 and Table 1, after 1.48 cm, 99.9% of the primary 150 MeV electrons have been stopped in tungsten. The absorption of the full electromagnetic shower takes more material, due to the combination of photons and electrons/positrons in the secondary shower. From Table 2, a 10 cm of tungsten will absorb more than 99.9% of the beam power, and hence is chosen as the dimension of the tungsten segments.

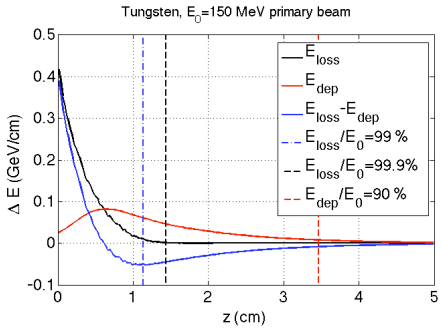


Figure 6: Longitudinal distribution of the energy loss of primary electrons (black) and the energy deposition (red) due to both primary electrons and the secondary shower.

Table 1: Longitudinal depth in cm corresponding to a particular fraction of energy loss by the primary electrons.

Material	Energy (MeV)	Distance fractional energy loss (cm)		
		70%	99%	99.9%
Tungsten	150	0.40	1.14	1.48
Tungsten	100	0.38	1.02	1.30
Tungsten	50	0.31	0.75	0.93
Graphite	150	14.09	30.72	35.79
Iridium	150	1.73	4.68	5.88
Iron	150	0.34	0.96	1.26

Table 2: Longitudinal depth to absorb a certain fraction of the total beam energy.

Material	Energy (MeV)	Distance of fractional total energy deposition (cm)		
		70%	99%	99.9%
Tungsten	150	1.73	5.88	8.78
Tungsten	100	1.53	5.68	8.58
Tungsten	50	1.13	5.23	8.13

The width of the dump segments is optimized based on multiple scattering of the primary electrons, and the transverse resolution needs of the measurement. As shown in Fig. 7, multiple scattering will contribute to a widening of the transverse distribution of the other of tens of microns. Table 3, 90% of the shower is contained within 1.6 mm of tungsten for 150 MeV electrons.

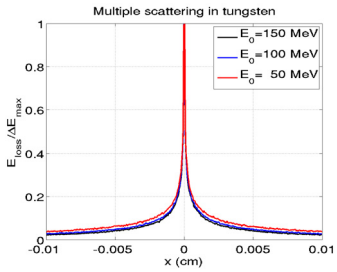


Figure 7: The effect of multiple scattering on the transverse position of the stopped primary electrons.

Table 3: Effect of multiple scattering on the transverse distribution of stopped primary electrons for different materials and beam energies.

Material	Energy (MeV)	Transverse width shower (cm)	
		90% e- stopped	99% e- stopped
Tungsten	150	0.16	0.57
Tungsten	100	0.21	0.64
Tungsten	50	0.27	0.68

Table 4: Summary of detector dimensions.

Parameter	Dimension
Tungsten collimator depth	10 cm
Tungsten collimator slit width	400 μm
Tungsten segment depth	2.0 cm
Tungsten segment width	3 mm

DESIGN OF THE TBL SPECTROMETER

From the energy distribution of the decelerated beam, as shown in Fig. 3, the resulting transverse distribution, down stream from the dipole magnet is calculated. The resulting distribution depends on the choice of the magnetic field in the dipole and the spectrometer drift length. An optimal layout is still to be finalised, but typical transverse distributions are given in Fig. 8.

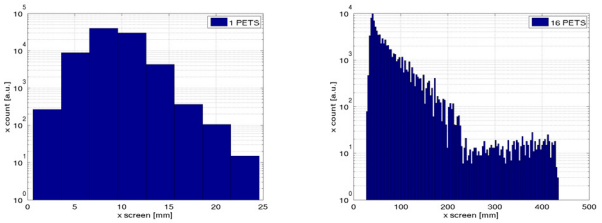


Figure 8: Typical transverse beam distributions downstream of the spectrometer dipole magnet for a beam of 1 PETS and 16 PETS, and the same dipole field.

The total energy deposition, in the realistic system has been studied as depicted in Fig. 9. The increase in temperature and the cumulative radioactive dose can be calculated from these values.

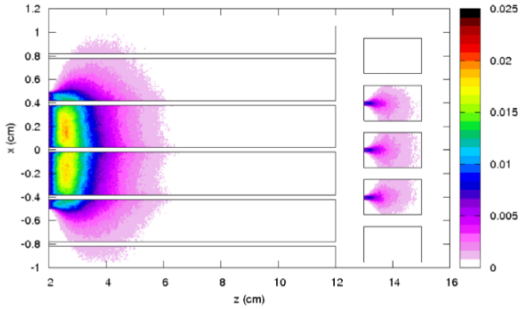


Figure 9: Energy deposition in the detector of a 150 MeV e- beam, given the final geometry of the collimator and active segments with dimensions as listed in Table 4.

CONCLUSIONS AND PERSPECTIVES

The main segmented dump design parameters have been identified for the time resolved energy measurement for the CTF3 TBL spectrometer. The design is based on an upstream collimator absorbing 90% of the beam power and a downstream active segmented dump with 3 mm wide segmentation. The mechanical design of the Dump will start soon and will be based on the temperature and radiation dose constraints estimated here. More simulations will be done in the future in order to quantify the impact of secondary particles on the measured charge.

ACKNOWLEDGEMENTS

Supported by the EU under contract PITN-GA-2008-215080.

REFERENCES

[1] G. Geschonke and A. Ghigo Eds, “CTF3 Design Report”, CERN/PS 2002-008 (RF).

[2] G. Guignard (Ed.), “A 3 TeV e+e- linear collider based on CLIC technology”, CERN 2000-008, 2000.

[3] S. Döbert, G. Rumolo, D. Schulte, I. Syratchev, D. Carrillo, “Progress on the CTF3 Test Beam”, LinProc. EPAC’06 and CLIC note 690, 2006.

[4] C. Welsh *et al.*, “Optimization of OTR screen surface” Review Advanced Material Science. 16 (2007) 73-79.

[5] T. Lefèvre *et al.*, “Segmented Beam Dump for Time resolved Spectrometry on a High Current Electron Beam”, DIPAC’07, Italy.

[6] "The FLUKA code: Description and benchmarking" G. Battistoni, S. Muraro, P.R. Sala, F. Cerutti, A. Ferrari, S. Roesler, A. Fasso`, J. Ranft, Proceedings of the Hadronic Shower Simulation Workshop 2006, Fermilab 6--8 September 2006, M. Albrow, R. Raja eds., AIP Conference Proceeding 896, 31-49, (2007).

INVESTIGATION OF EXTREMELY SHORT BEAM LONGITUDINAL MEASUREMENT WITH A STREAK CAMERA

C.A. Thomas*, I. Martin, G. Rehm, Diamond Light Source, Oxfordshire, UK

Abstract

During normal operation of synchrotron third generation light sources like Diamond, the measurement of the electron bunch profile, of the order of 10 ps, is perfectly done with a streak camera. However, in 'low alpha' operation, the shorter bunch length becomes extremely close to the resolution of the camera. In such a case, performing a good measurement and extracting the real information requires a good knowledge of the impulse response of the streak camera. We present analysis and measurement of the contributions to the point spread function (PSF) of the streak camera. The first contribution is the static PSF and is obtained by measuring a focussed beam without any sweep. The second contribution is the dynamic PSF, which is due to a chirp introduced by refractive optics. For pulse with large spectral bandwidth the dynamic PSF can be larger than 5 ps.

INTRODUCTION

Third generation synchrotron light sources are characterised by low emittance, small beam size, but also short bunch lengths. At Diamond we have been carrying out tests in the so-called low alpha mode, reducing the momentum compaction factor by up to a factor of 250, which gives a smallest theoretical bunch length of 0.7 ps, 15 times smaller than our 10.8 ps nominal bunch duration [1]. Measuring the real profile of such a short pulse is challenging. At Diamond, to measure bunch longitudinal profiles and length, we measure synchrotron radiation (SR) pulses with a dual sweep streak camera (SC) with a synchroscan at 250 MHz from Optronis GmbH. The manufacturer's specification of the camera gives 2 ps for the resolution with Rayleigh criterion and monochromatic light. This provides a good resolution for the normal operation mode of the camera but leads to extremely challenging measurement in low alpha mode.

We present measurement of the instrumental response of the streak camera that is decomposed into a static and dynamic response. The static response is measured as the point spread function of the image of a focussed photon beam on the SC, with no sweep from the electrodes. The dynamic response, as observed by previous authors [2, 3, 4], is the additional pulse lengthening measured while sweeping the electrodes of the SC, due to the dispersion in material traversed by the pulse. The decomposition of the PSF is firstly evidenced by means of spectral filters, and then measured with introduction of a spectrograph in the focussing optics of the SC.

* cyrille.thomas@diamond.ac.uk

STREAK CAMERA RESOLUTION

The SC is composed of a photocathode, a streak tube in which the electrons undergo a longitudinal constant accelerating voltage, and then a transverse varying high voltage from two sweep electrode pairs. The images are obtained by a phosphor screen, coupled to a multi channel plate (MCP) and a CCD camera [5]. The best probe of the resolution is to measure known short pulses. Measurement of broadband synchrotron light pulses in low alpha mode allows to evidence not only the static PSF, but also the dynamic PSF induced by group velocity dispersion of optical materials.

Electron Bunch Length in Storage Rings

In storage rings, the r.m.s length of small charge bunches is proportional to the relative energy spread of the relativistic electrons, σ_ϵ, to the momentum compaction factor, α_c, and inversely proportional to the synchrotron frequency, f_s. The expression governing the bunch length at very low charge is given (in s) by:

$$\sigma_{bunch} = \frac{\alpha}{2\pi f_s}\sigma_\epsilon \qquad (1)$$

For the Diamond storage ring in normal operation we have $\alpha = 1.7 \cdot 10^{-4}$, $f_s = 2.5$ kHz, and $\sigma_\epsilon = 10^{-3}$, which make the bunch length $\sigma_{bunch} \approx 10.8$ ps. In the low alpha mode reported here, we had $\alpha = 10^{-5}$, $f_s = 0.6$ kHz, and $\sigma_\epsilon = 10^{-3}$, which make the bunch length $\sigma_{bunch} \approx 2.6$ ps.

Setup and Measurements

Bunch length is measured with the SC using the visible part of the SR from a bending magnet. The spectrum from the diagnostics beamline is selected by the mirrors of the transport line and the vacuum-air sapphire window. It ranges from 200 nm to over 800 nm. Further filtering by UV absorption is introduced by the BK7 focussing lens.

In the low alpha mode operation the measurements of the electron bunch length were performed with white beam and with a series of spectral filters at the same current.

Preliminary, the static PSF has been measured for the white beam and also with 10 nm bandwidth filters at 490 nm and 560 nm, and with a 400-450 nm bandpass filter. As the static PSF is measured in pixels, it translates to a resolution in ps with the sweep unit scale calibration factor (0.1863, 0.3137 and 0.6374 ps/pixel for the 15, 25 and 50 ps/mm sweep speeds respectively). The results are reported in table 1. The smaller resolution, around 7.33 pixel, is for the narrow bandwidth filter at 560 nm. In all other cases, the PSF is larger at 10 pixels and even 11.66 pixels for the

Table 1: Bunch Length in Low Alpha mode. The measured bunch length, Σ, varies as function of the pulse bandwidth. This is shown by the corrected bunch length, Σ^*, after subtracting quadratically by the SC r.m.s PSF width, Δ_{PSF}, measured for each case, white beam (WB), with bandpass filter (BP) 400-450 nm, narrow band filters 490 ± 10 nm and 560 ± 10 nm. The PSF is measured in pixels and reported as , $\Delta_{PSF,ii}$ with the corresponding scales 50 ps / mm, 25 ps / mm and 15 ps / mm.

	WB	BP 400-450 nm	490 nm	560 nm
Δ_{PSF} (pixel)	9.88	11.66	9.81	7.33
$\Delta_{PSF,50}$ (ps)	6.23	7.44	6.25	4.67
$\Delta_{PSF,25}$ (ps)	3.1	3.66	3.0	2.3
$\Delta_{PSF,15}$ (ps)	1.85	2.17	1.83	1.36
Short bunch measurements at 25 ps/ mm				
Σ (ps)	6.53	5.92	5.14	4.88
Σ^* (ps)	5.72	4.62	4.1	4.2

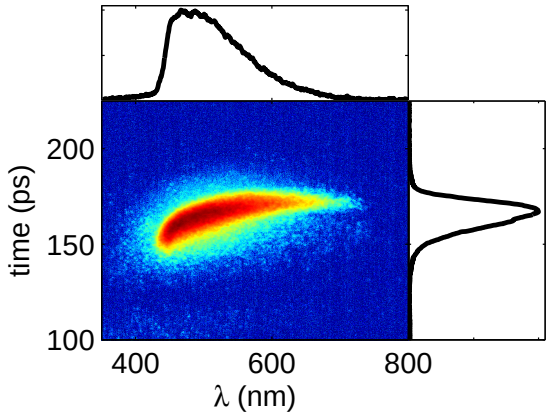


Figure 1: SC image presenting the pulse profile vs. wavelength. The chirp induced by the dispersion in the glass element traversed by the photon beam is clearly visible. The net result is a pulse broadening.

bandpass filter 400-450 nm. This suggests two effects: One and probably the main effect is the quality of the focussing system (BK7 singlet lens, slit and Nikkor achromat lens); and a possible additional effect of higher energy electrons spreading into the streak tube.

The bunch length has been measured in a short time, at 12 μA per bunch, varying less than 2 μA. This implies that the bunch length was the same for all measurements. The raw measurements vary with the bandwidth. However, the PSF largely contributes to the measurement as the bunch length is very close to the PSF width. In a first but good approximation, the contribution is quadratic, assuming the PSF and the measured pulses to be Gaussian. We then can write:

$$\Sigma^* = \sqrt{\Sigma^2 - \Delta_{PSF}^2} \qquad (2)$$

where Σ^* is the real r.m.s pulse duration, Σ is the measured r.m.s pulse duration, and Δ_{PSF} is the r.m.s static PSF of the SC.

Once the contribution of the PSF is removed, all the measurements should give the same bunch length. In fact, as described earlier in [2, 3], there is an additional broadening of pulses with wide spectral range due to the dispersion in the lenses' material and in the vacuum-air out-coupling window. We assume the broadening to be negligible for narrow bandwidth pulses, which is achieved with the 10 nm bandwidth filters. Consequently, the measurements with a pulse of large spectral band show a measurable broadening.

Direct Measurement with Spectrograph

A more accurate measurement of the pulse broadening due to the refractive materials is to measure a SR time resolved spectrum, i.e. the pulse profile vs. photon wavelength. For that we couple the SC with a spectrograph, keeping the same focussing optics as for the previous measurements. Figure 1 shows the results of such a time resolved spectrogram. The intensity spectrum is shown above the image, and on the right the profile of the integrated pulse over the spectrum. These measurement have been taken on a different day than the one in the previous section, so the machine parameter settings are different. For this measurements, we have $\alpha \approx -3 \cdot 10^{-6}$, $f_s \approx 340$ Hz, and the bunch current is $\approx 5.3\mu$A. Because the bunch has already some significant charge we expect to measure a larger pulse width than the 1.4 ps theoretically predicted.

Following the same approach as in the first section, we measured the static PSF of the spectrograms in the focussing mode. It is not fully optimised with a mean resolution of the order of 10 pixels r.m.s, but it is comparable with the previous experiment. In addition, the chromatic effects due to the first focussing lens make the optimisation of the static PSF difficult.

Figure 2 shows the centroid of the pulses vs. wavelength. The three curves presented are from the same pulses but at the three different sweep speeds offered by the synchroscan unit. The overlapping shows the independent calibration agreement. The quadratic polynomial fit (see figure caption) shows a higher order chirp probably due to the different glasses traversed by the photon beam, a sapphire window, a BK7 lens, and the achromatic Nikkor lens of the SC. The large chirp observed with the time resolved spectra explains the broadening measured with different spectral bandwidth pulses in the previous section (see table 1).

Figure 3 presents the pulse at 535 nm and the integrated pulse over the spectrum: the r.m.s width of the pulses are 3.3 ps and 6.7 ps respectively. The quadratic difference gives a first order estimate of the dynamic PSF of the order of 5.8 ps.

Finally we have measured with the 15 ps/mm sweep speed the pulse duration vs. wavelength as shown in Figure 4. In the range 400-600 nm, where the relative intensity is larger than 10% of the max, the corrected r.m.s width is on

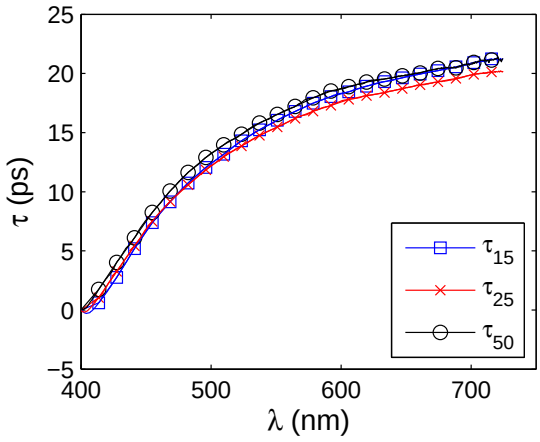


Figure 2: Centroid of the pulses vs. wavelength measured on Figure 1. τ_{ii} indicates the sweep speed. Fit of the curves converges to the second order polynomial: $y = -0.00026\,(\lambda - 400)^2 + 0.14\,(\lambda - 400) + 0.4$ (λ in nm and y in ps).

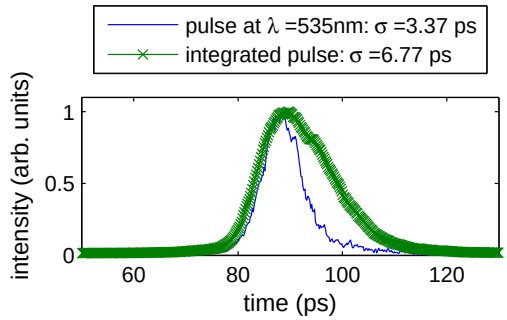


Figure 3: Pulse profile at 535nm compared to the integrated pulse over the spectrum.

average ≈ 3.5 ps with standard deviation 0.3 ps.

CONCLUDING REMARKS

We have characterised the instrument response of the SC. It is shown that the static PSF width is not uniform over the visible spectrum. This is due to mainly the chromatic effects of the lens system. However some spread due to the thermal energy of photons can also influence the width of the PSF. It is not measured here, and might be needed to further characterise the SC. We also presented the chirp induced by dispersion in glass materials and the effect on pulse width measurement. This is a well-known effect that is often forgotten. We associated this effect to a dynamic PSF introduced by the dispersion in the refractive optics of the SC. This leads to an additional spread in the pulse measurement that can be larger than 5 ps as shown by the time resolved spectra. Of course, this is unwanted and needs to be cured. The immediate solution is to use a narrow band filter so that the dispersion is negligible. However, this method also implies reducing the photon flux by more

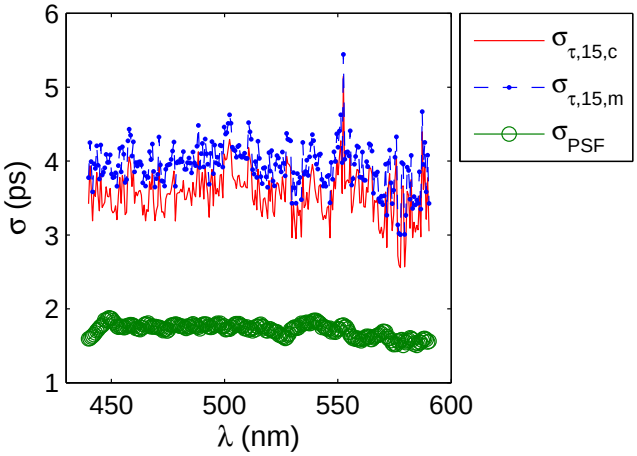


Figure 4: Pulse duration in the time-resolved spectrogram. The curves show measured and corrected r.m.s pulse width vs. wavelength. The relative spectrum intensity is shown in the inserted graph.

than 95%, which may prevent the ability to measure bunch length at very small current. Introducing a spectrograph in the measurement allows to measure precisely the induced chirp. In addition, it preserves the use of the full available power of the synchrotron radiation for the bunch length measurement. Thus, the low limit current for bunch length measurement should be pushed further down. Finally, the use of reflective focussing optics [4] presents the advantage of an almost dispersion free optical system. However, dispersion from the vacuum-air window still remains. In order to optimise the SC performance, we are currently designing a reflective focussing optics which includes a spectrograph. This should enable the SC to measure extremely short bunches closer to the manufacturer specification extended to the whole available SR spectral bandwidth, thus using at the same time all the available power. In addition, this new system keeps the ability to measure residual chirp.

REFERENCES

[1] I. Martin, R. Bartolini, J. Rowland, B. Singh, and C.A. Thomas. A Low Momentum Compaction Lattice for the Diamond Storage Ring. In *Proc. of PAC 2009, (Vancouver)*, 2009.

[2] J. Ihlemann, A. Helmbold, and H. Staerk. Chromatic time lag in picosecond-streak-camera objectives. *Review of Scientific Instruments*, 59:2502, November 1988.

[3] M. D. Duncan, R. Mahon, L. L. Tankersley, and J. Reintjes. Chromatic time lag in picosecond streak camera measurements. *Appl. Opt.*, 29(16):2369–2370, 1990.

[4] T. Obina and T. Mitsuhashi. Measurement Of Bunch Lengthening Effects Using A Streak Camera With Reflective Optics. Proceedings of DIPAC 2007, pages 256–258, May 2007.

[5] C. A. Thomas and G. Rehm. Diamond Optical Diagnostics: First streak camera measurements. Proceedings of EPAC 2006, pages 1112–1114, June 2006.

A COMPACT SINGLE SHOT ELECTRO-OPTICAL BUNCH LENGTH MONITOR FOR THE SwissFEL

B. Steffen*, V. Schlott, PSI, Villigen, Switzerland
F. Müller, PSI, Villigen and IAP Univ. Bern, Bern, Switzerland

Abstract

The knowledge and control of electron bunch lengths is one of the key diagnostics in XFEL accelerators to reach the desired peak current in the electron beam. A compact electro-optical monitor was designed and build for bunch length measurements at the SwissFEL. It is based on a mode locked ytterbium fiber laser probing the field-induced birefringence in an electro-optically active crystal (GaP) with a chirped laser pulse. The setup allows the direct time resolved single-shot measurement of the Coulomb field (THz-radiation) of the electron beam - and therefore the bunch length - with an accuracy as good as 200 fs. Simulations of the signals expected at the SwissFEL will be presented.

INTRODUCTION

Paul Scherrer Institut is planning a free electron laser for X-Ray wavelengths, the SwissFEL. The baseline design foresees to generate electron bunches with a charge between 200 and 10 pC and bunch lengths between 10 ps and a few fs. These bunches will be accelerated in a normalconducting linear accelerator (linac) to a particle energy of up to 6 GeV to radiate coherently at wavelengths between 0.1 and 7 nm in one of the two undulators. To test the feasibility of novel accelerator concepts and components needed for the generation of such high-brightness beams, their longitudinal compression and the preservation of the emittance, a 250 MeV Injector is currently being assembled at PSI (see Fig. 2).

Precise measurements of the temporal profile of extremely short electron bunches are indispensable for a detailed understanding of the bunch compression and lasing mechanisms in a FEL. Single-shot electro-optical (EO) detection techniques are ideally suited for this purpose since they are non-destructive and can be carried out during regular operation of the free-electron laser for user experiments [1, 2]. An important aspect is that they permit correlation studies between the measured time profile of electron bunches and other measured beam parameters as well as the properties of FEL pulses produced by the same bunch. A second technique for the single-shot direct visualization of longitudinal electron bunch profiles are transverse-deflecting structures (TDS) [3]. The TDS converts the temporal profile of the electron bunch charge density into a transverse streak on a view screen by a rapidly varying electromagnetic field. The measurement with the TDS offers the highest resolution but is inherently destructive, so it cannot be used as an online monitor of the bunch length.

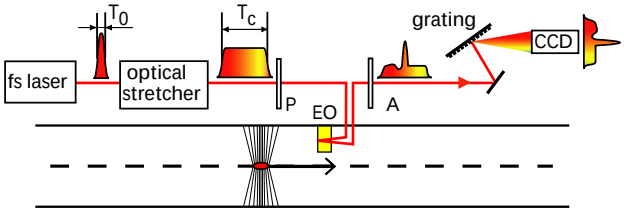


Figure 1: Schematic drawing of a spectrally encoded electro-optical detection setup. P: polarizer; EO: EO crystal; A: analyzer.

EO BUNCH LENGTH DETECTION

When a relativistic picosecond duration bunch passes within a few millimeters of an electro-optic crystal, its transient electric field is equivalent to a half-cycle THz pulse impinging on the crystal. The temporal profile of this equivalent half-cycle THz pulse provides a faithful image of the longitudinal charge distribution inside the electron bunch if the electrons are highly relativistic. The transient electric field induces birefringence in the electro-optic crystal. As the electric field propagates through the crystal, the birefringent properties of the crystal also propagate. This birefringence can be probed by a copropagating optical laser pulse [2].

Several variants of EO bunch diagnostics have been applied in electron bunch diagnostics [4, 5, 6], all sharing the underlying principle of utilizing the field-induced birefringence in an electro-optic crystal to convert the time profile of a bunch into a spectral, temporal, or spatial intensity modulation of a probe laser pulse.

THE COMPACT EO MONITOR

The presented compact EO bunch length monitor utilizes the spectral decoding technique, where the bunch shape information is encoded into a chirped laser pulse and then retrieved from its modulated spectrum using the known relationship between wavelength and longitudinal (temporal) position in laser pulse.

The chirped laser pulse passes through the polarizer and the EO crystal in the beampipe, where the polarization becomes elliptical. The ellipticity of the polarization is proportional to the electric field of the electron bunch and has the same temporal structure. The analyzer, a combination

* email: bernd.steffen@psi.ch

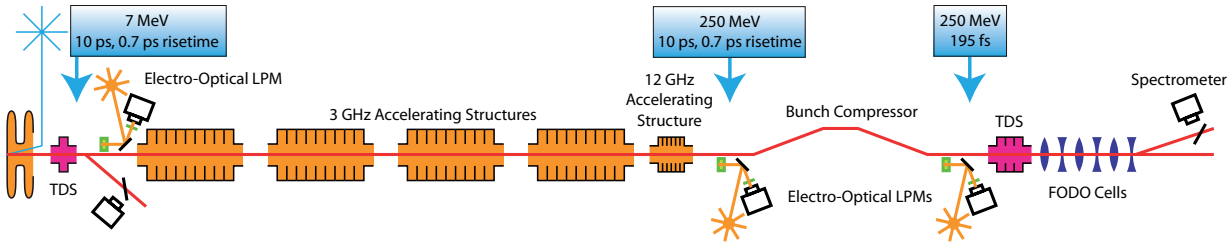


Figure 2: Schematics of the 250 MeV injector with the planned bunch length diagnostics. TDS: Transversely Deflecting Structure; FODO: Focusing - Drift - Defocusing - Drift; LPM: Longitudinal Profile Monitor.

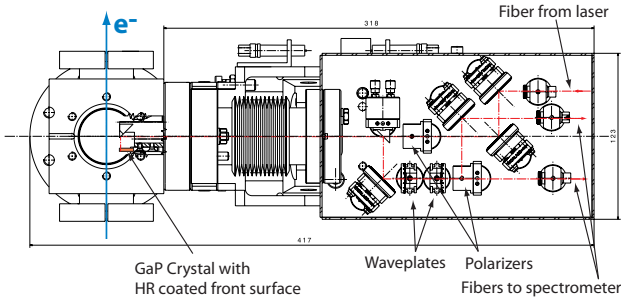


Figure 3: Assembly drawing of the compact EO monitor including the vacuum chamber (left).

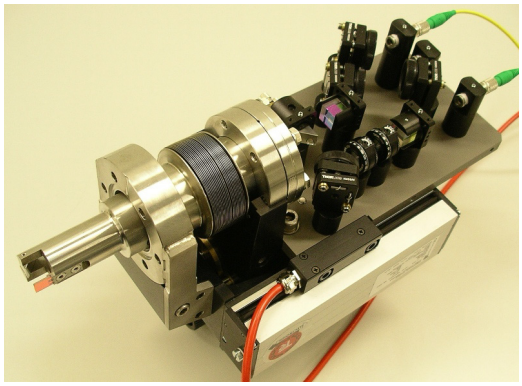


Figure 4: Photo of the EO monitor including the optics.

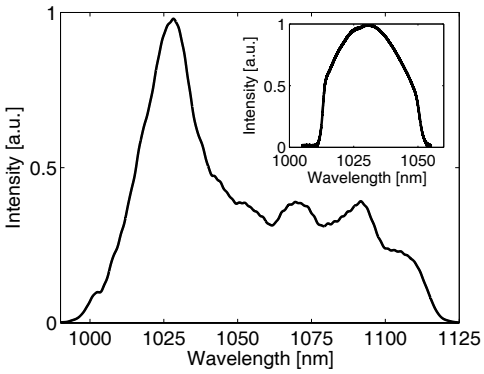


Figure 5: Broad spectrum of the amplifier as used for the EO monitor. Inset: Spectrum of the oscillator.

of wave plates and a polarizer, turns the elliptical polarization into an intensity modulation. The longitudinal charge distribution gets encoded in the spectrum of the laser pulse, which can then be detected using a spectrometer (Fig. 1).

The EO crystal used here is a Galliumphosphide (GaP) crystal with a reflective coating for the laser wavelength (1050 nm) at the front surface (towards the electron source) and an antireflective coating at the backside. Depending on the expected bunch length the monitor can be equipped with crystals of different thickness up to 5 mm. The laser enters the crystal at the backside, is reflected at the frontside and leaves the crystal at the backside again, while the Coulomb field of the electron bunch enters at the frontside, propagating towards the backside. This way the laser first counterpropagates with the electric field pulse of the bunch and afterwards copropagates. This leads to some artifacts in the EO signal shown in the next section, but the monitor can be build very compact and a an upstream mirror can be avoided that would disturb the Coulomb field and trigger wakefiels, which would also lead to spurious EO signals. The total length of the monitor including the space for the optic elements is less then 150 mm.

The crystal and the downstream mirror are mounted on a holder which is mounted on a motorized vacuum-feedtrough (Fig. 3 and 4). Outside the vacuum a small breadboard is fixed to the feedthrough which holds the required optics including the fibercouplers. This way all optic elements from the fiber coming from the laser to the fiber going to the spectrometer, including the EO crystal are rigidly coupled, avoiding any misalignment or timing changes when the crystal is moved closer to the electron beam or withdrawn from the beampipe.

As laser source for the monitor an amplified Yb-doped fiber laser system has been developed at the University of Bern. It delivers pulses with 20 to 200 nJ pulse energy and up to 100 nm useful bandwidth (Fig. 5). Details of the laser system and the synchronization to the accelerator are described elsewhere [7].

SIMULATIONS

The EO signals expected for the different positions along the 250 MeV injector have been simulated using a code based on the geometric response function [1, 8]. In the

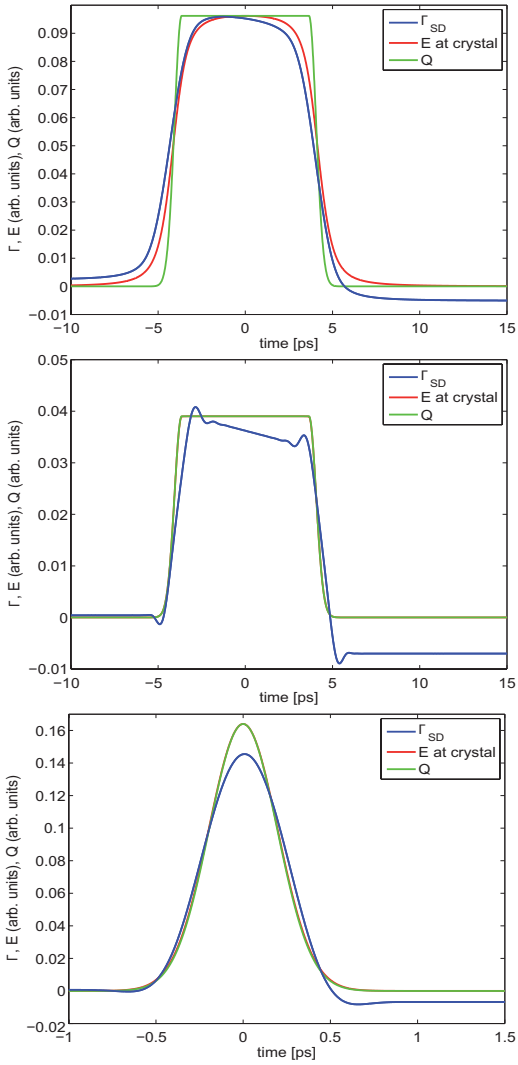


Figure 6: Simulated EO signals at different positions of the 250 MeV injector: after the gun (top, for a 5 mm thick GaP crystal and a laser pulse chirped to 5 ps(rms)), before the bunch compressor (center, for a 2 mm thick GaP crystal and a laser pulse chirped to 5 ps), and after the bunch compressor (bottom, for a 0.5 mm thick GaP crystal and a laser pulse chirped to 500 fs).

low energy region (7 MeV) right after the gun the dominant broadening is due the $1/\gamma$ opening angle of the Coulomb field, shown in Fig. 6 (top) for a distance of 3 mm between the path of the electron beam and the path of the laser. For the high energy region (250 MeV) before and after the bunch compressor the bunch shape can be well determined except from a shift of the baseline of the measurement after the bunch signal (Fig. 6 (center and bottom)).

This shift is due to an additional polarization rotation which the laser pulse accumulates when it sees the counter-propagating field of the electron bunch before the laser is reflected at the front surface of the EO crystal. This rotation is smaller in amplitude and of opposite sign as the rotation accumulated when the laser and bunch field are copropagating (Fig. 7). The relative amplitude of the two decreases with shorter electron bunches and thicker crystals. As long as the electron bunch is significantly shorter than the EO crystal multiplied with its refractive index, the signal coming from the part where the laser is copropagating can be well reconstructed from the sum signal.

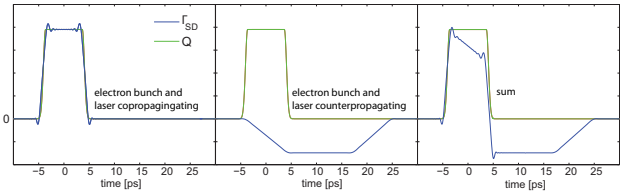


Figure 7: Simulated EO signals from a 10 ps long electron bunch passing a 1 mm thick GaP crystal, modulated on a copropagating laser pulse (left), a counterpropagating laser pulse (center) and the sum of the two (right).

CONCLUSION

Prototypes of the monitor and the laser have been build and are ready for first tests planned at the SLS linac in summer 2009. Further optimizations can be done by measuring shorter pulses during FEMTO slicing. In parallel we are planning a packaging of the laser for operation at the 250 MeV injector which is currently under construction.

REFERENCES

[1] B. Steffen, "Electro-optic methods for bunch length diagnostics at FLASH", PhD thesis, University of Hamburg, DESY-THESIS-2007-020, 2007.

[2] B. Steffen *et al.*, "Single-shot electron-beam bunch length measurements", Phys. Rev. ST Accel. Beams, 12:032802, 2009.

[3] O. H. Altenmueller *et al.*, "Investigations of Traveling-Wave Separators for the Stanford Two-Mile Linear Accelerator", Rev. Sci. Instrum. **35**, 438, 1964.

[4] I. Wilke *et al.*, "Single-shot electron-beam bunch length measurements", Phys. Rev. Lett., Vol 88, No 12, 2002.

[5] G. Berden *et al.* "Electro-optic technique with improved time resolution for real-time, nondestructive, single-shot measurements of femtosecond electron bunch profiles", Phys. Rev. Lett., 93:114802, 2004.

[6] A. L. Cavalieri *et al.*, "Clocking Femtosecond X Rays", Phys. Rev. Lett. **94**, 114801, 2005.

[7] F. Müller *et al.*, "Ytterbium fiber laser for electro-optical pulse length measurements at the SwissFEL", Proceedings DIPAC 09, Basel, TUPD31, 2009.

[8] S. Casalbuoni *et al.* "Numerical studies on the electro-optic sampling of relativistic electron bunches", Phys. Rev. ST Accel. Beams, 11:072802, 2008.

TOWARDS AN ULTRA-STABLE REFERENCE DISTRIBUTION FOR THE NEW PSI 250 MeV INJECTOR

S. Hunziker[#], V. Schlott, Paul Scherrer Institut, CH-5232 Villigen, Switzerland

Abstract

The PSI 250 MeV Injector, a precursor to the SwissFEL, with its extreme jitter and stability demands poses new challenges for the synchronization system. Our concept is double-tracked: low risk electrical and best potential performance and flexibility optical. The electrical distribution system, being established first, relies on reliable technology. Optimized to achieve a benchmark jitter performance of around 10 fs and a long term drift stability of some 10 fs in the most critical parts of the machine it will also backup the optical system. Sub 10 fs jitter and drift figures are being aspired for the latter. In this contribution, both system designs are presented, expected and first measured electrical and optical reference signal jitter and long term cable and coupler drifts are presented. A cable temperature stabilization system is discussed, too. Finally, a first jitter measurement of the optical master oscillator (OMO) laser will be presented.

INTRODUCTION

The 250 MeV Injector will be ≈65 m long and basically consist of an electron gun (with photocathode), S-band structures, an X-band structure and a bunch compressor as depicted in Fig. 1. These structures are driven by RF signals, which are synchronized to the distributed reference signal. Other "customers" of the reference distribution system are e.g. photocathode laser, timing system, diagnostics in general. The building is ready, first installations are being done now (Spring 2009). The reference distribution is one of the key challenges. Extremely tight timing jitter requirements demand for solutions on the edge of technical feasibility. On the other hand cost and reliability issues have to be considered. Both distribution concepts, the electrical and the optical one, are sketched in Fig. 2.

ELECTRICAL REFERENCE DISTRIBUTION

Architecture

The coaxial cable based baseline system consists of:

- Low phase-noise 214.14 MHz RF master oscillator (RF MO), will be ready by June 2009.
- RF power amplifier (P_{out}>37 dBm) providing required signal levels at the terminals (points where the reference signal is needed) reference inputs.
- Directional couplers, feeding and decoupling reference inputs of the various terminals, e.g. PLO (=phase locked oscillator for 1.5, 3.0 and 12 GHz) reference inputs, located along a trunk line.

Active subsystems are supplied with ultra-low noise linear power supplies.

Drift, Temperature Stabilization, RF MO

Multiple coaxial cables form the trunk line within the accelerator tunnel (depicted in red in Fig. 2). They are guided within a thermally isolated pipe, which is supplied with a temperature controlled heater cable (Fig. 3). The pipe is supported with hard foam plates on cable trays and periodically furnished with temperature sensors. Various cables (basically 3/8" and 7/8" coax, which are relatively inexpensive) are installed in parallel, offering the possibility to find the one with lowest drift after installation by optimizing the temperature within the pipe. It has been found that the temperature stability as well as the optimum operating temperature for minimum drift of low loss corrugated coaxial cables may strongly vary from production lot to production lot, which requires flexibility and redundancy during installation.

The measured temperature stability of various cables is listed in Table 1.

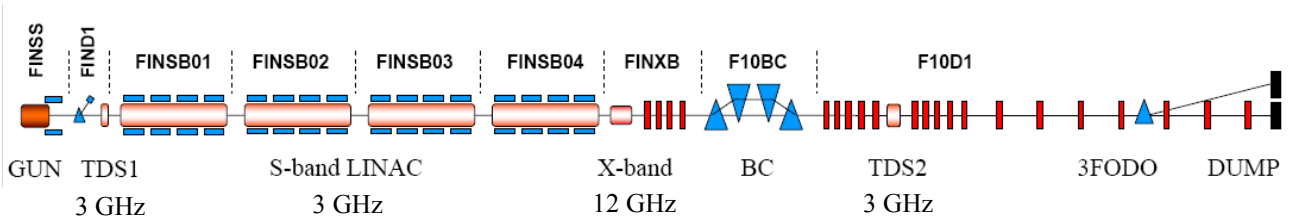


Figure 1: Simplified layout drawing of the PSI 250 MeV Injector [1].

[#]stephan.hunziker@psi.ch

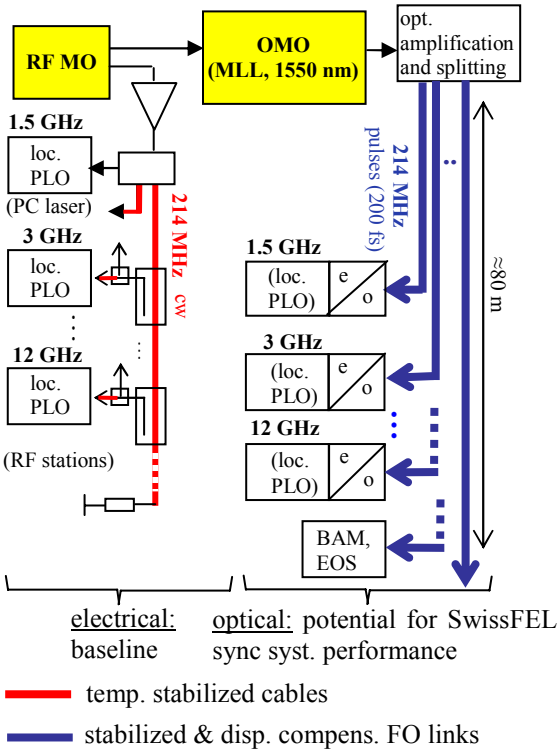


Figure 2: Simplified layout of electrical and optical reference distributions for the PSI 250 MeV Injector.

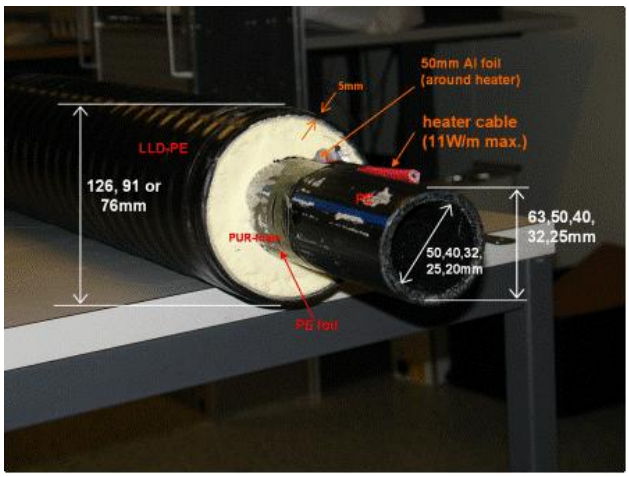


Figure 3: Temperature controlled cable pipe.

Corrugated low loss cables are the preferred choice for the trunk line, whereas flexible braided cables are used where small bending radii are required (e.g. within racks or to connect couplers and splitters). The temperature drift for the 7/8" cable seems to be quite high. The measured cables are obviously from a non-optimum production lot, whereas the 3/8" shows low drift, even though at higher than expected temperature. Typically the 7/8" Cellflex and the 3/8" Heliax (both temperature cycled at the manufacturer's site to minimize drift and relaxation effects) are expected to show approximately zero drift at ≈33 ºC (7/8") and at 27..30 ºC (3/8") respectively [2].

Expected drifts of the electrical system (in the critical front part of the machine over hours) are thus:

- 30 m of Heliax 3/8" (<0.2 °C stab.) <15 fs drift
- some m of Sucoflex 404 (<0.2 °C stab.) <10 fs drift
- directional coupler: ≈3 fs/°C drift
- total: <50 fs drift achievable

Specified and expected jitter values for the RF MO and the PLOs are shown in Table 2. The phase detectors inside the PLOs are extremely critical w.r.t. drift and therefore a weak point. They will be temperature stabilized to minimize drift between the RF stations' reference signals.

Table 1: Measured Coaxial Cable Drifts

Cable type	Temp. [ºC]	Drift [ppm/K]	Drift [fs/m/K]
Andrew Heliax 3/8" corrugated (low loss, low drift) $IL_{214\ MHz}$=5.5 dB/100 m	28.0	-2.9	-10.9
	30.0	-2.2	-8.1
	32.0	-1.5	-5.6
	34.0	-1.2	-4.6
	36.0	-0.3	-1.0
	38.0	+0.1	+0.5
RFS Cellflex 7/8", corrugated (very low loss) $IL_{214\ MHz}$=1.8 dB/100 m	27.5	-6.4	-23.6
	29.5	-6.7	-24.8
	31.5	-8.1	-30.0
	33.5	-6.4	-23.7
	35.5	-5.0	-18.3
	37.5	-5.4	-19.8
Huber+Suhner Sucoflex 404, braided (flexible, low drift) $IL_{214\ MHz}$=0.1 dB/m	26.0	-1.1	-4.2
	28.0	0.0	0.0
	30.0	-0.4	-1.4
	32.0	-5.3	-19.8

Table 2: RF MO and PLO Jitter Specifications and Expectations

Jitter (guar., typ.)	Δf=1 kHz..10 MHz, f_0=3 GHz	Δf=10 Hz..10 kHz, f_0=214.14 MHz
RF MO	-	13.0/9.5 fs
PLO, locked to MO	11.3/6.7 fs	-
specified	<10 fs	<20 fs

Figure 4 shows the block diagram of the RF MO. A Rb standard stabilizes the frequency (no long term phase differences between terminals due to ref. frequency drift). The close-in phase noise is optimized using two 10 MHz OCXOs (oven controlled x-tal oscillators) which are multiplied by 5 and mixed rather than doubling one oscillator's frequency, halving jitter (same for the 107.07 MHz oscillators). A 100 MHz frequency ref. unit, optimized for the medium offset frequency range, is locked to the 1st stage. A DDS (direct digital synthesis) adapts 107.07 MHz to the 100 MHz. First measurements of single blocks suggest that the typ. rather than the guaranteed jitter values will be reached.

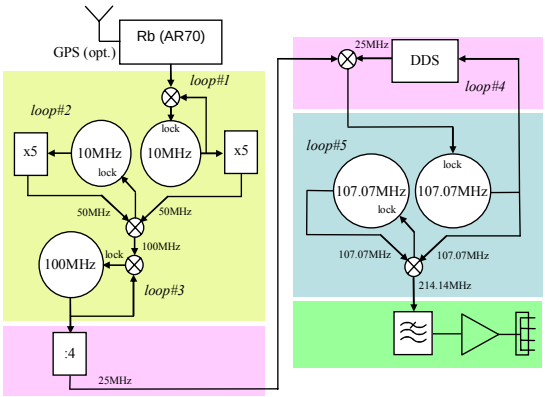


Figure 4: Block diagram of the RF master oscillator (214.14 MHz) [3].

OPTICAL REFERENCE DISTRIBUTION

Architecture, Link Stabilization

A star network (Fig. 2) of standard SM optical fiber bundles with plenty of redundant fibers offers high flexibility as every terminal in the facility can be patched with every other terminal at the OMO patch panel. Furthermore, many links will have to be compensated using DCF fibers, known from telecom applications [4] and phase stabilized as previously demonstrated for fs pulse transmission [5]. Link stabilization using optical cross-correlation is planned. Reliability-critical free-space delay lines used in these systems up to now may have to be replaced with more reliable components (e.g. in a combination of slow and fast delay correction). A commercial solution would be favored, the more so as e.g. Menlo Systems (www.menlosystems.com) is currently developing a link stabilization system as well as a Sagnac-loop based PLL. Temperature-stable LCP coated fibers [6] could be an alternative to active stabilization, at least for less critical links. The optical system is planned to be operational within the next two years

Optical Master Oscillator (OMO)

Basically, two OMO laser types are currently under evaluation, an Yb-doped hybrid (fiber, solid-state) femtosecond laser and a fiber laser. Both lasers are nearly transform limited soliton lasers (allows fiber-based dispersion compensation). Lowest jitter and highest stability up to now have been achieved with the former. Figure 5 shows the typical result of a phase noise and jitter measurement of the Onefive Origami 15 laser (1550 nm wavelength, 214.14 MHz rep. rate) [7]. This laser has an average optical output power of >120 mW (free space) or >70 mW (fiber coupled). For the measurement an Agilent E5052B SSA has been used. The influence of the setup noise has been minimized using SSA noise cancellation (10'000 correlations), a waveguide PD operated at max. V_{bias} (high saturation limit) and high photocurrent (≈2.5 mA), high carrier frequency, linear power supplies with additional filtering.

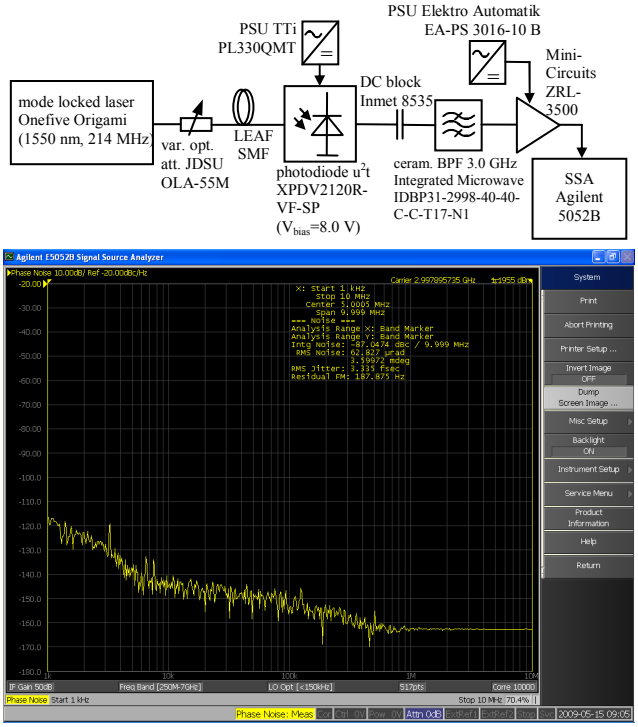


Figure 5: Measured phase noise of Onefive Origami 15 Soliton laser (□f=1 kHz..10 MHz, f_0=2.998 GHz=14th harmonic of rep. rate 214.14 MHz): Setup (top), phase noise spectrum, timing jitter of 3.3 fs (bottom).

PLOs

Generating ultra-low jitter synchronisation signals by extracting harmonics from the optical reference pulses is feasible, using optimized optical receivers (Fig. 5). As a next step, the drift performance of such receivers is being investigated and optimized. It has been shown by other groups that ultimate low drift (some fs) PLOs can be realized using optical-to-electrical phase detectors (Sagnac-loop PLL) [8]. As these PLOs are rather expensive, their use can be limited to situations where ultimate performance is really required. In other cases, direct harmonic extraction seems to be sufficient.

REFERENCES

[1] http://fel.web.psi.ch/
[2] http://www.wancom.com.cn/efiles/440-635.pdf
http://www.rfsworld.com/userfiles/pdf/Transmission_Line_Tech_Section.pdf
[3] http://www.inwave-gmbh.de
[4] R. Wilcox et al., "Fermi Timing and Synchronization System", Lawrence Berkeley Natl. Lab. LBNL-61165, 2006. repositories.cdlib.org/lbnl/LBNL-61165
[5] J. Kim et al., Opt. Lett. 32 (2007) 1044.
[6] T. Kakuta and S. Tanaka, Int. Wire & Cable Symp. Proc., p. 234 (1987).
[7] http://www.onefive.com
[8] J. Kim et al., Nature Photonics 2 (2008) 733.

ON THE LIMITATIONS OF LONGITUDINAL PHASE SPACE MEASUREMENTS USING A TRANSVERSE DEFLECTING STRUCTURE

C. Behrens* and C. Gerth,
Deutsches Elektronen-Synchrotron DESY, D-22603 Hamburg, Germany

Abstract

High-brightness electron bunches with low energy spread, small emittance and high peak currents are the basis for the operation of high-gain Free-Electron Lasers (FELs). As only part of the longitudinally compressed bunches contributes to the lasing process, time-resolved measurements of the bunch parameters are essential for the optimisation and operation of the FEL. Transverse deflecting structures (TDS) have been proven to be powerful tools for time-resolved measurements. Operated in combination with a magnetic energy spectrometer, the measurements of the longitudinal phase space can be accomplished. Especially in case of ultra-short electron bunches with high peak currents for which a time resolution on the order of 10 fs would be desireable, both the TDS and magnetic energy spectrometer have intrinsic limitations on the attainable resolution. In this paper, we discuss the fundamental limitations on both the time and energy resolution, and the relation between them.

INTRODUCTION

Recently developed Free-Electron Lasers for the generation of photons in the extreme ultraviolet and soft X-ray regime are based on an exponential gain of the radiation power in a single pass through a long undulator magnet system. These high-gain FELs put stringent demands on the electron bunch parameters. In order to initiate the lasing process and to reach power saturation in reasonable undulator lengths, a high charge density which is related to the peak current, a low energy spread, and a small emittance is mandatory.

Projected measurements of the electron bunch parameters are not sufficient to understand and to control the lasing process. For this reason, sliced electron bunch measurements are essential, which can be accomplished by Transverse Deflecting Structures (TDS). In combination with a magnetic energy spectrometer, the longitudinal phase space can be investigated.

In order to get the most information concerning the lasing process, the measurements may be carried out in front of the undulators. This is very challenging since the electron bunches are, in particular in front of the undulators, very short with bunch lengths in the femtosecond range and peak currents on the order of kiloampere.

* christopher.behrens@desy.de

GENERIC BEAMLINE LAYOUT

An experimental layout for sliced beam parameter measurements is presented schematically in Fig. 1. The entire beamline is equipped with quadrupole magnets to ensure the required optics for standard machine operation as well as for dedicated sliced beam parameter measurements. For operation without affecting the entire bunch train, e.g. bunch profile measurements, a fast kicker can be used to pick out individual bunches for off-axis screen operation. The magnetic energy spectrometer consists of at least one dipole magnet, followed by a drift section for building up dispersion.

Further requirements are imaging screens, e.g. OTR-screens or scintillators, and optical camera systems providing high spatial resolutions.

ACCELERATOR OPTICS

In order to obtain desired time[1] and energy resolutions, the accelerator optics has to be designed and adapted according to the following considerations.

In linear beam dynamics, the general transverse motion of charged particles can be described as combination of betatron motion and dispersion trajectory. The deflection plane of the energy spectrometer is assumed to be in the horizontal, e.g. the x-plane. The horizontal particle motion is then given by

$$x(s) = x_\beta(s) + D_x(s) \cdot \delta \,, \tag{1}$$

with the horizontal betatron motion $x_\beta(s)$, horizontal dispersion function $D_x(s)$, and relative momentum deviation δ. After passing the magnetic energy spectrometer, the horizontal rms beam size at screen location s_1 can be expressed by $\sigma_x = \sqrt{\sigma_{x_\beta}^2 + D_x^2 \cdot \sigma_\delta^2}$. In order to achieve energy resolutions on the order of σ_δ, the beam size due to dispersion and energy spread has to be larger than the natural rms beam size $\sigma_{x_\beta} = \sqrt{\epsilon_x \cdot \beta_x}$. This condition yields

$$D_x(s_1) \cdot \sigma_\delta > \sqrt{\epsilon_x \cdot \beta_x(s_1)} \,, \tag{2}$$

with the horizontal geometric emittance ϵ_x and beta function β_x. The reachable energy resolution is then given by

$$\sigma_\delta > \sqrt{\epsilon_x} \cdot \frac{\sqrt{\beta_x(s_1)}}{D_x(s_1)} \,. \tag{3}$$

[1] The time resolution expresses the resolution of the longitudinal coordinate ζ within the bunch. The relation is given by $t = \zeta/c$.

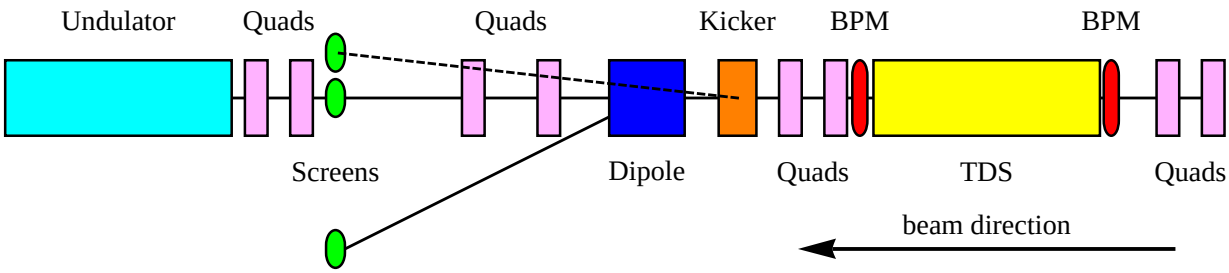


Figure 1: Beamline layout for dedicated sliced beam parameter measurements and investigations of the longitudinal phase space. The different components are labelled and assigned to colours. The electron beam direction is indicated by the arrow (from right to left).

For using a TDS in combination with a magnetic energy spectrometer, the deflection induced by the TDS has to be in the vertical. In case of a LOLA-type TDS [3], the particle motion is given by [1, 2]

$$y(s) = y_\beta(s) + S_y(s) \cdot \left(\zeta + \frac{\sin(\Psi)}{k \cdot \cos(\Psi)} \right) , \quad (4)$$

with the streak or shear function

$$S_y(s) = \sqrt{\beta(s_0)\beta(s)} \cdot \sin(\Delta\Phi_y) \cdot \frac{eV_0 k}{pc} \cdot \cos(\Psi) , \quad (5)$$

and the internal longitudinal bunch coordinate ζ. The parameters V_0 and k denote the deflecting voltage and the wavenumber. The beam energy is given by $E \approx pc$, and $\Delta\Phi_y$ is the vertical phase advance from location s_0 to s. The expression in (4) is valid for the approximation that the TDS is considered as to be a drift section with an instantaneous deflection at the centre of the structure. In order to avoid centroid deflections and achieve best resolution, the TDS is assumed to be operated near zero-crossing, i.e. the RF phase is set to $\Psi \approx 0$. Thereby, Eq. (4) is reduced to

$$y(s) = y_\beta(s) + S_y(s) \cdot \zeta , \quad (6)$$

which is of similar form as Eq. (1). In order to achieve a longitudinal resolution on the order of σ_ζ, the beam size at screen location s_1 due to streaking with the TDS has to be larger than the natural beam size due to betatron motion. This yields the condition

$$S_y(s_1) \cdot \sigma_\zeta > \sqrt{\epsilon_y \cdot \beta_y(s_1)} . \quad (7)$$

By using Eq. (5) and $\Psi \approx 0$, the attainable longitudinal resolution is then given by

$$\sigma_\zeta > \frac{\sigma_{y_\beta}(s_1)}{S(s_1)} = \frac{\sqrt{\epsilon_y} \cdot pc}{\sqrt{\beta(s_0)} \cdot \sin(\Delta\Phi_y) \cdot eV_0 k} . \quad (8)$$

TRANSVERSE DEFLECTING STRUCTURE

The considerations in the previous section represent the attainable resolutions for sliced beam parameter measurements in terms of linear beam dynamics. More detailed studies of the particle dynamics within the TDS reveal additional resolution limitations.

The physics of RF deflectors originates from the Panofsky-Wenzel theorem [4], which makes a general statement of the transverse momentum gained by fast particles moving through RF fields. The theorem states

$$\Delta\vec{p}_\perp = \left(\frac{e}{\omega}\right) \int_0^L (-i)\nabla_\perp E_z dz , \quad (9)$$

and it follows that transverse deflection is only possible if a transverse gradient of the longitudinal electric field $\nabla_\perp E_z$ is present. From $\nabla_\perp E_z \neq 0$ follows the existence a longitudinal accelerating field E_z. In case of uniform deflection over the whole aperture, i.e. abberation-free, it follows that E_z depends linearly on the transverse coordinates. Assuming that the field E_z can be factorised by $E_{z,\parallel}(z,t) \cdot E_{z,\perp}(x,y)$, the relative momentum gain within a TDS of length L can be expressed by

$$\delta = \frac{\Delta p}{p} = \left(-\frac{e}{pc} \int_0^L E_{z,\parallel} dz \right) \cdot E_{z,\perp} . \quad (10)$$

For abberation-free deflection, this leads to additional energy spread. In case of the LOLA-type TDS for vertical deflection, the longitudinal electric field is given by [3, 2]

$$E_z(x,y,z,t) = E_0\, k\, y \cos(\Psi(z,t)) . \quad (11)$$

For zero-crossing operation ($\Psi \approx 0$), the evaluation of Eq. (10) yields

$$\delta = \frac{eV_0 k}{pc} \cdot y , \quad (12)$$

with the equivalent deflecting voltage $V_0 = E_0 L$. Using Eq. (6), the additional energy spread induced by the TDS splits into two parts:

$$\delta = \frac{eV_0 k}{pc} \cdot y_\beta + \frac{eV_0 k}{pc} \cdot S \cdot \zeta . \quad (13)$$

The first part results in an rms energy spread given by

$$\sigma_\delta = \frac{eV_0 k}{pc} \cdot \sigma_y , \quad (14)$$

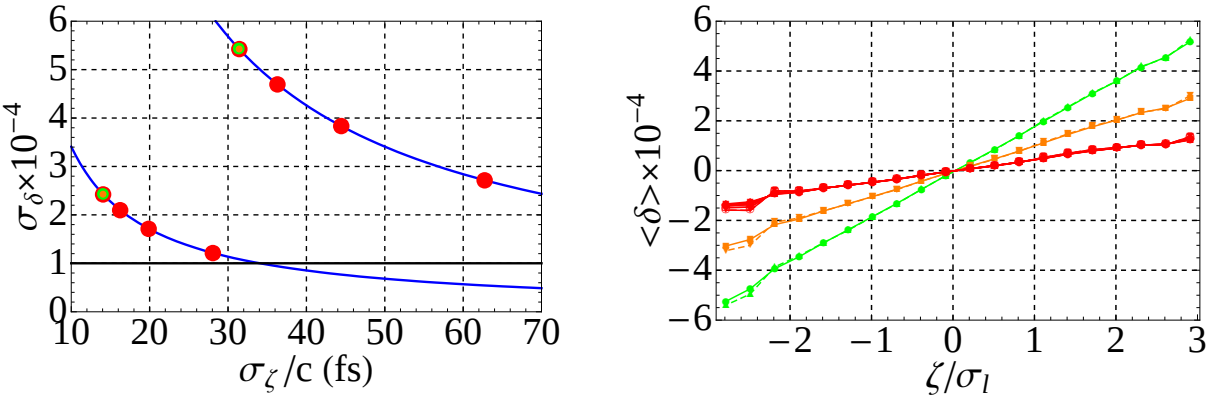


Figure 2: Left: Induced energy spread as a function of the longitudinal resolution. Dots indicate the results of simulations with the code `elegant`; blue lines represent the expression in Eq. (16). Right: Mean energy spread along the bunch for the cases in the left plot with the same colour coding. V_0: 20 MV (red), 30 MV (orange), and 40 MV (green).

whereas the second part corresponds to a linear energy correlation along the bunch. By means of the shear function in Eq. (5) and the vertical rms beam size in the TDS, the induced energy spread can be expressed by

$$\sigma_\delta = \frac{S(s_1)}{\sqrt{\beta_y(s_1)\beta_y(s_0)}\sin(\Delta\Phi)} \cdot \sqrt{\epsilon_y \cdot \beta_y(s_0)}\,. \quad (15)$$

With the longitudinal resolution introduced in Eq. (7), it follows

$$\sigma_\delta \cdot \sigma_\zeta > \frac{\epsilon_y}{\sin(\Delta\Phi)}\,. \quad (16)$$

Evaluating the second part of (13) with Eq. (5) and the assumption that the beta function β_y is almost constant in the TDS, yields

$$< \delta(\zeta) > \;\sim\; L \cdot \left(\frac{eV_0 k}{pc}\right)^2 \cdot \zeta\,, \quad (17)$$

which gives the mean energy spread along the bunch. It depends quadratically on the deflecting voltage V_0 and is not affected by the beta function β_y. In order to check the relations in (16) and (17), simulations using the code `elegant` [5] were performed. The simulation and Gaussian bunch parameters are listed in Table 1. The quoted beta functions represent the mean values within the TDS. According to the longitudinal resolutions σ_ζ/c given in Table 1 and the expression (16), the TDS induces energy spreads which are shown as dots in the left plot of Fig. 2. The lines are plotted according to (16) for a phase advance of $\Delta\Phi = \pi/2$ and two different emittance values. For each simulation point, also the mean energy spread is shown in the right plot. Three combinations of β_y and V_0 give the same resolutions, but due the dependency in Eq. (17), different slopes of the mean energy spread along the bunch are generated.

Table 1: Simulation and Initial Gaussian Bunch Parameters: beam energy $E = 1$ GeV, bunch length $\sigma_l = 50\ \mu$m, initial energy spread $\delta = 1 \cdot 10^{-4}$, normalised emittance $\epsilon_{N,y} = \epsilon_y \beta\gamma$, TDS wavenumber $k \approx 60\ \mathrm{m}^{-1}$ and length $L = 3.826$ m.

β_y	V_0	σ_ζ/c $\epsilon_{N,y} = 2\ \mu$m	σ_ζ/c $\epsilon_{N,y} = 10\ \mu$m
10 m	20 MV	29 fs	63 fs
20 m	20 MV	20 fs	45 fs
30 m	20 MV	17 fs	37 fs
40 m	20 MV	15 fs	32 fs
17.78 m	30 MV	15 fs	32 fs
10 m	40 MV	15 fs	32 fs

CONCLUSIONS

We have presented the required optics conditions in order to achieve a desired time and energy resolution for sliced beam parameter measurements. In case of the LOLA-type TDS, we have also shown that there exists a basic relation between the attainable energy spread and time resolution for longitudinal phase space measurements.

REFERENCES

[1] Michael Röhrs et al., "Time-resolved electron beam phase space tomography at a soft X-ray free-electron laser", accepted for publication in Phys. Rev. ST Accel. Beams, 2009

[2] Michael Röhrs, "Investigations of the Phase Space Distribution of Electron Bunches at the FLASH-Linac Using a Transverse Deflecting Structure", DESY-THESIS-2008-012, 2008

[3] O. A. Altenmueller, R. R. Larsen, and G. A. Loew, "Investigations of Traveling-Wave Separators for the Stanford Two-Mile Linear Accelerator", SLAC-PUB-0017, 1963

[4] W. K. H. Panofsky and W. Wenzel, "Some Considerations Concerning the Transverse Deflection of Charged Particles in Radio-Frequency Fields", Rev. Sci. Instrum., 27:967, 1956

[5] M. Borland, "elegant: A Flexible SDDS-Compliant Code for Accelerator Simulation", Advanced Photon Source LS-287, 2000

TEMPORAL PROFILES OF THE COHERENT TRANSITION RADIATION MEASURED AT FLASH WITH ELECTRO-OPTIC SPECTRAL DECODING

V. Arsov[1*], M-K. Bock, M. Felber, P. Gessler, K. Hacker, F. Loehl[2], F. Ludwig, K.-H. Matthiesen, H. Schlarb, A. Winter[3], DESY-Hamburg, Germany
S. Schulz, L. Wißmann, J. Zemella, Hamburg University, Germany

Abstract

We present absolute electric field time-profiles measured on the coherent transition radiation (CTR) beamline at FLASH using electro-optic spectral decoding (EOSD) in near crossed-polarizers scheme with a (20-200) μm thick GaP crystal in vacuum. The CTR spectrum is in the range 200 GHz - 100 THz and the pulse energy in the focus is over 10 μJ. The measured narrow CTR temporal profiles in the range 400 - 500 fs FWHM demonstrate that the short THz-pulses emitted by the compressed electron bunches are transported through the 19 m long beam line without significant temporal broadening.

INTRODUCTION

The reliable operation of the ultraviolet and x-ray free electron lasers require precise and non-destructive measurement of the electron bunch structure in the sub-100 fs scale. Recent numerical [1] and experimental [2], [3] works reveal the potential of the electro-optic detectors for such time-profile monitors. For even shorter, sub-10 fs structures, spectroscopy of coherent transition radiation (CTR) offers an alternative, although not allowing direct reconstruction of the longitudinal profile. For such diagnostic purposes 200 GHz - 100 THz broad-band CTR beamline is constructed and characterized [4]. The ability of the CTR beamline at FLAHS to preserve the narrow CTR pulses was first demonstrated using electro-optic balanced detection with 0.5 mm thick ZnTe crystal in air [5], followed by measurements with the same crystal in vacuum in near crossed-polarizers scheme [6]. To fully utilize the resolution of the electro-optic spectral decoding method, thinner crystals with better optical properties, such as GaP should be used. In this paper, we report electro-optic spectral decoding measurements at the CTR beamline of FLASH using a (20-200) μm wedge GaP crystal in vacuum.

EXPERIMENTAL SETUP

The setup for measurement of the CTR electric field temporal profiles is shown in Fig. 1.

The CTR beamline is installed in the straight section between the last accelerating module and the undulator at the 140 m of FLASH. The generation and transport of the ultrabroadband CTR radiation in the range of 200 GHz - 100 THz with energies more than 10 μJ is described thoroughly in [4]. The CTR is produced by kicking of a single bunch from a pulse train on an off-axis screen, inclined at 45° with respect to the accelerator axis. The 18.7 m long beam line is designed specially to minimize diffraction and to avoid waveguide effects, by using focusing mirrors and corrugated bellows. The pressure in the beamline is below 0.1 mbar and is isolated from the accelerator vacuum by a wedge diamond window.

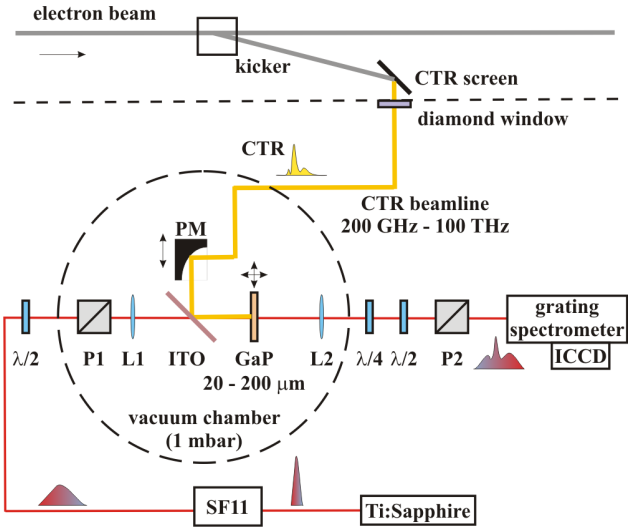


Figure 1: Schematic layout of the setup for EO detection of coherent transition radiation (CTR) transported from the linac to the laboratory through a 19 m beamline.

In a laboratory outside the linac tunnel, the beamline ends in a large vacuum vessel hosting several diagnostic experiments, taking full advantage of the broad band THz spectrum - interferometric, spectroscopic and electro-optic (EO).

The principles of single-shot electric field profile measurements using EO techniques is described in [3]. In this experiment, we apply the spectral decoding method. A τ_0 = 16 fs (Fourier-limited) pulse from a commercial Ti:Sapphire oscillator (Micra-5 from Coherent) is linearly chirped in a 10 cm long glass block (SF11) to $\tau_c \approx$ 5ps. The EO signal broadening, imposed by the chirp is $\sqrt{\tau_0 \cdot \tau_c} \approx 280$ *fs*. The laser center wavelength is 800 nm, the bandwidth 60 nm and the repetition rate 81 MHz. The typical output power of the laser is 500 mW.

Except for the first polarizer P1 and the lenses for the crystal, all other elements are placed on the same optical table. Shortly before the entrance port of the vacuum chamber, there is a half-wave plate, which in combination with the first polarizer P1 serves as a power attenuator. The energy on the EO the crystal is 2.5 nJ. The EO crystal

[1] now at PSI, Villigen, Switzerland
[2] now at Cornell University, USA
[3] now at ITER, Cadarache, France
[*] vladimir.arsov@psi.ch

is placed between the foci of two lenses with f = 300 mm. The laser focal spot radius is estimated to be 10 µm.

The distance between the last focusing mirror of the THz beamline (f_5 = 200 mm) and the parabolic mirror in the vacuum vessel (f = 150 mm) is 1.65 m. The distance between the center of the parabolic mirror and the EO crystal is 17.5 cm. According to simulations at this geometry for 2 THz the focal spot has a doughnut shape with outer radius 2 mm and inner radius 1 mm.

Both the EO crystal and the parabolic mirror are placed on motorized translation stages, allowing longitudinal tuning. In addition the EO crystal can be also translated horizontally (motorized) and turned azimuthally (manually). An indium-tin oxide (ITO) slab is used as a beam combiner.

For the present experiments a (20-200) µm wedge GaP crystal is used and results for thicknesses 175, 130, 70 and 20 µm are obtained. All measurements are made in vacuum below 0.1 mbar. For crystal thicknesses below 100 µm the THz pulse broadening is negligible [4], thus the overall system resolution is limited only by the chirp broadening (~300 fs).

The spectra are resolved with a 150 mm focal length spectrometer, a 600 l/mm grating and an intensified CCD camera with 1280 pixel. The spectral resolution is 0.122 nm/pix. The temporal calibration of the spectra is made before each data acquisition by sweeping the phase of the laser relative to the 1.3 GHz reference with 10 fs steps. The calibration constant is 8.6 fs/pix. Acquisition is made near crossed-polarizers, for which the EO signal is almost linear with the electric field [3].

The measurements are made with two bunches in the machine at 500 kHz repetition rate (second bunch kicked), energy 906 MeV and charge 0.8 nC.

RESULTS AND DISCUSSION

Typical raw CTR signals measured with 130 µm thick GaP crystal in vacuum are shown in Fig. 2. Each curve is an average of 20 acquisitions. In this example the EO signals are taken at Θ = –1° off-crossed polarizers. Four data sets are always saved: I(dark)-spectrum without laser and without THz, I(0,0)-spectrum at crossed polarizers and without THz, I(0,Θ)-spectrum at Θ° off-crossed polarizers and without THz, I(Γ,Θ)-spectrum at Θ° off-crossed polarizers and with THz.

Similar narrow signals in the range (420-520) fs are observed also for the rest of the measurements independent on the GaP thickness (20-175) µm. Within the accuracy of the setup resolution of ~300 fs these widths demonstrate the ability of the THz beamline to preserve the temporal structure of the CTR radiation produced by the sub-100 fs short electron bunches.

The measured electro-optic signals allow determination of the phase retardation Γ(τ) in the GaP crystal in the time domain and thus calculation of the absolute electric field profile of the CTR pulse. Near crossed polarizers the signal on the detector is [3]:

$$I_{det}(\Gamma,\Theta)=\frac{I_{laser}}{2}\cdot\left[1-\cos(\Gamma+4\Theta)\right]+I_{offset} \quad (1)$$

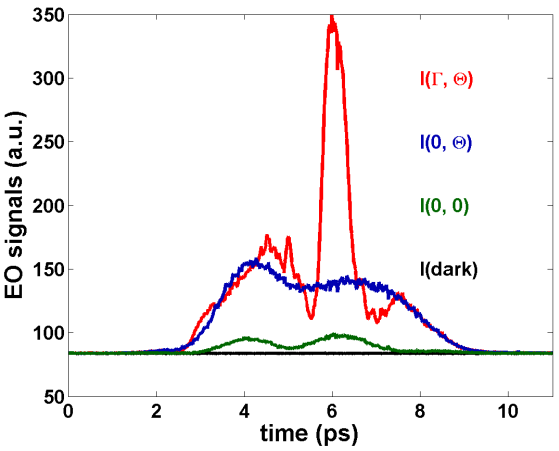


Figure 2: Raw single-shot EO signals of a CTR pulse, taken with 130 µm thick GaP crystal in vacuum. The deviation of from crossed polarizers is Θ = –1°.

Here it is assumed, that the quarter-wave plate is set for minimum transmission (crossed-polarizers, ϕ ≡ 0). The different backgrounds (Fig. 1) correspond to Γ and/or Θ set to zero, which allows solving (1) for Γ:

$$\Gamma_{\exp}(\tau)=\arccos\left[1-I_N(\tau)\right]-4\Theta \quad (2)$$

where I_N is the normalized signal:

$$I_N(\tau)=\frac{I(\Gamma,\Theta)-I(0,0)}{I(0,\Theta)-I(0,0)}\cdot(1-cos4\Theta) \quad (3)$$

On the other hand the phase retardation in the time domain can be computed using the electro-optic properties of the material in the frequency domain [3]:

$$\Gamma(\tau)=\frac{n_0^3 d}{\lambda_0}F^{-1}\left\{E(\omega)A_{tr}(\omega)G(\omega)r_{41}(\omega)\right\} \quad (4)$$

where n_0 is the refraction index for the optical group velocity (wavelength λ_0), d is the crystal thickness. For GaP and λ_0 = 800 nm n_0 = 3.568. F denotes a Fourier transformation. E(ω) is the THz Coulomb field in the frequency domain, $A_{tr}(\omega)$ is the frequency dependence of the amplitude transmission coefficient for the Coulomb field from vacuum into the EO crystal, G(ω) is the geometric response, which accounts the velocity mismatch between the THz and the optical pulses in the crystal and $r_{41}(\omega)$ is the electro-optic coefficient. The product of the last three factors is the effective response function, which is plotted on Fig. 3 for three different crystal thicknesses, used in the experiment.

Combining (2)-(4) one obtains an expression for the electric field in the time domain:

$$E(\tau)=F^{-1}\left\{\frac{\lambda}{n_0^3 d}\frac{F(\Gamma_{\exp}(\tau))(\omega)}{A_{tr}(\omega)G(\omega)r_{41}(\omega)}L(\omega)\right\} \quad (5)$$

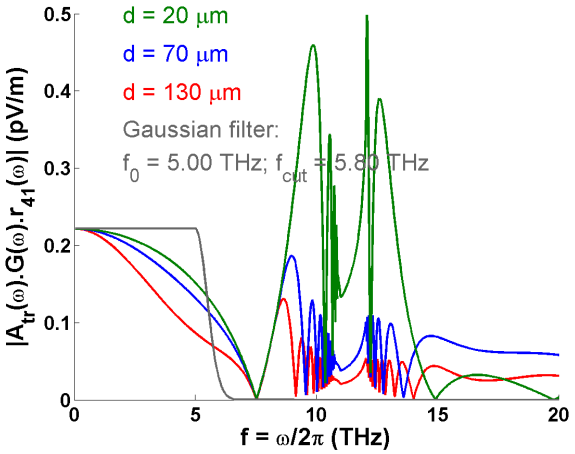


Figure 3: Effective response function of GaP and a Gaussian filter used for the retrieval of the Coulomb field

L(ω) is a low-pass filter, necessary to smoothly exclude the zeroes of the response function near the resonance. Here a Gaussian filter is used (Fig. 3). The choice of the central f_0 and the cut-off f_{cut} frequencies depends on the crystal thickness and the duration of the pulses. In order to fine-tune the filter for a given thickness, a model pulse is transformed according to equation (5) (Fig.4). In the shown example the GaP is 70 μm thick. Pulses with duration above 150 fs FWHM are reconstructed without distortion for Gaussian filter with f_0= 5 THz and f_{cut}=5.8 THz. For GaP thickness 130 μm the corresponding filter values are f_0= 3 THz and f_{cut}=3.8 THz. With the above parameter set, the absolute electric field profiles of the CTR pulses are calculated providing amplitudes 4 MV/m (Fig. 5a) for the 70 μm thick GaP crystal and 6 MV/m (Fig. 5b) for the thickness 130 μm. The obtained amplitudes can be attributed to the fact that different points in the focal plane have been sampled by the laser. The excellent agreement between the measured phase retardation Γ and the recovered with the above described numerical procedure electric field (Fig. 5) confirms the correctness of the method .

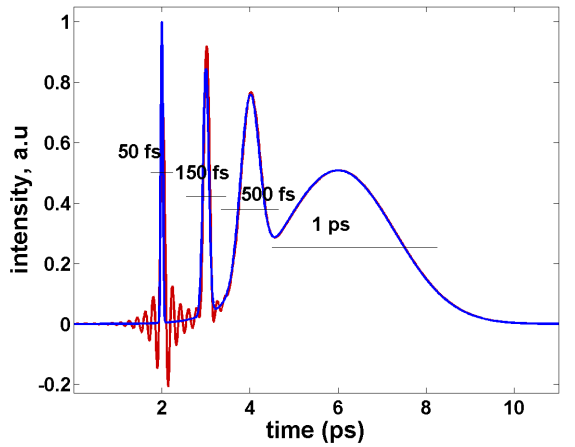


Figure 4: A model pulse Γ(τ) (blue curve) transformed according to eq. (5) (red curve) for GaP thickness 70 μm and Gaussian filter with f_0= 5 THz and f_{cut}=5.8 THz . The widths are FWHM.

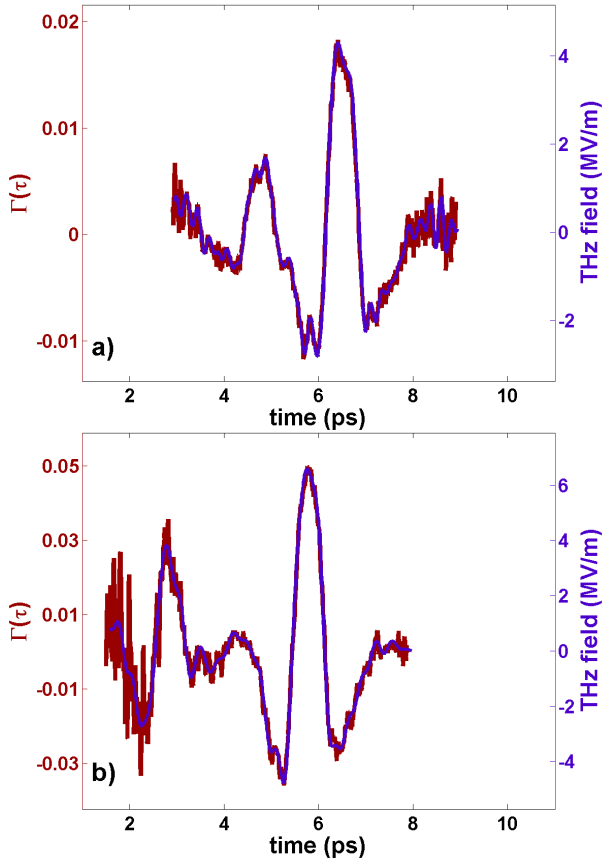


Figure 5: Phase retardation Γ and and recovered absolute electric field profiles for GaP thicknesses 70 μm (a) and 130 μm (b).

CONCLUSION AND OUTLOOK

Narrow CTR temporal profiles in the range 420-520 fs FWHM are measured with electro-optic spectral decoding with GaP in vacuum at crystal thickness 20-175 μm. Within the accuracy of the setup resolution of ~300 fs, these widths demonstrate that the THz beamline at FLASH preserves the narrow shape of the CTR pulse, produced by the compressed electron bunches. The measured profiles allow calculation of the absolute electric field. There is an excellent agreement between the measured phase retardation Γ and the numerically recovered electric field profile.

REFERENCES

[1] S. Casalbuoni et al., Phys. Rev. ST Accel. Beams **11**, 072802 (2008).
[2] G. Berden et al., Phys. Rev. Lett. **99**, 164801 (2007).
[3] B. Steffen et. al., Phys. Rev. ST Accel Beams **12**, 032802 (2009).
[4] S. Casalbuoni et al., Phys. Rev. ST Accel. Beams **12**, 030705 (2009).
[5] G. Berden et al., Proc. 10th EPAC, Edinburgh, Scotland (2006).
[6] V. Arsov et al, Proc. 29th FEL conference, Novosibirsk, Russia (2007).

BEAM POSITION MEASUREMENT WITH SUB-MICRON RESOLUTION

B. Keil, Paul Scherrer Institut, 5232 Villigen PSI, Switzerland

Abstract

This paper gives an overview of transverse sub-micron beam position measurement systems and techniques for 3rd and 4th generation light sources and collider projects. Topics discussed include mechanical, electrical, and digital design aspects, environmental influences, machine operation and design considerations, as well as system- and beam-based measurement and calibration techniques.

INTRODUCTION

Beam position measurement (BPM) systems belong to the most vital instrumentation systems of particle accelerators. The following sections discuss selected aspects of high-resolution BPMs, with a focus on the requirements of linac-based 4th generation (4G) FEL light sources in comparison to 3rd generation (3G) ring accelerators. However, due to the large technological overlap between light sources and colliders, most BPM-related topics are equally relevant for both accelerator types. The scope of the discussion in the following sections is limited to RF BPMs and does not cover the large variety of alternative beam position measurement techniques like mechanical or laser wires, screens, photon detectors, residual gas, beam loss or halo detectors.

REQUIREMENTS AND APPLICATIONS

Beam Stability

The main objective of submicron resolution BPMs in 3G light sources is the measurement of the electron beam position at the photon beam line source points. Typical photon beam stability requirements for experiments at the beam line end stations translate into σ/10 position and/or σ′/10 angular stability of the electron beam at the source point. Due to a typical emittance coupling in the order of 1% or less, the vertical beam stability is usually at least an order of magnitude more critical than the horizontal one. Vertical electron beam sizes of 2-5μm in low-beta insertion devices of modern low-emittance storage rings result in position stability requirements of a few 100nm.

Electron beam movements significantly below ~100Hz may be directly visible as an undesired modulation in the time structure of the recorded experimental data of photon beam line end stations. Movements at much higher frequencies are often averaged out by the experiment and are thus perceived as an effective increase of the electron beam emittance, with an accordingly reduced effective photon beam brilliance.

The required electron beam stability in 3G light sources is usually ensured by a fast orbit feedback (FOFB) system that measures and corrects the beam positions with sufficiently fast BPM electronics and corrector (dipole) magnets. Typical FOFB systems apply corrections at a rate of several kHz, with overall feedback loop latencies in the order of some 100μs to 1ms. This allows suppression of perturbations due to e.g. mechanical magnet vibrations, power supply noise, or changing insertion device gaps. Most FOFB systems suppress perturbations up to a cut-off frequency in the order of 100-200Hz [1].

BPM requirements for 3G storage rings are primarily driven by FOFB systems, since BPM electronics noise and drift as well as movements of BPM pickup mechanics are modulated back onto the beam or even amplified by the feedback loop if they exceed its cut-off frequency. Noise and drift of the BPM system within the FOFB bandwidth of some 100Hz should therefore be lower than the desired beam stability of typically some 100nm.

In contrast to 3G ring accelerators with continuously circulating bunches and typical bunch spacings of a few ns, 4G linac-based light sources often operate in single-bunch mode, at typical bunch repetition rates of 10-100Hz. This limits the cut-off frequency of beam-based transverse feedback systems to about 1-10Hz, thus not allowing to suppress perturbations induced e.g. by girder vibrations or power supply noise in the order of some 10Hz. Consequently, such 4G accelerators must be inherently stable and need a very careful design of mechanical and electrical subsystems in order to achieve sufficient beam stability. Therefore, the BPM requirements of 4G accelerators are not primarily driven by the requirements of fast feedbacks: Their BPMs only allow to observe fast perturbations and to identify their sources, but not their active suppression.

An exception are 4G linear or re-circulating energy recovery accelerators with bunch repetition rates above ~1kHz that may operate in CW mode, or superconducting pulsed accelerators with long accelerating RF pulses like ILC or the European X-Ray FEL (E-XFEL) where trains of several 1000 bunches with 200ns bunch spacing and ~10Hz repetition rate allow the implementation of intra bunch train feedback systems [2] with sub-microsecond latency that are able to suppress perturbations from DC up to a cut-off frequency in the order of 100kHz.

4G hard X-Ray FEL accelerators typically have round beams with σ~30-40μm in the undulators, while modern 3G accelerators with usual emittance couplings of 0.1-1% have flat beams with typically 2-5μm vertical size and at least an order of magnitude larger horizontal size. Thus, the absolute transverse stability requirements of 4G accelerators in both planes are similar to the horizontal plane in 3G rings and relaxed compared to the vertical plane in 3G rings. However, future 4G SASE FELs might operate at very low emittance and bunch charge (~10pC or less) in order to lase in single-spike mode with beam sizes below 10μm in the undulators [3], thus converging towards the vertical stability requirements of 3G rings.

Beam Based Calibration and Alignment

In 3G rings, the beam position displayed by an uncalibrated BPM and the real position as defined by the magnetic centers of adjacent (well-aligned) quadrupole magnets can differ by some 100μm due to mechanical tolerances of the pickup and imperfections of the electronics. This undesired offset is usually measured by varying the beam position in each quadrupole and determining the position where a change of the quadrupole focussing strength has minimal impact on the global beam orbit. BPM resolution and drift requirements for such beam based calibration methods in 3G rings are usually in the order of 10μm or more at ~1Hz bandwidth, which is relaxed compared to the requirements imposed by FOFB systems. The main goal of beam based BPM offset calibration with subsequent adjustment of the beam orbit to the quadrupole magnet centers is the reduction of coupling and thus vertical beam size, assuming that quadrupoles and sextupoles are sufficiently well aligned relative to each other.

In contrast to 3G rings, beam based BPM calibration and magnet alignment methods in 4G linac-based FELs may impose very high requirements on BPM performance. SASE linac FELs may have undulators with overall lengths in the order of 200m that typically consist of segments of a few meters length, with a quadrupole and BPM between adjacent segments. In order to achieve reproducible lasing and photon pulse saturation within the available undulator length, the trajectory of the electron bunch should not deviate more than ~σ/10 from a tangential straight line to the usually slightly curved beam trajectory over a few nominal gain lengths (typically over ~10-20m) at any position in the undulator.

A common method to obtain the required trajectory straightness and electron-photon beam overlap is the so-called dispersion-free steering (DFS) method [4] where the quadrupole magnet centers are adjusted iteratively by mechanical movers or dipole correction coils until the trajectory becomes (nearly) independent of the beam energy for a fixed beam position and angle at the undulator entrance. This is basically equivalent to a minimization of the integrated dipole field along the trajectory, which should thus result in an optimal trajectory straightness. One advantage with respect to other methods where e.g. the trajectory variation as a function of the quadrupole magnet current is measured is the fact that DFS accounts for all undesired dipole fields. Such fields may not only result from quadrupole magnet position offsets, but also e.g. from undulator field errors, external stray fields, or the Earth's magnetic field. It should be noted that the DFS method only requires the measurement of the relative position change with energy. Initial absolute position offsets of BPMs and quadrupoles relative to the ideal beam trajectory up to several σ due to mechanical alignment errors and electronics offsets are uncritical since such offsets are measured and corrected by the DFS method. The BPM resolution required for the DFS method in order to achieve typical acceptable quadrupole magnet alignment errors of ~1μm for hard X-ray FELs [5] scales with the maximum relative energy variation that can be applied: A variation in the order of some 10% may result in BPM resolution requirements in the order of σ/30, while a accelerator that only allows a few percent variation may need ~σ/300 resolution and drift over the duration of the measurement. However, depending on the way the measurement is performed and the accelerator is operated, this resolution and drift may not necessarily be required for single bunches but may be obtained by averaging over several bunches or measurement iterations.

ACCELERATOR DESIGN AND OPERATION ASPECTS

The design of an accelerator facility and the way it is operated have a large impact on the BPM requirements for a given accelerator performance goal. The following sections discuss some related design and operation considerations.

Bunch Shape

While the longitudinal and transverse charge distribution of a single electron bunch in a 3G light source is usually quasi-Gaussian due to synchrotron radiation damping, 4G accelerators may have very complex non-Gaussian asymmetric distributions in all 3 dimensions caused mainly by longitudinal bunch compression schemes in combination with nonlinearities of the accelerating RF fields.

In 4G SASE FELs, such charge distributions may entail that the part of the bunch with sufficient charge density for lasing has a transverse offset in the order of the bunch size relative to the center of charge that is measured by RF BPMs [6]. While this is irrelevant for beam-based magnet alignment techniques like e.g. the DFS method, it may cause problems for RF BPM based beam position feedbacks meant to correct the beam trajectory e.g. in the undulators: The BPMs may display a perfectly straight trajectory, while the part of the bunch with enough charge density for lasing performs large betatron oscillations around the desired straight trajectory so that the spatial overlap with its generated photon field is not sufficient for stable SASE operation. In order to avoid this, 4G accelerator facilities usually employ higher-harmonic RF systems that linearize the accelerating RF fields, leading to charge distributions with a sufficiently small offset of the lasing part of the bunch relative to the center of charge.

Magnet Lattice and BPM Pickup Locations

Many transverse feedback systems in 3G and 4G light sources and colliders use the singular value decomposition (SVD) method, where the changes of the corrector magnet kicks ΔK_j that are required to achieve a desired change of the beam positions ΔB_i are calculated using pseudo-inversion of the beam response matrix $M_{ij} = \Delta B_i / \Delta K_j$ that can be obtained either by measurement or by a theoretical optics model. M can be written as product

$M = U\Sigma V^T$, where U and V are orthonormal square matrices, and Σ is a diagonal matrix with only non-negative elements $\Sigma_{ii}=\lambda_i$, the so-called singular values of M that are usually sorted in descending order. The pseudo-inverse of M is $M^+=V\Sigma^+U^T$, with $\Sigma^+_{ii}=1/\lambda_i$ for $\lambda_i \neq 0$ and $\Sigma^+_{ii}= 0$ otherwise. The quotient $C=\max(\lambda_i)/\min(\lambda_i)$, $\lambda_i \neq 0$ is called conditioning number. The positions of BPMs and magnets in an accelerator as well as the beam optics should be designed in a way that minimizes C, since a large value of C means that at least one orbit perturbation pattern (represented by the i^{th} row vector of U^T that belongs to the smallest λ_i) requires a C-times larger RMS change of the corrector magnet kicks than another pattern (represented by the row vector that belongs to the largest λ_i) in order to obtain a certain RMS orbit change. Since (uncorrelated) BPM electronics noise contributes equally to all measured BPM patterns while real orbit perturbations are usually dominated by patterns belonging to large λ_i, a fast trajectory feedback in a accelerator with e.g. C=100 may cause ~10x larger noise-induced perturbations than in a accelerator with C=10.

Many accelerators with large C values therefore set small λ_i to 0 (singular value cut-off). This reduces the BPM-noise induced orbit perturbations, but also causes the feedback not to correct certain orbit perturbation patterns, so that the beam positions are usually not corrected exactly to the desired values. Alternatively, all λ_i below a certain limit (but still above the noise level) can simply be set to larger values before performing the pseudo-inversion. Then the respective perturbations are still corrected, but with a smaller feedback loop gain than other perturbations, thus reducing the amount of BPM noise being modulated onto the beam by the feedback [7].

In addition to a small conditioning number C, 3G and 4G accelerators should be designed with large beta functions at the locations of BPMs (preferably without increasing C), especially in case of BPMs adjacent to insertion devices that are used by orbit feedbacks, since the contribution of BPM electronics noise and drift to the photon beam movement for given optical functions at the photon beam source point scales with $1/\mathrm{sqrt}(\beta_{BPM})$.

Bunch Charge Stability

Differences between measured and real beam position due to electronics nonlinearities usually depend on the (average) beam current or bunch charge as well as on the temporal charge variation of subsequent bunches in linear and circular accelerators (for a constant average current). While this bunch charge dependence can be reduced by suitable electronics design and calibration techniques, it may still be large enough to have an undesired impact on beam stability. In 3G ring accelerators, this can be avoided by keeping the beam current at a nearly constant level by sufficiently frequent injections ("top-up injection") [8], and by using a "filling pattern feedback" [9] that not just keeps the overall beam current but also the relative charge distribution among the different RF buckets constant. Such feedbacks not only relax the BPM electronics requirements with respect to linearity and bunch charge dependence for a given beam stability goal, but they also improve the medium- and long-term photon beam stability drastically by keeping the thermal load on the beam pipe and photon beam line optics components nearly constant.

Environmental Aspects and Non-RF BPMs

Variations of the environmental temperature cause mechanical drift of BPM pickups as well as drift of BPM electronics components, e.g. gain and offset drift of amplifiers, attenuators, mixers or ADCs. The resulting temperature-dependent beam position offset due to mechanical pickup drift can be measured on-line with suitable sensors and added to the measured beam position. Temperature-induced drift of the beam position caused by BPM electronics components can be reduced by suitable design techniques. However, it may still be desirable or necessary to control and stabilize the air temperature and air flow speed in the area of BPM pickups and electronics in order to improve the beam stability. Additionally, non-RF BPMs like photon BPMs can be used to improve the photon beam stability in 3G and 4G light sources, e.g. by correcting the reference orbit of an RF BPM based FOFB in a way that keeps the photon beam positions constant [10]. Thus, any bunch charge and temperature drift effects of RF BPM electronics within the correction bandwidth of the photon BPM feedback become irrelevant for the photon beam stability.

BPM PICKUPS AND ELECTRONICS

Table 1 contains a qualitative overview of the properties of some RF BPM pickup types with respect to performance requirements, design effort, and costs. The table is based on a somewhat subjective selection and evaluation of existing pickups. A "+" (or "++") symbol indicates that it is usually less (or much less) challenging to meet a requirement or to keep the design effort or costs low, while a "-" (or "- - ") symbol denotes that it is more (or much more) challenging to reach the respective goal.

Table1: Qualitative Properties of Various BPM Pickups

	Button	Matched Stripline	Resonant Stripline, Normal Coupling	Single Cavity Normal Coupling	Two Cavities, Hybrid Coupling	
Signal/Noise	–	– / +	+	+	+	Performance
Monopole Mode Suppression	–	–	–	– / +	+	
Single-Bunch Resolution (@ Low Charge)	–	– / +	+	+	++	
Electronics Drift	– / +	– / +	– / +	– / +	+	
Weight 10mm Pipe	+ +	+	+	+	+	Budget
Weight 40mm Pipe	+ +	– / +	– / +	– / +	– / +	
Design Effort	+ +	– / +	– / +	– / +	–	
Fabrication Costs	+ +	– / +	– / +	– / +	– / +	
Tuning Effort	+ +	+ +	– / +	+	+	

Button Pickups

Most 3G storage rings use button pickups, since they are inexpensive, have minimal impact on the beam, and a broadband spectrum that allows to use commercial types

for different accelerator RF frequencies. Since submicron resolution is usually only required within the FOFB bandwidth below 1kHz where the overall integrated beam charge for 3G accelerators during user operation is usually >100μC, the signal-to-noise ratio is uncritical, and a resolution of some 100nm can be reached with moderate electronics design effort. This is different in 4G linac-based FELs, especially for single-bunch operation with 10-1000pC bunch charge at 10-100Hz rep rate, where the single-shot position resolution of button BPM systems is usually ranging from a few microns to tens or even hundreds of microns depending on bunch charge and pickup geometry.

Striplines

Matched or resonant stripline pickups are typically used for beam transport lines where single bunches have to be measured with higher precision than achievable with button pickups. The signal level and spectrum of stripline pickups enable higher signal-to-noise ratio, especially in case of resonant striplines The output signal of matched striplines consists of two pulses with opposite polarity, where the pulse spacing is twice the flight time along the four pickup strips. Resonant striplines are basically four λ/4 resonators with 90° rotation symmetry parallel to the beam. Their output signal is an exponentially decaying sine at the fundamental mode frequency (determined by the strip length) plus harmonics at odd integer multiples of that frequency. Since the four strips are individual resonators with mutual coupling, the pickup actually has four fundamental modes: A monopole mode proportional to the bunch charge, two dipole modes proportional to the product of bunch charge and horizontal or vertical position, and a quadrupole mode. The natural frequency separation between these modes is typically a few percent, although monopole and dipole mode frequencies can be matched by using non-uniform strip widths that increase towards the open end of the strip [11].

Monopole and dipole mode signals of resonant stripline and single-cell cavity BPMs (see below) can be separated using an external hybrid followed by bandpass filters. Resolution and drift are typically limited by the imperfect suppression of the monopole mode in the dipole channel of the electronics.

Cavities

While the performance of button and stripline BPMs is usually sufficient for beam transport lines, most 4G FEL undulators are equipped with cavity BPM pickups that allow to reach sub-micron resolution even at low charges. The simplest cavity BPM pickup consists of a single cylindrical cavity with four 90° rotation symmetric electrodes that couple directly to the resonator. The beam position is obtained by dividing the amplitude of the TM_{11} ("dipole") mode that is proportional to the product of bunch position and bunch charge through the TM_{01} ("monopole") mode amplitude that is only proportional to the bunch charge. A comparatively large spectral mode separation of typically some 10% allows easier monopole mode suppression in the electronics via band-pass filters as compared to stripline pickups. However, the different frequencies of dipole and monopole mode may cause significant temperature-induced position drift due to frequency-dependent properties of electronics components in monopole and dipole signal channel.

In order to overcome these drawbacks, several 4G linac FELs use cavity BPMs consisting of two adjacent, usually cylindrical cavities, one for the dipole and one for the monopole mode signal, with the same frequency of typically 3-12GHz for both signals. The dipole cavity often uses a mode-selective ("hybrid") coupling scheme [12] where more or less short waveguides couple only to the desired dipole mode while suppressing other modes, thus enabling a much lower drift- and resolution-limiting monopole mode leakage into the dipole signal channel.

Cost and Performance Aspects

Recent progress in the design of cost-optimized dual-cavity pickups with mode-selective couplers [13] allows their production at costs comparable to stripline pickups. Therefore 4G accelerators like the European XFEL plan to use dual-cavity pickups where high resolution is needed, and inexpensive button pickups elsewhere in the beam transport lines, without a third "medium-resolution" pickup type like matched or resonant striplines. However, striplines are still an attractive option for accelerators operating at very low bunch charge, e.g. for locations in the accelerator where the beam pipe diameter is too large for cavity BPMs (that tend to become large, heavy and expensive for large pipe diameters) and where the resolution of button pickups is not sufficient.

Electronics

Figure 1 shows simplified sketches of typical architectures of 3G ring button BPM (top) and 4G linac cavity BPM electronics (bottom). Modern 16-bit ADCs with 100-200MSamples/s and a bandwidth well above 500MHz allow direct sampling of button pickup signals at the main RF frequency of 3G ring accelerators, with a comparatively small analog input stage consisting mainly of bandpass and amplifier/attenuator stages.

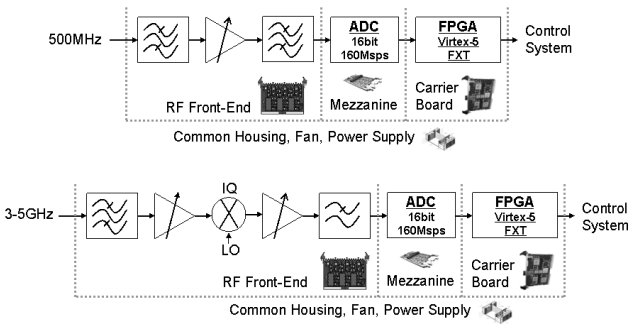


Figure1: BPM electronics for 3G and 4G light sources.

The main challenge is often not the required resolution of typically some 100nm at ~1kHz bandwidth but a low temperature drift and beam charge dependence in the same order as the resolution. Common electronics design

techniques to reduce drift and charge dependence include single- or multi-channel multiplexing schemes, real-time normalization on pilot signal tones, active temperature stabilization, or the compensation of nonlinearity and drift using lookup tables obtained by a lab calibration setup.

Since matched or resonant stripline pickup signals usually have a significant amount of their spectral energy within the bandwidth range of fast high-resolution ADCs, their signals can be sampled directly using similar electronics than storage ring button BPMs, typically with higher input stage gain, and resolutions down to a few microns for higher bunch charges. An alternative direct sampling approach for single-bunch linacs is the use of single-shot waveform digitizer chips that allow extremely cost-efficient recording of raw or bandpass-filtered BPM pickup signals at several GSamples/s [14].

Dual-cavity BPMs generate decaying sine signals with a typical frequency of 3-12GHz and loaded Q values in the order of 100 to several 1000. While higher frequencies theoretically enable higher resolution, lower frequencies allow larger pipe diameters, more flexibility and larger tolerances with respect to electronics components, as well as the use of several meters of cable from pickup to electronics instead of rigid waveguides that are used e.g. for X-band cavity BPMs in order to limit the signal attenuation to reasonably small values. Cavity BPM electronics usually employ IQ mixing to an IF in the order of 100MHz or to baseband before sampling the signals with high-resolution ADCs. An overview of existing high-resolution cavity BPM pickup and electronics designs can be found in Ref. [15].

Since ADC and digital signal processing electronics for 3G ring and 4G linac BPM electronics have very similar requirements, accelerator labs with both accelerators types may design generic BPM electronics consisting of pickup-specific RF front-ends and a common digital back-end and ADC type. In addition to FPGA- or ASIC-based digital IQ downconverters for direct sampling or IF-based BPM systems, digital back-ends [16,17] of modern BPM systems usually have serial multi-gigabit fiber optic or copper cable links that allows their integration into 3G ring FOFBs or 4G linac intra-bunchtrain feedback systems, with the possibility to use the same communication protocols, timing and control system interfaces for both accelerator types.

SUMMARY

Beam position measurement with sub-micron resolution and drift does not only involve BPM pickup and electronics technology, but should be based on an overall concept regarding the design and operation of an accelerator and its subsystems. The BPM system requirements for fast transverse feedbacks or beam based alignment in 3G and 4G light sources and colliders can be significantly relaxed by suitable accelerator design, alignment and operation techniques. BPM system architectures with accelerator-specific pickups and RF front-end electronics combined with generic digital-backend and ADC solutions enable large synergies between different accelerator types.

REFERENCES

[1] N. Hubert et al., *"Global Fast Orbit Feedback System Down to DC using Fast and Slow Correctors"*, these proceedings.

[2] B. Keil et al., *"Design of an Intra-Bunch-Train Feedback System for the European X-Ray FEL"*, Proc. DIPAC'07, Venice, Italy, 2007.

[3] Y. Kim et al., *"Beam Diagnostics and RF System Requirements for the SwissFEL Facility"*, these proceedings.

[4] T. Raubenheimer et al., *"A Dispersion Free Trajectory Technique for Linear Colliders"*, NIM A302:191-208, 1991.

[5] Y. Li et al., *"Impact of Quadrupole Offset and Undulator End-Kicks on the European-XFEL Facility Performance"*, DESY TESLA-FEL Report 2009-4, May 2009.

[6] B. Faatz et al., *"Status of FLASH and the European XFEL"*, SINAP'08, Shanghai, China, 2008.

[7] M. T. Heron et al, *"Performance and Future Developments of the Diamond Fast Orbit Feedback System"*, Proc. EPAC'08, Genoa, Italy, 2008.

[8] T. S. Ueng et al, *"Topping Up Experiments at SRRC"*, Proc. EPAC'96, Sitges, Barcelona, Spain, 1996.

[9] B. Kalantari et al., *"Bunch Pattern Control in Top-Up Mode at the Swiss Light Source"*, Proc. EPAC'04, Lucerne, Switzerland, 2004.

[10] T. Schilcher et al., *"Commissioning and Operation of the SLS Fast Orbit Feedback"*, Proc. EPAC'04, Lucerne, Switzerland, 2004.

[11] A. Citterio et al., *"Design of a Resonant Stripline Beam Position Pickup for the 250 MeV PSI XFEL Test Injector"*, these proceedings.

[12] Z. Li et al., *"Cavity BPM With Dipole-Mode Selective Coupler"*, Proc. PAC'03, Portland, Oregon, USA, 2003.

[13] H. Maesaka et al., *"Beam Position Monitor at the SCSS Prototype Accelerator"*, Proc. APAC'07, Indore, India, 2007.

[14] B. Keil et al., *"Application of a 5 GSPS Analogue Ring Sampling Chip for Low-cost Single-shot BPM Systems"*, Proc. EPAC'08, Genoa, Italy, 2008.

[15] D. Lipka, *"Cavity BPM Design, Related Electronics and Measured Performances"*, these proceedings.

[16] A. Kosicek, *"Libera Electron Beam Position Processor"*, Proc. PAC'05, Knoxville, Tennessee, USA, 2005.

[17] B. Keil et al., *"The PSI VPC Board - First Applications of a Common Digital Back-End for Electron and Proton Beam Instrumentation at PSI"*, Proc. DIPAC'05, Lyon, France, 2005.

CAVITY BPM DESIGNS, RELATED ELECTRONICS AND MEASURED PERFORMANCES

D. Lipka*, DESY, Hamburg, Germany

Abstract

Future accelerators like the International Linear Collider and Free-Electron Lasers require beam position measurements with submicron resolution in critical parts of the machines. This is achievable using the Cavity Beam Position Monitors (BPM). This paper presents the basic principles of this monitor type. Different institutes are working on the design of cavity BPM systems. An overview of recent developments with results and limitations is given.

INTRODUCTION

The international linear collider (ILC) will require high performance beam position monitors (BPM) to control the beam trajectory with high precision in order to maintain a stable collision of nanometer sized beams. The BPMs have to be located at specific positions along the linac up to the interaction point, where a few nanometer resolution is required. Additionally a spectrometer will be used in order to measure the beam energy. The spatial beam offset corresponds directly to the beam energy. To minimize the influence to the emittance the offset has to be small, therefore high precision BPMs are required for the ILC spectrometer with a resolution of 500 nm or better [1].

In case of Free-Electron Lasers (FEL) the overlap of the electron beam with the photon beam along the undulators less than 10 % of the transverse size is required. Typical transverse sizes of beams are of the order of 30 μm. Therefore a resolution better than 1 μm is required.

In comparison to other types of BPMs, like e.g. the button [2] or stripline [3] BPM, only the cavity BPM has the potential to achieve such high resolutions on a bunch by bunch time-scale. In this paper the cavity BPM principle is discussed, followed by the description of the electronics, resolution limitations and measurement methods. A few examples of such BPMs are presented.

THEORY OF CYLINDRICAL CAVITY BPMS

Electric Fields

The electric field **E** of a cavity can be derived from the d'Alembert equation

$$\Delta\mathbf{E} - \frac{1}{c^2}\frac{\delta^2\mathbf{E}}{\delta t^2} = 0 \qquad (1)$$

with c being the speed of light. For a cavity with radius R and length L only the z component is of interest. The solution can be represented as

$$E_{z,mnp}(r,\phi,z,t) = CJ_m\left(\frac{j_{mn}r}{R}\right)\cos(m\phi)e^{-i\left(\omega_{mnp}t \mp \frac{p\pi z}{L}\right)}. \qquad (2)$$

Here j_{mn} denotes the n-th zero of the Bessel function J_m of order m and

$$\omega_{mnp} = c\sqrt{\left(\frac{j_{mn}}{R}\right)^2 + \left(\frac{p\pi}{L}\right)^2} \qquad (3)$$

is the angular resonant frequency of the mode mnp. The two first modes have $j_{01} = 2.405$ and $j_{11} = 3.832$ [4]. The first mode (monopole mode, TM_{010}) does not depend on the spatial component ϕ, therefore a cylinder symmetric mode is generated, as shown in Fig. 1. The Bessel function of the order $m = 0$ does not depend of the radius r close to the cavity center. Therefore the field strength is proportional to the beam charge. The second mode (dipole mode, TM_{110}) depends on ϕ resulting in a field distribution as shown in Fig. 2. For a beam passing close to the cavity center the Bessel function of order $m = 1$ can be derived proportional to r. For that reason the field strength is proportional to the beam offset and charge.

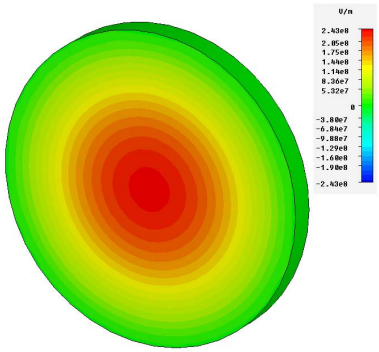


Figure 1: Field distribution of the first monopole mode in a cylindrical resonator. Simulation [5] is used.

Nowadays cylindrical cavities can be produced with very high accuracy. Therefore by measuring the field strength of the dipole mode a high resolution of the position information can be obtained.

Line Voltage

The normalized shunt impedance

$$\frac{R}{Q} = \frac{V^2}{\omega W} \qquad (4)$$

* dirk.lipka@desy.de

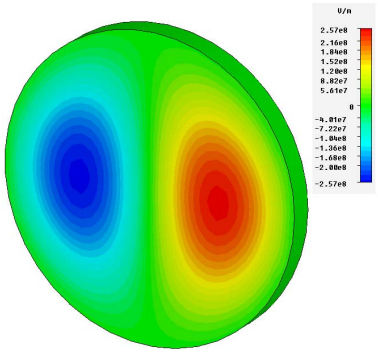


Figure 2: Field distribution of the first dipole mode in a cylindrical resonator (horizontal orientation), a second dipole mode with vertical orientation and the same resonance frequency is generated as well, not shown here. Simulation [5] is used.

characterizes the energy exchange between the beam and the cavity. Here W is the energy stored in the cavity and

$$V = \left| \int_0^L E_z dz \right|. \tag{5}$$

The integration path goes along the particle trajectory. It is convenient to define a shunt impedance $(R/Q)_0$ at a certain offset x_0 with respect to the electrical center of the cavity for the dipole mode

$$\frac{R}{Q} = \left(\frac{R}{Q}\right)_0 \frac{x^2}{x_0^2}. \tag{6}$$

The energy after passing a longitudinally Gaussian-like distributed bunch with a length σ_z and a charge q is given by [6]

$$W = \frac{\omega}{4}\left(\frac{R}{Q}\right)_0 \frac{x^2}{x_0^2} q^2 \exp\left(-\frac{\omega^2\sigma_z^2}{c^2}\right). \tag{7}$$

Only a fraction of the energy will be coupled out of the cavity depending on the external quality factor

$$Q_{ext} = \frac{\omega W}{P_{out}}. \tag{8}$$

Taking into account an output line with impedance Z the voltage is

$$\begin{aligned} V_{out} &= \sqrt{ZP_{out}} = \sqrt{Z\frac{\omega W}{Q_{ext}}} \\ &= \frac{\omega}{2}\sqrt{\left[\frac{Z}{Q_{ext}}\left(\frac{R}{Q}\right)_0\right]} q \frac{x}{x_0} \exp\left(-\frac{\omega^2\sigma_z^2}{2c^2}\right). \end{aligned} \tag{9}$$

The fraction $V_{out}/(qx)$ defines the sensitivity of the BPM.

The power dissipated in the cavity wall can be described by the internal quality factor Q_0

$$P_{diss} = \frac{\omega W}{Q_0}. \tag{10}$$

By combining both quality factors the loaded quality factor is

$$\frac{1}{Q_L} = \frac{1}{Q_0} + \frac{1}{Q_{ext}}. \tag{11}$$

The energy stored in the cavity decays proportional to the loaded quality factor

$$\tau = \frac{2Q_L}{\omega}. \tag{12}$$

For a single bunch measurement the signal should decay faster compared to the bunch spacing.

The line voltage parallel to the cavity axis results in

$$V_x(t) = V_{out} e^{-\frac{t}{\tau}} \sin(\omega t). \tag{13}$$

Note: There are two definitions of τ, the other is without factor 2 in (12), in this case the factor 2 has to be added in the denominator of the exponential in the equation (13).

The amplitude V_{out} depends on the product of beam offset and beam charge, therefore by measuring the amplitude and charge separately the offset can be obtained. The charge can be measured from the amplitude of a monopole mode. In most cases a second (reference) resonator tuned to the TM_{010} mode is used, also giving the relative phase between the dipole and the monopole mode and thus the direction of the beam offset.

Influence of the Beam Angle

If a beam enters the cavity under an angle α, each half of the resonator induces an offset with $\pm\alpha L/4$, see Fig. 3. The induced field is a dipole mode. The timing oscillation

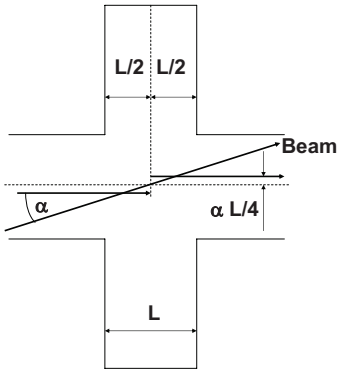


Figure 3: Sketch for the influence of the beam angle α.

in the equation (13) can be divided in each half of the resonator. The measured voltage is then

$$\begin{aligned} V_\alpha &= C^* \left[\sin(\omega(t + L/4c)) - \sin(\omega(t - L/4c))\right] \\ &= 2C^* \sin\left(\frac{\omega L}{4c}\right)\cos(\omega t). \end{aligned} \tag{14}$$

Note that the oscillation caused by a beam angle is shifted by 90° with respect to the signal caused by an offset. The fraction of the angle influence to the offset signal x is about $\omega L^2\alpha/(8\sqrt{2}cx)$. For short cavities the influence of the beam angle is reduced.

Influence of the Bunch Tilt

Consider a bunch with a tilt Θ with respect to the cavity axis, as shown in Fig. 4. In this case the bunch can be

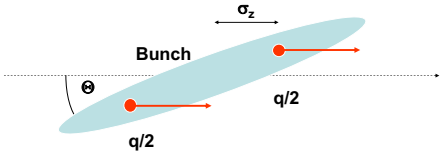


Figure 4: Sketch for the influence of the bunch tilt Θ.

divided into two parts each carrying a half of the bunch charge and contributing to the dipole mode. The measured voltage from the BPM in this case is:

$$V_\Theta = C^{**}\left[\sin\left(\omega(t+\sigma_z/c)\right) - \sin\left(\omega(t-\sigma_z/c)\right)\right] = 2C^{**}\sin\left(\frac{\omega\sigma_z}{c}\right)\cos\left(\omega t\right). \quad (15)$$

The signal is shifted by 90° with respect to the offset signal. The fraction of the tilt influence to the offset signal is about $\Theta\omega\sigma_z^2/(2cx)$. A shorter bunch will have less effect to the dipole mode.

Rejection the Monopole Mode

The resonance frequency of the monopole mode is different of that of the dipole mode but the amplitude of the monopole mode is orders of magnitude larger compared to the dipole mode. Furthermore, at a moderate loaded quality factor there is a contribution at the dipole mode frequency due to the given bandwidth of the monopole mode.

Therefore a spatial filter (a slot or a waveguide) has to be inserted on the resonator, as described in ref. [7]. Usage of the slot exploits the differences in the field distribution of the monopole and dipole modes in order to reject the tails from the monopole mode, as shown in Fig. 5. The monopole mode is damped in the slot but the dipole mode can still propagate. By inserting an antenna in the waveguide/slot the voltage of the dipole can be measured like represented in the equation (13).

Waveguides provide a larger orthogonal coupling reduction compared to antennas mounted directly in the cavity. One has to point out that the waveguides/slots have to be implemented with high precision. Otherwise it would shift the dipole mode distribution resulting in higher orthogonal coupling [9].

ELECTRONICS

The signal processing can be done as shown in Fig. 6. In a hybrid the two opposite signals (which have a phase shift of 180°) are subtracted. This reduces the influence of the monopole mode and doubles the amplitude of the dipole mode. Due to different cable length the phase of 180° can be shifted. Therefore phase shifters are connected before the hybrid to compensate the shift. In some cases the amplitude from the rejection of dipole and monopole modes

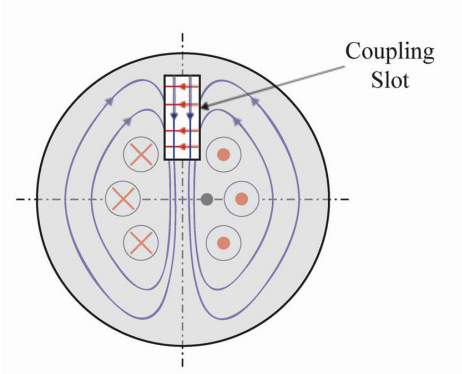


Figure 5: The dipole mode is selectively coupled out by means of two long, narrow, radial slots on one cavity face. The beam is indicated by a black dot, the electric field vector points circumferentially across the slot while the magnetic field vector points radially. The cavity has four slots (two for each plane to assure the symmetry). Details are given in ref. [8]

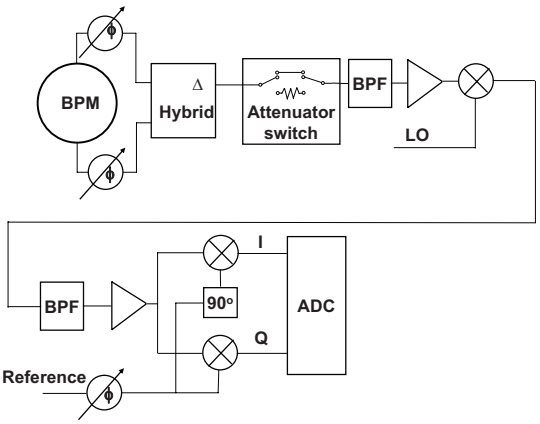


Figure 6: Block diagram of the electronics used for the signal processing of the dipole resonator.

due to spatial filter is large enough to dispense this part. This scheme is less sensitive to phase drifts due to temperature changes. To increase the dynamic range a switchable attenuator can be integrated in the electronics. A band-pass filter rejects higher order modes and an amplifier increases the amplitude.

If the following electronics can not be positioned close to the BPM, the signal has to be transmitted via long cables. The transmission of high frequency signals via cables is low, therefore down conversion with a local oscillator (LO) is done to an intermediate frequency. Two frequencies are multiplied:

$$A\sin\left(\omega_1 t+\phi_1\right)\cdot B\sin\left(\omega_2+\phi_2\right) = \frac{AB}{2}[\cos\left((\omega_1-\omega_2)t+(\phi_1-\phi_2)\right) - \cos\left((\omega_1+\omega_2)t+(\phi_1+\phi_2)\right)]. \quad (16)$$

Followed by a low-pass filter only the lower frequency $\omega_1 - \omega_2$ is received.

The intermediate frequency can be transported with lower attenuation to the other part of the electronics. Here a second band-pass filter for the intermediate frequency is used followed by an amplifier. Two parallel down conversions (I-Q demodulation) are used with a reference frequency either with a matched phase (realized with the phase shifter beforehand) and with reference frequency shifted by 90°. This reduces the influence of beam angle α and bunch tilt Θ, compare with equations (13), (14) and (15).

Two methods are in use for the I-Q demodulation: Homodyne and Heterodyne one. The first one uses the same frequency as the dipole mode. Therefore the same intermediate frequency enters the conversion. This results in a zero frequency, as follows from equation (16) and only the amplitude information is maintained. The Heterodyne method uses a reference frequency, which is different from the intermediate frequency. In this case a lower frequency provides the amplitude and phase information.

The used electronics can imply all components mentioned above as shown in Fig. 6, but some of those can be dispense. For example the remote controlled attenuation switch is used only when a large dynamic range is required, or the first down conversion is used only if the I-Q demodulator is positioned far away from the BPM. In case the resolution above 1 μm is required, the I-Q demodulation is not in use.

RESOLUTION

The position signal is influenced by the monopole signal, by the beam angle and bunch tilt, by orthogonal coupling and cavity noise. The latter can be calculated as

$$V_{noise} = \sqrt{4kTZBW}, \tag{17}$$

where k is the Boltzmann constant, T is the temperature, Z is the impedance (usually 50 Ω) and BW is the bandwidth of the entire system including the electronics. The amplifiers of the electronics will amplify also the cavity BPM noise. Additional electronics noise will contribute, degrading the resolution. The amplifiers and the ADC usually have the largest contributions to the noise. Therefore low noise components for the electronics with stabilized environment temperature have to be chosen.

MEASUREMENTS

The resolution of a cavity BPM is measured by using 3 BPMs placed one after another with distances $z_{ij} = z_i - z_j$ $(i, j = 1, 2, 3)$ to exclude the beam jitter. The outer BPMs (1,3) are measuring the beam position and predict the position on the BPM 2. The difference of several measurements gives the RMS value σ_2. For the resolution R_2 a geometric factor has to be taken into account as described in ref. [6]

$$R_2 = \frac{\sigma_2}{\sqrt{1^2 + \left(\frac{z_{12}}{z_{13}}\right)^2 + \left(\frac{z_{23}}{z_{13}}\right)^2}}. \tag{18}$$

Here one has to assume that all three BPM have the same resolution. For $z_{13}/2 = z_{12} = z_{23}$ the equation (18) simplifies to $R_2 = \sigma_2\sqrt{2/3}$.

Another method for the resolution measurement is the correlation of a large number of BPMs with a single BPM of a long beamline. In this case the resolution will be overestimated because the other BPMs are assumed to be noise free.

EXAMPLES OF RECENT MEASUREMENTS

SPring-8 Compact SASE Source Cavity BPM Prototype

The design of the cylindrical cavity BPM with 4.76 GHz resonance frequency can be found in [10]. First measurements have been made with 4 BPMs placed between the undulators. The electronics was build without I-Q demodulator. Therefore phase drifts for different machine conditions and beam angle and bunch tilt influences the resolution measurement. The resolution between 1.7 and 5.2 μm was obtained [10].

A new circuit has been realized with an I-Q demodulation, applying the homodyne method and the beamline was rearranged with only drifts between 3 BPMs. With this configuration the resolution improved to 0.2 μm [11].

Re-entrant Cavity BPM for the European XFEL

Cylindrical re-entrant cavity BPM built at Saclay with dipole mode resonance frequency of 1.724 GHz will be used in the cold accelerator at cryogenic temperature. The design is realized without slots, therefore the monopole mode at 1.255 GHz is filtered with hybrids, as described in details in ref. [12]. A single down conversion per plane is used, applying the homodyne method. The charge calibration is made by using the sum signal from the hybrid, corresponding to the monopole mode. Measurements at FLASH show a resolution of 4 and 8 μm, the difference is caused by different low-pass filters [12, 13]. This results fulfills the requirement for the resolution of 50 μm.

Undulator Cavity BPM for the European XFEL

The design of the cavity BPM is based on [10] adapted to the requirements of the European XFEL: smaller beam pipe (10 mm diameter) and a lower resonance frequency of 3.3 GHz. Few prototypes already produced at DESY, one is installed at FLASH. The measured frequency, loaded quality factor and sensitivity are in agreement with the prediction. An improvement of the orthogonal coupling has been done, see [9]. Next step is to include 3 BPM in FLASH with electronics to measure the resolution.

Linac Coherent Light Source Cavity BPM

The cylindrical cavity BPMs were developed at the Argonne National Laboratory with a dipole mode resonance

frequency of 11.384 GHz to be used between the undulators at LCLS. The detail of the design can be found in ref. [14]. The fields of the cavities are transmitted with waveguides to the receiver, below the undulator girder. The receiver uses a single-stage heterodyne method, as described in [15]. Measurements at the Advanced Photon Source low energy undulator test line result in resolution between 0.26 and 0.32 μm [16]. Meanwhile 33 cavity BPMs are used for the resolution measurements at LCLS with the cross correlation method. The median resolution of all BPMs is 0.44 μm for the horizontal, and 0.23 μm for the vertical plane, as described in ref. [17].

ILC Spectrometer With Cavity BPM

A prototype of an ILC spectrometer using cylindrical cavity BPMs as described in ref. [18] is installed at the SLAC end station A. The design is presented in [19] and provides a resonance frequency of about 2.9 GHz. The electronics consists of a I-Q demodulation with Heterodyne method, a single stage down-conversion is used. The middle BPM (of three) is mounted on a dual axis mover system. The BPMs vibrational motion of the horizontal plane is monitored by an interferometer system. It was shown that the non-rigid motion for the middle BPM is 620 nm, for the other two it is below 100 nm. Therefore by measuring the BPM resolution and assuming all three have the same behavior the non-rigid motion dominates the result. The measured resolution is about 0.5 μm [1] which fulfills the requirement.

Cavity BPM for the ILC Interaction Point

To control the interaction of the beam collisions the resolution of the BPM has to be few nanometers. Some iterations are made to improve the resolution. Cylindrical cavity BPMs are tested with a special metrology system to stabilize the non-rigid motion, which leads to the resolution of 15 nm [20] at the KEK Advanced test facility. The next tested prototype was a rectangular design for each transverse plane to suppress the orthogonal coupling. These prototypes were fixed on a heavy granite table. The steerers available for the calibration produce a certain offset. This system uses a hybrid to increase the weak amplitude and a homodyne method is applied for the I-Q demodulation. The resolution of $(8.72 \pm 0.28(\text{stat.}) \pm 0.35(\text{syst.}))$ nm was measured [21].

SUMMARY

The basic principles of the cavity BPM designs are presented. The influence of the beam angle and bunch tilt are discussed and the rejection of the monopole mode is described. An overview of the signal processing is shown and the main influence on the resolution is discussed. The examples from different institutes have shown that the cavity BPMs are able to provide resolutions at a few nanometer level.

REFERENCES

[1] M. Slater *et al.*, "Cavity BPM system tests for the ILC energy spectrometer", NIM A 592, 201-217, 2008.

[2] W. C. Barry, "Broad-Band characteristics of circular button pickups", Proceedings at the Accelerator Instrumentation Workshop, 1992.

[3] T. Suwada *et al.*, "Stripline-type beam-position monitor system for single-bunch electron-positron beams", NIM A 440, 307-319, 2000.

[4] M. Abramowitz and I. A. Stegun, "Handbook of Mathematical Functions", Dover Publications, Inc., New York, 1965.

[5] Computer Simulation Technology (CST), `http://www.cst.com`.

[6] S. Walston *et al.*, "Performance of a high resolution cavity beam position monitor system", SLAC-PUB-12492, 2007.

[7] V. Balakin *et al.*, "Experimental results from a microwave cavity beam position monitor", Proceedings PAC, 1999.

[8] V. Vogel *et al.*,"Performance of a nanometer resolution beam position monitor system", UCRL-CONF-216283, Nanobeam 2005.

[9] D. Lipka *et al.*,"Orthogonal coupling in cavity BPM with slots", These proceedings: MOPD02, 2009.

[10] H. Maesaka *et al.*,"Beam position monitor at the SCSS prototype accelerator", Proceedings APAC, 2007.

[11] H. Maesaka *et al.*, These proceedings: MOPD07, 2009.

[12] C. Simon *et al.*, "Beam position monitors using a Re-entrant cavity", Proceedings DIPAC, 2007.

[13] C. Simon *et al.*,"Performance of a reentrant cavity beam position monitor", Physical Review AB 11, 082802, 2008.

[14] G. Waldschmidt *et al.*,"Electromagnetic design of the rf cavity beam position monitor for the LCLS", Proceedings PAC, 2007.

[15] R. Lill *et al.*,"Design and performance of the LCLS cavity BPM system", Proceedings PAC, 2007.

[16] R. Lill, private communication, 2009.

[17] S. Smith, "LCLS Cavity BPM", These proceedings: TUOC03, 2009.

[18] A. Lyapin *et al.*, "A prototype energy spectrometer for the ILC at end station A in SLAC", Proceedings PAC, 2007.

[19] A. Lyapin *et al.*, "A prototype S-band BPM system for the ILC energy spectrometer", EUROTeV-Report-2008-072, 2009.

[20] S. Walston *et al.*, "Resolution of a high performance cavity beam position monitor system", Proceedings PAC, 2007.

[21] Y. Honda *et al.*, "Development of a high-resolution cavity-beam position monitor", Physical Review AB 11, 062801, 2008.

LCLS CAVITY BEAM POSITION MONITORS*

S. Smith, S. Hoobler, R.G. Johnson, T. Straumann, A. Young,
SLAC National Accelerator Laboratory, Menlo Park, CA 94025, U.S.A.
R.M. Lill, L.H. Morrison, E. Norum, N. Sereno, G.J. Waldschmidt, D. Walters,
Argonne National Laboratory, Argonne, IL 60439, U.S.A.

Abstract

The Linac Coherent Light Source (LCLS) is a free-electron laser (FEL) at SLAC producing coherent 1.5 Å x-rays. This requires precise, stable alignment of the electron and photon beams in the undulator. We describe the beam position monitor (BPM) system which allows the required alignment to be established and maintained. This X-band cavity BPM employs a TM_{010} monopole reference cavity and a single TM_{110} dipole cavity detecting both horizontal and vertical beam position. Processing electronics feature low-noise single-stage three-channel heterodyne receivers with selectable gain and a phase-locked local oscillator. Sub-micron position resolution is required for a single-bunch beam of 200 pC. We discuss the specifications, commissioning and performance of 36 installed BPMs. Single shot resolutions have been measured to be about 200 nm rms at a beam charge of 200 pC. Initial LCLS commissioning is described.

FEL COMMISSIONING

LCLS photocathode RF gun and injector systems were commissioned in 2007, followed by linac and bunch compressor systems in 2008. Beam was first taken through the undulator beamline (with no undulators installed) in December, 2008. After aligning each undulator segment individually, 21 undulator magnets were inserted in April 2009. We observed lasing at 1.5 Angstroms essentially immediately [1].

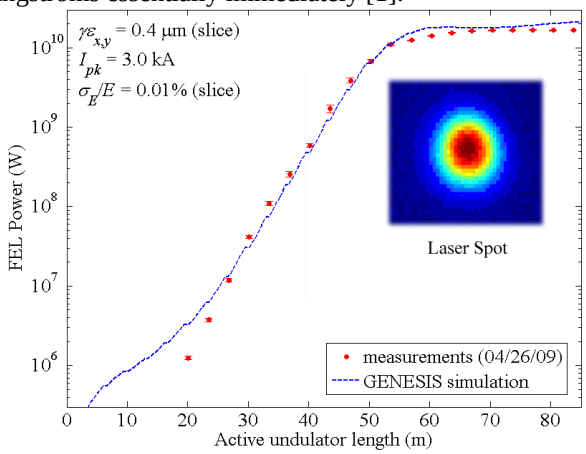


Figure 1: FEL power gain length measurement at 1.5 Å made by kicking the beam after each undulator sequentially (red points), a prediction (blue line) and the laser spot seen on a YAG screen.

*Work supported by U.S. Department of Energy under Contract Numbers DE-AC02-06CH11357 and DE-AC02-76SF00515.

BPM REQUIREMENTS

Laser saturation in the LCLS FEL requires the electron and photon beams be collinear in the 131 meter-long undulator to about 10% of the 37 μm rms transverse beam spot size over scales of the FEL amplitude gain length (~4m) [2,3]. BPM system requirements include centering accuracy, reproducibility, small physical size, radiation hardness, and sub-micron resolution at 200 pC.

SYSTEM DESIGN

The major subsystems for the LCLS undulator BPM system are the cavity BPM, receiver, and data acquisition components. The cavity BPM and downconverter reside in the tunnel while the analog-to-digital converters (ADC) and processing electronics are in surface buildings.

Thirty-four BPMs are installed on undulator girders while two are placed in the linac-to-undulator (LTU) transport line. The BPMs provide stable and repeatable beam position data for both planes on a pulse-to-pulse basis for up to a 120-Hz repetition rate.

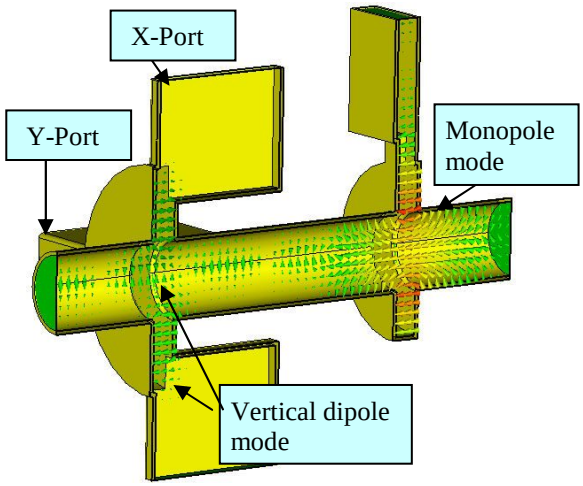


Figure 2: BPM Cavity schematic with electric fields of position (dipole) and reference (monopole) cavities.

X-Band Cavity

Figure 2 shows the electric field vectors in the cavity BPM simulated when the beam is offset[4,5]. Beam passes through the monopole reference cavity on the right, exciting the TM_{010} monopole mode signal resonant at 11.384 GHz. The TM_{110} dipole cavity is located 36 mm downstream through the 10-mm-diameter beam pipe. Monopole-dipole isolation is 130 dB, due to a below-

cutoff beampipe, copper losses, and poor coupling of the TM beampipe mode to the cavity dipole mode.

The position cavity dipole mode is resonant at 11.384 GHz, its output proportional to the product of beam position and bunch charge. The X and Y position modes are nominally degenerate in frequency, with the appropriate component chosen by the geometry of the couplers. The dipole coupler geometry is chosen to reject (the generally larger) monopole modes[4-8].

Iris couplers are precisely electrical discharge machined (EDM) into a solid copper block to ensure repeatable and accurate coupling. This technique ensures that the waveguide braze has little or no effect on the cavity performance. The dipole cavity was designed as a 4-port device with two opposing X couplers orthogonal to two opposing Y couplers. This is useful for cold testing and preserves symmetry. Unused ports are terminated with the potential for using them for future diagnostics.

Forty BPMs were built to a tolerance of ±10 MHz of design frequency. Accomplishing this without demanding unrealistic machining tolerances requires tuning. First, parts are inspected and cleaned. End caps are fitted to the body and clamped to a test fixture. Frequency and bandwidths are measured, then endcap beam pipe inner diameters are micro-machined as needed. BPMs are reassembled and checked to ensure the cavities are within the tolerance of +0, -10 MHz to compensate for frequency shift in the brazing process. End cap brazing was strictly controlled and a 10 MHz frequency shift was typically measured after the braze.

Dipole cavity final tuning was done with a sliding hammer in up to eight boss locations in the endcap to dimple the wall of the cavity. Four tuners in-line with the iris couplers are used for frequency adjustment. Four cross-talk tuners on the dipole cavity end cap are located at 45 degrees to the couplers. They reorient the dipole mode such that the modes are symmetric about the vertical and horizontal planes. These tuners are used to set the symmetry of the modes and optimize the isolation between planes.

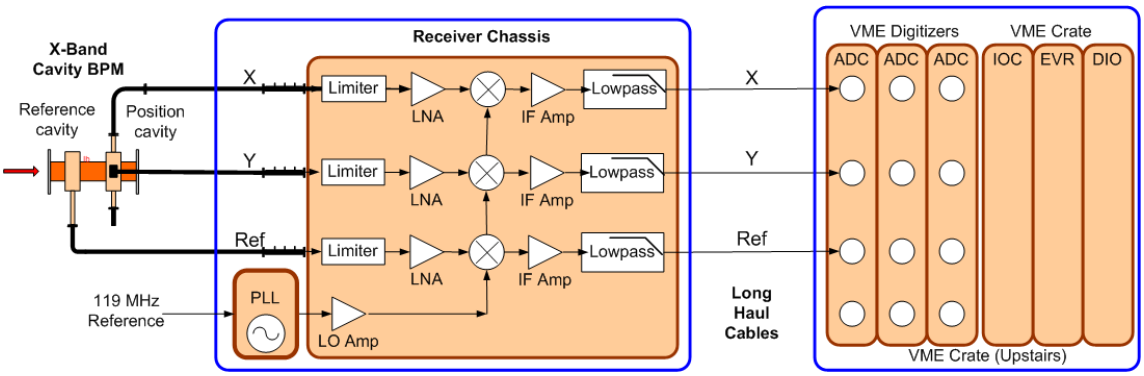


Figure 3: System block diagram. The receiver is mounted on the undulator stand while the digitizers are upstairs.

Receiver

A three-channel heterodyne receiver (Figure 3) mixes incoming X-band signals to a 25-50 MHz intermediate (IF) frequency. Each receiver input is limited to a 35 MHz bandwidth around 11.384 GHz. Filters also provide a broadband -10 dB return loss match to the cavities. Out-of-band filtering of -60 dB prevents higher modes from saturating the receiver input. Signals are first amplified in a low noise stage (LNA), then translated to the lower IF by mixing with a local oscillator (LO). The LNA is protected against high-power surges by a limiter that is rated at 50 W peak. The dynamic range of the electronics is extended by switching the gain of the receiver. Overall conversion gain/loss is +10 dB in the high gain mode and -15 dB in low gain. The LO is a low noise phase-locked dielectric resonant oscillator (PDRO) locked to the 119-MHz timing reference [9].

Digitizer

The X, Y, and Reference signals are digitized to 16 bits at a 119 MHz sampling rate in 4-channel VME digitizers designed and built at SLAC. Waveforms are transmitted over the backplane to a VME processor which reduces raw waveforms to beam position and charge.

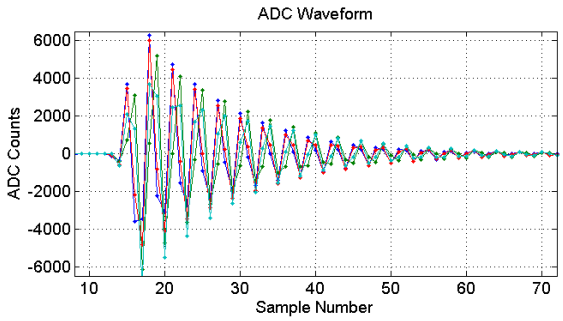


Figure 4: BPM raw waveforms sampled at 119 MHz.

ALGORITHM

Beam charge at each BPM is estimated by scaling the amplitude of the reference cavity. Each position waveform is reduced to amplitude and phase in an appropriate bandwidth around the cavity frequency. Normalized amplitudes are formed by dividing by the amplitude of the reference cavity and rotating by its phase. Position is estimated by rotating this complex normalized amplitude by a phase established with beam calibration, projecting out the position component, and scaling to microns. Finally a linear transformation

accounts for potential physical rotations of the BPM, non-orthogonality of the X and Y ports, and coupling between the ports.

CALIBRATION

Recovering beam position and charge from the digitized cavity waveforms requires knowledge of cavity phases and scales. Undulator BPMs are calibrated by mechanically moving the girder on which the BPM is fixed, fitting the phase and amplitude of the position signals normalized in phase and amplitude to the reference. Presently production BPM code calibrates by moving BPMs in 100 micron steps, much larger than typical 10 to 20 micron beam jitter. In principle we can use uncalibrated measurements from nearby BPMs to remove beam jitter during calibration, and calibrate with motion below alignment tolerances. The results of such a small-move calibration are shown in Figure 5. Transfer line BPMs, which are not mounted on movers, are calibrated by moving the beam on the BPM with a corrector.

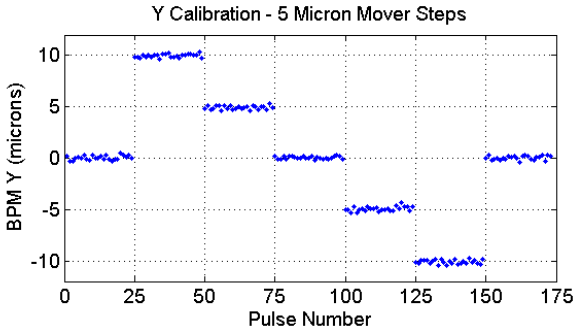


Figure 5: Calibration moving BPM in 5 micron steps.

PERFORMANCE

Resolution

We evaluate BPM resolution in the presence of >10 micron beam jitter by acquiring beam position synchronously over many beam pulses from many BPMs. A least-squares fit predicts position in each BPM as a linear combination of position measured in neighboring BPMs. Figure 6 shows this procedure applied to the 26th cavity BPM. It shows Y measured 120 times in 3 adjacent BPMs, Y versus that predicted from four closest neighbors, and the fit residual, or difference between measurement and prediction. The scatter of fit residual is an estimate of BPM resolution. Also plotted is a histogram of Y resolutions for 33 BPMs.

Stability

We evaluate two aspects of BPM stability. Calibration stability is evaluated by repeatedly calibrating about once a shift over three days. We find the scale drifting by less than 0.5% in 24 hours and the phase stable to 0.1 degree.

Secondly we record groups of about 100 beam pulses every 20 minutes over a 3.5 day period using a single calibration. Using adjacent BPMs to remove beam jitter, we plot measured beam position at each BPM. Typical stability is better than 1 micron drift over 24 hours.

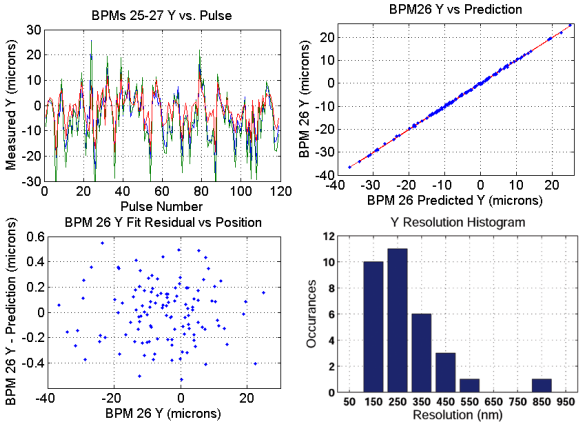


Figure 6: Upper-left: Y position measured at adjacent BPMs for 120 pulses. Upper right: Y at BPM26 vs. best fit prediction from its neighbors. Lower left: Fit residual, Lower right: Histogram of measured BPM resolutions.

REFERENCES

[1] P. Emma, "First Lasing of the LCLS X-Ray FEL at 1.5 A", to be published in Proceedings of PAC09, May, 2009.

[2] R. Hettel, et al, "Investigation of Beam Alignment Monitor Technologies for the LCLS FEL Undulator," BIW98, Stanford CA, May 1998, p. 413.

[3] P. Emma, J. Wu, "Trajectory Stability Modelling and Tolerances in the LCLS," EPAC06, Edinburgh, Scotland, June 2006, p. 151.

[4] R. Lill, et al, "Linac Coherent Light Source Undulator RF BPM System," FEL06, Berlin, Germany, July 2006, p. 706.

[5] G. Waldschmidt, R. Lill, L. Morrison, "Electromagnetic Design of the RF Cavity Beam Position Monitor for the LCLS", PAC 07, Albuquerque NM, May 2007, p. 1153.

[6] V. Balakin, "Experimental Results From a Microwave Cavity Beam Position Monitor", PAC99, New York, May 1999, p. 461.

[7] Z. Li, et al "Cavity BPM with Dipole-Mode-Selective Coupler", PAC03, Portland OR, May 2003, http://accelconf.web.cern.ch/AccelConf/p03/PAPERS/ROAB004.PDF

[8] S. Walston, et al, "Performance of a High Resolution Cavity Beam Position Monitor System." NIM A578, 2007.

[9] R. Lill, G. Waldschmidt, D. Walters, L. Morrison, S. Smith, "Design and Performance of the LCLS Cavity BPM System", PAC07, Albuquerque NM, p. 1153.

POSITION PICKUPS FOR THE CRYOGENIC STORAGE RING

F. Laux, M. Grieser, R. von Hahn, T. Sieber, A. Wolf, K. Blaum,
Max-Planck-Institut für Kernphysik, Heidelberg, Germany

Abstract

A cryogenic electrostatic storage ring (CSR) is under construction at the Max-Planck-Institut für Kernphysik in Heidelberg (MPI-K), which will be a unique facility for low velocity and in many cases also phase-space cooled ion beams. Amongst other experiments the cooling and storage of molecular ions in their rotational ground state is planned. To meet this demand the ring must provide a vacuum in the XHV range (10^{-13} mbar room temperature equivalent) which will be achieved by cooling the ion beam vacuum chambers to 2 - 10 K. This also provides a very low level of blackbody radiation. The projected beam current will be in the range of 1 nA - 1 μA. The resulting low signal strengths together with the cold environment put strong demands on the amplifier electronics. We plan to make use of a resonant amplifying system. Using coils made from high purity copper, we expect quality factors of $\sim$1000. The mechanical design has to provide stability and reproducibility of the alignment despite thermal shrinking when switching from room temperature operation to cryogenic operation. A prototype pickup has been built in order to test resonant amplification and the mechanical design using the wire method. The resonant amplification principle was tested in the MPI-K's Test Storage Ring (TSR).

INTRODUCTION

The CSR will be a fully electrostatic storage ring used to store atomic and molecular ion beams [1]. The beam optics consist of quadrupoles, 6° deflectors to separate the ion beam from neutral reaction products and 39° deflectors. It will be possible to merge the ion beam with neutrals and a laser beam. The experimental straight sections contain an electron cooler and a reaction microscope for reaction dynamic investigations. One linear section is uniquely reserved for diagnostics which will contain quartz profile monitors, Schottky pickups, an ionization rest gas monitor, a sensitive squid based cryogenic current comparator and two beam position monitors [2].

For the cold supply a commercially available Linde 4.5 K helium liquefier is combined with an additional connection box assuring the adaption to the CSR's helium pipe system. To reduce blackbody radiation, a maximum temperature of 10 K of the inner vacuum chamber is required. Efficient pumping of hydrogen as the main rest gas component is necessary to reach a vacuum in the XHV range which will be achieved by cooling parts of the vacuum chamber down to 2 K. For commissioning of the ring the ability of room temperature operation is required and part of the cryogenics concept is the possibility of baking out the system to at least 300 °C. The cryogenic concept leading to the ability to reach vacua in the desired range was successfully tested with the Cryogenic Trap Facility (CTF) [3].

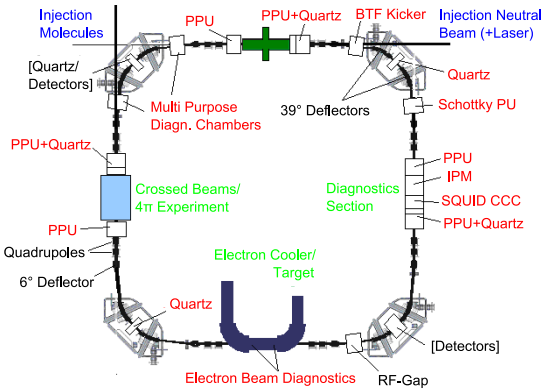


Figure 1: Overview over the CSR beam diagnostics system.

The extremely low temperatures, the large operational temperature range and the low pressures together with expected low signals are extremely challenging factors for the design of the storage ring components, particularly for the diagnostics equipment.

POSITION PICKUPS

Mechanical Design

In total six beam position monitors, each consisting of two pickups, are foreseen. One beam position monitor will be placed at each end of the diagnostics section as well as on both sides of the reaction microscope and of the third experimental section. The diagonal slit type linear pickups with a circular aperture will be used. The overall beam position monitor length will be $\sim$ 35 cm and the diameter of the electrodes will be 10 cm.

The pickups themselves will be situated in a grounded shielding chamber which has two functions. Firstly, it shields the pickup plates from the cryo-pump, which is a panel made from metal and coated with charcoal to provide a large absorption area. This layer introduces extra electrical capacity and an implied unsymmetry into the system and it added up to the loss budget lowering the quality factor of the resonant circuit. Secondly, the shielding separates the actual signal from disturbing signals on the ground set up by the storage ring chambers. A provision of small holes in the chamber that shield against high frequency electric fields but improves pumping will be con-

sidered. The grounded shielding chamber is terminated by massive plates having an aperture of 10 cm, which is the smallest aperture in the beam pipe. These plates also serve as mounting points for the electrode struts. The grounded shielding chamber is placed on a cylindrical metal pillar, which is itself mounted on the 40 K shield. This cylinder must be thin-walled to prevent heat flux from the 40 K shield to the grounded shielding chamber. It will additionally be interrupted by a ceramic insert to electrically disconnect the grounded shielding chamber from the ring ground. Since the ring is supposed to be operated between 2 - 300 K, the height of the optical elements such as the quadrupoles will vary and the vertical position of the pickups must vary likewise. The capability of the pickups for absolute position determination is required to be 0.5 mm. The suspension of the optical elements will be made from glass fiber reinforced plastics and the pickup suspension must be composed of materials that compensate for the temperature shrinkage. The electrically and thermally floating pickup chamber has to be thermally connected to the experimental vacuum chamber by copper bands with sapphire inserts that ensure the electrical separation of the ring ground and the shielding chamber ground.

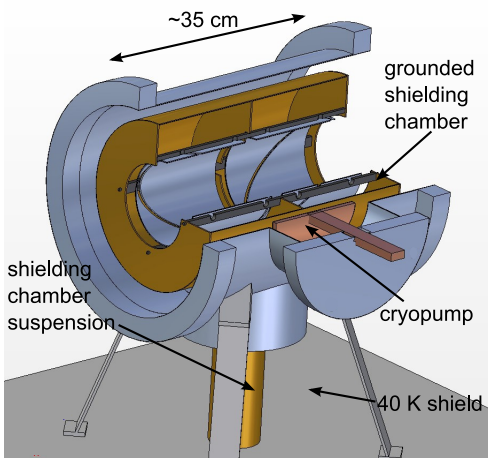


Figure 2: Preliminary mechanical design of the beam position monitor.

Amplification Principle

Table 1 summarizes some of the relevant beam parameters. The lower current limit derives from a minimum design current to operate the ring in connection with exotic large molecules with a low current source and in experiments with high reaction cross sections in which it will be necessary to lower the reaction rate to prevent from detector saturation.

For amplification of pickup signals in the kHz to MHz regime, originating from bunched beams with long bunch lengths, usually high impedance amplifiers with an input DC-resistance of 1 MΩ are used. This 'conventional' - non-resonant - method is planned to be used in the CSR

Table 1: Beam parameters

Mass range	1-100 amu
Energy range (1^+ ions)	20 - 300 keV
Frequency range	5 kHz - 200 kHz
Intensity range	1 nA - 1 μA

as well. Additionally it is planned to extend the system with the possibility of resonant amplification which is, to first order, set up by an inductance supplementing the circuit in parallel with the combined capacity of the pickup electrodes, the signal feedthroughs and other extra capacities. At resonance the impedances of both the capacity and the inductance have the same absolute value but phase shifted by π and thus the impedance of the total circuit equals its purely resistive part. The large range of planned frequencies is set by the extended mass range of the stored ions. A resonant system which would cover the first harmonic frequency range would have to have an extremely large and variable capacity or inductance range, which is not feasible. Therefore a system with a frequency range from 200 kHz to 400 kHz is planned, so that e.g. a beam coasting at 5 kHz had to be bunched to its 40^{th} harmonic. From the viewpoint of the coupling to the resonance circuit a narrow span of signal frequencies would allow optimal impedance matching to minimize noise transfer. In principle it is possible to bunch the beam to even higher harmonics to also move the signal frequency further away from the 1/f-noise regime. Additionally the manufacturing of the inductance for which we intend to use coils made from high purity copper became much simpler and the side effects of a high inductance coil such as self-capacity and wire resistance lowering the quality factor were of minor importance. There is, however, an upper limit for the harmonics with which the beam can be bunched, yet alone if the beam displacement is calculated from the pickup signal based on a calibration function obtained using a wire with an applied RF-frequency as a beam replacement. The EM wave generated by the wire has no component in the longitudinal direction and thus represents a TEM wave in the pickup and therefore a field of a beam with $\beta = 1$. As described by R. E. Shafer [4], for beams with $\beta \approx 1$ the difference signal divided by the sum, which is usually evaluated, if the beam displacement is determined, is frequency independent. There is, however, a dependence of the calibration curve on the frequency for low-β beams. Estimations using equations provided in [4] indicate that up to a harmonic number h=40 no low-β effects are expected. This number, together with the low frequency limit of a coasting beam, leads to the lower limit of the frequency range which must be covered by the resonant amplifying system. However, calculations of the low-β effects based on the finite elements method, are considered which include the special geometry of our pickup system, the result of which may shift the desired frequency range.

The tuning of the resonant circuit, that was used in test

measurements at the Test Storage Ring, was done with a tuning capacity, which is appropriate to withstand cryogenic temperatures and does not affect the quality factor of the resonant circuit. However its range of capacity change is not sufficient to tune the resonant circuit to frequencies in the desired range. As an alternative we will investigate piezo-element driven mechanic capacitors which have the advantage of a highly adjustable capacity range, but the disadvantage of slow variational speed.

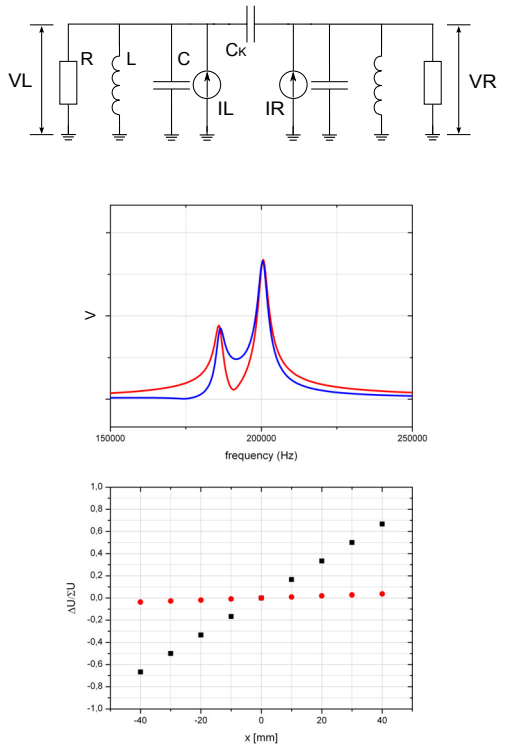


Figure 3: The effect of the coupling capacity on the resonant pickups. Upper plot: Equivalent circuit with the capacity of the pickup electrode (+cables etc.) and the coupling capacity C_k. The difference of the signal currents *IL* and *IR* is for a diagonally slit pickup linearly dependent on the beam displacement. For beam position measurements the left and right voltages *VL* and *VR* are processed. Middle: Frequency response with the resonant circuits tuned to 200 kHz and $C = 4$ pF. The curves (red: *VR*, blue: *VL*) are calculated for a beam position of $x = 30$ mm. Lower: Plot of the calibration curves. Black: Calibration curve for non-resonant amplification, i.e. without the inductances. The slope is decreased due to coupling with respect to the ideal case where $(VR - VL)/(VR + VL) = 1$ at $x = 50$ mm. Red: Calibration curve with resonant amplification. Its slope is decreased by a factor of 20 with respect to non-resonant amplification.

For the position measurement a simultaneous measurement of the signals from both pickup electrodes is preferable. Due to the large opposing areas of the pickup electrodes, there is always a considerably large coupling capacity present. Using non-resonant amplification, a high coupling capacity lowers the displacement sensitivity, which can be partially improved using grounded guard rings that are inserted in the gaps between the electrodes. If resonant amplification of both electrodes is used, the presence of a capacity between the electrodes causes a coupling of the resonant circuits, resulting in a double resonance and a drastically reduced displacement sensitivity (Fig. 3).

A measurement system as depicted in Fig. 4 is currently planned to be used, with which the position will be measured stepwise. With relays, one electrode will be short cut to ground. By this the coupling capacity simply adds up to the capacity of the active electrode which is itself connected to the resonant amplifying system. In a second step the relays are switched to the other electrode. This method doubles the acquisition time with respect to a narrow band measurement in one step. The switching time of relays, which is typically <5 ms, must additionally be considered.

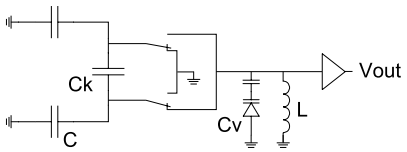


Figure 4: An amplification scheme using two relays and one tuning diode *Cv*.

OUTLOOK

A measurement with a copper coil at room temperature at the MPI-K's Test Storage Ring (TSR) has shown the expected increased signal by the quality factor of the resonance circuit. However, strong background signals from the RF-buncher of the TSR have significantly increased the uncertainty of the location measurement, in part because the background has unpredictable long term changes and at this time it was not possible to quickly switch between the electrodes. Changes of the amplifying system are currently underway which will reduce the background and allow for a quick electrode change to reduce measurement systematics.

REFERENCES

[1] M. Froese et al., "Cryogenic ion beam storage", PAC 09 Proceedings, Vancouver, May 2009.

[2] T. Sieber et al., "Beam diagnostics development for the Cryogenic Storage Ring CSR", WEPB23, DIPAC 07 Proceedings, Venice, May 2007.

[3] M. Lange et al., "Commissioning of the Heidelberg Cryogenic Trap for Fast Ion Beams (CTF)", MOPC110, EPAC 07 Proceedings, Genoa, June 2008.

[4] R. E. Shafer, "Beam position monitor sensitivity for low-β beams", Proc. Beam Instr. Workshop BIW, Santa Fe, 1994.

EXPERIENCE WITH THE COMMISSIONING OF THE LIBERA BRILLIANCE BPM ELECTRONICS AT PETRA III

A. Brenger, I. Krouptchenkov, G. Kube, F. Schmidt-Föhre, K. Wittenburg, DESY, Hamburg, Germany

Abstract

PETRA III, a new 3rd generation synchrotron radiation source, is presently under commissioning at DESY. Its beam position measurement system is based on the Libera Brilliance electronics. The BPM system is used for the machine start up and development. Later on, the system will be used for the orbit monitoring and orbit feedback. This paper presents the infrastructure and features of the BPM system together with the commissioning experience of the BPM electronics.

INTRODUCTION

In 2004 DESY decided to reconstruct its storage ring PETRA II into a new 3rd generation synchrotron radiation source PETRA III [1]. After two-years upgrade, one eighth of the 2.3-kilometer long ring was completely rebuilt and equipped with 14 undulator beamlines. The remaining seven eighth were completely removed, modernized and reinstalled. The electron beam position monitor (BPM) system that was installed in PETRA II did not meet the resolution and stability requirements of PETRA III. A simple upgrade was not possible; therefore it was decided to equip PETRA III with a completely new BPM-system. The BPM pickup stations, cables, BPM read-out electronics and all related infrastructure were renewed. Installation of the BPM system began in summer 2008 and commissioning with beam started in the end of March 2009.

BEAM POSITON MONITORS AND READ-OUT ELECTRONICS

PETRA III is equipped with 227 BPMs for the orbit measurement. There are 8 different types of electrostatic button pickup stations because the vacuum system of PETRA III has various types of vacuum chamber cross sections. Commercial RF button feedthroughs from PMB and Meggitt are used as pickups for the BPM blocks. All feedthroughs were individually tested and grouped together per BPM by similar test pulse response.

The requirements for the readout electronics are quite tight for new light sources. The BPM system for PETRA III has to support the machine commissioning as well as orbit feedback and the beam position observation. All of the BPMs have to be equipped with single turn and single pass, i.e. Turn-by-Turn (TbT) capabilities with the resolution of 50…100 µm (rms) in this operation mode. For standard user operation the orbit of the stored beam has to be kept constant with high accuracy: the beam should be stabilized to 1/10th of the beam width σ. For the BPMs located near the undulators required vertical resolution is 0.3µm (rms), i.e. the BPM system must have very high accuracy. Additionally, position data with TbT frequency about 130 kHz and resolution not worse than 50µm (rms) are needed for the Fast Orbit Feedback (FOFB) system. Other important requirements are the temperature drift (≤ 0.2 µm/°C) and 8-hours stability (1 µm peak to peak).

Libera Brilliance BPM electronics from Instrumentation Technologies was chosen as BPM read-out electronics. This beam position processor meets all technical requirements of the BPM electronics. Additionally it is an all-in-one solution that allows simplifying the infrastructure, and therefore the reliability of the system. Liberas were successfully used at other light sources like Soleil, Diamond, Elettra and ESRF.

In the beginning, the Libera Electron version was comprehensively tested in the laboratory and during a beam test at the ESRF [2]. Later on it was estimated that the monitor signals from the buttons might be higher than allowable input signal level of the Libera Electron [3]. Libera Brilliance, the next version of the beam position processor, has different characteristics of the input RF chain and allows operating with higher input signal levels. In addition the Brilliance version has better TbT resolution, temperature drift, beam current and bunch pattern dependency. Finally it was decided to equip PETRA III with the Libera Brilliance. The functional block diagram of Libera Brilliance together with the input chain is shown in Fig. 1.

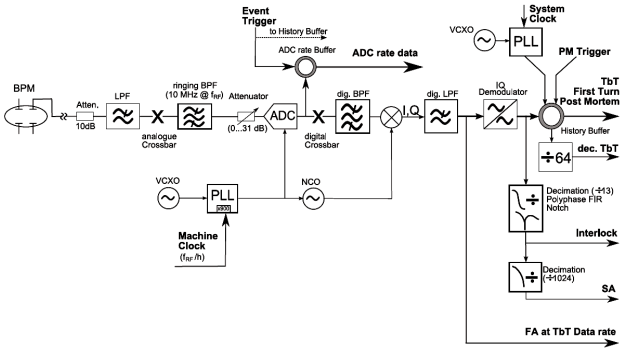


Figure 1: Functional block diagram of one channel of the Libera Brilliance BPM read-out electronics at PETRA III.

There are five data paths: ADC raw data, TbT data, decimated TbT data (factor 64), slow acquisition (SA) data for closed orbit measurement at approx. 10 Hz and fast acquisition (FA) data. External 10 dB attenuators are placed on each input in order to avoid damage of the

Libera's input circuit by high peak voltage. The performance of the attenuators was tested and meets the resolution requirements of the BPM system as well as the temperature stability using thermally-coupled mounting. The Libera Clock Splitter from Instrumentation Technologies is used to apply clock and trigger signals to each Libera device. Orbit interlock signals are directed to the Machine Protection System. The fast data stream with TbT update rate is used to collect the beam position at each BPM location for the FOFB system. Fast acquisition data from all BPM electronics located into the same rack are streamed via Libera's Rocked IO to the signal combiner and then towards the FOFB system. One BPM rack has up to 14 BPM electronics. Communication with the control system and feeding the slow acquisition data for closed orbit observation as well as slow orbit feedback are accomplished via Fast Ethernet switches.

BPM SYSTEM INFRASTRUCTURE

In order to achieve the required BPM resolution and stability, the BPM system must have proper environment and infrastructure. Important points are cables, pickup support and movement, temperature control and stabilization. High performance cables are used for the BPM-signal cabling. There are 3 types of cables depending on the distance between the pickups and the location of the read-out electronics. The maximal cable length is about 160m. A set of four cables should provide the signals with equal phases to the inputs of the electronics in order to fulfill beam current dependency requirements [4]. Therefore the cables have been precisely cut to equal lengths within 3-4 cm for each set. All of the input signal cables are additionally fixed in order to avoid unwanted vibrations that can affect the resolution of the system. All button pickups located in the new octant are joined to a High Frequency Movement Monitor in order to measure their position and movement with respect to the girder or ground floor. The resolution of this measurement system is better than 0.01 μm.

The BPM electronics are housed in 24 racks. 10 of them are placed in the new experimental hall. Temperature stabilization of the electronic racks is necessary in order to improve the reproducibility of the system. The hall has its own air conditioning system that provides temperature stabilization within ± 0.1 ^{o}C. Each rack has a fan-driven panel placed on the top in order to get proper ventilation. 14 BPM electronics rack are positioned in 8 halls around the remaining seven eighth of the ring. The BPM together with the FOFB racks are located into special air-conditioned huts as these halls have no temperature stabilization. The requirement to the beam stability is not too tight in these locations. The temperature inside the huts can be varied within ± 1^{o}C. An absolute value of this temperature is important and should not exceed a certain value. Therefore the temperature and the speed of the fan rotations inside the Libera are monitored by software.

COMMISSIONING OF THE BPM ELECTRONICS

Site acceptance tests of each unit have been performed after delivery of the BPM electronics. The results of the tests were within specifications [5]. After finishing the hardware installation and before beam start up, all BPM electronics have been verified together with the input signal cables to avoid wrong cabling. Server, client and dedicated MATLAB® application programs, required for the commissioning, were developed.

Turn by Turn Measurements

After first beam injection, the sum signal from the four buttons was used at the first stage of the commissioning for guiding the beam around the ring. TbT data together with the ADC raw data were used for the position measurements. It allowed to proceed with the injection improvement and to correct the beam position. Figure 2 shows the first sum signal from the beam at PETRA III.

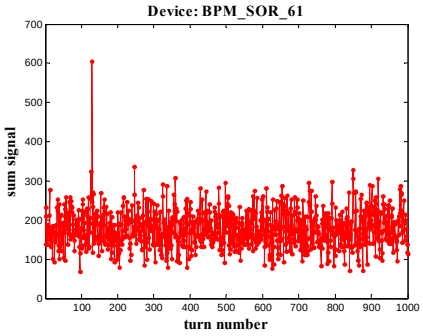


Figure 2: First beam at PETRA III. Response of a single BPM near injection. Due to an adjusted timing offset the first turn appears in turn no. 129.

After obtaining the position information from several BPMs one of the priorities became synchronization of the acquisition of all Liberas in the ring, i.e. first-turn sum signal should be observed at the same turn with respect to the acquisition trigger for all devices. Correct synchronization was set by finding proper external trigger, adjusting the hardware trigger delay inside Libera (available in the software release 1.80), and looking to the ADC data. Bunch signals have to be seen on the same position in the ADC samples for all BPMs. Additionally the phase of the Machine Clock (MC), coming with the revolution frequency, was adjusted in order to get correct beam phase with respect to the MC. Figure 3 shows first turn sum signals from all BPMs in the ring with the correct synchronization.

ADC raw data are very useful for finding certain hardware failures (e.g. noisy channels) in the beginning of the commissioning when the beam current is small and therefore the signals from the buttons are difficult to see. An essential application of the TbT data is the tune measurements. The tune measurements have been done as soon as a few hundreds turns were injected (Fig. 4).

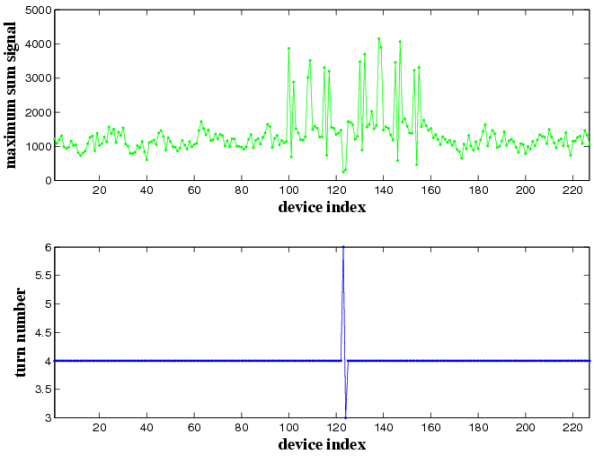


Figure 3: First turn sum signals from 227 BPMs observed at the same turn. Top: un-normalized sum signal. The narrow gap BPMs near the undulators are clearly visible. Bottom: Due to a readjusted delay the first turn appears in turn no. 4 now. BPM no. 121 and 122 are not installed.

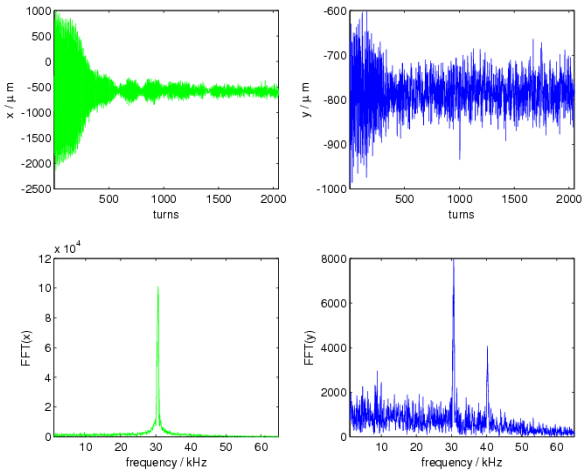


Figure 4: Horizontal and vertical turn by turn data together with FFT for tune measurement.

Slow Acquisition

The first stored beam was obtained shortly after the start of PETRA III commissioning [6]. Slow acquisition data have since been used for monitoring the closed orbit (Fig. 5). The SA data streams from all Liberas should be synchronized. Therefore their internal system and machine times had to be set simultaneously in advance for all devices. Automatic gain control was used to find the proper level for the attenuators in the Libera inputs. The resolution of dedicated monitors close to the undulators was better than 1µm in horizontal and about 0.5 µm in vertical plane at input signal levels of -45 dBm (1.9 mA; 6 GeV; 40 bunches) in SA mode. Interlock and post mortem functionality were successfully tested with beam.

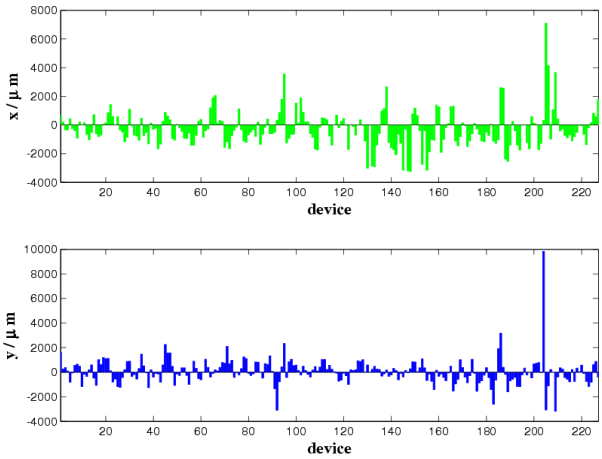


Figure 5: Orbit of the stored beam.

CONCLUSIONS

The PETRA III BPM system was completely renewed after reconstruction. Substantial effort was put into design, installation and testing of the system. As a result, the BPM system was put into operation in time and without any trouble. It enabled a successful start to the commissioning of PETRA III. Some features of Libera Brilliance BPM-readout electronics like trigger delays, possibility to use ADC data etc. helped a lot during the commissioning.

ACKNOWLEDGEMENTS

We thank our colleagues from Instrumentation Technologies for comprehensive support. We acknowledge R. Neumann, J. Klute and H-T. Duhme for very fruitful discussions. We also thank J. Neugebauer for his excellent work during the installation of the system.

REFERENCES

[1] Technical Design Report "PETRA III: A low Emittance Synchrotron Radiation Source" Editors K. Balewski et al., DESY 2004-035.

[2] K. Balewski et al., "Examination of the bunch current and bunch pattern dependence of the Libera BPM electronics", DESY technical note 2006-1.

[3] G. Kube and M. Werner, "Signal Level Calculation for the PETRA-III Beam Position Monitor System", DIPAC'07, Venice, Mestre, Italy, May 2007.

[4] G. Rehm et al., "Digital EBPMs at Diamond: operational experience and integration into a fast global orbit feedback", DIPAC'07, Venice, Mestre, Italy, May 2007.

[5] K. Wittenburg et al., "PETRA III Beam Position Monitor Electronic: Requirements and technical Specifications; Tendering and Contract Management"; Version 1.92 (2007).

[6] K. Balewski, "Commissioning Results of Beam Diagnostics for the PETRA III Light Source", these proceedings.

DUAL BEAM X-RAY BEAM POSITION MONITOR

C. Bloomer, J. Brandao-Neto, G. Rehm, C. Thomas, Diamond Light Source, Oxfordshire, UK

Abstract

Presented are the first results from the custom built I04 X-ray Beam Position Monitors at Diamond Light Source, using a single device to measure two adjacent beams in one front end. Synchrotron Light Sources are increasingly in demand by both academic and commercial users, and the number of 3rd generation light sources is growing rapidly. In order to make best use of the facilities a number of synchrotrons have adopted a scheme whereby two canted Insertion Devices occupy a single straight. Two beams are produced, separated by an angular divergence in the order of 1mRad, and both beams proceed down the same front end before being separated into two experimental hutches. This paper describes the techniques used at Diamond to accurately measure the position of both beams simultaneously with micron precision.

INTRODUCTION

A relatively new development in Synchrotron Sources is the concept of utilizing a single Insertion Device (ID) straight to produce two independent X-ray beams into two experimental stations. Such beamlines have been constructed and operated at both the APS [1], and at the ESRF [2]. At Diamond such a system has been designed and developed for the I04 Macromolecular Crystallography (MX) beamline. I04 has been operating now since January 2007 as an in-vacuum 23mm period undulator beamline, tunable over the wavelength range 0.5 - 2.5Å, to enable Multiwavelength Anomalous Diffraction (MAD) experiments to be carried out. J04 is a complimentary out of vacuum monochromatic undulator for MX fixed at 0.916Å that was installed in November 2008.

The IDs are located in the same straight, spatially separated by 1.9m and canted to produce beams separated by 0.98mRad (Fig. 1).

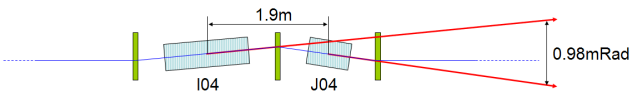


Figure 1: Schematic of I04 ID straight.

Both beams pass down the same front end and enter the first optics hutch where a beam splitter separates the beams further into two separate experimental cabins. This technique saves space within the synchrotron and allows more experiments to be performed for lower additional cost.

Each beam is capable of being independently tuned by altering each ID gap without the neighboring beam being affected. We verify this by observing the behavior of the electron orbit as the gap changes.

BEAM POSITION MEASUREMENTS

Traditional tungsten blade X-ray Beam Position Monitors (XBPMs) are capable of making sub-micron precision measurements of the position of a single beam. Four negatively biased blades intercept the edges of the X-ray beam (Fig. 2, left) and photons striking the surface of the blades liberate electrons. A low current monitor detects this loss of electrons as a current, and using the difference-over-sum method [3] one can deduce the position of the centre of the beam.

The four blade device is an elegant solution to the problem of accurately resolving beam positions, but unfortunately the system only works when dealing with a simple near-Gaussian beam distribution. Trying to resolve the centre of none-Gaussian distributions, such as that from a Helical Undulator, is much harder [4], and trying to resolve the distribution formed by two beams (Fig. 2, right) is impossible. Other Light Sources do not even attempt to measure the beam position in the front end in these circumstances.

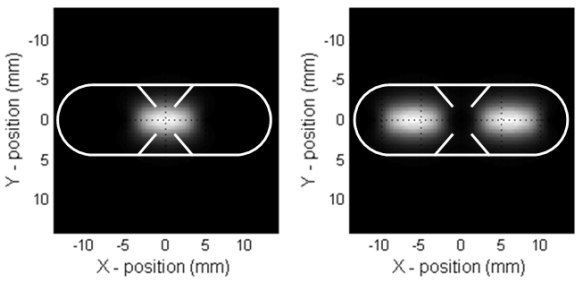


Figure 2: A standard four blade XBPM with the light from a normal ID (left) and light from two canted IDs (right). In this example the light from the two canted IDs has been normalised so they are of equal intensity.

EIGHT BLADED XBPM

However, a new XBPM designed and built as part of a collaboration between Diamond Light Source and FMB is capable of making sub-micron precision position measurements of both beams independently. Two sets of four blades are arranged within a single device using two blade holders (Fig. 3, Fig. 4). The two sets of four are treated

independently and connected to separate low current monitors.

This setup requires very precise positioning of the XBPM blades. At the location of XBPM-01, 12m from the centre of the straight, the beams are separated by only 11mm.

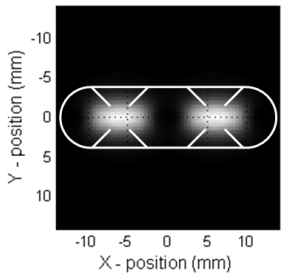


Figure 3: Eight blades, positioned correctly, are able to resolve the two beams.

In order to minimize noise or interference from one set of blades to the other (and to help ease overcrowding within the XBPM) the blade holders are longitudinally offset by 70mm (Fig. 4). This helps prevent liberated electrons from one set of blades interacting with the second set of blades.

The photo-electric cross section of tungsten dictates at what photon energy electrons are liberated. This cross section is weighted heavily towards low energy photons [5] and as a result most electrons liberated have an energy of less than 10keV. Electrons in the energy range of a few keV tend to be emitted approximately perpendicular to the photon path, as described by the Sauter distribution [6]. As a result free electrons released from one set of blades do not tend to interfere with the other set of blades in this configuration.

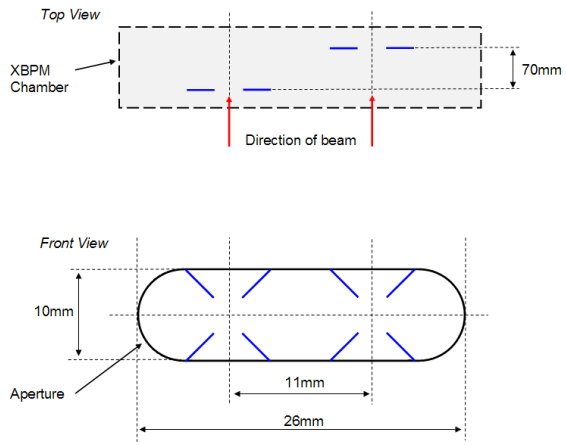


Figure 4: Dual beam XBPM schematic.

Each of the blades is biased at -70V in order to aid the liberation of electrons, and to ensure that free electrons are repelled.

Although the two beams are separated by 0.98mRad there is some overlap of their fringes. Each set of blades picks up a small amount of signal from the neighboring beam. However, we expect this cross talk to be a constant signal and thus can correct for it using a simple background subtraction script.

DETERMINING THE BEAM POSITIONS

The XBPMs are mounted on 2-axis stepper motors. By scanning the stepper motor back and forth across the aperture it is possible to build up an image of the flux seen at each position by each of the XBPM blades. This is a useful diagnostic aid for determining the position and approximate shape of the beam, and can be used to calibrate the XBPMs as relative beam movements can be compared to absolute and known stepper motor positions.

These scans can be performed with the ID closed in order to determine the effects of the beam, and also with the ID open as a way of gauging background contamination from other sources.

The scan presented below taken using XBPM-01 (Fig. 5) shows the flux seen by each XBPM blade when both IDs are closed to their nominal operating gaps (I04 to 7mm and J04 to 16mm). The image from each blade is scaled to the same limits, distances are in mm. The signal received (nA) has been normalised to a constant storage ring beam current of 1mA.

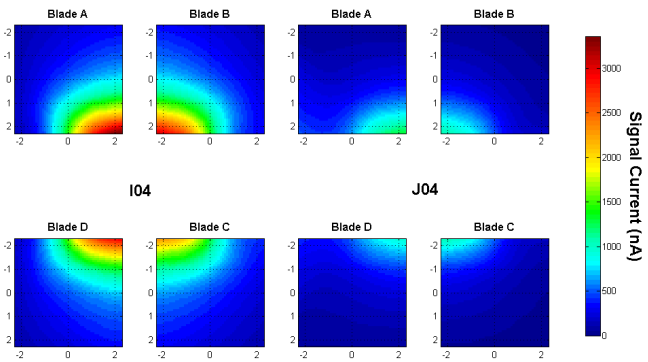


Figure 5: When both IDs are closed each beam is clearly visible.

This image clearly depicts the two beams passing down the front end, each beam centred on one of the sets of four blades. The J04 beam appears so much weaker than the I04 beam since it is produced by a 31mm period out of vacuum undulator whilst I04 is an in-vacuum 23mm period undulator. The lower photon count from J04 is exactly what one would expect from this device, but it does present some problems in accurately calculating the beam position since the signal detected has the potential to be skewed by stray radiation from the I04 beam.

Before an exact beam position can be calculated these stray radiation effects on one set of blades from the neighbouring beam must be determined. To do this one ID remains closed whilst the other is fully opened, and then the signal from both sets of blades is recorded.

The I04 blade signal at the nominal XBPM position

(0mm, 0mm) is 500nA per mA stored beam current. In order to determine how much of the signal comes from the 'wrong' beam, J04 is fully opened whilst I04 remains closed. In this arrangement J04 blade signal is 40nA per mA stored beam, 10% of the signal seen on I04. This signal is coming from the outer fringes of the I04 beam striking the J04 blades.

	I04 signals		J04 signals	
	$I04_{open}$	$I04_{closed}$	$I04_{open}$	$I04_{closed}$
$J04_{open}$	10	498	13	40
$J04_{closed}$	16	504	148	171

Table 1: Average blade signal received by each XBPM for various I04 and J04 undulator positions. Values are nA signal current per mA stored beam.

Since we know that the beam maintains a stable position we can assume that this signal remains constant as long as the I04 gap remains unchanged. By taking data at various I04 gaps a lookup table of background contamination is made, and the detected background signal seen on J04 is interpolated from this for any I04 gap. It becomes a simple matter to subtract one from the other to correct for the background signal.

This problem has less impact when considering the effect of the J04 beam on the I04 blades since the J04 beam is considerably less intense than I04. Only a small signal of a few nAs per mA stored beam contaminate the I04 blades. The corrections will still be applied though in order to eliminate even this small error.

CALIBRATED BEAM POSITION

Once the background signals have been subtracted a calibration of the XBPM is made. The response of the blades is measured against the known electron beam movements (Fig. 6). The fast orbit feedback system is used to alter the path of the electron beam through the IDs and produce parallel bumps. These known offsets are compared to the XBPM readings in order to provide calibrated position measurements in mm.

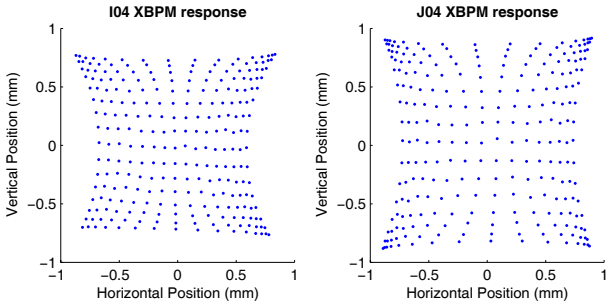


Figure 6: Response of the XBPM as the stepper motor position changes.

From this the two separate beam positions can be calculated using a simple asymmetry calculation [3].

CONCLUSIONS

The new twin beam XBPM is able to simultaneously resolve the position and pointing angle of two separate and independent ID beams in a single front end, despite only using one stepper motor to centre the XBPM. This device has enabled us to make accurate position measurements of the X-ray beam and thus confirm the alignment of the canted electron beam. Horizontally the separation of the two beams is measured to be 0.98mRad, and the vertical separation is measured to be 0.01mRad. This confirms the canting angle of the two IDs, as well as the quality of the ID trim tables to produce such small deviations from the expected alignment.

In summary this design of XBPM is verified to be capable of making sub-micron position measurements of adjacent beams from twin canted ID straights. The design is flexible enough to meet the requirements of a range ID parameters and positions within the front end (at DLS we have another set of these XBPMs installed for use on a U21 beamline). Their manufacture is not significantly more costly or time consuming compared to that of a normal XBPM, and their setup and calibration is relatively easy. These XBPMs are a very valuable addition to our diagnostics equipment.

ACKNOWLEDGEMENTS

We would like to thank FMB Berlin, for the design and manufacture of these devices, and Karstan Holldack for his valuable input.

REFERENCES

[1] P. den Hartog, G. Decker, and L. Emery. Dual Canted Undulators at the Advanced Photon Source. In *Proceedings of the 2003 IEEE Particle Accelerator Conference (PAC 03)*, page 833, 2003.

[2] D. Nurizzo, T. Mairs, M. Guijarro, V. Rey, J. Meyer, P. Fajardo, J. Chavanne, J. Biasci, C. Jean, S. McSweeney, and E. Mitchell. The ID23-1 structural biology beamline at the ESRF. *Journal of synchrotron radiation*, 13:227–238, 2006.

[3] E. van Garderen, J. Krempasky, M. Böge , J. Chrin , V. Schlott, T. Schmidt, and A. Streun. Characterisation of the Systematic Effects of the Insertion Devices with Photon Beam Position Monitors. In *Proceedings of the 2007 European Workshop on Beam Diagnostics and Instrumentation for Particle Accelerators (DIPAC 07)*, page 126, 2007.

[4] H. Aoyagi, T. Kudo, and H. Kitamura. Blade-type X-ray beam position monitors for SPring-8 undulator beamlines. *Nuclear Instruments and Methods in Physics Research A*, 467:252–255, July 2001.

[5] N. J. Carron. *An Introduction to the Passage of Energetic Particles through Matter*. Taylor & Francis, 2007.

[6] F. Sauter. Über den atomaren Photoeffekt in der K-Schale nach der relativistischen Wellenmechanik Diracs. *Annalen der Physik*, 403:454–488, 1931.

IMPROVEMENT OF THE FAST ORBIT CORRECTION ON THE ESRF STORAGE RING

E. Plouviez, L. Farvacque, J.M. Koch, J.L. Pons, F. Uberto, ESRF, Grenoble, France

Abstract

Until the end of 2008, the suppression of the closed orbit distortion on the storage ring of the ESRF was obtained using two separate systems: A slow system using 224 BPM and 96 correctors performing a correction every 30 seconds with a bandwidth of 1.5 10^{-2} Hz, and a fast system, using only 32 BPMs and 32 correctors but working at 4.4 KHz, damping the orbit distortion from 5 10^{-2} Hz up to 150 Hz; the 1.5 10^{-2} Hz to 5 10^{-2} Hz frequency span was left uncorrected [1].

This separation of the frequency range of the two systems by a dead frequency span avoided cross talks between them, but prevented the efficient cancellation of the very low frequency orbit distortions caused by the frequent modification of the insertion device (IDs) settings required by the beamlines operation. We found a way to coordinate the operation of the slow and fast systems in order to suppress this dead frequency span. This paper describes the principle and the beneficial effect of this new scheme, and its limitations. To overcome these limitations, we are now developing a single new orbit correction system that will damp the orbit distortion from DC to 150 Hz; this system will use the Libera Brillance BPM electronics recently implemented at ESRF, and new fast correctors. This new scheme is also briefly presented in this paper.

INITIAL SLOW AND FAST CORRECTION SCHEMES

Both slow and fast correction systems derive the orbit correction from the BPM data using a correction matrix obtained from the inversion of the response matrix of the BPMs to each corrector. These response matrixes are inverted using the SVD method; for the slow correction 96 Eigen vectors are used; for the fast correction 16 vectors are used. As mentioned in the abstract, the slow and fast orbit correction systems used at ESRF were able to operate independently by leaving the 1.5 10^{-2} Hz to 5 10^{-2} Hz frequency span uncorrected; the cancellation of the DC response of the fast system was obtained by the following algorithm: the vector I_{av}, average value of the currents in the fast system correctors magnets is continuously computed; using the response matrix of the BPMs of the fast system to the fast correctors, it computes the position offset at the location of the fast BPMs produced by this currents set I_{av}. If we subtract this offset to the reading of the fast BPMs, it will result in the cancellation of the fast correctors currents at low frequency; the proper choice averaging time used for the calculation of I_{av} and for the frequency of the fast BPMs offset subtraction allows us to set the cut off frequency of the cancellation of the DC response of the fast system to 5 10^{-2} Hz. At the startup of the fast system, the initial offset of the BPMs is set at the values read before the loop closing, so the initial value of the currents set in the fast correctors magnets should be null. When the IDs settings are fixed, there are very few orbit perturbations in this 1.5 10^{-2} Hz to 5 10^{-2} Hz frequency span, so the choice of this dead span looked good. But over the last years of operation of the ESRF storage ring we found that the most detrimental cause of orbit distortion had become the frequent changes of the settings of the insertion devices (gap and phase) which perturb the orbit precisely in this 1.5 10^{-2} Hz to 5 10^{-2} Hz frequency span. Each of the most troublesome IDs have then been equipped with a feedforward correction system which sets the field of two dedicated correctors magnets located at both ends of the ID as a function of the insertion device settings, using a look up table; however the maintenance and periodic calibration of a large number of these feedforward systems is very inconvenient. To overcome this problem, we have implemented a control of the slow and fast orbit correction system allowing them to coordinate their correction over the DC to 5 10^{-2} Hz frequency span allowing the fast correction system to cancel without delay the orbit distortion caused during a change of the settings of an ID occurring during the 30 s time interval between two slow orbit corrections.

PRINCIPLE OF THE COUPLING METHOD

We are using the following scheme to operate both systems down to DC; the slow system computes and applies an orbit correction every T_s period of 30 s; it is able to offset the closed orbit over a range of several mm; in this new scheme, the fast system should also works from DC to 150 Hz between two slow corrections, without the scheme described above for the cancellation of I_{av}; the correctors of the fast system are only able to offset the closed orbit by a fraction of mm; so, before the computation of a slow correction, the slow system reads the vector I_{av}, average value of the currents in the fast system correctors ; using the response matrix of the BPMs of the slow system to the fast correctors, it computes the orbit offset at the location of the slow BPMs which was caused by the current set I_{av}; then by adding this offset to the real orbit read by the its BPMs, the slow system will compute a correction which will be the sum of the correction that he would apply plus the static correction already applied by the fast system; when the slow system applies this total correction, the fast system automatically removes from the fast correctors the set of currents I_{av}; in this way the slow system downloads the DC part of the correction from the fast system every 30 seconds avoiding

the saturation of the power supplies of the fast correctors which have a much lower dynamic range than the slow correctors.

Adjustment of the Fast System Goal Orbit

The ideal orbit that the fast system working down to DC will try to reach is the orbit that was measured at its start up and which was set previously by the slow system; the ideal beam position set as a goal for both the slow and fast system at the location of the fast system BPMs is the same at the system start; however this is usually no longer true after, for instance, one hour of beam decay and ID setting changes, because the orbit distortion to cancel may have significantly changed, and due to the difference in the basis and number of the Eigen vectors used by both systems for the orbit correction computation.

The solution would be to continuously adjust the goal orbit of the fast system to follow the change of the optimum orbit set by the slow system; the solution that we found to achieve that was to eventually reintroduce a cancellation of the DC response of the fast system through a change of the fast BPM offset, as in the initial operating mode without coupling to the slow system, but this time with a cut-off frequency much lower than the 1.5 10^{-2} Hz cut-off frequency of the slow correction, and not higher as previously; now the bandwidths of the slow and fast system are not separated by a dead frequency span but overlap; in this way, the average value of the correction applied by the fast system between two slow corrections is almost unchanged compared to a fast correction down to DC and the I_{av} vector read by the slow system to cancel the DC current in the fast system magnets is also nearly unchanged; then the only effect of the suppression of the DC response of the goal orbit of the fast system is the automatic adjustment of the fast system to the slow drifts of the goal orbit of the slow system. The evolution of the currents of the fast magnets after storage ring refill, with this algorithm, is shown in Fig. 1, no divergence is visible.

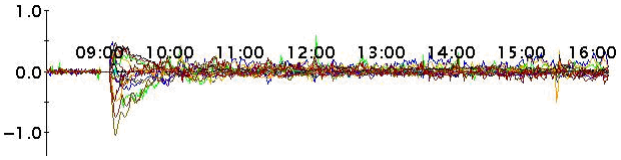


Figure 1: evolution of the horizontal fast correctors currents over a 7 hours beam decay.

EFFECT ON THE BEAM STABILITY

Effect on the Beam Stability

The plot of Fig. 2 shows a typical record of the position read by a horizontal fast BPMs, with a bandwidth of 0.1 Hz, without and with slow and fast correction coupling; after coupling, the low frequency orbit distortion occurring between two slow correction are very well damped by the fast system.

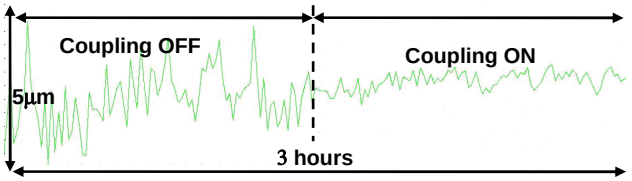


Figure 2: Effect of the operation of the fast orbit correction down to ultra low frequency.

Case of Local Orbit Perturbation

In the case of a single local perturbation, the correction produced by the fast system will not be very effective in the interval between the two correctors surrounding the perturbation; this interval will extend over at least one cell but can be as large a three or four cells, due to the low number of fast correctors (32 horizontal and 16 vertical correctors). Unfortunately we are faced with this type of single local perturbation in the case of the change of an ID setting. It is a major limitation of our present orbit correction scheme.

UPGRADE PROJECT

If we want to avoid having locally large local orbit distortion when the cause of the distortion is localized, we must drastically increase the number of fast BPMs and fast correctors. Since the former slow BPMs of our storage ring are now equipped with *Libera Brillance* electronics [2], we now already have a set of 224 very high resolution BPMs with an orbit measurement rate of 10 KHz. Concerning the correctors, we considered two options: to use the present set of 96 slow correctors with low bandwidth power supply, and increase the number of fast correctors, or to increase drastically the bandwidth of the slow correctors power supply, and use only one type of fast correctors.

Correctors Magnets

The present slow correctors are implemented by adding 3 pairs of auxiliary coils on the yoke of the sextupoles; using the proper combination of currents in these 3 coil pairs as shown in Fig. 3, we can produce any combination of vertical and horizontal kicks. The bandwidth of these correctors will be affected by the eddy currents in the sextupole core and at the surface of the vacuum chamber (the vacuum chamber all over our storage ring is made of 2mm stainless steel). Measurements showed that the vacuum chamber is the main cause of the magnet field attenuation due to eddy currents, compared to the eddy currents in the sextupole core; but the inductance of these correctors is also quite large: 0.6 H. However, it is possible to achieve, for the small currents amplitude needed for the fast correction, a bandwidth of 150 Hz for these correctors with a proper design of the power supply. This bandwidth is lower than the bandwidth of the present air cored fast correctors, but it should be possible to make up for it by a proper design of the controller of the orbit control loop, so the implementation of dedicated fast correctors is not an absolute requirement as it would be on ring built mostly with Aluminium vacuum vessels.

Simulations showed that using a PID type controller instead of the PI controller that we are using now is a solution; more sophisticated controllers like the IMC controller can also be used [3]. So for the future we will go for an upgrade of our orbit correction system using a single type of correctors, instead of mixing fast and slow correctors as in our present system.

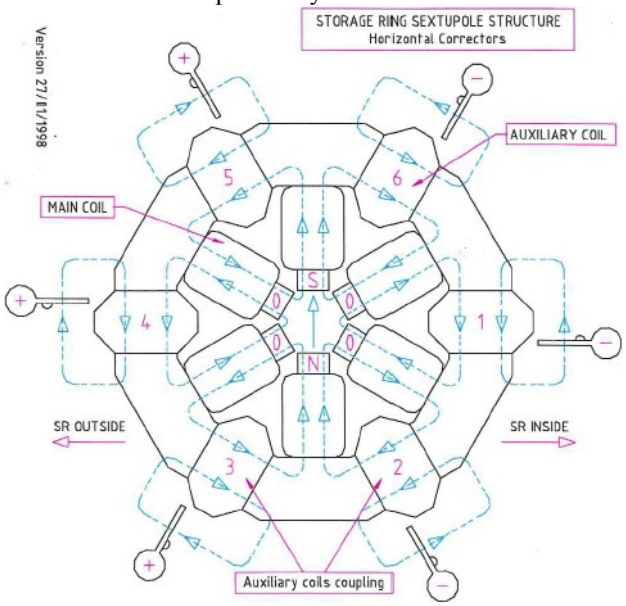


Figure 3: Layout of the auxiliary correctors in a sextupole.

New System Layout

The design of our new system will be based on the availability of the *Libera Brillance* electronics and an associated "Communication Controller" developed at DIAMOND [3] using the *Libera Rocket I/O* ports, which allows the measurement and broadcast of the beam position with a very good resolution at a rate of 10 KHz. As indicated above we want to use the corrector magnets embedded in the sextupole cores; we also want to use the existing cables connecting the magnets to the existing power supplies, so the new fast power supplies of the corrector will be located in the same cabinets as the old one, in 4 different technical galleries; this constraint sets the architecture and topology of our system;

Since the power supplies will be spread in 4 locations, we will also distribute the correction computation in the same locations, over 8 processors; For the choice of the processor, we noticed that SOLEIL and DIAMOND were using a PMC board embedding a *Xilinx Virtex 2 pro* FPGA to concentrate the 10 KHz BPM data for diagnostics purpose using the Communication Controller, and that a FPGA model and a Tango device server were already available for this application; the RS485 digital outputs for the digital control of the power supply are also available for this type of board; with a ready-to-use communication interface with the BPMs and the correctors, this board appears as an almost natural choice as a platform for the orbit correction calculation, after addition of the feedback algorithm in the FPGA model.

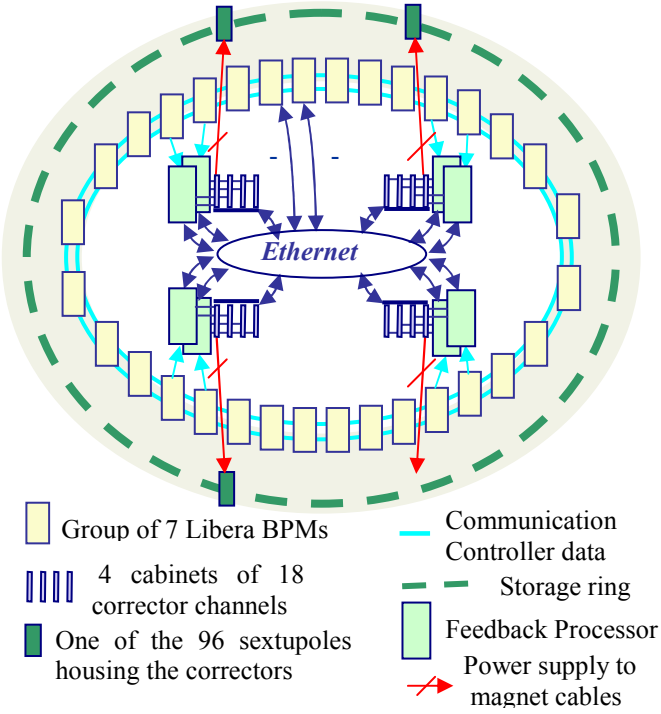


Figure 4: Layout of the future orbit correction system.

CONCLUSION

We have managed to combine the operation of two very heterogeneous orbit control systems using different BPMs, different correctors, with very different dynamic characteristics, to obtain a stable orbit correction on their combined frequency range of operation, without uncorrected frequency span. However, for the future upgrade of our orbit control system, we have decided, in order to end up with a simpler layout, to use only one type of BPMs and correctors; this choice is possible since the vacuum vessels of our storage ring are made of stainless steel instead of aluminium, which is a big advantage, at least in this respect.

REFERENCES

[1] E. Plouviez et al., " Fast orbit correction at the ESRF", 3rd International Workshop on Beam Orbit Stabilization, December 2004, Grindelwald, Switzerland.

[2] K. Scheidt, F. Epaud, "Installation and Commissioning of a Complete Upgrade of the BPM System for the ESRF Storage Ring ", this conference.

[3] M. T. Heron, M. G. Abbott, J. A. Dobbing,S. Duncan G. Rehm, J. Rowland, I. Uzun, "Performance and Future Developments of the Diamond Fast Orbit Feedback System", Proc EPAC 08, June 2008, Genova, Italy.

OPTIMISATION STUDIES OF A RESONANT CAPACITIVE PICK-UP FOR BEAM POSITION MONITORING OF LOW INTENSITY, LOW VELOCITY ANTIPROTON BEAMS AT FLAIR*

J. Harasimowicz†, C.P. Welsch, Cockcroft Institute and the University of Liverpool, UK

Abstract

The Ultra-low energy Storage Ring (USR) at the future Facility for Low-energy Antiproton and Ion Research (FLAIR) at GSI, Germany will decelerate antiproton beams of very low intensities from 300 keV down to 20 keV. Such beams can be easily disturbed by standard monitoring devices and the development of new sensitive diagnostic techniques is required. To overcome the limitations related to a very low number of particles, a low signal-to-noise ratio and ultra-low kinetic energies, a resonant capacitive pick-up has been proposed as a beam position monitor. In the planned solution, the signal gain will be realised by the use of a specially designed resonant circuit optimized to meet the requirements of the USR. The current overall design studies of the resonant capacitive pick-up, including simulations of the beam displacement sensitivity and linearity for different pick-up geometries and the equivalent resonant circuit characterisation, will be discussed.

INTRODUCTION

The novel Ultra-low energy Storage Ring (USR) is currently being developed for the future Facility for Low-energy Antiproton and Ion Research (FLAIR) [1]. It will be able to accept, store and decelerate a 300 keV beam of $\leq 2 \cdot 10^7$ antiprotons down to 20 keV.

For the standard operation of the USR, ∼100-ns-long bunches might be of the main interest. With the ring circumference of 42.6 m, the revolution time t_{rev} of the 300 keV antiproton beam will be equal to 5.6 μs. In this case, a harmonic mode h = 10, corresponding to the RF frequency f_{RF} = 1.78 MHz and RF buckets of about 560 ns, might be chosen. The RF field will typically be applied after the beam has reached a quasi-DC state which will lead to the generation of 10 bunches not longer than ≈150 ns. After the deceleration stage, the main RF frequency will have to be decreased to 459 kHz to follow the longer revolution time t_{rev} = 21.8 μs of 20 keV antiprotons resulting in bunches being not more than ≈550 ns long. Therefore, the standard operation of the USR will include ≈1.1 m long bunches of ultra-slow particles (β = 0.006–0.025) carrying a very low charge (300 fC) with the repetition rates in the range of ∼0.4–2 MHz.

In addition, a production of ultra-short (1–2 ns) bunches for in-ring experiments is also foreseen for the USR [2]. Initially, a 20 keV coasting beam is planned to be adiabatically captured into 50 ns stationary buckets formed by a 20 MHz cavity operating at a high harmonic mode. With h = 436 one gets only $\leq 5 \cdot 10^4$ particles (8 fC) per bunch. The final bunch length will depend on the initial RF voltage applied to capture the circulating beam. The desired ultra-short bunches of 1–2 ns duration, corresponding to ≈2 mm only, will then be formed by an additional double drift buncher with a voltage of ≈300 V.

Accurate beam position measurements, necessary for the successful operation of the USR, will require devices suitable for the proposed beam distributions. For the standard mode (h = 10) with the bunch repetition frequencies of the order of 1 MHz and the bunches much longer than the space available for a beam monitor, a capacitive diagonal-cut pick-up (PU) is a favourable solution. It offers a high linearity which is a huge advantage when the beam diameter can reach up 2 cm in some parts of the USR before electron cooling. However, this relatively simple device will not be suitable for the ultra-short, very slow bunches intended for the in-ring experiments. In this case, other monitors extracting information from electromagnetic fields of moving charged particles might also fail to measure the beam displacement. Figure 1 shows the transverse electric field calculated at a distance of 125 mm from the beam for 20 keV antiproton cos^2-like bunches formed with h equal to 10, 75, 200 and 436. For the highest h, the modulation of the signal is practically lost, thus none of the beam position pick-ups will work.

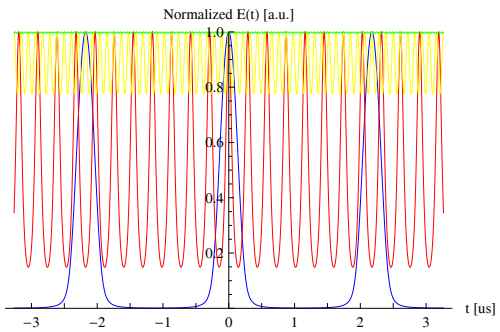


Figure 1: Normalized transverse electric field at a distance of 125 mm from the 20 keV cos^2-like bunches formed with h = 10 (460 kHz, blue curve), 75 (3.5 MHz, red curve), 200 (9.2 MHz, yellow curve), and 436 (20 MHz, green curve).

* Work supported by the EU under contract PITN-GA-2008-215080, by the Helmholtz Association of National Research Centers (HGF) under contract number VH-NG-328, and GSI Helmholtz Centre for Heavy Ion Research.

† Janusz.Harasimowicz@quasar-group.org

CAPACITIVE PICK-UP DESIGN AND SIGNAL ESTIMATIONS

As already mentioned, a diagonal-cut capacitive pick-up will be used for the beam position measurements. The whole monitor will consist of two units, each l = 100 mm long and able to monitor the displacement in one axis. In order to avoid beam-to-ground impedance jumps and so the beam instabilities, the PU should have the same diameter as the beam tube, thus the radius r = 125 mm has been assumed. The coupling capacitance between opposite PU plates and adjoining PU units can be minimised by introducing guard rings on ground potential [3]. Figure 2 shows the simulations performed for different PU geometries. In all cases, not only is high linearity achieved, but also the guard ring separating two plates results in a greater sensitivity to the beam displacement.

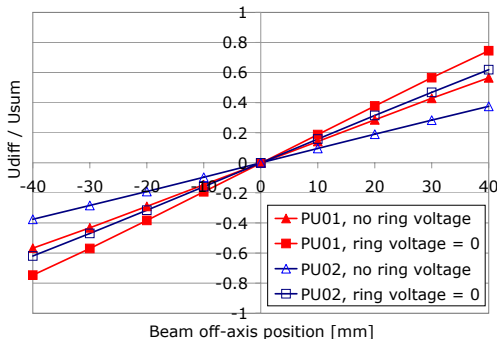


Figure 2: Response curves for two exemplary PU geometries with (squares) and without (triangles) ground voltage set to a guard ring introduced between PU plates.

For the 300 keV bunches at f_{RF} = 1.78 MHz consisting of $2 \cdot 10^6$ particles each and the foreseen PU length l = 100 mm, radius r = 125 mm and plate-to-ground capacitance $C \approx 100$ pF, the expected peak voltage can be as low as $\sim$100 μV [4]. If the coupling capacitance between two plates is ignored, one can assume a simple linear response $\Delta U/\Sigma U = x/r$, where ΔU is the differential signal between two opposite plates, ΣU is the sum signal and x is the beam displacement. In this case, the differential signal for x = 0.1 mm will be as small as 150 nV and a low-noise amplifier will be required. Nevertheless, even with the equivalent amplifier input noise lowered to 0.6 nV/$\sqrt{\text{Hz}}$ (e.g., see [5]), a 20 MHz bandwidth system necessary for the USR bunch structure observation will result in the signal-to-noise ratio $S/N \approx 0.3$ for 0.5 mm of beam displacement. Smaller bandwidth of 2 MHz could at least allow for the bunch-by-bunch observation, but in this case $S/N \approx 0.9$ is still quite low. If a resolution better than 0.5 mm is to be achieved, a further bandwidth reduction will be required. Therefore, it has been proposed to build the pick-up as a part of a resonant circuit well tuned to the repetition frequency. Due to the bandwidth restriction, it will not be possible to measure the individual bunch properties, but a much higher sensitivity can be expected.

EQUIVALENT CIRCUIT STUDIES

An equivalent circuit of a capacitive PU plate with an external inductance coil introduced to create a resonant solution is shown in Fig. 3. The image current I flowing from the pick-up into the circuit can be estimated for a point charge moving inside the PU; then the total bunch signal can be calculated by summing up the weighted contributions. Although cos^2-like bunches with the full width at the baseline T = 150 ns and f_{RF} = 1.78 MHz have been assumed for the purpose of this study, the differences in the signals from arbitrary charge distributions for low β values can be neglected [6]. Figure 4 shows the calculated image current. A sine function of the same amplitude of ≈500 nA has been used for the resonant circuit analysis.

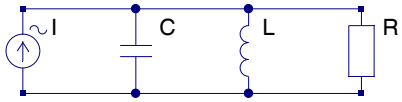


Figure 3: Equivalent circuit of the resonant capacitive PU plate with the image current I, plate-to-ground capacitance C, added inductance coil L and amplifier input resistor R.

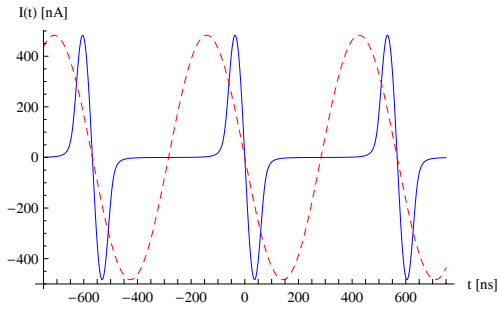


Figure 4: Image current flowing from the pick-up into an external circuit (blue curve) and a sine function with the same amplitude and repetition frequency (dashed red curve). The signal is generated on a PU plate of l = 100 mm and r = 125 mm by cos^2-like bunches with β = 0.025 and T = 150 ns.

The behaviour of two PU plates has been compared and studied in terms of the detectable voltage difference for I_{peak} = 500 nA, C = 100 pF, R = 1 MΩ, $\omega_0 = 2\pi f_{RF}$ and $L = 1/(\omega_0^2 C)$ = 80 μH. Signals from the off-centre beam has been estimated according to [7]. In the first assumption, ohmic losses $R_L << R$ in the inductance coil and the coupling capacitance C_c between the plates were ignored which resulted in the peak voltage of 0.5 V and the differential signal of 4 mV for 0.1 mm of beam displacement. However, damping and a shift of the resonance frequency $\omega_d = \omega_0\sqrt{1 - R_L^2 C/L}$ occurs when R_L is taken into account. With R_L = 50 Ω, the change in the resonance frequency Δf is smaller than 3 kHz, but the peak voltage and the differential signal for x = 0.1 mm decrease to about 8 mV and 50 μV respectively. When the coupling capaci-

tance is considered, the differential voltage at f_{RF} = 1.78 MHz may drop down even by three orders of magnitude for C_c as low as 2 pF and no R_L included; with R_L = 50 Ω, the same signal is decreased only by a factor of 2. In both cases, the effect is due to the resonant response distortion. Figure 5 shows the behaviour of the system for C_c = 10 pF and R_L = 50 Ω. As can be seen, the signal from each plate is maximized at the desired frequency, but the maximum of the differential signal, still about 50 μV, is shifted to f = 1.62 MHz. Therefore, a careful selection of the inductance and the frequency is necessary. One can also consider a different setup with one inductance coil only connecting two plates for the direct measurement of the differential signal. In this case, the signal is not increased above the previous value of 50 μV, but the required inductance $L \approx 130$ μH is higher.

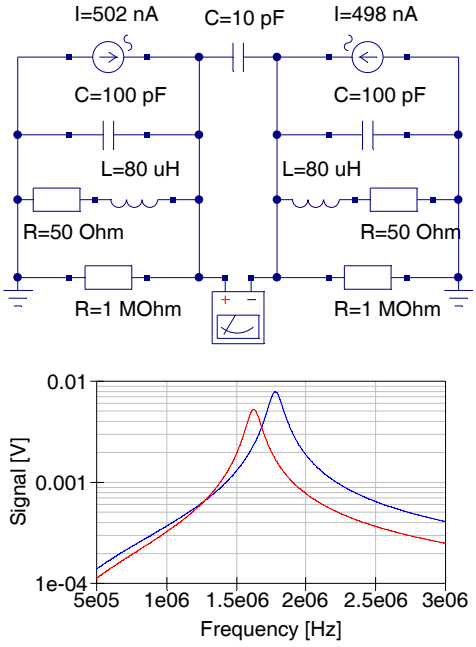


Figure 5: Equivalent circuit of two plates of the resonant capacitive PU and the resulting signal: peak voltage (blue curve) and differential voltage scaled by a factor of 100 for the picture clarity (red curve).

LOW-β EFFECT

The influence of the low β value on the pick-up response should be discussed as well. The sensitivity of the beam position monitor for a logarithmic ratio processing and small beam displacements can be expressed by a relativistic component multiplied by $(1 - G)$, where the correction factor for a non-relativistic beam is approximately [8]:

$$G \approx 0.139 \left(\frac{2\pi f_{RF} r}{\gamma\beta c}\right)^2 - 0.0145 \left(\frac{2\pi f_{RF} r}{\gamma\beta c}\right)^3 \quad (1)$$

Figure 6 shows the pick-up sensitivity deviation from the relativistic case for 300 keV and 20 keV beams. As can be noted, the correction factor increases with the increasing harmonic mode, but for the considered standard operation of the USR it should still be as low as 0.5%.

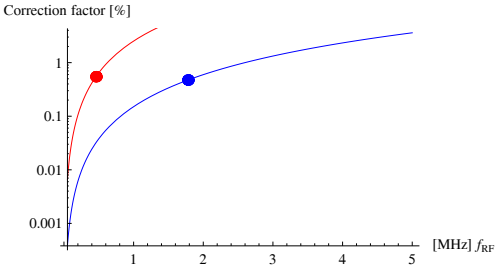


Figure 6: Correction factor calculated for 300 keV (blue) and 20 keV (red) bunches as a function of their repetition frequency (dots correspond to harmonic mode $h = 10$).

CONCLUSIONS

The studies of the foreseen capacitive pick-up design were presented. The diagonal-cut plates assure high linearity of the monitor, whereas grounded rings provide its greater sensitivity. Due to a very low number of particles and a low signal-to-noise ratio, a narrowband system is required and it has been decided to adopt a resonant circuit solution. Although the values of the considered circuit parameters were only estimated, the study provided an insight into the behaviour of the proposed system and the differential signal at least several times stronger is expected. Finally, it was shown that the sensitivity of the PU is strongly dependent on a harmonic mode h and not the β value itself.

REFERENCES

[1] C.P. Welsch and J. Ullrich, "FLAIR – a Facility for Low-energy Antiproton and Ion Research", Hyperfine Interact. 172, 71-80 (2006).

[2] A. Papash, C.P. Welsch, "On the Possibility of Realizing Shortest Bunches in Low-energy Storage Rings", Phys. Part. Nucl. Lett. 6(3), 216-226 (2009).

[3] P. Kowina et al., "Optimisation of 'Shoe-Box Type' Beam Position Monitors Using the Finite Element Methods", DIPAC'05 Proc., Lyon, France, 114-116 (2005).

[4] H. Koziol, "Beam Diagnostics for Accelerators", CERN Accelerator School, Loutraki, Greece (2004).

[5] M. LeGras et al., "The Closed-orbit Measurement System for the CERN Antiproton Decelerator", DIPAC'99 Proc., Chester, UK (1999).

[6] P. Strehl, "Beam Instrumentation and Diagnostics", Springer (2006).

[7] R.E. Shafer, "Beam Position Monitoring", AIP Conf. Proc. 212, 26-58 (1990).

[8] R.E. Shafer, "Beam Position Monitor Sensitivity for Low-β Beams", AIP Conf. Proc. 319, 303-308 (1994).

AN FPGA BASED DATA ACQUISITION SYSTEM FOR A FAST ORBIT FEEDBACK AT DELTA

G. Schuenemann, P. Hartmann, D. Schirmer, P. Towalski, T. Weis, K. Wille,
DELTA, Technical University of Dortmund, Germany
P. Marwedel, Technical University of Dortmund, Germany

Abstract

The demand for beam orbit stability for frequencies up to 1kHz resulted in the need for a fast orbit position data acquisition system at DELTA. The measurement frequency was decided to be 10kHz which results in a good margin for 1kHz corrections. It is based on a Xilinx University Program Virtex-II Pro Development System in conjunction with an inhouse developed Analog-Digital Converter board, featuring two Analog Devices AD974 chips. An inhouse developed software written in VHDL manages measurement and data pre-processing. A communication controller has been adopted from the Diamond Light Source [1] and is used as communication instance. The communication controller is versatile in its application. The data distribution between two or more of the developed measuring systems is possible. This includes data distribution with other systems utilizing the communication controller, e.g. the Libera beam diagnostic system[1].
To enhance its measuring capabilities one of the two onboard PowerPC cores is running a Linux kernel. A kernel module, capable of receiving the measurement data from the Field Programmable Gateway Array (FPGA) measurement core, was implemented [2], allowing for advanced data processing and distribution options. The paper presents the design of the system, the used methods and successful results of the first beam measurements.

INRODUCTION

Since DELTA faces the demand for improved beam orbit stability for supplying a higher brilliance synchrotron radiation, a suitable data acquisition system for fast orbit feedback had to be found. Measurements regarding the electron beam disturbances have shown a variety of sources [5]. Slow orbit shifts have been observed, caused by thermal drifts on a day to week scale. In addition ground motion and girder movement in the low frequency range of up to 10Hz (DELTA girder resonance) have also been observed. On the other hand much faster excitation is caused by the mains power frequency of 50Hz and its harmonics up to 300Hz. The existing analog position measurement system used for the slow orbit feedback at 0.1Hz may be operated at a maximum orbit position data rate of 10kHz. To exploit this capability a most versatile adoption to this data had to be found and a data acquisition system had to be designed and implemented without any interference with the existing global slow orbit feedback system, which is supplied with orbit data from the same orbit calculating devices. This approach includes cost effectiveness (by using existing orbit electronics) as well as modularity (modular system) and versatility (broad range of communication options).

GENERAL LAYOUT

DELTAs orbit feedback is a classic control loop. The data is acquired, corrections are calculated and applied to the beam by means of magnetic fields. Modern fast orbit feedback systems [1, 3] are based on turn-by-turn (TBT) beam position data reduced to kHz bandwidth. Only a minor number of Deltas BPMs are TBT measurement capable. Therefore the idea to use the existing analog Bergoz MX-BPMs in combination with TBT capable devices for a fast orbit data acquisition system came up. To achieve the systems desired versatility and modular design a decentralized solution was chosen. Initial design ideas were adopted from the concept of the Libera Electron fast orbit feedback at Diamond Light Source, England, including data interchange with any device running the underlying communication structure, the Diamond Communication Controller (DiamondCC) [1].

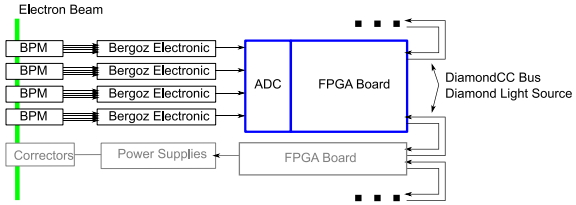


Figure 1: Data acquisition system (DAQ) layout. Additional bus participants can be connected if desired.

The system follows the idea of a classic control loop (see figure 1). The electron beam induces a voltage on the four beam pickup buttons. The position of the electron beam is calculated by the Bergoz MX-BPMs. The analog position value is then digitized by an ADC-board and transferred to the FPGA being part of the Xilinx University Program development board [6]. The FPGA takes over the task of pre-processing and then distributing the data amongst the feedback participants. These are typically either data pickup stations, correction calculation instances or data logging devices. The DiamondCC is the communication instance used for this data distribution. It features a synchronized, global position data exchange on a fast time basis, thereby avoiding the common bottleneck for orbit feedback applications. Adjustment to the possible maxi-

[1]Instrumentation Technologies d.o.o., Solkan, Slovenia

mum number of bus participants is accomplished through the number of communication interfaces. The necessary correction is then calculated by each corrector station and applied accordingly (see figure 1).

ORBIT POSITION GENERATION & DATA READOUT

The analog orbit position data at DELTA is generated by Bergoz MX-BPMs. These analog electronics use a multiplexer to sample each of the four orbit position pickup button signals to make use of a single amplifier stage and an additional sample/hold and position calculating circuit [4]. Due to the input multiplexing technique used, the maximum position data output rate is a quarter of the multiplexing frequency. Without a possible external clock this frequency is coasting with approximately 8kHz, resulting in a 2kHz position data rate. The maximum specified operation range however is a 40kHz multiplexer frequency creating a 10kHz position data rate. Measurements have shown that the MX-BPMs indeed are able to run at 40kHz, the only drawback being a fluctuation of the position signal at the start of the multiplexing cycle. Fortunately the start of this cycle is indicated by a trigger, thus making a workaround to this problem by clever timing possible (see figure 2).
These demands resulted in the development of the data readout board. The core component is the Digital Analog Converter, in our case the AD974 by Analog Devices was chosen, having a 16Bit, 200kHz data conversion rate in the required voltage range. Additionally it features four multiplexed inputs. It was decided to use one AD974 chip for the horizontal plane and one AD974 chip for the vertical plane. By using the multiplexing feature four Bergoz MX-BPMs can be read out with one ADC-Board. The data rate is split into a four times 50kHz signal rate, resulting in an five times oversampling of each Bergoz MX-BPM position signal. To enhance the signal quality and to filter higher frequency artefacts an optional 10kHz lowpass-filter for the input signal was integrated into the board. Apart from the data conversion part the ADC-board integrates the signal connectors for the additional control signals provided by the Bergoz MX-BPMs, e.g. the multiplexer sequence start signal (SYNC). Two additional triggers and two additional clock inputs are also installed for future use. As the communication of the FPGA-board requires special clocking, the quartz and suitable connectors are also installed on the printed circuit board.

ADC CONTROLLING & READOUT TIMING

The readout of the two ADCs is accomplished directly from the FPGA on the FPGA-board. The AD974 features different readout modes, set by configuration signals. In our case the fastest possible mode has been chosen. Due to internal design this is also the mode ensuring highest conversion precision [7]. The conversion is initiated by the FPGA. The conversion result, the digitized analog value, is then transferred from the ADC to the FPGA during the next conversion cycle. Special care has been taken on the FPGA side to synchronize the two AD974 chips and to detect possible errors. Two ensure a high quality readout signal a special, additional timing block was created on the FPGA.
The reason for this is the structure of the Bergoz MX-BPMs. Since four MX-BPMs are usually connected to one ADC-board, each multiplexer runs at a random clock around 8kHz. As soon as the external 40kHz clock is applied, the multiplexers start to run synchronized, except for the cycle of each individual multiplexer (from button one to button four), which is again random and indicated by the SYNC signal (see figure 2). This SYNC signal spoils the position readout. The workaround found is the application of the following procedure: Enabling of the external clock, checking whether the sequence of SYNC signals is suitable and re-applying the clock if necessary, hoping for a drift during the non-clocking period.

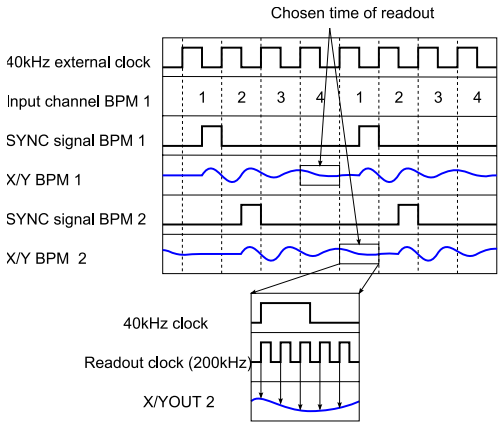


Figure 2: Signal sequence of two BPMs. The SYNC signal, always at position 1 of the Bergoz MX-BPMs multiplexer distorts the output signal. The time of readout has been adopted to the least distorted region of the signal.

Once a suitable sequence is found, the readout sequence is adjusted accordingly. The system is designed fault tolerant, thereby the number of Bergoz MX-BPMs is completely variable from one to four including hot-plugging.

DATA PRE-PROCESSING

In the ideal case one complete readout sequence takes $100\mu s$, resulting in four (one from each MX-BPM) times five (readouts of one position) by two (horizontal and vertical plane) datasets. At present only a very limited preprocessing of this data is undertaken. The last of each of the five position values is discarded and the other four are averaged for higher precision. These four by two datasets are then passed on to the communication instance.

DIAMOND COMMUNICATION CONTROLLER

Developed for the fast orbit feedback system at the Diamond Light Source, the DiamondCC has been designed for fast global data exchange. The communication is based on point to point two way connections, eliminating data collision problems. It is synchronized, clocked and deterministic. A trigger network connects all communication participants for synchronization. Once synchronized, the communication is split into 10kHz frames, each frame is completed when all position data is globally exchanged. It is a distributed communication protocol without a central server. The communication structure can be user-specified. Specific demands like fault-tolerance, lower delay or a varying number of communication participants can easily be implemented [1].
The DiamondCC was integrated onto the FPGA after adoption to the specific needs of this application. The DiamondCC was designed for I-Tech Libera Electron [8], therefore its data retrieval is adjusted to the Libera data chain. This data chain has been adopted to our ADC-Board. The most prominent alteration is the existence of four position values instead of one.

EXTERNAL CONNECTION

Instead of using the slow and the fast orbit data acquisition in parallel, a single fast data source with a reduced data rate to run a slow orbit feedback reduces the amount of complexity. The present control system has no DiamondCC interface, hence the PowerPC cores available on the FPGA fabric are utilized for this purpose. The averaged data is transferred from the pure FPGA side to one of the PowerPC cores running Linux. This enables a data exchange with an easily accessible system [2].

SOFTWARE DESIGN

The software has been designed and implemented in VHDL. The ADC-Board is controlled by the Bergoz Control unit, taking care of clocking, SYNC signal processing and readout timing. A second entity, the ADC Control Module, is solemnly for the control of the AD974 chips and reception of the digitized data. The data is passed on to the data processing unit and then on to the DiamondCC. The DiamondCC is controlled from the control module containing all global configuration informations and settings.

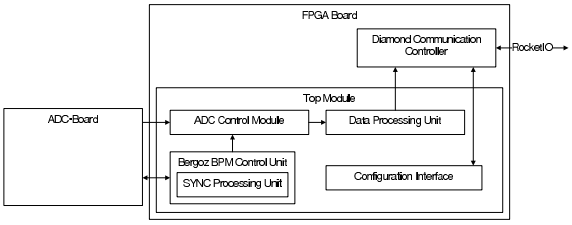


Figure 3: DAQ software layout.

CONCLUSION

The data acquisition system has proven its functionality in test measurements with beam (see figure 4) showing its broad capabilities as DAQ for a global fast orbit feedback. In a first step a local fast orbit feedback, using this fast communication structure, has been implemented successfully by P. Towalski [5]. In addition calculations have shown a precision increase in the order of one magnitude concerning the slow orbit feedback position data.

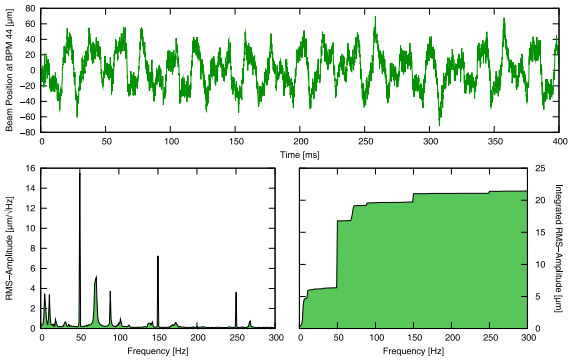


Figure 4: Horizontal beam position versus time (top), spectral rms orbit deviation versus frequency (bottom left) and integrated power density spectrum (bottom right).

ACKNOWLEDGEMENTS

I would like to thank the Diamond Light Source, Didcot, U.K. for providing the Diamond Communication Controller and assistance, especially G. Rehm, I.S. Uzun, M.G Abbott and N. Hubert from the SOLEIL Light Source, France, for his support on feedback related issues and the electronics lab of the physics faculty, especially N. Koch for his help with designing the ADC-board.

REFERENCES

[1] I.S. Uzun, “Inital design of the fast orbit feedback system for Diamond Light Source”, ICALEPCS, 2005.

[2] Peter Hartmann, DELTA Internal Report, 2008.

[3] N. Hubert, “The SOLEIL bpm and orbit feedback systems”, Proceedings of DIPAC 2007, Venice, Italy.

[4] J. Bergoz, “Multiplexed Beam Position Monitor User’s Manual”, Bergoz Instrumentation,Rev. 1.5.4.

[5] P. Towalski, “Implementation of a FPGA-based local fast orbit feedback at the DELTA storage ring”, DIPAC 2009, Basel, Swiss.

[6] Xilinx Inc., “Xilinx University Program Virtex-II Pro Development System Hardware Reference Manual”, v1.1, 04/2008.

[7] Analog Devices, “AD974 4-Channel, 16-Bit, 200kSPS Data Acquisition System Data Sheet”, Rev. A, 05/1999.

[8] Instrumentation Technologies, `http://www.i-tech.si`

BEAM TESTS WITH LIBERA IN SINGLE PASS MODE

A. Stella, M. Serio, INFN-LNF, Frascati, Italy
S. Bassanese , R. De Monte, M. Ferianis, ELETTRA, Trieste, Italy

Abstract

The single pass functionality available in the recent release of the Libera Brilliance software, takes particular interest when compared with the requirements of FEL machines, that need stable and precise control of the beam trajectory throughout Linacs and transfer lines in order to meet the stringent beam quality and transverse position constraints inside undulators.

Results from tests performed on Libera with beam from ELETTRA, SPARC and DAFNE operating in Sincrotrone Trieste and LNF Frascati are reported to characterize the resolution of single shot transverse beam position measurements.

INTRODUCTION

The Libera Brilliance detection electronics, developed by Instrumentation Technologies, implements the digital receiver technology to measure the beam position.

When used on a machine with stored beams, the narrow band signals from the pickups are downconverted to baseband with an undersampling technique for amplitude measurement.

Nevertheless one can perform accurate measurement of short single bunches signals, typical of transfer lines or Linacs, by working directly on the ADCs samples provided by the same boards used for the storage rings [1].

In the following chapter we report results of single pass tests obtained with beams from different accelerators, acquired as reported in Table 1.

Table 1: Beams parameters during measurements

	Bunch Charge	Acquisition Rate	FWHM Pulse Length
SPARC	0.08 nC	10 Hz	.5 ns
ELETTRA	.01÷1 nC	10 Hz	.2 ns
DAFNE	1 nC	2 Hz	.8 ns

SINGLE PASS DATA

Signals from beam position monitor (BPM) have been connected, through low attenuation coaxial cables, to Libera Brilliance.

Before sampling, the short single pulses are fed to the Libera RF front-end which includes passband filters of bandwidth larger than the accelerator revolution frequency and placed around a center frequency given by the RF frequency.

Raw data are collected from the four 16 bit ADCs buffer at a sampling frequency of ~116.8 MHz, which is customizable for each accelerator. To allow measurement on the stored beam it is usually chosen as a multiple of the revolution frequency. The buffer is 1024 samples long and acquisition can be started by an external trigger.

Beam Position Reconstruction

Stripline BPM have been used. The beam position is reconstructed from the amplitude difference of voltage signals from opposite pickups times the *k* sensitivity, according to:

$$x = k \cdot \frac{\Delta V}{\Sigma V}$$

Different BPM sensitivities *k*, dependent solely on the vacuum chamber geometry, must be taken into account when comparing results (Table 2).

Table 2: Pickup parameter

	BPM type	**chamber**	***k* [mm]**
DAFNE	Short circuited stripline	Circular	18.3 mm
ELETTRA	50 Ω matched stripline	Diamond shape	19.8 mm
SPARC	50 Ω matched stripline	Circular	10 mm

Libera release 2.00 provides a dedicate algorithm working over the raw buffer data and implemented directly onboard, to reconstruct the beam position

The amplitude from each electrode is assumed as the square root of the sum of the squared samples. Data used for this calculation are selected by setting an amplitude threshold on the waveform and taking into account only N points specified with the *pre-trigger* and *post-trigger* Libera parameters [2].

A further algorithm based on the Hilbert transform [3] has been applied offline to the sampled data. In this case the Hilbert transform has been used as amplitude envelope detector on the narrowband ADC samples.

The signal amplitude from each electrode has been extracted from the integral of the envelope amplitude.

RESOLUTION MEASUREMENTS

SPARC, the 150 MeV S-band photoinjector operating in Frascati (Italy) to produce high brightness electron beams for SASE-FEL experiments, has been equipped with stripline BPMs for trajectory measurement. Figure 1 shows a typical signal from a single stripline at the end of the coaxial cable and the sampled waveform available in the Libera ADC buffer.

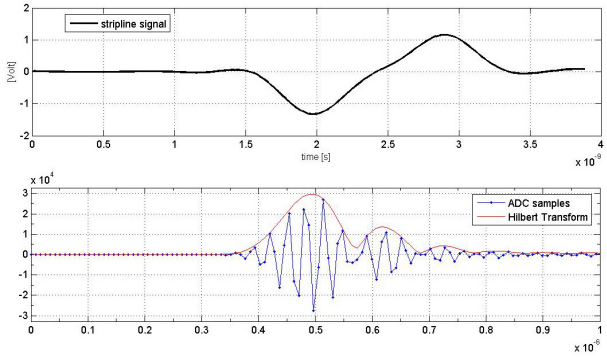


Figure 1: SPARC BPM signal (top) and Libera ADC sampled waveform (bottom), along with the computed Hilbert amplitude.

The data set acquired at SPARC is related to a bunch charge of ~80 pC. The results reported in Fig. 2 show the maximum of Libera ADCs counts for each acquisition on the left and the scatter plot of the beam positions on the right. The measured standard deviations of the (x,y) distributions are respectively 12.6 µm and 14.6 µm. However we cannot exclude a contribution to this values coming from actual beam jitter.

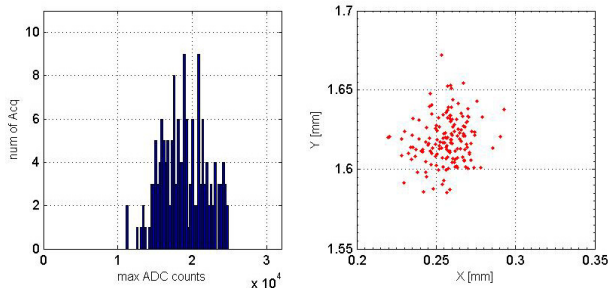


Figure 2: Histogram of maximum of ADC counts (left) and beam position (right) at a particular BPM at SPARC.

Measurements at the Elettra Synchrotron beam have been performed by sampling, at the location of a stripline BPM routinely used for tune measurements, non consecutives passages of a stable stored single bunch with a 10 Hz external trigger synchronous with the RF.

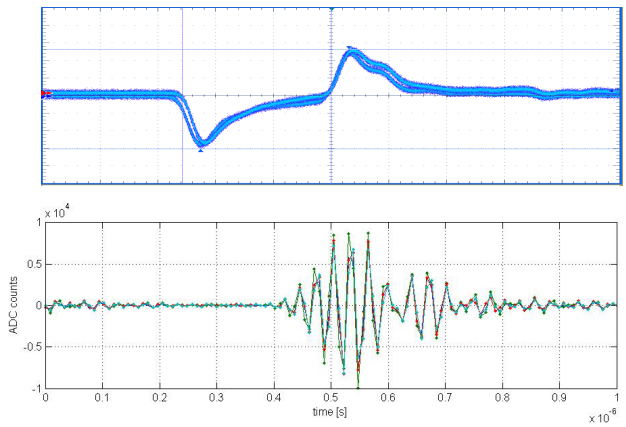


Figure 3: Stripline BPM signals at Elettra [400 mV/div vs 400 ps/div] (top) and Libera sampled data (bottom).

Several data sets of one hundred passages each, performed at different beam current, allowed to characterize the resolution vs. bunch charge. The results are reported in Fig. 4, where the beam position has been calculated using the two different algorithms described above.

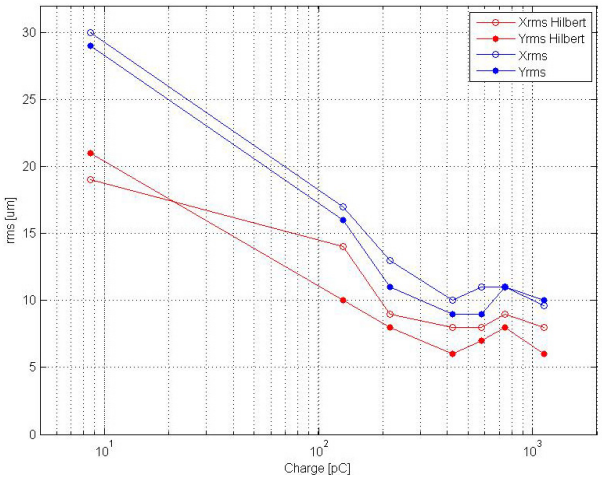


Figure 4: Measured resolution vs. bunch charge at Elettra.

The *Hilbert* method showed better accuracy in the reconstructed position without the needs to specify Libera parameters, at the price of an increased computing load after the acquisition.

A further set of measurements have been performed at a constant bunch current by equally splitting the signal from a single BPM electrode to the four Libera inputs, after the insertion of a variable attenuator.

With this setup, acquisitions for variable input levels have been collected by increasing the Libera sensitivity front-end with the programmable variable attenuators, in order to keep a stable signal level at the ADCs.

In Fig. 5 we report the measured resolution vs. the board sensitivity and the related linearity of the measured positions.

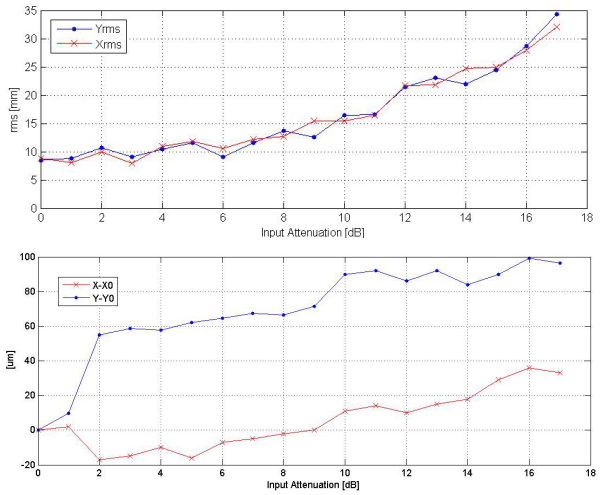


Figure 5: Position linearity (bottom) and resolution (top) vs. Libera input signal attenuation.

Measurements at DAFNE have been performed in the transfer lines used to connect the damping ring to the collider, with a bunch charge of ~1 nC.

Figure 6 (right) reports the histogram of the maximum ADC counts recorded for each acquisition, while Fig. 6 (left) shows beam positions for 100 consecutives pulses.

The (*x*,*y*) distribution is affected by the beam stability of the injection mostly horizontally, due to the operation of a pulsed bending magnet and kickers operating in the horizontal plane.

To evaluate the resolution in the presence of beam jitter, we used a least-square fit to evaluate a linear regression between the positions measured simultaneously at three BPMs over 100 consecutives beam pulses.

The standard deviation of the distribution of the residuals (i.e. the difference between the measured beam position and the predicted position as calculated from the fit equation) has been taken as an estimate of the resolution.

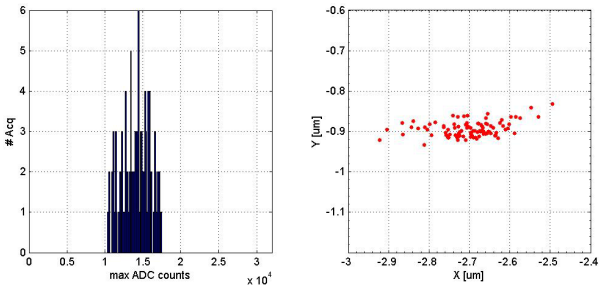


Figure 6: Histogram of maximum of ADC counts (left) and beam position (right) at a particular BPM in DAFNE.

Figure 7-8 show the vertical and horizontal position predicted with the best-fit linear combination of the other BPMs compared with the measured values.

The standard deviation of the residual distribution yielded a resolution of 9.7 μm for vertical position and 12.8 μm for radial position.

It must be noted that the measured resolutions should be related to the vacuum chamber aperture through the *k* constant of each BPM, for DAFNE the radius of the chamber is 37 mm.

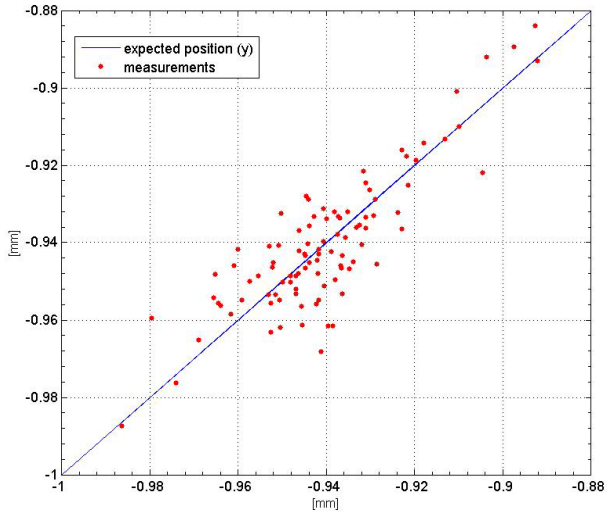


Figure 7: Expected vertical position vs. measured position for the BPSTT03 BPM in the DAFNE transfer line.

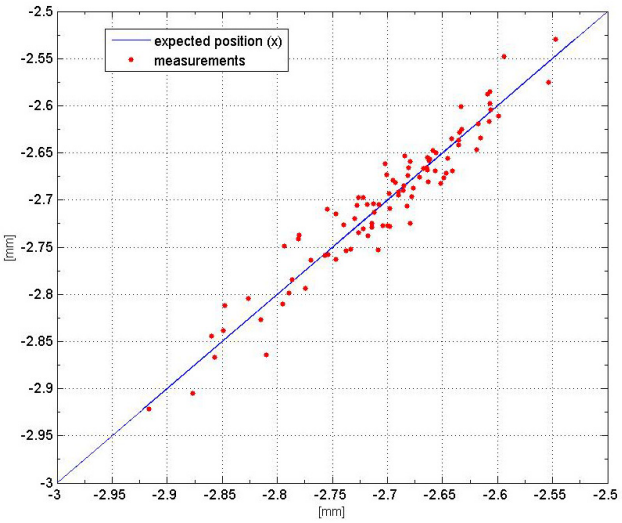


Figure 8: Expected horizontal position vs. measured position for the BPSTT03 BPM in the DAFNE transfer line.

CONCLUSIONS

Tests performed with real beam signals showed the feasibility of using Libera Brilliance for beam position measurements of single pass bunches. Very good results for RMS resolution have been reported.

ACKOWLEDGEMENTS

The authors wish to thank Matjaž Znidarčič (Instrumentation Technologies) for the invaluable help during data taking, O. Coiro, D. Pellegrini and C. Mencarelli for technical support at LNF, G. Di Pirro and G. Gatti for support during measurements at SPARC.

REFERENCES

[1] Instrumentation Technologies: “Libera Brilliance Single Pass Measurements”, (2009), http://www.i-tech.si

[2] Instrumentation Technologies, “Libera Brilliance: User Manual v2.00”, (2008), http://www.i-tech.si/

[3] Papoulis, A.: "The Fourier Integral and Its Applications", McGraw-Hill, (1962).

THE BPM MEASUREMENT SYSTEM IN HIRFL-CSR *

J.X. Wu#, J.W. Xia, G.Q. Xiao, R.S. Mao, T.C. Zhao, Y.J. Yuan, J.H. Zheng, IMP, Lanzhou, China

Abstract

HIRFL-CSR [1], a new heavy ion cooler-storage ring in China IMP, had been installed and started commission from 2005. We report here the BPM system on the main ring (CSRm) and the experimental ring (CSRe). The BPM structure, the signal processing system and on-line measurement experiments are presented. The measurement results such as turn-by-turn bunch observation, closed-orbit measurement, Schottky noise measurement are also presented in this paper.

INTRODUCTION

HIRFL-CSR is a new heavy ion cooler-storage ring synchrotron system in Lanzhou. It consists of a main ring (CSRm) and an experimental ring (CSRe) with multi-usages and multi-functions, shown in Fig. 1. The two existing cyclotrons SFC (K=69) and SSC (K=450) of the Heavy Ion Research Facility in Lanzhou (HIRFL) are used as its injector system. The heavy ion beams from HIRFL with the energy of 7-25MeV/u will be first injected into CSRm, accompanying with the accumulation, e-cooling and acceleration, and finally extracted slowly with the energy of 500-1100MeV/u for many external-target experiments, or extracted fast with the energy of 200-700MeV/u to produce radioactive ion beams (RIBs) or high Z beams at the primary target of the beam line. The secondary beams will be accepted and stored in CSRe for many internal-target experiments. From 2006 to 2008 all the commissioning activities of HIRFL-CSR were made, including stripping injection, multi-turn injection, cooling accumulation with hollow electron beams, ramping in a wide range with different RF harmonics, isochronous mode commission of CSRe, mass measurement of RIBs in CSRe with ToF and slow extraction from CSRm.

As the eyes of an accelerator, the diagnostic system is built together with the construction of the CSR. The whole CSR commission was proceeded and succeeded with the support and help of it. Of course the BPM system is the key part of the diagnostic system. The shoe-box type BPMs are used in CSR because of its good linear dependence with respect to the beam displacement [2]. There are 16 BPMs distributed around the CSRm and 11 around the CSRe. The structure is shown in Fig. 2. The length of the BPM is 300 mm and the cross section is 170*110 mm^2 for the CSRm and 250*130 mm^2 for the CSRe. To avoid the influence of the beam injection and extraction of the CSRm, the dimension of the BPM at these two positions is larger than others and its cross section is 240*170 mm^2.

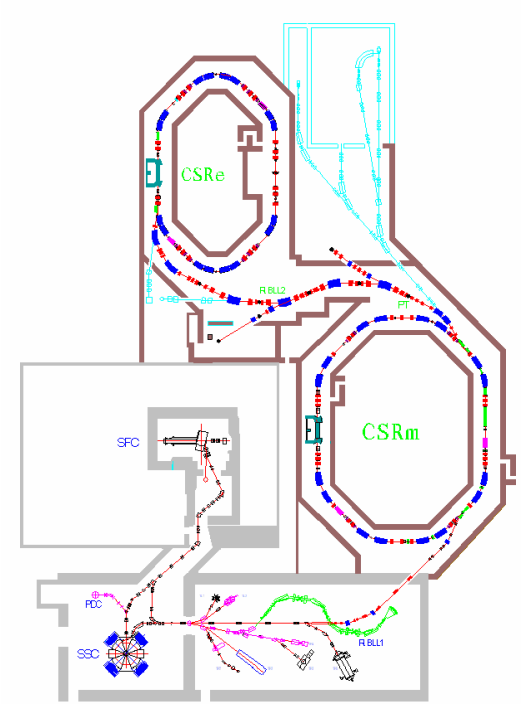


Figure 1: Overall layout of HIRFL-CSR.

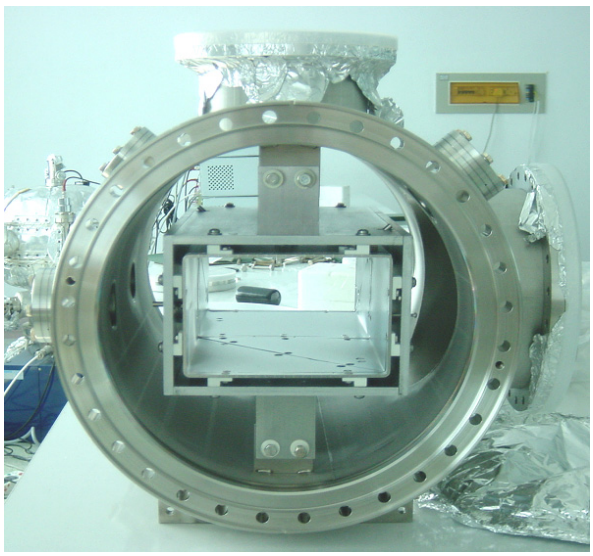


Figure2: The BPM structure of HIRFL-CSR.

BPM PROCESSING SYSTEM

As the beam frequency is low in CSR and the range of the frequency is 0.25~1.7MHz in CSRm and 0.5~2.0MHz in CSRe. So the broadband processing is used in the CSR BPM system, as in Fig.3. After pre-amplification, the BPM signal is directly digitized by a fast ADC. The low-noise amplifier has the bandwidth of DC-1GHz, the gain of 52dB and the noise figure of 1.7 $\mu V/\sqrt{Hz}$. It has a

*Work supported by the center government of China and NSFC
#wujx@impcas.ac.cn

good stability and linearity in the dynamic range. Then the plate signal is digitized with the NI PXI-5105. This digitizer has a 12-bit vertical resolution rate, 60 MS/s real-time sampling rate and 60 MHz analog bandwidth. After that, the digitized signals are done by the LABVIEW software to get the beam signal, beam position and orbit, to do the Fourier transform to get the beam frequency, energy, frequency spread and also the tune value of the machine and so on. The trigger of the ADC is from the accelerator trigger system and the sampling time can be controlled precisely. We can also put the amplified pickup signal directly into the spectrum analyzer through the switch to look at the longitudinal or transverse spectrum, the ramping process and to do the Schottky noise analysis.

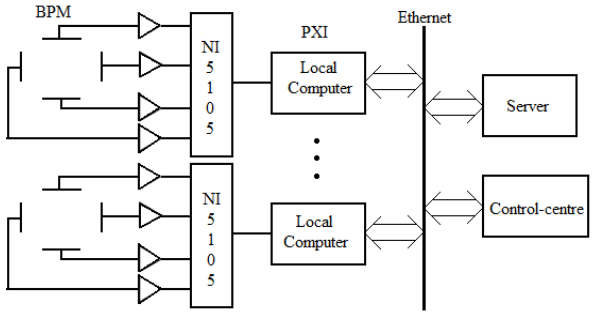


Figure 3: BPM processing system setup.

BEAM MEASUREMENT RESULTS

The BPM system played a vital role during the commissioning of the HIRFL-CSR. As mentioned above, we use the broadband processing system, so the single bunch can be monitored, turn-by-turn [3]. Figure 4 is the stored beam signal of C^{6+}- 6.89MeV/u from a BPM at the beginning of the CSRm commissioning. In this case the RF system of the CSRm wasn't used, thus the bunched beam from the cyclotron SFC would become as a costing beam gradually after the single-turn stripping injection, and the beam signal from BPM also became weak turn by turn. At the 20th turn the beam signal had already become very weak. Figure 5 is the BPM signals measured from a C^{6+} beam with the energy of 600MeV/u in CSRe. The four channels from up to down correspond to the signals from four electrodes of one pickup: left side and right side for horizontal measurement, upside and downside for vertical measurement. From that we can see that there was an oscillation in the vertical direction. The interval between the two signals is 0.557μs and that was the right revolution time of the beam at that energy in the CSRe.

Figures 6 and 7 are the longitudinal and transverse Schottky spectrum measurement in CSRe done by the LABVIEW software. From the results we got that the momentum dispersion was 2.39E-4, the tune value in x plane was 2.5177 and in y plane it was 2.5239. The designed tune value is 2.5300 in horizontal plane and 2.5258 in vertical plane. In Fig 7 there are 4 sidebands in each plane. But two of them are real transverse sidebands and the other two are the coupled signals from the other plane. We judged that by adjusting the corresponding quadruple magnet, if we adjust the quadruple strength in horizontal direction, then the horizontal sidebands would move, so from that we could distinguish them.

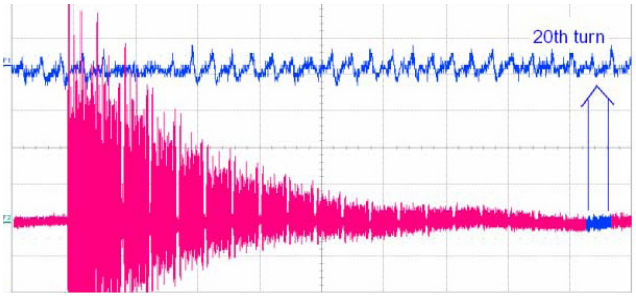


Figure 4: The stored beam signal from BPM in CSRm.

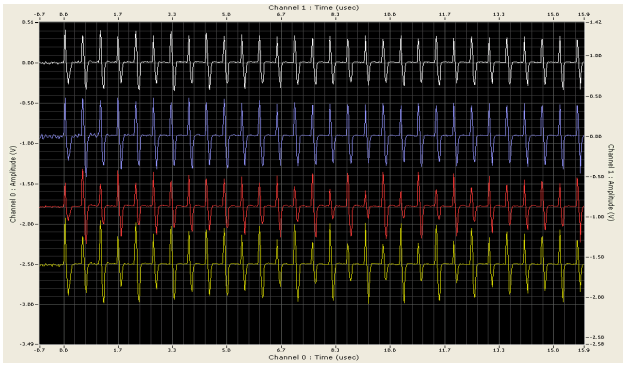


Figure 5: BPM signal from CSRe.

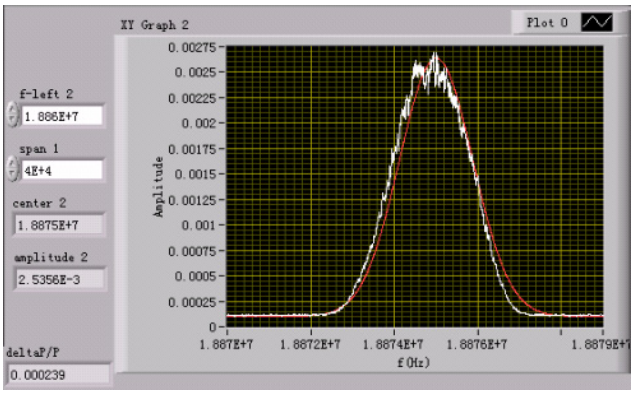


Figure 6: Momentum dispersion measurement in CSRe.

The closed-orbit measurement and correction were also done with the BPM system. Figure 8 is one of the closed-orbit measurement results in horizontal and vertical plane of CSRm. Furthermore, the BPM system can give the information about betatron and synchrotron oscillations, transfer functions, betatron amplitudes, and many other static and dynamic beam parameters.

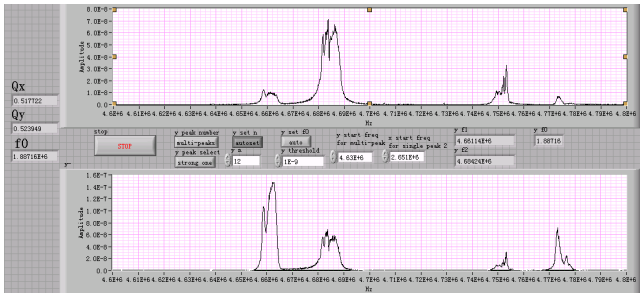


Figure 7: Tune measurement in CSRe.

.

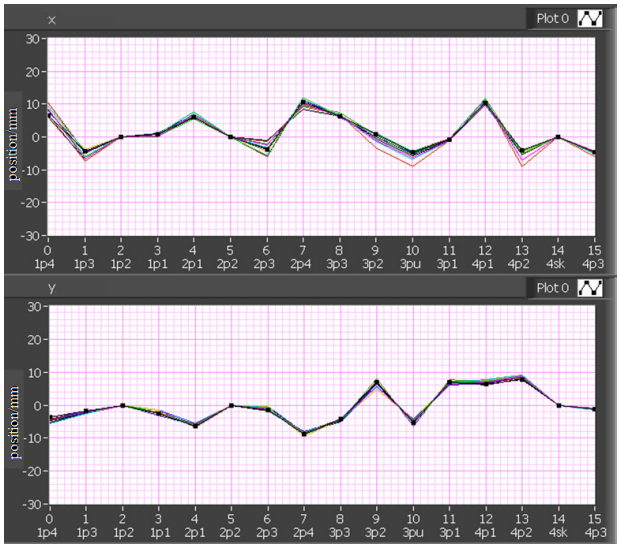


Figure 8: Closed orbit measurement of CSRm.

CONCLUSION

So far the BPM system has been successfully used in HIRFL-CSR. But for very weak beam or single particle measurement, it is impossible because the sensitivity is too low and the noise is too large. Now we are doing a resonant pickup to measure the very weak beam or single particle.

REFERENCES

[1] J.W. Xia et al, "Construction and commissioning of the HIRFL-CSR", APAC'04, Indore, India, Feb. 2007, THXMA03, p. 534.

[2] Peter Fork, "Lecture Notes on Beam Instrumentation and Diagnostics", Joint University Accelerator School, January – March 2008.

[3] G. Vismara, "The comparison of signal processing systems for beam position monitors", DIPAC 1999, Chester, UK, p.12.

BPM SYSTEM AND FAST ORBIT FEEDBACK UPGRADE FOR THE TAIWAN LIGHT SOURCE

C.H. Kuo, P.C. Chiu, K. H. Hu, Jenny Chen, C.Y. Wu, Demi Lee, K.T. Hsu
NSRRC, Hsinchu 30076, Taiwan

Abstract

The BPM electronics of the Taiwan Light Source (TLS) have been upgraded to the Libera Brilliance in August 2008 to improve performance and functionality. Orbit feedback system is also migrated into fast orbit feedback system to enhance orbit stability. Infrastructure of the orbit acquisition system and orbit feedback system has been reconstructed to accommodate the new BPM electronics and to satisfy requirements of fast orbit feedback loops. Gigabit Ethernet grouping was adopted for the data transfer of 10 KHz rate orbit date to the orbit feedback system. The efforts and performance of this upgrade will be summarized in this report.

INTRODUCTION

Orbit stability is an extremely important for a modern synchrotron light source. Generally, beam motion should be less than 10 % of its beamsize or even smaller. There are many efforts make to improve orbit stability of Taiwan Light Source (TLS) such as control of the ambient environment, removing various mechanical vibration passively, feed-forward compensation of insertion devices, locating faulty power supply and etc. Nevertheless, the limited loop bandwidth led incapability to suppress fast orbit excursion above 6 Hz. The fast orbit feedback system was thus proposed. The commissioning of the new fast orbit feedback system will come to an end soon. In the report, the upgrade progress and performance of the BPM system will be presented. Measurement of the system response and latency are discussed next. Finally, the infrastructure and performance of fast orbit feedback are summarized.

BPM SYSTEM UPGRADE AND ACQUIRED DATA MEASUREMENT

The Libera Brilliance [1] is employed to replace the existed BPM electronics for the TLS. Its integration started from 2007 until finish in August 2008. It was gradually deployed and performed without interfere routine operation. There are 59 Libera Brilliances online operation for more than 8 months. The adequate long-term reliability has been achieved. The typical Libera acquired slow and fast data which are extreme critical for FOFB performance will be shown in the latter.

Libera Grouping

The Libera provided a Gigabit Ethernet interface to transfer data with 10KHz update rate. The data sending in the same time, there is network packet collision and interrupt queue over buffer problem in the receiving node. That will take fatal jitter effect and data lost. To eliminate this phenomenon, Libera Brilliance units are grouped together by a redundant multi-gigabit links via the LC optical links and copper “Molex” cables. This link can exchange the data among all Libera Brilliance units to be a single and large packet size by FPGA and send the gathered data via Gigabit Ethernet. It is effective to reduce the packet numbers in network, banish jitter and data lost in the communication with processor [3,4].

Fast Data

Resolution is an important issue for fast orbit feedback system. The resolution of the Liberas FA data at 10 kHz is around 0.2~0.3 μm when the simulated beam current intensity is operated at 300 mA. Each unit slightly differs while the whole of 59 Liberas should be within 0.35μm.

Slow Data

Vertical orbit data is shown as Fig. 1. The standard deviation is around 0.1~0.8 with real beam corresponding to respective location.

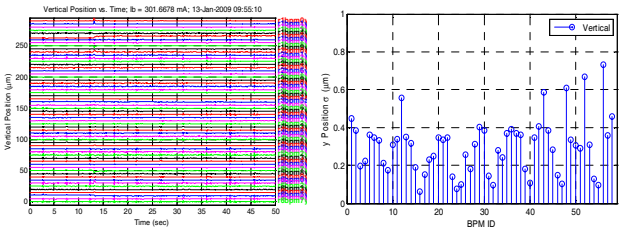


Figure 1: Slow data of vertical position and its RMS value.

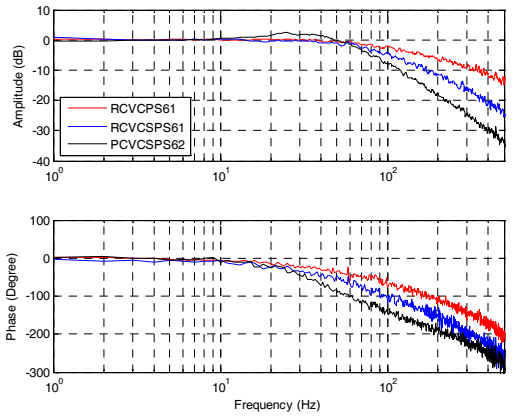


Figure 2: Three vertical correctors’ (RCVCPS61, RCVCSPS61, RCVCSPS62) response functions.

VARIOUS SYSTEM MEASUREMENT SUMMARY

There are several kinds of corrector magnets installed in the TLS due to historical reasons. They have different response. To understand the compound response of the power supplies, correctors, vacuum chamber and the stored beam, pseudo-random binary sequence (PRBS) excitation is employed to measure system response and latency.

Open Loop System Response

The various correctors are installed in the storage ring of the TLS at different period section; Fig. 2 shows the overall PRBS response of the three vertical correctors in section R6. It includes power supply, corrector, vacuum chamber, correctors to BPM readings. The dynamics of these three correctors differ from each other. There are some vertical correctors' bandwidth that can achieve to 80 Hz, but others may be below 30 Hz, through measurements around the whole storage ring. Choosing the proper correctors for FOFB is thus necessary.

Latency Time Evaluation

The estimated I/O latency time is around 500 μsec of which is at the peak location of the cross-correlation function between the corrector action and BPM response, as shown in Fig. 3.

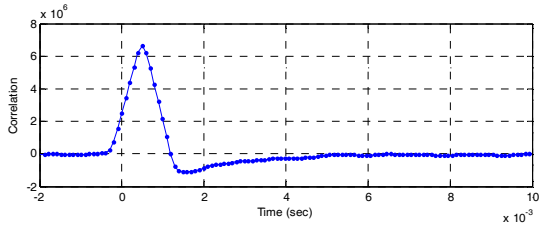


Figure 3: Cross-correlation function of PRBS sequence and BPM reading, the peak location corresponding to the overall latency from the DAC output the BPM reading.

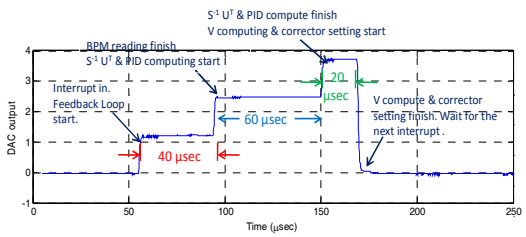


Figure 4: DAC output level is changed when each computing step is finished. The interval between two adjacent difference levels represents the respective latency for each computation.

Processing latency of the data acquisition and computation are also detailed evaluated as Fig. 4. Transfer BPM data, rearrangement and scaling takes around 40 μsec; $S^{-1}U^{T}$ matrix (response matrix $R=USV^{T}$) and PID computation around 60 μsec; V matrix computation and DAC settings 20 μsec. The time for whole feedback loop takes about 120 μsec. It infers that we can push feedback sampling frequency from the current 1.25 kHz to higher frequency under constrains of the current orbit feedback infrastructure which is implemented in economic way. The overall latency time is about 620 us that includes of calculation, chamber eddy current effect, bpm reading and corrector setting delay,… etc.

FOFB INFRASTRUCTURE AND ALGORITHM

The infrastructure of the new orbit feedback system is shown in Fig. 5. The orbit controls for the horizontal and vertical plane are separated from the old version to increase available computation power. The reflective memory is employed to shares fast orbit data without consuming extra CPU resource and support data acquisition for other subsystems.

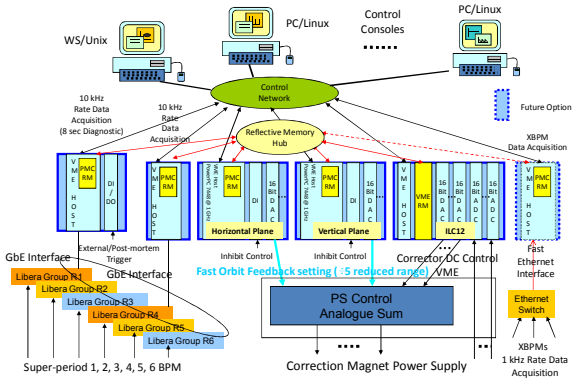


Figure 5: Infrastructure of the new FOFB and the related subsystems

Tikhonov Regularization

Orbit response matrix R is a linear mapping, between the orbit and the steering magnet relation. Singular value decomposition, as a most commonly is used to invert this mapping in the feedback correction algorithm [5,6]. Furthermore, to obtain a stable solution, Tikhonov regularization is also adopted [3,6].

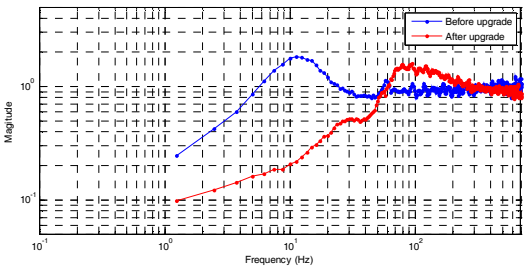


Figure 6: Noise sensitivity function comparison before and after FOFB upgrade.

PRELIMINARY PERFORMANCE TEST

Noise Sensitivity Function Measurement

The bandwidth and performance of FOFB are measured and estimated by PRBS. Fig. 6 shows that the new FOFB is promoted to suppress noise of bandwidth to around 60Hz from old 6Hz system after all components are upgraded. The new BPM performance in wideband is better than before. As a result, vertical orbit stability can be reasonably expected down to submicron from DC to 60Hz.

Orbit Stability for User Operation

The feedback system can improve beam stability as shown in Fig. 7 and Fig. 8. The standard deviation of all BPM reading can be reduced to 0.2 um from 0.8 um between feedback on and off in the normal user mode for vertical plane. Both of horizontal and vertical orbit displacement can be less than one micron in SA readings.

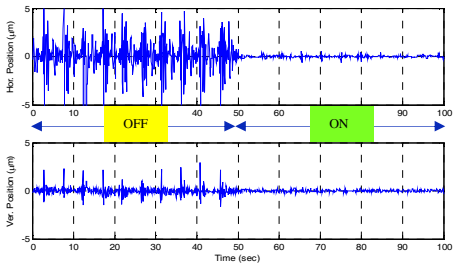


Figure 7: R6BPM7 SA data for FOFB ON/OFF.

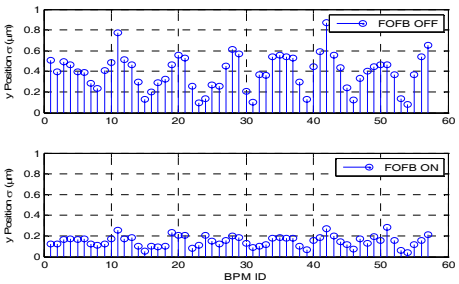


Figure 8: The standard deviation of vertical orbit displacement between FOFB on/off.

Figure 9 shows the R6BPM7 FA data spectrum comparison when FOFB on and off. The orbit stability can be suppressed to one micron at this location with higher β function therefore the overall RMS orbit stability should be submicron from DC to 50 Hz.

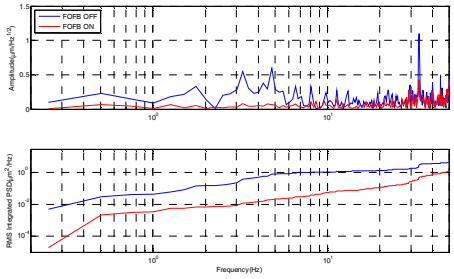
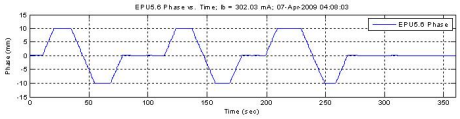


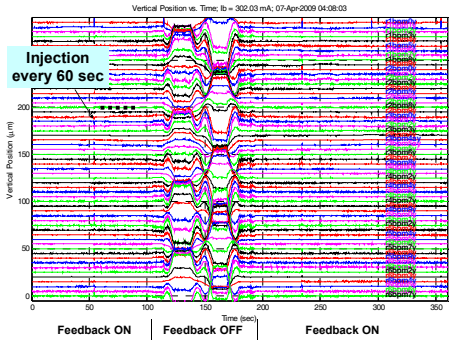
Figure 9: The spectrum and integrated PSD of R6BPM7 for FOFB on/off.

Effects of FOFB for Insertion Device Operation

Fast operations of gap and phase of the insertion devices are highly desirable. However, the old orbit feedback loop cannot effectively suppress the orbit excursion when insertion devices gap or phase motion is fast than the limited component and bandwidth. The wider bandwidth of the new orbit feedback loop can promote the motion speed. Fig. 10(a) shows the 1 mm/sec phase move of the EPU5.6. The orbit displacement is shown in Fig. 10(b). It is clearly observed that the feedback loop can eliminate the orbit excursion.



(a) History of the EPU5.6 phase motion at speed of 1 mm/sec.



(b) Beam position reading of all BPMs

Figure 10: Effect of the new FOFB to suppress orbit excursion of 1 mm/sec phase change of EPU5.6.

SUMMARY

Infrastructure of the FOFB for TLS has been revisited. Commissioning of the FOFB system is on going. Various R&D including modelling, measurement, control rules, and etc. are in proceed. Preliminary results and many exercises confirmed that the FOFB system effectively improve orbit stability.

REFERENCES

[1] I-Tech website: http://www.i-tech.si.
[2] C. H. Kuo, et al., "Fast Orbit Feedback System Upgrade with New Digital BPM and Power Supply in the TLS", DIPAC'07
[3] C. H. Kuo, et al., "Fast Orbit Feedback System Commissioning of the TLS", PAC'09
[4] A. Bardorfer, et al., "LIBERA GROUPING: Reducing the Data Encapsulation Overhead", Proceedings of the EPAC08, TUPC003
[5] A. Terebilo, et al. "Fast Global Orbit Feedback System in Spear3", EPAC06.
[6] J. Rowland, et al. "Status of The Diamond Fast Orbit Feedback system", ICALEPCS07.

PHOTODIODE-BASED X-RAY BEAM-POSITION MONITOR WITH HIGH SPATIAL-RESOLUTION FOR THE NSLS-II BEAMLINES*

P.S. Yoon†, NSLS-II, Brookhaven National Laboratory, Upton, NY 11973 USA
D. P. Siddons, NSLS, Brookhaven National Laboratory, Upton, NY 11973 USA

Abstract

We developed a photodiode-based monochromatic X-ray beam-position monitor (X-BPM) with high spatial resolution for the project beamlines of the NSLS-II. A ring array of 32 Si PIN-junction photodiodes were designed for use as a position sensor, and a low-noise HERMES4 ASIC chip was integrated into the electronic readout system. A series of precision measurements to characterize electrically the Si-photodiode sensor and the ASIC chip demonstrated that the inherent noise is sufficiently below tolerance levels. Following up modeling of detector's performance, including geometrical optimization using a Gaussian beam, we fabricated and assembled a first prototype. In this paper, we describe the development of this new state-of-the-art X-ray BPM along the beamline, in particular, downstream from the monochromator.

MOTIVATION

The end stations for user's experiments at NSLS-II are located far from the X-ray sources. Hence, a small number of displacement- and angular-errors in a radiation source can degrade the end experiments. Accordingly, there is a pragmatic demand for a novel X-ray beam-position monitor (X-BPM) with high spatial resolution. A suite of six project beamlines under design are to be commissioned in the NSLS-II infrastructure[1]. A new X-BPM system developed specifically for these beamlines will serve as a diagnostic device for aligning beamline components and for real-time monitoring of a series of the beamline optics elements. The beam shape changes during its transportation through various optical elements. Therefore, it is anticipated that the performance of the new X-BPM will be less dependent upon the beam optics. Moreover, the mode of operation should affect the beam as little as possible to meet the stringent requirements for beam stability.

PHOTODIODE-SENSOR DESIGN

Figure 1 depicts the ring array of 32 photodiode pads that were designed and fabricated at in-house facilities[1]. Boron ions are implanted on the front side of the wafer through 1 kA oxide, forming a p-n junction[2]. Phosphorous ions are implanted on the back side to make an ohmic contact with the front side. All 32 pads, configured as a polar array, are positioned between an inner ring radius of 5,050 μm and an outer ring radius of 6,763 μm. The active surface area of each pad is about 2.0 (mm^2), and each photodiode is 470-μm thick. In the photoconductive mode, the photodiodes are operated with reverse bias voltage of about 100. Upon impinging on a scatterer as a source of fluorescence radiation, the incident X-ray beam scatters and isotropically illuminates the backside of the ring photodiode. The photon sensor was devised for both back-side and front-side illumination. Our first prototype adopts a scheme of forward scattering using a silicon-nitride (Si_3N_4) substrate metalized with different species such as Cr, Ni, Ti, and Au. As Fig. 2 illustrates, the next version will utilize a backward-scattering scheme, employing *bi*-HERMES4 configuration that will be implemented later in the electronic readout.

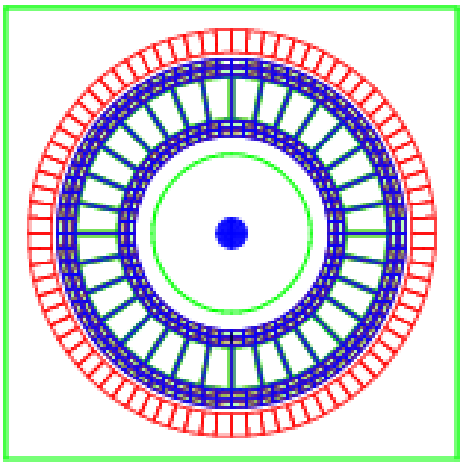


Figure 1: The ring array of segmented Si photodiodes. – drawing courtesy of the Instrumentation Division of BNL.

ELECTRICAL CHARACTERIZATION OF PHOTODIODE SENSOR

Achieving the desired level of detector performance requires a detailed electrical characterization of the optical sensor of the position-monitoring system. Hence, we undertook a comprehensive evaluation of each individual segment on the photodiode ring prior to completing the assem-

* This work was supported by the Department of Energy under contract number DE-AC02-98CH10886.
† yoon@bnl.gov
[1] There is a one-on-one correspondence between 32 pads and 32 ASIC channels.

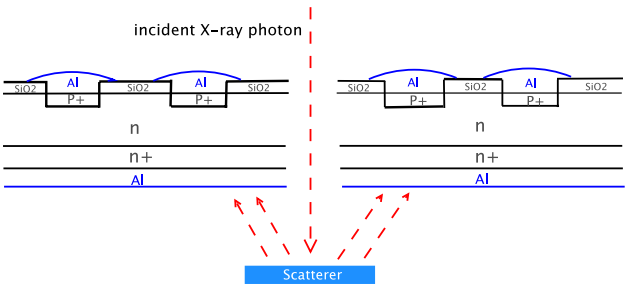


Figure 2: A schematic illustration of the backward-scattering scheme and the structure of the PIN-junction photodiode.

bly of our prototype detector. The inherent noise is reduced by reducing capacitance, followed by the segmentation of a photodiode array in parallel connections. I-V characteristics are acquired by sweeping the DC reverse-bias voltage, V_{rb} from 0 (V). One main design consideration for the ring-array Si photodiode is to ensure that most of an incident X-ray photon is absorbed within the depletion region of a reverse-biased junction. Because of the considerable width of depletion region (a few hundred μm), we selected the PIN junction. As shown in Fig. 3, leakage current measured from one pad is linear against the increasing reverse bias voltage on a log-log scale. Up to the operational bias voltage of 100 (V), the leakage current is held at the order of nA. As Fig. 4 shows, the depletion region is created at around 200 (V) from the C-V characteristic.

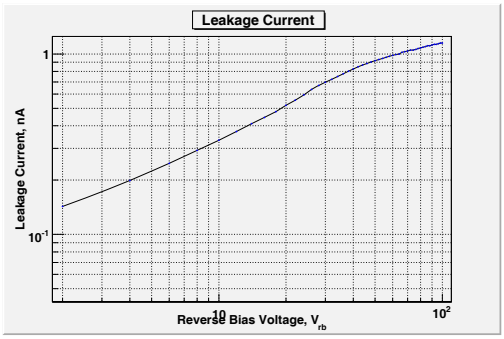


Figure 3: I-V characteristic curve.

GEOMETRICAL OPTIMIZATION

To maximize the detector's performance, an analytical model for optimizing its detector geometry was constructed. Because of the geometrical configuration of the ring-array photodiodes, the solid angle (Ω)[3, 4] of the photodiode sensor was calculated with parameterization as in Eqn. (1): In Fig. 5, the solid angle (Ω), which is an effective area seen by a beam, is plotted against the distance ($Z^{\star}$) between the sensor and the fluorescence target. From our calculations, it was determined that an optimized working distance is 3.0 (mm) and the peak solid angle ($\hat{\Omega}$) is 0.76 (sr).

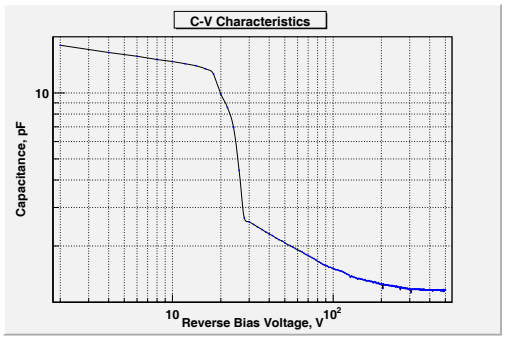


Figure 4: C-V characteristic curve.

$$
\begin{aligned}
&\Omega_{ring,\,7}(\underbrace{\rho^{*},\theta^{*},z^{*}}_{beam\ parameters\ (3)}\ ;\ \underbrace{\rho^{+},\rho^{-},\theta^{+},\theta^{-}}_{sensor\ parameters\ (4)})\\
&= -\arctan\left[\frac{\Delta\theta^{+}(\rho^{*2}-(\rho^{*}\rho^{+})+z^{*2})}{z^{*}\sqrt{(\Delta\rho^{+})^{2}+(\rho^{+}\Delta\theta^{+})^{2}+z^{*2}}}\right]\\
&+\arctan\left[\frac{\Delta\theta^{-}(\rho^{*2}-(\rho^{*}\rho^{+})+z^{*2})}{z^{*}\sqrt{(\Delta\rho^{+})^{2}+(\rho^{+}\Delta\theta^{-})^{2}+z^{*2}}}\right]\\
&+\arctan\left[\frac{\Delta\theta^{+}(\rho^{*2}-(\rho^{*}\rho^{-})+z^{*2})}{z^{*}\sqrt{(\Delta\rho^{-})^{2}+(\rho^{-}\Delta\theta^{+})^{2}+z^{*2}}}\right]\\
&-\arctan\left[\frac{\Delta\theta^{-}(\rho^{*2}-(\rho^{*}\rho^{-})+z^{*2})}{z^{*}\sqrt{(\Delta\rho^{-})^{2}+(\rho^{-}\Delta\theta^{-})^{2}+z^{*2}}}\right]
\end{aligned}
\tag{1}
$$

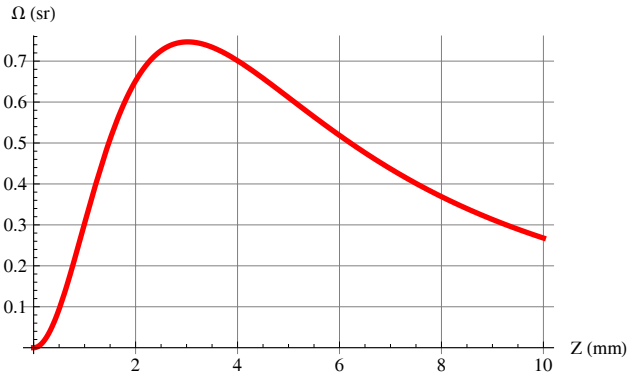


Figure 5: A plot of solid angle vs. working distance.

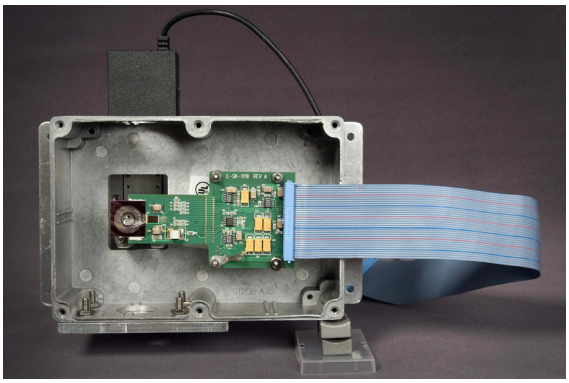
NEW ASIC DESIGN

We employed HERMES4, an application-specific integrated circuit (ASIC), which was redesigned at BNL for photon-counting application[5]. The new HERMES4 utilizing CMOS technology provides 32 channels, a charge pre-amplifier, a high-order charge shaper, a discriminators, an array of five 10-bit global DACs, and counters per channel. The HERMES4 was redesigned to read out input signals generated by the Si-photodiode sensor. The measured

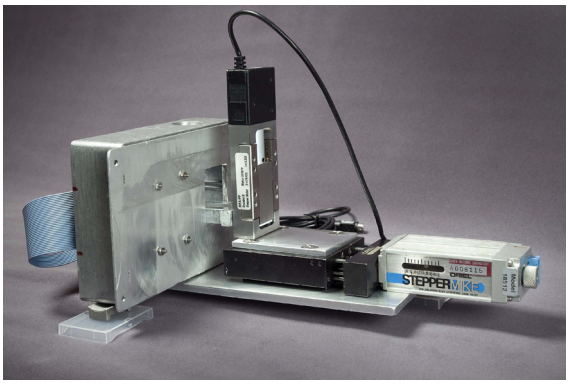
electronic resolution is good, *viz.*, 15 rms e^- at a peaking time of 4 μsec. The gain settings available on HERMES4 are 750 mV/fC and 1,500 mV/fC. The settable peaking times are 0.5, 1, 2, and 4 μsec. Stray capacitance is reduced by direct Al-wire wedge-bonding between the 32 channels and sensor pads.

PROTOTYPE ASSEMBLY

As shown in Fig. 6, four linear stages are incorporated into the prototype detector. The two stages are for positioning the X-BPM in horizontal and vertical directions. The third one is for scanning a fluorescence source along the axial direction, and the last one is for setting a working distance between the photon sensor and the fluorescence target.



(a) an open enclosure.



(b) an assembled detector.

Figure 6: (a) An open enclosure of the new X-BPM. (b) a completely-assembled prototype detector.

BENCH-TOP MEASUREMENTS

Prior to beamline tests of the new X-BPM, we carried out bench-top measurements. After irradiation of the detector from a sealed radiation source of Fe-55, consistent signals were generated from each individual pad (Fig. 7), and registered with the ASIC chip.

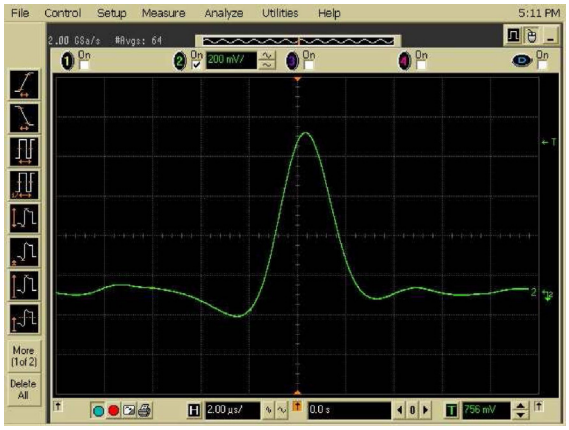


Figure 7: An example of a signal acquired after irradiation.

CLOSING REMARKS AND PLANS

Encouraged by the results from bench-top experiments and recent calibration runs on an existing beamline at NSLS, we are planning to undertake more detailed experiments to measure position sensitivity. Our analytical modeling enables us to predict the detector's performance in advance, and to develop enhanced photodiode sensors with larger solid angles. As a result, the new photodiode sensors will be used for the next version of prototypes.

ACKNOWLEDGMENTS

The authors gratefully acknowledge the support and provisions of the NSLS-II Experimental Facility Division, the NSLS Experimental Systems, and the Instrumentation Division of BNL.

REFERENCES

[1] NSLS-II Conceptual Design Report, BNL-77977-2006-V1-V2, December 2006

[2] Z. Li, and W. Chen *priv. comm.*, Brookhaven National Laboratory, 2009

[3] R. Alkire, "Design of Vacuum-Compatible High-Precision Monochromatic Beam-Position Monitor for Use with Synchrotron Radiation from 5 to 25 keV", J. of Synchrotron Rad., 2001, **7**

[4] C. DeCusatis, "Handbook of Applied Photometry", AIP Press, New York, 1997

[5] G. De Geronimo et al., "Readout ASIC for 3D Position-Sensitive Detectors", 2007 IEEE Nuclear Science Symposium Conference Record, Brookhaven National Laboratory

CHARACTERIZATION TESTS OF THE BEAM POSITION MONITOR SERIES PRODUCTION FOR THE TBL LINE OF THE CTF3 AT CERN*

C. Blanch-Gutierrez, J.V. Civera-Navarrete, A. Faus-Golfe, J.J. García-Garrigós
IFIC (CSIC-UV), Valencia, Spain

Abstract

A set of two Inductive Pick-Up (IPU) prototypes with its associated electronics for Beam Position Monitoring (BPM) in the Test Beam Line (TBL) of the 3^{rd} Compact Linear Collider (CLIC) Test Facility (CTF3) at CERN were designed, constructed, and tested by the IFIC team. One prototype and two units of the series production are already installed in the TBL line. In the first part of the paper we describe the characterization tests of these two prototypes carried out at CERN, and the first beam tests performed to one of them. The second part of this paper is dedicated to the description of the issues addressed by the start of the series production and the characterization tests of the first series units performed with a custom-made low-frequency wire setup. This setup which emulates the beam position variation allows to carry out the series tests in an automatized manner and with higher accuracy.

INTRODUCTION

The CLIC Test Facility will demonstrate the essential parts of the CLIC drive beam generation scheme consisting of a fully loaded linac, a delay loop and a combiner ring. The final CTF3 drive beam is delivered to the CLIC Experimental Area (CLEX) comprising the TBL and a two beam test stand. The TBL is designed to study and validate the drive beam stability during deceleration. The TBL consists of a series of FODO lattice cells and a diagnostic section at the beginning and end of the line to determine the relevant beam parameters. Each cell is comprised of a quadrupole, a BPM (labeled as BPS) and a Power Extraction and Transfer Structure (PETS) [1]. A 3D view of a TBL cell is shown in Fig. 1. The available space in CLEX allows the construction of up 16 cells with a length of 1.4 m per cell. The BPS's are IPU type and the expected performances for a TBL beam type (current range 1-32 A, energy 150 MeV, emittance 150 μm, bunch train duration 20-140 ns, microbunch spacing 83ps (12GHz), microbunch duration 4-20 ps, microbunch charge 0.6-2.7 nC) are summarized in Tab. 1.

BPS PROTOTYPES

A set of two prototypes of the BPS's labeled as BPS1 and BPS2 with its associated electronics has been designed, constructed and characterized by the IFIC team with the collaboration of the CTF3 team at CERN. The BPS has four electrodes setting up the vertical and horizontal coordinate planes. The current intensity induced by the beam is distributed through these electrodes depending on the beam proximity. The electrodes current is then sensed by their respective transformers in a conditioning circuit placed in a internal PCB. This gives the four output voltage signals (V_+, H_+, V_-, H_-) that will drive an external amplifier to yield three signals for determining the beam position: sum signal ($\Sigma = V_+ + H_+ + V_- + H_+$), to get the beam current intensity; and two difference signals ($\Delta V = V_+ - V_-$ and $\Delta H = H_+ - H_-$) which are proportional to the horizontal and vertical coordinates of the beam position. There is also two input calibration signals, Cal+ and Cal-, to check the correct function of the sensing PCB halves. A detailed description of the mechanics, electrical model and the electronics of this two prototypes can be found in [2].

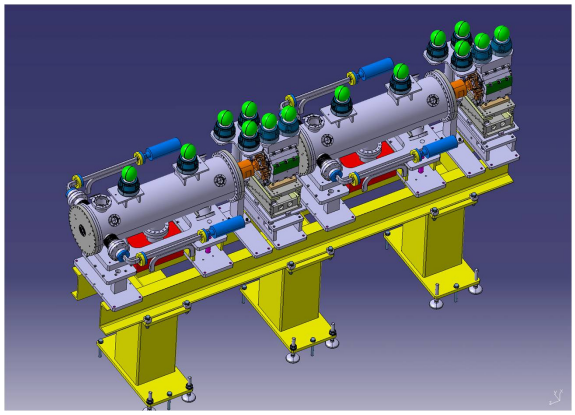


Figure 1: 3D view of a TBL cell with the PETS tanks, the BPSs and the quadrupoles.

Table 1: Expected BPS Characteristics

Analog bandwidth	10 kHz-100 MHz
Beam position range	±5 mm (H/V)
Beam aperture diameter	24 mm
Overall mechanical length	126 mm
Number of BPS's	16
Resolution at maximum current	$\leq$5 μm
Overall precision $\sigma_{H/V}$	$\leq$50 μm

Prototypes Characterization Tests

The BPS characterization parameters for each coordinate plane: sensitivity, overall precision (accuracy), electrical offset and cut-off frequencies with its associated time constants; has been determined with the wire method test in the BI-PI labs at CERN. This test is based on a test bench

* Work supported by FPA2007-31124-E

setup that allows moving the BPS with respect to a current wire that simulates the beam passing through the BPS under test. The BPS1 prototype reference performance coming from the first characterization tests are summarized in the Tab. 2. From the linearity test, which fits the normalized $\Delta(V,H)/\Sigma$ signals to the wire position in each coordinate plane, are obtained the main BPS characterization parameters: the sensitivity, as the proportional factor between the BPS signals and the beam position coordinate; the electrical offset from the true mechanical center or zero position; and the accuracy, as the rms linearity error in the range of interest. The frequency response test of the BPS output signals gives the cut-off frequencies that define the needed bandwidth (see Tab. 1) to let pass the rectangular pulse signal without deformation induced by the pulsed beam structure. The pulse-time constants derive inversely from these cut-off frequencies. In the most relevant case of the exponential droop time constant, it has to be a factor hundred larger than the beam pulse duration (140 ns) to ensure the desired flat-top pulse output signals of the BPS.

The performed tests in the wire setup yield good linearity results and reasonably low electrical offsets from the mechanical center. From the linearity errors analysis can be stated that the overall precision results have to be ameliorated, considering the effect of the very low excitation current in the wire (13 mA) and the misalignment for the horizontal plane electrodes. Concerning the frequency response measurements, the low cut-off frequencies for the Δ signals, f_{l_Δ}, are equal for the vertical and horizontal planes, and they are given for performing the compensation of droop time constants with the external amplifier, decreasing so these cut-off frequencies down to the specified bandwidth lower limit (10 kHz). The low cut-off frequencies for the sum (Σ) signals, f_{l_Σ}, corresponding also to each electrode output frequency response, are the same for both cases wire/beam and calibration excitation ($f_{l_\Sigma[Cal]}$), and they are under specifications (below 10 kHz), as well as, the high cut-off frequencies, f_h and $f_{h[Cal]}$, that we could determine to be above the required 100 MHz. The fact that the f_{l_Δ} are much higher than f_{l_Σ}, is due to a coupling effect among the BPS opposite electrodes for a displaced wire/beam. This effect leaves the electrodes frequency response equal and constant in magnitude, becoming the Δ signals insensitive to a wire/beam displacement, only for the low frequency components. Moreover, it was measured a significant, and never seen before, difference of around 100 kHz between the Δ low cut-off frequencies for the wire/beam and the calibration excitations, f_{l_Δ} and $f_{l_\Delta[Cal]}$ respectively. In the attempt of eliminate this difference, both low cut-off frequencies were lowered changing the output resistor values in a new PCB version, but the difference between f_{l_Δ} and $f_{l_\Delta[Cal]}$ remained unchanged. Both effects involving the Δ signals are related, and a new electrical model for taking into account those effects will be investigated in a future work.

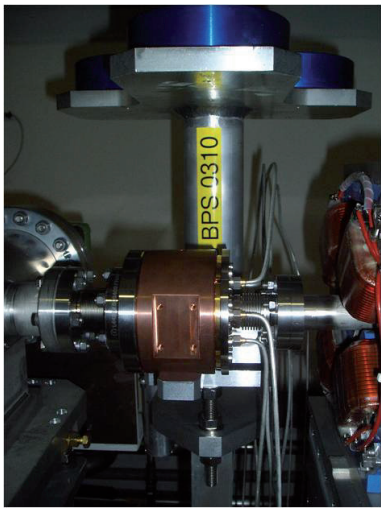


Figure 2: BPS1 and its support installed in the TBL line.

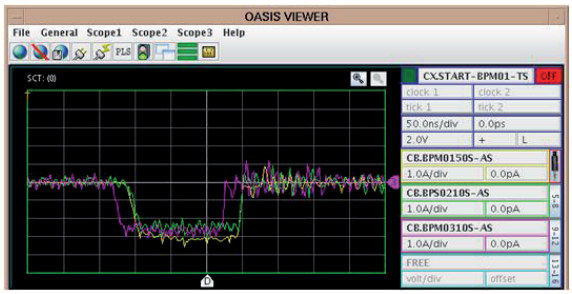


Figure 3: Σ beam pulse measurement of the BPS1 (yellow trace) in the TBL line.

First Beam Test

The BPS1 and its support was installed in the TBL line as it is shown in Fig. 2. In December 2008 some preliminary test with beam losses was performed. In these first series of measurements with beam we observed a ringing problem with calibration pulses which was investigated and solved in a collaborative effort. The results of the second series of beam measurements were satisfactory after solving the initial ringing problem and in Fig. 3 is shown the Σ signal corresponding to a beam pulse. The BPS2 remained at the IFIC labs for testing, performing the necessary improvements for the series and help in the design and construction of the new wire setup.

BPS SERIES PRODUCTION

The series production of the 15 unit (BPS1 + 15) has been started at the IFIC labs in November 2008. After solving some mechanical design adjustments based on the prototyping experience, the production of the different parts, described in [2], is finished. The PCBs for the full BPS series are also finished and validated, implementing the final version of the PCB design with some improvements with respect to the first prototype versions. Mainly, the redesign of the PCB was focused on trying to diminish the high coupling effects that exists between the BPS strip electrodes.

Table 2: BPS1 Prototype and BPS2/3 Series Performance

BPS1/2/3 Sensitivity and Linearity Parameters	
V Sensitivity S_V	41.09/43.16/43.70 m^{-1}
H Sensitivity S_H	41.43/42.60/42.10 m^{-1}
V Electric Offset EOS_V	0.03/-0.67/-0.84 mm
H Electric Offset EOS_H	0.15/0.50/0.52 mm
V overall precision σ_V ($\pm$5 mm)	78/89/94 μm
H overall precision σ_H ($\pm$5 mm)	109/90/98 μm
BPS1/2/3 Characteristic Output Levels	
Sum signal level Σ	16.5 V
Diff signals levels $\|\Delta V/H\|_{max}$	8.25 V
Centered beam level, $V_{sec}(0,0)$	4.125 V
BPS1/2/3 Frequency Response Parameters	
Σ low cut-off freq f_{l_Σ}	1.76/2.90/1.70 kHz
Δ low cut-off freq f_{l_Δ}	282/271/275 kHz
Σ[Cal] low cut-off freq $f_{l_{\Sigma[Cal]}}$	1.76/2.80/1.70 kHz
Δ[Cal] low cut-off freq $f_{l_{\Delta[Cal]}}$	180/163/171 kHz
High cut-off freq f_h	>100 MHz
High cut-off freq [Cal] $f_{h[Cal]}$	>100 MHz
BPS1/2/3 Pulse-Time Response Parameters	
Σ droop time const τ_{droop_Σ}	90/55/93 μs
Δ droop time const τ_{droop_Δ}	564/587/579 ns
Σ[Cal] droop const $\tau_{droop_{\Sigma[Cal]}}$	90/57/93 μs
Δ[Cal] droop const $\tau_{droop_{\Delta[Cal]}}$	884/976/931 ns
Rise time const τ_{rise}	<1.6 ns
Rise time const [Cal] $\tau_{rise[Cal]}$	<1.6 ns

The assembly of the full series, including the PCBs, is foreseen to start at the end of May 2009.

Due to installation schedule requirements two new units has been installed in the TBL line in advance of the rest of the series. The BPS2 which was previously manufactured as a second prototype, and the BPS3, a new assembled unit belonging to the series production, both incorporating the PCBs final version.

Series Characterization Tests

Prior to send these two units to CERN, their characterization test were performed at IFIC labs with the new low-frequency wire test setup (Fig. 4). It has been custom designed for the BPS series tests and built also at IFIC. The BPS2/3 characterization results are presented in Tab. 2.

The main features of this new test bench setup is that the BPS under test will be moved by a motorized XY and rotatory micromovers to change the relative wire position (0.25 mm) with respect to the BPS. For the sensitivity and linearity test the wire input is fed by a sinusoid signal in the pass-band of the BPS (1MHz) which comes from a Vector Network Analyzer (VNA) after passing through a current amplifier. The last will boost the wire current more than 250 mA, improving the signal to noise ratio of the previous tests made at CERN. The BPS external amplifier is connected to the BPS electrode outputs to send the Δ and Σ signals to the VNA. Then, a PC running LabVIEW acquire the $\Delta(V,H)/\Sigma$ and the wire position signals managing the VNA and the micromovers controller through GPIB bus. This allows to program the measurement of many samples for each BPS unit by automatizing all the equipment. The frequency and pulse response tests are performed in the same way but with the signals coming directly from the BPS outputs. Other setup characteristics are: the pneumatic isolation workstation to avoid wire vibrations, the 2/0.2 μm precision/resolution of the XY linear stages, and the rotatory stage with 0.2/0.009 μrad. These are enough features to obtain the desired accuracy in the position measurements and to estimate the minimum position resolution down to 5 μm according to TBL specifications. The critical part observed during these tests is that the wire must be aligned with the BPS very precisely. The BPS2/3 accuracy measures was affected by this issue, although both coordinate planes now show good balance. This will be corrected for the rest of the series characterization.

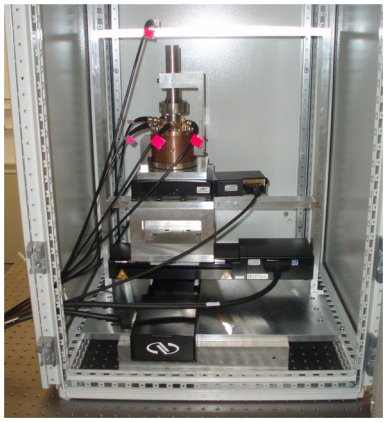


Figure 4: Low-frequency wire test setup in the IFIC labs.

CONCLUSION AND FUTURE TASKS

The series production of 15 units has already started. BPS1 prototype and BPS2/3 series units are already installed in the TBL. The rest of the series will be installed in July 2009. A custom low-frequency setup has been designed and constructed at IFIC labs to automatize the BPS series measurements. Furthermore, a high frequency setup is also being constructed at IFIC for measuring the longitudinal impedance in some of the series units.

ACKNOWLEDGMENTS

We would like to thank all members of the CTF3 team at CERN for their continuous help, especially to G. Geschonke, S. Döebert, L. Søby and F. Guillot. Thanks also to Trinos Vacuum Projects and Lemar for the participation in the BPS's manufacturing.

REFERENCES

[1] S. Doebert, et al "Status report of the CTF3 Test Beam Line", CTF3 Note 076.

[2] J.J. Garcia-Garrigos et al "Design and Construction of an Inductive Pick-Up for Beam Position Monitoring in the Test Beam Line of the CTF3", EPAC08.

PARTICLE IDENTIFICATION DEVICES IN MICE

V. Verguilov*, University of Geneva - DPNC, Geneva, Switzerland
V. Palladino, INFN-Napoli, Napoli, Italy

Abstract

The international Muon Ionization Cooling Experiment (MICE) is being built at the Rutherford Appleton Laboratory (RAL). It will carry out a systematic investigation of ionization cooling of a muon beam. This is one of the major technological steps needed in the development of a muon collider and a neutrino factory based on muon decays in a storage ring. MICE will use particle detectors to measure the cooling effect with high precision, achieving an absolute accuracy on the measurement of emittance of 0.1% or better. A PID system based on three Time-of-Flight stations, two Aerogel Cerenkov detectors, a KLOE-like calorimeter in combination with Electron-Muon Ranger calorimeter has been constructed in order to keep beam contamination (e, π) well below 1%. The MICE time-of-flight system will measure timing with a resolution better than 70 ps per plane, in a harsh environment due to high particle rates, fringe magnetic fields and electron backgrounds from RF dark current. The aim of this paper is to give a quick overview of the particle identification system in MICE.

OVERVIEW

The physics program at a neutrino factory is very rich and includes long-baseline ν oscillations, short-baseline ν physics and slow muon physics [1]. The performance of a Neutrino Factory depends not only on its clean beam composition ($50\%\nu_e, 50\%\overline{\nu}_\mu$ for the $\mu^+ \mapsto \overline{\nu}_\mu \nu_e e^+$ case), but also on the available beam intensity. The cooling of muons (accounting for $\sim 20\%$ of the final costs of the factory) is thus compulsory, increasing the performance up to a factor 10 [2], [3], [4], [5].

The process of ionization cooling of the transverse phase-space coordinates of a muon beam was proposed more than 20 years ago by A.N. Skrinsky [6]. Essentially it can be accomplished by passing it through an energy-absorbing material and an accelerating structure, both embedded within a focusing magnetic lattice. Both longitudinal and transverse momentum are lost in the absorber while the RF-cavities restore only the longitudinal component. The Muon Ionization Cooling Experiment (MICE) [7], [8], [9] at Rutherford-Appleton Lab is the first test of the ionization cooling concept for muon beams in the approximate momentum range 140 to 240 MeV/c. A minimum ionizing muon beam will be transversely cooled by stages of $-dE/dx$ in LH_2 absorbers and longitudinal energy restoration in a series of 201 MHz RF cavities; (Figure 1) The 6D emittance reduction is measured before and after the cooling stage by tracking individual muons through the system. To establish muon cooling the in-flight muon beam is positively identified by three time-of-flight (TOF) stations [10], by two threshold Cherenkovs (CKOVs), and by a low energy ranging electron-muon calorimeter (KL/EMR) near the beam exit.

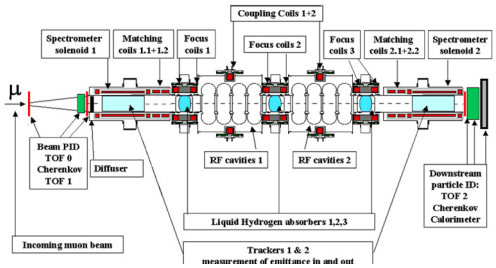


Figure 1: MICE Spectrometer Layout.

TIME OF FLIGHT DETECTORS

Three time-of-flight (TOF) stations are positioned in the MICE channel at the beginning (TOF0), midway(TOF1), and near the rear(TOF2). Each station is approximately 50cm × 50cm in active cross section and spaced apart by a ≈10 m flight path. The TOF stations are used in establishing a precision particle trigger which can be synchronized to within $\leq 70ps$ of the RF cavity phase of the experiment. The TOF 0/1/2 stations consist of 10/7/10 X-counter and 10/7/10 Y-counter arrays constructed of BC404/420 scintillator bar with dual R4998 PMT (TOF0) readout (Fig. 2). The HV dividers have been modified for high rate performance (≈2 MHz). The dual photomultiplier (PMT) readout gives typically σ_t=50-60 ps intrinsic timing resolution for each bar assembly. The bars are 2.5 cm thick, optimizing between light collection and energy loss. The transit time and associated dispersion, σ_{tt}, of the signal through the PMT, cable delay, and the discriminating electronics is not known and are measured measured for each channel by a calibration procedure which can use particle beam and/or cosmics. Leading edge discriminators have been

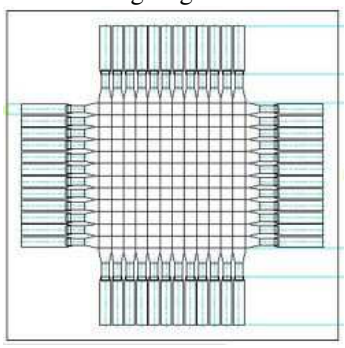


Figure 2: X/Y planes for TOF0 station. Each bar assembly is 4 cm wide.

adopted for the timing measurements. This introduces a dependence of the discrimination crossing time, "time-walk", with its associated dispersion σ_{tw}. To calculate the time-walk correction the difference of the time measured by the

* for the Mice Collaboration

PMTs and a reference time is measured for a series of data, and a correction function is applied offline. The projected time-of-flight resolution between 2 stations is given by

$$\Delta t_{12} = \sqrt{2(\sigma_t/\sqrt{2})^2 + \sigma_{tt}^2 + \sigma_{tw}^2} \leq 75\ ps \qquad (1)$$

The TOF data acquisition utilizes three TDC boards (CAEN V1290). The digital values recorded by the TDCs correspond to the absolute time since the last reset of each TDC board. A "particle trigger" signal is generated by hardware logic units in the data acquisition (DAQ) racks. It is given by the first dual coincidence of the PMTs connected to the same TOF0 bar unit. The first channel of each TDC board receives a copy of a particle trigger signal and this signal is used as a reference for all the PMT signals of the TOF stations. In the fall of 2008, components of the TOF0 and TOF1 stations were commissioned in the MICE beamline. For a set of pion runs, with time-walk corrections applied, the intrinsic detector resolutions were measured to be in the 55 ps to 65 ps range, very close to design specification. These intrinsic timing distributions are shown in Figure 3 and Figure 4. The time-of-flight distribution for the nominal 300 MeV/c pion tune is shown in Figure 5, displaying a good separation between positrons, muons, and pions in the beam at this early stage of analysis.

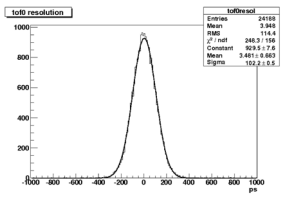


Figure 3: TOF0 detector's intrinsic timing.

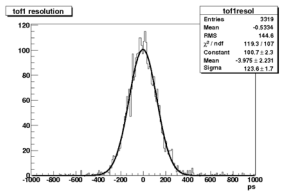


Figure 4: TOF1 detector's intrinsic timing.

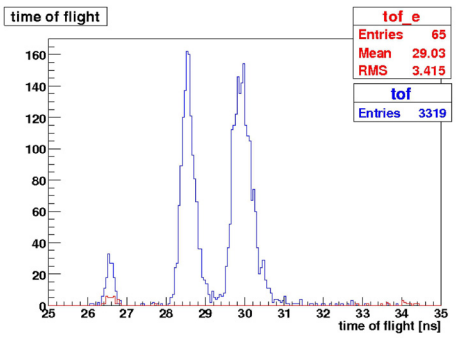


Figure 5: TOF1-TOF0 timing of e^+, μ^+, π^+ in nominal 300 MeV/c π^+ beam.

AEROGEL CHERENKOV COUNTERS

It is not possible to select a single material as Cerenkov radiator that is sensitive to muons and blind to pions over the entire range. To overcome this, high density aerogel Cherenkov radiators were selected, [11], with indexes of refraction and muon threshold momenta of n=1.07 (p^{μ}_{th}=278 MeV/c) and n=1.12 (p^{μ}_{th}=220 MeV/c). Each counter consists of a 2.3 cm thick aerogel radiator sealed behind a thin UV-transmitting window. The Cherenkov light is collected by four 8 inch 9354KB Electron Tubes PMTs. The PMT dividers have been designed to operate at $\leq$ 5 MHz beam rate with transistorized last dynode stages. The charge is collect in a 500 MHz flash ADC (CAEN V1721 500MS/s FADC) in the DAQ rack. A model of the aerogel Cherenkov detector with open PMT ports is shown in Figure 6.

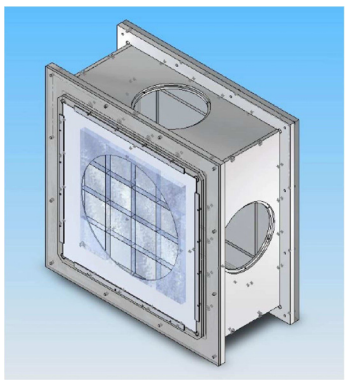


Figure 6: Model sketch of aerogel Cherenkov detector.

The saturation (β=1) photoelectron calibration for particles is found in 100 MeV/c positron runs. A typical PMT spectrum is shown in Figure 7. We collect between 20 and 25 photoelectrons in the aerogel counters. This yield gives sufficient photostatistics for a good muon tagging efficiency of 98% at low pion misidentification rate ($\leq 10^{-3}$) over the 220-360 MeV/c momentum range.

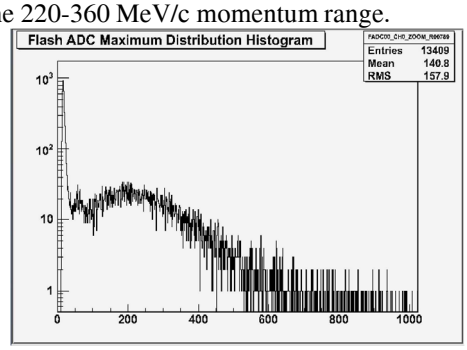


Figure 7: Typical light spectrum from single CKOV PMT, about 5-6 p.e. per channel $\times$ 4 .

KLOE LIGHT + ELECTRON-MUON RANGER

The downstream calorimeter (EMCAL) is a Pb-scintillating fiber calorimeter (KL), of the KLOE type [12], [13], with 1-mm diameter blue scintillating fibers glued between 0.3 mm thick grooved lead plates followed by a Electron-Muon Ranger (EMR), made of higly segmented 70 cm long fully active scintilators. The combination of both detectors will provide the final clean muon tag veto $\mu^+ \rightarrow e^+\overline{\nu_e}\nu_\mu$ decays at the 10^{-2} level. EMCAL system offers adequate energy resolution to perform muon and electron identification in the momentum range of interest for MICE.

KL The KL preshower calorimeter is constructed of 0.3mm grooved Pb with BF12 scintillating fiber inlay in

a KLOE-type layout. The original KLOE design represents 2.5 X_0 in depth, a 4 cm thick active depth. It has an energy resolution for electrons of $\Delta E/E(GeV = 7\%/\sqrt{(E(GeV))}$, and timing resolution of Δ_t = 70 ps / $\sqrt{E}$. The KL was commissioned in fall 2008 MICE run. Below we show a scan with 300 MeV/c pion beam into the calorimeter. The ionizing response shown in Figure 8 was nominally what is expected. Further calibrating exposures to electron beam are planned for fall 2009.

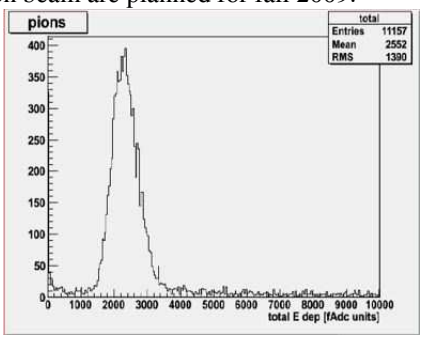


Figure 8: KL response to 300 MeV/c pion beam. The horizontal scale is in ADC channels.

EMR The EMR is currently under construction for MICE and utilizes a MINERνA-like design [14]. It will consist of 40 layers of 59 extruded scintillator bars with a triangular shape (Figure 9). Each bar is interfaced with a multianode PMT through WLS fibers (4 with a diameter of 0.8 mm); in total there will be 32 64-channel PMTs (Hamamatsu, H7645B) and 2 256-channel PMTs (Hamamatsu, H9500) to obtain an indication on the charge deposit in each layer, the analog signal of each PMT dynode will be digitized with a CAEN V1731; this will require 3 digitizers for the whole detector. With the foreseen electronics it is not possible to obtain the analog information of every bar without introducing dead time. The front-end electronics will allow to obtain a digital information for every bar, that is the time when the bar signal is over threshold. The system will not work in self triggering mode; the trigger will be given by an external detector (e.g. TOF0) or by the machine itself (the so-called "MICE spill gate") Simulations show that MICE can achieve a longitudinal momentum resolution of $\sigma_{P_z} \approx 4$ MeV/c for muons under 270 MeV/c, which range out in the calorimeter. See Figure 10. The error of this momentum is complementary to the MICE tracker measurement.

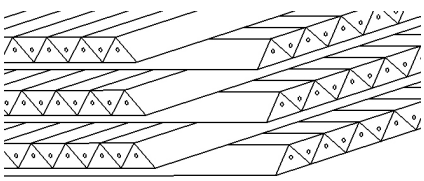


Figure 9: Sketch of MINERνA-like EMR calorimeter design to be used in MICE.

CONCLUSIONS

Muon cooling is necessary for building a neutrino factory. MICE, The Muon Ionization Cooling Experiment, based at RAL, UK will try to achieve a transversal cooling of a muon beam in the range 140 to 240 MeV/c. To reduce the systematics in the measurement of the cooling effect, a combination of PID detectors was designed and manufactured. Two Time-of-Flight detectors, two Aerogel Cerenkov detectors and a KLOE-like calorimeter were already installed and commissioned along the MICE beamline. Third Time-of-Flight detector as well as the second part of the EMCAL system - the Electron-Muon Ranger will be installed in the next year.

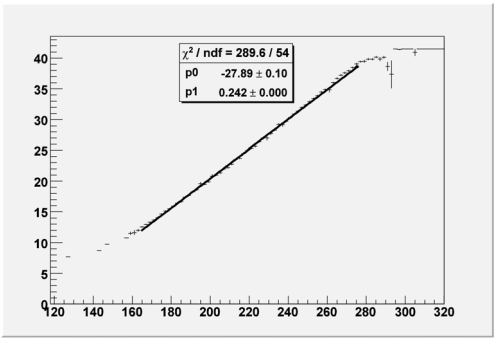


Figure 10: Muon range simulation in the EMR. $\sum E$ vs Layer # is plotted. The horizontal axis is in MeV/c. Muons above $\tilde{2}70$ MeV/c will range through.

REFERENCES

[1] M. Bonesini, A.Guglielmi Phys. Rep. 433 (2006) 65.
[2] D. Ayres *et al.,* "Expression of interest for R & D towards a Neutrino Factory based on a storage ring and a muon collider," physics/9911009.
[3] A. Blondel et al., "The Neutrino Factory: Beam and Experiments," Nucl. Instrum. Meth. A **451**, 102 (2000).
[4] C. H. Albright *et al.,* "The Neutrino Factory and Beta Beam experiments and development," physics/0411123, Nov. 2004.
[5] J. S. Berg *et al.,* "A cost-effective design for a Neutrino Factory," *Phys. Rev. ST Accel. Beams,* vol. **9**, art. 011001, 2006.
[6] A.N. Skrinsky, V.V. Parkhomchuk Sov. Jour. Nucl. Phys. 12 (1981) 3.
[7] P. Drumm, "MICE: The International Muon Ionisation Cooling Experiment," PAC 05-Knoxville, hep-ex/0509021, May 2005.
[8] M. Yoshida, "The International Muon Ionization Cooling Experiment (MICE)," NuFact 04-Osaka, *Nucl. Phys. Proc. Suppl.* vol. **149**, pp. 94-98, 2005.
[9] A. Blondel et al., MICE proposal, RAL, 2004; G. Gregoire et al., MICE Technical Report, RAL, 2005.
[10] M. Bonesini et al., The Design of the Time-of-Flight System for MICE", arXiv-0712.4370.
[11] D. A. Sanders et al., "A Cherenkov Rdiation Detector with High Density Aerogels", SORMA West 2008, Berkeley, CA, 2-5 Jun 2008.
[12] A. Aloisio *et al.*, KLOE coll., Nucl. Inst. and Meth. A 494 (2002), 326.
[13] F. Ambrosino *et al.*, "Calibration and performances of the KLOE calorimeter," Nucl. Instrum. Meth. A **598**, 239 (2009).
[14] "THE MINERvA EXPERIMENT," E.C. Schulte, Acta Phys.Polon.B37,2379-2386,2006.

BASEBAND TUNE MEASUREMENTS AT GSI SIS-18 USING DIRECT DIGITIZED BPM SIGNALS*

U. Rauch†, P. Hülsmann, GSI, Darmstadt, Germany and Goethe University, Frankfurt, Germany
P. Forck, P. Kowina, P. Moritz, GSI, Darmstadt, Germany

Abstract

A precise tune determination is crucial for stable operation of GSI SIS 18 synchrotron especially for intense beam conditions. In order to avoid nearby resonances in the tune diagram the fractional part of coherent betatron motion needs to be measured with a resolution of 10^{-3} also during ramping mode. This is achieved using a fast digital readout system for Beam Position Monitors (BPM) which delivers a bunch-by-bunch position. The tune is then determined in baseband directly by Fourier-transformation of the positions of a certain bunch typically over 2048 turns. This algorithm does not require any additional input parameter. Since particle losses due to emittance blow-up have to be avoided, excitation power has to be kept as low as possible. In order to find a working range where tune measurement can be implemented in normal machine operation without disturbing the beam several series of measurement have been performed using a digital random noise generator for beam excitation and an Ionization Profile Monitor for displaying alterations of beam profile.

SYSTEM OVERVIEW

The new data acquisition system for BPMs based on fast and direct signal digitization followed by digital signal processing offers a sensitive method for tune measurement [1, 2, 3]. By using the integrated bunch-by-bunch position information the coherent betatron motion can be extracted in baseband without external parameters. Such frequency spectrum is expressed in units of q and ranges from $0 < \mathrm{q} < 0.5$. The GSI heavy ion synchrotron has some particular machine parameters, namely the comparatively long bunches, the injection at non-relativistic velocity β = 15,5% and the acceleration frequency ramping from 0.8 to 5 MHz. The new method acts as a low pass filter with dynamically adapted filter bandwidth. Therefore it offers a high flexibility for the varying beam parameters at SIS 18, which cannot be realized by the sensitive analog baseband-q detection system BBQ [4].

As schematically shown in Fig. 1, the analog single plate BPM signals from all four plates of a shoebox type BPM [5] are fed to a high impedance amplifier and digitized. The digitization of the broadband BPM signal is performed using a sampling rate of 125 MSa/s which corresponds to a range of 18 to 140 Sa per bunch for SIS 18 typical beam parameters, depending on the revolution frequency. The signal is integrated bunch-by-bunch which minimizes thermal and digitization noise and the beam position is calculated.

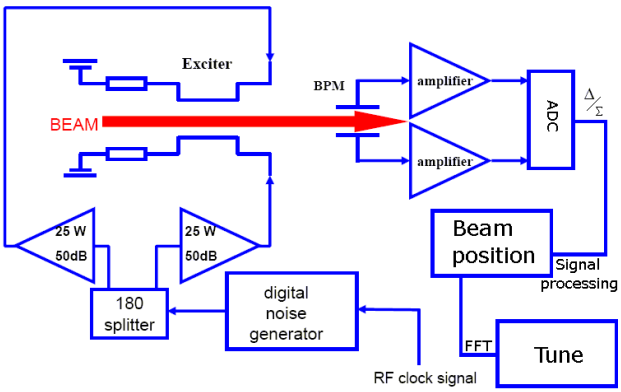


Figure 1: System schematics. The Beam Position Monitor is read out using a fast ADC. A white noise generator with limited bandwidth is connected to an exciter.

The position processing algorithm delivers a single value for vertical and horizontal position for each bunch and thus a certain bunch can be traced digitally. Signal shape and treatment as well as algorithm details for position evaluation have been described earlier [1, 2].

The coherent betatron motion cannot be observed for a stable and well adjusted beam, therefore the beam has to be slightly excited. This excitation is applied using a digital random noise generator connected to an exciter installed at SIS 18 (Fig. 1). It produces white noise with adjustable bandwidth on side bands of a carrier frequency f_c [6]. f_c is set by a frequency tracker connected to the SIS 18 rf signal. The noise bandwidth is set broad enough to cover the range of expected maximum tune deviation, which usually was chosen as $\Delta\mathrm{q} = 0.05$. The noise generator signal is split and each branch is amplified up to a maximal power of 25 W. Both signals are fed to a stripline exciter of 750 mm length and 200x70 mm horizontal/vertical aperture. Two independent exciters are installed at SIS 18 for horizontal and vertical plane respectively.

Excessive excitation of the beam must be avoided to prevent emittance blow-up. The search for a standard working range for tune measurement is subject of the studies presented in this contribution.

TUNE AND BEAM POSITION RESULTS

Detailed measurements have been performed with this system for various beam parameters. In the following we discuss the properties for a typical beam with the following parameters: $6.5 \cdot 10^9 Ar^{18+}$ ions accelerated from 11.4 to 300 MeV/u within 400ms, which corresponds to 220.000 turns. The vertical plane is discussed if not otherwise men-

* Work supported by EU, DIRAC secondary beams, 515873
† u.rauch@gsi.de

tioned. The achieved results serve as a representation for a typical beam response.

Fig. 2 shows an example for the development of tune along the acceleration ramp. Every 2048 turns one value for tune and for beam position are obtained, which gives a repetition rate of more than 100 FFTs per second at SIS 18. Moreover, Fig. 2 shows the system dependency on beam excitation: the excitation level applied to the beam, from which data for the middle graph has been used, is too low in order to safely observe the tune along the whole ramp. As can be seen, the detection interrupts at about 180.000 turns due to a low signal intensity. When the excitation level increases the frequency is detected more precisely due to a better signal to noise ratio over the whole cycle. The preset machine tune for this measurement was 3.23, a mean fractional tune of 0.221 with fluctuations ± 0.005 has been measured. Other comparable results can be found in [7].

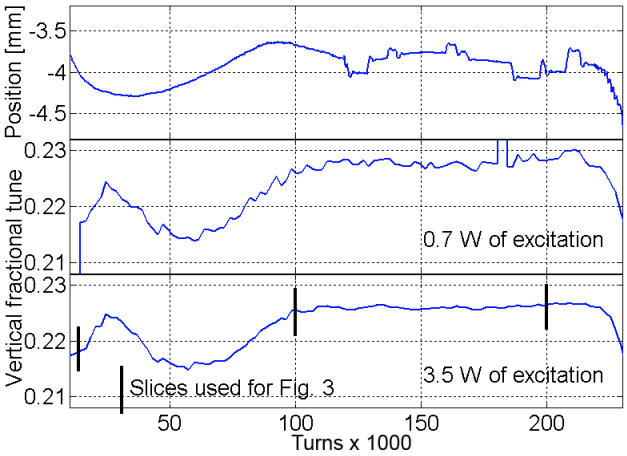


Figure 2: Vertical beam position and fractional tune, see text for beam parameters. Excitation at $q_{ex} = 0.23 \pm 0.05$ with amplitudes of $P_{ex} = 0.7$ W for middle graph and $P_{ex} = 3.5$ W for lower graph.

EXCITER WORKING RANGE

In order to investigate the correct working range for the excitation level, where the tune can be displayed properly without unnecessary emittance blow-up, a series of measurements has been performed. The exciter power was increased from zero to the maximum possible excitation power setting of 50W, which corresponds to a power spectral density (PSD) of 0.72 $\frac{mW}{Hz}$. Other beam conditions were untouched (Fig. 3). Out of the digitally stored position data for these different excitation levels spectra taken over 2048 turns are used.

As expected, an increase in excitation level leads to a linear increase in the tune signal amplitude. Up to a certain threshold for the excitation amplitude the frequency is not tracked safely. On the other hand, above about 10 W of exciter power, a PSD of 0.14 $\frac{mW}{Hz}$, the beam transmission suffers from particle losses.

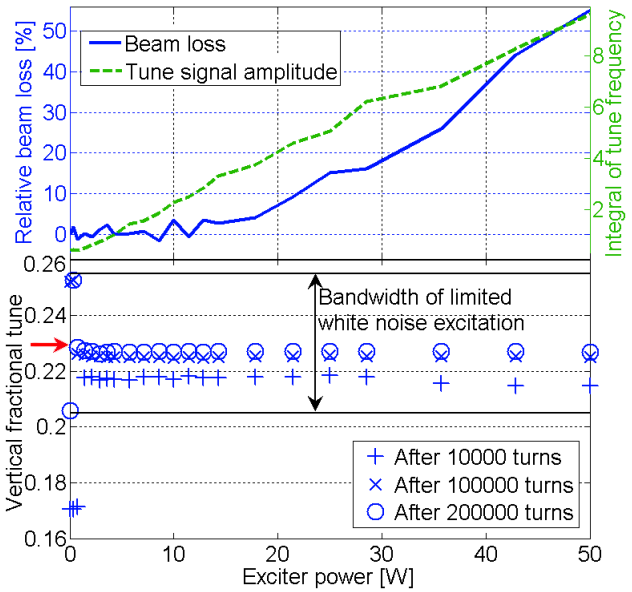


Figure 3: Beam response on noise excitation for dedicated times on ramp. Red arrow in lower part marks the machine preset tune value.

A possible way to mark the begin of the exciter working range is to analyze the variation of the obtained tune frequencies for a certain excitation amplitude. If the PSD is not large enough, noise dominates the spectrum and the result fluctuates statistically. Fig. 4 identifies the beginning of the working range. Each point represents the momentum value of 50 tune frequency spectra measured for each respective exciter amplitude setting. As the standard deviation of each value in the working range is typically close to its mean value, which is 0.0019 for this example, a small tolerance limit of $\Delta\sigma = 4 \cdot 10^{-4}$ can be found. This is the decisive parameter which defines the minimum excitation power to about 2 W, which equals to a PSD of 0.029 $\frac{mW}{Hz}$. The typical system resolution within the working range based on several measured machine tune spectra is better than $\Delta q = 2 \cdot 10^{-3}$, including machine fluctuations.

It is of interest whether beam excitation leads to an emittance blow-up, which has to be avoided. An Ionization Profile Monitor (IPM) installed at SIS 18 [8] has been used to observe the effect of beam profile broadening by monitoring one profile for both horizontal and vertical plane every 10 ms. By observing the profile alteration of several consecutive profiles of an excited beam, the difference between excited beam profiles and those taken from a non-excited beam can be compared. As shown in Fig. 5, the beam profiles show a broadening only for high excitation levels.

Again a series of measurements has been analyzed in order to find a range, where tune measurement is possible but no profile alteration can be measured. The broadening of the beam profile can be expressed by measuring its alteration of the standard deviation σ compared to a non-excited one. For this purpose profiles at the end of the ramp are taken and averaged over 20 cycles, leading to an error

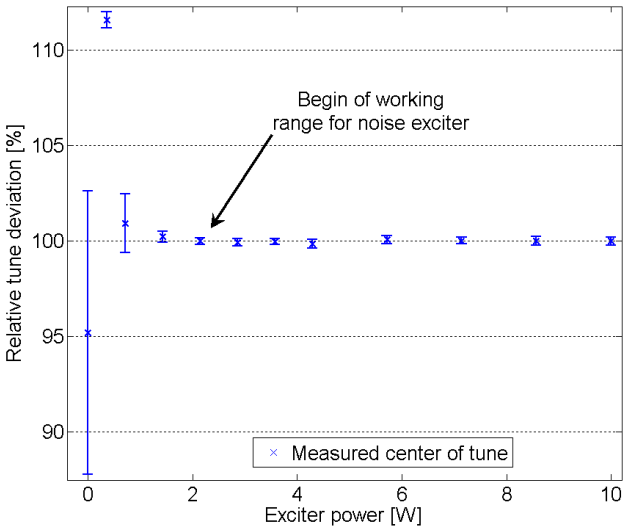


Figure 4: Points represent the mean value of 50 tune spectra with equal time offset to ramp start. Due to the fluctuations of obtained tune at low excitation the exciter power needed for the working range can be defined.

level below 5 %. As can be seen in Fig. 6 no effect on beam profiles at all could be detected for excitation levels below 8.5 W (PSD $= 0.12\frac{mW}{Hz}$). If the excitation level is increased, the profiles start to broaden and above 10 W of excitation power beam losses occur, as depicted in Fig. 3. Thus we have shown, that the working range for stable tune measurement without emittance blow-up is below 10 W, which gives a satisfying range. Fig. 6 shows in addition horizontal profile broadening. For higher excitation levels a slight width increase is visible, which serves as a sensitive method for measuring the horizontal-vertical tune coupling strength; further investigations are necessary.

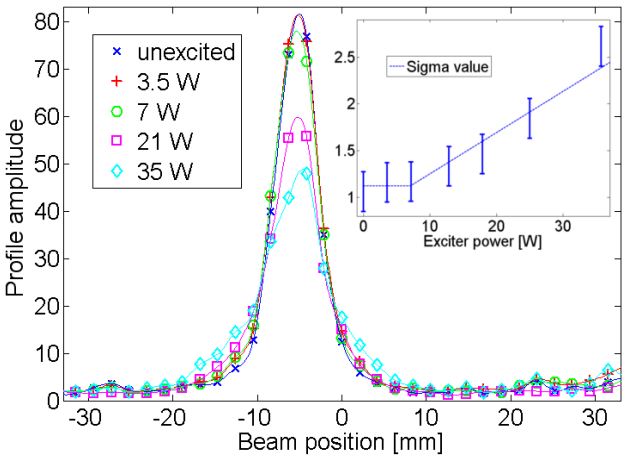


Figure 5: Vertical beam profiles of Ar^{18+}-beam measured by an IPM. Profile alteration by increasing exciter power is shown.

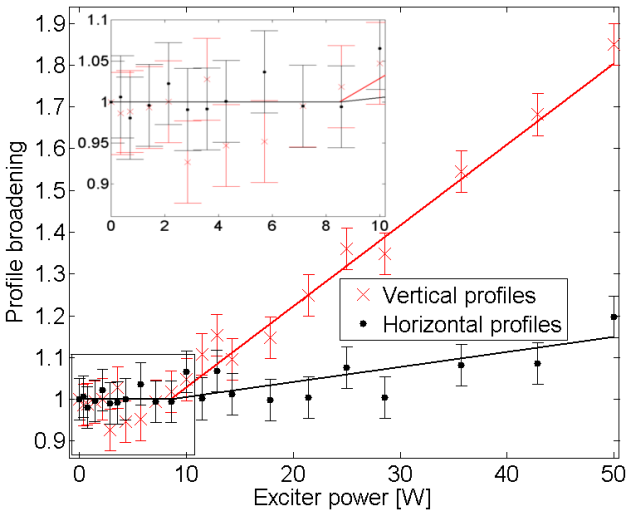


Figure 6: The increase of the standard deviation of beam profiles is shown as a function of exciter power. Points represent a mean value of 200 beam profiles of IPM, recorded at the end of the ramp.

CONCLUSIONS

The baseband digitization of BPM signals together with limited white noise excitation of the beam allows precise tune determination on the synchrotron ramp. The measurements yield reproducible results on a low excitation level using a PSD of below 0.1 $\frac{mW}{Hz}$, thus defining the right working range for tune measurements and preventing detrimental emittance blow-up. Displaying the measured machine tune with a resolution of $\Delta q < 2 \cdot 10^{-3}$ next to a precise beam position with a resolution below 30 μm [1, 3] gives a powerful tool for machine operation. Therefore, the presented system is a promising prototype for tune measurements at FAIR and is actually being implemented at SIS 18.

REFERENCES

[1] U. Rauch et al, Proc. of 5th Care-HHH-ABI workshop, Chamonix, Dec. 2007, http://adweb.desy.de/mdi/CARE/chamonix/Care-Proceedings-Chamonix.pdf
[2] K. Lang et al, Proc. of PCaPAC '08, Ljubljana, 2008
[3] A.Galatis et al : Proc. of EPAC 2006
[4] M.Gasior, Proc. of DIPAC'05, Lyon, France, 2005
[5] P. Kowina et al, Proc. of DIPAC'05, Lyon, France, 2005
[6] K. Blasche et al, SIS Status Report, GSI Scientific Report 2000, p.184
[7] U. Rauch et al, SIS Status Report, GSI Scientific Report 2008
[8] T.Giacomini, Proc. of BIW '04, Knoxville, USA, 2004

PHASE AND AMPLITUDE MEASUREMENT FOR THE SPIRAL2 ACCELERATOR

C. Jamet, W. Le Coz, C. Doutressoulles, T. Andre, E. Swartvagher, GANIL, Caen, France

Abstract

The SPIRAL2 project is composed of an accelerator and a radioactive beam section. Radioactive ions beams (RIBs) will be accelerated by the current cyclotron CIME and sent at GANIL experimental areas. The accelerator, with a RFQ and a superconducting Linac, will accelerate 5 mA deuterons up to 40MeV and 1 mA heavy ions up to 14.5 MeV/u. A new electronic device has been evaluated at GANIL to measure phase and amplitude of pick-up signals. The principle consists of directly digitizing pulses by under-sampling. Phase and amplitude of different harmonics are then calculated with a FPGA by an I/Q method. Tests and first results of a prototype are shown and presented as well as future evolutions.

SPIRAL2 ACCELERATOR DESCRIPTION

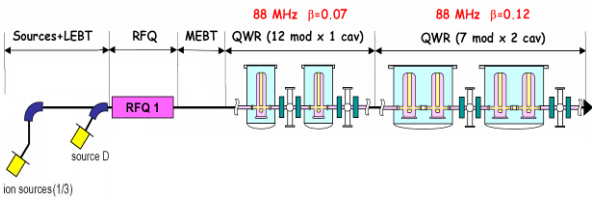


Figure 1: Accelerator Layout.

The accelerator is divided in 3 main parts, an injector, a superconducting linac and a high energy line. The injector part is composed of a deuteron/proton line, an ion line (LEBT), a RFQ and a MEBT line. Two kinds of superconductivity cavity are used for the Linac (β=0.07, β=0.12).

Table 1: Beam Intensity and Power

	Intensity	Energy	Power
LEBT1 (ions)	1 mA	20 keV/A	60 W
LEBT2 (deut.)	5 mA	40 keV	200 W
MEBT	5 mA	750 keV/A	7.5 kW
HEBT	5 mA	20 MeV/A	200 kW

BEAM ENERGY MEASUREMENT

During the RFQ and the MEBT commissioning, an Injector Test Bench (BTI) will be used to qualify beam characteristics. Beam energy will be measured at the exit of the RFQ by the "time of flight" method. Another beam energy measurement by TOF is foreseen in the HEBT at the exit of the superconducting LINAC.

Table 2: Phase Measurement Accuracy

	Energy Accuracy	Distance (mm)	Phase Accuracy
BTI	10^{-3}	1500 ± 0.2	± 0.5°
HEBT	5.10^{-3}	5000 ± 2	± 2 °

Intensity dynamic (50 µA < Ibeam < 5mA)
Beam ratio (CW to 100µs/100ms) 10^{-3}
Phase measurement gives the possibility to subtract the offset, an advantage compared to the time measurement.

INJECTOR TEST BENCH PICK-UP

3 pick-ups will be used to measure beam energy. The third pick-up allows determining the bunch number between two first pick-ups.

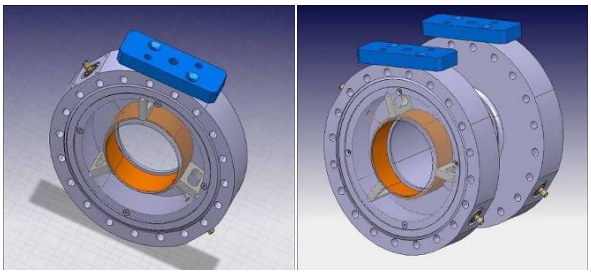


Figure 2: Pick-up Design. Diameter: 80 mm, Length: 30 mm.

PICK-UP SIGNAL SIMULATIONS

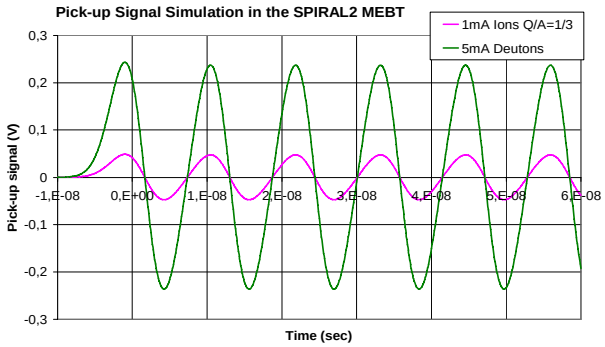


Figure 3: MEBT Pick-up Signal Simulation.

Signal amplitudes
- 1mA ions Q/A =1/3: Vh1 = 50 mV
- 5mA deuterons : Vh1 = 230 mV
Ratio h1/h2 = 13

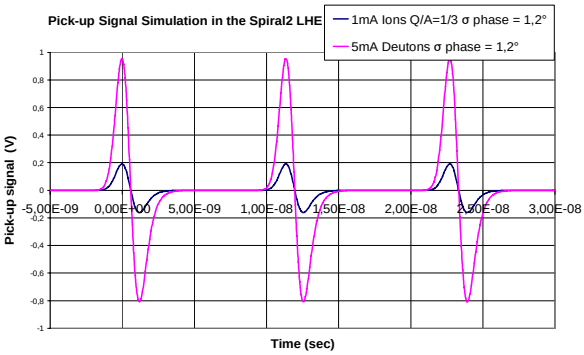


Figure 4: HEBT Pick-up Signal Simulation.

Signal amplitudes
- 1mA Ions Q/A= 1/3: Vh1= 27mV Vh2= 44mV
- 5mA Deuterons : Vh1= 136mV Vh2= 220mV
Ratio h1/h2 = 0,62

PHASE MEASUREMENT METHOD

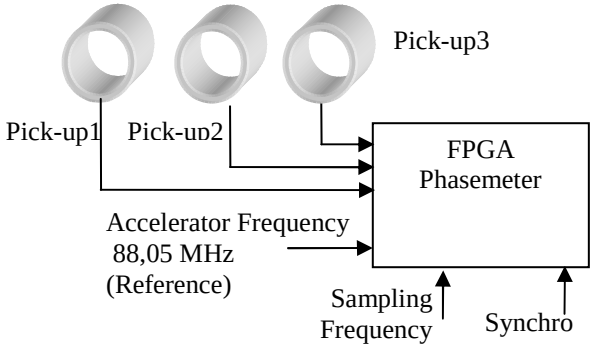


Figure 5: Assembly Scheme.

Three pick-up signals and the accelerator frequency signal will be connected directly to the FPGA phasemeter.

Under-sampling

Every signal is digitized at a sampling frequency lightly different from the signal frequency.

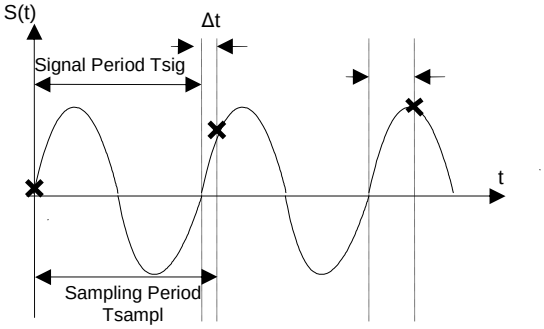


Figure 6: Under-sampling Timing.

$$\Delta t = Tsamp - Tsig \qquad Nb = \frac{Tsig}{\Delta t} \qquad Fsamp = Fsig\,\frac{Nb}{Nb+1}$$

Nb: number of samplings to reconstruct a signal period

Under-sampling uses ADCs at a lower frequency than a classical digitalisation frequency. The sample period is higher and allows digital signal processing directly by FPGA. The ADC accuracy increases and improves the dynamic measurement. The reference is also under-sampled and used in the FPGA digital signal processing.

I/Q Method

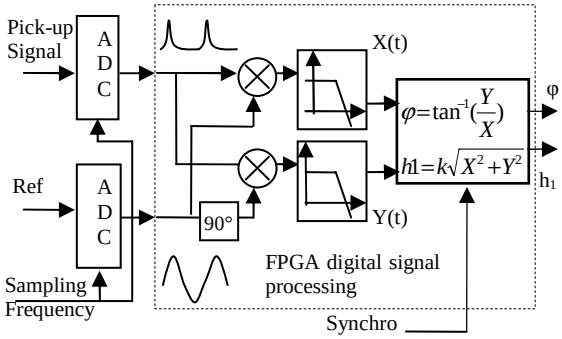


Figure 7: I/Q Diagram.

$$\begin{cases} X = \dfrac{A_{sig}A_{ref}}{2}\cos(\varphi) \\ Y = \dfrac{A_{sig}A_{ref}}{2}\sin(\varphi) \end{cases} \qquad \begin{cases} \varphi = \tan^{-1}\left(\dfrac{Y}{X}\right) \\ h1 = \dfrac{2}{A_{ref}}\sqrt{X^2+Y^2} \end{cases}$$

Digital signals are processed by an I/Q method in a FPGA. A synchronisation input is foreseen for pulsed beam, which indicates the beam presence.

Under-sampling and digital process simplify the analogic chain and remove mixers used classically with an I/Q method.

FPGA BOARD PROTOTYPE

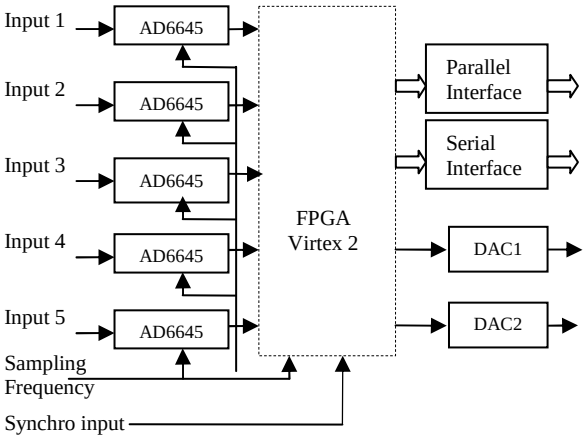


Figure 8: Board Diagram.

The FPGA board prototype is composed of analog to digital converters AD6645 Analog Devices (14 bits), a FPGA Virtex2 Xilinx, a double digital to analog converter AD9765, a parallel and a serial interface.

TEST BENCH DESCRIPTION

Tests and measurements are realized at a GANIL frequency (7MHz). The goal is to compare the measures in laboratory and on the accelerator.

CW Sinusoidal Signal

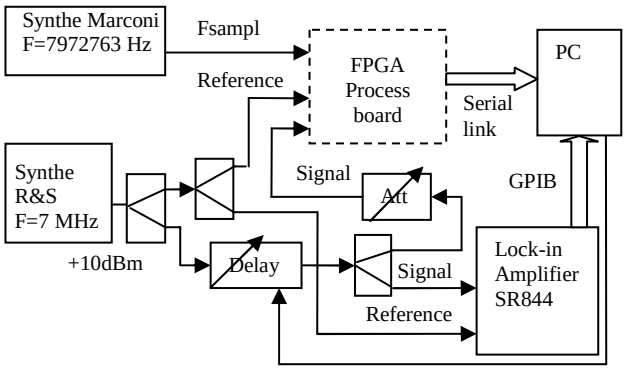


Figure 9: Test Bench Diagram.

Synthesizer R&S and splitters generate references and signals. FPGA Phase and module values are compared with the lock-in amplifier measures (SR 844 Stanford Research). The reference frequency is calculated to have 256 values per period in the FPGA process. Programmable Delay lines change the signal phase from 0° to 360°. Tests consist of measuring phase and module variations between FPGA and SR844 with shifting the signal phase. A variable attenuator decreases module signal from 0dB to 60 dB and allows comparing results with different signal levels.

RESULTS

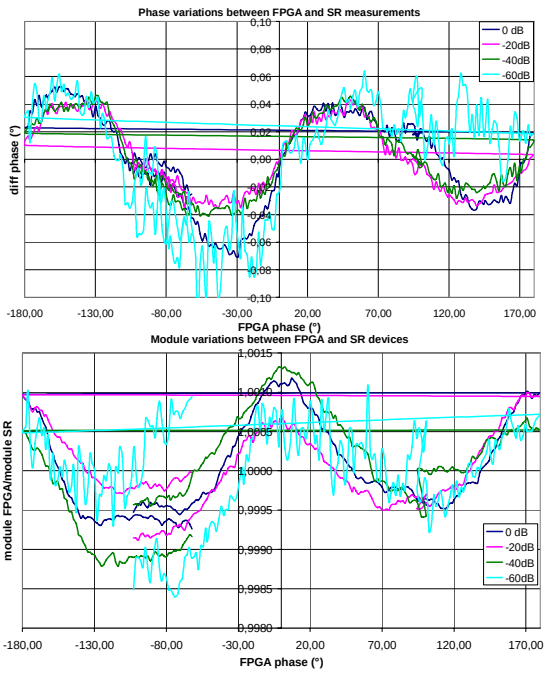


Figure 10: Phase and Module Variations.

Results are the same with a duty cycle (1ms/100ms), measurement time increases proportionally to the ratio.

CW Pulse Signal

A pulse generator (Avtech AVM-1-C) is installed in front of the attenuator. The pulse width is about 10 ns.

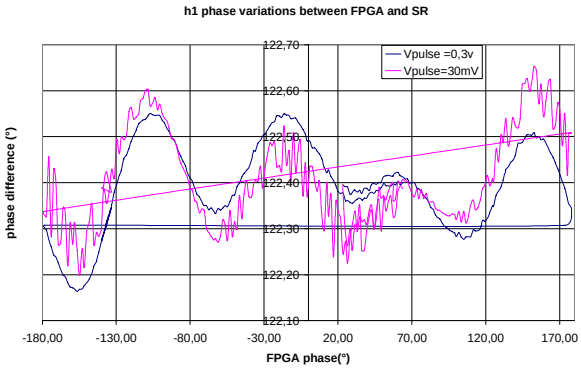


Figure 11: Phase Variations.

Main variations are due to the h2 and h3 harmonics of the reference signal. Results will be improved after filtering the reference by process.

CONCLUSIONS AND EVOLUTIONS

Under-sampling and numerical processing by I/Q method gives good results in laboratory. On a great dynamics (60dB), FPGA phasemeter is able to measure sinusoidal signal phase precisely (+/-0.1°). With pulse signals, improvements must be done to filter the reference signal and optimize the accuracy.

Pick-up signal digitalization gives also the possibility to calculate module and phase of different harmonics. This electronics can also give the opportunity to follow beam intensity on line.

The next step consists in using FPGA phasemeter on the GANIL accelerator, measuring the time of flight with two pick-ups, calculating the beam energy and comparing this value with the spectrometer measure.

A new prototype is also in development to improve analog input adaptation, sampling frequency distribution, integration with the FPGA.

REFERENCES

[1] P. Ausset et al., SPIRAL2 Injector Diagnostics, DIPAC09, Basel, Switzerland, paper id: MOPD27.

[2] C. Jamet et al., Injector Diagnostic Overview of SPIRAL2 Accelerator, DIPAC07, Venice, Italy.

[3] T. Junquera et al., Status of the Construction of the SPIRAL2 Accelerator at GANIL, LINAC08, Victoria, Canada.

[4] T. Junquera et al., The high intensity superconducting Linac for the SPIRAL2 project at Ganil, LINAC06, Knoxville, USA.

[5] P. Bertrand, JL Biarrotte and D. Uriot, Beam dynamics studies for the SPIRAL2 project, EPAC06, Edinburgh, Scotland, UK.

LONGITUDINAL EMITTANCE MEASUREMENT USING PARTICLE DETECTORS

T. Milosic, P. Forck, GSI, Darmstadt, Germany
D. Liakin, ITEP, Moscow, Russia

Abstract

A device for accessing the longitudinal phase space at low energy sections ($1.4\ MeV/u$) of the GSI heavy ion LINAC is presented. The interceptive measurement is based on the coincident detection of single particles by means of two detectors: The first detector provides measurement of secondary electrons emitted from a thin Al-foil by the impinging ion beam. Secondly, after a drift beam particles are registered directly by a fast diamond detector. This contribution describes the measurement setup in detail including the principle of particle number attenuation by Rutherford scattering in the Ta foil. The achievements concerning the required timing resolution are presented and the investigations are accompanied by recently recorded data. Finally an outlook towards post-processing is given.

MOTIVATION

The existing facility at GSI will be used as injector for the future project FAIR which requires optimizations of the existing accelerator facility. Depending on the kind of a certain optimization crucial information may be obtained from beam diagnostics. The device presented is located at the linear acceleration UNILAC and is aimed at providing information about the longitudinal phase space in order to improve injection into the Alvarez section (Fig. 1). Due to the location in front of the Alvarez tank spatial constraints led to a novel approach that is based on the time-of-flight (TOF) between two particle detectors [1].

WORKING PRINCIPLE

The measurement setup can basically be divided into three crucial parts. At first a mechanism has to provide feasible particle number attenuation to satisfy single particle coincidence measurements. Secondly, two timestamps are needed to account for the energy of the particle. Lastly,

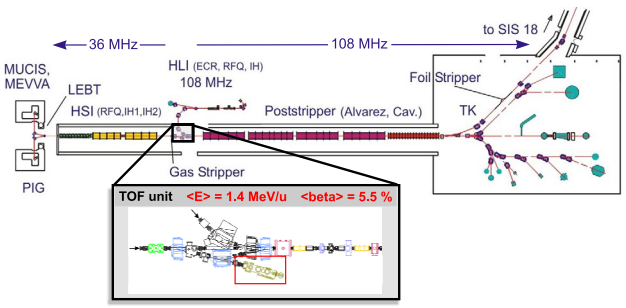


Figure 1: Setup located at GSI UNILAC after IH structures, accessible by the high current injector.

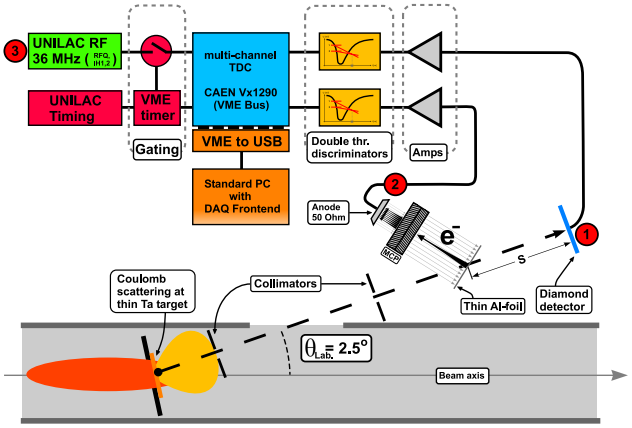


Figure 2: Device schematics. Single particles are detected indirectly at MCP module (2) and directly at diamond detector (1). UNILAC rf (3) is used as timing reference.

a method to determine the relative phase information is required to complete the longitudinal degrees of freedom within the phase space. The schematic of the measurement setup is depicted in Fig. 2.

Particle number attenuation is accomplished in two stages. Once the beam enters the device attenuation is carried out by coulomb scattering using a thin Ta foil of $210\ \mu g/cm^2$ and selecting scattered particles under an laboratory angle of $2.5°$ with respect to the beam axis. Two plates with $\varnothing\ 0.5\ mm$ and $1\ mm$ at a distance of $155mm$ act as a collimator to achieve a small solid angle of $\Omega \approx 10^{-4}$. This assumes incoming beam intensities that have already been lowered to several μA in order to prevent damages of the Ta foil. This allows for a single particle coincidence per bunch at maximum in conjunction with coulomb scattering utilising the aforementioned selection of particles under a certain solid angle. Primary beam attenuation needs different approaches for low current and high current measurements. The attenuation of the primary beam from a maximal current of $\approx 10\ mA$ to about $10\ \mu A$ is done using transverse defocusing at different locations along the UNILAC. By this space charge effects along the Linac structures are influenced. Variation of the gas pressure inside the stripper section provides an additional parameter to adjust the primary beam attenuation which is used in particular at high current measurements.

The detector setup consists of a Microchannel Plate (MCP, *Hamamatsu F4655-13*) and a diamond detector separated at $80\ cm$, the drift length relevant for the TOF.

Due to the high stopping power at $1.4\ MeV/u$, it is not possible to have a direct measurement of the traversing ions in both detectors. Therefore the MCP module has been designed to provide an indirect timing signal by measurement of secondary electrons emitted by a thin Al foil ($9\ \mu g/cm^2$) which is exposed to the particle trajectory. A potential of $-2\ kV$ with respect to the MCP front is applied to the Al foil. Electrons emitted from the Al foil are accelerated towards the MCP working at a potential of $\Delta U_{MCP} = -1.9\ kV$ and are assumed to have a sufficiently sharp peaked velocity distribution to legitimate a constant time offset imposed by their TOF. Signals are taken at the MCP anode using a bias tee connected to ground preventing damages of the DAQ electronics due to possible charge accumulation.

Eventually the ions are detected directly at a diamond detector. The diamond detector has a diameter of $8\ mm$ with a thickness of $200\ \mu m$ and is supplied by $200\ V$. Both detector signals are further processed by double threshold discriminators [3] and subsequently fed to a high resolution TDC (CAEN V1290). Derived from the UNILAC rf of $36.136\ MHz$ a logical pulse representing the period length is generated and recorded by the TDC. To reduce data overhead a prescaler of 10 is used on the regular rf data by analog gating. Linear regression is applied on the stable timing data to improve precision. The relative phase information is acquired by the time difference of the diamond time information with respect to the UNILAC rf reference. A custom-made VME beam timing module provides the macro pulse start timing.

The longitudinal phase space information is reconstructed by transformation of the TDC data into the relevant scales and subsequent filling appropriate histograms. With $\Delta t = t_{Dia} - t_{MCP}$ and assuming that $\Delta E \ll \langle E \rangle$ the relative energy deviation in linear approximation is given by

$$\frac{\Delta E}{\langle E \rangle} \approx \frac{dE}{E}\bigg|_{E=\langle E \rangle} = -2\frac{dt}{t}\bigg|_{t=t_{\langle E \rangle}} \approx -2\frac{\Delta t}{t_{\langle E \rangle}},$$

where $\langle E \rangle = E(t_{\langle E \rangle})$ is the mean energy and $t_{\langle E \rangle}$ is the TOF for a particle at mean energy. To account for relative cable offsets and latency effects at the MCP module, the design energy of $1.4\ MeV$ is used a priori, i.e. data evaluation is based on central moments. It should be noted however that without linear approximation it is particular difficult to determine the correct phase space since it is not invariant under translation in $t_{\langle E \rangle}$.

MEASUREMENT EXAMPLE

An example of data recorded with a high current setting is depicted in Fig. 3. The lower left pad shows the actual recorded data with its projection on bunch structure (upper left) and its relative energy deviation (lower right). In the upper right pad the expected longitudinal phase space at Alvarez injection has been calculated using the in-house Dynamion code. The measured phase space deviates significantly in the energy spread compared to the phase space

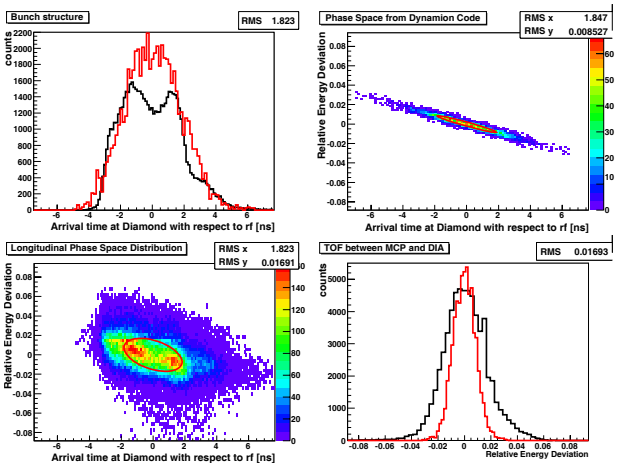


Figure 3: High current data recorded at HIPPI [2] '08 campaign - Ar^{10+} $6.5\ mA$. Histograms in black show projected measured data whereas red histograms show the projected Dynamion simulation.

received by the tracking code and gives a hint for the experimental resolution. This is also reflected in the actual values of emittance (rms) and Twiss parameters given in Tab. 1. Including the almost Gaussian shape of the energy projection this is a clear hint that a direct measurement is not capable of reconstructing the energy spread with the required resolution.

Table 1: Direct Measurement vs. Dynamion code (Fig. 3)

Fig. 3		**Measurement**	**Dynamion**
ε_{rms}	$[(keV/u)\,ns]$	0.03	0.004
α		0.5	3.9
β	$[ns/(kev/u)]$	200	862
γ	$[(keV/u)/ns]$	0.01	0.02
$Covar.$	$[(keV/u)\,ns]$	-0.014	-0.015
ΔE_{rms}	$[keV/u]$	24	12
ΔL^*_{rms}	$[ns]$	1.8	1.8

* Bunch length has been used as constraint in simulation.

TIMING REQUIREMENTS

To get a better understanding on the very high timing requirements it is useful to have a look at the expected energy width of an optimized beam at Alvarez entrance. ΔE_{rms} is expected to be around $1\%\langle E \rangle$ and thus

$$\Delta E^{expected}_{rms} \approx 14\ keV/u,$$

which corresponds to a difference in TOF of only about $240\ ps$ at the given drift length of $80\ cm$.

Uncertainties within the measurement can be classified into dissipative effects and the plain net timing resolution of the setup. Dissipative effects due to straggling occurring in both foils have been estimated using SRIM. The energy

spread for a monochromatic ensemble of incidenting particles is calculated to be about 1.7 keV/u for the different species of ions, Ar, Ta and U at the first foil (Ta) of 723 Å thickness and about 0.6 keV/u at the second foil (Al) of 334 Å thickness. As those affect the real physical phase space the corresponding relative error does not depend on the drift length.

On the other hand the timing resolution is a critical limitation which depends on several contributions from the electronics and detector setup. An input jitter of 35 ps has to be considered for each channel of the TDC. Varying signal shapes of MCP pulses do not allow for a better estimation of timing performance than at least 100 ps. Also discrimination of diamond pulses show a jitter of at least 50 ps. Additionally, as the MCP can not be mounted orthogonal to the beam axis, the foil is adjusted with an angle of 37.5° with respect to the particle trajectory. This implies an uncertainty of the drift length that can be estimated from the mean drift length and diamond radius to about $\Delta t_{foil}^{rms} \approx 24\ ps$. As there is no way of calibrating the device it is difficult to state quantitative error values especially for discrimination behaviour of the given signal shapes. Still, it is apparent from all recorded data sets that the device has a limiting energy resolution, and thus the inability to provide a direct measurement of the energy deviation.

PRELIMINIARY POST-PROCESSING

Resolution deficiencies can be treated numerically to some extend. If the response function of the setup is well known deconvolution can improve the interpretation of the recorded data. However, the process of deconvolution is very sensitive to noise which might be a limit of the present setup due to the low event rate. In Fig. 4 deconvolution has been applied to each vertical energy slice separately using the *TSpectrum class* implemented in *ROOT* for the data represented above in Fig. 3. The response function is chosen to be of Gaussian shape with an rms width of $1.25\%\langle E\rangle$. The original data has been processed with 100 iterations and 10 repetitions with a boost parameter of 1. To stress the fact of preliminary work these values should be considered of arbitrary character and do not represent a consistent procedure for now. A comparison of the data and simulation is given in Fig. 5 for different integral cutoff levels.

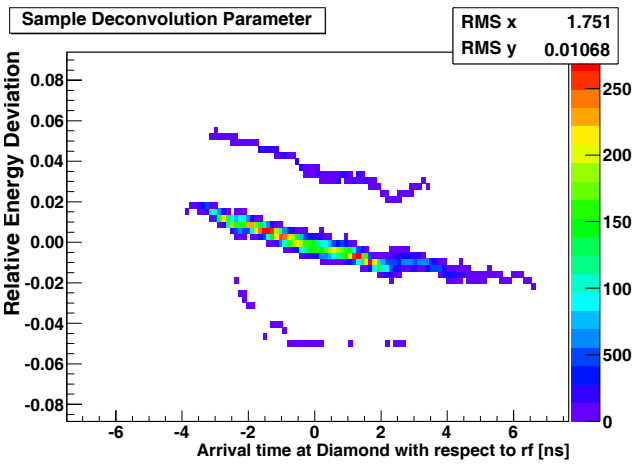


Figure 4: Preliminary post-processing using *Gold Deconvolution* as implemented in *ROOT*. Apart from the suppressed artefacts the resulting distribution tends towards the expected phase space as given in Fig. 3.

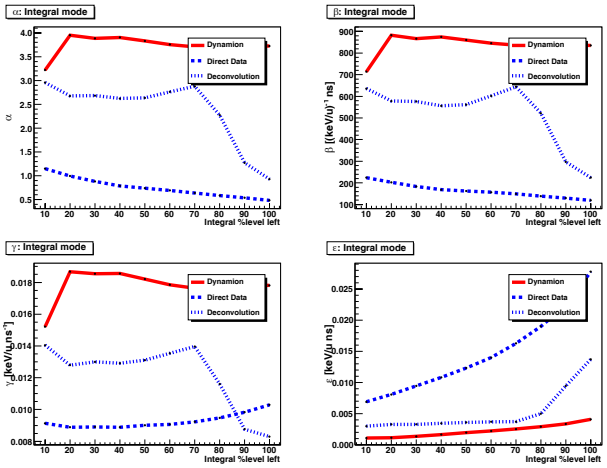


Figure 5: Comparison of *measured*, *deconvoluted* and *Dynamion* data. Integral cutoffs are evaluated by homogeneous removing of events ending on a certain fraction left.

CONCLUSION & OUTLOOK

A novel type of device for measurement of the longitudinal phase space based on TOF using particle detectors has been presented. The high timing requirements for the direct measurement of the energy can not be matched with the resolution achievable at the given drift length. Although a direct measurement is out of scope concerning the full longitudinal phase space, direct bunch length measurements have proven trustworthy as the timing requirements are significantly lower with typical bunch lengths starting at $2ns$. First attempts have been made to use post-processing techniques on the degree of freedom connected to the energy of the particles. Current efforts focus on finding a consistent method to apply deconvolution on a wide scale of recorded data.

REFERENCES

[1] P. Forck et al. "Measurement of the six Dimensional Phase Space at the New GSI High Current Linac", LINAC 2000, Monterey

[2] L. Groening et al. Phys. Rev. Lett. **89**, 094201 (2008).

[3] `http://www.gsi.de/informationen/tt/Double-Threshold-1_e.html`

BEAM PROFILING AND MEASUREMENT AT MIBL

O. F. Toader and F.U. Naab,
Michigan Ion Beam Laboratory, University of Michigan, Ann Arbor MI, U.S.A.

Abstract

Michigan Ion Beam Laboratory (MIBL) is equipped with a 1.7 MV tandem particle accelerator and a 400 kV ion implanter. Ion beams can be produced from a variety of ion sources and delivered to different beamlines. Precise beam profiling and current measurements are critical aspects of everyday activity in the laboratory and influence the success of each experiment. The paper will present the devices used at MIBL to precisely determine the parameters of the ion beams in order to produce successful proton irradiations and ion implantations.

INTRODUCTION

The Michigan Ion Beam Laboratory (MIBL) is located in Ann Arbor and is a part of the Department of Nuclear Engineering and Radiological Sciences at the University of Michigan. The laboratory is equipped with a 1.7 MV Tandetron accelerator, a 400 kV ion implanter and an ion beam assisted deposition system (IBAD). The accelerator is a solid-state gas insulated, high frequency device, capable of operation between 0.4 and 1.7 MV (Fig. 1).



Figure 1: 1.7 MV Tandetron accelerator.

Various beams can be produced, starting with protons (up to 300 μA) and continuing with D^+, He^+, C^+, O^+, N^+, heavier ions like Fe^+ and Ni^+ and many others. The Tandetron can operate with three types of sources: a Torvis by (NEC) [1] that reliably delivers proton and deuterium beams, a duoplasmatron 358 source (HVEE) [2] used mainly for Alfa particles for surface analysis and a sputtering source PS120 (Peabody Scientific) [3] used to produce heavy ions. The Tandetron has two beamlines; a 15^0 beamline for ion beam modification (implantation, and ion mixing) and radiation damage, and a 30^0 beamline for ion beam analysis, each terminated with a target chamber. Both beamlines contain a quadrupole triplet for focusing, an analyzing magnet, a raster-scanner and a steerer. The 15^0 beamline and the chamber are equipped with cryopumps that can routinely achieve pressures in the 10^{-9} Torr range. Beyond the main chamber on the 15^0 beamline there is an electrically isolated irradiation sub-chamber. A temperature controlled sample stage can be attached next for radiation damage experiments (between 50 and 600 °C). The 30^0 beamline contains an aperture system, a Faraday cup for charge collection, a beam viewer, a translation two-axis goniometer and detectors for backscattering and glancing angle measurements. It is turbo-pumped and equipped for rapid sample turn-around. Rutherford backscattering spectroscopy (RBS), nuclear reaction analysis (NRA), elastic recoil detection (ERD), and ion channelling are conducted in this chamber. All the control and monitor software programs for the proton irradiation and the Torvis source are written in Labview from National Instruments (NI) and were developed at MIBL

The 400 kV NEC is an air-insulated ion implanter (Fig. 2). The ion source Model 921 made by Danfysik [4] is designed for production of high current and high brightness ion beams. It is capable of ionizing materials that have low vapor pressure, and can produce ions by sputtering solid targets or by ionizing gases.



Figure: 2 NEC's 400 kV ion implanter.

The implanter can provide beams from most elements in the periodic table, with energies between 10 and 400 kV and with beam currents ranging from several microamperes to more than a milliampere (in some cases). Beam fluencies of up to 10^{20} atoms/cm^2 could be achieved in an area of a square inch in a few hours. Double ionization states for some elements (Ar^{2+}, O^{2+}, etc) allow for implants at energies of up to 800 kV. The target chamber and beam line operating pressure is in the 10^{-8} Torr range. A rotating carousel permits simultaneous loading of twelve 2-inch wafers, five 4-inch wafers or four 6-inch wafers for sequential implantation. The target chamber (3) is equipped with a 4-point Faraday cup system that allows for precise beam monitoring and dose measurements.

BEAM PROFILE MONITORS

Proton Irradiations

In the case of proton irradiations, the beam is raster scanned over an area that encompasses the samples to be irradiated and over a set of slits (apertures) that is used to monitor the current (Fig. 3). If the beam is not centered, (as determined by reading the amount of current detected on the 4-slits set) the beam can be corrected accordingly using the Tandetron's steerers.

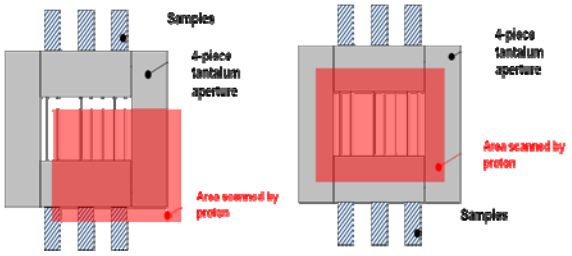


Figure 3: Beam alignment procedure.

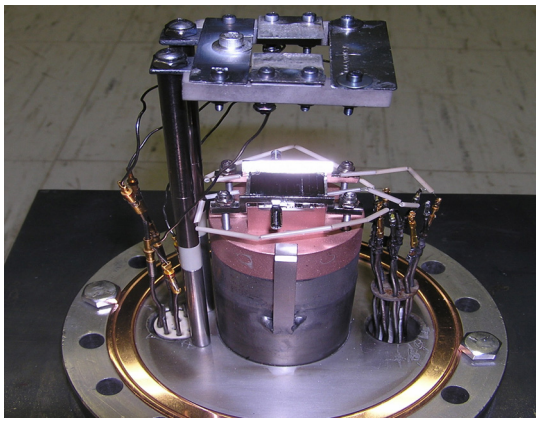


Figure 4: Actual irradiation stage.

This way we ensure that the stage (Fig. 4) where the samples are loaded is uniformly exposed to the beam

The Full-Width-Half-Maximum Profile

If the beam is not ~3 mm or less in diameter during the scanning process, there will be places on the sides of the irradiated area that will "see" less beam. The beam will spend less time on the edges than in the center of the stage, resulting a non-uniform irradiated set of samples. The beam profile gives the beam's spatial characteristics (shape and size) and determines its quality. The Beam Profile Monitor (BPM) outputs the signal to an oscilloscope. The X and Y profile of the beam as displayed on the oscilloscope resemble a Gaussian curve (Fig. 5).

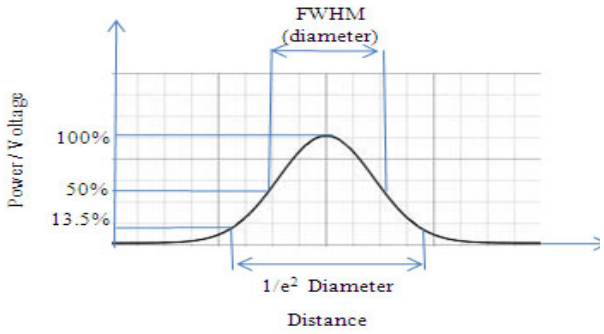


Figure 5: Typical Gaussian curve.

The Full-Width-Half Max (FWHM) specifies where the power drops to one half the maximum and represents the beam's "calculated" diameter. As the edge of the beam is not perfectly defined we generally agree that the beam's diameter is measured between two points that contain a selected percentage of the meaningful energy – and in the case of a Gaussian this is at the $(1/e^2)$*diameter. This is where the beam contains 4-sigma of the energy distribution and the beam power is at this point 13.5% of the power at maximum height.

Measuring the Beam Size

The FWHM is used in determining the width of the beam according to the BPM manufacturer's characteristics. The BPM is located close to the target (about 75 cm away) as a minimum beam is of crucial importance for the success of the irradiation experiments. MIBL is equipped with two BPMs – one on the Tandem and one on the Implanter. They were both manufactured by NEC [1]. The BPMs are model number BPM80 and BPM 82 respectively with controllers model S55A (Fig. 6 and 7).

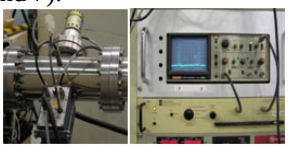


Figure 6: BPM and controller of the Tandetron.

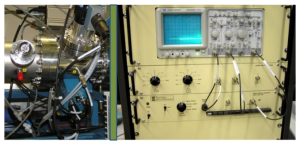


Figure 7: BPM and controller of the Implanter.

These BPMs consist of a helical tungsten wire that is driven horizontally and vertically across the beam at a frequency of about 19 cps. The position is electronically monitored and the secondary electrons generated by the interaction with the beam are collected, the charge amplified and displayed on an oscilloscope. The main advantages of this BPM setup are: long term stability and reproducibility, low current detection (~1 nA) and the capability to quantify and center the beam in the beamline. This is done by setting some reference points on the oscilloscope screen and knowing the relationship between the divisions on the screen and the location and size of the beam, the beam is steered in the correct location.

Measuring the Beam Size

If the two peaks (X and Y) correspond to the fiduciary marks of the BPM, by measuring the FWHM of the peaks (set identical for a circular beam) one can determine the diameter of the beam in the X and Y direction (Fig. 8). In the case depicted in Fig. 8, the FWHM is about 1.5 small units (one unit = 2 mm) on the scope, giving a beam diameter of ~3 mm and guaranteeing a successful irradiation. After the beam is centered and focused, is raster scanned (Fig. 9) to cover the desired area.

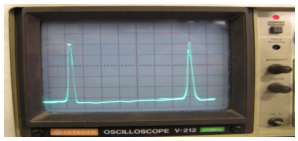


Figure 8: X and Y displays of the beam.

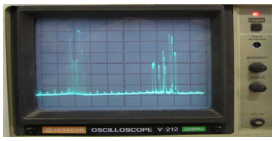


Figure 9: Beam during scanning.

A similar procedure is applied to the implanter to determine the beam's characteristics.

SUMMARY

Michigan Ion Beam Laboratory is a user's facility that can perform a wide range of services in the surface analysis, ion beam irradiation and ion implantation fields. It can produce a wide variety of ion beams with energies varying form 10 keV to 3.4 MeV and higher (for higher charge states). Beam measurements are a prerequisite part of a successful experiment. At MIBL this is guaranteed by a set of BPMs and current measurements performed before and during the runs.

REFERENCES

[1] National Electrostatic Corporation (NEC), http://www.pelletron.com.
[2] High Voltage Engineering Europa (HVEE), http://www.highvolteng.com.
[3] Peabody Scientific: http://www.peabodyscientific.com.
[4] Danfysik: http://www.danfysik.com

DESIGN AND OPERATION OF A CURRENT MONITOR UNDER HEAVY HEAT LOAD

P. A. Duperrex, P. Baumann, S. Joray, D. Kiselev, Y. Lee, U. Müller,
Paul Scherrer Institut, 5232 Villigen PSI, Switzerland

Abstract

For high intensity beam operation (3 mA, 1.8 MW) in the PSI 590 MeV 50 MHz cyclotron, a new current monitor for proton beams has been built. This monitor uses a re-entrant cavity tuned at the 2nd RF harmonic. Compared to the current monitors already in operation, the design has improved cooling. The circuit resonance has been optimized in the laboratory to minimize the gain drift due to temperature changes. Energy deposition simulations and thermal analysis were performed to estimate the cooling efficiency, and preliminary results indicate that the temperature rise of the resonator corresponds to values predicted with MARS. Anomalous gain drift is nevertheless observed even with an active cooling system. A drift compensation scheme using a pilot signal 600 kHz off the designed resonator frequency is being presently tested and the preliminary results are encouraging.

INTRODUCTION

A new proton beam current monitor called "MHC5" has been installed in the PSI 590 MeV proton cyclotron. The current monitor is located approximately 8 m behind a 4 cm thick graphite target used for muon and pion production. As a consequence, the monitor is exposed to scattered particles and their secondaries from this target. The resulting thermal load is the main concern for this monitor. This problem will be even acuter for future high intensity beam operation (3 mA, 1.8 MW). Thus the main improvements of the new monitor were an active water cooling system and a surface blackening to improve the radiation cooling.

MAIN FEATURES

Measurement Principle

The current monitor consists of a TM01-mode coaxial resonator, coaxially symmetric with the round proton beam pipe. The resonator is modelled as a quarter-wave transmission line, the open-end gap in the beam pipe couples some of the wall current into the resonator. The cavity is tuned at 101.26 MHz, the 2nd harmonic of the proton beam pulse frequency. This frequency is used because of the better signal-to-noise ratio, the RF noise components from the generator being mainly at the odd harmonics. No significant shape dependency of the 2nd harmonic amplitude for relative small beam pulses is expected [1]. The oscillating magnetic field in the resonator is used to measure the beam current.

Resonance Condition

For a given resonant frequency, using an external capacitor shunt reduces the physical length of the resonator. The corresponding resonance condition is given by:

$$\tan\left(\frac{2\pi L}{\lambda_m}\right) = \frac{\lambda_m}{2\pi c C Z_o}$$

with L the resonator length, C the capacitor shunt, Z_o the characteristic impedance of the transmission line, and λ_m the resonant wavelength.

Mechanical Design

The monitor is made of aluminium (anticorodal 110), with a 10µm coating layer of silver to improve the electrical conductivity. Compared to the monitors already into operation, the thermal coupling conductance was increased to improve the efficiency of the active water cooling. The monitor itself being in vacuum, the external surfaces have been chemically blackened to increase the emissivity of the monitor to provide an additional cooling. Four type K thermocouples monitor the resonator temperature.

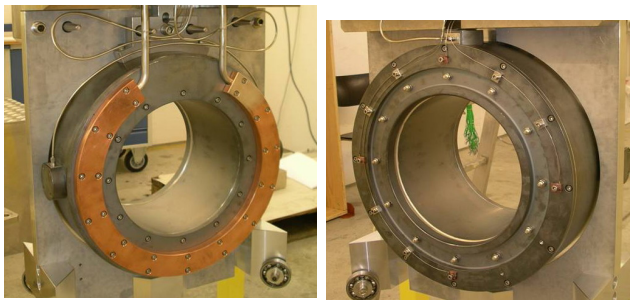


Figure 1: The new current monitor, showing the water cooling circuitry at the beam entry side (left). The four thermocouples are installed on the beam exit side (right).

Temperature Drift Compensation

Effect of temperature changes on the resonant frequency has been measured on a laboratory test bench before the installation of the monitor. External resonant circuits have been added to compensate the temperature drifts. Gain drifts smaller than 0.3dB were measured for the expected temperature variations during beam operation (30 to 70 ^{o}C).

POWER DEPOSITION

To predict the thermal load, the proton deposition rate in the current monitor MHC5 was simulated, using Monte Carlo methods with the MCNPX [2] and MARS [3] programs. In MCNPX, the effect of the magnetic quadrupoles QHG 21 & 22 located between the target and the current monitor cannot be taken into account due to the lack of magnetic module. In MARS, the quadrupole induced beam deflection is taken into account. The MCNPX and the MARS calculations respectively predict 562 W and 345 W energy deposition rate for 3 mA proton beam current. In MCNPX, the Coulomb scattering at the meson target is observed to be stronger, which causes more widely scattered beam thereafter, giving the higher energy deposition rate. In MARS, the beam is more focused due to the presence of quadrupole effect, and the current monitor is less exposed to scattered particle shower.

THERMAL ANALYSIS

Simulation Tools

The applied simulation methods for the thermal analysis include the coupled flow and heat simulations based on second order accurate finite volume scheme and the Monte Carlo simulations for particle transport. The coupled flow and heat simulations have been performed by the multiphysics commercial tool CFDACE+ [4]. For calculation of the heat exchange rate between MHC5 and water, the shear stress transport (SST) $k-\omega$ turbulence model [5] has been used. The mesh in the boundary layer region was refined until the desired value of the wall function is achieved.

Water Cooling Efficiency

For the laboratory test, the monitor MHC5 was thermally isolated and first heated by circulating 80 °C water through the cooling circuitry. As the monitor reached a thermally stable condition, the monitor was then suddenly cooled down using 30 °C water. The monitor temperature was observed to decrease exponentially in time during this cooling phase. The corresponding time constant was measured for different water speeds and then compared with the simulation results (Fig. 2). The time constants agree well within the 10 % error for water speeds larger than 0.5 m/s. There is relatively large disagreement in values, for the water velocities below 0.25 m/s. One reason is that the simulation setting uses the turbulence module which might describe the laminar flow region with low water speed inaccurately. Another reason is that there have been more uncertainties in accurately controlling the water velocity for small mass flux.

For reference, the transition from laminar to turbulent flow is expected to occur inside the 10 mm diameter water pipe at around 0.25 m/s. Then, the fully developed turbulent internal flow is formed at a water speed around 0.4 m/s (or Reynolds number $4\text{x}10^3$, see Ref. [6]). Once the turbulence is fully developed, the improvement of the cooling efficiency with increasing water inlet speed is marginal. This phenomenon is well reproduced by the simulation and the measurement.

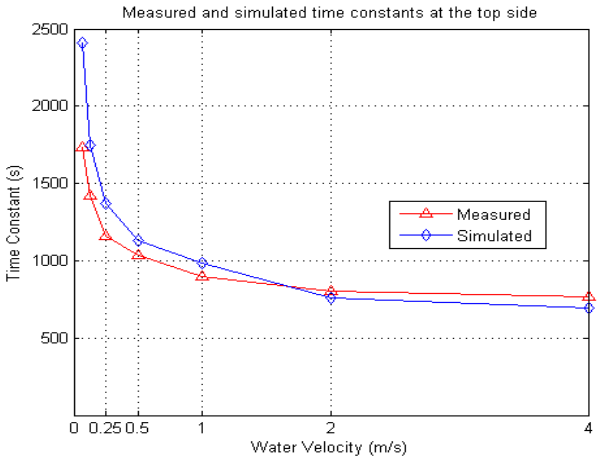


Figure 2: Comparison between measured and simulated time constants at the upper thermocouple location.

Based on these cooling efficiency tests, a speed of 2 m/s was chosen for the water inlet flow. Larger speeds would just accelerate the wearing out of the tube wall without improving the cooling.

Predicted Operating Temperature

For the prediction of the operating temperature of MHC5, a coupled flow and thermal simulation for the energy deposition rate given by MCNPX was performed.

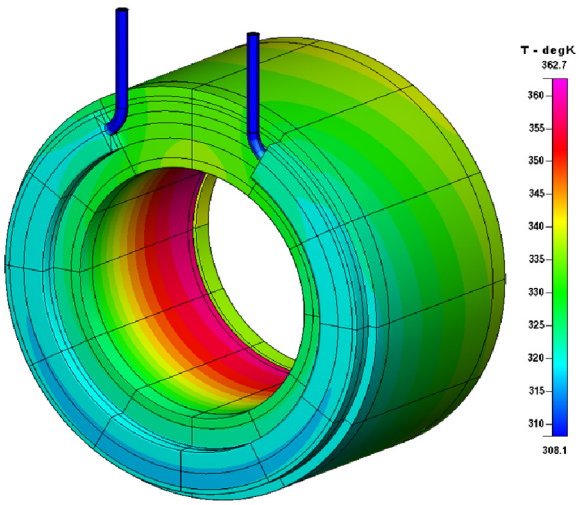


Figure 3: The simulated temperature profile of MHC5 for the proton beam current 3 mA. The temperatures range from 308°K to 363°K.

Figure 4 shows the simulated temperature distribution for a proton beam current 3 mA, with the peak temperature being 90 °C. For the energy deposition input from MARS, the peak temperature is simulated to be below 70 °C.

Comparison with Experiment

For the present operating beam current of 2 mA and for a inlet cooling water temperature of 38 °C, the MARS thermal simulation predicts a temperature of 48 to 49 °C at the upper PT100 sensor location. This is in excellent agreement with experimentally observed temperature (also 48 to 49 °C) for a 2 m/s cooling water speed. Thus, MARS delivers a realistic estimate of the power deposition.

PRELIMINARY RESULTS

Measurements of the beam current showed however significant and unexpected drifts for large currents (>1 mA). The drifts are clearly visible when the MHC5 current measurement is compared with a standard current monitor (MHC6) on the same beam line (Fig. 4). After each short beam interruption, MHC5 measurement drifts can be observed whereas MHC6 measurements remain stable. The temperature variations during these measurements were smaller than 5 °C and they could not account for the observed 10% current measurement drift. Transfer function measurements were thus performed during beam operation and the results clearly show changes larger than those observed during the bench tests.

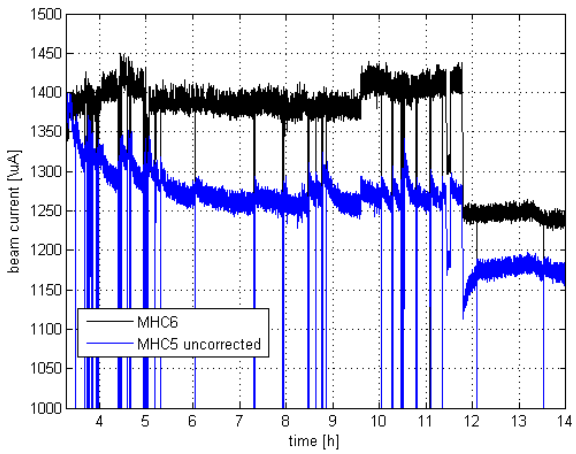


Figure 4: Time evolution of the beam current as measured with standard monitor (MHC6) and with the new monitor (MHC5). MHC5 drifts are clearly visible.

The use of a pilot signal (test signal 600 kHz off the cyclotron RF frequency) to monitor these drifts and to provide a calibration has been investigated. An off-line analysis using MATLAB shows that the pilot signal may indeed compensate the observed drift (Fig. 5) at least during stable beam operation (i.e. no long beam interruptions).

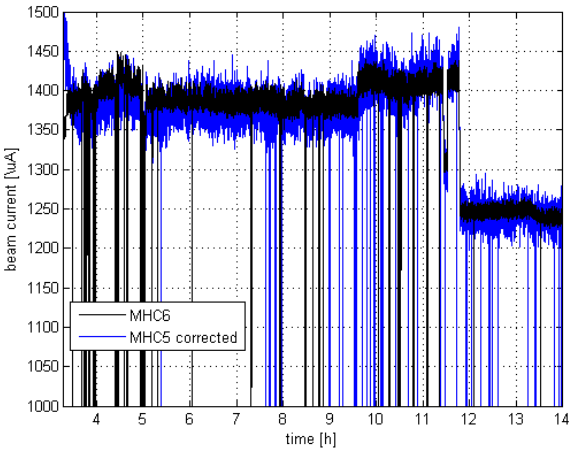


Figure 5: Time evolution of the MHC6 and of the corrected MHC5. The drifts could be compensated by using a pilot signal.

CONCLUSION

The preliminary measurements indicate that temperature measurements are in agreement with power deposition simulations when the magnetic field effects are taken into account (MARS). The beam current measurement drifts are larger than expected and remain for the moment unexplained. Correction schemes using a pilot signal are under investigation and the preliminary results are positive.

REFERENCES

[1] R. Reimann, M. Rüede, “Strommonitor für die Messung eines gepulsten Ionenstrahls”, Nucl. Instr. Meth. 129 (1975) 53.

[2] D.B. Pelowitz, ed., “MCNPX User’s Manual,” Version 2.5.0, LA-CP-05-0369

[3] N.V. Mokhov, C.C. James, “The MARS Code System User’s Guide,” Version 15, 2007.

[4] CFD-ACE+, http://www.esi-group.com.

[5] F.R. Menter, “Zonal Two Equation $k-\omega$ Turbulence Models for Aerodynamic Flows”, AIAA Paper 93-2906.

[6] J. P. Holman, “Heat Transfer,” McGraw-Hill, 2002.

A "NOT-INTERCEPTIVE" FARADAY CUP IN THE CNAO LOW ENERGY INJECTION LINES

G. Balbinot, J. Bosser, M. Caldara, L. Lanzavecchia, M. Pullia, A. Parravicini, Pavia, Italy
on behalf of the CNAO collaboration

Abstract

The CNAO, the first Italian synchrotron for deep hadron therapy [1, 2], is presently in its final step of installation. It will deliver beam of both Protons and Carbon ions, in three treatment rooms, in order to cure solid tumours with active scanning technique.

CNAO beams are generated by two ECR sources, able to produce both particle species, and transferred to a RFQ and a LINAC through a Low Energy Beam Transfer line (LEBT) at 8 keV/u and then accelerated up to 7 MeV/u before being injected in the synchrotron ring.

At the end of the LEBT line, just upstream the RFQ (L2-011A-IC1 in Fig. 1), an electrostatic Chopper deviates the beam on the vacuum chamber except for about 100 micro-seconds every 2 seconds, in order to shape the particles batch according to LINAC requirements and to minimize the beam losses at the RFQ entrance. An electrically insulated vacuum pipe section hit by the deviated beam allows reading the LEBT beam current: this detector is called Chopper Faraday Cup (CFC) and is based on the Faraday Cup working principle: it results a "not-interceptive" monitor that is able to measure, continuously, the source beam current ripples and stability, without affecting the beam delivered to the synchrotron. The CFC detector is presently under commissioning and preliminary results are presented.

CFC DESCRIPTION

The CFC is a detector installed in the LEBT line, devoted to monitor, continuously, source current ripples and stability, even during treatments, without affecting the beam delivered to the synchrotron: the goal is the monitoring of beam current slow variations due to sources instabilities and ripples. This implies that the system should be able, in the worst case, to have 1% resolution of the minimum nominal beam current, which corresponds to 1.5 μA, according to LEBT beam parameters at chopper level (Table 1).

The CFC key idea (Fig. 2) consists of insulating the vacuum chamber sector downstream the chopper and measuring the collected current: the cup measures the full beam intensity while the Electrostatic Chopper is powered. The result is an on-line monitor based on the Faraday Cup (FC) principle but not interceptive for the beam directed to the synchrotron: it will be blind only when the beam is directed into the LINAC section, that is nominally 100 μsec every 2 sec. Like a conventional Faraday Cup, the CFC is constituted by a body (A to B on Fig. 2), collecting the charge to be measured, and a repeller, aiming to push back the secondary emitted electrons produced by the beam-to-body interaction, whose escape would affect the measurement. The CFC body is the insulated section of the vacuum chamber where the beam is bent; it is showed grounded by a "resistance" in Fig. 2. The voltage across the "resistance" is proportional to the LEBT current. It is defined by inserting two insulating gaskets at its extremities. CFC length and diameter are optimized to the Chopper kick range and to the beam rigidity (Table 2).

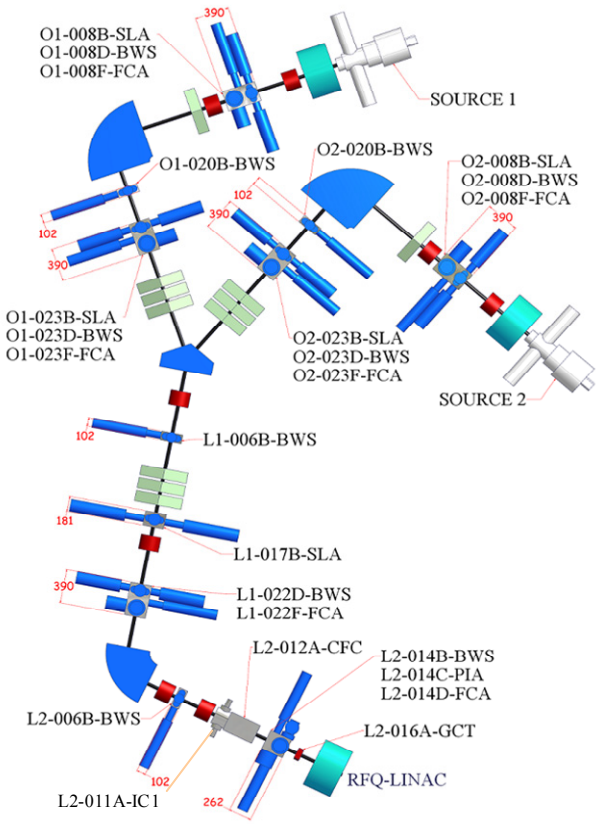


Figure 1: LEBT Instrumentation Layout with elements names. SLA are Slits, BWS are Wire Scanner in both planes, FCA is Faraday Cup, CFC is the Chopper Faraday Cup , PIA is Profile Grid, GCT is a current transformer and IC1 is the electrostatic chopper.

The repelling field, aimed to send back secondary electrons to the body, is generated by a metallic cylinder having an aperture where the beam is expected to pass (Fig. 2); this cylinder is inserted into the CFC tank and grounded, while the chamber is polarized with a positive voltage (V_{bias}= 50÷100V) and so protected with a Plexiglas cover (Fig. 3) for safety.

Table 1: Beam Parameters at LEBT Chopper

H_3^+ Current intensity at Chopper	0.70 mA
C^{4+} Current intensity at Chopper	0.15 mA
Beam Current stability	± 1.5%
Beam Current ripple	± 2 %
Beam before Chopper	Continuous
Beam after Chopper	100µs pulse at 0.5 Hz
Beam Energy	8 keV/u

Table 2: CFC Mechanical Parameters

	Material	Length	Inner diameter
Repeller	Al	360 mm	80 mm
Repeller support	Al	360 mm	65 mm
Body	Al	360 mm	90 mm
Insulators	Viton	3.53	156 mm

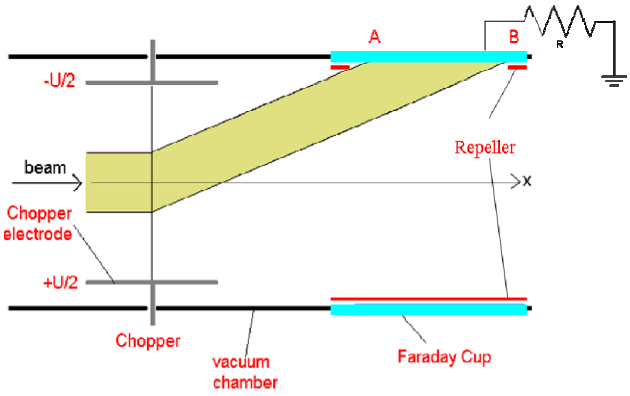


Figure 2: Schematic top view of the CFC working principle.



Figure 3: CFC with Plexiglas cover.

The beam enters the CFC continuously for most (99.995%) of the machine cycle time (2 sec) so over heating problem cannot be neglected. Large cooling fins (Fig. 3) on the outside of the CFC tank improve the air-cooling efficiency: at the maximum Carbon ion current the power to be dissipated is about 3.6 W. This kind of cooling is estimated to be sufficient to preserve the detector under these conditions. Moreover, two power feed-throughs (OFHC Copper, 1 pin, 9.5mm diameter) are used to ground the repeller and allow some heat transfer. Using Plexiglas shield, the air convection efficiency is reduced. On a test bench, a power of 150 W has been applied to the CFC: it reached the steady state temperature of 70°C, which is fully acceptable without any risk. Anyway, in order to increase the device safety, the CFC temperature is always monitored by an infrared thermometer remotely readable from the control room.

EXPERIMENTAL RESULTS

Particles deflection angle depends on the beam barycentre position and chopper electrodes polarisation value. It has been simulated by using the Simion 7.0 program. The first measurement is, indeed, the CFC current acquisition at different chopper deflection voltages (Fig. 5); a Proton probe beam of 100 µA, having a spot diameter of about 10 mm and positioned at the CFC mechanical centre, was available for such a test.

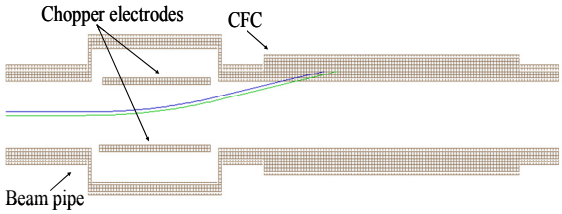


Figure 4: CFC Simion Code 7.0 simulation, top view: chopper electrodes polarized at ΔV=4kV.

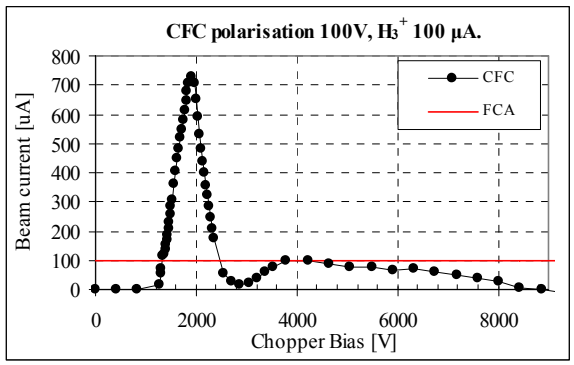


Figure 5: CFC measured current at different chopper deflection voltages (Chopper Bias [V] on abscissa) with a H_3^+ probe beam of 100 µA.

Figure 5 reports the average beam current read with the CFC body polarised at 100V at various chopper

deflection voltages and also compared with the current read on the FC upstream the dipole (L1-022F-FCA) and downstream the CFC (L2-014D-FCA) where the measured beam current is the same. The CFC readout current value is coincident with the one obtained with the classical FCs when the chopper electrodes are polarised at 4 kV. The peak at lower deflection voltage (~2kV), which is not the normal working setting, could be due to the fact that the beam interacts in a region where, for mechanical reasons, the electric field is stronger: peak amplitude is CFC polarisation voltage dependant. With these parameters (chopper electrodes at 4 kV and CFC polarisation at 100V), the beam current measured on the CFC has been plotted versus the FC upstream the dipole current by changing beam intensity (Fig. 6) modifying the slit aperture at L1-017B-SLA.

The CFC has a linear response coefficient that is 5% below that of the normal Faraday-Cup; the error could be due to a not optimized secondary electrons repelling which could be improved increasing the CFC polarisation voltage. Looking at the horizontal profiles downstream the CFC (Fig. 7), it appears that the repelling field asymmetry affects the beam trajectory even at 100V polarisation, kicking the beam on the right with respect to the tank centre. In order to solve this problem, the CFC electronics has to be modified as described in following chapter.

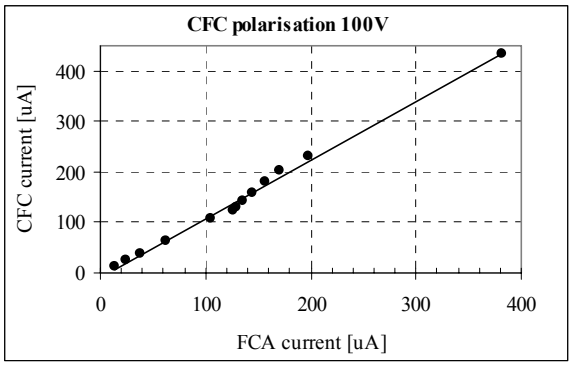


Figure 6: CFC current at different H_3^+ beam intensity.

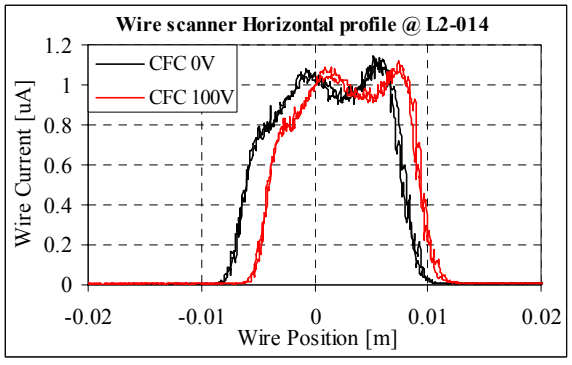


Figure 7: CFC polarisation effect on H_3^+ beam profiles.

ELECTRONICS CHAIN

Figure 8 sketches the electronic chain connected to the CFC is used to polarise the cup and to acquire the beam current. Appling on the CFC a polarisation (0÷1250V) through a voltage-regulated power supply like FUG MCP140-1250 with floating outputs, a DC current of few microamperes entering the cup can be read imposing the power supply to generate a current larger than the beam into a resistor (R2 in Fig. 8) to ground: the PS regulation reacts when beam adds to the normal current in order to keep the voltage constant. Measuring the variation of the power supply current monitor output ("IMON" in Fig. 8), the CFC beam current can be computed. Using a capacitor (C2), the monitoring of beam pulse duration injected in the RFQ and LINAC is also possible.

During the measurements, the relay that grounds the cup is opened; the problem of beam deflection due to the repeller could be solved closing the relay when the beam is no more bent by the chopper but sent into the LINAC. This solution is presently under investigation.

CONCLUSION

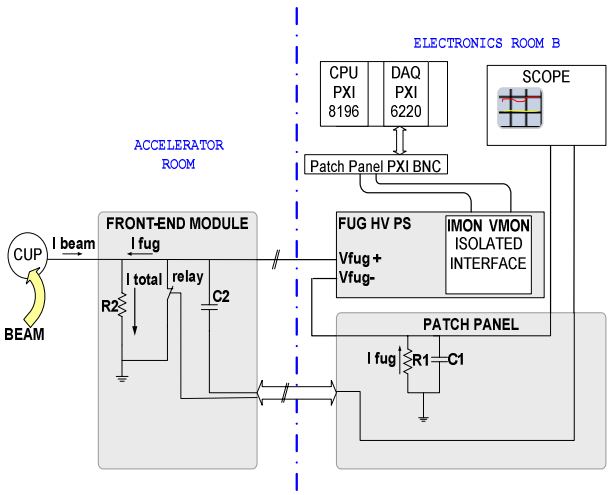


Figure 8: CFC electronics chain.

Insulating the vacuum pipe downstream the electrostatic chopper, it's possible to monitor a Proton beam current using the Faraday Cup working principle, without intercepting the beam for treatments: the preliminary results show that the CFC response is linear by 5%. Problems remain on the repelling field system that can perturb the beam trajectory: once solved with a modified electronic chain, the detector commissioning with a full, Carbon and Proton, beam, can be performed.

REFERENCES

[1] S. Rossi, "Developments in proton and light-ion therapy", EPAC 2006.

[2] M.Pullia, "Status Report on the Centro Nazionale di Adroterapia Oncologica (CNAO)", EPAC 2008.

BEAM BASED MEASUREMENTS OF THE RF AMPLITUDE STABILITY AT FLASH USING A SYNCHROTRON RADIATION MONITOR

Ch. Gerth, F. Ludwig and Ch. Schmidt
Deutsches Elektronen-Synchrotron DESY, D-22603 Hamburg, Germany

Abstract

To exploit the short radiation pulses in pump-probe experiments at single-pass free-electron lasers, stabilization of the longitudinal profile and arrival time of the electron bunches is an essential prerequisite. Beam energy fluctuations, induced by the cavity field regulation in the accelerating modules, transform into an arrival time jitter in subsequent magnetic chicanes used for bunch compression due to the longitudinal dispersion. The development of beam based monitors is of particular importance for the validation and optimization of the cavity field regulation. In this paper we present bunch-resolved energy jitter measurements that have been recorded with a synchrotron radiation monitor at the Free-electron LASer in Hamburg (FLASH). The (rms) beam energy jitter was determined to be $8.8\ 10^{-5}$, and the cavity field detectors of the accelerating module have been identified as the main noise source within the cavity regulation system with an (rms) amplitude fluctuation of $6.5\ 10^{-5}$. The reduction of deterministic cavity field imperfections by applying a feedforward learning algorithm for the cavity field regulation is demonstrated.

INTRODUCTION

Stable and reliable user operation of the Free-electron LASer in Hamburg (FLASH) requires precise control and stabilization of the RF accelerating amplitudes and phases. This is in particular true for RF accelerating fields prior to bunch compressors, as the ultra-short electron bunches with high peak currents are produced by off-crest acceleration in combination with magnetic dipole chicanes. Small fluctuations in the energy chirp rate may cause unacceptable peak current and bunch arrival time jitters. For instance at FLASH, RF amplitude and phase stabilization of about 10^{-4} and 0.01° are required to achieve peak current variations on a percent level.

A schematic of the FLASH injector is shown in Fig. 1. The RF photo-cathode gun is directly followed by the super-conducting 1.3 GHz accelerating module ACC1 which accelerates the electrons to a beam energy of typically 130 MeV. The module comprises eight 9-cell niobium cavities with a very high quality factor, i.e. very narrow bandwidth and very long response times. The maximum feedback gain g_0 that can be applied in the low-level RF (LLRF) system for the regulation of ACC1 is limited due to instabilities generated by the digital control loop, and, therefore, imperfect compensation of effects such as beam loading may occur.

A deviation of the beam energy $\Delta E/E$ transforms into a horizontal beam displacement Δx in the dispersive section of the bunch compressor (BC) downstream of ACC1 and a beam arrival time difference Δt at the end of the BC given by (first order transport theory, $\beta \simeq 1$):

$$\Delta x = R_{16} \cdot \frac{\Delta E}{E} \quad \text{and} \quad \Delta t = R_{56} \cdot \frac{\Delta E}{E}, \qquad (1)$$

where $R_{16} \approx 300 - 400$ mm and $R_{56} \approx 140 - 230$ mm are the the horizontal and longitudinal dispersion of the BC. The beam energy can be determined by recording the beam position Δx with a synchrotron radiation (SR) monitor.

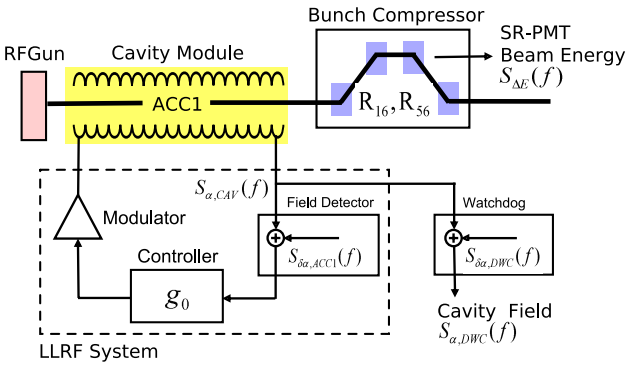


Figure 1: Schematic of FLASH injector.

SR MONITOR

The SR emitted in the third dipole of the first BC at FLASH is imaged by a SR monitor which comprises an intensified CCD camera (SR-Camera) and a multi-array photomultiplier tube (SR-PMT). By utilizing a beam splitter, both the SR-camera and SR-PMT can be used simultaneously.

The SR-camera [1] records the full x-y projection of the electron bunches. By adjusting the gate and delay of the camera timing, single bunches or any number of subsequent bunches can be chosen out of a bunch train. However, the readout of the CCD is too slow to resolve more than one electron bunch within a bunch train.

Two adjacent anodes of the SR-PMT [2] are used to measure the centre-of-gravity beam position which is given by the normalized difference signal s of both anodes:

$$s = \frac{I_1 - I_2}{I_1 + I_2}, \qquad (2)$$

where I_1 and I_2 are the signal intensities of each anode.

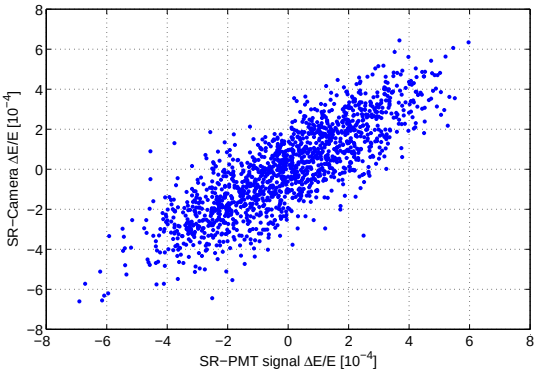


Figure 2: Correlation plot for 500 bunches recorded simultaneously with the SR-PMT and SR-camera.

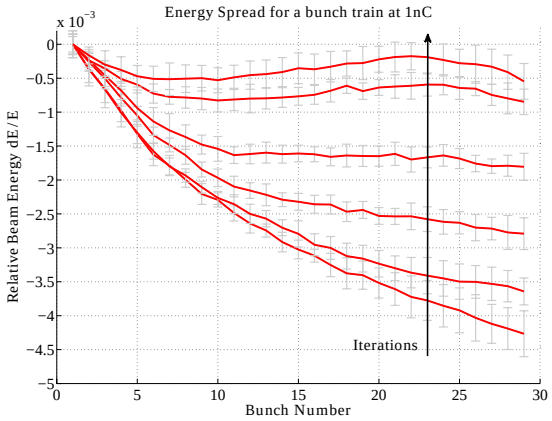


Figure 3: Removing beam induced RF field deviations along the bunch train with a learning FF algorithm.

The fast SR-PMT signals are digitized by analog-to-digital converters (ADC) which enables bunch-resolved beam energy measurement within the bunch trains. By changing the dipole current and, therewith, the beam position, both the SR-camera (in pixel) and SR-PMT (in V) can be calibrated as a relative change in the magnetic field corresponds to a relative change in beam energy.

An upper limit for the energy resolution can be estimated by recording simultaneously the relative energy jitter with the SR-camera and SR-PMT. Figure 2 shows the correlation of the energy jitter measured for 500 subsequent bunch trains. The difference of the measured energy jitter is $1.08 \pm 0.04\,10^{-4}$ which gives an upper limit for the resolution of both detectors. Assuming that both detectors have the same resolution, the resolution of each detector would be $1.08 \pm 0.04\,10^{-4}/\sqrt{(2)} = 7.6 \pm 0.3\,10^{-5}$.

LEARNING FEEDFORWARD

The RF field regulation is subject to various disturbance sources which can be distinguished into stochastic and deterministic disturbances. The effect of both disturbances can be minimized to a certain level by usage of a feedback compensator. Repetitive disturbances can also be suppressed by using the knowledge from previous regulations to adapt the system input drive for the following ones. The basic update algorithm [3] is given by:

$$u_{k+1}(t) = u_k(t) + L(t)\, e_k(t)\,, \qquad (3)$$

where u is defined as the system input and e the deviation of the measured RF output to the given setpoint. L is a linear, non-causal, time-varying filter based on the identified system model.

Figure 3 shows the energy slope along bunch trains with 29 bunches measured with the SR-PMT for several iterations of a learning feedforward (FF) algorithm. Note that stochastic effects were eliminated by normalising the energy of the first bunch for each bunch train to zero. As can be seen, the energy slope over the bunch train is about $4\ 10^{-3}$ (lowest curve) even with the feedback controller turned on. Only a few iterations of the leaning FF algorithm were necessary to reduce the energy slope caused by beam loading.

The standard deviation of the beam energy of all bunches in the bunch train relative to the corresponding mean value is shown in Fig. 4. The convergence speed of the learning FF algorithm is high enough to achieve a rms beam energy stability of below 10^{-4} within a bunch train after several iterations. Each iteration step corresponds to a measurement over 10 bunch trains.

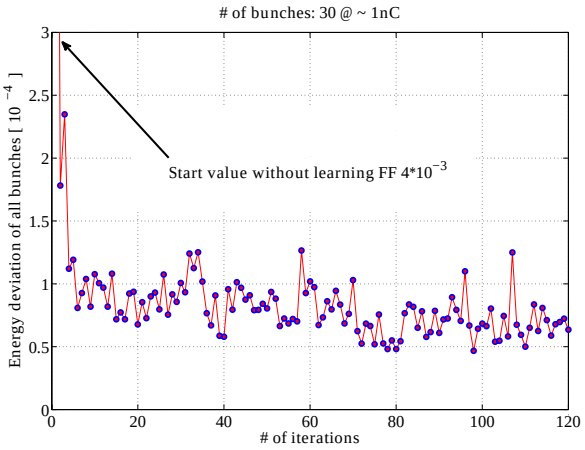


Figure 4: Minimization of the rms energy deviation of all bunches within a bunch train by applying the learning FF algorithm.

BEAM STABILITY

The cavity field amplitude and phase fluctuations within the LLRF regulation system depend mainly on the controller loop gain and amplitude and phase noise of each subsystem: cavity, master reference, field detectors, modulator and klystron [4]. To clarify how the LLRF system contributes to the beam energy and bunch arrival time fluc-

tuations, we have determined its correlation to the cavity vector sum field of ACC1. For minimum noise contribution and closed loop operation of the regulation system, the measured closed-loop cavity vector-sum-field noise decreases with increasing loop gain and is not suitable for correlation measurements. Nevertheless, the cavity field noise in correlation to the beam energy jitter can be detected by using a second noise 'watchdog' system which is operated simultaneously in open loop mode as depicted in Fig. 1. Solving both LLRF systems using algebraic methods presented in [4] and neglecting phase noise contributions, both the beam energy noise $S_{\Delta E}(f)$ and cavity field noise $S_{\alpha,DEV}(f)$ detected by the watchdog system are given by

$$S_{\Delta E}(f) = S_{\alpha,CAV}(f) \quad (4)$$

$$S_{\alpha,DEV}(f) = S_{\delta\alpha,DEV}(f) + S_{\alpha,CAV}(f)\,, \quad (5)$$

where $S_{\alpha,CAV}(f)$ is the vector sum amplitude noise of the cavity field and $S_{\delta\alpha,DEV}(f)$ the field detector noise. Using a perfect controller with a gain of $g_0 \gg 1$, which eliminates most of the regulation noise, indicated by a nearly noiseless cavity vector sum signal, shifts the field detector noise directly onto the beam in closed loop operation. Using $S_{\alpha,CAV}(f) = S_{\delta\alpha,ACC1}(f)$ and Eq. (5), the correlation between the beam energy fluctuations and the detected cavity field noise is given by

$$\gamma_{\delta E,\alpha}(f) = \left(1 + \frac{S_{\delta\alpha,DEV}(f)}{S_{\delta\alpha,ACC1}(f)}\right)^{-\frac{1}{2}}. \quad (6)$$

The correlation between the beam energy jitter measured with the SR-PMT and the cavity field measured with the watchdog system is shown in Fig. 5 for 6000 bunch trains at 6 degree off-crest operation of ACC1. Long-term drifts were eliminated in the data. Except for some occasional deviations, the measurements are in accordance with Eq. (6) for $\gamma_{\delta E,\alpha}(f) = 1/\sqrt{2} \approx 0.707$, only assuming that the field detectors have the same noise spectral density.

The upper part of Fig. 5 shows the rms amplitude field detector noise measured with the watchdog system, The value of $9.2\ 10^{-5}/\sqrt{2} = 6.5\ 10^{-5}$ is in agreement with an independent characterization of the field detectors at FLASH of $6.5\ 10^{-5}$ amplitude and $5.0\ 10^{-5}$ phase stability using the master reference. The expected noise reduction factor of $\sqrt{8}$ using the vector sum principle of 8 single field detectors, each characterized to be $1.5\ 10^{-4}$, has been demonstrated in machine operation. Using Eq. (1), the rms arrival time jitter caused by the LLRF system, dominated by the field detector noise, amounts to about 40 fs.

A slightly higher beam energy jitter of $8.8\ 10^{-5}$ measured with the SR-PMT (Fig. 5 (middle)) indicates either the presence of additional uncorrelated beam charge or bunch arrival time fluctuations entering the accelerating module of the same order or resolution limitations by the SR-PMT. These limitations might decrease the correlation (Fig. 5 (bottom)). Other effects increasing the correlation, e.g. phase noise fluctuations, controller imperfections and higher order cavity passband modes, will be investigated in the future.

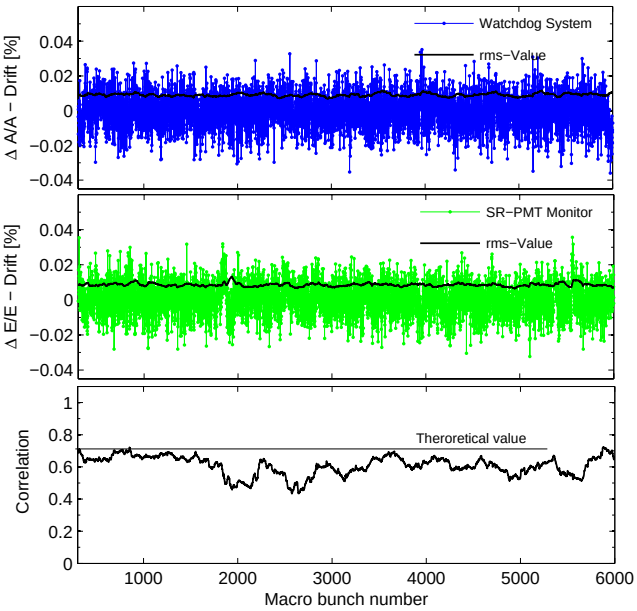


Figure 5: (top) Cavity vector-sum field amplitude fluctuations measured with the watchdog system, (middle) beam energy fluctuations measured with the SR-PMT, (bottom) correlation between watchdog system and SR-PMT.

CONCLUSIONS

A SR monitor based on a multi-anode photomultiplier tube, installed in the first bunch compressor at FLASH, has been used to measure the beam energy jitter compared to the field regulation in the first accelerating module. We have demonstrated that deterministic disturbances, e.g. beam loading, can be suppressed to a rms value below 10^{-4} over a bunch train by applying a learning feedforward algorithm. Using a noise watchdog system, the cavity field detectors have been identified as the main noise source within the cavity regulation system with an amplitude fluctuation of $6.5\ 10^{-5}$. The beam energy jitter measured with the SR-PMT was determined to be $8.8\ 10^{-5}$.

REFERENCES

[1] Ch. Gerth, "Synchrotron Radiation Monitor for Energy Spectrum Measurements in the Bunch Compressors at FLASH", DIPAC'07, Venice, TUPC03.

[2] A. Wilhelm and Ch. Gerth, "Synchrotron Radiation Monitor for Bunch-Resolved Beam Energy Measurements at FLASH", DIPAC'09, Basel, TUPD43.

[3] S. Kirchhoff *et al.*,"An Iterative Learning Algorithm for Control of an Accelerator based Free Electron Laser", Proceedings of 2008 CDC, Cancun, 2008.

[4] F. Ludwig *et al.*, "Phase stability of the next generation RF field control for VUV- and X-Ray free electron laser", EPAC'06, Edinburgh, TUPCH188.

DETECTORS FOR ABSOLUTE LUMINOSITY MEASUREMENT AT DAFNE

G. Mazzitelli#, M. Boscolo, F. Bossi, B. Buonomo, F. Murtas, G. Sensolini, P. Raimondi, INFN LNF, Frascati, Italy
N. Arnaud, D. Breton, L. Burmistrov, A. Stocchi, A. Variola, B. Viaud, LAL, Orsay, France
P. Valente, INFN Roma, Rome, Italy
P. Branchini, INFN Roma Tre, Rome, Italy
M. Schioppa, INFN Cosenza, Rende, Italy

Abstract

The Frascati electron-positron collider DAFNE is testing the crabbed waist scheme, aiming to reach a large improvement of the specific and integrated luminosity of the accelerator. In order to have a reliable, fast and accurate measurement of the absolute luminosity, a number of dedicated detectors have been designed, built, tested, calibrated and put into operation.

INTRODUCTION

At the Frascati DAFNE accelerator, running at the Φ meson peak (√s=1.02 GeV), the idea of enhancing the luminosity of an electron/positron collider with the introduction of a large Piwinski angle and low vertical beta function compensated by crab waist [1], is being tested. The accelerator has been modified to test the crab waist sextupoles compensation scheme and has restarted operations at the beginning of year 2008. Dedicated detectors have been installed for the measurement of the luminosity and the backgrounds.

Luminosity Detectors

Three different types of detectors using different physical processes are used, with different degrees of statistical and systematic accuracy:

- resonant decay $e^+e^- \rightarrow \Phi \rightarrow K^+K^-$: a set of scintillators (Kaon monitor) has been installed around the vertical axis (θ~90°) by the SIDDHARTA collaboration to count back-to-back high-ionization tracks: a rate of about 25 Hz at 10^{32} is expected.
- The elastic (Bhabha) scattering $e^+e^- \rightarrow e^+ e^-$: two calorimetric detectors have been placed on both sides of the interaction region (IR) to detect back-to-back tracks with energy deposit of about the beam energy ~510 MeV. Even though the polar angle is limited due to the presence of the low-β quadrupoles, the rate expected in the covered acceptance of 18°≤θ≤27° is high enough (~440 Hz at a luminosity of 10^{32} cm^{-2} s^{-1}) to provide a clean measurement on-line.

The radiative Bhabha process: $e^+e^- \rightarrow e^+e^-\gamma$; it has the advantage of a very high rate and that the emission of highly collimated photons (95% of the signal in contained in a cone of 1.7 mrad aperture), but it is heavily affected by backgrounds. In particular beam losses due to interactions with the residual gas in the beam-pipe, Touschek effect, and particles at low angles generated close to the IR. Very limited space is available at very small angles, close to the beam pipe, so that compact crystal calorimeters have been realized, in order to count events with a radiated photon.

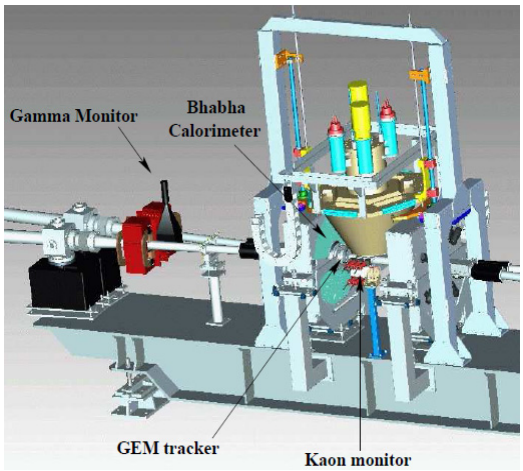


Figure 1: View of the DAFNE interaction region, with the detectors for luminosity measurement around the SIDDHARTA experiment setup.

BHABHA DETECTORS

The Bhabha monitors consist of two different detectors: a couple of calorimeters and two GEM trackers of annular shape, on either sides of the IR.

Calorimeters

Two modules of calorimeters surround each of the two final permanent quadrupole magnets, located at a distance of 32.5 cm on both sides of the IR, as shown in Fig. 1. Each of the four modules are segmented in the azimuth angle in five sectors, 30° wide. A 1/6 of the acceptance, i.e. the ±15° region, has not been instrumented, both for leaving space for the supporting structure, and for the high rate of background events expected on the machine plane.

Each sector is a sandwich of 12 trapezoidal tiles of 1cm thick scintillator, wrapped with Tyvek, alternated with lead plates: eight 5 mm thick plates towards the interaction point and three 1cm thick plates in the back part, for a total thickness of 19 cm. This choice was

driven by the compromise between the need of having a good longitudinal containment of 510 MeV electron showers (the total depth corresponds to about 12.5 X_0), and the necessity of having a detector not exceeding the permanent quadrupole length.

Each of the 240 scintillator tiles (produced by injection-molding in IHEP, Protvino) has three radial grooves on one face, 2 mm deep (one in the middle and two 1 cm from the edge of the tile) inside which wavelength shifting (WLS) fibers of 1 mm diameter are placed; the 36 WLS fibers of a sector are collected to an optical adapter to fit the photocathode of a Photonis-Philips XP 2262B photomultiplier. The assembly of the five sectors of a calorimeter module, before the coupling of fibers to the photomultiplier, is shown in Fig. 2.

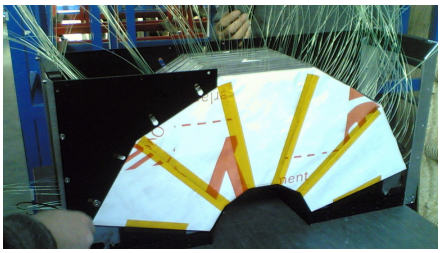


Figure 2: One of the four Bhabha calorimeter modules, each composed by five sectors of 12 scintillator trapezoidal tiles sandwiching 11 lead plates.

The DAQ is based on the KLOE experiment system: the analog signals are actively splitted to be digitized by a constant fraction discriminator for time measurement (using the KLOE TDC, 1.04 ns resolution), and for the pulse height measurement by the KLOE charge ADC, with a 0.25 pC resolution.

An energy resolution of 15% at 510 MeV has been measured, before the installation in the IR with a 510 MeV test-beam at the Frascati BTF, and afterwards with collisions data. This is adequate to define the trigger threshold for selecting Bhabha events. For each of the four modules indeed the analog sum of the five sectors signals is discriminated with a given threshold; then the trigger for a candidate Bhabha event is simply given by the coincidences of two back-to-back modules.

The Triple GEM Trackers

In front of each calorimeter, at a distance of 18.5 cm from the IR, a ring of triple-GEM detectors [2] is installed around the beam pipe. The trackers are divided in two units, with an half-moon shape; the top (bottom) half covering azimuth angles between 14° and 166° (194° and 346°), as shown in Fig. 3. Each of the four GEM units is segmented into 32 pads: eight cells in azimuth (covering 19° each) are arranged in four rings of equal radial extension. When a charged particle crosses the 3 mm drift gap, it generates electrons that will be multiplied by the three GEM foils separated by 2/1/2 mm. Each of the GEM planes is made of a thin (50μm) kapton foil sandwiched between two copper clads and perforated by a dense set of holes (70μm diameter, 140 μm pitch).

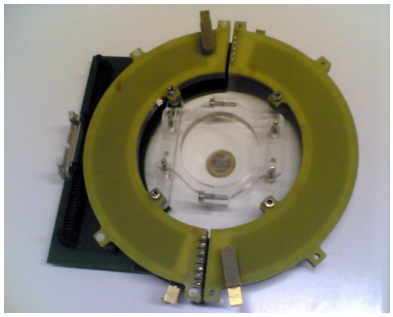


Figure 3: Triple-GEM ring detectors, composing one of the two trackers installed on each side of the IR.

As a high potential difference (about 400 kV) is applied between the copper sides, the holes act as multiplicating channels and the gain of each layer is about 20 (8,000 in total).

The GEM trackers have been included into the main DAQ system, read by KLOE TDC modules.

RADIATIVE BHABHA DETECTORS

Two gamma monitor detectors are located 170 cm away from the IR, collecting the photons radiated by electron or positron beam. Each detector is made of four $PbW0_4$ crystals (squared section of $30\times30mm^2$ and 110mm high) assembled together along z, in order to have a 30 mm face towards the photon beam, and a total depth of 120 mm corresponding to about $13X_0$. Each crystal is readout by a Hamamatsu R7600 compact photomultiplier. Each of the crystal signals is splitted: one half is sent to the charge ADC of the data acquisition system, while the other is sent to an analog mixer. The analog sum of the four crystals is then discriminated and the counts are read by the DAFNE Control system, providing a prompt estimate of the luminosity for machine optimization.

Because of the boost introduced by the beam crossing angle, the trajectories of the photons are shifted towards the inner side (along x coordinate) of the machine; the gamma monitors and GEM trackers are then placed along the beam pipe at x=–5cm and rotated by 4^o in the horizontal plane with respect to the beam axis.

Thanks to the high rate, those detectors are very useful as a fast feedback for the optimization of machine luminosity versus background, more than providing a measurement of the luminosity, since the relative contribution of background is changing with the machine conditions.

SIMULATION

In order to get the absolute luminosity from the measured coincidence rate in the Bhabha calorimeters, the event rate should be corrected for the detectors' acceptance and selection efficiency. In order to compute these factors we developed a full simulation of the whole

experimental set-up, based on the GEANT3 package. This includes all the materials and fields present in the interaction region as well as a simulation of the detectors response.

The BHWIDE package is used to generate Bhabha events with a full treatment of the radiation [3]. The contamination due to the Touschek background is investigated by interfacing an ad hoc generator [4] with the simulation.

The simulation predicts a measured Bhabha event rate of ~440 Hz when the luminosity equals 10^{32} cm^{-2} s^{1}. The rate actually measured at the IP is compared with this number to derive the actual luminosity. The simulation is also used to evaluate the systematic uncertainties affecting this measurement. Using only the calorimeters, an uncertainty of 11% can be estimated. It drops to 7% when the GEMs are also used.

We also used the simulation to determine the optimal location for the GEMs. They're shifted in the horizontal plane by 5 mm in the direction of the boost to compensate for the loss of back-to-back-ness caused by this boost.

RESULTS

The four calorimeters, the GEM trackers and the crystal gamma detectors are acquired by KLOE farm data acquisition prototype. The trigger condition (T1FREE) consists of the OR of the two possible coincidences of opposite, upside-down modules when the energy released in the modules is above a threshold of about 200MeV.

The precise knowledge of the effective energy threshold in our trigger is essential for the determination of the acceptance with the Monte Carlo simulation. A good estimate of the threshold can be obtained looking at the ratio of the events triggering a given module, with respect to the total acquired events. The threshold profile that one obtains by taking this ratio (bottom plot in Fig. 4) is not a step function due to smearing introduced by the electronics.

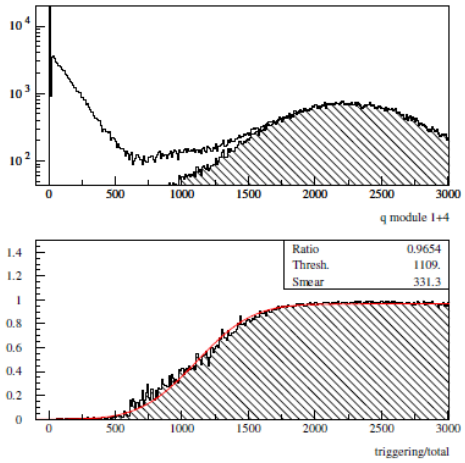


Figure 4: Determination of the trigger threshold by taking the ratio of triggering/total events in one module.

The equivalent energy of the threshold can then be determined from the knowledge of the peak in the energy deposit, which corresponds to the beam energy (510 MeV).

Single and coincidence rates are acquired by the DAFNE control system, in order to provide a fast reading of luminosity and background condition very useful for machine parameters optimization.

The T1FREE rate is affected by background contamination, especially during beam injections. In order to get an accurate and clean luminosity estimate, an online filtering process runs on the DAQ farm, providing an offline estimate of the rate (T2FARM), corrected by the measured percentage of background events. This correction is computed analyzing blocks of events (1000 events, corresponding to about 1 s at 2.5×10^{32}), and by looking at the time distribution of the two triggering modules. In order to isolate genuine Bhabha's, the online filter selects events in around around $\Delta t=0$ in a $\pm3\ \sigma$ window (±6 counts). The amount of background beneath the peak is also taken into account: events in the sideband (of the same time width) are counted and subtracted.

All online and filtered data are stored by DAFNE control system with a sampling time of 15 seconds and are available for analysis and on web for online presentation (Fig. 5).

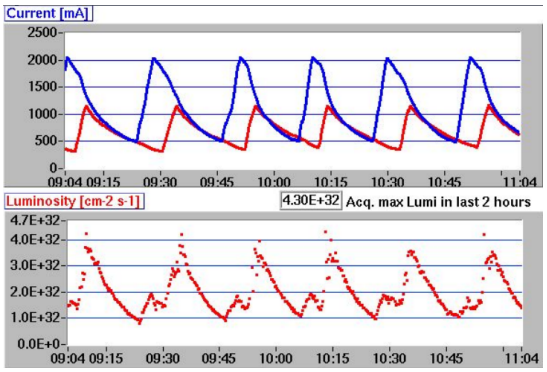


Figure 5: Online display of the currents in the machine (upper plot) and the luminosity measured by our luminometers (bottom plot, including the correction for the acceptance and background subtraction).

ACKNOWLEDGEMENTS

We would like to thank L. Iannotti, V. Romano and the LNF SSCR service for the mechanical works, and all the electronic staff of the Accelerator Division; G Corradi, M. Pistilli, D. Tagnani for the GEM electronics and detector construction. We also would like to thank W. Placzek for the support on BHWIDE code.

REFERENCES

[1] D. Alesini et al, LNF-06/033 (IR), 2006.
[2] G. Bencivenni, et al., NIM A488: 493-502, 2002.
[3] S. Jadach et al, Phys.Lett. B390: 298-308, 1997.
[4] M. Boscolo et al, PAC2007, Albuquerque, New Mexico, USA, 2007.

HIGH DYNAMIC RANGE SPECTRAL ANALYSIS IN THE kHz BAND

M. Gasior, A. Boccardi, CERN, Geneva, Switzerland

Abstract

Many beam instrumentation signals of large circular accelerators are in the kHz range and can thus be digitised with powerful high resolution ADCs. A particularly large dynamic range can be achieved if the signals are analysed in the frequency domain. This report presents a system employing audio ADCs and FPGA-based spectral analysis, initially developed for tune measurement applications. Technical choices allowing frequency domain dynamic ranges beyond 140 dB are summarised.

INTRODUCTION

The large market for PC sound cards and audio processing devices has resulted in the availability of excellent and inexpensive audio ADCs. Often they have two channels and are accompanied by two (or more) DACs in a single chip, commonly referred to as "codec". Good audio ADCs have 24-bit resolution with excellent linearity given by the Σ/Δ architecture and datasheet signal-to-noise ratios (SNRs) in the order of 100-120 dB, corresponding to some 16-20 effective number of bits. The remaining bits normally contain noise, but as this is to a large extent white noise, it can be lowered by spectral analysis or time domain filtering, resulting in an increased dynamic range. Since the frequency domain SNR improves as $\sqrt{N/2}$ for an N-point FFT, for 4K-point FFT one gains some 33 dB and for 64K-point FFT the gain is about 45 dB, giving potential SNRs above 160 dB.

As illustrated in Fig. 1, the presented spectral analysis system is based on an audio codec, connected to a digital acquisition board (DAB) through an LVDS link. The DAB, hosting a large FPGA and memory, is a standard CERN acquisition/processing VME board used for most of the LHC beam instrumentation systems. In the discussed system the DAB stores the acquired data and performs FFT calculation, prior to transmitting raw data and calculated spectra to a VME front-end computer (FEC). The FEC, connected to the control infrastructure by a fast Ethernet link, makes the data available for end applications [1].

As the DAB-based real-time FFT analysis providing 180 dB dynamic range is described in [2], this paper focuses on the remaining crucial aspects of the system, making it a powerful, inexpensive high dynamic range acquisition and spectral analysis system.

24-BIT ADC/DAC MODULE

The system described in this paper was built primarily for the LHC tune and chromaticity measurement systems [1], which process two beam signals and provide two excitation signals that are band-limited to half the revolution frequency ($f_r \approx 11.2$ kHz for the LHC). An audio stereo codec with two ADCs and two DACs was the natural choice for the core of the system. Since system prototypes were studied at the CERN SPS ($f_r \approx 43$ kHz) and BNL RHIC ($f_r \approx 78$ kHz), the design is compatible with all these machines.

The 24-bit ADC/DAC circuit was built not as a VME module, but in a NIM format, at the expense of having an additional crate in the system. This solution offered more room to accommodate input and output insulation transformers, which have substantial dimensions as they carry low frequency signals of relatively large amplitudes. Furthermore, NIM chassis typically offer lower levels of electromagnetic interference, since they usually contain analogue electronics in shielded modules, and as they provide power supplies of good quality that are less subject to perturbations from complex digital modules rare in NIM chassis.

From the many audio codecs available in the market Cirrus Logic CS4272 was selected, a 28-pin chip containing two 24-bit ADCs and two 24-bit DACs with differential inputs and outputs. The choice was a compromise between the chip performance and complexity, mainly of the configuration protocol. Its datasheet SNR is 111 dB and the maximal sampling frequency (f_s) 200 kHz, however, its best SNR was found to be for f_s below 50 kHz.

The codec inputs and outputs allow differential architecture for the input amplifiers and low pass filters (LPFs) as well as for differential output interpolation LPFs. This increases the immunity to interference and the dynamic range.

Despite the fact that the 24-bit ADC/DAC module

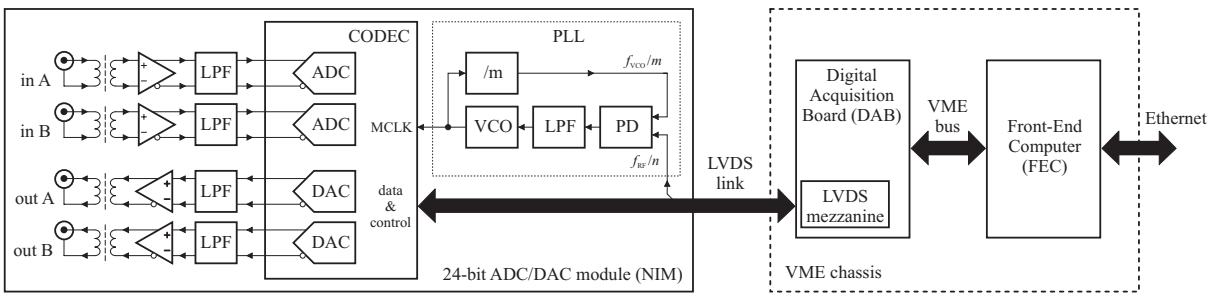


Figure 1: Block diagram of the kHz range spectral analysis system.

circuits work at low frequencies, in order to maximise the dynamic range, its four-layer PCB was designed according to high frequency design rules, such as using only small surface mount components, low inductance power supply decoupling, solid ground planes and no thermal reliefs on the component layers.

The inputs and outputs of the NIM module have insulation transformers. The purpose of the input transformers is to prevent ground loop currents that may arise if the module and the source of the analysed signal (typically an analogue front-end) are distant from each other and if their local grounds are not exactly on the same potential. This is especially common in the vicinity of large power systems. In case the signal cable connecting the module and the source is grounded on both ends, any ground potential difference will drive a current through the cable ground conductor. This current creates in turn a voltage on the cable resistance and the voltage appears on the input of the ADC. Introducing insulation transformers between the two ground domains reduces the ground currents to the one flowing through the inter-winding capacitance of the transformer. While in the kHz range this current can be kept small, insulation transformers significantly reduce ground loop interference for low frequencies.

The purpose of the output insulation transformers is to prevent ground loops for the input of the remote system connected to the DACs (e.g. high power transverse damper amplifiers).

Unfortunately, the insulation transformers for the kHz range have to be of substantial size and wound on a high permeability core with many windings. To minimise their size and number of turns, the NIM module has 50 Ω input and output impedance, contrary to typical audio systems. Low input/output impedance also helps to achieve good transformer insulation.

The drawback of using insulation transformers is measurable signal distortion that depends on signal amplitude and frequency. This was one of the reasons to limit the full scale (FS) amplitude to 2.8 Vpp for the inputs and to 2.5Vpp for the outputs.

It was observed that the insulation transformers captured some stray magnetic fields (e.g. of the NIM power supply transformer, however below the –100 dBFS level), thus they are useful only if the ground loop interference dominates, which is usually the case in large accelerator installations.

For tune measurement applications it is necessary that the ADC sampling is synchronised to the machine revolution frequency f_r. The ADC sampling clock is thus derived from the machine RF system. In addition, typically for the Σ/Δ architecture, the master clock (MCLK) frequency supplied to the codec is a multiple of f_s. To fulfil these requirements the codec MCLK was produced by a PLL synchronised to the RF frequency (f_{RF}), as shown on the system block diagram in Fig. 1.

To minimise MCLK jitter, the voltage controlled oscillator (VCO) was built as an LC generator tuned with a varicap diode. Since f_r variations for all considered machines are small (e.g. maximal relative change of LHC f_r is some 25 ppm), the VCO tuning range was limited to some ±1 %, determined by potential drifts of resonator components. The phase detector (PD) is a part of an integrated PLL circuit, followed by a passive low-pass filter. The MCLK jitter was measured to be about 5 ps_{rms}.

Since the system is supposed to work for three machines, the required clocking flexibility was achieved by programming the f_{RF} divider in the FPGA and the VCO frequency divider in the NIM module, as shown in Table 1, listing also other parameters of the clocking scheme. With such a scheme, it was possible to maintain a similar VCO frequency for all machines, and only the simple LPF of the PD is machine specific, in order to achieve an optimal PLL dynamic for different loop gains.

For the LHC system f_s is a fourth multiple of f_r and samples are filtered and decimated to f_r, in order to improve the system SNR by 6 dB.

Tune measurement of smaller CERN accelerators required extending the system bandwidth to a few MHz and this was achieved by replacing the 24-bit ADC/DAC module with two DAB mezzanines, one accommodating two 16-bit, 40 MHz ADCs and the second with two 12-bit, 40 MHz DACs. The FPGA signal processing required only a few minor changes. The achieved ADC SNR, largely sufficient for the small accelerators, is lower by some 30 dB with respect to the system based on the audio codec.

Table 1: Codec Clocking Parameters

	f_r [kHz]	$\frac{f_s}{f_r}$	$\frac{f_{MCLK}}{f_s}$	$\frac{f_{RF}}{f_r}$	f_{RF} [MHz]	n	m	f_{MCLK} [MHz]
LHC	11.25	4	384	3564	40.08	297	128	17.27
SPS	43.4	1	384	924	40.08	77	32	16.66
RHIC	78.0	1	192	360	28.08	60	32	14.98

RESULTS

Beam measurements obtained with the described system are presented in [1, 2] and this report focuses on lab measurement results shown in Fig. 2, documenting an ultimate SNR performance of the system in the LHC version.

In typical applications of the system the DAC signal quality is much less important than the performance of the ADCs. However, for the presented measurements the DAC signals were put on the ADC inputs, as the DAC signal quality surpasses all typical lab sine wave sources.

Figure 2a shows a 4K-point FFT magnitude spectrum for a measurement done with the DAC signals (in blue), alongside with a measurement with no ADC input signal, averaged 100 times (in red). As the DAC signal amplitude was close to the FS, many harmonics of the fundamental tone are present. They are related to nonlinearities of the two insulation transformers and the rest of the chain, in particular the DAC output amplifier driving low impedance load. The noise floor for the measurement without signal is about –152 dBFS, clearly seen due to the averaging. It rises (≈2 dB) for low frequencies, because of

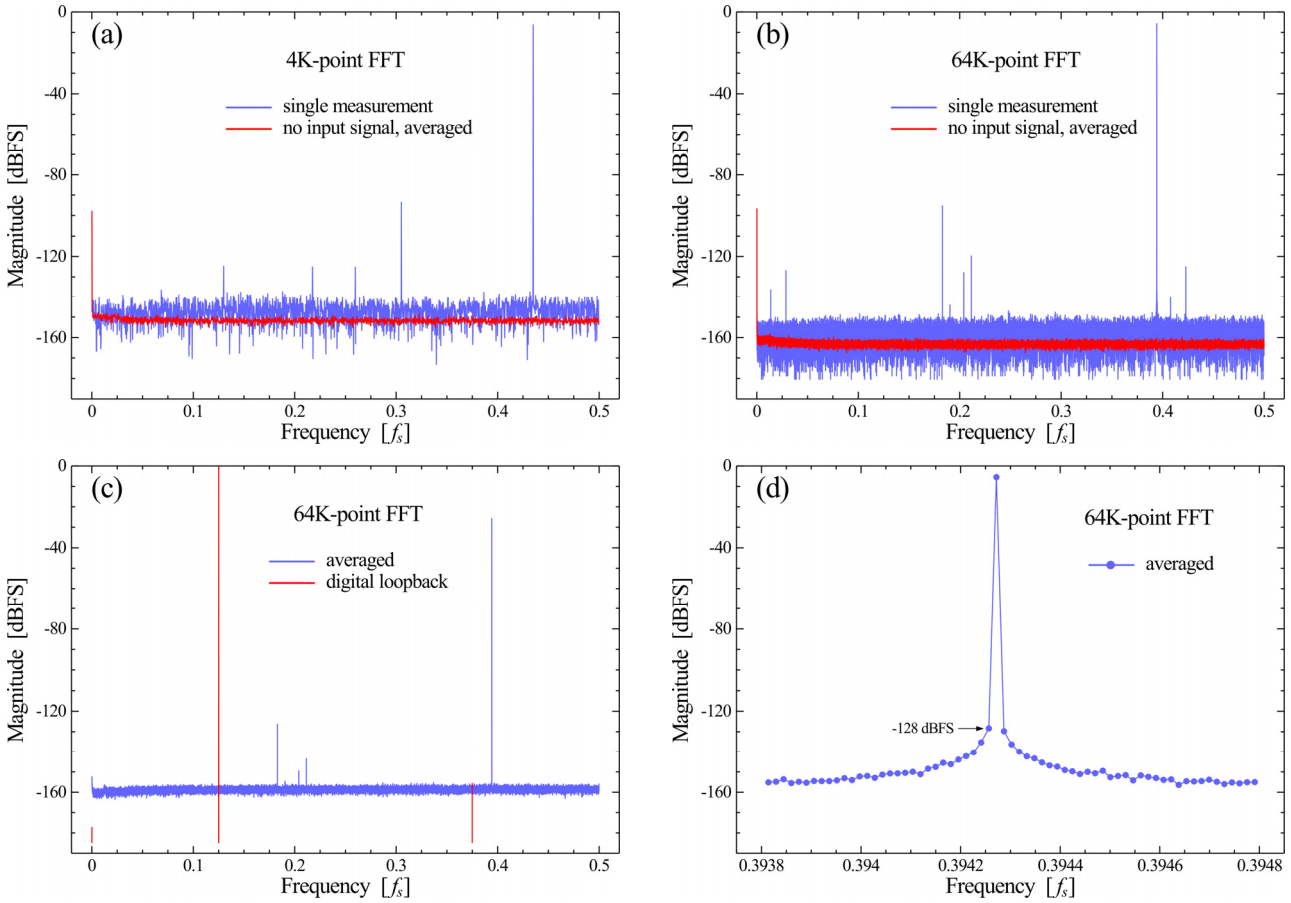


Figure 2: Results of lab measurements with the system LHC version.

low-pass filtered noise from an ADC input bias resistors. If from the –152 dBFS noise floor are subtracted SNR improvements due to the FFT (33 dB) and the time domain averaging by four (6 dB), one gets the time domain noise floor of –113 dBFS, which is compatible with the datasheet typical SNR of 111 dB.

Corresponding measurements for a 64K-point FFT magnitude spectrum are shown in Fig. 2b. The noise floor, having similar low frequency slope, reduces to about –163 dBFS, i.e. by 11 dB, which is close to the theoretical 12 dB related to the FFT length increase by factor 16.

Figure 2c shows an average of 100 spectra with a lower DAC output (in blue) and a spectrum obtained with the digital signal processing in the loopback mode (in red). In this mode calculated DAC samples directly undergo processing normally performed on the ADC data. It can be seen that smaller DAC amplitude decreases the harmonic level. The noise floor, now being the superposition of the ADC and DAC noise performance, is higher by ≈4 dB than the one with no input signal shown in Fig. 2b. The loopback spectrum contains only three non-zero bins: the fundamental tone, the third harmonic and the DC component, both accommodating all the quantisation noise related to digital sine generation and truncations in signal processing. The achieved spurious component level is a measure of quality of the sine generation and the remaining bins containing zeros (which have been omitted on the logarithmic scale plot) show the dynamic range of the FFT calculation [2].

Figure 2d shows the fundamental tone averaged 100 times and zoomed within $0.001 f_s$ (65 bins).

CONCLUSIONS

The described high dynamic range frequency analysis system was built primarily for the LHC tune and chromaticity measurement applications. At the expense of designing algorithms and code for the FPGA of the DAB and building the NIM 24-bit ADC/DAC module, the CERN Beam Instrumentation Group gained a powerful and inexpensive system, which is used also for the LHC 4.7 GHz Schottky monitor [3] and special RF system diagnostics based on wall current monitor signals [4].

REFERENCES

[1] M. Gasior et al., “An overview of the LHC transverse diagnostics systems”, BIW’08.

[2] A. Boccardi et al., “The FPGA-based continuous FFT tune measurement system for the LHC and its test at the CERN SPS”, PAC’07.

[3] F. Caspers et al., "The 4.8 GHz LHC Schottky pick-up system”, PAC’07.

[4] E. Shaposhnikova et al., "Longitudinal Schottky spectrum of the peak bunch amplitude signal”, PAC’09.

MACHINE PROTECTION SYSTEM FOR PETRA III

T. Lensch, M. Werner
Deutsches Elektronen Synchrotron DESY, Hamburg, Germany

Abstract

The basic design for the machine protection system (MPS) for the light-source PETRA III is discussed. High synchrotron radiation can damage absorbers and vacuum chambers. Therefore the MPS identifies alarm conditions from different systems, including the beam position monitors (BPM), temperature and vacuum systems and creates a dump command within 100us. For diagnostic purposes a post-mortem trigger is implemented and a first alarm detection is planned. The initial commissioning of the MPS with its alarm-delivering systems is described.

INTRODUCTION

The former electron and proton preaccelarator PETRA II was reconstructed into a high brilliant X-ray source. PETRA III will operate at 6 GeV. The circumference of the accelerator is 2.3 km. In the first step a beam current of 100mA is planned, the goal is 200mA [1]. The experiments are placed behind 14 undulator beamlines. Absorbers and beam chambers in the damping wiggler section and the undulator section have to be protected against synchrotron radiation. Closed vacuum shutters in the whole storage ring have to be protected as well against the electron beam. A dump trigger from the MPS is connected to the RF system which stops delivering power to the beam. The beam will be lost within 1ms at a dedicated scraper. In addition the beam shutters will be driven into the beam.

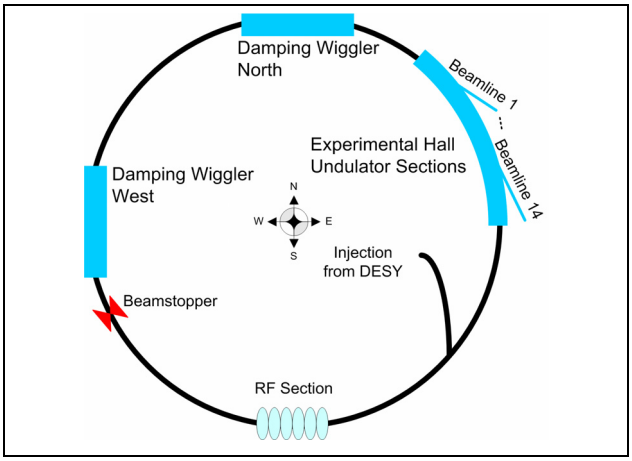


Figure 1: Overview PETRA.

MPS SPECIFICATION

The MPS should provide a dump trigger within 100µs after alarms are received. After a beam loss the MPS should provide a post mortem trigger which is delivered to other systems. In order to locate the initial alarm which triggered the dump, a first alarm detection should also be implemented.

About 170 alarms are connected to the MPS to protect the machine against damage from synchrotron radiation or the electron beam. Further 50 alarms are connected to the MPS for optimizing the first alarm detection. The alarms are distributed over nine PETRA halls but with main contributions from the damping wiggler sections and the experimental hall. Partially alarms are merged to one alarm for the MPS. The Tables 1 - 3 give an overview of all alarms connected to the MPS.

Table 1: Dump Triggering Alarms

System	Total Count of Alarms	Inputs at MPS
Beam Position Monitors	95	95
Temperature	260	17
Vacuum Shutters	35	8
Fast Vacuum Shutters	14	14
Personnel Interlock	1	1
Getter pumps	26	13
Vacuum Hand Shutters	14	4
Water Flow	33	5
Screen Monitor	1	1
Total	**479**	**158**

Table 2: Alarms for Masking Other Inputs

System	Inputs at MPS
Undulator Gaps	14
Damping Wiggler Gaps	2
Total	**16**

Table 3: Alarms First Alarm Detection

System	Total Count of Alarms	Inputs at MPS
Magnet Power Supplies	700	42
RF System	8	8
Total	**708**	**50**

A dump button is implemented into the software console program in addition to a hardware dump button. Both dump buttons are connected to standard alarm inputs.

Every alarm input is masked with an individual beam current threshold. In the damping wiggler sections and the undulator sections several alarm inputs have to be combined. Figures 1 - 3 show the different assemblies.

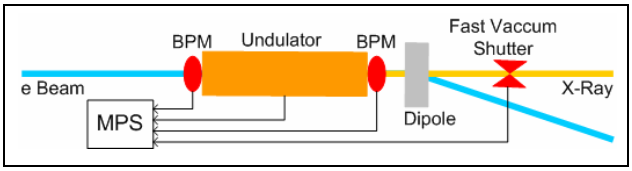


Figure 2: Single Undulator Section.

For a single undulator module section a dump is triggered if one of the BPMs or the fast vacuum shutter gives an alarm and the undulator gap is closed.

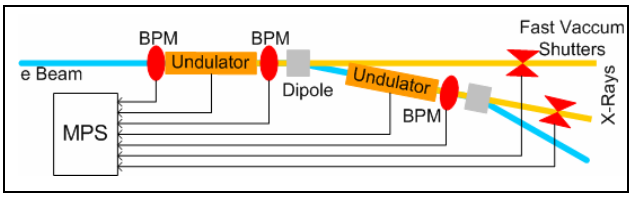


Figure 3: Double Undulator Section.

For a double undulator section a dump is triggered if one of the three BPMs gives an alarm in combination with one or both undulator gaps or if a fast vacuum shutter gives an alarm in combination with the corresponding undulator gap.

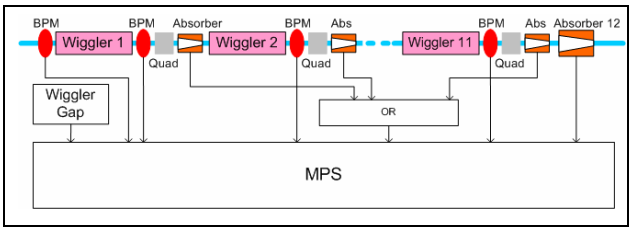


Figure 4: Damping Wiggler Section.

In a damping wiggler section a dump trigger is created if a minimum of two BPMs or the summary alarm of water flow sensors gives an alarm in combination with the closed wiggler gap. The water flow sensor in the last absorber in the section creates an alarm itself.

MPS DESCRIPTION

The MPS is a distributed system without a central unit. In every PETRA hall a crate is located which collects up to 112 alarms and provides a dump trigger as well as a post mortem trigger. The MPS crates are linked together with a redundant optical fibre loop. The connection to the control system is done through the SEDAC fieldbus, which is an inhouse development. All modules needed for the MPS were developed and built at DESY.

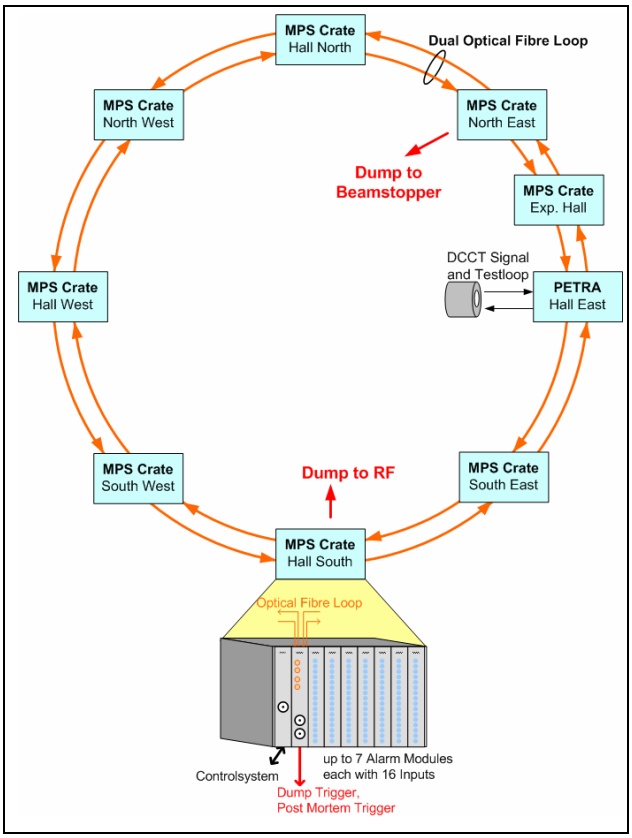


Figure 5: Overview of MPS Components.

Alarm Inputs

Alarm delivering systems provide a potential free contact to the MPS. An alarm corresponds to an open contact. An MPS input provides a 5V / 10mA source combined with a differential input to read the contact as shown in Fig. 6. The advantage in comparison to a 24V technique is very fast alarm detection (~1µs). By the use of shielded differential cables EMI problems are reduced to a minimum.

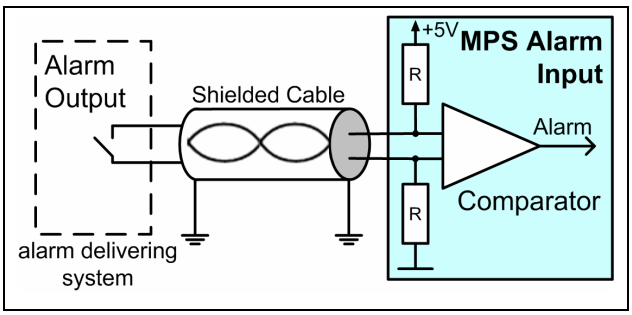


Figure 6: Differential Alarm Input.

Signal Flow Inside an Input Module

All alarm inputs can be configured by software with individual beam current thresholds. The active beam current is received from a dedicated DCCT beam current monitor through the optical fibre link. It is possible to

combine the 16 inputs within a module into an and/or matrix. Figure 7 shows the alarm flow.

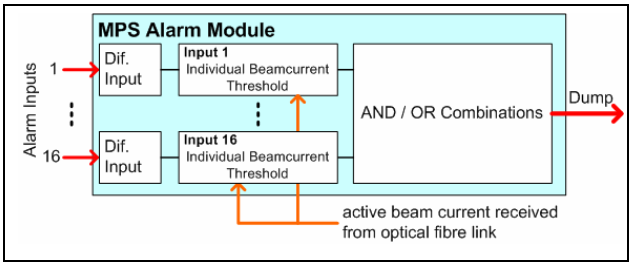


Figure 7: Alarm flow.

BEAM CURRENT MEASUREMENT

The beam current is measured with a dedicated DCCT and transferred via the optical fibre loop to the whole system. An integrated test loop through the toroid is used for an ongoing test of the complete DCCT installation as shown in Fig. 8. Such a permanent test is important since a zero-reading of a non-working monitor disables alarms.

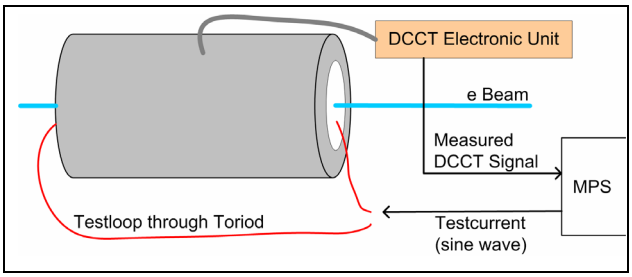


Figure 8: DCCT Layout.

REDUNDANT OPTICAL FIBRE LOOP

The MPS crates in the 9 PETRA halls are linked together with a redundant optical fibre loop. The following information is transmitted:

- beam current from the DCCT
- timing synchronisation of all MPS crates (planned)
- post mortem trigger
- dump trigger

The redundancy serves two purposes: The machine availability is increased by allowing machine operation when one fibre is damaged. For a timing synchronisation the second fibre is also needed.

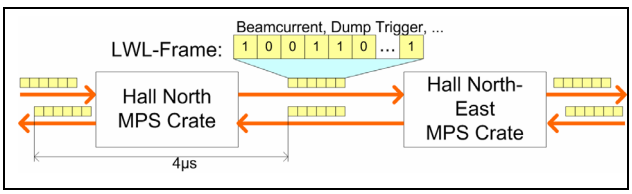


Figure 9: Redundant Optical Fibre Loop.

CONTROL SYSTEM

The server and console programs are implemented in JAVA. In the console program each alarm input is represented by an icon. The different icon styles and colours show the input status. Choosing a column gives more detailed information about a module and its alarm inputs. Figure 10 shows the console program.

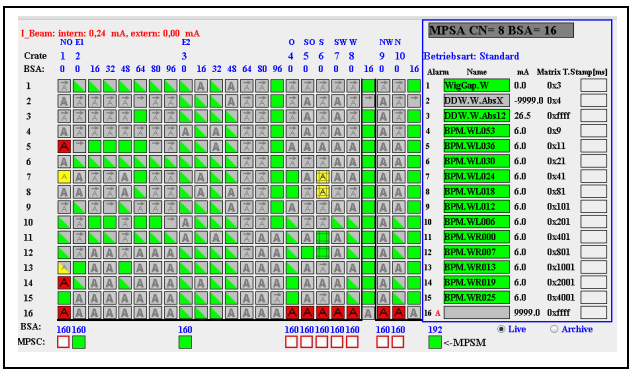


Figure 10: MPS Console Program.

MPS Data Archive

When states of the alarm inputs change this information is saved with a timestamp in an event archive. In a special mode of the console program the archive data can be viewed in the same way as live data.

COMMISSIONING

In the end of January the MPS started its first test operation and since April with the first turns in PETRA the system is active. With increasing machine current more alarm inputs are activated and viewed in the control room. The first experiences are positive. Up to now no malfunction such as unwanted dumps were noticed.

CONCLUSIONS AND OUTLOOK

The MPS is a tool which keeps the machine safe. Presently 10 crates are installed with a possible total number of 1120 alarms over 9 PETRA halls. Additional crates can easily be integrated in the system. With a firmware upgrade it is possible to combine any alarm inputs throughout the whole MPS by transferring the input status over the optical fibre loop.

The effect of the planned timing synchronisation will be a post mortem trigger and a first alarm detection with an accuracy of ~1µs.

REFERENCES

[1] The Technical Design Report (TDR) "PETRA III: A low Emittance Synchrotron Radiation Source" Ed. K. Balewski et al., DESY 2004-035

LHC BLM SINGLE CHANNEL CONNECTIVITY TEST USING THE STANDARD INSTALLATION

J. Emery, B. Dehning, E. Effinger, G. Ferioli, C. Zamantzas, CERN, Geneva, Switzerland
H. Ikeda, KEK, Ibaraki, Japan; E. Verhagen, IceCube, UW-Madison, USA

Abstract

For the LHC beam loss measurement system (BLM), the high voltage supply of the ionisation chambers and the secondary emission detectors is used to test their connectivity. A harmonic modulation of 0.03 Hz results in a current signal of about 100pA measured by the beam loss acquisition electronics. The signal is analyzed and the measured amplitude and phase are compared with individual channel limits for the 4000 channels. It is foreseen to execute an automatic procedure for all channels every 12 hours which takes about 20 minutes.

The paper will present the design of the system, the circuit simulations, measurements of systematic dependencies of different channels and the reproducibility of the amplitude and phase measurements.

TEST PURPOSE AND PRINCIPLE

The primary purpose of this test is to ensure the integrity of the cabling of each beam loss monitor. By adding a small harmonic modulation signal on the high voltage supply of the monitors, it is possible to detect a small current on the measurement side (Fig. 1). If anywhere in the signal chain a cable is missing, disconnected or discontinued for any reason, the measurement will not show any harmonic variation of the current.

The second goal is to survey the integrity of the components. The measured amplitude and phase of every channel (monitor or spare) is compared to a predefined threshold measured for every channel. If one of them is outside the limits, the test will fail and the beam permit [1] will not be raised.

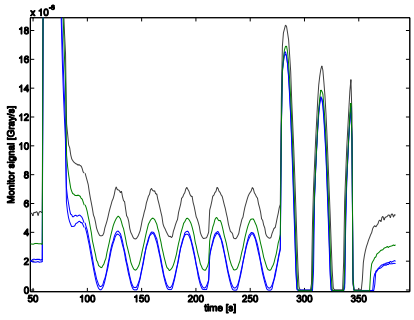


Figure 1: Four ionisation chamber signals modulated.

LHC BLM SYSTEM

The LHC BLM system is organised in eight different groups. Each group has a high voltage power supply, which covers two half arcs and one straight section. For each group, there are three or four crates, which can hold up to 256 channels each, connected to one ionisation chamber (IC) or two in certain case (IC2) or one secondary emission monitor (SEM). Each monitor has a low pass filter with a serial resistor and a capacitor used to stores charges. With this structure, the surface power supply can be small. When a beam loss or a variation of the high voltage occurs, charges are moving to the tunnel card BLECF [2]. This card integrates charges for 40µs and sends the result digitally to the surface electronic threshold comparators BLETC [3]. Longer integration windows (running sums) are then computed. When a connectivity test is performed, the central processing unit (CPU) sends one of the running sums every second to the combiner and survey card BLECS for analysis (Fig. 2).

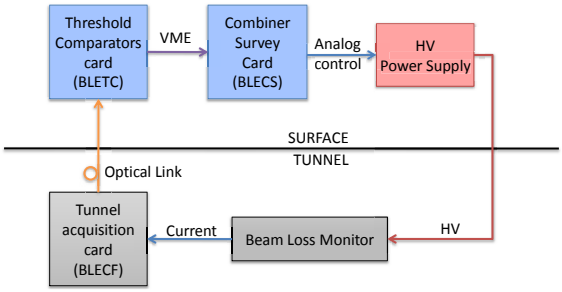


Figure 2: The LHC BLM system looped for the connectivity test.

Connection to the Beam Interlock System

The LHC BLM system is connected to the beam interlock system through the CIBUS interface [1]. There are two of these interfaces per point. One is for unmaskable and the other for maskable channels. The BLM system receives from this interface the status of the global beam permits (beam info). The BLM logic used to generate the beam permits includes the results of various system tests including the connectivity test.

Hardware Timers and Test Triggering

The LHC BLM system includes two hardware timers to ensure regular testing of the system. The first timer is linked to the "system test" which includes the connectivity test. The second one is linked to the online check [4] which ensures agreement between settings held inside the front-end and in the LSA database. If the tests are not triggered within a fixed time, the next injection will be blocked through the beam permits lines. To allow LHC operation again, the tests have to be triggered and their results need to be satisfactory.

When a test is requested by the internal timer, the BLM system raises a status bit and the LHC sequencer (or a manual operation) triggers the test. No test can start if there is beam inside the machine (hardware check of the beam info).

TEST DESCRIPTION

The connectivity test, also called modulation test, consists of adding a small harmonic signal to the control voltage of the high voltage power supply of the monitors (Fig. 1). This variation is propagated to the monitors, which are reacting by generating a current. This variation is measured with the standard acquisition chain (Fig. 2) and the results transferred to the combiner card by the CPU at the nominal rate of one per second. The combiner is performing an analysis of the resulting signal and calculates the peak to peak amplitude of the signal and its phase difference compared to the modulation introduced in the system.

Simplified Equivalent Circuit

The equivalent circuit of the system is shown in Fig. 3. The high voltage supply is connected to the detector through an 11MΩ resistor. The parallel capacitor (C_{filter}) is used as a supply of charges when a fast loss occurs. The IC, IC2 or SEM is represented by $C_{monitor}$. The input circuit of the tunnel card is represented as a resistor and capacitor, the virtual ground of the integrator is represented as a shunt resistor. The contribution of the cables capacity and resistivity is small compared to the component values for the frequency range (1mHz to 1Hz); they are ignored for this simulation.

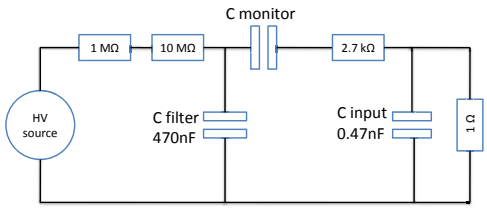


Figure 3: Simplified equivalent circuit.

Simulation Results

The simulation of the equivalent circuit shows the behaviour of the system depending on the harmonic frequency injected in the system (Bode diagram Fig. 4 and 5). The goal is to find a good working point to test the integrity of the cabling. We are also interested in the dependence of this diagram to the variation of the key component values: The monitor capacity ($C_{monitor}$), as it varies with the monitor type, and the C_{filter}, as it is directly under a lot of stress (radiation) and may lose its capacitive property.

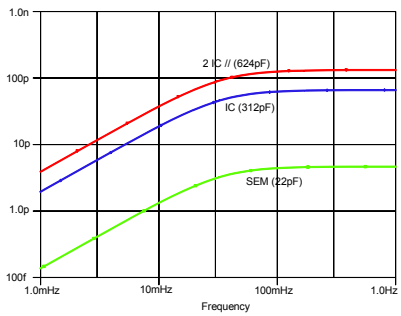


Figure 4: Magnitude of the Bode diagram for the 3 monitor types (SEM, IC and IC2).

The working frequency of 0.03Hz was selected as it gives the best sensitivity (in phase) for a variation of the C_{filter} (Fig. 5) with small magnitude changes (not shown). In Fig. 4, the magnitude of the signal at this frequency is nearly optimal and the monitor type can easily be distinguished. The variation of $C_{monitor}$ doesn't contribute at all to the phase change (not shown).

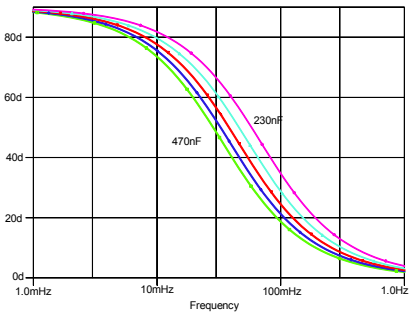


Figure 5: Phase of the Bode diagram for different values of C_{filter}.

Implementation of the Test

The generation and the processing of the test are done inside the combiner and survey card. When a test is triggered, the field programmable gate array (FPGA) starts generating the modulation signal added to the high voltage. The CPU provides the measurements every second to the card for processing. Once the complete set of the 256 channels has been written, the amplitude and the phase are calculated using the cross correlation between the measured signal and the initial recorded modulation.

Threshold Comparison and Results Availability

When the results of the test are available, they are compared to the channel specific thresholds to compute final passed/failed information for each channel. A global status with the 256 channels of the crate is being used to generate the beam permit signal.

The results of the test are automatically logged to the LHC logging system and are available shortly after the end of the test.

MEASUREMENTS ANALYSIS

An analysis of the behaviour of the system has been conducted to validate the test. The results are also used to produce thresholds to be loaded inside the front-end for the automatic test.

Data Retrieving

The measurements and the status generated by the electronics (passed/failed for each channel) are automatically stored in the Measurement database, from where they are sent to the Logging database without filtering for long term availability. The information is grouped per threshold comparator card and per crate. To link a channel to a detector name, the Layout database is accessed. To know if a channel is connected to the

maskable or unmaskable beam interlock interface, the LHC Software Architecture (LSA) database is accessed.

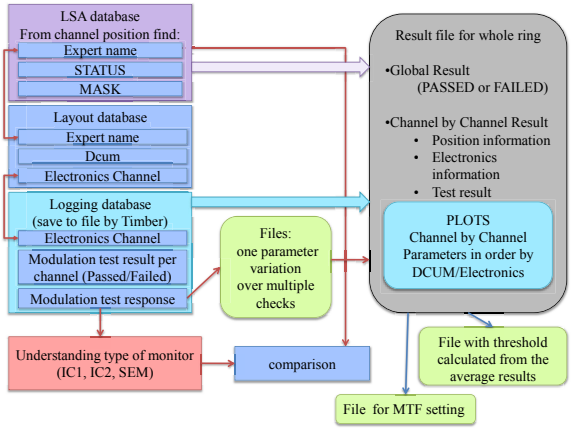


Figure 6: Overview of the analysis for system validation, parameter optimisation and threshold calculation.

Detector Recognition

The type of the detector can be identified as shown in the simulation by looking at the level of the induced current. By applying a simple rule it is possible to place the channel into four categories. Fig. 7(a) shows that starting from a modulation voltage of 8V, the SEM, the IC, the double IC (IC2) and the SPARE channels are clearly identified and not overlapping.

This detector identification is compared with the database expert name and appears in the report.

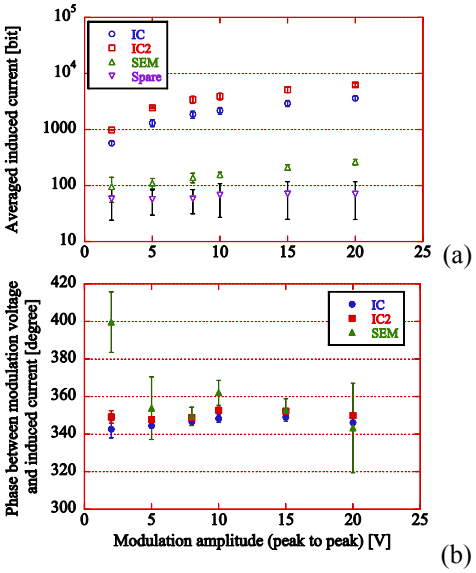


Figure 7: Average induced current (a) and phase (b) versus different modulation amplitudes. Data are collected from the LHC point 8 right and straight section including spare channels.

Modulation Voltage Optimisation

In order to optimise the harmonic modulation voltage control, different settings were studied. The average and variance of the harmonic induced current and phase for the three different detector types and the spare channels (without monitor) shown in Fig. 7(a) and 7(b) is used.

The SEM signal shows a large variance at low voltage (Fig. 8), since the absolute value of the induced current is very small. For 15V and above, the error increases for IC (and IC2) probably due to saturation effects. We chose 10V for the modulation amplitude for good signal to noise ratio and reproducibility of the measurements for all monitor types.

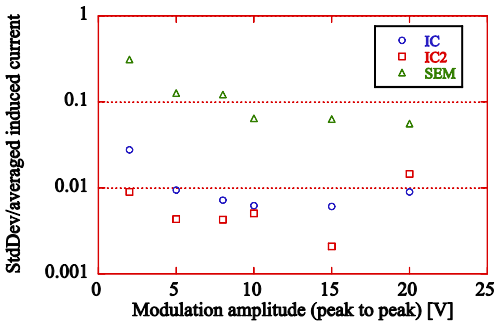


Figure 8: Measurement reproducibility versus modulation amplitude. Different options are being investigated to reduce the SEM error.

Thresholds Production

The individual thresholds, to be set inside the electronics for each channel, are the minimum and the maximum boundaries for the harmonic induced current and the phase. To calculate them, the average value over multiple measurements for each parameter (Fig. 7) is taken and a 15% margin (Fig. 8) is added.

SUMMARY

The BLM system of the LHC is now capable of self testing its connections and removing ambiguities due to cabling malfunction. The system sensitivity and measurement reproducibly (better than 1% for the IC and 5% for the SEM) exposed in this paper allows the distinction between monitor types and different setups. Component value changes due to radiation or ageing can be detected with high sensitivity. The threshold comparison automatically blocks beam injection in case of system nonconformity.

REFERENCES

[1] Engineering Specification, *"The Beam Interlock System For The LHC"*, LHC Project Document No. LHC-CIB-ES-0001-00-10, version 1.0, 17-02-2005.

[2] E. Effinger, B. Dehning, J. Emery, G. Ferioli, C. Zamantzas, *"Single Gain Radiation Tolerant LHC Beam Loss Acquisition Card"*, Proceedings of DIPAC'07, Venice-Mestre, Italy.

[3] C. Zamantzas, B. Dehning, E. Effinger, J. Emery, G. Ferioli, *"The LHC Beam Loss Monitoring System's Surface Building Installation"*, Proceedings of LECC'06, Valencia, Spain.

[4] C. Zamantzas, B. Dehning, J. Emery, J. Fitzek, F. Follin, S. Jackson, V. Kain, G. Kruk, M. Misiowiec, C. Roderick, M. Sapinski, *"Configuration and Validation of the LHC Beam Loss Monitoring System"*, these proceedings.

UPGRADE OF THE TIMING SYSTEM AT THE AUSTRALIAN SYNCHROTRON

E. van Garderen, M. ten Have, G. LeBlanc, A. Starritt, K. Zingre
Australian Synchrotron, Melbourne, Australia

Abstract

The Australian Synchrotron (AS) timing system is based on a hybrid design: an Event Generator-Event Receiver (EVG-EVR) system creates the injection trigger and various clocks, while a network of digital delay generators adjusts pulse delays and widths. This architecture, combined with a storage ring fill pattern monitor, allows the targeting of injection into specific buckets in the storage ring. Nevertheless, more demanding needs from the machine and the beamlines require an upgrade of the system. Delay generators will be removed and replaced by EVRs. This will allow fixed or variable frequency clocks to be made available to beamlines or to trigger diagnostic hardware in a flexible way, while reducing jitters to below 100 ps.

INTRODUCTION

The Australian Synchrotron is a 3rd generation light source [1]. It consists of a 100 MeV linac, a 100 MeV to 3 GeV booster synchrotron and a 3 GeV storage ring composed of 14 sectors. The storage ring can store up to 200 mA. First beam was delivered to users in 2007 and, currently, eight of the nine beamlines are in operation.

The timing system was partly commercially delivered. Its in-house design was limited to the storage ring fill pattern monitor, AC synchronization and a down-graded EVG/EVR-200 to provide just the storage ring orbit clock for diagnostics and the injection trigger.

The first improvement in 2007 included the upgrade to the EVG/EVR-230RF with Radio Frequency (RF) recovery. The event system gun transmitter (GTX) and receiver (GRX) were also added to improve jitter performance of the electron gun while replacing the original LiteLink fibre optics transmission system.

This upgrade will replace all the delay generators and other smaller parts to improve reliability and maintainability, with easy-to-program signals.

TIMING REQUIREMENTS

The AS injection process uses a static injector [2] with a repetition rate of 1 Hz. Buckets are targeted by delaying the whole injector from the gun to the injection of the electrons into the storage ring instead of just the extraction from the booster. All trigger signals are therefore fixed with respect to the gun that can be delayed in $\sim$2 ns steps, given by the RF from the Master Oscillator: f_{RF} = 499.671838 MHz $\pm$ 20 kHz. Moreover, the injection system is synchronized to the 50 Hz mains frequency (AC sync) to minimize the influence of the AC heated linac modulator and gun.

Table 1: Summary of relevant timing requirements

Clocks	**Frequency**
RF	499.671 MHz
Event Clock	125 MHz
SROC	1.38 MHz
Items	**Trigger Delay/Width**
GUN	
Gun single-bunch	181.4 μs / 1 ns
Gun multi-bunch	181.4 μs / up to 150 ns
LINAC	
500 MHz pre-buncher	175 μs / 140 ns
3 GHz electron multiplier	184 μs / 140 ns
MAGNETS	
Booster injection septum	0 ns / 300 μs
Booster injection kicker	175 μs / 10 μs
Booster ramping magnets	2 ms / 500 μs
Booster extraction septum	601 ms / 100 μs
Booster extraction kicker	601 ms / 5 μs
SR injection septum	601 ms / 1 μs
SR injection kicker	601 ms / 830 ns

The 90 keV gun can be run in single-bunch or multi-bunch modes. Multi-bunch mode is limited by the size of the booster ring and speed of the kicker magnets for up to a bunch train of 75 buckets. The single-bunch trigger requires a very low jitter of a few tens of picoseconds to optimize capture in the booster, whereas the multi-bunch trigger does not have those tight demands because bunches are separated by the 500 MHz modulation of the gun.

Most triggers require TTL, CML or LVPECL levels terminated into 50 Ω and a few optical links. All triggers should have low jitter performance of a few hundreds of picoseconds, as discussed further. Table 1 summarizes important trigger requirements.

PRESENT ARCHITECTURE

The current hybrid timing features the event system [3] from Micro Research Finland, including a VME-EVG-230RF, two VME-EVR-230RF, an optical fanout VME-OUT-12, a GTX VME-GUNTX-200, plus a stand-alone GRX GUNRC-202, and delay generators DG535s from Stanford Research Systems and with details shown in Fig. 1.

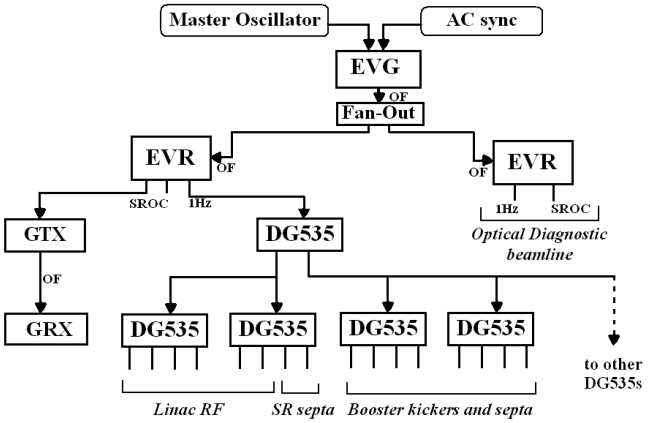


Figure 1: Overview of the current timing system. See text for description of the abbreviations.

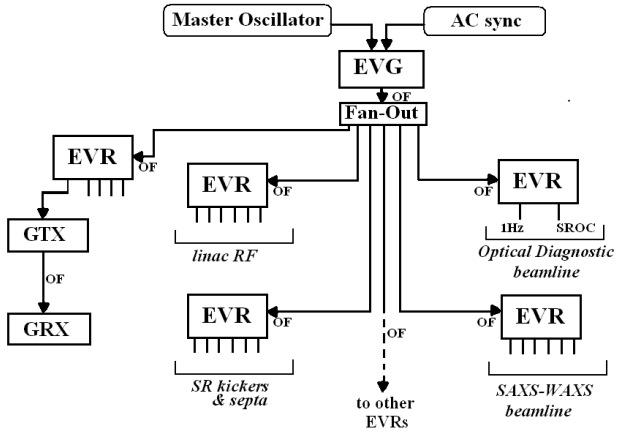


Figure 2: Overview of the future timing system.

High speed counters inside the EVG derive the Storage Ring Orbit Clock SROC (1.38 MHz) from the f_{RF} divided by the storage ring harmonic number (360), and the event clock (125 MHz) $f_{RF}/4$. The 1 Hz master trigger, however, results from the AC divided by 50 and is internally synchronized with SROC. The event clock is used as the clock signal for the EVG and EVRs; the EVG and the EVR are therefore phase locked with the RF. Signals from the EVG are transmitted to the EVRs by multi-mode optical fibres (OF) via the fanout.

The first EVR decodes the master clock and converts it into an injection trigger by adding 8 ns step delays, equivalent to an event clock cycle or 4 buckets. The injection trigger is then delivered to the network of DG535s, which generate fixed triggers to the end devices. This EVR also provides the necessary CML signals to the GTX which generates 2 ns step delays and drives the GRX via OF. Each storage ring bucket is therefore targeted by delaying the gun by a calculated amount of 2 ns steps, which is a combination of 8 ns coarse delays from the EVR and 2 ns fine ones from the GTX. The second EVR supplies the 1 Hz master trigger, injection trigger, RF and SROC signals to the optical diagnostics beamline.

Need for Improvement

A major drawback of this architecture was the high jitter observed on triggers with delays larger than 1 ms, as reported in [4]. In particular, the storage ring kickers, with a delay of 600 ms, were subject to 5 ns jitter. However, instabilities could be reduced by changing DG535s from an internal to an external timebase, fed from a 10 MHz reference clock supplied by the master oscillator.

Nevertheless, an upgrade was desired to improve the performance of the machine and to deliver the timing system to the beamlines in an advanced way. EVR cards were found to be accurate and flexible, providing multiple outputs which can be triggered out of different clocks, with a very low jitter (25 ps rms). They also offer various types of outputs to avoid external level converters. It was therefore decided to replace all delay generators by EVRs.

FUTURE ARCHITECTURE

The new timing system is composed of an EVG and twelve EVRs: seven for the machine and five for the beamlines (see Fig. 2). Machine EVRs are located in various areas of the facility in order to reduce cable lengths to end devices.

Five events are created by the EVG: the master trigger, the injection trigger, SROC, SROC/N1 and SROC/(N1*N2), where N1 and N2 are integers. The two latter clocks are required by the optical diagnostic beamline to trigger diagnostics equipment such as the streak camera.

The starting time of all clocks has been carefully chosen to avoid most conflicts between events, in order to prevent jitter in signals derived from the injection trigger.

Considering internal delays inherent to the EVG programming of events and event sources priority [5], the timing scheme as been designed as follows (see Fig. 3):

The master trigger is delayed by 91 event clocks (e.c.). The first possible injection trigger, targeting buckets 1 to 4, is set 92 e.c. later than the master trigger. Injection triggers aiming at later buckets are further delayed in 1 e.c. steps. In that way, conflicts between master trigger, injection trigger and SROC related clocks result in the latter being delayed by 1 e.c.. The priority is thus left to the master trigger and the injection trigger. Interferences with the injection trigger are observed for buckets 357 to 360 only, which coincide with SROC. However, those buckets are currently not used in user beam mode fill patterns. Similarly, the slower SROC related clock has a lower priority than the faster one.

The timing system software is based on EPICS. It executes an EPICS base-3.14.8.2 IOC running on a Redhawk (real time RHEL derivative) Linux box. This IOC also manages fill pattern and ultimately bucket selection using an EPICS seq-2.0.11 sequencer program. For the IOC new records (with new names) have been defined together with new EVG/EVR device drivers, although these are based on

the existing records and drivers. This allows for a combinations of old and new systems to run at the same time for testing and calibration. The OPI software uses the existing AS OPI framework, which is based on the Borland Delphi development system. It creates a Windows executable that runs both natively on Windows boxes and under Wine on Linux machines. New forms have been developed for the new functionality and integrated into the overall accelerator control OPI program. Fig. 4 shows part of the EVR control form for one of the pulse delay channels, and illustrates how the operator can control and monitor pulse enable/disable, polarity, select the trigger event and specify the delay and the width.

The signal cabling has also been replaced in the upgrade. Short ENVIROFLEX_316_D cables now provide a link from the LEMO outputs of the EVRs to a nearby SMA patch panel followed by low attenuation highly screened microwave cables of type S04272B in order to maintain good phase stability, fast rising edges and reduce noise.

External level converters have been replaced by OF and LVPECL universal boards inserted in EVR cards to drive booster kickers and Liberas [6], respectively. Replacement of the repeaters for the ramped booster power supplies is also considered due to poor matching and the inability to drive 50 Ω.

Pros and Cons

The new timing system is flexible, easily programmable and introduces no jitter degradation over long delays due to RF synchronization which automatically readjusts all delays if f_{RF} changes. It also offers the option of reconstructing f_{RF} on CML outputs, which is a convenient alternative to pulling cables from the master oscillator. Moreover, the variety of output boards available (LVPECL, OF, NIM) makes conversion equipment obsolete.

Unlike the delay generators, which allowed modification of the amplitude of signals, EVRs provide a maximum amplitude of 3 V, demanding a change to the trigger levels of some devices.

EVR cards need to be tuned regularly [7]. Failure to do so results in unstable signals which are no longer phase matched with the RF. In those cases, jitters up to 800 ps have been observed.

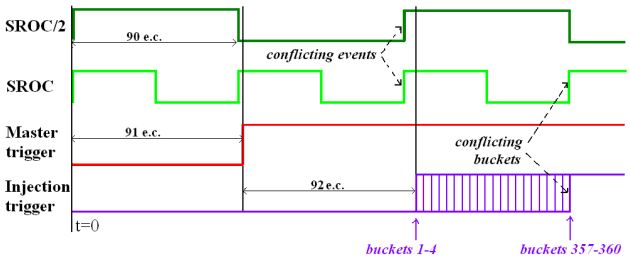


Figure 3: Schematics of various clocks generated by the EVG. See text.

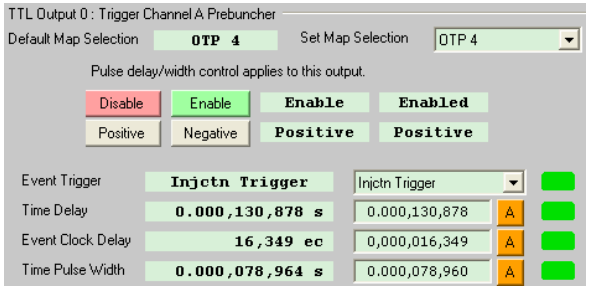


Figure 4: Detail of the EVR user interface.

CONCLUSION

The current Australian Synchrotron timing system is about to be upgraded from a hybrid system to a complete event system with multiple stations distributed via fibre optics around the machine and to the beamlines. The upgrade is intended to cover the increasing demands of users, to provide better flexibility and performance, and to reduce jitters below 100 ps.

Ten new EVR cards have been deployed throughout the facility to eventually replace all delay generators. The control software of the EVG and EVRs, including user interfaces, has been improved to conform with the new requirements. Injection into the storage ring using the new architecture was successful. Presently, a few adjustments still need to be performed before all delay generators are removed.

ACKNOWLEDGEMENTS

The authors are grateful to T. Korhonen and J. Pietarinen for their precious help in understanding and programming the event systems.

REFERENCES

[1] J. Boldeman, D. Einfeld, Nucl. Instr. and Meth., A **521**, 2004, p. 306-317.

[2] M.J. Spencer et al., "Diagnostics and Timing at the Australian Synchrotron", EPAC'06, Edinburgh 2006.

[3] T. Korhonen, "Review of Accelerator Timing Systems", ICALPEC'99, Trieste 1999.

[4] DG535 data sheet, www.thinksrs.com/downloads/PDFs/Catalog/DG535c.pdf

[5] Micro-Research Finland, Event Generator, www.mrf.fi/index.php?option=com_content&task=view&id=39&Itemid=47

[6] Y.-R. E. Tan et al., "Commissioning the Australian Synchrotron with Libera EBBPS and Matlab", APAC'07, Indore 2007.

[7] J. Pietarinen, "VME Event Reciever (VME-EVR-230RF), Technical Reference, Firmware version E504", March 2009.

FIRST MEASUREMENTS OF THE LONGITUDINAL PHASE SPACE DISTRIBUTION USING THE NEW HIGH ENERGY DISPERSIVE SECTION AT PITZ*

J. Rönsch†, G. Asova‡, J. Bähr, C. Boulware, H.J. Grabosch, L. Hakobyan§, M. Hänel, Y. Ivanisenko
M. Khojoyan¶, M. Krasilnikov, B. Petrosyan, S. Rimjaem, A. Shapovalov‖, L. Staykov**,
R. Spesyvtsev, F. Stephan, DESY, 15738 Zeuthen, Germany
S. Lederer, DESY, 22761 Hamburg, Germany
J. Rossbach, Hamburg University, 22761 Hamburg, Germany
D. Richter, HZB für Materialien und Energie, 12487 Berlin, Germany

Abstract

The Photo Injector Test facility at DESY, Zeuthen site, (PITZ) develops and optimizes high brightness electron sources for Free Electron Lasers (FELs) like FLASH and the European XFEL. A new multi-purpose dispersive section was designed [1, 2] and installed to characterize the momentum distribution, the longitudinal phase space distribution and the transverse slice emittance of the electron bunch for an electron energy up to 40 MeV. The spectrometer consists of a 180 degree dipole magnet followed by a slit, a quadrupole magnet and two screen stations. One of the screen stations allows the measurement of the longitudinal phase space distribution. The first measurement results and corresponding beam dynamics simulations of the momentum and the longitudinal phase space distributions will be reported in this contribution. The resolution of the system will be analysed and compared to the design expectations.

INTRODUCTION

The main goal of PITZ is to test and to optimize L-Band RF photo injectors for Free-Electron Lasers (FELs) like FLASH and XFEL at DESY in Hamburg and to study the emittance conservation by using a matched booster cavity. The demands on such a photo injector are a small transverse emittance, a charge of about 1 nC and short bunches (of about 20 ps). Besides the accelerating (gun and booster) cavities, the electron beam line of PITZ consists mainly of diagnostics elements. In 2008 a new multi-purpose dispersive section was installed downstream the booster cavity to characterize the momentum distribution, the longitudinal phase space distribution and the transverse slice emittance [3] of the electron bunch for an energy up to 40 MeV.

* This work has partly been supported by the European Community, contract numbers RII3-CT-2004-506008 and 011935, and by the 'Impuls- und Vernetzungsfonds' of the Helmholtz Association, contract number VH-FZ-005.

† jroensch@ifh.de
‡ On leave from INRNE, Sofia, Bulgaria
§ On leave from YerPhI, Yerevan, Armenia
¶ On leave from YerPhI, Yerevan, Armenia
‖ On leave from MEPHI, Moscow, Russia
** On leave from INRNE, Sofia, Bulgaria

THE SETUP

Figure 1 shows the layout of the new installed first high-energetic dispersive arm (HEDA1). It consists of a 180 degree dipole spectrometer (deflecting in vertical direction) followed by an insertable slit, a quadrupole magnet (DISP2.Q1) and two screen stations (DISP2.Scr1&2). The first screen stations (DISP2.Scr1) is equipped with a YAG-screen imaged onto a 8-bit TV-camera[1] for momentum measurements and a Cherenkov radiator (Silica aerogel, thickness of 5 mm and a refractive index of n = 1.05) [4] to measure the longitudinal phase space distribution using an extended optical read-out and a streak camera [5]. All the results presented in this paper have been made using DISP2.Scr1. DISP2.Scr2 is currently mainly used for transverse slice emittance measurements [3] which are not presented in this paper.

The position where a particle hits the screen after passing the dipole magnet depends on the momentum, the transverse position and the angle of the particle before it enters the dipole spectrometer, according to the first order transport matrix:

$$y_{DA} = R_{11} y_0 + R_{12} y'_0 + R_{16} \frac{\Delta p_0}{p_0}, \qquad (1)$$

where y_0, y'_0 and $\frac{\Delta p_0}{p_0}$ are the position, divergence and relative momentum deviation of the particle at the entrance of the dipole magnet and R_{11}, R_{12} and R_{16} are the dipole matrix elements. For a 180 degree dipole spectrometer without pole face rotation these values become:

$$R_{11} = -1, \quad R_{12} = -L_{DA}, \quad R_{16} = 2r, \qquad (2)$$

with L_{DA} the drift length between the dipole exit and the screen station where the measurement is performed and r the deflecting radius.

When the dipole magnet is switched off the vertical position of a particle at longitudinal position L_{drift} downstream the dipole entrance is given by:

$$y = 1 y_0 + L_{drift} y'_0. \qquad (3)$$

[1] In the future this 8-bit camera will be replaced by a 12 bit camera with a higher sensitivity

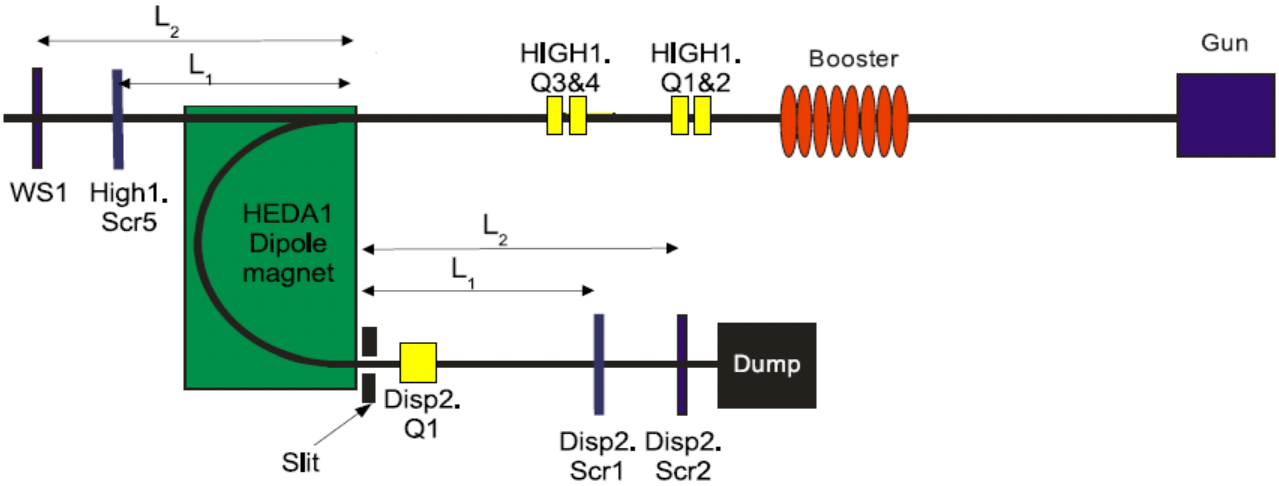


Figure 1: Schematics of the design of the first high-energetic dispersive arm (HEDA1).

This means, when the vertical beam size is minimized at a screen located $L_{drift} = L_{DA}$ (labeled L_1 in figure 1) downstream the dipole entrance also the influence of the initial beam size and divergence to the momentum spread measurement is minimized.

In front of the dipole magnet two quadrupole-doublets are situated, mainly the quadrupole-doublet HIGH1.Q1&2 is used to focus the beam to reach a high resolved momentum measurement.

MEASUREMENTS OF THE MOMENTUM DISTRIBUTION

Figure 2 shows a measured momentum distribution compared to simulations for a main solenoid current of 390 A, a maximum accelerating field of 60 MV/m at the photo cathode, a charge of 250 pC, a gun phase of maximum momentum gain + 10° and a booster phase of maximum momentum gain + 10°. The beam was focused on the reference screen (HIGH1.Scr5) in vertical direction, in order to minimize the influence of the beam size and divergence to the resolution. Both distribution show a good agreement, nevertheless some difference are visible in the distributions. These differences are caused by the residual influence of beam size and divergence as well as inaccuracies in the entrance parameters of the ASTRA simulation (e.g. of the cathode laser distribution).

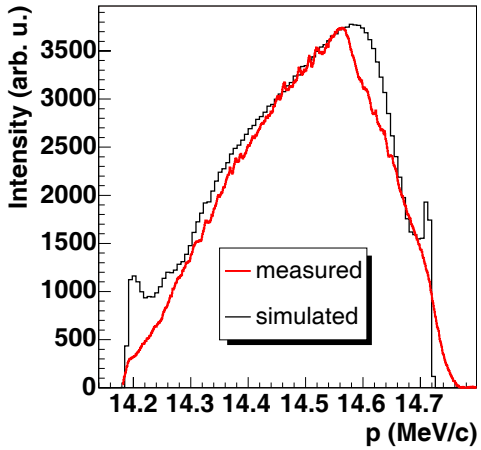


Figure 2: Comparison of measured and simulated momentum distribution for a charge of 250 pC, a gradient of 60 MV/m at the cathode, gun phase of maximum momentum gain + 10° and booster phase of maximum momentum gain +10°.

MEASUREMENTS OF THE LONGITUDINAL PHASE SPACE DISTRIBUTION

Figure 3 shows the measured longitudinal phase space distribution for a maximum accelerating field of 60 MV/m at the photo cathode, a gun phase of maximum momentum gain and a booster phase of maximum momentum gain - 10°. In figure 4 the corresponding simulated longitudinal phase space distribution is shown.

The shape of the measured longitudinal phase space distribution for gun and booster phase of maximum momentum gain is comparable to the simulated one, but the area of the phase space distribution and thus the longitudinal emittance and the slice momentum spread is still larger in the measurement than in the simulation. This limitation is mainly caused by the resolution of the streak camera of 2 ps (Hamamatsu C5680) and the optical transmission line. Therefore the simulated longitudinal phase space distribution was convoluted with the response function of the streak camera (shown in figure 5) to estimate the limitation of the resolution of the measurement by the streak camera. This distribution including the streak camera resolution smears out the details in the simulated longitudinal phase space distribution and small modulations are not recognizable anymore. It is much closer to the measure-

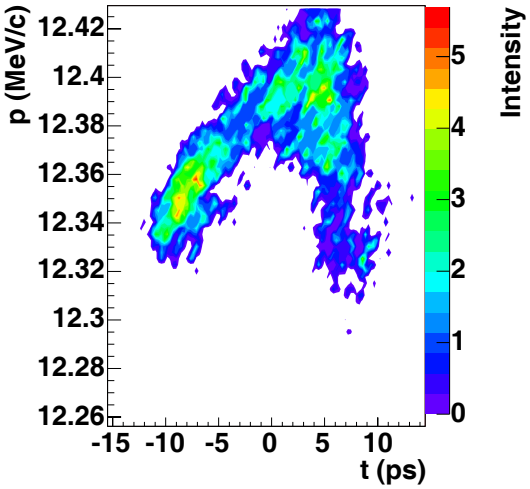


Figure 3: Measured longitudinal phase space distribution for a gradient of 60 MV/m at the cathode, gun phase of maximum momentum gain and booster phase of maximum momentum gain $-10°$.

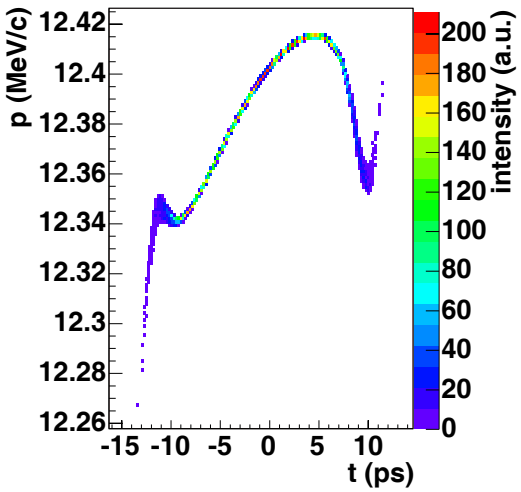


Figure 4: Simulated longitudinal phase space distribution for a gradient of 60 MV/m at the cathode, gun phase of maximum momentum gain and booster phase of maximum momentum gain $-10°$.

ment, even there are still discrepancies between measurement and simulation. The low intensive head of the bunch seen in the simulation is not visible in the measurement, most probably this is a problem of sensitivity. One also has to take into account that the measurement is an average of 100 bunches and a small phase or gradient jitter of the accelerating cavities is impacting the bunch momentum and blurs the longitudinal phase space with its narrow slice momentum spread.

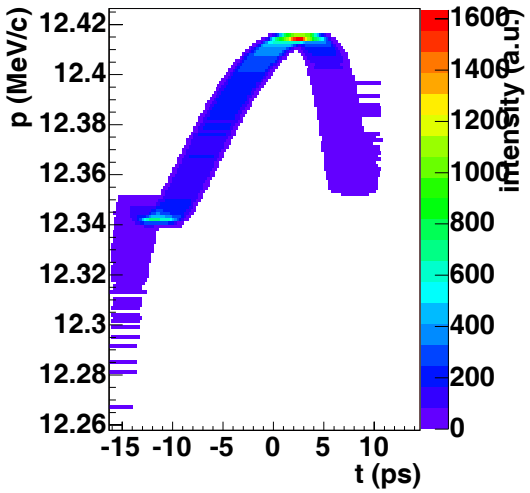


Figure 5: Simulated longitudinal phase space distribution for a gradient of 60 MV/m at the cathode, gun phase of maximum momentum gain and booster phase of maximum momentum gain $-10°$ convoluted with the resolution of the streak camera.

SUMMARY

The measurement of the momentum distribution and longitudinal phase space distribution using the new multipurpose dispersive section (HEDA1) has been presented. A reproduction of the measured momentum distribution by simulations has been shown. Also the measured longitudinal phase space distribution could be reproduced by ASTRA simulations taking into account the resolution of the streak camera used for the measurement.

ACKNOWLEDGMENT

Special thanks to S. Khodyachykh and A. Oppelt for their work during the design phase.

REFERENCES

[1] S. Khodyachykh et al., "Design of Multipurpose Dispersive Section at PITZ", Proceedings of the 28th FEL Conference, Berlin, September 2006.

[2] S. Khodyachykh et al., "Design and Construction of the Multipurpose Dispersive Section at PITZ", Proceedings of DIPAC 2007, Venice, Mestre, Italy 2007.

[3] Ye. Ivanisenko, C. Boulware, L. Staykov, F. Stephan, "Slice Emittance Measurement Using an Energy Chirped Beam in a Dispersive Section at PITZ", Proceedings of the 30th FEL Conference, Gyeongju, S. Korea, 2008

[4] J. Baehr, V. Djordjadze, D. Lipka, A. Onuchin, F. Stephan, "Silica aerogel radiators for bunch length measurements", Nuclear Instruments and Methods in Physics Research A 538 (2005) 597-607

[5] J.Baehr et al., "Optical System for Measuring Electron Bunch Length and Longitudinal Phase Space at PITZ: Extension and Methodical Investigations", Proceedings of DIPAC 2007, Venice, Mestre, Italy 2007

MEASUREMENT DEVICES FOR THE SPARC SYNCHRONIZATION SYSTEM

M. Bellaveglia, D. Alesini, A. Gallo, C. Vicario,
INFN-LNF, Via Enrico Fermi 40, Frascati, Italy

Abstract

The SPARC FEL facility is under commissioning at the Frascati National Laboratories of INFN. The synchronization system is working as expected and various devices are used to monitor its performances. In particular this paper is focused on a comparison between the results obtained using different methods and instruments to perform laser, RF and beam synchronization measurements. Both electro-optical and full electrical techniques are used to obtain information about the phase noise of the RF fields inside the accelerating structures, the phase noise of the IR laser oscillator, the time of arrival of the laser UV pulse on the cathode and the time of arrival of the accelerated electron bunch at a selected reference position along the linac.

INTRODUCTION

The SPARC project is now under its commissioning phase at the Frascati National Laboratories of INFN. First FEL lasing in the SASE regime has been observed and other experimental activities are on the way [1]. The synchronization system is working as expected. Its performance has been recently upgraded using a new scheme and also new diagnostic devices have been installed, as described later in this document.

System Layout

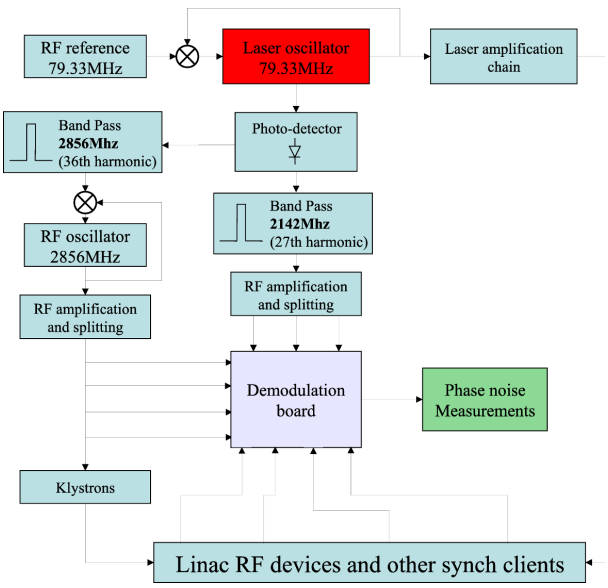


Figure 1: Layout of the synchronization system of SPARC.

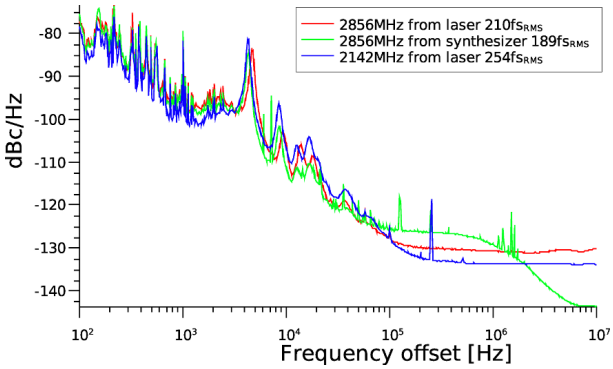


Figure 2: Phase noise spectra of the RF reference signals with integrated absolute jitter (from 100 Hz to 10 MHz).

The synchronization system has been modified and upgraded respect to the one operating during the last SPARC run [2]. We chose to use the Ti:Sa oscillator of the photocathode laser as optical master oscillator (OMO) instead of using a RF synthesizer. Doing this, we can bypass the electro-mechanical PLL used to synchronize the laser cavity oscillation to the RF reference. This loop has a bandwidth of $\approx$ 5 kHz and was the main limitation of the SPARC synchronization system. Using the new scheme and starting from the laser cavity frequency, we can lock the RF synthesizer to that, using a PLL with a larger bandwidth ($\approx$ 1 MHz). Thus the RF-to-laser relative jitter results pretty much reduced, as reported later in this paper. The long term frequency stability of the laser cavity is granted by a $79.\overline{3}$ MHz signal coming from a RF synthesizer and squared by dedicated standard NIM electronics. The PLL around the oscillator cavity make use of both the fundamental and the 9^{th} harmonic to lock the laser repetition rate.

Reference Generation

As described in Figure 1, the RF reference signals are obtained by the $79.\overline{3}$ MHz pulse train coming from a solid state 10 GHz bandwidth photodetector illuminated by the laser Ti:Sa oscillator. In particular we used two filters to isolate the 27^{th} (2142 MHz) and the 36^{th} (2856 MHz) harmonic of the laser repetition rate. The signal has been also pre-filtered after the photodetector to eliminate the fundamental frequency and the unwanted harmonics that could generate distortion in the RF amplification process. Actually a commercial RF synthesizer from Rhode&Schwarz is used to generate the reference sent to the RF power stations. We used its FM port to close a PLL to have a copy of

the 2856 MHz laser reference that is distributed in the system. Due to the pretty large PLL bandwidth (about 1 MHz) the two SSB phase noise spectra are very similar at low frequencies as shown in Figure 2. We also report in the same figure the spectrum of the 2142 MHz signal coming from the photodetector and used for diagnostic purpose. The measurements have been performed using a Agilent E5052A Signal Source Analyzer.

DEVICES AND MEASUREMENTS

All the signals coming from the RF devices and from other diagnostics elements of the synchronization system are gathered into the demodulation boards located in the SPARC tunnel. The phase detection relative to the RF references is accomplished by mixers and the information is digitalized and sent into the control system by a dedicated CPU. All the synchronization measurements are easily performed in the control room using custom applications.

RF Phase Noise

To reduce the phase noise of the RF power signals inside the accelerating structures relative to the RF reference, we implemented PLLs working around the two klystrons [3], that are the main noise sources in the RF network. The loop has a large bandwidth, so that its transient has a duration of about 1 µs and it can easily operate inside a single 4.5 µs RF pulse. This allowed us to compress the noise of a factor ≈ 10 resulting in a relative jitter less than 100 fs_{RMS} measured at various RF probes along the linac. The phase information for each RF square pulse is obtained sampling the RF demodulated signal with a 60 Msample/s-12bit digitizer card and averaging the data over about 200 samples. The long term phase stability is provided by slow feedback loops acting at RF low level. They use motorized delay lines to keep the phase stable, compensating possible temperature drifts [3].

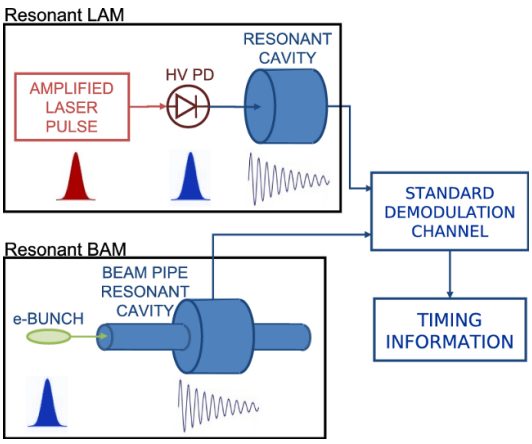
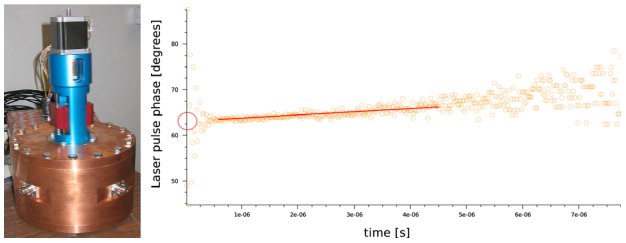


Figure 3: Block diagram of the BAM and LAM devices.

LASER Time of Arrival Monitor (LAM)

The innovative idea for SPARC is to have timing information on the single laser UV pulse at the end of the amplification chain and to use it to build a pulse-to-pulse phase lock feedback. Normally one needs a continuous sinusoidal waveform to analyze its spectrum and give an estimation of the phase stability of an oscillator. Unfortunately, in the case of a pulse train with 10 Hz of repetition rate it is almost impossible to extract this information. To overcome the problem, we implemented the experimental setup shown in Figure 3. The measured signal comes from a cavity tuned at 2142 MHz, fed by a high voltage electric pulse (with a peak of $70 \div 100$ V) formed by a fast photodiode illuminated by the laser UV 10 ps pulse, with a repetition rate of 10 Hz. This photodetector is a biplanar vacuum photodiode with a rise time less than 100 ps operating at 5 kV bias voltage. A resonant cavity shown in Figure 4a has been designed and built to accomplish these measurement. It works with a solenoidal $TE011$ mode and has a high Q factor ($Q_0 = 60000$, $Q_L = 20000$). This grants an exponential decaying RF pulse with a duration of about 3 µs and allows to perform a consistent measurement. Due to the interference of the signals with the strong electric fields inside the accelerating structure, the cavity has been designed with a central frequency of 2142 MHz, equal to the 3/4 RF SPARC frequency. This device is also equipped with a motorized tuner that can be remotely controlled. The out-coming signal is then compared with the 2142 MHz RF reference obtained from the Ti:Sa oscillator.



(a) (b)

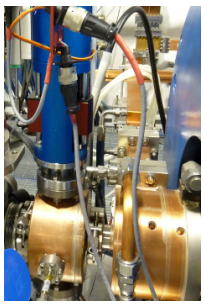
Figure 4: (a) Picture of the resonant cavity for the LAM and (b) an acquired phase data for a single UV pulse with emphasis on the analysis algorithm.

After the signal sampling, performed using a 60 Msample/s-12bit digitizer card, we obtain the phase data shown in Figure 4b. To extract a single phase value associated to each laser shot we had to overcome two problems: (i) due to a non perfect tuning of the cavity, a slope can be present in the phase signal and (ii) the initial part of the signal is distorted by the presence of some higher cavity mode excited by the short electric pulse. Thus we post-process the data performing a fit in the central part of the pulse using a linear model and we reconstruct the phase information at the pulse initial time. This tasks are performed at the machine repetition rate of 10 Hz and allow us to have a real time information of the laser time arrival. The best result we obtained after the

synchronization system upgrade is a jitter of 220 fs_{RMS}.

e-bunch Time of Arrival Monitor (BAM)

Resonant Cavity BAM The principle used in the resonant cavity BAM [4] is identical to the one reported in the previous section about the LAM. The only difference is that the exciting electric pulse comes from the e.m. field of the electron bunch propagating inside the beam pipe, as shown in Figure 3. The consequent cavity free oscillations are carried outside by 2 antennas connected to vacuum coaxial feedthroughs and are sampled as described in the LAM section. Two pill-box like cavities have been designed and realized at LNF and a resonant frequency of 2142 MHz has been chosen to avoid interference coming from the 2856 MHz power signal present in the accelerating structures. The first cavity has been installed between the first two accelerating sections and the second one will be installed at the end of the linac. A picture and some of the main parameters of the first cavity are shown in Figure 5a and b. The BAM cavities are equipped with two tuning ports. The larger port accommodates a fixed tuning plunger to coarsely tune the cell, while the smaller port host a remotely controlled tuner plunger to finely correct the cavity natural resonant frequency of the fundamental mode to < 10 kHz respect to the reference 3/4 RF to limit the detected phase slippage during the measurement time slot. The coupling of the antennas is designed to produce large detectable signals (≈ 2 V for 1 nC bunch) which will eventually require no extra RF front-end amplification before being demodulated. The use of BAMs on the SPARC linac will allow to direct monitor the electron bunch synchronization and, by differentially comparing the measurements of 2 different BAMs, to finally qualify the ultimate resolution attainable by the pulse resonant stretching method which is fully based on electrical microwave techniques.



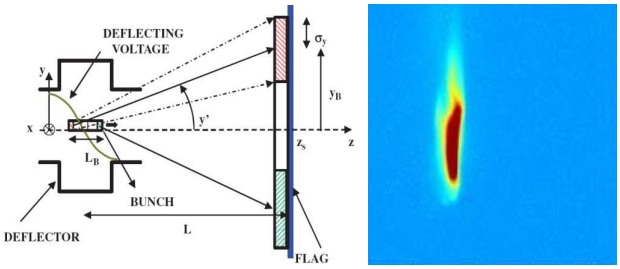
(a)

Operating mode	$TM010$
Frequency	$f_0 = 2142$ MHz
Unloaded Q factor	$Q_0 = 16000$
R/Q factor	$R/Q = 40\,\Omega$
Antenna ext. Q fact.	$Q_{ext} = 30000$
Loaded Q factor	$Q_L = 7500$
Decay time	$\tau_d = 1\,\mu$s
Output peak voltage @1 nC bunch charge	$V_{pk} \approx 2$V

(b)

Figure 5: (a) A picture of the BAM cavity and (b) some of its useful parameters.

RF deflector BAM This BAM technique uses the SPARC RF deflector developed at SPARC that is a 5-cell SW structure reaching a maximum transverse deflecting voltage of more than 3 MV with an input power of nearly 2 MW. This device has been designed for longitudinal profile and slice emittance measurements that have been already performed at SPARC [5]. A sketch of the deflector working principle and a sample of the measured longitudinal bunch shape are reported in Figure 6a and b. Due to the deflection, the longitudinal distribution of the bunch is projected into the vertical plane of a target placed after the RF deflector. After a necessary calibration, the BAM in this case works analyzing some tens of raw images acquired by a digital camera and extrapolating the information about the jitter of the beam centroid vertical position. Also the phase noise of the RF field inside the deflecting structure affects the measurement, changing the deflecting force that the beam centroid "feels". The contribution has been estimated measuring the phase noise from a deflector vacuum probe. Thus we could easily eliminate this systematic error that is of the order of 100 fs_{RMS}. The residual jitter of the bunch arrival time is finally estimated to be ≈ 140 fs_{RMS}.



(a) (b)

Figure 6: (a) Sketch of the RF deflector working principle and (b) an acquired image showing the longitudinal beam shape.

CONCLUSION

After implementing a synchronization system upgrade we measured the signals jitter observing a significant improvement on the performance respect to the previous configuration. The photocathode laser time arrival monitor measured a ≈ 200 fs_{RMS} jitter while the RF deflector bunch time of arrival monitor measured 140 fs_{RMS}. The resonant BAM will be tested as soon as possible during the next SPARC run. Also correlated measurements will be performed between BAM, LAM, gun launching phase and other other RF signals sampled along the linac to completely characterize the sources of noise in the system.

REFERENCES

[1] M. Ferrario et el., "Recent Results of the SPARC FEL Experiments", Proc. of PAC09, Vancouver, Canada

[2] A. Gallo et al., "The SPARC RF synchronization system", Proc. of PAC05, Knoxville, Tennessee

[3] A. Gallo et al., "Performances of the SPARC laser and RF synchronization systems", Proc. of EPAC08, Genoa, Italy

[4] D. Alesini et al., SPARC technical note RF-09/001, `http://www.lnf.infn.it`

[5] C. Vaccarezza et al., "Slice emittance measurements at SPARC photoinjector with a RF deflector", Proc. of EPAC08, Genoa, Italy

YTTERBIUM FIBER LASER FOR ELECTRO-OPTICAL PULSE LENGTH MEASUREMENTS AT THE SWISSFEL

F. Müller*, S. Hunziker, V. Schlott, B. Steffen, D. Treyer, Paul Scherrer Institute (PSI), Switzerland
T. Feurer, University of Bern, Switzerland

Abstract

Pulsed Yb fiber lasers emit at 1030 nm which provides a better phase matching in standard EO crystals (GaP, ZnTe) than the wavelength of Ti:Sa lasers (800 nm). We present a mode locked ytterbium fiber laser which is phase locked to the RF. A subsequent fiber amplifier is used to boost the power and to broaden the spectrum due to nonlinear effects. The produced pulses have a spectral width of up to 100 nm and are therefore suitable for EO bunch length measurements, especially for spectral decoding.

INTRODUCTION

In accelerator diagnostics the knowledge of the electron bunch length and the temporal structure plays an important role. Electro optical (EO) techniques offer the possibility for non destructive single shot pulse length measurements [1]. This laser based method requires an environmentally stable and robust laser system with a small jitter and a broad spectrum. Ytterbium (Yb) fiber lasers fulfill these criteria. Yb has a number of interesting properties as a small quantum defect which leads to high pump efficiencies, a long upper state lifetime, a broad gain spectrum and a good phase matching to the THz field in GaP and ZnTe crystals [2, 3]. Combined with the advantages of fiber based systems, as compactness, freedom from misalignment and robustness, Yb fiber laser systems offer an attractive alternative to Ti:Sa lasers for EO measurements. Besides, the price of an Yb laser system is only a fraction of the costs of a Ti:Sa laser system. The EO setup contains the fiber laser and a compact bunch length monitor [4].

LASERSYSTEM

Setup

The laser consists of an oscillator and a single pass amplifier. A schematic of the oscillator is depicted in Fig. 1. The ring resonator has a fiber and a free space part. The latter is basically necessary for dispersion compensation and for the mode locking mechanism, which is based on nonlinear polarization evolution (NPE) [5]. The polarization state is controlled by the three wave plates, which allow to rotate the polarization in a way, that the short and intense part of the pulse remains in the oscillator where the rest, which underwent less polarization rotation is coupled out by the polarizer. This fast and passive effect is responsible for mode locking. The unidirectional way of propagation is defined by the isolator. The amplification and the pumping is done in fiber. The piezo stretcher modulates the resonator length and therefore the repetition rate, which is used to synchronize the laser to a reference signal.

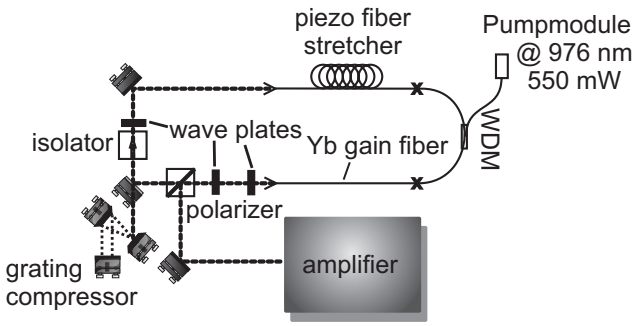


Figure 1: Scheme of the oscillator; WDM, wavelength division multiplexer

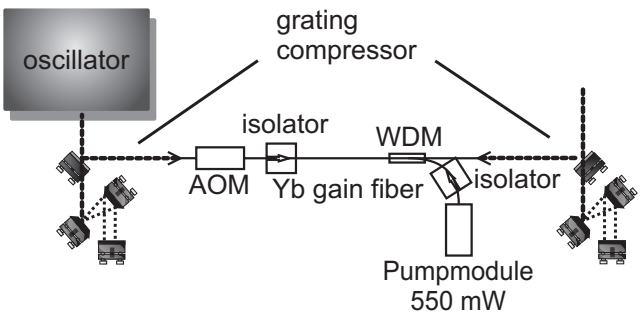


Figure 2: Scheme of the amplifier; AOM, acousto optic modulator; WDM, wavelength division multiplexer

The amplifier is shown in Fig. 2. After the oscillator a first grating compressor modulates the pulse width in order to compensate the dispersion of the following fiber section. The AOM reduces the repetition rate which allows to boost the pulse energy without increasing the average power. Near the end of the fiber, the amplified pulses become short, the intensity increases and strong nonlinear effects occur which broaden the spectrum.

The according spectra are shown in Fig. 3. In the inset plot the spectrum of the oscillator is depicted, which has a spectral width of about 40 nm. It has the typical parabolic shape of self similar pulses [6]. After amplifi-

* felix.mueller@psi.ch

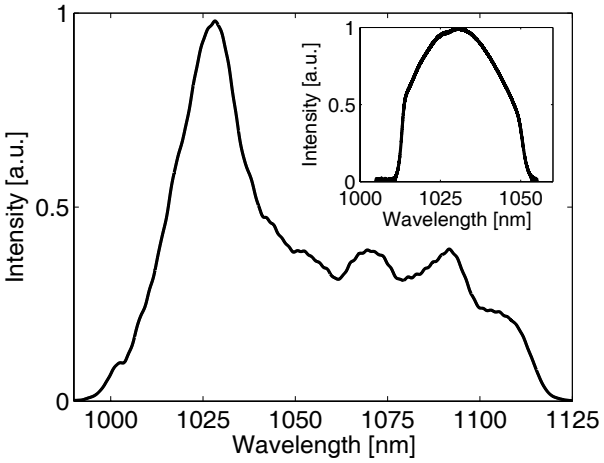


Figure 3: Broad spectrum of the amplifier as used for the EO monitor. Inset: Spectrum of the oscillator

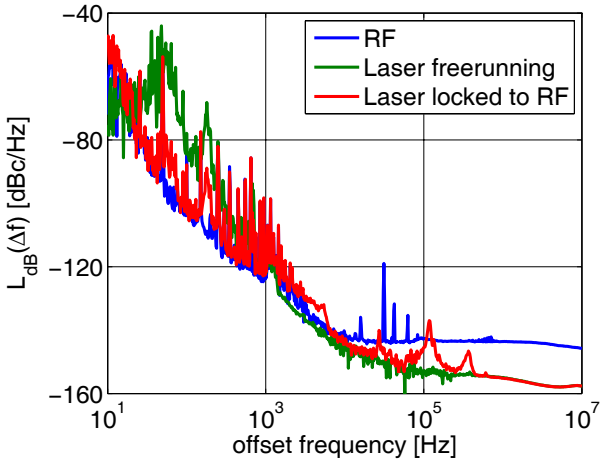


Figure 4: Phase noise measurement of the reference signal, the free running and the locked laser

cation, the broadened spectrum goes from 1 μm to 1.1 μm, providing more than 100 nm of useful bandwidth. For spectral decoding [7, 8] the spectral width directly determines the resolution respectively the temporal range of measurement. Due to the large product of intensity and interaction length in fibers, the oscillator as well as the amplifier produce chirped pulses of up to 10 ps FWHM. The spectral phase of the oscillator is mainly linear, which means that the pulse length can be easily compressed with standard grating compressors down to 60 fs FWHM. After the amplifier the phase has also higher order terms which complicates the pulse compression. The pulses can still be compressed to less than 50 fs FWHM but with some remaining pedestals.

Table 1: Specifications of the Laser System

	Oscillator	**Amplifier**
Average power	50 mW	20 - 100 mW
Repetition rate	50 MHz	0.1 - 1 MHz
Pulse length	60 fs	50 fs
Pulse energy	2 nJ	20 - 200 nJ
Spectral bandwidth	40 nm	100 nm
Central wavelength	1030 nm	1050 nm

Some of the specifications of the laser are summarized in Table 1.

Synchronization

EO Measurements are based on a spatial and temporal overlap between a chirped laser pulse and the electric field of an electron bunch in a nonlinear crystal. This requires a good synchronization to a reference signal (RF) and a low jitter of the laser above the loop bandwidth. The phase locked loop (PLL) modulates the resonator length with a piezo fiber stretcher and locks the 10th harmonic of the repetition rate to the reference clock (500 MHz).

In Fig. 4 the phase noise measurement of the reference signal and of the fiber laser is illustrated. The phase noise of the free running laser for low offset frequencies is typically quite high, where it decreases rapidly for higher frequencies and becomes even smaller than the phase noise of the reference signal. Hence, the laser has to be locked only up to about 1 kHz offset frequency. This loop bandwidth can be seen in the measurement of the locked laser. It follows the reference signal as long as it is more stable and stays freeruning above. The remaining integrated jitter between 1 kHz and 10 MHz is 41 fs.

PREPARATIONS FOR EO MEASUREMENTS AT THE SLS

First EO measurements will take place at the Swiss Light Source (SLS) at PSI where the bunch length of the electron bunches is between 2 ps (LINAC) and 70 ps (storage ring) FWHM. Additionally, there is an ongoing experiment (FEMTO slicing) which generates much shorter pulses by cutting a temporally short part (100 fs) out of the main bunch [9, 10]. An amplified femtosecond Ti:Sa laser pulse interacts with the electrons and modulates their energy. After a dispersive element the energy modulation transforms into a longitudinal one.

The simulated charge distribution is depicted in Fig. 5 for several turns at the THz beamline [11]. Directly after the interaction the modulation has more or less the same temporal length as the laser pulse. Due to the damping of the machine, this modulation becomes longer from turn to turn and finally vanishes. This behavior is shown for turn 0 up to turn 3, which shows the temporal shape after three round trips. The coherent synchrotron radiation can be used to test the EO setup with a whole set of pulse lengths from several ps down to 100 fs, which is the lower limit of the EO techniques due to the limited bandwidth of the EO crystals [2]. Since this modulation of the electron

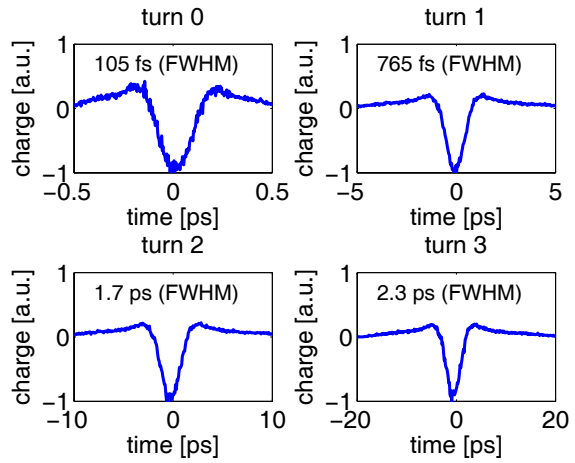


Figure 5: Charge distribution of the sliced bunches from turn 0 to turn 3

bunch is done with a second synchronized laser, the laser to laser stability and the relative jitter plays a decisive role for pulse length measurements. The jitter determines how long the chirped laser pulse has to be in order to get a temporal overlap. It can be deduced from a cross correlation between these two pulses. This measurement delivers a first characterization of the whole laser setup. It has been done in a collinear cross correlation setup in a BBO crystal of 50 μm thickness. The initial pulse length of the lasers were 60 fs (Yb) and 100 fs FWHM (Ti:Sa). In case of an ideal synchronization with no jitter, one would get the cross correlation as depicted in Fig. 6 (blue curve), any jitter results in further broadening this curve.

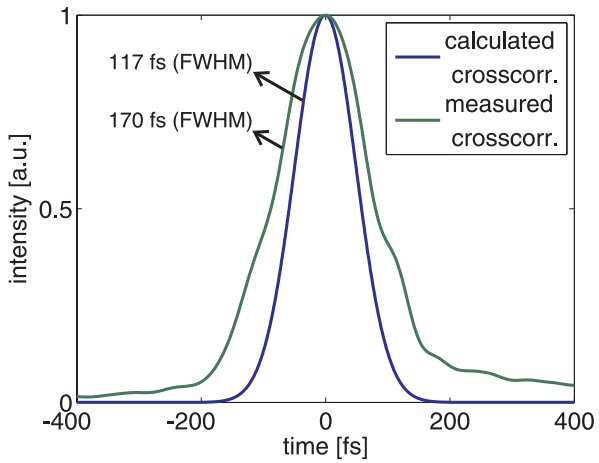


Figure 6: Calculated jitter-free (blue curve) and measured (red curve) cross correlation of the Yb and the Ti:Sa Laser.

The relative jitter between the two lasers is about 120 fs, which is suitable for the planned experiments.

CONCLUSION AND OUTLOOK

A mode locked Yb fiber laser has been built, which suffices the requirements for EO pulse length measurements. The synchronization has been characterized and successfully tested with a cross correlation experiment. First measurements with the EO setup, consisting of the laser and the EO monitor, are planned at the SLS linac during summer 2009. Further optimizations can be done by measuring shorter pulses during FEMTO slicing. In parallel we are planning a packaging of the laser for operation at the 250 MeV Injector which is currently under construction.

REFERENCES

[1] D. Oepts et al., "Picosecond electronbunch length measurement using an electro-optic sensor", Proceedings of the 21st International FEL Conference, Hamburg, 1999.

[2] B. Steffen, "Electro-optic methods for bunch length diagnostics at FLASH" PhD thesis, University of Hamburg, DESY-THESIS-2007-020, 2007.

[3] S. Casalbuoni et al., "Numerical studies on the electro-optic sampling of relativistic electron bunches", Phys. Rev. ST Accel. Beams, 11:072802, 2008.

[4] B. Steffen et al., "A Compact Single Shot Electro-Optical Bunch Length Monitor for the SwissFEL" Proceedings DIPAC 09, Basel, TUPB42, 2009.

[5] M. Hofer et al., "Mode locking with cross-phase and self-phase modulation", Optics Letters, Vol. 16, No. 7, April 1, 1991.

[6] V. Kruglov et al., "Self-similar propagation of high-power parabolic pulses in optical fiber amplifiers", Optics Letters, Vol. 15, No. 24, December 15, 2000.

[7] Z. Jiang et al., "Electro-optic measurement of THz field pulses with a chirped optical beam", Appl. Phys. Lett., 72(16):1945, 1998.

[8] I. Wilke et al., "Single-shot electron-beam bunch length measurements", Phys. Rev. Lett., Vol 88, No 12, 2002.

[9] A. Zholents et al., "Femtosecond X-Ray Pulses of Synchrotron Radiation", Phys. Rev. Lett., Vol 76, No 6, 1996.

[10] P. Beaud et al., "Spatiotemporal Stability of a Femtosecond HardX-Ray Undulator Source Studied by Control of Coherent Optical Phonons", Phys. Rev. Lett., 99, 174801, 2007.

[11] D. Kalantaryan et al., "Laser beam interaction and calculation of the sliced bunch radiation spectra for the SLS FEMTO beam line", Proceedings of EPAC08, Genoa, Italy, 2009.

ULTRA-FAST MM-WAVE DETECTORS FOR OBSERVATION OF MICROBUNCHING INSTABILITIES IN THE DIAMOND STORAGE RING

G. Rehm, A.F. Morgan, Diamond Light Source, Oxfordshire, U.K.
R. Bartolini, I.P. Martin, DLS, Oxfordshire and John Adams Institute at Oxford, U.K.
P. Karataev, John Adams Institute at RHUL, London, U.K.

Abstract

The operation of the Diamond storage ring with short electron bunches using low alpha optics for generation of Coherent THz radiation and short X-ray pulses for time-resolved experiments is limited by the onset of microbunching instabilities. We have installed two ultra-fast (time response is about 250 ps) Schottky Barrier Diode Detectors sensitive to radiation within the 3.33-5 mm and 6-9 mm wavelength ranges. Bursts of synchrotron radiation at these wavelengths have been observed to appear periodically above certain thresholds of stored current per bunch. The fast response allows a bunch-by-bunch and turn-by-turn detection of the burst signal, which facilitates study of the bursts structure and evolution. In this paper we present our first results for various settings of alpha and also discuss future plans.

INTRODUCTION

Diamond Light Source has recently started an experimental programme for the generation of short radiation pulses in the storage ring. Dedicated low-alpha optics[1] have been developed and tested for users providing radiation pulses as short as 1 ps r.m.s. Both X-ray time resolved experiments and THz users are expected to benefit from such operating mode. In order to study microbunching instabilities and the potential for coherent emission at mm and sub-mm wavelengths, additional diagnostic instrumentation has been installed.

EXPERIMENTAL SETUP

Schottky Barrier Diode (SBD) detectors are common devices at microwave and mm-wave applications. In comparison to other detectors for mm and sub-mm-wavelengths like bolometers and Golay cells they have a very fast response, allowing turn by turn observation of emissions. The only alternative with similarly fast response are hot electron bolometers, which are more expensive, delicate and space consuming due to the required dewar. While at microwave frequencies SBD detectors are typically packaged with coaxial connectors, for mm-wave frequencies they are waveguide mounted, which limits their bandwidth. Coupling to free space fields is then achieved using a horn antenna, for instance of pyramidal design.

Table 1: Specifications of the two Schottky Barrier Diode Detectors (terminated into 50 Ω) and Connected Standard Gain Horn Antennas [2, 3]

Detector Model	DXP-22-RPFW0	DXP-12-RPFW0
Frequency range	33-50 GHz	60-90 GHz
Video sensitivity	40 mV/mW	23 mV/mW
Video bandwidth	1 GHz	1 GHz
Horn Model	SGH-22-RP000	SGH-12-RP000
Gain [dB]	24	24
Input aperture	55 mm· 42 mm	30 mm· 23 mm

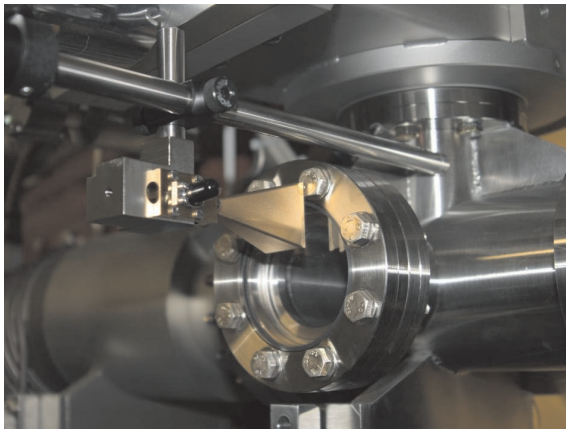


Figure 1: Photo of the 60-90 GHz detector with horn antenna mounted next to the visible light extraction.

For the evaluation of SBD detectors to detect mm-wave synchrotron radiation emissions, we have mounted two types of detector with the according horn antenna near the window of the visible light extraction used for optical diagnostics (streak camera and fill pattern measurement from photon counting). The two detectors from Millitech differ in their frequency range, sensitivity and dimensions, and were mounted one at a time, as the current setup does not provide the space to mount both at the same time without interfering with the visible light transport. The frequencies of the two detectors have been chosen close to the vacuum vessel cutoff, estimated to be 54 GHz from the relation $f_c = 2h\sqrt{h/\rho}$ with our total vertical aperture $h = 38$ mm and the bending radius $\rho = 7.13$ m.

Figure 1 show the setup where the detector can be seen mounted off centre near the window, so that visible light which comes from a mirror inside the vessel [5] can still pass beneath the horn antenna. The detector is oriented to

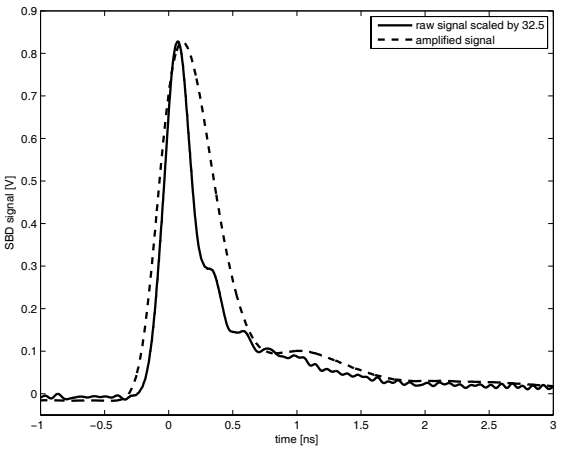


Figure 2: Pulse shape from 30-50 GHz detector without and with amplifier. Both traces are averages of 512 acquisitions triggered only on strong pulses.

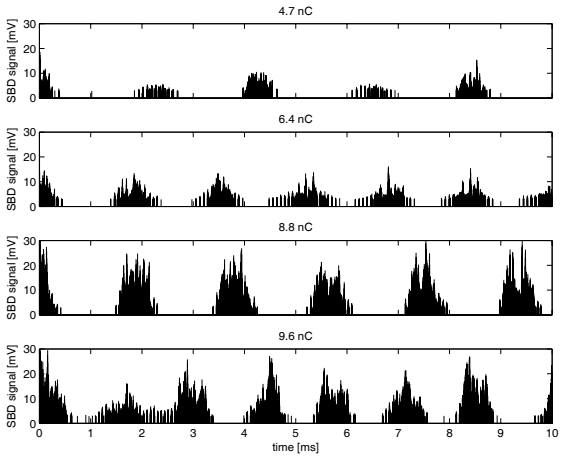


Figure 3: SBD signal (60-90 GHz, unamplified) for increasing single bunch charge with normal optics.

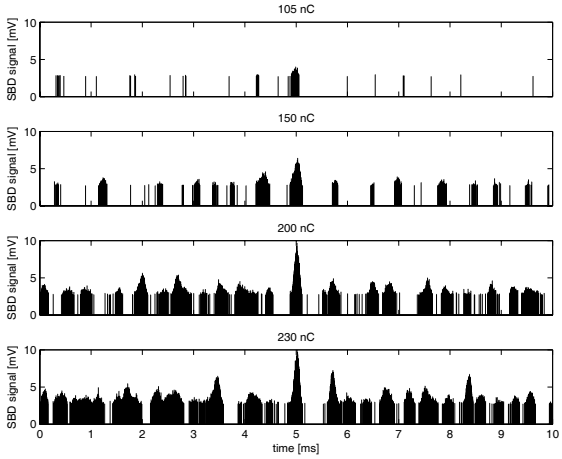


Figure 4: SBD signal (60-90 GHz, unamplified) for increasing single bunch charge with low-alpha optics.

receive the horizontal polarisation. The detector signal was then transported through a 25 m long RG-213 cable to an Agilent DSO-91304A oscilloscope outside the storage ring tunnel. During later experiments and to increase sensitivity, a FEMTO HSA-X-1-40 amplifier with 40 dB gain in a 10 kHz to 1.1GHz bandwidth was added, at first near the oscilloscope and subsequently near the detector, with the latter greatly reducing noise pickup. A typical pulse shape from the detector receiving strong mm-wave pulses from a 5.6 nC single bunch is shown in Figure 2 illustrating also the influence of the amplifier on pulse shape and amplitude.

It was found that both the 30-50 GHz and the 60-90 GHz detectors produced comparable signals under similar conditions. It is not clear whether this means that there are actually emissions below the estimated 54 GHz vacuum pipe cutoff frequency, or whether the 30-50 GHz detector is sensitive to radiation at frequencies above its upper specification limit. Further experiments with a filter fitted on the lower frequency detector and both detectors in place at the same time will be carried out in the future.

OBSERVATION OF MM-WAVE BURSTS

Without the pulse amplifier, mm-wave emissions could only be detected from bunches above a certain charge threshold. For normal user optics with a momentum compaction factor $\alpha = 1.7 \cdot 10^{-4}$ and theoretical zero current bunch length of 11 ps r.m.s the charge threshold was at around 3.7 nC, while for low-alpha optics with a momentum compaction factor $\alpha = -1 \cdot 10^{-6}$ and theoretical zero current bunch length of 1 ps r.m.s the charge threshold was at around 100 pC.

Beyond these thresholds, the burst intensity increases and the structure and frequency of the bursts changes irregularly as can be seen in Figures 3 and 4. The emissions were bursts with a complex and partially irregular structure typically 1 ms long (with further structure at 80 μs intervals) with 2 ms spacing. We presume these bursts to originate from microbunching instabilities introducing coherently emitting structure into parts of the electron distribution inside a bunch.

On a longer time scale, 10-300 ms long periods of stronger peak intensity have been observed, still showing essentially the same structure of bursts. This can be seen in from the spectrogram in Figure 5 which shows the persistent spectral features at 500 Hz and 12 kHz corresponding to the time structure as described above.

OBSERVATION OF CONTINUOUS MM-WAVE EMISSIONS

With the amplifier fitted, it was also possible to observe the mm-wave signal emitted on every turn from each bunch, for instance in the normal user fill with 700 of 936 bunches filled to 670 pC on average, as shown in Figure 6. However, it can be seen from the inset that the

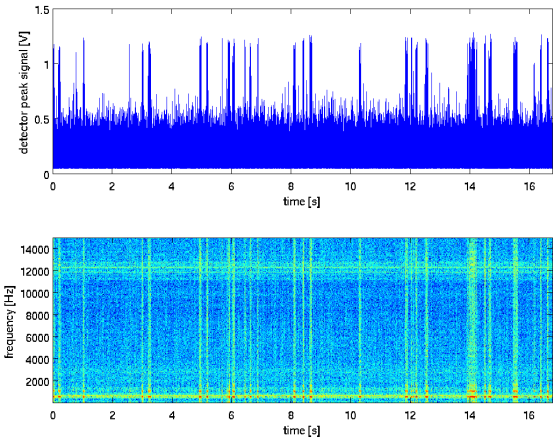


Figure 5: SBD signal (30-50 GHz, amplified) shows rare strong bursts with continuous weaker bursts between. Colour coded spectrogram is generated from block FFT of 2048 points at 500 kS/s.

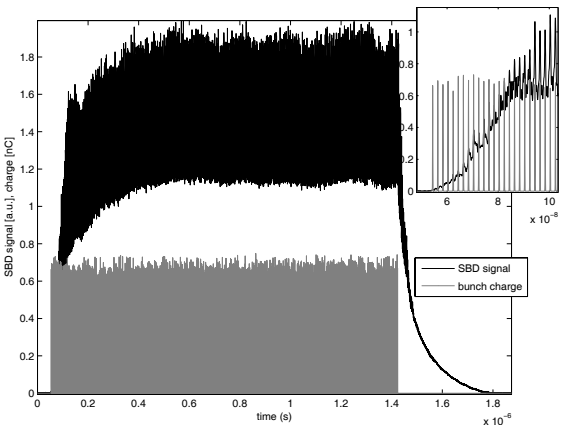


Figure 6: SBD signal (30-50 GHz, amplified) from normal 3/4 fill in user optics.

sensitivity of the detector appears to increase for the first few bunches. This is thought to be a result of self-biassing of the detector connected to the high pass input filter of the amplifier: As a voltage across the coupling capacitor builds up with subsequent bunches, the working point of the detector shifts. This will require further investigation as it clearly limits the ability to detect emissions from single bunches.

Still, with the increased sensitivity due to the added amplifier, it was possible to observe stable continuous emissions (see Figure 7) from a single bunch in low-alpha optics with a momentum compaction factor $\alpha = -3 \cdot 10^{-6}$ and theoretical zero current bunch length of 1.3 ps r.m.s. The intensity of these emissions increases faster than the charge in the bunch, ie the normalised intensity per charge increases. This could suggest partially coherent emissions, but will need further investigation.

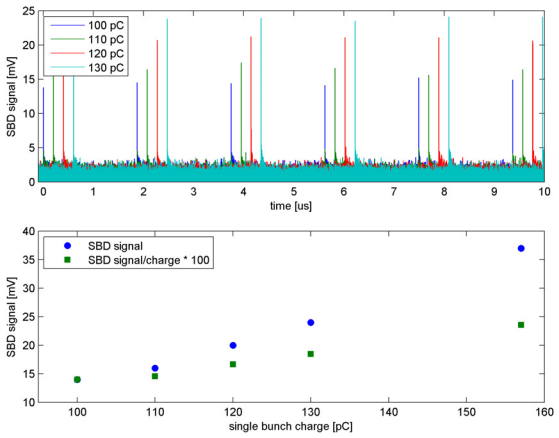


Figure 7: SBD signal (30-50 GHz, amplified) from every turn of an increasing single bunch in low-alpha optics.

CONCLUSION AND OUTLOOK

We have presented first measurements with an ultra fast mm-wave detector based on a compact Schottky Barrier Diode detector. The fast response and high sensitivity in combination with a pulse amplifier have allowed investigation of continuous and bursting mm-wave emissions over timescales of individual single bunch signals with sub-ns resolution to many seconds, documenting the complex structure of bursting emissions. Initial variations of parameters such as bunch charge or momentum compaction factor have shown the usefulness of the detector and helped optimising the setup, but clearly more rigourous investigations will have to follow.

Furthermore, we intend to move the detector into a location where more than one can be used at the same time and improve the extraction of mm-waves. To this end, we intend to build a special mm-wave extraction by modifying one of the beam port absorbers on an unused bending magnet port. This will also provide enough space to allow the installation of a Michelson or Martin-Puplett interferometer to characterise the spectral content of the mm-wave emissions further. In addition, with the IR beamline B22 becoming operational later in 2009 we should have one more valuable source of measurements.

REFERENCES

[1] I. Martin, R. Bartolini, J. Rowland, B. Singh, C. Thomas, "A Low Momentum Compaction Lattice for the Diamond Storage Ring", in *Proceedings of PAC 2009*

[2] "Millitech Series DXP General Purpose Detectors", *www.millitech.com/pdfs/specsheets/IS000026-DXP.pdf*

[3] "Millitech Series SGH Standard Gain Pyramidal Horns", *www.millitech.com/pdfs/specsheets/IS000025-SGH.pdf*

[4] "FEMTO 1.1GHz High Speed Amplifier", *www.femto.de/datasheet/HSA-X-1-40.pdf*

[5] N.P. Hammond, K. Kay, G. Rehm, "Developments in the Diamond Storage Ring", in *Proceedings of MEDSI 2008*

FIRST LIGHT FOR OPTICAL TRANSITION RADIATION MONITOR AT THE J-PARC*

A. Toyoda, K. Agari, E. Hirose, M. Ieiri, Y. Katoh, A. Kiyomichi, M. Minakawa, T. Mitsuhashi, R. Muto, M. Naruki, Y. Sato, S. Sawada, Y. Shirakabe, Y. Suzuki, H. Takahashi, M. Takasaki, K.H. Tanaka, H. Watanabe, Y. Yamanoi, High Energy Accelerator Research Organization (KEK), 1-1 Oho, Tsukuba, Ibaraki, Japan
H. Noumi, Research Center for Nuclear Physics (RCNP), 10-1 Mihogaoka, Ibaraki, Osaka, Japan

Abstract

We have continuously developed the Optical Transition Radiation (OTR) monitor with optics system based on the Newtonian telescope to measure a profile for a high intensity proton beamline. Now we installed the OTR monitors of production version on the J-PARC hadron beamline, and successfully observed a first OTR light. This led to the establishment of high S/N profile measurement with minimum beam disturbance. At this commissioning stage, beam intensity is expected to be as small as 1.2 KW, but expected to increase up to 750 kW, so that maintenance work becomes important. To improve ease of maintenance, we plan to replace the focusing lens system with reflective mirror system with higher resistance to radiation. A result of beam profile measurement, an estimation of dependence of an OTR background on a beam loss, and a future plan for an upgrade of our optics system will be presented.

INTRODUCTION

We have finished constructing first stage J-PARC hadron facility to provide high intensity proton beam whose design intensity is 750 kW for various particle and nuclear physics experiments such as strangeness nuclear physics, exotic hadron physics, kaon rare decay physics, and so on. A 50 GeV proton beam is slowly extracted via switchyard (SY) section into T1 target (Ni disk; 30 % beam loss). It is crucial to minimize a beam loss to observe the beam status by various monitors for such high intensity beamline. For this purpose, the OTR monitor is one of the best solutions because the OTR is a surface phenomenon so that we can minimize a screen thickness. Thus the OTR is widely used at electron and proton facility for the profile measurement [1-3]. We have developed the OTR monitor for a profile measurement at the upstream part of the SY section.

OPTICS DESIGN AND INSTALLATION

We performed a test experiment at KEK 12-GeV PS with proto-type OTR monitor, and realized that it is important to reduce background and radiation to detector system [4]. Therefore, we prepared an OTR optics system like Catadioptric-type telescope and planned to put this system 5 m away from a beamline. Detailed design and optimization are described in Ref. [4].

After the fine tuning of each component of optics system, we installed the OTR chamber and optics system, and finely aligned them with a beamline. As shown in Fig. 1, OTR1 is installed just upstream of a q01 quadrupole magnet, OTR2 is just upstream of a q02 quadrupole magnet, and OTR3 is just upstream of a v04 vertical steering magnet.

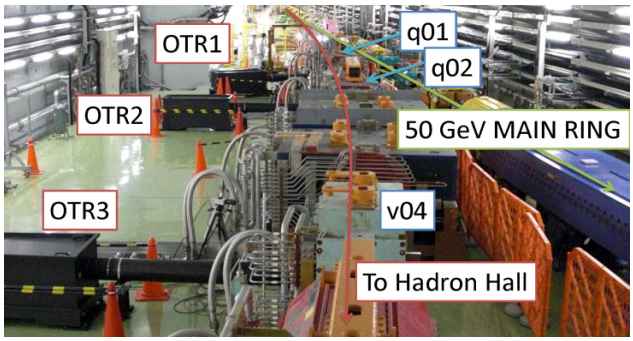


Figure 1: Layout of OTR monitors.

Figure 2 shows the OTR optics layout. There is an OTR screen (Al foil, 7 μm thickness) with rotating drive mechanism which enables to remove and install the screen remotely inside the OTR chamber. An OTR light emitted downward at the screen is first reflected by a planer mirror, and introduced into the dark box containing the OTR optics.

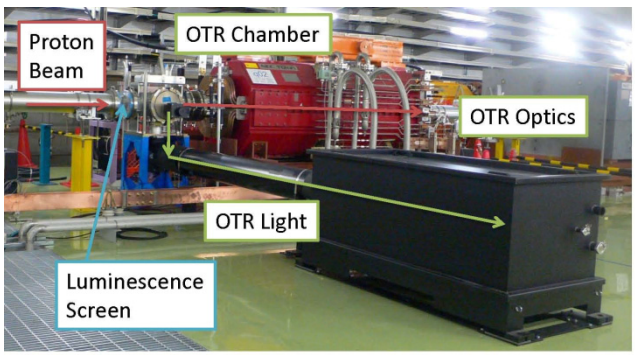


Figure 2: OTR optics installation upstream of q02.

*Work supported by Grant-in-Aid for Young Scientists (B) (20740155), and Grant-in-Aid for Scientific Research (A) (17204019)

For OTR2 and OTR3, a Luminescence screen composed of alumina ceramic is installed just upstream of OTR for a comparison of a beam profile. An Image Intensifier (IIT) is prepared to measure a weak OTR signal.

For OTR1, instead of an OTR screen, a Luminescence screen is installed to check the OTR optics. A light output of a Luminescence screen is expected too high to use IIT, so that we remove IIT for this layout.

FIRST OTR LIGHT AT THE J-PARC

The commissioning was started on January 27th, 2009. A proton beam is successfully transported to a beam dump at 19:35 on the same day. Slow extraction beam tuning was performed until the end of this past February. Final beam performance was as low as 120 W (1.5 x 10^{11} protons/spill) due to accelerator troubles. Spill cycle was 1/6 Hz, and beam duration was about 100 ms.

Despite this low intensity, we successfully measured the OTR light as shown in Fig. 3. Each shot is accumulated image for 40 ms. Consecutive three profile images reflecting the beam duration are measured. There is no long persistent component coming from such as the infrared ray, so that this signal should mainly come from the OTR.

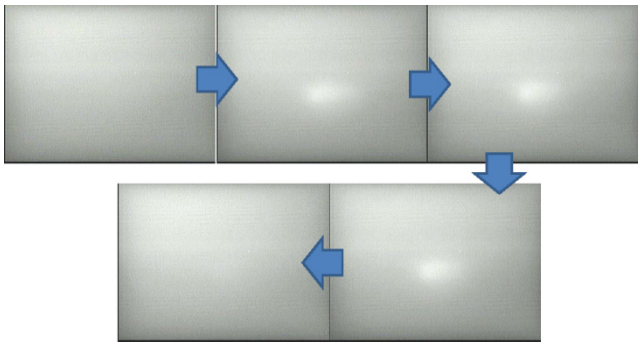


Figure 3: Typical sequential shots of the measured OTR light at v04.

ANALYSIS RESULT

Captured images are averaged, and its background is subtracted for both OTR data and Luminescence data. Figure 4 shows the resulting images for OTR data and Luminescence data, respectively.

We projected these image data into X and Y axis. We evaluated beam position and width by fitting resulting histograms with Gaussian signal + first order polynomial background function.

Figure 5 shows analysis result for beam position measured by the OTR and the Luminescence screen. Decay turtle [5] calculation result is also plotted for comparison. OTR data is in good agreement with Luminescence screen data within statistical and systematic error of about 1 mm. Measured position is deviated from turtle data due to lack of time for beam tuning.

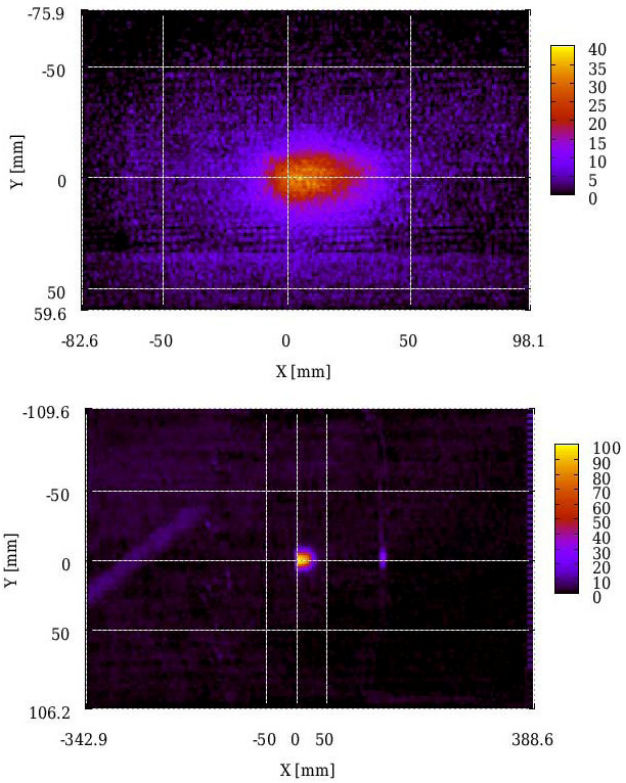


Figure 4: A typical OTR image (top) and a Luminescence screen image (bottom) at v04. Each screen size is 100 mm x 100 mm.

Figure 6 shows analysis result for beam width in the same way as the position result. Luminescence screen data coincide with decay turtle data except for q01-Y. We need to pay attention to data of OTR1 which is composed of Luminescence screen and OTR optics system. OTR1 data is in good agreement with turtle data so that it is expected that Luminescence screen at q01in probably has some problem. OTR overestimated beam width by 8 mm for q02, 14 mm for v04, respectively.

DISCUSSION AND FUTURE PLAN

Possible reasons of the OTR width overestimation is as follows.

- detector non-linearity
- OTR emission non-linearity

The other possibilities such as infrared ray effect, OTR at vacuum foil, OTR opening angle effect, diffuse reflection effect are estimated by computer simulation, and concluded that these effects are too small to cause such large width broadening . In the former case, we already checked a linearity of new optics system with J-PARC beam, so that IIT non-linearity is most suspected.

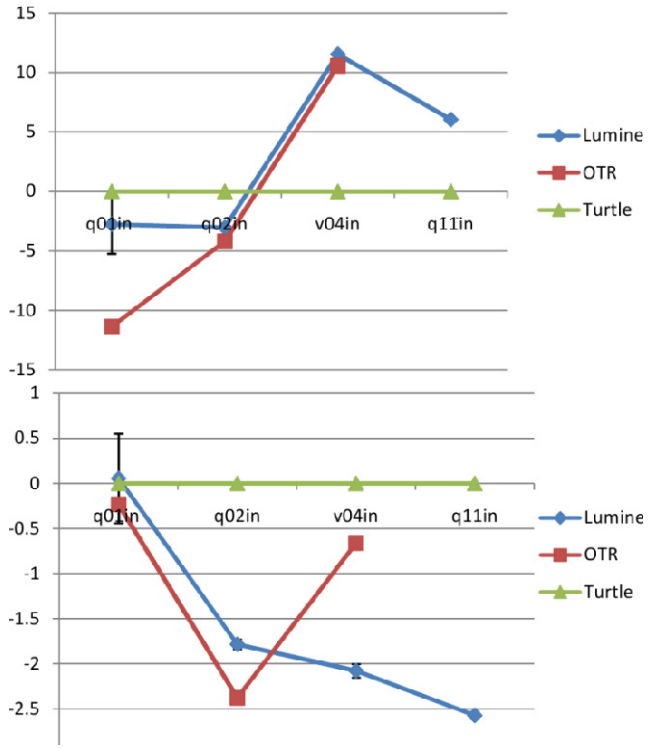


Figure 5: Position for X axis (top) and that for Y axis (bottom). Red line is for OTR, blue line is for Luminescence (Lumine), and green line is for turtle calculation.

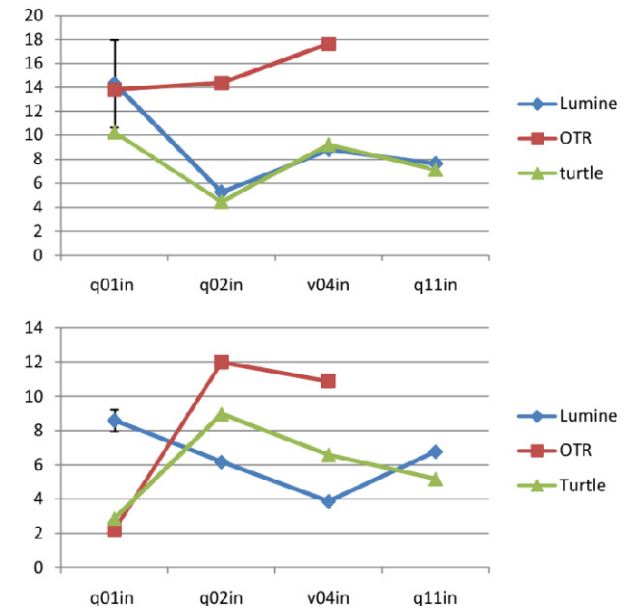


Figure 6: Width for X axis (top) and that for Y axis (bottom). Red line is for OTR, blue line is for Luminescence (Lumine), and green line is for turtle calculation.

This is probably caused by faster beam extraction of about 100 ms and spiky beam time structure due to the accelerator trouble. IIT has gain control system to protect MCP from strong light input, but this system is not enough quick for such rapid change of intensity. This can cause the instability of IIT gain leading to the non-linearity. We plan to check IIT linearity by standard light source. After the confirmation of detector non-linearity, we can check the OTR non-linearity in the next J-PARC beam time from this October.

We also have a plan to upgrade this OTR optics system. Our current optics uses coupling lenses to compensate insufficient magnification of main reflector. These lenses do not have good resistance to radiation, so that maintenance work will become a problem in the near future. To solve this problem, we now develop new OTR optics system without any lenses as shown in Fig. 7. Two reflectors are combined like Gregorian telescope, but sub reflector is placed nearer to main reflector to improve magnification. Design work including aberration minimization, magnification adjustment, and so on is completed with computer simulation, and new OTR optics system will be made and installed into J-PARC extraction beamline this Summer.

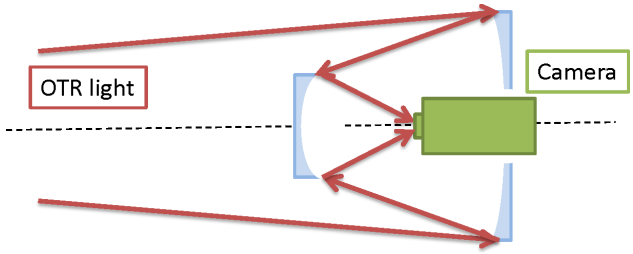


Figure 7: Conceptual design of new OTR optics.

SUMMARY

We successfully observed the first OTR light with our OTR detector at the J-PARC. Beam position for the OTR coincides well with that for Luminescence screen, but the OTR is confirmed to overestimate a signal width. We plan to recheck the detector response and perform a test experiment in the next beam time. New OTR optics system will also be tested in the beam time.

REFERENCES

[1] L. Wartski et al., Appl. Phys. 46 (1975) 3644.
[2] J. Bosser et al., Nucl. Inst. Meth., A238 (1985) 45.
[3] V.E. Scarpine et al., IEEE Trans. Nucl. Sci., 51 (2004) 1529.
[4] A. Toyoda et al., "Optical transition radiation monitor for high intensity proton beam at the J-PARC", Proceedings of DIPAC2007, (2008) 30.
[5] K.L. Brown, Ch. Iselin, D.C. Carey, Decay Turtle, CERN 74-2 (1974).

BEAM TRANSVERSE PROFILE MONITOR BASED ON RESIDUAL GAS IONIZATION FOR IFMIF-EVEDA ACCELERATOR

J. Marroncle, P. Abbon, F. Jeanneau, J.-P. Mols, J. Pancin, CEA Saclay, DSM/IRFU, France

Abstract

Within the framework of IFMIF-EVEDA project, a high-intensity deuteron (125 mA - 9 MeV) prototype accelerator will be built and tested at Rokkasho (Japan) in order to validate the future IFMIF accelerator. One of the most challenging diagnostics is the Beam Transverse Profile Monitor (BTPM), which has to be a non-interceptive device. Two R&D programs have been initiated: one based on residual gas fluorescence developed by CIEMAT Madrid (see J. Carmona et al. contribution) and another one based on residual gas ionization developed at CEA Saclay [1]. The principle of the last one is to measure the current induced by ionization electrons, drifting under an electric field influence, towards several strips to get a one-dimension projection of the transverse beam profile. Preliminary results of a first prototype tested on the IPHI Saclay accelerator will be shown, as well as a new prototype design. In the new design several improvements have been carried out. The new detector will be tested soon with continuous and pulsed beam at higher energy.

INTRODUCTION

The International Fusion Materials Irradiation facility (IFMIF) aims at producing an intense flux of 14 MeV neutrons, in order to characterize materials envisaged for future fusion reactors. The primary mission of IFMIF is to provide a materials irradiation database for the design, construction, licensing and safe operation of the future Fusion Demonstration Reactor (DEMO) [2]. In such a reactor, high neutron fluxes may generate up to 30 dpa/fpy (displacements per atom / full power year). IFMIF facility is based on two high power continuous drivers (175 MHz) delivering 125 mA deuteron beams at 40 MeV each, colliding with a liquid lithium target.

In the framework of the "Broader Approach", the IFMIF-EVEDA (Engineering Validation and Engineering Design Activities) project includes the construction of an accelerator prototype with the same characteristics as IFMIF, except a lower energy of 9 MeV instead of 40 MeV for the incident deuteron energy. Most of the components of the accelerator are developed by France, Italy and Spain. Accelerator parameters are

- 125 mA cw deuteron beam at 175 MHz (5.7 ns)
- Vacuum pipe pressure level: 10^{-5} mbar (at target region) and below 10^{-7} mbar elsewhere.

In such high current accelerator, non-interceptive diagnostics are required. This paper will focus on a Beam Transverse Profile Monitor (BTPM) based on beam residual gas ionization.

Firstly, we will present the main beam test results which were obtained using a first prototype. A new prototype was designed with respect to conclusions coming from the previous test. This will be described in a second part.

FIRST PROTOTYPE

This monitor is based on the ionization induced by the beam particles on the residual gas of the accelerator beam pipe [3] (Fig. 1). An electric field is applied between two parallel plates, on which electrons and ions are collected. A high voltage is applied to the upper plate while the lower plate is grounded. The lower plate consists of 32 conductive strips covering a 4x3 cm^2 surface. On each side of the active area 9 thin pads are set regularly in voltage in order to insure the electric field uniformity (each resistor is 60 MΩ). This monitor is fixed on a flange (DN100), which is held on the accelerator beam pipe.

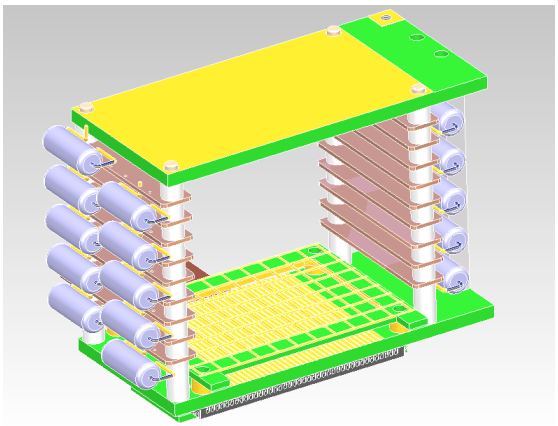


Figure 1: First prototype drawings.

Front-End Electronics

The currents induced by charges on the strips are read-out by a front-end electronic card developed in our group. The 32 channels are connected, via a kapton bus, to this card (Fig. 2).

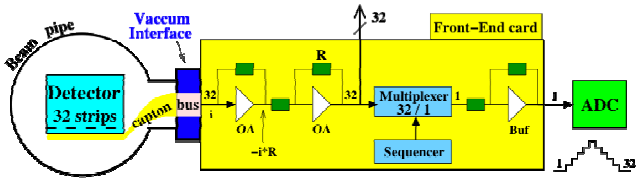


Figure 2: Front-end electronic sketch.

A transimpedance circuit converts all strip currents in voltage at 33 MHz. After the amplifiers, multiplexer and sequencer stages, a profile of the beam is given every 1060 ns.

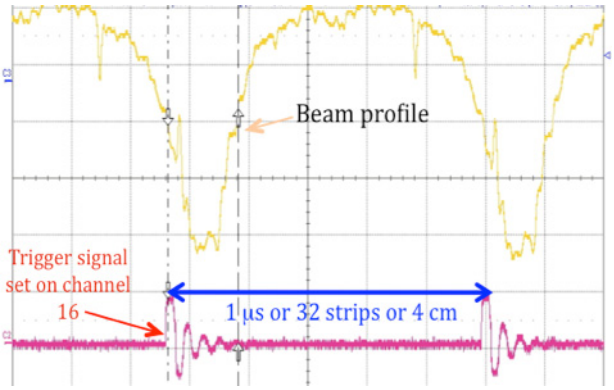


Figure 3: Beam profile seen on an oscilloscope every 1060 ns, which correspond to the 32 strips, lay out over 40 mm.

The oscilloscope picture of such a profile can be seen in Fig. 3. This card reads the strip currents with a bandwidth below 3 MHz and has a sensitivity down to 1 nA due to a high gain of 1.2 mV/nA. The equivalent input noise is around 0.8 nA.

Monitor Beam Test

This monitor was tested in July 2008 at Saclay, on the IPHI (Injector of Proton at High Intensity) source accelerator [4]. A continuous proton beam of 75 and 95 keV was delivered at beam intensity up to 12 mA for our test. Firstly we have checked that we observed an ionization signal by varying the residual gas pressure at constant beam intensity (1.2 mA). The pressure ratio is about 3.5 and this is this is good agreement with the data reported in Fig. 4 for different HV values.

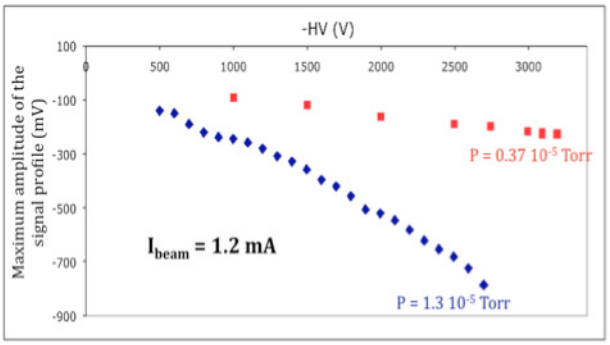


Figure 4: Maximum amplitude response for a 1.2 mA beam intensity at 2 vacuum pressures.

Extrapolating our data to IFMIF conditions at the beam dump level (I_{beam}=125 mA, E=40 MeV, P=10^{-5} mb) [5], have shown that enough signal can be picked up with such a monitor. So, no ionization amplifiers, like MCPs (Multi Channel Plates) which are radiation sensitive, are required in this hard radioactive environment (γ and neutrons). Some other lessons were withdrawn from these tests, which have been taken into account to build the second prototype.

They concern mainly:

- Electric breakdown and short cuts,
- Water-cooling system conditioned for higher beam intensity.
- Beam profile resolution,
- Good behavior of the electronic Front-end.

SECOND PROTOTYPE

The second prototype was designing taking into account these remarks. Figure 5 shows this new prototype, which is still in design progress.

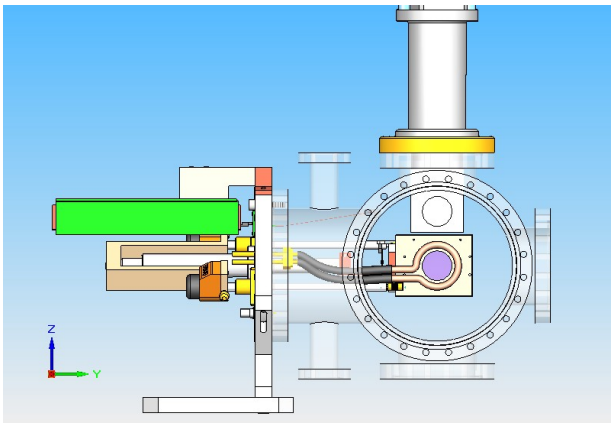


Figure 5: In horizontal, the monitor mounted on a piston, with its front-end electronic card on the left (green). In vertical, the SEM grid profiler is shown.

Improvements

The main improvements withdrawn from the first prototype test are listed below.

A cooling water system is fixed on a copper shield with an aperture to let the beam pass through it. It will allow to work at higher beam intensity.

A secondary emission grid monitor (vertical) will allow to compare profiles obtained with both monitors in same beam conditions. These monitors with a help of pistons can be moved in beam position without modifying machine conditions.

Numerous electric breakdowns appeared during the test. Ceramic will be used to avoid them. For example, two kinds of strip plane are designed: one with strips deposited on a ceramic plane, and the other one with conductive wires, welded on contacts deposited on ceramic. Plastic insulators are replaced by ceramic ones.

Electronics: only currents are measured up to now. Current integration is necessary to manage low currents encountered at high energy for which ionization cross sections decrease drastically, and to work at low beam pipe pressure.

Tests

Two campaigns of tests are foreseen with this prototype:

- On IPHI source, at the beginning of July 2009. Tests will be done at high intensity and low energy, but with an un-pulsed beam.
- At higher beam energy with a pulsed beam, in order to check the behavior of the BTPM (image current at the vacuum wall…)

During these tests, we should have to pay attention on the space charge, which play an important role on the resolution of the beam profile (due to electrons and ions trajectories).

CONCLUSION

At full current and cw beam operation, no interceptive profiler can be set in the beam of IFMIF-EVEDA. A non-interceptive transverse beam profile prototype, based on residual gas ionization, has been presented. Promising beam test results were used to improve this new prototype. It will be tested in July 2009.

REFERENCES

[1] P. Abbon et al., "Beam Transverse Profile Monitor for IFMIF-EVEDA", Bad Kreuznach; adweb.desy.de/mdi/CARE/Bad_Kreuznach/ABI_workshop_2008.html, December 11-12, 2008.
[2] IFMIF Comprehensive Design Report, January 2004.
[3] P. Abbon et al., "Beam Transverse Profile Monitor for IFMIF-EVEDA accelerator", BIW 2008, Lake Tahoe, May 2008.
[4] P.-Y. Beauvais et al., "Installation of the French high-intensity proton injector at Saclay", Linac 2006, Knoxville, p. 153.
[5] E. Surrey et al., Report for TASK EVEDA technology programme, 2007.

TARGET MATERIALS FOR A LOW ENERGY PEPPER-POT EMITTANCE DEVICE

M. Ripert, A. Peters, HIT, Heidelberg, Germany

Abstract

The ion cancer therapy facility HIT in Heidelberg [1] is producing ions (H, He, C and O) from two ECR sources at an energy of 8 keV/u with different beam currents from about 80 µA up to 2 mA. Typical sizes for the beam in the LEBT range from are 5 – 30 mm. Matching the always slightly changing output from the ECR sources to the first accelerating structure, an RFQ, demands a periodical monitoring of the beam emittance. For that, a special pepper-pot measurement device is under design, whose most important parts are a damage-resistant pepper-pot mask and a vacuum-suitable scintillator material. The material lifetime, the list of feasible materials, the modelling of the target damage will be discussed.

PEPPER-POT SCINTILLATOR SCREEN DESIGN

As part of the ongoing development at HIT, and to provide necessary information for beam dynamics, high quality emittance and beam profile measurements are needed. A pepper-pot device is under investigation to provide a 4-D emittance measurement.

Location

The Pepper-Pot Scintillator Screen system should fit within the existing beam line components (vacuum boxes already used with beam diagnostics equipment like Faraday cups, profile grids and slits). The N1DK1 vacuum boxes will be equipped with a fast iris shutter, a pepper-pot mask and a scintillator screen. The N1DK2 vacuum boxes will contain a 45 degrees tilted mirror inside and a CCD camera outside. (Figure 1)

The Pepper-Pot Principle

The pepper-pot mask, which is perpendicular to the beam and contains a regular array of identical holes, splits the beam into beamlets. The beamlets drift toward the scintillator screen where they are imaged. The determination and the arrangements of the optical component must be designed in such a way that it meets its basic function requirements:

- The production of an image of a suitable size,
- The system should fit into the available space.

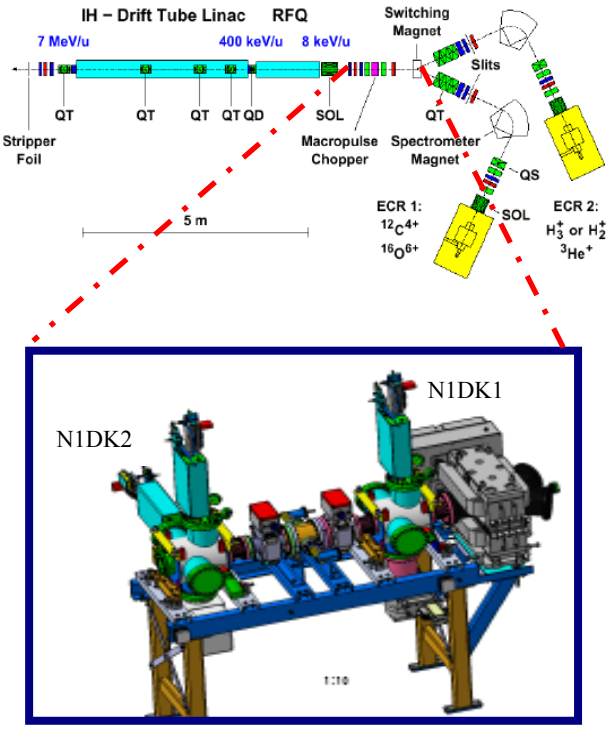


Figure 1: The Low Energy Beam Transport at HIT and the position of the Pepper-Pot Scintillator Screen device within the LEBT.

Some considerations [2] in the choice of the aperture parameters have to be followed so that:

- The beamlets images on the scintillator screen are larger than the mask aperture d,
- The pepper-pot mask thickness, Ls, should be small enough to prevent any smearing effects due to multiple slit scattering
- The separation spacing, w, should be much larger than the mask aperture d to prevent the beamlets from overlapping at the screen.

Different optical systems have been designed along the previous set of rules [2] depending on the minimum beamlet width. From the arguments given above, a set of the pepper-pot parameters (Table1) with a 0.2 mm hole diameter, 1.5 mm separation, and 0.1 mm maximum depth was calculated.

Due to a beam size of 10–20mm on the mask and at 8 keV / u energy, the drift length from the mask to the measurement screen is approximately between 65 and 150 mm.

Table 1: Pepper-pot parameters

Parameters	value
RMS beam size σ	10-20 mm
Pepper-pot Hole Diameter d	0.2 mm
Pepper-pot Hole Spacing w	1.5 - 2 mm
Pepper-pot mask thickness Ls	< 0.1 mm
Drift Length Ld	65-150 mm
Minimum Beamlet width	0.2 -0.24 mm
Resolution Pepper Pot	3.2 - 1.6 mrad

Scintillator Screen

The pepper pot mask and the measurement screen will be aligned perpendicularly to the beam because of their small separation distance. The beam images will be thus produced by a transparent scintillator such as crystals (ruby, YAG : Ce / Pr) or glass materials (quartz …) and will be captured by a suitable CCD camera.

BEAM TARGET INTERACTION

When an ion impinges on a solid, it loses kinetic energy through interactions with atoms. This transfer of energy from the ion to the target atoms results in ion reflection and backscattering, atomic sputtering and deposition, solid damage and heating. The impinging ions come finally to rest in the solid through a set of nearby adjacent inelastic and elastic collisions of atoms, called a collision cascade.

However, ions implanted into a solid can modify the physical properties of the solid due to both chemical and structural change in the target. Heating of the target by an ion beam leads to a fast thermodynamic response of the target. Consequently, during and after the irradiation, the distribution of the target density is changing. The energy loss dynamic of the ion beam within the material should be also investigated.

At the target, the beam maybe focused to a small spot where the deposition process dominates and also the thermal forces. For that, an estimation of the deposited beam energy is compared to the energy needed to melt the physical volume of the target [3]. Since the penetration depth is much smaller than the physical dimension of the target, a better estimation will be to calculate the energy required to melt the range volume. Obviously this estimation can only be coherent if no heat transfer around the range volume takes place during the beam pulse. This is not the case. In order to fully understand the thermal aspects of intense pulsed beam on materials, the time dependence heat transfer has to be taken into account. The timescale for heat to spread through the thickness of the material should be simulated. Similarly, the space evolution of the heated material should be replicated.

DAMAGE OF THE TARGET

The damage of the target consists of three principles. One consists in the change of the molecular structure which is unrecoverable. The molecular bond breaking is followed by atom displacement, creation of vacancies, and also sputtering, surface roughness, surface segregation. The other one is the preservation of the molecule integrity. The hit atom doesn't have enough energy to leave the site and then it will vibrate releasing this given energy as phonons. The phonons energy is deposited into the material lattice which can increase the present damage. Finally, the mixing of these two phenomena takes over and provides distortions to the target: mixing of layers and also atomic mixing [4]. A direct consequence of these damages could be a diminution in the light output, and in the durability of the material.

Consequently, changes in the properties are related to the structure damage of the target. Clearly, a simulation of the energy loss through the material would provide important information about the change in the properties of matter within the target.

Atomic mixing (figure 2), also called the slowing down process of intense ion beams into matter is the most important process. It consists of three main effects:

- Cascade Mixing (1),
- Recoil Implantation (2),
- And Diffusion (3).

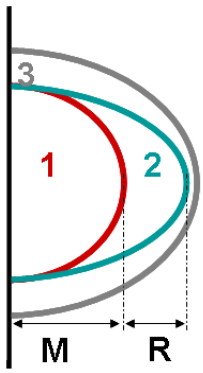


Figure 2: Atomic mixing [3].

The cascade mixing zone (1), the recoil implantation zone (2) and the diffusion factor (3) have to be distinguished and correlated to the structure damage of

the target and to the physical output parameters (heat, light output, durability).
A model should be used to quantify the influence of these mixing effects.

SIMULATIONS

TRIM [5], the Transport of Ions in Matter code, is based on the Binary collision approximation. It means that each incident ion finds the same unmodified substance. Any effects as ion deposition or surface erosion are neglected. TRIM doesn't treat any recoil phonon coupling in a solid.

Under irradiation with different ions, the ratio of electronic to nuclear stopping powers varies for both the primary ion and the secondary recoils produced.

Helium impinging into SiO_2 with a density equal 2.32 g/cm3 is represented in figure 3-a. Each time an ion has a collision with a target atom, there is one vacancy created (red dots). The target atom then recoils and all its collision that causes vacancies are plotted with green (for silicon atoms) and blue dots (for oxygen atoms). When the recoil atom stops it is plotted with green or blue dark dots. A single ion may produce half hundred vacancies (red), whereas a single recoil atom gets few vacancy plotted (green and blue). Consequently, the ion energy has been transferred to the target through principally inelastic scattering (i.e. electronic energy loss). The recoil cascade is slightly visible.

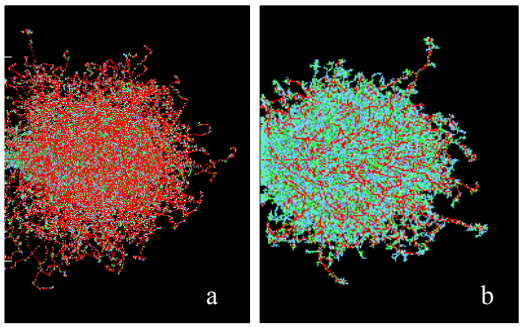


Figure 3: TRIM simulation of Helium (a) and Carbon (b) ion impinging into SiO_2 at 8 keV/u with the total number of ions equal to 1000. The longitudinal range and straggle (in parentheses) of Helium and Carbon are 866 Å (133 Å) and 282 Å (133 Å).

As you can see on the preceding picture (figure 3-b) the Carbon ion track shows red dots, representing vacancies for which the target atoms (Si and O) are knocked away from their lattice. However, Carbon ion beam–target interaction shows mostly some blue (Oxygen atoms) and green dots (Silicon atoms). There is enough energy for the target atom to recoil and cause other vacancies until it does not have enough energy, so that the target atom will vibrate back to its original position site releasing its energy as phonons. By vibrating back to their original position, the recoil atoms (blue/green) track follows the same initially created (red dots) and thus, they superpose. This picture can be misleading by assuming that the nuclear energy dissipation (15%) dominates the electronic energy dissipation (27%).

Since atomic mixing and recoil implantation distort the depth profile simultaneously, a model for which all interactions experienced by an atom should be used. Monte Carlo Codes coupled with thermal processes or Molecular Dynamic approximation [6] take into considerations the distortions caused by mixing effects such as the slowing down process within a material. Even if TRIM is a B.C approximation, this program should be used for the input of parameters needed for the M.C or M.D code.

CONCLUSION

Of concern is the temperature at the surface giving rise to stresses that could result in erosion, atomic mixing in the collision cascade. A model is needed in this area to better understand the beam target interaction and its effects on the target, and to find solutions such as the choice of the target.

The optical layout of the ion beam through the Pepper-Pot Scintillator Screen system should be finalised using one of this code: SIMION, the ion and electron optics simulation software or PARMILIA, the Phase And Radial Motion in Ion LInear Accelerators software.

Further developments this year will include a beam test of possible transparent materials. Short and long time effects should be studied.

REFERENCES

[1] T. Haberer, "Commissioning of Hadron Therapy synchrotrons: HIT and CNAO", Particle Accelerator Conference (2009).
[2] S. G. Anderson, J. B. Rosenzweig, G. P. LeSage, J. K. Crane, Space-charge effects in high brightness electron beam emittance measurements", Phys. Rev. ST Accel. Beams 5, 014201 (2002).
[3] P. Strehl, "Beam Instrument and Diagnostics", Springer Ed, 2006.
[4] G. Kupris, H. Rößler, G. Ecke, S. Hofmann, Interpretation of sputter depth profiles by mixing simulations", Fresenius J. Anal. Chem. 1995,353, 307.
[5] J. F. Ziegler, J.P. Biersack, and M. D. Ziegler, The Stopping and Ranges of Ions in Matter (pergamon, New York, 1985).
[6] K. Nordlund, Molecular dynamics simulation of ion ranges in the 1-100 keV energy range, Comput. Mater. Sci. 3, 448 (1995).

SYNCHROTRON RADIATION MONITOR AND MIRROR AT SSRF

K.R. Ye, Y.B. Leng, J. Chen, J. Yu, G.B. Zhao, W.M. Zhou, Sinap, Shanghai, 210200, China
T. Mitsuhashi, KEK, Japan

Abstract

SR monitor for the measurements of beam profile, sizes, and bunch length has been designed and constructed at the Shanghai synchrotron radiation Facility (SSRF). A water-cooled beryllium mirror is installed to extract the visible SR. This beryllium mirror was designed via thermal analysis based on ANSYS. The extracted visible SR is relayed to dark room by three mirrors. The measurement system includes, imaging system, SR interferometers (SRI), streak camera and fast-gated camera etc are set in the dark room. Both the horizontal and the vertical beam sizes are monitored by SRI, and bunch length and temporal profile of the beam are measured by streak camera. The existed system suffers with dynamic problem for beam physics studies. The commissioning of synchrotron radiation monitor system has been performed in SSRF since December, 2007. The results obtained at SSRF are presented.

GENERAL OVERVIEW

A diagnostics beamline has been installed in the BM02 bending magnet of the SSRF storage ring. The designed parameter of the SSRF is listed in Table1.

Table 1: Designed parameter of Storage Ring

parameters	Value
Energy (GeV)	3.5
Beam current (mA)	200-300
Critical photon energy (keV)	9.96
Emittance εx (nm.rad)	3.9
Beam profileσx (μm) 1% coupling	53
Beam profileσy (μm)	22
Bunch Length (ps)	14.4

Synchrotron radiation monitor measures beam profile and beam size of the synchrotron radiation light source for performance optimization, routine operation check and various beam physics study. The monitor should be able to measure a small transverse beam dimension and motion [1]. Using this monitor, we can characterize the electron beam size, phase-space ellipse and emittance. It is described that the general design of the SRM, extraction mirror design, and measurement equipments such as SR interferometer and streak camera in this paper.

Instruction

The source point of for SRM is bending magnet near injecting point. The synchrotron light is extracted by a water-cooled beryllium mirror. Then three mirrors guide the light to the dark room. The synchrotron light interferometers [2] [3] is set in the dark room and they measure horizontal and vertical beam sizes. Also a focusing system is applied to obtain the image of beam profile. The result beam profile is passed on the display in the control. Bunch length measurements is performed with a streak camera (HAMAMATSU C5680) that uses a scan streaking of 125MHz (1/4 RF) and also dual time streaking is available. (Fig.1). The general arrangement of the SRM system is shown in Fig.1.

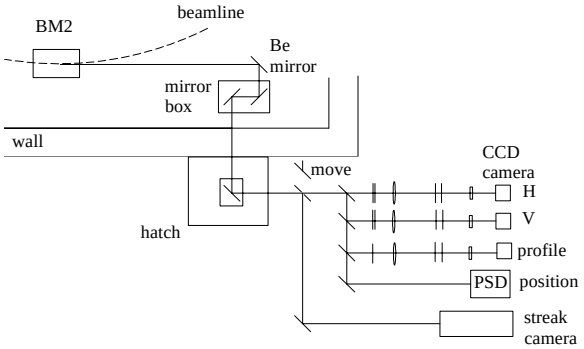


Figure 1: General arrangement of synchrotron radiation monitor.

EXTRACTION MIRROR

The vertical opening angle of visible SR is roughly 3mrad. 4mrad opening will be available in the horizontal direction. The visible part of the synchrotron radiation is reflected by water-cooled Beryllium mirror.

Water-cooled Beryllium Mirror

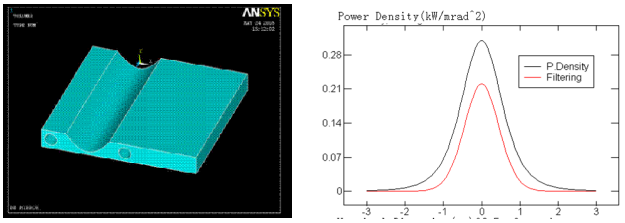
The first mirror is set 9m apart from the source point, which reflects the visible light by 90° downward. Thermal distortion of the Be mirror for a given absorbed heat load by X-rays is simulated using the technique of finite-element analysis. The deformation of the mirror has been studied in detail in comparison with other materials. The result shows Be is best material for the extraction mirror.

Thermal Distortion Analyse

A thermal-mechanical analysis experiments with electron beams show: the quality factor for different metals dynamic formation is indicated. The thermal distortion values for metals between 0^0C to 400^0C, these

effects were especially good in Beryllium mirrors than Invar and Copper mirrors [4].

We designed the mirror shape having a parabolic shape in the backside as shown in Fig.2. Most of the X-ray will pass through the central thin part of the mirror. The incident and the transmit power densities are shown in the right side graph in Fig.2.



(a) (b)

Figure 2: (a): The design of mirror which has two water-cooling tubes. (b): Power Density distributions.

The deformation of Be mirror is simulated by ANSYS and XOP [5] for varying the shape, size, and diameter of cooling tube. We fixed outer-dimension of beryllium mirror is 80mm(wide), 60mm(high), 12mm(thickness). With the diameter of water-cooling tube will 8mm, the centric deformation of mirror surface results 3.9μm with inlet water temperature 26^0C. The highest temperature of mirror will be 56^0C.

The results of Be mirror deformation and temperature distribution for number of water cooling tube 7 and 2 are shown in Fig. 3

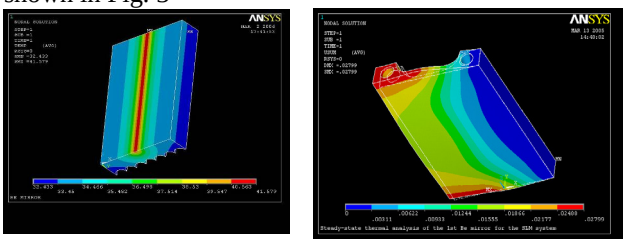


Figure 3: Analyse the deformation of two types of mirror those have seven cooling tubes (right) and two cooling tubes (left).

The convection coefficient will depend on cooling water velocity. The dependence of convection coefficient against cooling water temperature is shown in Fig 4 with various tube diameters. From this figure, the effect of the tube diameter is smaller than the velocity of cooling water. Because the diameter of the tube 6mm-7mm is easy to handle, we used the 6mm tube. Increase of Water temperature by 3-4 ºC while beam current rise from 10mA to 100mA was observed in real operation of the mirror.

Actually, the key point in the design of the mirror is to make deformation smooth and symmetry about the centre of mirror. So we chose two tubes those arranged in symmetry. In the case to use the SR interferometer, we need only two pencils of light.

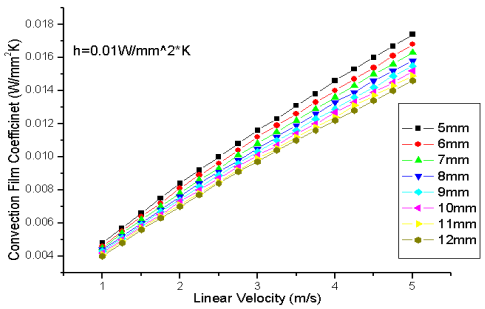


Figure 4: Convection coefficient as a function of cooling water velocity with various diameters of water cooling tubes.

It isn't important for interferometer that 1 to 2 μm deformation of the mirror. We can calibrate the interferometer with ray trace technique. So, the beryllium mirror with two cooling tube which haves a parabolic shape in backside is applied in the SSRF.

IMAGING SYSTEM AND SR INTERFEROMETER

The synchrotron radiation monitor consists of an imaging system to obtain a profile of electron beam and SR interferometers to measure the beam sizes. This imaging system is also used for observing a beam image position. A result of beam image and image position are shown in Fig. 5

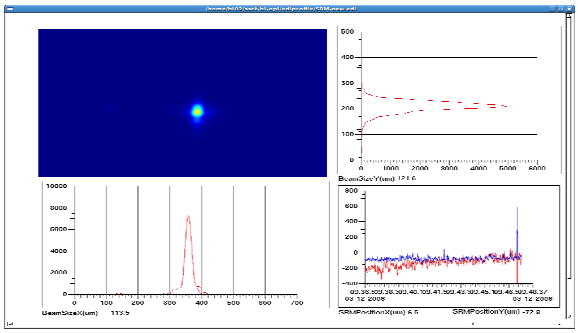


Figure 5: Result of beam profile measurement, and beam image positions.

Two Harsherian-type reflective SR interferometers are installed to measure the both of vertical and horizontal beam sizes. The double slit is set at 18 meter apart from source point. A focusing mirror, f=2000mm, is used as an objective mirror. A small off-axis diagonal mirror is set for the convenience of the observation. A band-pass filter, which has 80nm bandwidth at 550nm, is used to limit the wavelength of input light. The σ-polarization of SR is selected by dichroic polarization filter. The arrangement of SR interferometers are shown in Fig. 6 . A ray tracing method using a Hartman square mask is used to calibration of SR interferometer due to the first mirror deformation.

The measured interferogram are fitted by the intensity distribution of the form. The image analysis system works

extracting the orthogonal profile, center position, and least square fit to evaluate the beam sizes.

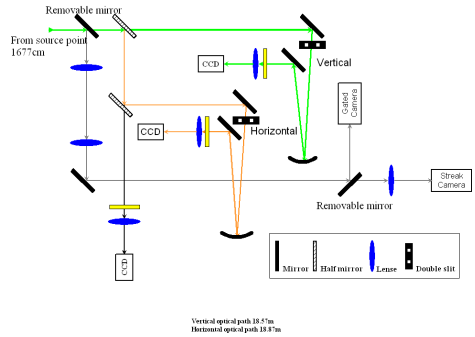


Figure 6: Arrangement of SR interferometers.

An example of observed vertical interferogram is indicated in Fig. 7.

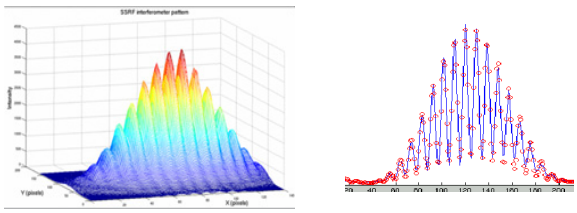


Figure 7: An example of observed vertical interferogram.

Application software is located at workstation /Unix and PC/Linux control console, supporting commercial software Matlab and LabVIEW. The high level physical application environment has been set up and done the online test of device control using MatLab and middle layer with the SSRF centre database.]

Preliminary commissioning of the SRM is performed recently. The glass window has been used to overcome the effect of air flow. The linearity between electron beam intensity and radiation image intensity in such system is good. Accompany with neutral density filter. The dynamic range can be extended to 10^3 and with excellent linearity.

Beam size of electron in storage ring has been achieved by synchrotron radiation interferometer successfully . The results of vertical beam size measurement for beam regulation are shown in Fig.8. When beam current is 200mA, using a wave length λ = 550nm, with acquired data 600 times, the results of vertical RMS beam size is 34.3±0.4um, and horizontal RMS beam size is 52.3± 0.4um.

The beam size measurement also used to adjust the transverse feedback system for SSRF storage ring. It is shown as in Fig.9, when beam current is getting higher than 40mA, the vertical beam size is getting large. If beam current change from 40mA to 100mA; the vertical beam size becomes larger from 35 um to more than 100 um. When the multi-bunch transverse feedback is work; the vertical beam size becomes smaller and stable. The observed beam size with transverse feedback is 35 μm just same as in the low current. The variation is observed for xy coupling parameters from this measurement

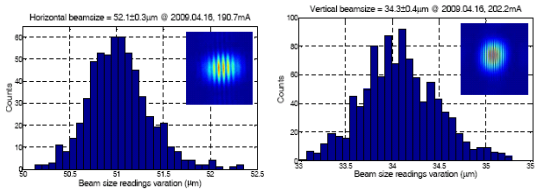


Figure 8: The results of beam size (RMS) measurement.

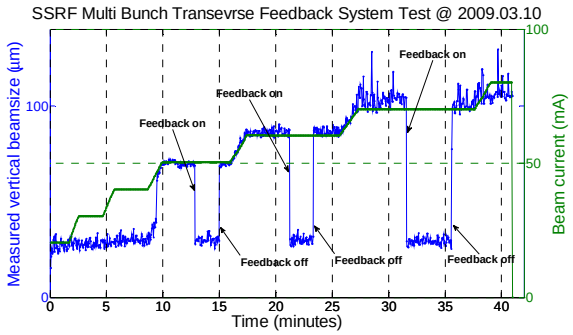


Figure 9: Beam size measurement for transverse feedback.

CONCLUSIONS

The SR monitor to measure the beam size, and bunch length etc. is constructed at the SSRF. The transverse RMS beam sizes in both horizontal and vertical direction are measured in the rage of a few mA to 200mA. The observed horizontal beam size is 52.3±0.4μm and it is good agreed with designed value. The observed vertical beam size is 34.3±0.4μm, and it is stable with transverse feedback system. From this observed vertical beam size, eminttance coupling is 1.2%.

ACKNOWLEDGEMENTS

The author express thanks for beamline mechanical group help and discuss with us. The support provided by the Technical Services Division in particular the colleagues in the mechanical, vacuum, alignment and control groups.

REFERENCES

[1] T. Mitsuhashi, “Beam Profile and Size Measurement by SR Interferometer ” in Beam measurement, Ed. by S. Kurokawa et.al., P399-427, World Scientific (1999).

[2] T. Mitsuhashi, “Measure of Small Transverse Beam Size Using Interferometer” DIPAC 2001, P26-30.

[3] Y. Yamamotoa, I. Sakaib, T. Mitsuhashic, D. Amanod, H. Iwasaki, “Interferometric measurement of the beam size in the compact storage ring,”. Nucl. Instr. and Meth. A 467–468 (2001) P921–924.

[4] A.P.Sabersky, “Momitoring the beams in Spear with synchrotron light” SLAC-PUB-1207(A) March 1973.

[5] http://www.esrf.eu/computing/scientifi

TWO-DIMENSIONAL IONIZATION BEAM PROFILE MEASUREMENT*

M. Poggi, L. Boscagli, A. Dainese, R. Ponchia, INFN Laboratori Nazionali di Legnaro, Viale dell'Universita' 2, 35020, Legnaro, Padova, Italy
H.W. Mostert, J.L. Conradie, M.A. Crombie J.G. de Villiers, K.A. Springhorn, iThemba LABS, P.O. Box 722, Somerset West 7130, South Africa

Abstract

Equipment for non-destructive, two-dimensional beam profile measurement was developed for the high intensity beam project foreseen at INFN, Legnaro and the K200 variable-energy, separated-sector cyclotron at iThemba LABS. Ions, produced by the interaction of the beam with residual gas, are accelerated in an electrostatic field towards microchannel plates (MCP) for signal amplification. With the first of the two prototypes that were built, ions are accelerated in an electric field between two parallel plates and after passing through an aperture in one of the plates, move through the electric field between two curved plates and consequently bent through ninety degrees before reaching the MCP. The aperture in the plate provides one profile dimension and the spread in the energy of the produced ions the other dimension. In the second prototype two one-dimensional systems, rotated through ninety degrees with respect to each other, were installed in close proximity of each other. The beam profiles measured with both prototypes were compared with those measured with a nearby profile grid. Measurements were made on various beams and with intensities between 10 nA and 1μA.

BACKGROUND

One-dimensional residual gas beam profile monitors (RGBPMs) are already used successfully. Space limitations and the need to measure both dimensions of the beam at the same location, initiated the investigation of two-dimensional systems. iThemba LABS designed the first prototype, RGBPM-1, and was tested at the 6 MV Van der Graaff accelerator on site. It is based on the energy spread analyses method [1].

THE DESIGN OF RGBPM-1

In order to improve on previous designs, a different geometry, shown in Fig. 1, was developed for the analyzing field. Only electrostatic fields are used. Residual gas ions are accelerated in the collecting field and pass through a 1 mm extraction slit. The curved electrodes produce the analyzing field that bends the trajectory of the ions by approximately 90 degrees. Curved electrodes are chosen to assure that the electrostatic field remains perpendicular to the ion path. The aim is to obtain a linear projection of the two dimensional profile on the MCP surface. Ions created further from the slit obtain additional acceleration, and because of their higher energy will be deflected less in the analyzing field. Those that are created in the collecting field at position *a* in Fig. 1 are deflected more than those created at position *c*. The vertical position information can therefore be recovered on the MCP. The horizontal information gathered in the collecting field is maintained in the analyzing field and is therefore also available on the MCP, as in the case of a one-dimensional system.

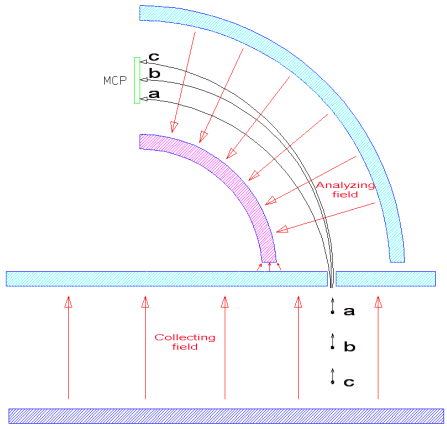


Figure 1: The electrostatic field in RGBPM-1.

Electric field calculations and particle orbit simulations were done with the program TOSCA [2], to determine the geometry as well as the potentials required on the electrodes. The calculations confirmed that beam profile information in both the horizontal and vertical directions can be obtained with this method as shown in Figures 2 and 3. For the current design, with central radius of the

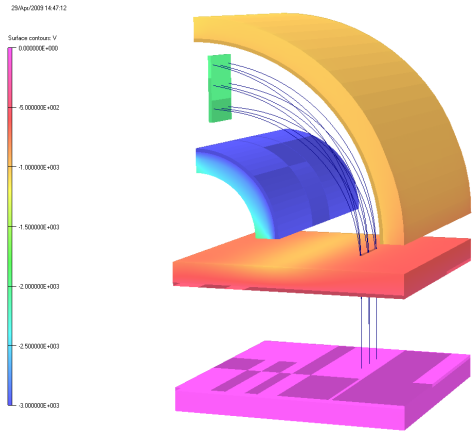


Figure 2: Calculated ion paths in the electrostatic fields of RGBPM-1.

*Supported by Istituto Nazionale di Fisica Nucleare, Italy and National Research Foundation, South Africa, project-code 15

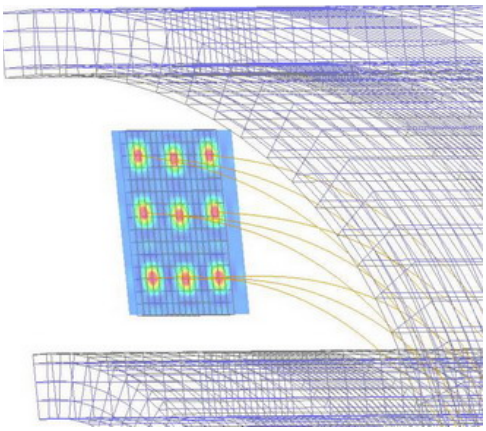


Figure 3: Projection of different beam positions onto the MCP of the RGBPM-1.

analyzing field of 40 mm, the magnification is 0.75 with respect to the measured profile in the vertical plane.

IMPLEMENTATION

A special X-Y matrix multilayer printed circuit board was designed as a position-sensitive collecting anode behind the MCP. This anode is at virtual earth potential. Current measurement electronics, using the ACF2101 integrating current to voltage converter, measures the amplified signal from the MCP. The printed circuit board has a resolution of 40 horizontal and 40 vertical channels with a pitch of 0.75 mm. A profile grid with a wire spacing of 1 mm was installed 7 cm downstream from the MCP to verify the measurements. The RGBPM-1 is installed in a beam diagnostic vacuum chamber in the beam lines and fits into the available space, without interfering with a nearby installed profile grid monitor.

Fig. 4 shows the profiles measured with the RGBPM-1 and a harp. The measured profile of the RGBPM-1 is nearly a factor 2 larger than the measured profile on the grid profile monitor, both in the vertical and the horizontal planes. TOSCA calculations indicate that this broadening effect is not due to distortion of the analyzing and collecting fields, as shown in Fig. 3, but could possibly be owing to space charge effects, or because the

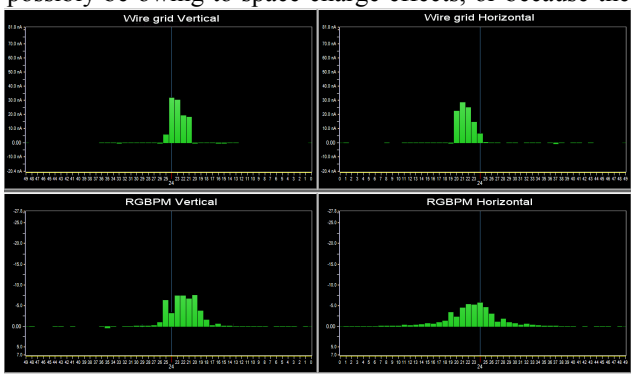


Figure 4: The horizontal and vertical RGBPM-1 profiles, bottom, compared with the profiles measured with a wire grid on top.

ions produced in the rest gas are not completely at rest. This has to be investigated

THE DESIGN OF RGBPM-2

The second design, developed at INFN at Legnaro, Italy, is based on the combination of two one-dimensional systems, rotated through ninety degrees with respect to each other, installed in close proximity as shown in Fig. 5. It was tested on the 15MV tandem at INFN, Legnaro as a

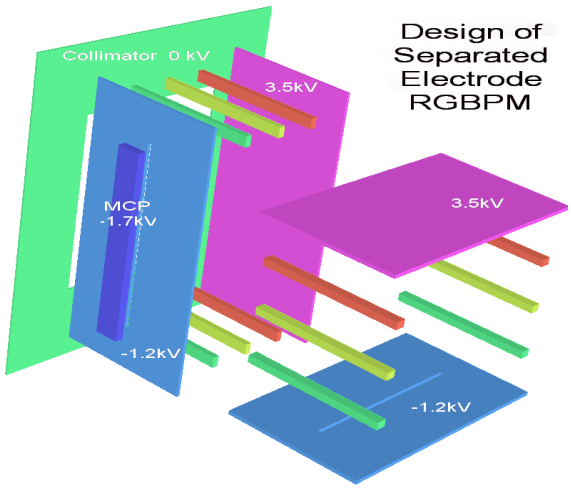


Figure 5: Calculated construction of the RGBPM-2 with the relevant voltages shown on the electrodes.

non-interceptive beam profile monitor for the high intensity beam project foreseen at INFN. The mechanical arrangement comprises two parallel plates for each plane, 50 mm apart with a collection voltage and extraction slit. A pair of rectangular MCPs followed by a position sensitive collecting anode is facing the slit, for each plane. The opening for the beam is 50 x 50 mm^2.

A photo of the monitor is shown in Fig. 6. The operating principle of the detector is described comprehensively in reference [3]. The copper bars, visible on the photo, keep the collecting field more uniform. The signal from the MCP is measured on a position sensitive anode, with a pitch of 1.25 mm (40 channels covering 50 mm). The electric fields of this monitor were also

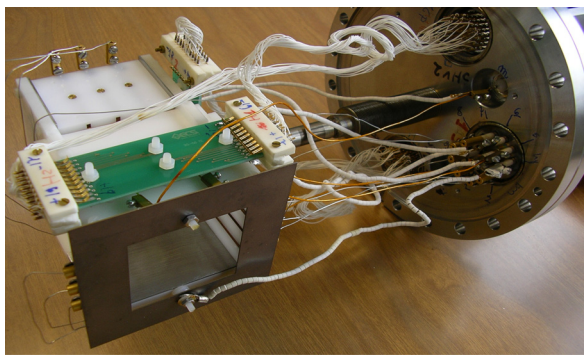


Figure 6: The residual gas beam profile monitor RGBPM-2. The 50 x 50 mm^2 opening for the beam is defined by a square tantalum protection screen in front of the monitor.

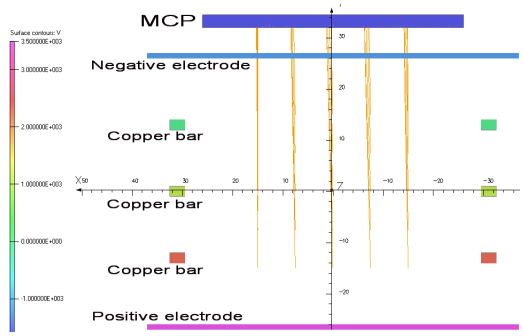


Figure 7: Twenty five particles, starting on a 30 mm x 30 mm XY-grid are tracked through the calculated electric field of the vertical profile monitor of RGBPM-2. The distortion of the profile is about 1mm due to non homogeneity of the electric field.

calculated with the program TOSCA. Particles were tracked in a plane perpendicular to the beam direction at the position of the vertical and horizontal micro channel plates to determine the distortion of the measured beam profile at the microchannel plates, due to the non-homogeneity of the electric field and likely influence between the horizontal and vertical collecting fields. The calculation, Fig. 7, shows that the beam profile in the vertical is distorted with less than 1 mm.

The collecting electrostatic field is approximately 1 kV/cm and the MCP side facing the collecting plane is at -1700 V, with about 800 V on each MCP. A grid system was installed 15 cm downstream from the RGBPM-2 detector to compare the profiles, in both the horizontal and vertical directions. The pitch of the grid is 0.75 mm. Several tests were made using various ion beams at different beam intensities. The profiles measured with the RGBPM-2 are strongly influenced by the presence of the profile grid intercepting the beam. When the grid is inserted to intercept the beam, the scattered electrons from the wires produce a lot of noise on the RGBPM-2. It

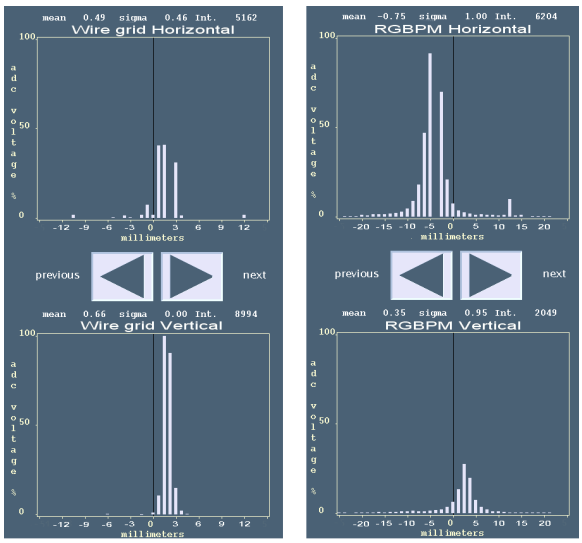


Figure 8: The profile of a 60 nA beam of 99 MeV oxygen ions measured with the grid is shown on the left. The profile measured with the RGBPM-2 is shown on the right.

is evident that the RGBPM-2 profiles are wider than those measured with the profile grid by approximately a factor of two as can be seen in Fig. 8. To explain this, four hypotheses are investigated: cross talk between the anode strips, transversal velocity of the produced ions, additional ionization caused by fast electrons produced by primary ionization and space charge effects. Work is in progress to improve the ion collecting field by experimenting with higher collector voltages.

CONCLUSION

The RGBPM-1 is a more compact and cheaper monitor compared to RGBPM-2, since it uses only one set of MCPs. It is however more difficult to operate, because the beam position display in the analyzing plane has to be calibrated against another beam position monitor. The RGBPM-1 monitor is also less sensitive than RGBPM-2 since the ionized rest gas is distributed over a larger area on the MCP. Even though the RGBPM-2 consists of two sets of electrodes, it still fits into a single vacuum chamber with insignificant mutual electrical influence. The calculations confirm these marginal distortions as shown in Fig. 7. It is possible to get good beam profile information with beam intensities from 10 nA at a pressure of 10^{-6} mbar without the addition of external gas. As a non-intercepting device, both RGBPM-1 and RGBPM-2 are useful beam position monitors. In both cases the RGBPMs were compared with a nearby profile wire grid system to determine their accuracy. The measured beam profile of both the RGBPM-1 and RGBPM-2 is about a factor of two larger than the beam profile measured with profile grid monitor. If the increase in the measured beam profile could possibly be due to space charge effects and because the ions produced in the residual gas are not really at rest, a higher collector voltage and mathematical methods [4] could possibly resolve this problem, and is the subject of future development.

REFERENCES

[1] J. C. Muller, et al, s, “Beam profile measurements using residual gas in the beam line”, http://www.kvi.nl/~annrep/ar1997/node61.html.
[2] http://www.vectorfields.co.uk/.
[3] B. Hochadel et al., “A residual-gas ionization beam profile monitor for the Heidelberg Test Storage Ring TSR”, Nucl. Instr. and Meth. A343 (1994) p 401.
[4] R. E. Williamson et al, “Analysis of measurement error in residual gas ionization profile monitors in a high intensity proton beam”, EPAC ’08, Genoa, TUPC109.

INVESTIGATION OF THE LIGHT YIELD OF LUMINESCENT SCREENS FOR HIGH ENERGY AND HIGH BRILLIANT ELECTRON BEAMS

G. Kube, DESY, Hamburg, Germany
W. Lauth, Institut für Kernphysik, Mainz, Germany

Abstract

Transverse beam profile diagnostics at electron accelerators is usually performed with optical transition radiation (OTR) monitors. For intense beams however, thermal load in the screen material may result in resolution degradation and even screen damage. To overcome this problem the beam can be swept over the screen, but the strong OTR light emission directivity will reduce the optical system's collection efficiency. In order to overcome these difficulties, luminescent screens can be used because of their robustness and isotropic light emission. Since only little information is available about scintillator properties for applications with high energy electrons, a test experiment has been performed in order to study the light yield of different screen materials under electron bombardment.

INTRODUCTION

For the European XFEL with a maximum beam energy of 20 GeV and an average beam power of up to 300 kW it is planned to install a beam profile monitor in the dump section in order to control beam position and size and to avoid damage of the dump window. OTR is widely used for transverse beam profile measurements with high energy electrons. Advantages of OTR are the radiation generation directly at the screen boundary in an instantaneous emission process, and the rather high light output emitted in a small lobe with an opening angle defined by the beam energy. For intense beams however, the thermal load from the particle interaction with the screen material results in a degradation of the image resolution and possible screen damage. To overcome this problem the beam can be swept over the screen, but in this case the strong OTR light emission directivity has the drawback of reducing the collection efficiency of the optical system. Therefore it is planned to use luminescent screens because of their robustness and isotropic light emission. While the use of luminescent screens at hadron machines is widespread (see e.g. Refs. [1, 2] and the references therein), there is little information about scintillator properties for applications with high energy electrons. At the SLC linac for example, screens based on phosphor (Gd_2O_2S:Tb or P43) deposited on a thin aluminum foil were in use, showing no sign of damage after bombardment with up to 4×10^{18} e/cm^2 [3]. To study the light yield of other scintillator materials, a test experiment has been performed which is described in the following.

EXPERIMENTAL SETUP

Figure 1 shows the sketch of the experimental setup. The experiment was performed at the 855 MeV beam of the Mainz Microtron MAMI (University of Mainz, Germany) [4] in the beamline of the X1 collaboration, close to the beam dump which is located behind the vertical deflecting bending magnet BM2. The screens were mounted directly

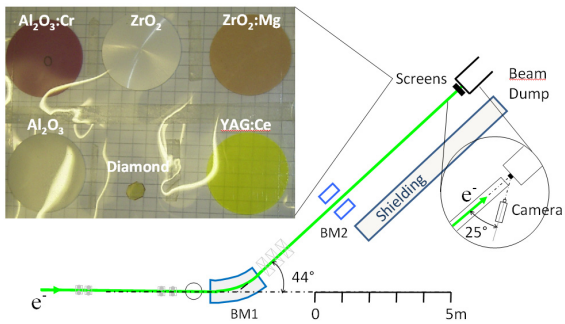


Figure 1: Screen test set–up in the X1 beamline at MAMI. The inset shows a photo of the screen materials under investigation.

in front of the dump in air. During beam exposure which lasted approximately one minute with a cw beam current of a few nA, the emitted luminescence light was observed via a standard Vidicon camera. The camera was located at a distance of about 1 m from the screens such that the loss of scintillation light intensity due to total reflection in the screen material was neglectable.

Table 1: Overview of the Screen Materials and Thicknesses Together with the Applied Beam Current

material	d / mm	current / nA
YAG:Ce	1	0.5
Diamond	0.2	1.9
Al_2O_3	1	1.9
Al_2O_3:Cr (Chromox)	1	0.5
ZrO_2 (Z700-20A)	1	32.4
ZrO_2:Mg (Z507)	1	32.4

Six different screens have been tested which are listed in Table 1 together with their thickness and the applied cw beam current. An industrial diamond crystal (Sumitomo Electric Industries [6]) together with four ceramic screens (BCE Special Ceramics [7]) were investigated with respect to their luminescence yield. The YAG:Ce crystal (Saint

Gobain Crystals [5]) served as reference.

DATA TAKING AND ANALYSIS

For each scintillator material, 10 images were taken with and 5 without beam. Each resulting mean background image was subtracted from the corresponding mean signal image in order to determine the background corrected profile image. The resulting image was normalized to the cw current according to Table 1 and then fitted in a pre–defined range of interest (ROI) with a normal distribution. Figure 2 shows the fit result for the Al_2O_3 screen as an example. Afterwards the light yield was determined by summing up the background corrected normalized intensity over a range of $\pm 6\sigma$ with respect to the profile maximum.

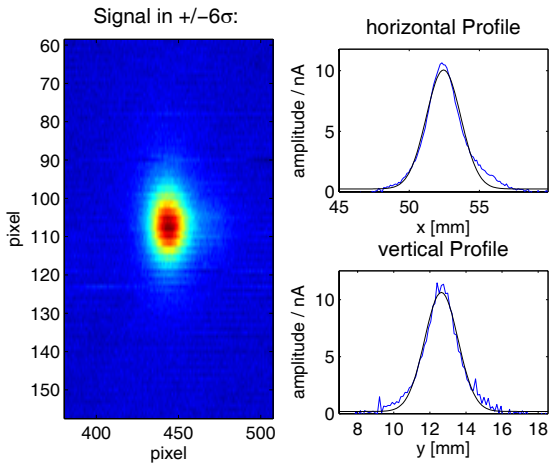


Figure 2: Left: background corrected beam image in range of interest for intensity integration. Right: normalized projected beam profiles and fit with normal distribution.

The results are summarized in Table 2. The horizontal and vertical (1σ) widths from the fit in the central parts of the projected profiles are listed together with the relative intensities, integrated over the corresponding ROIs. The intensities are expressed in units of the YAG:Ce intensity.

Table 2: Horizontal and Vertical (1σ) Widths Together with the Integrated Normalized Intensities for each Screen Material

material	σ_x **[mm]**	σ_y **[mm]**	I_{norm} **[a.u.]**
YAG:Ce	0.91	0.77	1
Chromox	0.93	0.73	72.6×10^{-3}
Al_2O_3	1.04	0.80	41.8×10^{-3}
Diamond	-	-	24.9×10^{-3}
ZrO_2:Mg	0.67	0.46	1.6×10^{-3}
ZrO_2	0.86	0.62	0.6×10^{-3}

The diamond crystal showed intense luminescence effects, and a light spot was clearly visible. However, due to its small size (c.f. Fig 1), part of the light was reflected at the crystal boundaries and some could even escape out of its volume. Therefore it was not possible to determine the projected profiles, and in the subsequent analysis this measurement will not be considered.

In case of the YAG crystal the $\pm 6\sigma$ range for intensity integration was not sufficient. As can be seen from Fig. 3 the profile no longer resembles a normal distribution and the intensity contribution in the tails is larger than in the measured profiles with other screens, see e.g. Fig. 2. The strong asymmetry is due to the fact that the beam was hitting the crystal close to its border and the range of light emission is restricted to the crystal volume. In order to account for this intensity loss for the light yield determination, the intensity integral from the profile maximum to -17σ was determined and the result was multiplied by a factor of 2.

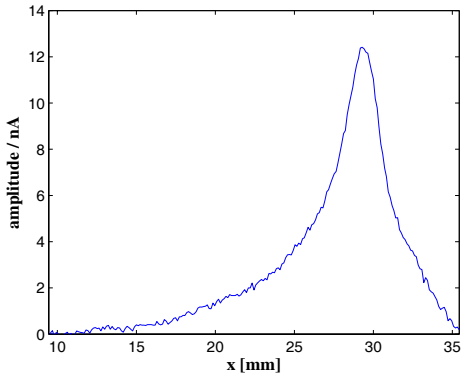


Figure 3: Horizontal profile as measured with the YAG:Ce screen.

The effect of image blurring in profile diagnostics with YAG screens is reported in Refs. [8, 9, 10] and explained by saturation of the scintillating sites inside the crystal and space charge ionization enhancement. For this experiment however, an effect due to saturation doesn't seem applicable because of the low beam charge density and the fact that a fit of the central part of the profile with a normal distribution results in profile widths comparable to those from the other screens, see Table 2. It is more likely that the increased intensity in the tails is due to light reflection from the backside of the scintillator crystal. However, the explanation of this effect needs further investigation.

Comparing the transverse beam sizes in Table 2 it is striking that the results of the measurements with ZrO_2 ceramics are both smaller than the others. Furthermore, during the course of the experiment it was possible to observe immediately a discolouration of the screen at the positions where the beam hits the ceramics, c.f. Fig. 4. By heating the samples at 150° in air for a few hours both screens recovered. After the irradiation which lasted only about one minute per target, both screens showed additionally a strong activation in the order of 30 μSv/h. As consequence the use of ZrO_2 screens seems not to be suitable for electron beam diagnostics.

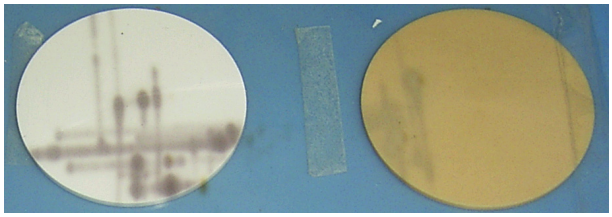


Figure 4: ZrO_2 screen (left) and ZrO_2:Mg screen (right) after electron bombardment. The positions where the beam hits the ceramics are clearly visible as dark spots or lines.

Efficiency Estimation

In this subsection a rough estimate for the scintillator efficiency will be given. While the intention of the test experiment was not to measure absolute values, the estimation is based on published values for the YAG:Ce efficiency as reference together with simplified experimental assumptions:

For the light yield of YAG:Ce crystals values between 8 [5] and 20.3 photons/keV [11] can be found in the literature. For the following analysis an efficiency of 8 photons/keV is assumed because it is the value as quoted from the crystal supplier.

Furthermore, to simplify it is assumed that the difference in the scintillator light outputs is caused by the different energy depositions of the beam electrons in the scintillator materials. None of the screens under investigation belongs to the category of cross-luminescent scintillators, therefore the processes of energy conversion (i.e. the formation of 'hot' electrons and holes in the scintillator host material), their thermalization, and the energy transfer to the luminescent centers (either extrinsic, i.e. doping ions, or intrinsic) were considered to be the same for all materials. The energy deposition is calculated with the Geant4 code [12] under the assumption that the energy loss is caused by the host material, and not by the activators because of their small concentration.

Table 3 summarizes the estimated light yield for the scintillators under investigation. Additionally it is assumed that

Table 3: Estimated Scintillator Efficiencies Together with Calculated Deposited Energy According to Ref. [12]

material	ΔE **[keV]**	**light yield [photons/keV]**
YAG:Ce	680	8 (Ref. [5])
Chromox	619	0.639
Al_2O_3	619	0.367
ZrO_2:Mg	829	0.011
ZrO_2	829	0.004

the camera sensitivity is constant, i.e. the emission spectrum of the individual scintillators is not taken into account.

Finally the self absorption inside the scintillator material is not taken into account, i.e. the luminescent light emission originates from the entire scintillator thickness. According to Ref. [13] it is a general scintillator property to be transparent in the sense that energy levels involved in the radiative transition are contained in the forbidden energy band to avoid reabsorption of the emitted light or photo–ionization of luminescent centers.

CONCLUSION

As can be concluded from Table 3 the YAG:Ce screen provides the highest output, more than one order of magnitude compared to a Chromox ceramic. However, the measured beam shape from the YAG screen was distorted, the reason for this profile degradation needs further investigation. With simplified assumptions the light yield difference between Chromox and the standard Al_2O_3 ceramic for electron bombardment amounts to only a factor of 2. For heavy ion bombardment, on the other hand, it was found out that a Chromox screen gives about one order of magnitude more intensity than an Al_2O_3 ceramic [14]. Finally the use of ZrO_2 ceramics seems not to be suitable for electron beam diagnostics because of the low light output, the material degradation under bombardment, and the rather high screen activation.

ACKNOWLEDGMENT

The authors would thank T. Hoffmann and E. Gütlich (GSI Darmstadt) for providing the YAG screen and the ceramic scintillators, B. Struth (DESY–Hasylab) for providing the diamond crystal, and S. Weisse (DESY Zeuthen) for support with the camera server.

REFERENCES

[1] R. Jung, G. Ferioli, and S. Hutchins, Proc. DIPAC'03, Mainz, Germany, May 2003, IT03, p.10 (2003).

[2] C. Bal *et al.*, Proc. DIPAC'05, Lyon, France, June 2005, POM013, p.57 (2005).

[3] M. Ross *et al.*, SLAC_PUB_3640 (1985).

[4] J. Ahrens *et al.*, Nuclear Physics News **4** (1994) 5.

[5] `http://www.detectors.saint-gobain.com`.

[6] `http://www.sei.co.jp/index.en.html`.

[7] `http://www.bce-special-ceramics.de/index.html`.

[8] A.H. Lumpkin *et al.*, Nucl. Instr. and Meth. **A 429** (1999) 336.

[9] A. Murokh *et al.*, Proc. 2^{nd} ICFA Advanced Accelerator Workshop on the Physics of High Brightness Beams, p.564 (2000).

[10] A. Murokh *et al.*, Proc. PAC'01, Chicago, Illinois, June 2001, p.1333 (2001).

[11] M. Moszyński *et al.*, Nucl. Instr. and Meth. **A 345** (1994) 461.

[12] S. Agostinell *et al.*, Nucl. Instr. and Meth. **A 506** (2003) 250. J. Allison *et al.*, IEEE Trans. Nucl. Sci. **53** No. 1 (2006).

[13] P. Lecoq *et al.*, *Inorganic Scintillators for Detector Systems*, (Springer Verlag, Berlin–Heidelberg, 2006).

[14] E. Gütlich, Diploma Thesis (in German), Fachhochschule Wiesbaden (Germany) 2008.

CARBON FIBER DAMAGE IN ACCELERATOR BEAM

M. Sapinski, B. Dehning, A. Guerrero, J. Koopman, E. Metral, CERN, Geneva, Switzerland

Abstract

Carbon fibers are commonly used as moving targets in Beam Wire Scanners. Because of their thermomechanical properties they are very resistant to particle beams. Their strength deteriorates with time due to radiation damage and low-cycle thermal fatigue. In case of high intensity beams this process can accelerate and in extreme cases the fiber is damaged during a single scan. In this work a model describing the fiber temperature, thermionic emission and sublimation is discussed. Results are compared with fiber damage test performed on SPS beam in November 2008. In conclusions the limits of Wire Scanner operation on high intensity beams are drawn.

INTRODUCTION

In order to validate beam heating model [1] and to determine the breakage mechanism of the $33\ \mu\mathrm{m}$ carbon fiber, a damage test has been performed on the SPS beam at CERN in November 2008. The final goal of the test was to verify the predictions of the limits for the wire damage in LHC beam and conclude about the specifications of the future Scanner.

EXPERIMENTAL CONDITIONS

A rotational Wire Scanner equipped with electronics which allow to measure wire resistivity and thermionic emission during the scan has been used in the experiment. The scanner contains two wires which scan the beam in horizontal and vertical directions. It can reach the scan speed of $6\ \mathrm{m/s}$ and performs two scans called IN and OUT. The speeds of both scans and interval between them are set independently. This interval has been set to at least 1 second to allow cooling the wire. In this test the scan IN was always performed with maximum speed and the speed of scan OUT was gradually slowed down from scan to scan in the following sequence: 6, 3, 1.5, 1, 0.8, 0.7, 0.6, 0.5 m/s. Two other Wire Scanners have been used during the test to constrain additionally the beam parameters.

A special beam cycle on CERN SPS accelerator has been prepared for this test. Beam intensity has been maximized and reached about $\mathrm{N_{prot}} = 2.4{\cdot}10^{13}$ circulating protons. In order to diminish the effect from RF-coupling [2] the beam has been debunched. A 12-second long flat-top plateau has been kept providing enough time to perform measurements in stable beam conditions. Beam momentum was 400 GeV/c.

WIRE BREAKAGE

The wires have been broken in conditions summarized in Table 1, where σ_l is the beam width along and σ_t perpendicular to the scan direction (the beam is assumed to have Gaussian transverse profiles). The breakage occurred after a sequence of scans, therefore the wire has already been weaken by preceding scans. In addition the wires installed in the scanner have been used since at least a year and have performed unknown number of scans (typically a few thousand).

Table 1: Beam Conditions at Wire Breakage

scan speed	$\mathrm{N_{prot}}$	σ_l [mm]	σ_t [mm]
0.5 m/s	$2.41 \cdot 10^{13}$	0.57	0.73
0.7 m/s	$2.18 \cdot 10^{13}$	0.73	0.57

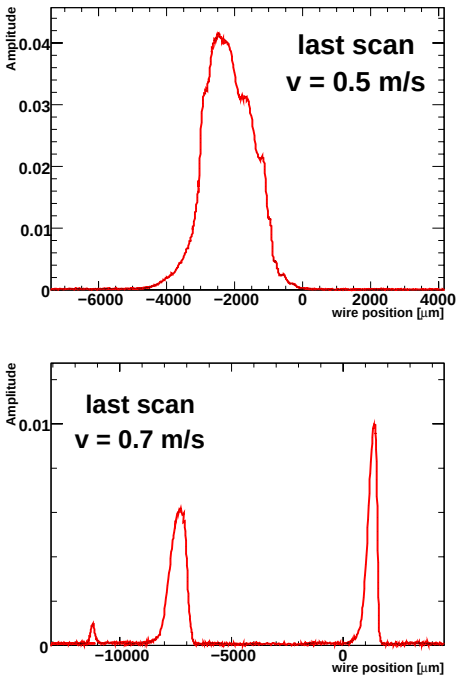


Figure 1: The last profiles after which the wire has been found broken. Upper plot shows breakage of vertical wire: deviations from Gaussian profile are visible. The bottom plot shows breakage of the horizontal wire: multiple peaks suggest that the wire has already fragmented.

In Fig. 1 the beam profiles registered during the last scans are shown. The deviations from Gaussian shape and

multiple peaks are symptoms of the wire deterioration and breakage. The measurement of the wire resistivity after these scans showed that the wire has been broken.

POSTMORTEM ANALYSIS

After the experiment the Wire Scanner has been opened and both wires have been recovered. They have been photographed with scanning electron microscope. The images obtained with 1000 times magnification, taken in three positions: at the center of the beam impact, 0.5 mm away and 1 mm away are presented in Fig. 2. They clearly show that the main process deteriorating the wire is sublimation due to the high temperature. In the center of the beam-impact location the remaining wire diameter is only about $7.5\ \mu\mathrm{m}$, what is equal to the sublimation of 95% of the material. At 0.5 mm from the beam-impact center the beam traces are visible and sublimation removed about a half of the material. At 1 mm from the beam center the fiber is intact.

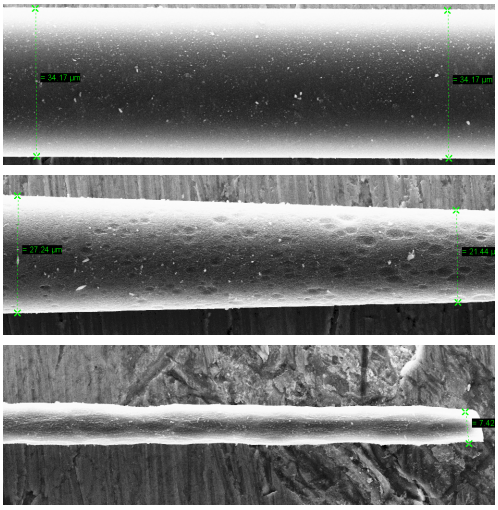


Figure 2: Fiber fracture at three distances from the beam impact location: 1 mm (upper plot), 0.5 mm (middle plot) and at beam center location (bottom plot).

In conclusion the wire breakage mechanism during these scans can be explained as a sublimation of the wire material until the moment when the mechanical properties of the wire does not allow to withstand forces which appear during the scan.

MODEL PREDICTIONS

The model described in [1] gives predictions of the temperature evolution of the wire during the scan. This temperature is a parameter of another model which describes the carbon sublimation.

Temperature evolution

The simulated evolution of the maximum temperature of the wire in the point where wire crosses the beam maximum is shown in Fig. 3 for scans with 0.5 and 0.7 m/s. At the speed of 0.5 m/s a plateau of about 2 ms in temperature evolution due to the equilibrium between beam heating and cooling by thermionic emission is observed.

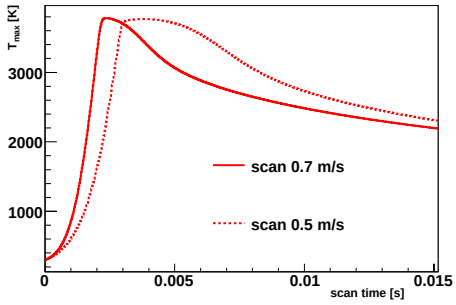


Figure 3: Simulated evolution of the maximum temperature of the wires during final scans.

Sublimation

The estimation of the sublimation rate is based on parametrization from [3]. In Fig. 4 the percentage of the wire diameter expected to sublimate during scan as a function of the velocity is shown. Scans with speeds of 0.5-0.7 m/s lead to sublimation of 8-12% of the wire diameter. The whole scan sequence used in the damage test should leave about $12 - 14\ \mu\mathrm{m}$ of the wire. This expectation is almost two times higher then the wire diameter measured on post-mortem samples.

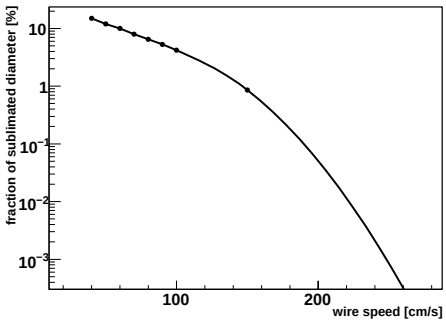


Figure 4: Simulated sublimation of the wire material in the wire center during scans with decreasing velocity.

From Figure 4 it is concluded that the sublimation process removes significant amount of material for all wire speeds slower then $2\ m/s$. This allows to determine the safety factor of 4, with respect to breakage conditions, as assuring a safe scanner operation. This factor can be obtained by decreasing the beam intensity or by increasing the wire velocity.

EXTRAPOLATION TO LHC CONDITIONS

From the model [1] it has been estimated that only a small part of about 5-7% of the nominal LHC beam at col-

lision (ie. $1.6 - 2.2 \cdot 10^{13}$ protons) can be scanned with $\mathrm{v_{wire}} = 1\ \mathrm{m/s}$ before the wire breakage. These values correspond almost to the breakage limit ie. only a small safety factor is assumed.

In case of fast scans the cooling processes can be neglected in estimation of the maximum temperature reached by the wire. Therefore the $\mathrm{T_{max}}$ depends on the number of particles which pass the wire center during the scan. As the peripheral parts of the scan can be neglected, a good parameter is beam density in the center, as seen by a wire with diameter $\mathrm{d_{wire}}$ moving with a speed $\mathrm{v_{wire}}$ in accelerator with revolution time τ_{revol}. It is expressed by Equation 1[1].

$$\rho_{0,\mathrm{tot}} = \frac{\mathrm{N_{prot} d_{wire}}}{2\pi\sigma_{\mathrm{x}}\sigma_{\mathrm{y}}\mathrm{v_{wire}}\tau_{\mathrm{revol}}}[\frac{\mathrm{protons}}{\mathrm{mm^2}}] \qquad (1)$$

In case of the two wire breakages described in this paper the $\rho_{0,\mathrm{tot}}$ is $2.4 \cdot 10^{13}$ and $1.6 \cdot 10^{13}\ \mathrm{protons/mm^2}$. This value for the wire moving with $1\ \mathrm{m/s}$ through the LHC beam is $4.7 \cdot 10^{14}\ \mathrm{protons/mm^2}$, ie. about 30 times more. Therefore for full LHC beam at 7 TeV the safe scan conditions are below 3% of nominal intensity. This is about 2 times less then predicted by the model [1].

NEW WIRE SCANNER

A project has been started at CERN with a goal to manufacture a fast and accurate Wire Scanners which could safely scan LHC beams [4, 5]. A proper choice of the wire can boost the Scanner performance. The following remarks are results of bibliographical research, modelling and experiments.

- The model [1] shows a weak dependence of the wire maximum temperature from the wire diameter,
- Thinner wires produce less particles which could quench the downstream magnet; on LHC the quench limit has been estimated to be about 4.5% of the full beam intensity at 7 TeV,
- Because of internal wire structure [6] a thinner wire (for instance 7 $\mu\mathrm{m}$) produced using a graphitization procedure in the last stage of preparation process has better mechanical properties then typical $30\ \mu\mathrm{m}$ wire,
- The wire breakage at Tevatron Main Injector [7] has shown that a wire with diameter of $4\ \mu\mathrm{m}$ broke at about $\mathrm{T_{max}} = 3200\ \mathrm{K}$, what might indicate that very thin wires have worse performance,
- Thin wires might have larger oscillation amplitude what might limit the scanner accuracy,
- The accuracy of the beam profile measurement is ultimately limited by the wire thickness.

A solution proposed for LHC are multiwires made of a few fibers twisted together. They should have enhanced strength as a bunch of thin fibers is stronger than a single thick wire. The vibration amplitude of multiwires should be smaller then in case of single wires. The method of optimal fabrication of such wires is being developed.

CONCLUSIONS

The wire damage test has been performed on high-intensity SPS beam. The test has shown that the wire damage mechanism is the sublimation and the following mechanical breakage. The results of the model [1] are probably too optimistic and the safe scanning of LHC beam with $\mathrm{v_{wire}} = 1\ \mathrm{m/s}$ at collision energy is limited to intensity of about $4 \cdot 10^{12}$ protons. A new Wire Scanner project will provide with fast and precise devices. It is proposed to use multiwire in the new Scanner as it will provide better thermomechanical performance than a single wire.

ACKNOWLEDGEMENTS

The authors wish to thank: Barbara Holzer for help during the damage experiment, Jesse Gudrun for taking post-mortem images of the wire with scanning electron microscope, Michel Sillanoli for taking a good care of the wire while removing it from the scanners after the test, which allowed to perform post-mortem analysis. Finally authors were happy to participate in a few fruitful discussions with Serge Rebouillat, an expert in physics and chemistry of the carbon fibers.

REFERENCES

[1] M. Sapinski, "Model of carbon wire heating in accelerator beam," CERN-AB-2008-030.

[2] M. Sapinski, T. Kroyer, "Operational limits of wire scanners on LHC beams, " proceedings of Beam Instrumentation Workshop, May 2008.

[3] S. Dushman, "Scientific foundations of vacuum technique," Wiley Inc., New York 1966.

[4] `https://project-wire-scanner.web.cern.ch/project-wire-scanner`.

[5] M. Koujili et al., "Fast And High Accuracy Wire Scanner," these proceedings.

[6] J-B. Donnet, S. Rebouillat, T.K. Wang, J. Peng, "Carbon Fibers", Taylor & Francis Inc, 1998.

[7] Martin Hu, private communication, 2008.

[1] Maximum temperature depends weakly on the wire diameter, in this Equation the beam density is averaged over $\mathrm{d_{wire}}$.

STATUS OF THE LASER-BASED BEAM PROFILE INSTRUMENT FOR THE RAL FRONT END TEST STAND

D.A. Lee, P. Savage, Imperial College London, U.K.
J. Pozimski, Imperial College London U.K. / STFC/RAL, Chilton, Didcot, U.K.
C. Gabor, STFC/RAL/ASTeC, Chilton, Didcot, U.K.

Abstract

The RAL Front End Test Stand is under construction with the aim of demonstrating production of a high-quality, chopped 60 mA H^- beam at 3 MeV and 50 pps. In addition to the accelerator development, novel laser-based diagnostics will be implemented. This paper reports on a device that will be able to measure multiple profiles of the beam density distribution in such a way that the full 2D density distribution can be reconstructed. The device is currently being commissioned. The status of the device is presented together with results of the commissioning and plans for future development.

INTRODUCTION

The Front End Test Stand is currently under construction at RAL. It will eventually consist of a high-brightness, 65 keV H^- ion source; a three solenoid Low Energy Beam Transport (LEBT); a 324 MHz, four-vane Radio Frequency Quadrupole (RFQ) that will accelerate the beam to 3 MeV; a Medium Energy Beam Transport (MEBT) section incorporating a beam chopper; and a comprehensive suite of diagnostics.

First beam was achieved from the ion source on 30 April (see Figure 1 and [1] for details). Regular operation is anticipated to begin by the end of June 2009, at which time beam commissioning of the laser-based profile monitor described in this paper will begin. A laser-based emittance monitor that will measure the emittance after the MEBT at 3 MeV is also under development; it is described in [2].

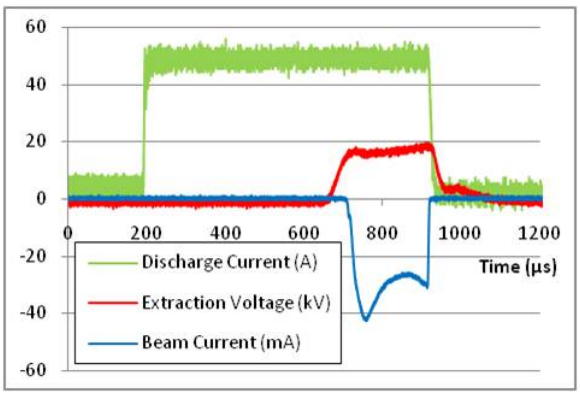


Figure 1: An oscilloscope trace of the first beam from the FETS ion source [1]

LASER-BASED H^- BEAM DIAGNOSTICS

Lasers can be used to diagnose H^- beams by the photodetachment of the outer electron of the H^- ions, via the process $H^- + \gamma \rightarrow H^0 + e^-$. The detached electrons or neutralised H^0 atoms can then be used to diagnose the beam; in the case of the profile monitor, the electrons are used. (The emittance monitor uses the neutralised H^0 atoms.) The detached electrons are separated from the ions (and the neutralised H^0) by a dipole magnet and the number of electrons is measured by a Faraday cup. This technique is illustrated in Figure 2. For the instrument described in this paper, due to the low energy of the electrons detached from the 65 keV H^- ions, it is also necessary to accelerate the electrons (in this case by a 2 kV electric field) to reduce any possible deflection by stray fields.

By having a laser with a beam diameter significantly smaller ($\sim$1 mm) than the ion beam diameter ($\sim$50 mm), stepping the laser beam across the ion beam and counting the number of electrons detached at each laser position, a projection of the ion beam onto a plane can be built up. A series of mirrors mounted on movable stages inside the vacuum vessel be used to step the laser beam across the ion beam. Additionally, the mirrors can be rotated and so the laser beam can pass through the ion beam at a variety of angles such that a projection onto any arbitrary plane can be measured. This is illustrated in Figure 3. A series of measurements at a variety of angles can be combined tomographically to give a full, correlated 2D beam profile. For this instrument, the measurements will be combined using the Algebraic Reconstruction Technique [3, 4].

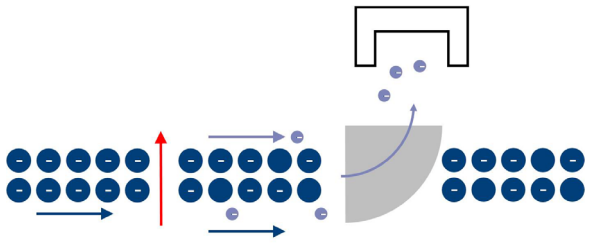


Figure 2: An illustration of the laser-based profile monitor principle. The laser (red) detaches some electrons (light blue) from the H^- ions (dark blue), which are then deflected by a dipole magnet (grey) into a Faraday cup.

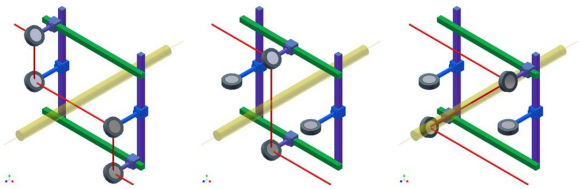


Figure 3: Three possible mirror configurations. The mirrors can rotate about their centrelines and move along x or y, depending on their positioning. The laser beam is shown in red and the ion beam in yellow

INSTALLATION AND OPTICS STATUS

The vessel in which the beam profile measurement will be made and the components required to make the measurement are complete and installed. They are shown in Figure 4. A vessel that will house the pepperpot system constructed for the characterisation of the FETS ion source [5] is also complete. This will allow for comparison between the initial laser-based profile measurements and ones from a scintillator screen.

Initially, two of the four pairs of stages will be installed (the back of the linear stages can be seen in Figure 4), giving coverage of half (180°) of the beam.

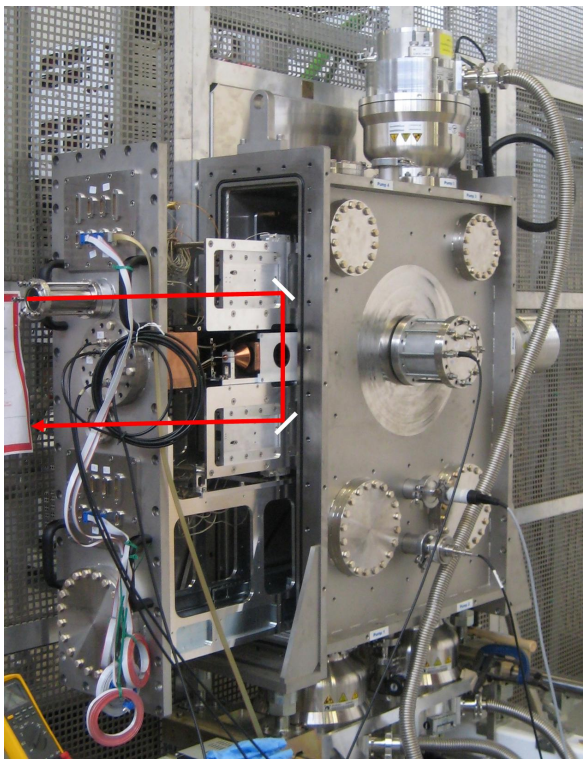
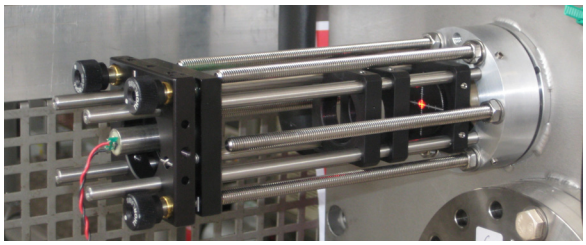
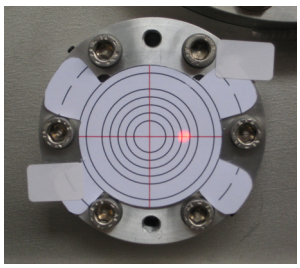


Figure 4: The vacuum vessel and the components required to make the beam density distribution measurement. In the centre of the picture the detector's copper Faraday cup can be seen. The central position of the mirrors is shown schematically in white, with the corresponding laser path in red.

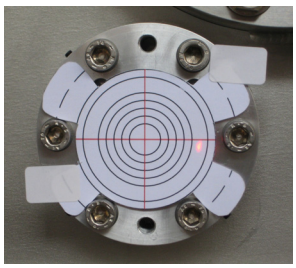
Due to the high power of the Nd:VO_4 laser that will be used to make the beam profile measurements, a lower power laser is being used to align the internal components of the vessel. In initial tests of the alignment, the rotary stages were configured to send the laser beam vertically down, as shown in Figure 4. The linear stages were then moved over their full travel (corresponding to a change in the path length of 400 mm) and the output position of the laser was found to vary by 7 mm. This corresponds to a mis-alignment of 0.0175 radians. This level of mis-alignment is tolerable as the beam does get coupled out from the vessel but may be corrected with shims between the stages and the frame on which they are mounted. A photograph of the alignment test setup is shown in Figure 5. It is anticipated that for the final alignment check a quantitative study will be performed using a position-sensitive laser power meter.



(a) The alignment laser jig, mounted on the laser input window. The output window is positioned 220 mm below the input window.



(b) A target mounted on the output window. The target's radii are 5 mm, 7.5 mm, 10 mm and so on. The movable stages are nearest to the vessel wall that the windows are mounted in (i.e. this is the configuration with the shortest path length).

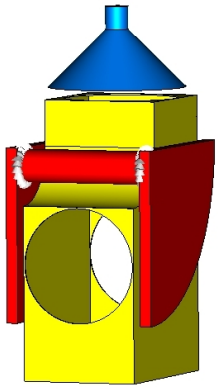


(c) For this picture the stages were moved to the furthest position from the vessel wall with the windows mounted in (such that the extra path length is 400 mm). Note that the spot has moved by ∼7 mm, compared to it's position in Figure 5b.

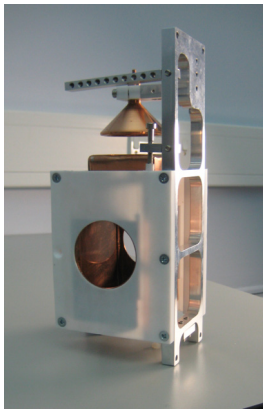
Figure 5: The optical alignment setup and results of initial alignment tests.

DETECTOR STATUS

The electron detector assembly consists of a copper sheath to accelerate the electrons, a dipole magnet to deflect them and a Faraday cup to collect them. It is shown in Figure 6. It is a compact assembly as the beamline length available for the vessel in which it is mounted is only 200 mm. The vessel has to be this short to prevent the divergent ion source beam becoming larger than the aperture of the first solenoid of the LEBT.



(a) A schematic of the detector. The magnet is shown in red, the accelerating sheath in yellow and the Faraday cup in blue.



(b) A photograph of the detector, shown in it's mechanical assembly. The magnet is not shown in this picture.

Figure 6: The detector, viewed from upstream. Electrons are deflected up into the Faraday Cup whilst the H^- ions pass straight through. The detector is $\sim$16 cm high.

Magnetic Field Measurements

In the design phase, the detector was simulated and it's performance assessed [6]. Subsequently, the bending component of the dipole magnet's field has been mapped at Daresbury Laboratory [7] to verify the simulation. The field was mapped on a 5 mm grid in the region where the electrons will be subjected to the dipole's field. The discrepancy between the measurement and simulation, averaged over all of the measurement points, is 0.23%. A summary of the results are shown in Figure 7.

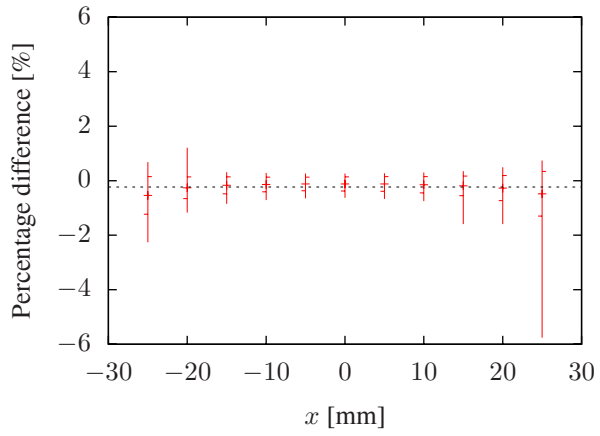


Figure 7: The discrepancy between the simulated and measured values of the x-component of the dipole's field. Each measurement was compared to the simulated value at it's position and then the discrepancies in each x-plane were averaged. The crosses show the average percentage difference for each plane; the ticks, $\pm 1\sigma$ from the average point; and the extent of the lines, the maximum discrepancies.

The largest discrepancies are seen in the region nearest to the pole pieces. Any discrepancies are expected to be largest in this region due to possible difficulties meshing the surface of the pole pieces in the simulation. Additionally, as most of the beam is transported through the middle section of the dipole, the discrepancies near the pole pieces do not affect the beam transport as much. Consequently, the measured dipole field is sufficiently close to the simulated field that no measurable difference between the simulated and actual performance is anticipated.

CONCLUSIONS & OUTLOOK

The status of an laser-based instrument to measure the full, correlated transverse beam density distribution of the H^- beam after the ion source of the Front End Test Stand has been presented, along with some commissioning results.

The movable components have been shown to have a mis-alignment of 0.0175 radians which, whilst sufficient for the measurement of the ion beam's profile, may be improved. The field of the dipole magnet used in the detector has been compared to the simulated field. The average discrepancy between the two fields is 0.23%, which should not influence the detector's performance noticeably.

With all the components installed, commissioning with beam will begin when the ion source is in regular operation (anticipated for the end of June) and the instrument should be able to perform beam projection measurements routinely soon after that.

In the longer term, the extra two pairs of stages will be added to enable all 360° of the ion beam to be covered and then full, correlated 2D profile measurements will be able to be made.

REFERENCES

[1] D. Faircloth *et al.*, "Initial Results from the Front End Test Stand High Performance H^- Ion Source at RAL", MO6RFP040, PAC'09, Vancouver, May 2009, http://www.JACoW.org.

[2] C. Gabor *et al.*, "Design Report of a Non Destructive Emittance Instrument for RAL's Front End FETS", TUPB22, DIPAC'09, Basel, May 2009, http://www.JACoW.org.

[3] D. Raparia *et al.*, "The Algebraic Reconstruction Technique (ART)", 2P057, PAC'97, Vancouver, May 1997, http://www.JACoW.org.

[4] D. Lee *et al.*, "A laserwire beam profile measuring device for the RAL Front End Test Stand", TUPB11, DIPAC'07, Venice, May 2007, http://www.JACoW.org.

[5] S. Jolly *et al.*, "Beam Diagnostics for the Front Front End Test Stand at RAL", WE02A01, DIPAC'07, Venice, May 2007, http://www.JACoW.org.

[6] D. A. Lee *et al.*, "Laser-based Ion Beam Diagnostics for the Front End Test Stand at RAL", TUPC058, EPAC'08, Genoa, June 2008, http://www.JACoW.org.

[7] http://www.astec.ac.uk/id_mag/id_lab.htm

DESIGN OF A NEW EMITTANCE METER FOR LINAC4

B. Cheymol, E. Bravin, C. Dutriat, T. Lefevre, CERN, Geneva, Switzerland

Abstract

LINAC4 is the first step in the upgrade of the injectors chain of the Large Hadron Collider (LHC). This Linac will accelerate H^- ions from 45 keV to 160 MeV. During the commissioning phase of LINAC4 transverse emittance measurements will be required at 45 keV, 3 MeV and 12 MeV. For this purpose a slit&grid system is currently being developed. The material and the geometry of the wires and of the slit need to be optimized in order to minimize the negative effects of the energy deposition and maximize the signals. This document describes the results of the studies carried out during the design of the emittance meter.

LINAC4

LINAC4 is an H^- linear accelerator with a maximum energy of 160 MeV intended to replace the present 50 MeV proton linac (LINAC2) as injector for the Proton Synchrotron Booster (PSB). In the present configuration the PSB represents the bottleneck in terms of beam brightness for the LHC. By injecting into the PSB a beam of higher energy and by using the phase-space painting technique, possible thanks to the use of H^- ions, the brightness and intensity of the beams produced by the PSB will double. In order to push the performances of the LHC even further additional upgrades of the injectors are foreseen. In the second step both the PSB and the Proton synchrotron (PS) will be replaced by a superconducting proton linac (SPL) and a new proton synchrotron, the PS2. [1]

EMITTANCE MESSUREMENT

The transverse phase-spaces (x and y) describe the distribution of particles in x and x' (y and y'), where x (y) is the position of the particles and x' (y') the angle between the trajectory of the particle and the longitudinal axis of the beam (z). The aim of the emittance meter is to sample the transverse phase-spaces from which the emittance can be calculated.

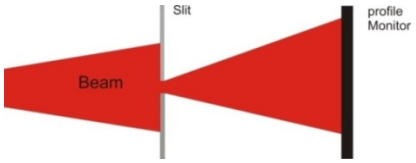


Figure 1: Slit and grid system.

As show in Fig. 1 and Fig. 2 a slit and grid system can be used to sample the transverse phase-space. In this technique the slit is used to select particles within a narrow slice in position, then, in the following drift space, the angular distribution of the particles transmitted through the slit is transformed into a position distribution and sampled using a profile monitor, in our case a secondary emission grid. By scanning the slit across the beam, the whole phase-space is reconstructed.

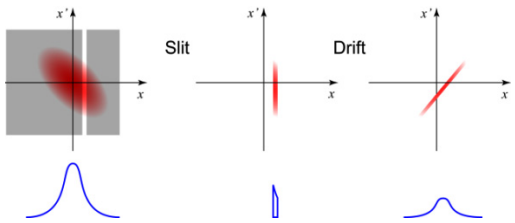


Figure 2: Phase-space sampling using a slit and grid system.

Each wire of the grid is connected to a separate acquisition channel and sampled at 250 kHz, this allows the observation of the evolution of the emittance along the linac pulse. The diameter and the material of the wires are chosen in order to reduce the thermal effects induced by the beam and provide an adequate signal.

In order to sample both transverse planes two slits and two SEM-grids are needed. (see Fig. 3)



Figure 3: The emittance meter of LINAC4.

MULTIPLE SCATTERING AND THERMAL EFFECTS ON THE SLIT

Particles scattered on the edges of the slit could perturb the measurement of the distributions and lead to errors in the calculation of the emittance. The geometry of the slit and its material must be carefully selected in order to minimize this effect.

The effect of multiple scattering on the edges has been simulated for the four slit geometries shown in Fig. 4 and for different energies using the FLUKA Monte-Carlo code [2].

Supported by the EU under contract PITN-GA-2008-215080

Table 1: Simulation of Slit Efficiency at 3 MeV in Different Materials

	Carbon	Copper	Titanium	Steel	Aluminium
% particles after the slit	8.5	8.7	8.9	8.39	8.95
% scattered	6,29	3,98	5,85	3,91	6,731
% scatt. and hitting the SEM-grid	4,14	1,1	2,39	0,94	3,22

The results for a beam of 3 MeV and for the geometry indicated in Fig. 4-a are shown in Table 1. The simulations show that for the mentioned case less than 4% of particles collected by the SEM-grid are scattered on the edges of the slit.

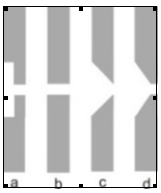


Figure 4: Different slit geometries used in the simulation. Each slit has an aperture of 100 μm and a maximum thickness of 1 mm.

The range of H^- ions in copper and stainless steel is shorter than the range in the lower Z materials while the scattering angle is larger; for this reason using higher Z materials reduces the fraction of the ions reaching the SEM-grid after interacting with the edges.

Comparisons of the different geometries shown in Fig. 4 in the case of stainless steel show that geometry (d) gives results similar to geometry (a), geometry (b) gives the best results and geometry (c) gives the worse results, with about 30% of the particles that reach the SEM-grid being scattered. It is important to note that geometry (b) is not well suited for sampling the phase-space. In this configuration the aperture of the slit is smaller than its thickness and the selection operated by the slit is no longer just in position, but also in angle. The result is that the measured phase-space distribution is flowed by an angular cut and the emittance is underestimated.

As FLUKA does not allow tracking particle below 100 keV in order to study the case of 45 keV simulations with beam energies of 200 kev and 300 keV have been used. For these two cases less than 0.01% of the particles passing through the slit are scattered on the slit edges. This result is due to the fact that the particles hitting the slit are stopped over a very short distance inside the material and as consequence only a very small fraction is able to escape. At 45 keV, the range of the H^- ions in steel is even shorter, so a similar result can be expected.

The energy deposition in the slit and the corresponding increase of temperature for the 3 MeV case have been also simulated with FLUKA showing that the increase in temperature exceeds the limits of stainless steel if the full beam intensity (400 μs) is sent on the slit.

In this case the maximum temperature increase is about 1500°C, which is above the melting point. For a shorter pulse of 200 μs the maximum increase of temperature remains acceptable, around 750°C, further studies are needed in order to understand the effects of the 1 Hz repetition rate.

Table 2: Maximum Temperature Increase on the Slit

Beam energy	**45 keV**		**3 MeV**	
pulse	200 μs	400 μs	200 μs	400 μs
Stainless steel	11.2°C	22.6°C	760°C	1512°C
Carbon	29.25°C	58°C	2100°C	4000°C

SECONDARY EMISSION

The signals from the wires have several components:

- secondary emission (SE) caused by the H^- ions entering the wire
- secondary emission caused by protons and electrons exiting the wire
- direct charge deposition of protons and electrons stopped inside the wire

The SE signal can be calculated using the theory of Sternglaas [3]. In this theory the Secondary Emission Yield (SEY) is described as

$$SEY = \Lambda * dE/dx$$

where Λ is a parameter that depends on the properties of the material and dE/dx is the stopping power for the given material and particle type.

Measurements of the stripping cross section for H^- and H^0 on carbon at 2 MeV and 7 Mev are available in literature [4]. The ionization cross sections depend on $\frac{1}{\beta^2}$ (relativistic factor) of the ions and on the Z of the material. In order to obtain values suitable for our studies the experimental results are interpolated using the mentioned dependencies, see Table 3.

Table 3: Measured and Extrapolated Ionization cross Sections

Stripping H^- in a H atom		
Beam Energy	Experimental cross section	Calculated cross section
2 MeV	$1 \cdot 10^{-16}\,cm^2$	
3 MeV		$0.66 \cdot 10^{-16}\,cm^2$
7 MeV	$0.35 \cdot 10^{-16}\,cm^2$	
12 MeV		$0.26 \cdot 10^{-16}\,cm^2$

Stripping H^0 in a H^+ ions		
Beam Energy	Experimental cross section	Calculated cross section
2 MeV	$0.4 \cdot 10^{-16}\,cm^2$	
3 MeV		$0.264 \cdot 10^{-16}\,cm^2$
7 MeV	$0.15 \cdot 10^{-16}\,cm^2$	
12 MeV		$0.11 \cdot 10^{-16}\,cm^2$

Figure 5 shows the ratio of the different hydrogen ions mixture as a function of the depth inside a carbon foil.

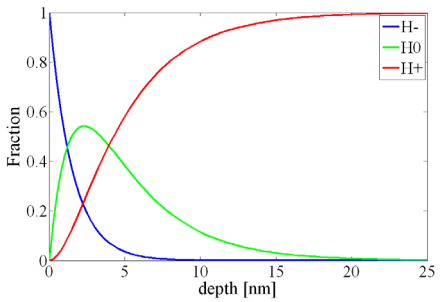


Figure 5: Relative fraction of hydrogen ions inside a carbon foil for a 3 MeV impinging H^- beam.

The secondary emission is an effect that takes place in a very thin layer near the surface of the material. Below a few MeV the H^- ions are stripped in the first few nanometers and the secondary emission of the incoming particle is dominated by the proton while for beam energies above 3 MeV the ionization happens after the SE layer and the secondary emission is dominated by the H^- ions. The SEY of the H^- ions is again calculated with the Sternglass formula assuming that the stopping power of the H^- ions is the same as that of protons.

The secondary emission of the exiting particles depends on the ions energy and on the wire properties and geometry as the H^- ions will be decomposed into the 3 constituents and these will lose energy and eventually be stopped inside the material.

SIGNALS

An example of the evolution of the signal induced by H^- ions on a 40 µm wire (carbon and tungsten) as a function of the H^- energy is shown in Fig. 6.

At very low energies, the SE is the dominant source for the signal, and it shows a strong dependency on the ions energy as expected from the theory.

Above a few MeV the SE is much reduced and the signal is dominated by the direct charge deposition of the stopped electrons, becoming thus negative. Increasing further the energy of the ions, the two electrons acquire sufficient energy to cross the wires; at this point the secondary emission becomes again the dominant effect, but this time with a much smaller yield. In this case the SE of both the proton and of the electrons exiting the wire has to be considered. For a carbon wire of 40 µm in diameter, the threshold energy for the electrons crossing the wire is around 110 MeV. When crossing this threshold the signal drops to much smaller amplitudes. In the case of tungsten the transition happens around 160 MeV which corresponds to the maximum energy of LINAC4.

As for the slit, the energy deposition on the wires and the corresponding increase of temperature has been studied using FLUKA. As most of the particles are stopped by the slit, only 0.05% of the initial particles are transmitted through it, the total energy deposited in the wires is very small and the increase in temperature, even in the worst case, is only of about 20°C (tungsten).

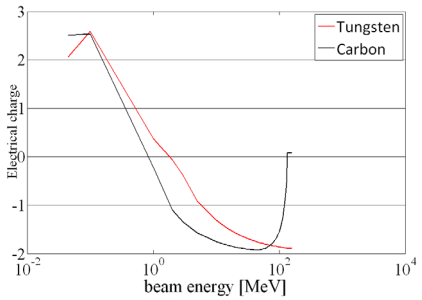


Figure 6: Electrical charge induced on a 40 µm wire by H^- ions as function of the ions energy.

CONCLUSION

Monte Carlo simulations of the LINAC4 emittance meter have been performed in order to study the efficiency of the slit and estimate the thermal loads and the amplitude of signals from secondary emission. The results for a beam of 3 MeV show that by choosing an adequate geometry the multiple scattering on the slit edges will not perturb the sampling of the phase-space. A thermal analysis shows that the slit will be damaged if the full beam intensity is sent on it and thus the emittance must be measured using a shorter beam pulse. The thermal load induced by the beam on the wires and the consequent increase in temperature is very small, well below the threshold for thermionic emission and far away from the limits of the material chosen for the wires.

Further simulations are being produced for beams of 12 MeV and higher, in order to design suitable slits for higher energies.

REFERENCES

[1] Linac4 technical design report, CERN-AB-2006-084 ABP/RF.

[2] FLUKA official website ww.fluka.org.

[3] E.J. Sternglass, Theory of Secondary Electron Emission by High-Speed Ions, Phys.Rev. 108(1957) 1.

[4] A. S. Artemov, Yu. K. Baigachev, A. K. Gevorkov and A. O. Sidorin, Zh. Tekh. Fiz. 68, 102–105 (August 1998).

SYNCHROTRON RADIATION MONITOR FOR BUNCH-RESOLVED BEAM ENERGY MEASUREMENTS AT FLASH

A. Wilhelm and C. Gerth*
Deutsches Elektronen-Synchrotron DESY, D-22603 Hamburg, Germany

Abstract

A synchrotron radiation monitor based on a multi-anode photomultiplier tube (PMT) has been installed in the first magnetic bunch compressor chicane at the Free-electron LASer in Hamburg (FLASH). The synchrotron radiation emitted in the third dipole of the magnetic chicane is imaged by a telescope onto two anodes of the PMT. In this way the horizontal beam position of the electron bunches is recorded which corresponds to the beam energy as the beam position is governed by the beam energy in the dispersive section of the magnetic chicane. The fast PMT signals are digitized by analog -to-digital converters which enables bunch-resolved beam energy measurement within the trains of the up to 800 bunches generated by the superconducting linear accelerator of FLASH. In this paper we describe the experimental setup of the synchrotron radiation monitor and present first commissioning results for various accelerator settings.

INTRODUCTION

Various diagnostic techniques based on the detection of synchrotron radiation (SR) have been utilised for decades for the characterisation of electron and proton beams in storage rings [1, 2]. In single-pass free-electron lasers (FEL), off-crest acceleration in combination with magnetic dipole chicanes is a common scheme for longitudinal bunch compression to produce ultra-short electron bunches with high peak currents. Due to the relatively large dispersion of these magnetic chicanes, the beam energy and energy spread can directly be deduced from a beam position measurement in the dispersive section of the magnetic chicane.

In the first bunch compressor (BC) at the Free-electron LASer in Hamburg (FLASH), a SR monitor based on photomultiplier tube (SR-PMT) has been added to an existing SR monitor based on an intensified CCD camera (SR-camera) [3]. The super-conducting linear accelerator of FLASH is capable of generating trains of up to 800 bunches with a spacing of 1 μs at a repetition rate of 5 Hz. By adjusting the gate and delay of the SR-camera, the full x-y projection of a single bunch (or any number of subsequent bunches) out of a bunch train can be recorded. However, the readout of the CCD is too slow to resolve more than one electron bunch within a bunch train. In contrast, by recording the signals of the two adjacent anodes of the SR-PMT the centre-of-gravity beam position for all individual bunches can be measured.

* christopher.gerth@desy.de

SR MONITOR SETUP

A schematic overview of the SR monitor installed in the first BC at FLASH is presented in Fig. 1. The BC, which consists of 4 horizontally deflecting dipole magnets, is located downstream of a RF photo-cathode gun and a super-conducting 1.3 GHz accelerating module (ACC1) which accelerates the electrons to a beam energy of typically 130 MeV. The large horizontal aperture of the flat vacuum chamber (200 mm $\times$ 8 mm cross section) allows one to operate the BC at bend angles in the range 15° - 21°. The critical wavelength of the emitted SR lies in the visible at around 400 nm for a bend angle of 18°.

An Ag-coated laser mirror (Linos, 20 mm $\times$ 30 mm) deflects the SR emitted at the entrance of the third dipole downwards by 90° (not shown in Fig. 1) onto a beam splitter. The transmitted SR is imaged by a camera lens (Sigma, f = 180 mm) onto an intensified CCD camera (PCO, dicam pro). The part of the SR that is reflected by the beam splitter is deflected by another mirror by 90° and then imaged by a camera lens (Tamron, f = 300 mm) with a teleconverter (3x) onto two anodes of a multi-anode photomultiplier tube (PMT). The PMT of type Hamamatsu R5900U-00-M4 comprises four anodes each having a size of 8 x 8 mm^2. The PMT was operated at a voltage of 720 V for which a linear dependence between the output signal and the electron bunch charge, i.e. SR intensity, was measured. The fast current signal of the PMT have a pulse height of about 1 V (with 50 Ohm input impedance) and a width of 4 ns (FWHM). The signals are broadened to 20 ns (FWHM) by Gauss filters with a cut-off frequency of 15 MHz to eliminate high-frequency noise and reduce the effect of timing jitter ($\sim$ 1 ns) of the 14-bit analog-to-digital converters (ADC). The ADCs are synchronised to the bunch repetition rate of 1 MHz and can be read out by the machine control system. The normalized difference signal s of both ADC channels gives then the centre-of-gravity beam position $s = (I_1 - I_2)/(I_1 + I_2)$, where I_1 and I_2 are the signal intensities of both anodes measured with the ADCs. The whole SR monitor setup is mounted on a mover which can be moved horizontally to be able to adjust to the electron beam trajectory for different bend angles of the BC.

Energy Calibration

The horizontal beam size in the BC is governed by the beam energy spread as an energy deviation $\Delta E/E$ transforms into a horizontal displacement Δx by 1st-order transport theory via $\Delta x = R_{16} \cdot \Delta E/E$ due to the large horizontal dispersion of about $R_{16} \approx 300 - 400$ mm [4].

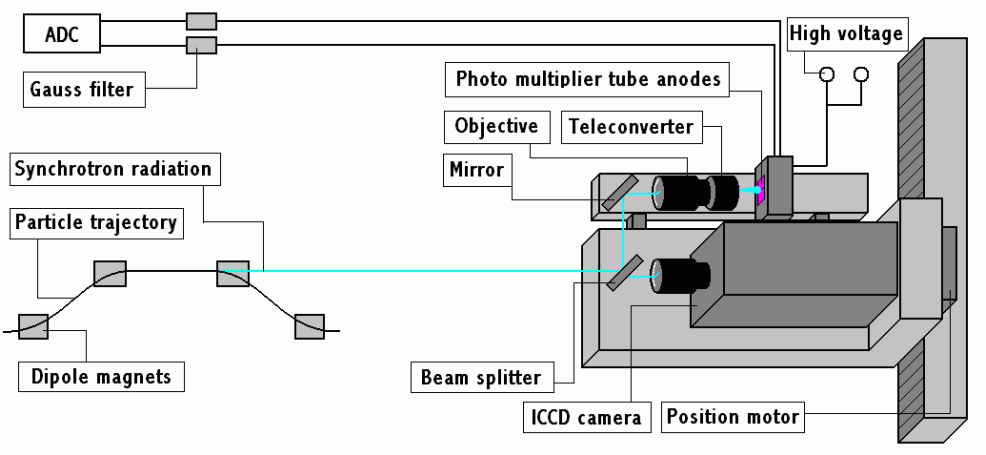


Figure 1: Schematic overview of the SR monitor setup. For further explanation see text.

Figure 2(a) shows the horizontal beam profile recorded with the SR-camera for 3 different accelerating phases of module ACC1. The corresponding calibration curves for the SR-PMT signal s are shown in Fig. 2(b). The calibration was accomplished by changing the dipole current - a relative change in the magnetic field corresponds to a relative change in beam energy - and recording simultaneously the SR-PMT signal. As can be seen, the calibration curve of the SR-PMT depends on the horizontal beam profile. The horizontal beam profile is dominated by the accelerator optics and phase of ACC1. Hence, after changing accelerator settings a re-calibration of the SR-PMT becomes necessary.

A calibration curve has been constructed from a horizontal beam profile recorded with the SR-camera by dividing the beam profile shown in Fig. 3(a) into two parts, calculating the normalised difference signal s for the integral intensity of each part and moving the parting line across the profile. This calibration curve (solid red line) is shown in Fig. 3(b) together with the corresponding calibration measurement with the SR-PMT (blue dots). A crosstalk of 8% between the two parts was assumed for the dashed line which is in good agreement with measurement points. This crosstalk may be due to crosstalk in the PMT, crosstalk in the electronics or a broadened profile, e.g. if the PMT is not positioned exactly in the image plane.

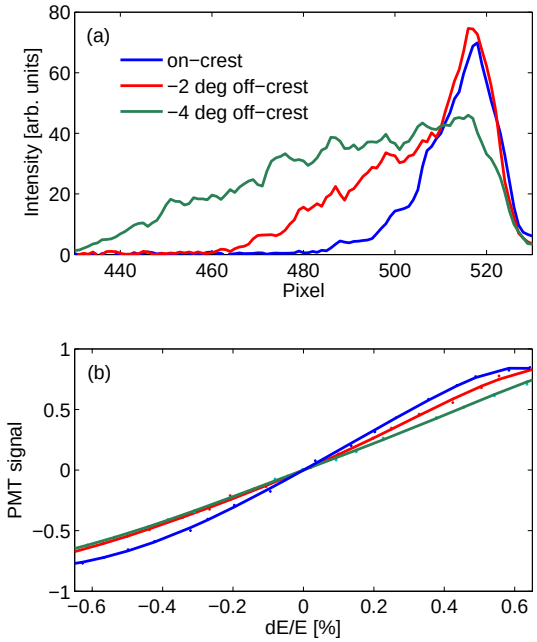


Figure 2: (a) Horizontal beam profiles measured with the SR-camera for 3 ACC1 phases; (b) Corresponding energy calibration of SR-PMT signal.

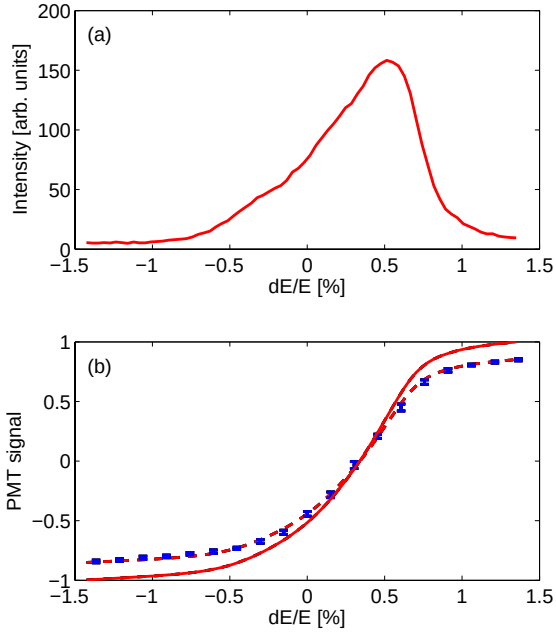


Figure 3: (a) Beam profile measured with the SR-camera; (b) Calibration curves of SR-PMT (dots) and deduced from beam profile (solid) with 8% crosstalk (dashed).

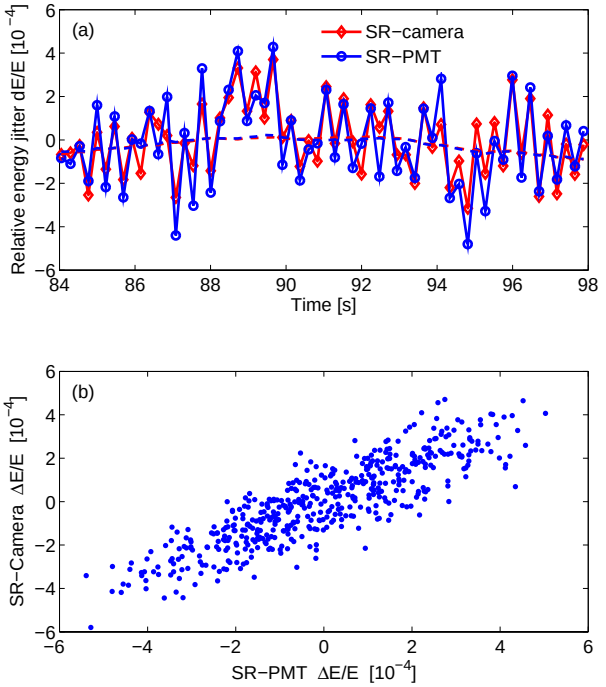


Figure 4: (a) Beam energy of single bunches measured with the SR-PMT and SR-camera for 60 subsequent bunch trains; (b) Correlation plot for 500 measurement points of the SR-PMT and SR-camera.

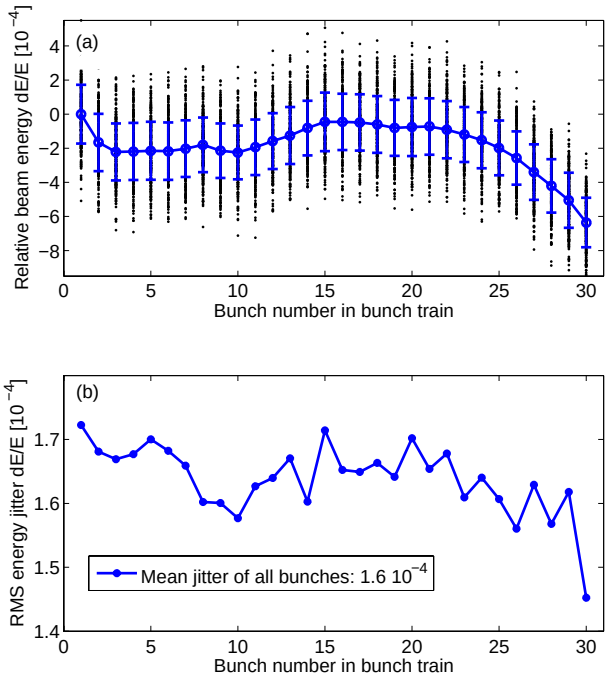


Figure 5: (a) Beam energy measured with the SR-PMT for 300 subsequent bunch trains with 30 bunches; (b) Corresponding rms energy jitter of each bunch.

MEASUREMENTS

An upper limit for the energy resolution of both SR monitors can be estimated by recording simultaneously the relative energy jitter with the SR-camera and SR-PMT.

Figure 4(a) shows the beam energy of single bunches measured with the SR-camera and SR-PMT during user operation of FLASH for 60 subsequent bunch trains out of a measurement of 500 bunch trains. The correlation of the measured beam energies for all 500 measurement points is shown in Fig. 4(b). The difference of the measured beam energy is $1.08 \pm 0.04\ 10^{-4}$ which gives an upper limit for the resolution of both SR monitors. Assuming that both SR monitors have the same resolution, the resolution of each detector would be $1.08 \pm 0.04\ 10^{-4}/\sqrt{(2)} = 7.6 \pm 0.3\ 10^{-5}$. Very similar values were obtained by correlating the beam energy measured with the SR-PMT for two adjacent bunches. The energy difference for adjacent bunches in a bunch train is very small due to the very high quality factor, i.e. very narrow bandwidth, of the superconducting cavities.

Figure 5(a) shows the beam energy measured with the SR-PMT for 300 subsequent bunch trains with 30 bunches (black dots). The mean values of each of the 30 bunches (blue dots) represent the energy slope along the bunch train (mean value of first bunch was normalised to zero). The measurement was recorded during the application of an adaptive feedforward algorithm to compensate beam loading effects (see Ref. [5] for more details). The rms beam energy jitter measured for each of the 30 bunches is about $1.6\ 10^{-4}$ and shown in Fig. 5(b).

SUMMARY

A new type of synchrotron radiation monitor based on a multi-anode photomultiplier tube has been installed in the first bunch compressor chicane at FLASH for bunch-resolved beam energy measurements. A relative energy resolution of about $1 \cdot 10^{-4}$ or below was achieved.

REFERENCES

[1] G. Kube, "Review of Synchrotron Radiation based Diagnostics for Transverse Profile Measurements", DIPAC'07, Venice, MOO1A03, http://www.JACoW.org.

[2] K. Holldack, "Review of Emittance and Stability Monitoring using Synchrotron Radiation Monitors", DIPAC'01, Grenoble, http://www.JACoW.org.

[3] Ch. Gerth, "Synchrotron Radiation Monitor for Energy Spectrum Measurements in the Bunch Compressors at FLASH", DIPAC'07, Venice, TUPC03, http://www.JACoW.org.

[4] P. Castro, "Beam trajectory calculations in the bunch compressors of TTF2 ", DESY Technical Note 03-01, April 2003.

[5] Ch. Gerth *et al.*, "Beam Based Measurements of the RF Amplitude Stability at FLASH using a Synchrotron Radiation Monitor", DIPAC'09, Basel, TUPD22, http://www.JACoW.org.

HIGH ENERGY EMITTANCE MEASUREMENT AT SPARC*

E. Chiadroni†, D. Alesini, M. Bellaveglia, M. Castellano, L. Cultrera, G. Di Pirro, M. Ferrario, L. Ficcadenti, D. Filippetto, G. Gatti, E. Pace, C. Vaccarezza, C. Vicario, INFN/LNF, Frascati, Italy
A. Cianchi, B. Marchetti, University of Rome Tor Vergata and INFN-Roma Tor Vergata, Rome, Italy
A. Mostacci, University La Sapienza, Rome, Italy
C. Ronsivalle, ENEA C.R. Frascati, Frascati, Italy

Abstract

The characterization of the transverse phase space of electron beams with high charge density and high energy is a fundamental requirement for particle accelerator facilities. The knowledge of characteristics of the accelerated electron beam is of great importance for the successful development of the SPARC FEL, a R&D photo-injector facility for the production of high brightness electron beams to drive SASE and SEEDED FEL experiments in the visible and UV wavelength. Here high energy emittance measurements are discussed.

INTRODUCTION

In order to achieve the SPARC [1] goals a precise characterization of the beam phase space at high energy is needed. In this paper we present the results for both transverse and longitudinal emittance measurements, together with the slice emittance analysis. In particular we discuss systematic effects observed in the transverse emittance measurement with the quadrupole scan technique using two quadrupoles arranged as a doublet.

Typical operation energy is around 140 MeV. For this stage of commissioning we have operated with a photocathode driven laser pulse with gaussian longitudinal profile (6-8 ps FWHM). The bunch charge was around 200 pC. The laser spot on the cathode was around 300 μm rms. Downstream from the last accelerating section several tools for a full characterization of the beam parameters are installed (Fig. 1).

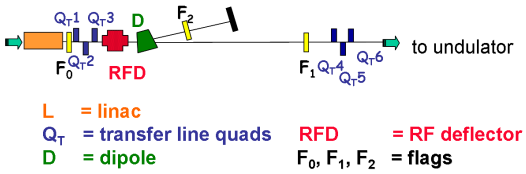


Figure 1: Layout of the high-energy experimental area.

TRANSVERSE EMITTANCE

The high energy transverse emittance measurement at SPARC is performed by means of a quadrupole scan [2] downstream from the third accelerating section. The transverse beam size is measured on the flag F_1 for different current values of quadrupoles Q_T1, Q_T2, Q_T3 (see Fig. 1); two quadrupoles have equal currents but opposite sign, and the third is used to control the beam spot shape. Quadrupoles are treated as thick lenses.

Typical Measurement

Usually, Q_T1 and Q_T3 are used with opposite polarity and Q_T2 is set at zero current, in order to reduce the overlapping of quadrupole fields. The transverse emittance is then determined by evaluating the Twiss parameters, $\beta\varepsilon$, $\alpha\varepsilon$ and $\gamma\varepsilon$, from the χ^2 minimization. The measured beam sizes, compared to the ones retrieved from the fit, are plotted in Fig. 2 as function of the quadrupole current.

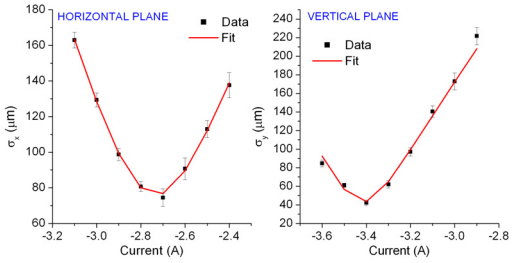


Figure 2: Comparison between the rms beam size measured at the flag F_1 (black squares) and the one retrieved from the χ^2 minimization (red curve) as function of the quadrupole current (125 pC, 140 MeV).

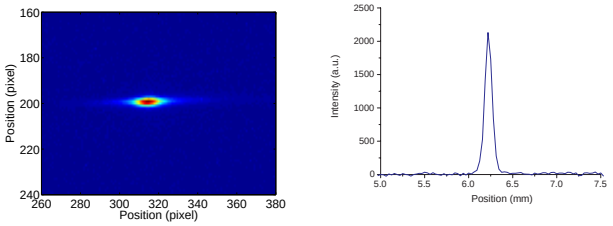
For a beam of 125 pC of charge and 140 MeV energy, the projected transverse emittance measured is $\varepsilon_{nx} = 1.52 \pm 0.05$ mm mrad and $\varepsilon_{ny} = 2.3 \pm 0.1$ mm mrad. The error on the emittance is estimated from the error propagation of the variance of the measurement error and accounts only for the statistical part. The high value of the projected emittance obtained with this charge is mainly due to inhomogeneities on the cathode surface.

Analysis of the Systematic Effects

The goodness of the least square fit on the experimental data is evaluated by backtracking the results in order to estimate the rms beam size on the flag F_0 at the end of the linac, where a comparison with a direct measurement can be performed.

* Work supported by MIUR Contract RBAP04XM5-001
† enrica.chiadroni@lnf.infn.it

In the case considered in Fig. 2, the beam has a regular distribution as also shown from its projection (Fig. 3).

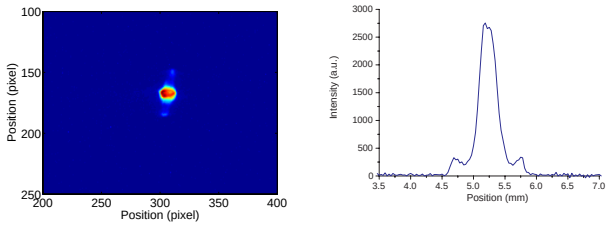


(a) (b)

Figure 3: Vertical (a) beam waist of a typical beam and its projection (b) as the one analysed for the emittance measurement. The pixel calibration is 31.25 μm/pixel.

It is then found that the agreement between the back-tracked and the measured rms beam size at the end of the linac agrees within 3% in the horizontal and 7% in the vertical plane. The worse agreement in the vertical plane is also confirmed by the calculated reduced χ^2, 6 in the vertical plane with respect to 1 in the horizontal one.

Depending on the laser beam alignment on the cathode, the beam exhibited "side structures" due to strong disuniformities in the emission from the cathode (Fig. 4).



(a) (b)

Figure 4: Beam with side structures in a region close to the vertical waist (a) and its projection (b). The pixel calibration is 30.30 μm/pixel.

These tails behave differently changing the focusing strength: they overlap into the beam core in the waist and get further from it as the focusing power weakens. Fig. 5 shows the quadrupole scan in the vertical direction. Here the different behavior of the tails results in a "bump" close to the waist, where they are taken into account in the calculation of the rms beam size.

Two-quadrupoles Compared to One-quadrupole Scan

The main advantage in using two quadrupoles as a doublet in the emittance measurement is that, if the beam has a round shape, it preserves its symmetry during the scan and the emittance can be measured simultaneously in both planes. However, in order to observe a waist in both planes, the range of currents considered is wider, i.e. the focusing

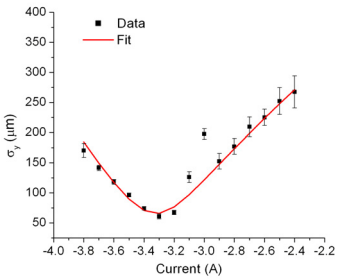


Figure 5: Quadrupole scan showing the effect of a beam with side structures (300 pC, 141 MeV).

strength is stronger and the beam undergoes a stronger focalization.

At this regard a quadrupole scan with a single quadrupole has been done (Fig. 6 shows the horizontal plane) and the results have been compared to the scan with two quadrupoles (Fig. 7(a), black squares). These measurements have been done with a beam of 200 pC charge, 7 ps FWHM pulse length and 145 MeV energy.

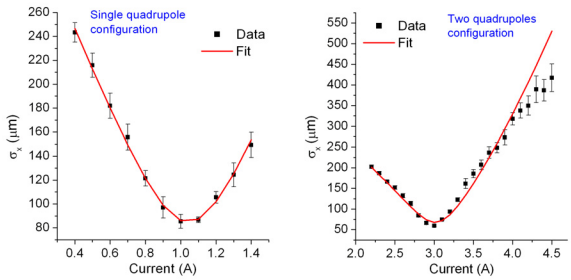
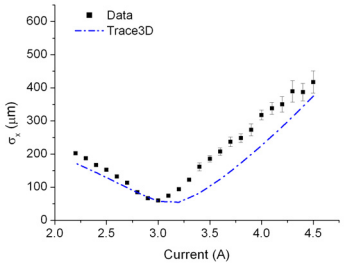


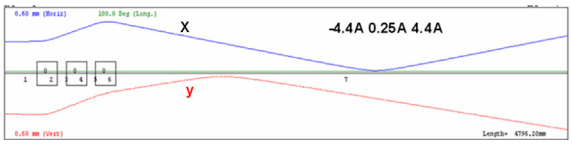
Figure 6: Quadrupole scan in single magnet and two magnets configuration. (200 pC, 7 ps FWHM pulse length and 145 MeV).

The Twiss parameters measured in the single quadrupole configuration have been then used as starting point for the TRACE3D simulation of the quadrupole scan with two quadrupoles. For the points before the waist, Fig. 7(a) shows a good agreement between measurements done in the single quadrupole and two quadrupoles configurations. After the beam waist, where the focusing strength is more intense, a non perfect agreement is observed. In the worst case, the emittance measured in the two quadrupoles configuration results to be about 30% higher than the one from single quadrupole scan.

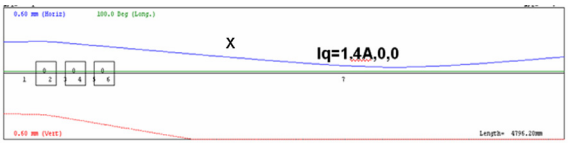
Fig. 7, (b) and (c), shows how between the quadrupole triplet and the flag F_1, the beam, due to the higher focusing strengths, undergoes a more abrupt focalization in the two quadrupoles configuration with respect to the single quadrupole one, emphasizing those effects like chromaticity which depend on the quadrupole intensity. More systematic investigations on this comparison are needed.



(a)



(b)



(c)

Figure 7: (a) Two magnets quadrupole scan compared to a TRACE3D simulation. (b), (c) Trace 3D envelope in the two quadrupole and single quadrupole configuration, respectively. The y axis extends from 0 to 0.6 mm for both x and y envelope curve. 200 pC, 7 ps FWHM pulse length and 145 MeV.

SLICE EMITTANCE

The quadrupole scan technique, combined to the radio-frequency deflector (labeled as *RFD* in Fig. 1) [3], allows also the investigation of the beam slice emittance. By powering the RFD, the beam is vertically deflected and a quadrupole scan is performed only in the horizontal direction, with the constraint of keeping constant the vertical beam size over the whole scan. The vertical beam size with the RFD off, rescaled by the RFD calibration coefficient, defines the resolution of the measurement. In Fig. 8 the slice emittance measurement (blue dots) for the beam considered in Fig. 2 and a laser spot size on the cathode of 320x300 μm rms is compared with a PARMELA simulation performed assuming 150k particles, a rms thermal emittance ϵ_{th}=0.75 mm-mrad per radius (mm) and a slice length of 200μm.

LONGITUDINAL EMITTANCE

The SPARC RFD with deflection plane in the vertical direction, combined to the horizontal dispersive region represented by the dipole (labeled as *D* in Fig. 1), allows to measure the longitudinal trace space in a single shot [5]. A typical measurement at SPARC is shown in Fig. 9 and by means of a 2D image analysis the beam longitudinal emittance can be retrieved. In the actual working point of

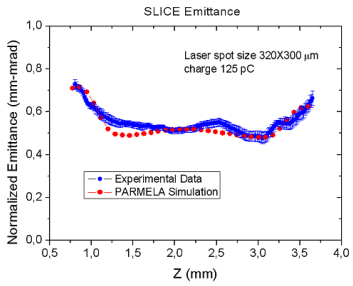


Figure 8: Slice emittance measurement compared to a PARMELA simulation. Z is the longitudinal position along the beam.

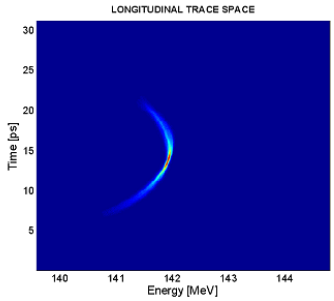


Figure 9: Longitudinal trace space at 140 MeV.

1.5 MV in the RFD, the estimated longitudinal emittance is about 209 mm-keV in good agreement with the simulation.

CONCLUSIONS

The tools for characterizing the 6D SPARC phase space at the end of the linac, where a 140 MeV energy is reached, have been completed. In the present operation we were limited by a strong transverse disuniformity on the cathode, which results in high values of transverse emittance. The goodness of the χ^2 test on the experimental data has been validated by the good agreement between the rms beam size measured at flag F_1 and the those retrieved by back-tracking to the flag F_0. A preliminary comparison between the two quadrupoles and single quadrupole scan has been done. More investigations are planned.

REFERENCES

[1] SPARC Conceptual Design Report, January 2004 - `http://www.lnf.infn.it/acceleratori/sparc/`.

[2] M. Minty and F. Zimmermann, "Measurement and control of charged particle beams", Springer (2003) p. 99.

[3] D. Alesini et al., Nucl. Instr. and Meth. in Phys. Res. A **568** (2006) 488.

[4] B. Marchetti et al., "Beam Slice Characterizazion at SPARC High Brightness Photoinjector", PAC'09, Vancouver.

[5] S. Korepanov, D. Alesini et al. "An RF Deflector for the Longitudinal and Transverse Beam Phase Space Analysis at PITZ", DIPAC'07, Venice.

SCREEN MONITOR DESIGN FOR THE SwissFEL

R. Ischebeck, B. Beutner, B. Steffen, V. Schlott, Paul Scherrer Institut, Villigen, Switzerland

Abstract

A screen monitor containing OTR foils and scintillator crystals has been designed to measure the transverse profile of electron bunches in the SwissFEL. In conjunction with quadrupole magnets in FODO cells and a transverse deflecting structure, the screen monitors will be used to measure transverse and longitudinal phase space projections of the electron pulses in the 250 MeV Injector. Tomographic methods will be used to reconstruct the phase space distributions.

INTRODUCTION

Paul Scherrer Institut is planning a free electron laser for X-Ray wavelengths, the SwissFEL [1]. The baseline design foresees to generate electron bunches with a charge between 10 and 200 pC and a normalized emittance below 0.4 μm in an RF photocathode gun. These bunches will be accelerated in a normal-conducting linear accelerator (linac) to a particle energy of up to 6 GeV and sent through one of two undulators with 15 and 40 mm period, respectively, where they radiate coherently at wavelengths between 0.1 and 7 nm. The repetition rate of this device will be 100 Hz initially, with an option to upgrade to 400 Hz. The baseline design foresees one electron bunch per RF pulse, but future extensions could allow for up to three electron bunches.

To test the feasibility of the concepts behind the generation of such high-brightness beams, their longitudinal compression and the preservation of the emittance, a 250 MeV Injector is currently being assembled. Commissioning will start early 2010, and by the end of the year PSI will submit a proposal to build the SwissFEL to the Swiss Government.

The 250 MeV Injector will have three diagnostic sections: one directly after the RF photocathode gun, at a particle energy of 7 MeV, one before and one after the bunch compressor, at an energy of 250 MeV (see Fig. 1 and Table 1). The repetition rate of this accelerator will be 10 Hz. Ideally, one would like to know the entire phase space distribution of the bunches, i.e. the phase space coordinates of each electron in the bunch. However, no method exists to measure the entire distribution directly. Instead, the distribution is projected onto sub-spaces such as the (x, y) plane which will be measured by screen monitors or the time axis which will be measured by coherent radiation and by electro-optical methods. Phase space transformations are applied to the electron beam prior to the measurements to infer the distributions in the other dimensions. If these transformations are linear, they can then be described by a matrix formalism. By scanning these transformations and measuring projections at each step, a Radon transform of the phase space distribution is acquired. Inverse Radon transformations are used to reconstruct the phase space. Maximum entropy methods [2] are particularly useful because there are often relatively few projections, which are furthermore not uniformly distributed.

SCREEN MONITORS

A total of 32 screen monitors will be built for the 250 MeV Injector. Besides measuring projected and slice emittance, they serve as prototypes for optical monitors of the SwissFEL. Screens convert the transverse electron distribution into visible light. At particle energies around 7 MeV in the gun region, scintillating crystals are used to image the beam. For higher energies, the scintillators will

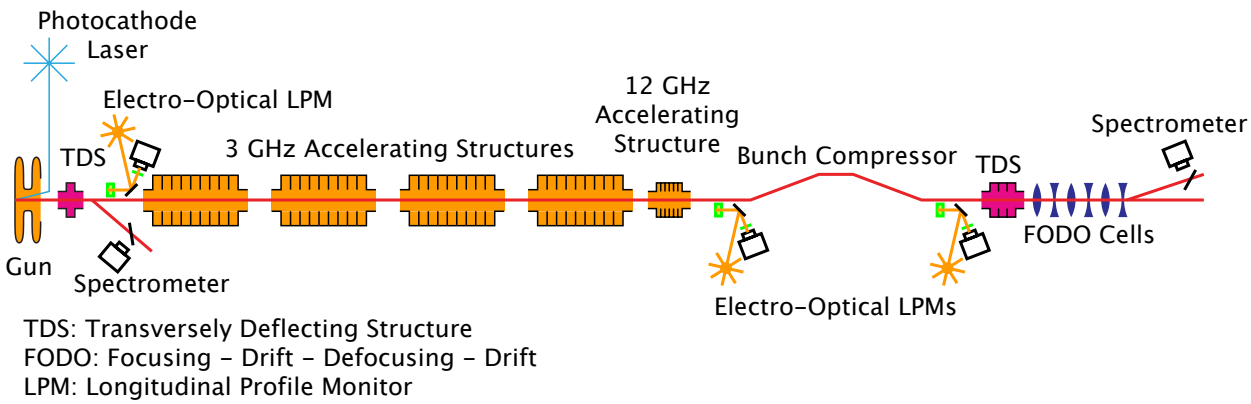


Figure 1: Schematic overview of the diagnostics for the 250 MeV Injector.

Table 1: Overview of the Diagnostics Planned for the 250 MeV Injector. BBC: before bunch compressor, ABC: after bunch compressor.

Quantity	Method	Gun	BBC	ABC	Notes
Projected emittance	OTR screens, phase advance scan, quadrupole scan	√	√	√	Alternatively, phosphor screens may be used
	OTR screens, FODO lattice			√	
	Wire scanners, phase advance scan	√	√	√	
Horizontal slice emittance	Transverse deflector, OTR screens, quad scan or FODO lattice	√		√	Bunch compressor is horizontal
Bunch length	Electro-optical	√		√	non-destructive, single-pulse
	Transverse deflector	√		√	
Bunch arrival time	Bunch arrival monitor		√	√	
Transverse position	BPMs	√	√	√	non-destructive, single-pulse
Energy spread	Spectrometer dipole	√		√	
Slice energy spread	Transverse deflector, spectrometer dipole	√		√	
Charge	ICMs	√	√	√	non-destructive, single-pulse
	OTR screens	√	√	√	It will have to be seen whether this measurement is affected by COTR
	Phosphor screens	√	√	√	Saturation of the phosphor may affect this measurement

be complemented by optical transition radiation (OTR) foils and wire scanners. The screens are mounted to a ladder and positioned in the beam with a vacuum feedthrough by a stepper motor actuator. The position is monitored by an absolute encoder mounted to the feedthrough. A scale engraved in the ladder serves both as a focusing target and as pixel size calibration. In the gun region, the scintillators are mounted at right angle to the beam; a mirror reflects the light out of the vacuum chamber. For the high energy diagnostic sections (located around the bunch compressor), the screens are mounted at an angle of 45° to the beam; OTR is emitted at a right angle through the vacuum window. The cameras will be able to image either screen, depending on the position of the screen ladder. Figure 2 shows the designs of the screen holders.

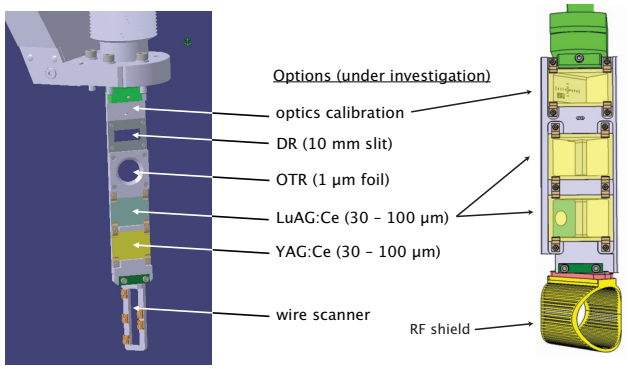


Figure 2: Screen holders for the low-energy diagnostic area (left) and the high-energy diagnostic areas (right). Several screens are available for the different operating modes.

CAMERAS AND OPTICAL SYSTEMS

The wide parameter range in beam sizes and the wide dynamic range in the expected intensity requires different methods for imaging and detection of the light. At each screen monitor location, two cameras can be installed, with a removable beam splitter for selection: An overview system that images the entire screen with reasonable resolution (projected pixel size 23 μm) will be used during commissioning and to find the beam if it is off center. This can be achieved with commercially available perspective control lenses, which at the same time allow for correction of the inclined object plane in the high-energy diagnostic sections. For screens where a higher resolution is required, a second camera that images the central part of the screen is used. In the gun region, where the screens are at right angle to the optical axis, commercial micro-photo lenses will be used. Screens in the 250 MeV diagnostics areas are at an angle of 45° to the optical axis. An optical system that corrects for this tilt and images these screens with a 1:1 imaging ratio is currently being investigated. Three types of photodetectors are under investigation:

- Room temperature CCDs are the baseline design. They are able to detect scintillation light and OTR at high bunch charges.
- Room temperature CMOS detectors offer exposure times down to 50 ns and may be used to distinguish individual electron bunches emitted during a single RF pulse, as well as to map dark current from the cathode.
- Cooled CCD detectors have a superior signal-to-noise ratio and offer therefore the possibility to use OTR at low bunch charges, or to measure bunches dispersed by the RF deflector.

CONTROLS

The screen monitors are controlled and read out by the EPICS control system [3]. Camera readout is not done by a realtime operating system, but a special hardware trigger will allow to synchronize the data stream with all other devices in the linac. This way, a pulse-to-pulse correlation can be established. Images can be displayed at a rate of 1...2 Hz, and simple analysis procedures can be performed in real time. For further analysis, the data can be written to HDF5 files, compatible to the Nexus format [4].

DATA ANALYSIS

Phase space transformations in the (x, x') and (y, y') planes are controlled by quadrupole magnets. By scanning multiple quadrupole magnets, or in FODO cells, the phase space is rotated while the beam size is kept constant. Thus, a Radon transform of the phase space is acquired. An inverse Radon transform, based on the maximum entropy algorithm, is used to reconstruct the phase space [5]. Two transverse deflecting RF structures will be installed in the 250 MeV Injector, one in the gun region and one behind the bunch compressor. Both allow to streak the beam vertically, i.e. do a (y, y', t) phase space transformation. With this additional transformation, the longitudinal bunch structure as well as the slice emittance can be measured.

FUTURE DEVELOPMENTS

Coherent optical transition radiation is possible for high bunch compression ratios, resulting in ultra-short bunches of femtosecond duration. This effect depends strongly on the wavelength of the radiation, and simulations have not yet predicted where the cutoff wavelength will be for the monitors in the 250 MeV Injector and the SwissFEL. To pursue research in this topic, we are considering the construction of an Offner imaging system based on reflective optics (Fig. 3). This would allow imaging the OTR source at a wide range of wavelengths.

An alternative refractive microscope system allows to image an object plane inclined by $45°$ to the optical axis onto a CCD at $90°$. Optimization and determination of such a system are ongoing.

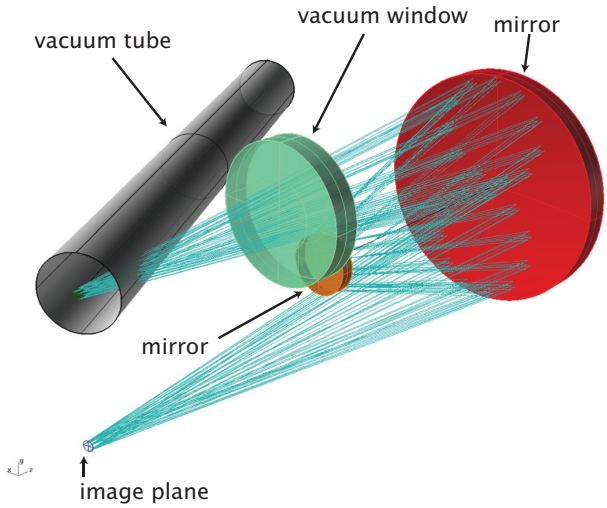


Figure 3: Offner reflective optics to image OTR over a wide wavelength range.

ACKNOWLEDGEMENTS

The authors would like to thank Dipl.-Ing. Jakob Neubert for optical design work, Federico Piffaretti for the mechanical design as well as Markus Baldinger and Albert Kammerer for the installation of a prototype monitor.

REFERENCES

[1] Paul Scherrer Institut, SwissFEL, `http://fel.web.psi.ch`, 2009.

[2] G.N. Minerbo, "MENT: A Maximum Entropy Algorithm for Reconstructing a Source from Projection Data", Comp. Graphics Image Proc., 48, 1979.

[3] Andrew Johnson, "EPICS – Experimental Physics and Industrial Control System", `http://www.aps.anl.gov/epics`, 2009.

[4] Mark Könnecke and Uwe Filges, "NeXus Software Status", `arXiv:physics/0210072v1`, 2002.

[5] J.J. Scheins, "Tomographic Reconstruction of Transverse and Longitudinal Phase Space Distributions Using the Maximum Entropy Algorithm", Technical report, DESY, 2004.

UNDULATOR RADIATION MEASUREMENTS AT LCLS USING *K*-EDGE X-RAY ABSORPTION TECHNIQUES*

A.S. Fisher#, J. Frisch, R. Iverson, H. Loos and J. Welch
SLAC National Accelerator Laboratory, Menlo Park, CA, USA

Abstract

The sharp *K*-edge absorption energies in nickel and yttrium were exploited at LCLS to measure spectral features of spontaneous and FEL x-rays. By scanning the electron beam energy so that the first and third harmonic x-rays scanned across the nickel and yttrium *K*-edges, the resulting spectral features allowed the precise determination of the position of central ray and the resonant photon energy.

BACKGROUND

The LCLS is in the final stages of commissioning. We have been producing strong FEL x-ray beams with most of the complement of undulator segments installed, but the full suite of x-ray diagnostics has not yet been available. However, we are getting information about the x-ray beam properties from a temporary YAG crystal/camera combination and an insertable nickel foil. This timely information serves to confirm our expectations for the properties of the undulator radiation, provides initial photon-energy calibrations, and provides pointing data needed for precise undulator-strength comparisons to be made in coming weeks as the new x-ray diagnostics are commissioned.

THEORY AND METHOD

X-rays that have energy just sufficient to excite electrons bound in the *K* shell of an atom (the *K*-edge energy) are preferentially absorbed by the atom compared to x-rays whose energy is just below the *K*-edge. Figure 1 shows an example of the sharp change in transmission at the *K*-edge of yttrium in a YAG crystal. At the LCLS FEL facility we generate both FEL and spontaneous undulator x-rays whose energy depends on the electron beam energy. By changing the electron beam energy, the energy of the resulting x-rays can be made to sweep across the *K*-edge energy either of the yttrium component of a cerium doped YAG crystal, or of a nickel foil that can be inserted into the x-ray beam.

X-rays absorbed in the YAG crystal generate visible photons, detected by a camera. If the photons have energies just above the yttrium *K*-edge, they are preferentially absorbed in the YAG and therefore cause a brighter area. When the nickel foil is inserted in front of the YAG crystal, photons with energy above the nickel *K*-edge are preferentially absorbed by the nickel and leave a relatively dark area on the YAG. In either case, the *K*-edges provide precise x-ray energy discrimination.

*Work supported in part by the DOE Contract DE-AC02-76SF00515, and performed in support of the LCLS project at SLAC.
#afisher@slac.stanford.edu

Of the two sources of x-rays used, FEL radiation is much simpler in that it consists mainly of a narrow beam of x-rays, primarily at the first harmonic. The spontaneous undulator radiation is more complex: spatially broader and consisting of many comparably strong harmonics. The on-axis, fundamental photon energy is determined from the resonance equation:

$$\lambda = \frac{\lambda_u}{2\gamma^2}\left(1+\tfrac{1}{2}K^2\right) \quad (1)$$

where λ is the x-ray wavelength, λ_u is the undulator period, γ is the electron energy in units of electron rest mass, and K is the undulator strength parameter (3.5, with some tunability, for LCLS). In the case of spontaneous undulator radiation, for angles small compared to K/γ, the spectrum contains many harmonics and is shifted by angle according to:

$$\lambda = \frac{\lambda_u}{2m\gamma^2}\left(1+\tfrac{1}{2}K^2+\gamma^2\theta^2\right) \quad (2)$$

Here θ is the angle from the central ray to the observation point and m is the harmonic number. From symmetry arguments, even harmonics must have no field on axis, while odd harmonics have a maximum on axis.

INSTRUMENTATION

The temporary diagnostic system shown in Fig. 2 is approximately 50 m downstream from the last undulator. This system contains, in order: a remotely controlled 1-μm-thick Be foil to block visible coherent light, a remotely controlled 10-μm Ni foil for *K*-edge measurements, and a fixed 100-μm-thick Ce-doped YAG crystal

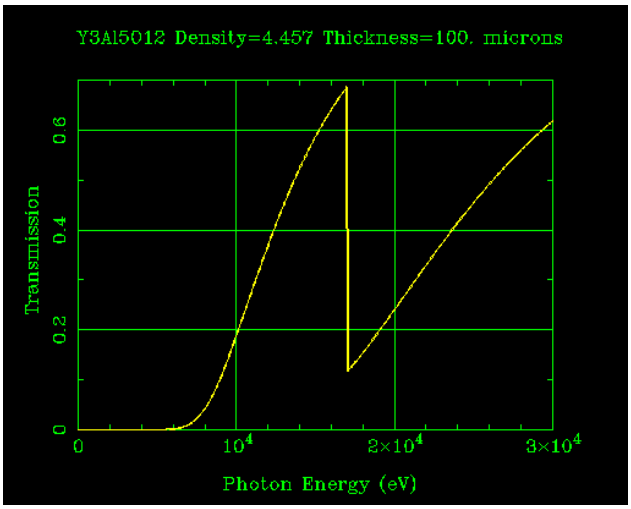


Figure 1: Transmission coefficient versus photon energy for YAG [2]. The yttrium K-edge occurs around 17 keV.

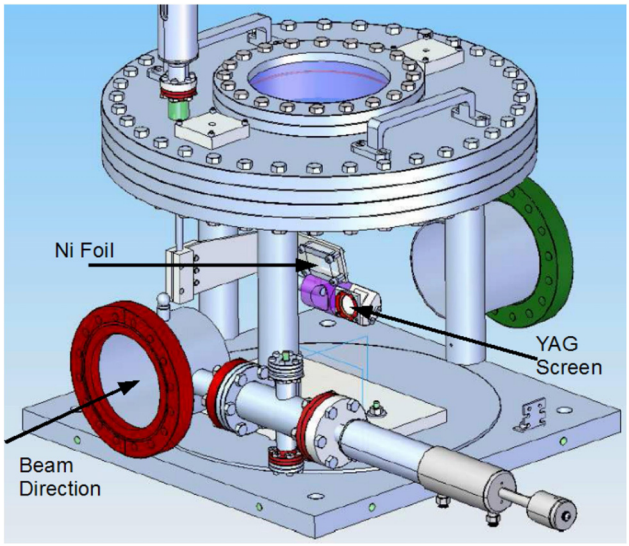


Figure 2: Temporary diagnostic assembly used in the measurements described this paper.

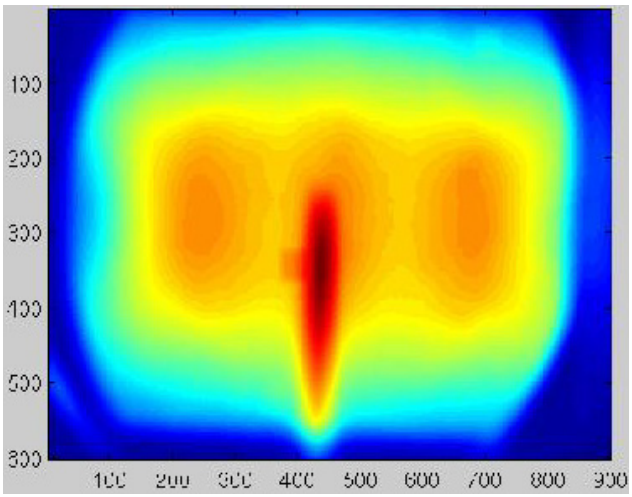


Figure 3: Spontaneous x-rays from one undulator segment as seen on the YAG crystal about 50 m downstream of the undulator. The central red stripe is cause by synchrotron radiation from the last dipoles. The three orange "humps" are the spatial signature of the 3rd harmonic.

as a fluorescence detector. A camera with 12-bit intensity resolution images the YAG at normal incidence using a mirror directly behind the crystal.

MEASUREMENTS

X-ray spatial and spectral measurements are described in this section. Most involve very effective image subtraction and smoothing techniques.

Harmonic Spatial Distributions

Angle-energy correlation of spontaneous synchrotron radiation, combined with the spectral discrimination of *K*-edges can be used to image various spatial harmonics present in the undulator spontaneous radiation. For example, even without image subtraction, third-harmonic structure is clearly visible in the image of Fig. 3.

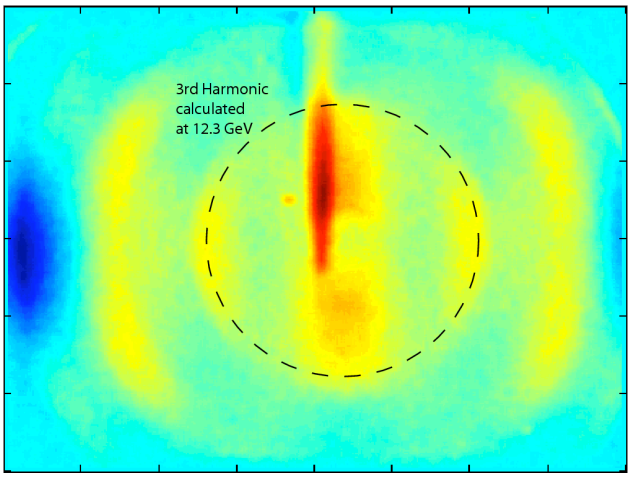


Figure 4: Difference of images taken with 12.3- and 11.3-GeV beams of spontaneous emission from one undulator segment. The dashed ring shows the predicted peak of 3rd-harmonic radiation, coinciding with the two partial rings in the image. Additional harmonics are also visible: the 2nd has two lobes above and below the middle, and the 5th harmonic appears as partial rings at higher angles.

Off-axis rays can be highly red-shifted. At high enough angles, several harmonics will have a resonant energy that is near the *K*-edge of the nickel foil. By subtracting images made with suitably chosen electron-beam energies, these harmonics become visible, as shown in Fig. 4, where we see three harmonics with the expected symmetries.

Determination of the Central Ray

Determining the central ray of spontaneous radiation is important in calibrating the x-ray energy spectrum and avoiding systematic errors when comparing two spectra. Even small errors, of order a few microradians, will shift the energy spectrum outside the tolerance of a few parts in 10^4 needed for undulator strength measurement.

The central ray has the most blue-shifted photon-energy spectrum. Figure 5 shows two images, taken with central energies just above and just below the nickel *K*-edge. While the central ray cannot be determined in either image alone, the difference image below gives a clear measurement of the position of the central ray from an undulator segment. X-rays emitted on axis have the highest energy spectrum and are the first to be preferentially absorbed by the nickel as the electron-beam energy is scanned upward. Figure 6 shows this clearly, with a dark central spot corresponding to the central ray. (Darkening also depends, of course, on using the appropriate sign in the image subtraction.)

FEL Spectrum

A calibration of the FEL photon energy around the first harmonic is shown in Fig. 7, where total intensity of the FEL image was plotted against the electron-beam energy

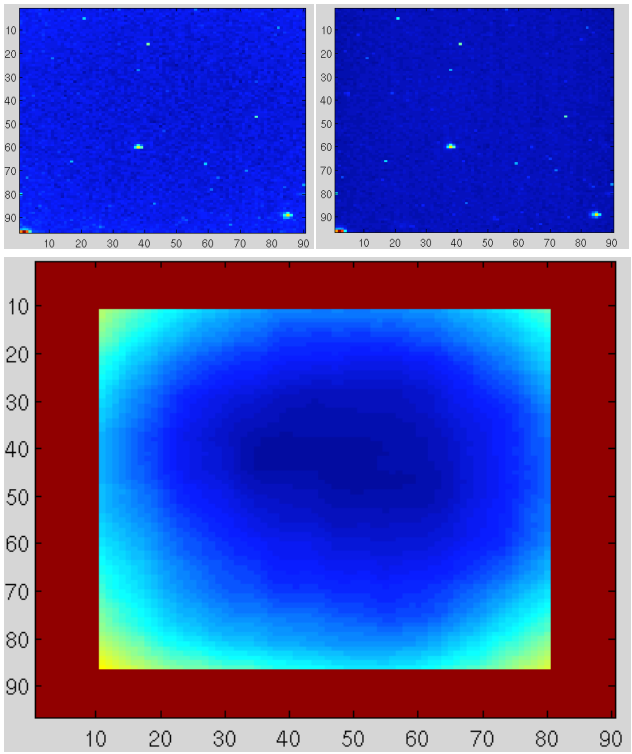


Figure 5: The upper two images were taken at slightly different electron energies corresponding to on-axis x-rays above (left) and below (right) the Ni *K*-edge. These are combined and filtered to produce a relatively clean image, shown enlarged in the lower frame, of only photons near the *K*-edge. The center of the resulting hole can be determined to within a few pixels.

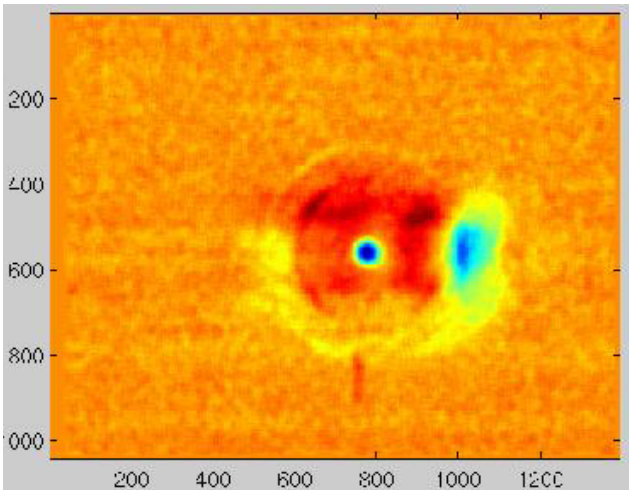


Figure 6: Difference image taken across the nickel K-edge. The dark central spot occurs coincides with the central rays from the undulator segment.

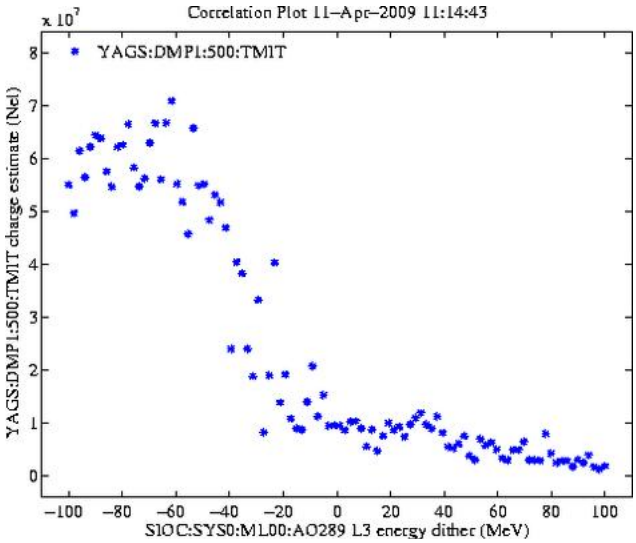


Figure 7: Energy scan of the FEL radiation, which is mostly 1st harmonic, incident on a 10-μm nickel foil. This scan calibrates the machine energy in GeV and the strength of the undulator segment against the nickel *K*-edge, where the transmission drops.

shift. When the electron energy is such that the central photon energy is right on the nickel *K*-edge, the signal drops by half. This occurs around −30 MeV relative to the electron reference energy of 13.740 GeV, i.e., at 13.710 GeV. Tabulated values give the *K*-edge of Ni at 8330 eV. If the true electron energy is 13.710 GeV, (the value derived from magnetic measurements of dipole magnets), then based on the design undulator period and measured strength, the resonant photon energy should be at 8363 eV—about 0.4% higher than the tabulated value. The difference could be explained by an error in the electron beam reference energy of 0.2%.

REFERENCES

[1] P. Emma, J. Welch, Z. Huang, H.-D. Nuhn, P. Stefan, R. Dejus, B. Yang and R. Bionta, Proc. FEL06, 2006.
[2] http://henke.lbl.gov/optical_constants/filter2.html

BEAM LOSS AND BEAM PROFILE MONITORING WITH OPTICAL FIBERS

F. Wulf, Helmholtz-Zentrum Berlin für Materialien und Energie, Germany
M. Körfer, DESY, Hamburg, Germany

Abstract

Beam losses and beam profiles at particle accelerators are determined by measuring the ionizing radiation outside the vacuum chamber. Four different radiation sensor systems using optical fiber will be presented. Two are based on the increase of radiation-induced attenuation of (Ge+P)-doped multimode graded index fibers, whereas the other two systems detect the Cerenkov light generated by relativistic electrons penetrating radiation hard fibers. The used fiber is an undoped multimode step-index fiber with 300 µm core diameter. Dosimetry at high dose levels uses the radiation induced Bragg wavelength shift of Fiber Bragg Gratings. The selection of a suitable fiber for the individual application is an important requirement and depends on the type, doping, used wavelength and annealing behavior. In addition, the dose range, dose rate and temperature must be considered. After an extensive selection procedure, two types of fibers for the particular application were chosen. One is used as a dosimetry sensor for the *slow* local and distributed beam loss position monitor (BLPM) and the other for *fast* beam loss monitor (BLM) as well as beam profile monitors (BPM). At six accelerators, all systems are used for in-situ particle loss control by measuring the ionization dose and/or Cerenkov light. These monitors provide a technique to improve the beam performance. This paper summarizes the basics of these measurement technologies and the experience at linear accelerators and at storage rings.

INTRODUCTION

Beam loss monitor systems (BLM systems) are an essential part of linear accelerators and storage rings. They allow the understanding of beam loss mechanisms during commissioning and operation and provide an option for an emergency shutdown. A proper understanding of beam loss events can improve machine performance, which consequently reduces also the radiation level for the used accelerator components. Well-known beam loss systems [1], like a) long and short ionization chamber, b) combination of scintillator and photomultiplier and c) PIN photo-diodes, d) scintillation counter, e) electron multipliers, f) cryogenic calorimeters have still some deficiency [2,3,4,5,6,7]. They do not cover the complete sections of the accelerator, particularly large undulator systems, and have an insufficient position and time resolution. It would be of great advantageous to monitor continuously on-line localized beam losses around the complete accelerator complex. Particular total dose measurements at the susceptible undulator magnets are desirable because they are made of radiation sensitive alloys. With in the framework of the TESLA/ILC (International Linear Collider) [8] and FLASH (Free-Electron-Laser Hamburg) [9] design study. New concepts of BLM systems based on special types of optical fiber sensors were developed [10,11,12]. They have been tested during real operation at different accelerator facilities*.

OPTIMIZATION AND SELECTION OF OPTICAL FIBERS

Since 30 years it is well known that the radiation induced attenuation (RIA) of particular optical fibers [13,14,15,16,17,18,19] is a function of the total ionization dose (TID). This mechanism allows a reliable dose measurement up to a level of a few thousand Gray. For high dose applications the changes of the refractive index or Bragg wavelength shift (BWS) can be used. The radiation induced emission of Cerenkov light or luminescence mechanism are used for fast detection of radiation sources without calibration of TID. Fibers can also be made sensitive for thermal and fast neutrons [20,21,22]. The nonsatisfying applications in the past rely at most on insufficient knowledge and control of the producing process of the fibers. An individual characterization of each lot is therefore indispensable. This is a key function for further usage of fiber radiation sensors. The influence of core material, cladding thickness, drawing speed of the fiber and coating material of pure silica core step-index fibers have been investigated in detail [23].

CLASSIFICATION OF BEAM LOSS MONITOR SYSTEMS

As shown in Fig. 1 the BLM systems are distinguished in two categories. One system measure the TID generated by the beam losses as a function of RIA. With an optical power meter, the RIA is measured at local position along the beam line, especially at the undulator. The resolution of the absorbed dose of the so called *local sensor system* is about 60 mGy with an updating time - depending of the number of used sensors - in the range of ms [25]. The *distributed sensor system* makes use of Optical Time Domain Reflectormeter (OTDR) measurements. As a result of the attenuation measurement, the position and TID along the beam line or undulators can be calculated. At FLASH, typical sensor length is less then 100 m. The update time is in the range of some seconds with a position resolution of about 1.5 m. The dose resolution for the presented measurement setup is about 3 Gy [25]. The system of the second category detects the generated Cerenkov light in the fiber over a length of about 40 m with a

* PITZ, MAX-LAB, BESSY II, DELTA, SLS

position resolution of 25 cm, a response time below millisecond and a time resolution of nanosecond. This short time response makes the system also applicable for emergency shutdown.

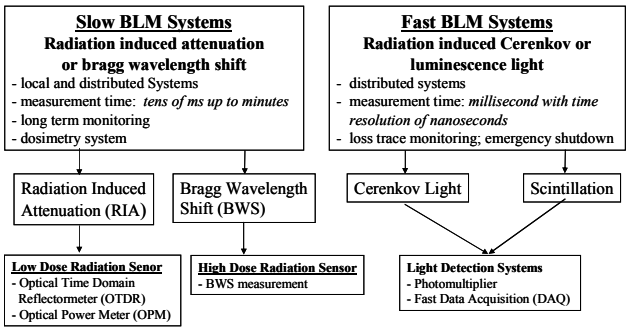


Figure 1: Classification flow chart of beam loss monitors systems using optical fiber sensor.

SLOW BEAM LOSS MONITOR SYSTEMS (DOSIMETER SYSTEM)

Slow BLM (response time between ms and minutes) require a dosimetry fiber with an excellent linearity between the TID and the RIA. They must have a large dose range in combination with small fading and annealing behavior respectively. The fiber must be insensitive against dose rate, temperature and radiation type and their energy. The simultaneous usage of the same fiber for the local and distributed sensor beam loss monitor system requires also a selection with respect to the bandwidth of the fiber. Low bandwidth show higher mode dispersion and increase the pulse broadening of the light pulse, which reduces the achievable position resolution. With an Optical Time Domain Reflectormeter using a 3 nm pulse width and a laser wavelength of 850 nm, a bandwidth of 800 MHz ∗ km is sufficient [24]. The long term experience at the FHG INT[#] and HMI[#] in optical fiber characterization facilitate the collaboration to an intensive selection process. As a result, for the dose measurement a (Ge+P) doped multimode gradient-index (MM GI) fiber [25] and for the measurement of the Cerenkov light a multimode step-index fiber (MM SI) [32, 33] was selected.

The following function approximates the RIA of fibers:

$$RIA\ [\mathrm{dB/m}] = c\,(\lambda) \bullet D^{f(\lambda)} \qquad [26]\ (1)$$

The constant c [dB/m Gy] expresses the radiation sensitivity, which is a strong function of the used measurement wavelength λ [nm] and D [Gy] the accumulated dose. The exponent f is the linearity factor close to 1 for fibers with low annealing effect. The fitting parameters for the MM GI fiber are:

λ= 678 nm: c = 0.0369 dB/m Gy, f = 0.972 and for
λ= 829 nm: c = 0.0042 dB/m Gy, f = 1.025

The fibers response passes into a non-linear function above a RIA level of 1 kGy and saturate at higher dose level. It was shown, that the RIA of a P-doped MM-GI covered with a heat resistant polyimide coating can be regenerated in short time at temperatures above 350°C with very little changes of their optical properties [27].

Local Dosimeter Systems

The functional principle of the local sensor system developed for sensitive TID measurements at selected accelerator positions is shown in Fig. 2. The sensor fiber is linked by radiation resistant fiber to the light source and on the other side to the optical power meter. For temperature control and calibration of the set up, one fiber is directly connected between light source and power meter. A typical set up used at an undulator consist of 16 measurement channels. The light source guided to the 16 output pigtails of a 1:16 splitter made of 50/125 m GI fiber. Depending of the expected dose, the number of windings (typical 5-20) for each sensor can be adjusted. The coils of the sensor are mounted together with optical connectors on a holder (Fig. 3). This holder is mounted in prepared cut out of the vacuum chamber (Fig. 4).

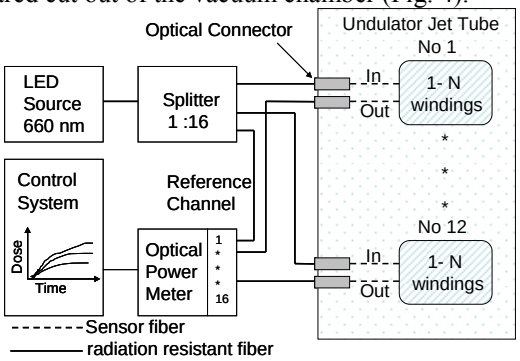


Figure 2: Functional principle of a local sensor system.

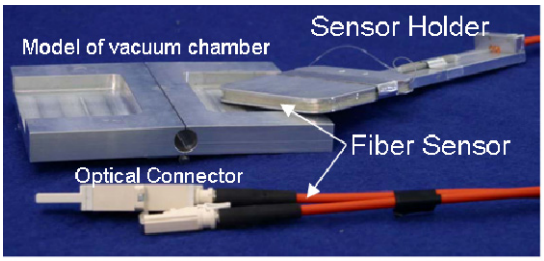


Figure 3: Sensor holder of the local sensor system.

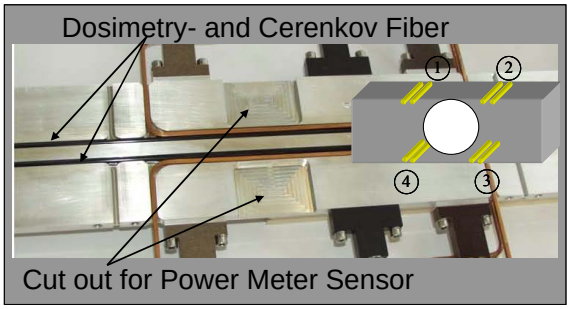


Figure 4: Detail of the vacuum chamber line of the undulator show the cut out for the power meter sensor, the OTDR and Cerenkov fiber.

Fraunhofer INT, Euskirchen, Germany, Hahn-Meitner Institut Berlin, now Helmholtz-Zentrum Berlin für Materialien und Energie, Germany

Each output of the sensor module is connected to a power meter, which is controlled by a PC [25] and the data are forwarded to the accelerator control system. The TID values of the local sensor with optical power meter are in good agreement with reference TLD measurements [25,28].

Local Dosimeter System for High Dose Measurement

Fiber Bragg Gratings can be used as radiation sensor in high dose environment by measuring the Bragg wavelength shift (BWS) as a function of the absorbed dose [29]. The influence of the production process leads to a factor of three in BWS using the identical process parameter. A variation of the process parameter provides a BWS difference of nearly a factor of ten [30]. Up to a dose level of 100 kGy the fiber show no saturation and is almost independent of the radiation dose rate. They can be used up to a level of 1 MGy [30].

Distributed Dosimeter System

With standard Optical Time Domain Reflectormeter technology, the change of the attenuation caused by the local irradiation along the beam line is measured. Only a few OTDR systems are available with adequate small pulse width and short wavelength combined with multi-mode modules[+]. The expected RIA and the dynamic range of the OTDR equipment defines the maximum sensor length for a given monitor section. Behind a fiber segment with a high RIA the following fiber section can not be measured. With a high precision optical switch many segments can be monitored with one OTDR system. At the FLASH undulator four fibers are placed in equidistant radial distance around the vacuum chamber (Fig. 4). That makes it possible to calculate the direction of the highest Bremsstrahlung level (highest beam loss) around the beam line. In the same way but with a larger distance to the beam line, four fibers are installed along the beam line.

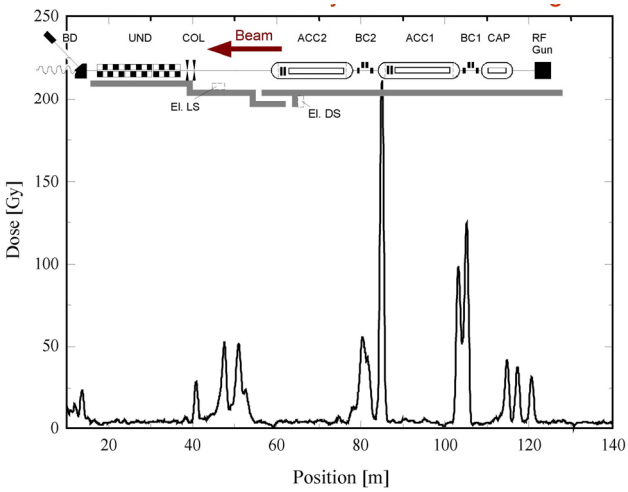


Figure 5: Measured TID along the entire beam line at the TESLA Test Facility, DESY Hamburg [31].

+ like Tektronix Fiber Master TFP2A

The accumulated dose during a long-term operation of 3 weeks at the TESLA Test Facility is shown in Fig. 5.

FAST BEAM LOSS MONITOR SYSTEMS (CERENKOV LIGHT)

Many previous publications describe the measurement of ionizing radiation by detection of the generated Cerenkov light in optical fibers. The implementation and systematic optimization of this technology was missing. The precondition is the selection of an optimal fiber as explained in the previous chapter. Two measurement systems are installed. The measurement set up for the undulator section and upstream beam line section is shown in Fig. 7. At the undulators four fibers are grouped together in equidistant radial distance around the vacuum chamber sharing the same cut outs with the OTDR fiber (Fig. 4). The fibers are connected in the tunnel to photomultipliers (PMT), which are selected with respect to their sensitivity.

Fast Beam Loss Monitor

Fast BLM require radiation resistant fiber with high bandwidth and large core diameter. Electrons with energies above 175 keV generate Cerenkov light in pure quartz fiber (n=1.46). Based on this effect, powerful BLM systems like beam loss position monitor (BLPM) [32] and beam profile monitor (BPM) [33] were developed. They use Fiber with pure silica core and high OH-content which are in general radiation resistant. However, F-doped fiber could reach higher radiation level without increasing the RIA [34]. The presented BLM systems use a multi-mode step-index fiber with a core diameter of 300 µm. The core diameter is a good compromise between the irradiation sensitivity and a required bandwidth. A black nylon buffer shields the fiber against the ambient light. The total diameter of the fiber is only 900 µm. In contrast scintillation fibers have high attenuations values and are radiation sensitive. This fiber type cannot be used for measurements over long distance or in applications with high dose level.

Typical curves of the Cerenkov light generated in the optical fibers over a length of six undulators during routine operation at FLASH are shown in Fig. 6.

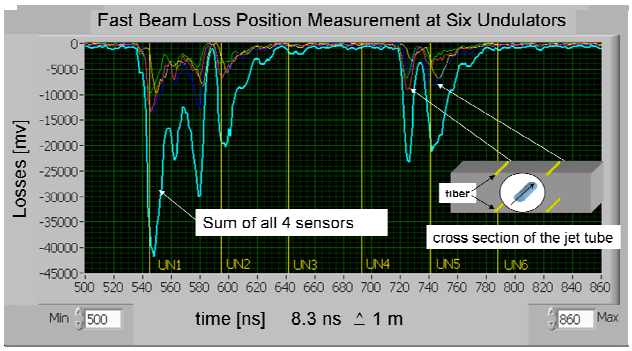


Figure 6: Screen shot at FLASH, in March 2009. At six undulators the Bremsstrahlung level at four positions is shown. An adjustable persistence mode improves the quality of the visualisation.

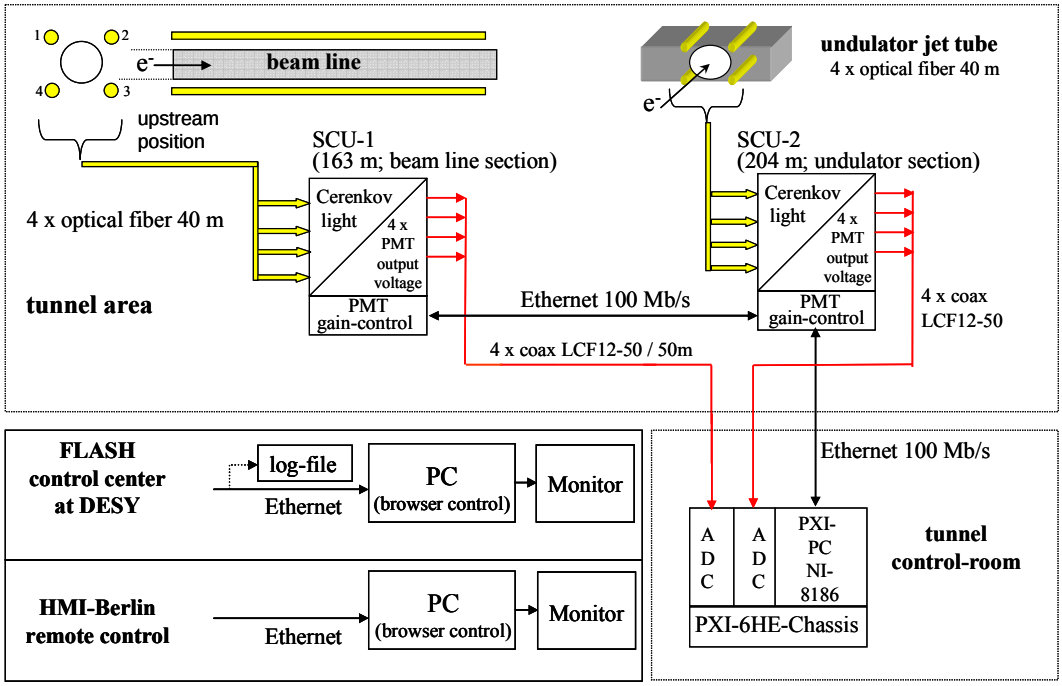


Figure 7: Measurement set up for BLPM and BPM at FLASH. One sensor group controls the undulator and a second one the beam line.

Measurement Set Up

The outputs of low noise preamplifiers are connected to fast ADCs (1 GS/s; 1 GHz bandwidth) installed outside the radiation area of the tunnel in a modular PXI-System. The system is synchronized with the bunch clock and controlled by an embedded CPU. The system is integrated in the FLASH control system. Selected events can be logged together with the machine status. Maintenance is executed via remote control from the HMI. This system is used for BLPM and BPM.

Beam Loss Position Monitor

The position of the radiation source is calculated by the time difference between a maximum peak height of the light pulse and the bunch clock trigger. The accurate location of the secondary shower with respect to the beam line layout can be determined by vacuum components like optical transition radiation (OTR) screen or wire scanner with their know position. It has been shown, that the position can be determined with an accuracy of about 25 cm measured at PITZ [35]. Due to the fact, that the velocity of relativistic electrons in vacuum (~ c) is higher than the light velocity in the fiber (~ 0.66•c) the measured light signals are expanded or compressed depending on the position of the PMTs relative to the beam line. If the PMTs are installed at the upstream position, the measured light signals are stretched by a factor of 2.5 relatively to the electrons in the vacuum chamber. Installing the PMTs at the downstream position, the signals are compressed by a factor of two. This gives the possibility to detect single bunches at the downstream position with five times higher repetition rate as at the upstream position. However, with the same bandwidth and sample rate the position resolution is than five times lower [36]. In Fig. 8 the principle result of BLPM measurement is shown. The losses are generated by an inserted OTR-screen. The intensity of the loss shower increases at the first quadrupole. The local minima of the signal are caused by the shielding effect of the components (quadrupoles, vacuum pumps e.g.) and transversal distance variation of the fiber with respect to the beam line. Nevertheless, using the maximum values of the signals, an envelope function can be calculated to define the direction of the centroid of the Bremsstrahlung shower as shown in Fig. 9.

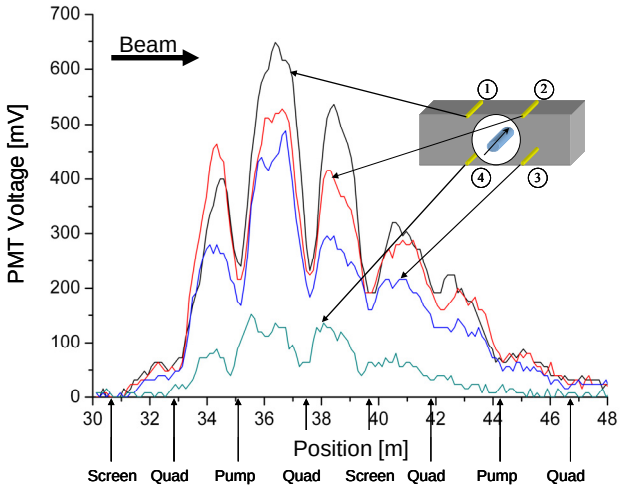


Figure 8: Typical results of the BLPM measurement at an interesting section of the beam line. The shielding effect of the beam components causes the minima of the signal amplitude.

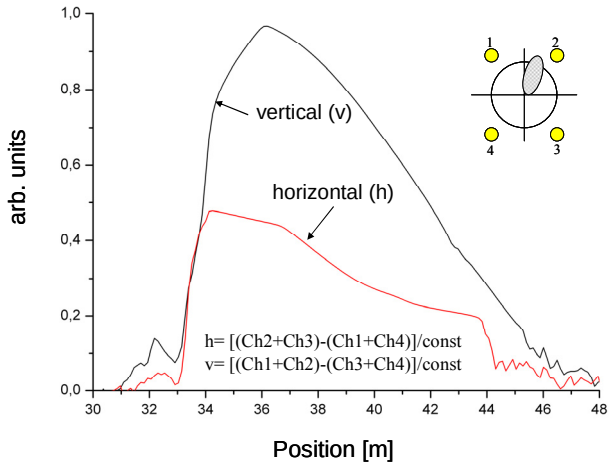


Figure 9: Enveloped function of the Bremsstrahlung shower as shown in Fig. 8.

Beam Profile Monitor

Beam profile measurement is an essential part of the beam diagnostic. Conventional systems use wire scanner systems (WS) [37] where only a fraction of the generated Bremsstrahlung in longitudinally direction is measured by a PMT at the end of a beam line section. The efficiency of this measurement principle is additionally reduced due to the shielding effect of the beam line components. The built in BLPM can be used to measure the Bremsstrahlung in the longitudinal as well as in the transversal direction, particularly direct after the wire scanner. The interesting parts of the beam are the beam core and tails. The measurement of the beam profile requires a large dynamic range of the detection system. In addition, parallel to the installed Cerenkov fiber group a second set of fibers are used. This gives the opportunity to measure at the same time with low and high amplification ranges of the PMT. This is necessary, because the sensitivity of the PMT after high illumination level needs a too long recovery time with respect to the fast movement of the wire scanner itself. Figure 10 shows the good correlation between measurements with standard WS systems and the new BPM system. Detailed experimental results are given in [33]. A novel pre-amplifier increases the sensitivity of the BPM system by a factor of 10. This offers more detailed information about the beam tails. The combination of BLPM and BPM using the same measurement system gives fast information about the beam quality.

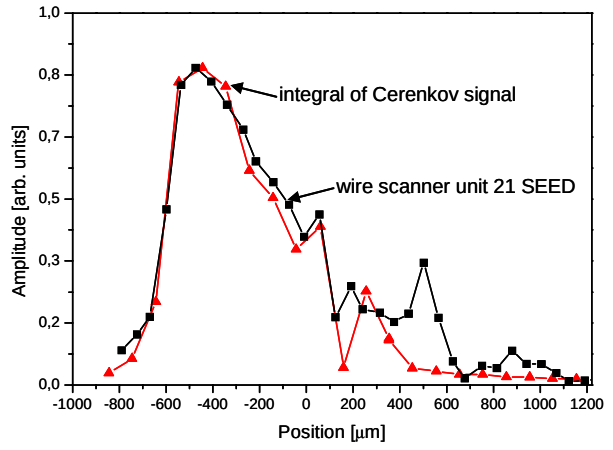


Figure 10: Horizontal beam profile measured with a standard wire scanner system compared to results obtained with an optical fiber BPM system. The maximum values are normalized. The measurements were taken one after another.

CONCLUSIONS

It has been shown that fiber used in *slow* beam loss monitor (BLM) systems - like distributed dosimeter system - and in *fast* BLM systems - like beam loss position monitor (BLPM) and beam profile monitor (BPM) - are useful tools for the optimization and control process of particle accelerators. In general, fiber sensors can be used in nearly inaccessible gaps or regions with high electrical or electromagnetic fields. It is an indispensable precondition, that a careful selection of the sensor fiber is necessary to meet the essential requirements. The local dosimeter system can be placed anywhere with individually adapted sensitivity and detection area. These sensors measure local doses with a resolution of some tens of milligrays in real time. Various numbers of sensors - connected together via an optical switch and splitter - can be measured in few milliseconds. Distributed dosimeters use the same fiber type. The fibers are installed up to several hundred meters along the accelerator beam line, tunnel or undulators, measuring the total ionization dose (TID) down to a few Gray with a position resolution of about 1.5 m. The measurement time is in a range of some minutes, depending on the required dose accuracy. The system is applicable to supervise the radiation level of the total accelerator environment. The (Ge+P) doped multimode gradient-index fiber with a heat resistant polyimide coating can be regenerated with very little changes of their optical properties. In a high dose environment the usage of Fiber Bragg Gratings seems to be a possible solution.

Fast BLM systems like BLPM and BPM enable the operator to control the beam loss along the entire beam line in transversal and longitudinal dimensions. It allows the identification of single bunches within one bunch train. The system response is in the range of millisecond with a time resolution of nanoseconds and a position resolution of about 25 cm. This allows an interactive control of the beam optimization process and gives the opportunity to trace the stability over all setting parameters of the beam. In addition, this system is applicable for fast emergency shut down. Optimized BPM systems provide a beam profile measurement with higher sensitivity to the beam core and beam tail compared to FLASH undulator wire scanner system. The important parameters of BLM with optical fibers are summarized in table 1. In the last years the presented BLM systems are not only used at FLASH but also at PITZ at DESY Zeuthen [35], Germany, MAX-Lab [38], Lund University, Sweden and at storage rings at BESSY II, Berlin, Germany and DELTA [39,40] in Dortmund, Germany.

ACKNOWLEDGEMENT

The development of the beam loss monitor systems was initiated by the Hahn-Meitner Institut Berlin - new name since 1.1.2009: Helmholtz-Zentrum Berlin für Materialien und Energie (HZB) - in collaboration with the DESY, Hamburg and the Fraunhofer Institut Naturwissenschaftlich-Trendanalysen (Fraunhofer INT), Euskirchen. We thank W. Goettmann of HZB, H. Henschel, J. Kuhnhenn, U. Weinand, O. Köhn, of Fraunhofer INT, and R. Awwad, of DESY, for the strong engagement over many years developing the powerful measurement set ups, data acquisition systems, the optimization and selection process of optical fibers and valuable contributions to the successful execution of this challenging research project.

Table 1: Summary of the Beam Loss Monitor Systems

Application	Slow BLM Systems			Fast BLM Systems
	Distributed Dosimeter System	**Local Dosimeter System**	**Local Dosimeter System (High Dose)**	**Beam Loss Position Monitor and Beam Profile Monitor**
Measurement principle:	Optical Time Domain Reflectormeter	Optical Power Meter	Bragg Wavelength shifting (Δ BWS)	Cerenkov Light
Bunch resolution	No	No	No	Yes, within one train
Measurement time (detection response)	minutes	ms to minutes	ms to sec	≤ ms with time resolution of 1 ns
Range of maximum dose TID [Gy]	3 – 450 limited by OTDR	0.06- 2000 limited by fiber type	$2 * 10^3$- 10^6 limited by fiber type	only a rough estimation possible, fiber can used until $1 * 10^5$
Wavelength range	850 - 1330 nm	860 nm	820 nm - 1,55 µm $\Delta\lambda_B$ = 5-350 pm	200 - 850 nm
Position resolution	1.5 m	0.05 m	0,5 m	0.25 m
Reasonable fiber length*	≤ 5 km typical ≤100 m sections	-	-	≤ 1 km typical 50 - 100 m sections

* Depending on max. Dose and required position resolution

REFERENCES

[1] K. Wittenburg, "Beam loss monitoring and control", Proceedings of the 8th EPAC 2002, Paris, France, pp 109-113.

[2] K.Wittenburg, "Beam loss detection", Proc 1st DIPAC93 CERN PS/93-35 (DB) pp11-20.

[3] B.Joly, U.Weinrich, G.A.Naylor, "Beam loss monitors at the ESRF", Proc. DIPAC 1999, Chester, UK, IT 3, pp 3-6.

[4] H.Burkhardt, "How to use Beam Loss Monitors at the LHC?" Proc. Chamonix XI Workshop, Jan. 2001, CERN-SL-2001-003 DI.

[5] P. Michel, J. Teichert, R. Schurig, H. Langenhagen, "Beam Loss Detection at Radiation Source ELBE", Proc. DIPAC 2003, CT05, pp 65-67.

[6] J. Roelfe et al., "Long Ion Chambers Systems for the SLC", SLAC-PUB-4925, 3/1989.

[7] K. Wittenburg, "Beam Loss Detection" DESY; Hamburg, Proc. 1st European Workshop on Beam Diagnostics and Instrumentation for Particle Accelerators, Montreux, Switzerland, 3-5.5.1993,CERN PS/93-35 (BD).

[8] http://zms.desy.de/research/accelerators/international_linear_collider_ilc/index_eng.html.

[9] http://zms.desy.de/research/accelerators/free_electron_laser_flash/index_eng.html.

[10] Henschel, O. Köhn, M. Körfer, Th. Stegmann, F. Wulf," Preliminary Trials with Optical Fiber Dosimeters at TTF", TESLA Report No. 2000-25, August 2000, pp 1-9.

[11] H. Henschel,M. Körfer, K. Wittenburg, F. Wulf , "Fiber Optic Radiation Sensing Systems for TESLA", TESLA Report No. 2000-26, September 2000, pp 1-18.

[12] E. Janata, M. Körfer, "Radiation Detection by Cerenkov Emission in Optical Fibers at TTF", TESLA Report No. 2000-27, 28. December 2000, pp 1-11

[13] R.D. Maurer, E.J. Schiel, S. Kronenberg, R.A. Lux, "Effect of Neutron- and Gamma-Radiation on Glass Optical Waveguides", Appl. Opt. Vol. 12, No. 9, pp. 2024-2026, 1973.

[14] B.D. Evans, G.H. Sigel, "Permanent and Transient Radiation Induced Losses in Optical Fibers", IEEE Trans. Nucl. Sci. Vol. 21, No. 6, pp. 113-118, 1974

[15] P.L. Mattern, L.M. Watkins, C.D. Skoog, J.R. Brandon, E.H. Barsis, "The Effects of Radiation on the Absorption and Luminescence of Fiber Optic Waveguides and Materials", IEEE Trans. Nucl. Sci. Vol. 21, No. 6, pp. 81-95, 1974.

[16] W. Gaebler, D. Bräuning, "Application of optical fiber waveguides in radiation dosimetry", 1st Intern. Conf. on Fiber Optic Sensors, pp. 185-189, London 1983.

[17] W. Gaebler, "Characteristics of Fiber Optic Radiation Detectors", SPIE Vol. 403: Optical Fibers in Broadband Networks, Instrumentation and Urban and Industrial Environments, pp. 142-145, 1983.
[18] W. Gaebler, "Glasfasern als Strahlungssensoren", Atomenergie-Kerntechnik, Vol. 43, No. 1, p. 64, 1983.
[19] H. Bueker, F. W. Haesing, "Fiber-Optic Radiation Sensors", SPIE Col. 2425, 1994, pp. 106-114.
[20] H. Henschel, O. Köhn, S. Metzger, M. Decréton, P. Devos, O. Deparis, J. Kirchhof, St. Grimm, "Neutron fluence and dose measurements by optical fibers", SPIE Vol. 2867, pp. 290-295, 1997.
[21] B.R.L. Siebert , H. Henschel, "Calculation of fast neutron dose in plastic-coated optical fibres", IEEE Trans. Nucl. Sci., Vol. 45, No. 3, pp. 1570-1575, 1998.
[22] H. Henschel, O. Köhn, W. Lennartz, S. Metzger, H.U. Schmidt, J. Rosenkranz, B. Glessner, B.R.L. Siebert, "Comparison between fast neutron and gamma irradiation of optical fibres", IEEE Trans. Nucl. Sci., Vol. 45, No. 3, pp. 1543- 1551, 1998.
[23] Kuhnhenn, J. and H. Henschel, "Influence of coating material, cladding thickness, and core material on the radiation sensitivity of pure silica core step-index fibers", 8th European Conference on Radiation and Its Effects on Components and Systems (RADECS 2005), Cap d'Agde, France.
[24] H. Henschel, M. Körfer, and F. Wulf: "Fibre optical radiation sensing system for TESLA", DIPAC 2001 Proceedings, Paper CT-04.
[25] H. Henschel, M Körfer, J. Kuhnhenn. U. Weinand, F. Wulf., "Fibre optic radiation sensor systems for particle accelerators", Nuclear Instruments and Methods in Physics Research Section A: Accelerators, Spectrometers, Detectors and Associated Equipment, 2004. 526(3): p. 537-550.
[26] D.L. Griscom, M.E. Gingerich, E.J. Friebele, "Radiation-Induced Defects in Glasses: Origin of Power-Law Dependence of Concentration on Dose", Phys. Rev. Lett. Vol. 71, No. 7, pp. 1019-1022, 1993.
[27] J. Kuhnhenn, H. Henschel, O. Köhn, U. Weinand, "Thermal annealing of radiation dosimetry fibres", RADECS 2004, Torrejon de Ardoz, Proc. pp 39-42
[28] H. Henschel, M Körfer, J. Kuhnhenn. U. Weinand, F. Wulf., "Optical Fibre Dosimeter for SASE FEL Undulators", Proc. of DIPAC 2003, Mainz, Germany, 5-7 May, PT 31, p 248.
[29] K. Krebber, H. Henschel, U. Weinand, "Fibre Bragg gratings as high dose radiation sensors?", Measurement Science and Technology, Volume 17, Issue 5, pp. 1095-1102 (2006).
[30] Henning Henschel, Stefan K Hoeffgen, Katerina Krebber, Jochen Kuhnhenn, and Udo Weinand, "Influence of Fiber Composition and Grating Fabrication an the Radiation Sensitivity of Fiber Bragg Gratings", IEEE Transaction on Nuclear Science, Vol. 55, No. 4, August 2008, pp 2235-2242.
[31] H. Henschel, M. Körfer, J. Kuhnhenn, U. Weinand, F. Wulf, "Fibre optic sensor Solutions for particle accelerators", Proc. 17th International Conference on Optical Fibre Sensors, 23-27 May 2005, Bruges, Belgium, pp 515-518, and Poster.
[32] W. Goettmann, F. Wulf, M. Körfer, J. Kuhnhenn, "Beam Loss Position Monitor using Cerenkov Radiation in Optical Fibers", Proc. of DIPAC 2005, Lyon, France, POW026, pp 301-303.
[33] W. Goettmann, M. Körfer, F. Wulf,"Beam Profile Measurement with Optical Fiber Sensors at FLASH", Proc. of DIPAC 2007, Vience, Italy, TUPB 25, pp 123-125.
[34] Thijs Wijnands, Luit Kort De Jonge, Jochen Kuhnhenn, Stefan Klaus Hoeffgen, and Udo Weinand, "Optical Absorption in commercial Single Mode Optical Fibers in a High Energy Physics Radiation Field", IEEE Transactions on Nuclear Science, Vol.55 (2008), No.4, pp.2216-2222.
[35] H.-J. Grabosch, W. Goettmann, "Results of Test Measurements, Simulation of Beam-Loss with FLUKA", SEI Tagung, Report; HMI-B 619, ISSN 0936-0891, Ruhr Universität Bochum, 24. - 26. Sept. 2007, pp 176-191.
[36] W. Goettmann, et. al., "Strahlverlustmessung durch Messung der Cerenkovstrahlung in Lichtwellenleitern" SEI Herbststagung, 26. – 28. Sept. 2005 Berlin, HMI-B 2005, ISSN 0936-0891, pp 49-61.
[37] N. von Bargen et al., "Prototype of a Wire Scanner for TTF II", TESLA Report 2002-8.
[38] J. Bahrdt, et al., "Status of the undulator system on the seeded HGHG-FEL test bench at MAX-lab", International Free Electron Laser Conference 2007, Novosibirsk (2007).
[39] G. Schmidt, E. Kasl, K. Wille, M. Körfer, H. Henschel, J. Kuhnhenn, "Optical Fibre Beam Loss Monitors for Storage Rings at DELTA", Proc. EPAC 2002, Paris, France, pp 1969-1971.
[40] F. Rüdiger, G. Schmidt, K. Wille, M. Körfer, W. Göttmann,"Beam Loss Position Monitoring with optical Fibres at DELTA", Proc. EPAC June 23- 27, 2008, Genoa, Italy, TUOCM03, p 1032.

INTENSITY AND PROFILE MEASUREMENT FOR LOW INTENSITY ION BEAMS IN AN ELECTROSTATIC CRYOGENIC STORAGE RING

T. Sieber, K. Blaum, M. Grieser, F. Laux, M. Lange, D. Orlov, R. von Hahn, A. Wolf
MPI-K Heidelberg, Germany

Abstract

The cryogenic storage ring CSR is a 35 m circumference electrostatic ring, designed for molecular- and atomic physics experiments at MPI-K Heidelberg. It will operate at pressures down to 10^{-13} mbar and temperatures <10 K. The beam intensities will be in the range of 1 nA to 1 µA, particle energies with between 20 - 300 keV.

An intensity measurement for coasting beams below 1µA requires magnetic field detection devices, which are much more sensitive than existing DC beam transformers. The highest sensitivity is currently achieved using DC SQUID based cryogenic current comparators (CCCs). At GSI, a prototype of such a CCC was successfully tested in the mid 90's, reaching a resolution of ~250 pA/Hz$^{1/2}$. Recently a resolution of 40 pA/Hz$^{1/2}$ could be achieved under laboratory conditions at Jena University, however, the CCC sensitivity in an accelerator environment depends strongly on efficient shielding and mechanical decoupling.

We describe our work on adaptation and improvement of the CCC beam transformer for the CSR. Furthermore a concept for an ionisation profile monitor is discussed, which in addition to low beam intensities, has to cope with extremely low gas densities at 10^{-13} mbar.

INTRODUCTION

The CSR [1] combines a number of challenges for diagnostics development: Low currents, low ion energies, extremely low pressure, high bakeout temperatures and not least the cryogenic environment. To illustrate these boundary conditions, Table 1 shows the relevant parameters of the ring at one glance.

Table 1: Parameters of the CSR

Type	Electrostatic
Circumference	35.2 m
Corner deflectors	2x39°, 2x6°
Acceptance	100 mm mrad
Mass range	1 – 100 amu
Energy range (1^+ ions)	20 – 300 keV
Intensity range	1 nA – 1 µA
Revolution Frequency	5 - 220 kHz
Operation temperature	2 - 300 K
Bakeout temperature	< 350°C
Vacuum pressure	1×10^{-13} mbar
Mat. cold chamber	316 L
Mat. isolation chamber	Al
Outer tank cross sect.	~ 1 m^2

The mass range of A ≤ 100 in the table is at the moment considered a reasonable design value. Studies with much heavier molecules with A ≤ 2000 (at much lower intensities than 1 nA) are foreseen in a later stage of CSR operation.

In the summer 2008 the setup of the CSR prototype ion trap (Cryogenic Trap for fast ions, CTF) was completed. Numerous vacuum tests have been performed with the prototype, demonstrating a pressure in the low 10^{-13} mbar range [2], which was determined by measuring the lifetimes of stored ion beams (τ_{max} = 320 s for N_2^+). The first molecular physics experiment campaign with the CTF has been successfully completed by the time of this report. For the CSR itself, the mechanical design work for the main components has been finished. The assembly of the first ring corner will start in the fall of 2009.

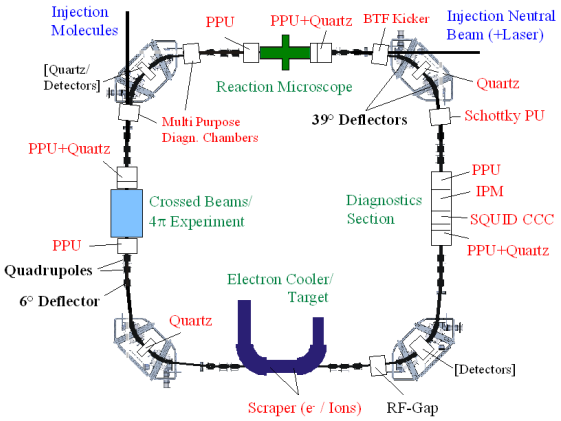


Figure 1: Layout of the CSR and diagnostics system.

The general concept for the beam diagnostics system of the CSR is shown in Figure 1. In contrast to existing or planned electrostatic rings, the CSR will have an extensive set of diagnostics devices, which is similar to the equipment of our Test Storage Ring (TSR). The four linear sections include two main experimental areas, an electron cooler/target and a section which is dedicated to beam diagnostics. Beam injection is foreseen in two corners of the ring (ions and neutral particles/laser).

For measurement of the beam intensity we have developed a mechanical and cryogenics design for a beam transformer, based on a Cryogenic Current Comparator (CCC) with a SQUID sensor, which will also be a prototype for the FAIR project at GSI.

To measure the beam profile in a non-interceptive way, we investigated the possibility of an ionisation profile monitor (IPM) at 10^{-13} mbar. At this residual gas pressure,

the problem of dramatically decreasing count rates must be solved. On the other hand, increasing cross sections for charge exchange at low energies might lead to particle losses. Nonetheless we see no alternative to an IPM for the CSR.

BEAM INTENSITY MEASUREMENT

Since the first prototype of a CCC beam transformer was tested at GSI [3], the device has been steadily optimized, mainly at Jena University. On the electronics side, the bandwidth could be increased (increased slew rate) as well as the phase-locking to the periodic voltage signal from the SQUID, resulting in much higher performance and lower background noise. On the side of the pickup coil, the shielding was optimised and new materials for the toroidal core (see Fig. 2) have been investigated. The currently achieved resolution of 40 $pA/Hz^{1/2}$ under laboratory conditions [4], confirm our expectation of current measurements in the sub nA range.

The principle of the CCC beam transformer is shown in Figure 2. It basically consists of a superconducting shielding, which houses a superconducting coil on a toroidal core of high permeability. The shielding only allows the azimuthal magnetic field from the ion beam to penetrate inside, all other field components are strongly attenuated (-120 dB). If the ion beam enters the CCC, a surface current is generated due to the Meissner Effect, which is - independent from beam orientation - equal to the beam current. The shielding represents the primary winding of a transformer with the secondary winding being the pickup coil, which is again coupled to the SQUID circuit via a flux transformer for inductance matching.

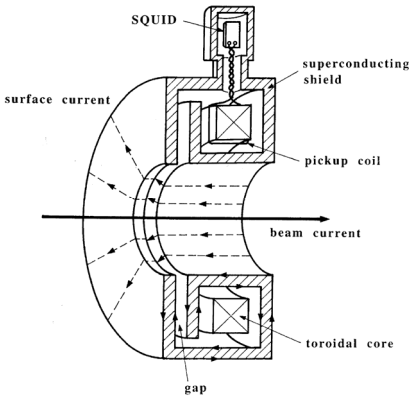


Figure 2: Principle of the CCC beam transformer [3].

For an increased performance of the system numerous ferrite materials have been tested recently in a dedicated setup at FSU Jena [6], suggesting a change from the formerly used VITROVAC® to the so called NANOPERM® material, the latter showing a high permeability over a large frequency range ($\mu_r \approx 50000$, f ≈ 1 Hz - 70 kHz), which fullfills the demand of a high inductivity pickup coil with the lowest possible number of windings (N=1). A high bandwidth is not crucial for the application in CSR, but essential for peak current measurements at FAIR.

The mechanical and cryogenic design of the CCC for CSR and FAIR takes into account that all components of the CCC have to be cooled down to liquid helium temperature, with a temperature stability of 50 mK to minimise noise and zero shift. Since the CSR also has an operation mode at room temperature, its CCC will have a separate thermal shielding, which must be closed towards the (potentially warm) beam tube and will be installed inside the inner (40 K) thermal shield (see figure 3). The SQUID and the toroidal core of the pickup coil define an upper temperature limit of only 80° C, which means the CCC shield has to be water cooled during bakeout. The liquid helium container, which houses the superconducting shielding and the attached SQUID electronics, will be suspended with wires inside the aluminum shield.

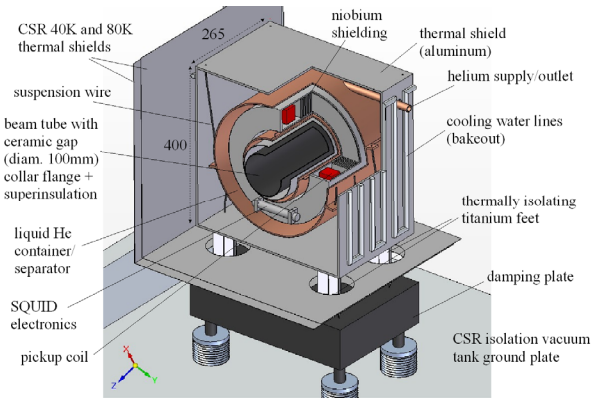


Figure 3: CCC beam transformer installation for the CSR.

Some effort is necessary for the suppression of mechanical vibrations. The shield itself is placed (with thermally isolating Ti feet) on a massive ground plate, which is - decoupled from the CSR isolation vacuum chambers by bellows - mounted on vibration damping feet on a separate support outside the isolation vacuum. Vibrations from the streaming helium in the cooling lines or from the refrigerator were measured in our prototype setup and found to be neglectable.

The CSR offers (besides a helium supply and the absence of vibration from cooling devices) the advantage of being completely non-magnetic - this concerning its optical elements as well as the used materials ($\mu_r < 0.01$). Nonetheless we are currently in the process of designing the superconducting shielding of our CCC to reach a performance, which is (despite the differing shielding geometry) identical to the shielding in the DESY setup.

BEAM PROFILE MEASUREMENT

At a vacuum pressure of 1×10^{-13} mbar, the count rate for residual gas ionisation by a 300 keV, 1 µA Proton beam is calculated with $R = \sigma\, n\, v\, \eta\, N$ to be 10 Hz. Here σ is the ionisation cross section, taken from [6], n is the

residual gas density, v is the beam velocity, η is the ratio of the effective detector length to the ring circumference and N is the number of stored ions. A count rate of 10 Hz is slightly above the MCP noise level and does not allow for reasonable beam profile measurements. Therefore, the pressure must be increased to at least 10^{-11} mbar in a short, well defined section of the ring.

A number of other design criteria must be taken into account: To have proper imaging of the beam profile, high field homogeneity over a large area (beam diameter up to 8cm) is essential. At the same time, the kick on the circulating beam must be minimized. MCP operation at low temperature has been investigated in [7] and seems feasible. The IPM must be highly redundant (due to bad accessibility once installed in CSR) and have a good thermal conductivity.

To match these criteria we designed an IPM (Fig. 4), which basically consists of two identical twin IPMs with reverse polarity in x- and y-direction (kick compensation, redundancy). The MCP is screened from the extraction voltage by a grid, the whole structure is built from copper and the insulators are made from sapphire.

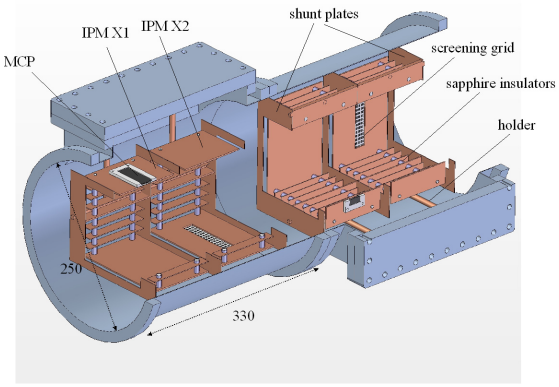


Figure 4: The IPM for CSR.

The voltages on the field shaping electrodes can be, due to the low residual gas temperature, comparatively low (100 V). On the one hand this reduces the influence of the IPM on the circulating beam, on the other hand the low IPM field can suffer from deformation caused by the MCP voltage, even if the MCP is screened with a grid. As a reasonable compromise we found an IPM voltage of U_{El} = ± 600 V (U_{MCP} = -2 kV), which gives a resolution of Δx = 45 µm. By doing field analysis and particle tracking of a 20 keV proton beam with the TOSCA® code and then calculating the influence on the closed orbit with MAD, it turned out that at ± 600 V the closed orbit shift is 1.1 mm in the y-direction and 0.5 mm in the x-direction. The uniformity of the field is given by E_x/E_y < 2 % at the worst point in an area of 70 x 100 mm below the MCP. The values are acceptable and have to be seen as a worst case estimation, because the screening grid was approximated with a large mesh (3 x 3 mm) with 1mm wires due to limited available memory. Using a real 85% transmission grid, the IPM voltages as well as the closed orbit shift will be much lower.

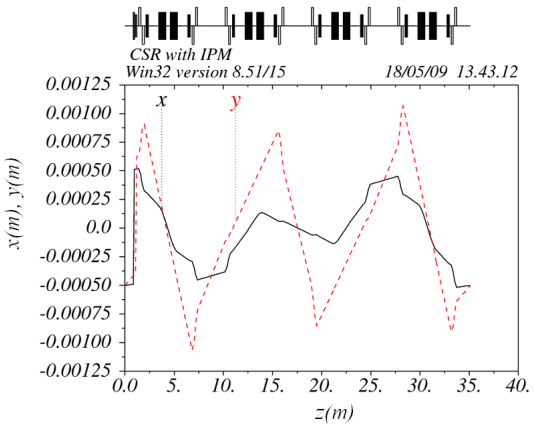


Figure 5: Closed orbit distortion of a 20 keV proton beam caused by the IPM voltage from MAD.

To increase the gas pressure in the IPM section, we are currently investigating the possibility of heating a test chamber in our CSR prototype setup. Theoretically, 10% of a monolayer of hydrogen can decrease the pressure from our present 10^{-13} mbar to 10^{-11} mbar for about 30 days, if the chamber is heated with its bakeout wires with a current of 200 mA (W ≈ 800 mW). We are considering a scheme of carefully heating the IPM chamber itself as well as neighbouring chambers, possibly in connection with a H_2 gas inlet.

OUTLOOK

After the geometry of the CCC shielding is fixed, a toroidal core with appropriate dimensions will be tested for its mechanical properties (microphony) at FSU Jena. Manufacturing of the shielding and setup of the prototype is planned until the end of 2009.

For the IPM tests in the CSR prototype, we have designed a small (5 x 5 cm) test IPM, which will be installed after the current experimental runs.

REFERENCES

[1] A. Wolf et al., “The Heidelberg CSR: Low Energy Ion-Beams in a Cryogenic Electrostatic Storage Ring”, Proc. COOL05, Galena, USA (2005), p. 473

[2] M. Froese et al., ”Cryogenic Ion Beam Storage”, Proc. PAC09, Vancouver, Canada (2009), in preparation

[3] A. Peters et al., “A Cryogenic Current Comparator for Nondestructive Beam Intensity Measurements”, Proc. EPAC94, London UK (1994), p. 290

[4] W. Vodel et al., “Current status of the SQUID based Cryogenic Current Comparator” Proc. DIPAC07, Venice, Italy (2007), p. 301

[5] R. Geithner, PhD thesis, Solid State Physics Department, FSU Jena, in preparation

[6] D.S.F Crothers, J.F. McCann, J. Phys B, At. Mol. Phys. 16 (1983), p. 3229

[7] S. Rosén et al., Rev. Sci. Instr. 78 (11), pp. 113301-113301-5 (2007)

DATA ACQUISITION AND ERROR ANALYSIS FOR PEPPERPOT EMITTANCE MEASUREMENTS

S. Jolly, Imperial College, London, UK
J. Pozimski, STFC/RAL, Chilton, Didcot, Oxon, UK/Imperial College, London, UK
J. Pfister, IAP, Frankfurt am Main, Germany
O. Kester, NSCL, East Lansing, Michigan, USA
D. Faircloth, C. Gabor, A. Letchford, S. Lawrie, STFC/RAL, Chilton, Didcot, Oxon, UK

Abstract

The pepperpot provides a unique and fast method of measuring emittance, providing four dimensional correlated beam measurements for both transverse planes. In order to make such a correlated measurement, the pepperpot must sample the beam at specific intervals. Such discontinuous data, and the unique characteristics of the pepperpot assembly, requires special attention be paid to both the data acquisition and the error analysis techniques. A first-principles derivation of the error contribution to the rms emittance is presented, leading to a general formula for emittance error calculation. Two distinct pepperpot systems, currently in use at GSI in Germany and RAL in the UK, are described. The data acquisition process for each system is detailed, covering the reconstruction of the beam profile and the transverse emittances. Error analysis for both systems is presented, using a number of methods to estimate the emittance and associated errors.

INTRODUCTION

The use of pepperpots in measuring transverse emittance is widespread. The pepperpot is unique in providing an instantaneous measurement of the 4 dimensional emittance of a beam in a single shot. To do so the pepperpot sacrifices position resolution by measuring the beam only at discrete intervals through an intercepting screen. With suitably fast analysing software, this provides the opportunity of measuring and visualising the emittance of the beam in real time. The disadvantage of using a pepperpot is that they are highly destructive to the beam, primarily due to the intercepting screen, and the discontinuous nature of the position measurement that results from segmenting the beam.

To fully categorise emittance measurement error, a first principles analysis of the propagation of errors through the calculation of *rms* emittance has been carried out. This results in a general formula for the calculation of errors from any method of emittance measurement. This error analysis procedure is demonstrated for two contrasting pepperpot designs.

PEPPERPOT SYSTEMS

Error analysis has been carried out for two pepperpot systems: from the HITRAP project at GSI [1] and the Front End Test Stand (FETS) at RAL [2].

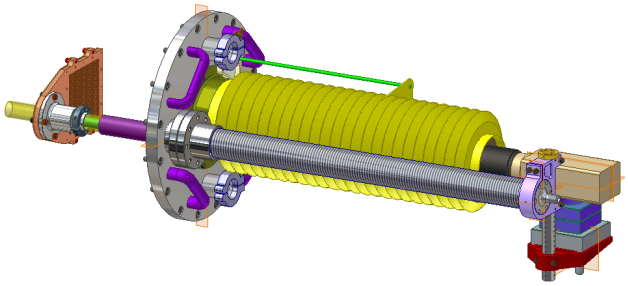


Figure 1: 3-D model of the FETS pepperpot assembly [3].

A CAD model of the FETS pepperpot assembly is shown in Fig. 1: full description of the FETS pepperpot device is given in [3]. The intercepting screen is a 100 μm thick tungsten foil with a square array of 41×41 holes, each 50 ± 5 μm in diameter, on a 3 ± 0.01 mm pitch, giving a total imaging area of $120 \times 120\,\mathrm{mm}^2$. The beam is imaged with a quartz scintillator, 10 mm from the tungsten screen, and a 2048×2048 pixel PCO 2000 high speed camera: the camera-to-screen distance of 1100 mm gives a resolution of 65 μm per pixel and an angular resolution of 6.5 mrad. Data is recorded from the camera direct to a multi-image TIFF file and analysed with Matlab. Calibration is carried out using a series of calibration marks on the rear copper plate facing the camera: 4 lines, forming a 125 mm×125 mm square around the intercepting screen, provide the necessary calibration information on the size, location and rotation of the pepperpot holes.

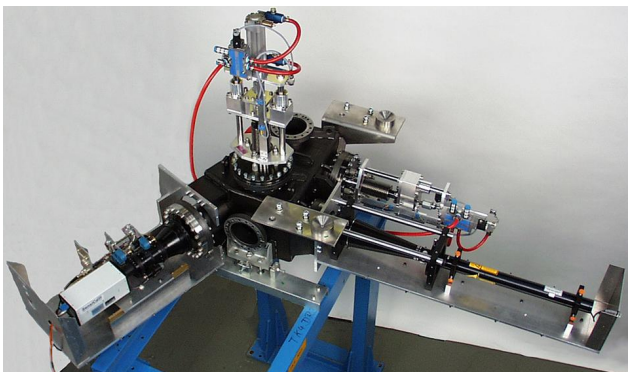


Figure 2: The HITRAP pepperpot setup (*cf.* [5]).

The setup of the GSI pepperpot system for the HITRAP

experiment is outlined in [4], with recent modifications detailed in [5]: the complete system is shown in Fig. 2. The pepperpot can be equipped with various intercepting screens: for recent measurements a 100 μm thick tungsten foil was used, with an array of 19×19 holes, each $100 \pm 10\,\mu$m in diameter, on a 1.6 ± 0.02 mm pitch, to image an area of $29 \times 29\,\mathrm{mm}^2$. An Al_2O_3 scintillator is mounted 150 mm from the screen: pepperpot images are recorded with a cooled fast shutter CCD camera with a 1280×1024 pixel resolution, giving an angular resolution of 0.3 mrad. A laser is used to calibrate the system: an image is recorded of the resulting light spots on the imaging screen, these calibration spots are projected to horizontal and vertical axes and the maxima are defined as calibration positions for each individual row and column.

EMITTANCE ERROR ANALYSIS

In order to calculate an error on the emittance, it is necessary to derive an emittance error formula by propagating the errors on each measured quantity through the formula for emittance. The *rms* emittance is used as it is mathematically well defined, allowing such a first-principles approach to be used. Such an approach is valid only if the errors on each variable are also well defined: this is addressed in the next section. In the x-plane, the definition of ε_{rms} is:

$$\varepsilon_{rms} = \sqrt{\langle x^2 \rangle \langle x'^2 \rangle - \langle x x' \rangle^2} \tag{1}$$

$$= \sqrt{\frac{\left(\sum_{i=1}^{N} \rho_i x_i^2\right)\left(\sum_{j=1}^{N} \rho_j x_j'^2\right) - \left(\sum_{i=1}^{N} \rho_i x_i x_i'\right)^2}{\left(\sum_{i=1}^{N} \rho_i\right)^2}} \tag{2}$$

To calculate an error on the emittance, a variance, $\sigma^2_{\varepsilon_{rms}}$, and hence a standard deviation, $\sigma_{\varepsilon_{rms}}$, must be derived. The variance on one term of the $\sum_{i=1}^{N} \rho_i x_i^2$ series is given by:

$$\sigma^2_{\rho x^2} = 4\rho^2 x^2 \sigma_x^2 + x^4 \sigma_\rho^2 \tag{3}$$

Since, for addition, variances also add, the variance for the complete series, $\sigma^2_{\sum \rho x^2}$ is:

$$\sigma^2_{\sum \rho x^2} = \sum_{i=1}^{N} \left(4\rho_i^2 x_i^2 \sigma^2_{x_i} + x_i^4 \sigma^2_{\rho_i}\right) \tag{4}$$

... since every position measurement, x_i, has its own error, σ_{x_i}, and each intensity measurement, ρ_i, has its own error σ_{ρ_i}. The same calculation holds true for $\sum_{j=1}^{N} \rho_j x_j'^2$ and its associated variance, $\sigma^2_{\sum \rho x'^2}$:

$$\sigma^2_{\rho x'^2} = 4\rho^2 x'^2 \sigma^2_{x'} + x'^4 \sigma^2_\rho \tag{5}$$

$$\sigma^2_{\sum \rho x'^2} = \sum_{j=1}^{N} \left(4\rho_j^2 x_j'^2 \sigma^2_{x_j'} + x_j'^4 \sigma^2_{\rho_j}\right) \tag{6}$$

The variance for the product of these two terms, $\sigma^2_{\sum \rho x^2 \sum \rho x'^2}$, is given by:

$$\sigma^2_{\sum \rho x^2 \sum \rho x'^2} = \left(\sum_{i=1}^{N} 4\rho_i^2 x_i^2 \sigma^2_{x_i} + x_i^4 \sigma^2_{\rho_i}\right)\left(\sum_{j=1}^{N} \rho_j x_j'^2\right)^2 + \left(\sum_{i=1}^{N} 4\rho_i^2 x_i'^2 \sigma^2_{x_i'} + x_i'^4 \sigma^2_{\rho_i}\right)\left(\sum_{j=1}^{N} \rho_j x_j^2\right)^2 \tag{7}$$

Two more variances are needed: for the xx' and ρ^2 terms in Eqn. 2. Following the same procedure:

$$\sigma^2_{\rho x x'} = x^2 x'^2 \sigma_\rho^2 + \rho^2 x'^2 \sigma_x^2 + \rho^2 x^2 \sigma_{x'}^2 \tag{8}$$

$$\sigma^2_{\sum \rho x x'} = \sum_{i=1}^{N} \left(x_i^2 x_i'^2 \sigma^2_{\rho_i} + \rho_i^2 x_i'^2 \sigma^2_{x_i} + \rho_i^2 x_i^2 \sigma^2_{x_i'}\right) \tag{9}$$

$$\sigma^2_{(\sum \rho x x')^2} = 4\left(\sum_{i=1}^{N} x_i^2 x_i'^2 \sigma^2_{\rho_i} + \rho_i^2 x_i'^2 \sigma^2_{x_i} + \rho_i^2 x_i^2 \sigma^2_{x_i'}\right) \times \left(\sum_{j=1}^{N} \rho_j x_j x_j'\right)^2 \tag{10}$$

And:

$$\sigma^2_{\sum \rho} = \sum_{i=1}^{N} \sigma^2_{\rho_i} \tag{11}$$

$$\sigma^2_{(\sum \rho)^2} = 4\left(\sum_{i=1}^{N} \sigma^2_{\rho_i}\right)\left(\sum_{j=1}^{N} \rho_j\right)^2 \tag{12}$$

As such, the variance for the numerator in Eqn. 2 is:

$$\sigma^2_{\sum \rho x^2 \sum \rho x'^2 - (\sum \rho x x')^2} = \left(\sum_{i=1}^{N} 4\rho_i^2 x_i^2 \sigma^2_{x_i} + x_i^4 \sigma^2_{\rho_i}\right)\left(\sum_{j=1}^{N} \rho_j x_j'^2\right)^2 + \left(\sum_{i=1}^{N} 4\rho_i^2 x_i'^2 \sigma^2_{x_i'} + x_i'^4 \sigma^2_{\rho_i}\right)\left(\sum_{j=1}^{N} \rho_j x_j^2\right)^2 + 4\left(\sum_{i=1}^{N} x_i^2 x_i'^2 \sigma^2_{\rho_i} + \rho_i^2 x_i'^2 \sigma^2_{x_i} + \rho_i^2 x_i^2 \sigma^2_{x_i'}\right)\left(\sum_{j=1}^{N} \rho_j x_j x_j'\right)^2 - 8\left(\sum_{i=1}^{N} \rho_i^2 x_i^4 x_i'^4 \sigma^2_{\rho_i} + \rho_i^4 x_i^2 x_i'^4 \sigma^2_{x_i} + \rho_i^4 x_i^4 x_i'^2 \sigma^2_{x_i'}\right) \tag{13}$$

The subtraction comes about through the cancellation of terms in Eqn. 2. Propagating the errors through the division and square root gives a variance on ε_{rms}, $\sigma^2_{\varepsilon_{rms}}$:

$$\sigma_\varepsilon^2 = \frac{\left(\sum_{i=1}^N \rho_i^2 x_i^2 \sigma_{x_i}^2 + \frac{x_i^4 \sigma_{\rho_i}^2}{4}\right)\left(\sum_{j=1}^N \rho_j x_j'^2\right)^2}{\varepsilon^2\left(\sum_{k=1}^N \rho_k\right)^4} + \frac{\left(\sum_{i=1}^N \rho_i^2 x_i'^2 \sigma_{x_i'}^2 + \frac{x_i'^4 \sigma_{\rho_i}^2}{4}\right)\left(\sum_{j=1}^N \rho_j x_j^2\right)^2}{\varepsilon^2\left(\sum_{k=1}^N \rho_k\right)^4} + \frac{\left(\sum_{i=1}^N x_i^2 x_i'^2 \sigma_{\rho_i}^2 + \rho_i^2 x_i'^2 \sigma_{x_i}^2 + \rho_i^2 x_i^2 \sigma_{x_i'}^2\right)\left(\sum_{j=1}^N \rho_j x_j x_j'\right)^2}{\varepsilon^2\left(\sum_{k=1}^N \rho_k\right)^4} - \frac{2\left(\sum_{i=1}^N \rho_i^2 x_i^4 x_i'^4 \sigma_{\rho_i}^2 + \rho_i^4 x_i^2 x_i'^4 \sigma_{x_i}^2 + \rho_i^4 x_i^4 x_i'^2 \sigma_{x_i'}^2\right)}{\varepsilon^2\left(\sum_{k=1}^N \rho_k\right)^4} + \frac{\varepsilon^2\left(\sum_{i=1}^N \sigma_{\rho_i}^2\right)}{\left(\sum_{k=1}^N \rho_k\right)^2} \quad (14)$$

The error on the *rms* emittance, $\sigma_{\varepsilon_{rms}}$, is the square root of this value.

PEPPERPOT EMITTANCE ERRORS

The next stage is to identify the errors on each measured quantity and use these to calculate $\sigma_{\varepsilon_{rms}}$. For pepperpot measurements, the dominant errors are: the spacing of the holes for σ_x; the camera resolution and pepperpot-to-scintillator distance – defining the angular resolution – for $\sigma_{x'}$; and the inherent beam variation and signal noise in the measurement apparatus for σ_ρ. Certain errors, such as the shape and diameter of the holes, contribute to both σ_x and σ_ρ: however, the dominant contribution to σ_x is clearly the hole spacing, and careful analysis of the hole size would allow this error to be removed. It is assumed that the hole size is smaller than the relative pixel size of the camera, allowing simple angles to be calculated through ray tracing, and that the camera orientation defines the beam orientation. As such, calibration errors contribute only to errors on $\sigma_{x'}$.

The emittance values derived from measurements for the two systems, along with the corresponding error estimate for each contributing error, is shown in Table 1. Where errors are negligible, or error analysis has not been carried out, no figure is shown. For the FETS system, an additional angle error of $\sim$1 mrad per mm is included due to the inaccuracy of the calibration. Two sources of intensity error are considered: beam noise, corresponding to the stochastic pulse-to-pulse variation in the beam, and the noise floor,

Table 1: Percentage Emittance Error Contributions for Pepperpot Measurements

	FETS		HITRAP	
	Value	σ (%)	Value	σ (%)
Beam radius (mm)	45	–	17	–
ε_x (π mm mrad)	0.61	–	0.24	–
Hole spacing (mm)	3	1.8	1.6	2.2
Angle res. (mrad)	6.5	1.6	0.3	0.2
Beam noise (%)	10	1.3	10	0.3
Noise floor (%)	2	~ 0	10	1.2
σ_ε (π mm mrad)	0.029	4.8	0.010	3.9

a pessimistic figure representing the constant level of background noise (quoted as a percentage of the maximum signal). For the FETS system, each source of error contributes approximately equally to the final error figure of $\pm 4.8\%$: For the GSI system, the dominant error is clearly the hole spacing, with a contribution from the background noise: the angle resolution is considerably better than the FETS system and this is reflected in the error values. An interesting effect is that the beam noise contributes significantly more for the FETS system but is dominated by the noise floor in the HITRAP system: this is a result of the smaller beam and lower light intensity producing a less intense pepperpot image for the HITRAP pepperpot. This also contributes to the larger position error.

CONCLUSIONS

The formula for calculating *rms* emittance errors has been applied successfully to 2 different pepperpot setups, with promising results. Further work is required to categorise errors not included in this analysis, since these affect the accuracy of the emittance measurement while not contributing to the error estimate. This has particular importance when dealing with cut selection, something dealt with in considerable detail by the SCUBEEx algorithm (see [6] and Refs therein). As such, this method constitutes a minimum estimate of the emittance error.

ACKNOWLEDGEMENTS

The authors gratefully acknowledge the contributions of Roger Barlow, Louis Lyons and Martin Jolly in the analysis and derivation of emittance errors.

REFERENCES

[1] J Pfister *et al.*, EPAC'08, THPP037, p. 3449.

[2] A Letchford *et al.*, EPAC'08, THPP029, p. 3437.

[3] S Jolly *et al.*, DIPAC'07, WEO2A01, p. 218.

[4] T Hoffmann *et al.*, BIW 2000, AIP Conf. Proc. 546, p. 432.

[5] J Pfister *et al.*, LINAC'08, TUP074, p. 555.

[6] M Stockli *et al.*, Rev. Sci. Instrum. **75** (2004) 1646.

BEAM DIAGNOSTIC DEVELOPMENTS FOR FAIR*

M. Schwickert, P. Forck, P. Kowina, T. Giacomini, H. Reeg, A. Schlörit,
GSI Helmholtzzentrum für Schwerionenforschung GmbH, Darmstadt, Germany

Abstract

The FAIR (Facility for Antiproton and Ion Research) accelerator complex is currently designed and projected at GSI. The unique features of the main machine SIS100, like e.g. the acceleration of high intensity beams of 2.5×10^{13} protons and 5×10^{11} Uranium ions, the operation close to the space charge limit leading to a large tune spread and the extreme UHV conditions of the cryogenic system for fast ramped superconducting magnets, impose challenging demands on the beam diagnostic components. This contribution describes the general concept of beam diagnostics for FAIR and reports on the present status of prototype studies. Exemplarily the achievements for a novel type of dc transformer, beam position monitors and the ionization profile monitor are discussed and first measurements with prototype setups are presented.

FAIR ACCELERATOR COMPLEX

Presently GSI entered the final planning phase for the international FAIR project [1]. The existing GSI accelerators, UNILAC and SIS18, together with a new high-current proton LINAC will act as injectors. In its final stage FAIR will consist of two heavy ion synchrotrons (SIS100, SIS300) and four storage rings (CR, RESR, NESR, HESR). The main features of FAIR are: acceleration of all ion species from protons to Uranium, high currents of primary beams, generation of radioactive beams for fixed target experiments or injection in storage rings, as well as antiproton production, accumulation and storage ring experiments. For the planned large variety of physical experiments the multiplexed operation of the whole facility with different settings for ion species, energy etc. on a pulse-to-pulse basis, has been an important design criterion. In this contribution we focus on diagnostics for the fast ramped superconducting synchrotron SIS100 and the high energy beam transport section of FAIR.

REQUIREMENTS FOR DIAGNOSTICS

A set of general strategies has been considered in order to facilitate the construction of the facility with world-unique complexity. A main paradigm is the facility-wide standardization of diagnostic devices. Even though the requirements of the synchrotrons and storage rings differ, it is planned to use identical diagnostic installations wherever applicable. Standardization also covers the front-end software FESA [2] as an integrative platform for all diagnostic devices at FAIR. Concerning the hardware it is planned to use commercially available components to a maximum extent, in order to reduce manpower and spares inventory.

*Work partly supported by EU-FP6 DIRAC-phase1, -secondary-Beams

FAIR beam parameters impose strict requirements for all diagnostic devices. A strong constraint with regard to mechanics is the extreme UHV condition down to 5×10^{-12} mbar in SIS100. In this main synchrotron, high currents (up to the space charge limit) of primary beams in low charge states will be stored and accelerated with a large incoherent tune spread of up to $\Delta Q\approx0.5$. An important prerequisite is the precise beam alignment since in certain locations the synchrotron acceptance is limited to 6 times the rms beam width. For the High Energy Beam Transport section of FAIR the acceptance is even lower, four times the rms beam width. The goal for diagnostics in transport lines and storage rings is to achieve a high resolution and low detection limit. Additionally, the HEBT diagnostic devices have to deal with slow and fast extracted beams, respectively. Due to the requirement for online measurements and in order to prevent device destruction at high beam intensities, non-intercepting diagnostics is preferred and focused on in this contribution.

BEAM CURRENT MEASUREMENT

Novel DC Current Transformer (NDCCT)

For the GSI-built synchrotron DCCT, it was found that at high beam currents (>70mA) and bunch frequencies around 1.2 MHz the feedback loop of the DCCT loses control and the setting of the correct working point becomes unreliable. Therefore an alternative device based on state-of-the-art sensor technology is presently under development at GSI [3]. The NDCCT makes use of integrated GMR sensors (giant magneto-resistance) inside the gap of a split flux concentrator (amorphous alloy or ferrite toroid). The GMR signals are corrected and amplified by a differential pre-amplifier. Additionally, an AC transformer path is implemented by a secondary winding. Special requirements for the NDCCT are: low noise characteristic, high resolution (~100 µA), capability to measure beam currents from 100 µA to 150 A (2 A DC), bunch frequency up to 5 MHz, long-term zero-point stability and high absolute accuracy.

The utilized GMR sensor (AA-0002, Nonvolatile Electronics Co.) consists of 4 meandered resistors and 2 flux concentrators, building up a Wheatstone bridge. Studies on the frequency response revealed that the sensor circuitry spans inductive loops and, above a certain threshold frequency, the frequency response of the GMR sensor becomes disturbed. The upper frequency threshold was found to be a result of macroscopic effects like unwanted induced voltages in the sensor, eddy currents and skin effects in the GMR's NiFe-layer, leading to a reduced bridge voltage above the cut-off frequency of 1 MHz, as depicted in Fig. 1. The GMR frequency response is shown for different core materials (CMD5005,

VITROVAC6025F) and different magnetic remanences. An important goal for the NDCCT design is to reach an overall resolution in the 100 µA region. The NDCCT resolution is dominated by system noise, while the noise contribution of the passive ACT-part is negligible with respect to the GMR noise. The lower resolution limit was estimated by detection of the broadband sensor noise (GMR+pre-amp). For S/N=2, the measurement of the minimum power spectrum density yields 88 nV/√Hz.

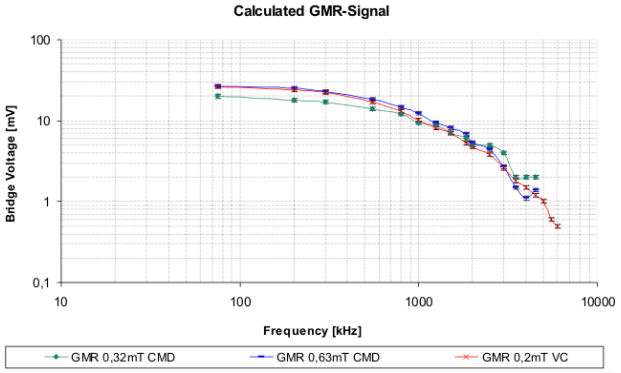


Figure 1: GMR signal vs. frequency.

Due to the system cut-off frequency of 1 MHz, the sampling rate has to be 2 MHz leading to signal amplitude of ~88 µV. Thus, the calculated minimum detectable beam current is as low as 220 µA. The electromagnetic interference of the unshielded test setup was found to be quite high and reduction of the interfering signals will be studied after the design of the readout electronics has been finished.

Cryogenic Current Comparator (CCC)

Because the CCC allows non-intercepting beam current measurements down to the nA-range [4] its installation inside HEBT beamlines is foreseen. The measurement principle of a CCC is based on the effect that for an ideal superconductor the magnetic flux is expelled from the bulk material through shielding currents on the materials surface. The magnetic field of a passing ion beam is measured by a superconducting toroid including a single winding pick-up coil with a ferromagnetic core. The coil signal is fed into a DC SQUID and digitized. In order to achieve a high current resolution in the nA-range both, the SQUID and the pick-up coil, have to be effectively shielded against external magnetic fields. A detailed investigation on noise contributions of the ferromagnetic core material was carried out. The theoretical calculations have shown that, apart from a good attenuation of external fields, the CCC resolution strongly depends on the choice for the coil material. Thus a wide range of ferromagnetic materials has been investigated with respect to their permeability as a function of temperature (down to 4.2 K) and frequency (dc to 10 kHz) [5]. The best choice for the core material is NANOPERM (Magnetec GmbH). The next step is to manufacture a prototype coil structure and to implement it in a vacuum chamber with cryostat. Further details of the CCC prototype development can be found in [6].

PROFILE MEASUREMENT

Ionization Profile Monitor

The ionization profile monitor (IPM) allows non-intercepting detection of transverse beam profiles. Profiles of the circulating beam inside the synchrotron are monitored by detection of the ionized residual gas molecules (e.g. H_2). Here a transverse electric field is applied to accelerate either (depending on polarity) the ionized gas atoms of the residual gas or the emitted electrons towards a spatial resolving Micro-Channel Plate phosphor module. An electric field of 50 V/m is realized with an inhomogeneity of less than 1% by dedicated field forming electrodes to ensure position preservation. Additionally, if electrons shall be detected, a guiding B-field of ~30 mT is required, as calculated using FEM simulations.

The IPM installation in SIS18 is operative since 2003 and the device has become almost a standard tool for beam tuning. Exemplarily, Fig. 2 shows measurement results for the beam profile evolution at different levels of noise excitation leading to significant emittance blow-up.

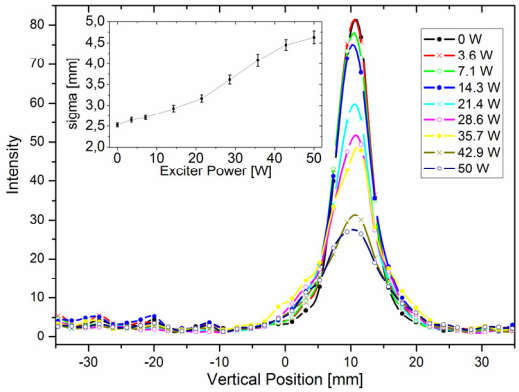


Figure 2: IPM measurements of vertical beam profile for different exciter settings. Insert: beam width sigma (Gaussian fit to beam profiles) vs. exciter power.

As part of an EU-FP6 project the new development of an advanced IPM for SIS18 was launched as a prototype for FAIR IPMs. As a first step a test bench was constructed to investigate a new concept for MCP installation. The test bench includes an UV lamp for calibration of the MCPs (100×48 mm^2), including a phosphor screen for the conversion of the electron signal to blue light. This P47 screen has a decay time of 100 ns. For the advanced IPM two measurement modes are foreseen: 1) high spatial resolution by CCD, 2) turn-by-turn readout by PMT. In mode 1 the goal is to reach a high spatial resolution of 0.1 mm at the cost of a lower time resolution of typically 10 ms. For this mode a triggered GigE CCD camera (framerate 200 frames/s) digitizes the fluorescent image of the MCP. The standalone front-end software for CCD readout exists and is presently tested. The proof of principle of this measurement mode was achieved by successful beam tests with protons at the COSY synchrotron (FZ Jülich, Germany, cf. [7]). For the turn-by-turn measurement a

multi-anode photo-multiplier with 32 channels will be used. The read out of the anodes is performed using a dedicated digitizer board, including purpose built FPGA and DSP electronics (framerate: 10 MSlices/s), designed and manufactured by the collaboration partner ITEP (Moscow) [8]. The goal of this measurement mode is to reach a time resolution of 100 ns at a reduced spatial resolution of 0.8 mm. The novel electronics has been manufactured and the prototype is presently tested.

BEAM POSITION MONITORS

The development of beam position monitors (BPM) in SIS100 is subdivided into five subprojects: 1) pick-up design for BPM installation inside cryostats [9], 2) cryogenic signal feed-throughs, 3) design of transformers for impedance matching, 4) low noise, 50 Ohm input impedance amplifiers [10] and 5) data acquisition using LIBERA digitizer boards [11]. Since a comprehensive description of all subprojects is out of the scope of this contribution, we focus on impedance matching and data acquisition. Because of the required resolution of the BPM system inside the cryogenic environment (accuracy 100 µm, mechanical stability 50 µm) metalized ceramics were preferred for the pick-up plates instead of bulk metal electrodes. Details on the FEM simulations for optimization of shoe-box BPMs are given in [9].

The BPM signals are fed into matching transformers because a direct mounting of pre-amplifiers inside the cryostat would exceed the allowed thermal load. Secondly, the expected radiation level close to the BPM (some ten kGy/yr) is too high. Therefore the cable length will reach approx. 5 m, calling for 50 Ohm cables in connection with low impedance amplifiers. To fulfil these requirements transformers for impedance matching have to be used, which have been investigated with respect to their frequency dependent transfer function. After extensive studies of various materials in the frequency range 0.1-100 MHz VITROPERM500F (Vakuumschmelze GmbH&Co.KG) was chosen. Additional measurements of transfer functions at liquid Nitrogen and liquid Helium temperatures have shown no saturation effects [12].

As a second parallel subproject the new data acquisition system has been designed and is currently being tested. As shown in Fig. 3, each of the 12 BPMs of SIS18 is now connected to a LIBERA digitizer (4×14 Bit ADC, 125 MSa/s, [11]). For the broadband analysis of bunch signals by calculating the integrals of the sampled difference and sum data, two steps are implemented in the FPGA: a) window generation [13] and b) baseline restoration [14]. Whereas the algorithm for direct base-band digitization resides in the FPGA, raw data as well as calculated beam positions can be transmitted via 1 GbE Rocket I/Os to data concentrators. This concept allows investigating the position data on a bunch-by-bunch manner. To handle the data rate of 700 MB/s for the 12 BPMs a dedicated network connects the LIBERAs to 2 high performance concentrator servers (Intel quad core PC).

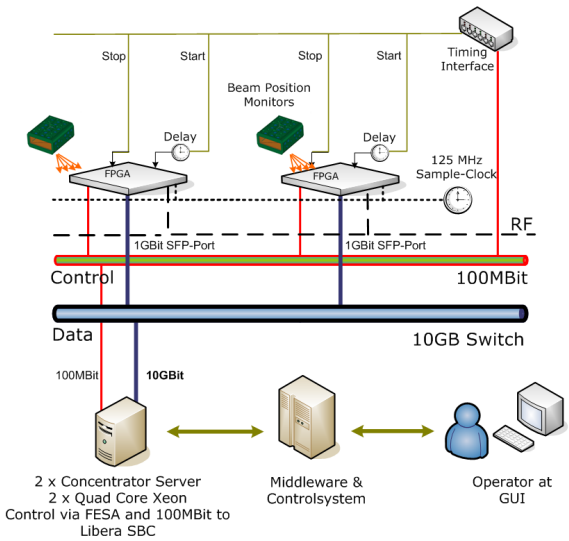


Figure 3: Layout of the new BPM data acquisition system for SIS18.

An industrial partner [15] was contracted to implement the data path from the FESA-controlled LIBERA, via middleware to a JAVA based GUI. Additionally, the system is also capable of online tune measurements by FFT calculation on the position data. The new BPM system is now installed at SIS18 and first tests with beam have been successfully completed.

CONCLUSIONS

We have shown that the demanding beam parameters of FAIR require in many cases advanced diagnostic devices that are currently being developed at GSI. First prototype tests at existing accelerators yield encouraging results. The authors acknowledge W. Vodel, R. Geithner, T. Sieber and A. Peters for the CCC collaboration, U. Raich, J. Belleman for fruitful discussions on the BPM layout and J. Dietrich and D. Liakin for the collaborative work on the IPM.

REFERENCES

[1] www.gsi.de/fair/reports/index.html
[2] M. Arruat et al., ICALEPCS 2007, Knoxville, Tennessee, USA, WOPA04, p. 310.
[3] A. Schlörit, H. Reeg, GSI Scientific Report 2008, to be published.
[4] A. Peters et al., DIPAC1999, Chester, UK, PS05, p. 109.
[5] W. Vodel et al. Proc. PAC 2009, Vancouver, CA, TH5RFP046, to be published.
[6] T. Sieber et al., WEOA02, these proceedings.
[7] V. Kamerdzhiev et al., TUPB12, these proceedings.
[8] D. Liakin et al., EPAC08, Genoa, IT, TUPC060, p. 1194.
[9] P. Kowina et al., MOOC03, these proceedings.
[10] J. Schölles et al., DIPAC05, Lyon, FR, POT021, p. 190.
[11] www.i-tech.si
[12] M. Freimuth et al., GSI-Scientific Report 2008, to be published.
[13] P. Kowina, GSI-Scientific Report 2007, p. 78.
[14] A. Galatis et al., EPAC06, Edinburgh, Scotland, TUPCH012, p. 1019.
[15] www.cosylab.si

BEAM DIAGNOSTICS AND RF SYSTEMS REQUIREMENTS FOR THE SwissFEL FACILITY

Y. Kim*, B. Beutner, H. Braun, A. Citterio, M. Dehler, A. Falone, R. Ganter, T. Garvey, S. Hunziker, R. Ischebeck, B. Keil, M. Pedrozzi, S. Reiche, T. Schilcher, V. Schlott, B. Steffen
Paul Scherrer Institut, CH-5232 Villigen PSI, Switzerland

Abstract

In this paper, we describe four very different operating modes of the SwissFEL facility, the requirements of the challenging beam diagnostics and ultra-stable RF systems needed for two special operating modes with 10 pC, and current developments of beam diagnostics and RF systems for the PSI 250 MeV injector test facility.

INTRODUCTION

SwissFEL will supply coherent, ultra-bright, and ultra-fast XFEL photon beams covering the wavelength range from 0.1 nm to 7 nm. To build the whole facility within about 800 m, PSI will use a 2.5 cell S-band RF gun, a 530 m long normal conducting RF linac, and a 70 m long in-vacuum undulator using the NdFeB with diffused Dy for the hard X-ray beamline and a 70 m long Apple-II type undulator for the polarization controllable soft X-ray beamline [1–3]. SwissFEL will be operated with four very different operating modes according to the overall electron bunch length compression factor, which determines RF jitter tolerances. To begin with, SwissFEL will be operated with a compression factor of 75. After improving the RF systems and beam diagnostics step by step, the facility could be operated with a compression factor of about 2400 to supply a fully coherent single spike XFEL photon pulse. In this paper, we review the requirements of the beam diagnostics and RF systems for two highly challenging operating modes with 10 pC, which have compression factors of 240 and 2400, respectively.

MODES & REQUIREMENTS

To begin with, SwissFEL will be operated with three nominal modes with 10 pC and 200 pC, which have compression factors of 75, 125, and 240 [1]. In the nominal operating modes, a higher single bunch charge of 200 pC will be used to supply more photons per pulse, and a lower single bunch charge of 10 pC will be used to supply shorter photon pulses [1, 3]. For one upgraded mode with 10 pC, RF systems and beam diagnostics will be greatly improved, and attosecond XFEL photon pulses can be generated by increasing the compression factor up to about 2400. For the upgraded operating mode with 10 pC, the soft X-ray beamline will supply transversely as well as longitudinally coherent 250 as (rms) long single spike photon pulses in a range of wavelengths from 0.7 nm to 7 nm, while the hard X-ray beamline will supply transversely coherent 250 as (rms) long multiple spike photon pulses in a range of wavelengths from 0.1 nm to 0.7 nm. Detailed information on the four different operating modes and minimum required and expected beam parameters are summarized in Table 1 [1,3].

Table 1: Parameters of the SwissFEL Project.

Operating Mode		Nominal		Upgraded
Parameters	unit	long pulse	short pulse	atto pulse
beam energy E	GeV	5.8	5.8	5.8 / 3.4
single bunch charge	pC	200	10	10
core-slice emittance	μm	0.43 / 0.38	0.18	0.25
slice rms E-spread	MeV	0.35 / 0.25	0.25	1.00
peak current	kA	2.7 / 1.6	0.7	7
projected emittance	μm	0.65	0.25	0.45
rms bunch length	fs	31 / 47	6.2	2.4
compression factor	·	125 / 75	240	2400
undulator period	mm	15	15	15 / 40
undulator parameter	·	1.2	1.2	1.2 / 1.05
saturation length	m	48 / 55	50	30 / 25
shortest wavelength	nm	0.1	0.1	0.1 / 0.7
rms photon length	fs	12 / 19	2.3	0.25
number of photon	10^9	31 / 32	1.7	3.2 / 31
rms bandwidth	%	0.03 / 0.03	0.035	0.05 / 0.35
single spike pulse	·	no / no	no / no	no / yes
longitudinal coherence	·	no / no	no / no	no / yes
transverse coherence	·	yes / yes	yes / yes	yes / yes

To check the beam quality at the entrance of the undulator for two highly challenging operating modes with 10 pC, we have optimized linac layouts for SwissFEL with the ASTRA and ELEGANT codes, and performed start-to-end (S2E) simulations as summarized in Fig. 1. Here, all key beam dilution effects such as space charge effects up to 150 MeV, short-range transverse and longitudinal wakefields in all linac structures, incoherent synchrotron radiation (ISR) and coherent synchrotron radiation (CSR) in the BC dipoles, and fringe-field and chromatic effects in all magnets are considered. From those S2E simulations, we realized that the lower charge operating modes with 10 pC can supply much better beam quality than the minimum required beam qualities, which are summarized in Table 1.

As shown in Fig. 1(top), in the case of the nominal mode with 10 pC, the rms transverse beam size, the normalized rms projected emittance, and the normalized core-slice emittance at the entrance of an undulator are about 8.5 μm,

* Mail : Yujong.Kim@PSI.ch

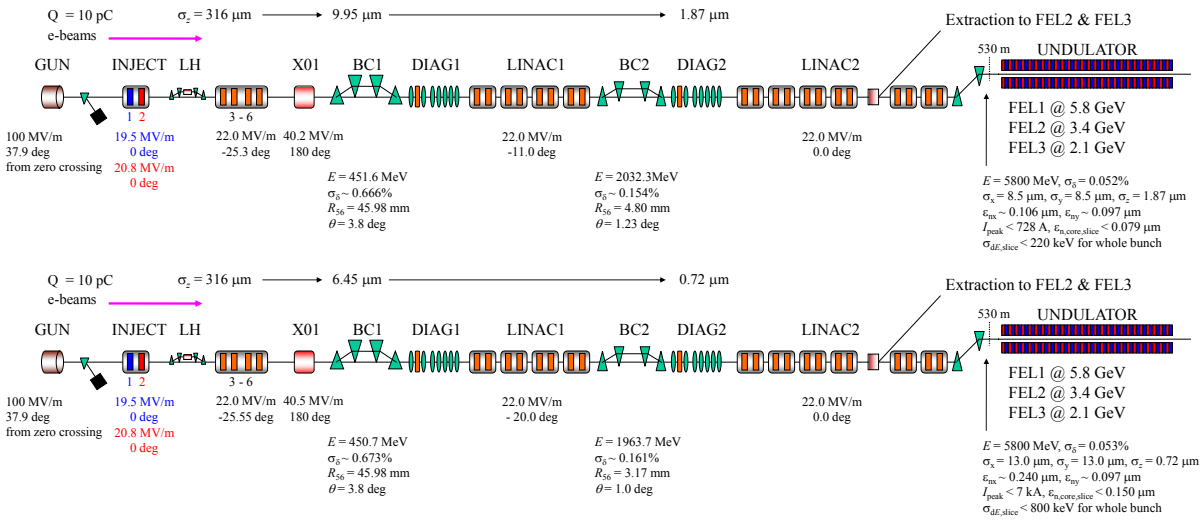


Figure 1: Two special operating modes with 10 pC: nominal mode (top) and upgraded mode (bottom).

0.11 μm, and 0.08 μm, respectively. Since the beam size and emittances are very small in this operating mode, the resolution of the beam based alignment (BBA) or the offset between the ideal design orbit and quadrupole (QM) in the linac should be smaller than 2 μm (rms) to keep emittance growth in the linac smaller than 2% (rms) [1]. Since the transverse rms beam size at the entrance of an undulator is about 8.5 μm (rms), the BPM resolution for undulators should be smaller than 1 μm (rms) to maintain a good overlap between photon beams and electron beams for lasing. Additionally, the resolution of OTR screens in the linac should be smaller than 2 μm (zero-to-peak *i.e.*, z-to-p) to detect 5% projected emittance growth in the linac. Even though the peak current is only 728 A, the photon beam power can be saturated within 50 m of undulator due to the ultra-low core-slice emittance. The requirements for the nominal operating mode with 10 pC are summarized in Table 2. Here, we assume that the repetition rate is 100 Hz, and six S-band klystrons and two X-band klystrons will be used in the injector linac [1]. To determine RF tolerances for the nominal mode with 10 pC, we assume that an active orbit feedback system is working in front of the undulator beamline, and we used the following four criteria on XFEL performance; beam arrival time error $\triangle T_{arrival} \leq 30$ fs (z-to-p), saturation power error $\triangle P_{sat}/P_{sat} \leq 30\%$ (z-to-p), central wavelength error $\triangle \lambda_0/\lambda_0 \leq 0.001\%$ (z-to-p), and power saturation length error $\triangle L_{sat}/L_{sat} \leq 15\%$ (z-to-p) from 80% core slices for 60 seconds.

As summarized in Table 1 and as shown in Fig. 1(bottom), the 250 as (rms) long photon pulses can be generated by compressing the electron bunch length down to about 2.4 fs (rms). For the upgraded operating mode with 10 pC, the longitudinal beam diagnostic systems, the RF reference timing distribution system, and the RF low level systems are extremely challenging due to the ultra-short electron bunch and the photon pulse length as summarized in Table 3. Here, we assume that

Table 2: Requirements of Nominal Mode with 10 pC.

Parameters	Tolerances
gun laser arrival time error	$\leq$ 5 fs (rms)
single bunch charge error	$\leq$ 1% (rms)
INJECT S-band $\triangle\phi_s$ per klystron (total six)	$\leq$ 0.01 deg (rms)
INJECT S-band $\triangle V_s/V_s$ per klystron (total six)	$\leq$ 0.01% (rms)
X-band $\triangle\phi_x$ per klystron (total two)	$\leq$ 0.06 deg (rms)
X-band $\triangle V_x/V_x$ error per klystron (total two)	$\leq$ 0.06% (rms)
gun solenoid misalignment after BBA	$\leq$ 20 μm (z-to-p)
S-band structure misalignment after BBA	$\leq$ 100 μm (z-to-p)
S-band solenoid misalignment after BBA	$\leq$ 50 μm (z-to-p)
X-band structure misalignment after BBA	$\leq$ 50 μm (z-to-p)
BC dipole misalignment after BBA	$\leq$ 50 μm (z-to-p)
BC dipole roll error after BBA	$\leq$ 25 μrad (z-to-p)
BBA resolution	$\leq$ 2 μm (rms)
screen resolution to detect 5% emittance growth	$\leq$ 2 μm (z-to-p)
gun solenoid power supply error $\triangle I_{sol}/I_{sol}$	$\leq$ 10 ppm (rms)
BC dipole power supply error $\triangle I_{bc}/I_{bc}$	$\leq$ 10 ppm (rms)
QM power supply error $\triangle I_{qm}/I_{qm}$	$\leq$ 10 ppm (rms)
steerer power supply error $\triangle I_{st}/I_{st}$	$\leq$ 10 ppm (rms)
girder vibration amplitude from 2 Hz to 200 Hz	$\leq$ 50 nm (rms)
undulator BPM resolution	$\leq$ 0.85 μm (rms)

six S-band klystrons and six X-band klystrons will be used in the injector linac to operate SwissFEL facility at 400 Hz [1]. Due to a much stronger power fluctuation, a much higher uncorrelated energy spread, and a much shorter photon pulse, we have used four somewhat different criteria to determine RF tolerances for the single spike operating mode with 10 pC; $\triangle T_{arrival} \leq 5$ fs (z-to-p), $\triangle P_{sat}/P_{sat} \leq 100\%$ (z-to-p), $\triangle \lambda_0/\lambda_0 \leq 0.01\%$ (z-to-p), $\triangle L_{sat}/L_{sat} \leq 15\%$ (z-to-p) from 80% core slices for 60 seconds. Here we also assume that an active orbit feedback system is working in front of the undulator beamline. For the upgraded operating mode, the other

Table 3: Requirements of Upgraded Mode with 10 pC.

Parameters	Tolerances
gun laser arrival time error	$\leq$ 1 fs (rms)
single bunch charge error	$\leq$ 1% (rms)
INJECT S-band $\triangle\phi_s$ per klystron (total six)	≤ 0.005 deg (rms)
INJECT S-band $\triangle V_s/V_s$ per klystron (total six)	$\leq 0.005\%$ (rms)
X-band $\triangle\phi_x$ per klystron (total six)	≤ 0.005 deg (rms)
X-band $\triangle V_x/V_x$ per klystron (total six)	$\leq 0.025\%$ (rms)
BC1 dipole power supply error $\triangle I_{bc1}/I_{bc1}$	≤ 7.5 ppm (rms)
LINAC1 $\triangle\phi_1$ per klystron	≤ 0.015 deg (rms)
LINAC1 $\triangle V_1/V_1$ per klystron	$\leq 0.010\%$ (rms)
BC2 dipole power supply error $\triangle I_{bc2}/I_{bc2}$	≤ 7.5 ppm (rms)
LINAC2 $\triangle\phi_2$ per klystron	≤ 0.017 deg (rms)
LINAC2 $\triangle V_2/V_2$ per klystron	$\leq 0.011\%$ (rms)

requirements which are not shown in Table 3 are the same as those for the nominal mode with 10 pC in Table 2.

CURRENT DEVELOPMENTS

As discussed in the previous section, challenging transverse beam diagnostic systems are required for the nominal operating mode with 10 pC due to its small beamsize and the low emittance, and highly challenging longitudinal beam diagnostic systems, RF reference timing distribution system, and RF low level systems are required for the upgraded operating mode with 10 pC due to its short electron bunch length. To develop these diagnostic systems and RF systems, PSI is constructing a 250 MeV injector test facility, and its first commissioning will start at the end of 2009 [5]. Accelerator design concepts and two advanced beam diagnostic sections of the 250 MeV injector test facility are described in references [1, 4, 5].

Here we give some examples of current developments of beam diagnostics and RF systems for the 250 MeV injector. Further details can be found from references [1, 5–13]. The 250 MeV injector will use two different technologies to distribute the RF reference timing. One is an electrical timing distribution system with a temperature controlled coaxial cable. The other is an optical timing distribution system with a mode locked laser (MLL) based optical master oscillator. At the moment, an ultra-low timing jitter of 3.3 fs (rms) for 1 kHz to 10 MHz has been demonstrated with the latter technology [6]. To get a wide dynamic range from 10 pC to 200 pC, the injector test facility will use various screen methods which are all attached on a ladder actuator [7]. To measure the projected emittance in the presence of coherent optical transition radiation (COTR) emission, a wire scanner will be installed on the ladder. Additionally, we are testing a cooled CCD camera to improve the signal-to-noise ratio during 10 pC operation as well as a fast gated CCD camera to obtain an individual beam image during two or three bunch operation [7]. The injector test facility will test two different BPMs. The first one is the resonant stripline BPM with a required resolution of about 10 μm (rms) for 10 pC and 200 pC, and the second one is an RF cavity BPM with a sub-micron rms resolution [8, 9]. To minimize the projected emittance growth due to transverse wakefields in an X-band linac structure, the injector test facility will use a HOM coupler based structure alignment system, which can align tilts, bends, offset, and cell-to-cell misalignment of the X-band structure within a few μrad or μm (rms) [10]. For the single-shot measurement of electron longitudinal profile or bunch length with a resolution of 100 fs (rms), the injector will use an electro-optical (EO) crystal based compact bunch length monitor [11]. To measure electron bunch length with a much higher resolution, the injector will use two transverse deflecting structures (TDSs). At the gun region, there is a single cell deflecting structure (TDS1) to measure the slice emittance, the bunch length, and the longitudinal phase space [12]. Its expected time resolution is about 42 fs (rms) for 10 pC electron beams. Without changing any optics, to measure various parameters such as electron bunch length, slice emittance, slice energy spread, longitudinal phase space, beam arrival time jitter, projected emittance, Twiss parameters, and optics matching, the injector has an advanced beam diagnostic section after the bunch compressor [1,5,13]. In the advanced diagnostic section, there are specially designed asymmetric three and half FODO cells and a five cell deflecting structure (TDS2) to measure bunch length with a time resolution of about 11 fs (rms) for 10 pC [1, 5].

SUMMARY

Due to two low charge, 10 pC operating modes, the requirements on beam diagnostic systems, the RF reference timing distribution system, and the RF low level system are highly challenging for stable operation of the SwissFEL facility. To develop these required technologies for SwissFEL, the PSI 250 MeV injector test facility is under construction. Since there are strong random orbit fluctuations in undulators due to CSR kick and RF jitters, we are also investigating its impact on the orbit feedback system and XFEL performance during the upgraded mode.

REFERENCES

[1] Y. Kim *et al*., in *Proc. FEL2009*, Liverpool, UK.
[2] T. Schmidt *et al*., in *Proc. FEL2009*, Liverpool, UK.
[3] S. Reiche *et al*., in *Proc. FEL2009*, Liverpool, UK.
[4] Y. Kim *et al*., in *Proc. EPAC200*8, Genoa, Italy.
[5] M. Pedrozzi *et al*., in *Proc. FEL2009*, Liverpool, UK.
[6] S. Hunziker *et al*., in these proceedings.
[7] R. Ischebeck *et al*., in these proceedings.
[8] A. Citterio *et al*., in these proceedings.
[9] B. Keil *et al*., in these proceedings.
[10] M. Dehler *et al*., in these proceedings.
[11] B. Steffen *et al*., in these proceedings.
[12] A. Falone *et al*., in *Proc. PAC2009*, Vancouver, Canada.
[13] B. Beutner *et al*., in *Proc. FEL2009*, Liverpool, UK.

RECENT RESULTS FROM THE OPTICAL REPLICA SYNTHESIZER EXPERIMENT IN FLASH

G. Angelova-Hamberg, V. Ziemann, Uppsala University, Sweden
P. van der Meulen, P. Salén, M. Larsson, Stockholm University, Sweden
H. Schlarb, J. Bödewadt, A.Winter, F. Löhl, E. Saldin, E. Schneidmiller, M. Yurkov, DESY, Germany
S. Khan, DELTA, TU Dortmund, Germany
A. Meseck, Helmholtzzentrum Berlin, Germany

Abstract

We present very promising recent results from the optical replica synthesizer experiment in FLASH where we manipulate ultrashort electron bunches in FLASH with a laser in order to stimulate them to emit a coherent light pulse from which the temporal structure of the electron bunches can be obtained using laser diagnostic (FROG) methods.

INTRODUCTION

Monitoring and tuning the bunch properties are essential for the reliable operation of linac-based SASE free-electron lasers such as FLASH [1], XFEL [2], or LCLS [3]. This need has triggered the development of new diagnostic methods based on a transversely deflecting cavity [4] or electro-optical sampling [5]. The optical replica synthesizer (ORS), a complementary scheme that was introduced in Ref. [6], is similar to an optical klystron FEL seeded by an infrared laser as is shown in Fig. 1. In the modulator the interaction of the laser with the transversely oscillating electrons causes an energy modulation. A dispersive section turns this energy modulation into a density modulation at the wavelength of the light. In a following radiator undulator the micro-bunched beam radiates coherently and the emitted light pulse allows to deduce the longitudinal profile of the electron beam. Hence the name optical replica synthesizer.

The optical replica pulse is analyzed in a FROG (frequency resolved optical gating) device [7], which is based on recording the spectrally resolved auto-correlation. Subsequent application of a pulse retrieval algorithm reveals both amplitude and phase of the incident electric field and thus of the longitudinal profile of the electron bunch. A very compact second harmonic FROG device called Grenouille [8] is available commercially and the traces are analyzed with the VideoFROG [9] software.

The complete system of seed laser, laser transport line, two undulators, the chicane and two optical stations for timing and FROG analysis was installed in FLASH during a shutdown period in spring 2007. In the remainder of this report we briefly describe the hardware components and the commissioning progress that culminated in the recent observation of FROG traces.

HARDWARE

The laser system is located in a newly erected building next to the FLASH tunnel and connected to the accelerator tunnel by a pipe through which the laser beam is transported. The laser itself is based on a Erbium-doped fiber oscillator [10] operating at 1550 nm that is phase-locked to the radio-frequency (RF) system of the accelerator. The phase-lock is accomplished by comparing the phase of the 24^{th} harmonic of the laser oscillator round-trip frequency at 1.3 GHz with the RF signal and adjusting the length of the optical fiber that is wound on a piezo-crystal by applying a voltage to the crystal. The timing is thus stabilized to about 50 fs. The relative timing of laser and RF can be adjusted by changing the phase of the RF signal with a vector-modulator. The stabilized pulses are amplified and frequency-doubled in a 1 mm PPLN crystal and subsequently passed to a Clark-MXR CPA-2001 regenerative Titanium-Sapphire amplifier that is based on chirped-pulse amplification and pumped by a Nd:YAG laser. This system delivers pulses with a center wavelength of 772 nm, up to 1 mJ energy per pulse and a full-width at half-maximum (FWHM) pulse length down to 150 fs.

To reach the accelerator, the laser pulse travels through a 12 m long laser transport system with remotely controlled motorized mirrors and a two-lens telescope that provides a narrow laser waist in the laser-electron interaction zone inside the modulator. For diagnostic purposes the laser beam can be reflected back to the laser building with a mirror where the position and size of the laser waist can be measured. With the mirror retracted the laser pulse is injected into the accelerator beam pipe through a back-tangent window located near the second dipole of a dog-leg chicane.

Inside the accelerator beam pipe the laser pulse co-propagates with the electron beam, passes the modulator undulator and is extracted by a silver-coated silicon OTR screen installed in the middle of the four-magnet chicane on the first optical station OS1. The optical station accommodates a camera, photo diodes with 1.5 GHz bandwidth, and a power meter in order to analyze the laser pulse and to determine the relative timing of the laser pulse and the electron beam by observing the laser pulse and the synchrotron radiation pulse from the electron beam generated in the modulator on a photo diode. The electron beam continues to propagate through the radiator undulator and pass a second optical station (OS2) where the light created at or re-

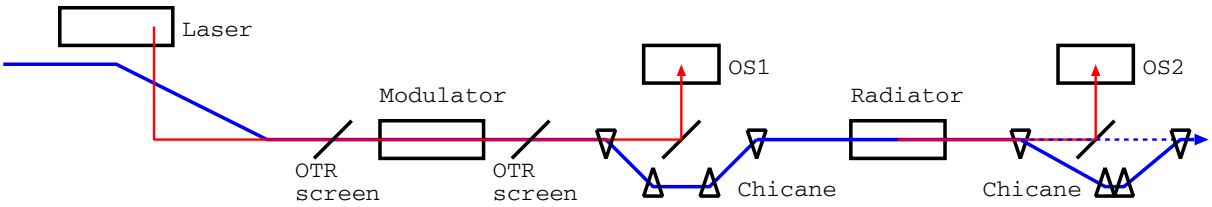


Figure 1: Schematics of the Optical Replica Synthesizer.

flected from a silver-coated silicon OTR screen is guided to an optical table. There it is recorded by a Basler A331 camera or analyzed with a power meter or the GRENOUILLE which is used to reconstruct the longitudinal intensity profile and the phase of the replica pulse. For the ORS experiments the electron beam will be directed around the OTR screen on OS2 by a second chicane, as is shown by the thin line in Fig. 1. Alternatively the electron beam can also be directed onto the OTR screen by switching off the chicane in order to observe the coherent radiation stemming from the micro-bunched beam [11]. Both the modulator and radiator undulator have 5 periods + 2 correction periods with 0.2 m period length and a peak field up to 0.45 T. The magnet gap is 40 mm in order to accommodate 38 mm beam pipe. The modulator is vertically deflecting and the radiator is horizontally deflecting which allows separating the vertically polarized laser pulse from the horizontally polarized replica pulse generated in the radiator.

EXPERIMENT PREPARATION

We received normally a few experimental shifts every few months to commission the system and careful preparation of the laser system such that the laser oscillator is mode-locked and that the laser timing is phase-locked to the RF is essential. We then continue to carefully flatten the electron orbit to below 0.1 mm in the section between the modulator undulator and OS2 and then record the electron position on OTR screens adjacent the modulator. Note that normally the modulator is turned off to avoid its synchrotron radiation reaching the downstream OTR screen because that increases the recorded spot size on the screen and reduces the precision of the overlap-finding procedure. Once the electron beam is aligned we inject the laser pulses and direct them onto the same transverse position on the OTR screens with mirrors. Once the transverse overlap is achieved we turn on the modulator undulator and the first chicane and observe the laser pulse and the synchrotron radiation pulse from the modulator on the photo-diode on OS1 while the electron beam passes on further downstream. Observing the signal on a fast oscilloscope and adjusting the relative timing between electron beam and laser pulse with the vector modulator we can match the arrival time of electron beam and laser pulse on the photodiode to better than a few 100 ps. Fine-tuning the temporal overlap is done by passing the electron beam through the OTR screen on OS2, as indicated by the dotted line on Fig. 1, and observing the OTR light as the timing is varied with the vector modulator on a sub-ps time scale. Once the laser pulse and the electron beam overlap inside the modulator an energy modulation of the electron beam results which is transformed into a density modulation in the chicane. When the micro-bunched electron beam intercepts the screen on OS2 it causes the emission of coherent transition radiation that is enhanced by several orders of magnitude compared to the ordinary OTR light. Plotting the average intensity within a 'region of interest' (the red underlaid spot on Fig. 2) versus the timing clearly indicates the overlap and can actually be used to record the bunch profile and longitudinal-transverse correlations of bunches that are a few pico-seconds long. A typical scan is shown in Fig. 3. Details of the procedure are reported in Refs. [11, 12]. Once the longitudinal overlap is established we turn the radiator undulator on and tune it to resonance. The electron beam is made to bypass the OTR screen on OS2 by turning on the second four-magnet chicane as is in-

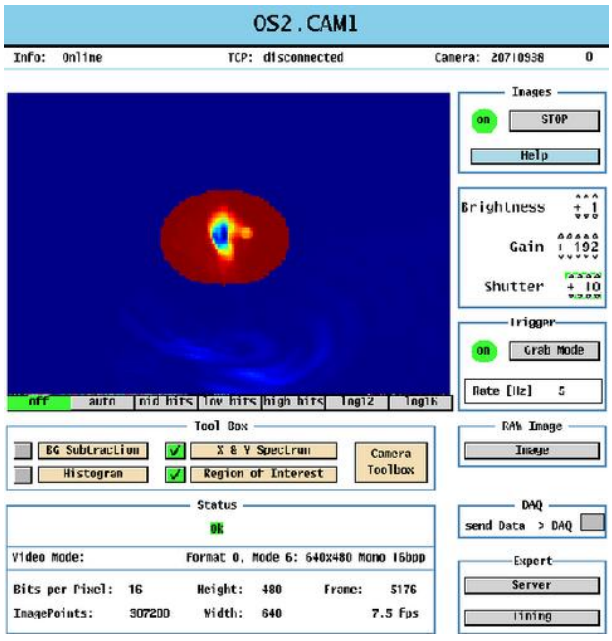


Figure 2: The beam spot on a camera observing the screen on OS2 with the region of interest indicated by the bigger read circle.

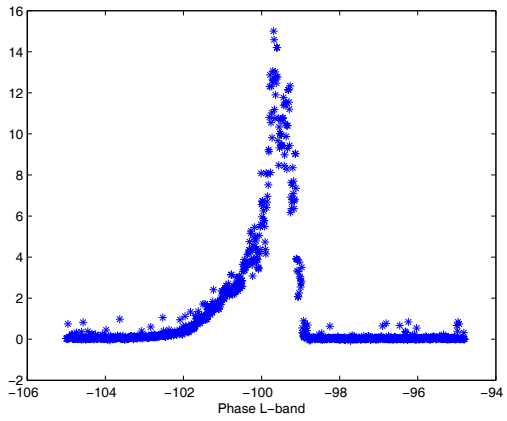


Figure 3: The average intensity within the region of interest as a function of the relative timing between laser pulse and electron beam.

dicated on Fig. 1. In this way the electron bunch propagates further downstream through the SASE undulator and the micro-bunched electron bunches emit a coherent radiation pulse in the radiator undulator that is passed through a set of irises to facilitate the alignment into the GRENOUILLE located on an optical table under the accelerator beam pipe.

RESULTS

During shifts in January and March with 700 and 900 MeV electrons with SASE conditions, i.e. that the bunches are compressed to exhibit a current spike and the SASE undulator lases, we performed the preparatory work elaborated above and after careful alignment of the radiation from the radiator undulator on the input iris of the GRENOUILLE that is controlled by the VideoFROG software [9] we could finally record FROG traces with compressed electron bunch and a laser pulse length of 400 fs (FWHM). The analysis of these traces is under way but incomplete. In particular we were unable record simultaneous profiles with the transversely deflecting cavity LOLA [4] due to various unfortunate circumstances. More time to do scans of various parameters such as varying the electron bunch length and comparing with simultaneous LOLA measurements or varying the R_{56} of the first chicane is definitely needed.

It is noteworthy that during the time the ORS was running and the second chicane around OS2 was turned on such that the electron beam passed through the downstream SASE undulator and also the Far-Infrared undulator [13], which is located downstream of the SASE undulator. We performed initial tests to observe coherent enhancement of the radiation from the FIR undulator when tuned to the bunching wavelength 772 nm of the ORS. This opens up possibilities to mix the coherently enhanced radiation with an external pump-probe laser for timing purposes.

CONCLUSIONS

We have observed and started to analyze the first FROG traces from a compressed electron bunch in the optical replica synthesizer experiment in FLASH. Despite generous allotment of beam time we were unable to do careful systematic analyses by performing scans with bunches of different lengths because of the rather long experiment preparation time. Fortunately, the promising results have led to the conclusion to relocate the ORS setup with undulators and optical tables to the rebuilt sFLASH after the coming shutdown such that there will be further opportunities for experiments.

Support from the FLASH crew during installation and running the experiment is highly appreciated. Extensive financial support from the UU-SU-KTH FEL-center is acknowledged.

REFERENCES

[1] J. Rossbach, *Observation of self-amplified spontaneous emission in the wavelength range from 80 to 180 nm at the TESLA test facility FEL at DESY,* Nucl. Inst. Meth. A475 (2001) 13.

[2] P. Audebert, et.al., *TESLA XFEL: The first stage of the X-ray laser laboratory - Technical Design Report,* DESY 2002-167.

[3] The LCLS Design Study Group, *LCLS Design Study Report,* SLAC-R-593, 2002.

[4] O. Grimm et al., *Longitudinal bunch shape diagnostics with coherent radiation an a transverse deflecting cavity in TTF2,* Proceedings of FEL04, p. 395.

[5] G. Berden, et al., *Electro-Optic Technique with Improved Time Resolution for Real-Time, Nondestructive, Single-Shot Measurements of Femtosecond Electron Bunch Profiles,* Phys. Rev. Lett. 93 (2004) 114802.

[6] E. Saldin, E. Schneidmiller, M. Yurkov, *A simple method for the determination of the structure of ultrashort relativistic electron bunches,* Nucl. Inst. and Methods **A 539** (2005) 499.

[7] R. Trebino, *Frequency Resolved Optical Gating,* Kluwer Academic, Boston, 2000.

[8] `www.swampoptics.com`

[9] `www.mesaphotonics.com`

[10] A. Winter, P. Schmüser, F. Loehl, H. Schlarb, W. Jalmuzna, *Status of the Laser Master Oscillator System at FLASH,* Proceedings of PAC07, p. 191.

[11] G. Angelova, et al., *Observation of two-dimensional longitudinal-transverse correlations in an electron beam by laser-electron interactions,* Physical Review Special Topics - Accelerators and Beams 11 (2008) 070702.

[12] G. Angelova, et.al., *Results from the optical replica experiment in FLASH,* Proceedings of EPAC08, p. 1332.

[13] M. Gensch et al., *New infrared undulator beamline at FLASH,* Infrared physics and Technology 51 (2008) 423.

PHYSICS REQUIREMENTS FOR LINAC STABILIZATION AND TECHNICAL SOLUTIONS

J. Carwardine, Argonne National Laboratory, Argonne, IL 60439, U.S.A.

Abstract

This paper gives a general overview of active and passive stabilization systems, which are mainly required for future X-FEL and high-energy linear colliders. Key physics criteria for beam stability for X-FELS and linear colliders will be introduced and resulting technical implications discussed. New and innovative approaches to the design and development of state-of-the-art linear accelerator components and stabilization systems will be reviewed, and recent results shown from selected prototypes and new machine installations.

INTRODUCTION

Achieving performance specifications of modern accelerators places narrow tolerances on a wide range of technical parameters. The location of magnetic optics elements in space, their field strengths, and particle energy all must remain within tight bounds.

Within the context of stabilizing beams with dimensions measured in microns, there are many potential sources of drift and jitter that must be taken into account.

Sources of drift and slow changes include air and cooling water temperatures, ground motion due to settlement and lunar cycles. Medium timescale disturbances include girder vibration excited by ground motion, cooling pipes, or mechanical pumps. Faster disturbances include power supply ripple, rf jitter, switching magnet jitter, etc.

In our discussion of linac beam stabilization, we will focus on four large-scale pulsed electron linacs: LCLS and the European XFEL (both x-ray photon sources); and ILC and CLIC (both linear colliders). Table 1 lists some of their main parameters [1-4].

Table 1: Main Linac Parameters

	ILC	CLIC	EU-XFEL	LCLS	
Max. Energy	2x 250	2x 1500	20	13	GeV
ML Length	2x 12	2x 21	1.6	1	km
Cavity type	S/C	N/C	S/C	N/C	
RF Freq	1.3	12	1.3	12 + 2.8	GHz
RF source	Klystron	Drive beam	Klystron	Klystron	
Pulse rate	5	50	10	120	Hz
Pulse length	970	0.15	650	--	μs
Bunches / Pulse	2670	312	3250	1	
Bunch length	300	44	25	20	μm
Bunch size	640 nm x 5.7 nm	45 nm x 0.9 nm	20-30 μm	37 μm	

S/C: Superconducting N/C: normal conducting

These represent the most recent generation of linacs: LCLS is in commissioning and XFEL is under construction; while ILC and CLIC remain in development and proof-of-principle stages respectively.

All four machines present significant technical challenges, in part due to their large scale and complexity. From a beam stabilization perspective, these include distribution of precision rf phase references to many locations over distances of kilometers to tens of kilometers and stabilizing beams with dimensions of nanometers.

This next section gives a brief overview of the four machines and discusses their performance and stabilization criteria. Some examples of technical solutions will also be discussed.

PHOTON SOURCES: LCLS AND EU-XFEL

For certain classes of photon user experiments, FEL-based sources such as LCLS and XFEL dramatically exceed the capabilities of storage ring light sources by:

- Peak brightness is many orders of magnitude higher than the present storage ring photon sources
- Sub-picosecond photon pulse lengths compared with 10's to 100's ps from storage rings
- Photon beams are transversally fully coherent

The ultra-short pulse lengths will make it possible to study the time evolution of chemical processes that occur in timeframes of 100's femtoseconds to picoseconds, while the high coherence will open up new classes of imaging experiments.

A comparison of peak and average brightness with other light sources is shown in Fig. 1.

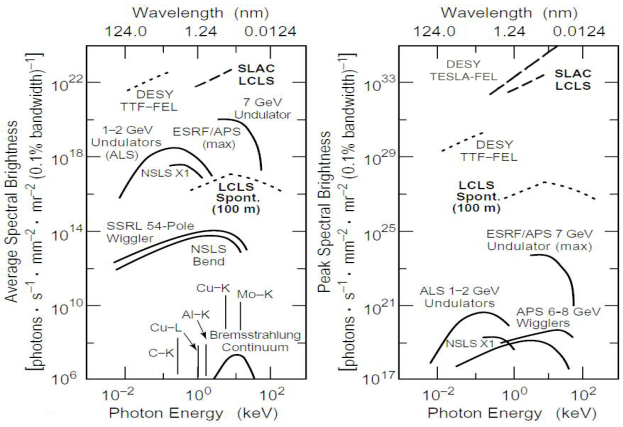


Figure 1: Average and peak brightness calculated for photon sources that are operating or under construction.

Lasing occurs through a process of Self-Amplified Spontaneous Emission (SASE). Referring to Fig. 2, synchrotron radiation is emitted in a narrow forward cone as the beam travels through the alternating magnetic field of a long undulator.

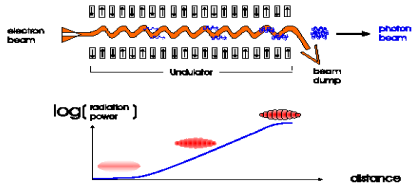


Figure 2: Principle of the FEL process.

The electric field of the synchrotron radiation density-modulates the electron beam longitudinally at the wavelength of the light (micro-bunching). Particles within an optical wavelength emit synchrotron light coherently, and consequently the intensity of the light grows as the square of the number of particles. The more intense light enhances the density modulation and the process grows exponentially until it reaches saturation after about ten gain-lengths of the undulator. The process requires high-energy electron beams with low emittance, high peak currents, and small energy spread.

A schematic layout of the XFEL accelerator is shown in Fig. 3 [5]. (A schematic layout of LCLS is shown in Fig. 8 to follow). Both XFEL and LCLS accelerators comprise an rf gun, followed by two bunch compressors and the main linac.

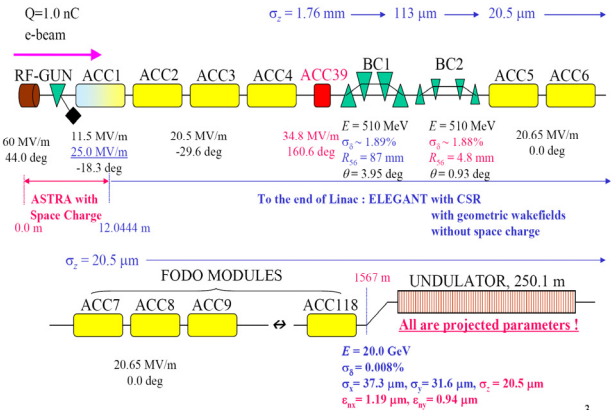


Figure 3: Schematic layout of the XFEL accelerator.

Stringent tolerances are placed on RF cavity phase and amplitude to achieve the necessary energy stability, bunch length, and peak bunch current. Example tolerances and sensitivities for XFEL are shown in Table 2 [6] and for LCLS are documented in the references [7]. Stabilizing pulsed cavity fields to the level of 0.01% and 0.01 degrees is state of the art. RF phase reference distribution to this level of performance goes beyond the state of the art.

Experiment techniques used by the ultra-fast science community place difficult timing and synchronization requirements on XFEL and LCLS. Pump-probe experiments require that the photon bunch and the pulse from a local pump laser to illuminate the sample with a precise delay of a fraction of the photon bunch duration. Synchronization to the 10's of femtosecond level is beyond the present state of the art.

Table 2: Example RF Tolerances & Sensitivities (XFEL)

	Sensitivity(p2p)	Tol. (p2p)	Tol. (rms)	Threshold
dT	± 0.729 ps	± 0.300 ps	0.100 ps	saturation length
dQ/Q	± 5.452%	± 3.000%	1.000%	saturation length
ACC1C1234 phase	± 0.133 deg	± 0.045 deg	0.015 deg	saturation length
ACC1C1234 dV/V	± 0.129%	± 0.045%	0.015%	arriving time
ACC1C5678 phase	± 0.072 deg	± 0.045 deg	0.015 deg	saturation power
ACC1C5678 dV/V	± 0.063%	± 0.045%	0.015%	arriving time
ACC234 phase	± 0.048 deg	± 0.045 deg	0.015 deg	arriving time
ACC234 dV/V	± 0.045%	± 0.045%	0.015%	arriving time
ACC39 phase	± 0.064 deg	± 0.045 deg	0.015 deg	saturation power
ACC39 dV/V	± 0.142%	± 0.045%	0.015%	arriving time
BC1 dI/I	± 0.013%	± 0.012%	0.004%	arriving time
ACC56 phase	± 0.721 deg	± 0.045 deg	0.015 deg	arriving time
ACC56 dV/V	± 0.913%	± 0.045%	0.015%	saturation length
BC2 dI/I	± 0.201%	± 0.012%	0.004%	arriving time
ACC78910 phase	±10.037 deg	± 0.045 deg	0.015 deg	SASE wavelength
ACC78910 dV/V	± 0.060%	± 0.045%	0.015%	SASE wavelength

LINEAR COLLIDERS: ILC AND CLIC

In recent years, high-energy physics experiments have explored the 100 GeV energy range using hadron colliders such as the Tevatron at Fermilab and lepton colliders such as LEP at CERN. Attention is now shifting to the TeV energy range, which will be first explored at the Large Hadron Collider at CERN. A widely anticipated result from the LHC is discovery of the Higgs Boson and validation of the so-called Standard Model of particle physics. While hadron colliders provide a wealth of physics through a broad spectrum of particle-particle interactions, lepton colliders provide precision measurements over a narrow spectrum of particle interactions. As such, information from both types of collider is necessary to develop a complete understanding of physics in the energy range. To complement the LHC, development is in progress for an e+/e- linear collider.

Present linear collider development efforts are converging on the International Linear Collider, which uses superconducting accelerating cavities to reach a center-of-mass energy of 500 GeV. As shown in Fig. 4, the ILC comprises the following major elements:

- Polarized electron source
- Undulator-based positron source
- Damping rings to develop very low emittance beams
- One or two bunch compressors
- Two counter-posing accelerating linacs
- Beam delivery systems to focus the beams and bring them into collision at the Interaction Point

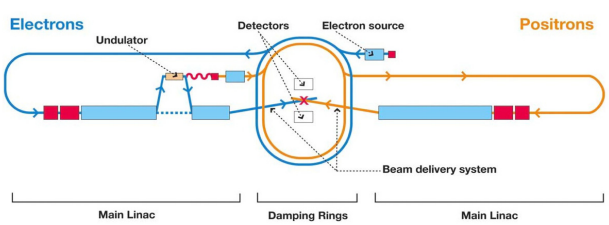


Figure 4: ILC top-level layout.

While it is anticipated that 500 GeV center-of-mass will be sufficient to explore the new physics of the Higgs, some theories that go beyond the standard model predict that energy well above 500 GeV might be required. A separate R&D effort is ongoing at CERN to prove and develop a novel linac concept with the intention of reaching center-of-mass energies up to 3 TeV. The Compact Linear Collider (CLIC) uses normal-conducting accelerating structures that receive their RF power from a second high power electron beam that travels parallel to the main accelerator (Fig. 5).

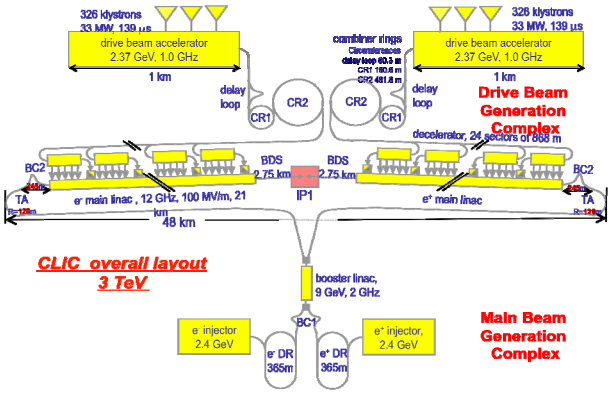


Figure 5: Schematic layout of CLIC.

Both the ILC and CLIC are of an unprecedented scale and complexity. For example, each ILC main linac has some 8,000 superconducting cavities housed in 1,000 cryomodules, powered by 320 10 MW rf klystrons. In the case of CLIC, the complexity is increased by the existence of the drive beam accelerators.

Stability challenges originate at the interaction point where the two beams collide. To achieve the highest luminosity, optics for the electron and positron beam delivery systems must be optimally matched at the IP, and the two beams must be synchronized to intersect perfectly at the IP. Tolerances for optics matching, arrival times, and trajectory errors must have impacts that are small, relative to the bunch dimensions.

A luminosity loss budget example for CLIC is shown in Table 3, clearly illustrating the degree of stability needed to stabilize nanometer-scale beams. Whether it is feasible to stabilize large structures to the sub-nanometer level is under study by the CLIC Stabilization Group [9].

Table 3: Example Luminosity Loss Budget for CLIC

Source	budget	raw tolerance
Damping ring extraction jitter	1%	
Magnetic field variations	?%	
Bunch compressor jitter	1%	
Quadrupole jitter in main linac	1%	$\Delta\epsilon_y = 0.4$ nm $\sigma_{jitter} \approx 1.5$ nm
Structure pos. jitter in main linac	0.1%	$\Delta\epsilon_y = 0.04$ nm $\sigma_{jitter} \approx 200$ nm
Structure angle jitter in main linac	0.1%	$\Delta\epsilon_y = 0.04$ nm $\sigma_{jitter} \approx 170$ nradian
RF jitter in main linac	1%	
Crab cavity phase jitter	1%	$\sigma_\phi \approx 0.01°$
Final doublet quadrupole support jitter	1%	$\sigma_{jitter} \approx 0.18$ nm
Other quadrupole jitter in BDS	1%	
...	?%	

EXAMPLES OF TECHNICAL SOLUTIONS

In this section, examples of technical solutions and approaches to meeting stabilization requirements will be discussed.

Precision Timing and Synchronization

A major challenge for large linacs is to implement a timing and synchronization system with the needed accuracy and stability:

- Ultra-stable RF phase references must be distributed over kilometer distances to multiple RF stations while maintaining the relative phase between stations and the absolute phase relative to the beam. Stability of the phase references must exceed the 0.01-degree stability required in the rf cavities
- ILC and CLIC require the electron and positron bunch arrival times at the interaction point to be synchronized within a fraction of a bunch length
- LCLS and XFEL pump-probe experiments require synchronization of the FEL photon bunch with a pump laser at the <10 fs scale

Significant progress is being made in developing methods for distributing ultra-stable phase references and in timing synchronization. Schemes for actively stabilized links using pulsed and CW lasers are being developed. An rf phase reference transmission scheme developed at LBL uses a CW laser modulated by rf (Fig. 6). Stability of <100 fs rms over 12 hrs has been reported for fiber lengths of 2 km [10].

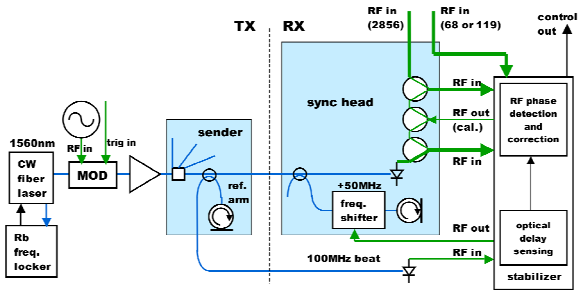


Figure 6: LBL optical RF distribution system.

Bunch arrival monitors using electro-optical sampling techniques provide a means to phase-lock a bunch train and to tag each bunch with an arrival time. Principles of the bunch arrival monitor (BAM) are shown in Fig. 7.

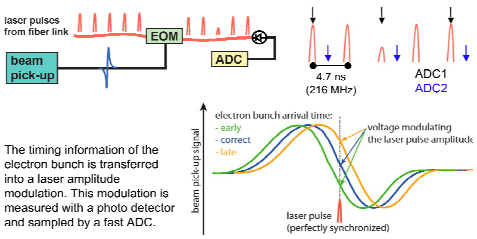


Figure 7: Bunch Arrival Time Monitor.

Reference laser pulses pass through an electro-optical modulator that is driven by the signal from a beam pick-up. Changes in the arrival time of the electron beam cause different modulation voltages at the laser pulse arrival time. The resulting change in laser amplitude is detected using a photo detector. The resolution of these devices is improving rapidly, and single-bunch measurement resolutions of <6 fs have been recently reported [11].

Time-tagging each bunch allows pump-probe experiments to identify bunches where the arrival time of the photon bunch is within the desired time window relative to the pump laser. Other ways to tag bunches with their relative arrival time is to correlate light from the pump laser and photon pulse using a streak camera.

LCLS Longitudinal Feedback System

A pulse-by-pulse longitudinal feedback system has been implemented in at LCLS to stabilize beam energy and bunch lengths [12, 13]. The overall topology is shown in Fig. 8. Beam energy is measured at the end of each linac section and regulated by adjusting the amplitude of the rf drive to the accelerating structures. Both phase and amplitude of the rf drive to the bunch compressors are regulated in order to stabilize both the beam energy and the bunch length.

Bunch lengths are measured using coherent synchrotron radiation in the chicanes of the two bunch compressors and energy is measured using high-resolution bpms after each section. Rather than implanting cascaded feedback loops around each linac section, all the feedback loops are integrated into a single global computation with multiple inputs and outputs.

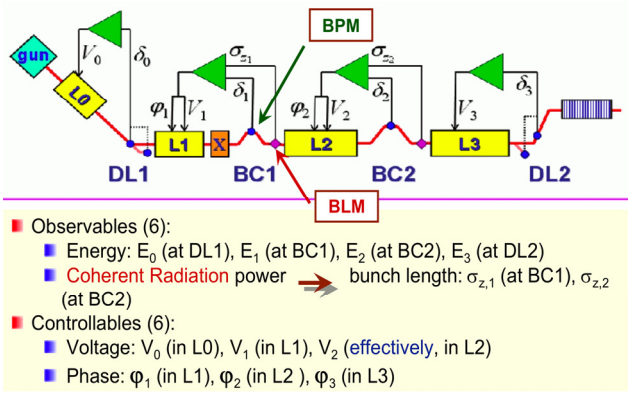


Figure 8: LCLS longitudinal feedback system.

With the longitudinal feedback on, energy stabilities of ~0.03% rms have been measured after each linac section, and peak bunch currents at BC1 and BC2 have been stabilized to ~5% rms and ~10% rms respectively.

Beam Position Monitors

Specifications for stability and precision of the undulator bpms are very demanding because of the micro-scale transverse beam sizes and pointing stability requirements of a fraction of the beam size.

Table 4 shows some key performance specifications for bpms in the undulator section of LCLS [14].

Table 4: LCLS bpm Specifications

Parameter	Specification
Transverse beam size	~37μm
Resolution	< 1μm
Offset Stability over 10hrs	< +/- 1μm
Offset Stability over 30days	< +/- 3μm

The bpms are x-band cavity type, and comprise a monopole TM010 reference cavity and a single TM110 dipole cavity for detecting both horizontal and vertical position. X-band signals are down-converted to an IF of 20-50 MHz before being digitized at 119 MHz. Mounting the bpms on precision mechanical movers has simplified the processes of calibration of bpm offsets and gains.

Single-shot resolutions of ~200 nm rms have been measured with a beam charge of 200 pC. Figure 9 shows an example vertical position scan when the bpm assembly is moved in 5-micron steps [15].

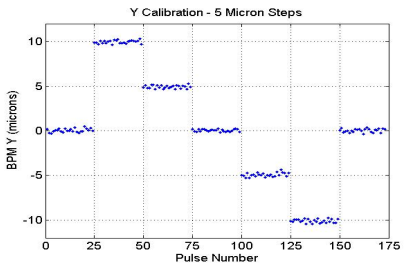


Figure 9: LCLS cavity bpm resolution measurement.

XFEL Intra-Train Transverse Feedback System

Stable SASE operation requires the electron and photon beams to be collinear in the undulators to within ~10% of the beam size (~3 μm rms), and therefore the electron beam trajectory must be stable through the undulators to the same order. Long bunch trains of the XFEL make it possible to implement intra-train trajectory feedback. Figure 10 shows the proposed topology for an XFEL intra-train feedback system, using two upstream and two downstream bpms to monitor the beam trajectory and two rf kickers to make position and angle corrections [16]. The feedback regulator will be implemented digitally.

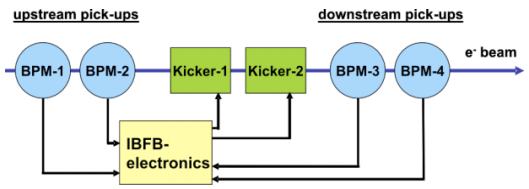


Figure 10: Proposed topology for XFEL intra-train feedback.

The proposed scheme computes the correction kicks using the upstream bpms and an optics model rather than using the downstream bpms in a more conventional feedback loop. This reduces latencies because cable lengths are shorter and also as correction signals are

traveling in the same direction as the beam. At a slower rate, the downstream bpms are used to check and update the optics model based on the response to the applied kicks. A prototype system is currently being developed for testing on FLASH.

OUTLOOK

The latest generation of FEL based light sources, such as LCLS and XFEL present some significant technical challenges. The ILC and CLIC will present even greater challenges. Equally, significant progress is being made towards achieving the end-user requirements of LCLS and XFEL. Experience tells us, that as we start to meet the needs of accelerator users, even more challenging expectations begin to emerge. For example, just as we begin to develop the technology to provide femtosecond timing precision, there is already talk of experiments requiring attosecond-scale precision. It is this type of thinking and forward progression that keeps the field of diagnostics ever advancing.

REFERENCES

[1] XFEL Technical Design Report, DESY 2006-097, 2006
[2] LCLS Conceptual Design Report, SLAC-R-593, 2002
[3] ILC Reference Design Report, ILC-REPORT-2007-001, 2007
[4] CLIC 3 TeV Design and Parameters, CLIC-Note-764, 2008
[5] W. Decking, "Beam Stability Challenges at the European XFEL," Workshop on Beam Stability, Hamburg, Germany, 2004
[8] D. Schulte, "Some Stabilization Specifications," CLIC08 Workshop, CERN, Swizerland, 2008
[9] http://clic-stability.web.cern.ch/clic-stability/
[10] R. Wilcox, "Recent results of RF synchronization at LBL," Second Timing and Synchrotron Workshop, Trieste, 2009
[11] F. Loehl, "Beam Arrival Monitor Implementation Challenges," Second Timing and Synchrotron Workshop, Trieste, 2009
[12] P. Kreicik, "Feedback Concepts: Experience at SPPS, LCLS Plans," 37th ICFA Advanced Beam Dynamics Workshop on Future Light Sources," Hamburg, Germany, 2006
[13] P. Emma, private communication
[14] S. Smith "LCLS Cavity Beam Position Monitors" these proceedings.
[15] R. Lill, private communication
[16] B. Keil et al., "Design of an Intra-train Feedback System for the European XFEL," DIPAC 2007, Venice, Italy

List of Authors

Italic papercodes indicate primary authors

— A —

Abbon, P. TUPD34
Adli, E. *MOPD29*, TUPB40
Adroit, G. TUPB14
Agari, A. TUPD33
Ait Amira, Y. TUPB11
Aleksandrov, A.V. *MOPD21*, TUOA03
Alesini, D. *TUOA01*, TUPD30, TUPD44
Andre, C.A. MOPD42, TUPB02
Andre, T.A. MOPD27, MOPD30, TUPD17
Anelli, F. A. MOPD44
Angelova Hamberg, G. WEOB02
Anger, P. *MOPD30*
Anthony, L.S. MOPD01
Aoyagi, H. *TUPB24*
Arnaud, N. TUPD23
Arsov, V. R. *TUPB46*
Artikova, S.T. TUPB30
Artinian, S. MOPD11
Arutunian, S.G. *MOPD41*, *TUPB28*
Asano, Y. TUPB24, TUPB29
Asova, G. TUPD29
Ausset, P. *MOPD27*

— B —

Baehr, J.W. MOPD26, TUPD29
Balbinot, G. *MOPD31*, *TUPD21*
Balewski, K. *MOOB02*
Bart Pedersen, S. MOOC02
Bartolini, R. TUPD32
Bassanese, S. TUPD10
Baumann, P. TUPD20
Becker, F. MOPD42, *TUPB02*
Behrens, C. *TUPB44*
Bellaveglia, M. MOPD44, *TUPD30*, TUPD44
Belleman, J.M. *MOOC02*
Belohrad, D. B. *MOPD43*
Benedetti, G. TUPB15
Bergoz, J.F. MOPD41
Berkovits, D. TUPB20
Beutner, B. TUPD45, WEOB01
Bieniosek, F.M. TUPB02
Biscari, C. MOPD31
Bizen, T. TUPB24
Blaizot, M. TUPB07
Blanch Gutierrez, C. TUPD14
Blaum, K. TUPD02, WEOA02
Blokland, W. *TUOA03*
Bloomer, C. *TUPD04*
Boccardi, A. TUPD24
Bocci, A. *TUPB13*
Bock, M.K. TUPB46
Boedewadt, J. *TUPB16*, WEOB02
Boehme, C. *TUPB10*, TUPB12
Boscagli, I. TUPD38
Boscolo, M. TUPD23
Bosser, J. MOPD31, TUPD21
Bossi, F. TUPD23
Botha, A.H. MOPD01
Boulware, C.H. TUPD29
Bousonville, M. *TUPB35*
Brañas, B. MOPD06, TUPB06
Branchini, P. TUPD23
Brandao-neto, J.R. TUPD04
Braun, H.-H. WEOB01
Bravin, E. TUPD42
Brenger, A. MOOB02, MOPD20, TUPD03
Bressi, E. MOPD31
Breton, D. TUPD23
Briegel, C.I. MOPD19
Buonomo, B. TUPD23
Burmistrov, L. TUPD23

— C —

Caldara, M. MOPD31, TUPD21
Calvo Giraldo, E. MOPD09
Carlson, K. TUPB25
Carmichael, L.R. TUPB25
Carmona, J.M. *TUPB06*
Carwardine, J. *WEOB03*
Caspers, F. MOPD02
Cassinari, L. MOOC01
Castellano, M. TUOA01, TUOA02, TUPD44
Cestelli Guidi, M. TUPB13
Chen, J. TUPD37
Chen, Y.Z. MOOB03
Chevallay, E. MOPD25
Cheymol, B. *TUPD42*
Chiadroni, E. TUOA01, *TUOA02*, *TUPD44*
Chiu, P.C. TUPD12
Cianchi, A. TUOA01, TUOA02, TUPD44
Citterio, A. MOPD04, *MOPD12*, WEOB01
Civera-Navarrete, J.V. TUPD14
Clozza, A. TUPB13
Cocq, D. MOPD09
Conradie, J.L. MOPD01, TUPB10,

	TUPD38
Corsini, R.	MOPD29
Cousineau, S.M.	TUOA03
Crisp, J.L.	*TUPB23*, TUPB25
Crombie, M.A.	TUPD38
Cultrera, L.	*MOPD44*, TUOA01, TUPD44
Cuzon, S.C.	TUPB07

— D —

Dabrowski, A.E.	MOPD25, TUPB40
Dainese, A.	TUPD38
D'Auria, G.	MOPD04
Davtyan, M.M.	MOPD41
De Freitas, J.	TUPB11
de Maria, R.	*MOPD17*
De Monte, R.	TUPD10
De Santis, S.	TUPB23
De Sio, A.	TUPB13
De Villiers, J.G.	MOPD01, TUPD38
Decker, G.	MOPD16, MOPD41
Dehler, M. M.	*MOPD04*, MOPD12, WEOB01
Dehning, B.	TUPB11, TUPB31, TUPB32, TUPB33, TUPD26, TUPD40
Delannoy, A.	MOPD30, TUPB07
Delsink, J.L.G.	MOPD01
Denard, J.	MOOC01
Di Pirro, G.	MOPD44, TUOA01, TUPD44
Dietrich, J.	MOPD01, TUPB10, TUPB12
Djerdir, A.	TUPB11
Doebert, S.	MOPD25, MOPD29, TUPB40
Doutresssoulles, C.	MOPD27, TUPD17
Drago, A.	TUPB13
Dubrovsky, A.	MOPD29
Ducoudret, B.	MOPD27
Duhme, H.T.	MOOB02
Dunkel, K.	TUPB20
Duperrex, P.-A.	*TUPD20*
Dutriat, C.	TUPD42

— E —

Eddy, N.	MOPD19, TUPB23
Effinger, E.	TUPB32, TUPB33, TUPD26
Egberts, J.	*TUPB30*
Egger, D.	MOPD25
Ego, H.	MOOA03, MOPD07
Eisen, Y.	TUPB20
El-Ashmawy, M.M.	MOPD04
Elsener, K.	MOPD25
Emanuele, E.P.	TUPB13
Emery, J.	TUPB31, TUPB33, *TUPD26*
Ensinger, W.	TUPB04
Epaud, F.	MOPD05
Ewald, F.	*TUPB09*

— F —

Faircloth, D.C.	WEOA03
Falkenstern, F.	*MOPD40*
Falone, A.	MOPD04, WEOB01
Farvacque, L.	TUPD05
Faus-Golfe, A.	TUPD14
Fedosseev, V.	MOPD25
Felber, M.	TUPB46
Feldman, D.W.	MOOC04
Fellenz, B.J.	MOPD19
Ferianis, M.	TUPD10
Ferioli, G.	TUPD26
Ferrario, M.	TUOA01, TUPD44
Feurer, T.	TUPD31
Ficcadenti, L.	TUOA01, TUPD44
Filippetto, D.	MOPD44, TUOA01, TUPD44
Fiorito, R.B.	MOOC04
Fisher, A.S.	*TUPB03*, *TUPD46*
Fitzek, J.	TUPB31
Flanagan, J.W.	MOPD08
Follin, F.	TUPB31
Fontbonne, J.-M.	MOPD30
Forck, P.	MOOC03, MOPD42, TUPB02, TUPB04, TUPB12, TUPD16, TUPD18, WEOA04
Fourie, D.T.	*MOPD01*
Fox, J.D.	MOPD17
Foy, J.-C.	TUPB07
Frisch, J.C.	TUPD46
Fukami, K.	TUPB24

— G —

Gabor, C.	*TUPB22*, TUPD41, WEOA03
Gallo, A.	TUPD30
Gambicorti, L.	TUPB13
Gangnant, P.	TUPB07
Ganter, R.	WEOB01
Garcia-Garrigos, J.J.	*TUPD14*
Garvey, T.	WEOB01
Gasior, M.	*TUPD24*
Gatti, G.	TUOA01, TUPD44
Geloni, G.	*TUPB37*
Gerth, C.	TUPB44, *TUPD22*, TUPD43
Gessler, P.	TUPB46
Gevorkian, Zh.S.	TUPB28
Gharibyan, V.	MOOB02

Giacomini, T. TUPB12, WEOA04
Gianfelice-Wendt, E. MOPD19
Gobin, R. TUPB14
Goldblatt, A. TUPB03
Gonzalez, J.L. *MOPD09*
Goodwin, R.W. TUPB25
Grabosch, H.-J. TUPD29
Grieser, M. TUPD02, WEOA02
Grilli, A.G. TUPB13
Grudiev, A. MOPD04
Gudkov, D. MOPD04
Günzel, T.F. MOPD18
Gueroult, E. MOPD30, TUPB07
Guerrero, A. TUPB05, TUPD40
Guetlich, E. *TUPB04*

— H —

Hacker, K.E. TUPB46
Hänel, M. TUPD29
Hakobyan, L. TUPD29
Halfon, S. TUPB20
Harasimowicz, J. *TUPD06*, *TUPD06*
Hartmann, P. MOPD13, TUPD08
Harutyunyan, G.S. MOPD41
Haseitl, R. *MOPD42*, TUPB02
Hertel, N. MOPD24
Higashiya, A. MOOA03
Hirose, E. TUPD33
Höfle, W. MOPD17
Hoffmann, D.H.H. TUPB02
Hoffmann, F. MOPD40
Holzer, B.J. *MOOA01*
Honkavaara, K. TUOA02
Hoobler, S. TUOC03
Houarner, C. TUPB07
Hsu, K.T. *MOPD33*, TUPD12
Hu, K.H. MOPD33
Hu, Z.G. TUPB21
Hubert, N. *MOOC01*
Hülsmann, P. TUPD16
Huening, M. *MOPD14*
Hug, A. TUPB02
Hunziker, S. *TUPB43*, TUPD31, WEOB01

— I —

Ibarra, A. MOPD06, TUPB06
Ieiri, M. TUPD33
Ikeda, H. TUPD26
Ilinski, P. TUPB37
Inoue, S.I. MOOA03, MOPD07
Intermite, A. *TUPB27*
Iriso, U. *MOPD18*, *MOPD32*, *TUPB15*
Ischebeck, R. TUPB16, *TUPD45*, WEOB01
Itoga, T. TUPB24, TUPB29
Ivanisenko, Ye. MOPD26, TUPD29
Iverson, R.H. TUPD46

— J —

Jackson, S. *TUPB31*
Jacquot, B. MOPD30
Jamet, C. MOPD27, MOPD30, *TUPD17*
Jeanneau, F. TUPD34
Johnson, R.G. TUOC03
Jolly, S. *WEOA03*
Jonas, R. MOPD14
Jones, O.R. *MOOA02*, MOPD09, MOPD43
Joray, S. TUPD20
Jore, M. MOPD26

— K —

Kain, V. TUPB31
Kalinin, A. *MOPD11*
Kamerdzhiev, V. TUPB10, *TUPB12*
Karataev, V. TUPD32
Kasprowicz, G. MOOC02
Katoh, Y. TUPD33
Kaufmann, W. MOOC03
Kaya, C. *TUPB38*
Keil, B. MOPD12, *TUOC01*, WEOB01
Kester, O.K. WEOA03
Khan, S. MOPD13, WEOB02
Khojoyan, M.K. TUPD29
Kim, Y. *WEOB01*
Kiselev, D.C. TUPD20
Kitamura, H. TUPB24
Kiyomichi, A. TUPD33
Klute, J. MOOB02
Knaack, K.K. MOOB02
Koch, J.M. TUPD05
Koerfer, M. WEOA01
Koopman, J. TUPB05, TUPB11, TUPD40
Kotzian, G. MOPD17
Koujili, M. *TUPB11*
Kourbanis, I. TUPB23
Kowina, P. *MOOC03*, TUPD16, WEOA04
Krasilnikov, M. MOPD26, TUPD29
Krouptchenkov, I. MOOB02, *TUPD03*
Kruk, G. TUPB31
Kube, G. MOOB02, MOPD20, TUOA02, TUPD03, *TUPD39*
Kuehnel, K.-U. TUPB08
Kuo, C.H. MOPD33, *TUPD12*
Kuske, P. MOPD40

Kuszynski, J. MOPD40
Kyberd, P. *MOPD23*

— L —

Lanzavecchia, L. TUPD21
Larsson, M. WEOB02
Lauth, W. TUPD39
Laux, F. *TUPD02*, WEOA02
Lawrie, S.R. WEOA03
Le Coz, W. MOPD27, TUPD17
LeBlanc, G. TUPD27
Lederer, S. TUPD29
Ledu, G. MOPD30
Lee, D.A. *TUPD41*
Lee, Y. TUPD20
Lefevre, T. MOPD25, TUPB03, TUPB40, TUPD42
Lehnert, U. TUPB38
Leng, Y.B. TUPD37, *MOOB03*
Lensch, T. MOOB02, *TUPD25*
Lepoittevin, F. MOPD27
Letchford, A.P. TUPB22, WEOA03
Liakin, D.A. TUPB12, TUPD18
Liebing, J. MOOB02
Lill, R.M. TUOC03
Lipka, D. *MOPD02*, *TUOC02*
Loehl, F. TUPB46, WEOB02
Lokhovitskiy, A.E. *TUPB05*
Loos, H. TUPD46
Ludwig, F. TUPB46, TUPD22
Ludwig, M. MOPD43, MOPD45
Lund-Nielsen, J. MOPD14

— M —

Maazouzi, C. MOPD27
Maesaka, H. *MOOA03*, MOPD02, *MOPD07*
Malyutin, D.A. TUOA03
Mao, R.S. *TUPB21*, TUPD11
Marcelli, A. TUPB13
Marchetti, B. TUOA01, TUPD44
Mardor, I. TUPB20
Maréchal, X.-M. *TUPB29*
Marroncle, J. MOPD06, *TUPD34*
Martin, I.P.S. TUPB41, TUPD32
Marwedel, P. TUPD08
Matsubara, S.M. MOOA03, MOPD07
Matthiesen, K.-H. TUPB46
Maxey, C. MOOC04
Mazzitelli, G. TUPD23
McManamy, T.J. MOOC04
Meseck, A. WEOB02
Mete, O. *MOPD25*, *MOPD25*
Métral, E. TUPD40
Milosic, T. *TUPD18*
Minakawa, M. TUPD33
Misiowiec, M. TUPB31
Mitsuhashi, T.M. MOPD08, TUPD33, TUPD37
Møller, S.P. MOPD24
Mols, J.-Ph. TUPD34
Morgan, A.F.D. TUPD32
Moritz, P. MOOC03, TUPD16
Morrison, L.H. TUOC03
Mostacci, A. TUOA01, TUPD44
Mostert, H.W. *TUPD38*
Mueller, F. TUPB42, *TUPD31*, *TUPD31*
Mueller, U. TUPD20
Murtas, F. TUPD23
Muto, R. TUPD33

— N —

Naab, F.U. TUPD19
Nadji, A. MOOC01
Nadolski, L.S. MOOC01
Nariyama, N. TUPB24
Naruki, M. TUPD33
Neumann, Re. MOOB02
Neumann, Ru. MOOB02, MOPD20
Ni, P.N. TUPB02
Nielsen, J.S. *MOPD24*
Noelle, D. MOPD02, *TUOA04*
Norum, W.E. TUOC03
Noumi, H. TUPD33

— O —

Obina, T. MOPD08
Odier, OP. *MOPD45*
Oganesyan, K.B. TUPB28
Ohshima, T. MOOA03, MOPD07
Olivetto, C.O. MOPD27
Olmos, A. MOPD32
Olvegaard, M. *TUPB40*
Orlov, D. WEOA02
Orr, N. MOPD30
Otake, Y. MOOA03, MOPD07

— P —

Pace, E. MOPD44, TUOA01, TUPD44, TUPB13
Palladino, V.C. TUPD15
Pancin, J. TUPD34
Parravicini, A. MOPD31, TUPD21
Pedrozzi, M. WEOB01
Perez, F. MOPD18, MOPD32, TUPB15
Perry, A. TUPB20
Peters, A. TUPD36
Petrarca, M. MOPD25
Petrosyan, B. TUPD29

Pfister, J. WEOA03
Piel, C. TUPB20
Pinayev, I. MOPD16
Piotrowski, J.P. TUPB13
Plouviez, E. *TUPD05*
Podadera Aliseda, I. *MOPD06*, TUPB06
Poggi, M. TUPD38
Polzin, B. TUPB16
Ponchia, R. TUPD38
Pons, J.L. TUPD05
Pottin, B. TUPB14
Pozimski, J.K. TUPB22, TUPD41, WEOA03
Priebe, G. MOOB02
Prieto, P.S. MOPD19
Prost, L.R. TUPB25
Pullia, M. MOPD31, TUPD21
Putignano, M. *TUPB08*, TUPB27, *TUPB08*

— R —

Raco, A.R. TUPB13
Raguin, J.-Y. MOPD04
Raich, U. MOOC02
Raimondi, P. TUPD23
Ramos, D. TUPB11
Rauch, U. *TUPD16*
Rausch, J. TUPB35
Rechenmacher, R. MOPD19
Reeg, H. WEOA04
Rehm, G. TUPB41, TUPD04, *TUPD32*
Reiche, S. WEOB01
Richter, R. TUPD29
Riddone, G. MOPD04, MOPD29
Rimjaem, S. *MOPD26*, TUPD29
Ripert, M.B. *TUPD36*
Roderick, C. TUPB31
Rodnizki, J. TUPB20
Roensch, J. MOPD26, *TUPD29*
Rohwer, P.F. MOPD01
Ronsivalle, C. TUOA01, TUPD44
Rossbach, J. TUPB16, TUPD29
Roux, R. MOPD25
Ruber, R.J.M.Y. MOPD29
Ruescas, C. MOPD27
Ruf, M. *MOPD10*
Rumolo, G. MOPD17

— S —

Saewert, G.W. TUPB25
Saldin, E. TUPB37, WEOB02
Salen, P.M. WEOB02
Salvant, B. MOPD17
Samoshkin, A. MOPD04
Sannibale, F. *MOOB01*
Sapinski, M. TUPB11, TUPB31, *TUPD40*
Sato, Y. TUPD33
Savage, P. TUPD41
Savalle, A. MOPD30
Savioz, J.-J. MOPD43
Sawada, S. TUPD33
Scheidt, K.B. *MOPD05*
Schilcher, T. WEOB01
Schioppa, M. TUPD23
Schirmer, D. MOPD13, TUPD08
Schlarb, H. TUPB16, TUPB46, WEOB02
Schlörit, A. WEOA04
Schlott, V. MOPD12, TUPB42, TUPB43, TUPD31, TUPD45, WEOB01
Schmidt, Ch. TUPD22
Schmidt, G. MOPD13
Schmidt, L. MOPD10
Schmidt-Foehre, F. MOOB02, MOPD14, *MOPD20*, TUPD03
Schneidmiller, E. TUPB37, WEOB02
Schroeder, H.-Ch. MOOB02
Schuenemann, G. MOPD13, *TUPD08*
Schulte, D. MOPD29
Schulz, L. MOPD12
Schulz, S. TUPB46
Schwickert, M. *WEOA04*
Seiya, K. TUPB23
Senee, F. *TUPB14*
Sensolini, G. TUPD23
Sereno, N. TUOC03
Serio, M. TUPD10
Setzer, S. MOPD10
Shapovalov, A. TUPD29
Shea, T.J. *MOOC04*
Shemyakin, A.V. TUPB25
Shintake, T. MOOA03, MOPD02, MOPD07
Shirakabe, Y. TUPD33
Shkvarunets, A.G. MOOC04
Siddons, D.P. TUPD13
Sieber, T. TUPD02, *WEOA02*
Siemens, M. MOPD02
Singh, O. *MOPD16*
Smith, S.R. *TUOC03*
Sorchetti, R.S. TUPB13
Spairani, M. MOPD31
Spesyvtsev, R. TUPD29
Springhorn, K. TUPD38
Stadler, M. MOPD02
Starostenko, A.A. TUOA03
Starritt, A. C. TUPD27
Staykov, L. TUPD29
Steffen, B. *TUPB42*, TUPD31,

TUPD45, WEOB01
Stella, A. *TUPD10*
Stephan, F. MOPD26, TUPD29
Stocchi, A. TUPD23
Straumann, T. TUOC03
Susen, R. MOOB02
Suzuki, Y. TUPD33
Swartvagher, E. MOPD27, TUPD17
Syratchev, I. MOPD29

— T —

Tadano, M. MOPD08
Takahashi, H. TUPD33
Takai, R. MOPD08
Takasaki, M. TUPD33
Tanaka, K.H. TUPD33
Tanaka, T. TUPB24
Tang, B. TUPB21
ten Have, M.L.M. TUPD27
Terunuma, N. MOPD19
Thomas, C.A. *TUPB41*, TUPD04
Thomsen, K. *TUPB18*
Thoulet, S. MOPD43, MOPD45
Toader, O.F. *TUPD19*
Tobiyama, M. *MOPD08*
Tomizawa, H. MOOA03
Towalski, P. *MOPD13*, TUPD08
Toyoda, A. *TUPD33*
Treyer, D.M. MOPD02, MOPD12, TUPD31
Trompetter, D. TUPB20
Tuske, O. TUPB14

— U —

Uberto, F. TUPD05
Urakawa, J. MOPD19

— V —

Vaccarezza, C. TUOA01, TUPD44
Valente, P. *TUPD23*
van der Meulen, P. WEOB02
van Garderen, E.D. *TUPD27*
van Schalkwyk, P.A. MOPD01
Varenne, F. MOPD30
Variola, A. MOPD26, TUPD23
Vasiniuk, I.E. MOPD41
Venturini, G.G. *TUPB32*, *TUPB33*
Verguilov, V.Z. *TUPD15*
Verhagen, E. TUPD26
Viaud, B.F. TUPD23
Vicario, C. MOPD44, TUOA01, TUPD30, TUPD44
Vignet, J.L. *TUPB07*, MOPD27, MOPD30
Vilalte, S. MOPD29
Vilcins, S. MOOB02, MOPD02
vom Stein, P. TUPB20
von Hahn, R. TUPD02, WEOA02
Voy, D.C. MOPD19

— W —

Wagner, A. TUPB16
Walasek-Hoehne, B. TUPB02, TUPB04
Waldschmidt, G.J. TUOC03
Walters, D.R. TUOC03
Wang, C.Y. MOPD33
Warner, A. *TUPB25*
Watanabe, H. TUPD33
Wehrle, U. MOPD17
Weiland, T. MOOC03
Weis, T. MOPD13, TUPB10, TUPD08
Weissman, L. *TUPB20*
Welch, J.J. TUPD46
Welsch, C.P. TUPB08, TUPB27, TUPB30, TUPD06
Wendt, M. *MOPD19*
Werner, M. MOOB02, *TUPB26*, TUPD25
Wiebers, Ch. MOOB02
Wilhelm, A.B.J. *TUPD43*
Wille, K. TUPD08
Winter, A. TUPB46, WEOB02
Wissmann, L.-G. TUPB46
Wittenburg, K. MOOB02, MOPD20, TUPD03
Wolf, A. TUPD02, WEOA02
Wolfheimer, F. MOOC03
Wu, J.X. TUPB21, *TUPD11*
Wuensch, W. MOPD04
Wulf, F. *WEOA01*

— X —

Xia, J.W. TUPB21, TUPD11
Xiao, G.Q. TUPB21, TUPD11
Xu, H.S. TUPB21
Xu, Z.G. TUPB21

— Y —

Yabashi, M. MOOA03
Yamanoi, Y. TUPD33
Yanagida, K. MOOA03
Yang, B.X. MOPD16
Ye, K.R. *TUPD37*, MOOB03
Yoon, P.S. *TUPD13*
Young, A. TUOC03
Yu, J. TUPD37
Yuan, Y.J. TUPB21, TUPD11
Yurkov, M.V. TUPB37, WEOB02

— Z —

Zamantzas, C. TUPB32, TUPB33, TUPB31, TUPD26
Zemella, J. TUPB46
Zennaro, R. MOPD04
Zhao, G.B. TUPD37
Zhao, T.C. TUPB21, TUPD11
Zheng, J.H. TUPD11, TUPB21
Zhou, W.M. TUPD37, MOOB03
Ziemann, V.G. MOPD29, *WEOB02*
Zingre, K. TUPD27
Zwaska, R.M. TUPB23

Institutes List

ACCEL
Bergisch Gladbach
- Dunkel, K.
- Trompetter, D.
- vom Stein, P.

ANL
Argonne, Illinois
- Carwardine, J.
- Decker, G.
- Lill, R.M.
- Morrison, L.H.
- Norum, W.E.
- Sereno, N.
- Waldschmidt, G.J.
- Walters, D.R.
- Yang, B.X.

ASCo
Clayton, Victoria
- LeBlanc, G.
- Starritt, A. C.
- Zingre, K.
- ten Have, M.L.M.
- van Garderen, E.D.

BERGOZ Instrumentation
Saint Genis Pouilly
- Artinian, S.
- Bergoz, J.F.

BESSY GmbH
Berlin
- Falkenstern, F.
- Hoffmann, F.
- Kuszynski, J.

BINP SB RAS
Novosibirsk
- Malyutin, D.A.
- Starostenko, A.A.

BNL
Upton, Long Island, New York
- Pinayev, I.
- Siddons, D.P.
- Singh, O.
- Yoon, P.S.
- de Maria, R.

Brunel University
Middlesex
- Kyberd, P.

CEA
Gif-sur-Yvette
- Abbon, P.
- Adroit, G.
- Gobin, R.
- Jeanneau, F.
- Marroncle, J.
- Mols, J.-Ph.
- Pancin, J.
- Pottin, B.
- Senee, F.
- Tuske, O.

CELLS-ALBA Synchrotron
Cerdanyola del Vallès
- Benedetti, G.
- Günzel, T.F.
- Iriso, U.
- Olmos, A.
- Perez, F.

CERN
Geneva
- Bart Pedersen, S.
- Belleman, J.M.
- Belohrad, D. B.
- Boccardi, A.
- Bosser, J.
- Bravin, E.
- Calvo Giraldo, E.
- Caspers, F.
- Chevallay, E.
- Cheymol, B.
- Cocq, D.
- Corsini, R.
- Dabrowski, A.E.
- De Freitas, J.
- Dehning, B.
- Doebert, S.
- Dubrovsky, A.
- Dutriat, C.
- Effinger, E.
- Elsener, K.
- Emery, J.
- Fedosseev, V.
- Ferioli, G.
- Fitzek, J.
- Follin, F.
- Gasior, M.
- Goldblatt, A.
- Gonzalez, J.L.
- Grudiev, A.
- Gudkov, D.
- Guerrero, A.
- Holzer, B.J.
- Höfle, W.
- Jackson, S.
- Jones, O.R.

- Kain, V.
- Kasprowicz, G.
- Koopman, J.
- Kotzian, G.
- Koujili, M.
- Kruk, G.
- Lefevre, T.
- Lokhovitskiy, A.E.
- Ludwig, M.
- Mete, O.
- Misiowiec, M.
- Métral, E.
- Odier, OP.
- Olvegaard, M.
- Petrarca, M.
- Raich, U.
- Ramos, D.
- Riddone, G.
- Roderick, C.
- Rumolo, G.
- Salvant, B.
- Samoshkin, A.
- Sapinski, M.
- Savioz, J.-J.
- Schulte, D.
- Syratchev, I.
- Thoulet, S.
- Venturini, G.G.
- Wehrle, U.
- Wuensch, W.
- Zamantzas, C.
- Zennaro, R.

CIEMAT
Madrid
- Brañas, B.
- Carmona, J.M.
- Ibarra, A.
- Podadera Aliseda, I.

CNAO Foundation
Milan
- Balbinot, G.
- Bressi, E.
- Caldara, M.
- Lanzavecchia, L.
- Parravicini, A.
- Pullia, M.
- Spairani, M.

Cockcroft Institute
Warrington, Cheshire
- Harasimowicz, J.

DELTA
Dortmund
- Hartmann, P.
- Khan, S.
- Schirmer, D.
- Schmidt, G.
- Schuenemann, G.
- Towalski, P.
- Weis, T.
- Wille, K.

DESY Zeuthen
Zeuthen
- Asova, G.
- Baehr, J.W.
- Boulware, C.H.
- Grabosch, H.-J.
- Hakobyan, L.
- Hänel, M.
- Ivanisenko, Ye.
- Khojoyan, M.K.
- Krasilnikov, M.
- Petrosyan, B.
- Rimjaem, S.
- Roensch, J.
- Shapovalov, A.
- Spesyvtsev, R.
- Staykov, L.
- Stephan, F.

DESY
Hamburg
- Arsov, V. R.
- Balewski, K.
- Behrens, C.
- Bock, M.K.
- Brenger, A.
- Duhme, H.T.
- Felber, M.
- Geloni, G.
- Gerth, C.
- Gessler, P.
- Gharibyan, V.
- Hacker, K.E.
- Honkavaara, K.
- Huening, M.
- Ilinski, P.
- Jonas, R.
- Klute, J.
- Knaack, K.K.
- Koerfer, M.
- Krouptchenkov, I.
- Kube, G.
- Lederer, S.
- Lensch, T.
- Liebing, J.
- Lipka, D.
- Loehl, F.
- Ludwig, F.
- Lund-Nielsen, J.
- Matthiesen, K.-H.
- Neumann, Re.
- Neumann, Ru.
- Noelle, D.

- Polzin, B.
- Priebe, G.
- Saldin, E.
- Schlarb, H.
- Schmidt, Ch.
- Schmidt-Foehre, F.
- Schneidmiller, E.
- Schroeder, H.-Ch.
- Siemens, M.
- Susen, R.
- Vilcins, S.
- Wagner, A.
- Werner, M.
- Wiebers, Ch.
- Winter, A.
- Wittenburg, K.
- Yurkov, M.V.

DPNC
Genève
- Verguilov, V.Z.

Diamond
Oxfordshire
- Bloomer, C.
- Brandao-neto, J.R.
- Martin, I.P.S.
- Morgan, A.F.D.
- Rehm, G.
- Thomas, C.A.

ELETTRA
Basovizza
- Bassanese, S.
- D'Auria, G.
- De Monte, R.
- El-Ashmawy, M.M.
- Ferianis, M.

ENEA C.R. Frascati
Frascati (Roma)
- Ronsivalle, C.

EPFL
Lausanne
- Egger, D.
- Mete, O.

ESRF
Grenoble
- Epaud, F.
- Ewald, F.
- Farvacque, L.
- Koch, J.M.
- Plouviez, E.
- Pons, J.L.
- Scheidt, K.B.
- Uberto, F.

FYSIKUM, AlbaNova, Stockholm University
Stockholm
- Larsson, M.
- Salen, P.M.
- van der Meulen, P.

FZD
Dresden
- Kaya, C.
- Lehnert, U.

FZJ
Jülich
- Dietrich, J.
- Kamerdzhiev, V.

Fermilab
Batavia
- Carlson, K.
- Kourbanis, I.
- Rechenmacher, R.
- Saewert, G.W.
- Seiya, K.
- Shemyakin, A.V.
- Warner, A.
- Wendt, M.
- Zwaska, R.M.
- Briegel, C.I.
- Carmichael, L.R.
- Crisp, J.L.
- Eddy, N.
- Fellenz, B.J.
- Gianfelice-Wendt, E.
- Goodwin, R.W.
- Prieto, P.S.
- Prost, L.R.
- Voy, D.C.

GANIL
Caen
- Andre, T.A.
- Anger, P.
- Blaizot, M.
- Cuzon, S.C.
- Delannoy, A.
- Doutresssoulles, C.
- Ducoudret, B.
- Foy, J.-C.
- Gangnant, P.
- Gueroult, E.
- Houarner, C.
- Jacquot, B.
- Jamet, C.
- Le Coz, W.
- Ledu, G.
- Lepoittevin, F.
- Savalle, A.

- Swartvagher, E.
- Varenne, F.
- Vignet, J.L.

GSI
Darmstadt
- Andre, C.A.
- Becker, F.
- Bousonville, M.
- Forck, P.
- Giacomini, T.
- Guetlich, E.
- Haseitl, R.
- Hug, A.
- Hülsmann, P.
- Kaufmann, W.
- Kowina, P.
- Milosic, T.
- Moritz, P.
- Rauch, U.
- Reeg, H.
- Schlörit, A.
- Schwickert, M.
- Walasek-Hoehne, B.

HIT
Heidelberg
- Peters, A.
- Ripert, M.B.

Helmholtz-Zentrum Berlin für Materialien und Energie GmbH
Berlin
- Kuske, P.
- Meseck, A.
- Richter, R.
- Wulf, F.

IAP Univ. Bern
Bern
- Feurer, T.
- Mueller, F.

IAP
Frankfurt am Main
- Pfister, J.

IFIC
Valencia
- Blanch Gutierrez, C.
- Civera-Navarrete, J.V.
- Faus-Golfe, A.
- Garcia-Garrigos, J.J.

IKP
Mainz
- Lauth, W.

IMP
Lanzhou
- Hu, Z.G.
- Mao, R.S.
- Tang, B.
- Wu, J.X.
- Xia, J.W.
- Xiao, G.Q.
- Xu, H.S.
- Xu, Z.G.
- Yuan, Y.J.
- Zhao, T.C.
- Zheng, J.H.

IN2P3-LAPP
Annecy-le-Vieux
- Vilalte, S.

INFN Gruppo di Cosenza
Arcavacata di Rende (Cosenza)
- Schioppa, M.

INFN-Napoli
Napoli
- Palladino, V.C.

INFN-Roma II
Roma
- Cianchi, A.
- Marchetti, B.

INFN-Roma
Roma
- Valente, P.

INFN/LNF
Frascati (Roma)
- Alesini, D.
- Anelli, F. A.
- Bellaveglia, M.
- Biscari, C.
- Bocci, A.
- Boscolo, M.
- Bossi, F.
- Buonomo, B.
- Castellano, M.
- Cestelli Guidi, M.
- Chiadroni, E.
- Clozza, A.
- Cultrera, L.
- Di Pirro, G.
- Drago, A.
- Ferrario, M.
- Ficcadenti, L.
- Filippetto, D.
- Gallo, A.

- Gatti, G.
- Grilli, A.G.
- Marcelli, A.
- Mazzitelli, G.
- Murtas, F.
- Pace, E.
- Raco, A.R.
- Raimondi, P.
- Sensolini, G.
- Serio, M.
- Sorchetti, R.S.
- Stella, A.
- Vaccarezza, C.
- Vicario, C.

INFN/LNL
Legnaro, Padova
- Boscagli, I.
- Dainese, A.
- Poggi, M.
- Ponchia, R.

INOA
Firenze
- Gambicorti, L.

IPHC
Strasbourg Cedex 2
- Maazouzi, C.
- Olivetto, C.O.
- Ruescas, C.

IPN
Orsay
- Ausset, P.

ISA
Aarhus
- Hertel, N.
- Møller, S.P.
- Nielsen, J.S.

ITEP
Moscow
- Liakin, D.A.

Imperial College of Science and Technology, Department of Physics
London
- Jolly, S.
- Lee, D.A.
- Pozimski, J.K.
- Savage, P.

JAI
Egham, Surrey
- Karataev, V.
- Bartolini, R.

JASRI/SPring-8
Hyogo-ken
- Aoyagi, H.
- Bizen, T.
- Ego, H.
- Fukami, K.
- Maréchal, X.-M.
- Nariyama, N.
- Tomizawa, H.
- Yanagida, K.

KEK
Ibaraki
- Flanagan, J.W.
- Ikeda, H.
- Mitsuhashi, T.M.
- Muto, R.
- Obina, T.
- Shirakabe, Y.
- Tadano, M.
- Takai, R.
- Takasaki, M.
- Tanaka, K.H.
- Terunuma, N.
- Tobiyama, M.
- Urakawa, J.
- Agari, A.
- Hirose, E.
- Ieiri, M.
- Katoh, Y.
- Kiyomichi, A.
- Minakawa, M.
- Naruki, M.
- Sato, Y.
- Sawada, S.
- Suzuki, Y.
- Takahashi, H.
- Toyoda, A.
- Watanabe, H.
- Yamanoi, Y.

LAL
Orsay
- Arnaud, N.
- Breton, D.
- Burmistrov, L.
- Jore, M.
- Roux, R.
- Stocchi, A.
- Variola, A.
- Viaud, B.F.

LBNL
Berkeley, California

- Bieniosek, F.M.
- De Santis, S.
- Ni, P.N.
- Sannibale, F.

LPC
Caen
- Fontbonne, J.-M.
- Orr, N.

MPI-K
Heidelberg
- Artikova, S.T.
- Blaum, K.
- Egberts, J.
- Grieser, M.
- Intermite, A.
- Kuehnel, K.-U.
- Laux, F.
- Orlov, D.
- Putignano, M.
- Sieber, T.
- Wolf, A.
- von Hahn, R.

NERS-UM
Ann Arbor, Michigan
- Naab, F.U.
- Toader, O.F.

NSCL
East Lansing, Michigan
- Kester, O.K.

NSRRC
Hsinchu
- Chiu, P.C.
- Hsu, K.T.
- Hu, K.H.
- Kuo, C.H.
- Wang, C.Y.

ORNL
Oak Ridge, Tennessee
- Aleksandrov, A.V.
- Blokland, W.
- Cousineau, S.M.
- Maxey, C.
- McManamy, T.J.
- Shea, T.J.

PSI
Villigen
- Baumann, P.
- Beutner, B.
- Braun, H.-H.
- Citterio, A.
- Dehler, M. M.
- Duperrex, P.-A.
- Falone, A.
- Ganter, R.
- Garvey, T.
- Hunziker, S.
- Ischebeck, R.
- Joray, S.
- Keil, B.
- Kim, Y.
- Kiselev, D.C.
- Lee, Y.
- Mueller, F.
- Mueller, U.
- Pedrozzi, M.
- Raguin, J.-Y.
- Reiche, S.
- Schilcher, T.
- Schlott, V.
- Schulz, L.
- Stadler, M.
- Steffen, B.
- Thomsen, K.
- Treyer, D.M.

RCNP
Osaka
- Noumi, H.

RI Research Instruments GmbH
Bergisch Gladbach
- Piel, C.

RIKEN/SPring-8
Hyogo
- Asano, Y.
- Higashiya, A.
- Inoue, S.I.
- Itoga, T.
- Kitamura, H.
- Maesaka, H.
- Matsubara, S.M.
- Ohshima, T.
- Otake, Y.
- Shintake, T.
- Tanaka, T.
- Yabashi, M.

Rome University La Sapienza
Roma
- Mostacci, A.

SINAP
Shanghai
- Chen, J.
- Leng, Y.B.

- Ye, K.R.
- Yu, J.
- Zhao, G.B.
- Zhou, W.M.

SLAC
Menlo Park, California
- Fisher, A.S.
- Fox, J.D.
- Frisch, J.C.
- Hoobler, S.
- Iverson, R.H.
- Johnson, R.G.
- Loos, H.
- Smith, S.R.
- Straumann, T.
- Welch, J.J.
- Young, A.

SOLEIL
Gif-sur-Yvette
- Cassinari, L.
- Denard, J.
- Hubert, N.
- Nadji, A.
- Nadolski, L.S.

SSRF
Shanghai
- Chen, Y.Z.
- Leng, Y.B.
- Ye, K.R.
- Zhou, W.M.

STFC/DL/ASTeC
Daresbury, Warrington, Cheshire
- Kalinin, A.

STFC/RAL
Chilton, Didcot, Oxon
- Letchford, A.P.
- Pozimski, J.K.

STFC/RAL/ASTeC
Chilton, Didcot, Oxon
- Gabor, C.

STFC/RAL/ISIS
Chilton, Didcot, Oxon
- Faircloth, D.C.
- Lawrie, S.R.
- Letchford, A.P.

Siemens Med
Erlangen
- Setzer, S.

Soreq NRC
Yavne
- Berkovits, D.
- Eisen, Y.
- Halfon, S.
- Mardor, I.
- Perry, A.
- Rodnizki, J.
- Weissman, L.

TEMF, TU Darmstadt
Darmstadt
- Weiland, T.
- Wolfheimer, F.

TU Darmstadt
Darmstadt
- Hoffmann, D.H.H.

TU Dortmund University
Dortmund
- Marwedel, P.

TUD
Darmstadt
- Rausch, J.

Technical University Darmstadt
Darmstadt
- Ensinger, W.

The University of Liverpool
Liverpool
- Harasimowicz, J.
- Putignano, M.
- Welsch, C.P.

U. Erlangen-Nurnberg LHFT
Erlangen
- Ruf, M.
- Schmidt, L.

UFC
Besançon
- Ait Amira, Y.

UMD
College Park, Maryland
- Feldman, D.W.
- Fiorito, R.B.
- Shkvarunets, A.G.

UTBM
Belfort
- Djerdir, A.

UW-Madison/PD
Madison, Wisconsin
- Verhagen, E.

Uni HH
Hamburg
- Boedewadt, J.
- Rossbach, J.
- Schulz, S.
- Wilhelm, A.B.J.
- Wissmann, L.-G.
- Zemella, J.

UniDo/IBS
Dortmund
- Boehme, C.

University of Oslo
Oslo
- Adli, E.

Università degli Studi di Firenze
Firenze
- De Sio, A.
- Emanuele, E.P.
- Pace, E.

Università di Roma II Tor Vergata
Roma
- Cianchi, A.

Uppsala University
Uppsala
- Angelova Hamberg, G.
- Ruber, R.J.M.Y.
- Ziemann, V.G.

VIGO System S.A.
Ozarow Maz.
- Piotrowski, J.P.

YSU
Yerevan
- Harutyunyan, G.S.

YerPhI
Yerevan
- Arutunian, S.G.
- Davtyan, M.M.
- Gevorkian, Zh.S.
- Oganesyan, K.B.
- Vasiniuk, I.E.

iThemba LABS
Somerset West
- Anthony, L.S.
- Botha, A.H.
- Conradie, J.L.
- Crombie, M.A.
- De Villiers, J.G.
- Delsink, J.L.G.
- Fourie, D.T.
- Mostert, H.W.
- Rohwer, P.F.
- Springhorn, K.
- van Schalkwyk, P.A.

roma3
Rome
- Branchini, P.

Participants List

— A —

Adli, Erik
CERN
Geneva, Norway

Ahluwalia, Helga
DESY
Hamburg, Germany

Alabau-Gonzalvo, Javier
IFIC
Valencia, Spain

Aleksandrov, Alexander
ORNL
Oak Ridge, USA

Alesini, David
INFN/LNF
Frascati, Italy

Anger, Pascal
GANIL
Caen, France

Arsov, Vladimir
PSI
Villigen, Switzerland

Artinian, Sebastien
BERGOZ Instrumentation
Saint Genis Pouilly, France

Arutunian, Suren
YerPhI
Yerevan, Armenia

— B —

Badano, Laura
TERA
Trieste, Italy

Balbinot, Giovanni
CNAO
Milan, Italy

Balewski, Klaus
DESY
Hamburg, Germany

Becker, Frank
GSI
Darmstadt, Germany

Behrens, Christopher
DESY
Hamburg, Germany

Bellaveglia, Marco
INFN/LNF
Frascati, Italy

Belleman, Jeroen
CERN
Geneva, Switzerland

Bellodi, Giulia
CERN
Geneva, Switzerland

Belohrad, David
CERN
Geneva, Switzerland

Bergoz, Julien
BERGOZ Instrumentation
Saint Genis Pouilly, France

Bloomer, Christopher
Diamond
Chilton, UK

Boccardi, Andrea
CERN
Geneva, Switzerland

Bocci, Alessio
INFN/LNF
Frascati, Italy

Bödewadt, Jörn
University Hamburg
Hamburg, Germany

Böhme, Christian
University Dortmund
Dortmund, Germany

Bousonville, Michael
GSI
Darmstadt, Germany

Brossard, Julien
LAL
Orsay, France

Bruderer, Sylvain
MagentaSys
Genolier, Switzerland

Bugmann, Marlen
PSI
Villigen, Switzerland

— C —

Cameron, Peter
BNL
Upton, USA

Carmichael, Linden
Fermilab
Batavia, USA

Carmona, José Miguel
CIEMAT
Madrid, Spain

Carwardine, John
ANL
Argonne, USA

Cassinari, Lodovico
SOLEIL
Gif-sur-Yvette, France

Catin, Madeleine
CERN
Geneva, Switzerland

Cerne, Robert
i-tech
Solkan, Slovenia

Chen, Yongzhong
SINAP
Shanghai, China

Cheymol, Benjamin
CERN
Geneva, Switzerland

Chiadroni, Enrica
INFN/LNF
Frascati, Italy

Chrin, Jan
PSI
Villigen, Switzerland

Citterio, Alessandro
PSI
Villigen, Switzerland

Le Coz, William
GANIL
Caen, France

Craievich, Paolo
ELETTRA
Trieste, Italy

Crisp, James
Fermilab
Batavia, USA

Cultrera, Luca
INFN/LNF
Frascati, Italy

— D —

Dabrowski, Anne
CERN
Geneva, France

Dedič, Jože
Cosylab
Ljubljana, Slovenia

Dehler, Micha
PSI
Villigen, Switzerland

Dehning, Bernd
CERN
Geneva, Switzerland

Denard, Jean-Claude
SOLEIL
Gif-sur-Yvette, France

Dietrich, Jürgen
FZJ
Jülich, Germany

Duperrex, Pierre-Andre
PSI
Villigen, Switzerland

Duraffourg, Michel
CERN
Geneva, Switzerland

Dölling, Rudolf
PSI
Villigen, Switzerland

— E —

Effinger, Ewald
CERN
Geneva, Switzerland

Egberts, Jan
MPI-K
Heidelberg, Germany

Emery, Jonathan
CERN
Geneva, Switzerland

Ewald, Friederike
ESRF
Grenoble, France

— F —

Falkenstern, Fjodor
BESSY
Berlin, Germany

Ferianis, Mario
ELETTRA
Trieste, Italy

Fisher, Alan
SLAC
Menlo Park, USA

Focker, Gerrit Jan
CERN
Geneva, Switzerland

Forck, Peter
GSI
Darmstadt, Germany

Fourie, Dirk
iThemba LABS
Somerset West, South Africa

— G —

Gabor, Christoph
STFC/RAL/ASTeC
Chilton, UK

García-Garrigós, Juan
IFIC
Valencia, Spain

van Garderen, Elsa
ASCo
Clayton, Australia

Garvey, Terence
PSI
Villigen, Switzerland

Gassner, David
BNL
Upton, USA

Geloni, Gianluca
DESY
Hamburg, Germany

Gerth, Christopher
DESY
Hamburg, Germany

Gonzalez, Jose
CERN
Geneva, Switzerland

Grabosch, Hans-Jürgen
DESY
Hamburg, Germany

Grewe, Marc
ACCEL
Bergisch Gladbach, Germany

Guéroult, Eloise
GANIL
Caen, France

Gütlich, Eiko
GSI
Darmstadt, Germany

— H —

Hagmann, Mark
NewPath
Salt Lake City, USA

Hamdi, Abdallah
CEA
Gif-sur-Yvette, France

Handschin, Thomas
Agilent
Basel, Switzerland

Harasimowicz, Janusz
University Liverpool
Liverpool, UK

Haseitl, Rainer
GSI
Darmstadt, Germany

Holzer, Bernhard
CERN
Geneva, Switzerland

Hubert, Nicolas
SOLEIL
Gif-sur-Yvette, France

Hunziker, Stephan
PSI
Villigen, Switzerland

— I —

Ikeda, Hitomi
KEK
Tsukuba, Japan

Intermite, Angela
MPI-K
Heidelberg, Germany

Iriso, Ubaldo
CELLS-ALBA
Cerdanyola del Vallès, Spain

Ischebeck, Rasmus
PSI
Villigen, Switzerland

Ispiryan, Karo
YerPhI
Yerevan, Armenia

Itoga, Toshiro
RIKEN/SPring-8
Hyogo, Japan

— J —

Jamet, Christophe
GANIL
Caen, France

Jamison, Steven
STFC/DL/ASTeC
Daresbury, UK

Jenny, Marcel
Agilent
Basel, Switzerland

Johnson, Ronald
SLAC
Menlo Park, USA

Jolly, Simon
Blackett Laborabory
London, UK

Jones, Owain
CERN
Geneva, Switzerland

— K —

Kalinin, Alexander
STFC/DL/ASTeC
Daresbury, UK

Kamerdzhiev, Vsevolod
FZJ
Jülich, Germany

Kaya, Caglar
FZD
Dresden, Germany

Keil, Boris
PSI
Villigen, Switzerland

Kim, Yujong
PSI
Villigen, Switzerland

Körfer, Markus
DESY
Hamburg, Germany

Koshelev, Andrey
IHEP
Protvino, Russia

Kowina, Piotr
GSI
Darmstadt, Germany

Krouptchenkov, Igor
DESY
Hamburg, Germany

Kube, Gero
DESY
Hamburg, Germany

Kuo, Changhor
NSRRC
Hsinchu, Taiwan

Kyberd, Paul
Brunel University
Uxbridge, UK

Källberg, Anders
MSL
Stockholm, Sweden

— L —

Laux, Felix
MPI-K
Heidelberg, Germany

Leban, Peter
i-tech
Solkan, Slovenia

Leng, Yongbin
SINAP
Shanghai, China

Lensch, Timmy
DESY
Hamburg, Germany

Letourneur, Stéphane
LAL
Orsay, France

Lipka, Dirk
DESY
Hamburg, Germany

Lokhovitskiy, Arkady
CERN
Geneva, Switzerland

Lund-Nielsen, Jorgen
DESY
Hamburg, Germany

— M —

Maesaka, Hirokazu
RIKEN/SPring-8
Hyogo, Japan

Mao, Ruishi
IMP
Lanzhou, China

de Maria, Riccardo
CERN
Geneva, Switzerland

Marinkovic, Goran
PSI
Villigen, Switzerland

Marroncle, Jacques
CEA
Gif-sur-Yvette, France

Marx, Michaela
DESY
Hamburg, Germany

Mazzitelli, Giovanni
INFN/LNF
Frascati, Italy

Mete, Oznur
EPFL
Lausanne, Switzerland

Metzger, Marius
Hamamatsu Photonics
Basel, Switzerland

Milosic, Timo
GSI
Darmstadt, Germany

De Monte, Raffaele
ELETTRA
Trieste, Italy

Morgan, Alun
Diamond
Chilton, UK

Mostert, Hendrik
iThemba LABS
Somerset West, South Africa

Müller, Felix
PSI
Villigen, Switzerland

— N —

Nielsen, Jørgen
ISA
Aarhus, Denmark

Nölle, Dirk
DESY
Hamburg, Germany

— O —

Obina, Takashi
KEK
Tsukuba, Japan

Odier, Patrick
CERN
Geneva, Switzerland

Oevermann, Christel
DESY
Hamburg, Germany

Olvegård, Maja
CERN
Geneva, Switzerland

Oswald, Benedikt
PSI
Villigen, Switzerland

— P —

Payne, Stephen
STFC/RAL/ISIS
Chilton, UK

Peréz, Francis
CELLS-ALBA
Cerdanyola del Vallès, Spain

Pertica, Alex
STFC/RAL/ISIS
Chilton, UK

Peschel, Marc
ACCEL
Bergisch Gladbach, Germany

Peters, Andreas
HIT
Heidelberg, Germany

Pleško, Mark
Cosylab
Ljubljana, Slovenia

Plouviez, Eric
ESRF
Grenoble, France

Podadera Aliseda, Ivan
CIEMAT
Madrid, Spain

Pollet, Patrick
PSI
Villigen, Switzerland

Poucki, Vladimir
i-tech
Solkan, Slovenia

Putignano, Massimiliano
KIP
Heidelberg, Germany

— R —

Raich, Uli
CERN
Geneva, Switzerland

Rauch, Udo
GSI
Darmstadt, Germany

Reggiani, Davide
PSI
Villigen, Switzerland

Rehm, Günther
Diamond
Chilton, UK

Rimjaem, Sakhorn
DESY
Hamburg, Germany

Ripert, Marion
HIT
Heidelberg, Germany

Roberti, Cristiana
ELETTRA
Trieste, Italy

Roggo, Martin
LeCroy
Meyrin, Switzerland

Ruber, Roger
Uppsala University
Uppsala, Sweden

Ruf, Marcel
Uni Erlangen-Nürnberg
Erlangen-Nürnberg, Germany

— S —

Sachwitz, Martin
DESY
Hamburg, Germany

Sannibale, Fernando
LBNL
Berkeley, USA

Schaa, Volker RW
GSI
Darmstadt, Germany

Scheidt, Kees
ESRF
Grenoble, France

Schilcher, Thomas
PSI
Villigen, Switzerland

Schippers, Marco
PSI
Villigen, Switzerland

Schlott, Volker
PSI
Villigen, Switzerland

Schmidt-Föhre, Frank
DESY
Hamburg, Germany

Schudel, Erwin
Linktronix
Thalwil, Switzerland

Schünemann, Gerrit
DELTA
Dortmund, Germany

Schwickert, Marcus
GSI
Darmstadt, Germany

Senée, Franck
CEA
Gif-sur-Yvette, France

Serio, Mario
INFN/LNF
Frascati, Italy

Sexton, Daniel
JLAB
Newport News, USA

Shea, Thomas
ORNL
Oak Ridge, USA

Sieber, Thomas
MPI-K
Heidelberg, Germany

Singh, Om
BNL
Upton, USA

Smale, Nigel
FZ Karlsruhe
Karlsruhe, Germany

Smith, Stephen
SLAC
Menlo Park, USA

Stadler, Markus
PSI
Villigen, Switzerland

Steffen, Bernd
PSI
Villigen, Switzerland

Stella, Angelo
INFN/LNF
Frascati, Italy

Storch, Martin
Linktronix
Thalwil, Switzerland

Streun, Andreas
PSI
Villigen, Switzerland

Summ, Patrick
Optronis GmbH
Kehl, Germany

— T —

Teytelman, Dmitry
Dimtel
San Jose, USA

Thomas, Cyrille
Diamond
Chilton, UK

Thomsen, Knud
PSI
Villigen, Switzerland

Tinta, Dejan
i-tech
Solkan, Slovenia

Toader, Ovidiu
NERS-UM
Ann Arbor, USA

Towalski, Patryk
DELTA
Dortmund, Germany

Toyoda, Akihisa
KEK
Tsukuba, Japan

Treyer, Daniel
PSI
Villigen, Switzerland

— U —

Unser, Klaus

Prevessin, France

— V —

Verguilov, Vassil
DPNC
Geneva, Switzerland

Verzilov, Victor
TRIUMF
Vancouver, Canada

Vignet, Jean-Luc
GANIL
Caen, France

Vock, Cecile
PSI
Villigen, Switzerland

— W —

Wacker, Gerald
Roschi Rohde & Schwarz
Ittigen, Switzerland

Warner, Arden
Fermilab
Batavia, USA

Weeks, Allen
i-tech
Solkan, Slovenia

Wehrli, Thomas
PSI
Villigen, Switzerland

Weinert, Klaus
MEN
Nürnberg, Germany

Weis, Thomas
DELTA
Dortmund, Germany

Weissman, Leonid
Soreq NRC
Yavne, Israel

Wendt, Manfred
Fermilab
Batavia, USA

Werner, Matthias
DESY
Hamburg, Germany

Whitehead, Sarah
STFC/RAL/ISIS
Chilton, UK

Wittenburg, Kay
DESY
Hamburg, Germany

Wu, Junxia
IMP
Lanzhou, China

Wulf, Friedrich
BESSY
Berlin, Germany

— Y —

Ye, Kairong
SSRF
Shanghai, China

Yoon, Phil
BNL
Upton, USA

— Z —

Zamantzas, Christos
CERN
Geneva, Switzerland

Ziemann, Volker
Uppsala University
Uppsala, Sweden

DIPAC 2009 Sponsors





bergoz
Instrumentation

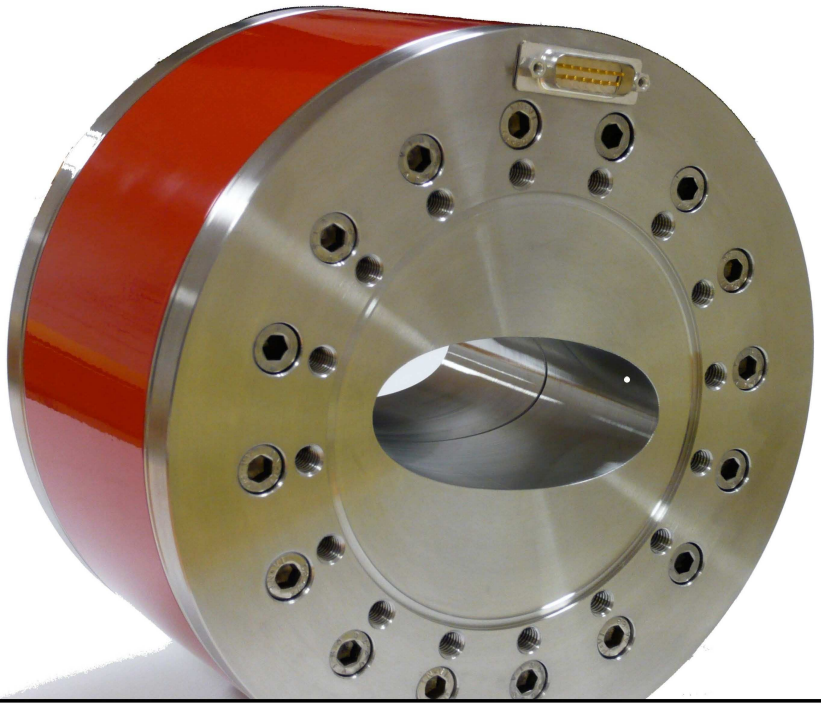
Presents...

In-flange DC current monitor for
Synchrotron
Low emittance beam
CW source
ERL

Resolution < 500 nA
Matched pairs

Saves space:
120 mm axial length
UHV

HOM tested on SPEAR3
storage ring
500 mA 20ps MB beam




Instrumentation Technologies
When your users demand stability. www.i-tech.si
Many instruments. Many people. Working together.
Stability means knowing your machine has innovative solutions. For users, stability means a machine achieving its full potential, enabling them to do more science. For us, stability means synchronized, connected, dynamic state-of-the-art instrumentation, working together as one system.
Because we know that the machine is more than just the sum of its parts.
Libera

How many of your control system projects did you really finish on time and on budget?

How many had the scope, time and budget defined at all?

How often did you write up the documentation?

Over 30 labs use Cosylab, the specialized control system integrator for accelerators



Our teams of 35 engineers and physicists provides professional execution of:

EPICS, TANGO, LabView, TINE, FESA, PVSS-2, ACS

Operator Screens and Displays

On-site Contractual Work and Courses

Requirements Gathering and Specifications

Project Management and Turn Key Solutions

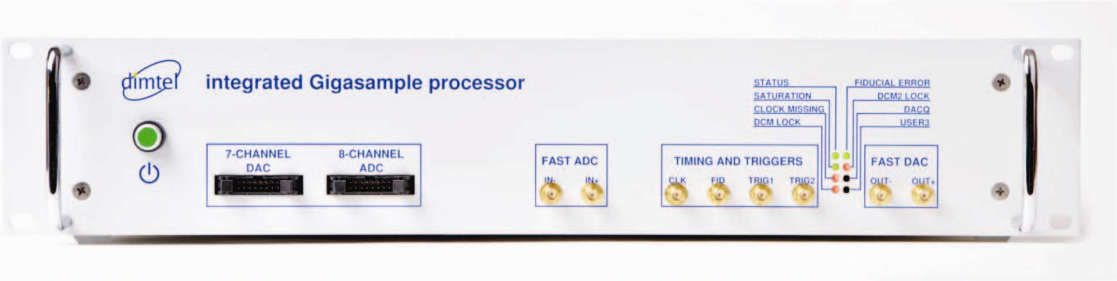
Custom Software and Electronics Development

Integration and Installation of Devices and Instrumentation

our passion: to deliver high quality and be respected for that

Analog and Digital Signal Processing for Particle Accelerators

Integrated Gigasample Processor (iGp)



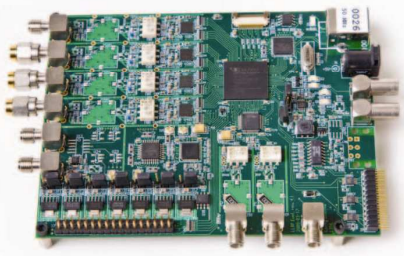
- 500+ MHz processing channel.
- 16-tap bunch-by-bunch FIR filtering for feedback.
- Support for any harmonic number.
- Control and diagnostics via EPICS.
- High-speed external triggers, fiducial synchronization.
- Low-speed ADCs/DACs, general-purpose digital I/O.

Front and Back End (FBE)

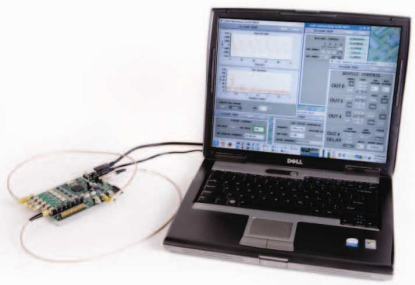


- 1.5 GHz front-end detection frequency.
- Two-cycle comb generator.
- 1-1.5 GHz back-end frequency.
- Integrated EPICS controls through iGp.
- Adjustable elements: front and back-end LO phase shifters; front and back-end attenuators.

Low-Level RF Board



- Four 14-bit 125 MSPS ADCs
- Two 14-bit 260 MSPS DACs.
- FPGA signal processing.
- RF down- and up-conversion chains.
- Can also be configured for IF processing.
- USB is used for control and diagnostic interface.
- EPICS support.



Our clients:

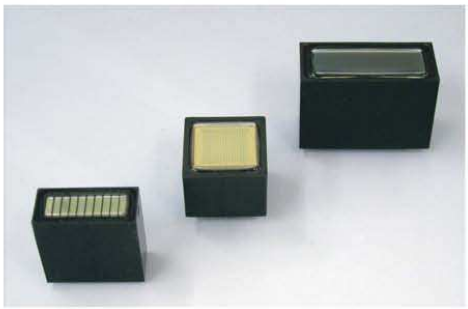
- BEPC-II, IHEP, China
- CESR-TA, Cornell University, USA
- The Cockroft Institute, UK
- Duke University FEL Laboratory, USA
- KEK, Japan
- LBNL, USA
- LNF-INFN, Italy
- NSRRC, Taiwan

Dimtel, Inc. 2059 Camden Avenue, Suite 136, San Jose, CA 95124
Phone: +1 650 862 8147 • Fax: +1 603 907 0210 • E-mail: info@dimtel.com

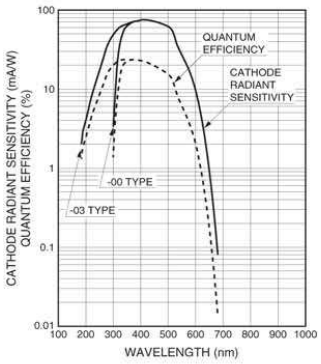
LINEAR ARRAY MULTIANODE PMT SERIES
H9530, H10515, H7260

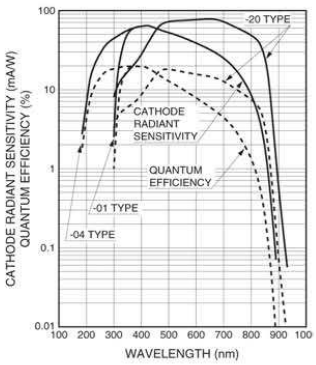
Applications

- Beam Diagnostic
- Biomedical fluorescence detection
  (Cell sorter / Cell analyzer / MTP reader /
  DNA analytical instrument)
- Laser scanning micsorscopy
- Spectroscopy
- Environmental monitoring

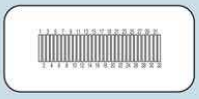


Spectral response





Selection guide of linear array multianode PMT module / assembly

Anode Type	8 ch			16 ch		32 ch	
							
Type No.	H9530	NEW H9530M	Devlp. H9530G	Devlp. H10515	Devlp. H10515M	H7260	Devlp. H7260M
PMT	●	●	●	●	●	●	●
Divider Circuit	●	●	●	●	●	●	●
Pre Amplifier		●	●		●		●
High Voltage Power Supply		●	●		●		●
Gain Control Function			●				

HAMAMATSU

PHOTON IS OUR BUSINESS

www.hamamatsu.ch

World's Fastest Real-Time Oscilloscope



30 GHz
Bandwidth

80 GS/s
Sample Rate

512 Mpts
Analysis Memory

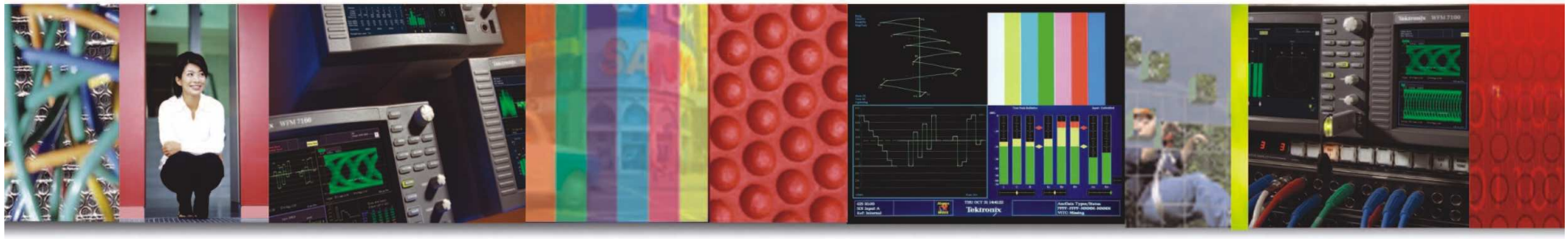
The new oscilloscope experience is now available from 4 to 30 GHz of bandwidth.

The WaveMaster 8 Zi series of oscilloscopes provides industry leading performance, advanced Eye Doctor™ signal integrity tools and superior serial data analysis. X-Stream II architecture provides 10 to 100 times faster processing, and instantaneous responsiveness leverages the deepest toolbox in the industry. Bandwidth upgrade capability through the full range of 4 to 30 GHz models affords outstanding investment protection.

www.lecroy.com/europe

LeCroy

INNOVATION



Tektronix

Generalvertretung Schweiz: linktronix

Visit us in the Foyer at Hotel Mercure

www.linktronix.ch

Rugged and Powerful VMEbus SBC A20

for Harsh and Communication Intensive Applications



The Atlas Experiment at CERN, http://atlas.ch

- Intel® Core™ 2 Duo down to Celeron® M
- 2eSST VMEbus master and slave
- 2 PMC or XMC slots
- Six PCI Express® lanes
- 1 VGA, 1 Gb Ethernet and 1 USB at the front
- Up to 4 GB DDR2 DRAM soldered-on

MEN Mikro Elektronik GmbH
Klaus Weinert, Channel Manager
Phone +49-911-99 33 5-163
Fax +49-911-99 33 5-901
E-Mail Klaus.Weinert@men.de
www.men.de

MagentaSys
Sylvain Bruderer
Phone +41-22-366-33-33
Fax +41-22-366-33-16
E-mail Sylvain.bruderer@magentasys.com
www.magentasys.com

men®
mikro elektronik
gmbh • nürnberg

Freedom in magnetic measurement

Take this magnetometer anywhere!
Get easy 3-axis measurements – up to 20 T, with an accuracy of ±1%. Almost reduced to its cable, the THM1176 is the world's most compact magnetometer. A revolutionary integrated sensor provides access to very small gaps.

Plug the USB connector either into your PC or into the optional PDA and start collecting your data.
Display the results numerically or graphically.
Modify the software as you want – the source code is provided.
In a word: freedom in magnetic measurement.

THM1176: the only handheld 3-axis Hall magnetometer





www.metrolab.com

METROlab
Magnetic precision has a name

Optronis

Make time visible

OPTOSCOPE-SC



Streak Camera Family

Streak Cameras with modular design

for analysis of ultrafast optical signals

- **down to 2 ps Temporal Resolution**
- **up to 250 MHz Synchroscan Operation**
- **up to 4 MHz Triggered Operation**
- **Modular and flexible design**
- **Perpendicular Sweep**
- **Ethernet interface**

Optronis

Honsellstr. 8

77694 Kehl, Germany

E-Mail: info@optronis.com

www.optronis.com

1000 Sweeps/s, 40 MHz Bandbreite, Touchscreen

Weltneuheit!
Noch schneller als der bisher schnellste!

Signalanalysator R&S®FSV –
die neue Referenz in der Mittelklasse

Der R&S®FSV ist schneller, breitbandiger, genauer und bedienfreundlicher als alles, was Sie sonst in dieser Preisklasse bekommen können:

- Schnellster Signalanalysator auf dem Markt mit bis zu 1000 Sweeps/s im Fernsteuerbetrieb
- 40 MHz Analysebandbreite – für alle Breitbandtechnologien wie WLAN 802.11n, LTE und WiMAX sowie allgemeine OFDM-Signale
- Intuitive Bedienung über Touchscreen und Bedienfeld
- Höchste Pegelgenauigkeit: Messunsicherheit <0,4 dB bis 7 GHz
- Sehr gute HF-Performance
- Umfangreiche Leistungsmessfunktionen, Wechselfestplatte, GBit-LAN-Schnittstelle, einfache Hardware-Nachrüstung



www.roschi.rohde-schwarz.ch

Rohde & Schwarz –
The Driving Force in Spectrum Analysis

ROHDE&SCHWARZ
ROSCHI ROHDE & SCHWARZ AG

MANAGEMENTSYSTEM ISO 9001 / 14001 SQS 097 star

Arbeitsgebiete Messtechnik

Allgemeine Messtechnik
ROHDE&SCHWARZ
HAMEG Instruments
FLUKE
TOMCO
NF

EMV Messtechnik
ROHDE&SCHWARZ
BONN Elektronik
LANGER
HAEFELY TECHNOLOGY
OPHIR

AC/DC Quellen und Lasten
ROHDE&SCHWARZ
HAMEG Instruments
xantrex
Sorensen
TOELLNER
ELGAR

Optische Messtechnik
ADVANTEST

Board-Tester
ROHDE&SCHWARZ
PRÜFTECHNIK Schneider & Koch

Physik und Elektrochemie
AMETEK
Princeton Applied Research
SIGNAL RECOVERY
solartron analytical

Broadcast und Mobilfunk
ROHDE&SCHWARZ

Software & Services
KOCH IT AG

Laboreinrichtungen
hera

Ausbildungssysteme
Horstmann

Unser Instandhaltungskonzept
- Herstellerunabhängig
- Akkreditiertes Kalibrierlabor
- Online Instandhaltungsmanagement